Science Advances

9 JUNE 2023

AAAS

SOCIAL SCIENCES

Global impacts of extractive and industrial development projects on Indigenous Peoples' lifeways, lands, and rights

Arnim Scheidel[1], Álvaro Fernández-Llamazares[2,1]*, Anju Helen Bara[3], Daniela Del Bene[1], Dominique M. David-Chavez[4], Eleonora Fanari[1], Ibrahim Garba[5], Ksenija Hanaˇek[1,6], Juan Liu[7,1], Joan Martínez-Alier[1], Grettel Navas[8], Victoria Reyes-García[1,9], Brototi Roy[1,10], Leah Temper[11], May Aye Thiri[1], Dalena Tran[1], Mariana Walter[1], Kyle Powys Whyte[12]

To what extent do extractive and industrial development pressures affect Indigenous Peoples' lifeways, lands, and rights globally? We analyze 3081 environmental conflicts over development projects to quantify Indigenous Peoples' exposure to 11 reported social-environmental impacts jeopardizing the United Nations Declaration on the Rights of Indigenous Peoples. Indigenous Peoples are affected in at least 34% of all documented environmental conflicts worldwide. More than three-fourths of these conflicts are caused by mining, fossil fuels, dam projects, and the agriculture, forestry, fisheries, and livestock (AFFL) sector. Landscape loss (56% of cases), livelihood loss (52%), and land dispossession (50%) are reported to occur globally most often and are significantly more frequent in the AFFL sector. The resulting burdens jeopardize Indigenous rights and impede the realization of global environmental justice.

INTRODUCTION

Indigenous leaders, scholars, and knowledge holders have long highlighted how their stewardship practices offer key solutions to maintain biodiversity, mitigate climate change, and engender positive social change more broadly (*1*–*3*). One of the ways in which Indigenous Peoples achieve these stewardship roles is by protecting their territories from extractive and industrial development pressures (*3*–*6*).

Although Indigenous Peoples have contested land encroachment and oppression from the advent of colonialism to the present (*7*–*9*), many continue to be severely affected by development projects causing environmental conflicts worldwide (*10*–*13*). Such social conflicts over extractive and industrial projects and their adverse social-environmental burdens occur despite numerous efforts to recognize and enforce Indigenous rights, including through national legislations and global policy instruments like the International Labor Organization's (ILO) Convention 169 and the United Nations Declaration on the Rights of Indigenous Peoples (UNDRIP) (*14*, *15*).

In environmental conflicts, Indigenous Peoples face severe impacts, such as livelihood loss and land dispossession (*16*), environmental pollution (*17*, *18*), threats to their knowledge systems (*19*), racial- and gender-based violence (*20*–*23*), as well as intimidations and assassinations (*12*, *24*). Global reports about Indigenous rights violations have provided extensive qualitative evidence about such impacts, for instance, by compiling local testimonies, oral histories, and in-depth narratives from diverse case studies (*25*). Except for recent analyses on direct violence and killings affecting Indigenous Peoples in environmental conflicts (*10*, *26*), such global studies have left unanswered questions about the frequency of occurrence of the social-environmental impacts that conflictive development projects put on Indigenous Peoples' lifeways, lands, and rights worldwide.

To address this knowledge gap, we present here the largest quantitative analysis of reported social-environmental burdens that Indigenous Peoples bear in environmental conflicts worldwide. We quantify the extent to which Indigenous groups are affected by conflictive extractive and industrial development projects and provide extensive data on their exposure to a range of associated social-environmental impacts. Our results provide large-scale evidence of the magnitude of environmental burdens faced by numerous Indigenous Peoples worldwide and bring into focus the Indigenous rights violations associated with these burdens.

Methodologically, we build upon comparative and statistical approaches in political ecology aiming to reveal trends and patterns of environmental conflict characteristics in a more systematic way (*10*, *27*). Theoretically, our analysis is grounded in scholarship approaching environmental justice from the perspectives of Indigenous communities (*28*, *29*), showing that global environmental injustice is a structural undercurrent for many of the challenges faced by contemporary Indigenous Peoples (*29*–*32*). We share the views from Indigenous intellectual traditions where knowledge is understood as being fundamentally interwoven with practice and ethics (*1*, *33*–*35*). Largely drawing from these perspectives and following calls for the use of quantitative research approaches to

[1]Institut de Ciència i Tecnologia Ambientals (ICTA-UAB), Universitat Autònoma de Barcelona, Barcelona, Spain. [2]Helsinki Institute of Sustainability Science (HELSUS), Faculty of Biological and Environmental Sciences, University of Helsinki, Helsinki, Finland. [3]Department of Development Studies, Central University of South Bihar, Gaya, India. [4]Department of Forest and Rangeland Stewardship, Colorado State University, Fort Collins, CO, USA. [5]Native Nations Institute, University of Arizona, Tucson, AZ, USA. [6]Faculty of Social Sciences, Global Development Studies, University of Helsinki, Helsinki, Finland. [7]College of Humanities and Development Studies, China Agricultural University, Beijing, PR China. [8]Facultad de Gobierno, Universidad de Chile, Santiago, Chile. [9]Institució Catalana de Recerca i Estudis Avançats (ICREA), Barcelona, Spain. [10]Department of Environmental Science and Policy, Central European University, Vienna, Austria. [11]Department of Natural Resource Sciences, McGill University, Montreal, QC, Canada. [12]School for Environment and Sustainability, University of Michigan, Ann Arbor, MI, USA.
*Corresponding author. Email: alvaro.fernandez-llamazares@helsinki.fi

inform policy concerned with Indigenous issues (*36*, *37*), we discuss the implications of our results for upholding Indigenous Peoples' rights and enhancing environmental justice, broadly understood here as the advancement toward the eradication of adverse social-environmental burdens compromising peoples' lifeways, lands, and rights.

Our analysis draws on the most comprehensive dataset available: 3081 environmental conflict cases, documented through the global Environmental Justice Atlas (EJAtlas) (data S1), which we collected through a crowdsourced and collaborative data collection process (*38*). Scholars have previously used selected EJAtlas data for diverse thematic, sectoral, and country-wide analyses of environmental conflicts [e.g., (*21*, *38*, *39*)] and for global characterizations of environmental conflicts and determinants of the occurrence of direct violence (*10*, *27*). This study examines the global EJAtlas dataset thoroughly from the lens of Indigeneity and through the consideration of a wide range of social-ecological impacts beyond direct violence. For this purpose, we identify through an extensive review process the names of the specific Indigenous groups involved in conflicts (see Supplementary Text) and combine the EJAtlas dataset with data on the spatial extent of Indigenous Peoples' lands (*40*) and data on the status of the languages spoken by the affected Indigenous groups (*41*, *42*). On this basis, we show the global overlap of conflictive extractive and industrial development projects with Indigenous Peoples' lands, describe the specific Indigenous groups most frequently affected in our dataset, and identify threats to Indigenous language use.

We assess the reported frequency of 11 adverse impacts globally and across six sectors and discuss their implications for environmental justice and Indigenous rights as recognized in UNDRIP.

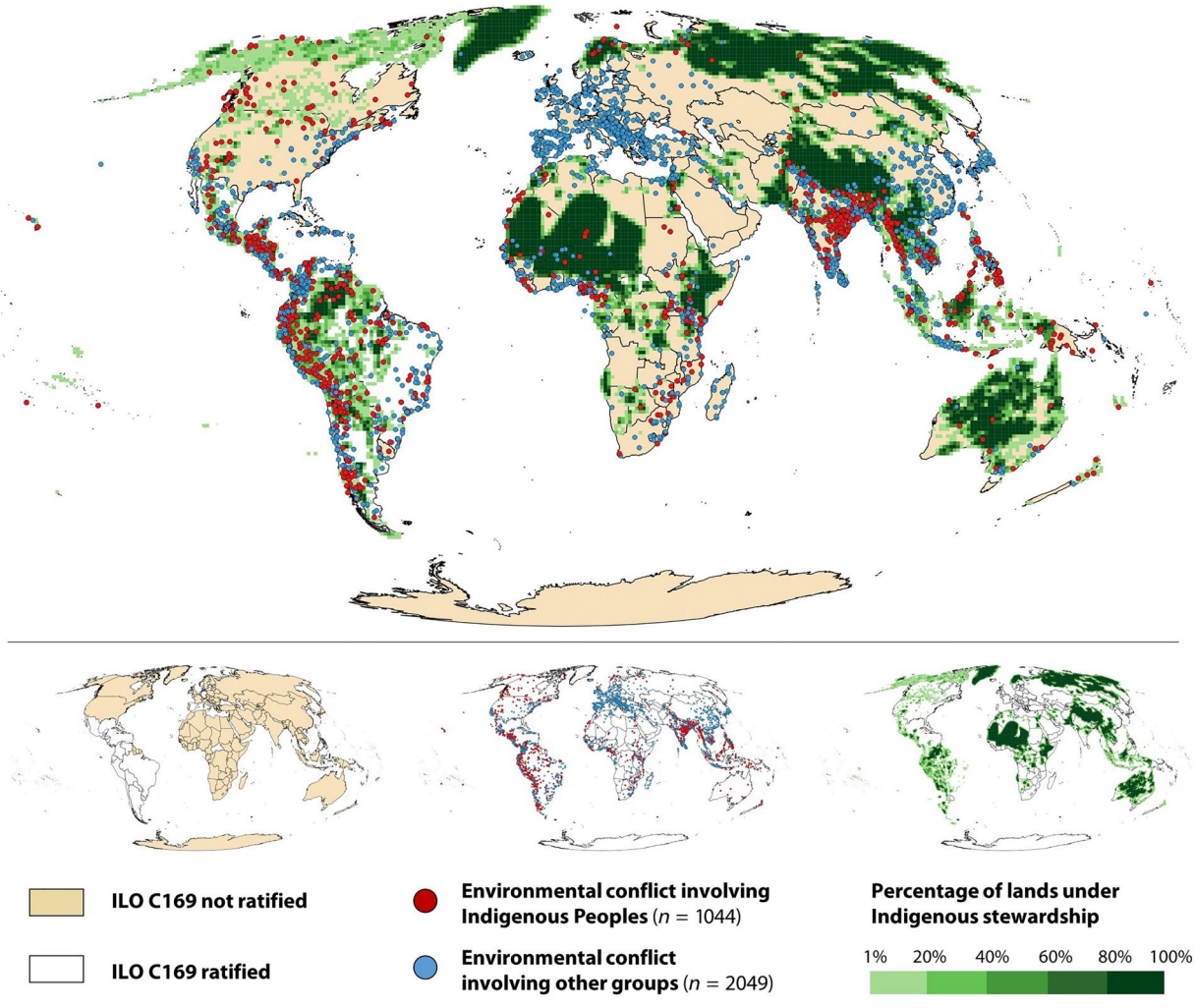

Fig. 1. Map of environmental conflicts involving Indigenous Peoples and other groups (*n* = 3081), ILO C169 signatory countries, and Indigenous Peoples' lands. The resolution is by necessity imprecise, as boundaries between Indigenous and other lands are often under dispute. Unmapped areas do not necessarily indicate an absence of Indigenous Peoples or an absence of conflicts, but areas for which an Indigenous connection cannot be inferred on the basis of publicly available geospatial data or no conflict data are available (*40*). A total of 95% of the environmental conflicts involving Indigenous Peoples began during or after the 1970s, while more than 50% of cases began between 2007 and 2020. Note that social-environmental impacts occurring in environmental conflicts have long-term effects that compromise Indigenous Peoples' lifeways well beyond the year when the conflict started. ILO C169 signatory countries are provided in table S3. UNDRIP was adopted in 2007 in the General Assembly by a majority of 144 states (table S4).

The assessed impacts include (i) livelihood loss, (ii) land dispossession, (iii) displacement, (iv) traditional knowledge loss, (v) landscape loss, (vi) militarization, (vii) impacts on women, (viii) deforestation, (ix) biodiversity loss, (x) water degradation, and (xi) soil degradation. The assessed sectors include (i) mining; (ii) fossil fuels; (iii) dams; (iv) the agriculture, forestry, fisheries, and livestock (AFFL) sector; (v) industries and other infrastructures, and (vi) other sectors (see Materials and Methods and tables S1 and S2 for definitions).

We acknowledge that the range of impacts analyzed here is necessarily incomplete and that crowdsourced convenience samples, such as the one analyzed here, have inherent data limitations arising from potential sample selection and reporting biases (see Materials and Methods for a detailed discussion). However, for global social-ecological phenomena for which the total population of cases is unknown and where access to information is constrained, the use of such datasets is often the only available alternative to advance our understanding of their patterns of occurrence. In this context, our study provides the largest global quantitative assessment of reported adverse social-environmental impacts to which Indigenous Peoples have been exposed in conflictive development projects. The findings are relevant to enhance current knowledge about the extent to which extractive and industrial development pressures affect Indigenous Peoples' lifeways, lands, and rights globally and can inform current policy efforts to uphold Indigenous Peoples' rights enshrined in UNDRIP.

RESULTS

Indigenous Peoples comprise about 6.2% of the world's population (*43*) and steward about a quarter of the world's terrestrial surface (Fig. 1) (*40*). According to our dataset, they are involved in at least 34% of documented environmental conflicts over extractive and industrial development projects (Fig. 2). This finding converges with evidence derived from other datasets, which shows that Indigenous Peoples often find themselves on the frontlines of industrial-extractive expansion (*11*, *26*). Most countries where conflicts occur endorse UNDRIP (table S4). However, only 24 countries have ratified the legally binding ILO C169 convention (Fig. 1 and table S3).

In the 1044 environmental conflicts involving Indigenous Peoples (data S2), we find at least 740 distinct Indigenous groups affected, representing at least 15% of the approximately 5000 Indigenous groups known worldwide. The Quechua (51 conflicts), Mapuche (31), Gond (30), Aymara (20), Nahua (20), Ijaw (20), Munda (19), Kichwa (19), Guaraní (18), and Karen (18) are the 10 Indigenous groups more frequently featured in the EJAtlas dataset. Substantial data gaps remain, particularly for Central Asia, Russia, and the Pacific (data S3). The actual number of affected Indigenous groups is expected to be much higher, particularly when considering that some regions have limited data coverage. Furthermore, an additional 7% of conflict cases involve other non-Indigenous place-based communities with long-term connections to their lands, including most prominently Quilombolas (35 conflicts) and other Afrodescendant communities (29).

The social-environmental impacts faced by many Indigenous Peoples in conflictive extractive and industrial development projects, as well as their long-term effects on livelihoods, lands and well-being, undermine the fulfillment of UNDRIP. Our results show the frequency of reported impacts at the global level and across sectors (Fig. 3; see Materials and Methods for a discussion of data limitations). Loss of landscape is reported most often in our dataset, with a global frequency of 56% of all cases, jeopardizing specifically UNDRIP article 25 on the right to maintain Indigenous spiritual relations with their traditionally used territories. Livelihood loss and land dispossession are reported globally in 52 and 50% of all cases, respectively. These impacts raise concerns over the fulfillment of UNDRIP articles 20 and 21, both addressing the rights to maintain, secure, and improve their economic and social systems and conditions, as well as article 26 on the right to exercise control over their lands, territories, and resources.

Other frequently reported impacts include deforestation (43%), biodiversity loss (43%), water degradation (40%), and soil degradation (31%), which severely compromise UNDRIP article 29 on the right to the protection and conservation of their environment and the productive capacities of their territories. In addition, displacement (43%) threatens article 10 protecting Indigenous Peoples from relocation without free, prior, and informed consent. Knowledge loss (43%) jeopardizes their right to maintain and protect their traditional knowledge (article 31); militarization (32%) provokes social and political concerns over the unrightful presence of armed forces in Indigenous territories (article 30); while specific impacts on women (20%) compromise the fulfillment of their special needs enshrined in UNDRIP article 22.

Extractive and industrial development also threatens Indigenous linguistic diversity (*44*). While environmental injustice puts stressors on all Indigenous languages, groups with smaller speaker populations are often less resilient to external pressures (*44*, *45*). A total of 45.7% of the Indigenous groups affected by environmental conflicts over development projects speak languages that are critically pressured (Fig. 2; see Materials and Methods for data sources and limitations). Threats to Indigenous language use and the different contexts of language awakening are generally concomitant to broader cultural pressures that undermine UNDRIP article 13.

According to our dataset, four sectors account for more than three-quarters of all environmental conflicts involving Indigenous Peoples: mining (24.7%), fossil fuels (20.8%), the AFFL sector (17.5%), and dams (15.2%) (Fig. 2). While the mining sector is implicated in the highest number of conflicts involving Indigenous Peoples (n = 258), the AFFL sector is associated with an alarmingly high frequency of reported impacts (Fig. 3). Specifically, deforestation (74% of cases), land dispossession (74%), livelihood loss (69%), and biodiversity loss (69%) are reported to occur significantly more frequently in the AFFL sector, compared to other sectors and the global average (table S5).

These impacts produce severe social-environmental burdens on Indigenous communities across all inhabited continents (Fig. 1) and pose a major barrier to advancing environmental justice and Indigenous rights globally. Our results highlight that efforts toward achieving zero tolerance of Indigenous rights violations (*46*) are urgently needed.

DISCUSSION

Our findings provide quantitative evidence of the breadth and depth of environmental injustices that many Indigenous Peoples face globally. Indigenous Peoples' lands intersect some of the world's most unexploited natural areas (*40*, *47*, *48*), which have been a target for extractive and industrial development and a

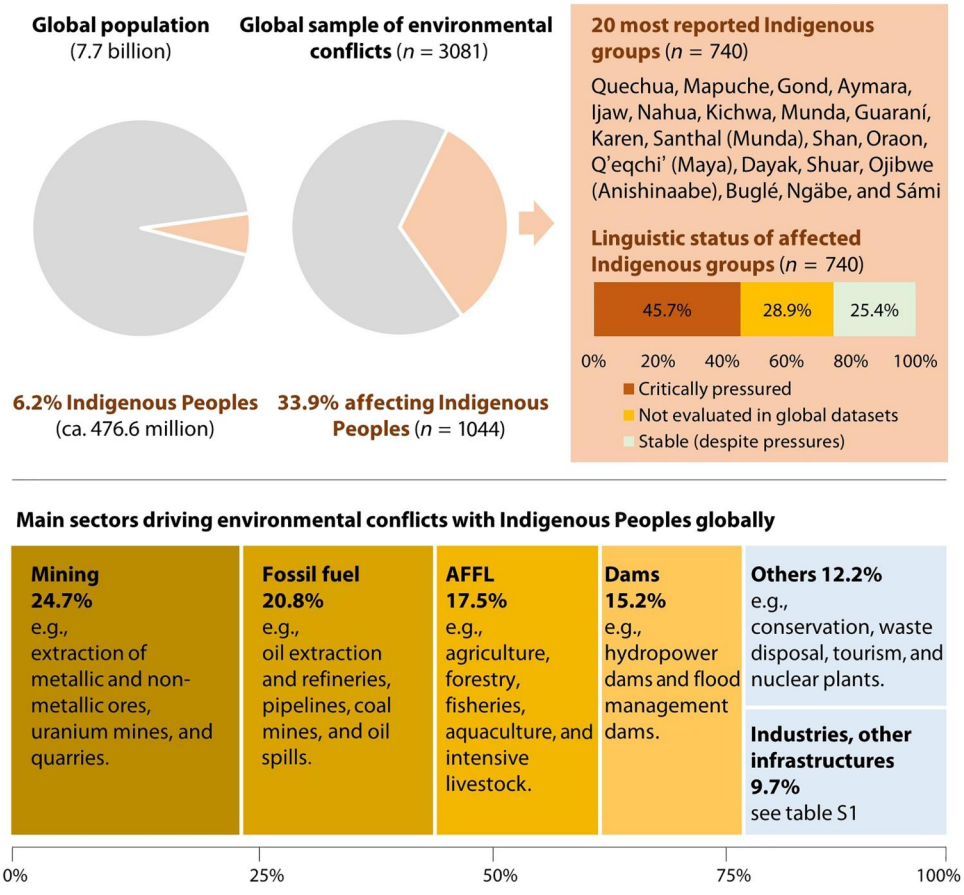

Fig. 2. Overview of environmental conflicts involving Indigenous Peoples. (**Top**) Left: Environmental conflicts involving Indigenous Peoples compared to the share of the Indigenous population of the world population. Right: Most reported Indigenous groups affected by environmental conflicts and their linguistic situation. (**Bottom**) Sectors causing environmental conflicts with Indigenous Peoples globally. Sectoral definitions and examples are provided in table S1. Population estimates refer to 2019 (*43*).

breeding ground for environmental conflicts from colonialism to the present (*7*, *11*–*13*). By showing that Indigenous Peoples' lifeways, lands, and rights continue to be substantially disrupted by the resource demands of the world economy's metabolism (*49*), this study complements previous Indigenous scholarship highlighting the colonial-economic drivers of environmental injustices (*29*, *30*). The resulting burdens are concomitant with multidimensional patterns of violence (*39*) and exacerbate legacies of intergenerational trauma and land dispossession (*50*).

Because of methodological limitations in gathering data on environmental conflicts globally, we note that our dataset cannot be considered complete and that potential reporting biases remain. The results should therefore be interpreted with caution, particularly regarding the number of Indigenous groups affected and the limited number of reported impacts discussed here. Furthermore, our data do not include information about how reported impacts are distributed within Indigenous communities and the possible differences in opinions among community members regarding the desirability of extractive and industrial development projects (*51*, *52*).

Nevertheless, the findings demonstrate the sheer size of Indigenous rights violations associated to industrial ways of life. International instruments like the ILO C169 convention and UNDRIP can play an important role for advancing Indigenous rights. Our results show that current levels of ratification, implementation, and monitoring are insufficient to ensure respect for such rights. The ILO C169 convention is now the only legally binding global instrument that safeguards the application of the principle of free, prior, and informed consent, yet most countries with lands under Indigenous stewardship and with environmental conflicts affecting Indigenous Peoples have not ratified it (Fig. 1).

While most countries endorse UNDRIP, results suggest that signatory nations are not upholding their commitments to protect Indigenous rights (Fig. 3). UNDRIP rights violations occur across all sectors addressed in this study, whereas land dispossession, livelihood loss, and environmental degradation are significantly more reported in the AFFL sector. These issues can be addressed by strengthening the protection of Indigenous rights over their lands (*53*, *54*). Furthermore, due diligence of corporations within the AFFL sector may be enacted if shareholders and consumers demand additional scrutiny, accountability, and action. Last, efforts to advance UNDRIP will require further attention to industries and corporations, causing environmental harm and violating environmental rights, which now remain insufficiently addressed in the declaration (*55*).

Reported social-environmental impacts of conflictive development projects affecting Indigenous Peoples
(UNDRIP articles specifically jeopardized by reported impacts)

	Global average	AFFL	Dams	Fossil fuels	Mining	Industries, infra-structures	Other
Loss of landscape (articles 25 and 29)	56% ***53–59%***	62% ***54–69%***	58% ***50–66%***	55% ***48–62 %***	53% ***46–59 %***	56% ***46–66 %***	52% ***43–61 %***
Livelihood loss (articles 20 and 21)	52% ***49–55%***	69% ***62–75%***	48 % ***40–56%***	47% ***40–54 %***	47% ***40–53 %***	48% ***38–58 %***	54% ***45–62 %***
Land dispossession (article 26)	50% ***47–53%***	74% ***67–80%***	53 % ***45–61%***	44% ***38–51 %***	40% ***34–46 %***	39% ***30–49 %***	49% ***40–58 %***
Deforestation (article 29)	43% ***40–46%***	74% ***67–80%***	50 % ***42–58%***	35% ***28–41 %***	39% ***33–45 %***	29% ***21–39 %***	22% ***15–30 %***
Biodiversity loss (article 29)	43% ***40–47%***	69% ***62–75%***	40% ***32–48%***	45% ***38–52 %***	34% ***28–40 %***	34% ***25–44 %***	35% ***27–44 %***
Displacement (article 10)	43 % ***40–46%***	54% ***47–61%***	52% ***44–60%***	41% ***34–47 %***	34% ***28–40 %***	34% ***25–44 %***	48% ***39–57 %***
Knowledge loss (articles 24 and 31)	43% ***40–46%***	49% ***41–56%***	42% ***34–50%***	44% ***37–51 %***	39% ***33–45 %***	39% ***30–49 %***	43% ***35–52 %***
Water degradation (article 29)	39% ***37–42%***	43% ***36–51%***	37% ***30–45%***	43% ***37–50%***	48% ***42–55%***	26% ***18–36%***	23% ***16–31%***
Militarization (article 30)	32% ***29–35%***	30% ***24–37%***	33% ***26–41%***	26% ***21–33%***	40% ***34–46%***	27% ***19–37%***	29% ***22–38%***
Soil degradation (article 29)	31% ***28–34%***	33% ***27–41%***	18% ***12–25%***	35% ***29–42%***	43% ***37–49%***	22% ***15–32%***	21% ***15–30%***
Impacts on women (article 22)	20% ***18–23%***	23% ***18–30%***	21% ***15–28%***	19% ***14–25%***	21% ***16–27%***	21% ***14–31%***	16% ***10–24%***
Number of cases (*n*)	1044	183	159	217	258	100	127

Fig. 3. Heatmap of reported social-environmental impacts and UNDRIP rights (in parentheses) jeopardized across sectors, causing environmental conflicts with Indigenous Peoples (*n* = 1044). Confidence intervals (95%) of reported frequencies are shown in bold italics in the figure and in detail in table S5. Additional uncertainty in reported frequencies may result from potential data reporting biases (see Materials and Methods for discussion on data limitations). Impact categories are not mutually exclusive; percentages do not add up to 100% (table S1).

Current initiatives aimed at upholding Indigenous rights, and advancing environmental justice may leverage the quantitative evidence provided in this study. Such initiatives include, for example, governmental efforts to develop corporate due diligence policies and trade agreements conditional upon upholding UNDRIP responsibilities, as well as civil society and Indigenous divestment campaigns targeting corporations involved in rights violations. The case data presented here on an aggregate level are openly available through the EJAtlas (data S2) and include comprehensive and case-specific data on the specific sectors and entities involved in environmental conflicts with Indigenous Peoples. These data can be used accordingly to inform due diligence policies, accountability initiatives, and divestment campaigns, thereby supporting the transformation of the global economy toward one that respects environmental justice and Indigenous Peoples' rights.

MATERIALS AND METHODS

Environmental conflict data

Environmental conflicts generally describe a diverse range of contentious mobilizations related to environmental issues (*56*). Here, we specifically address those types of environmental conflicts that are documented in the global EJAtlas, an online database that gathers information on conflict cases through a large network of contributors. In the EJAtlas, an environmental conflict case refers to the contentious mobilizations of civil society actors in which explicit social-environmental claims are made against a specific project or economic activity that is pursued by state, corporate, and, sometimes, also illicit actors (e.g., illegal loggers). Only cases that are verifiable through secondary sources previously published elsewhere are included in the EJAtlas. These sources include scholarly papers, civil society reports, lawsuits, formal complaints, news

articles, and others. The use of multiple sources enables to cross-check and triangulate information, thereby helping to reduce, to some extent, reporting biases produced by using only a single type of source (e.g., media sources and civil society reports) (*57*). The completeness and quality of all information about conflict cases are checked by a permanent team of moderators who are co-authors of this article. Detailed information regarding the origin, conceptual background, methodology, and general characteristics of the EJAtlas database can be found in (*10*), (*38*), and (*58*).

Sample characteristics

The sample analyzed in this study includes 3081 environmental conflicts, of which 1044 cases involve Indigenous Peoples (see data S1 and S2). This sample only includes extractive and industrial development projects that resulted in environmental conflicts, but not cases of industrial extraction in general. One conflict case includes multiple conflict events and repeated mobilizations over the same project causing the conflict. Each case entry details these events through coded fields accompanied by qualitative descriptions. The sample covers conflicts occurring predominantly during the last decades: 95% of the conflicts began during or after the 1970s, while more than 50% of the cases occurred between 2007 and 2020. We chose this large temporal coverage to include the widest information available on how often specific social-environmental impacts are reported across conflicts involving Indigenous Peoples. Furthermore, the discussed social-environmental impacts (e.g., deforestation, land dispossession, and livelihood loss) ramify through complex pathways and generate legacies that compromise Indigenous Peoples′ lifeways well beyond the year when the conflict began. The consideration of long-lasting impacts is therefore profoundly relevant to understand the challenges faced by contemporary Indigenous Peoples. For a detailed documentation of the case selection procedure used here, see Supplementary Text.

The analyzed EJAtlas sample is a large convenience sample of documented environmental conflicts over a diverse range of extractive and industrial projects, whereas the total number of environmental conflicts worldwide is unknown. The use of this type of sample has become common in environmental conflict research (*10*, *26*, *27*) and is often the only available option to enhance our understanding of global social-environmental phenomena with an unknown population and constrained data access (*10*, *38*). For example, quantitative studies of large-scale land acquisitions and their social-ecological implications commonly rely on crowdsourced databases such as the Land Matrix (*59*–*61*). Another database that offers crowdsourced data on environmental conflict events globally are Global Witness′ annual statistics of killings of environmental defenders (*46*), used, for example, in analyses of environmental conflicts involving Indigenous Peoples (*26*, *27*). However, this dataset does not provide information on the social-environmental impacts of the projects provoking the conflicts. The EJAtlas database offers the largest global coverage of reported social-environmental impacts affecting Indigenous Peoples in environmental conflicts. It enables us to improve our understanding of the reported frequency of these, at a scale that has not been possible so far.

Sample limitations

Because of the inherent characteristics of crowdsourced convenience samples, important limitations for data interpretation apply. First, the data used here are only a sample and not a complete inventory of environmental conflicts, which is not possible to obtain at the global level. Thus, the number of groups of Indigenous Peoples identified here represents a conservative lower boundary of the minimum of Indigenous Peoples affected by conflictive resource use projects worldwide but does not indicate the actual number of affected groups that is unknown. At the country level and for regions with adequate media coverage, independent academia, and strong civil society, we encourage to contrast our results with further systematic research, such as systematic screenings (*62*). Second, data gaps on environmental conflicts remain for specific geographic regions, i.e., Russia and Mongolia, Central Asia, and the Pacific. This is because of several reasons, including a lack of collaborators, or censorship, among other factors (*10*). Environmental conflicts involving Indigenous groups from these areas are therefore underrepresented in the sample. Third, information retrieved from secondary data sources, such as formal lawsuits, scholarly papers, or newspaper reports may, in some cases, dismiss the involvement of specific Indigenous groups despite their presence, for example, because of a lack of legal recognition of specific groups or lack of focus on Indigenous issues, among other reasons. Thus, the identified percentage of conflicts involving Indigenous Peoples (Fig. 2) represents a conservative and geographically biased estimate, while the actual number is possibly higher and more ubiquitous.

Analysis of reported impacts

The EJAtlas provides information on a range of reported social-environmental impacts, caused by a conflictive project. Information about these impacts is retrieved from the same secondary sources used to create and verify conflict entries, i.e., scholarly papers, civil society reports, lawsuits, formal complaints, and newspaper articles. The use of such nonacademic knowledge sources (e.g., newspaper accounts) has become commonplace in the study of protest events (*63*), and local reports about social-ecological impacts have become important data sources to complement other scientific impact assessments, particularly in the context of limited data availability (*64*, *65*). Furthermore, reported and perceived impacts are important to consider, because they partake in creating people′s realities and affected communities often act in response to them (*17*, *66*).

The reported impacts assessed in this study include (i) livelihood loss, (ii) land dispossession, (iii) displacement, (iv) traditional knowledge loss, (v) landscape loss, (vi) militarization, (vii) impacts on women, (viii) deforestation, (ix) biodiversity loss, (x) water degradation, and (xi) soil degradation. These impacts were selected on the basis of the criteria of data availability and relevance for the UNDRIP. Furthermore, given the cross-sectoral and global scope of our analysis, we selected only impacts that apply to a wide range of projects, while we did not assess more specific impacts linked to specific project types or sectors (e.g., EJAtlas impact variables "oil spills" or "mine tailings"). All impacts are mutually not exclusive, i.e., they can occur simultaneously in the same conflict. Table S2 provides definitions of all the impact variables used in this study.

We note that these impacts represent only a selection of impacts to which Indigenous Peoples may be exposed in conflictive extractive and industrial development projects. Furthermore, reported data (e.g., newspaper sources) may be subject to various forms of biases, including selection biases (e.g., impacts considered as worthy of media coverage), description biases (e.g., accuracy of impact description and framing of the event), and diverging

understanding of their specific causes (*63*, *67*). As a case in point, "impacts on women" appear in our dataset less frequently than other impacts, which our team has attributed to the fact that gender aspects are not considered equally important across all regions (*68*), thus generating a selection bias. Moreover, while we report impacts on women as an important aspect of gendered impacts, data availability and reporting bias limits the assessment of other important gendered impacts, such as impacts on people who self-identify as lesbian, gay, bisexual, transgender, queer and questioning, and two-spirit (LGBTQ2S), among others. More generally, we note that extractive and industrial development projects may provoke other human rights violations beyond the UNDRIP concerns discussed here (*69*, *70*). In addition, our dataset does not include information on intracommunity dynamics vis-à-vis conflictive projects, although there is evidence that the burdens and benefits of such projects are frequently unevenly distributed within communities and that different community members may have different opinions regarding their desirability (*51*, *52*).

We acknowledge these data limitations and the restricted scope of our analysis and note that the absence of data on these and other issues in our analysis does not imply their absence in environmental conflicts over extractive and industrial development projects. While potential reporting biases introduce some degree of uncertainty over the global frequencies of reported impacts, in addition to the confidence intervals (table S5), we believe that our results are, nevertheless, of high scholarly relevance as they push the boundaries of the knowledge frontier of Indigenous Peoples' realities vis-à-vis extractive and industrial development pressures. Our dataset provides a contextually rich yet globally relevant evidence basis to inform current efforts toward achieving zero tolerance of Indigenous rights violations (*46*).

Sectoral analysis

We classified environmental conflicts into six mutually exclusive categories according to the main sectors that provoked the conflicts: (i) AFFL, (ii) dams, (iii) mining, (iv) fossil fuels, (v) industries and other infrastructures, and (vi) other conflicts. To arrive at this classification, all environmental conflict cases involving Indigenous Peoples were manually screened to identify the main sector causing the conflict. In cases where several sectors were involved in environmental conflicts, the sector highlighted by the case contributor as the main sector, causing the conflict was chosen to classify the case. Table S1 provides definitions and examples of the sectoral categories used in this study.

Data on Indigenous Peoples' lands and languages

The definition of Indigeneity adopted here largely aligns with those of the ILO Indigenous and Tribal Peoples Convention 1989 (no. 169) article 1 [(*14*); see Supplementary Text for details]. We used the boundaries of Indigenous lands mapped in (*40*), who identified Indigenous lands across 87 countries or politically distinct areas. This dataset represents the most comprehensive assessment of terrestrial lands where Indigenous Peoples have customary ownership, management, or governance arrangements in place, regardless of legal recognition (*47*, *48*). It is based on 127 publicly available sources, including cadastral records, participatory maps, and census data. We acknowledge that voids in these maps do not necessarily imply an absence of Indigenous Peoples or their lands but rather areas for which an Indigenous connection cannot be determined from publicly available geospatial resources. Given that some of the boundaries of Indigenous Peoples' lands are fiercely disputed, we present information only as a percentage of land in 100-km^2 grid cells. We also note that, while data by Garnett *et al.* (*40*) report on Indigenous Peoples' lands, the EJAtlas data report on Indigenous actors involved in environmental conflicts. However, they may have moved to places where no Indigenous stewardship arrangements are in place. These characteristics and differences of the two datasets explain why some conflicts appearing in Fig. 1 are in areas where no Indigenous Peoples' lands are identified in (*40*). In addition, we gathered data on the linguistic status of the languages spoken by the Indigenous groups in our database, from the UNESCO's Atlas of the World's Languages in Danger (*41*), and the Ethnologue (*42*). See data S3 and Supplementary Text for details, as well as limitations about these datasets.

Statistical analysis

We used descriptive statistics to quantify and characterize the exposure of Indigenous Peoples to reported social-environmental impacts and to assess their frequency of occurrence across extractive and industrial sectors. To understand the uncertainty in our observations of reported conflicts involving Indigenous Peoples compared to reported conflicts not involving Indigenous Peoples, we conducted a bootstrap analysis, in which we sampled and summarized, with replacement, 1044 new observations from the original dataset. This step was repeated for 1000 iterations to approximate the distribution of the statistics of conflicts involving Indigenous Peoples. The bootstrap results showed a normal distribution, with a proportion of conflicts involving Indigenous Peoples at 33.8%, with a 95% confidence interval of 32.3 to 35.45%. Confidence intervals were then calculated for all assessed impacts (table S5). We used Pearson's chi-square tests of independence to examine the associations between sectors and impacts affecting Indigenous Peoples (table S5). Reported P values are two-tailed. The significance level was set at 5%.

Research positionality

We are an epistemically, culturally, and disciplinarily diverse group of authors, concerned with global environmental injustices. Each of us brought distinct perspectives to this research, on the basis of our personal and professional experiences, including our numerous engagements with civil society groups, Indigenous Peoples, grassroots organizations, and local communities working within the epistemic community of environmental justice. This positionality inevitably affects our analysis and interpretation. Four coauthors (A.H.B., D.M.D.-C., I.G., and K.P.W.) self-identify as Indigenous and bring perspectives from their cultural contexts and communities to this work (i.e., Oraon, Arawak Taíno, Karai-Karai, and Potawatomi communities, respectively). Although our overall framework is heavily influenced by Western epistemic traditions, we strive to address environmental justice from Indigenous perspectives, as informed by Indigenous intellectual and scholarly traditions (*28*–*35*). We are aware that Indigenous Peoples are not a homogenous and generalized group of people but sovereign and unique nations of peoples and communities with different values and aspirations. We understand the collective rights of Indigenous Peoples as a fundamental human right, and we respect and acknowledge the efforts associated with the development and implementation of UNDRIP (*15*).

Supplementary Materials

This PDF file includes:
Supplementary Text
Tables S1 to S6
Legends for data S1 to S3

Other Supplementary Material for this manuscript includes the following:
Data S1 to S3

REFERENCES AND NOTES

1. Umeek (E. Atleo), *Principles of Tsawalk. An Indigenous Approach to a Global Crisis* (UBC Press, 2011).
2. Forest Peoples Programme, International Indigenous Forum on Biodiversity, Indigenous Women's Biodiversity Network, Centres of Distinction on Indigenous and Local Knowledge, Secretariat of the Convention on Biological Diversity, *Local Biodiversity Outlooks 2* (Forest Peoples Programme, 2020).
3. ICCA Consortium, *Territories of Life Report* (ICCA Consortium, 2021).
4. C. G. Armstrong, C. Brown, Frontiers are frontlines: Ethnobiological science against ongoing colonialism. *J. Ethnobiol.* **39**, 14–31 (2019).
5. S. Díaz, J. Settele, E. S. Brodizio, H. T. Ngo, J. Agard, A. Arneth, P. Balvanera, K. A. Brauman, S. H. M. Butchart, K. M. A. Chan, L. A. Garibaldi, K. Ichii, J. Liu, S. M. Subramanian, G. F. Midgley, P. Miloslavich, Z. Molnár, D. Obura, A. Pfaff, S. Polasky, A. Purvis, J. Razzaque, B. Reyers, R. Roy Chowdhury, Y.-J. Shin, I. Visseren-Hamakers, K. J. Willis, C. N. Zayas, Pervasive human-driven decline of life on Earth points to the need for transformative change. *Science* **366**, eaax3100 (2019).
6. R. Schuster, R. Germain, J. Bennett, N. J. Reo, P. Arcese, Vertebrate biodiversity on indigenous-managed lands in Australia, Brazil, and Canada equals that in protected areas. *Environ. Sci. Policy* **101**, 1–6 (2019).
7. G. Hill, *500 Years of Indigenous Resistance* (PM Press, 2010).
8. L. B. Simpson, *As We Have Always Done: Indigenous Freedom Through Radical Resistance* (University of Minnesota Press, 2017).
9. A. Spice, Fighting invasive infrastructures. *Environ. Soc.* **9**, 40–56 (2018).
10. A. Scheidel, D. Del Bene, J. Liu, G. Navas, S. Mingorría, F. Demaria, S. Avila, B. Roy, I. Ertör, L. Temper, J. Martínez-Alier, Environmental conflicts and defenders: A global overview. *Glob. Environ. Change* **63**, 102104 (2020).
11. J. R. Owen, D. Kemp, J. Harris, A. M. Lechner, É. Lèbre, Fast track to failure? Energy transition minerals and the future of consultation and consent. *Energy Res. Soc. Sci.* **89**, 102665 (2022).
12. N. Estes, *Standing With Standing Rock: Voices From the #NoDAPL Movement* (University of Minnesota Press, 2019)
13. R. Kuokkanen, At the intersection of Arctic indigenous governance and extractive industries: A survey of three cases. *Extr. Ind. Soc.* **6**, 15–21 (2019).
14. International Labour Organization (ILO), "Indigenous and Tribal Peoples Convention" (No. 169, 1989).
15. United Nations, *United Nations Declaration on the Rights of Indigenous Peoples* (United Nations General Assembly, 2007).
16. J. Dell'Angelo, G. Navas, M. Witteman, G. D'Alisa, A. Scheidel, L. Temper, Commons grabbing and agribusiness: Violence, resistance and social mobilization. *Ecol. Econ.* **184**, 107004 (2021).
17. Á. Fernández-Llamazares, M. Garteizgogeascoa, N. Basu, E. S. Brondizio, M. Cabeza, J. Martínez-Alier, P. McElwee, V. Reyes-García, A state-of-the-art review of indigenous peoples and environmental pollution. *Integr. Environ. Assess. Manag.* **16**, 324–341 (2020).
18. M. Liboiron, *Pollution Is Colonialism* (Duke University Press, 2021)
19. Á. Fernández-Llamazares, D. Lepofsky, K. Lertzman, C. G. Armstrong, E. S. Brondizio, M. C. Gavin, P. O'. B. Lyver, G. P. Nicholas, P. Pascua, N. J. Reo, V. Reyes-García, N. J. Turner, J. Yletyinen, E. N. Anderson, W. Balée, J. Cariño, D. M. David-Chavez, C. P. Dunn, S. T. Garnett, S. Greening, S. Jackson, H. Kuhnlein, Z. Molnár, G. Odonne, G.-B. Retter, W. J. Ripple, L. Sáfián, A. S. Bahraman, M. Torrents-Ticó, M. B. Vaughan, Scientists' warning to humanity on threats to indigenous and local knowledge systems. *J. Ethnobiol.* **41**, 144–169 (2021).
20. K. Deonandan, R. Tatham, B. Field, Indigenous women's anti-mining activism: A gendered analysis of the El Estor struggle in Guatemala. *Gend. Dev.* **25**, 405–419 (2017).
21. D. L. Tran, J. Martínez-Alier, G. Navas, S. Mingorría, Gendered geographies of violence: A multiple case study analysis of murdered women environmental defenders. *J. Political Ecol.* **27**, 1189–1212 (2020).
22. R. Kuokkanen, *Restructuring Relations. Indigenous Self-Determination, Governance and Gender* (Oxford Univ. Press, 2019)
23. I. Altamirano-Jiménez, Indigenous women refusing the violence of resource extraction in Oaxaca. *AlterNative* **17**, 215–223 (2021).
24. J. H. Knox, *Environmental Human Rights Defenders - A Global Crisis* (Universal Rights Group, 2017).
25. J. Martínez-Cobo, *Problem of Discrimination Against Indigenous Populations* (United Nations Permanent Forum on Indigenous Issues, 1986).
26. N. Butt, F. Lambrick, M. Menton, A. Renwick, The supply chain of violence. *Nat. Sustain.* **2**, 742–747 (2019).
27. P. Le Billon, P. Lujala, Environmental and land defenders: Global patterns and determinants of repression. *Glob. Environ. Change* **65**, 102163 (2020).
28. M. K. MacKenzie, S. K. Serrano, K. L. Kaulukukui, Environmental justice for Indigenous Hawaiians: Reclaiming land and resources. *Nat. Resour. Environ.* **21**, 37–42 (2007).
29. D. McGregor, S. Whitaker, M. Sritharan, Indigenous environmental justice and sustainability. *Curr. Opin. Environ. Sustain.* **43**, 35–40 (2020).
30. K. P. Whyte, The Dakota access pipeline, environmental injustice, and U.S. colonialism. *Red Ink* **19**, 154–169 (2017).
31. K. P. Whyte, Settler colonialism, ecology, and environmental injustice. *Environ. Soc.* **9**, 125–144 (2018).
32. K. P. Whyte, Too late for indigenous climate justice: Ecological and relational tipping points. *Wiley Interdiscip. Rev. Clim. Change* **11**, e603 (2020).
33. N. J. Reo, *Inawendiwin* and relational accountability in Anishnaabeg studies: The crux of the biscuit. *J. Ethnobiol.* **39**, 65–75 (2019).
34. L. Simpson, E. Manitowabi, Theorizing resurgence from within Nishnaabeg thought, in *Centering Anishinaabeg Studies: Understanding the World through Stories*, J. Doerfler, N. J. Sinclair, H. K. Stark, Eds. (Michigan University Press, 2013), pp. 279–294.
35. D. McGregor, J.-P. Restoule, R. Johnston, *Indigenous Research: Theories, Practices, and Relationships* (Canadian Scholars' Press, 2018).
36. M. Walter, Using the 'power of the data' within Indigenous research practice. *Aust. Aboriginal Stud.* **2**, 27–34 (2005).
37. A. Hayward, L. Wodtke, A. Craft, T. Robin Martens, J. Smylie, S. McConkey, A. Nychuk, C. Healy, L. Star, J. Cidro, Addressing the need for indigenous and decolonized quantitative research methods in Canada. *SSM Popul. Health* **15**, 100899 (2021).
38. L. Temper, F. Demaria, A. Scheidel, D. Del Bene, J. Martínez-Alier, The Global Environmental Justice Atlas (EJAtlas): ecological distribution conflicts as forces for sustainability. *Sustain. Sci.* **13**, 573–584 (2018).
39. G. Navas, S. Mingorría, B. Aguilar, Violence in environmental conflicts: The need for a multidimensional approach. *Sustain. Sci.* **13**, 649–660 (2018).
40. S. T. Garnett, N. D. Burgess, J. E. Fa, Á. Fernández-Llamazares, Z. Molnár, C. J. Robinson, J. E. M. Watson, K. K. Zander, B. Austin, E. S. Brondizio, N. F. Collier, T. Duncan, E. Ellis, H. Geyle, M. V. Jackson, H. Jonas, P. Malmer, B. McGowan, A. Sivongxay, I. Leiper, A spatial overview of the global importance of Indigenous lands for conservation. *Nat. Sustain.* **1**, 369–374 (2018).
41. United Nations Educational, Scientific and Cultural Organization (UNESCO), *Atlas of the World's Languages in Danger* (United Nations, 2021).
42. D. M. Eberhard, G. F. Simons, C. D. Fennig, *Ethnologue: Languages of the World* (SIL International, 2021).
43. International Labour Organization (ILO), *Implementing the ILO Indigenous and Tribal Peoples Convention No. 169: Towards an Inclusive, Sustainable and Just Future* (International Labour Organization, 2019).
44. J. Ferguson, M. Weaselboy, Indigenous sustainable relations: Considering land in language and language in land. *Curr. Opin. Environ. Sustain.* **43**, 1–7 (2020).
45. K. L. Rehg, L. Campbell, *The Oxford Handbook of Endangered Languages* (Oxford Univ. Press, 2018).
46. Global Witness, *Last Line of Defence: The Industries Causing the Climate Crisis and Attacks Against Land and Environmental Defenders* (Global Witness, 2021).
47. J. E. Fa, J. E. M. Watson, I. Leiper, P. Potapov, T. D. Evans, N. D. Burgess, Z. Molnár, Á. Fernández-Llamazares, T. Duncan, S. Wang, B. J. Austin, H. Jonas, C. J. Robinson, P. Malmer, K. K. Zander, M. V. Jackson, E. Ellis, E. S. Brondizio, S. T. Garnett, Importance of Indigenous Peoples' lands for the conservation of Intact Forest Landscapes. *Front. Ecol. Environ.* **18**, 135–140 (2020).
48. A. Estrada, P. A. Garber, S. Gouveia, Á. Fernández-Llamazares, F. Ascensão, A. Fuentes, S. T. Garnett, C. Shaffer, J. Bicca-Marques, J. E. Fa, K. Hockings, S. Shanee, S. Johnson, G. H. Shepard, N. Shanee, C. D. Golden, A. Cárdenas-Navarrete, D. R. Levey, R. Boonratana, R. Dobrovolski, A. Chaudhary, J. Ratsimbazafy, J. Supriatna, I. Kone, S. Volampeno, Global importance of Indigenous Peoples, their lands, and knowledge systems for saving the world's primates from extinction. *Sci. Adv.* **8**, eabn2927 (2022).
49. R. Muradian, M. Walter, J. Martínez-Alier, Hegemonic transitions and global shifts in social metabolism: Implications for resource-rich countries. Introduction to the special section. *Glob. Environ. Change* **22**, 559–567 (2012).

50. J. Farrell, P. Burow, K. McConnell, J. Bayham, K. P. Whyte, G. Koss, Effects of land dispossession and forced migration on Indigenous peoples in North America. *Science* **374**, eabe4943 (2021).
51. I. Kelman, J. S. Loe, E. W. Rowe, E. Wilson, N. Poussenkova, E. Nikitina, D. B. Fjærtoft, Local perceptions of corporate social responsibility for arctic petroleum in the Barents region. *Arct. Rev. Law Politics* **7**, 152–178 (2016).
52. V. Reyes-García, Á. Fernández-Llamazares, J. Bauchet, R. Godoy, Variety of indigenous peoples' opinions of large infrastructure projects: The TIPNIS road in the Bolivian Amazon. *World Dev.* **127**, 104751 (2020).
53. A. Moreton-Robinson, *Sovereign Subjects Indigenous Sovereignty Matters* (Allen & Unwin, 2007)
54. I. Watson, *Indigenous Peoples as Subjects of International Law* (Routledge, 2014).
55. A. Giunta, Looking back to move forward: The status of environmental rights under the UN Declaration on the Rights of Indigenous Peoples. *Int. J. Hum. Rights* **23**, 149–173 (2019).
56. P. Le Billon, Environmental conflict, in *The Routledge Handbook of Political Ecology* (Routledge, 2015), pp. 598–608.
57. R. Sundberg, E. Melander, Introducing the UCDP georeferenced event dataset. *J. Peace Res.* **50**, 523–532 (2013).
58. L. Temper, D. Del Bene, J. Martinez-Alier, Mapping the frontiers and front lines of global environmental justice: The EJAtlas. *J. Polit. Ecol.* **22**, 255–278 (2015).
59. C. Liao, K. Nolte, J. A. Sullivan, D. G. Brown, J. Lay, C. Althoff, A. Agrawal, Carbon emissions from the global land rush and potential mitigation. *Nat. Food* **2**, 15–18 (2021).
60. M. F. Müller, G. Penny, M. T. Niles, V. Ricciardi, D. D. Chiarelli, K. F. Davis, J. Dell'Angelo, P. D'Odorico, L. Rosa, M. C. Rulli, N. D. Mueller, Impact of transnational land acquisitions on local food security and dietary diversity. *Proc. Natl. Acad. Sci. U.S.A.* **118**, e2020535118 (2021).
61. L. Rosa, M. C. Rulli, S. Ali, D. D. Chiarelli, J. Dell'Angelo, N. D. Mueller, A. Scheidel, G. Siciliano, P. D'Odorico, Energy implications of the 21st century agrarian transition. *Nat. Commun.* **12**, 2319 (2021).
62. C. Raleigh, A. Linke, H. Hegre, J. Karlsen, Introducing ACLED: An armed conflict location and event dataset. *J. Peace Res.* **47**, 651–660 (2010).
63. J. Earl, A. Martin, J. D. McCarthy, S. A. Soule, The use of newspaper data in the study of collective action. *Annu. Rev. Sociol.* **30**, 65–80 (2004).
64. V. Reyes-García, D. García-del-Amo, P. Benyei, Á. Fernández-Llamazares, K. Gravani, A. B. Junqueira, V. Labeyrie, X. Li, D. M. S. Matias, A. McAlvay, P. G. Mortyn, A. Porcuna-Ferrer, A. Schlingmann, R. Soleymani-Fard, A collaborative approach to bring insights from local observations of climate change impacts into global climate change research. *Curr. Opin. Environ. Sustain.* **39**, 1–8 (2019).
65. G. D. Blanco, Á. Fernández-Llamazares, G. D. Blanco, J. Baker, M. S. M. Tagliari, M. Albuquerque Hayata, M. L. Campos, N. Hanazaki, The impacts of mining on the food sovereignty and security of Indigenous Peoples and local communities: A global review. *Sci. Total Environ.* **855**, 158803 (2023).
66. A. A. Granderson, Making sense of climate change risks and responses at the community level: A cultural-political lens. *Clim. Risk Manag.* **3**, 55–64 (2014).
67. L. Q. Sneyd, A. Legwegoh, E. D. G. Fraser, Food Riots: Media perspectives on the causes of food protest in Africa. *Food Secur.* **5**, 485–497 (2013).
68. D. Tran, Realities beyond reporting: Women environmental defenders in South Africa. *Fem. Media Stud.*, 10.1080/14680777.2022.2045335 (2022).
69. J. Burger, *Indigenous Peoples, Extractive Industries and Human Rights* (European Union, 2014).
70. Inter-American Commission on Human Rights (IACHR), *Indigenous Peoples, Afro-Descendent Communities, and Natural Resources: Human Rights Protection in the Context of Extraction, Exploitation, and Development Activities* (Organization of American States, 2015).

Acknowledgments: We dedicate this work to all the Indigenous communities defending their territories from adverse development pressures. We thank all case contributors to the EJAtlas who have made this research possible. We thank S. T. Garnett and colleagues for compiling and sharing data on Indigenous Peoples' lands, L. Vadez-Reyes for help in data gathering, S. Álvarez Fernández for statistical support, and S. Díaz for constructive feedback on an earlier version of this manuscript. **Funding:** This work was supported by Balzan Prize Foundation (2020 Balzan Prize for Environmental Challenges, to J.M.-A.); Ramón y Cajal research grant, Spanish Ministry of Science (RYC2020-029088-I, to A.S.) and Spanish Ministry of Science and Innovation (RYC2021-034198-I, to Á.F.-L.); Helsinki Institute of Sustainability Science (HELSUS; to Á.F.-L.); ERC Consolidator Grant (FP7-771056-LICCI, to V.R.-G.); La Caixa Foundation fellowship (ID 537 100010434, code LCF/BQ/DI19/11730049, to D.T.; ID 100010434, code LCF/BQ/DI19/11730058, to M.A.T.; code LCF/BQ/DI20/11780015, to E.F.); Fundamental Research Funds for the Central Universities (CAU-2022TC061, to J.L.); María de Maeztu Programme for Units of Excellence of the Spanish Ministry of Science and Innovation (CEX2019-000940-M, to A.S., Á.F.-L., B.R., D.D.B., D.T., E.F., J.L., J.M.-A., K.H., M.A.T., M.W., and V.R.-G.). **Author contributions:** Conceptualization: Á.F.-L., A.S., D.M.D.-C., K.P.W., I.G., A.H.B., L.T., and D.D.B. Methodology: D.D.B., L.T., J.M.-A., A.S., Á.F.-L., D.M.D.-C., K.P.W., I.G., A.H.B., and V.R.-G. Investigation: A.S., Á.F.L., M.A.T., D.D.B., E.F., K.H., J.L., J.M.-A., G.N., V.R.-G., B.R., L.T., D.T., M.W., A.H.B., D.M.D.-C., I.G., and K.P.W. Visualization: A.S., Á.F.-L., V.R.-G., and D.M.D.-C. Funding acquisition: J.M.-A., L.T., A.S., and Á.F.-L. Project administration: D.D.B., J.M.-A., L.T., M.W., A.S., and G.N. Supervision: Á.F.-L. and A.S. Writing—original draft: all authors. Writing—review and editing: A.S. and Á.F.-L. **Competing interests:** The authors declare that they have no competing interests. **Data and materials availability:** All data needed to evaluate the conclusions in the paper are present in the paper and/or the Supplementary Materials. The data are also available in the Global Atlas of Environmental Justice (www.ejatlas.org).

Submitted 19 September 2022
Accepted 2 May 2023
Published 7 June 2023
10.1126/sciadv.ade9557

NEUROSCIENCE

$CD4^+$ T cells aggravate hemorrhagic brain injury

Samuel X. Shi[1]†, Yuwen Xiu[1,2,3]†, Yan Li[2]†, Meng Yuan[2], Kaibin Shi[2], Qiang Liu[3], Xiaoying Wang[1]*, Wei-Na Jin[2]*

Leukocyte infiltration accelerates brain injury following intracerebral hemorrhage (ICH). Yet, the involvement of T lymphocytes in this process has not been fully elucidated. Here, we report that $CD4^+$ T cells accumulate in the perihematomal regions in the brains of patients with ICH and ICH mouse models. T cells activation in the ICH brain is concurrent with the course of perihematomal edema (PHE) development, and depletion of $CD4^+$ T cells reduced PHE volumes and improved neurological deficits in ICH mice. Single-cell transcriptomic analysis revealed that brain-infiltrating T cells exhibited enhanced proinflammatory and proapoptotic signatures. Consequently, $CD4^+$ T cells disrupt the blood-brain barrier integrity and promote PHE progression through interleukin-17 release; furthermore, the TRAIL-expressing $CD4^+$ T cells engage DR5 to trigger endothelial death. Recognition of T cell contribution to ICH-induced neural injury is instrumental for designing immunomodulatory therapies for this dreadful disease.

INTRODUCTION

The prognosis of intracerebral hemorrhage (ICH) is devastating (*1*). Evidence from preclinical and clinical studies suggests the detrimental role of lymphocyte-driven inflammatory response in ICH pathophysiology (*2*–*4*). These orchestrated pathways of neuroinflammation are thought to contribute toward the evolution of brain edema and secondary injury following ICH, which deteriorates patient neurological outcomes (*3*, *5*). However, the detailed mechanisms involving lymphocyte-driven neuroinflammatory processes remain only partially understood, and no targeted treatment for post-ICH brain inflammation is currently available in clinical practice.

Blood components exuded from the hematoma and damage-associated molecular patterns released by injured neural cells activates an acute immune response following ICH (*5*, *6*). Besides activated intrinsic brain cells such as microglia and astrocytes, lymphocytes assemble in the regions proximal to the hematoma in the acute and post-acute phase of ICH. Lymphocyte subsets—$CD4^+$ T, $CD8^+$ T, B, and natural killer cells—are observed within a day after ictus and peak around 3 days after (*7*–*9*).

T cells, which represent a major lymphocyte population, are among the brain-infiltrating immune cells observed in the acute stage of experimental ICH; however, their actions are comparatively less known compared to innate immune cells (*7*, *8*). In their adaptive modality, $CD4^+$ T cells are generally activated by T cell receptor recognition of cognate antigens presented by major histocompatibility complex II of antigen-presenting cells in the presence of costimulatory signals. Upon activation, $CD4^+$ T cells proliferate and produce a variety of cytokines/chemokines (*10*, *11*). Alternatively, in the absence of antigen recognition, T cells can respond to danger signals and produce cytokines (*12*–*15*), suggesting their potential involvement in the genesis or progression of the neuroinflammatory cascade in the acute stage of ICH. To dissect the roles of T cells in acute ICH brain injury, we used brain tissue sections of ICH patients and mouse models to query the potential mechanisms underlying T cell actions in ICH injury. Our study findings provide a rationale for further investigations toward the development of immunotherapies targeting T lymphocytes to modulate the development and progression of secondary brain tissue damage in ICH.

RESULTS

$CD4^+$ T cells accumulate in perihematomal regions in ICH patients and mouse models

To uncover the role of T cells in the pathophysiology of ICH, we first identified T cells presence in brain tissue obtained from the perihematomal region from patients with ICH within 72-hour onset who underwent craniectomy to remove hematoma. Brain tissues were stained for cell type markers (CD4, CD8, and CD19) and phenotypic markers [CD69 and interleukin-17 (IL-17)]. An increased average count of lymphocytes was detected in ICH tissues compared to the location-matched control brain tissues (Fig. 1, A and B). In ICH tissues, average $CD4^+$ counts outnumbered $CD8^+$ and B cells; $CD4^+$ cells were observed as early as 24 hours after ICH in individual brain samples (Fig. 1, A and B). In addition, T cells in the ICH group displayed a marked expression of CD69 and IL-17 compared to cells in the control group (Fig. 1, C and D), indicating a proinflammatory state of the $CD4^+$ T cell in patient-derived tissue. The accumulation of $CD4^+$ T cells in perihematomal regions suggests active $CD4^+$ T cell participation in the early immune response to ICH (Fig. 1, A to D).

An established animal model induced by autologous blood injection was used to experimentally confirm the observations in ICH patient-derived brain tissue. Infiltrating lymphocytes were counted in the perihematomal region of murine brains at 24 and 72 hours after ICH induction. Correspondingly, an increased accumulation of $CD4^+$ T cells in the regions surrounding the hematoma at both 24 and 72 hours after ICH induction was observed (Fig. 1, E to G). We further noted the close proximity of these infiltrating $CD4^+$ T cells with $CD31^+$ endothelial cells, indicating their

[1]Clinical Neuroscience Research Center (CNRC), Department of Neurosurgery and Neurology, Tulane University School of Medicine, New Orleans, LA, USA. [2]Center for Neurological Diseases, China National Clinical Research Center for Neurological Diseases, Beijing Tiantan Hospital, Capital Medical University, Beijing, China. [3]Department of Neurology, Tianjin Medical University General Hospital, Tianjin, China.
*Corresponding author. Email: weina.jin@ncrcnd.org.cn (W.-N.J.); xwang51@tulane.edu (X.W.)
†These authors contributed equally to this work.

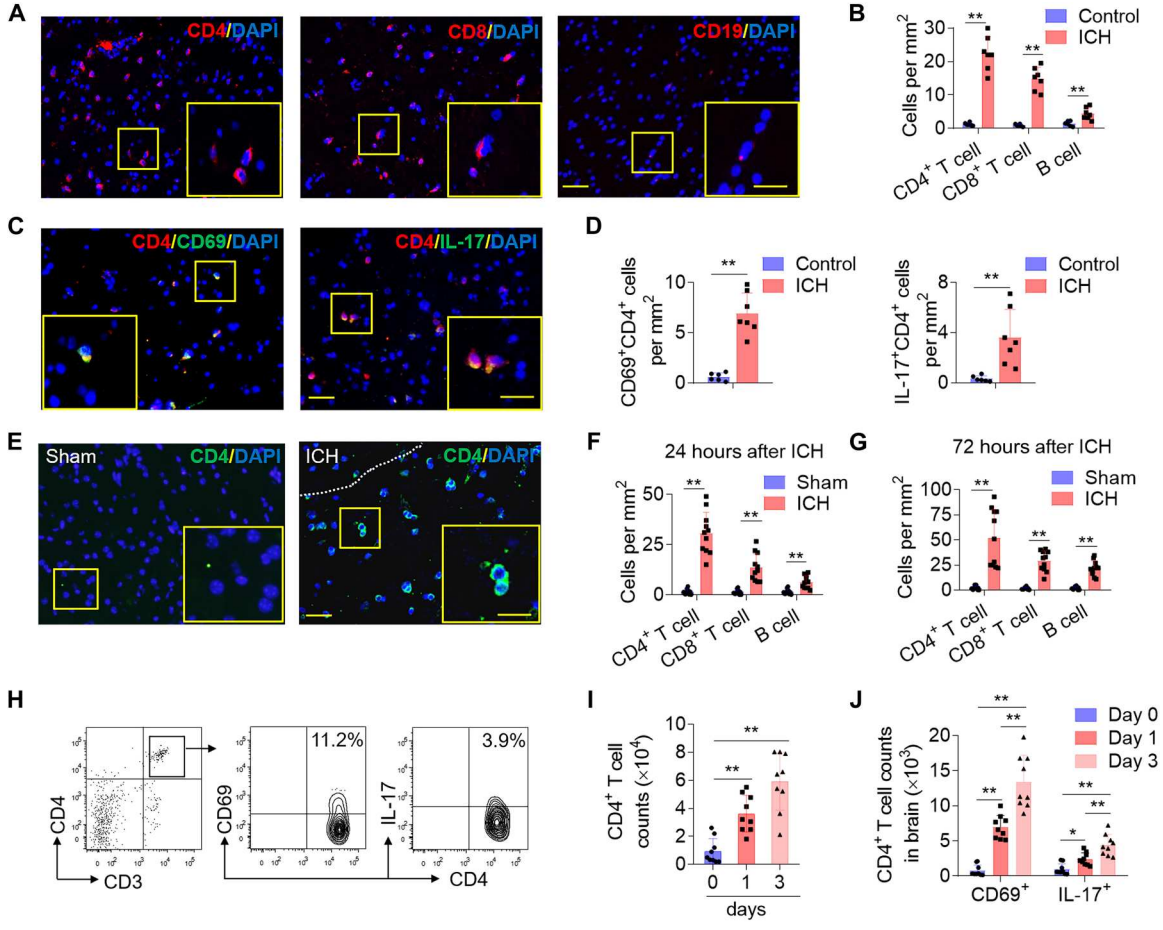

Fig. 1. CD4$^+$ T cells accumulate in perihematomal areas following ICH. Perihematomal tissues were obtained from brain basal ganglia of patients with ICH within 72-hour onset who underwent urgent evacuation of hematoma. Brain tissues for control cases were obtained from individuals that passed from non-neurologic diseases and were without history of neurological or neuropsychiatric conditions, and selected tissue sections were region-matched with ICH tissues. (**A** and **B**) Immunostaining (A) and quantification (B) of lymphocyte subsets (T and B cells) in brain sections from patients with ICH in the perihematomal area after ICH and control subjects without neurological disorders. (**C** and **D**) Immunostaining (C) and quantification (D) shows brain-infiltrating CD4$^+$ T cells expression of the activation marker CD69 and IL-17 in perihematomal edema (PHE) after ICH. Scale bars, 40 μm and (inset) 20 μm. Quantification was averaged as positive cells per mm^2. In (B) and (D), patients with ICH: $n = 7$; controls: $n = 6$. Mann-Whitney test. Means ± SD, *$P < 0.05$ and **$P < 0.01$. (**E** to **J**) ICH was induced by injection of autologous blood in C57BL/6 mice. Brain tissue was harvested at 24 or 72 hours after ICH. (E) Immunostaining of ICH brain slices show infiltrating CD4$^+$ T cells. White dashed lines outline the hematoma area. (F and G) Quantification of lymphocyte subsets in the perihematomal region of ICH brain 24 hours (F) and 72 hours (G) after ICH induction. Scale bars, 40 μm and (inset) 20 μm. Quantification was averaged as positive cells per mm^2. $n = 11$ mice per group. Two-tailed unpaired Student's t test. (H to J) Flow cytometry plots and quantification show CD4$^+$ T cell counts and the expression of CD69 and IL-17 in brain-infiltrating CD4$^+$ T cells from days 0 to 3 after ICH. $n = 9$ mice per group. In (I) and (J), one-way analysis of variance (ANOVA) followed by Tukey post hoc test. Means ± SD, *$P < 0.05$ and **$P < 0.01$. DAPI, 4′, 6-diamidino-2-phenylindole.

perivascular accumulation (fig. S1). Furthermore, CD4$^+$ T cells increasingly expressed CD69 and IL-17 in a time-dependent manner, detected as early as 24 hours following experimental ICH (Fig. 1, H to J, and fig. S2). To ensure that observed CD4$^+$ T cells were not derived from the injected autologous blood, blood from ubiquitin C promoter–green fluorescent protein (UBC-GFP) mice (universal cellular GFP expression) was injected into wild-type mice. Detection of GFP signal following ICH induction showed that less than 10% of CD4$^+$ T cells in the perihematomal area were GFP$^+$, indicating that most of these cells were actively recruited from the circulation (fig. S3).

CD4$^+$ T cells are significantly activated in the ICH brain

To characterize the temporal and spatial trends of T cell activation following ICH (*16*), we leveraged a fluorescence resonance energy transfer (FRET)–based genetically encoded calcium indicator, TN-XXL, to visualize T cell activation (Fig. 2A) (*17*, *18*); we tested the compartment-specific T cell activation modalities in ICH mice (Fig. 2B). TN-XXL is composed of calcium-sensitive double C-terminal lobe of troponin C (TnC)–linked dual parts: cyan fluorescent protein (CFP) and cpCitrine. Upon cell activation, increased cytoplasm free calcium binds to the TnC, which then undergoes a reversible conformational change and transfers energy from the CFP to the cpCitrine, resulting in a signature drop in CFP fluorescence and concurrent increase in cpCitrine fluorescence (FRET$^+$). The ratiometric change in fluorescent intensities reflects the cellular

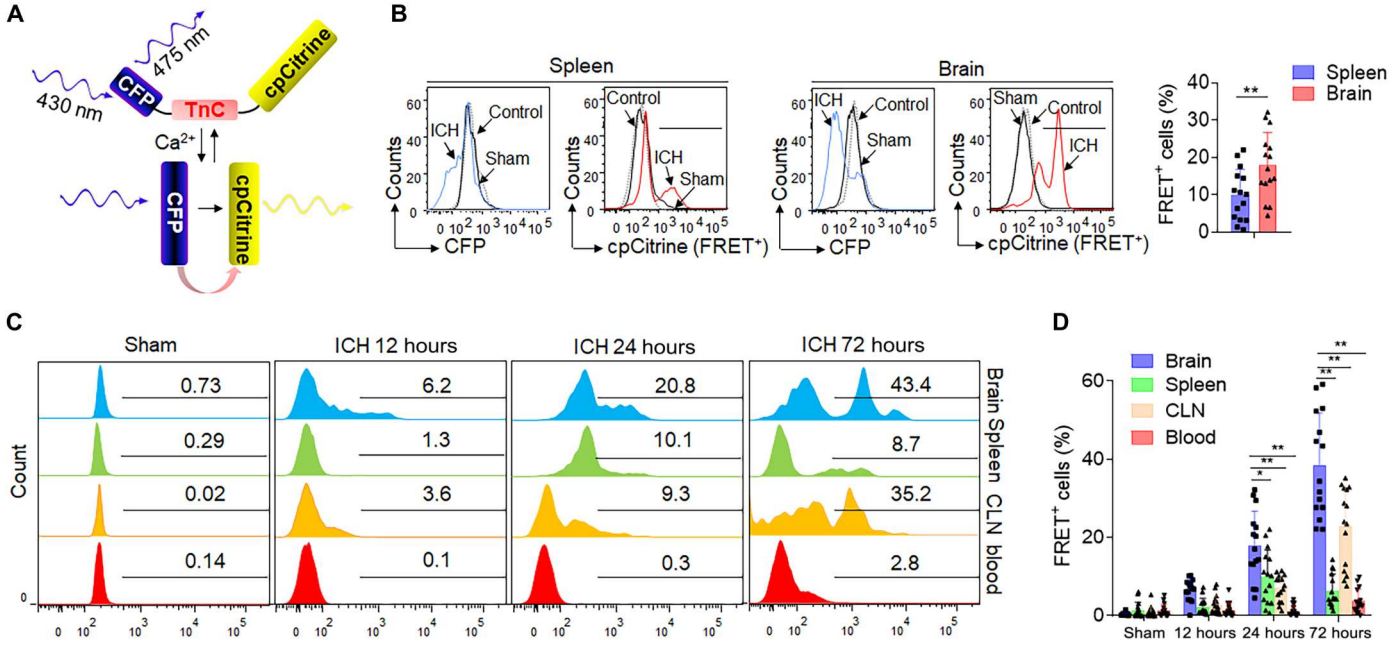

Fig. 2. CD4$^+$ T cells are significantly and time-dependently activated in the brain after ICH. CD4$^+$ T cells were fluorescence-activated cell sorter (FACS) sorted from C57BL/6 mice and retrovirally transduced with TN-XXL plasmid. A total of 1×10^7 TN-XXL–expressing CD4$^+$ T cells were then injected into Rag2$^{-/-}$ mice 24 hours before ICH. Twenty-four hours after ICH, FRET of TN-XXL–expressing CD4$^+$ T cells in the brain, spleen, CLNs, and blood was detected using flow cytometry. (**A**) Schematic representation of the calcium indicator TN-XXL, containing donor fluorophore CFP, cpCitrine acceptor, and calcium-sensitive domain TnC, before and after binding of calcium. (**B**) After binding to free calcium, TnC undergoes a conformational change that leads to energy transfer from the donor to the acceptor fluorophore, resulting in a drop in CFP fluorescence and an increase in cpCitrine fluorescence with CD4$^+$ T cells activation after ICH injury. Flow cytometry gating strategy showing negative control (mock transduced), sham operation, and ICH surgery groups in the spleen and brain separately. Bar graphs shows the FACS-based FRET measurements in TN-XXL–expressing CD4$^+$ T cells within the spleen and brain at 24 hours after ICH. $n = 15$ per group. Two-tailed unpaired Student's t test. (**C** and **D**) Flow cytometry histogram and measurements of FRET level in TN-XXL–expressing CD4$^+$ T cells within indicated organs from 0 to 72 hours after ICH. $n = 15$ per group. Two-way ANOVA followed by Tukey post hoc test. Mean ± SD. *$P < 0.05$ and **$P < 0.01$.

activation status. CD4$^+$ T cells isolated from wild-type mice were retrovirally transduced with TN-XXL and intravenously transferred into Rag2$^{-/-}$ mice, followed by autologous blood ICH induction. Notably, FRET$^+$CD4$^+$ T cells were primarily observed in the injured brain and detected as early as 12 hours after ICH (Fig. 2, C and D). FRET$^+$CD4$^+$ T cells in the brain were increasingly activated in a time-dependent manner compared to cells in peripheral compartments including the spleen, cervical lymph nodes (CLNs), and blood (Fig. 2D). We also observed an increase of activated CD4$^+$ T cells in the CLNs, but not as prominently as in the brain after ICH (Fig. 2D). These results show that CD4$^+$ T cells are significantly activated in the hemorrhagic brain and in a time-dependent manner following ICH.

ICH induces distinguishing transcriptomic features of T cells in the brain versus periphery

To further depict the landscape of the composition and functional states of brain-infiltrating immune cells following ICH, single-cell RNA sequencing (scRNA-seq) was performed to identify the molecular characteristics of CD45$^+$ cells in the brain versus those in peripheral compartments of ICH mice (Fig. 3). CD45$^+$ cells were sorted from mouse splenocytes or brain at day 3 after ICH or sham procedures and were subjected to unbiased scRNA-seq. Besides, the CD45^{hi} cells were also isolated from sham brain (Sham brain_ CD45^{hi}) to obtain enough T cells for subclustering and data processing. After stringent quality control, a total of 41,385 individual cells, with an average of 2372 genes per cell, were obtained (Fig. 3, A and B, and fig. S4). Thirteen cell clusters were defined on the basis of their distinct molecular features (Fig. 3, C to E). In the ICH brain, the T cell subset exhibited a higher activation score compared to the activation of other CD45$^+$ clusters (Fig. 3F). Moreover, the T cell cluster in ICH brain exhibited a notable higher activation score compared to sham brain and spleen groups (Fig. 3G). The distinct difference in activation scores alludes to the conspicuous activation state of the T cells within the ICH brain.

To visualize the intrinsic structure and uncover the potential functional subtypes of the overall T cell population within the context of ICH, unsupervised clustering and uniform manifold approximation and projection (UMAP) were performed for reclustered CD3$^+$ cells from CD45$^+$ (sham spleen, ICH spleen, and ICH brain) or CD45^{hi} (sham brain) populations. Nine distinct T cell subclusters emerged from the sham spleen, sham brain, ICH spleen, and ICH brain, defined as naïve CD4$^+$ T, naïve CD8$^+$ T, activated CD4$^+$ T, activated CD8$^+$ T cell clusters, etc. (Fig. 4, A and B, and fig. S5). Within the ICH brain, activated CD4$^+$ T cells were significantly increased as compared to sham brain (Fig. 4C). Compared with sham brain, ICH-brain CD4$^+$ T cells included up-regulated genes related to inflammation (*Jun*, *Fosb*, *Ifngr1*, and *Spp1*), chemotaxis (*Ccl3* and *Ccl4*), metabolism (*ApoE* and *Ttr*), and apoptotic-triggering death ligands (*Fasl* and *Tnf*) (Fig. 4D). Kyoto Encyclopedia of Genes and Genomes (KEGG) pathway enrichment analysis of

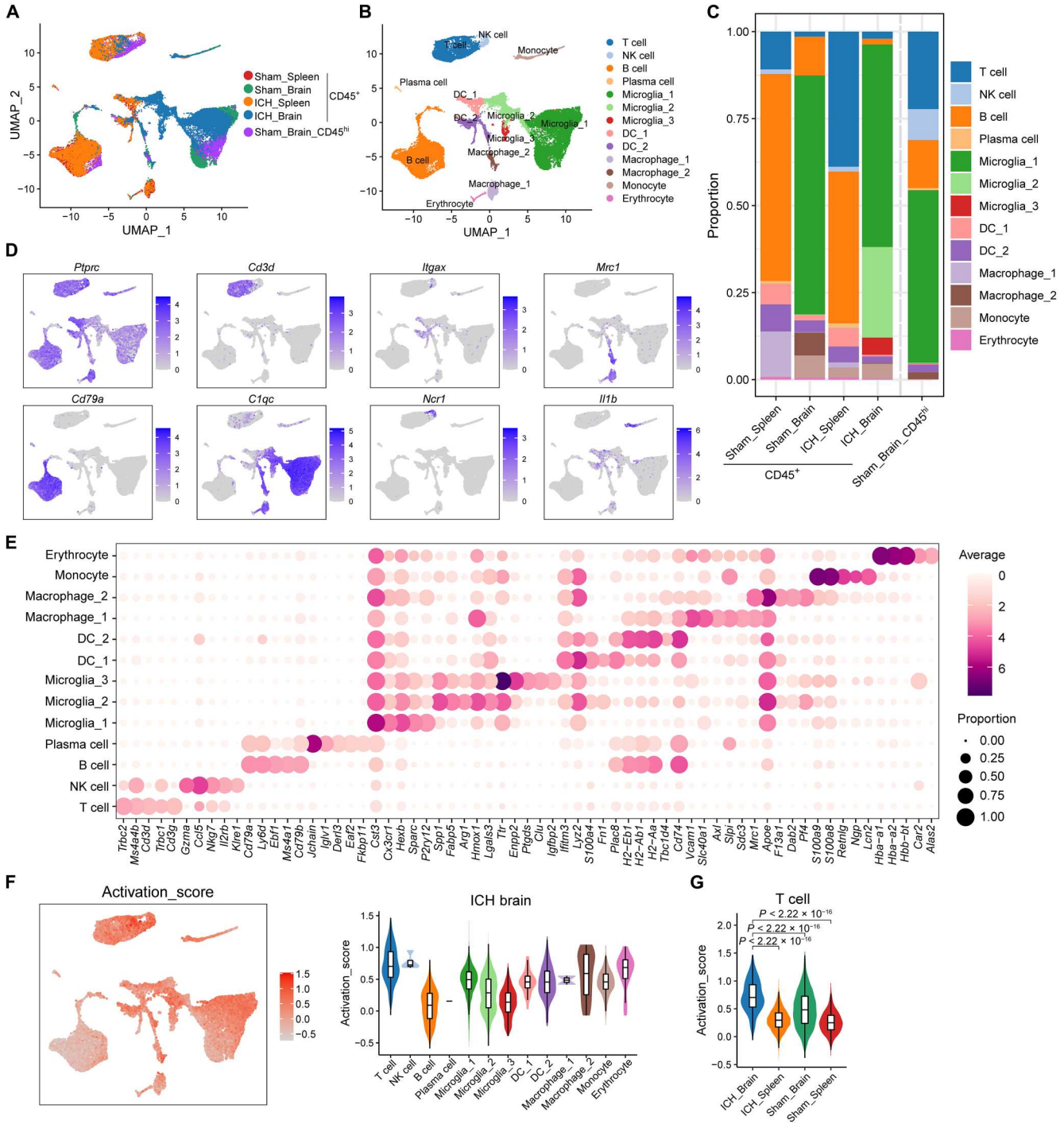

Fig. 3. Single-cell analysis of CD45$^+$ cells isolated from the brain and spleen of ICH mice. CD45$^+$ cells were isolated from splenocytes or brain tissues of C57BL/6 mice 72 hours after autologous blood injection induced ICH using FACS. CD45$^+$ cells splenic (Sham spleen) or brain (Sham brain_CD45$^+$) cells from sham-operated mice were used as controls for unbiasedly single-cell RNA mapping. The optimized FACS sorting was performed on CD45^{hi} cell population to obtain enough CD4$^+$ T cells in sham brains for subclustering and data processing (Sham brain_ CD45^{hi}). scRNA-seq was performed using the 10X Genomics Chromium platform. (**A** and **B**) Uniform manifold approximation and projection (UMAP) plot along components 1 and 2 for all high-quality single cells from sham brain_CD45$^+$ (n = 10487 cells), sham brain_CD45^{hi} (n = 5589 cells), sham spleen (n = 8747 cells), ICH brain (n = 10,487 cells), and ICH spleen (n = 9147 cells), colored by group and cell type. (**C**) Stacked bar chart showing the constitution of 13 cell clusters in sham spleen, sham brain_CD45$^+$, sham brain_CD45^{hi}, ICH spleen, and ICH brain. (**D**) UMAP plots show selected marker genes for determining cell identity. (**E**) Dot plots show average (dot color) and percentage (dot size) expression of top five marker genes for each cluster. (**F**) UMAP plot illustrating activation feature scores (*Ms4a4b*, *Ms4a6b*, *Cxcl10*, *Itk*, *Prkcq*, *Ccnd1*, *Ccnd2*, *Ccnd3*, *Hmox1*, *Ccl5*, *Dusp1*, *Klf4*, *Jun*, and *Junb*) calculated using AddModuleScore function in Seurat (left). Violin plot with box plot inside showing the comparison of activation scores between T cells and other CD3$^-$CD45$^+$ clusters in ICH Brain (right). (**G**) Violin plot with box plot inside illustrating the comparison of T cell activation scores between indicated groups. In (A) to (G), data were pooled from 15 mice in each group.

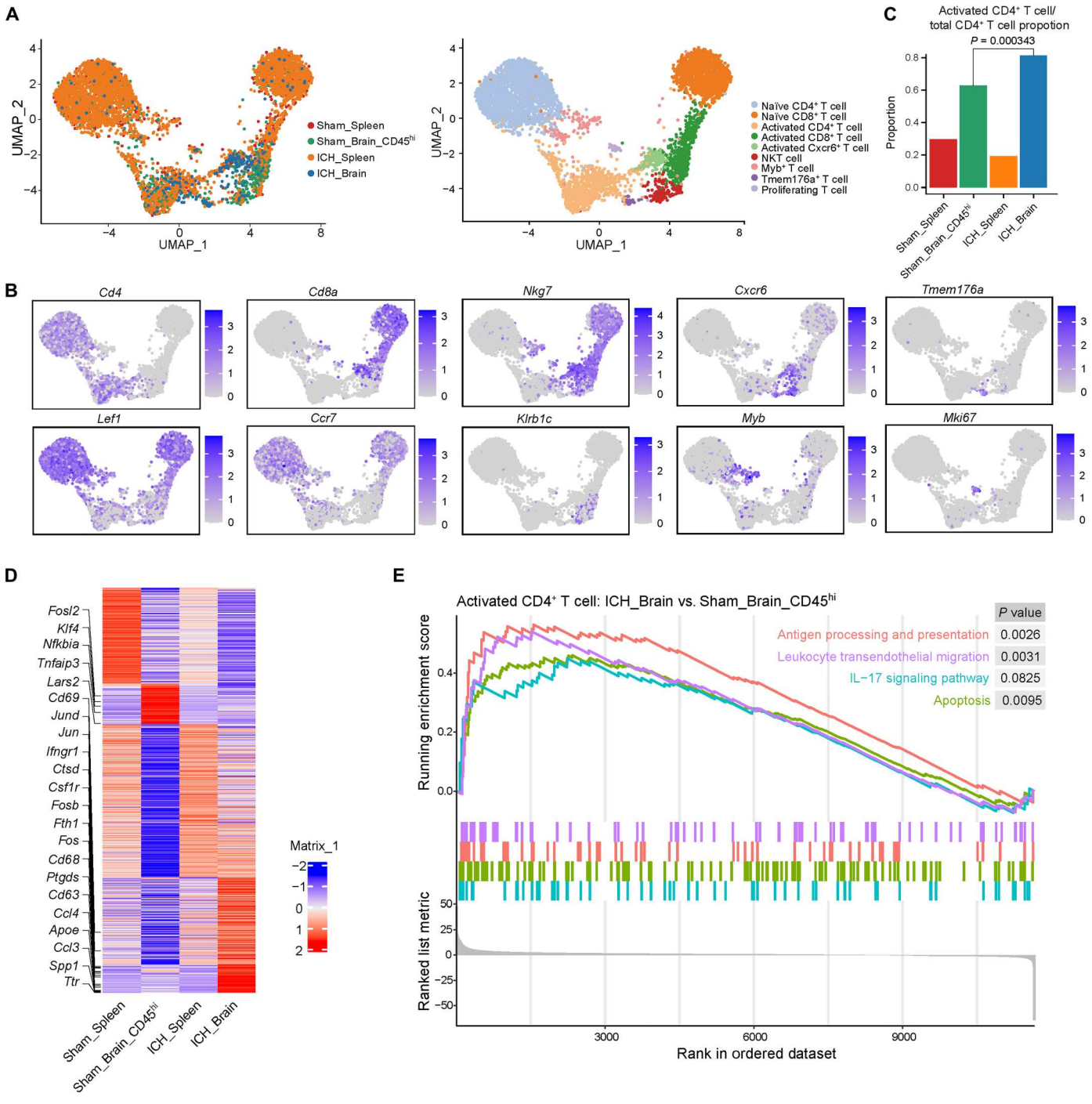

Fig. 4. Brain CD4$^+$ T cells bear unique molecular signatures versus peripheral T cells after ICH. CD3$^+$ T cells were reclustered from CD45$^+$ cell populations isolated from the spleen or brain tissues of C57BL/6 mice at 72 hours after ICH induced by autologous blood injection, based on the scRNA-seq data. (**A**) UMAP plot showing T cell subtypes of CD45$^+$ cells from sham spleen, sham brain (CD45^{hi}), ICH spleen, and ICH brain. (**B**) UMAP displaying expression of maker genes for T cell subtype identity. (**C**) Proportion of activated CD4$^+$ T cells within total CD4$^+$ T cells from sham spleen, sham brain (CD45^{hi}), ICH spleen, and ICH brain. $P = 0.000343$ by Fisher's exact test. (**D**) Heatmap showing relative average expression of differentially expressed genes in activated CD4$^+$ T cells across ICH brain, ICH spleen, sham brain, and sham spleen group. (**E**) Selected significantly enriched Kyoto Encyclopedia of Genes and Genomes pathways by gene set enrichment analysis between activated CD4$^+$ T cells from ICH brain and those from sham brain. In (A) to (E), data were pooled from 15 mice in each group.

activated CD4$^+$ T cells identified a pronounced up-regulation of antigen processing and presentation, apoptosis, leukocyte transendothelial migration, and IL-17 signaling pathways within the injured brain (Fig. 4E). From these high-resolution sequencing data, we can extrapolate possible targets relevant to their actions in secondary ICH injury. Yet, the salient results here find that T cells are activated in the ICH brain and display distinct signatures from peripheral T cells at day 3 after ICH.

Brain-infiltrating CD4$^+$ T cells promotes focal inflammation through IL-17

Upon uncovering the brain-specific signatures of post-ICH CD4$^+$ T cells where the IL-17 signaling pathway was highly enriched, A Proteome Profiler Mouse XL Cytokine Array of brain-sorted CD4$^+$ T cells, 24 and 72 hours after ICH, validated the protein expression of the enriched pathways. Compared to CD4$^+$ T cells isolated from the sham brain, CD4$^+$ T cells of the ICH brain registered a greater production in an array of proinflammatory cytokines, with IL-17 remaining the most expressed (Fig. 5, A and B). IL-17 has known proinflammatory functions, which initiate and drive inflammation in a tissue-dependent manner in response to injury or infection (*19*–*21*). This prompted us to interrogate the specific effects of increased IL-17 production from brain-infiltrated CD4$^+$ cells in acute ICH injury. To this end, CD4$^+$ T cells from IL-17$^{-/-}$ mice were isolated, and the IL-17$^{-/-}$CD4$^+$ T cells were intravenously transferred to Rag2$^{-/-}$ mice, which are devoid of mature lymphocytes. Compared to Rag2$^{-/-}$ mice receiving IL-17$^{+/+}$ CD4$^+$ cells, Rag2$^{-/-}$ mice receiving IL-17$^{-/-}$ CD4$^+$ cells exhibited reduced perihematomal edema (PHE) volumes (Fig. 5, C and D), improved endothelial survival, and preservation of blood-brain barrier (BBB) integrity (fig. S6) at 1 and 3 days after ICH induction. The increased expression of inflammatory cytokines reinforces the activated status of CD4$^+$ T cells in the ICH brain, and their increased production of IL-17 appears to be a primary cytokine-mediated method fueling perihematomal inflammation injury and worsening secondary ICH injury.

CD4$^+$ T cells induced brain endothelial cell apoptosis involving the TRAIL-DR5 pathway

As revealed by single-cell sequencing, another potential pathway, which may underlie CD4$^+$ T cell contribution to ICH injury, is through death ligand–mediated cell apoptosis (Fig. 4, D and E). To specifically investigate the apoptosis panel in CD4$^+$ T subsets, RT2 Profiler PCR Array of CD4$^+$ T lymphocytes corroborated the transcriptomic findings and identified the expression of a variety of apoptotic-related genes. At day 1 after ICH, brain-infiltrating CD4$^+$ T cells overexpressed a variety of antiapoptotic genes (*Naip1*, *Nol3*, and *Tnfrsf11b*), a transcription factor for apoptotic regulation (Atf5), and the immune stimulatory factor (Cd70) (Fig. 6, A and B). Critically, brain-infiltrating CD4$^+$ T cells were also found to

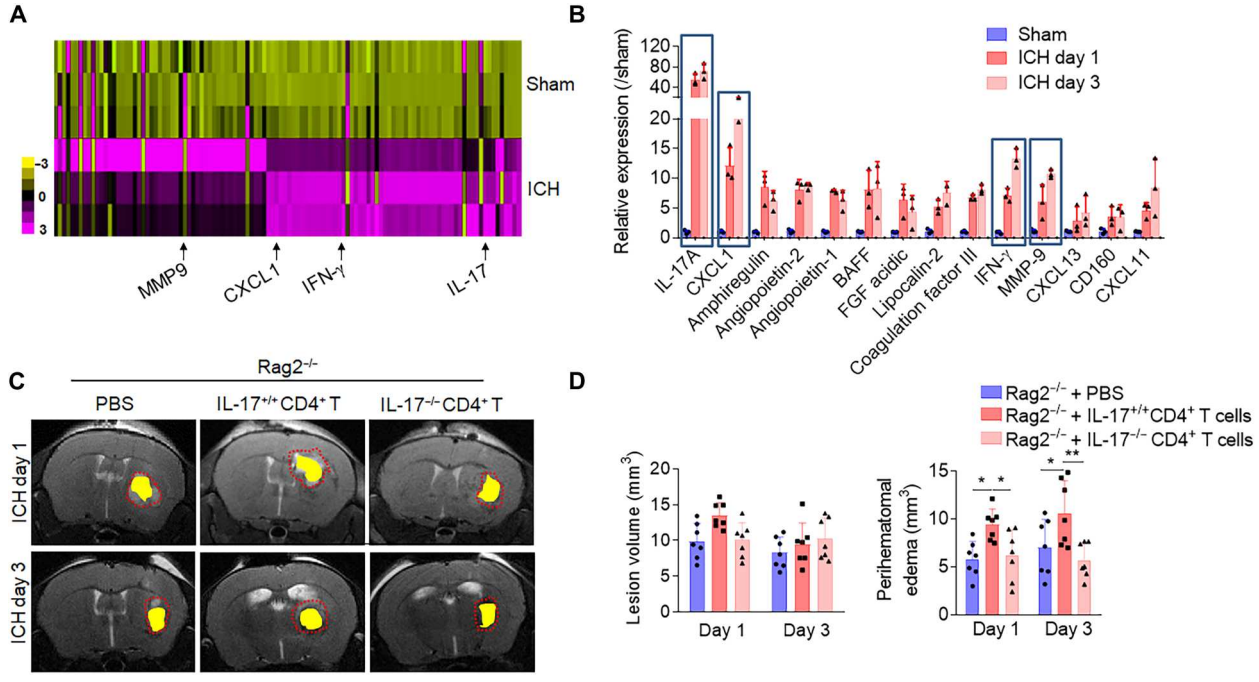

Fig. 5. Detrimental effects of brain-infiltrating CD4$^+$ T cells in ICH involves IL-17. (**A** and **B**) CD4$^+$ T cells were isolated from brain of C57BL/6 mice 24 hours and 3 days after ICH induced by autologous blood injection or sham control, and cells were then lysed for Proteome Profiler Mouse XL Cytokine Array analysis. (A) Heatmap shows relative changes of cytokine and chemokine profiles in lysates of CD4$^+$ T cells from ICH brain versus sham mice. Results were based on clustering of immunoassay measurements of the listed proteins. Purple shades represent fold change of up-regulated proteins, and yellow shades demark fold change of decreased proteins. (B) Bar graph shows highly up-regulated expression of selected cytokines/chemokines. $n = 3$ duplicates from 15 mice. One-way ANOVA followed by Tukey post hoc test. (**C** and **D**) CD4$^+$ T cells were isolated from the spleen of IL-17$^{-/-}$ mice or their IL17$^{+/+}$ littermates. IL-17$^{-/-}$ versus IL17$^{+/+}$ CD4$^+$ T cells were adoptively transferred into Rag2$^{-/-}$ mice to evaluate the role of CD4$^+$ T cell–derived IL-17 in ICH injury. Quantification of lesion volume and PHE volume was calculated in the indicated groups of collagenase induced ICH. $n = 7$ mice per group. One-way ANOVA followed by Tukey post hoc test. Means ± SD. *$P < 0.05$ and **$P < 0.01$. BAFF, B cell–activating factor; FGF, fibroblast growth factor; MMP9, matrix metalloproteinase 9.

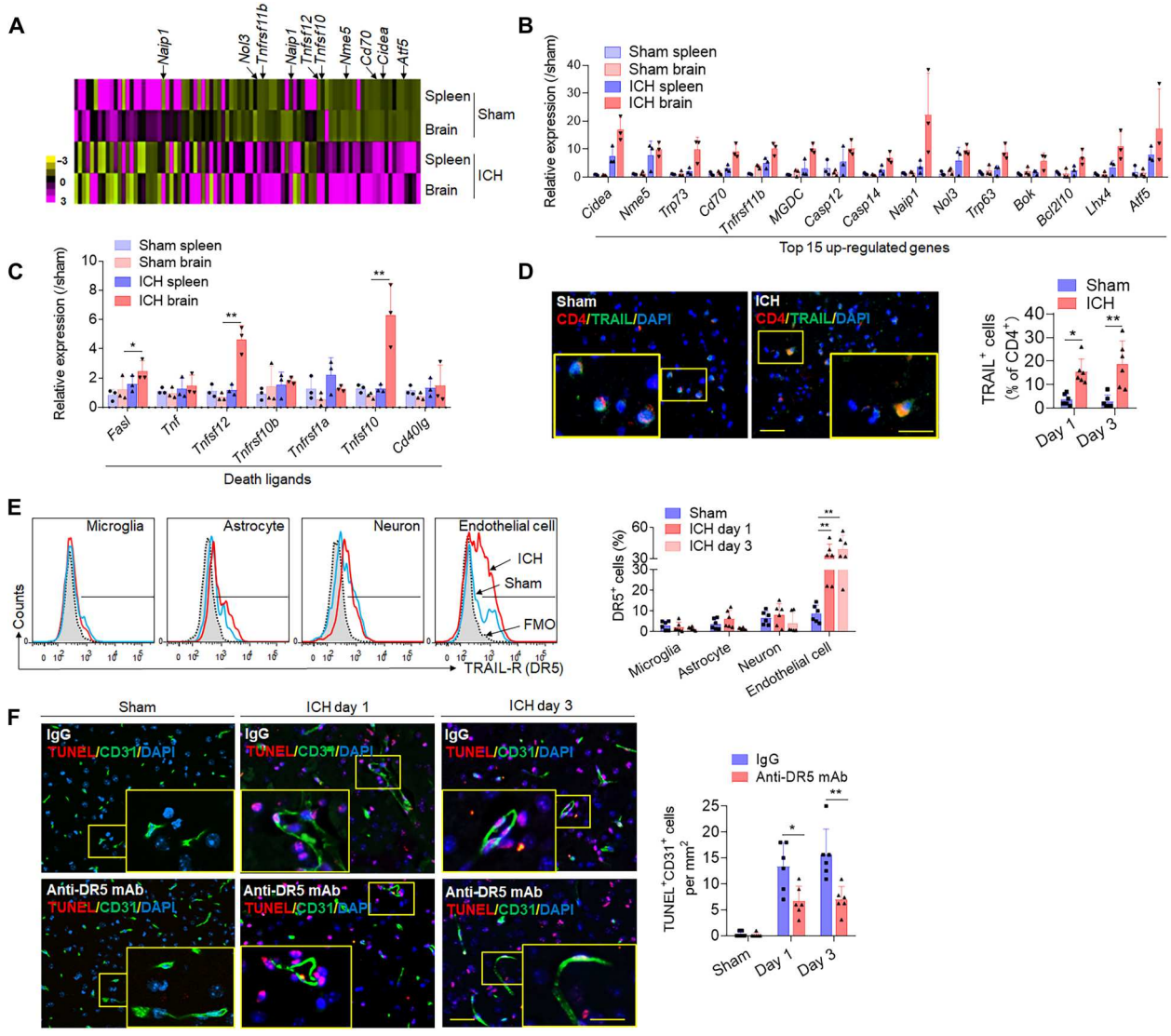

Fig. 6. CD4$^+$ T cells induce apoptosis of endothelial cells through death receptor signaling. CD4$^+$ T cells were isolated from splenocytes or brain of mice 24 hours after autologous blood injection induced ICH or sham control. FACS-sorted CD4$^+$ T cells were used for RT2 Profiler PCR Array analysis of 87 apoptosis related genes. (**A**) Heatmap shows relative changes of expression of cell apoptotic-related genes in CD4$^+$ T cells from the brain or spleen of ICH mice versus sham mice. (**B**) Quantification of top 15 up-regulated apoptosis associated genes. (**C**) Bar graph shows genes of death receptor ligands in CD4$^+$ T cells of ICH or sham mice. In (B) and (C), $n = 3$ duplicates from 15 mice. One-way ANOVA followed by Tukey post hoc test. (**D**) Immunostaining of death receptor ligand TRAIL in brain CD4$^+$ T cells of ICH or sham mice. Quantification was averaged as percentage of death receptor ligand–positive cells in CD4$^+$ T cells. Scale bars, 40 μm and (inset) 20 μm. $n = 6$ mice per group. Mann-Whitney test. (**E**) Flow cytometry plots and bar graph show expression of TRAIL receptor (DR5) in different brain cell types of sham and ICH mice, including microglia (CD45^{int}CD11b$^+$), astrocytes [glial fibrillary acidic protein positive (GFAP$^+$)], neuron (NeuN$^+$), and endothelial cells (CD31$^+$). FMO, fluorescence minus one. $n = 6$ mice per group. One-way ANOVA followed by Tukey post hoc test. (**F**) CD31$^+$ endothelial cell apoptosis was analyzed by TUNEL staining in sham mice and ICH mice with anti-DR5 monoclonal antibody (mAb) or IgG group. Scale bars, 40 μm and (inset) 20 μm. Quantification was averaged as positive cells per mm^2 in the perihematomal region. $n = 6$ mice per group. Mann-Whitney test. Means ± SD. *$P < 0.05$ and **$P < 0.01$.

up-regulate the death receptor ligands *Tnfsf10*, *Tnfsf12*, and *Fasl* (Fig. 6C). Immunostaining of murine ICH brain slices visualizes a notable increase in the expression of tumor necrosis factor–related apoptosis-inducing ligand (TRAIL), encoded by the *Tnfsf10* gene, on CD4$^+$ T cells (Fig. 6D). After gating for brain intrinsic cells expressing the TRAIL cognate receptor DR5, flow cytometry analysis revealed that DR5 was expressed by multiple brain intrinsic cell types; however, ICH robustly increased DR5 expression on brain endothelial cells (Fig. 6E). Considering that BBB disruption is a key pathophysiological hallmark of the ICH injury and driver of secondary injury and that endothelial cells are a critical cellular component of the neurovascular unit and participant in the evolution of brain edema, we postulate that CD4$^+$ T cells may exert direct endothelial cell injury via TRAIL-DR5 interaction, resulting in increased BBB disruption and brain edema. We tested this notion using a TRAIL-specific antibody to neutralize the interaction. Anti-DR5 monoclonal antibody (mAb) treatment effectively blocked CD31$^+$ endothelial cell death (Fig. 6F) and brain injury after ICH (fig.

S7). These results highlight how brain-homing $CD4^+$ T cells induce apoptosis of brain intrinsic cells through antigen-independent mechanisms, partly involving the TRAIL-DR5 pathway in ICH mice.

Depletion $CD4^+$ T cells reduced secondary ICH injury

To ascertain their contribution to secondary brain injury in ICH, $CD4^+$ T cells were depleted with an anti-CD4 mAb before ICH induction in mice. Flow cytometry quantification verified the efficacy of $CD4^+$ T cell depletion, without influencing other cell populations in peripheral blood of control mice (fig. S8). Ablation of $CD4^+$ T cells in both autologous blood and collagenase models of hemorrhagic stroke demonstrated T cell participation in the processes of secondary brain injury. $CD4^+$ depleted animals recorded reductions in PHE volume and improvement of functional outcomes at days 1, 3, and 7, compared to mice receiving IgG control, in both ICH models (Fig. 7). Depletion of $CD4^+$ cells before model induction ameliorated parameters of secondary injury, functionally supporting the detrimental capacity of $CD4^+$ T cells in acute ICH injury.

BBB permeability and neuroinflammation are key contributors toward PHE expansion. To further elucidate their roles, we looked into $CD4^+$ T cell influence on BBB integrity and local inflammation following ICH. $CD4^+$ depletion before ICH preserved the expression of major tight junction proteins, claudin-5 and ZO-1, at 3 days after ICH (Fig. 8A). In addition, $CD4^+$ T cell depletion reduced matrix metalloproteinase 9 (MMP9) protein in the ICH brain at day 3 (Fig. 8A); MMP9 is an immunemodulatory molecule that damages the matrices of the BBB following stroke and is considered a surrogate marker of BBB disruption (*22*, *23*). In $CD4^+$ T cell–depleted animals, we observed reduced leakage of Evans blue (EB) into the brain parenchyma (Fig. 8B) and a reduction brain $CD31^+$ endothelial cell death (Fig. 8, C and D). Last, we evaluated whether brain-infiltrated $CD4^+$ T lymphocytes affect the focal inflammatory milieu by quantifying leukocyte trafficking into the ICH brain of $CD4^+$ T cell–depleted mice. Compared to immunoglobulin G (IgG)–treated control mice, counts of brain-infiltrating neutrophils and monocytes were notably reduced in $CD4^+$ T cell–depleted mice at day 3 after ICH induction (Fig. 8, E and F, and fig. S9). These findings inform how infiltrating $CD4^+$ T cells engage in critical processes known to drive secondary injury following cerebral hemorrhage; considering $CD4^+$ ablation in ICH preserved BBB integrity, attenuated local inflammation, reduced lesion volume, and improved sensorimotor function in animal models. These broad responses may point to the multifaceted involvement of $CD4^+$ T cells in secondary ICH injury. Together, these results suggest that $CD4^+$ T cells are acutely recruited to the ICH brain where they exacerbate BBB disruption and focal inflammation to contribute to the secondary brain injury.

DISCUSSION

This study provides the first thorough evidence that $CD4^+$ T cells accelerate PHE development in ICH. As documented here, activated $CD4^+$ T cells accumulate in the perihematomal region and drive local inflammation via the production of IL-17 and engagement of endothelial cell death receptors, resulting in diminishing BBB integrity and augmented brain edema (fig. S10). Monoclonal antibody depletion of $CD4^+$ T cells before ICH induction limits PHE and lesion volume, attenuates local brain inflammation, maintains key tight junction proteins, and improves functional outcomes through the acute time points after ICH. The varied responses elicited by the absence of $CD4^+$ in ICH pathophysiology not only indicates their expansive effector functions but may also illustrate the complex interaction and possible redundant pathways encompassed in the pathophysiology of ICH secondary injury.

PHE is a cause of progressive tissue injury after ICH, and the extent of brain edema surrounding the hematoma directly correlates with poor outcomes in patients with ICH (*24*). PHE represents an attractive therapeutic target in part because of the extended time window during which it occurs; however, it has thus far not been successfully therapeutically modulated with available drugs, as shown by clinical trials. For example, in MISTIE III trial (Minimally Invasive Surgery Plus Alteplase for Intracerebral Hemorrhage Evacuation), Shah *et al.* reported that a minimally invasive procedure for hematoma clearance failed to show superiority to standard medical care (*25*). Inflammation contributes to the development and progression of PHE and thus subsequent neurological deterioration (*26*, *27*). In targeting ICH-induced neuroinflammation, numerous studies have explored the potential of multiple sclerosis disease-modifying drugs in the setting of stroke (*28*). Two clinical trials involving natalizumab showed that it does not confer any benefits, but four human studies with fingolimod have showcased its potential in improving recovery prospects (*29*, *30*). Therefore, there is an unmet need for the development of alternative immune-modulatory approaches in alleviating ICH injury.

After brain injury, peripheral immune cells are activated and infiltrated the injured brain where they propagate acute neuroinflammation and contribute to secondary brain injury (*8*, *31*, *32*). $CD4^+$ T cells have been suggested to be the predominant infiltrating leukocyte populations in the acute stage in experimental ICH (*8*). Emerging literatures support a role for meningeal vessels as a route for immune cell migration and post-stroke inflammation, as well (*33*, *34*). Studies, depleting lymphocyte infiltration to the brain or limiting their influx, show that T cells absence generally alleviates acute neuroinflammation and injury after ICH (*35*). Given their broad effector actions, several studies detailed T cell action in ICH related to inflammation (*36*), BBB injury (*37*), neurotoxicity (*38*), and edema formulation (*39*). Despite these reported studies, the fine kinetics and specific T cell activation in ICH brain were previously unknown. In this study, we detail their activation status by leveraging the TN-XXL approach, which tracks their differential activation in vivo. This approach revealed $CD4^+$ T cells to be substantially and time-dependently activated in the hemorrhagic brain, suggesting that the microenvironment of the ICH brain primes the infiltrating T cells.

scRNA-seq of $CD4^+$ T cell identified specific proinflammatory and proapoptotic signatures unique to the ICH brain versus their profiles in peripheral compartments. Of inflammatory genes altered in brain $CD4^+$ T cells following ICH, the IL-17 pathway stood out in its degree of enrichment. One recent study by Yang *et al.* (*40*) showed prominent accumulation of T helper 1 (T_H1) and T_H17 cell subsets of $CD4^+$ T cells at 14 days after ICH and suggested that modulating $CD4^+$ T cell differentiation may alleviate post-ICH outcomes. Our data show an early increase in $CD4^+$ T cells and the IL-17^+CD4^+ T cell (T_H17) subset in patients with ICH, which is consistent and enhances the results from the aforementioned study. From this present data, we deduce that $CD4^+$ T

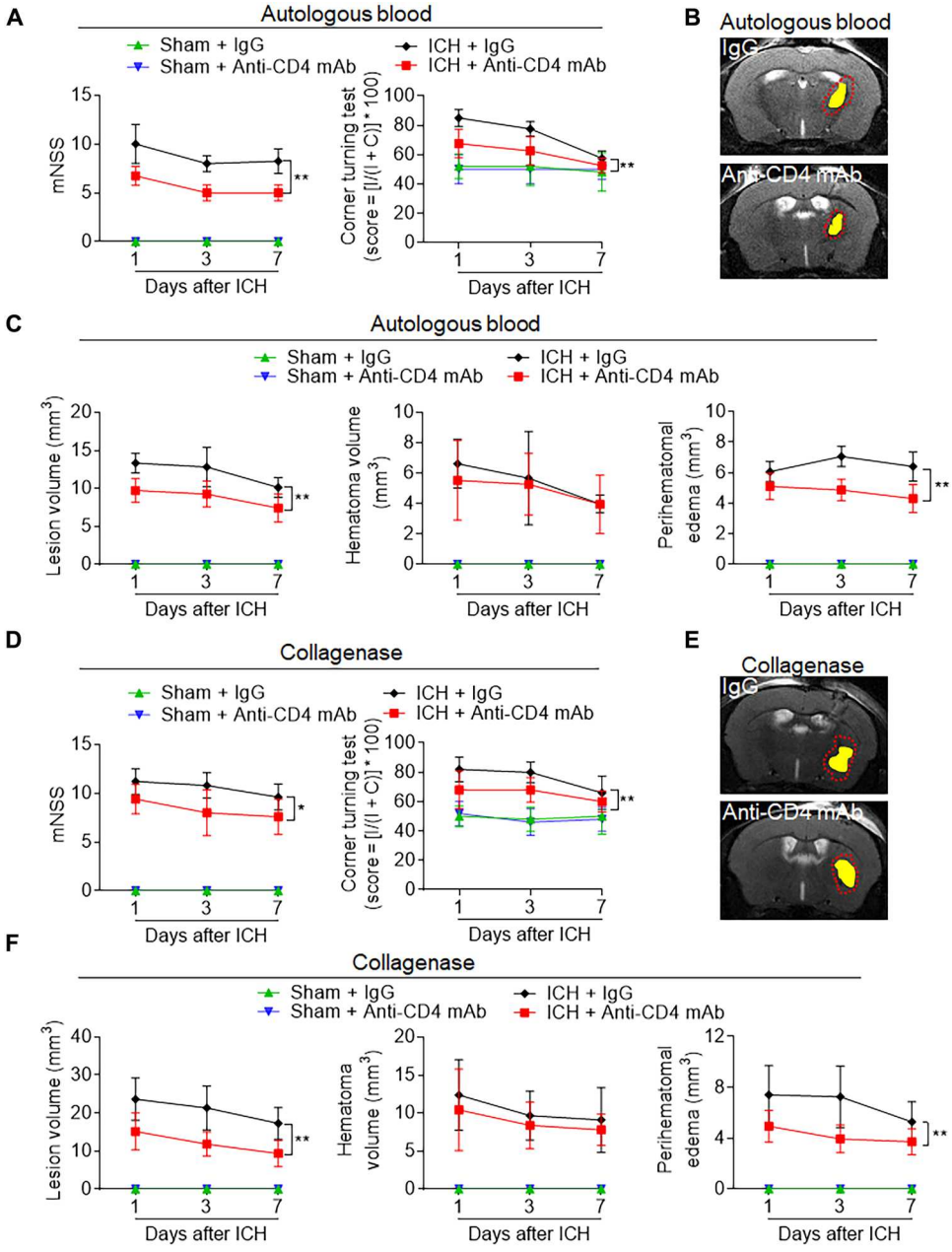

Fig. 7. Depletion of CD4$^+$ T cells ameliorates neurodeficits and ICH injury in mice. C57BL/6 mice received intraperitoneal injection of 50 μg of anti-CD4 mAb or IgG control 24 hours before ICH induction with injection of autologous blood or collagenase. (**A**) Behavioral tests including modified neurological scale score (mNSS) and corner turning test were performed in indicated groups of autologous blood–induced ICH mice. (**B**) Multimodal 7-T magnetic resonance imaging (MRI) was used to visualize lesion (T2) and hematoma (SWI) in autologous blood–induced ICH mice. PHE volume was calculated by subtracting the hematoma volume from lesion volume. Representative MRI for hematoma and PHE in mice receiving anti-CD4 mAb or IgG following ICH induction for 24 hours. (**C**) Quantification of lesion volume, hematoma, and PHE volume in the indicated groups of autologous blood–induced ICH mice. (**D**) Behavioral tests in indicated groups of collagenase induced ICH mice. (**E**) Representative MRI for hematoma and PHE in mice receiving anti-CD4 mAb or IgG following ICH induction for 24 hours. Yellow shadows represent hematoma, and red lines delineate the lesion area. (**F**) Quantification of lesion volume and PHE volume in the indicated groups of collagenase-induced ICH mice. In (A) to (F), $n = 7$ mice per group. Two-way ANOVA followed by Tukey post hoc test. Means ± SD. *$P < 0.05$ and **$P < 0.01$.

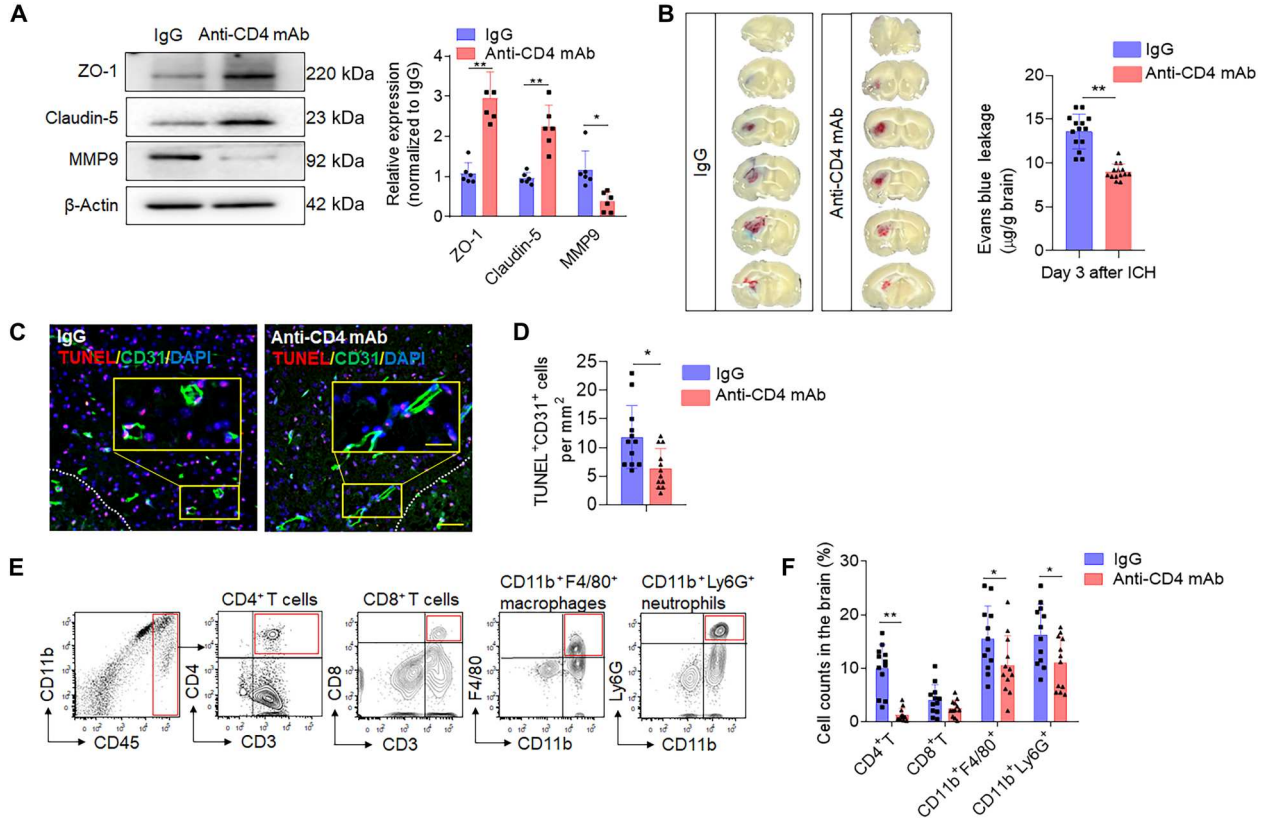

Fig. 8. Depletion of CD4$^+$ T cells reduces BBB permeability and leucocyte infiltration in ICH mice. C57BL/6 mice received intraperitoneal injection of 50 μg of anti-CD4 mAb or IgG control 24 hours before ICH induction with injection of autologous blood. (**A**) Brain tissue was collected at day 3 after ICH. Western blot shows tight junction protein level (claudin-5 and ZO-1) and MMP9 expression in ICH mice receiving anti-CD4 mAb or IgG control. Right: Quantification of ZO-1, claudin-5, and MMP9 in brain homogenates of ICH mice. $n = 6$ mice per group. Mann-Whitney test. (**B**) Concentrations of evans blue were measured at day 3 after ICH, with anti-CD4 mAb or IgG injection. $n = 14$ per group. Two-tailed unpaired Student's t test. (**C** and **D**) Immunostaining (C) and quantification (D) of TUNEL in CD31$^+$ endothelial cells of ICH mice received IgG control or anti-CD4 mAb separately. White dashed lines outline the hematoma area. Scale bars, 40 μm and (inset) 20 μm. $n = 12$ mice per group. Two-tailed unpaired Student's t test. (**E** and **F**) Single-cell suspensions from brain tissue were collected at day 3 after ICH. (E) Gating strategy of brain-infiltrating neutrophils (CD11b$^+$CD45^{hi}Ly6G$^+$), monocytes/macrophages (CD11b$^+$CD45^{hi}F4/80$^+$), CD4$^+$ T cells (CD45^{hi}CD3$^+$CD4$^+$), and CD8$^+$ T cells (CD45^{hi}CD3$^+$CD8$^+$) was shown. (F) Counts of the immune cell populations in ICH brains from mice receiving anti-CD4 mAb or IgG. $n = 12$ mice per group. Two-tailed unpaired Student's t test. Means ± SD. *$P < 0.05$ and **$P < 0.01$.

cells augment acute local inflammation in the ICH brain and worsen secondary injury primarily through IL-17 production.

We further demonstrate that CD4$^+$ T cells can induce apoptosis of intrinsic brain cells by expressing death receptor ligands, and their interaction with cells bearing cognate death receptors was restricted after receptor blockade. We highlight a series of apoptotic-related genes and death ligands up-regulated in brain CD4$^+$ T cells following ICH, particularly their surface expression of TRAIL. The unique role of TRAIL in the nervous system is revealed by the widespread expression of its receptor DR5 on various brain cell types, including neurons, astrocytes, and endothelial cells. Notably, DR5 was found to be significantly up-regulated in endothelial cells following ICH. The detrimental role of TRAIL-DR5 pathway in BBB injury was attributed with reduced endothelial cell apoptosis in the ICH brain by DR5 mAb pretreatment. These findings expose an innovative mechanism by which cells in the ICH brain can be damaged by invading T cells through the engagement of cell death receptors.

This study has several limitations. First, restricted by the source of control samples, we adopted postmortem tissue sections for control, as previously published (*9*). Second, female mice were not used. In addition, several treatments such as T cell depletion and antibody neutralization were given before ICH. The effect of treatment after injury is warranted in future preclinical studies. On the basis of single-cell sequencing data, the impact of other activated T cell subsets on ICH brain injury warrants study. Moreover, our data demonstrates that CD4$^+$ T cells are also activated in the CLN after ICH, supplementing a recent study that brain-to-CLN pathway may be involved in acute brain injury (*41*). Further studies could determine the dynamic activation of T cells within the ICH brain and CLN, as well as their specific features in the respective two compartments.

As a major cellular component of the adaptive immune system, T cells are usually activated by specific antigens presented on the surface of antigen-presentng cells (*42*), a process elapsing from days to weeks until maturity. Yet, the early T cells activation we observe in acute ICH injury indicates the involvement of antigen-independent mechanisms. This study identifies how T lymphocytes respond and participate in ICH pathology. Together, our results broaden the understanding of T lymphocyte–mediated

neuroinflammation in relation to PHE expansion after ICH, providing insights toward targeted intervention for ICH.

MATERIALS AND METHODS

Human brain tissues

Collection of human samples was performed according to protocols approved by the Institutional Review Boards of Tianjin Medical University General Hospital (Tianjin, China) and Beijing Tiantan Hospital (Beijing, China). For immunostaining of human brain tissues, six cases of control postmortem and seven ICH human brain sections were included. All seven patients had primary ICH at the basal ganglia. Fresh brain tissues of perihematomal regions were collected from patients with ICH undergoing hematoma evacuation within 72 hours after onset. Brain tissues for control cases were obtained from deceased individuals with non-neurologic diseases and without history of neurological or neuropsychiatric conditions. The selected tissue sections were region-matched with ICH tissues. Lymphocytes populations were counted at 12 different view fields for each brain slide and then quantified by averaging positive cells per mm^2. Image analysis was performed using ImageJ software (National Institutes of Health, MD, USA). Quantification was performed in a double-blinded manner. The average age between ICH and control subjects did not differ significantly [ICH: 54.7 ± 9.52 years old (y/o); control: 56.5 ± 8.55 y/o; means ± SEM; $P > 0.05$; unpaired t test].

Mice

All animal experiments were performed in accordance with the ARRIVE (Animal Research: Reporting In Vivo Experiments) guidelines and obtained approved protocols from respective Institutional Animal Care and Use Committee (IACUC). All studies were performed with adult 3- to 4-month-old male mice. C57BL/6 (RRID: MGI:2159769), $Rag2^{-/-}$ (RRID: NSRRC_0035), UCB-GFP (RRID:IMSR_JAX:004353), and $IL\text{-}17^{-/-}$ mice (RRID:IMSR_JAX:034140) and $IL17^{+/+}$ littermates were purchased from the Jackson Laboratory (Bar Harbor, Maine). All mutant mice were backcrossed to the C57BL/6 background for 12 generations. Animals were housed under pathogen-free conditions, with maximum of five animals per cage, standardized light-dark cycle conditions, and free access to food and water.

Induction of murine ICH model

ICH in mice was induced by intra-striatal injection of autologous blood or bacterial collagenase as previously described (*4*, *43*). Briefly, mice were anesthetized with ketamine/xylazine mixture by intraperitoneal injection and positioned prone in a stereotactic head frame. A ~1-mm-diameter hole was drilled on the right side of the skull (2.3 mm lateral to midline, 0.5 mm anterior to bregma). In the autologous blood model, 30 μl of nonheparinized blood was withdrawn from angular vein and infused via infusion pump to the coordinates; 5 μl was initially injected at a rate of 1 μl/min at a depth of 3.0 mm, and the remaining 25 μl was injected at an identical rate at 3.7 mm depth. The needle was left for 15 min to prevent backflow and then gently withdrawn. In the collagenase model, 0.0375 U of bacterial collagenase (type IV, Sigma-Aldrich, St. Louis, MO) in 0.5 μl of saline was administered at the same coordinates at rate of 0.5 μl/min. An identical surgical procedure with equal volume of sterile saline injection for sham-operated groups. Cranial burr hole was sealed with bone wax, and incision was sutured. Body temperature was maintained at 37.0° ± 0.5°C throughout the procedures. The total mortality rate of mice subjected to ICH was ~4.8%.

Evaluation of neurological deficit

Neurological outcome of ICH mice was evaluated by modified neurological scale score (mNSS) and corner test as reported previously (*4*, *44*). The mNSS consisted of motor, sensory, reflex, and balance assessments with the highest possible score being 18. The rating scale was as follows: A score of 13 to 18 indicates severe injury, 7 to 12 indicates moderate injury, and 1 to 6 indicates mild injury. Following surgery, each mouse was assessed on a scale from 0 to 18 after recovery from the ICH surgical procedure. Mice with a score of <6 or above a score of 13 at 24 hours after ICH (before treatment) were not included in the study.

Magnetic resonance imaging

Brain lesion size and PHE in ICH mice were evaluated with 7-T small animal magnetic resonance imaging scanner (Bruker, Billerica, MA). T2-weighted images of the brain were acquired with fat-suppressed rapid acquisition with relaxation enhancement sequence (repetition time, 4000 ms; echo time, 60 ms; slice thickness, 0.5 mm) to visualize lesion volume. Susceptibility-weighted images (SWIs; repetition time, 21.0 ms; echo time, 8.0 ms; 0.3-mm thickness) visualized hematoma volume. T2 and SWI images were manually traced and calculated by summing the volume by the distance between sections via ImageJ (National Institutes of Health), PHE volume was calculated as difference of lesion and hematoma volumes (*44*). Magnetic resonance imaging data were analyzed by two experimenters blinded to experimental conditions.

Administration of monoclonal antibodies

Ultra-LEAF–purified anti-CD4 mAb (100470, GK1.5, BioLegend, San Diego, CA) was intraperitoneally injected to deplete $CD4^+$ T cells, with a dose of 50 μg at 24 hours before ICH induction and every 5 days until the end of experiments. IgG antibody (Rat IgG2b, 400671, BioLegend) was used as control for anti-CD4 mAb. Anti-DR5 mAb (119909, MD5-1, BioLegend) was administered intraperitoneally at a dosage of 100 μg at 24 hours before ICH induction. Purified hamster IgG isotype antibody (400902, HTK888, BioLegend) was used as a control for anti-DR5 mAb.

Immunostaining

Immunostaining procedure of brain slices was conducted as previously described (*4*). Primary antibodies were incubated at 4°C overnight at vendor concentration. After washing with cold PBS, slices were incubated with fluorescence-conjugated secondary antibodies at room temperature for 1 hour. Slides were washed and mounted with a mounting medium containing 4′, 6-diamidino-2-phenylindole (DAPI; ab104139, Abcam, Cambridge, UK). Primary antibodies used were as follows: anti-human CD4 (EPR6855, ab133616, Abcam), anti-human CD8a (D8A8Y, 85336, Cell Signaling Technology), anti-human CD69 (EPR21814, ab233396, Abcam), anti-human IL-17 (4K5F6, ab189377, Abcam), anti-human IL-4 (PA5-25165, Invitrogen), anti-human interferon-γ (IFN-γ) (15365-1-AP, Proteintech), anti-human Foxp3 (12632, Cell Signaling Technology), anti-mouse CD4 (GK1.5, MAB554-100, R&D Systems), anti-mouse CD8 (EPR20305, ab209775, Abcam), anti-human/mouse CD19 (6OMP31, 14-0194-82, eBioscience), anti-human/mouse

TRAIL-R2 (DR5, PA5-19895, Invitrogen), and anti-mouse CD31 (D8V9E, 77699, Cell Signaling Technology). Secondary antibodies used were as follows: Alexa Fluor 594 anti-rat IgG (ab150160, Abcam), Alexa Fluor 594 anti-rabbit IgG (ab150080, Abcam), Alexa Fluor 488 anti-rabbit IgG (ab150077, Abcam), Alexa Fluor 488 anti-mouse IgG (ab150113, Abcam), and Alexa Fluor 488 Anti-rat IgG (ab150157, Abcam). TUNEL (terminal deoxynucleotidyl transferase–mediated deoxyuridine triphosphate nick end labeling) staining used the in situ 5-bromo-2′-deoxyuridine–Red DNA Fragmentation (TUNEL) Assay Kit (ab66110, Abcam). All Images were acquired on a fluorescent microscope (Olympus, model BX-61, Center Valley, PA, USA). Image analysis was performed using ImageJ software (National Institutes of Health, MD, USA).

Cell isolation and passive transfer of CD4$^+$ T cells

CD4$^+$ T cells were sorted from pooled splenocytes of wild type, IL-17$^{-/-}$ mouse strains, or IL17$^{+/+}$ littermates. Spleen tissues were separated and placed on a premoistened 70-μm cell strainer and then gently homogenized with the end of a 1-ml syringe plunger. The strainer was washed with 10 ml of erythrocyte lysis buffer (349202, BD FACS, San Jose, CA, USA), and the eluted cells were incubated for 5 min at room temperature and washed with 40 ml of phosphate-buffered saline (PBS). Cell suspensions were simultaneously incubated for 30 min with alloohycocyanin (APC)-conjugated anti-CD4 (RM4-4, 116013), and phycoerythrin (PE)–conjugated anti-CD3 (17A2, 100205). Then, CD4$^+$ T cells were purified via two rounds of cell sorting selection (CD4$^+$CD3$^+$) with the high-speed sort of FACS Aria III flow cytometer. Purity of sorted CD4$^+$ T cells was verified by flow cytometry before transfer. Highly purified (>99%) CD4$^+$ T cells (1×10^7) were injected into tail vein of Rag2$^{-/-}$ recipient mice.

Cytokine array

Cytokine secretion profile of ICH brain CD4$^+$ T cells was evaluated by Proteome Profiler Mouse XL Cytokine Array. CD4$^+$ cells were sorted from the whole brain of ICH or sham mice. Cytokine levels in these samples were detected using the Mouse XL Cytokines Array Kit (R&D Systems Inc. Minneapolis, MN) according to the manufacturer′s instructions.

Flow cytometry

Preparation of single-cell suspensions for flow cytometry from the spleen, brain, CLNs, and blood were prepared as previously reported (*4*, *45*). Briefly, mice were euthanized by lethal anesthesia via isoflurane, and then the brain and spleen were removed. Brain tissues were minced and incubated with collagenase IV and deoxyribonuclease at 37°C for 30 min. After removing the myelin debris by centrifugation in 30% Percoll, single cells were suspended in 1% bovine serum albumin. Spleen tissues were minced and strained through a 70-μm cell strainer; red blood cells were removed using a lysis buffer. For CLN tissue, the ventral neck area of mice was dissected, and bilateral CLNs were removed before or after ICH. The lymph node tissues were minced and strained through a 70-μm cell strainer. Thereafter, single-cell suspensions were placed in conical centrifuge tubes (10^6 cells per tube) and stained with fluorescently conjugated antibodies. For intracellular staining, cells were fixed in fixation buffer for 20 min after surface marker staining. After washing twice in permeabilization buffer, cells were incubated with antibodies in the staining buffer for 45 min. All flow cytometry antibodies were sourced from BioLegend, unless otherwise indicated. Antibodies used were as follows: CD45-APC-Cy7 (30-F11, 103116), CD4-APC (RM4-4, 116013), CD4-PE (GK1.5, 100408), CD3–fluorescein isothiocyanate (FITC) (17A2, 100204), CD3-PE (17A2, 100205), CD8a-BV421 (53-6.7, 100737), CD69-BV421 (H1.2F3, 104527), IL-17A–PE-Cy7 (TC11-18H10.1, 506921), F4/80-FITC (BM8, 123017), Ly6G-APC (1A8, 127613), CD11b-PE-Cy7 (17A2, 101216), TRAIL-R2-FITC (MD5-1, A15750, Invitrogen), NeuN-AF647 (EPR12763, ab190565, Abcam), CD31-BV421 (390, 102423), glial fibrillary acidic protein–PE (1B4, 561483, BD Bioscience), IL-4–APC (11B11, 504106), IFN-γ–BV605 (XMG1.2, 505839), CD25-BV421 (PC61, 102034), and Foxp3-PE (MF-14, 126404). Samples were run on FACSAria (BD Biosciences) and analyzed using FACS Diva and FlowJo X software (Informer Technologies, Ashland, OR).

Single-cell RNA sequencing

CD45$^+$ single cells were sorted by flow cytometry for sequencing. The optimized fluorescence-activated cell sorter (FACS) sorting were performed on CD45^{hi} cell population to obtain enough CD4$^+$ T cells in sham brains for subclustering and data processing (Sham brain_2 in Fig. 3A).10X Genomics platform of Tulane University Single Cell Sequencing Core and Huada Gene (Shenzhen, PRC) prepared the barcode libraries with the Single Cell 3′ Reagent Kit v2 (10X Genomics) along the manufacturer′s instructions. RNA-seq performed at a sequencing depth of approximately 50,000 reads per cell.

scRNA-seq data processing

Raw files (FASTQ format) were processed with Cell Ranger software (v5.0.1), which performed mapping to the mm10 transcriptome, filtering, barcode counting, and unique molecular identifier (UMI) counting and lastly generated feature-by-barcode UMI matrix. Scrublet (*46*) software was used to remove potential doublets for individual samples. Seurat (v3.1.5) was used for downstream analysis. Low-quality cells, <500 genes expressed or with <2500 UMIs, were excluded at the initial quality control step. Cells >15% mitochondrial UMIs were removed. Library-size normalization was performed on the UMI-collapsed gene expression values for each cell barcode by scaling the total number of transcripts and multiplying by 10,000. Data were then log-transformed for further downstream analysis.

Two thousand genes with highest variance were initially identified using the FindVariableGenes function. Batch effects were corrected by using the fastMNN function of batchelor R package (*47*), a fast version of the mutual nearest neighbors (MNNs) method, and the first 20 components of MNN was considered to reduce the dimensionality. Cells were clustered with Seurat′s FindClusters function. For visualization, we applied run UMAP to cluster cells on scatter plots. Marker genes were defined as genes with an adjusted P value < 0.05 tested with a nonparametric Wilcoxon rank-sum test (table S1). KEGG pathway enrichment analysis was performed by gene set enrichment analysis function in clusterProfiler (v3.14.3) (*48*). Activation feature scores were calculated by using AddModuleScore function in Seurat with an array of cell activated feature genes based on published literatures (*Ms4a4b*, *Ms4a6b*, *Cxcl10*, *Itk*, *Prkcq*, *Ccnd1*, *Ccnd2*, *Ccnd3*, *Hmox1*, *Ccl5*, *Dusp1*, *Klf4*, *Jun*, and *Junb*) (*49*–*57*).

Apoptosis-related gene evaluation

Apoptosis-related genes in FACS-sorted $CD4^+$ T cells from the spleen or brain of ICH or sham mice were evaluated by the 87 gene RT2 Profiler PCR Array Kit (330231, QIAGEN). mRNAs were extracted from isolated cells with TRIzol reagent (Invitrogen). The expression of apoptosis-related genes was determined according to the manufacturer's protocol.

In vivo detection and T cell activation via TN-XXL

TN-XXL pcDNA3 was a gift from Oliver Griesbeck (Addgene plasmid # 45797; http://n2t.net/addgene:45797; RRID:Addgene_45797). FACS-isolated $CD4^+$ T cells from wild-type mice spleen were transfected with TN-XXL as reported (*18*, *58*). Briefly, isolated cells were suspended in retrovirus supernatant supplemented with polybrene (8 μg/ml; Sigma-Aldrich) and IL-2 (10 ng/ml). Transfection was achieved by centrifuge at 450 relative centrifugal force for 90 min at room temperature. Cells were washed and then intravenously transferred to recipient mice. Mock transduced (vector without TN-XXL) $CD4^+$ T cells were used as a control. TN-XXL–expressing or mock-transduced $CD4^+$ T cells were then injected into $Rag2^{-/-}$ mice. The FRET of TN-XXL–expressing $CD4^+$ T cells in the brain and peripheral tissues was detected using flow cytometry. TN-XXL consists of CFP as FRET donor and cpCitrine as FRET acceptor. These proteins are linked by the calcium-sensitive double C-terminal lobe of TnC. After binding to free calcium, TnC undergoes a conformational change that leads to energy transfer from the donor to the acceptor fluorophore, resulting in a drop in CFP fluorescence and an increase in cpCitrine fluorescence. FACSCanto system was used for intracellular calcium measurements, with a 405-nm laser for excitation of CFP and 465/30 nm and 530/30 nm bandpass filters for CFP and FRET emission, respectively, along with a 488-nm laser with a 530/30-nm bandpass filter for excitation and emission of cpCitrine.

Western blot

Mice treated with anti-CD4 mAb or IgG control were euthanized days 1 and 3 after ICH. After pericardiac perfusion with cold PBS, ipsilateral brain were harvested and homogenized in radioimmunoprecipitation assay lysis buffer (Thermo Fisher Scientific, Waltham, MA) with 1 mM phenyl-methanesulfonyl fluoride (Thermo Fisher Scientific, Waltham, MA) and phosphatase inhibitor cocktail (sc-45065, Santa Cruz Biotechnology, Dallas, TX). The supernatant from centrifugation-collected total proteins was separated by 10% SDS–polyacrylamide gel electrophoresis and transferred onto a nitrocellulose membrane (Amersham Biosciences, Piscataway, NJ). Immunoblot analysis for primary antibody incubation of ZO-1 (a0659, ABclonal), claudin 5 (29767-1-AP, Proteintech), and MMP9 (RM1020, ab283575, Abcam) at 4°C overnight. β-Actin (3700, Cell Signaling Technology) was internal control. Membrane was incubated with horseradish peroxidase–conjugated anti-rabbit or anti-mouse secondary antibody (Thermo Fisher Scientific, Waltham, MA) for 1 hour at room temperature. Chemiluminescent intensity was measured with ImageQuant LAS 4000 (GE Healthcare Life Sciences, Uppsala, Sweden).

EB analysis

To determine BBB permeability, EB dye (Sigma-Aldrich, St. Louis, MO) was used for each group of mice. Mice were intravenously injected with EB dye (2% in saline, 4 ml/kg) 4 hours before euthanization. The ipsilateral hemisphere was weighed and then homogenized into a tube with 2 ml of formamide (Sigma-Aldrich, St. Louis, MO). After incubation in water bath at 60°C for 72 hours, supernatants were collected and the optical density at 600 nm was measured by a microplate reader (Thermo Fisher Scientific, Varioskan Flash, USA). The concentration of EB was calculated with the following formula: EB content in brain tissue (μg/g wet brain) = EB concentration × formamide (ml)/wet weight (g).

Statistical analysis

Animals were randomly assigned to treatment conditions. Randomization was based on the random number generator function in Microsoft Excel software. All results were analyzed by investigators blinded to the treatment. The exclusion criteria are described in the individual method sections. No power analysis predetermined sample sizes were applied; however, the sample sizes were similar to those reported in our prior publications (*59*, *60*). Data are presented as the means ± SD. Statistical significance was determined by two-tailed unpaired Student's *t* test for parametric data in univariate analysis, Mann-Whitney test for nonparametric data, one-way analysis of variance (ANOVA) followed by Tukey post hoc test for three or more groups, and two-way ANOVA to assess the entire time course variation, accompanied by Tukey post hoc test for multiple comparisons. Fisher's exact test was used to determine differentially expressed genes in scRNA-seq between indicated groups. $P < 0.05$ was considered statistically significant. All statistical analyses were performed using Prism 8.0 software (GraphPad, San Diego, CA, USA).

Supplementary Materials

This PDF file includes:

Figs. S1 to S10
Table S1

View/request a protocol for this paper from *Bio-protocol*.

References and notes

1. Q. Bai, M. Xue, V. W. Yong, Microglia and macrophage phenotypes in intracerebral haemorrhage injury: Therapeutic opportunities. *Brain* **143**, 1297–1314 (2020).
2. Y. Fu, J. Hao, N. Zhang, L. Ren, N. Sun, Y. J. Li, Y. Yan, D. Huang, C. Yu, F. D. Shi, Fingolimod for the treatment of intracerebral hemorrhage: A 2-arm proof-of-concept study. *JAMA Neurol.* **71**, 1092–1101 (2014).
3. Y. Fu, Q. Liu, J. Anrather, F. D. Shi, Immune interventions in stroke. *Nat. Rev. Neurol.* **11**, 524–535 (2015).
4. S. X. Shi, Y. J. Li, K. Shi, K. Wood, A. F. Ducruet, Q. Liu, IL (Interleukin)-15 Bridges Astrocyte-Microglia Crosstalk and Exacerbates Brain Injury Following Intracerebral Hemorrhage. *Stroke* **51**, 967–974 (2020).
5. K. Shi, D. C. Tian, Z. G. Li, A. F. Ducruet, M. T. Lawton, F. D. Shi, Global brain inflammation in stroke. *Lancet Neurol.* **18**, 1058–1066 (2019).
6. R. F. Keep, Y. Hua, G. Xi, Intracerebral haemorrhage: Mechanisms of injury and therapeutic targets. *Lancet Neurol.* **11**, 720–731 (2012).
7. M. C. Loftspring, J. McDole, A. Lu, J. F. Clark, A. J. Johnson, Intracerebral hemorrhage leads to infiltration of several leukocyte populations with concomitant pathophysiological changes. *J. Cereb. Blood Flow Metab.* **29**, 137–143 (2009).
8. E. Mracsko, E. Javidi, S. Y. Na, A. Kahn, A. Liesz, R. Veltkamp, Leukocyte invasion of the brain after experimental intracerebral hemorrhage in mice. *Stroke* **45**, 2107–2114 (2014).
9. Z. Li, M. Li, S. X. Shi, N. Yao, X. Cheng, A. Guo, Z. Zhu, X. Zhang, Q. Liu, Brain transforms natural killer cells that exacerbate brain edema after intracerebral hemorrhage. *J. Exp. Med.* **217**, e20200213 (2020).
10. T. Korn, A. Kallies, T cell responses in the central nervous system. *Nat. Rev. Immunol.* **17**, 179–194 (2017).

11. M. Lever, P. K. Maini, P. A. van der Merwe, O. Dushek, Phenotypic models of T cell activation. *Nat. Rev. Immunol.* **14**, 619–629 (2014).
12. J. T. Walsh, S. Hendrix, F. Boato, I. Smirnov, J. Zheng, J. R. Lukens, S. Gadani, D. Hechler, G. Golz, K. Rosenberger, T. Kammertons, J. Vogt, C. Vogelaar, V. Siffrin, A. Radjavi, A. Fernandez-Castaneda, A. Gaultier, R. Gold, T. D. Kanneganti, R. Nitsch, F. Zipp, J. Kipnis, MHCII-independent CD4+ T cells protect injured CNS neurons via IL-4. *J. Clin. Invest.* **125**, 699–714 (2015).
13. G. Caron, D. Duluc, I. Fremaux, P. Jeannin, C. David, H. Gascan, Y. Delneste, Direct stimulation of human T cells via TLR5 and TLR7/8: Flagellin and R-848 up-regulate proliferation and IFN-gamma production by memory CD4+ T cells. *J. Immunol.* **175**, 1551–1557 (2005).
14. M. Komai-Koma, L. Jones, G. S. Ogg, D. Xu, F. Y. Liew, TLR2 is expressed on activated T cells as a costimulatory receptor. *Proc. Natl. Acad. Sci. U.S.A.* **101**, 3029–3034 (2004).
15. C. Kleinschnitz, N. Schwab, P. Kraft, I. Hagedorn, A. Dreykluft, T. Schwarz, M. Austinat, B. Nieswandt, H. Wiendl, G. Stoll, Early detrimental T-cell effects in experimental cerebral ischemia are neither related to adaptive immunity nor thrombus formation. *Blood* **115**, 3835–3842 (2010).
16. J. Zhang, K. Shi, Z. Li, M. Li, Y. Han, L. Wang, Z. Zhang, C. Yu, F. Zhang, L. Song, J.-F. Dong, A. La Cava, K. N. Sheth, F.-D. Shi, Organ- and cell-specific immune responses are associated with the outcomes of intracerebral hemorrhage. *FASEB J.* **32**, 220–229 (2018).
17. N. I. Kyratsous, I. J. Bauer, G. Zhang, M. Pesic, I. Bartholomaus, M. Mues, P. Fang, M. Worner, S. Everts, J. W. Ellwart, J. M. Watt, B. V. L. Potter, R. Hohlfeld, H. Wekerle, N. Kawakami, Visualizing context-dependent calcium signaling in encephalitogenic T cells in vivo by two-photon microscopy. *Proc. Natl. Acad. Sci. U.S.A.* **114**, E6381–E6389 (2017).
18. M. Mues, I. Bartholomaus, T. Thestrup, O. Griesbeck, H. Wekerle, N. Kawakami, G. Krishnamoorthy, Real-time in vivo analysis of T cell activation in the central nervous system using a genetically encoded calcium indicator. *Nat. Med.* **19**, 778–783 (2013).
19. H. Kebir, K. Kreymborg, I. Ifergan, A. Dodelet-Devillers, R. Cayrol, M. Bernard, F. Giuliani, N. Arbour, B. Becher, A. Prat, Human TH17 lymphocytes promote blood-brain barrier disruption and central nervous system inflammation. *Nat. Med.* **13**, 1173–1175 (2007).
20. I. M. Stromnes, L. M. Cerretti, D. Liggitt, R. A. Harris, J. M. Goverman, Differential regulation of central nervous system autoimmunity by T(H)1 and T(H)17 cells. *Nat. Med.* **14**, 337–342 (2008).
21. H. Park, Z. Li, X. O. Yang, S. H. Chang, R. Nurieva, Y. H. Wang, Y. Wang, L. Hood, Z. Zhu, Q. Tian, C. Dong, A distinct lineage of CD4 T cells regulates tissue inflammation by producing interleukin 17. *Nat. Immunol.* **6**, 1133–1141 (2005).
22. Y. Shigemori, Y. Katayama, T. Mori, T. Maeda, T. Kawamata, Matrix metalloproteinase-9 is associated with blood-brain barrier opening and brain edema formation after cortical contusion in rats. *Acta Neurochir. Suppl.* **96**, 130–133 (2006).
23. T. L. Barr, L. L. Latour, K. Y. Lee, T. J. Schaewe, M. Luby, G. S. Chang, Z. El-Zammar, S. Alam, J. M. Hallenbeck, C. S. Kidwell, S. Warach, Blood-brain barrier disruption in humans is independently associated with increased matrix metalloproteinase-9. *Stroke* **41**, e123–e128 (2010).
24. S. Urday, W. T. Kimberly, L. A. Beslow, A. O. Vortmeyer, M. H. Selim, J. Rosand, J. M. Simard, K. N. Sheth, Targeting secondary injury in intracerebral haemorrhage--perihaematomal oedema. *Nat. Rev. Neurol.* **11**, 111–122 (2015).
25. V. A. Shah, R. E. Thompson, G. Yenokyan, J. N. Acosta, R. Avadhani, R. Dlugash, N. McBee, Y. Li, B. M. Hansen, N. Ullman, G. Falcone, I. A. Awad, D. F. Hanley, W. C. Ziai, One-Year Outcome Trajectories and Factors Associated with Functional Recovery Among Survivors of Intracerebral and Intraventricular Hemorrhage With Initial Severe Disability. *JAMA Neurol.* **79**, 856–868 (2022).
26. X. Hu, T. M. De Silva, J. Chen, F. M. Faraci, Cerebral vascular disease and neurovascular injury in ischemic stroke. *Circ. Res.* **120**, 449–471 (2017).
27. C. Iadecola, J. Anrather, The immunology of stroke: From mechanisms to translation. *Nat. Med.* **17**, 796–808 (2011).
28. A. M. Aloizou, V. Siokas, G. Pateraki, I. Liampas, C. Bakirtzis, Z. Tsouris, G. Lazopoulos, D. Calina, A. O. Docea, A. Tsatsakis, D. P. Bogdanos, E. Dardiotis, Thinking outside the ischemia box: Advancements in the use of multiple Sclerosis drugs in ischemic stroke. *J. Clin. Med.* **10**, 630 (2021).
29. J. Elkins, R. Veltkamp, J. Montaner, S. C. Johnston, A. B. Singhal, K. Becker, M. G. Lansberg, W. Tang, I. Chang, K. Muralidharan, S. Gheuens, L. Mehta, M. S. V. Elkind, Safety and efficacy of natalizumab in patients with acute ischaemic stroke (ACTION): A randomised, placebo-controlled, double-blind phase 2 trial. *Lancet Neurol.* **16**, 217–226 (2017).
30. Y. Fu, N. Zhang, L. Ren, Y. Yan, N. Sun, Y. J. Li, W. Han, R. Xue, Q. Liu, J. Hao, C. Yu, F. D. Shi, Impact of an immune modulator fingolimod on acute ischemic stroke. *Proc. Natl. Acad. Sci. U.S.A.* **111**, 18315–18320 (2014).
31. M. Durocher, B. Knepp, A. Yee, G. Jickling, F. Rodriguez, K. Ng, X. Zhan, F. Hamade, E. Ferino, H. Amini, P. Carmona-Mora, H. Hull, B. P. Ander, F. R. Sharp, B. Stamova, Molecular Correlates of Hemorrhage and Edema Volumes Following Human Intracerebral Hemorrhage Implicate Inflammation, Autophagy, mRNA Splicing, and T Cell Receptor Signaling. *Transl. Stroke Res.* **12**, 754–777 (2021).
32. E. Mracsko, R. Veltkamp, Neuroinflammation after intracerebral hemorrhage. *Front. Cell. Neurosci.* **8**, 388 (2014).
33. R. Cai, C. Pan, A. Ghasemigharagoz, M. I. Todorov, B. Forstera, S. Zhao, H. S. Bhatia, A. Parra-Damas, L. Mrowka, D. Theodorou, M. Rempfler, A. L. R. Xavier, B. T. Kress, C. Benakis, H. Steinke, S. Liebscher, I. Bechmann, A. Liesz, B. Menze, M. Kerschensteiner, M. Nedergaard, A. Erturk, Panoptic imaging of transparent mice reveals whole-body neuronal projections and skull-meninges connections. *Nat. Neurosci.* **22**, 317–327 (2019).
34. J. H. Ahn, H. Cho, J. H. Kim, S. H. Kim, J. S. Ham, I. Park, S. H. Suh, S. P. Hong, J. H. Song, Y. K. Hong, Y. Jeong, S. H. Park, G. Y. Koh, Meningeal lymphatic vessels at the skull base drain cerebrospinal fluid. *Nature* **572**, 62–66 (2019).
35. W. B. Rolland, T. Lekic, P. R. Krafft, Y. Hasegawa, O. Altay, R. Hartman, R. Ostrowski, A. Manaenko, J. Tang, J. H. Zhang, Fingolimod reduces cerebral lymphocyte infiltration in experimental models of rodent intracerebral hemorrhage. *Exp. Neurol.* **241**, 45–55 (2013).
36. L. L. Mao, H. Yuan, W. W. Wang, Y. J. Wang, M. F. Yang, B. L. Sun, Z. Y. Zhang, X. Y. Yang, Adoptive regulatory T-cell therapy attenuates perihematomal inflammation in a mouse model of experimental intracerebral hemorrhage. *Cell. Mol. Neurobiol.* **37**, 919–929 (2017).
37. X. Zhang, W. Liu, J. Yuan, H. Zhu, Y. Yang, Z. Wen, Y. Chen, L. Li, J. Lin, H. Feng, T lymphocytes infiltration promotes blood-brain barrier injury after experimental intracerebral hemorrhage. *Brain Res.* **1670**, 96–105 (2017).
38. L. Gao, P. P. Li, T. Y. Shao, X. Mao, H. Qi, B. S. Wu, M. Shan, L. Ye, H. W. Cheng, Neurotoxic role of interleukin-17 in neural stem cell differentiation after intracerebral hemorrhage. *Neural Regen. Res.* **15**, 1350–1359 (2020).
39. Q. Zhong, K. Zhou, Q. L. Liang, S. Lin, Y. C. Wang, X. Y. Xiong, Z. Y. Meng, T. Zhao, W. Y. Zhu, Y. R. Yang, M. F. Liao, Q. W. Gong, L. Liu, A. Xiong, J. Hao, J. Wang, Q. W. Yang, Interleukin-23 secreted by activated macrophages drives γδT cell production of interleukin-17 to aggravate secondary injury after intracerebral hemorrhage. *J. Am. Heart Assoc.* **5**, e004340 (2016).
40. H. Yang, X. Gao, W. Xiao, J. Su, Y. Li, W. Ni, Y. Gu, Minocycline Alleviates White Matter Injury following Intracerebral Hemorrhage by Regulating $CD4^+$ T Cell Differentiation via Notch1 Signaling Pathway. *Oxid. Med. Cell. Longev.* **2022**, 3435267 (2022).
41. E. Esposito, B. J. Ahn, J. Shi, Y. Nakamura, J. H. Park, E. T. Mandeville, Z. Yu, S. J. Chan, R. Desai, A. Hayakawa, X. Ji, E. H. Lo, K. Hayakawa, Brain-to-cervical lymph node signaling after stroke. *Nat. Commun.* **10**, 5306 (2019).
42. S. L. Swain, K. K. McKinstry, T. M. Strutt, Expanding roles for $CD4^+$ T cells in immunity to viruses. *Nat. Rev. Immunol.* **12**, 136–148 (2012).
43. M. Li, Z. Li, H. Ren, W. N. Jin, K. Wood, Q. Liu, K. N. Sheth, F. D. Shi, Colony stimulating factor 1 receptor inhibition eliminates microglia and attenuates brain injury after intracerebral hemorrhage. *J. Cereb. Blood Flow Metab.* **37**, 2383–2395 (2017).
44. S. X. Shi, K. Shi, Q. Liu, Brain injury instructs bone marrow cellular lineage destination to reduce neuroinflammation. *Sci. Transl. Med.* **13**, (2021).
45. Y. Gan, Q. Liu, W. Wu, J. X. Yin, X. F. Bai, R. Shen, Y. Wang, J. Chen, A. La Cava, J. Poursine-Laurent, W. Yokoyama, F. D. Shi, Ischemic neurons recruit natural killer cells that accelerate brain infarction. *Proc. Natl. Acad. Sci. U.S.A.* **111**, 2704–2709 (2014).
46. S. L. Wolock, R. Lopez, A. M. Klein, Scrublet: Computational identification of cell doublets in single-cell transcriptomic data. *Cell Syst.* **8**, 281–291.e9 (2019).
47. L. Haghverdi, A. T. L. Lun, M. D. Morgan, J. C. Marioni, Batch effects in single-cell RNA-sequencing data are corrected by matching mutual nearest neighbors. *Nat. Biotechnol.* **36**, 421–427 (2018).
48. G. Yu, L. G. Wang, Y. Han, Q. Y. He, clusterProfiler: An R package for comparing biological themes among gene clusters. *OMICS* **16**, 284–287 (2012).
49. Y. Sui, W. Zeng, MS4A4A Regulates Arginase 1 Induction during Macrophage Polarization and Lung Inflammation in Mice. *Eur. J. Immunol.* **50**, 1602–1605 (2020).
50. L. A. Hohsfield, A. R. Najafi, Y. Ghorbanian, N. Soni, E. E. Hingco, S. J. Kim, A. D. Jue, V. Swarup, M. A. Inlay, K. N. Green, Effects of long-term and brain-wide colonization of peripheral bone marrow-derived myeloid cells in the CNS. *J. Neuroinflammation* **17**, 279 (2020).
51. R. Reschke, J. Yu, B. Flood, E. F. Higgs, K. Hatogai, T. F. Gajewski, Immune cell and tumor cell-derived CXCL10 is indicative of immunotherapy response in metastatic melanoma. *J. Immunother. Cancer* **9**, e003521 (2021).
52. S. De Munck, M. Provost, M. Kurikawa, I. Omori, J. Mukohyama, J. Felix, Y. Bloch, O. Abdel-Wahab, J. F. Bazan, A. Yoshimi, S. N. Savvides, Structural basis of cytokine-mediated activation of ALK family receptors. *Nature* **600**, 143–147 (2021).
53. T. N. Sims, T. J. Soos, H. S. Xenias, B. Dubin-Thaler, J. M. Hofman, J. C. Waite, T. O. Cameron, V. K. Thomas, R. Varma, C. H. Wiggins, M. P. Sheetz, D. R. Littman, M. L. Dustin, Opposing effects of PKCtheta and WASp on symmetry breaking and relocation of the immunological synapse. *Cell* **129**, 773–785 (2007).
54. J. Zhang, X. Bu, H. Wang, Y. Zhu, Y. Geng, N. T. Nihira, Y. Tan, Y. Ci, F. Wu, X. Dai, J. Guo, Y. H. Huang, C. Fan, S. Ren, Y. Sun, G. J. Freeman, P. Sicinski, W. Wei, Cyclin D-CDK4 kinase

destabilizes PD-L1 via cullin 3-SPOP to control cancer immune surveillance. *Nature* **553**, 91–95 (2018).

55. A. M. Mitterstiller, D. Haschka, S. Dichtl, M. Nairz, E. Demetz, H. Talasz, M. P. Soares, E. Einwallner, H. Esterbauer, F. C. Fang, S. Geley, G. Weiss, Heme oxygenase 1 controls early innate immune response of macrophages to Salmonella Typhimurium infection. *Cell. Microbiol.* **18**, 1374–1389 (2016).
56. K. L. Jeffrey, M. Camps, C. Rommel, C. R. Mackay, Targeting dual-specificity phosphatases: Manipulating MAP kinase signalling and immune responses. *Nat. Rev. Drug Discov.* **6**, 391–403 (2007).
57. T. Herta, A. Bhattacharyya, M. Rosolowski, C. Conrad, C. Gurtner, A. D. Gruber, P. Ahnert, B. Gutbier, D. Frey, N. Suttorp, S. Hippenstiel, J. Zahlten, Krueppel-Like Factor 4 Expression in Phagocytes Regulates Early Inflammatory Response and Disease Severity in Pneumococcal Pneumonia. *Front. Immunol.* **12**, 726135 (2021).
58. M. Mank, A. F. Santos, S. Direnberger, T. D. Mrsic-Flogel, S. B. Hofer, V. Stein, T. Hendel, D. F. Reiff, C. Levelt, A. Borst, T. Bonhoeffer, M. Hubener, O. Griesbeck, A genetically encoded calcium indicator for chronic in vivo two-photon imaging. *Nat. Methods* **5**, 805–811 (2008).
59. Q. Liu, W. N. Jin, Y. Liu, K. Shi, H. Sun, F. Zhang, C. Zhang, R. J. Gonzales, K. N. Sheth, A. La Cava, F. D. Shi, Brain ischemia suppresses immunity in the periphery and brain via different neurogenic innervations. *Immunity* **46**, 474–487 (2017).
60. W. N. Jin, K. Shi, W. He, J. H. Sun, L. Van Kaer, F. D. Shi, Q. Liu, Neuroblast senescence in the aged brain augments natural killer cell cytotoxicity leading to impaired neurogenesis and cognition. *Nat. Neurosci.* **24**, 61–73 (2021).

Acknowledgments

Funding: This study was supported in part by the American Heart Association (grant ID: 833696) and National Science Foundation of China (82122021). **Author contributions:** X.W. and W.-N.J. formulated the concept and designed the studies. S.X.S., Y.X., Y.L., W.-N.J., and K.S., M.Y. performed the experiments and analyzed the results. S.X.S., K.S., Q.L., and W.-N.J. interpreted the results and drafted the manuscript. **Competing interests:** The authors declare that they have no competing interests. **Data and materials availability:** All data needed to evaluate the conclusions in the paper are present in the paper and/or the Supplementary Materials. scRNA-seq data have been deposited in the NCBI Gene Expression Omnibus (GEO) (www.ncbi.nlm.nih.gov/geo/query/acc.cgi?acc=GSE230414).

Submitted 18 March 2022
Accepted 1 May 2023
Published 7 June 2023
10.1126/sciadv.abq0712

PSYCHOLOGICAL SCIENCE

Randomized evaluation of a school-based, trauma-informed group intervention for young women in Chicago

Monica P. Bhatt[1]*, Jonathan Guryan[2], Harold A. Pollack[3,4], Juan C. Castrejon[1]†, Molly Clark[1]†, Lucia Delgado-Sanchez[1]‡, Phoebe Lin[1]†, Max Lubell[1]†, Cristobal Pinto Poehls[1]‡, Ben Shaver[1]‡, Makenzi Sumners[1]†

This study explores whether a school-based group counseling program for adolescent girls, implemented at scale, can mitigate trauma-related mental health harms. In a randomized trial involving 3749 Chicago public high school girls, we find that participating in the program for 4 months induces a 22% reduction in posttraumatic stress disorder symptoms and find significant decreases in anxiety and depression. Results surpass widely accepted cost-effectiveness thresholds, with estimated cost-utility well below $150,000 per quality adjusted life year. We find suggestive evidence that effects persist and may even increase over time. Our results provide the first efficacy trial of such a program specifically designed for girls, conducted in America's third largest city. These findings suggest the promise of school-based programs to mitigate trauma-related harms.

INTRODUCTION

Decades of psychology research establish the developmental mental health harms of trauma exposure, particularly during adolescence. The coronavirus disease 2019 (COVID-19) global pandemic has sharply increased these mental health challenges: the proportion of mental health–related emergency department visits for children aged 5 to 11 and 12 to 17 years increased approximately 24 and 31%, respectively, in 2020 compared to previous years (*1*). While these experiences are not unique to young women, their burdens are often disproportionately borne by girls, particularly Black and Latinx girls. These burdens include effects on mental health, development, and schooling attainment (*2*). Young women who have been exposed to a traumatic event such as violence are more likely to report symptoms of posttraumatic stress disorder (PTSD) than their male peers (*3*); depressive disorders are more common among women (*4*); and women are more likely than men to develop an anxiety disorder over their life spans (*5*–*7*). Exposure to trauma, through its effect on mental health, also influences academic performance and increases the likelihood of high school dropout (*8*). In Chicago, for example, students' exposure to local homicides is associated with notable reductions in academic performance and scores on standardized tests (*9*).

Despite the marked increase in trauma exposure for adolescent girls and accompanying mental health challenges, there is a dearth of evidence regarding what works to address these challenges. Upon beginning this study, the influential Blueprints for Healthy Youth Development identified only six promising or model programs to address anxiety, depression, and PTSD in adolescents; none focused on girls specifically [see, e.g., (*10*)].

Existing data also suggest that investing in programming for young women may provide benefits beyond the individuals served. For example, research suggests that programs that help males tend to primarily benefit participating individuals, whereas programs that help females yield greater benefits for families and communities (*11*).

Here, we provide evidence that it is possible to reduce PTSD, anxiety, and depression among adolescent girls through a school-based, group counseling program informed by cognitive behavioral therapy (CBT), acceptance and commitment therapy (ACT), and narrative therapy. The program that we study includes a curriculum that intentionally helps student participants to develop self-awareness, build self-esteem and self-efficacy, and enhance their own individual competencies to make positive and healthy decisions.

Students randomized to treatment received programming through Youth Guidance's Working on Womanhood (WOW) program. WOW is a school-based, trauma-informed, relationship-centered, group counseling and mentoring program designed specifically by and for Black and Latinx women to disrupt the cycle of intergenerational trauma.

WOW's 39-lesson curriculum is designed around five core themes: self-awareness, emotional intelligence, healthy relationships, visionary goal setting, and leadership. The program is delivered by master-level social workers and counselors. Each of these staff members works with 50 to 55 girls across four to five groups in a school. Groups meet once per week, during the school day. For needs that cannot be addressed in a group setting, WOW counselors provide individual counseling and referrals to other services. The positive network created by WOW is posited to improve peer relationships and social supports while strengthening girls' ties with important adults, such as parents, teachers, and counselors. The program model and curriculum were refined and revised following a formal formative evaluation in 2018 (*12*).

WOW is rooted in CBT, ACT, and narrative therapy as well as key learnings from other school-based mentoring programs. CBT helps individuals recognize and understand connections among

[1]Crime Lab and Education Lab, University of Chicago, Chicago, IL, USA. [2]School of Education and Social Policy, Northwestern University, Evanston, IL, USA. [3]Crown Family School of Social Work, Policy and Practice, University of Chicago, Chicago, IL, USA. [4]University of Chicago Health Lab, University of Chicago, Chicago, IL, USA.
*Corresponding author. Email: mbhatt@uchicago.edu
†These authors contributed equally to this work.
‡These authors contributed equally to this work.

thoughts, feelings, and behavior as well as the context within which those thoughts, feelings, and behaviors are developed. Previous research has found that CBT is effective in providing symptomatic relief for specific psychiatric disorders, including depression (*13*–*17*), PTSD (*18*), and anxiety disorders (*19*–*21*). CBT has also been found to be effective when adapted to a school-based setting for youth exposed to trauma in urban settings (*21*). There is evidence that school-based CBT can improve school grades (*22*, *23*) and reduce negative behavioral outcomes such as violent crime arrests (*24*).

ACT is used primarily to strengthen psychological flexibility, consisting of six primary components: diffusion, acceptance, self as context, contact with the present moment, values, and committed action. Psychological flexibility promotes behavior change in the service of chosen values by connecting the present moment with what the situation affords. Narrative therapy is a psychotherapeutic approach based on the notion that people construct narratives to define themselves and give meaning to their daily experiences and life events; by supporting narrating their life experiences in richer and more gratifying ways, the individual becomes empowered to consider life alternatives not previously considered. The narrative therapy process has seven core components: collaboration, externalizing the problem, identifying empowerment, identifying values, linking past story to new narrative, inviting witness to new narrative, and documenting gains (*25*, *26*). These therapies and treatments have been used to treat depression and anxiety, with no discernible differences documented to date on individual outcomes. The WOW program draws from each therapeutic tradition to form the foundation of the program curriculum (*27*).

METHODS

Research design

To scrutinize the causal impact of WOW on mental health outcomes, we conducted a cluster-randomized controlled trial in which we randomized girls to receive an offer of the WOW program or business as usual electives and services within nonrandomly preselected neighborhood high schools. Our research team and Youth Guidance together selected 10 study site Chicago Public Schools (CPS) high schools to be invited to participate in a randomized control trial during academic year 2017–2018 and 2018–2019. Each school had sufficient enrollment to provide the necessary number of treatment and control students, could accommodate WOW, and is located in an underserved community on Chicago′s south or west side that has experienced high rates of violent crime (see Fig. 1).

All schools had excess demand and eligibility for the WOW program, allowing for program slots to be offered via a fair lottery given program constraints (approximately 50 girls could be served per school). In accordance to the human subject protocol approved by the University of Chicago Institutional Review Board, consent was waived for randomization into the treatment and control assigned conditions; subsequently, students were consented to participate in the program as well as for participation in baseline and follow-up surveys.

Girls who were randomized to be offered the WOW program were contacted by Youth Guidance counselors and consented into program participation. Girls who participated joined group-based counseling sessions once per week during an elective period during schools in which WOW counselors administered the WOW curriculum and built rapport with WOW groups. Girls who were not randomized to receive an offer from WOW were eligible to receive all other status quo services and elective offerings in the building.

Sample eligibility

During the first week of academic year 2017–18, we received lists of all 9th to 11th grade girls from schools participating in the study. In practice, many of these lists came with extra information—e.g., including additional grades and/or male students—and had to be cleaned before the randomization stage. We used CPS administrative data to randomize 3749 young women who met Youth Guidance′s guidelines for participating in WOW, which included: (i) at least 75% overall school attendance during 2016–2017 academic year; (ii) no specific diagnosis of significant intellectual disability, per CPS records by the end of academic year 2016–2017; and (iii) no signs of proactive aggression, self-harm, or active suicidal ideation. A student is considered to have a significant intellectual disability if they were listed in any of the following six disability categories: autistic; emotional and behavior disorder; educable mental handicap; intellectual disability − profound; severe/profound handicap; trainable mental handicap. These guidelines were intended to ensure that the eligible students had a reasonable chance of engaging with and benefiting from WOW by attending a sufficient number of sessions and by being able to productively participate in and understand group activities.

The combined roster lists contained 3875 potential candidates ready to enter the randomization stage; of those, 126 individuals (about 3.25%) were excluded from the randomization because of not meeting WOW′s requirements for participation. On the basis of these requirements, we randomized >95% of all 9th to 11th grade girls in schools participating in the study.

Randomization

We randomly assigned 3749 eligible 9th, 10th, and 11th grade girls to either a treatment group or control group. Because WOW programming capacity varied by school and sometimes by grade, we carried out a random assignment conditional on school-by-grade "randomization blocks" and varied the probability of assignment to the treatment condition across randomization blocks. Within each randomization block, students were randomly selected for either the treatment group, which was offered the chance to participate in WOW, or for the control group, for whom all business as usual services and electives were available. A total of 1232 young women in the study were assigned to the treatment group; 2517 women were assigned to the control group in fall 2017.

Two additional randomization phases followed the one described above. First, we randomly selected a sample of 626 students (of the 3749 students in the study) for recruitment for a baseline survey, conducted before the beginning of WOW programming; this sample was created in a way such that the number of students assigned to the treatment group was as similar as possible to the number assigned to the control group. The final number of participants within each group has a random component to it. We can only define ex ante the desired sampling probabilities within each randomization block. When creating a random sample for the baseline survey, we used sampling probabilities such that within each block, we expected an equal number of participants landing in

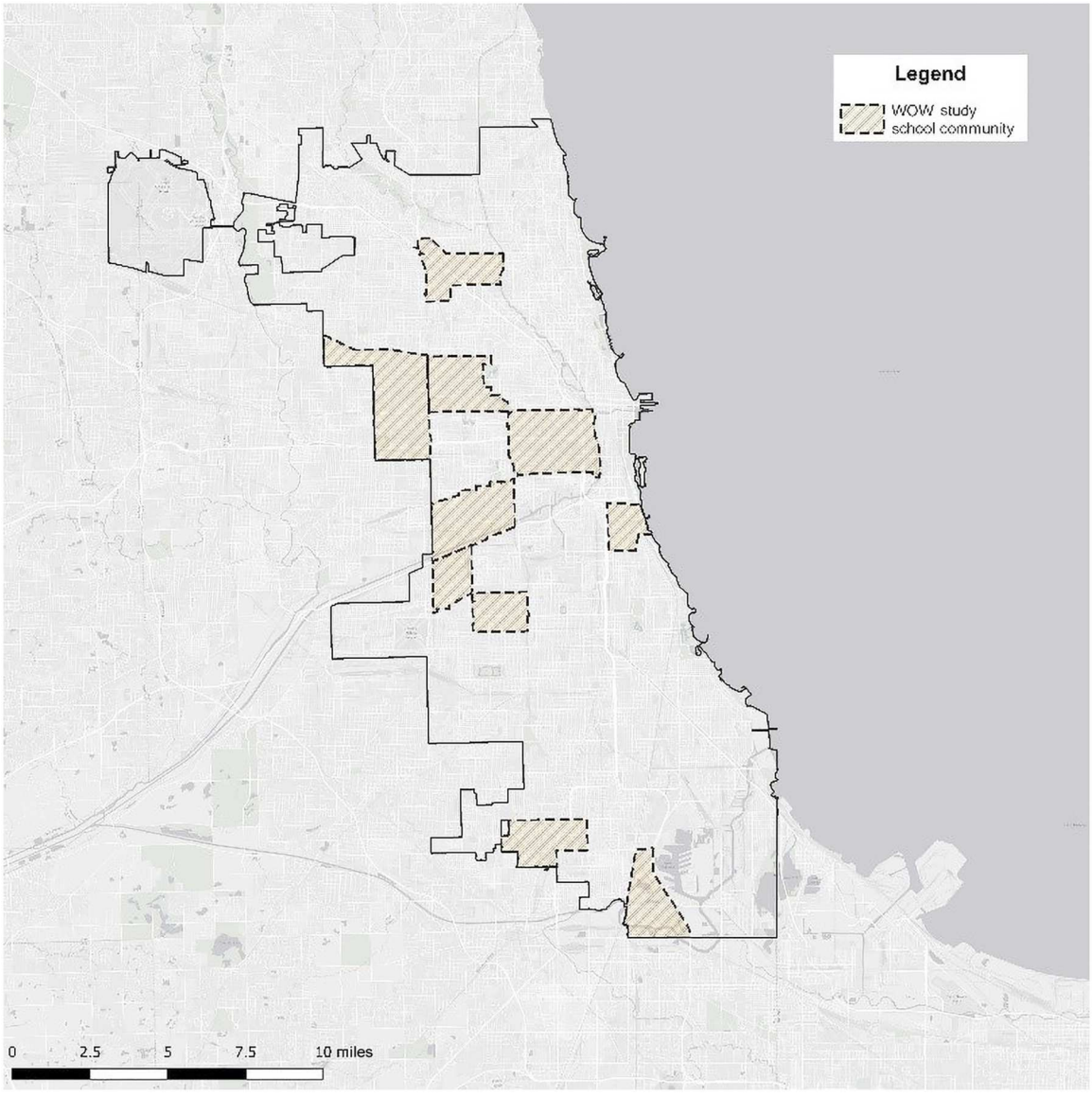

Fig. 1. WOW study school communities. WOW, Working on Womanhood.

the treatment versus control group. It just happened to be the case that we ended up with an equal number of 313 participants on each group for this case. For the follow-up survey sample, the methodology used was the same as the one used for the baseline survey sample, only that now targeting a larger sample size (~2000). The final number of participants assigned to the treatment group was that of 1008; with 1003 being assigned to the control group. From 626 randomly selected students, we had 346 responses for an effective response rate of 55%.

Second, we randomly selected a sample of 2011 students (of the 3749 students in the study) to be recruited for a follow-up survey, conducted toward the end of the first year of WOW programming; this sample was also created in a way such that the number of students in the study assigned to the treatment group was as similar as possible to the number assigned to the control group. A total of 1487 selected students responded to the follow-up survey of the 2011 offered, with an effective response rate of 84%.

We do not see differential outcome missingness for survey respondents for either survey across treatment and control groups. In the baseline survey, of the 313 students in the study assigned to the treatment group, 175 (~56%) were effectively surveyed; and of the 313 students assigned to the control group, 171 (~55%) were effectively surveyed. All other students in the study were either unable to be located or declined to participate in the baseline survey. In the case of the follow-up survey, of the 1008 students in the study assigned to the treatment group, 759 (~76%) were effectively surveyed; and of the 1003 students assigned to the control group, 728 (~73%) were effectively surveyed. Eight students assigned to the follow-up survey sample declined to participate in the study before the follow-up survey began and were excluded from the targeted sample altogether. Five of 1008 participants

assigned to the treatment group in the follow-up survey belong to the group of eight that were excluded from the follow-up survey ex ante. Within the control group, 3 of 1003 cases belong to the group of eight that were excluded from the follow-up survey ex ante. The consort diagram (see Fig. 2) shows the overall structure at each point, depicting the analytic sample for administration of a baseline survey as well as a follow-up survey (see "Data collection" section for more details on survey administration).

Analytic samples

We include analysis from two different analytic samples assigned based on the randomization procedures above here. The follow-up survey student sample is a randomly selected subset of the cohort I sample. We describe each analytic sample below, for reference:

Cohort I sample

Our cohort I sample includes girls randomized in fall 2017 (N = 3749). Eighty-five percent of young women in our study are Black and Hispanic/Latinx. About one-half of young women in the study reported speaking Spanish as their primary language at home (Table 1). The majority of students in cohort I are free and reduced price lunch recipients. We find a slightly higher proportion of students with limited English proficiency (LEP) in the treatment group and a somewhat higher proportion of youth in the control group who are flagged as having a learning disability in cohort I.

Follow-up survey sample: Selected students

The first follow-up survey sample included 2011 study youth randomly sampled for survey participation. Girls selected to be part of the follow-up survey sample were representative of girls in the cohort I sample (Table 1). Of the 2011 youth, we found that eight girls had declined survey participation at baseline and were excluded from the study; therefore, 1003 treatment youth and 1000 control youth were assigned to the survey. We find that the randomly selected follow-up survey sample students are similar to the cohort I sample and are balanced across treatment and control groups (Table 1).

Follow-up survey sample: Respondents

In addition, we find a balanced sample among follow-up survey respondents as well (Table 2). A total of 2003 students in the study were offered the opportunity to complete a follow-up survey between June and November 2018. We received 1487 completed surveys, with an effective response rate of 84%, with 759 treatment youth and 728 control youth completing the survey. A total of 1487 participants responded to at least one question of either the Student Health Survey (SHS) or Behavioral Assessment System for Children (BASC-3) questionnaires. We received 1484 completed surveys. Nonresponders in the follow-up were more likely to be Hispanic, averaged an additional day of unexcused absence, and had slightly lower grade point averages (GPAs) than respondents did. We find balance on observed covariates within this sample, with no statistically significant differences in response rates across students assigned to treatment and control (Table 2).

Data collection

Survey measures

In consultation with Youth Guidance and our team's expert mental health researcher (K. Grant, DePaul University), we compiled a comprehensive survey that contained several rigorous diagnostic instruments. We selected the nationally normed and clinically validated BASC-3 (*28*) to measure anxiety and depression (among several

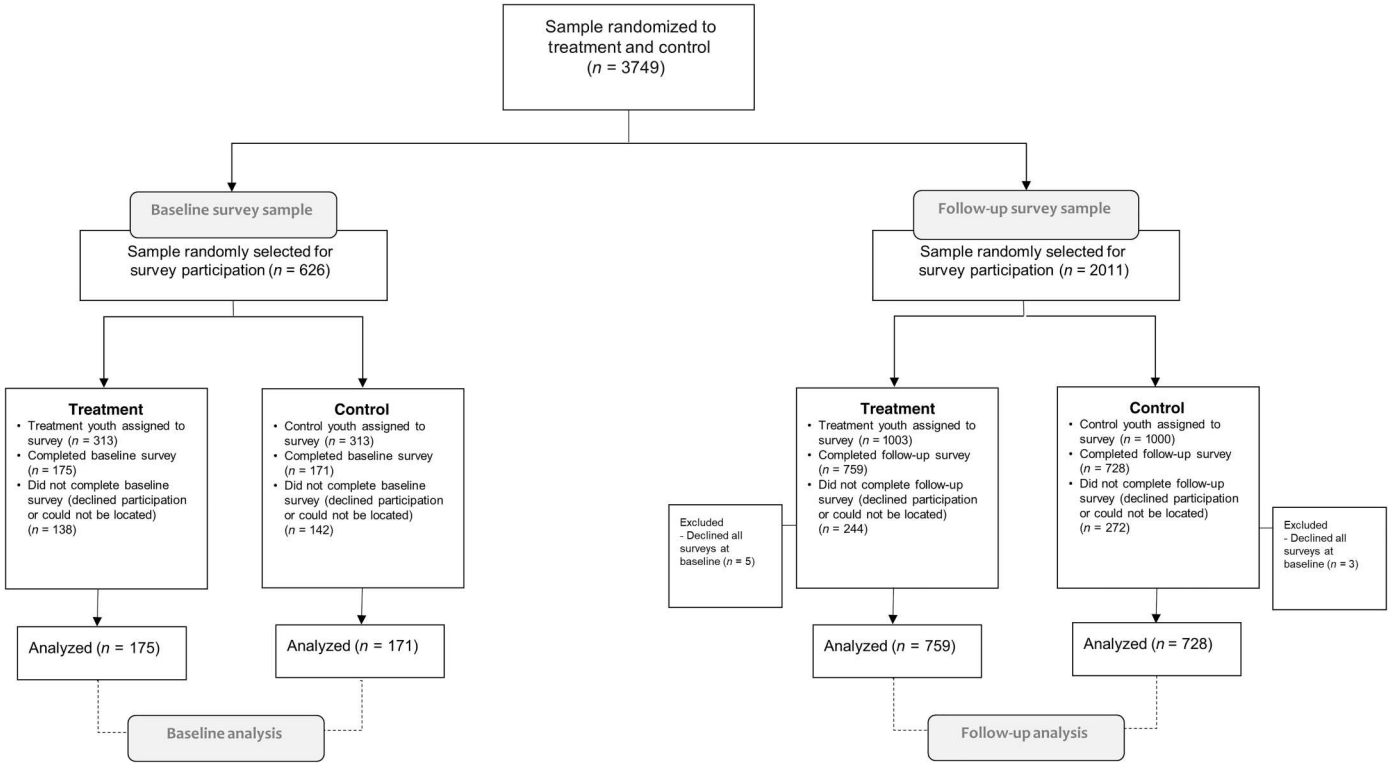

Fig. 2. WOW study consort diagram: Cohort I.

Table 1. Balance table: Cohort I and follow-up survey sample. Significance between the mean differences for the treatment versus control groups was estimated using a linear regression with block-level fixed effects. All missing cases were imputed using block-level averages. A joint *F* test was performed on demographic/academic covariates grouped together to test their joint significance. *P* values estimated using heteroscedasticity robust SEs. ***$P < 0.001$; **$P < 0.01$; *$P < 0.05$; +$P < 0.1$. GPA, grade point average; LEP, limited English proficiency. Obs., observations.

	Cohort I			Follow-up survey sample		
Variable	**Treat mean**	**Control mean**	***P* value**	**Treat mean**	**Control mean**	***P* value**
Old for grade	0.149	0.122	0.135	0.151	0.127	0.118
Age as of randomization	15.15	15.12	0.256	15.16	15.13	0.19
Learning disability	0.096	0.073	0.099+	0.091	0.081	0.393
Free/reduced lunch recipient	0.952	0.951	0.929	0.946	0.954	0.402
Black	0.393	0.328	0.705	0.402	0.407	0.871
Hispanic	0.582	0.64	0.859	0.574	0.57	0.944
Out-of-school suspensions	0.067	0.07	0.319	0.072	0.072	0.985
In-school suspensions	0.101	0.081	0.729	0.109	0.107	0.91
Unexcused absences	8.92	9.43	0.412	8.96	9.37	0.417
Excused absences	4.1	4.47	0.26	4.03	4.36	0.161
Days present at school	162.7	162.8	0.62	162.6	162.9	0.631
GPA	2.86	2.81	0.235	2.86	2.84	0.532
Disciplinary incidents	0.287	0.25	0.898	0.298	0.278	0.567
Violent disciplinary incidents	0.025	0.027	0.312	0.027	0.025	0.805
Any disciplinary incidents?	0.157	0.14	0.861	0.162	0.156	0.666
LEP indicator	0.11	0.099	0.063+	0.102	0.097	0.703
Primary language Spanish	0.497	0.538	0.397	0.491	0.474	0.403
Obs.		3749			2003	
Joint *F* tests		$F_{17, 3702} = 1.044$			$F_{17, 1956} = 0.732$	
		Prob > *F* = 0.406			Prob > *F* = 0.772	

other mediators and secondary outcomes), enabling us to compare our study sample to the national distribution of young women aged 15 to 18. We also elected to use the well-established Child and Adolescent Trauma Screen (CATS) to measure trauma exposure and PTSD symptomology. We relied on the BASC-3 to gather self-reported data on our hypothesized mechanisms of self-esteem and self-efficacy. The self-efficacy measurement was supplemented using the Self-Efficacy Questionnaire for Children drawn from Muris (*29*).

We drew upon a variety of validated instruments and other survey questions to complement these instruments with a range of additional survey items that explored physical and sexual health, risk-taking behavior, self-image, future orientation, relationships, and more. We used the Difficulties in Emotional Regulation Scale–Short Form (*30*) to measure emotional regulation and the Future Outlook Inventory (*31*–*33*) to capture future orientation. Our surveys also included items from the National Longitudinal Study of Adolescent to Adult Health (Add Health) (*34*), which provided information on reproductive health outcomes and substance use.

Baseline survey

We administered a preprogram survey in the fall of school year 2017–2018 to obtain mental and physical health outcome measures not well captured in administrative data. We used this baseline survey data to test for and establish balance between treatment and control groups, improve the precision of our estimates, and provide information on the overall mental health characteristics of our population of interest.

Because of funding constraints, we could not conduct a baseline survey of our entire sample to complement the administrative data to which we had access for the full study sample. We were able to draw a random subset of 626 students from our full sample, blocking on school and grade, for baseline survey. Of the 626, we successfully consented, assented, and surveyed 346 to achieve a response rate of 55.3%. As shown in Tables 1 and 2 below, we achieved good balance in our surveyed sample on demographic and other variables, including our primary outcomes and proposed mechanisms.

Follow-up survey

Our research team conducted a follow-up survey from May to October 2018 to capture first-year post-program impacts on key outcomes for our first study cohort, which received services from fall 2017 to spring 2019. We worked with the Survey Research Center at the University of Michigan's Institute for Social Research (ISR) to administer the follow-up survey to a random sample of approximately 2000 students using the survey instruments that we used for the baseline survey. We used a two-phase sampling to obtain responses from a representative subsample of hard-to-locate respondents, with a goal of an effective response rate of 85%, which ISR had achieved in our previous studies of CPS

Table 2. Balance table: Follow-up survey respondents. Significance between the mean differences for the treatment versus control groups was estimated using a linear regression with block-level fixed effects. All missing cases were imputed using block-level averages. A joint *F* test was performed on demographic, academic, and mental health covariates grouped together to test their joint significance. Obs(*w*) refers to the weighted sample size, i.e., the sum of the sample weights used in the statistical tests. *P* values estimated using heteroscedasticity robust SEs. ***$P < 0.001$; **$P < 0.01$; *$P < 0.05$; +$P < 0.1$. PTSD, posttraumatic stress disorder.

Variable	Treat	Control	Est	*P* value	Obs	Obs(*w*)
Mental health indicators						
Anxiety raw score	15.893	15.969	−0.066	0.938	329	329
Anxiety per score	59.25	58.565	0.603	0.839	329	329
Anxiety at risk or clinically significant	0.208	0.267	−0.064	0.165	329	329
Depression raw score	8.754	8.553	0.337	0.677	326	326
Depression per score	61.395	60.535	1.363	0.678	326	326
Depression at risk or clinically significant	0.257	0.277	−0.016	0.745	326	326
PTSD raw score	12.641	13.38	−0.372	0.805	333	333
PTSD at risk or clinically significant	0.388	0.362	0.049	0.364	333	333
Demographic indicators						
Old for grade	0.15	0.133	0.011	0.541	1487	1621.4
Age as of randomization	15.179	15.112	0.008	0.687	1487	1621.4
Learning disability	0.093	0.066	0.024+	0.085	1487	1621.4
Free/reduced lunch recipient	0.945	0.945	−0.002	0.87	1487	1621.4
Black	0.435	0.422	0.001	0.944	1487	1621.4
Hispanic	0.55	0.561	0.001	0.941	1487	1621.4
Out-of-school suspensions	0.07	0.071	−0.004	0.84	1487	1621.4
In-school suspensions	0.119	0.116	−0.007	0.824	1487	1621.4
Unexcused absences	8.589	8.925	−0.422	0.425	1487	1621.4
Excused absences	3.935	4.108	−0.324	0.217	1487	1621.4
Days present at school	163.327	163.874	−0.146	0.867	1487	1621.4
GPA	2.883	2.883	0.02	0.587	1487	1621.4
Disciplinary incidents	0.309	0.272	0.025	0.614	1487	1621.4
Violent disciplinary incidents	0.023	0.028	−0.006	0.481	1487	1621.4
Any disciplinary incidents?	0.171	0.14	0.027	0.143	1487	1621.4
LEP indicator	0.106	0.093	0.012	0.463	1487	1621.4
Primary language Spanish	0.473	0.469	0.012	0.564	1487	1621.4
	Number of obs. =	326	[Obs(w) = 326]			
Joint *F* test I (mental health and demographic)	$F_{25, 271}$ =	1.03				
	Prob > *F* =	0.428				
	Number of obs. =	1487	[Obs(*w*) = 1621.4]			
Joint *F* test II (demographic only)	$F_{17, 1440}$ =	0.918				
	Prob > *F* =	0.553				

students (*24*). We use the follow-up survey items in two ways: (i) to assess program impact and (ii) to identify potential mediators of treatment effects.

Administrative data

Master data sharing agreements with CPS and the Chicago Police Department (CPD) provided the administrative data foundation for our statistical analysis of education and arrest outcomes. Because the study sample was drawn from CPS administrative data, we had access to longitudinal student-level records for every student in the treatment and the control groups, including student-level school records on attendance, course grades, test scores, graduation and college enrollment, and school disciplinary actions. Students who switch schools or drop out are tracked and analyzed by original group assignment. Our data suggest that 3% of CPS 9th and 10th graders switch schools each year; 9% drop out or leave Chicago. These data were available before the intervention, throughout the intervention period, as well as after intervention, even for students who changed schools as long as they remained connected to CPS and were particularly valuable to

track youth for in-person surveys, as students could have changed schools, dropped out, or changed addresses during the study period.

Our team also has a master data sharing agreement with the CPD to access arrest data (*35*). These include data on the identity of the offender, date and location of the crime event, and criminal charges (for juvenile and adult offenders). We also had access to CPD victimization data covering juvenile and adult arrests citywide. We matched our study sample to these arrest records using probabilistic matching on name and date of birth. This study was approved by The University of Chicago Institutional Review Board, protocol IRB17-0585.

Data analysis

Because of our randomized experimental design, our analysis plan is straightforward. We estimate both the intent-to-treat (ITT) effect and the treatment-on-the-treated (TOT) effect. The ITT estimate comes from estimating Eq. 1

$$Y_i = \pi_0 + \pi_1 Z_i + X_i \pi_2 + B_i + \varepsilon_i \quad (1)$$

where Y_i is an outcome for participant i measured after random assignment, Z_i is an indicator for having been offered WOW programming, B_i is a full set of randomization block fixed effects, ε_i is a random error term, and X_i is a set of baseline controls to improve precision. These include age, school, and grade fixed effects; an indicator for having a learning disability, an indicator for having limited English proficiency, an indicator for being old for grade, and indicators for black and Latinx; and the following academic measures measured in the 2016–2017 baseline school year: number of each type of grade received (A to D and F), days present, days of out-of-school suspensions, and days of in-school suspensions. We also include indicators for ever being arrested for a violent, drug, or property related charge. Missingness of baseline covariates is balanced across treatment and controls groups. Missing baseline covariates were imputed using randomization block means by treatment status. For each imputed baseline covariate, we included an indicator identifying those observations that were imputed.

To estimate the TOT effect, we use random assignment (Z_i) as an instrumental variable (IV) for participation (D_i), as in Eqs. 2 and 3 (*36*, *37*). The first-stage equation is

$$D_i = \gamma_0 + \gamma_1 Z_i + X_i \gamma_2 + B_i + \mu_i \quad (2)$$

where D_i is an indicator for having participated in WOW programming (defined as having participated in at least one WOW group session), the γs are parameters to be estimated, μ_i is a random error term, and all other variables are defined as above. The relationship of interest is

$$Y_i = \beta_0 + \beta_1 D_i + X_i \beta_2 + \beta_i + \vartheta_i \quad (3)$$

The identifying assumption here is that treatment assignment has no effect on the outcomes of those assigned to treatment who do not participate. The IV estimate for the parameter B_i (Eq. 3) is essentially a ratio of two ITT estimates—the ITT effect on the outcome of interest in the numerator and the ITT effect on participation in the denominator.

RESULTS

Baseline descriptive statistics

We used the baseline survey to test for and establish balance between treatment and control groups, improve the precision of our estimates, and describe the overall mental health characteristics of our population of interest. Of our 346 survey respondents at baseline, we observe no statistically significant differences in our 13 baseline measures.

At baseline, young women in the study had suffered, on average, at least two serious traumatic experiences in their lifetimes; nearly 30% had personally witnessed someone being attacked, stabbed, shot at, hurt badly, or killed. More than 45% had someone close die suddenly or violently. Twenty-four percent scored within the clinical range or the at-risk range for anxiety; 27% scored within the clinical range or the at-risk range for depression (*38*).

The baseline survey also helps us understand the baseline prevalence of depression, anxiety, and PTSD within this population (N = 346). Approximately 17% of girls surveyed at baseline appeared at risk for depression and anxiety. About 10% appeared within the clinically significant range for depression and about 7% for anxiety. Findings on trauma exposure do not account for experiences of direct physical abuse, sexual abuse, or sexual assault due to mandatory reporting requirements and may be a conservative estimate. Our baseline surveys indicate that 38% of 10th and 11th grade young women in our study sample exhibit signs of PTSD; the observed prevalence of probable PTSD among these young women is twice that of service members returning from Iraq and Afghanistan. Our depression and anxiety measures are drawn from the BASC-3 SRP-A. The clinically significant range is defined as 2 SDs above the mean when scores are normalized to the appropriate national norm. In our case, we use general female, aged 15 to 18. Almost 30% scored within the probable PTSD range on the CATS, and on average, girls reported 2.5 exposures to traumatic events.

Follow-up survey outcomes

We observed large and statistically significant treatment-control differences in PTSD, depression, and anxiety scores (see Figs. 3 to 5).

We find that participation in WOW causes a 22% decrease in PTSD symptom severity scores, which measures the frequency and intensity of PTSD symptoms, and a 38% decrease in scores that indicate "moderate trauma-related distress." We also find that WOW participation causes significant decreases in measures of anxiety (9.77%) and depression (14.1%) (see Table 3).

We analyze academic outcomes in the administrative data for the full sample of 3749 girls randomized to treatment and control conditions. We observed no clinically or statistically significant differences between treatment and control participants in overall attendance, GPA, or freshman on-track status. Treatment and control participants displayed virtually identical outcomes on these measures (see Table 4).

Economic policy analysis (cost-utility results)

Our main results suggest that WOW improved mental health outcomes for young women participating in the program relative to those who did not. Building on these findings, we used cost-utility analysis to examine the economic value of such mental health improvements relative to WOW's associated program costs. We focused on observed treatment effects in reducing

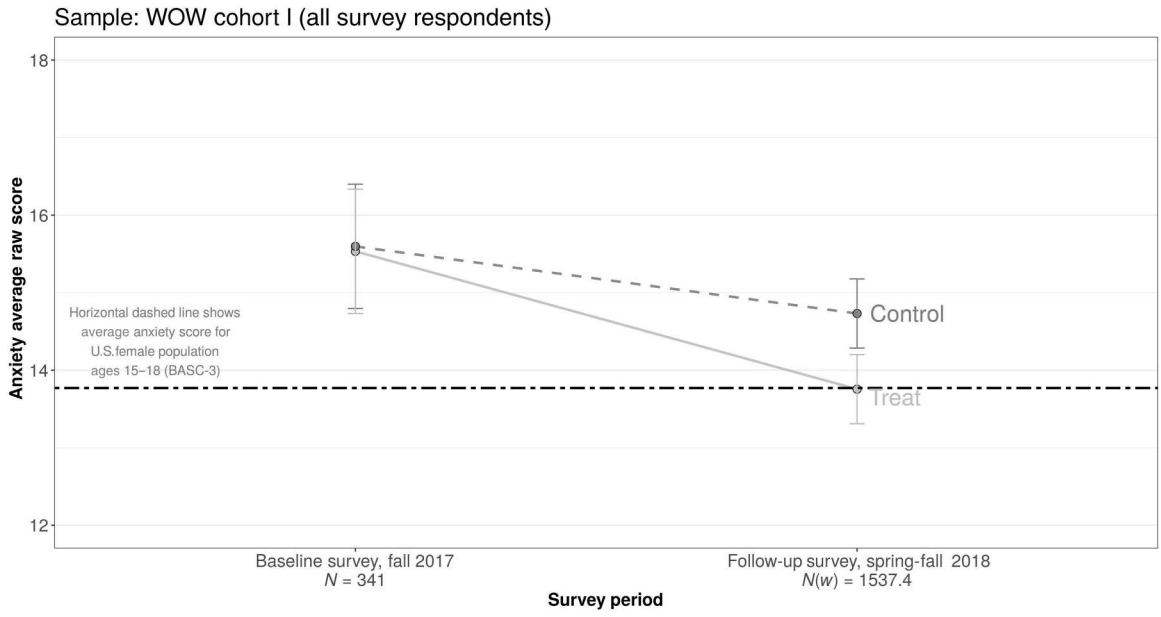

Fig. 3. Mental health trajectory for anxiety (effect of being offered WOW). Note that control means shown in the plot are regression adjusted for both the baseline and follow-up samples. Treatment means are calculated as the adjusted control means plus the estimated effect of being offered WOW. Confidence intervals are at the 95% significance level. BASC-3, Behavioral Assessment System for Children. *N*(*w*), weighted sample size.

depression and PTSD symptoms, converting these mental health benefits to changes in quality adjusted life year (QALY) units gained through the intervention. Briefly summarized, QALYs are constructed by multiplying the length of time that a program effect is presumed to occur by a utility weight that corresponds to the quality of life of individual. One year in perfect health is equivalent to one QALY as is 2 years in a very poor health state with the assigned utility weight of 0.5 (1 year * 1 = 1 QALY = 2 years * 0.5).

To generate an estimate of the cost per QALY gained through WOW, we applied utility weights for depression and PTSD, drawn from existing research, to the responses in the follow-up survey administered to the young women in the study. For depression, we assumed that an individual who is depression-free has a utility weight of 1 (perfect health) and that an individual who satisfies screening criteria for clinically significant depression has a utility weight of 0.59 (*39*). We also assumed that an individual at risk for clinically significant depression has a utility weight between 0.59 and 1 proportionate to their BASC-3 depression *t* score. The assignment of utility weights for PTSD followed a similar pattern. We assumed an individual who is PTSD-free has a utility weight of 1 and that an individual with clinically significant PTSD has a utility weight of 0.61 (*40*). Those at risk for PTSD receive a utility weight between 0.61 and 1 proportionate to their survey CATS PTSD score.

The program cost was estimated to be $2300 per actual participant in WOW. This number was obtained from Youth Guidance, the WOW program provider. That cost figure is based on a caseload of 55 youths served per counselor. It includes the direct salary and benefit costs of counselors and the curriculum specialists who provide training and coaching. It also includes further expensing of program management, other direct programming expenses, and overhead costs for information technology, human resources, and Youth Guidance financial and program evaluation/quality assurance required to operate the program.

We performed an ITT analysis to compare mental health outcomes among all youth invited to participate in WOW with those observed in the control group. On the basis of the program take-up rate of 65%, we converted our program cost data to be comparable to the ITT measure. The cost per program participant in the ITT treatment-assigned group was thus $2300*0.6525 or $1501.

Following the medical cost-effectiveness literature, we then computed the cost per QALY gained by computing an incremental cost-effectiveness ratio (ICER) for each outcome

$$\left(\frac{\text{Cost}_T - \text{Cost}_C}{\text{QALY}_T - \text{QALY}_C}\right) = \left(\frac{\$1501 - \$0}{\text{QALY}_T - \text{QALY}_C}\right)$$

where Cost_T refers to the average cost of implementing WOW calculated within the full treatment-assigned group (e.g., $2300*0.6525 = ~$1500 for the PTSD case). For the cost-benefit analysis, we use the average program cost across the entire treatment group; because not everyone in the treatment group enrolls in WOW, the per-person program cost of $2300 needs to be scaled down by the participation rate before we can plug it into the ICER′s equation. The percentage of study participants from the treatment group enrolled in the WOW program is 65.3%. Note that this percentage varies slightly across the different mental health constructs, as not everyone responded to all questions in the survey (e.g., it is 64.92% for depression, 65.25% for PTSD, etc.). We take an estimate of β_1 from the following regression model as an estimate of QALYT − QALYC

$$\text{QALY}_i = \beta_0 + \beta_1 \text{WOW}_1 + BX + BXmiss + \mu_i + \varepsilon_i$$

where

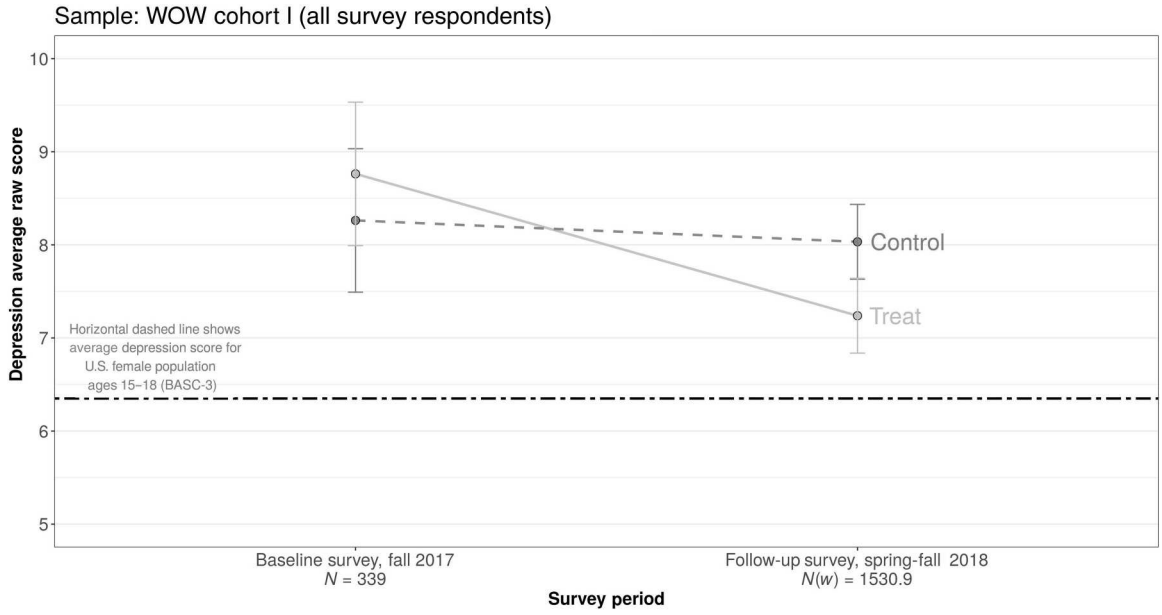

Fig. 4. Mental health trajectory for depression (effect of being offered WOW). Note that control means shown in the plot are regression adjusted for both the baseline and follow-up samples. Treatment means are calculated as the adjusted control means plus the estimated effect of being offered WOW. Confidence intervals are at the 95% significance level.

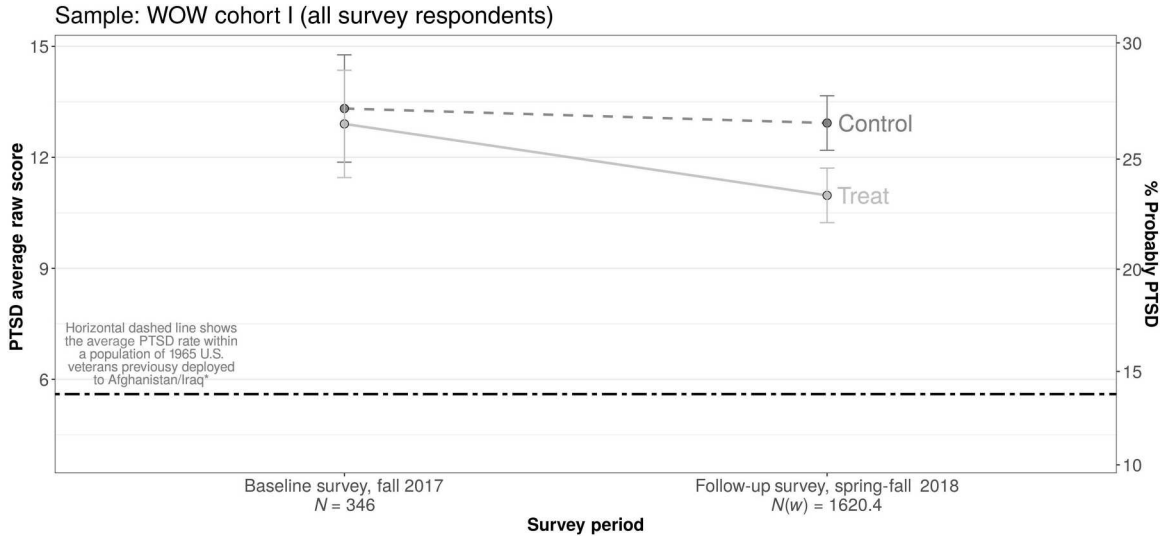

Fig. 5. Mental health trajectory for PTSD (effect of being offered WOW). Note that control means shown in the plot are regression adjusted for both the baseline and follow-up samples. Treatment means are calculated as the adjusted control means plus the estimated effect of being offered WOW. Confidence intervals are at the 95% significance level. The left-hand *y* axis indicates average posttraumatic stress disorder (PTSD) raw scores [Child and Adolescent Trauma Screen (CATS)]; the right hand one shows the percentage with probably PTSD. The horizontal line showing the probable PTSD incidence for the veterans' population should only be read using the right-hand *y* axis; the average PTSD raw scores (CATS) scale is only valid for the WOW sample (*38*).

1) $QALY_i$ is an individual's utility weight multiplied by an assumed effect duration of 365 days. (We perform sensitivity analyses of assumed effect duration below.)
2) WOW_i is a WOW treatment binary indicator.
3) X is a vector of baseline covariates.
4) *Xmiss* is a dummy indicator identifying those cases where the baseline covariates included in X were imputed, using randomization block-level means.
5) μ_i is block-level fixed effects.
6) ε_i is normally distributed random error term.

We compute an ICER for depression and PTSD separately, where the cost per QALY refers to the cost per QALY gained in terms of just that outcome.

We also compute the cost per QALY gained for the combination of PTSD and depression. To avoid complex assumptions about the

Table 3. Mental health primary outcomes: Anxiety, depression, and PTSD. Baseline covariates include: days present; number of in-school suspensions; number of out-of-school suspensions; number of each type of grade received (A to D and F); dummies for ages 14 to 15, 15 to 16, and 17+; and indicators for having a learning disability, having LEP, being in 9th or 10th grades, being old for grade, being Black, being Hispanic, and ever being arrested in each of the three arrest categories: violence, drug, and property. *N*(*w*) refers to the weighted sample size, i.e. the sum of the sample weights used in the statistical tests. *P* values estimated using heteroscedasticity robust SEs. ***$P < 0.001$; **$P < 0.01$; *$P < 0.05$; +$P < 0.1$. IV, instrumental variable.

Sample	*N*(*w*)	Control mean	Intention to treat	Effect of participation (IV)	Control compiler mean	*N*(*w*)	Control mean	Intention to treat	Effect of participation (IV)	Control compiler mean	*N*(*w*)	Control mean	Intention to treat	Effect of participation (IV)	Control compiler mean
			Anxiety raw score					**Depression raw score**					**PTSD raw score**		
Baseline	341	15.98	−0.064 (0.821)	−0.096 (1.178)	16.01	339	8.53	0.5 (0.789)	0.752 (1.132)	8.5	346	13.77	−0.416 (1.485)	−0.62 (2.116)	14
Year one FU	1537.4	14.83	-. 976* (0.455)	−1.513* (0.692)	15.48	1530.9	8.02	−0.794+ (0.41)	−1.227* (0.625)	8.7	1620.4	12.93	−1.956** (0.752)	−3.016** (1.14)	13.91
			Anxiety at risk					**Depression at risk**					**PTSD at risk**		
Baseline	341	0.18	−0.029 (0.041)	−0.044 (0.059)	0.21	339	0.17	−0.013 (0.042)	−0.019 (0.06)	0.16	346	0.09	0.053 (0.033)	0.079+ (0.047)	0.06
Year one FU	1537.4	0.15	0.006 (0.021)	0.01 (0.032)	0.16	1530.9	0.13	−0.009 (0.019)	- 0.013 (0.028)	0.13	1620.4	0.13	−0.042* (0.017)	−0.065* (0.026)	0.17
			Anxiety clinically significant					**Depression clinically significant**					**PTSD clinically significant**		
Baseline	341	0.08	−0.033 (0.026)	−0.049 (0.037)	0.11	339	0.1	0.001 (0.034)	0.001 (0.049)	0.13	346	0.29	−0.009 (0.049)	−0.013 (0.07)	0.3
Year one FU	1537.4	0.04	−0.003 (0.011)	−0.005 (0.017)	0.05	1530.9	0.09	−0.019 (0.017)	−0.029 (0.026)	0.12	1620.4	0.27	−0.035 (0.024)	−0.055 (0.036)	0.28
			Anxiety at risk or clinically significant					**Depression at risk or clinically significant**					**PTSD at risk or clinically significant**		
Baseline	341	0.27	−0.062 (0.045)	−0.094 (0.065)	0.32	339	0.28	−0.012 (0.049)	−0.018 (0.071)	0.29	346	0.37	0.044 (0.053)	0.066 (0.076)	0.36
Year one FU	1537.4	0.2	0.003 (0.023)	0.004 (0.035)	0.21	1530.9	0.22	−0.027 (0.023)	−0.042 (0.035)	0.25	1620.4	0.39	−0.078** (0.026)	−0.12** (0.04)	0.44

Table 4. Academic primary outcomes: Cohort I. Baseline covariates and randomization block-fixed effects included in all models. Baseline covariates include: days; present number of in-school suspensions; number of out-of-school suspensions; number of each type of grade received (A to D and F); dummies for ages 14 to 15, 15 to 16, and 17+; and indicators for having a learning disability, having LEP, being in 9th or 10th grades, being old for grade, being Black, being Hispanic, and ever being arrested in each of the following arrest categories: violence, drug, and property. Year 1(2) outcomes for cohort I correspond to Chicago Public Schools (CPS) academic year 2017–2018 (2018–2019). Misconduct data from CPS was only available up to academic year 2018–2019 at the moment this table was constructed. PSAT/SAT test are not administered to senior year students; i.e., the sample used for estimates does not include participants that were enrolled in 12th grade during the testing year. The freshman on-track indicator is only applicable for cohort I CPS students enrolled in 9th grade at the beginning of academic year 2017–2018 (N = 1,199). *P* values estimated using heteroscedasticity robust SEs. ***$P < 0.001$; **$P < 0.01$; *$P < 0.05$; +$P < 0.1$.

Sample	*N*	Control mean	Intention to treat	Effect of participation (IV)	Control compiler mean	Control mean	Intention to treat	Effect of participation (IV)	Control compiler mean	Control mean	Intention to treat	Effect of participation (IV)	Control compiler mean
			GPA				Failed any course				Credits earned		
Cohort I (year 1)	3749	2.61	0.003 (0.026)	0.005 (0.042)	2.67	0.29	0.01 (0.015)	0.017 (0.024)	0.23	6.65	0.007 (0.031)	0.011 (0.05)	6.78
Cohort I (year 2)	3749	2.62	−0.009 (0.025)	−0.015 (0.041)	2.69	0.28	0.003 (0.014)	0.006 (0.023)	0.24	6.64	0.025 (0.033)	0.042 (0.054)	6.72
			Days present				School persistence index				Any school incidence		
Cohort I (year 1)	3749	154.68	0.892 (0.809)	1.469 (1.32)	158.35	0	0.015 (0.02)	0.025 (0.032)	0.13	0.15	0.002 (0.012)	0.004 (0.02)	0.18
Cohort I (year 2)	3749	148.59	−0.504 (0.949)	−0.828 (1.55)	152.08	0	−0.018 (0.018)	−0.029 (0.029)	0.06	0.12	0.018 (0.012)	0.029 (0.019)	0.14
			Any L4-6 school incident				In-school suspension				Out-of-school suspensions		
Cohort I (year 1)	3749	0.08	0.004 (0.01)	0.006 (0.016)	0.09	0.08	0.008 (0.015)	0.012 (0.025)	0.1	0.11	0.004 (0.015)	0.007 (0.024)	0.11
Cohort I (year 2)	3749	0.06	0.004 (0.008)	0.007 (0.013)	0.06	0.06	0.033* (0.015)	0.054* (0.025)	0.05	0.06	0.005 (0.01)	0.008 (0.017)	0.06
			PSAT/SAT math score (SD)				PSAT/SAT math score (SD)				Freshman on-track		
Cohort I (year 1)	3749	0	−0.019 (0.029)	−0.031 (0.047)	0	0	−0.044 (0.029)	−0.072 (0.048)	0.02	0.86	0.025 (0.018)	0.043 (0.031)	0.88
Cohort I (year 2)	2595	−0.03	−0.053 (0.035)	−0.09 (0.06)	0.04	−0.02	−0.031 (0.034)	−0.053 (0.058)	0.03				

cumulative impact of co-occurring conditions, we assigned each student in the study a utility weight that corresponds to the minimum utility weight that they scored across depression and PTSD. Although anxiety is one of our primary outcomes, we do not include it in the main CBA analysis, because we were unable to find utility weights in the literature that mapped well onto the anxiety questions asked in the BASC-3. Table 5 reports the cost per QALY gained for each outcome.

The Institute for Clinical and Economic Research reports two standard thresholds to use for economic evaluations of pharmaceutical pricing as well as medical and public health interventions in the United States: $150,000 and $100,000 per QALY (*41*). Comparing the cost per QALY gained from WOW to these thresholds, WOW appears to be highly cost-effective when evaluated solely in terms of its impact on PTSD or on the combined PTSD/depression outcome. It is borderline cost-effective when evaluated solely as a depression prevention intervention.

To assess the sensitivity of these results to variance in the estimates of the program effects, we performed a bootstrap analysis to examine the variation in our computed ICER for the combined outcome using 100,000 repetitions. We find that WOW meets the $150,000 threshold in 92.4% of samples and the $100,000 threshold in 81.2% of samples. Figure S8 is the cumulative distribution function of the bootstrapping results.

As a further robustness check, we conducted a bounding exercise where we generate utility weights for a third mental health outcome, anxiety, using the utility weights for depression and students′ responses to anxiety questions of the BASC-3. This does not change our fundamental result. When we combine utility weights using the minimum quality-of-life weights for an individual across their PTSD, depression, and imputed anxiety scores and construct an ICER, we find that the cost per QALY gained to be $67,505. Assuming the quality of life for anxiety is no better than the quality of life for depression, this ICER provides an estimate of the cost per QALY gained across our three primary outcomes.

Table 5. Cost per QALY gained. Showing cost per QALY gained assuming a 365-day benefit. We also show the number of posited benefit days required to meet relevant cost-benefit thresholds. QALY, quality adjusted life year.

Outcome	Cost per QALY gained presuming a 365-day benefit	Days of posited benefit required to meet the $150,000 per QALY threshold	Days of posited benefit required to meet the $100,000 per QALY threshold
Depression as the only valued outcome	$180,522 per QALY	439	659
PTSD as the only valued outcome	$64,274 per QALY	156	235
Combined depression and PTSD	$58,025 per QALY	141	212

A second uncertainty (see Table 5) relates to the posited duration of program effects. If the true program effect were shorter than 365 days, then we may overstate program cost-utility. Examining the combined depression/PTSD outcome, we find that the intervention meets the $100,000 benchmark with a posited intervention duration of 235 days of benefit. The intervention meets the $150,000 benchmark with a posited benefit duration of 156 days.

Study limitations

Our analysis has several study limitations that must be considered in evaluating our results. Within-school randomization creates some potential for spillovers, which could have led us to understate program effects. Spillovers occur if control students directly enroll in WOW, if WOW staff provides informal mentoring or other supports to control-group students, or if treatment group services indirectly benefit control-group students in other ways.

Our mental health outcomes were based on the BASC-3 instrument rather than a diagnostic clinical interview. Our results thus should not be taken as providing clinical diagnosis for any specific individual. Because we could not conduct diagnostic clinical interviews, we adopted a conservative approach to the quality-of-life impact of co-occurring depression and PTSD symptoms, in which we assumed that the quality of life was equivalent to the minimum value obtained for each condition independent of comorbidity. To the extent that the quality-of-life impact of co-occurring symptoms is worse than the impact of either condition alone, we may understate the harms associated with co-occurring conditions.

Given study exigencies arising from the COVID-19 pandemic, we could not gather data on long-term mental health outcomes among WOW participants or controls. Our findings are thus based on respondents′ mental health status as captured in the follow-up survey. We were therefore not able to measure whether WOW induced benefits that lasted beyond the study period. We also could not observe intervention benefits that may have faded out for some participants before the follow-up survey was administered. WOW was also designed to be a 2-year program. We may understate the program′s full benefits given the timing of our mental health surveys.

Given these limitations, we conducted sensitivity analyses to examine the duration of program benefit required for WOW to pass the standard cost-effectiveness threshold. As noted above, WOW′s observed mental health benefits associated with reduced PTSD and depression symptoms would need to last approximately 157 days (roughly 5 months) for WOW to be deemed cost-effective, based on the $150,000-per-QALY threshold.

DISCUSSION

Young women, particularly those attending school in low-income, predominantly minority communities experience high rates of depression, PTSD, and other mental health challenges. Designing and fielding feasible and cost-effective interventions to address these challenges remains a key challenge.

The WOW intervention induces marked and statistically significant improvement in depression, anxiety, and PTSD symptoms among the young women who participate in this intervention. WOW was not designed to move academic outcomes such as

standardized test scores and grades. In addition, over the period observed, WOW did not improve these outcomes.

Evaluated on the basis of its ability to ameliorate mental health symptoms, WOW appears highly cost-effective when judged on the basis of standard cost-utility metrics used to evaluate medical and public health interventions. These benefits were achieved within the challenging real-world environment of 10 Chicago public high schools. At a per-participant cost of $2300, WOW provides one promising model that can be replicated at scale within resource-challenged public schools across the country.

The burden of mental health is often unseen and overlooked, particularly for young women of color, in part because it is not always associated with externalizing behaviors. This study marks one of the first studies of adolescent mental health for young women of color that documents prevalence of mental health challenges such as anxiety, depression, and PTSD in Chicago. It also provides rigorous evidence about how to systematically reduce the prevalence of these challenges at scale through an innovative, group-based, in-school model of therapy.

These findings are previously unknown in part because of the limited evidence base for existing interventions and programs intended to address the high rates of trauma exposure and consequent anxiety, depression, and PTSD found among young women in our study. Our results suggest that group-based, in-school therapy programs like WOW can be effective in reducing these rates and highlight the dearth of alternate services available to the young women in our study. More attention should be directed to WOW and other feasible, cost-effective interventions that support the mental health of young women.

This study was conducted in 10 schools within the real-world environment in America′s third largest city and in its third largest school district. The study included the vast majority of young women in these schools; approximately 95% of female students were randomized to either the treatment or control conditions.

Given that approximately 70% of adolescents′ mental health services are received in a school-based setting, this study marks an important advancement in quantifying the efficacy of the WOW approach of combining CBT, ACT, and narrative therapy into group-based counseling. Despite this advancement, there were young women who had more profound mental health challenges and more significant needs that were not appropriate for group-based intervention; future work should examine interventions to support the needs of these girls.

In our analysis of costs and benefits, we applied the best cost-utility metrics available. More analyses are needed to specifically study young women and to provide cost-effective and outcome measures tailored to this population. Young women experience high mental health disease burdens but are understudied in the literature.

It is also important to evaluate school-based, mental health interventions by the same yardsticks that we use to evaluate other interventions to extend life and improve health. If as a society we are willing to cover the cost of medication to support mental health through Medicaid and other payment sources, then we should also finance psychosocial interventions that prove to be cost-effective when viewed through the lens of these same cost-utility metrics.

Supplementary Materials

This PDF file includes:
Figs. S1 to S12
Tables S1 to S21
Legends for data files S1 to S3

Other Supplementary Material for this manuscript includes the following:
Data files S1 to S3

REFERENCES AND NOTES

1. R. T. Leeb, R. H. Bitsko, L. Radhakrishnan, P. Martinez, R. Njai, K. M. Holland, Mental health–related emergency department visits among children aged <18 years during the COVID-19 pandemic—United States, January 1–October 17, 2020. *MMWR Morb. Mortal. Wkly Rep.* **69**, 1675–1680 (2020).
2. J. A. Fairbank, F. W. Putnam, W. W. Harris, The prevalence and impact of child traumatic stress, in *Handbook of PTSD: Science and Practice*, M. J. Friedman, T. M. Keane, P. A. Resick, Eds. (Guilford Press, ed 1, 2007). [chapter 13].
3. K. M. Fitzpatrick, J. P. Boldizar, The prevalence and consequences of exposure to violence among African-American youth. *J. Am. Acad. Child Adolesc. Psychiatry* **32**, 424–430 (1993).
4. C. J. L Murray, A. D. Lopez, The global burden of disease, in *Global Burden of Disease and Injury* (Harvard Univ. Press, Cambridge, ed. 1, 1996), pp. 117–200.
5. J. Angst, A. Dobler-Mikola, The Zurich Study–A prospective epidemiological study of depressive, neurotic and psychosomatic syndromes. IV. Recurrent and nonrecurrent brief depression. *Eur. Arch. Psychiatry Neurol. Sci.* **234**, 408–416 (1985).
6. S. E. Bruce, K. A. Yonkers, M. W. Otto, J. L. Eisen, R. B. Weisberg, M. Pagano, M. T. Shea, M. B. Keller, Influence of psychiatric comorbidity on recovery and recurrence in generalized anxiety disorder, social phobia, and panic disorder: A 12-year prospective study. *Am. J. Psychiatry* **162**, 1179–1187 (2005).
7. D. A. Regier, M. E. Farmer, D. S. Rae, B. Z. Locke, S. J. Keith, L. L. Judd, F. K. Goodwin, Comorbidity of mental disorders with alcohol and other drug abuse: Results from the epidemiologic catchment area (ECA) study. *JAMA* **264**, 2511–2518 (1990).
8. M. V. Porche, L. R. Fortuna, J. Lin, M. Alegria, Childhood trauma and psychiatric disorders as correlates of school dropout in a national sample of young adults. *Child Dev.* **82**, 982–998 (2011).
9. P. Sharkey, The acute effect of local homicides on children's cognitive performance. *Proc. Natl. Acad. Sci. U.S.A.* **107**, 11733–11738 (2010).
10. D. F. Tolin, E. B. Foa, Sex differences in trauma and posttraumatic stress disorder: A quantitative review of 25 years of research. *Psychol. Bull.* **132**, 959–992 (2006).
11. S. C. Rambaud, J. L. Pascual, R. Moro-Visconti, E. M. Santandreu, Should gender be a determinant factor for granting crowdfunded microloans? *Humanit. Soc. Sci. Commun.* **9**, 1–13 (2022).
12. R. E. Ford-Paz, L. Crown, K. Lawton, H. Goldenthal, G. Day, C. A. Coyne, T. Gill, N. Harris, S. Blakemore, C. Cicchetti, Working on Womanhood (WOW): A participatory formative evaluation of a community-developed intervention. *Eval. Program Plann.* **72**, 237–249 (2019).
13. D. A. Brent, D. Holder, D. Kolko, B. Birmaher, M. Baugher, C. Roth, S. Iyengar, B. A. Johnson, A clinical psychotherapy trial for adolescent depression comparing cognitive, family, and supportive therapy. *Arch. Gen. Psychiatry* **54**, 877–885 (1997).
14. G. N. Clarke, P. Rohde, P. M. Lewinsohn, H. Hops, J. R. Seeley, Cognitive-behavioral treatment of adolescent depression: Efficacy of acute group treatment and booster sessions. *J. Am. Acad. Child Adolesc. Psychiatry* **38**, 272–279 (1999).
15. P. M. Lewinsohn, G. N. Clarke, H. Hops, J. Andrews, Cognitive-behavioral treatment for depressed adolescents. *Behav. Ther.* **21**, 385–401 (1990).
16. P. Rohde, G. N. Clarke, D. E. Mace, J. S. Jorgensen, J. R. Seeley, An efficacy/effectiveness study of cognitive-behavioral treatment for adolescents with comorbid major depression and conduct disorder. *J. Am. Acad. Child Adolesc. Psychiatry* **43**, 660–668 (2004).
17. A. Wood, R. Harrington, A. Moore, Controlled trial of a brief cognitive–behavioural intervention in adolescent patients with depressive disorders. *J. Child Psychol. Psychiatry* **37**, 737–746 (1996).
18. P. Smith, W. Yule, S. Perrin, T. Tranah, T. Dalgleish, D. M. Clark, Cognitive-behavioral therapy for PTSD in children and adolescents: A preliminary randomized controlled trial. *J. Am. Acad. Child Adolesc. Psychiatry* **46**(8), 1051–1061 (2007).
19. P. M. Barrett, A. L. Duffy, M. R. Dadds, R. M. Rapee, Cognitive-behavioral treatment of anxiety disorders in children: Long-term (6-year) follow-up. *J. Consult. Clin. Psychol.* **69**, 135–141 (2001).

20. T. In-Albon, S. Schneider, Psychotherapy of childhood anxiety disorders: A meta-analysis. *Psychother. Psychosom.* **76**, 15–24 (2006).
21. P. C. Kendall, E. Flannery-Schroeder, S. Panichelli-Mindel, M. Southam-Gerow, A. Henin, M. Warman, Therapy for youths with anxiety disorders: A second randomized clinical trial. *J. Consult. Clin. Psychol.* **65**, 366–380 (1997).
22. B. D. Stein, L. H. Jaycox, S. H. Kataoka, M. Wong, W. Tu, M. N. Elliott, A. Fink, A mental health intervention for schoolchildren exposed to violence: A randomized controlled trial. *JAMA* **290**, 603–611 (2003).
23. S. Kataoka, L. Jaycox, M. Wong, E. Nadeem, A. Langley, L. Tang, B. Stein, Effects on school outcomes in low-income minority youth: Preliminary findings from a community-partnered study of a school trauma intervention. *Ethn. Dis.* **21**, 71–79 (2011).
24. S. B. Heller, A. K. Shah, J. Guryan, J. Ludwig, S. Mullainathan, H. A. Pollack, Thinking, fast and slow? Some field experiments to reduce crime and dropout in Chicago. *Q. J. Econ.* **132**, 1–54 (2017).
25. J. White, Wellbeing and education: Issues of culture and authority. *J. Phil. Edu.* **41**, 17–28 (2007).
26. M. White, D. Epston, in *Narrative Means to Therapeutic Ends* (Norton & Co, New York, London, 1990).
27. R. T. Lopes, M. M. Gonçalves, P. P. P. Machado, D. Sinai, T. Bento, J. Salgado, Narrative therapy vs. cognitive-behavioral therapy for moderate depression: Empirical evidence from a controlled clinical trial. *Psychother. Res.* **24**, 662–674 (2014).
28. C. R. Reynolds, R. W. Kamphaus, K. J. Vannest, BASC3: Behavior Assessment System for Children. *PsychCorp* (2015).
29. P. Muris, A brief questionnaire for measuring self-efficacy in youths. *J. Psychopathol. Behav. Assess.* **23**, 145–149 (2001).
30. E. A. Kaufman, M. Xia, G. Fosco, M. Yaptangco, C. R. Skidmore, S. E. Crowell, The Difficulties in Emotion Regulation Scale Short Form (DERS-SF): Validation and replication in adolescent and adult samples. *J. Psychopathol, Behav. Assess.* **38**, 443–455 (2016).
31. M. F. Scheier, C. S. Carver, Optimism, coping, and health: Assessment and implications of generalized outcome expectancies. *Health Psychol.* **4**(3), 219–247 (1985).
32. A. Strathman, F. Gleicher, D. S. Boninger, C. S. Edwards, The consideration of future consequences: Weighing immediate and distant outcomes of behavior. *J. Pers. Soc. Psychol.* **66**, 742–752 (1994).
33. P. G. Zimbardo, Strategies for Coping with Social Traps: Times Perspectives Influences, paper presented at the 98th Annual Convention of American Psychological Association, Boston, August 1990.
34. K. M. Harris, J. R. Udry, National Longitudinal Study of Adolescent to Adult Health (Add Health). *Carolina Population Center, University of North Carolina-Chapel Hill [distributor], Inter-university Consortium for Political and Social Research [distributor]*. (1994–2018).
35. P. J. Cook, S. T. Parker, H. A. Pollack, Sources of guns to dangerous people: What we learn by asking them. *Prev. Med.* **79**, 28–36 (2015).
36. J. D. Angrist, G. W. Imbens, D. B. Rubin, Identification of causal effects using instrumental variables. *J. Am. Stat. Assoc.* **91**, 444–455 (1996).
37. H. S. Brown, Accounting for no-shows in experimental evaluation designs. *Eval. Rev.* **8**, 225–246 (1984).
38. T. Schell, G. Marshall, Survey of Individuals Previously Deployed for OEF/OIF, in *Invisible Wounds of War: Summary and Recommendations for Addressing Psychological and Cognitive Injuries* (RAND Corporation, ed. 1, 2008), pp. 87–116.
39. J. R. Lave, R. G. Frank, H. C. Shulberg, M. S. Kamlet, Cost-effectiveness of treatments for major depression in primary care practice. *Arch. Gen. Psychiatry* **55**, 645–651 (1998).
40. E. Gospodarevskaya, L. Segal, Cost-utility analysis of different treatments for post-traumatic stress disorder in sexually abused children. *Child Adolesc. Psychiatry Ment. Health* **6**, 15 (2012).
41. Institute for Clinical and Economic Review, Overview of the ICER value assessment framework and update for 2017-2019 (2017).

Acknowledgments: We thank our partners at Youth Guidance including L. Crown, G. Day, N. Harris, R. Clarkin, R. Langan, R. Crosby, and M. Adler-Morrison and the WOW program team. We thank J. Broom, S. Dickson, and J. Sell for their help in accessing the data that we analyzed here. We also thank K. Grant for assistance with the selection of study instruments and A. Tentner for review of ACT and narrative therapy treatment modalities. **Funding:** This paper was made possible by the support of the AbbVie Foundation; Arnold Ventures; Paul M. Angell Family Foundation; Edna McConnell Clark Foundation; Logan; MacArthur; Polk; and grant number 2016-JU-FX-0002 from the Office of Juvenile Justice and Delinquency Prevention, Office of Justice Programs, U.S. Department of Justice. Points of view or opinions in this document are those of the authors and do not necessarily represent the views of the U.S. Department of Justice, National Institutes of Justice or any other funder. Any errors are of course our own. **Author contributions:** M.P.B.: Conceptualization, methodology, investigation, validation, resources, supervision, project administration, and writing (original draft and review and editing). J.G.: Conceptualization, methodology, investigation, validation, formal analysis, and writing (review and editing). H.A.P.: Conceptualization, methodology, investigation, funding acquisition, and writing (review and editing). J.C.C.: Project administration and writing (original draft). M.C.: Supervision, project administration, and resources. L.D.-S.: Formal analysis. P.L.: Supervision, resources, formal analysis, and project administration. M.L.: Supervision, project administration, formal analysis, and resources. C.P.P.: Data curation, investigation, formal analysis, writing (original draft and review and editing), software, visualization, and validation. B.S.: Investigation, formal analysis, software, and validation. M.S.: Supervision, project administration, resources, and formal analysis. **Competing interests:** The authors declare that they have no competing interests. **Data and materials availability:** All data needed to evaluate the conclusions in the paper are present in the paper and/or the Supplementary Materials. The data used for this study are owned and controlled by the Chicago Public Schools (CPS); the Education Lab was granted limited restricted use of these data through a data use agreement between the University of Chicago and CPS that prohibits further sharing of the data. The data are defined in contract as Confidential Information that remains the exclusive property of CPS, and the University is not permitted to share any Confidential Information with a third party such as *Science Advances* without the previous contractual consent of CPS, even if the data are deidentified. Furthermore, the data are subject to federal privacy protections outlined in the Family Educational Rights and Privacy Act (FERPA) that prohibits disseminating any data below a minimum standard of aggregation. The University retains the right to publish research results, however, including aggregated statistics from our research findings. Although the University is unable to directly share data from this research with Science, it is possible for researchers to directly access these same data from CPS through a standard process. Researchers may submit an external data request form on the CPS website, which can be found at the following link: www.cps.edu/about/district-data/conduct-primary-research. Our Master Data Use Agreement with the Chicago Police Department similarly prohibits our resharing of their confidential information, or the dissemination of any information without approval in accordance with the Illinois Juvenile Court Act. Our contract with CPD states that: "Data provision will include juvenile arrest and victimization records that, per the Illinois Juvenile Court Act (705 ILCS 405/5- 905-1-f), requires explicit approval from 'the judge of juvenile court and the chief executive of the agency that prepared the particular recording.' Judge M. P. Toomin of the Circuit Court of Cook County and Chicago Police Superintendent D. O. Brown both provided written support for the Requestor's receipt of juvenile arrest and victimization records. The Requestor acknowledges the confidential nature of the criminal justice information supplied and agrees that disclosure to anyone not directly identified in the approved application in any manner that allows the identification of the individuals whose records have been obtained from the CPD is totally prohibited under any circumstances. Should the Requestor engage in any project involving use of the records by a third party not mentioned in this document, the Requestor will notify the Chicago Police Department. Upon review and approval by CPD, third party use will be documented in a separate agreement signed by representatives of the third party. To conceal the identities of persons whose records are supplied to the Requestor, the Requestor agrees to refrain from copying any data not absolutely necessary for the use identified in the application or its security and retain such data only so long as is necessary to conduct the program described in the application to CPD." The University of Chicago Education Lab is required to permanently destroy identifying information in both administrative records and in any survey or health data collected during the study period upon conclusion of the study. Deidentified analytic datasets will be securely stored for a period of up to 10 years following project completion, unless data partners request destruction at an earlier date. After 10 years following study conclusion, all administrative data obtained for the study (that our study team does not have ownership of) will be permanently deleted from our servers. However, deidentified survey data that were collected by our research team during the study period will be published together with this paper.

Submitted 24 March 2022
Accepted 3 May 2023
Published 7 June 2023
10.1126/sciadv.abq2077

NEUROSCIENCE

Altered fear engram encoding underlying conditioned versus unconditioned stimulus–initiated memory updating

Shuai-Wen Teng[1], Xin-Rong Wang[1], Bo-Wen Du[1], Xiao-Lin Chen[1], Guan-Zhou Fu[1], Yun-Fei Liu[1], Shu-Qi Xu[1], Jia-Chen Shuai[1], Zhe-Yu Chen[1,2,3]*

It is known that post-retrieval extinction but not extinction alone could erase fear memory. However, whether the coding pattern of original fear engrams is remodeled or inhibited remains largely unclear. We found increased reactivation of engram cells in the prelimbic cortex and basolateral amygdala during memory updating. Moreover, conditioned stimulus– and unconditioned stimulus–initiated memory updating depends on the engram cell reactivation in the prelimbic cortex and basolateral amygdala, respectively. Last, we found that memory updating causes increased overlapping between fear and extinction cells, and the original fear engram encoding was altered during memory updating. Our data provide the first evidence to show the overlapping ensembles between fear and extinction cells and the functional reorganization of original engrams underlying conditioned stimulus– and unconditioned stimulus–initiated memory updating.

INTRODUCTION

Pathological memory is harmful but difficult to treat. Clinically, exposure therapy is commonly used to treat such cases, which is a process of fear extinction by repeatedly presenting the conditioned stimulus (CS) in the absence of the unconditioned stimulus (US) (*1*). However, it is not always effective as fear memory still exists with the phenomenon such as spontaneous recovery (SR) (*2*), which indicates that extinction normally leaves the original memory intact. It is reported that fear memory could be erased without SR by extinction training at the reconsolidation window (10 min to 6 hour) induced by either CS retrieval or US retrieval, which suggests that post-retrieval extinction treatment could induce fear memory updating (*3*, *4*). In particular, specific CS retrieval before extinction (CS + Ext) could selectively erase the reactivated CS rather than other cue-associated fear memory, while US retrieval before extinction (US + Ext) could prevent multiple CS–associated fear memory with that US (*5*). Although it is reported that reactivation of original memory engrams in the dentate gyrus (DG) contributes to remote contextual fear memory attenuation (*6*), little is known whether the coding pattern of memory engrams is altered during post-retrieval extinction–induced memory updating.

Memory engram cells referred to a population of neurons that are activated by learning and must be reactivated for recall (*7*). In the contextual fear memory paradigm, previous studies found that artificial activation of engram cells could induce stored memory retrieval, and extinction training suppressed the reactivation of original engram cells while activating distinct extinction engram ensembles in the DG (*7*–*9*). Moreover, fear and extinction cells were also found in basolateral amygdala (BLA), and the balance of activity between subpopulations of BLA projection neurons determines the relative expression of fear and extinction memories (*10*, *11*). It is reported that prelimbic cortex (PrL) is critical for auditory fear memory expression, and the existence of fear engram cells in PrL is well established (*12*, *13*). However, whether there exist extinction cells in PrL remains unknown. In addition, the relationship between fear and extinction cells and the dynamic modification of fear engram encoding underlying memory updating are still unclear. In particular, whether memory erasure is mediated by the inhibition or updating of fear engrams has always been a question.

To answer the question, by using activity-dependent neuronal-tagging technology, neuronal tracing technique combined with optogenetic manipulation and in vivo calcium imaging (*7*, *14*, *15*), we identified the fear and extinction cells in PrL and BLA and investigated the dynamic encoding of memory engram ensembles in PrL and BLA during CS- versus US-initiated memory updating.

RESULTS

First, the mice were fear-conditioned using three tone-shock pairings and were then divided into four experimental groups. Context only, extinction only, CS(30 min) + Ext, and CS(24 hours) + Ext groups were included to examine whether time window–controlled post-retrieval extinction paradigm could erase fear memory. Consistent with previous study (*3*), SR, renewal, and reinstatement were found in the CS(24 hours) + Ext group but not in the CS(30 min) + Ext group (fig. S1, A to C). In addition, memory saving could be tested by retraining to determine whether memory was erased (*3*), and we found that the freezing levels during the memory saving test performed at 24 hours after retraining in the CS(24 hours) + Ext group were significantly higher than those in home cage and CS(30 min) + Ext groups. Moreover, there was no difference in the memory saving test between the CS(30 min) + Ext group and the home cage group, which suggests that there was no memory

[1]Department of Anatomy and Neurobiology, Shandong Provincial Key Laboratory of Mental Disorders, School of Basic Medical Sciences and Qilu Hospital, Cheeloo College of Medicine, Shandong University, Jinan, Shandong 250012, P.R. China. [2]Institute of Brain Science, Shuguang Hospital Affiliated to Shanghai University of Traditional Chinese Medicine, Shanghai 201203, P.R. China. [3]Institution of Traditional Chinese Medicine Innovation Research, Shandong University of Traditional Chinese Medicine, Jinan 250355, P.R. China.
*Corresponding author. Email: zheyuchen@sdu.edu.cn

savings in the CS(30 min) + Ext group (fig. S1D). These results suggested that the CS(30 min) + Ext paradigm could erase fear memory. While BLA, PrL, and infralimbic cortex (IL) have been reported to be respectively involved in cued fear learning, retrieval, and extinction processes (*16*, *17*), it remains unknown whether they play roles in memory erasure. Therefore, we examined the c-Fos expression at 90 min after the CS + Ext paradigm and found that PrL and BLA but not IL showed increased c-Fos–positive cell numbers in the CS(30 min) + Ext group compared with the CS(24 hours) + Ext group (fig. S1, E and F). Next, we want to know whether the reactivation of fear engram cells contributes to the increased c-Fos expression during memory erasure. We used double transgenic c-fos:tTA and TRE:H2B-GFP TetTag mice and c-Fos antibody to label and detect the memory engram cell reactivation during memory erasure. By using doxycycline (Dox)–dependent manner, the mice underwent auditory fear conditioning (AFC) training under the Dox-off condition to label the fear memory engram cells, and the cells activated by extinction, retrieval, or erasure were labeled with the c-Fos antibody, where the GFP^+c-Fos^+ cells indicate the reactivated engram cells (Fig. 1, A to C). In BLA and PrL, the GFP^+ cell number showed no difference between CS(30 min) + Ext, CS(30 min) + Ctx, and CS(24 hours) + Ext groups (Fig. 1D). The engram cell reactivation ratio in the CS(30 min) + Ctx group was significantly higher than that in the CS(24 hours) + Ext group; however, the CS(30 min) + Ext group showed the highest engram reactivation ratio among the three groups (Fig. 1E). In addition, in both BLA and PrL, the engram cell reactivation was above chance in either the CS(24 hours) + Ext group, the CS(30 min) + Ctx group, or the CS(30 min) + Ext group, and the reactivation in the CS(30 min) + Ext group was significantly greater than that in the CS(24 hours) + Ext or CS(30 min) + Ctx group (Fig. 1F). These findings indicate the increased memory engram cell reactivation in BLA and PrL during memory erasure, which might contribute to CS-initiated memory updating.

The activation of fear engram cells in PrL but not BLA is crucial for CS-initiated memory updating

To investigate the role of BLA and PrL engram cells in CS-initiated memory updating, we first bilaterally targeted injections of AAV_9-c-fos:tTA and AAV_9-TRE:eNpHR3.0-EYFP into BLA or PrL of wild-type (WT) mice to label the fear engram cells induced by AFC training (Fig. 2, A to C). Optogenetic inhibition of BLA or PrL fear engram cells during retrieval could significantly decrease the freezing levels in the retrieval test, while it has no effect on the following extinction performance (Fig. 2, D to F). Optogenetic inhibition of PrL but not BLA fear engram cells during retrieval led to increased freezing levels during the SR test, indicating fear memory recovery (Fig. 2, E and F). It suggests that both BLA and PrL fear engram cells are necessary for fear memory retrieval, while fear engram cells in PrL but not BLA are essential for CS-initiated memory updating.

To further investigate whether artificially activating BLA or PrL fear engram cells 30 min before Ext could induce memory erasure, we labeled the BLA or PrL engram cells induced by AFC training by bilaterally targeted injections of AAV_9-c-fos:tTA and AAV_9-TRE:ChR2-mCherry (Fig. 3, A to C). Optogenetic activation of BLA or PrL fear engram cells in the context B without CS recall at 30 min before Ext could induce freezing behavior and has no effect on the following extinction training (Fig. 3, D to F), which is consistent with previous study that artificial activation of memory engram cells could induce memory expression (*8*). Moreover, there is no freezing recovery during the SR test following optogenetic activation of BLA or PrL fear engram cells at 30 min before extinction (Fig. 3, E and F). To rule out the influence of single CS retrieval or optogenetic activation of fear engrams on the subsequent memory test, we further analyzed the freezing levels during the first trail of Ext in different experimental groups. The freezing levels during the first trail of Ext exactly reflect the memory levels without extinction. Therefore, analyzing the freezing levels during the first trail of Ext in Ext only, CS(24 hours) + Ext, and CS(30 min) + Ext groups (data from fig. S1) could investigate the effect of CS retrieval only on the subsequent memory test. The freezing levels during the first trail of Ext in the optogenetic activation of the PrL or BLA engrams (data from Fig. 3) could reveal the effect of optogenetic manipulation on the subsequent memory test. We found that the freezing levels were no different across Ext only, CS(24 hours) + Ext, and CS(30 min) + Ext groups, which suggests that single CS exposure during the retrieval session could not affect the subsequent fear memory test (fig. S2A). Similarly, the freezing levels during the first trail of Ext showed no difference between the ChR2 group and the mCherry group under the PrL or BLA engram manipulation (fig. S2B). These results suggest that neither single CS exposure nor single optogenetic activation of memory engrams could affect the subsequent fear memory test. Together, our results suggest that BLA or PrL fear engram cell activation at 30 min before extinction is sufficient for CS-initiated memory updating.

To clarify the differential role of PrL and BLA fear engram cells in CS-initiated memory updating, we bilaterally targeted injections of AAV_9-c-fos:tTA and AAV9-TRE:ChR2-mCherry into PrL for fear engram cell activation, and AAV_9-c-fos:tTA and AAV_9-TRE:eNpHR3.0-EYFP were simultaneously injected into BLA for fear engram cell inhibition (fig. S3A). Activation of PrL fear engram cells and simultaneous inhibition of BLA engram cells at 30 min before extinction did not induce freezing behavior in the retrieval test, while it could block freezing recovery during the SR test, indicating erased fear memory (fig. S3B). We next inhibited the PrL fear engram cells and simultaneously activated BLA engram cells at 30 min before extinction; mice freezing levels in the retrieval test were significantly increased compared with the control group (fig. S3, C and D). However, freezing levels during the SR test were increased compared with that during the extinction memory (EM) test, indicating fear memory recovery (fig. S3D). Thus, our data suggest that the activation of BLA engram cells is critical for fear expression but not CS-initiated memory updating, whereas the activation of PrL fear engram cells is necessary and sufficient for CS-initiated memory updating. Our data also demonstrate that it is the activation of fear engram cells but not the freezing behavior that is critical for fear memory updating. To illustrate the mechanism that artificial activation of BLA fear engram cells could induce memory erasure, we further bilaterally injected AAV_9-TRE:ChR2-mCherry into BLA in double transgenic c-fos:tTA and TRE:H2B-GFP TetTag mice, which could allow us to examine the PrL engram cell reactivation upon BLA engram cell activation (fig. S3E). BLA fear engram cells induced by AFC training were labeled by ChR2-mCherry, and optogenetic activation of BLA engram cells could induce increased freezing levels in the context without CS recall (fig. S3, F and G). Furthermore, we found that the c-Fos expression and the engram cell reactivation in PrL were increased upon

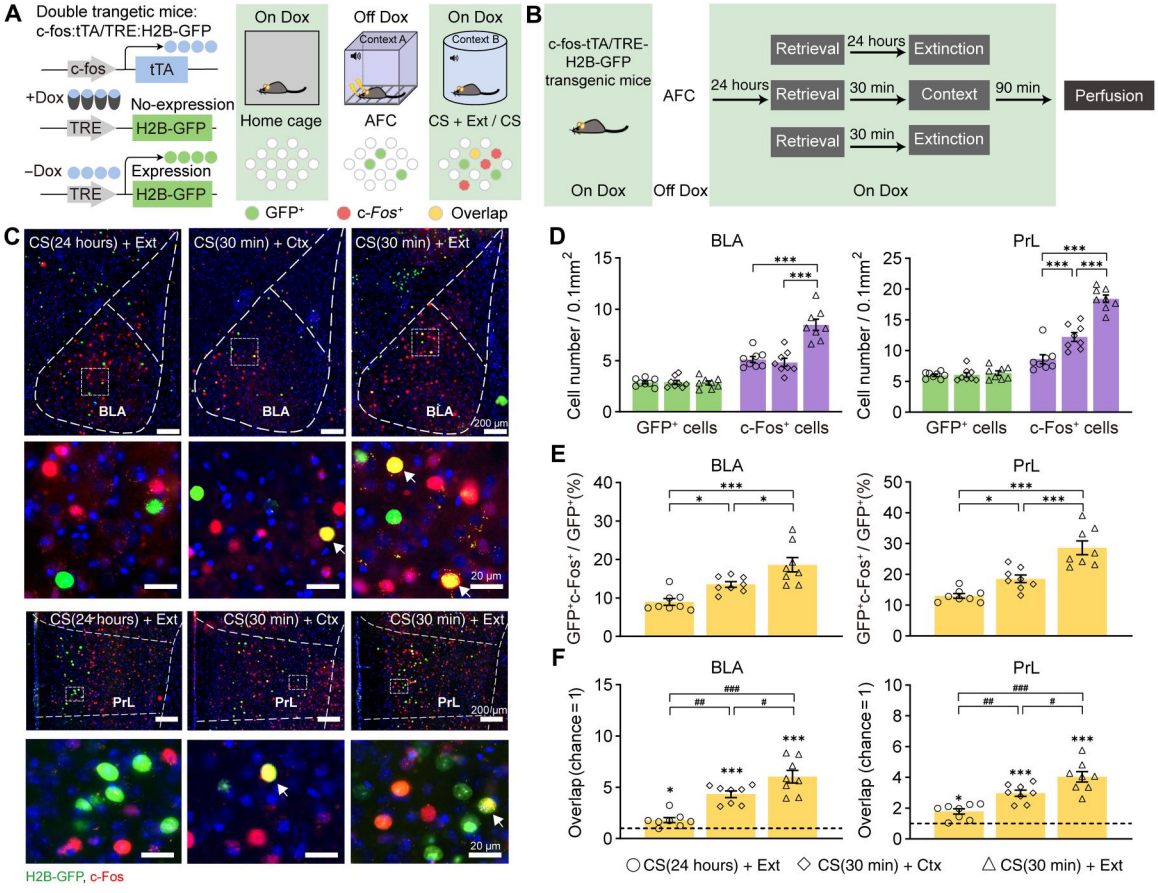

Fig. 1. The engram cells in BLA and PrL show increased reactivation during CS-initiated memory updating. (**A**) Labeling strategy of the inducible double transgenic TetTag mouse and the experimental design used in the CS or CS + Ext paradigm. Activated neurons upon AFC training express H2B-GFP (green), while neurons activated by CS or CS + Ext express endogenous c-Fos (red) and the overlapped cells were labeled (yellow). (**B**) Experimental schedule of engram cell labeling in CS(24 hours) + Ext, CS(30 min) + Ctx, and CS(30 min) + Ext groups. (**C**) Representative images of GFP^+ (green) and c-Fos^+ (red) immunofluorescence in BLA (top) and PrL (bottom) during CS(30 min) + Ext, CS(30 min) + Ctx, and CS(24 hours) + Ext. The white arrowheads marked colabeled $GFP^+c\text{-}Fos^+$ cells. (**D**) The CS(24 hours) + Ext, CS(30 min) + Ctx, and CS(30 min) + Ext groups showed similar GFP^+ cell density, but the c-Fos^+ cell density was significantly higher in the CS(30 min) + Ext group in both PrL and BLA (unpaired *t* test, $^{***}P < 0.001$; $n = 8$ animals per group). (**E**) $GFP^+c\text{-}Fos^+/GFP^+$ levels were significantly higher in the CS(30 min) + Ext group than in CS(24 hours) + Ext and CS(30 min) + Ctx groups [one-way analysis of variance (ANOVA) with Tukey's multiple comparisons test, $^{*}P < 0.05$, $^{***}P < 0.001$]. (**F**) Compared with the chance (dashed line) level, the overlap between GFP^+ and c-Fos^+ cells [$GFP^+c\text{-}Fos^+$/4′,6-diamidino-2-phenylindole (DAPI)] was greater in CS(30 min) + Ext, CS(30 min) + Ctx, and CS(24 hours) + Ext groups, but the overlap was higher in the CS(30 min) + Ext group than in the CS(30 min) + Ctx or CS(24 hours) + Ext group (paired *t* test, $^{*}P < 0.05$, $^{***}P < 0.001$, $^{***}P < 0.001$; one-way ANOVA with Tukey's multiple comparisons test, $^{\#}P < 0.05$, $^{\#\#}P < 0.01$, $^{\#\#\#}P < 0.001$). Data are presented as means ± SEM.

optogenetic activating BLA engram cells (fig. S3, H and I), which suggests the functional connection between BLA and PrL fear engram cells and is consistent with our conclusion that the activation of PrL engram cells is critical for CS-initiated memory updating.

Identification of extinction cells in PrL

Contextual extinction training has been reported to induce the activation of extinction cells, which shows high reactivation and suppresses the reactivation of fear cell ensembles in the EM test (*9*). We hypothesized that the cross-talk between fear and extinction ensembles may be critical for memory updating. As reported, fear cells and extinction cells have been identified in BLA, whereas PrL was reported to be involved in memory expression via inputs to BLA but not extinction (*11*). A recent study described that extinction ensembles existed in the medial prefrontal context (mPFC), and they found that the extinction engram connectivity of BLA → mPFC and ventral hippocampus (vHPC) → mPFC is available but weakened during fear recovery. However, the subregion of mPFC was not clarified in their study, and whether there exist extinction ensembles in PrL remains unclear (*18*). Previous studies showed that the IL plays an essential role in memory extinction (*19*–*21*), and IL efferent into PrL is required for extinction learning in traced fear conditioning (*16*, *22*). Therefore, we injected the retrograde virus AAV_2-hSyn-EGFP into BLA to label the BLA projecting PrL cells ($EGFP^+$) and simultaneously injected the anterograde trans-synaptic virus AAV_1-hSyn-Cre into IL and AAV_9-DIO-mCherry into PrL to label the PrL cells receiving IL projections ($mCherry^+$). Mice were subjected to the AFC training after 2 weeks and divided into three groups for context only: retrieval and extinction treatment followed by c-Fos immunofluorescence staining (Fig. 4, A and B). Consistent with our previous data (fig. S1, F and G), the c-Fos cell number in

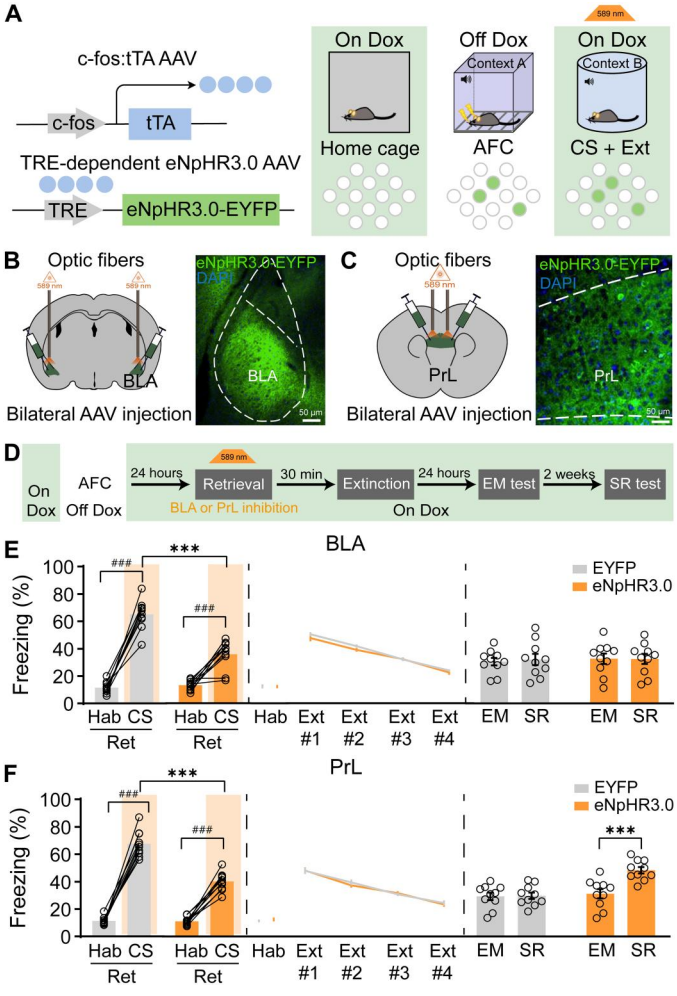

Fig. 2. The activation of engram cells in PrL but not BLA was necessary for CS-initiated fear memory updating. (**A**) Labeling strategy of engram cells with eNpHR3.0-EYFP. (**B**) Coronal sections of BLA with eNpHR3.0-EYFP (green). (**C**) Coronal sections of PrL with eNpHR3.0-EYFP (green). (**D**) Schematic and experimental design of the optogenetic inactivation of engram cells in BLA or PrL. (**E**) Optogenetic silencing of engram cells in BLA during retrieval (Ret) reduced the freezing levels (one-way ANOVA with Tukey's multiple comparisons test, $^{***}P < 0.001$; paired *t* test, $^{###}P < 0.001$; $n = 10$ animals per group). Freezing behavior during extinction showed no difference. The freezing levels during the SR test and EM test showed no difference. (**F**) Optogenetic silencing of engram cells in PrL during retrieval reduced the freezing levels (one-way ANOVA with Tukey's multiple comparisons test, $^{***}P < 0.001$; $n = 10$ animals per group). Freezing behavior during extinction showed no difference. The freezing levels during the SR test were significantly increased compared to the EM test by optogenetic silencing of engram cells in PrL, but there was no difference in the EYFP group [repeated-measures (RM) two-way ANOVA with Sidak's multiple comparisons test, $^{***}P < 0.001$]; freezing levels of habituation showed the freezing levels in the context during the pre-CS or preactivation period. Data are presented as means ± SEM.

the retrieval group was increased compared with those in context only and extinction groups (Fig. 4C). The c-Fos cell number in the extinction group showed an increased trend ($P = 0.1821$) but did not reach statistic difference compared with the context only group. Next, we analyzed the c-Fos$^+$mCherry$^+$ and c-Fos$^+$EGFP$^+$ colabeled cell number across groups. We found that the number of mCherry$^+$ and EGFP$^+$ cells showed no difference across groups, whereas the percentage of colabeled c-Fos$^+$mCherry$^+$ cells was higher in the extinction group compared with context only and retrieval groups (Fig. 4, C and D). Moreover, the overlap level of c-Fos$^+$mCherry$^+$ cell during extinction was significantly higher than that in context and retrieval (Fig. 4D). In contrast, the percentage of colabeled c-Fos$^+$EGFP$^+$ cells and the overlap level of c-Fos$^+$EGFP$^+$ cells were significantly higher in the retrieval group compared with context only and extinction groups (Fig. 4E). These results suggest that PrL cells receiving IL projections displayed increased activation during extinction, while PrL cells projecting to BLA were activated during retrieval. We next investigate the functional roles of these two cell populations by optogenetics. AAV_1-hSyn-Cre was injected into IL, AAV_9-DIO-eNpHR3.0-EYFP was injected into PrL, and the optic fiber was implanted into PrL to manipulate PrL cells receiving IL projections (Fig. 5, A and B). AAV_9-hSyn-eNpHR3.0-EYFP was injected into PrL, and the optic fiber was implanted into BLA to manipulate the PrL-BLA projections (Fig. 5, D and E). We found that inhibition of PrL cells receiving IL projections has no effect on memory retrieval but impairs extinction performance, while inhibition of PrL-BLA projections impairs memory retrieval but has no effect on the rate of within-session extinction and EM test (Fig. 5, C and F). These data suggest that there were two distinct ensembles in PrL, where BLA projecting PrL neurons were mainly responsible for fear encoding, while PrL neurons receiving IL inputs were involved in memory extinction.

CS-initiated memory updating induced increased fear and extinction overlapping ensembles in PrL but not BLA

To further investigate the cross-talk between fear and extinction cells, we monitor Ca^{2+} activity at the single-cell level in PrL and BLA of freely moving mice by using miniaturized microscope. We injected AAV_5-hSyn-GCaMP6f into PrL or BLA of WT mice and implanted a graded refractive index (GRIN) lens (Fig. 6, A, B, and D). After enough recovery time, the mice experienced the AFC training followed by memory extinction or erasure paradigm (Fig. 6A). We functionally identified fear cells and extinction cells in PrL and BLA (Fig. 6, C and E). Fear cells were selectively activated during fear retrieval, while extinction cells were selectively activated during the last trial of extinction, which is according to the definition of a previous study (*23*). To examine the relationship between fear and extinction cells during memory extinction or erasure, we calculated the vector distance by cosine distance between fear and extinction cells in PrL and BLA (Fig. 6, F to I), which allowed us to analyze the similarity of population activity patterns between fear and extinction cells (*24*). Cosine distance is good for the analysis of population activity pattern structure as it is independent of activity intensity. We found that the cosine distance between fear and extinction cells in the CS(30 min) + Ext group was smaller than that in the CS(24 hours) + Ext group in PrL, while there is no difference in BLA (Fig. 6, G and I). These data suggest that population activity patterns between fear and extinction cells were much more closely related during CS-initiated memory updating compared with that during memory extinction in PrL but not in BLA. The discrepancy in population activity similarity between fear and extinction cells in PrL and BLA during CS-initiated memory updating may explain the differential role of fear engrams in PrL and BLA in memory updating.

With the greater similarity between fear and extinction cells in PrL during CS-initiated memory updating, we asked whether there

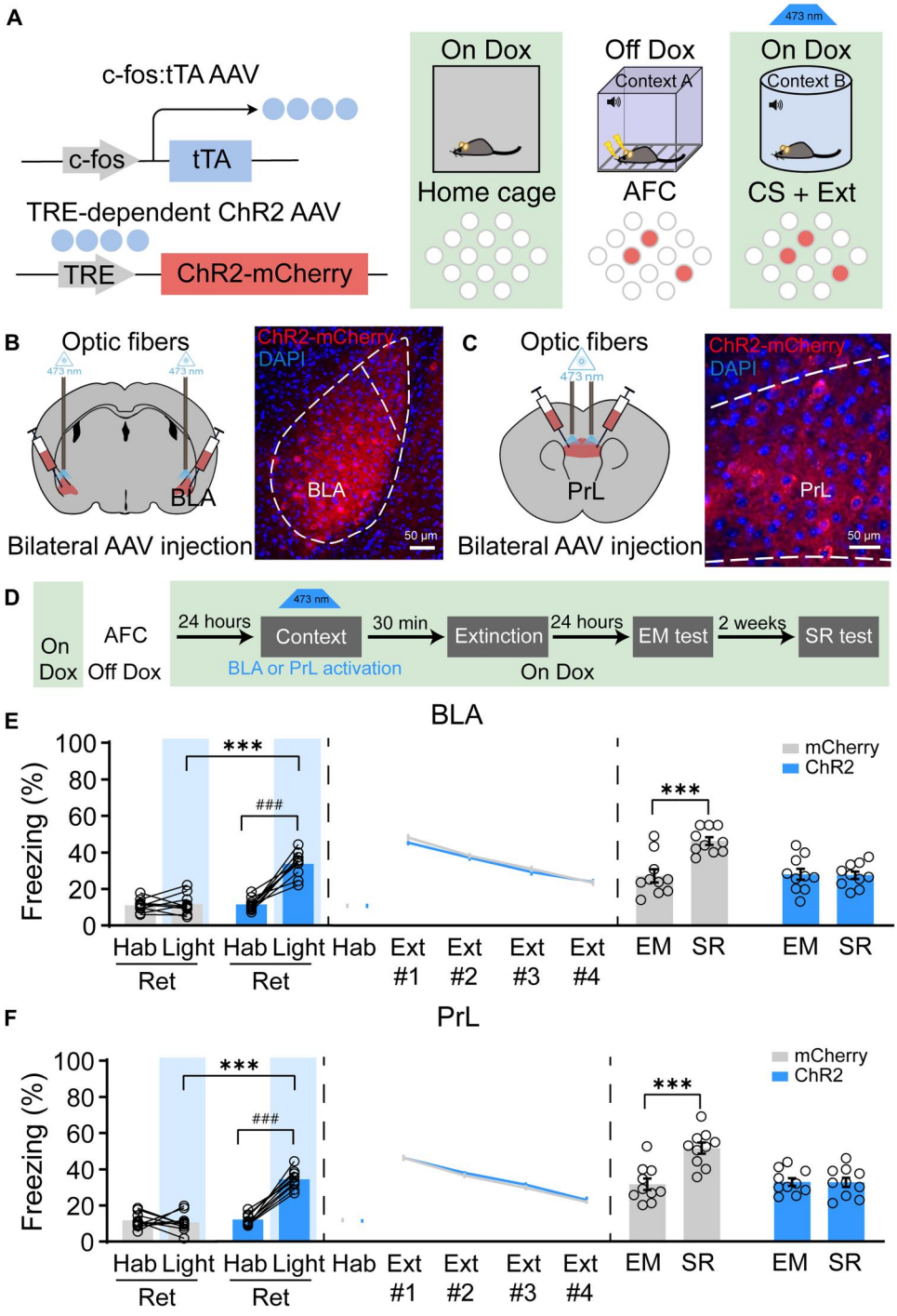

Fig. 3. The activation of engram cells in either PrL or BLA could induce CS-initiated fear memory updating. (**A**) Labeling strategy of engram cells with ChR2-mCherry. (**B**) Coronal sections of BLA with ChR2-mCherry (red). (**C**) Coronal sections of PrL with ChR2-mCherry (red). (**D**) Schematic and experimental design of the optogenetic activation of engram cells in BLA or PrL. (**E**) Optogenetic activation of engram cells in BLA in context B without CS-induced increased freezing levels (one-way ANOVA with Tukey's multiple comparisons test, $^{***}P < 0.001$; paired t test, $^{\#\#\#}P < 0.001$; $n = 10$ animals per group). Freezing behavior during extinction showed no difference. The freezing levels during the SR test were significantly increased compared to the EM test in the mCherry group, but there was no difference in the ChR2-mCherry group in which the engram cells in BLA were activated by optogenetics (RM two-way ANOVA with Sidak's multiple comparisons test, $^{***}P < 0.001$). (**F**) Schematic and experimental design of the optogenetic activation of engram cells in PrL. Optogenetic activation of engram cells in PrL in context B without CS-induced increased freezing levels (one-way ANOVA with Tukey's multiple comparisons test, $^{***}P < 0.001$; paired t test, $^{\#\#\#}P < 0.001$; $n = 10$ animals per group). Freezing behavior during extinction showed no difference. The freezing levels during the SR test were significantly increased compared to the EM test in the mCherry group, but there was no difference in the ChR2-mCherry group in which the engram cells in PrL were activated by optogenetics (RM two-way ANOVA with Sidak's multiple comparisons test, $^{***}P < 0.001$). Data are presented as means ± SEM.

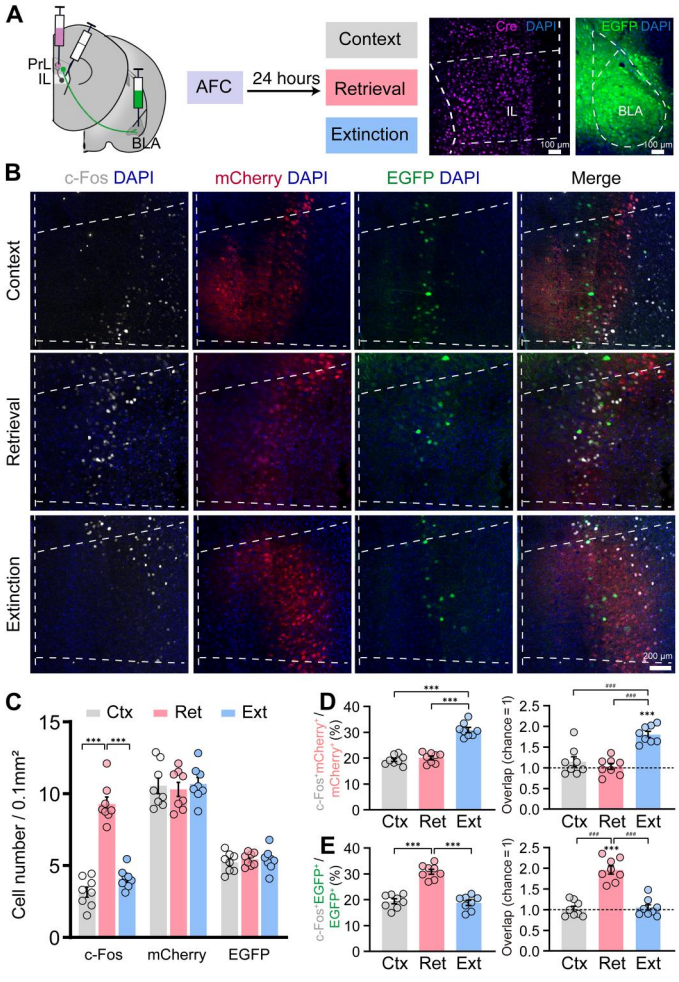

Fig. 4. PrL neurons receiving IL inputs showed high activation during memory extinction. (**A**) Labeling strategy of the anterograde and retrograde tracing in PrL and the behavioral experimental design; coronal sections of IL with anti-Cre immunostaining (left) and coronal sections of BLA with retroAAV$_2$-hSyn-EGFP expression (right). (**B**) Representative images of c-Fos$^+$ (white), mCherry$^+$ (red), and EGFP$^+$ (green) cells in PrL during context, retrieval, and extinction. (**C**) The three groups (Ctx, context; Ret, retrieval; Ext, extinction) showed similar mCherry$^+$ and EGFP$^+$ cell density, but the c-Fos$^+$ cell density during retrieval was significantly higher than in context and extinction groups (one-way ANOVA with Tukey's multiple comparisons test, $^{***}P < 0.001$; $n = 8$ animals per group). (**D**) c-Fos$^+$mCherry$^+$/mCherry$^+$ levels were significantly higher in the extinction group than in context and retrieval groups; compared with the chance (dashed line) level, the overlap between mCherry$^+$ and c-Fos$^+$ cells (c-Fos$^+$mCherry$^+$/DAPI) was greater in the extinction group, and the overlap was higher in the extinction group than in context and retrieval groups (paired *t* test, $^{***}P < 0.001$; one-way ANOVA with Tukey's multiple comparisons test, $^{###}P < 0.001$). (**E**) c-Fos$^+$EGFP$^+$/EGFP$^+$ levels were significantly higher in the retrieval group than in context and extinction groups; compared with the chance (dashed line) level, the overlap between EGFP$^+$ and c-Fos$^+$ cells (c-Fos$^+$EGFP$^+$/DAPI) was greater in retrieval groups, and the overlap was higher in the retrieval group than in context and extinction groups (paired *t* test, $^{***}P < 0.001$; one-way ANOVA with Tukey's multiple comparisons test, $^{###}P < 0.001$). Data are presented as means ± SEM.

were overlapping ensembles in memory updating, as it was reported that overlapping ensembles could alter the fear memory (*25*). The Venn diagram showed the number of fear cells, extinction cells, and overlapped cells in example mice in the memory extinction or CS updating group, respectively (Fig. 6, J and K). We found that the overlapped percentage of fear and extinction cells in PrL was higher in the CS(30 min) + Ext group compared with that in the CS(24 hours) + Ext group, although the percentage of fear or extinction cells was similar (Fig. 6L). Unexpectedly, neither the percentage of fear or extinction cells nor the overlapped percentage was different between CS(24 hours) + Ext and CS(30 min) + Ext groups in BLA (Fig. 6M), which suggested that the overlapping ensembles in PrL might be the mechanism underlying CS-initiated memory updating.

The original fear engram encoding in PrL was altered during CS-initiated memory updating

Having known that there is increased similarity and overlapping between fear cells and extinction cells during CS-initiated memory updating in PrL but not in BLA, we hypothesized that the original fear cell ensembles in PrL but not BLA were remodeled during CS-initiated memory updating. We first analyzed the reactivation of fear and extinction cells during different sessions to support our hypothesis. In the CS(24 hours) + Ext group, compared with those during the first trial of extinction, we found that the reactivation of fear cells was decreased with extinction training in both PrL and BLA, while it showed recoverable reactivation during SR (fig. S4, A and D). In addition, extinction cell reactivation in both PrL and BLA during SR was significantly lower than that during the EM test, which suggests that fear cell reactivation was positively related with the freezing level, while extinction cell reactivation was negatively related with freezing levels (fig. S4, B, C, E, and F). Our results were consistent with a previous study that shows that fear engrams were inhibited during EM, while the increased engram reactivation induced SR (*9*). Differentially, in the CS(30 min) + Ext group, the reactivation of fear cells and extinction cells in PrL showed no difference across different sessions, although the freezing levels were lower in EM and SR tests compared with the first trial of extinction (fig. S4, A to C). On the contrary, in BLA, the relationship between reactivation of fear cell and extinction cell with the freezing levels across different sessions in the CS(30 min) + Ext group was consistent with that in the CS(24 hours) + Ext group (fig. S4, E and F). These results suggested that the coding pattern of original fear cell ensembles might be altered in PrL but not in BLA during CS-initiated memory updating.

Furthermore, to provide functional evidence to support our hypothesis, we performed the optogenetic activation study. We trained four groups of mice for our manipulation, PrL-CS(24 hours) + Ext, PrL-CS(30 min) + Ext, BLA-CS(24 hours) + Ext, and BLA-CS(30 min) + Ext (Fig. 7A). With the similar training curve, similar freezing levels in the retrieval test, and similar extinction curve, we found that activation of PrL or BLA fear engram cells could induce fear memory expression either before extinction or after extinction in the CS(24 hours) + Ext group (Fig. 7, B and D). In the CS(30 min) + Ext group, activation of PrL or BLA fear cells before extinction could induce increased freezing levels (Fig. 7, C and E). However, optogenetic activation of PrL fear engram cells at 24 hours or 14 days after extinction could not induce freezing behavior, whereas BLA fear engram cell activation could still increase freezing

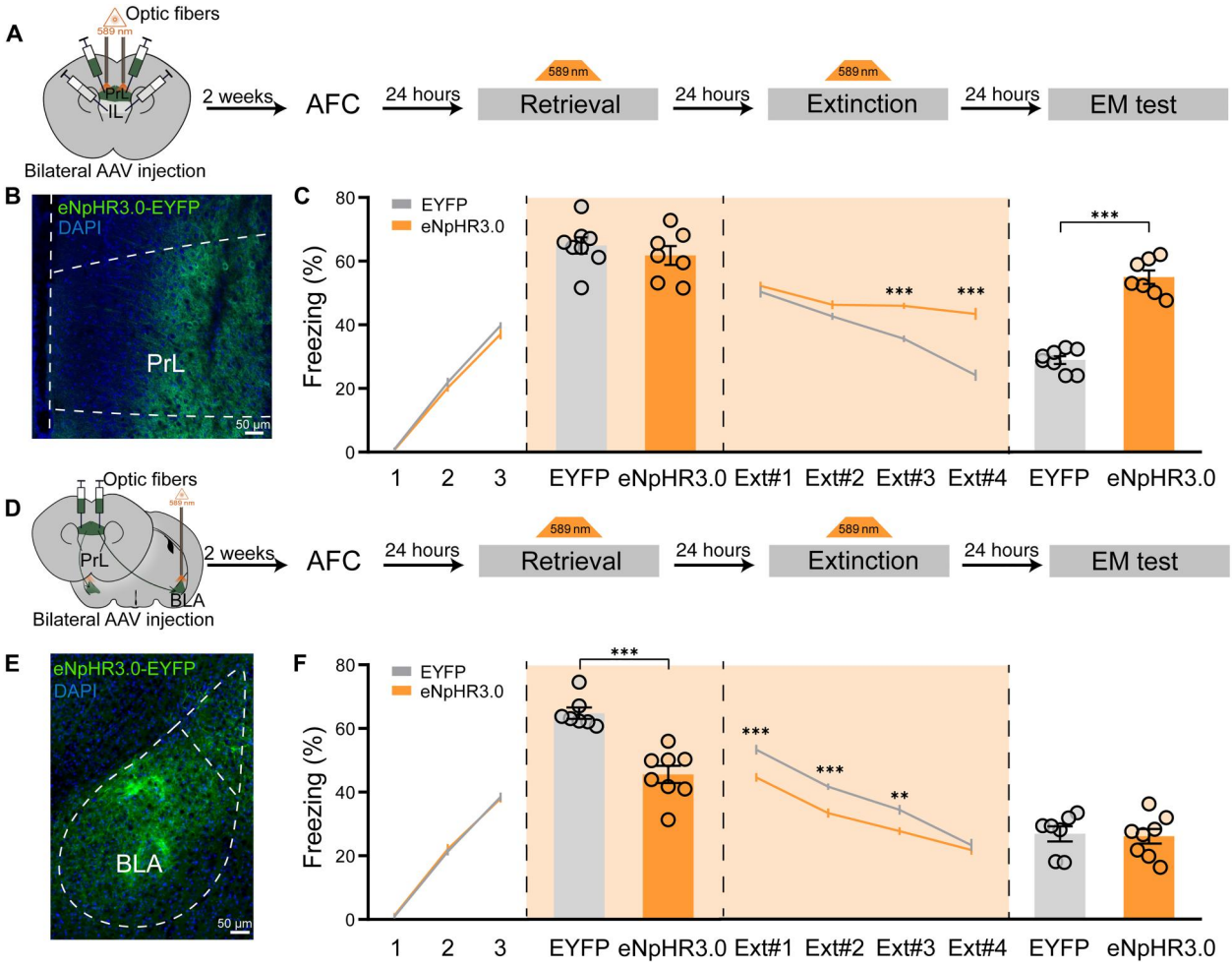

Fig. 5. PrL neurons receiving IL inputs regulate memory extinction. (**A**) Labeling strategy of PrL neurons receiving IL projection with injection of DIO-eNpHR3.0-EYFP in PrL and injection of AAV_1-hSyn-Cre in IL; schematic and experimental design of the optogenetic inactivation of PrL neurons receiving IL projection. (**B**) Coronal sections of PrL with DIO-eNpHR3.0-EYFP (green). (**C**) Optogenetic inhibition of PrL neurons receiving IL projection has no effect on retrieval but impairs EM acquisition, and the freezing levels during the EM test were significantly increased in the eNpHR3.0 group compared to the EYFP group (RM two-way ANOVA with Sidak's multiple comparisons test, ***$P < 0.001$; $n = 8$ animals in the EYFP group, $n = 7$ animals in the eNpHR3.0 group). (**D**) Labeling strategy of PrL projections into BLA with injection of AAV_9-hSyn-eNpHR3.0-EYFP in PrL; schematic and experimental design of the optogenetic inactivation of PrL to BLA projections. (**E**) Coronal sections of BLA with PrL axons expressing eNpHR3.0-EYFP (green). (**F**) The freezing levels during retrieval were significantly decreased in the eNpHR3.0 group compared with the EYFP group. The freezing levels during Ext#1, Ext#2, and Ext#3 in the eNpHR3.0 group were significantly lower than those in the EYFP group, while the rate of within-session extinction showed no difference (RM two-way ANOVA with Sidak's multiple comparisons test, **$P < 0.01$, ***$P < 0.001$; $n = 8$ animals per group). Data are presented as means ± SEM.

(Fig. 7, C and E). These data provided functional evidence that the original engram coding information in PrL but not BLA was rewritten during CS-initiated memory updating.

US-initiated memory updating induced increased fear and extinction overlapping ensembles in BLA

The above results were focused on the specific CS-related memory updating; next, we want to know the selectivity of the dynamic coding remodeling of the original fear cell ensembles as there were multiple CS associations to US in actual situation. Therefore, the CS1-US and CS2-US behavioral paradigm was used to investigate that the differences between memory erasure procedures depended on the post-CS extinction and post-US extinction. CS1 and CS2 were two different tones that the mouse could distinguish and learn with US association, respectively. After the fear conditioning experiment with CS1 and CS2, the mice could learn CS1- and CS2-related fear memory, respectively. Then, the post-CS or post-US extinction behavioral paradigm was applied to erase the fear memory. To clarify the difference of neural ensembles activation during CS- or US-initiated memory erasure in PrL, we tracked the Ca^{2+} activity of cells in PrL during post-CS or US extinction procedures (fig. S5, A and B). The behavior paradigm showed that the CS1(30 min) + Ext paradigm could specifically erase the CS1 fear memory while leaving the CS2 memory intact (fig. S5A), whereas the US(30 min) + Ext paradigm could erase both the CS1 and CS2 memory, which was consistent with previous studies (fig. S5B) (*5*, *26*). We accordingly identified CS1 fear cells, CS2 fear cells, and CS1 extinction cells in PrL (fig. S5, C and D). Although we found that both CS1 and CS2 fear cells in PrL showed high reactivation levels during US retrieval (fig. S7A), the cosine distance

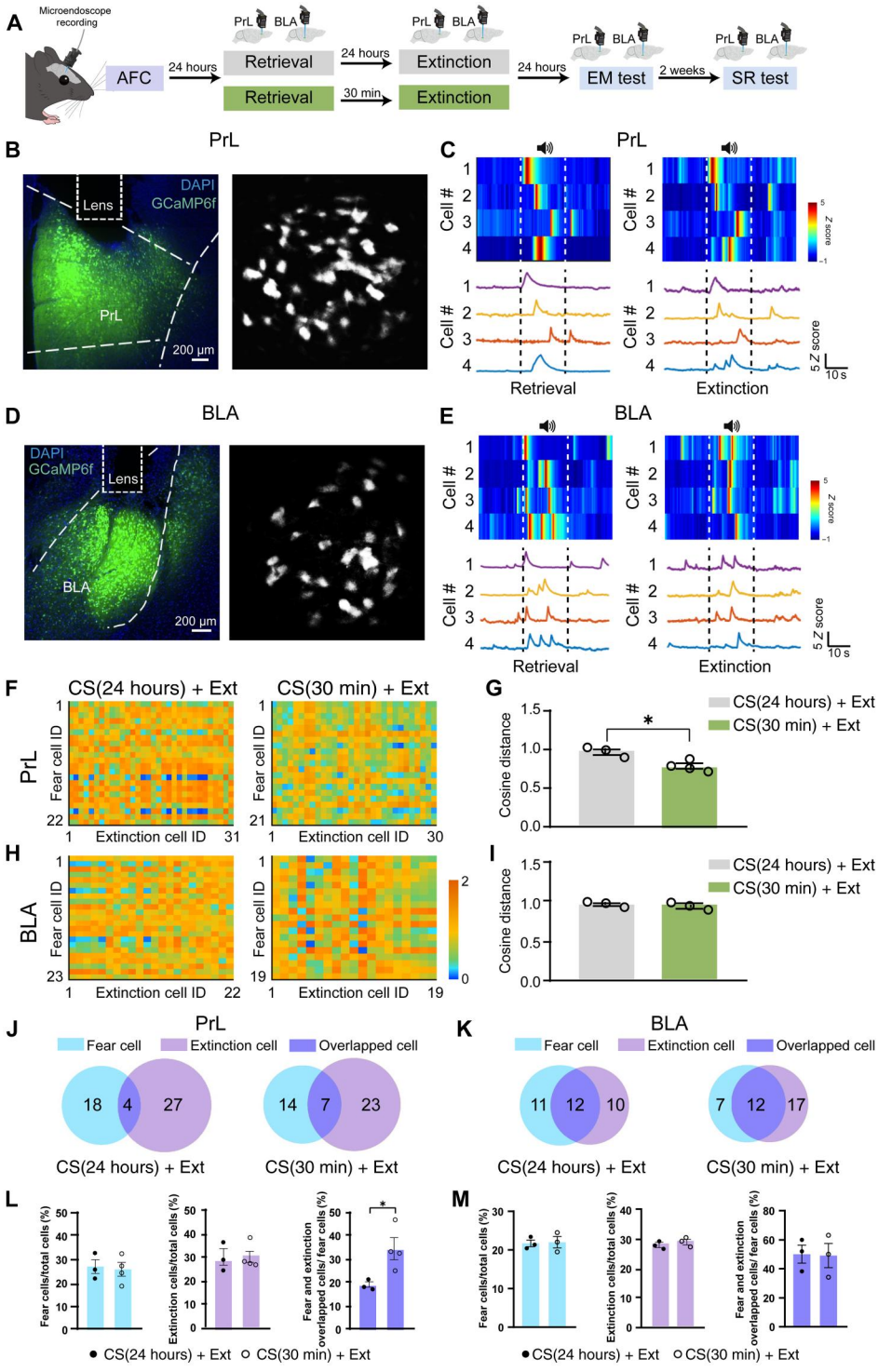

Fig. 6. The vector distance and overlapped cells between fear cells and extinction cells during CS-initiated memory updating. (**A**) Monitoring of Ca^{2+} activity of PrL and BLA during different behavioral paradigm in a freely moving mouse by using miniaturized microscope. (**B**) Virus injection and GRIN lens implantation (left) and maximum intensity projection image (right) in PrL. (**C**) Example cells selected activated during retrieval or the last trail of extinction in PrL. (**D**) Virus injection and GRIN lens implantation (left) and maximum intensity projection image (right) in BLA. Scale bar, 50 μm. (**E**) Example cells selected activated during retrieval or the last trail of extinction in BLA. The matrix showed the cosine distance from example mice between fear cells and extinction cells in PrL (**F**) or BLA (**H**) in CS(24 hours) + Ext and CS(30 min) + Ext groups. (**G**) The cosine distance between fear and extinction cells of PrL in the CS(30 min) + Ext group was significantly smaller than that in the CS(24 hours) + Ext group [two-way ANOVA with Sidak's multiple comparisons test, $^*P < 0.05$; $n = 3$ animals; 335 neurons in the CS(24 hours) + Ext group; $n = 4$ animals, 434 neurons in the CS(30 min) + Ext group]. (**I**) The cosine distance between fear and extinction cells of BLA showed no difference between CS(24 hours) + Ext and CS(30 min) + Ext groups [$n = 3$ animals, 396 neurons in the CS(24 hours) + Ext group; $n = 3$ animals, 375 neurons in the CS(30 min) + Ext group]. The Venn map showed the distribution of fear and extinction cells in PrL (**J**) or BLA (**K**) from example mice in CS(24 hours) + Ext and CS(30 min) + Ext groups. The percentage of fear cells (fear cells/total cells), extinction cells (extinction cells/total cells), and overlapped cells (fear and extinction overlapped cells/fear cells) of the CS(30 min) + Ext group in PrL (**L**) or BLA (**M**) (RM two-way ANOVA with Sidak's multiple comparisons test, $^*P < 0.05$). Data are presented as means ± SEM.

between CS1 fear cells and CS1 extinction cells was smaller than that between CS2 fear cells and CS1 extinction cells in PrL in both CS1(30 min) + Ext and US(30 min) + Ext groups (fig. S5, E and F). Furthermore, the overlapped percentage of CS1 fear and CS1 extinction cells in PrL was greater than that of CS2 fear and CS1 extinction cells in both CS1(30 min) + Ext and US(30 min) + Ext groups (fig. S5, G and H). These results provide another evidence to support the essential role of increased fear and extinction overlapping ensembles in PrL for specific CS but not US retrieval–initiated memory updating.

Then, we tracked the Ca^{2+} activity of cells in BLA during the CS1- and US-initiated memory updating paradigm, and the CS1 fear, CS2 fear, and CS1 extinction cells in BLA were identified (Fig. 8, A to D). We found that the reactivation of both CS1 and

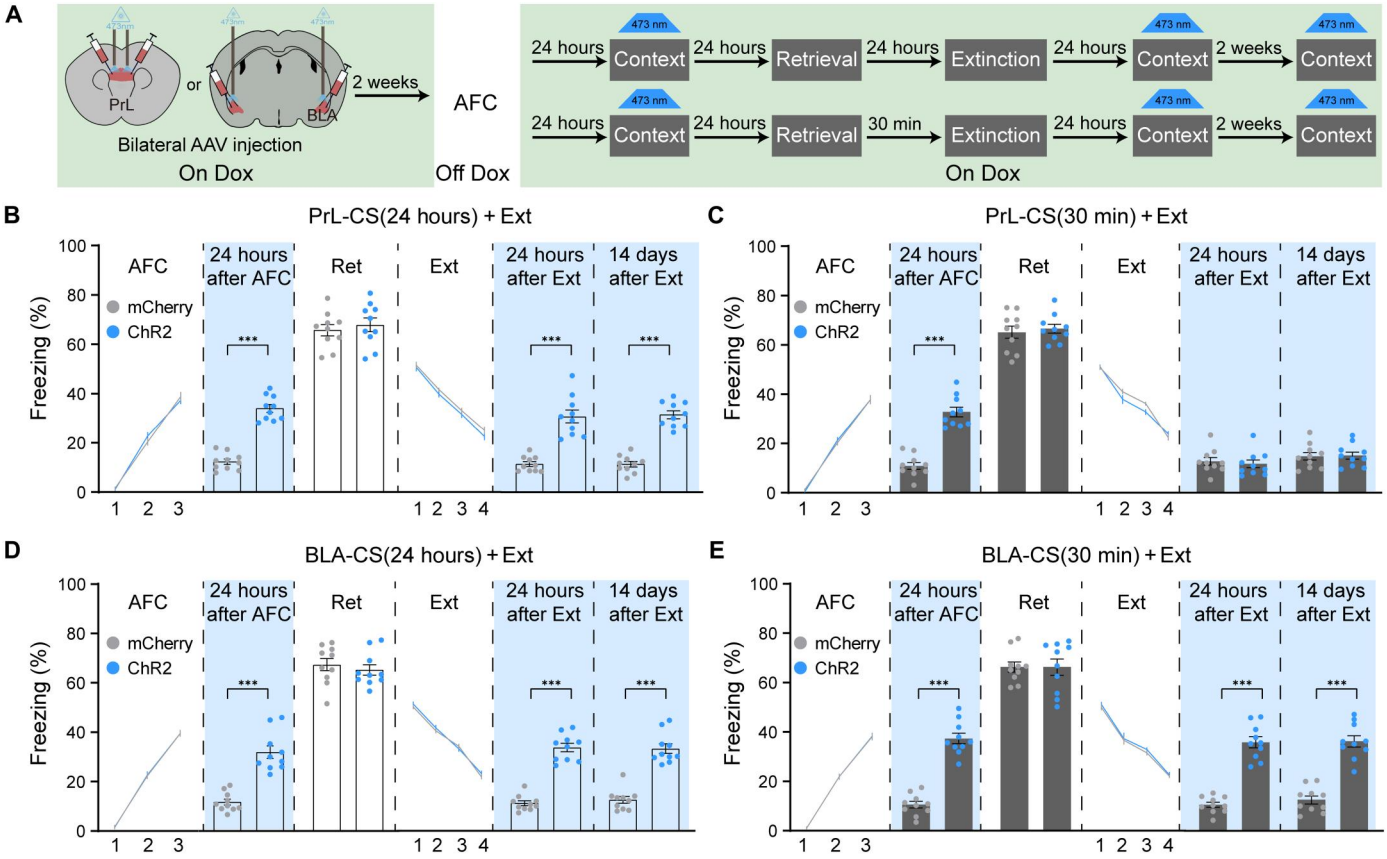

Fig. 7. The encoding of engram cells in PrL but not BLA was updated during CS-initiated memory updating. (**A**) Schematic and experimental design of the optogenetic activation of engram cells in PrL or BLA at different time points. The freezing levels with activation of PrL engram cells in context B without retrieval at 24 hours after AFC and 24 hours or 14 days after extinction in the PrL-CS(24 hours) + Ext group (**B**) and the PrL-CS(30 min) + Ext group (**C**) (RM two-way ANOVA with Sidak's multiple comparisons test, ***$P < 0.001$; $n = 10$ animals per group). The freezing levels with activation of BLA engram cells in context B without retrieval at 24 hours after AFC and 24 hours or 14 days after extinction in the BLA-CS(24 hours) + Ext group (**D**) and the BLA-CS(30 min) + Ext group (**E**) (RM two-way ANOVA with Sidak's multiple comparisons test, ***$P < 0.001$; $n = 10$ animals per group). Data are presented as means ± SEM.

CS2 fear cells in BLA was higher than by chance during US retrieval (fig. S7B). In the CS1(30 min) + Ext group, we found that the cosine distance between CS2 fear cells and CS1 extinction cells showed no difference compared with that between CS1 fear cells and CS1 extinction cells in BLA. In contrast, the cosine distance between CS1/CS2 fear cells and CS1 extinction cells in BLA in the US(30 min) + Ext group was smaller compared with that in the CS1(30 min) + Ext group (Fig. 8, E and F). In addition, the overlapped cells between CS1/CS2 fear and CS1 extinction cells in BLA in the US(30 min) + Ext group were increased compared with those in the CS1(30 min) + Ext group (Fig. 8, G and H). These data further confirm that the overlapping ensembles between fear and extinction cells were essential for post-retrieval memory updating and suggest that CS- versus US-initiated memory updating occurred in PrL and BLA, respectively.

Next, we performed the optogenetic experiment to investigate the functional role of BLA engram cells in US-initiated memory updating. The BLA engram cells induced by CS1-US or CS2-US training was labeled by bilateral injection of AAV_9-c-fos:tTA and AAV_9-TRE:eNpHR3.0-EYFP (fig. S6A). Optogenetic inhibition of either CS1 or CS2 engram cells in BLA during US retrieval has no effect on CS1 extinction but increases the freezing levels in the SR test, which suggests that the activation of CS1/CS2 engram cells in BLA is necessary for US-initiated fear memory erasure (fig. S6, B and C). In addition, we analyzed the overlap of CS1 and CS2 fear cells in PrL and BLA during fear memory updating. We found that the overlap level of CS1 and CS2 fear cells in BLA was significantly higher than that in PrL, which explains how the inhibition of either CS1 or CS2 engram cells in BLA could block both CS-associated memory erasures by US(30 min) + Ext (fig. S7C).

The original fear engram encoding in BLA was altered during US-initiated memory updating

We further asked whether BLA engram cell encoding was altered during US-initiated fear memory updating. We labeled BLA engram cells induced by CS1-US or CS2-US training by bilateral injection of AAV_9-c-fos:tTA and AAV_9-TRE:ChR2-mCherry (Fig. 9A). With the similar training and extinction curve, we found that activation of CS1 or CS2 BLA fear engram cells could induce fear memory expression before US(30 min) + Ext, while optogenetic activation of CS1 or CS2 BLA fear engram cells at 24 hours or 14 days after extinction could not induce freezing behavior upon US-initiated memory updating (Fig. 9, B and C). In contrast, activation of CS1 BLA fear engram cells either before CS1(30 min) +

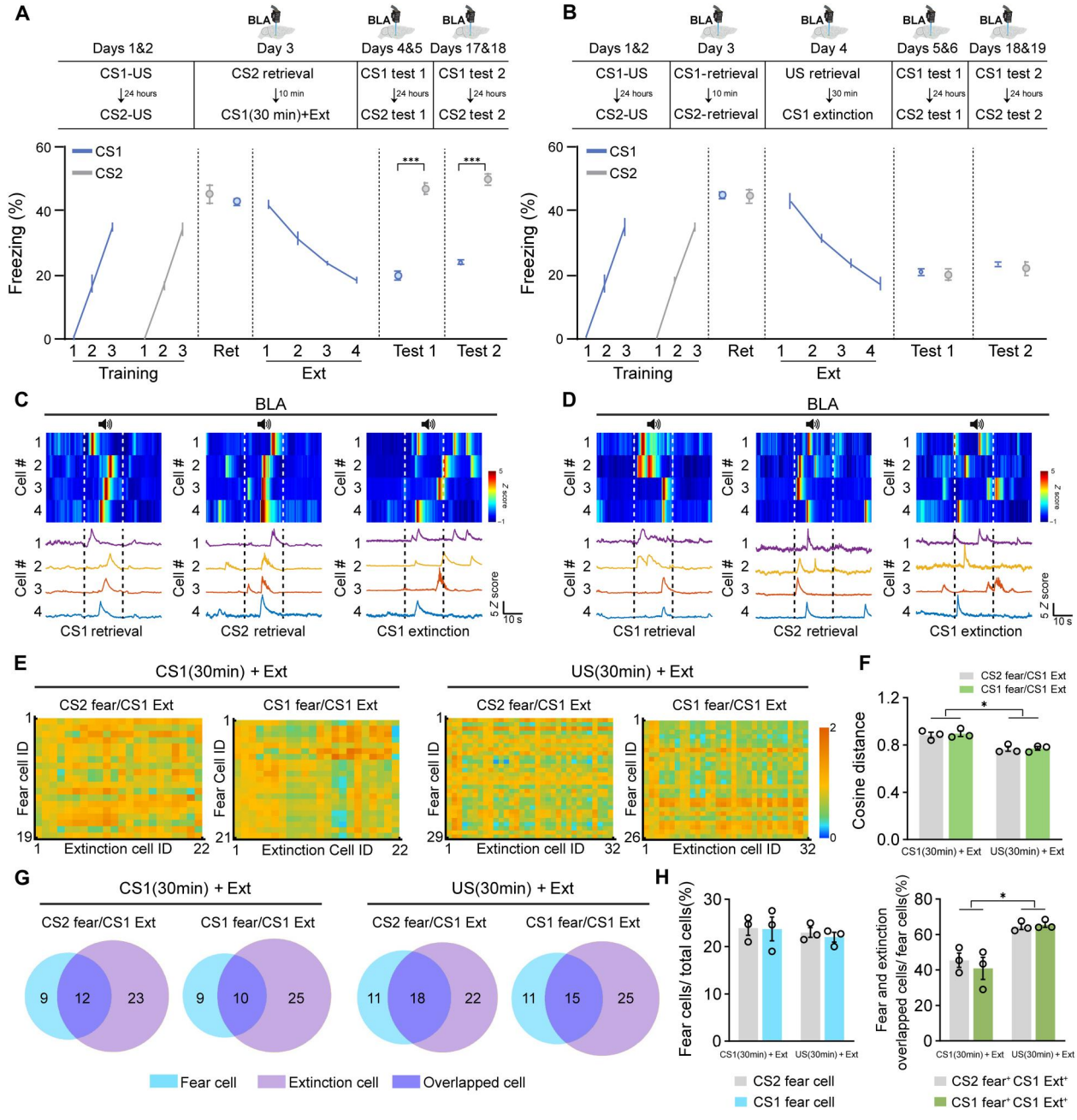

Fig. 8. The vector distance and overlapped cells between fear cells and extinction cells in BLA during US-initiated memory updating. Monitoring of Ca^{2+} activity of BLA during different sessions of CS1(30 min) + Ext (**A**) or US(30 min) + Ext (**B**) in a freely moving mouse by using miniaturized microscope (RM two-way ANOVA with Sidak's multiple comparisons test, ***$P < 0.001$). Example cells selected activated during CS1 retrieval, CS2 retrieval, and the last trail of CS1 extinction in BLA during CS (**C**)– or US (**D**)–initiated memory updating. (**E**) The matrix showed the cosine distance from one example mouse between CS1 fear cells and CS1 extinction cells and CS2 fear cells and CS1 extinction cells of BLA. (**F**) Compared with the CS1(30 min) + Ext group, CS1 fear cells and CS1extinction cells or CS2 fear cells and CS1 extinction cells showed closer cosine distance in the US(30 min) + Ext group [two-way ANOVA with Sidak's multiple comparisons test, *$P < 0.05$; $n = 3$ animals, 320 neurons in the CS1(30 min) + Ext group; $n = 3$ animals, 328 neurons in the US(30 min) + Ext group]. (**G**) The Venn map showed the distribution of CS1 fear cells, CS2 fear cells, and CS1 extinction cells in BLA from one example mouse. (**H**) The percentage of CS1 and CS2 fear cells (fear cells/total cells) in BLA showed no difference. Compared with the CS1(30 min) + Ext group, the percentage of CS2 fear cells or CS1 fear cells and CS1 extinction overlapped cells (fear and extinction overlapped cells/fear cells) in the US(30 min) + Ext group was significantly higher (two-way ANOVA with Sidak's multiple comparisons test, *$P < 0.05$). Data are presented as means ± SEM.

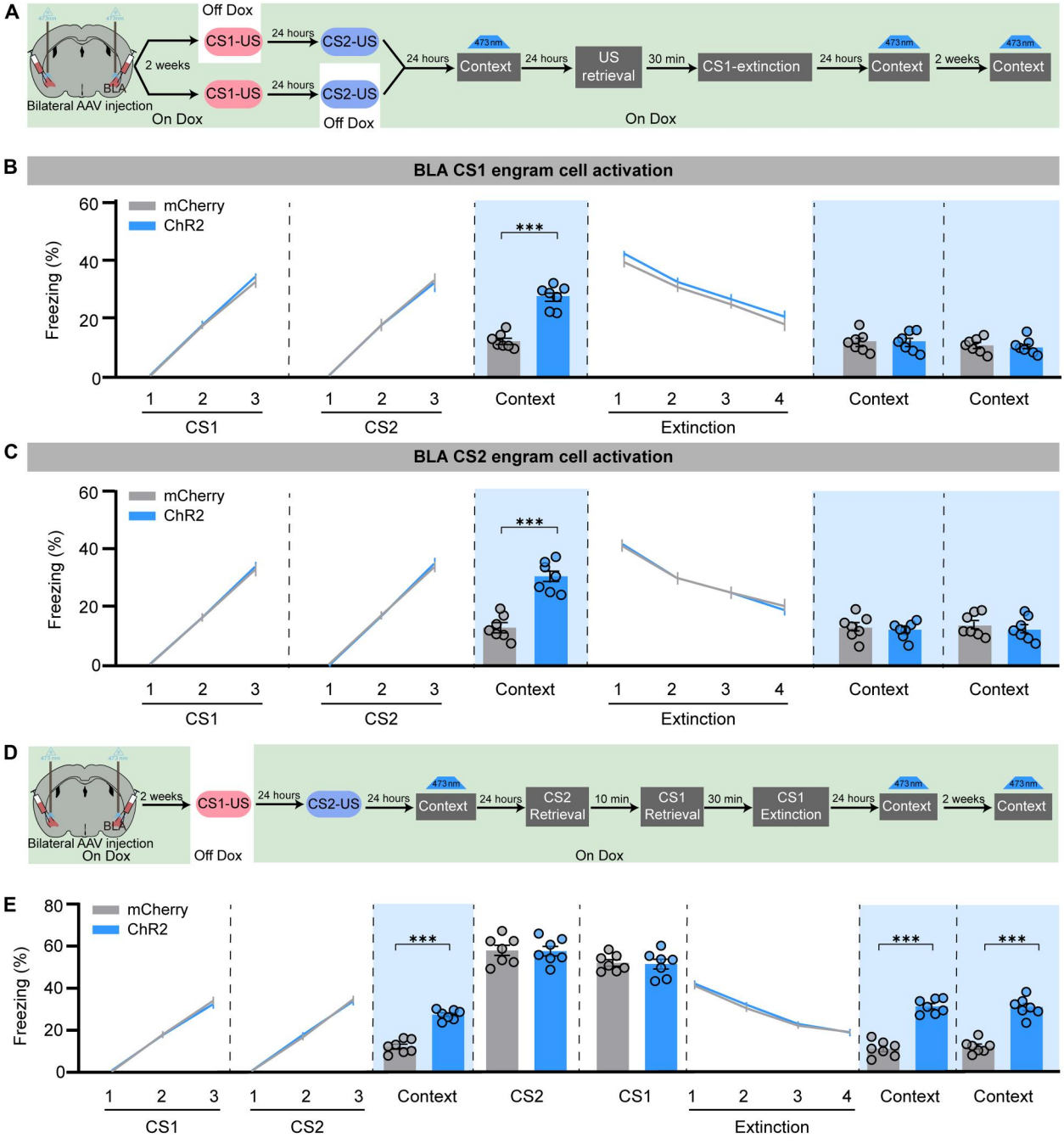

Fig. 9. The encoding of fear engram cells in BLA was altered during US-initiated memory updating. (**A**) Schematic and experimental design of the optogenetic activation of CS1 or CS2 engram cells in BLA at different time points. The freezing levels with activation of CS1 fear engram cells (**B**) or CS2 engram cells (**C**) in BLA in context B without retrieval at 24 hours after CS2-US conditioning and 24 hours or 14 days after extinction during US-initiated memory updating (RM two-way ANOVA with Sidak's multiple comparisons test, ***$P < 0.001$; $n = 7$ animals per group). (**D**) Schematic and experimental design of the optogenetic activation of CS1 engram cells in the BLA at different time points during CS1(30 min) + Ext. (**E**) The freezing levels with activation of CS1 fear engram cells in BLA in context C without retrieval at 24 hours after CS2-US conditioning and 24 hours or 14 days after extinction during CS1-initiated memory updating (RM two-way ANOVA with Sidak's multiple comparisons test, ***$P <$ 0.001; $n = 7$ animals per group). Data are presented as means ± SEM.

Ext or 24 hours or 14 days after CS1(30 min) + Ext could still induce freezing behavior in the CS-initiated memory updating group (Fig. 9D). These data suggest that the original engram coding information in BLA was rewritten in US-initiated memory updating but not in CS-initiated memory updating. To explore the mechanism underlying US-initiated memory updating in BLA, we compared the BLA activation pattern by c-Fos staining after CSs retrieval or US retrieval (fig. S8A). We found that CS2 and CS1 retrieval induced increased c-Fos$^+$ cells in BLA compared with the context only group, while the c-Fos$^+$ cell number in US retrieval was significantly greater than that during CS2 and CS1 retrieval (fig. S8, B and C). These data suggest that US retrieval may induce a more generalized BLA activation, which might account for the phenomena that US instead of CS retrieval could induce BLA engram encoding updating. Last, we labeled the activated cells during US retrieval in BLA by bilateral injection of AAV_9-c-fos:tTA and AAV_9-TRE:ChR2-mCherry into BLA (fig. S8D). We optogenetically activated these US-activated cells for 20 s at 30 min before extinction, which could increase the freezing levels and has no effect on CS1 extinction performance. However, we found that the freezing levels at the CS2 EM test and CS1 and CS2 SR tests were lower in the ChR2 group compared with the mCherry group, which suggest that activation of US-induced engram cells 30 min before extinction could induce US-initiated memory updating (fig. S8E). Moreover, artificial activation of US-induced engram cells at 24 hours or 14 days after extinction could still induce freezing behavior, which suggest that the innate US fear cells in BLA were unable to reverse the valence but might contribute to the reshaping of memory engram cells. Overall, our data show the physiological and functional evidence to support our hypothesis that the original fear cell ensemble coding pattern in PrL was remodeled during CS-initiated memory erasure, while US-initiated memory erasure induced BLA engram encoding updating.

DISCUSSION

We first investigated the role of PrL and BLA engram cells in memory updating. It is reported that reactivation of memory engrams in the DG is critical for remote contextual fear attenuation (*6*), which suggests that fear attenuation might involve memory engram ensemble updating, but little is known about the role of engram cells in memory erasure. Instead, we found that, compared with extinction alone, the post-CS extinction paradigm induced increased auditory fear engram cell reactivation in PrL and BLA. Notably, we demonstrated that manipulating fear engram cells in PrL but not BLA could bidirectionally regulate CS-initiated memory erasure. The BLA engram cells have been reported to play an essential role in fear memory acquisition, consolidation, and retrieval (*27*). We found that the reactivation of BLA fear ensemble is indispensable for US- but not CS-initiated memory updating. Inhibiting BLA fear engram cells during CS retrieval blocked freezing but could still induce memory erasure. In contrast, activating BLA fear engram cells while inhibiting PrL fear engram cells induced freezing behavior but blocked memory erasure, which suggested that the reactivation of PrL engrams but not the freezing level is essential for CS-initiated memory updating. In contrast, inhibiting BLA fear engram cells blocked US-initiated fear memory updating. These studies suggested that CS- and US-initiated memory updating depends on the reactivation of engram cells in PrL or BLA, respectively.

Next, our present work demonstrated that the increased overlapping ensembles between fear and extinction cells are essential for memory updating. A previous study found that contextual extinction training suppresses reactivation of the fear acquisition ensemble and recruits a different EM ensemble in DG, which is examined at the EM test and SR stage (*9*). The activation of fear cells induces fear memory expression, while the activation of extinction cells promotes EM expression. It is reported that distinct BLA neurons encode fear and extinction (*10*, *11*). Recently, BLA pyramidal neurons were found to be composed of two genetically, functionally, and anatomically distinct neuronal populations, which encode positive and negative valences, respectively (*28*). Further study found that BLA fear EM engram is formed and stored in the positive valence encoding cells, which express protein phosphatase 1-regulatory inhibitor subunit 1B (Ppp1r1b$^+$) (*29*). A previous study showed that PrL was crucial for memory expression but not extinction (*30*); here, we found that BLA projecting PrL neurons mainly encode fear expression, while PrL neurons receiving IL inputs were highly activated in memory extinction and were essential for memory extinction, which provides functional evidence that extinction cells in PrL exist. Our data indicate that there were distinct fear and extinction ensembles in PrL, which provides a basis for the fear and extinction ensemble interaction and information updating in PrL.

Using a miniature fluorescence microscope, we found that the vector distance between fear cells and extinction cells in PrL but not BLA was closer in CS-initiated memory updating compared with the extinction alone group. Moreover, CS-initiated memory updating induced significantly increased overlapping between fear and extinction cells in PrL but not BLA, which is selective to CS-specific cells. To our knowledge, it is the first evidence to show the increased overlapped ensembles between fear and extinction cells during memory updating. Memory formation is dynamic in nature, and acquisition of new information is often influenced by previous experiences. In our study, the retrieval 30 min before extinction shifted the allocation of extinction cells into previous fear cells. According to the memory allocation hypothesis (*31*–*33*), a temporary increase in neuronal excitability could bias the representation of a subsequent memory to the neuronal ensemble encoding the first memory. It is reported that the overlap between the hippocampal CA1 ensembles activated by two distinct contexts acquired within a day is higher than when they are separated by a week (*34*). Although fear and extinction cells encode different values, we found that CS retrieval 30 min but not 24 hours before extinction induced higher overlap between fear and extinction cells in PrL but not BLA. The increased overlap of two neuronal representations might be due to increases in intrinsic neuronal excitability triggered by activation of the transcription factor cyclic adenosine monophosphate (cAMP) response element–binding protein (CREB) of the first memory engram cells (*31*, *35*–*37*). Fear and EM that unfold in close temporal proximity (hours apart) would share a more overlapped cell ensemble and could therefore become integrated into an intertwined mnemonic structure.

Furthermore, in contrast to CS retrieval, US-initiated memory updating could erase both CS1- and CS2-associated memory and induce increased overlapping between fear and extinction cells in BLA. Previous studies reported that US is a powerful reminder to

trigger reconsolidation in the amygdala, which, when pharmacologically interfered, results in selective disruption of the multiple CS–associated memory (*26*, *38*). During US-initiated memory updating, we found that the vector distance is closer and the overlap is greater between both CS1/CS2 fear and CS1 extinction cells in BLA compared with those during CS-initiated memory updating. In contrast, in PrL, the increased overlap and decreased vector distance were only observed between CS1 fear and extinction cells. These data suggested that in contrast to CS retrieval, US-initiated memory updating occurred in the BLA fear ensembles.

Last, our study provides an opportunity to investigate the dynamic mnemonic encoding during memory updating. How the engram cells are organized to constitute a corresponding memory is a long-lasting question. We found that the reactivation of engram cells by natural cue, US, or optogenetic manipulation could be a prerequisite for memory malleability to integrate the new information outside the original memory trace and orchestrated to constitute an updated memory. What is the underlying mechanism by which memory is encoded within the engram cells? As formalized by Morris and colleagues (*39*), the modification of the pattern of synaptic connections mediated by synaptic plasticity is the mechanism whereby the brain stores memory. Using synaptic optoprobe, Kasai and colleagues (*40*) found that the acquired motor learning was disrupted by the optical shrinkage of the potentiated spines but was not affected by the identical manipulation of spines evoked by a distinct motor task in the same cortical region, which suggests that acquired motor memory depends on the formation of a task-specific, dense synaptic ensemble. Optogenetic manipulation of the plasticity at synapses specific to one memory affected the recall of only that memory and did not affect another linked fear memory encoded in the shared ensemble (*41*), which suggests that synapse-specific connectivity of engram cells guarantees the identity and storage of individual memories. Using the dual-eGRASP (GFP reconstitution across synaptic partners) technique, it is reported that there is enhanced connectivity and larger spine morphology between engram cells after fear conditioning and there was weakened connectivity between engram cells after extinction (*42*, *43*). However, the question whether the memory information was updated in memory erasure with no fear recovery was unanswered. Previous studies showed that optogenetic activation of engram cell could induce memory recovery from amnesia resulting from anisomycin-induced disruption of reconsolidation, and similar results are also found in mouse models of Alzheimer′s disease and infantile amnesia (*44*–*46*), which suggest that the strength of engram cell connectivity critically contributes to the memory retrieval. In contrast, we found that optogenetic activation of the PrL or BLA engram cells after CS- or US-initiated memory updating could not induce memory recovery, whereas activating the engram cells after extinction did. In addition, it has been reported that the valence associated with the hippocampal DG memory engram could be bidirectionally reversed; however, the BLA engrams were not able to reverse the valence of the memory (*47*). Consistent with this report, we found that the reactivation of BLA engram cells is not sufficient for the memory valence updating; however, US stimulus, which triggers a more generalized BLA activation, could induce the BLA engram encoding updating. In addition, only a part of fear cells showed increased activity at the end of extinction during CS- or US-initiated memory updating, suggesting that a part of cell activation pattern alteration might be sufficient for switching the function of the total cell ensembles, which was also reported in previous studies (*34*, *47*).

These results provide physiological and functional evidence to support our hypothesis that memory information is stored in the specific pattern of connections among engram cells. Memory updating instead of extinction alters fear engram encoding rather than induces a memory retrieval deficit, which may result from the increased overlapping fear and extinction ensembles initiated by the CS/US representation. Moreover, CS-/US-initiated memory updating is specific to learning-associated memory encoding as the valence of innate fear engrams (shock labeled) was unchanged.

Overall, we demonstrate that memory updating reshaped the neural ensemble representations of the original memory, which depends on the overlapped ensembles between fear and extinction cells, whereas memory extinction temporarily inhibited but not reshaped the original fear cells. Our study provides some previously unidentified insights into understanding how the value of memory was updated and switched.

MATERIALS AND METHODS

Mice

Adult male C57BL/6J mice, c-fos:tTA transgenic mice [The Jackson Laboratory; strain B6.Cg-Tg(Fos-tTA, Fos-EGFP*)1Mmay/J; stock number 018306], and TRE:H2B-GFP transgenic mice [The Jackson Laboratory: strain Tg(tetO-HIST1H2BJ/GFP)47Efu/J; stock number 005104] weighing between 23 and 25 g (8 weeks old) at the beginning of the experiment and mice (three to four mice per standard laboratory cage) were housed and maintained at 22° ± 2°C on a 12-hour light-dark cycle with water and food available ad libitum. Care was taken to minimize pain or discomfort for the animals. All procedures were conducted according to the National Institutes of Health (NIH) *Guide for the Care and Use of Laboratory Animals* and were approved by the institutional animal care and use committee of Shandong University.

Auditory fear conditioning

There are four groups with different behavioral treatments in our study, and all groups received AFC training. After the AFC training was performed, the mice received different treatments, which were context only, extinction only, R(30 min) + Ext, and R(24 hours) + Ext groups.

For AFC, the mice were habituated for 3 min without any stimulation in a fear conditioning box (context A, which was measured 25 cm × 25 cm × 25 cm and located inside of a custom-built sound isolation box). Each box contained a modular test cage with an electrifiable floor grid and an ambient light supply. The inner walls were painted black and were cleaned with alcohol before testing. Grid floors were connected to a scrambled shock source. Auditory stimuli were delivered via a speaker in the chamber wall. Delivery of stimuli was controlled with a personal computer and a specific software (Freezing, Panlab), and then mice were fear-conditioned with three tone (CS: 20 s, 3 kHz, 80 dB)–footshock (US: 0.75 mA, 1 s) pairings. The interstimulus interval (ITI) between each CS was 120 s. After an additional 120 s following the last shock, the mice were placed back to their home cages.

Retrieval
The retrieval session was performed 24 hours after AFC; context only and extinction only mice were put into a chamber consisting of a white box context B with different floor, color, shape, and smell from fear conditioning box context A without any stimulation for 200 s. The R(30 min) + Ext and R(24 hours) + Ext mice were presented with an isolated CS after 120-s habituation, then there was 60-s duration for resting, and the mice were returned to the home cage to wait for the extinction training.

Extinction training
Mice underwent extinction training in context B. The extinction protocol was conducted as described previously (*3*) with little modification. Context only mice were placed into the extinction box context B for 1880 s without any stimulation, while extinction only mice, R(30 min) + Ext mice, and R(24 hours) + Ext mice were placed into context B for 180 s, then extinction only mice received 40 tone-alone (20 s) presentations with 20-s ITIs to conform to the total number of CSs, and CS(30 min) + Ext mice and CS(24 hours) + Ext mice received 39 tone-alone (20 s) presentations with 20-s ITIs. Extinction trials were binned into Ext#1, Ext#2, Ext#3, and Ext#4, with Ext#1 representing the average of trails 1 to 9 for CS(30 min) + Ext mice and CS(24 hours) + Ext mice and trails 1 to 10 for the extinction only group, and Ext#2, Ext#3, and Ext#4 representing the average of every 10 trails of 30 trails remaining.

EM test
Twenty-four hours after extinction, the mice received four tone-alone (20 s) presentations with 30-s ITIs to measure the EM in the extinction chamber (context B).

SR test
Two weeks after the EM test, the mice received four tone-alone (20 s) presentations with 30-s ITIs to measure the SR freezing in the extinction chamber (context B).

Renewal
Twenty-four hours after the EM test, the mice were tested for the freezing for CS back in the acquisition context (context A).

Reinstatement
Twenty-four hours after the EM test, the mice received five footshocks without any CS recall. The next day, the mice were tested for the freezing levels in response to the CS in the same context.

Retraining
Twenty-four hours after the EM test, the mice were reconditioned with a single CS-US pair in context B.

Memory test
Twenty-four hours after retraining, the mice were tested for the freezing levels to CS.

CS1 and CS2 AFC
We used the CS1-US and CS2-US (CS1: 20 s, 3 kHz, 80 dB; CS2: auditory pips, 5-Hz pulses of auditory pips, 5-ms rise and fall, 20 s, 8 kHz, 80 dB; US: 0.4 mA, 1-s footshock) fear conditioning paradigm to distinguish two auditory fear memories in one mouse. On day 1, the mice were fear-conditioned with three CS1-US pairings with a 120-s ITI between each pairing in context A. Twenty-four hours later, the mice were trained with CS2-US, which was the same as CS1-US procedure in context C.

For the CS1(30 min) + Ext experiment, the mice first underwent CS2 retrieval (retrieval was performed as described above) in context B on day 3. Ten minutes later, the mice underwent CS1 retrieval, and the extinction training of CS1 was performed 30 min later. On days 4 and 5, the mice underwent CS1 retrieval and CS2 retrieval to test the CS1- and CS2-related fear memory (performed as described above). On days 17 and 18, the mice underwent memory measurement (performed as described above) to CS1 and CS2 to test the memory recovery.

For the US(30 min) + Ext experiment, the mice first underwent CS1 and CS2 retrieval with a 10-min ITI in context B on day 3. The US retrieval, in which a single US was provided, was performed, and the extinction training of CS1 was performed 30 min later in a novel context D on day 4. On days 5 and 6, the mice underwent CS1 and CS2 retrieval to test the CS1- and CS2-related fear memory. On days 18 and 19, the mice underwent memory measurement to CS1 and CS2 to test the memory recovery.

In all processes, the freezing was measured by a high-sensitivity weight transducer (load cell unit), which could record and analyze the animal movement intensity. The freezing level was scored during each experimental phase by the software (Freezing, Panlab). The freezing levels of retrieval, extinction, EM, SR, renewal, and reinstatement were scored during the presentation of the tone, while extinction trials were binned into four sessions, which was previously described in the extinction training of AFC. For the optogenetic activation experiment in Figs. 2, 5, and 7 and figs. S3 and S8, the freezing was scored during the activation period (20 s), which was the same as single CS duration. The freezing levels in the context during the pre-CS or preactivation period were scored as the freezing levels of habituation in Fig. 2 and fig. S3.

Immunohistochemistry and imaging
To prepare fixed brain tissue, the mice were transcardially perfused with 0.9% normal saline and 4% paraformaldehyde (PFA; pH 7.4) 90 min after the behavioral treatment, and brains were removed into 4% PFA overnight at 4°C for post-fixation. Then, the brains were sliced to 40-μm coronal sections via vibratome (VT1200S, Leica, Germany) and stored in antifreeze at −20°C.

For labeling c-fos–positive cells or Cre recombinase immunostaining, sections were incubated in blocking solution [0.4% Triton X-100 and 15% donkey serum in phosphate-buffered saline (PBS)] for 2 hours at room temperature and then incubated in 0.1% PBST (0.1% Triton X-100 in PBS) containing anti–c-fos rabbit antibody (1:3000; 2250S, Cell Signaling Technology) or anti-Cre recombinase mouse antibody (1:500; 2250S, Cell Signaling Technology) for 12 hours at 4°C. Free-floating sections were washed three times with 0.1% PBST and then incubated with donkey anti-rabbit conjugated to Alexa 594 (1:1000 in 0.1% Triton X-100 in PBS; A21207; Invitrogen) and donkey anti-rabbit conjugated to Cy5 AffiniPure (1:1000 in 0.1% Triton X-100 in PBS; 711-175-152, The Jackson Laboratory) for c-Fos staining or donkey anti-mouse conjugated to Alexa 647 (1:1000 in 0.1% Triton X-100 in PBS; A31571; Invitrogen) for Cre staining for 2 hours at room temperature. Subsequently, immunolabeled sections were washed with PBS three times, mounted on slides, dehydrated, and immersed in ProLong Gold antifade reagent with 4′,6-diamidino-2-phenylindole (DAPI). Multiple

images were captured at 20× objective (pixel size, 0.65 μm) using a Zeiss LSM880 confocal microscope (Zeiss, Germany) at Translational Medicine Core Facility of Shandong University.

Cell counting

For counting the c-Fos$^+$, GFP$^+$, EGFP$^+$, or mCherry$^+$ cells, six coronal BLA sections (from bregma −0.82 mm to bregma −1.94 mm) and five coronal sections containing IL and PrL (from bregma 1.94 mm to bregma 1.34 mm) were used to analyze in all experiments. The NIH ImageJ was used to count the number of c-Fos$^+$, GFP$^+$, or mCherry$^+$ neurons and calculate the area of BLA, PrL, and IL in each section. Overlap in Fig. 1 was calculated by (EGFP$^+$c-Fos$^+$/DAPI$^+$), while (c-Fos$^+$/DAPI$^+$) × (GFP$^+$/DAPI$^+$) was calculated as the chance level of overlap in BLA and PrL, as previously reported (*7*). Overlap in Fig. 2 was calculated by (EGFP$^+$c-Fos$^+$/DAPI$^+$) or (mCherry$^+$c-Fos$^+$/DAPI$^+$), while (c-Fos$^+$/DAPI$^+$) × (EGFP$^+$/DAPI$^+$) or (c-Fos$^+$/DAPI$^+$) × (mCherry$^+$/DAPI$^+$) was calculated as their chance level of overlap in PrL.

Stereotactic injection and fiber optic implants

The mice were fixed on a stereotaxic apparatus (RWD Life Science), while the mice were anesthetized with isoflurane on an anesthetic machine (RWD Life Science). Viruses were injected using a glass micropipette through a microelectrode holder filled with mineral oil. A microsyringe pump (Nanoliter 2010 Injector, WPI) and its controller (Micro4, WPI) were used to control the speed with 40 nl/min of the injection. The needle was slowly lowered to the target site and remained there for 10 min after the injection. For the inhibition/activation of PrL engram cells, the mice were bilaterally injected with 100 nl of pAAV$_9$-c-fos:tTA-pA (Addgene, plasmid no. 34856) and AAV$_9$-TRE-eNpHR3.0-EYFP (OBIO, AG26972) or AAV$_9$-TRE:ChR2-mCherry (OBIO, PT0515) into PrL [anterior-posterior (AP): +1.94 mm, medial-lateral (ML): ±0.5 mm, dorsal-ventral (DV): −2.1 mm] and were bilaterally implanted with optical fiber into PrL (AP: +1.94 mm, ML: ±0.5 mm, DV: −1.9 mm) under the on-Dox condition. For the inhibition/activation of BLA engram cells, the mice were bilaterally injected with 100 nl of AAV$_9$-c-fos:tTA and AAV$_9$-TRE-eNpHR3.0-EYFP or AAV$_9$-TRE:ChR2-mCherry into BLA (AP: −1.46 mm, ML: ±0.33 mm, DV: −4.68 mm) and were bilaterally implanted with optical fiber into BLA (AP: −1.46 mm, ML: ±3.3 mm, DV: −4.4 mm) under the on-Dox condition.

For inhibition of PrL neurons receiving IL projection, 100 nl of AAV$_1$-hSyn-Cre-pA (Taitool, S02992-1) was bilaterally injected into the IL (AP: +1.94 mm, ML: ±0.5 mm, DV: −3.3 mm) with a 20° angle, while 80 nl of rAAV-Ef1α-DIO-eNpHR3.0 -EYFP-WPRE-pA (BrainVTA, PT-0006) was injected into PrL (AP: +1.94 mm, ML: ±0.5 mm, DV: −2.1 mm), and optical fiber was also implanted in PrL (AP: +1.94 mm, ML: ±0.5 mm, DV: −1.9 mm). For inhibition of PrL-BLA projections, 100 nl of AAV$_9$-eNpHR3.0-EYFP (BrainVTA, PT-0010) was bilaterally injected into PrL (AP: +1.94 mm, ML: ±0.5 mm, DV: −2.1 mm), and optical fiber was implanted into BLA (AP: −1.46 mm, ML: ±3.3 mm, DV: −4.4 mm).

Activity-dependent cell labeling

To label the engram cells, we crossed c-fos:tTA transgenic mice with TRE:H2B-GFP transgenic mice and subjected the double transgenic mice to AFC, or we injected AAV$_9$-c-fos:tTA and AAV$_9$-TRE-eNpHR3.0-EYFP or AAV$_9$-TRE:ChR2-mCherry into WT mice for engram cell labeling. The double transgenic mice were maintained with the Dox-food condition (40 mg/kg) from their birth, and WT mice were treated with Dox-containing diet 2 weeks before surgery (*7*, *48*). The mice were taken off Dox for 24 hours to open a window for fear memory engram labeling in context A. Then, the animals were exposed to context A for fear conditioning, and Dox diets were resumed immediately after AFC training.

Optogenetic manipulation of PrL and BLA engram cells

In this study, we tested whether the activation/inhibition of PrL and BLA engram cells labeled by ChR2–mCherry or eNpHR3.0-EYFP is sufficient or necessary for memory updating by optogenetic manipulation 30 min before extinction. A context distinct from the AFC training chamber (context B) was used, and all mice had patch cords fitted to the optic fiber implant before testing. For light-induced freezing behavior, ChR2 was stimulated at 4 Hz (15-ms pulse width) for PrL engram cells or at 20 Hz (15-ms pulse width) for BLA engram cells using a 473-nm laser (10 mW). The manipulation session was 200 s, and mouse received 20-s optical stimulation starting from 120 s. At the end of 200 s, the mouse was detached and returned to its home cage. In addition, eNpHR was stimulated for both PrL and BLA engram cells using a 589-nm laser (5 mW) during a retrieval trail; the laser was on during the tone onset and off at the end of tone. Following behavioral experiments, brain sections were prepared to confirm efficient viral labeling in target areas. Animals lacking adequate labeling were excluded before behavior quantification.

Calcium imaging surgery and data acquisition

Ca^{2+} imaging of PrL and BLA neurons was performed on WT mice. AAV$_5$-hsyn-GCaMP6f (Taitool, S02245) was injected into right PrL (AP: 1.94 mm, ML: +0.5 mm, DV: −2.15 mm) or BLA (AP: −1.46 mm, ML: +3.3 mm, DV: −4.68 mm), then a GRIN lens (0.5-mm diameter, 4.1-mm length; Inscopix) was implanted on PrL, and a GRIN lens (0.5-mm diameter, 6.1-mm length; Inscopix) was implanted on BLA after 2-week injection. Last, a baseplate (Inscopix) was attached above the GRIN lens by ultraviolet-light curable glue 2 weeks after GRIN lens implantation. The Ca^{2+} imaging data were captured (20 frames/s) using the Inscopix miniature microscope and nVista acquisition software (Inscopix, CA, USA) during retrieval, extinction, EM test, and SR test. In all the fear memory–related behavior experiments, a Transistor-Transistor-Logic (TTL) signal was used to synchronize the calcium signal and the behavioral time points.

Calcium imaging data processing and cell sorting

The processing of calcium imaging data and calcium signal extraction was accomplished by using the Inscopix Data Processing Software (IDPS, Inscopix) with the following steps. First, the raw videos were preprocessed by cropping it to a specified pixel region. Then, the images were then downsampled (×2) and filtered by using a spatial band-pass filter to remove low and high spatial frequency information (low cutoff: 0.005 pixel^{-1}; high cutoff: 0.500 pixel^{-1}). Next, each frame of the movies was estimated to minimize the difference between the transformed frame and the reference frame (blood vessels) using the rigid image registration algorithm for motion correction (*49*). After this step, each pixel value was normalized by $\Delta F(t) - F_0/F_0$, where F_0 is the mean value by averaging the

signal of the entire video. Last, the spatial locations and calcium signals of individual cells were identified using the principal components analysis (PCA)/independent components analysis (ICA) algorithm (*29*). Ideally, each component was supposed to be one neuron, but it also identified some confounding components that may be nonneurons or nonbiological signals, so we manually removed those components by comparing their signal transients, locality, and morphology.

Identifying fear cells and extinction cells

To define the responsive cells, a Wilcoxon rank sum test was performed for the calcium signal of cells between the tone period and the equivalent no-tone period with a significance threshold of $P < 0.05$, according to a previous report (*23*). A cell was defined as fear cell if its signals during the tone period of retrieval were higher than those during the equivalent no-tone period with a significance threshold of $P < 0.05$, while cells whose signals during the last trail of the extinction period were higher than those during the equivalent no-tone period with the same threshold were defined as extinction cells, and US retrieval responsible cells were defined as the cells that show higher signal during the 20-s period from the US retrieval onset compared with signals during the 20-s period with no US. The reactivated fear cells or extinction cells in fig. S4 were defined as fear cells or extinction cells with the higher signals, which were examined during the tone period compared with signals during the no-tone period by the Wilcoxon rank sum test in different sessions. The reactivated fear cells or extinction cells during US retrieval in fig. S7 were defined as fear cells or extinction cells with the higher signals, which were tested during the 20-s period from the US onset compared with signals during the 20-s period with no US by the Wilcoxon rank sum test in US retrieval. The fear or extinction cell reactivation ratio in fig. S4 was calculated by reactivated fear cells/total fear cells or reactivated extinction cells/total extinction cells, while the reactivation level during US retrieval normalized to chance in fig. S7 was calculated by (reactivated fear cells/total cells)/[(fear cells/total cells) × (US retrieval responsible cells/total cells)]. The overlap of CS1 and CS2 fear cell was calculated by CS1 and CS2 co-responsible cells/total cells, while (CS1 fear cells/total cells) × (CS2 fear cells/total cells) was the chance level.

The distance between fear cells and extinction cells

To calculate the vector distance between fear cells and extinction cells, we performed the cosine distance calculation. The population vector x was defined as the normalized Ca^{2+} signal of fear cells in retrieval and population vector y was defined as the normalized Ca^{2+} signal of extinction cells in last trail of extinction. The cosine distance of two population vector x and y was calculated by the following formula

$$\text{cosine distance} = 1 - \cos\theta = 1 - \frac{\sum(x_i y_i)}{\sqrt{\sum x_i^2 \sum y_i^2}}$$

Statistics

GraphPad Prism 8.0 (GraphPad Software, San Diego, CA, USA) was used to analyze the data with Student's *t* test and one-way or two-way analysis of variance (ANOVA), followed by Tukey's multiple comparisons test or Sidak's multiple comparisons test. For single-factor experiments involving two or more than two groups, Student's *t* test or one-way ANOVA was used. For experiments composed of multiple factors, a two-way ANOVA with test for interaction was used. All data were displayed as means ± SEM, and the significance was set at $P < 0.05$.

Supplementary Materials

This PDF file includes:

Figs. S1 to S8

View/request a protocol for this paper from *Bio-protocol*.

REFERENCES AND NOTES

1. M. K. Tanner, H. S. Hake, C. A. Bouchet, B. N. Greenwood, Running from fear: Exercise modulation of fear extinction. *Neurobiol. Learn. Mem.* **151**, 28–34 (2018).
2. K. M. Myers, M. Davis, Mechanisms of fear extinction. *Mol. Psychiatry* **12**, 120–150 (2007).
3. M.-H. Monfils, K. K. Cowansage, E. Klann, J. E. LeDoux, Extinction-reconsolidation boundaries: Key to persistent attenuation of fear memories. *Science* **324**, 951–955 (2009).
4. D. Schiller, M.-H. Monfils, C. M. Raio, D. C. Johnson, J. E. LeDoux, E. A. Phelps, Preventing the return of fear in humans using reconsolidation update mechanisms. *Nature* **463**, 49–53 (2010).
5. J. Liu, L. Zhao, Y. Xue, J. Shi, L. Suo, Y. Luo, B. Chai, C. Yang, Q. Fang, Y. Zhang, Y. Bao, C. L. Pickens, L. Lu, An unconditioned stimulus retrieval extinction procedure to prevent the return of fear memory. *Biol. Psychiatry* **76**, 895–901 (2014).
6. O. Khalaf, S. Resch, L. Dixsaut, V. Gorden, L. Glauser, J. Graff, Reactivation of recall-induced neurons contributes to remote fear memory attenuation. *Science* **360**, 1239–1242 (2018).
7. T. Kitamura, S. K. Ogawa, D. S. Roy, T. Okuyama, M. D. Morrissey, L. M. Smith, R. L. Redondo, S. Tonegawa, Engrams and circuits crucial for systems consolidation of a memory. *Science* **356**, 73–78 (2017).
8. S. Ramirez, X. Liu, P. A. Lin, J. Suh, M. Pignatelli, R. L. Redondo, T. J. Ryan, S. Tonegawa, Creating a false memory in the hippocampus. *Science* **341**, 387–391 (2013).
9. A. F. Lacagnina, E. T. Brockway, C. R. Crovetti, F. Shue, M. J. McCarty, K. P. Sattler, S. C. Lim, S. L. Santos, C. A. Denny, M. R. Drew, Distinct hippocampal engrams control extinction and relapse of fear memory. *Nat. Neurosci.* **22**, 753–761 (2019).
10. C. Herry, S. Ciocchi, V. Senn, L. Demmou, C. Muller, A. Luthi, Switching on and off fear by distinct neuronal circuits. *Nature* **454**, 600–606 (2008).
11. V. Senn, S. B. E. Wolff, C. Herry, F. Grenier, I. Ehrlich, J. Grundemann, J. P. Fadok, C. Muller, J. J. Letzkus, A. Luthi, Long-range connectivity defines behavioral specificity of amygdala neurons. *Neuron* **81**, 428–437 (2014).
12. L. Dixsaut, J. Graff, The medial prefrontal cortex and fear memory: Dynamics, connectivity, and engrams. *Int. J. Mol. Sci.* **22**, 12113 (2021).
13. H. C. Bergstrom, The neurocircuitry of remote cued fear memory. *Neurosci. Biobehav. Rev.* **71**, 409–417 (2016).
14. L. G. Reijmers, B. L. Perkins, N. Matsuo, M. Mayford, Localization of a stable neural correlate of associative memory. *Science* **317**, 1230–1233 (2007).
15. X. Liu, S. Ramirez, P. T. Pang, C. B. Puryear, A. Govindarajan, K. Deisseroth, S. Tonegawa, Optogenetic stimulation of a hippocampal engram activates fear memory recall. *Nature* **484**, 381–385 (2012).
16. F. H. Do-Monte, K. Quiñones-Laracuente, G. J. Quirk, A temporal shift in the circuits mediating retrieval of fear memory. *Nature* **519**, 460–463 (2015).
17. S. Maren, G. J. Quirk, Neuronal signalling of fear memory. *Nat. Rev. Neurosci.* **5**, 844–852 (2004).
18. X. Gu, Y. J. Wu, Z. Zhang, J. J. Zhu, X. R. Wu, Q. Wang, X. Yi, Z. J. Lin, Z. H. Jiao, M. Xu, Q. Jiang, Y. Li, N. J. Xu, M. X. Zhu, L. Y. Wang, F. Jiang, T. L. Xu, W. G. Li, Dynamic tripartite construct of interregional engram circuits underlies forgetting of extinction memory. *Mol. Psychiatry* **27**, 4077–4091 (2022).
19. M. R. Milad, G. J. Quirk, Neurons in medial prefrontal cortex signal memory for fear extinction. *Nature* **420**, 70–74 (2002).
20. J. Peters, L. M. Dieppa-Perea, L. M. Melendez, G. J. Quirk, Induction of fear extinction with hippocampal-infralimbic BDNF. *Science* **328**, 1288–1290 (2010).
21. J. Xin, L. Ma, T. Y. Zhang, H. Yu, Y. Wang, L. Kong, Z. Y. Chen, Involvement of BDNF signaling transmission from basolateral amygdala to infralimbic prefrontal cortex in conditioned taste aversion extinction. *J. Neurosci.* **34**, 7302–7313 (2014).
22. A. Mukherjee, P. Caroni, Infralimbic cortex is required for learning alternatives to prelimbic promoted associations through reciprocal connectivity. *Nat. Commun.* **9**, 2727 (2018).

23. K. M. Hagihara, O. Bukalo, M. Zeller, A. Aksoy-Aksel, N. Karalis, A. Limoges, T. Rigg, T. Campbell, A. Mendez, C. Weinholtz, M. Mahn, L. S. Zweifel, R. D. Palmiter, I. Ehrlich, A. Luthi, A. Holmes, Intercalated amygdala clusters orchestrate a switch in fear state. *Nature* **594**, 403–407 (2021).
24. T. Frank, N. R. Monig, C. Satou, S. I. Higashijima, R. W. Friedrich, Associative conditioning remaps odor representations and modifies inhibition in a higher olfactory brain area. *Nat. Neurosci.* **22**, 1844–1856 (2019).
25. K. Z. Tanaka, A. Pevzner, A. B. Hamidi, Y. Nakazawa, J. Graham, B. J. Wiltgen, Cortical representations are reinstated by the hippocampus during memory retrieval. *Neuron* **84**, 347–354 (2014).
26. J. Debiec, L. Díaz-Mataix, D. E. A. Bush, V. Doyère, J. E. Ledoux, The amygdala encodes specific sensory features of an aversive reinforcer. *Nat. Neurosci.* **13**, 536–537 (2010).
27. M. Bocchio, S. Nabavi, M. Capogna, Synaptic plasticity, engrams, and network oscillations in amygdala circuits for storage and retrieval of emotional memories. *Neuron* **94**, 731–743 (2017).
28. J. Kim, M. Pignatelli, S. Xu, S. Itohara, S. Tonegawa, Antagonistic negative and positive neurons of the basolateral amygdala. *Nat. Neurosci.* **19**, 1636–1646 (2016).
29. X. Zhang, J. Kim, S. Tonegawa, Amygdala reward neurons form and store fear extinction memory. *Neuron* **105**, 1077–1093.e7 (2020).
30. D. Sierra-Mercado, N. Padilla-Coreano, G. J. Quirk, Dissociable roles of prelimbic and infralimbic cortices, ventral hippocampus, and basolateral amygdala in the expression and extinction of conditioned fear. *Neuropsychopharmacology* **36**, 529–538 (2011).
31. A. J. Silva, Y. Zhou, T. Rogerson, J. Shobe, J. Balaji, Molecular and cellular approaches to memory allocation in neural circuits. *Science* **326**, 391–395 (2009).
32. T. Rogerson, D. J. Cai, A. Frank, Y. Sano, J. Shobe, M. F. Lopez-Aranda, A. J. Silva, Synaptic tagging during memory allocation. *Nat. Rev. Neurosci.* **15**, 157–169 (2014).
33. A. F. de Sousa, A. Chowdhury, A. J. Silva, Dimensions and mechanisms of memory organization. *Neuron* **109**, 2649–2662 (2021).
34. D. J. Cai, D. Aharoni, T. Shuman, J. Shobe, J. Biane, W. Song, B. Wei, M. Veshkini, M. La-Vu, J. Lou, S. E. Flores, I. Kim, Y. Sano, M. Zhou, K. Baumgaertel, A. Lavi, M. Kamata, M. Tuszynski, M. Mayford, P. Golshani, A. J. Silva, A shared neural ensemble links distinct contextual memories encoded close in time. *Nature* **534**, 115–118 (2016).
35. A. P. Yiu, V. Mercaldo, C. Yan, B. Richards, A. J. Rashid, H. L. Hsiang, J. Pressey, V. Mahadevan, M. M. Tran, S. A. Kushner, M. A. Woodin, P. W. Frankland, S. A. Josselyn, Neurons are recruited to a memory trace based on relative neuronal excitability immediately before training. *Neuron* **83**, 722–735 (2014).
36. A. J. Rashid, C. Yan, V. Mercaldo, H.-L. L. Hsiang, S. Park, C. J. Cole, A. De Cristofaro, J. Yu, C. Ramakrishnan, S. Y. Lee, K. Deisseroth, P. W. Frankland, S. A. Josselyn, Competition between engrams influences fear memory formation and recall. *Science* **353**, 383–387 (2016).
37. J. H. Han, S. A. Kushner, A. P. Yiu, C. J. Cole, A. Matynia, R. A. Brown, R. L. Neve, J. F. Guzowski, A. J. Silva, S. A. Josselyn, Neuronal competition and selection during memory formation. *Science* **316**, 457–460 (2007).
38. L. Diaz-Mataix, J. Debiec, J. E. LeDoux, V. Doyere, Sensory-specific associations stored in the lateral amygdala allow for selective alteration of fear memories. *J. Neurosci.* **31**, 9538–9543 (2011).
39. S. J. Martin, P. D. Grimwood, R. G. Morris, Synaptic plasticity and memory: An evaluation of the hypothesis. *Annu. Rev. Neurosci.* **23**, 649–711 (2000).
40. A. Hayashi-Takagi, S. Yagishita, M. Nakamura, F. Shirai, Y. I. Wu, A. L. Loshbaugh, B. Kuhlman, K. M. Hahn, H. Kasai, Labelling and optical erasure of synaptic memory traces in the motor cortex. *Nature* **525**, 333–338 (2015).
41. K. Abdou, M. Shehata, K. Choko, H. Nishizono, M. Matsuo, S. I. Muramatsu, K. Inokuchi, Synapse-specific representation of the identity of overlapping memory engrams. *Science* **360**, 1227–1231 (2018).
42. J. H. Choi, S. E. Sim, J. I. Kim, D. I. Choi, J. Oh, S. Ye, J. Lee, T. Kim, H. G. Ko, C. S. Lim, B. K. Kaang, Interregional synaptic maps among engram cells underlie memory formation. *Science* **360**, 430–435 (2018).
43. D. I. Choi, J. Kim, H. Lee, J. I. Kim, Y. Sung, J. E. Choi, S. J. Venkat, P. Park, H. Jung, B. K. Kaang, Synaptic correlates of associative fear memory in the lateral amygdala. *Neuron* **109**, 2717–2726.e3 (2021).
44. T. J. Ryan, D. S. Roy, M. Pignatelli, A. Arons, S. Tonegawa, Engram cells retain memory under retrograde amnesia. *Science* **348**, 1007–1013 (2015).
45. D. S. Roy, A. Arons, T. I. Mitchell, M. Pignatelli, T. J. Ryan, S. Tonegawa, Memory retrieval by activating engram cells in mouse models of early Alzheimer's disease. *Nature* **531**, 508–512 (2016).
46. A. Guskjolen, J. W. Kenney, J. de la Parra, B. A. Yeung, S. A. Josselyn, P. W. Frankland, Recovery of "lost" infant memories in mice. *Curr. Biol.* **28**, 2283–2290.e3 (2018).
47. R. L. Redondo, J. Kim, A. L. Arons, S. Ramirez, X. Liu, S. Tonegawa, Bidirectional switch of the valence associated with a hippocampal contextual memory engram. *Nature* **513**, 426–430 (2014).
48. B. K. Chen, N. J. Murawski, C. Cincotta, O. McKissick, A. Finkelstein, A. B. Hamidi, E. Merfeld, E. Doucette, S. L. Grella, M. Shpokayte, Y. Zaki, A. Fortin, S. Ramirez, Artificially enhancing and suppressing hippocampus-mediated memories. *Curr. Biol.* **29**, 1885–1894.e4 (2019).
49. J. Schwenkgrub, E. R. Harrell, B. Bathellier, J. Bouvier, Deep imaging in the brainstem reveals functional heterogeneity in V2a neurons controlling locomotion. *Sci. Adv.* **6**, eabc6309 (2020).

Acknowledgments: We thank Experimental Center, Shandong University of Traditional Chinese Medicine, and Translational Medicine Core Facility of Shandong University for consultation and instrument availability that supported this work. **Funding:** This study was supported by the STI2030 Major Projects (2021ZD0202804), the National Natural Science Foundation of China (no. 32171029), and the Natural Science Foundation of Shandong Province (no. ZR2020ZD17). **Author contributions:** This study was conceptualized and designed by Z.-Y.C. and S.-W.T. S.-W.T. carried out the experiments and analyzed data. B.-W.D., J.-C.S., and G.-Z.F. contributed to transgenic mice keeping, histology, staining, and quantification. S.-Q.X. contributed to the behavioral experiment. S.-W.T., X.-R.W., X.-L.C., Y.-F.L., and G.-Z.F. processed and analyzed the calcium imaging data. The paper was written by Z.-Y.C. and S.-W.T. **Competing interests:** The authors declare that they have no competing interests. **Data and materials availability:** All data needed to evaluate the conclusions in the paper are present in the paper and/or the Supplementary Materials.

Submitted 23 September 2022
Accepted 3 May 2023
Published 7 June 2023
10.1126/sciadv.adf0284

NEUROSCIENCE

SARS-CoV-2 infection and viral fusogens cause neuronal and glial fusion that compromises neuronal activity

Ramón Martínez-Mármol[1], Rosina Giordano-Santini[1]†, Eva Kaulich[1]†, Ann-Na Cho[2], Magdalena Przybyla[2], Md Asrafuzzaman Riyadh[1], Emilija Robinson[2], Keng Yih Chew[3], Rumelo Amor[4], Frédéric A. Meunier[1,5], Giuseppe Balistreri[4,6], Kirsty R. Short[3], Yazi D. Ke[2], Lars M. Ittner[2], Massimo A. Hilliard[1]*

Numerous viruses use specialized surface molecules called fusogens to enter host cells. Many of these viruses, including the severe acute respiratory syndrome coronavirus 2 (SARS-CoV-2), can infect the brain and are associated with severe neurological symptoms through poorly understood mechanisms. We show that SARS-CoV-2 infection induces fusion between neurons and between neurons and glia in mouse and human brain organoids. We reveal that this is caused by the viral fusogen, as it is fully mimicked by the expression of the SARS-CoV-2 spike (S) protein or the unrelated fusogen p15 from the baboon orthoreovirus. We demonstrate that neuronal fusion is a progressive event, leads to the formation of multicellular syncytia, and causes the spread of large molecules and organelles. Last, using Ca^{2+} imaging, we show that fusion severely compromises neuronal activity. These results provide mechanistic insights into how SARS-CoV-2 and other viruses affect the nervous system, alter its function, and cause neuropathology.

INTRODUCTION

Infectious diseases that involve the nervous system are caused by a wide spectrum of agents, including bacteria, fungi, parasites, and viruses (*1*). Viruses from diverse families, such as rabies virus, herpes simplex virus, Epstein-Barr virus, Zika virus, reovirus, and severe acute respiratory syndrome coronavirus 2 (SARS-CoV-2) can infect neurons (*2*–*8*). Viral brain infections are characterized by multiple neurological symptoms, including headache, fever, confusion, epileptic seizures, and loss of taste or smell. In more severe cases, viral brain infections can lead to encephalitis and meningitis, as well as potentially irreversible neuronal deficits such as paralysis and death. Clinical symptoms can originate from the loss of infected neurons (*9*); however, some viruses do not kill their host cells, and the chronic neurological sequelae of these infections cannot be explained by neuronal death (*10*). Other neuropathological mechanisms must therefore underlie the progression of these viral infections, leading to brain dysfunction. In non-neuronal tissues, enveloped viruses and reoviruses use specialized molecules called fusogens to fuse with host membranes and enter cells (*11*). These viruses then hijack the cellular machinery to produce viral components, with newly synthesized viral fusogens redecorating the cell membrane and conferring the ability to fuse with neighboring cells. This results in the formation of multinucleated syncytia, which allow viral propagation "from within," without the need for virion release into the extracellular space (*12*–*14*). As defined more than 100 years ago by Santiago Ramón y Cajal, the nervous system is composed of discrete neurons that act as individual units and do not base their development or communication on cellular fusion. Preserving neuronal individuality is critical for the correct function of the nervous system, and it is still poorly understood whether viral infection and the resulting presence of viral fusogens can cause neuronal fusion and the formation of syncytia, thereby permanently altering the neuronal circuitry and function.

RESULTS

SARS-CoV-2 infection causes neuron-neuron, neuron-glia and glia-glia fusion in murine hippocampal cultures and in human-derived brain organoids

SARS-CoV-2 causes primarily a respiratory disease, but increasing evidence has revealed the presence of viral RNA and proteins also in the brain and a multitude of neuropsychiatric syndromes (*8*, *15*, *16*), which appear in the early stages of the disease and persist for months after infection, in what has recently been termed long COVID (*17*). Viral fusogens are involved in the recognition, binding, and entrance of viruses into their host cells. During infection, these proteins are expressed de novo to form new viral particles, trafficking from secretory organelles to the host plasma membrane and causing cell-cell fusion (*18*, *19*). To determine whether viral neuroinfection induces the fusion of neurons, we used SARS-CoV-2 and a fluorescence fusion assay, whereby different intracellular fluorophores transfer between fused cells. SARS-CoV-2 uses the human angiotensin-converting enzyme 2 (hACE2) as its main receptor on the surface of the host cell (*20*), and neuropilin 1 (NRP1) as a cofactor to enhance infectivity (*21*). Among other tissues, hACE2 is expressed in neuronal and glial cells in the human central nervous system (*22*). Mouse neurons express mACE2 (*23*), which shares 81.86% interspecies homology with the human protein but lacks key residues for spike S binding (*20*), resulting in modest to weak affinity for SARS-CoV-2 (*24*). We,

[1]Clem Jones Centre for Ageing Dementia Research, Queensland Brain Institute, The University of Queensland, Brisbane, QLD 4072, Australia. [2]Dementia Research Centre, Macquarie Medical School, Faculty of Medicine, Health and Human Sciences, Macquarie University, Sydney, NSW 2109, Australia. [3]School of Chemistry and Molecular Biosciences, Faculty of Science, The University of Queensland, Brisbane, QLD 4072, Australia. [4]Queensland Brain Institute, The University of Queensland, Brisbane, QLD 4072, Australia. [5]School of Biomedical Sciences, The University of Queensland, Brisbane, QLD 4072, Australia. [6]Department of Virology, Faculty of Medicine, University of Helsinki, Helsinki FIN-00014, Finland.
*Corresponding author. Email: m.hilliard@uq.edu.au
†These authors contributed equally to this work.

therefore, expressed hACE2 in murine-derived brain cells. Immediately after embryonic hippocampal dissection, a population of these brain cells was electroporated with a plasmid encoding hACE2 and another encoding green fluorescent protein (GFP); a second population of hippocampal cells was electroporated with a plasmid encoding hACE2 and another encoding mCherry. The two neuronal populations were then plated together and maintained for 5 days in vitro (5 DIV; Fig. 1A). The original ancestral SARS-CoV-2 was amplified in Vero cells expressing human transmembrane protease serine 2 (TMPRSS2) and titrated by plaque assay (*25*). The neuronal cultures were infected with 2×10^5, 2×10^3, or 20 plaque-forming units (PFUs) or were mock-infected with control culture medium. Seventy-two hours post-infection (hpi), the cultures were fixed and examined by confocal fluorescence microscopy, revealing the presence of fused neurons [positive for the neuronal marker microtubule-associated protein 2 (MAP2)], as characterized by the presence of both the GFP and mCherry fluorescent proteins for all the SARS-CoV-2 titers used (Fig. 1, B and C). Antibody staining revealed that fused neurons were positive for the fusogenic spike S protein (Fig. 1D and fig. S1, A and B) (*26*), which was distributed across the surface of infected neurons (Fig. 1E). In contrast, neuronal fusion was not observed in the mock control, and the spike S protein was not detected (Fig. 1B and fig. S1, A and B). Upon SARS-CoV-2 infection, glial cells expressing hACE2 were also positive for the spike S protein (fig. S1, C and D), and we observed additional fusion phenotypes, including neuron-glia (fig. S2, A to C) and glia-glia fusion (fig. S2, D to F). In agreement with previous findings (*2*), we found that high doses of neuronal SARS-CoV-2 infection resulted in cell damage, a phenotype that was not apparent at the lowest doses used within 72 hpi (fig. S1, E and F).

We next investigated whether viral infection induced the fusion of human neurons by infecting human embryonic stem cell (hESC)–derived three-dimensional (3D) brain organoids with SARS-CoV-2. Such organoids have become one of the preclinical models of choice to study SARS-CoV-2 pathogenesis (*27*) and have been used to demonstrate that the virus can infect human neurons with endogenous expression of ACE2 (*8*, *27*–*30*). To visualize whether organoid infection induced neuronal fusion, 43- to 50-day-old brain organoids were generated using a modification of previously reported protocols (*31*) and were transduced with adeno-associated virus (AAV) expressing GFP. This resulted in the stable expression of GFP in sparse neurons. The transduced organoids were then cultured for an additional 10 days before being infected with SARS-CoV-2 or with mock control and were fixed 72 hpi. Similar to what was observed after infection of 2D neuronal cultures, we found that SARS-CoV-2–infected brain organoids exhibited neuronal syncytia formed by GFP-interconnected neurons (Fig. 1, F and G).

Viral fusogens cause neuron-neuron, neuron-glia, and glia-glia fusion

To study whether and how the mere presence of viral fusogens on the surface of host cells affect the nervous system, we used the spike S protein of SARS-CoV-2 and the p15 fusogen isolated from the baboon orthoreovirus (BRV), which infects the brain of these primates, causing meningoencephalomyelitis (*5*, *32*). p15 is a fusion-associated small transmembrane fusogen. Unlike the spike S protein, p15 is the only viral protein required by the BRV to form a syncytium (*33*), with no receptor protein on the host cell being needed to mediate fusion (*34*, *35*). We first expressed p15 in embryonic mouse primary hippocampal neurons and visualized the presence of fusion through the fluorescence fusion assay described above. Immediately after isolation, a population of neurons was cotransfected by electroporation with a plasmid containing p15 and another containing GFP; a second population of neurons was cotransfected with a plasmid containing mCherry and an empty control vector. The two neuronal populations were then plated together and maintained in culture for 7 DIV (Fig. 2A). Our results revealed that the expression of p15 was sufficient to induce neuronal fusion, as detected by the presence of neurons containing both the GFP and mCherry fluorescent proteins [Fig. 2, B (first row) and C], a phenotype that was never observed when the control vector was cotransfected in the absence of p15 [Fig. 2, B (second row) and C]. To determine whether the fluorophore diffusion was caused by the fusogenic properties of p15, we generated an inactive version of this fusogen, p15Δ21-22, in which two residues of the N terminus of the transmembrane domain were truncated (*36*). Expression of this inactive fusogen completely abolished neuronal fusion [Fig. 2, B (third row) and C].

Unlike p15, the spike S protein must bind to the hACE2 receptor to trigger fusion, requiring both spike S and hACE2 to be expressed to promote neuronal fusion mediated by the viral fusogen. Using a similar approach to that described for p15, we electroporated two neuronal populations, one with a plasmid expressing GFP plus a plasmid containing a codon-optimized version of the spike S protein (*37*) and the other with a plasmid expressing mCherry plus a plasmid containing the hACE2 receptor. The two populations were then plated together and cultured for 7 DIV. The expression of the fusogen spike S and its receptor hACE2 in adjacent cells resulted in the fusion of these neurons and the mixing of the fluorescent proteins [Fig. 2, D (first row) and E]. The presence of both the fusogen and its specific receptor was required to initiate cellular fusion, as the expression of either spike S or hACE2 alone did not generate any fusion events [Fig. 2, D (second and third rows) and E]. To determine whether the fusion of neurons was caused by the fusogenic properties of spike S, we used two fusion-inactive versions of this protein, spike S-2P and spike S-6P (HexaPro). We first generated the spike S-2P variant, which contains two consecutive proline substitutions (K986P and V987P) in the C-terminal S2 subunit (*38*). These two mutations retain spike S in a prefusion conformation, blocking its fusion capacity (*39*). Spike S-6P contains four additional proline substitutions (F817P, A892P, A899P, and A942P) that further stabilize the prefusion conformation and increase protein expression and the ability to withstand heat stress (*40*). Our results reveal that neither of these versions of inactive spike S induces neuronal fusion (Fig. 2, F and G). Spike S maturation is driven by proteases, such as TMPRSS2. Viral entry and cell-to-cell fusion are enhanced by TMPRSS2 and NRP1 (*21*). Thus, we monitored their expression and detected both TMPRSS2 (fig. S3, A to C) and NRP1 (fig. S3, D to F) in our neuronal cultures, suggesting that these proteins could be involved in the brain infectivity and neuronal fusion induced by SARS-CoV-2. With both p15 and spike S, we observed not only neuron-neuron fusion but also neuron-glia and glia-glia fusion when the fusogens were expressed in these cell types (fig. S4), a result that mimics our observation with SARS-CoV-2 infection.

Neuronal fusion implies a temporary or permanent diffusion of cytoplasmic material between cells (*41*). To confirm that this was

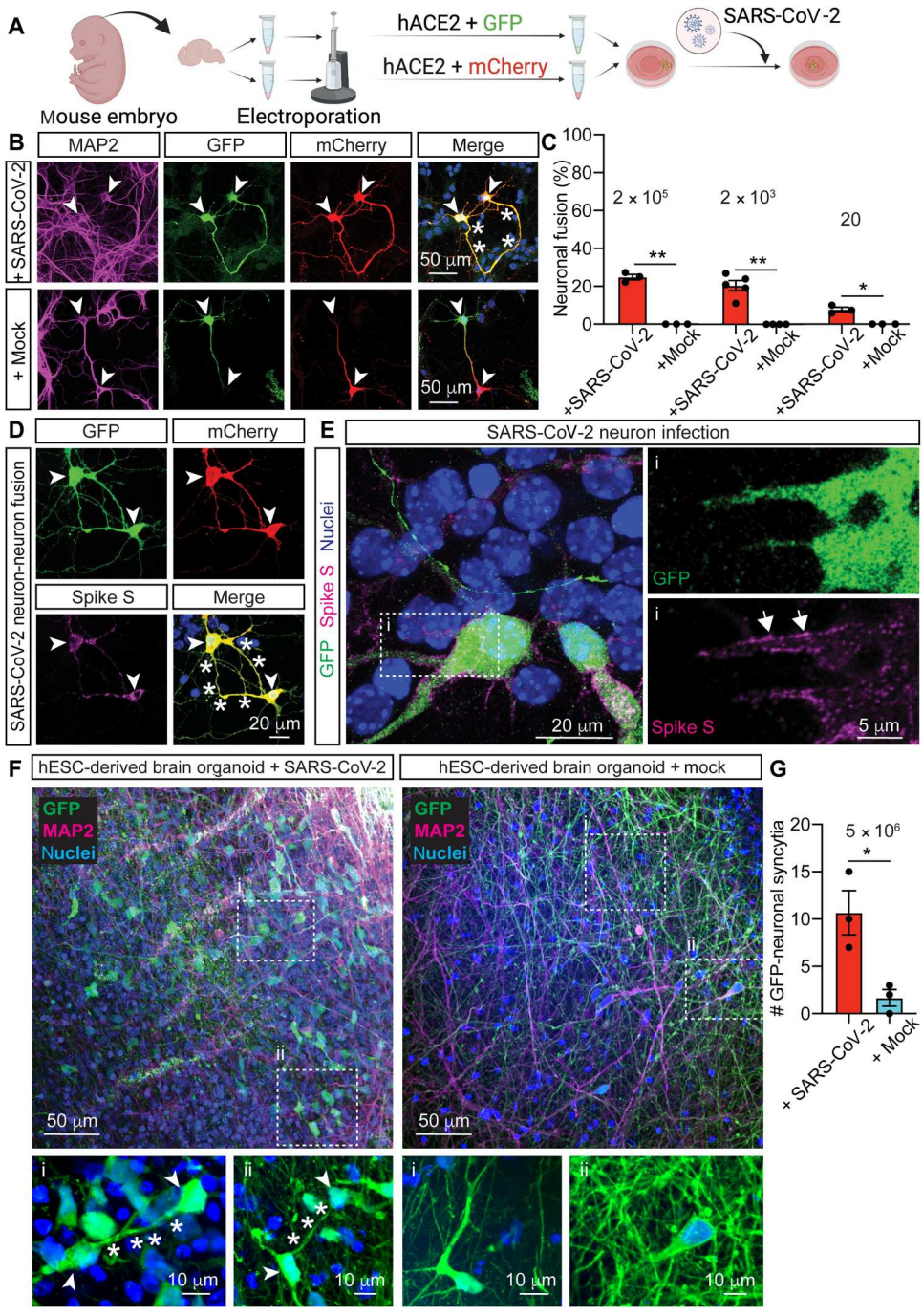

Fig. 1. SARS-CoV-2 infection induces neuronal fusion. (**A**) Scheme of the fluorescence fusion assay. Two independent populations of hippocampal neurons were electroporated with either hACE2 and GFP or hACE2 and mCherry. After electroporation, the neurons were cultured together and 5 days later were infected with SARS-CoV-2 or mock control. (**B**) Representative images of SARS-CoV-2–infected fused neurons (top row) identifiable by GFP (green) and mCherry (red) appearing in both neurons (yellow in merge), and nonfused mock control (bottom row). (**C**) Quantification of neuronal fusion expressed as the percentage of fused neurons out of the total fluorescent neurons in close proximity (< 200 μm). (**D**) Representative images of fused neurons positive for spike S staining. (**E**) Representative images showing the distribution of spike S in infected neurons. The boxed area (i) is at higher magnification in the right panels, with GFP (top) and spike S (bottom) distributed along the surface of the infected neuron (arrows). (**F**) Representative images of hESC-derived brain organoids infected with SARS-CoV-2 (left) or with mock control (right). Boxed areas (i and ii) are magnified in the bottom panels, with examples of GFP-neurons (arrowheads) fused at their neurites (asterisks). (**G**) Quantification of neuronal syncytia per organoid. In (B) and (F), immunocytochemistry shows nuclei (blue), neuronal MAP2 (magenta), GFP (green), and mCherry (red). In (D) and (E), immunocytochemistry shows nuclei (blue), GFP (green), mCherry (red), and SARS-CoV-2 spike S (magenta). In all images, arrowheads indicate somas, asterisks indicate fused neurites, and arrows indicate spike S protein on the membrane. Data in (C) and (G) represent means ± SEM. In (C), $n = 3$ independent infections, with three dishes per infection, and 19 to 60 neurons per dish. In (G), $n = 3$ brain organoids were infected. Unpaired two-tailed Welch's t tests were used in (C) and (G). $^*P \leq 0.05$ and $^{**}P < 0.01$.

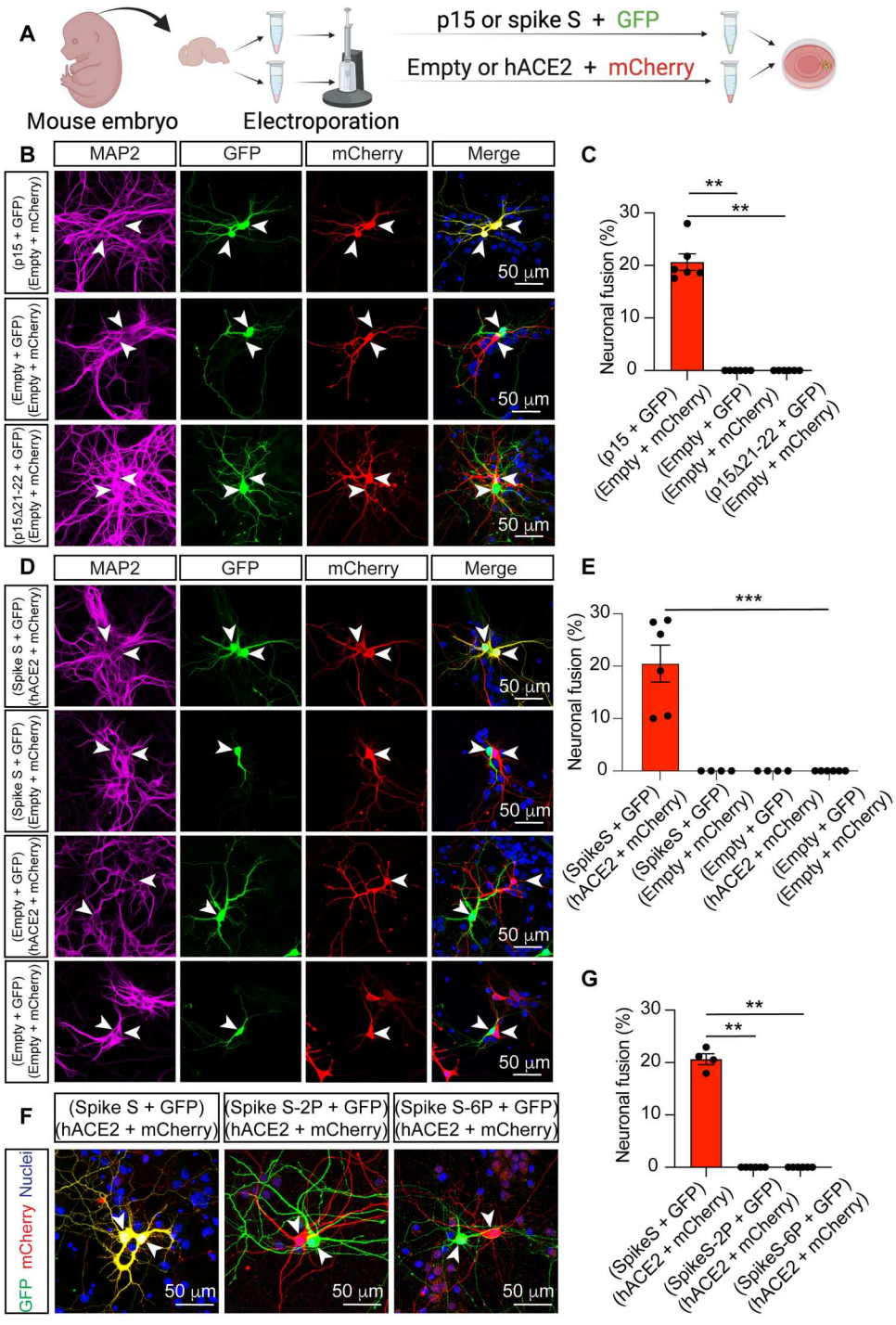

Fig. 2. Expression of the viral fusogens p15 and spike S is sufficient to induce neuronal fusion. (**A**) Scheme of the fluorescence fusion assay. Two independent populations of hippocampal neurons were electroporated with either fusogen (p15 or spike S) and GFP, or empty vector or hACE2 and mCherry. After electroporation, the neurons were cultured together for 7 days. (**B**) Representative images of fused neurons (top row) identifiable by GFP (green) and mCherry (red) fluorescence appearing simultaneously in adjacent neurons (yellow in merge) and nonfused control neurons (middle and lower rows). Fusion was observed upon expression of p15 but not with the nonfusogenic mutant p15Δ21-22 or by the empty vector. (**C**) Quantification of neuronal fusion as the percentage of transfected neurons that fuse out of the total number of fluorescent neurons in close proximity (≤ 200 μm). (**D**) Representative images of fused neurons induced by the expression of spike S and hACE2 (top row) and nonfused control neurons (remaining three rows). (**E**) Quantification of neuronal fusion as the percentage of transfected neurons that fuse out of the total number of fluorescent neurons in close proximity (≤ 200 μm). (**F**) Representative images showing the lack of fusion associated with the inactive spike S mutants S-2P and S-6P, compared to the WT. (**G**) Quantification of neuronal fusion as the percentage of transfected neurons that fuse (yellow) out of the total number of fluorescent neurons in close proximity (≤ 200 μm). Images in (B), (D), and (F) show immunocytochemistry for nuclei (blue), neuronal MAP2 (magenta), GFP (green), and mCherry (red). In all images, arrowheads indicate somas. Data in (C), (E), and (G) are displayed as means ± SEM; $n > 150$ neurons analyzed in four to six independent dishes from more than two cultures, one-way analysis of variance (ANOVA) Kruskal-Wallis test followed by Dunn's post hoc test comparing all groups to the empty vector control. $^{**}P < 0.01$ and $^{***}P < 0.001$.

the case, we used a variation of our fluorescence fusion assay. We cotransfected neurons with the photoconvertible fluorescent protein Kaede, which shifts from green to red fluorescence upon illumination with ultraviolet (UV) light (350 to 400 nm), together with either p15 or spike S and hACE2. After identification of interconnected adjacent green fluorescent neurons, we photoconverted the green Kaede fluorophore by applying brief pulses of UV light in a small region of one neuron (donor). The newly generated red photoconverted Kaede molecules rapidly diffused to the adjacent neuron (acceptor; fig. S5, A and E and movie S1). This diffusion was measured as a decrease in the red fluorescence within the donor neurons (fig. S5, B and F), with a concomitant increase in the acceptor neurons (fig. S5, C, D, G, and H), thereby conclusively demonstrating the existence of an active cytoplasmic bridge between p15-fused neurons and between spike S–hACE2–fused neurons. In the absence of fusion, red Kaede remained confined within the photoconverted neuron (fig. S5, A, E, and I to K). The

fused neurons retained their morphology, extended processes, and remained viable.

Viral fusogens induce neuronal fusion in vivo and in hESC-derived neurons

To determine whether the presence of viral fusogens can induce neuronal fusion in vivo, we generated transgenic *Caenorhabditis elegans* strains in which p15 and GFP were expressed simultaneously under the control of the *mec-4* promoter (*Pmec-4::p15* and *Pmec-4::GFP*), which is active in the six mechanosensory neurons (ALM left and right, AVM, PVM, and PLM left and right; fig. S6A). Similar to what we observed in mammalian neurons in culture, no fusion events with nearby neurons or tissues were detected in control animals expressing GFP under the *mec-4* promoter, and GFP was exclusively confined to the mechanosensory neurons [fig. S6, A (i) and B]. In contrast, we observed the appearance of additional GFP-positive cells in the head, mid-body, and tail of animals expressing the p15 fusogen [strains carrying p15 transgene *vdEx1266* or *vdEx1268*; fig. S6, A (ii to v) and B]. On the basis of its stereotypic location and morphology, we identified ALN as the most prevalent additional GFP-positive neuron [fig. S6, A (ii) and C]. The ALN neurons are a pair of sensory neurons located in the tail of the animal that extend their axons in close association with the axons of the ipsilateral ALM mechanosensory neurons (*42*). Other frequently GFP-positive neurons were the pair of LUA interneurons [fig. S6, A (iii) and C], which are located in the tail of the animal and extend anterior neurites in close proximity with those of the PLM neurons and the PVD mechanosensory neurons [fig. S6, A (v) and C], which are positioned in the mid-body of the animal with two extensively branched dendrites and a long axon (*42*). Despite over 90% of the GFP-positive cells being neurons, we also identified fluorescence in the hypodermal cells [fig. S6, A (iv) and C], which have a glial-like function forming a tissue in which the PLM and ALM axons are embedded (*43*, *44*). Similar to mammalian neurons, the expression of the inactive fusogen p15Δ21-22 within the mechanosensory neurons (*Pmec-4::p15Δ21-22*) did not result in fusion with neurons or hypodermal cells (fig. S6B). A temporal analysis of neuronal fusion observed during different stages of *C. elegans* life cycle revealed that the percentage of animals showing additional GFP-fused cells increased during the larval stages (L1 to L3), remaining constant in adulthood (fig. S6C). During our analysis of p15 expressed in mechanosensory neurons, we observed additional phenotypes that included defects in axonal guidance and axonal maintenance (visible as axonal breakages), as well as loss of mechanosensory neurons (fig. S6, D and E).

Next, to determine whether fusion could occur in vivo in the mammalian brain, we expressed p15 in the brains of adult mice. We designed AAV vectors expressing either GFP alone (+empty) or GFP and p15 (+p15) under the control of the neuronal human *Synapsin 1* (*hSyn*) promoter. AAVs were bilaterally injected into the hippocampus and the cortex of 11-week-old wild-type (WT) mice. Seven and 14 days after the AAV injections, the brains were removed for immunohistochemical analysis of neurons expressing p15 (fig. S7). Similar to what we observed in neuronal cultures and in *C. elegans* mechanosensory neurons, p15 expression resulted in neuronal fusion presenting as clusters of interconnected GFP-positive cells (fig. S7, A to E, and movie S2). Neuronal fusion was observed both in the hippocampus and in the cortex (fig. S7, F to I), representing up to 15% of transduced hippocampal neurons at 14 days after AAV infection (fig. S7H). Moreover, neuronal fusion resulted in a significant increase of total GFP-positive neurons (fig. S7, G and I) arising from the diffusion of GFP into adjacent cells, a value that increased with transduction time from 7 to 14 days (fig. S7J).

We next sought to determine whether fusion could also be observed in human-derived neurons by expressing either p15 or spike S in two different hESC-derived neuronal systems: cortical neurons differentiated in 2D cultures and 3D brain organoids. We first differentiated cortical neurons from hESCs and neuronal progenitor cells for 40 to 50 DIV and cotransfected them with GFP and either p15, spike S, or the inactive spike S-6P. Three days after the expression of the fusogens, the neuronal cultures were inspected, revealing the formation of neuronal clusters of interconnected GFP-positive cells that resembled the neuronal syncytium observed after p15 expression in murine neurons (fig. S8, A to C). The fact that cellular clusters were also observed when the spike S protein was expressed is a direct indication that neuronal fusion can occur using the endogenous hACE2 receptors expressed in these human cells. In the absence of fusogens or in the presence of the spike S-6P inactive mutant, no cell fusion was observed (fig. S8, A to C). We then differentiated brain organoids from hESCs until 43 to 50 DIV and expressed a similar combination of plasmids, consisting of the fluorescent protein mCherry and either p15, spike S, or the inactive spike S-6P. We maintained the organoids for three additional days before imaging them. Increments in the formation of mCherry-positive cell clusters were only detected in response to the expression of p15 or spike S (fig. S8, D and E), with both the empty vector and the spike S-6P mutant failing to induce cell fusion (fig. S8, D and E).

Neurons fuse at their neurites and exchange large organelles

In most tissues, syncytia are normally formed at the level of the cell bodies. However, the unique neuronal morphology with long processes prompted us to ask whether fusion can occur at the level of the neurites and, thus, at a distance from the neuronal cell bodies. We found that, upon SARS-CoV-2 infection, neuronal fusion occurred between the somas, as well as between the neurites far from the somas (Fig. 1D and fig. S9, A and B). Similarly, fusion driven by p15 and spike S resulted in fusion bridges of variable lengths that could extend over hundreds of micrometers (Fig. 3, A and B). This is remarkable, as it implies that neuronal fusion can easily be missed if searching for classical multinucleated syncytia. Next, we asked whether the observed fusion bridges allowed the exchange of cellular components larger than fluorescent proteins. To address this question, we performed a variation of the tethered fluorophore assay (*45*). As a consequence of cell-cell fusion, small cytoplasmic elements such as fluorophores and other soluble proteins can diffuse between cells, whereas larger organelles such as mitochondria remained tethered to the cellular microtubule cytoskeleton. We combined the expression of the soluble fluorescent protein mCardinal, with that of the photoactivatable mitochondrial marker mito-mPA-GFP, which allows visualization of mitochondrial movement. Our results reveal not only the presence of mCardinal in both fused neurons but also the movement of mitochondria between them (Fig. 3, C to E, and movie S3). To further confirm that the mitochondria movement was bidirectional, we tagged mitochondria with two different fluorophores, mito-mPA-GFP and

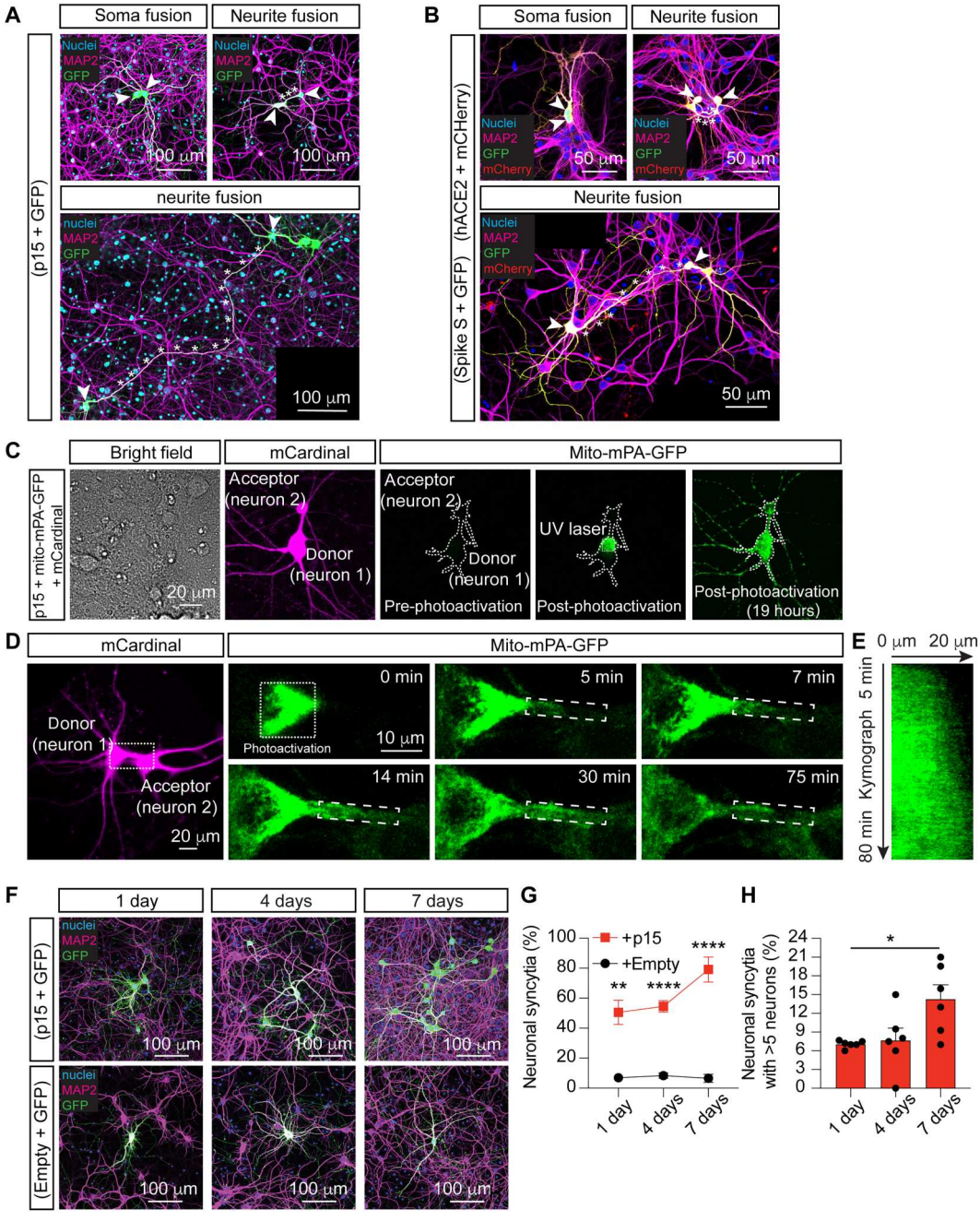

Fig. 3. Fused neurons form long neuronal bridges and exchange large organelles. (**A**) Representative fused neurons (arrowheads) transfected with p15 and GFP. (**B**) Representative fused neurons (arrowheads) transfected with either spike S and GFP or hACE2 and mCherry before being cocultured. In both (A) and (B), fusion is observed at the somas (top left) or the neurites (top right and bottom), with neuronal bridges (asterisks) of variable lengths. Immunocytochemistry for nuclei (blue), MAP2 (magenta), GFP (green), and mCherry (red). (**C** and **D**) Representative fused hippocampal neurons cotransfected at 7 DIV with p15, mCardinal, and mito-mPA-GFP. (C) mito-mPA-GFP is caged and becomes visible only after UV photoactivation. In fused neurons, mitochondria diffuse from the donor to the acceptor neuron. (D) The boxed area is magnified in the time series panels, with photoactivated mito-mPA-GFP moving anterogradely along the neuronal bridge. (**E**) Kymograph of mito-mPA-GFP moving between fused neurons in (D). (**F**) Representative neurons fusing over time. Hippocampal neurons cotransfected at 7 to 10 DIV with p15 and GFP (top) or with empty vector and GFP in control (bottom) and cultured for 1, 4, or 7 days. Immunocytochemistry for nuclei (blue), MAP2 (magenta), and GFP (green). (**G**) Quantification of neuronal syncytia as the percentage of fused neurons out of the total number of GFP-positive neurons. (**H**) Quantification of the average number of neurons per syncytium (more than five neurons). In all images, arrowheads indicate somas and asterisks indicate fused neurites. Data in (G) and (H) are means ± SEM, $n > 350$ neurons analyzed in more than four independent dishes from four cultures. Two-way ANOVA in (G) followed by Geisser-Greenhouse correction and Šidák post hoc test comparing treatments (+empty vector versus +p15) within conditions (days in culture). One-way ANOVA Kruskal-Wallis test followed by Dunn's post hoc tests was used in (H) to compare all groups to 1 day. *$P < 0.05$, **$P < 0.01$, and ****$P < 0.0001$.

mito-mPA-mCherry 1, revealing an exchange of these organelles between the fused neurons (fig. S10).

Last, we asked whether neuronal fusion was restricted to two adjacent neurons or if it was a propagating event that generated syncytia with a larger number of interconnected neurons. To address this possibility, we monitored neurons cotransfected with p15 and GFP for the appearance of syncytia over a 7-day period (Fig. 3F). Expressing GFP under the *CMV* promoter ensures that high levels of fluorescence are detected as early as 4 hours after transfection. In the absence of fusogen, the number of isolated GFP-expressing neurons remained constant; by contrast, in the presence of p15, the number of neuronal syncytia increased over time, appearing as clusters of interconnected GFP-positive neurons that progressively incorporated new cells (Fig. 3, F to H). Moreover, through live confocal imaging performed over a period of 50 hours, we observed the progressive appearance of GFP in surrounding neurons, revealing the occurrence of fusion events (movie S4). Similarly, after p15 expression in hESC-derived brain organoids, the mCherry-positive cells progressively organized into clusters and their numbers increased over time (fig. S11).

Fused neurons exhibit compromised neuronal activity

Our results suggest that fused neurons remain viable during long periods of time. However, whether fusion has an effect on neuronal activity remains unknown (*46*). To answer this question, we fused differentiated neurons (14 to 18 DIV) using p15 and visualized spontaneous neuronal activity with the fluorescent Ca^{2+}-sensitive indicator Cal-520. Individual neurons expressing mCherry and the control empty vector exhibited spontaneous activity (fig. S12, A and B), an effect that was not observed in glial cells (fig. S12, C and D). The majority (~90%) of fused neurons resulted in synchronized neuronal activity (Fig. 4, A and C, and movie S5), with overlapping of Ca^{2+} peaks (Fig. 4, D, G, and I), whereas the remaining 10% displayed a complete loss of neuronal activity. A close evaluation of the latter subpopulation of cells revealed that it corresponded to those neurons that were fused tightly at the level of their somas (Fig. 4, J to L). In contrast, nonfused neurons presented a variable pattern of neuronal activity (Fig. 4, B and E, and movie S6), ranging from highly synchronized to completely asynchronized (Fig. 4, F, H, and I). Every neuron that fused with glial cells presented a complete loss in neuronal activity (fig. S12, E to G). Regardless of the synchronization of fused neurons, the frequency of neuronal activity was not altered (fig. S13). To further investigate the mechanisms responsible for the simultaneous firing of fused neurons, we analyzed the Ca^{2+} levels along the neuronal bridge formed between these neurons (fig. S14, A and B, and movie S7). The intracellular Ca^{2+} concentration increased within the bridges (fig. S14, C to E), forming Ca^{2+} peaks that reflected the patterns of neuronal activity (fig. S14, F and G).

DISCUSSION

Neuroinfectious diseases transmitted by viruses represent an emerging public health threat due to the increasing appearance of new zoonotic neurotropic viruses (*47*). Viral infections of the nervous system cause a broad spectrum of acute neurological symptoms, including meningitis, encephalitis, meningoencephalitis, paralysis, and stroke, with long-term neurological sequelae or even fatal outcomes commonly observed in severe situations. Respiratory viruses such as the human respiratory syncytial virus, the influenza virus, the emerging coronaviruses (CoV), and the human metapneumovirus, among others, are now also included in the list of potential neurotropic viruses (*48*). Long-term and chronic neurological manifestations derived from viral neuroinfections are gaining increased attention, especially after the coronavirus disease 2019 (COVID-19) pandemic where long COVID has recently been termed to describe a multitude of symptoms of neurological nature that persist for months after the infection (*17*) and affect millions of people worldwide (*49*). To date, the pathophysiological mechanisms associated with the neurological symptoms derived from viral infections are only started to be elucidated, with fusion being a possible mechanism of transmission and spreading (*50*–*56*). Our results indicate that viral infections, driving the expression of viral fusogens, can initiate the irreversible fusion of brain cells, causing alteration in neuronal communication and revealing a possible pathomechanism of neuronal malfunction caused by infection. The impact on neuronal fusion will depend on the viral load in the brain and the specific areas infected; for example, in the case of SARS-CoV-2, neuronal fusion depends on the expression of hACE2 and, potentially, other accessory entry factors such as TMPRSS2 and NRP1 in neighboring neurons. Our results also imply that other viral infections can potentially cause neuronal fusion. Several viruses can cause severe neurological symptoms and/or death, such as HIV, rabies virus, Japanese encephalitis virus, vesicular stomatitis virus, poliovirus, measles virus, herpes simplex virus, varicella-zoster virus, Zika virus, cytomegalovirus, dengue virus, Nipah virus, and chikungunya virus, among others. Cell-to-cell contact has been shown to be involved in the spreading of HIV (*14*), measles (*51*), and SARS-CoV-2 (*57*), but viral-mediated neuronal fusion remained poorly understood.

Fused neurons can result in compromised neuronal circuitry and altered animal behavior, as previously shown for *C. elegans* chemosensory neurons that ectopically express endogenous fusogens (*46*). Our results demonstrate that neurons infected by viruses or expressing their viral fusogens can acquire the ability to fuse with neighboring neurons and glial cells, both in vitro and in vivo. This, in turn, results in the sharing of large molecules and even organelles and in compromised neuronal activity. While the latter can have direct implications on brain function and animals′ behavior, sharing large molecules implies a possible mechanism for the spread of toxic aggregates as observed in several neurodegenerative diseases and could also represent a mechanism of viral spreading that eludes the immune system (*12*). Retroviruses induce the formation of viral cytonemes, consisting of filopodial bridges that facilitate cell-to-cell transmission (*58*). Tunneling nanotubes are similar cellular bridges that allow communication between cells (*59*) and have been reported to mediate the transport of toxic α-synuclein aggregates (*60*). Our results demonstrate the formation of neuronal bridges that can extend hundreds of micrometers, allowing the exchange of small proteins and large mitochondria between interconnected neurons. Given the diverse range of structures that can be transported through these viral fusogen-mediated cellular structures, it is tempting to speculate that infecting viruses and other toxic aggregates may also use these pathways to spread to neighboring cells. In the case of SARS-CoV-2, the potential of fusion-mediated spreading of infection would be determined by the delivery of viral fusogen to the cell surface, which we have shown to occur, and by the pattern of ACE2-expressing neurons (*22*) that are in contact

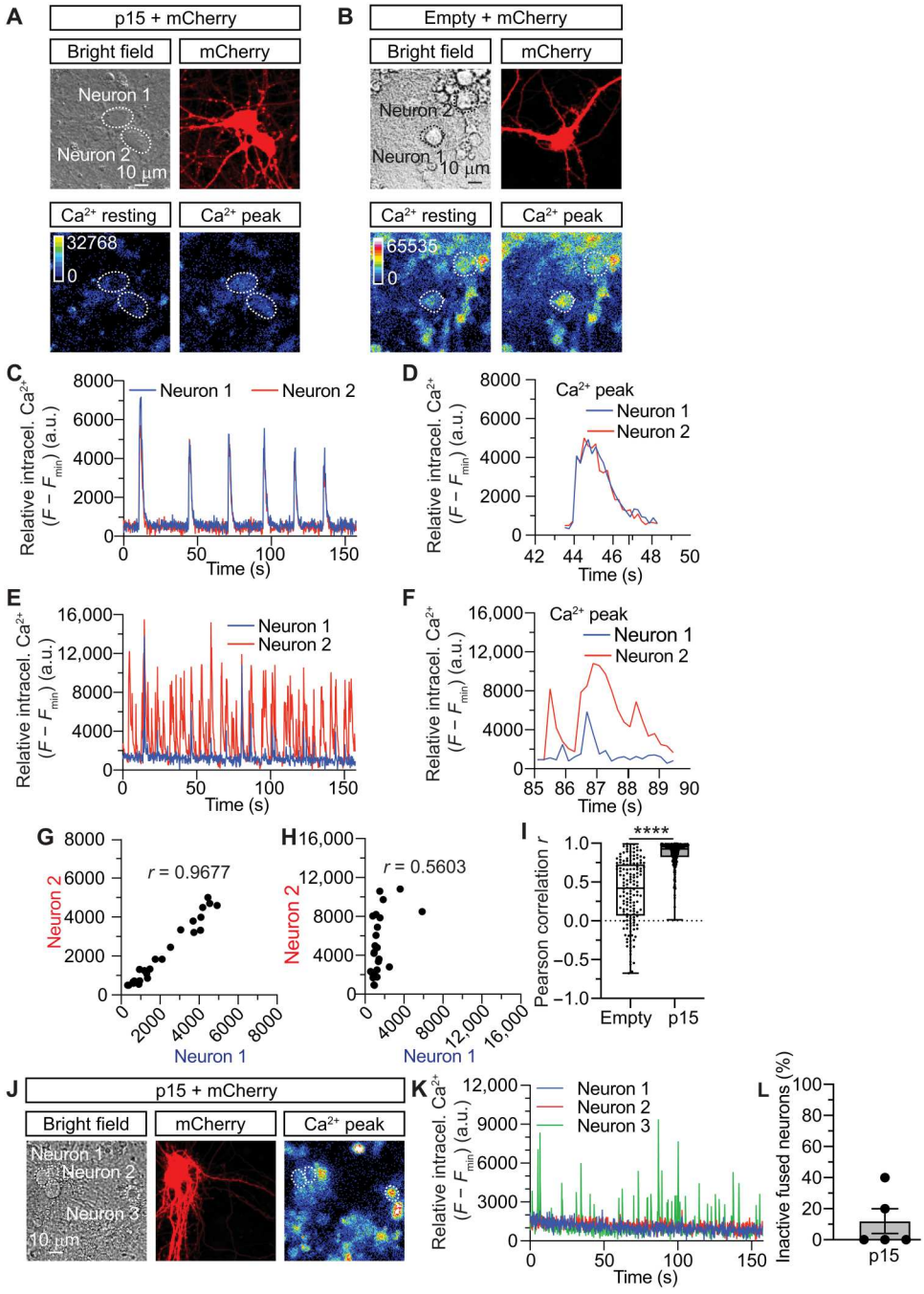

Fig. 4. Neuronal fusion results in altered synaptic activity. (**A** and **B**), Representative hippocampal neurons (neuron 1 and neuron 2) cotransfected at 12 DIV with p15 and mCherry [(A), fused neurons] or with an empty control vector and mCherry [(B), nonfused neurons] and imaged 3 days later at 15 DIV after incubation with the Ca^{2+} indicator CAL-520. Bottom: Pseudocolored images of the intracellular Ca^{2+} levels in resting conditions and during an activity peak. (**C**) Plot of the relative intracellular Ca^{2+} intensity levels over time from fused neurons 1 and 2 of (A). (**D**) Detail of one of the intracellular Ca^{2+} peaks plotted in (C). (**E**) Plot of the relative intracellular Ca^{2+} intensity levels over time from nonfused neurons 1 and 2 of (B). (**F**) Detail of one of the intracellular Ca^{2+} peaks plotted in (E). (**G** and **H**) Scatterplot of Pearson's correlation coefficient for the intracellular Ca^{2+} intensity levels of fused neurons (G) and nonfused neurons (H) of traces in (D) and (F), respectively. (**I**) Quantification of the average Pearson correlation (*s*) for the intracellular Ca^{2+} peaks from nonfused (empty) and fused (p15) neurons. (**J**) Images of two fused-but-inactive hippocampal neurons (neuron 1 and neuron 2) next to a nonfused active neuron (neuron 3). (**K**) Plot of the relative intracellular Ca^{2+} intensity levels of the fused neurons 1 and 2 and the nonfused neuron 3, from (J). Note the absence of intracellular Ca^{2+} peaks detected in neurons 1 and 2. (**L**) Percentage of inactive fused neurons. Data in (I) are means ± SEM. $n = 147$ Ca^{2+} peaks in nonfused (empty) and $n = 318$ Ca^{2+} peaks in fused (p15) neurons. Data in (L) are means ± SEM. All the data are obtained from >25 neurons imaged in five independent experiments. Unpaired two-tailed Welch's *t*-test was used in (I). ****$P < 0.0001$. a.u., arbitrary units.

with a single infected neuron, even at large distances from their respective cell somas. The neuropathological consequences of virus-induced neuronal fusion events could underlie the remarkable association between herpes simplex virus infection and Alzheimer's disease (*4*), HIV and Parkinson's disease (*61*), Epstein-Barr virus and multiple sclerosis (*62*), and Zika virus or Japanese encephalitis virus with epileptic seizures (*3*, *63*). An important consideration that emerges from our results is that fused neurons remain viable albeit with altered circuitry and function. This uncharacterized, difficult-to-detect event could explain some of the neurological consequences of viral infections of the nervous system.

Most of the current immunization approaches for COVID-19 are based on expressing the spike S protein in the host cells as an epitope to trigger the immune system response (*64*). These nucleic acid-based vaccines deliver the antigen encoded as mRNA, such as in the Pfizer-BioNTech BNT162b2 and the Moderna mRNA-1273 vaccines (*65*), or as adenovirus-enclosed DNA, such as in the Oxford-AstraZeneca ChAdOx1 nCoV-19/AZD1222 (*66*) and Johnson & Johnson Ad26.COV2.S (*39*) vaccines. The current versions of the Moderna, Pfizer-BioNTech, and Johnson & Johnson SARS-CoV-2 vaccines encode the full-length spike S protein with two mutations (spike S-2P) that stabilize the prefusion conformation and inactivate its fusogenicity (*39*, *64*, *67*, *68*). We used this same mutant form of spike S-2P as a negative control, demonstrating the complete lack of fusogenicity when two consecutive prolines were added at positions 986 and 987. However, our findings demonstrate that it will be critical to consider the fusogenic potential when designing any future vaccines in which viral fusogens are to be expressed in mammalian cells.

MATERIALS AND METHODS

Molecular biology

Standard molecular biology methods were used. The *p15* DNA sequence was obtained from the National Center for Biotechnology Information (www.ncbi.nlm.nih.gov/gene/). The plasmid was then designed using the software "A Plasmid Editor," and the insert was generated by Integrated DNA Technologies. The Pmec-4::p15 plasmid was constructed by subcloning *p15* between Msc I and Nhe I. The CMV::p15 plasmid was generated by subcloning *p15* into the pmaxCloning vector (Lonza, no. VDC-1040) between Hind III and Not I. The CMV::p15Δ21/22 plasmid was generated as previously described (*36*) by deletion of the amino acids 21 and 22 of the N terminus of the transmembrane domain. The CMV::SARS-CoV-2–S-2P plasmid was generated by introducing two prolines at the 986 (K986P) and the 987 (V987P) positions of the *SARS-CoV-2–S* gene of the pCMV14-3X-Flag–SARS-CoV-2 S plasmid. Mutations were generated using the QuikChange II Site-Directed Mutagenesis Kit (p15Δ21/22 forward primer, 5′-CCACCGCCAAATGCTTTTGTTGAAAGCAGTTCTACTG-3′; p15Δ21/22 reverse, primer 5′-CAGTAGAACTGCTTTCAACAAAAGCATTTGGCGGTGG-3′; SARS-CoV-2–S-2P forward, plasmid 5′-CCTGAGTCGCCTTGATCCGCCGGAAGCTGAAGTTC-3′; and SARS-CoV-2–S-2P reverse plasmid, 5′-GAACTTCAGCTTCCGGCGGATCAAGGCGACTCAGG-3′). Positive clones were confirmed by Sanger sequencing. The KaedeN1 plasmid was a gift from M. Davidson (Addgene, plasmid no. 54726; http://n2t.net/addgene:54726; RRID:Addgene_54726) (*69*). The mito-mPA-GFP plasmid was a gift from R. Youle (Addgene, plasmid no. 23348; http://n2t.net/addgene:23348; RRID:Addgene_23348) (*70*). The mito-7-mPA-mCherry1 plasmid was a gift from M. Davidson (Addgene, plasmid no. 57189; http://n2t.net/addgene:57189; RRID:Addgene_57189) (*71*). The pCMV14-3X-Flag-SARS-CoV-2 S plasmid was a gift from Z. Qian (Addgene, plasmid no. 145780; http://n2t.net/addgene:145780; RRID:Addgene_145780) (*37*). The pcDNA3.1-SARS2-Spike plasmid was a gift from F. Li (Addgene, plasmid no. 145032; http://n2t.net/addgene:145032; RRID:Addgene_145032) (*72*). The SARS-CoV-2 S-6P plasmid was a gift from J. McLellan (Addgene, plasmid no. 154754; http://n2t.net/addgene:154754; RRID:Addgene_154754) (*40*). The pcDNA3.1-hACE2 plasmid was a gift from F. Li (Addgene, plasmid no. 145033; http://n2t.net/addgene:145033; RRID:Addgene_145033) (*72*).

Animal ethics and mouse strains

All experimental procedures using animals were conducted under the guidelines of the Australian Code of Practice for the Care and Use of Animals for Scientific purposes and were approved by the University of Queensland Animal Ethics Committee (2019/AE000243) or the Macquarie University Animal Ethics Committee (2021/018). WT (C57BL/6 background) mice were maintained on a 12-hour light/12-hour dark cycle and housed in a PC2 facility with ad libitum access to food and water.

Culture of cell lines

Human embryonic kidney (HEK) 293T cells (American Type Culture Collection; 293T/17, ATCCCRL-11268) were cultured in a humidified atmosphere at 37°C with 5% CO_2 and maintained in Dulbecco's modified Eagle's medium (DMEM; Gibco–Thermo Fisher Scientific) supplemented with 10% fetal bovine serum (Gibco–Thermo Fisher Scientific), 1× GlutaMAX (Gibco–Thermo Fisher Scientific), and penicillin (100 U/ml)–streptomycin (100 μg/ml; Sigma-Aldrich–Merck). Vero E6 cells expressing TMPRSS2 were cultured in the same medium as the HEK-293T cells supplemented with puromycin (30 μg/ml; Sigma-Aldrich–Merck). Cells were transfected using the Lipofectamine LTX reagent according to the manufacturer's instructions (Invitrogen–Thermo Fisher Scientific).

Murine neuronal culture

Primary hippocampal neurons were obtained from mice at embryonic day 16. Isolated hippocampi were prepared as previously described (*73*, *74*). Briefly, 250,000 neurons were plated onto poly-L-lysine–coated 35-mm glass-bottom dishes (In Vitro Scientific) in Neurobasal medium (Gibco) supplemented with 5% fetal bovine serum (HyClone), 2% B-27, 2 mM GlutaMAX, and penicillin/streptomycin (50 U/ml; Invitrogen). The medium was changed to serum-free/antibiotic-free medium 24 hours after seeding, and half the medium was changed every week.

hESC-derived neurons

hESC-derived cortical neurons were differentiated from hESCs (H9, WIC-WA09-MB-001; WiCell) using a modification of a previously published protocol (*75*). Briefly, the hESCs were maintained on Matrigel (#354230; Corning) in Essential 8 medium (#A1517001; Life Technologies). hESCs were dissociated with Accutase (#AT-104-500; Innovate Cell Technologies) at 37°C for 1 min and seeded on AggreWell 800 (#34815; STEMCELL Technologies) in Essential 8

medium with ROCK inhibitor Y-27632 (10 μM, #72308, STEMCELL Technologies). After 24 hours, spheroids were collected and transferred into ultralow-attachment plates (#CLS3471; Sigma-Aldrich) with Essential 6 medium (#A1516401; Life Technologies) containing dorsomorphin (2.5 μM; #P5499, Sigma-Aldrich), SB-431542 (10 μM; #1614, Tocris) and cultured until day 13. The spheroids were then collected and placed into Matrigel (Corning)–coated six-well plates with DMEM/F12 (#11330057; Thermo Fisher Scientific), supplemented with 1× N2 (#17502048; Thermo Fisher Scientific). The resultant neural progenitor cells were passaged until day 30 and then replated on poly-L-lysine–coated (10 μg/ml; #P2636; Sigma-Aldrich) and laminin-coated (20 μg/ml; #23017015; Thermo Fisher Scientific) plates and maintained in Neurobasal medium (#21103049; Thermo Fisher Scientific) supplemented with B-27 (Thermo Fisher Scientific), GlutaMAX (#35050061; Thermo Fisher Scientific), brain-derived neurotrophic factor (BDNF; #78133; STEMCELL Technologies), ascorbic acid (200 μM; #72132; STEMCELL Technologies), GDNF (20 ng/ml; #78139.1, STEMCELL Technologies), and cyclic adenosine monophosphate (1 μM; #A6885; Sigma-Aldrich) up to 50 days.

Brain organoids

hESC-derived brain organoids were produced as previously reported (*76*). Briefly, hESCs were incubated with Accutase (#AT-104-500; Innovate Cell Technologies) at 37°C for 1 min. Dissociated single cells were seeded on AggreWell 800 (#34815, STEMCELL Technologies). One thousand single cells were added per well in Essential 8 medium supplemented with 10 μM ROCK inhibitor Y-27632 and centrifuged at 100*g* for 3 min. The AggreWell 800 plates were incubated at 37°C and 5% CO_2. After 24 hours, the organoids were transferred into ultralow-attachment 60ϕ dishes (#CLS3261, Sigma-Aldrich) in Essential 6 medium supplemented with 2.5 μM dorsomorphin, 10 μM SB-431542, and 2.5 μM XAV-939 (#3748, Tocris). The medium was changed every day for 5 days. On day 6, the medium was changed into Neurobasal A (#10888; Thermo Fisher Scientific) containing GlutaMAX (#35050; Thermo Fisher Scientific) and B-27 without vitamin A (#12587; Thermo Fisher Scientific). The medium was supplemented with epidermal growth factor (20 ng/ml; #236-EG; R&D Systems) and basic fibroblast growth factor (20 ng/ml; #233-FB; R&D Systems) until day 24, when it was switched to Neurobasal A medium containing GlutaMAX and B-27 without vitamin A and supplemented with BDNF (20 ng/ml) and neurotrophin-3 (20 ng/ml; #78074; STEMCELL Technologies) until day 43. Last, the medium was changed to Neurobasal A containing GlutaMAX and B-27 without vitamin A. For the viral labeling of brain organoid neurons, the adenovirus (AAV) *hSyn-eGFP* were constructed as previously described (*77*). Viral transduction was performed on 43 to 50 DIV organoids in ultralow-attachment 96-well plates (Corning) using 5×10^{11} titers of virus and exchanging the medium after 3 days. Transduced organoids were maintained for 10 additional days before SARS-CoV-2 infection.

SARS-CoV-2 preparation and infection

SARS-CoV-2 isolate hCoV-19/Australia/QLD02/2020 (QLD02) (used as the original ancestral virus) was provided by Queensland Health Forensic and Scientific Services, Queensland Department of Health. The virus was amplified in Vero cells expressing human TMPRSS2 (hTMPRSS2) and titrated by plaque assay. To evaluate the neuronal fusogenicity of SARS-CoV-2, 2D neuronal cultures were inoculated with 2×10^5, 2×10^3, or 20 PFUs or were mock-infected with control culture media, resuspended in neuronal culture medium, and incubated at 37°C until fixation (30 min) with paraformaldehyde [4% in phosphate-buffered saline (PBS)] 72 hours later. 3D hESC-derived brain organoids were inoculated with 2×10^4 PFUs or were mock-infected, all resuspended in brain organoid culture medium and incubated at 37°C until fixation (30 min) with paraformaldehyde (4% in PBS) 72 hours later. All experiments involving live SARS-CoV-2 and SARS-CoV followed the approved standard operating procedures in the Biosafety Level 3 facility from the School of Chemistry and Molecular Biosciences at the Faculty of Science of The University of Queensland.

Electroporation and transfection

When required, murine neurons were electroporated using the Invitrogen Neon transfection system (#MPK1025, Thermo Fisher Scientific) following the manufacturer's instructions. Briefly, immediately after dissection, isolated neurons were washed twice in Ca^{2+}-Mg^{2+}–free PBS and resuspended in buffer R containing 1 to 2 μg of the DNA to electroporate. The conditions for the electroporation were as follows: voltage, 1500 V; width, 10 ms; and three pulses. Alternatively, the neurons were transfected after 7 to 12 DIV using the Lipofectamine 2000 (#11668027, Invitrogen) reagent as previously described (*73*). Following the manufacturer's instructions, human neurons were transfected with Lipofectamine 3000 (#L3000015, Thermo Fisher Scientific) and 1.6 μg of plasmid DNA at 40 to 50 DIV; human brain organoids were transfected with Lipofectamine 3000 and 2.4 μg of plasmid DNA at 43 to 50 DIV. The transfection medium was replaced after 24 hours.

C. elegans strain maintenance, genetic crosses, and manipulation

Standard techniques were used for *C. elegans* maintenance, genetic crosses, and manipulations (*78*). Experiments were performed on hermaphrodite animals grown at room temperature (~22°C) on nematode growth medium plates, seeded with OP50 *Escherichia coli*. Transgenic strains generated during this study were obtained by standard microinjection techniques (*79*) and include *vdEx1266* [*Pmec-4::p15*; 5 ng/μl], *vdEx1268* [*Pmec-4::p15*; 5 ng/μl]; *vdEx1417* [*Pmec-4::p15Δ21/22*; 15 ng/μl], *vdEx1487* [*Pmec-4::p15Δ21/22*; 5 ng/μl], and *vdEx1489* [*Pmec-4::p15Δ21/22*; 5 ng/μl]. All injection mixes had a total concentration of 100 ng/μl and contained the transgene of interest, empty pSM plasmid as a filler, and a co-injection marker for the identification of transgenic animals. As the cell cycle transfer of extrachromosomal arrays (*vdEx*) is unstable, some animals lose the transgene. This provides an internal control for each transgenic strain, with these controls being referred to as "non-transgenic siblings" or *transgene (−)*.

Murine brain AAV transduction and brain histochemistry

AAV expressing either e*GFP* alone (control) or e*GFP* and the viral fusogen *p15* under the *hSyn* promoter were stereotactically injected at the level of the cortex (2 mm posterior to bregma, 2 mm bilateral to midline, and 0.8 mm deep) and the hippocampus (2 mm posterior to bregma, 2 mm lateral to midline, and 2 mm deep) of adult WT mice (11 weeks old). Control and p15-injected animals were randomly divided into two groups based on the duration of the

transduction, and brains were processed either 7 or 14 days after infection. Briefly, mice were anesthetized and transcardially perfused with cold PBS. Brains were then removed, post-fixed with 4% (w/v) paraformaldehyde (PFA) in PBS overnight, and cryoprotected with 30% (w/v) sucrose in PBS overnight. Frozen brains were cryosectioned at 80 μm; they were permeabilized with 0.5% (v/v) Triton X-100 (#X100; Sigma-Aldrich) in PBS for 30 min and blocked in 5% (w/v) BSA (#A7906; Sigma-Aldrich), 1% horse serum (#26050070; Thermo Fisher Scientific), and 0.1% (v/v) Triton X-100 overnight. The brains were then incubated with primary antibodies to GFP (#ab290; Abcam) and NeuN (#ab091; Merck/MilliporeSigma) at 4°C for 3 days. Following PBS washing, they were incubated at 4°C for 2 days with Alexa Fluor–conjugated secondary antibodies (#A32732 or #A-11039; Thermo Fisher Scientific), and nuclei were counterstained with DAPI (4′,6-diamidino-2-phenylindole; #D1306; Invitrogen) before being washed with PBS and prepared for confocal imaging.

Immunofluorescence staining

Murine neurons and cells were fixed with a solution of 4% PFA in PBS for 10 min. Neurons were rinsed in PBS and permeabilized with a solution of 0.1% Triton-X-100 in PBS for 10 min. They were then washed with PBS and incubated in blocking solution (5% horse serum and 1% BSA in PBS) for 1 hour at room temperature. After blocking, the neurons were incubated with the primary antibodies to GFP (#AB16901, Merck Millipore), mCherry (#ab167453, Abcam), NRP1 (#ABIN1173423, Antibodies-online.com), TMPRSS2 (#ab109131, Abcam), and MAP2 (#188004, Synaptic Systems), diluted in primary antibody solution (1% BSA in PBS) overnight at 4°C. The antibody anti-TMPRSS2 required an antigen retrieval step performed after fixation. After incubation with the primary antibodies, the cells were then washed with PBS and incubated with the secondary antibodies Alexa Fluor 488 goat anti-chicken (#A-11039, Thermo Fisher Scientific), Alexa Fluor 555 goat anti-rabbit (#A32732, Thermo Fisher Scientific), Alexa Fluor 647 goat anti-guinea pig (#A21450, Thermo Fisher Scientific), and DAPI (#62248, Thermo Fisher Scientific) in the secondary antibody solution (5% horse serum in PBS) for 1 hour at room temperature. Last, the neurons were washed and mounted in VECTASHIELD PLUS Antifade mounting medium (#H-2000, Vector Laboratories). The staining protocol was slightly modified for human neurons; they were fixed for 5 min, permeabilized with 0.1% (v/v) Triton-X-100 for 10 min, blocked with 5% (w/v) BSA (#A9418, Sigma-Aldrich), and stained for MAP2 only. Organoids were fixed with 4% PFA for 30 min at room temperature. PBS-rinsed organoids were permeabilized with 0.5% (v/v) Triton X-100 (#X100; Sigma-Aldrich) in PBS for 30 min and blocked in 5% (w/v) BSA for 5 hours. The organoids were then incubated with primary antibodies to MAP2 (#ab5392, Abcam) at 4°C for 3 days. Following PBS washing, they were incubated with Alexa Fluor–conjugated secondary antibodies (#A11039 or #A21437, Thermo Fisher Scientific) at 4°C for 3 days. Nuclei were counterstained with DAPI for 30 min and washed with PBS before imaging.

Confocal microscopy of fixed samples

Immunofluorescence imaging was carried out using a Zeiss Plan Apochromat 40×/1.2 numerical aperture (NA) water-immersion objective on a confocal/two-photon laser scanning microscope (LSM 710; Carl Zeiss) built around an Axio Observer Z1 body (Carl Zeiss), equipped with two internal gallium arsenide phosphide (GaAsP) photomultiplier tubes (PMTs) and three normal PMTs for epi (descanned) detection, or using a confocal microscope (LSM 880, Carl Zeiss) built around an Axio Observer Z1 body (Carl Zeiss), equipped with two internal gallium arsenide phosphide (GaAsP) PMTs and three normal PMTs for epi (descanned) detection. Both systems were controlled by Zeiss Zen Black software. Images were further processed and analyzed with Fiji-ImageJ (*80*). Imaging of organoids and mice brain slices was performed using a Yokogawa W1 inverted spinning disc confocal controlled by SlideBook 6.0 software (3I Inc.). Large-field imaging of tissue sections was performed using a 20×/0.8 NA air objective and a Hamamatsu Flash4.0 scientific complementary metal-oxide semiconductor (sCMOS) camera. High-resolution *Z*-stacks were performed using a 63×/1.4 NA oil-immersion objective and a Photometrics Evolve electron-multiplying charge-coupled device (EMCCD) camera.

Confocal and epifluorescence live imaging

C. elegans animals were immobilized using 0.05% tetramisole hydrochloride on 3.5% agar pads. The animals were imaged with a Zeiss Axio Imager Z1 microscope equipped with a Photometrics camera (Cool Snap HQ2) and analyzed using MetaMorph software (Molecular Devices) and Fiji-ImageJ. Cytoplasmic GFP was visualized with 470/80-nm excitation and 525/50-nm emission filters, and mitochondria tagged with a monomeric red fluorescent protein (mRFP) were visualized with 545/25-nm excitation and 605/70-nm emission filters. Animals were imaged on a spinning-disk confocal system (Marianas; 3I Inc.) consisting of an Axio Observer Z1 (Carl Zeiss) equipped with a CSU-W1 spinning-disk head (Yokogawa Corporation of America), an ORCA-Flash4.0 v2 sCMOS camera (Hamamatsu Photonics), and a 100×/1.4 NA Plan-Apochromat objective. Image acquisition was performed using SlideBook 6.0 and processed using Fiji-ImageJ.

A photoactivation assay was performed to demonstrate the exchange of mitochondria between fused mammalian neurons. For live-cell imaging of mito-mPA-GFP diffusion, a UV pulse was applied on a 10 μm–by–10 μm region of interest (ROI). Before photoactivation, mito-mPA-GFP is not visible as it remains caged (non-fluorescent). After irradiation with UV light, mPA-GFP irreversibly photoconverts to a green-emitting fluorescent protein. Photoconversion resulted in the emergence of green mitochondria that slowly moved from one neuron to the other along the fusion bridge. Green images were collected every 5 min; seventy-two images were acquired after photoconversion, and one last image was acquired 13 hours later. To identify a bidirectional transfer of mitochondria between fused neurons, 5 DIV neurons expressing either spike S, blue fluorescent protein (BFP), and mito-mPA-mCherry 1 or hACE2, BFP, and mito-mPA-GFP were imaged. Fused BFP-positive neuronal syncytia were identified by using a 405-nm excitation laser. This identification step also photoconverted both mito-mPA-GFP and mito-mPA-mCherry 1, making them visible and allowing the identification of interchanged mitochondria between fused neurons.

Fluorescence photoconversion was used to show the diffusion of large molecules between fused mammalian neurons. For live-cell imaging of Kaede diffusion, fusogen/empty vector-Kaede–transfected neurons were bathed in imaging buffer [145 mM NaCl, 5.6 mM KCl, 2.2 mM $CaCl_2$, 0.5 mM $MgCl_2$, 5.6 mM D-glucose, 0.5 mM

ascorbic acid, 0.1% BSA, and 15 mM Hepes (pH 7.4)]. Neurons were visualized at 37°C on a Zeiss Plan Apochromat 40x/1.2 NA water-immersion objective on a confocal/two-photon laser scanning microscope (LSM 710; Carl Zeiss). In transfected neurons, a UV pulse was applied on a 5 μm–by–5 μm ROI. Photoconversion resulted in the emergence of a spot of red fluorescence that rapidly diffused through the soma and proximal neurites. Simultaneous green and red images were collected every 785 ms; five images were acquired before photoconversion, and 50 images were acquired after photoconversion. Photoconversion and diffusion of the fluorophore were performed on neurons separated by 25 to 100 μm. In control conditions, UV light was applied first outside the neuron, 50 μm away from the soma, and then inside the soma.

Ca^{2+} imaging to visualize spontaneous neuronal activity was performed on differentiated neuronal primary cultures (14 to 18 DIV). Neurons were transfected with mCherry together with either the control empty vector or p15 and imaged 3 days later. Neurons were incubated at 37°C for 2 hours in Neurobasal medium supplemented with 2 mM GlutaMAX, 2% B-27, 10 μM Cal-520 AM (Abcam), and 0.03% Pluronic F-127 (Sigma-Aldrich). Following incubation, neuronal cultures were washed three times, transferred to imaging buffer, and imaged at 37°C on a Zeiss Plan Apochromat 40×/1.2 NA water-immersion objective on a confocal/two-photon laser scanning microscope (LSM 710; Carl Zeiss).

Neuron-neuron, neuron-glia, and glia-glia fusion quantification in mammalian neuronal cultures, human-derived brain organoids, and murine brain sections

Cell-cell fusion efficiency in neuronal cultures was quantified as the percentage of transfected neurons (GFP or mCherry) with their somas within a radius ≤200 μm and that contained simultaneously both GFP and mCherry. Neuron-neuron fusion was identified as more than two fused cells that were both positive for MAP2 staining. Neuron-glia fusion was identified by one of the fused cells being positive for MAP2. Glia-glia fusion was identified by neither of the fused cells being positive for MAP2. Neuronal syncytia were quantified as the percentage of interconnected neurons within a distance ≤200 μm. Neuron-neuron fusion in human-derived brain organoids and in murine brain sections was quantified as the percentage of pairs of transfected neurons that appear as tightly interconnected, with no gaps between them. In brain tissues, neuronal fusion was inspected within voxels of 0.01236 mm^3. Over 100 voxels through each brain region (hippocampus or cortex) were analyzed per animal. *Z*-stacks of images were deconvolved using Huygens software (Scientific Volume Imaging), and the 3D analysis of neuronal fusion was performed using the 3D viewer plugin from Fiji-ImageJ.

Statistical analysis

Results were analyzed statistically using GraphPad Prism software (GraphPad Software Inc.). The D′Agostino and Pearson test was used to test for normality. The unpaired two-tailed nonparametric Mann-Whitney *U* test was used for comparison of two groups, when the data were not normally distributed. The unpaired two-tailed Welch's *t* test was used for comparison of two groups, when the data were distributed following normality. For datasets comparing more than two groups, we performed one-way analysis of variance (ANOVA) Kruskal-Wallis test followed by Dunn's post hoc test for multiple comparisons, one-way ANOVA Brown-Forsythe and Welch tests followed by the Games-Howell's post hoc test for multiple comparisons, or two-way ANOVA followed by Geisser-Greenhouse correction and the Šidák post hoc test for multiple comparisons. Statistical comparisons were performed on a per-dish, per-neuron, per–human-derived organoid, or per-animal basis, depending on the experiment, as stated in the figure legends. Two to four technical replicate dishes were imaged, and two to five independent cultures were used per condition. One hundred to 103 *C. elegans* nematodes, three mice brains, and three to eight human-derived organoids were used per condition, as stated in the figure legends. Each mouse dissection provided neurons from a pool of at least six different embryos. Values are represented as means ± SD or means ± SEM. The tests used are indicated in the respective figure legends. A *P* value below 0.05 was accepted as significant.

Supplementary Materials

This PDF file includes:
Figs. S1 to S14
Legends for movies S1 to S7

Other Supplementary Material for this manuscript includes the following:
Movies S1 to S7

View/request a protocol for this paper from *Bio-protocol*.

REFERENCES AND NOTES

1. C. C. John, H. Carabin, S. M. Montano, P. Bangirana, J. R. Zunt, P. K. Peterson, Global research priorities for infections that affect the nervous system. *Nature* **527**, S178–S186 (2015).
2. E. Song, C. Zhang, B. Israelow, A. Lu-Culligan, A. V. Prado, S. Skriabine, P. Lu, O. E. Weizman, F. Liu, Y. Dai, K. Szigeti-Buck, Y. Yasumoto, G. Wang, C. Castaldi, J. Heltke, E. Ng, J. Wheeler, M. M. Alfajaro, E. Levavasseur, B. Fontes, N. G. Ravindra, D. Van Dijk, S. Mane, M. Gunel, A. Ring, S. A. J. Kazmi, K. Zhang, C. B. Wilen, T. L. Horvath, I. Plu, S. Haik, J. L. Thomas, A. Louvi, S. F. Farhadian, A. Huttner, D. Seilhean, N. Renier, K. Bilguvar, A. Iwasaki, Neuroinvasion of SARS-CoV-2 in human and mouse brain. *J. Exp. Med.* **218**, e20202135 (2021).
3. I. N. de Oliveira Souza, P. S. Frost, J. V. Franca, J. B. Nascimento-Viana, R. L. S. Neris, L. Freitas, D. Pinheiro, C. O. Nogueira, G. Neves, L. Chimelli, F. G. De Felice, E. A. Cavalheiro, S. T. Ferreira, I. Assuncao-Miranda, C. P. Figueiredo, A. T. Da Poian, J. R. Clarke, Acute and chronic neurological consequences of early-life Zika virus infection in mice. *Sci. Transl. Med.* **10**, eaar2749 (2018).
4. D. M. Cairns, N. Rouleau, R. N. Parker, K. G. Walsh, L. Gehrke, D. L. Kaplan, A 3D human brain-like tissue model of herpes-induced Alzheimer's disease. *Sci. Adv.* **6**, eaay8828 (2020).
5. S. Kumar, E. J. Dick Jr., Y. R. Bommineni, A. Yang, J. Mubiru, G. B. Hubbard, M. A. Owston, Reovirus-associated meningoencephalomyelitis in baboons. *Vet. Pathol.* **51**, 641–650 (2014).
6. M. J. Schnell, J. P. McGettigan, C. Wirblich, A. Papaneri, The cell biology of rabies virus: using stealth to reach the brain. *Nat. Rev. Microbiol.* **8**, 51–61 (2010).
7. N. Zhang, Y. Zuo, L. Jiang, Y. Peng, X. Huang, L. Zuo, Epstein-Barr virus and neurological diseases. *Front. Mol. Biosci.* **8**, 816098 (2021).
8. B. Z. Zhang, H. Chu, S. Han, H. Shuai, J. Deng, Y. F. Hu, H. R. Gong, A. C. Lee, Z. Zou, T. Yau, W. Wu, I. F. Hung, J. F. Chan, K. Y. Yuen, J. D. Huang, SARS-CoV-2 infects human neural progenitor cells and brain organoids. *Cell Res.* **30**, 928–931 (2020).
9. D. E. Griffin, J. M. Hardwick, Perspective: Virus infections and the death of neurons. *Trends Microbiol.* **7**, 155–160 (1999).
10. A. N. van den Pol, Viral infection leading to brain dysfunction: More prevalent than appreciated? *Neuron* **64**, 17–20 (2009).
11. S. Martens, H. T. McMahon, Mechanisms of membrane fusion: Disparate players and common principles. *Nat. Rev. Mol. Cell Biol.* **9**, 543–556 (2008).
12. A. A. Compton, O. Schwartz, They might be giants: Does syncytium formation Sink or spread HIV infection? *PLOS Pathog.* **13**, e1006099 (2017).
13. S. S. Frankel, B. M. Wenig, A. P. Burke, P. Mannan, L. D. Thompson, S. L. Abbondanzo, A. M. Nelson, M. Pope, R. M. Steinman, Replication of HIV-1 in dendritic cell-derived syncytia at the mucosal surface of the adenoid. *Science* **272**, 115–117 (1996).

14. S. Kalinichenko, D. Komkov, D. Mazurov, HIV-1 and HTLV-1 transmission modes: mechanisms and importance for virus spread. *Viruses* **14**, 152 (2022).
15. J. Meinhardt, J. Radke, C. Dittmayer, J. Franz, C. Thomas, R. Mothes, M. Laue, J. Schneider, S. Brunink, S. Greuel, M. Lehmann, O. Hassan, T. Aschman, E. Schumann, R. L. Chua, C. Conrad, R. Eils, W. Stenzel, M. Windgassen, L. Rossler, H. H. Goebel, H. R. Gelderblom, H. Martin, A. Nitsche, W. J. Schulz-Schaeffer, S. Hakroush, M. S. Winkler, B. Tampe, F. Scheibe, P. Kortvelyessy, D. Reinhold, B. Siegmund, A. A. Kuhl, S. Elezkurtaj, D. Horst, L. Oesterhelweg, M. Tsokos, B. Ingold-Heppner, C. Stadelmann, C. Drosten, V. M. Corman, H. Radbruch, F. L. Heppner, Olfactory transmucosal SARS-CoV-2 invasion as a port of central nervous system entry in individuals with COVID-19. *Nat. Neurosci.* **24**, 168–175 (2021).
16. Y. Kase, H. Okano, Neurological pathogenesis of SARS-CoV-2 (COVID-19): From virological features to clinical symptoms. *Inflamm. Regen.* **41**, 15 (2021).
17. S. Spudich, A. Nath, Nervous system consequences of COVID-19. *Science* **375**, 267–269 (2022).
18. A. Sapir, O. Avinoam, B. Podbilewicz, L. V. Chernomordik, Viral and developmental cell fusion mechanisms: Conservation and divergence. *Dev. Cell* **14**, 11–21 (2008).
19. Z. Zhang, Y. Zheng, Z. Niu, B. Zhang, C. Wang, X. Yao, H. Peng, D. N. Franca, Y. Wang, Y. Zhu, Y. Su, M. Tang, X. Jiang, H. Ren, M. He, Y. Wang, L. Gao, P. Zhao, H. Shi, Z. Chen, X. Wang, M. Piacentini, X. Bian, G. Melino, L. Liu, H. Huang, Q. Sun, SARS-CoV-2 spike protein dictates syncytium-mediated lymphocyte elimination. *Cell Death Differ.* **28**, 2765–2777 (2021).
20. R. Yan, Y. Zhang, Y. Li, L. Xia, Y. Guo, Q. Zhou, Structural basis for the recognition of SARS-CoV-2 by full-length human ACE2. *Science* **367**, 1444–1448 (2020).
21. L. Cantuti-Castelvetri, R. Ojha, L. D. Pedro, M. Djannatian, J. Franz, S. Kuivanen, F. van der Meer, K. Kallio, T. Kaya, M. Anastasina, T. Smura, L. Levanov, L. Szirovicza, A. Tobi, H. Kallio-Kokko, P. Osterlund, M. Joensuu, F. A. Meunier, S. J. Butcher, M. S. Winkler, B. Mollenhauer, A. Helenius, O. Gokce, T. Teesalu, J. Hepojoki, O. Vapalahti, C. Stadelmann, G. Balistreri, M. Simons, Neuropilin-1 facilitates SARS-CoV-2 cell entry and infectivity. *Science* **370**, 856–860 (2020).
22. S. Khan, J. Gomes, Neuropathogenesis of SARS-CoV-2 infection. *eLife* **9**, e59136 (2020).
23. M. F. Doobay, L. S. Talman, T. D. Obr, X. Tian, R. L. Davisson, E. Lazartigues, Differential expression of neuronal ACE2 in transgenic mice with overexpression of the brain renin-angiotensin system. *Am. J. Physiol. Regul. Integr. Comp. Physiol.* **292**, R373–R381 (2007).
24. T. N. Starr, S. K. Zepeda, A. C. Walls, A. J. Greaney, S. Alkhovsky, D. Veesler, J. D. Bloom, ACE2 binding is an ancestral and evolvable trait of sarbecoviruses. *Nature* **603**, 913–918 (2022).
25. D. E. Gordon, G. M. Jang, M. Bouhaddou, J. Xu, K. Obernier, K. M. White, M. J. O'Meara, V. V. Rezelj, J. Z. Guo, D. L. Swaney, T. A. Tummino, R. Hüttenhain, R. M. Kaake, A. L. Richards, B. Tutuncuoglu, H. Foussard, J. Batra, K. Haas, M. Modak, M. Kim, P. Haas, B. J. Polacco, H. Braberg, J. M. Fabius, M. Eckhardt, M. Soucheray, M. J. Bennett, M. Cakir, M. J. McGregor, Q. Li, B. Meyer, F. Roesch, T. Vallet, A. M. Kain, L. Miorin, E. Moreno, Z. Z. C. Naing, Y. Zhou, S. Peng, Y. Shi, Z. Zhang, W. Shen, I. T. Kirby, J. E. Melnyk, J. S. Chorba, K. Lou, S. A. Dai, I. Barrio-Hernandez, D. Memon, C. Hernandez-Armenta, J. Lyu, C. J. P. Mathy, T. Perica, K. B. Pilla, S. J. Ganesan, D. J. Saltzberg, R. Rakesh, X. Liu, S. B. Rosenthal, L. Calviello, S. Venkataramanan, J. Liboy-Lugo, Y. Lin, X.-P. Huang, Y. Liu, S. A. Wankowicz, M. Bohn, M. Safari, F. S. Ugur, C. Koh, N. S. Savar, Q. D. Tran, D. Shengjuler, S. J. Fletcher, M. C. O'Neal, Y. Cai, J. C. J. Chang, D. J. Broadhurst, S. Klippsten, P. P. Sharp, N. A. Wenzell, D. Kuzuoglu-Ozturk, H.-Y. Wang, R. Trenker, J. M. Young, D. A. Cavero, J. Hiatt, T. L. Roth, U. Rathore, A. Subramanian, J. Noack, M. Hubert, R. M. Stroud, A. D. Frankel, O. S. Rosenberg, K. A. Verba, D. A. Agard, M. Ott, M. Emerman, N. Jura, M. von Zastrow, E. Verdin, A. Ashworth, O. Schwartz, C. d'Enfert, S. Mukherjee, M. Jacobson, H. S. Malik, D. G. Fujimori, T. Ideker, C. S. Craik, S. N. Floor, J. S. Fraser, J. D. Gross, A. Sali, B. L. Roth, D. Ruggero, J. Taunton, T. Kortemme, P. Beltrao, M. Vignuzzi, A. García-Sastre, K. M. Shokat, B. K. Shoichet, N. J. Krogan, A SARS-CoV-2 protein interaction map reveals targets for drug repurposing. *Nature* **583**, 459–468 (2020).
26. J. Lan, J. Ge, J. Yu, S. Shan, H. Zhou, S. Fan, Q. Zhang, X. Shi, Q. Wang, L. Zhang, X. Wang, Structure of the SARS-CoV-2 spike receptor-binding domain bound to the ACE2 receptor. *Nature* **581**, 215–220 (2020).
27. Y. Han, L. Yang, L. A. Lacko, S. Chen, Human organoid models to study SARS-CoV-2 infection. *Nat. Methods* **19**, 418–428 (2022).
28. A. Ramani, L. Muller, P. N. Ostermann, E. Gabriel, P. Abida-Islam, A. Muller-Schiffmann, A. Mariappan, O. Goureau, H. Gruell, A. Walker, M. Andree, S. Hauka, T. Houwaart, A. Dilthey, K. Wohlgemuth, H. Omran, F. Klein, D. Wieczorek, O. Adams, J. Timm, C. Korth, H. Schaal, J. Gopalakrishnan, SARS-CoV-2 targets neurons of 3D human brain organoids. *EMBO J.* **39**, e106230 (2020).
29. L. Pellegrini, A. Albecka, D. L. Mallery, M. J. Kellner, D. Paul, A. P. Carter, L. C. James, M. A. Lancaster, SARS-CoV-2 infects the brain choroid plexus and disrupts the blood-CSF barrier in human brain organoids. *Cell Stem Cell* **27**, 951–961.e5 (2020).
30. F. Jacob, S. R. Pather, W. K. Huang, F. Zhang, S. Z. H. Wong, H. Zhou, B. Cubitt, W. Fan, C. Z. Chen, M. Xu, M. Pradhan, D. Y. Zhang, W. Zheng, A. G. Bang, H. Song, J. C. de la Torre, G. L. Ming, Human pluripotent stem cell-derived neural cells and brain organoids reveal SARS-CoV-2 neurotropism predominates in choroid plexus epithelium. *Cell Stem Cell* **27**, 937–950.e9 (2020).
31. Y. Miura, M. Y. Li, F. Birey, K. Ikeda, O. Revah, M. V. Thete, J. Y. Park, A. Puno, S. H. Lee, M. H. Porteus, S. P. Pasca, Generation of human striatal organoids and cortico-striatal assembloids from human pluripotent stem cells. *Nat. Biotechnol.* **38**, 1421–1430 (2020).
32. R. Duncan, F. A. Murphy, R. R. Mirkovic, Characterization of a novel syncytium-inducing baboon reovirus. *Virology* **212**, 752–756 (1995).
33. S. Dawe, R. Duncan, The S4 genome segment of baboon reovirus is bicistronic and encodes a novel fusion-associated small transmembrane protein. *J. Virol.* **76**, 2131–2140 (2002).
34. K. M. C. Chan, A. L. Arthur, J. Morstein, M. Jin, A. Bhat, D. Schlesinger, S. Son, D. A. Stevens, D. G. Drubin, D. A. Fletcher, Evolutionarily related small viral fusogens hijack distinct but modular actin nucleation pathways to drive cell-cell fusion. *Proc. Natl. Acad. Sci. U.S.A.* **118**, e2007526118 (2021).
35. D. Top, J. A. Read, S. J. Dawe, R. T. Syvitski, R. Duncan, Cell-cell membrane fusion induced by p15 fusion-associated small transmembrane (FAST) protein requires a novel fusion peptide motif containing a myristoylated polyproline type II helix. *J. Biol. Chem.* **287**, 3403–3414 (2012).
36. E. K. Clancy, R. Duncan, Helix-destabilizing, beta-branched, and polar residues in the baboon reovirus p15 transmembrane domain influence the modularity of FAST proteins. *J. Virol.* **85**, 4707–4719 (2011).
37. X. Ou, Y. Liu, X. Lei, P. Li, D. Mi, L. Ren, L. Guo, R. Guo, T. Chen, J. Hu, Z. Xiang, Z. Mu, X. Chen, J. Chen, K. Hu, Q. Jin, J. Wang, Z. Qian, Characterization of spike glycoprotein of SARS-CoV-2 on virus entry and its immune cross-reactivity with SARS-CoV. *Nat. Commun.* **11**, 1620 (2020).
38. D. Wrapp, N. Wang, K. S. Corbett, J. A. Goldsmith, C. L. Hsieh, O. Abiona, B. S. Graham, J. S. McLellan, Cryo-EM structure of the 2019-nCoV spike in the prefusion conformation. *Science* **367**, 1260–1263 (2020).
39. R. Bos, L. Rutten, J. E. M. van der Lubbe, M. J. G. Bakkers, G. Hardenberg, F. Wegmann, D. Zuijdgeest, A. H. de Wilde, A. Koornneef, A. Verwilligen, D. van Manen, T. Kwaks, R. Vogels, T. J. Dalebout, S. K. Myeni, M. Kikkert, E. J. Snijder, Z. Li, D. H. Barouch, J. Vellinga, J. P. M. Langedijk, R. C. Zahn, J. Custers, H. Schuitemaker, Ad26 vector-based COVID-19 vaccine encoding a prefusion-stabilized SARS-CoV-2 Spike immunogen induces potent humoral and cellular immune responses. *NPJ Vaccines* **5**, 91 (2020).
40. C. L. Hsieh, J. A. Goldsmith, J. M. Schaub, A. M. DiVenere, H. C. Kuo, K. Javanmardi, K. C. Le, D. Wrapp, A. G. Lee, Y. Liu, C. W. Chou, P. O. Byrne, C. K. Hjorth, N. V. Johnson, J. Ludes-Meyers, A. W. Nguyen, J. Park, N. Wang, D. Amengor, J. J. Lavinder, G. C. Ippolito, J. A. Maynard, I. J. Finkelstein, J. S. McLellan, Structure-based design of prefusion-stabilized SARS-CoV-2 spikes. *Science* **369**, 1501–1505 (2020).
41. B. Neumann, K. C. Nguyen, D. H. Hall, A. Ben-Yakar, M. A. Hilliard, Axonal regeneration proceeds through specific axonal fusion in transected *C. elegans* neurons. *Dev. Dyn.* **240**, 1365–1372 (2011).
42. Z. F. Altun, B. Chen, Z. W. Wang, D. H. Hall, High resolution map of *Caenorhabditis elegans* gap junction proteins. *Dev. Dyn.* **244**, 903 (2015).
43. M. Chalfie, J. E. Sulston, J. G. White, E. Southgate, J. N. Thomson, S. Brenner, The neural circuit for touch sensitivity in *Caenorhabditis elegans*. *J. Neurosci.* **5**, 956–964 (1985).
44. S. Coakley, F. K. Ritchie, K. M. Galbraith, M. A. Hilliard, Epidermal control of axonal attachment via β-spectrin and the GTPase-activating protein TBC-10 prevents axonal degeneration. *Nat. Commun.* **11**, 133 (2020).
45. B. Neumann, S. Coakley, R. Giordano-Santini, C. Linton, E. S. Lee, A. Nakagawa, D. Xue, M. A. Hilliard, EFF-1-mediated regenerative axonal fusion requires components of the apoptotic pathway. *Nature* **517**, 219–222 (2015).
46. R. Giordano-Santini, E. Kaulich, K. M. Galbraith, F. K. Ritchie, W. Wang, Z. Li, M. A. Hilliard, Fusogen-mediated neuron-neuron fusion disrupts neural circuit connectivity and alters animal behavior. *Proc. Natl. Acad. Sci. U.S.A.* **117**, 23054–23065 (2020).
47. K. Gruber, Preventing zoonotic pandemics: Are we there yet? *Lancet Microbe* **2**, e352 (2021).
48. K. Bohmwald, N. M. S. Galvez, M. Rios, A. M. Kalergis, Neurologic alterations due to respiratory virus infections. *Front. Cell. Neurosci.* **12**, 386 (2018).
49. C. Chen, S. R. Haupert, L. Zimmermann, X. Shi, L. G. Fritsche, B. Mukherjee, Global prevalence of post-acute sequelae of COVID-19 (PASC) or Long COVID: A meta-analysis and systematic review. medRxiv 2021.11.15.21266377 (2021). https://doi.org/10.1101/2021.11.15.21266377.
50. S. Watanabe, Y. Shirogane, S. O. Suzuki, S. Ikegame, R. Koga, Y. Yanagi, Mutant fusion proteins with enhanced fusion activity promote measles virus spread in human neuronal cells and brains of suckling hamsters. *J. Virol.* **87**, 2648–2659 (2013).
51. Y. Shirogane, H. Harada, Y. Hirai, R. Takemoto, T. Suzuki, T. Hashiguchi, Y. Yanagi, Collective fusion activity determines neurotropism of an en bloc transmitted enveloped virus. *Sci. Adv.* **9**, eadf3731 (2023).

52. Y. Sato, S. Watanabe, Y. Fukuda, T. Hashiguchi, Y. Yanagi, S. Ohno, Cell-to-cell measles virus spread between human neurons is dependent on hemagglutinin and hyperfusogenic fusion protein. *J. Virol.* **92**, e02166-17 (2018).
53. Y. Iwasaki, H. Koprowski, Cell to cell transmission of virus in the central nervous system. I. Subacute sclerosing panencephalitis. *Lab. Invest.* **31**, 187–196 (1974).
54. M. U. Ehrengruber, E. Ehler, M. A. Billeter, H. Y. Naim, Measles virus spreads in rat hippocampal neurons by cell-to-cell contact and in a polarized fashion. *J. Virol.* **76**, 5720–5728 (2002).
55. M. M. Rajah, A. Bernier, J. Buchrieser, O. Schwartz, The mechanism and consequences of SARS-CoV-2 spike-mediated fusion and syncytia formation. *J. Mol. Biol.* **434**, 167280 (2022).
56. L. Braga, H. Ali, I. Secco, E. Chiavacci, G. Neves, D. Goldhill, R. Penn, J. M. Jimenez-Guardeno, A. M. Ortega-Prieto, R. Bussani, A. Cannata, G. Rizzari, C. Collesi, E. Schneider, D. Arosio, A. M. Shah, W. S. Barclay, M. H. Malim, J. Burrone, M. Giacca, Drugs that inhibit TMEM16 proteins block SARS-CoV-2 spike-induced syncytia. *Nature* **594**, 88–93 (2021).
57. C. Zeng, J. P. Evans, T. King, Y. M. Zheng, E. M. Oltz, S. P. J. Whelan, L. J. Saif, M. E. Peeples, S. L. Liu, SARS-CoV-2 spreads through cell-to-cell transmission. *Proc. Natl. Acad. Sci. U.S.A.* **119**, e2111400119 (2022).
58. N. M. Sherer, M. J. Lehmann, L. F. Jimenez-Soto, C. Horensavitz, M. Pypaert, W. Mothes, Retroviruses can establish filopodial bridges for efficient cell-to-cell transmission. *Nat. Cell Biol.* **9**, 310–315 (2007).
59. C. Zurzolo, Tunneling nanotubes: Reshaping connectivity. *Curr. Opin. Cell Biol.* **71**, 139–147 (2021).
60. S. Abounit, L. Bousset, F. Loria, S. Zhu, F. de Chaumont, L. Pieri, J. C. Olivo-Marin, R. Melki, C. Zurzolo, Tunneling nanotubes spread fibrillar α-synuclein by intercellular trafficking of lysosomes. *EMBO J.* **35**, 2120–2138 (2016).
61. N. Khanlou, D. J. Moore, G. Chana, M. Cherner, D. Lazzaretto, S. Dawes, I. Grant, E. Masliah, I. P. Everall; the HNRC Group, Increased frequency of α-synuclein in the substantia nigra in human immunodeficiency virus infection. *J. Neurovirol.* **15**, 131–138 (2009).
62. K. Bjornevik, M. Cortese, B. C. Healy, J. Kuhle, M. J. Mina, Y. Leng, S. J. Elledge, D. W. Niebuhr, A. I. Scher, K. L. Munger, A. Ascherio, Longitudinal analysis reveals high prevalence of Epstein-Barr virus associated with multiple sclerosis. *Science* **375**, 296–301 (2022).
63. T. Solomon, N. M. Dung, R. Kneen, T. T. T. Le, M. Gainsborough, A. Nisalak, N. P. Day, F. J. Kirkham, D. W. Vaughn, S. Smith, N. J. White, Seizures and raised intracranial pressure in Vietnamese patients with Japanese encephalitis. *Brain* **125**, 1084–1093 (2002).
64. F. Krammer, SARS-CoV-2 vaccines in development. *Nature* **586**, 516–527 (2020).
65. F. P. Polack, S. J. Thomas, N. Kitchin, J. Absalon, A. Gurtman, S. Lockhart, J. L. Perez, G. P. Marc, E. D. Moreira, C. Zerbini, R. Bailey, K. A. Swanson, S. Roychoudhury, K. Koury, P. Li, W. V. Kalina, D. Cooper, R. W. Frenck Jr., L. L. Hammitt, Ö. Türeci, H. Nell, A. Schaefer, S. Ünal, D. B. Tresnan, S. Mather, P. R. Dormitzer, U. Şahin, K. U. Jansen, W. C. Gruber; C4591001 Clinical Trial Group, Safety and efficacy of the BNT162b2 mRNA Covid-19 vaccine. *N. Engl. J. Med.* **383**, 2603–2615 (2020).
66. Y. Watanabe, L. Mendonca, E. R. Allen, A. Howe, M. Lee, J. D. Allen, H. Chawla, D. Pulido, F. Donnellan, H. Davies, M. Ulaszewska, S. Belij-Rammerstorfer, S. Morris, A. S. Krebs, W. Dejnirattisai, J. Mongkolsapaya, P. Supasa, G. R. Screaton, C. M. Green, T. Lambe, P. Zhang, S. C. Gilbert, M. Crispin, Native-like SARS-CoV-2 spike glycoprotein expressed by ChAdOx1 nCoV-19/AZD1222 vaccine. *ACS Cent. Sci.* **7**, 594–602 (2021).
67. K. S. Corbett, D. K. Edwards, S. R. Leist, O. M. Abiona, S. Boyoglu-Barnum, R. A. Gillespie, S. Himansu, A. Schafer, C. T. Ziwawo, A. T. DiPiazza, K. H. Dinnon, S. M. Elbashir, C. A. Shaw, A. Woods, E. J. Fritch, D. R. Martinez, K. W. Bock, M. Minai, B. M. Nagata, G. B. Hutchinson, K. Wu, C. Henry, K. Bahl, D. Garcia-Dominguez, L. Ma, I. Renzi, W. P. Kong, S. D. Schmidt, L. Wang, Y. Zhang, E. Phung, L. A. Chang, R. J. Loomis, N. E. Altaras, E. Narayanan, M. Metkar, V. Presnyak, C. Liu, M. K. Louder, W. Shi, K. Leung, E. S. Yang, A. West, K. L. Gully, L. J. Stevens, N. Wang, D. Wrapp, N. A. Doria-Rose, G. Stewart-Jones, H. Bennett, G. S. Alvarado, M. C. Nason, T. J. Ruckwardt, J. S. McLellan, M. R. Denison, J. D. Chappell, I. N. Moore, K. M. Morabito, J. R. Mascola, R. S. Baric, A. Carfi, B. S. Graham, SARS-CoV-2 mRNA vaccine design enabled by prototype pathogen preparedness. *Nature* **586**, 567–571 (2020).
68. X. Xia, Domains and functions of spike protein in SARS-Cov-2 in the context of vaccine design. *Viruses* **13**, 109 (2021).
69. G. J. Kremers, K. L. Hazelwood, C. S. Murphy, M. W. Davidson, D. W. Piston, Photoconversion in orange and red fluorescent proteins. *Nat. Methods* **6**, 355–358 (2009).
70. M. Karbowski, D. Arnoult, H. Chen, D. C. Chan, C. L. Smith, R. J. Youle, Quantitation of mitochondrial dynamics by photolabeling of individual organelles shows that mitochondrial fusion is blocked during the Bax activation phase of apoptosis. *J. Cell Biol.* **164**, 493–499 (2004).
71. A. G. York, A. Ghitani, A. Vaziri, M. W. Davidson, H. Shroff, Confined activation and subdiffractive localization enables whole-cell PALM with genetically expressed probes. *Nat. Methods* **8**, 327–333 (2011).
72. J. Shang, G. Ye, K. Shi, Y. Wan, C. Luo, H. Aihara, Q. Geng, A. Auerbach, F. Li, Structural basis of receptor recognition by SARS-CoV-2. *Nature* **581**, 221–224 (2020).
73. M. Joensuu, R. Martinez-Marmol, P. Padmanabhan, N. R. Glass, N. Durisic, M. Pelekanos, M. Mollazade, G. Balistreri, R. Amor, J. J. Cooper-White, G. J. Goodhill, F. A. Meunier, Visualizing endocytic recycling and trafficking in live neurons by subdiffractional tracking of internalized molecules. *Nat. Protoc.* **12**, 2590–2622 (2017).
74. T. Fath, Y. D. Ke, P. Gunning, J. Gotz, L. M. Ittner, Primary support cultures of hippocampal and substantia nigra neurons. *Nat. Protoc.* **4**, 78–85 (2009).
75. S. R. Guttikonda, L. Sikkema, J. Tchieu, N. Saurat, R. M. Walsh, O. Harschnitz, G. Ciceri, M. Sneeboer, L. Mazutis, M. Setty, P. Zumbo, D. Betel, L. D. de Witte, D. Pe'er, L. Studer, Fully defined human pluripotent stem cell-derived microglia and tri-culture system model C3 production in Alzheimer's disease. *Nat. Neurosci.* **24**, 343–354 (2021).
76. S. J. Yoon, L. S. Elahi, A. M. Pasca, R. M. Marton, A. Gordon, O. Revah, Y. Miura, E. M. Walczak, G. M. Holdgate, H. C. Fan, J. R. Huguenard, D. H. Geschwind, S. P. Pasca, Reliability of human cortical organoid generation. *Nat. Methods* **16**, 75–78 (2019).
77. A. Ittner, S. W. Chua, J. Bertz, A. Volkerling, J. van der Hoven, A. Gladbach, M. Przybyla, M. Bi, A. van Hummel, C. H. Stevens, S. Ippati, L. S. Suh, A. Macmillan, G. Sutherland, J. J. Kril, A. P. Silva, J. P. Mackay, A. Poljak, F. Delerue, Y. D. Ke, L. M. Ittner, Site-specific phosphorylation of tau inhibits amyloid-β toxicity in Alzheimer's mice. *Science* **354**, 904–908 (2016).
78. S. Brenner, The genetics of *Caenorhabditis elegans*. *Genetics* **77**, 71–94 (1974).
79. C. C. Mello, J. M. Kramer, D. Stinchcomb, V. Ambros, Efficient gene transfer in C. elegans: Extrachromosomal maintenance and integration of transforming sequences. *EMBO J.* **10**, 3959–3970 (1991).
80. J. Schindelin, I. Arganda-Carreras, E. Frise, V. Kaynig, M. Longair, T. Pietzsch, S. Preibisch, C. Rueden, S. Saalfeld, B. Schmid, J. Y. Tinevez, D. J. White, V. Hartenstein, K. Eliceiri, P. Tomancak, A. Cardona, Fiji: An open-source platform for biological-image analysis. *Nat. Methods* **9**, 676–682 (2012).

Acknowledgments: We thank the Queensland Brain Institute's Advanced Microscopy Facility's team for excellent support during the imaging acquisition, R. K. Sullivan and the Queensland Brain Institute's Histology Facility for excellent support during the processing and preparation of histological samples, and A. Kumar for laboratory assistance. We also thank P. Bartlett, J. Götz, P. Bazzicalupo, and R. Tweedale for comments and critical appraisal of the manuscript. We thank the members of the Hilliard laboratory for insightful discussions and comments. Some strains were provided by the *Caenorhabditis* Genetics Center, which is funded by NIH Office of Research Infrastructure Programs (P40 OD010440), and the International *C. elegans* Gene Knockout Consortium. Graphic schemes were created with Biorender.com. **Funding:** This work was supported by Academy of Finland Research Grant 318434 (to G.B.), The University of Helsinki Funds (to G.B.), NHMRC Ideas Grant GNT2010917 (to F.A.M. and G.B.), Senior Research Fellowship GNT1155794 (to F.A.M.), NHMRC Investigator Grant GNT2007919 (to K.R.S.), NHMRC Investigator Grant GNT1197860 (to M.A.H.), Project Grant GNT1068871 (to M.A.H.), NHMRC Project Grant GNT1129367 (to M.A.H. and F.A.M.), Australian Research Council (ARC) Discovery Project Grant DP160104359 (to M.A.H.), NHMRC Career Development Fellowship GNT1123564 (to Y.D.K.), NHMRC Principal Research Fellowship GNT1136241 (to L.M.I.), NHMRC Equipment Grant (QBI Histology Facility), ARC Linkage Infrastructure Equipment and Facilities Grant LE130100078 (QBI Advanced Microscopy Facility), HFSP Human Frontier Science Program Fellowship LT000762/2012 (to R.G.-S.), and Advance Queensland Women's Academic Fund (to R.G.-S.). **Author contributions:** Conceptualization: R.M.-M., R.G.-S., and M.A.H. Methodology: R.M.-M., R.G.-S., G.B., Y.D.K., L.M.I., M.A.H., K.R.S., K.Y.C., and R.A. Investigation: R.M.-M., R.G.-S., E.K., A.-N.C., M.A.R., E.R., K.Y.C., M.P., and R.A. Visualization: R.M.-M., R.G.-S., E.K., A.-N.C., and E.R. Funding acquisition: L.M.I., Y.D.K., F.A.M., and M.A.H. Project administration, L.M.I., Y.D.K., and M.A.H. Supervision: L.M.I., Y.D.K., K.R.S., and M.A.H. Writing (original draft): R.M.-M., R.G.-S., and M.A.H. Writing (review and editing): R.M.-M., R.G.-S., E.K., G.B., F.A.M., Y.D.K., LM, K.Y.C., K.R.S., and M.A.H. **Competing interests:** The authors declare that they have no competing interests, except for K.R.S. K.R.S. is a consultant for Sanofi, Roche, and Novo Nordisk. The opinions and data presented in this manuscript are of the authors and are independent of these relationships. **Data and materials availability:** All data are available in the paper and/or the Supplementary Materials. Requests for materials should be addressed to M.A.H. (m.hilliard@uq.edu.au).

Submitted 11 December 2022
Accepted 1 May 2023
Published 7 June 2023
10.1126/sciadv.adg2248

EVOLUTIONARY BIOLOGY

Genotypes selected for early and late avian lay date differ in their phenotype, but not fitness, in the wild

Melanie Lindner[1,2]*, Jip JC Ramakers[3], Irene Verhagen[4], Barbara M Tomotani[1,5], A Christa Mateman[1], Phillip Gienapp[6], Marcel E Visser[1,2]*

Global warming has shifted phenological traits in many species, but whether species are able to track further increasing temperatures depends on the fitness consequences of additional shifts in phenological traits. To test this, we measured phenology and fitness of great tits (*Parus major*) with genotypes for extremely early and late egg lay dates, obtained from a genomic selection experiment. Females with early genotypes advanced lay dates relative to females with late genotypes, but not relative to nonselected females. Females with early and late genotypes did not differ in the number of fledglings produced, in line with the weak effect of lay date on the number of fledglings produced by nonselected females in the years of the experiment. Our study is the first application of genomic selection in the wild and led to an asymmetric phenotypic response that indicates the presence of constraints toward early, but not late, lay dates.

INTRODUCTION

Anthropogenic global warming has led to drastic changes in the environment and species must cope with these changes. Many species use ambient temperature as a cue to match the timing of seasonally expressed life-history traits to the year-specific environment (*1*). For many seasonally reproducing consumer species, ambient temperature predicts when food resources are plentiful. By using temperature as a cue, consumer species can match the timing of offspring provisioning with the timing of maximum food resource abundance. In many systems, however, consumer and resource species differ in how strongly they respond to increasing temperatures (*2*, *3*). They might differ in temperature sensitivity per se (i.e., the number of days phenology shifts per 1°C in temperature change) and/or in the time period at which they are temperature sensitive, and the temperature in these time periods may change at different rates (*4*). This way, increasing temperatures can uncouple the timing of offspring provisioning from the timing of maximum food resource abundance, leading to a phenological mismatch between consumer and resource species with potentially severe consequences on reproductive success of the consumer species (*5*). The poster child example for this in evolutionary ecology is the phenological mismatch between great tits (*Parus major*) and their caterpillar prey (*6*–*8*). In this system, the match between the food demands of great tit young and caterpillar biomass abundance is a strong selection pressure on first egg laying date (hereafter lay date). Hence, an advancement in the phenology of caterpillar biomass without a concomitant advancement in lay dates and thus chick rearing period is expected to negatively affect the reproductive success of great tits (*6*) and population stability in the long run (*7*, *9*).

Quantitative genetic studies have long used data from individual-based long-term study populations to estimate the strength of directional selection and the magnitude of additive genetic variation underlying focal traits to predict the potential for a microevolutionary response to selection (*10*, *11*). Despite many examples of directional selection [e.g., (*11*–*15*)], microevolutionary responses to selection in the wild that match the expectations based on estimates of quantitative genetic studies are rare (*16*) and often populations are in so-called evolutionary stasis (*16*). There are potential statistical and biological explanations for why this might be the case (*17*), and one of them is that we might not know whether the predicted response would indeed lead to an increased fitness if predicted responses lie outside the currently observed distribution. In other words, we have no data to estimate the fitness consequences of these shifted trait values and cannot assess whether the predicted response to directional selection would have positive or negative consequences for fitness.

For great tit populations, which are phenologically mismatched with their main food resource for chick feeding, a directional mean shift in phenotypes does not necessarily result in higher fitness (*5*). In one scenario, early lay dates that reduce the phenological mismatch between offspring provisioning and maximum food abundance are expected to have higher reproductive success when the phenological mismatch is the main selection pressure, i.e., fitness is maximized with a reduced mismatch [figure 1 in (*5*)]. Then, a phenological mismatch is considered true mistiming between consumer and resource species. In an alternative second scenario, other ecological variables, in addition to the match between consumer and resource phenology, are important determinants of fitness (*5*). For example, poor environmental conditions in early spring, such as cold temperatures and limited food resources, might lead to high fitness costs (e.g., increased mortality) for females that attempt to breed early enough to reduce the phenological mismatch. With these additional fitness components in place, the phenotype that maximizes fitness might maintain (a certain degree of) the phenological mismatch [figure 2 in (*5*)]. Then, the phenological

[1]Department of Animal Ecology, Netherlands Institute of Ecology (NIOO-KNAW), Wageningen, Netherlands. [2]Chronobiology Unit, Groningen Institute for Evolutionary Life Sciences (GELIFES), University of Groningen, Groningen, Netherlands. [3]Mathematical and Statistical Methods–Biometris, Wageningen University & Research (WUR), Wageningen, Netherlands. [4]Wageningen University & Research (WUR) Library, Wageningen, Netherlands. [5]Department of Arctic and Marine Biology, UiT The Arctic University of Norway, Tromsø, Norway. [6]Michael-Otto-Institut, NABU, Bergenhusen, Germany.
*Corresponding author. Email: m.lindner@nioo.knaw.nl (M.L.); m.visser@nioo.knaw.nl (M.E.V.)

mismatch is considered an adaptive mismatch between consumer and resource species. Only when earlier phenotypes have increased fitness (i.e., the phenological mismatch constitutes true mistiming; first scenario), do we expect to see a shift in the distribution of trait values as a response to directional selection [figure 4 in (*17*)]. We, however, lack sufficient data at the very ends of the current lay date distribution to test whether a phenological mismatch constitutes mistiming (if earlier females with a reduced phenological mismatch had higher fitness) or an adaptive mismatch (if earlier females had lower fitness than females that retain a certain degree of the phenological mismatch).

Understanding the evolutionary consequences of a phenological mismatch requires to move phenotypes toward earlier lay dates in the wild and assess the fitness consequences. To directionally push phenotypes toward earlier or later lay dates, some kind of experimental manipulation is needed. It has, however, proven challenging to perform "clean" manipulations of avian breeding time in the wild (*18*). Methods that previously attempted to manipulate lay dates constitute manipulations on the phenotypic level, such as the exposure to a single long day (*19*), manipulation of photoperiod perception (*20*), a leptin implant treatment (*21*), or the use of supplemental food in the time before laying (*22*). These manipulations either failed to advance lay dates or are known to induce a bias in reproductive success as a consequence of the manipulation. Hence, these methods are unsuitable for estimating the fitness components of advanced lay dates, but see (*23*) for a successful population-specific phenotypic manipulation of lay dates.

Genomic selection offers a previously unexplored approach to induce directional shifts in lay dates of seasonally breeding birds that have genomic breeding values (GEBVs) for extremely early and late lay dates (*24*). In contrast to traditionally applied procedures for artificial selection, where one selects on the expressed phenotype or breeding values (BVs) estimated using pedigree-based relatedness, genomic selection is based on GEBVs, the additive effect of an individual's genotype on the phenotype relative to the population mean phenotype estimated using genomic approaches (*25*). Calculating GEBVs for a wild bird species allowed us to follow females, which are expected to have extremely early or late lay dates based on their GEBVs, throughout their lifetime. This way, the fitness consequences of individuals that are expected to have extremely early and late lay dates can be assessed while differentiating between (i) the fitness costs in the time from fledging to first-time recruitment and first egg lay date and (ii), if a female succeeds to recruit, the fitness benefits in the form of lifetime reproductive success. While genomic selection via GEBVs is a powerful tool for artificial selection commonly applied in animal and plant breeding (*26*) and its potential for studies in the wild has been acknowledged (*25*), we are currently not aware of any study in which genomic selection has been used in this way. Note, however, that GEBVs have previously been estimated in a wild population (*27*). This lack of application is likely explained by limitations in sample size and statistical power, as a large number of individuals genotyped at a sufficient marker density is required. These limitations are especially relevant for phenological traits that generally have low heritability [~0.2 for lay dates in our study population (*24*)] and might require a training population with a sample size of thousands.

Here, a training population of >2000 great tit females from a long-term study population at the Hoge Veluwe National Park (The Netherlands) with known lay dates and genotyped at >500,000 single-nucleotide polymorphisms (SNPs) was used to estimate GEBVs using the "genomic best linear unbiased prediction" (GBLUP) approach (*24*, *28*). GEBVs were used as the criterion for the selection procedure in such a way that birds with extremely negative and positive GEBVs were selected for the early and late selection lines for lay date. A detailed description of the selection procedure can be found in (*29*), and a short description can be found in Materials and Methods. We bred F3 generation breeding pairs of the early and late selection line from 2017 to 2019 and moved the F4 generation eggs they laid into the Hoge Veluwe study population. In the following year(s), we identified and monitored any selection line females of the F4 generation that recruited into the study population as breeding bird to record the realized lay dates and assess the fitness consequences.

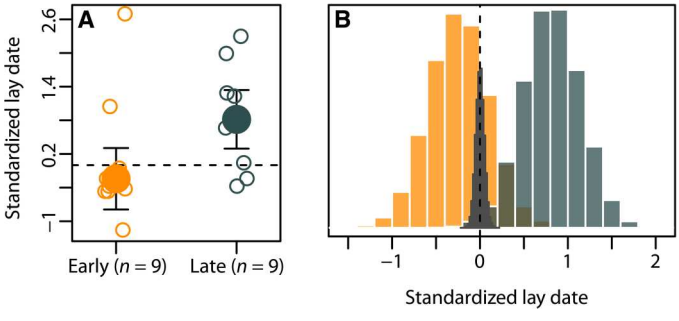

Fig. 1. Posterior predictions of standardized lay dates. (**A**) Posterior means of mean-standardized lay dates with 89% credible interval for female recruits form the early (yellow, $n = 8$) and late (blue, $n = 9$) selection line (posterior mean difference in standardized lay dates (late-early): 1.06; 89% credible interval: 0.30;1.81). The crossed-out data point indicates an outlier female that was removed from the data before analysis (see text S5 for a formal outlier analysis). (**B**) Posterior distribution of mean-standardized lay dates for female recruits from the early (yellow) and late (blue) selection line and for local female recruits (dark gray, $n = 433$) [posterior mean difference in standardized lay dates (local-early): 0.24, 89% credible interval: −0.31;0.80; posterior mean difference in standardized lay dates (local-late): −0.82, 89% credible interval: −1.34;−0.29]. The posterior mean of standardized lay dates for local female recruits is shown as vertical dashed line. Lay date observations were standardized as z scores using a year-specific SD of 3.26, 5.45, and 4.82 days for 2018, 2019, and 2020, respectively.

RESULTS

Phenotypic response to genomic selection in the wild

Lay date

We recorded the lay dates of female selection line recruits at the local study population in the years 2018 to 2020 to test whether genomic selection for early and late lay dates translated into a phenotypic response in the wild. In total, 936 F4 selection line eggs produced by F3 selection line breeding pairs in aviaries were introduced into the wild study population at the Hoge Veluwe of which <20 females locally recruited as breeding birds. Female recruits from the early selection line ($n = 8$) had earlier lay dates than female recruits from the late selection line ($n = 9$) (posterior mean difference in standardized lay dates (late-early): 1.06, 89% credible interval: 0.30;1.81, Fig. 1A and tables S1 and S2) when a potential outlier observation was removed (see text S5 for a formal outlier analysis and fig. S11). The finding did not change when the outlier remained

included (fig. S12). The posterior mean difference in standardized lay dates translated into a mean difference in lay dates of 3.45 (2018), 5.77 (2019), and 5.10 (2020) days. As lay dates were standardized, the posterior distribution of standardized lay dates for nonselection line female recruits (hereafter local female recruits; n = 433) was centered at zero (posterior mean of standardized lay dates: 0.00, 89% credible interval: −0.08;0.08; Fig. 1B and tables S1 and S2). While we did not succeed to advance the lay dates of female recruits from the early selection line relative to the lay dates of local female recruits [posterior mean difference in standardized lay dates (local-early): 0.24, 89% credible interval: −0.31;0.80], we succeeded to delay the lay dates of female recruits from the late selection line relative to lay dates of local female recruits [posterior mean difference in standardized lay dates (local-late): −0.82, 89% credible interval: −1.34;-0.29, Fig. 1B and tables S1 and S2]. This interpretation is also supported by the posterior distribution of standardized lay dates for female recruits from the early and late selection line (posterior mean of standardized lay dates for female recruits from the early selection line: −0.24, 89% credible interval: −0.79;0.31; posterior mean of standardized lay dates for female recruits from the late selection line: 0.82, 89% credible interval: 0.30;1.34; Fig. 1A and tables S1 and S2). Hence, the genomic selection experiment for early and late lay dates led to a somewhat asymmetric phenotypic response in the wild (Fig. 1B). However, there is no difference between the selection lines in their phenotypic response relative to local female recruits (posterior mean of difference in standardized lay dates relative to local females between selection lines: 0.57, 89% credible interval: −0.20;1.35; tables S1 and S2).

Phenological mismatch

We assessed whether the difference in lay date between female recruits from the early and late selection line (Fig. 1) translated into a difference in phenological mismatch, i.e., the difference in days between the expected chick rearing period and the period of maximum caterpillar biomass availability. Female recruits from the early selection line (n = 8) showed a reduced phenological mismatch relative to female recruits from the late selection line (n = 9) [posterior mean difference in standardized phenological mismatch (late-early): 1.90, 89% credible interval: 0.44;3.38; Fig. 2 and tables S3 and S4]. The phenological mismatch of female recruits from either selection line did not differ from the phenological mismatch of local female recruits, with a posterior mean difference in standardized phenological mismatch of 0.93 (local-early) (89% credible interval: −0.17;2.02) and −0.97 (local-late) (89% credible interval: −2.02;0.07; Fig. 2 and tables S3 and S4) for female recruits from the early and late selection line, respectively. For local female recruits (n = 433), the number of days of the phenological mismatch differed between years (fig. S1 and tables S5 and S6). While females were on average mismatched by 13.38 days in 2018 (89% credible interval: 12.70;14.05) and 9.74 days in 2020 (89% credible interval: 9.17;10.31), they were, on average, better matched in 2019 with a negative mismatch of 2.62 days (89% credible interval: −3.22;-2.02; tables S5 and S6), i.e., they laid, on average, 2.62 days too early rather than too late.

Consequences of genomic selection for fitness in the wild

To test for fitness differences between lines we analyzed the first-year survival of selection line fledglings [in the form of (i) mortality before laying and (ii) probability to locally recruit as a breeding bird and (iii) lifetime number of fledglings produced when recruited]. We then estimated the (iv) total fitness of selection line fledglings as the product of their local recruitment probability and the lifetime number of fledglings produced.

Consequences of genomic selection on mortality before laying

One proxy for survival is the potentially selective disappearance of early selection line females before their first breeding event. This selective disappearance might arise as a consequence of higher mortality risk for females that attempt to breed early, when the environment makes it challenging to produce eggs at that time [i.e., second scenario (*5*)]. For this, we tested whether early selection line females were less likely than late selection line females to recruit into the local study population as a breeding bird when females were identified in late winter [n = 7 (early) and n = 15 (late)] or during nest building in early spring [n = 13 (early) and n = 16 (late)]. We did not find any difference between early and late selection lines females in local recruitment probability irrespectively of whether females were identified in January or early spring (figs. S2 and S3 and tables S7 to S10). This analysis, however, is limited by low statistical power.

Consequences of genomic selection on local recruitment probability

Another proxy for survival is the local recruitment probability [i.e., the probability that a fledgling survives to locally breed the following year(s)], for which we did not find a difference between early (n = 318) and late (n = 331) selection line fledglings [posterior mean difference (late-early): −0.005, 89% credible interval: −0.035;0.026; Fig. 3A and tables S10 to S12] or between selection line fledglings and nonselection line fledglings (hereafter local fledglings; n = 1675) [posterior mean difference (local-early): −0.018, 89% credible interval: −0.044;0.005; posterior mean difference (local late): −0.014, 89% credible interval: −0.038;0.009; tables S10 to S12]. Overall, local recruitment probability of local fledglings was low at the study site and showed a decrease throughout spring and an increase with fledgling weight (Fig. 3B and table S10), in line with the expectation that birds that fledge early and are heavier at the time of fledging are more likely to recruit (*30*).

We moved the F4 selection line eggs in mixed-selection line broods from the aviaries into the Hoge Veluwe study site. With this, we aimed to rear selection line individuals in a common environment in which early and late selection line individuals did not differ in their realized hatch date and subsequent fledging date. We formally tested this assumption and, indeed, did not find a difference in fledging date between early and late selection line fledglings [posterior mean difference in standardized fledging date (late-early): 0.074; 89% credible interval: −0.010;0.158; fig. S4 and tables S13 and S14]. Hence, our experimental design removed any differences between selection lines that, e.g., might arise as a consequence of the maternal lay date (i.e., the lay date of F3 selection line females in the aviaries) and, in turn, might induce a bias in local recruitment probability.

We, furthermore, tested for a difference in the fledgling weight of early and late selection line fledglings, which might be a correlated response to genomic selection for lay date. We found that early selection line fledglings were lighter than late selection line fledglings [posterior mean difference in standardized fledgling weight (late-early): 0.10, 89% credible interval: 0.01;0.18; fig. S5 and tables S15 and S16]. Moreover, early selection line fledglings were lighter than local fledglings [posterior mean difference in standardized fledgling weight (local-early): 0.16; 89% credible interval: 0.09;0.23; tables S15

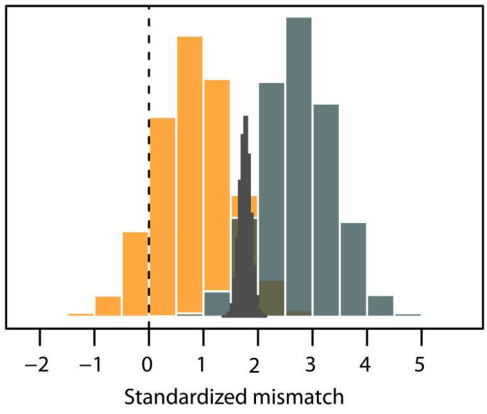

Fig. 2. Posterior predictions of standardized mismatch. Posterior distribution of mean-standardized mismatch for female recruits from the early (yellow, $n = 8$) and late (blue, $n = 9$) selection line and for local female recruits (dark gray, $n = 433$) [posterior mean difference in standardized phenological mismatch (late-early): 1.90, 89% credible interval: 0.44;3.38; posterior mean difference in standardized phenological mismatch (local-early): 0.93, 89% credible interval: −0.17;2.02; posterior mean difference in standardized phenological mismatch (local-late): −0.97, 89% credible interval: −2.02;0.07]. The vertical dashed line indicates the lay date that corresponds to the lay date that results in a perfectly matched phenology. Mismatch was standardized as *z* scores using a year-specific SD of 3.26, 5.45, and 4.82 days for 2018, 2019, and 2020, respectively.

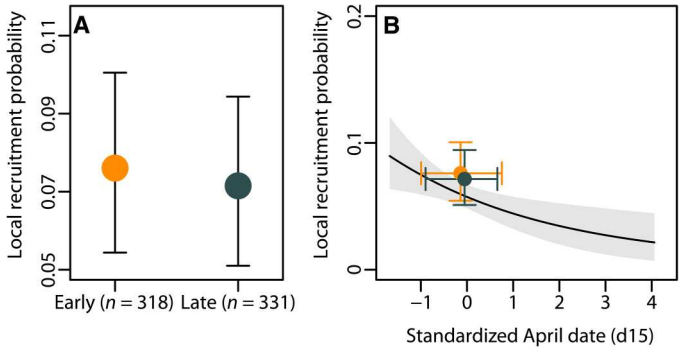

Fig. 3. Posterior predictions of local recruitment probability. (**A**) Posterior means of mean local recruitment probability with 89% credible interval for early (yellow, $n = 318$) and late (blue, $n = 331$) selection line fledglings [posterior mean difference (late-early): −0.005, 89% credible interval: −0.035;0.026]. (**B**) Mean local recruitment probability of early (yellow) and late (blue) selection line fledglings in comparison to local fledglings (black/gray, $n = 1675$). For selection line fledglings, vertical locations of filled circles and error bars correspond to the posterior means of local recruitment probability with 89% credible interval, and horizontal location of filled circles and error bars correspond to mean-standardized April date at d15 with 89% credible interval. For local fledglings, the black line and gray shaded area represent the posterior mean of local recruitment probability over standardized April dates at d15 with 89% credible interval. April dates were standardized as *z* scores using a SD of 10.29 days.

and S16], while there was no difference in fledgling weight between late selection line fledglings and local fledglings [posterior mean difference in standardized fledgling weight (local-late): 0.06, 89% credible interval: −0.00;0.13; tables S15 and S16].

As we can only calculate the consequences of genomic selection on total fitness for females and not for males (and hence need to propagate sex-specific posterior distributions for local recruitment probability; see the "Consequences of genomic selection on reproductive success" section), we estimated the sex-specific local recruitment probability for selection line fledglings using 159 early and 167 late female selection line fledglings as well as 158 early and 164 late male selection line fledglings. There was no difference in the local recruitment probability between selection lines, sexes, or their interactions (tables S17 and S18).

Consequences of genomic selection on reproductive success

To assess reproductive success, we used the lifetime number of fledglings produced by female selection line recruits, i.e., female selection line fledglings that recruited into the local study population and were identified as a breeding bird, as a proxy for reproductive success. The reported difference in lay date (Fig. 1) and phenological mismatch (Fig. 2) between female selection line recruits from the early ($n = 8$) and late ($n = 9$) line did not translate into a difference in reproductive success [posterior mean difference in the standardized lifetime number of fledglings produced (late-early): 0.31; 89% credible interval: −0.53;1.15; Fig. 4A and tables S19 and S20]. This, however, is in line with the overall weak effect of lay dates on the lifetime number of fledglings produced by local female recruits ($n = 254$) at the study population in the years of the experiment (posterior mean: −0.13, 89% credible interval: −0.25;0.00; Fig. 4B and tables 21 and S22). Moreover, the quality of fledglings produced did not differ between female recruits from the early ($n = 61$) and late ($n = 68$) selection line in terms of fledgling weight, tarsus length, and third primary (P3) length (figs. S6 to S8 and tables S23 to S28).

In addition to assessing differences in reproductive success, we tested whether female recruits from the early and late selection line differed in other aspects that have potential effects on reproductive success. However, female recruits from the early and late selection line did not differ in their daily energy expenditure during chick feeding or daily chick feeding frequency (figs. S9 and S10 and tables S29 to S32). Overall, female recruits from the early and late selection line did not differ in reproductive success when the lifetime number of fledglings produced was used as a proxy for reproductive success.

Consequences of genomic selection on total fitness

Females from the selection lines for early and late avian lay date did not differ in their total fitness, when the total fitness was defined as the product of the local recruitment probability of female selection line fledglings and the lifetime number of fledglings produced by female selection line recruits (table S32). Overall, genomic selection for avian lay date did not lead to any fitness consequences in the wild in the years we performed the experiment.

DISCUSSION

Whether species will be able to cope with global warming-induced changes to their environment depends on how well they can adapt to these new environmental conditions, for instance, by shifting their phenology (*2*, *3*). We, however, lack sufficient data at the very end of the current lay date distribution, making it impossible to estimate whether a further advancement of lay dates would indeed lead to an increase in fitness, i.e., is selected for. We used the Dutch great tit long-term study population at the Hoge Veluwe National Park with the aim to induce directional shifts in the currently observed distribution of lay dates, without inducing a bias in the fitness measurement, as is often the case for phenotypic manipulations (see Introduction). For this, we aimed to create birds

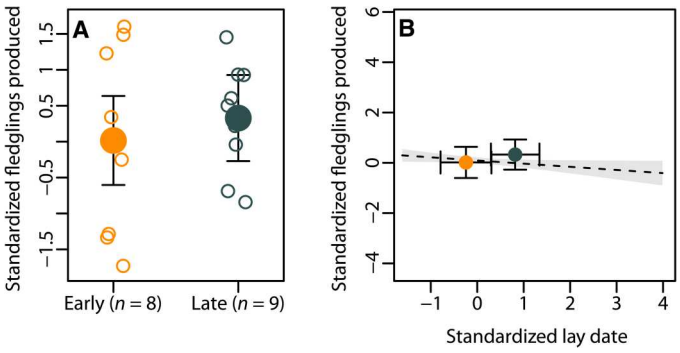

Fig. 4. Posterior predictions of the lifetime number of fledglings produced. (**A**) Posterior means of the mean-standardized lifetime number of fledglings produced with 89% credible interval for female recruits from the early (yellow, $n = 8$) and late (blue, $n = 9$) selection line [posterior mean difference in the standardized lifetime number of fledglings produced (late-early): 0.31; 89% credible interval: −0.53;1.15]. (**B**) Mean lifetime number of fledglings produced by female recruits from the early (yellow) and late (blue) selection line in comparison to the standardized lifetime number of fledglings produced by local female recruits (black/gray, $n = 254$). For female selection line recruits, vertical locations of filled circles and error bars correspond to the posterior mean-standardized lifetime number of fledglings produced with 89% credible interval, and horizontal location of filled circles and error bars correspond to posterior mean-standardized lay dates with 89% credible interval. For local female recruits, black dashed line and gray shaded area show posterior means of the standardized lifetime number of fledglings produced with 89% credible intervals over standardized lay dates. The lifetime number of fledglings produced was standardized as *z* scores using a year-specific SD of 3.13, 3.53, and 3.14 fledglings for 2018, 2019, and 2020, respectively. Lay date observations were standardized as *z* scores using a year-specific SD of 3.26, 5.45, and 4.82 days for 2018, 2019, and 2020, respectively.

with extremely early and late expected lay dates based on their GEBVs, which would allow us to test for the fitness consequences of extremely early and late lay dates, including breeding attempt failure or mortality of females that attempt to lay eggs very early and under harsh conditions. We obtained birds with extreme phenotypes from a genomic selection experiment in which the breeding pairs were selected on the basis of their GEBVs for lay dates (rather than lay dates per se) (*24*, *29*). We moved F4 selection line eggs that were laid in aviaries to the local study population to hatch, fledge, and recruit there as a breeding female the following year(s). We found differentiation in lay dates between female recruits from the early and late selection line, indicating that genomic selection for lay dates was indeed successful. However, while genomic selection delayed lay dates relative to the lay dates of local female recruits, we failed to advance lay dates relative to lay dates of local female recruits. Although the difference in lay dates between female recruits from the early and late selection line translated into a reduced phenological mismatch for female recruits from the early selection line, there was no difference in the lifetime number of fledglings produced. This was in line with the overall weak effect of lay date on the lifetime number of fledglings produced by local female recruits during the same time period.

Genomic selection led to a difference in lay dates in the wild, showing that the difference in GEBVs for lay dates of female recruits from the early and late selection line indeed translated into a phenotypic response under wild conditions. While we refer to this response as asymmetric, because genomic selection delayed lay dates relative to the lay dates of local female recruits while it failed to advance lay dates relative to lay dates of local female recruits, it is important to emphasize that the two selection lines did not statistically differ in their response to selection. Nevertheless, the phenotypic response observed in the wild is in line with the phenotypic response observed in half-open aviaries, where F3 generation females from the early and late selection line of the genomic selection experiment also showed a difference in lay dates (*29*). Moreover, early selection line females showed a smaller shift in lay dates over generations (mean lay date in days from 1 April; F1: 13.9 days ±2.5 and F3: 12.6 days ±2.4) than late selection line females [mean lay date in days from 1 April; F1: 15.9 days ±3.6 and F3: 22.2 days ±3.4; (*29*)]. However, it is difficult to directly compare lay dates in the wild with lay dates in aviaries because of the complex and environment-dependent nature of the trait (*31*, *32*). Nevertheless, the asymmetric shift in lay dates in aviaries, where ad libitum food is supplied, indicates that food availability early in spring per se is unlikely to explain the asymmetric response in lay dates.

The asymmetric response to genomic selection can potentially be explained by a methodological limitation with regard to the efficiency of genomic selection. Especially in wild study systems, we are limited by small sample sizes and statistical power as a large number of individuals genotyped at a sufficient marker density is required. These limitations are especially relevant for phenological traits that generally have low heritability [~0.2 for lay dates in the local study population; (*24*)] and might require a sample size of thousands. Here, a rather large training population of >2000 wild great tit females with known lay dates and genotyped at >500,000 SNPs was used for estimating GEBVs. However, estimated accuracy of GEBVs for lay date was moderate [~0.2; (*24*)] and rather low for what is normally reported in domesticated species [e.g., dairy cattle (*33*) and crop species (*34*)]. Comparably, low accuracy of GEBVs for lay dates might be explained by lower sample size than typically available for domesticated species [>20,000 genotyped individuals; (*34*, *35*)] and higher number of independently segregating genome segments (*36*). Moreover, the experimental design did not include any replicated lines, which makes it difficult to differentiate any direct response to genomic selection from genetic drift. On the basis of a fixation index (F_{st}) outlier analysis using a method that supposedly can distinguish drift from selection, we previously established a strong response to genomic selection at the genetic level (*29*). This indicates that the phenotypic differentiation observed in aviaries and the wild is at least partly a response to the genomic selection experiment rather than genetic drift alone.

An alternative explanation for the asymmetric phenotypic response to genomic selection is the presence of environmental constraints early in the breeding season that limit a translation of GEBVs for early lay dates into early phenotypes. (*37*). Harsh environmental conditions during the energy-intense period of egg production can directly affect female condition by reducing female survival probability (*38*), decreasing foraging efficiency (*39*) and increasing energetic costs for the production of eggs (*40*, *41*) or have carry-over effects on brood success, for example, in the form of reduced caring capacity during chick feeding (*42*). Especially, the direct effects on female condition before egg laying might cause females, which are genetically primed to have early lay dates, to fail their breeding attempt and are consequently not recorded as a local recruit. However, we did not find any indication that early and

late selection line females differed in their survival in late winter or early spring. This indicates that the lack of advancement is not simply explained by females that attempted to lay their eggs early but died in the attempt to do so, as a consequence of environmental constraints in early spring. Moreover, although early selection line females were selected for GEBVs for extremely early lay dates, it is possible that environmental variables (e.g., ambient temperature) set some kind of a hard threshold for the earliest lay dates (*43*). [However, see (*44*) for details on the concept of lay date as threshold trait.] Albeit we do not find any clear indication for environmental constraints on early lay dates, we cannot exclude their presence.

In addition to the phenotypic response to genomic selection, we assessed the fitness consequences of genomic selection for lay dates in the form of two fitness components: the fitness costs of advanced lay dates before egg laying in terms of apparent survival until local recruitment and the fitness benefits of a reduced phenological mismatch in terms of lifetime reproductive success. While we discussed apparent survival probability in the context of environmental constraints in early spring (see above), it is important to clarify that our experimental design allowed us to test for a difference in local recruitment probability as a direct consequence of expected early and late lay dates based on GEBVs for lay date. Lay date and subsequent fledging date are known to affect the local recruitment probability of fledglings (*30*, *45*). When moving the F4 selection line eggs from the aviaries into the Hoge Veluwe study population, we prepared the clutches such, that both early and late selection line eggs were included in each clutch and, this way, ensured that early and late selection line individuals were reared in a common environment that did not propagate the differences in lay dates between early and late F3 generation selection line females in the aviaries (i.e., the lay date of genetic mothers of early and late selection line individuals). Hence, our experimental design allowed us to test for a difference in local recruitment probability as a direct consequence of expected early and late lay dates based on GEBVs for lay date.

In line with our expectations, the difference in lay date between female recruits from the early and late selection line indeed translated into a reduced phenological mismatch for female recruits from the early selection line (relative to female recruits from the late selection line). In contrast to our expectation based on previous findings (*6*), the reduced phenological mismatch, however, did not result in a difference in the lifetime number or quality of fledglings produced between female recruits from the early and late selection line. Although there was strong directional selection for advanced lay dates in past decades as a consequence of the phenological mismatch at the local study population (*6*, *46*, *47*), we recently showed that natural variability in temperature has reduced the phenological mismatch in recent years and decreased selection pressures on lay dates (*4*). The small number of selection line recruits led to low statistical power for detecting a difference in fitness between female recruits from the early and late selection line. However, even when using all local female recruits of the study population, we did not detect any effect of lay date on the lifetime number of fledglings produced, such that a larger sample size would likely not have change our findings. Using projected temperatures from a large ensemble of climate simulations, we showed that global warming will again lead to an intensified phenological mismatch between great tits and caterpillar biomass peak date in the long run (*4*).

Global warming has shifted phenological traits in many species, but whether species are able to further track increasing temperatures depends on the fitness consequences of a shifted phenology. To test this, *we* here applied genomic selection for lay dates in a long-term study population of great tits and assessed the consequences of expected early and late lay dates based on GEBVs for lay dates in the wild. While genomic selection led to a differentiation in lay dates under wild conditions, we did not advance lay dates relative to lay dates of local females recruits from the wild study population. Moreover, the differentiation in lay dates between female recruits from the early and late selection line did not translate into a difference in reproductive success, which is in line with reduced selection on lay dates in the years of the experiment in the study population. Such a reduction of selection despite the presence of a phenological mismatch in most years indicates that the consequences of lay dates on reproductive success are multifaceted and may not be explained by the phenological (mis)match during chick provisioning alone. In the light of future global warming, it is important to identify the constraints that led to an asymmetric phenotypic response to genomic selection, as climate projections hint toward anew increased selection pressures toward early lay dates (*4*).

MATERIALS AND METHODS

Genomic selection lines for early and late lay dates

Genomic selection is commonly applied in animal and plant breeding and has proven a powerful tool for artificial selection (*26*), but we are not aware of a study where genomic selection has been applied in a wild population. Here, we applied genomic selection for early and late lay date (i.e., the date a female initiates egg laying in a respective year) in a wild long-term study population of great tits at the Hoge Veluwe National Park (The Netherlands). A wild training population of >2000 great tit females from the study population with known lay dates and genotyped at >500,000 SNPs was used to estimate GEBVs using the GBLUP approach (*24*, *28*). In this approach, the pedigree-based relatedness matrix within an animal model is replaced by a SNP-based relatedness matrix. The animal model constitutes a specific form of a mixed-effect model frequently used in quantitative genetic studies (*48*) and the BLUPs for the additive genetic effect constitute the (genomic) BVs. Using GEBVs rather than lay dates as entity of selection had two advantages: (i) GEBVs of males can be estimated and hence males can be used for the selection procedure, and (ii) GEBVs can be estimated in the nestlings and supersede the need to wait for females to express the phenotype during their first year of breeding before being selected into breeding pairs. A detailed description on how the GEBVs for lay dates were estimated is provided in (*24*).

To initiate the selection lines for early and late lay dates, 28 breeding pairs from the Hoge Veluwe study population were selected in 2014 as "parental" generation based on their BVs for lay date (*29*). Rather than the parental generation itself, all nestlings of the parental generation were taken to the aviary facilities at the Netherlands Institute of Ecology (NIOO-KNAW) on the 10th day after hatching (d10) where they were hand raised until independence [see (*49*) for details] and constituted the F1 generation. The nestlings were genotyped to estimate their GEBVs for lay date, and individuals with the most extreme GEBVs were selected into breeding pairs (n = 20 breeding pairs per selection line) to breed in aviaries while maintaining as much of the genetic variation within line as possible [see (*29*) for details]. Eggs laid during the breeding season of 2015 (that constituted the F2 generation) were moved

into the nests of wild foster parents that undertook the brood care. At d10, the nestlings were again brought to the aviary facilities at the NIOO-KNAW for further hand raising and continuation of the selection lines (via GEBVs). The procedure was repeated until the F3 generation was produced. A detailed description of the selection procedure is provided in (*29*).

Selection line eggs moved into the wild

To introduce selection line females with expected early and late lay date based on their GEBVs into the wild, we moved F4 generation selection line eggs (i.e., eggs laid in the aviaries by F3 selection line females) into the local study population. During the breeding seasons of 2017–2019, we housed same-selection line breeding pairs of the F3 generation in half-open aviaries with nest boxes and nest building material [under housing conditions as described in (*29*)]. Every morning shortly after sunrise (earliest at 6 a.m.), we checked all nest boxes for newly laid eggs, which we replaced by artificial eggs. We marked all collected eggs with a unique identification code and stored them for up to 14 days at ambient temperature (or 10°C when ambient temperature exceeded 10°C) on an egg turner (Automatic Egg Turner, GQF, Georgia, US). To rear F4 selection line individuals in a common environment that does not propagate any difference in maternal lay date between the selection lines, we prepared mixed-selection line clutches with (up to 12) eggs from both selection lines. With the mixed-selection line clutches, we aimed to rear selection line individuals in a common environment in which early and late selection line individuals did not differ in their realized hatch date and subsequent fledging date. In a few cases where there were no eggs from one of the selection lines available, we prepared same-selection line clutches (11 of 72 clutches in 2017 and 3 of 94 clutches in 2020; table S33). To optimized the use of limited nests available in the local study population at the Hoge Veluwe, we moved the selection line clutches in two steps. First, we moved clutches to nests of incubating females at one of two intermediate locations [the great tit populations in Bennekomse Bos (n = 2549) and Heikamp (n = 400), The Netherlands], such that the foster females started to incubate the selection line clutches in the wild. After 5 days of incubation, we selected the eggs that showed embryonic development that were, in the second step, moved to nest boxes at the local study population at the Hoge Veluwe, the final location (n = 936). This way, we discarded any eggs that were unfertilized or got damaged during handling of the eggs before the move to the final location. Depending on the number of eggs within a clutch that showed embryonic development, we merged eggs from different clutches to increase clutch size. At the local study population, we selected nests where females had initiated incubation approximately 5 days before the final egg movement to match the developmental time of the pre-incubated selection line eggs with the development time of the discarded eggs from the wild foster parents.

We monitored the foster nests with selection line eggs at the local study population in line with the standard protocol at the local study population (see text S1) with minor modifications and additions. The standard protocol includes a "capture" of nestlings on d15 during which we equipped selection line nestlings with passive integrated transponder (PIT) tags (2.6-mm EM4102 PIT bird tag, Eccel Technology Ltd., Leicester, UK) in addition to the aluminum rings that have unique identifier codes. The PIT tags have unique PIT-tag IDs and were used to identify nestlings that fledged and recruited into the local study population the following year(s) (see below). During the d15 capture, we also measured the weight, tarsus length, and length of the P3 feather and took a 10 μl of blood sample stored in 1 ml of Queen′s buffer. We used the blood samples to assign the selection line nestlings to their genetic parents (i.e., F3 generation selection line breeding pairs) via molecular markers following a previously established protocol [see e.g. (*50*)].

We moved a total of 936 F4 generation selection line eggs from the NIOO-KNAW to the local study population at the Hoge Veluwe of which 475 and 461 eggs were derived from the selection lines for early and late lay dates, respectively. The number of eggs moved to the study population differed between years, with 358, 456, and 122 eggs in 2017, 2018, and 2019, respectively (table S34).

Selection line birds in the wild

In the years following the introduction of selection line eggs to the local study population (i.e., in 2018–2020), we monitored female fledglings from the selection lines for early and late lay dates that recruited into the local study population. We monitored nest boxes of female selection line recruits in accordance with the standard protocol at the study site (see text S1) with minor modifications and additions. Instead of identifying selection line females during the capture of adults at d7, we identified and localized selection line females during the start of their nest building activities in late March (see text S2), which, in combination with sightings from roosting inspections in January (see text S2), also provided an estimate of apparent winter survival of selection line fledglings before their first breeding attempt. We measured the daily energy expenditure of female selection line recruits in the 24-hour period between the d10 capture and a subsequent capture at d11 (see text S3). Last, we measured the daily feeding frequency of female selection line recruits on d12 and d13 using PIT-tags and transponder readers (see text S4).

Statistical analysis

For statistical interference, we applied generalized linear multilevel models using Stan′s Hamiltonian Monte Carlo algorithm to estimate the respective posterior probability distributions. We implemented the models in R v4.0.3 (*51*) using the R package rethinking v2.13 (*52*) with R package cmdstanr v0.3.0.9000 (*53*) as an interface to Stan [CmdStan v2.28.2; (*54*)]. Following McElreath (*55*), we report the 89% credible interval (instead of the commonly used 95% interval) with the posterior means to discourage readers from conducting unconscious hypothesis testing. For all models, we set the number of iterations for sampling to 10,000 for each of four independently sampled chains that were distributed over four processor cores. Half of the iterations for sampling were used as warmup (and do not contribute to the predicted posterior distributions). Trace and trank plots of the Markov chain Monte Carlo (MCMC) output for the models described below and in the appendices are presented in figs. S13 to S44. The R code for the analyses is publicly available at Dryad (doi:10.5061/dryad.2280gb5ws).

Phenotypic response to genomic selection in the wild

Lay date. We assessed the phenotypic response to genomic selection in the wild by testing for a difference in lay dates between female recruits from the early and late selection line as well as between female selection line recruits and local female recruits. We included the lay dates of all females that recruited to the local study sites between 2018 and 2020, i.e., all females that had a lay date

in those years. For female selection line recruits (n = 9 for the early and n = 9 for the late selection line), we used the lay date in the first year of breeding as the number of females that bred in more than 1 year was too small to account for repeated measurements. For local female recruits, we focused on all first egg lay dates recorded within a year (irrespective of the female) to get the least biased representation of the year-specific distribution of lay dates (n = 433 lay dates over the three-year period). Because of the small number of female selection lines recruits, we did not account for year effects but used within-year standardized lay dates for the analysis. For the standardization, we used all observed lay dates of local female recruits within a year (i.e., excluding the lay dates of female selection line recruits) to derive estimates of the year-specific mean and SD that are representative for the local study population. We used these year-specific estimates to calculate year-specific z scores of lay dates for female selection line recruit and local female recruits, i.e., we subtracted the year-specific mean from each observed lay date within that year and divided the resulting difference by the year-specific SD. We detected a potential outlier observation for an early female selection line recruit (fig. S11 and see text S5 for details) and removed it from the statistical analysis (reducing the dataset to n = 8 for female recruits from the early and n = 9 for female recruits from the late selection line). However, repeating the statistical analysis while keeping the outlier observation included did not qualitatively change the results (fig. S12).

We specified a linear regression model to estimate the posterior distribution of standardized lay dates (Eq. 1). Within the regression model, we specified an intercept α and an effect of the selection line $\beta l_{\text{Line[i]}}$ with weakly regularizing priors

$$\begin{gathered} L_i \sim \text{Normal}(\mu_i, \sigma) \\ \mu_i = \alpha + \beta l_{\text{Line[i]}} \\ \alpha \sim \text{Normal}(0, 1.5) \\ \beta l_j \sim \text{Normal}(0, 1.5), \textit{for } j = 1..3 \\ \sigma \sim \text{Half} - \text{Normal}(0, 1) \end{gathered} \tag{1}$$

Phenological mismatch. We tested whether differential lay dates between female recruits from the early and late selection line translated into a difference in phenological mismatch. Using the same dataset as above (see the "Lay dates" section), we calculated the expected year-specific dates of highest resource demands for chick feeding by adding 33 days to the year-specific lay dates (*56*). We used the expected year-specific dates of highest resource demands and the year-specific caterpillar biomass peak dates (which were April date 37, 48, and 40 for 2018, 2019, and 2020, respectively) to calculate the year-specific phenological mismatch as the difference between both (i.e., we subtracted the year-specific caterpillar biomass peak dates from the expected year-specific dates of highest resource demands). We estimated the predicted posterior distributions for the phenological mismatch across years for female selection line recruits and local female recruits and estimated the difference in phenological mismatch between those groups. We standardized the calculated phenological mismatches within a year by estimating the year-specific SD of phenological mismatch excluding female selection line recruits and divided each calculated phenological mismatch within a year by the year-specific SD. (We did not mean center the data.) To estimate the posterior distribution of the standardized phenological mismatch, we specified a linear regression model (Eq. 2). Within the regression model, we specified an intercept α and an effect of the selection line $\beta l_{\text{Line[i]}}$ with weakly regularizing priors

$$\begin{gathered} \text{MM}_i \sim \text{Normal}\ (\mu_i, \sigma) \\ \mu_i = \alpha + \beta l_{\text{Line[i]}} \\ \alpha \sim \text{Normal}(0, 1.5) \\ \beta l_j \sim \text{Normal}(0, 1.5), \textit{for } j = 1..3 \\ \sigma \sim \text{Half} - \text{Normal}(0, 1) \end{gathered} \tag{2}$$

To gain insights on the magnitude of the phenological mismatch in the local study population within the years of the experiment, we estimate the year-specific phenological mismatch and the pairwise differences in year-specific phenological mismatch. The analysis is presented in text S6.

Consequences of genomic selection for fitness

We assessed the fitness consequences as the lifetime number of fledglings a female selection line fledgling produced. The more common alternative to the approach taken here would be to assess fitness as the lifetime number of local recruits produces per female selection line recruit. However, such a "mixed fitness" measure is a function of the fitness of both the female's reproductive success and the offsprings' survival (from zygote to recruitment) and, hence, is prone to bias (*57*). Our genomic selection experiment allows us to unequally look at fitness from fledgling to fledgling as we can assign an expected lay date phenotype already at the fledgling stage, which is not possible for local fledglings. Our fitness measure is a "mixed-fitness" measure in its own right, but the potential bias on our fitness measure resulting from offspring survival is notably reduced when the period from zygote to fledgling is considered rather than the period from zygote to recruitment.

We derived an estimate of the fitness consequences of the genomic selection experiment in two steps; we considered proxies for the survival of female selection line fledglings (e.g., local recruitment probability) and proxies for reproductive success (e.g., the lifetime number of fledglings produced by female selection line fledglings that recruited into the local study population). We, lastly, combined estimates of local recruitment probability and the lifetime number of fledglings produced by female selection line fledglings to estimate a proxy of the total fitness of early and late selection line females.

Potential selective disappearance of early selection line females. One proxy for the survival of female selection line fledglings that we assessed is the potential selective disappearance of early selection line females before their first breeding event. This selective disappearance might arise as a consequence of environmental fitness costs for females that attempt to breed early [i.e., second scenario (*5*)]. For this, we tested whether early selection line females were less likely than late selection line females to recruit into the local study population when females were identified in late winter or during nest building in early spring. The analyses are described in text S2.

Local recruitment probability. Another proxy for the survival of female selection line fledglings we assessed is the local recruitment probability (which is later used for calculating the total fitness; see the "Consequences of genomic selection on total fitness" section). We consider fledglings that returned to the local study population in the year(s) following the year of fledging as a local recruit. For the analysis, we included records from all fledglings that fledged from 2017 to 2019. In those years, there were a total of 2347 fledglings at

the local study population of which 649, 752, and 946 fledged in 2017, 2018, and 2019, respectively. The 2347 fledglings included 318 early and 331 late selection line fledglings and 1698 local fledglings (table S35). We excluded 23 local fledglings for which no data on fledgling weight (measured on d15) were available. Local recruitment was encoded as a binary variable with one for fledglings that locally recruited and zero for all other fledglings. To estimate the posterior distribution of local recruitment probability at the fledgling level, we specified a generalized linear multivariate model assuming a binomial distribution over local recruitment probability (Eq. 3) following (*55*). The Binomial distribution is defined by two parameters: the constant probability of success p (here local recruitment) over each of n trials. Here, we consider local recruitment probability p_i at the level of individual fledglings (for i = 1..2324) and hence set the number of trials for each fledgling n_i to 1 (a special case of the Binomial distribution that is also referred to as Bernoulli distribution). We used a logit link function to bind the linear model for p_i to values between 0 and 1. Within the generalized linear multivariate model, we specified year- and brood-specific intercepts $\alpha_{Year[i]}$ and $\gamma_{Brood[i]}$ to account for the hierarchical structure of our data (i.e., brood nested within year), an effect of the selection line $\beta l_{Line[i]}$, an effect of a proxy for fledging date βd (April dates on d15), and an effect of fledgling weight βw. We standardized the fledgling weight and the proxy for fledging date (April date on d15) using z scores (i.e., we subtracted the mean fledgling weight or fledging date from each observation and divided the resulting difference by the SD of fledgling weight or fledging date). We overall used weakly regularizing priors, and for the year- and brood-specific intercepts, we specified the priors as a function of other parameters (termed hyperparameters), $\overline{\alpha}$, σ_α, and σ_γ, for which we also used weakly regularizing priors (termed hyperpriors). This specification of adaptive priors allowed us to pool information across years and broods meaning that the model adaptively learns about the prior that is common to the above specified intercepts.

$$
\begin{gathered}
R_i \sim \text{Binomial}(1, p_i) \\
\text{logit}(p_i) = \alpha_{Year[i]} + \gamma_{Brood[i]} + \beta l_{Line[i]} + \beta d * \text{Date}_{[i]} + \beta w * \text{Weight}_{[i]} \\
\beta l_j \sim \text{Normal}(0, 1.5), for\ j = 1..3 \\
\beta d \sim \text{Normal}(0, 1.5) \\
\beta w \sim \text{Normal}(0, 1.5) \\
\alpha_j \sim \text{Normal}(\overline{\alpha}, \sigma_\alpha), for\ j = 1 \ldots 3 \\
\gamma_j \sim \text{Normal}(0, \sigma_\gamma), for\ j = 1..95 \\
\overline{\alpha} \sim \text{Normal}(0, 1.5) \\
\sigma_\alpha \sim \text{Half} - \text{Normal}(0, 1) \\
\sigma_\gamma \sim \text{Half} - \text{Normal}(0, 1)
\end{gathered}
\tag{3}
$$

To aid approximation of the posterior distribution for local recruitment probability, we increased the target acceptance rate during sampling of the posterior to 99% (default: 95%) and reparametrized the model. Steep regions of the parameter space can be difficult to explore and, this way, harm the efficiency of the chains [which is a common problem in multilevel models (*55*)]. A reparameterization into a mathematically equivalent but numerically different version can increase the efficiency of chains. The alternative model (Eq. 4) constitutes a noncentered reparameterization of the initial model (Eq. 3) in which the parameters embedded within the adaptive priors of α_j and γ_j (i.e., the hyperparameters $\overline{\alpha}$, σ_α, and σ_γ) were moved out of the definition. For this, we defined some new variables $z_{Year[i]}$ and $x_{Brood[i]}$ that followed a standard Normal distribution and reconstructed the original variables by reversing the transformation within the definition of the linear model ($\overline{\alpha} + z_{Year[i]}\sigma_\alpha$ and $x_{Brood[i]}\sigma_\gamma$, respectively)

$$
\begin{gathered}
R_i \sim \text{Binomial}(1, p_i) \\
\text{logit}(p_i) = \overline{\alpha} + z_{Year[i]}\sigma_\alpha + x_{Brood[i]}\sigma_\gamma + \beta l_{Line[i]} + \beta d * \text{Date}_{[i]} + \beta w * \text{Weight}_{[i]} \\
\beta l_j \sim \text{Normal}(0, 1.5), for\ j = 1..3 \\
\beta d \sim \text{Normal}(0, 1.5) \\
\beta w \sim \text{Normal}(0, 1.5) \\
z_j \sim \text{Normal}(0, 1), for\ j = 1..3 \\
x_j \sim \text{Normal}(0, 1), for\ j = 1..95 \\
\overline{\alpha} \sim \text{Normal}(0, 1.5) \\
\sigma_\alpha \sim \text{Half} - \text{Normal}(0, 1) \\
\sigma_\gamma \sim \text{Half} - \text{Normal}(0, 1)
\end{gathered}
\tag{4}
$$

In the above-described model for local recruitment probability (Eqs. 3 and 4), we included effects of fledgling weight and a proxy for fledging date as both are suggested to affect recruitment probability (*30*). However, fledgling weight might be affected by fledging date as we expect higher availability of food resources in early spring. To better understand whether both effects should be included, we compared different models that included effects of both fledging date and fledgling weight, an effect of fledgling weight only, and an effect of fledging date only. For model comparison, we used the Pareto-smoothed importance sampling (PSIS) cross-validation approximation implemented within the rethinking R package [for more details, see (*55*)]. PSIS provides feedback about its own reliability by emphasizing observations with very high weight (i.e., Pareto k values > 0.5) that might make the PSIS scores unreliable. Here, no Pareto k values > 0.5 were noted, and comparison showed that the model including effects for both fledging date and fledgling weight had the lowest PSIS score (PSIS with SEs = 1084.79 ± 61.72; table S36). However, the difference between the best and second-best model, the model including an effect for fledgling weight only, was 1.3 with an SE of the difference of 4.68, indicating that both models performed similarly well.

As fledging date is suggested to affect recruitment probability (*30*), we designed the experiment with the aim to rear selection line individuals in a common environment in which early and late selection line individuals did not differ in their realized hatch date and subsequent fledging date. We formally tested this assumption, and the analysis is described in text S7. Moreover, we tested for a difference in fledgling weight of early and late selection line fledglings; hence, a difference might be a correlated response to genomic selection for lay date. The analysis is described in text S8.

The above-described model for local recruitment probability (Eq. 4) allowed us to assess the local recruitment probability of selection line fledglings in comparison to local fledglings but did not allow us to estimate the local recruitment probability for female selection line fledglings, as the sex of fledglings was only determined (via molecular markers; see above) for selection line fledglings, but nor for all other fledglings at the local study site. The 318 early selection line fledglings included 159 females and 158 males, and the 331 late selection line fledglings included 167 females and 164 males (note that for one early selection line fledgling, the molecular sex determination failed, such that one early selection line fledgling was excluded from the analysis). As the sex of local fledglings that

did not recruit remained unknown, we fitted another model that retained only data from selection line fledglings. This way, we could estimate the sex-specific local recruitment probability for selection line fledglings. We used the same model structure as for the above-described model (Eq. 4) but additionally specified an effect of sex using a weakly regularizing prior (i.e., normal distribution with mean = 0 and SD = 1.5). The posterior distributions of the recruitment probability for early and late female selection line fledglings were used to estimate the total fitness (see the "Consequences of genomic selection on total fitness" section).

Lifetime number of fledglings produced. We used the lifetime number of fledglings produced by female fledglings that recruited into the local study population as a proxy for reproductive success. We calculated the lifetime number of fledglings produced by female recruits for all females with known lay dates (n = 9 for female recruits from the early and n = 9 for female recruits from the late selection line and n = 433 for local female recruits; see the "Lay dates" section). We first calculated the lifetime number of fledglings produced within each year and performed a within-year standardization, then imputed the total number of fledglings for local female recruits where one or more broods were potentially affected by research-related manipulations (which is only the case for local females recruits, not for female selection line recruits) and, last, used the within-year standardized total number of fledglings for each year to calculate the sum across years resulting in the standardized lifetime number of fledglings (for details see text S9). This way, our final dataset included eight and nine female recruits from the early and late selection line, respectively, and 254 local female recruits.

We first focused on female selection line recruits to test for a difference in reproductive success between the selection lines (which is later used for calculating the total fitness; see the "Consequences of genomic selection on total fitness" section). We estimated the posterior distribution of the standardized lifetime number of fledglings produced by female selection line recruits by specifying a linear regression model (Eq. 5). Within the regression model, we specified an intercept α and an effect of the selection line $\beta l_{\mathrm{Line[i]}}$ with weakly regularizing priors

$$\begin{aligned} \mathrm{LNF_i} &\sim \mathrm{Normal}(\mu_i, \sigma) \\ \mu_i &= \alpha + \beta l_{\mathrm{Line[i]}} \\ \alpha &\sim \mathrm{Normal}(0, 1.5) \\ \beta l_j &\sim \mathrm{Normal}(0, 1.5), for\ j = 1..3 \\ \sigma &\sim \mathrm{Half-Normal}(0, 1) \end{aligned} \tag{5}$$

To test for an effect of lay date on the lifetime number of fledglings produced by fledglings that recruited into the local study population, we fitted another model using the data from local (i.e., nonselection line) female fledglings that recruited into the local study population. To estimate the posterior distribution of the standardized lifetime number of fledglings produced by local female recruits, we specified a linear regression model (Eq. 6). Within the regression model, we specified an intercept α and an effect of lay date βd with weakly regularizing priors

$$\begin{aligned} \mathrm{LNF_i} &\sim \mathrm{Normal}(\mu_i, \sigma) \\ \mu_i &= \alpha + \beta d * \mathrm{Lay\ date_{[i]}} \\ \alpha &\sim \mathrm{Normal}(0, 1.5) \\ \beta d &\sim \mathrm{Normal}(0, 1.5) \\ \sigma &\sim \mathrm{Half-Normal}(0, 1) \end{aligned} \tag{6}$$

In addition to the lifetime number of fledglings produced by female selection line fledglings that recruited into the local study population as a proxy for reproductive success, we also assessed the quality of fledglings produced in terms of fledgling weight, tarsus length, and P3 length (all measured at d15). The analyses are described in text S10.

Moreover, we tested whether the genomic selection experiment for early and late lay dates resulted in other correlated responses (in addition to lay dates) that might affect fitness in their own right such as the daily energy expenditure during chick feeding or daily chick feeding frequency. The analyses are described in texts S3 and S4, respectively.

Consequences of genomic selection on total fitness. To derive estimates of the total fitness, we multiplied the posterior distribution of the standardized lifetime number of fledglings produced by female selection line recruits with the posterior distributions of the recruitment probability of female selection line fledglings to estimate the posterior distribution of the total fitness of selection line fledglings while propagating the uncertainty of the estimates.

Supplementary Materials

This PDF file includes:
Texts S1 to S10
Figs. S1 to S44
Legends for tables S1 to S36

Other Supplementary Material for this manuscript includes the following:
Tables S1 to S36

View/request a protocol for this paper from *Bio-protocol*.

REFERENCES AND NOTES

1. H. E. Chmura, C. T. Williams, A cross-taxonomic perspective on the integration of temperature cues in vertebrate seasonal neuroendocrine pathways. *Horm. Behav.* **144**, 105215 (2022).
2. C. Parmesan, G. Yohe, A globally coherent fingerprint of climate change impacts across natural systems. *Nature* **421**, 37–42 (2003).
3. S. J. Thackeray, P. A. Henrys, D. Hemming, J. R. Bell, M. S. Botham, S. Burthe, P. Helaouet, D. G. Johns, I. D. Jones, D. I. Leech, E. B. Mackay, D. Massimino, S. Atkinson, P. J. Bacon, T. M. Brereton, L. Carvalho, T. H. Clutton-Brock, C. Duck, M. Edwards, J. M. Elliott, S. J. G. Hall, R. Harrington, J. W. Pearce-Higgins, T. T. Høye, L. E. B. Kruuk, J. M. Pemberton, T. H. Sparks, P. M. Thompson, I. White, I. J. Winfield, S. Wanless, Phenological sensitivity to climate across taxa and trophic levels. *Nature* **535**, 241–245 (2016).
4. M. E. Visser, M. Lindner, P. Gienapp, M. C. Long, S. Jenouvrier, Recent natural variability in global warming weakened phenological mismatch and selection on seasonal timing in great tits (Parus major). *Proc. Royal Soc. B Biol. Sci.* **288**, 20211337 (2021).
5. M. E. Visser, P. Gienapp, Evolutionary and demographic consequences of phenological mismatches. *Nat. Ecol. Evol.* **3**, 879–885 (2019).
6. M. E. Visser, A. J. van Noordwijk, J. M. Tinbergen, C. M. Lessells, Warmer springs lead to mistimed reproduction in great tits (Parus major). *Proc. R. Soc. Lond. B* **265**, 1867–1870 (1998).
7. V. Reed, S. Grotan, B.-E. Jenouvrier, M. E. Saether, Population growth in a wild bird is buffered against phenological mismatch. *Science* **340**, 488–491 (2013).

8. M. D. Burgess, K. W. Smith, K. L. Evans, D. Leech, J. W. Pearce-Higgins, C. J. Branston, K. Briggs, J. R. Clark, C. R. du Feu, K. Lewthwaite, R. G. Nager, B. C. Sheldon, J. A. Smith, R. C. Whytock, S. G. Willis, A. B. Phillimore, Tritrophic phenological match–mismatch in space and time. *Nat. Ecol. Evol.* **2**, 970–975 (2018).
9. E. G. Simmonds, E. F. Cole, B. C. Sheldon, T. Coulson, Phenological asynchrony: A ticking time-bomb for seemingly stable populations? *Ecol. Lett.* **23**, 1766–1775 (2020).
10. P. R. Grant, B. R. Grant, Predicting microevolutionary responses to directional selection on heritable variation. *Evolution* **49**, 241–251 (1995).
11. L. E. B. Kruuk, J. Slate, A. J. Wilson, New answers for old questions: The evolutionary quantitative genetics of wild animal populations. *Annu. Rev. Ecol. Evol. Syst.* **39**, 525–548 (2008).
12. L. E. B. Kruuk, J. Slate, J. M. Pemberton, S. Brotherstone, F. Guinness, T. Clutton-Brock, Antler size in red deer: Heritability and selection but no evolution. *Evolution* **56**, 1683–1695 (2002).
13. B. C. Sheldon, L. E. B. Kruuk, J. Merila, Natural selection and inheritance of breeding time and clutch size in the collared flycatcher. *Evolution* **57**, 406–420 (2003).
14. D. H. Nussey, E. Postma, P. Gienapp, M. E. Visser, Selection on heritable phenotypic plasticity in a wild bird population. *Science* **310**, 304–306 (2005).
15. P. Marrot, A. Charmantier, J. Blondel, D. Garant, Current spring warming as a driver of selection on reproductive timing in a wild passerine. *J. Anim. Ecol.* **87**, 754–764 (2018).
16. J. Merilä, B. C. Sheldon, L. E. B. Kruuk, Explaining stasis: Microevolutionary studies in natural populations. *Genetica* **112-113**, 199–222 (2001).
17. B. Pujol, S. Blanchet, A. Charmantier, E. Danchin, B. Facon, P. Marrot, F. Roux, I. Scotti, C. Teplitsky, C. E. Thomson, I. Winney, The missing response to selection in the wild. *Trends Ecol. Evol.* **33**, 337–346 (2018).
18. S. Verhulst, J.-Å. Nilsson, The timing of birds' breeding seasons: A review of experiments that manipulated timing of breeding. *Phil. Trans. R. Soc. B* **363**, 399–410 (2008).
19. L. te Marvelde, S. V. Schaper, M. E. Visser, A single long day triggers follicle growth in captive female great tits (Parus major) in winter but does not affect laying dates in the wild in spring. *PLOS ONE* **7**, e35617 (2012).
20. L. Salis, S. P. Caro, R. A. Hut, L. Vernooij, M. E. Visser, Manipulation of photoperiod perception advances gonadal growth but not laying date in the great tit. *J. Avian Biol.* **50**, e02197 (2019).
21. L. te Marvelde, M. E. Visser, Manipulation of life-history decisions using leptin in a wild passerine. *PLOS ONE* **7**, e34090 (2012).
22. S. Daan, C. Dijkstra, R. Drent, T. Meijer, Food supply and the annual timing of avian reproduction in *Volume I: Proceedings XIX International Ornithological Congress, 1986* (Univ. of Ottawa Press, 1989), vol. 1, pp. 392–407.
23. P. Gienapp, M. E. Visser, Possible fitness consequences of experimentally advanced laying dates in Great Tits: Differences between populations in different habitats. *Funct. Ecol.* **20**, 180–185 (2006).
24. P. Gienapp, M. P. L. Calus, V. N. Laine, M. E. Visser, Genomic selection on breeding time in a wild bird population. *Evol. Lett.* **3**, 142–151 (2019).
25. A. Charmantier, D. Garant, L. E. B. Kruuk, *Quantitative Genetics in the Wild* (Oxford University Press, New York, NY, 2014).
26. M. E. Goddard, B. J. Hayes, Mapping genes for complex traits in domestic animals and their use in breeding programmes. *Nat. Rev. Genet.* **10**, 381–391 (2009).
27. C. E. Regan, J. M. Pemberton, J. G. Pilkington, P. T. Smiseth, A. J. Wilson, Linking genetic merit to sparse behavioral data: Behavior and genetic effects on lamb growth in Soay sheep. *Behavioral Ecology* **31**, arz166 (2019).
28. S. Clark, J. van der Werf, Genomic best linear unbiased prediction (gBLUP) for the estimation of genomic breeding values. *Methods Mol. Biol.* **1019**, 321–330 (2013).
29. I. Verhagen, P. Gienapp, V. N. Laine, E. M. Grevenhof, A. C. Mateman, K. Oers, M. E. Visser, Genetic and phenotypic responses to genomic selection for timing of breeding in a wild songbird. *Funct. Ecol.* **33**, 1708–1721 (2019).
30. N. Verboven, M. E. Visser, Seasonal variation in local recruitment of great tits: The importance of being early. *Oikos* **81**, 511 (1998).
31. M. E. Visser, S. P. Caro, K. van Oers, S. V. Schaper, B. Helm, Phenology, seasonal timing and circannual rhythms: Towards a unified framework. *Phil. Trans. R. Soc. B* **365**, 3113–3127 (2010).
32. P. Gienapp, V. N. Laine, A. C. Mateman, K. van Oers, M. E. Visser, Environment-dependent genotype-phenotype associations in avian breeding time. *Front. Genet.* **8**, 102 (2017).
33. P. M. VanRaden, C. P. Van Tassell, G. R. Wiggans, T. S. Sonstegard, R. D. Schnabel, J. F. Taylor, F. S. Schenkel, Invited review: Reliability of genomic predictions for North American Holstein bulls. *J. Dairy Sci.* **92**, 16–24 (2009).
34. Z. Lin, B. J. Hayes, H. D. Daetwyler, Genomic selection in crops, trees and forages: A review. *Crop Pasture Sci.* **65**, 1177 (2014).
35. K. Schöpke, H. H. Swalve, Review: Opportunities and challenges for small populations of dairy cattle in the era of genomics. *Animal* **10**, 1050–1060 (2016).
36. K. van Oers, A. W. Santure, I. De Cauwer, N. E. van Bers, R. P. Crooijmans, B. C. Sheldon, M. E. Visser, J. Slate, M. A. Groenen, Replicated high-density genetic maps of two great tit populations reveal fine-scale genomic departures from sex-equal recombination rates. *Heredity* **112**, 307–316 (2014).
37. M. E. Visser, L. te Marvelde, M. E. Lof, Adaptive phenological mismatches of birds and their food in a warming world. *J. Ornithol.* **153**, 75–84 (2012).
38. M. E. Visser, C. M. Lessells, The costs of egg production and incubation in great tits (Parus major). *Proc. R. Soc. Lond. B* **268**, 1271–1277 (2001).
39. M. I. Avery, J. R. Krebs, Temperature and foraging success of Great Tits *Parus major* hunting for spiders. *Ibis* **126**, 33–38 (1984).
40. S. C. Kendeigh, V. R. Dol'nik, V. M. Gavrilov, Avian energetics in *Granivorous Birds in Ecosystemss: Their Evolution, Populations, Energetics, Adaptations, Impact and Control*, J. Pinowski, S. C. Kendeigh, Eds. (Cambridge Univ. Press, 1977), pp. 127–204.
41. L. te Marvelde, S. L. Webber, H. A. J. Meijer, M. E. Visser, Energy expenditure during egg laying is equal for early and late breeding free-living female great tits. *Oecologia* **168**, 631–638 (2012).
42. P. Monaghan, R. G. Nager, D. C. Houston, The price of eggs: Increased investment in egg production reduces the offspring rearing capacity of parents. *Proc. R. Soc. Lond. B* **265**, 1731–1735 (1998).
43. A. J. V. Noordwijk, R. H. McCleery, C. M. Perrins, Selection for the timing of great tit breeding in relation to caterpillar growth and temperature. *J. Anim. Ecol.* **64**, 451–458 (1995).
44. J. M. Reid, P. Acker, Conceptualizing the evolutionary quantitative genetics of phenological life-history events: Breeding time as a plastic threshold trait. *Evol. Lett.* **6**, 220–233 (2022).
45. M. E. Visser, N. Verboven, Long-term fitness effects of fledging date in great tits. *Oikos* **85**, 445–450 (1999).
46. J. J. C. Ramakers, P. Gienapp, M. E. Visser, Phenological mismatch drives selection on elevation, but not on slope, of breeding time plasticity in a wild songbird. *Evolution* **73**, 175–187 (2019).
47. A. Husby, M. E. Visser, L. E. B. Kruuk, Speeding up microevolution: The effects of increasing temperature on selection and genetic variance in a wild bird population. *PLOS Biol.* **9**, e1000585 (2011).
48. A. J. Wilson, D. Réale, M. N. Clements, M. M. Morrissey, E. Postma, C. A. Walling, L. E. B. Kruuk, D. H. Nussey, An ecologist's guide to the animal model. *J. Anim. Ecol.* **79**, 13–26 (2010).
49. P. J. Drent, K. van Oers, A. J. van Noordwijk, Realized heritability of personalities in the great tit (*Parus major*). *Proc. R. Soc. Lond. B* **270**, 45–51 (2003).
50. T. J. Greives, S. A. Kingma, B. Kranstauber, K. Mortega, M. Wikelski, K. Oers, A. C. Mateman, G. A. Ferguson, G. Beltrami, M. Hau, Costs of sleeping in: Circadian rhythms influence cuckoldry risk in a songbird. *Funct. Ecol.* **29**, 1300–1307 (2015).
51. R Core Team, R: A language and environment for statistical computing (R Foundation for Statistical Computing, 2021); (https://www.R-project.org/.
52. R. McElreath, *rethinking: Statistical Rethinking book package* (2020).
53. J. Gabry, R. Češnovar, cmdstanr: R Interface to "CmdStan" (2020);https://mc-stan.org/cmdstanr,https://discourse.mc-stan.org).
54. Stan Development Team, Stan Modeling Language Users Guide and Reference Manual (2019);https://mc-stan.org).
55. R. McElreath, *Statistical rethinking: A Bayesian course with examples in R and Stan* (CRC Press/Taylor & Francis Group, ed. 2, 2020).
56. L.-M. Chevin, M. E. Visser, J. Tufto, Estimating the variation, autocorrelation, and environmental sensitivity of phenotypic SELECTION. *Evolution* **69**, 2319–2332 (2015).
57. C. E. Thomson, J. D. Hadfield, Measuring selection when parents and offspring interact. *Methods Ecol. Evol.* **8**, 678–687 (2017).

Acknowledgments: We thank M. Kaandorp, B. van Lith, and P. de Vries for supporting the fieldwork; the animal caretakers at the NIOO-KNAW for taking care of the birds; M. van der Sluijs and colleagues in the molecular laboratory at NIOOK-NAW for the support with the molecular sex determination; M. Kaandorp and L. Vernooij for database support; and K. van Oers for useful discussions. We would like to thank the board of the National Park "de Hoge Veluwe" for their permission to work within their reserve. We thank A. Wilson, A. Phillimore, and one anonymous reviewer for constructive comments that greatly improved the manuscript. **Funding:** This work was supported by a European Research Council Advanced grant (339092–E-Response) to M.E.V.
Ethics statement: This study was performed under the approval by the Animal Experimentation Committee (DEC), Amsterdam, The Netherlands, protocol NIOO14.10 and addendum 2 to this protocol. **Author contributions:** Conceptualization: M.E.V. and P.G. Methodology: M.E.V., J.J.C.R., and M.L. Investigation: M.L., J.J.C.R., B.T., I.V., and A.C.M. Visualization: M.L. Supervision: M.E.V. Writing—original draft: M.L. Writing—review and editing: M.L., M.E.V., P.G., J.J.C.R., M.L., I.V., and A.C.M. **Competing interests:** The authors declare that they have no competing interests. **Data and materials availability:** All data needed to evaluate the conclusions in the paper are present in the paper and/or the Supplementary

Materials. Data and the R code used for analysis are publicly available at Dryad (doi:10.5061/dryad.2280gb5ws).

Submitted 29 August 2022
Accepted 1 May 2023
Published 7 June 2023
10.1126/sciadv.ade6350

PLANETARY SCIENCE

Giant tidal tails of helium escaping the hot Jupiter HAT-P-32 b

Zhoujian Zhang[1,2]*, Caroline V. Morley[2], Michael Gully-Santiago[2], Morgan MacLeod[3], Antonija Oklopčić[4], Jessica Luna[2], Quang H. Tran[2], Joe P. Ninan[5], Suvrath Mahadevan[6,7,8], Daniel M. Krolikowski[2,9], William D. Cochran[10], Brendan P. Bowler[2], Michael Endl[11], Gudmundur Stefánsson[12], Benjamin M. Tofflemire[2], Andrew Vanderburg[13], Gregory R. Zeimann[14]

Capturing planets in the act of losing their atmospheres provides rare opportunities to probe their evolution history. This analysis has been enabled by observations of the helium triplet at 10,833 angstrom, but past studies have focused on the narrow time window right around the planet's optical transit. We monitored the hot Jupiter HAT-P-32 b using high-resolution spectroscopy from the Hobby-Eberly Telescope covering the planet's full orbit. We detected helium escaping HAT-P-32 b at a 14σ significance,with extended leading and trailing tails spanning a projected length over 53 times the planet's radius. These tails are among the largest known structures associated with an exoplanet. We interpret our observations using three-dimensional hydrodynamic simulations, which predict Roche Lobe overflow with extended tails along the planet's orbital path.

INTRODUCTION

Atmospheric escape is the primary physical process sculpting the population of short-period, irradiated exoplanets. One piece of observational evidence of this process is the observed dearth of short-period Neptune-mass planets (*1*). Several mechanisms likely contribute to the atmospheric escape, including photoevaporation and core-powered mass loss (*2*–*9*), which predict distinct correlations between mass-loss rates and properties of the radiation environment [e.g., x-ray and ultraviolet (UV) fluxes of host stars] and planets (e.g., equilibrium temperatures). Directly measuring mass loss for a large ensemble of exoplanets can differentiate between these processes, and these measurements have been enabled by the helium 10,833-Å triplet (*10*–*12*), which is a robust probe of exospheres accessible from the ground and immune to high absorption from the interstellar medium that hampers similar studies based on Lyman α.

Using the Habitable-zone Planet Finder Spectrograph (HPF) (*13*–*15*) on the Hobby-Eberly Telescope (HET) (*16*–*18*), we observed HAT-P-32 b with time-series high-resolution ($R \approx 55{,}000$) spectra to detect a helium outflow and investigate atmospheric escape. HAT-P-32 b is a hot Jupiter transiting a late-F star, HAT-P-32 A, on a 2.15-day orbit with an in-transit duration of 3.12 hours (*19*, *20*). This planet has an inflated radius (1.79 ± 0.03 Jupiter radii) that almost fills its Roche lobe. A recent study (*21*) found hydrogen and helium outflows escaping HAT-P-32 b using the Calar Alto high-Resolution search for M dwarfs with Exoearths with Near-infrared and optical Échelle Spectrographs (CARMENES) (*22*) on the Calar Alto 3.5-m telescope. They collected high-resolution ($R \approx 80{,}000$) spectra of the host star over two nights right around the planet's optical transits and monitored for 6 hours each night centered on the middle of transits, leading to the detection of the planet's excess helium absorption with a maximum transit depth of 5.3%.

With HET/HPF, we monitored HAT-P-32 Ab with time-series spectroscopy, covering orbital phases spanning the planet's full orbital period. We collected spectra during three planet transits on 9 August 2020 universal time (UT), 19 September 2020 UT, and 6 October 2020 UT and during out-of-transit periods within 2 days of each transit. We also monitored the stellar activity of HAT-P-32 A with irregular cadence from 1 August 2020 UT to 25 December 2020 UT (Table 1). Our data were reduced using the HPF pipeline code Goldilocks and the muler Python package (*23*–*26*), which perform bias and nonlinearity corrections, cosmic-ray rejection, flat fielding, wavelength calibration, and careful subtraction of sky emission features. We obtained a total of 77 high-quality spectra with a median signal-to-noise ratio (S/N) of 85 per pixel (142 per resolution element) near 10,833 Å. All spectra were shifted to the stellar rest frame based on barycentric corrections and our computed absolute radial velocities (RVs).

RESULTS

We measured helium equivalent widths (EWs) for all HPF spectra of HAT-P-32 A + b and detected a long-duration (12 hours), statistically significant (14σ) excess absorption feature near the transit of HAT-P-32 b (Fig. 1). The helium excess is not correlated with any stellar activity indicators (fig. S1) and spans ≈4× longer than the planet's optical transit duration. To facilitate the transmission spectroscopic analysis, we divided the data into five subsets according to

[1]Department of Astronomy and Astrophysics, University of California, Santa Cruz, Santa Cruz, CA 95064, USA. [2]Department of Astronomy, The University of Texas at Austin, Austin, TX 78712, USA. [3]Center for Astrophysics, Harvard and Smithsonian, Cambridge, MA 02138, USA. [4]Anton Pannekoek Institute for Astronomy, University of Amsterdam, Amsterdam, Netherlands. [5]Department of Astronomy and Astrophysics, Tata Institute of Fundamental Research, Mumbai, India. [6]Department of Astronomy and Astrophysics, The Pennsylvania State University, University Park, PA 16802, USA. [7]Center for Exoplanets and Habitable Worlds, University Park, PA 16802, USA. [8]ETH-Zürich, Institute for Particle Physics and Astrophysics, Zürich, Switzerland. [9]Steward Observatory, The University of Arizona, 933 N. Cherry Ave, Tucson, AZ 85721, USA. [10]Center for Planetary Systems Habitability and McDonald Observatory, The University of Texas at Austin, Austin, TX 78730, USA. [11]McDonald Observatory and the Department of Astronomy, The University of Texas at Austin, Austin, TX 78712, USA. [12]Department of Astrophysical Sciences, Princeton University, Princeton, NJ 08544, USA. [13]Department of Physics and Kavli Institute for Astrophysics and Space Research, MIT, Cambridge, MA 02139, USA. [14]Hobby-Eberly Telescope, The University of Texas at Austin, Austin, TX 78712, USA.
*Corresponding author. Email: zhangdirac@gmail.com

Table 1. The HET/HPF observing log of HAT-P-32 Ab. For each date, we list the number of the observed spectra (N_{spec}) and their mean S/N (per pixel) near 10,833 Å, as well as the range of air mass and orbital phase covered by these data. Each spectrum was acquired with an exposure time of 820 s. The HPF spectral resolution element contains a median of 2.8 pixels. We also divide our spectra into five subsets based on their orbital phase as indicated in the "Type" column, including START (with the orbital phase in [−0.5, −0.15]), PRE ([−0.15, −0.03]), TRANSIT ([−0.03, +0.03]), POST ([+0.03, +0.08]), and END ([+0.08, +0.5]).

Date (UT)	Type	N_{spec}	Mean S/N	Air mass	Orbital phase
Transit event 1					
7 August 2020	POST	3	57	[1.31, 1.20]	[+0.05, +0.06]
8 August 2020	START	4	91	[1.30, 1.19]	[−0.49, −0.48]
9 August 2020	TRANSIT	6	68	[1.36, 1.16]	[−0.03, −0.01]
Transit event 2					
18 September 2020	START	3	89	[1.14, 1.20]	[−0.37, −0.36]
19 September 2020	TRANSIT	6	84	[1.35, 1.16]	[−0.01, +0.01]
19 September 2020	END	2	112	[1.16, 1.18]	+0.10
20 September 2020	START	4	93	[1.15, 1.24]	[−0.44, −0.43]
22 September 2020	END + START	4	95	[1.15, 1.24]	[+0.49, +0.51]
Transit event 3					
5 October 2020	END	4	96	[1.29, 1.18]	[+0.42, +0.43]
6 October 2020	PRE	6	74	[1.31, 1.14]	[−0.12, −0.10]
6 October 2020	TRANSIT	6	93	[1.14, 1.31]	[−0.02, 000]
7 October 2020	END	4	96	[1.15, 1.24]	[+0.45, +0.46]
8 October 2020	START	4	83	[1.29, 1.18]	[−0.19, −0.18]
Stellar activity monitoring					
1 August 2020	END	2	99	[1.21, 1.18]	+0.28
4 September 2020	POST	4	59	[1.31, 1.19]	[+0.04, +0.05]
5 September 2020	START	1	84	1.17	−0.48
11 October 2020	END	2	116	[1.18, 1.21]	+0.31
12 October 2020	START	4	100	[1.17, 1.27]	[−0.23, −0.22]
2 December 2020	END	2	66	[1.30, 1.26]	+0.32
9 December 2020	START	2	90	[1.17, 1.20]	[−0.33, −0.32]
23 December 2020	END	2	71	[1.20, 1.23]	+0.17
25 December 2020	END	2	74	[1.17, 1.20]	[+0.09, +0.10]

their orbital phases ϕ (Fig. 1), which we denote as START ($-0.5 \leq \phi \leq -0.15$; 23 spectra), PRE ($-0.15 < \phi \leq -0.03$; 6 spectra), TRANSIT ($-0.03 < \phi < +0.03$; 18 spectra), POST ($+0.03 \leq \phi \leq +0.08$; 7 spectra), and END ($+0.08 < \phi \leq +05$; 23 spectra). We constructed the out-of-transit reference spectra for each of the three transits by combining the corresponding START and/or END spectra (fig. S2) and used them to normalize the other data to produce transmission and residual (=transmission − 1) spectra.

We detected strong excess helium absorption from PRE, TRANSIT, and POST residual spectra and measured the time-dependent wavelength shift for each subset to characterize the velocity of HAT-P-32 b′s escaping atmosphere (Fig. 2). We modeled the excess helium absorption feature in each residual spectrum (figs. S3 and S4) using a Gaussian profile to determine its transit depth and central wavelength, and then we converted the latter into an RV of the escaping atmosphere (in the stellar rest frame) by comparing with the rest wavelength of the helium triplet. As shown in Fig. 2, RVs of the helium excess during the optical transits of HAT-P-32 b are consistent with those of the planet′s orbital motion, reaffirming the planetary origin of the helium; the observed features have slightly higher RVs (i.e., toward the star) than the planet′s orbital RV, which could result from mass transfer from the planet to its host star. These observations are consistent with both Roche lobe overflow and mass loss controlled by planetary and stellar magnetic fields [e.g., (*27*)]. Before (PRE) and after (POST) the planet′s optical transit, the observed escaping atmosphere does not track the planet′s orbital motion and, instead, has only a small line-of-sight velocity shift in the stellar rest frame, suggesting that the helium gas from the planet′s upper atmosphere mostly moves within the sky plane perpendicular to the observers′ line of sight; this property is consistent with the spatially extended geometry of the gas (as indicated by the long duration of our detected helium excess; see Fig. 1), with gas far from the planet orbiting the star. Helium excess features in POST residual spectra are noticeably blue-shifted, implying that material trailing the planet is moving outward in the planetary system.

The maximum depth of the detected helium excess is measured to be ≈8.2% during the optical transit of HAT-P-32 b; the helium

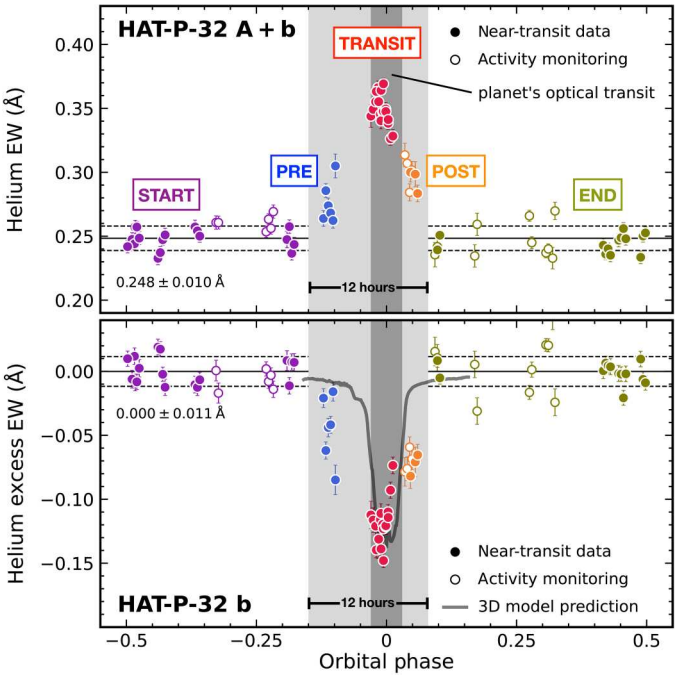

Fig. 1. Measured helium excess in HAT-P-32 A+b planetary system. EWs of the helium 10,833-Å triplet, measured from the observed spectra of HAT-P-32 A + b (top) and computed residual spectra of HAT-P-32 b (bottom), exhibit long-duration (12 hours), significant (14σ) excess near the planet's transits. Solid circles represent data obtained within two nights of each optical transit, and open circles represent the stellar variability monitoring data obtained from out-of-transit periods. We divided the data into five categories in terms of orbital phase, with boundaries highlighted by gray-shaded regions. Our three-dimensional (3D) hydrodynamic simulation is shown as the gray solid line. The time-series helium EWs are asymmetric with respect to the planet's optical transit (dark gray), demonstrating the leading tail of the helium atmosphere escaping HAT-P-32 b.

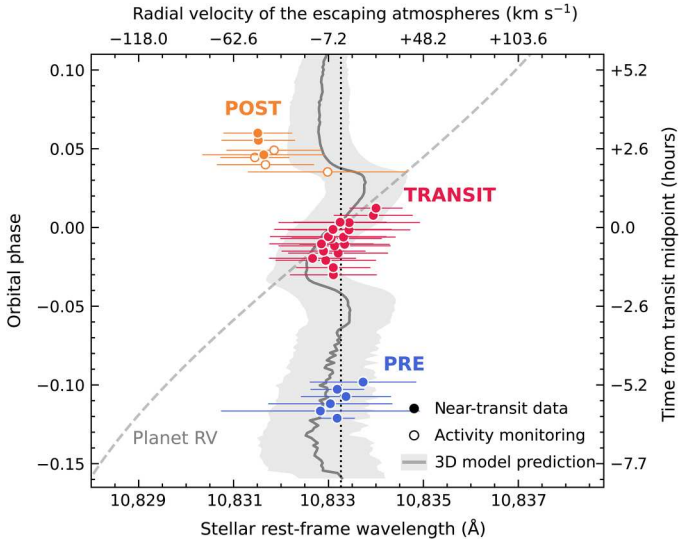

Fig. 2. Measured central wavelengths and RVs of HAT-P-32 b's escaping helium atmosphere as a function of orbital phase in the stellar rest frame. The observed helium excess features in PRE (blue), TRANSIT (red), and POST (orange) residual spectra were fitted by Gaussian profiles to determine the central wavelengths and the standard deviations (circles with horizontal bars), which were then converted to RVs of the escaping atmosphere based on the rest wavelength of the two strongest components of the helium triplet (vertical dotted line at 10,833.26 Å). Circle symbols have the same format as those shown in Fig. 1. The gray dashed line represents the planet's RV. The central wavelength and SD of helium excess from our simulations are shown as the gray solid line with shadow.

excess in the 12-hour period surrounding optical transit is 5 to 6% (Fig. 3). Our in-transit helium excess depth is about 1.5 times higher than the value (5.3%) measured by CARMENES because their "out-of-transit data" were taken when the escaping helium is still in transit. Our detected excess helium absorption spans 3 to 4 Å in the stacked TRANSIT residual spectrum, comparable with the observed residual spectra from CARMENES (*21*), and spans 1.5 to 2 Å in the stacked PRE and POST residual spectra. While other planets show trailing tails of material (*12*, *28*–*30*), HAT-P-32 b has both a (longer) leading and (shorter) trailing tail.

DISCUSSION

Helium outflow from three-dimensional hydrodynamic models

Comparing our observations to three-dimensional (3D) hydrodynamic simulations of the HAT-P-32 A + b system provides physical insight into the geometry of the outflow. We generated 3D hydrodynamic models following (*31*) to examine the interactions between the planetary outflow and stellar winds in the tidal gravitational field of the HAT-P-32 A + b system (Fig. 4). Because of the small orbital separation and high star-to-planet mass ratio, HAT-P-32b nearly fills its Roche lobe. Our models show extended, columnar tails of planetary outflow both leading and trailing the planet along the orbital path. These tails provide excess helium absorption even at phases far from the planet's optical transit that match our observations. Our model also predicted that the mass loss rate of the planet is $\approx 1.7 \times 10^{-14}\ M_\odot\ \mathrm{year}^{-1}$, implying that the planet will lose its atmosphere over a time scale of $M_\mathrm{p}/\dot{M}_\mathrm{p} \approx 4 \times 10^{10}$ years.

As shown in Fig. 1, our 3D model does not accurately explain the observed relative depth of the PRE and POST phases as compared to the mid-transit, which we used as a point of reference. However, as traced in Fig. 2, the model predicted that the extended tidal tails lie in approximately the stellar rest frame, not the planet's rest frame, as seen in our HPF data. Our simulations (Figs. 2 and 4) reveal how these extended tails span the star-planet environment of the HAT-P-32 A + b system. Sophisticated models that account for the momentum deposition by the stellar radiation field on the planetary outflow, orbital eccentricity of the planet, ram pressure of stellar wind, and the thermodynamics of the planetary outflow will be useful to probe the range of physical processes shaping this interaction.

The exceptional escaping helium of HAT-P-32 b

HAT-P-32 b's escaping helium atmosphere is exceptional among known detections: It has the largest depth and longest duration found to date. The duration of the helium transit implies the tidal tails have a sky-projected length of 53 times the planet's radius (seven times the host star's radius), among the largest structures ever observed in a planetary system. Our study verifies the importance of long-baseline monitoring of planet-host systems to characterize systems with extended tails. Many surveys have targeted K-type planet-host stars since their UV spectra can readily populate

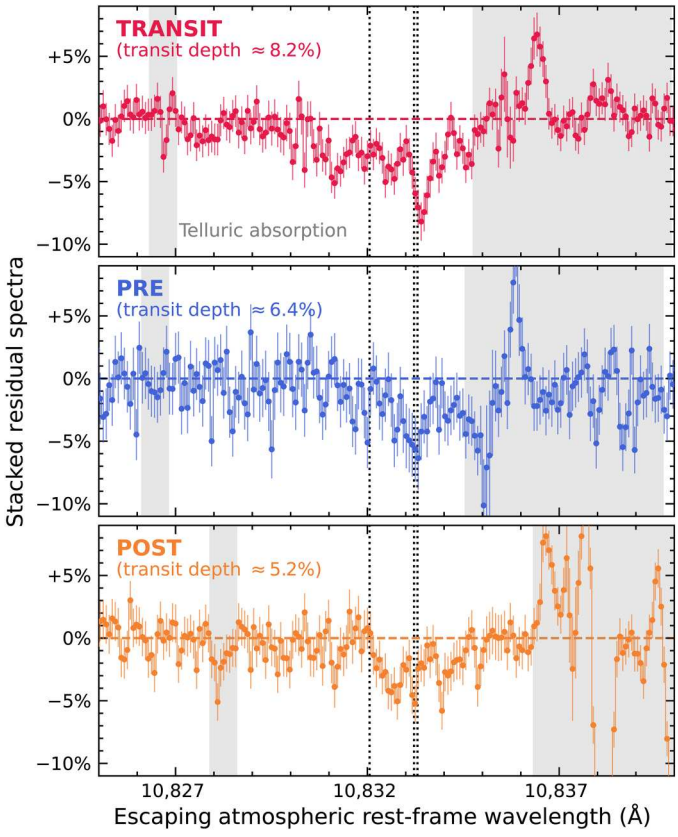

Fig. 3. Stacked residual spectra of HAT-P-32 b. Before the stacking, each residual spectrum has been corrected by its RV of the escaping helium atmosphere, such that their helium excess features all line up with the rest wavelength of the strongest component of the helium triplet. We detected strong excess helium absorption from TRANSIT (top), PRE (middle), and POST (bottom) residual spectra, spanning 1.5 to 4 Å in wavelength with a maximum depth of 8.2%, 6.4%, and 5.2%, respectively. The rest wavelength of the helium triplet is marked by vertical dotted lines. Telluric absorption features with a transmission of <99.9% are shown as gray shades.

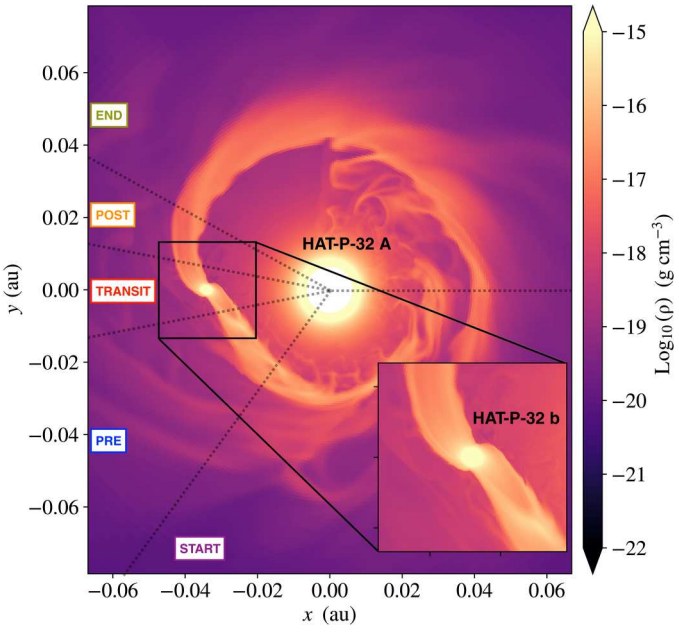

Fig. 4. Slice through the orbital plane of a simulated system approximating HAT-P-32 A + b. The frame rotates with the planetary mean motion, so the position of observers rotates clockwise, with regions of START, PRE, TRANSIT, POST, and END shown in observations divided by black dotted lines. The logarithm of gas density is shown in the color scale. A low-density but relatively fast stellar wind expands from HAT-P-32 A at the coordinate origin and interacts with the outflow from HAT-P-32 b. The outflow from HAT-P-32 b is stretched into long, column-like tails leading and trailing the planet along the orbital path. These tidal tails are shaped by the advection of slow-moving planetary outflow in the star-planet gravitational field.

the helium metastable state (*32*); HAT-P-32 Ab's strong helium excess empirically demonstrates that F stars also provide a suitable environment for mechanisms triggering the planets' mass loss. Our observations of HAT-P-32 b show that this planet-star configuration, where the planet largely fills its Roche lobe, can lead to extended outflowing material.

On the potential variability of HAT-P-32 b's helium excess

We examined the potential variability of HAT-P-32 b's escaping helium atmosphere by comparing measured helium excess EWs across different dates (Fig. 5). During the planet's optical transit, the helium excess EWs mostly varied by less than 0.03 Å across three events. Near the planet's egress (observed during the second transit event) and slightly after the optical transit (shown by the POST subset), EWs of helium excess varied by less than 0.02 Å. In the PRE subset, all our observations were collected on the same night with the third transit event. In this subset, the measured helium excess EWs varied by 0.06 Å, and the helium excess absorption appears to become stronger with the increasing orbital phase. More observations of HAT-P-32 A + b over the orbital phase of the PRE subset will be useful to assess the variability of the planetary helium outflow slightly before the optical transit. To conclude, these HPF observations do not suggest a significant variability of HAT-P-32 b's helium excess over our monitoring baseline from 7 August 2020 to 25 December 2020. As a point of comparison, in our 3D hydrodynamic simulations, the overall column density of metastable helium and its mean RV do not appear significantly variable despite instabilities at the interface between the planetary and stellar winds.

Comparing the helium excess revealed by the HPF spectra with those from the CARMENES data (*21*), observed on 1 September 2018 and 9 December 2018, will examine the longer-term variability of the planet's helium excess. The published CARMENES spectroscopic observations span from about 4 hours before (≈−0.08 in orbital phase) to 3 hours after (≈+0.06 in orbital phase) the midpoint of the planet's optical transit, meaning they coincide with the PRE, TRANSIT, and POST subsets in our analysis (Fig. 1). New CARMENES observations that cover a longer time baseline (especially with orbital phases of our START and END subsets) than those already acquired by (*21*) will construct the reference spectra that are needed to reanalyze the CARMENES-based helium excess. Comparing these results with the HPF measurements will investigate the long-term variability for HAT-P-32 b's outflow.

The diversity of planetary systems with escaping helium atmospheres

We compared properties of HAT-P-32 Ab with all other planetary systems that have either detections or upper-limit constraints of the

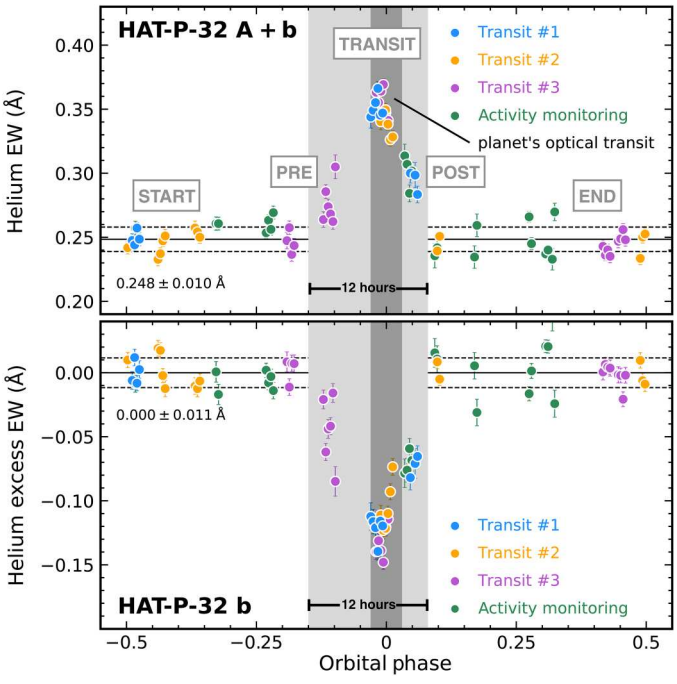

Fig. 5. The measured helium EWs of HAT-P-32 A + b and the helium excess EWs of HAT-P-32 b from different dates are consistent over a given range of the planet's orbital phase. The data presented here are exactly the same as Fig. 1 but are color-coded by observation dates, including those observed during the first (blue), second (orange), and third (purple) transit event, as well as the long-term stellar activity monitoring (green). More observations slightly before the planet's optical transit are needed to examine whether the planet's helium excess is variable in the PRE subset.

escaping helium atmospheres, to investigate what physical parameters are causing the unusually extended helium atmosphere of HAT-P-32 b and driving the mass loss of exoplanets in general. We compiled all these systems in table S1. Following (*12*), we computed the equivalent height of each planet's helium atmosphere δR_p and its ratio to the planet's atmospheric scale height at the equilibrium temperature H_{eq}, leading to a metric, $\delta R_p/H_{eq}$, that quantifies the strength of the helium excess signal [also see (*33*–*35*)]. The census was divided into two subsets with planetary radii above and below 0.4 R_{Jup}, which represent gas giants and sub-Neptunes, respectively. In Fig. 6, we investigated $\delta R_p/H_{eq}$ as functions of the planets' Roche-lobe filling, planetary surface gravity, the planet's bolometric equilibrium temperature, incident x-ray and UV (XUV) flux from the host stars, and the host stars' effective temperatures. Here, the Roche-lobe filling stands for the ratio between the planetary radii R_p to the Roche lobe radii R_{RL}, with the latter computed via equation 2 of (*36*).

With the existing census, Fig. 6 does not suggest clear trends between $\delta R_p/H_{eq}$ and other physical properties investigated here. Among gas giants, HAT-P-32 b has the largest $\delta R_p/H_{eq}$ and the longest-duration helium excess. This property lines up with its much larger Roche-lobe filling, lower surface gravity, and higher XUV incident flux, all of which are expected to foster the planet mass loss. However, several planets (e.g., WASP-69 b and WASP-107 b) with lower Roche-lobe fillings and XUV incident fluxes achieved comparable $\delta R_p/H_{eq}$ as HAT-P-32 b. In addition, WASP-76 b has very similar properties as HAT-P-32 b, but its potential helium outflow was not significantly detected as shown by (*37*), although partially due to the contamination of the telluric absorption near the helium triplet.

Note that the three planets with the deepest helium excess depths, WASP-69 b, WASP-107 b, and HAT-P-32 b, also have longer-duration extended excess absorption than the planets' optical transits. A variety of system physical properties must conspire to create extended, deep helium signals; surface gravity—and therefore escape velocity—seems to be important since these three planets have some of the lowest in the sample. The observed diversity calls for further observational and theoretical studies of planets with both detections and nondetections of excess helium absorption with long-baseline monitoring, to probe the mass loss mechanisms of exoplanets.

MATERIALS AND METHODS

Known properties of the HAT-P-32 system

Located at a distance of 283 ± 2 pc (*38*), HAT-P-32 A is a moderately rapidly rotating ($v \sin i = 20.7 \pm 0.5$ km s^{-1}) late-F dwarf with a near-solar metallicity ([Fe/H]= −0.04 ± 0.08 dex) and an isochrone-based age of 2 to 4 Ga [e.g., (*19*, *39*)]. The hot Jupiter HAT-P-32 b was found by Hartman *et al.* (*19*) from optical transit light curves and the host star's multiepoch RVs. The observed RV jitter (≈80 m s^{-1}) of HAT-P-32 A prevents precise measurements of the planet's orbital eccentricity, so Hartman *et al.* (*19*) provided two sets of orbital solutions for HAT-P-32 b by assuming a circular orbit (i.e., $e = 0$) or allowing the eccentricity to vary (leading to $e = 0.163 \pm 0.061$). On the basis of new RV data and/or transit light curves, Wang *et al.* (*20*) and Knutson *et al.* (*40*) refined the planet's orbital eccentricity as $e = 0.159^{+0.051}_{-0.028}$ and $e = 0.20^{+0.19}_{-0.13}$, respectively. However, the secondary eclipse timing of the planet detected by Zhao *et al.* (*41*) clearly suggests a lower $e = 0.007^{+0.070}_{-0.006}$. Throughout this work, we thus adopt a circular planet orbit for HAT-P-32 b. Various orbital analyses converge on the planet's orbital semi-major axis of ≈0.034 arbitrary units (au) (*19*, *20*, *41*). HAT-P-32 b has a mass of 0.59 ± 0.03 M_{Jup}, a radius of 1.79 ± 0.03 R_{Jup}, a low density of 0.14 ± 0.02 g cm^{-3}, and a high equilibrium temperature of 1836 ± 7 K (*19*, *21*). With HAT-P-32 b's mass and irradiation, a core-less planet (the limiting case that provides the highest possible radius) would have a radius of 1.1 to 1.2 R_{Jup} [e.g., (*42*)], meaning that HAT-P-32 b is an inflated hot Jupiter. This planet likely has a polar orbit, with a sky-projected obliquity of 85.0° ± 1.5°, based on the Rossiter-McLaughlin effect (*43*). The HAT-P-32 A + b system also has an M1.5 stellar companion, HAT-P-32 B, with a projected separation of 2.94″ or 830 au (*41*, *44*, *45*). With such a wide orbit, HAT-P-32 B is not responsible for the detected significant RV trend (−38 ± 5 m s^{-1} year^{-1}) of HAT-P-32 A (*20*, *40*).

HET/HPF observations, data reduction, and postprocessing

HET is designed with a fixed elevation of 55° and a tracking window of ±8° (*16*, *17*). As a consequence, HAT-P-32 (declination = 46.687852°) is only observable over a track length of 1.5 to 3.3 hours per night. The strategy of our survey is to observe the target over the full track when the planet's optical transit occurs and to collect out-of-transit spectra on both of the two nights before and

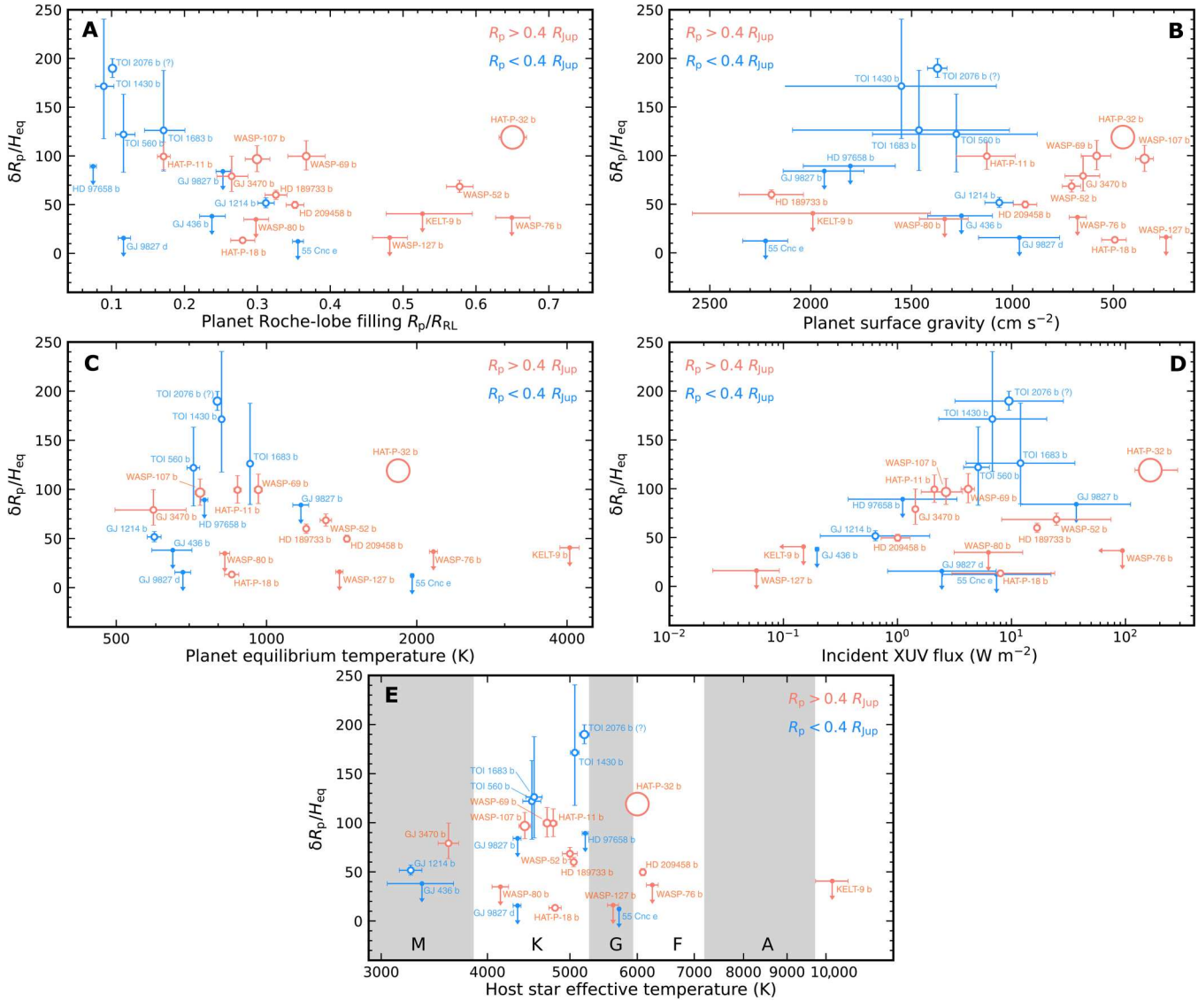

Fig. 6. Census of planetary systems with detections and upper-limit constraints of excess helium absorption (table S1), divided into gas giants (orange) and sub-Neptunes (blue). The *y* axes of all panels present the objects' equivalent heights of helium upper atmosphere in units of the scale height at equilibrium temperatures, $\delta R_p/H_{eq}$. The *x* axis in (**A**) is Roche-lobe filling R_p/R_{RL}, which is the radius ratio between the planet and its Roche lobe. The *x* axes in (**B** to **E**) represent these planets' surface gravities, equilibrium temperatures, incident XUV flux from their host stars, and their host stars' effective temperatures, respectively. Symbol size for detections is proportional to the ratio between the transit duration of helium excess and that of the planets' optical transits. Most systems have such ratios as 1, while WASP-69 b (*12*), WASP-107 b (*28*), and HAT-P-32 b have larger ratios of 1.2, 1.4, and 3.8, respectively, meaning that their helium upper atmospheres are extended. In addition, TOI 2076 b exhibited excess helium absorption until 50 min after the planet's egress; we computed a ratio of 1.3 although the monitoring baseline did not extend the full optical transit and preingress periods (*60*). Furthermore, Gaidos *et al.* (*61*) recently cautioned that the excess helium absorption signature of TOI 2076 b is likely due to its host star's variability. In addition, TOI 1430 b exhibits excess helium absorption slightly before the planet's ingress (*60*); longer-baseline monitoring would validate this feature so we simply assumed a ratio of 1.

two nights after the transit event to construct the reference spectra used to calibrate the transmission spectra. We also monitored HAT-P-32 A + b from 1 August 2020 UT to 25 December 2020 UT with irregular cadence to investigate its stellar activity. Our observing log is summarized in Table 1.

Our raw HPF data were reduced using the Goldilocks pipeline (*23*–*25*), which extracts the 1D simultaneous spectra from the target fiber, sky reference fiber, and the laser frequency comb (LFC) fiber from 2D images, spanning from 8100 to 12,800 Å. Given the relaxed requirement about the RV precision for the science goal of our survey and to avoid any scattered light in the target star fiber, the LFC was turned off. We applied standard 1D postprocessing for these spectra using our newly developed muler framework (*26*) that also provides quick-look quality assurance.

To remove sky emission lines, we combined the observed spectra from both the target and the sky fibers. These two types of fibers have different throughputs, so the direct/naive subtraction between target and sky fiber spectra is not sufficient. The sky-to-

target throughput calibration was determined by our muler framework. Specifically, we analyzed twilight flats regularly acquired during the HPF operations. In this configuration, both target and sky fibers were illuminated by the scattered sunlight. Computing the ratio of the solar spectra acquired by these two fibers, we thus derived a wavelength-dependent scaling factor that should be applied to the sky fiber before the sky subtraction. We found the sky fiber has a ≈7% more throughput than the target fiber. We further validated this sky-to-target throughput calibration using another dataset acquired during the HPF nighttime operations. In this dataset, both target and sky fibers were pointed at blank patches of the sky, leading to two sets of spectra populated with only sky emission lines. Comparing the strengths of these skylines from both fibers led to a similar calibration term determined from the twilight flats (also see the documentation and tutorials of muler). Overall, the sky subtraction based on muler leads to 14 improvements over the naive sky subtraction, with negligible residual structure seen in most bright skylines near the helium triplet. The performance of our sky subtraction is also verified by another independent method that can derive the sky-to-target throughput calibration using a given target's observed spectrum without requiring twilight flats or blank sky observations (*46*). As an additional step to further minimize the impact of skylines on our analysis, we masked a skyline doublet that is close to the helium spectral feature; this doublet is located at 10,832.103 and 10,832.412 Å (*47*). For each spectrum, we first converted a wavelength range of 10,832.103 to 10,832.412 Å into its stellar rest frame (see below) and then used linear interpolation to approximate the fluxes.

Corrections to telluric absorption were not performed given we planned our observations strategically when telluric bands were widely separated from the helium spectral feature of HAT-P-32 Ab, as shifted by Earth's barycentric motion (see Fig. 3).

Our reduced spectra are all in vacuum wavelengths. All spectra have S/Ns above 45 per pixel, i.e., >75 per resolution element, near the helium triplet at 10,833 Å; the median S/N is 85 per pixel. During the observation, the stellar companion B is outside the HPF target fiber, the radius of which (0.85″) is only 29% of the angular separation between A and B components (2.94″) (*44*, *45*). In addition, the B-to-A flux ratio is about 0.017 near the helium triplet at 10,833 Å [see figure 4 of (*41*)]; this ratio is comparable to the noise-to-signal ratio of A's observed fluxes, with a median of 0.012 (=1/85). Thus, the stellar companion would have comparable fluxes with A's flux uncertainties, even if both stellar components were observed by the same fiber. Therefore, the stellar companion HAT-P-32 B has negligible contamination to our observations of HAT-P-32 A + b.

HPF relative RVs of HAT-P-32 A

We measured the relative RVs of HAT-P-32 A from the HET/HPF spectra following (*48*). We first applied the barycentric correction to all spectra using Astropy (*49*, *50*) and then multiplied each spectrum by a third-order polynomial, with coefficients determined in the steps described below, to match the fluxes of the science spectrum (observed on 19 September 2020 UT) with the highest S/N among our entire dataset. To create a master template, we carried out a cubic basic (B-spline) regression to data points from all these scaled spectra via the least-squares minimization implemented with a κ-sigma clipping that removes significant outliers from the residuals. We then jointly fitted the relative RV and the third-order polynomial coefficients for each spectral order of each spectrum by minimizing the χ^2 between the given spectrum and the master template, over a grid of velocities (from −5 to +5 km s^{-1} with steps of 50 m s^{-1}) following (*51*). During this process, we also masked the telluric absorption and sky emission features. We determined the RV value and variance of a given spectral order based on the χ^2-velocity parabola and computed the final relative RV for each spectrum as the weighted mean and SE of RVs among all spectral orders. The spectrum with the highest S/N in our dataset thus provides the baseline for the measured relative RVs. Our resulting HPF relative RVs has typical uncertainties of 131 m s^{-1}.

Given that HAT-P-32 A has an absolute RV of −23.21 ± 0.26 km s^{-1} based on (*19*), we thus added this value to the relative RV of each spectrum to obtain an absolute RV, with uncertainties added in quadrature. The computed absolute RVs of our data have a typical uncertainty below 0.3 km s^{-1}, corresponding to a wavelength shift of only <0.01 Å near the helium triplet. We used the computed absolute RV of each spectrum to shift it into the stellar rest frame.

EW measurements of helium and the calcium infrared triplets

We measured the EWs of the helium triplet in the stellar rest frame by integrating the line flux over 10,831.5 to 10,834.5 Å, with the pseudo-continuum approximated by a linear fit of the fluxes from two surrounding wavelength regions of 10,824 to 10,826 Å and 10,840 to 10,841 Å. The flux uncertainties are propagated into our resulting EWs in an analytical fashion. We also measured the EWs of the calcium infrared triplet (Ca II IRT) at 8500, 8544, and 8644 Å, which probe the stellar chromospheric activity. These lines are thus used to validate that our observed significant excess helium absorption has a planetary rather than stellar origin [e.g., (*21*, *52*)]. To compute the EW of each triplet component, we defined the line wavelength as 8498 to 8503 Å with the pseudo-continuum established from 8491 to 8495 Å and 8505 to 8509 Å for Ca II λλ8500; line wavelength as 8540 to 8549 Å with the pseudo-continuum from 8536 to 8537.5 Å, 8552 to 8556 Å, and 8562 to 8570 Å for Ca II λλ8545; and line wavelength as 8661 to 8668 Å with the pseudo-continuum from 8658 to 8660 Å, 8672 to 8676 Å, and 8680 to 8688 Å for Ca II λλ8665. For a given spectrum, we adopted the EW of the Ca II IRT as the sum of all three components' EWs. As shown in fig. S1, our measured Ca IRT EWs of spectra in PRE, TRANSIT, and POST subsets, when the escaping helium atmosphere and/or the planet are in transit, are all consistent with those of out-of-transit data in START and END subsets. Therefore, the observed helium excess spectral features likely originate from the planet's upper atmosphere. This conclusion is supported by the observed low activity level from the ground-based optical light curves [e.g., (*53*)] and was also drawn by Czesla *et al.* (*21*) based on CARMENES data.

Construction of the reference, transmission, and residual spectra

We resampled each spectrum in the stellar rest frame to the same wavelength grid of the spectrum that has the highest S/N at 10,833 Å. Then, we normalized the spectrum in the neighborhood of the helium triplet, with the pseudo-continuum established from a linear fit of fluxes from 10,824 to 10,826 Å and 10,840 to 10,841 Å as used in our EW measurements. For data collected from each of the

three transit events and also from the long-term stellar activity monitoring, we derived a reference spectrum by computing the average of all spectra corresponding to orbital phases below −0.15 (i.e., START) or above +0.08 (i.e., END). We propagated the flux uncertainties in an analytical fashion and obtained a total of four reference spectra. As shown in fig. S2, our computed reference spectra all have consistent shapes and values in the neighboring wavelengths of the helium triplet, with different fluxes from the telluric absorption lines that are clearly separated from the helium feature. We then divided each normalized PRE, TRANSIT, and POST spectrum by its corresponding reference spectrum to produce transmission and residual (transmission 1) spectra (figs. S3 and S4). A telluric band, spanning 10,835 to 10,840 Å in the stellar rest frame, is near but separated from the helium feature in our residual spectra. Thus, our analysis cannot detect if there is any helium excess from a clump of the planet's escaping atmosphere with an RV toward the host star with values of 48 to 187 km s^{-1}; such signal is not predicted by our subsequent 3D hydrodynamic simulation for our target (see below).

Gaussian models of the excess helium absorption

The observed wavelengths of helium excess reflect the RVs of helium upper atmosphere escaping HAT-P-32 b. To identify these wavelengths, we fitted a Gaussian profile $G(\lambda) = -A_G \exp\left[-(\lambda - \mu_G)^2/2\sigma_G^2\right]$ to each residual spectrum over 10,825 to 10,840 Å, with A_G, μ_G, and σ_G describing the transit depth, central wavelength, and SD wavelength of each excess absorption feature. We excluded telluric bands redward of the helium triplet, as well as wavelengths of sky emission lines whose fluxes were replaced by linear interpolation during the data processing. Some residual spectra observed near the end of the planet's optical transit show broad absorption features that have slightly shorter wavelengths and shallower depths than the helium excess (e.g., the residual spectrum of the second transit event with the orbital phase near 0.012; fig. S3). These features line up with the weakest component of the helium triplet (Fig. 3) but contain an absorption component that is even more blueshifted [also see (*21*)]. We chose to exclude wavelengths of such feature in our fitting process, given that the goal of fitting Gaussian profiles is to identify wavelengths of the primary component of the excess helium absorption.

On the basis of our fitted A_G values, the depth of helium excess from each residual spectrum in the PRE (6 spectra in total), TRANSIT (18 spectra in total), and POST (7 spectra in total) subsets spans 2 to 3%, 4 to 7%, and 2 to 4%, respectively. The transit depth in each subset is further increased after stacking all residual spectra (Fig. 3). In addition, our observed helium excess has full widths at half maximum of 1.5 to 3 Å (i.e., $2.355\sigma_G$), comparable with the detected helium excess in other planetary systems [e.g., (*11*, *12*)]. To compute the RV of the escaping helium atmosphere of HAT-P-32 b, we further compared the fitted central wavelength μ_G of each residual spectrum with the mean rest wavelength of the strongest two components of the helium triplet at 10,833.26 Å. Our fitted μ_G, σ_G, and computed escaping RVs are presented in Fig. 2.

Planetary orbital RV in the stellar rest frame

We computed the planet's RV in the stellar rest frame as a function of the planet's orbital phase (ϕ) based on the following equation

$$RV_p(\varphi) = -\left(1 + \frac{1}{M_p/M_*}\right) \times K_* \{\cos[\nu(\varphi) + \omega_*] + e\cos\omega_*\} \quad (1)$$

where M_p/M_* is the planet-to-star mass ratio, K_* is the semiamplitude of the host star's RV, ω_* is the argument of the periastron of the host star's orbit induced by the exoplanet, and e is the planet's orbital eccentricity. The true anomaly, ν, is converted from a given orbital phase based on the planet's orbital period (P) and eccentricity (e), time of periastron (T_P), and the time of the planet's optical transit (T_C).

We computed $RV_p(\phi)$ for a circular planet orbit and adopted $M_p/M_* = 4.81 \times 10^4$ (*21*), $K_* = 83.4$ m s^{-1} (*21*), $P = 2.1500082$ days (*20*), and $T_C = 2{,}456{,}237.031$ BJD_{TDB} (*20*). We simply assumed $\omega_* 0°$ and $T_P = T_C - P/4$ for using Eq. 1. We did not incorporate the uncertainties of orbital parameters in our calculation, given our analysis compares the planet's RV with measured RVs of the escaping helium atmosphere under a qualitative perspective. Our computed $RV_p(\phi)$ is presented in Fig. 2.

Stacked residual spectra and the light curve of excess helium absorption

We shifted all residual spectra to an "escaping atmospheric rest frame" based on the computed RVs of the helium upper atmosphere escaping HAT-P-32 b, such that the helium excess feature in each shifted residual spectrum all lines up with the rest wavelength of the strongest component of the helium triplet at 10,833.26 Å. We then computed the stacked residual spectrum based on the weighted flux mean and uncertainty of all data in each of the PRE, TRANSIT, and POST subsets (Fig. 3). In addition to the excess helium absorption features, the stacked PRE residual spectrum shows a deep absorption feature near 10,835 Å, which is caused by the telluric absorption mainly contributed by the PRE residual spectrum with an orbital phase of −0.098 and −0.111 (fig. S4). The wavelength of this feature is outside the wavelength range used to compute the helium EWs (Fig. 1). To compute the light curve of excess helium absorption (Fig. 1), we integrated each residual spectrum in the escaping atmospheric rest frame over a window centered at 10,833.26 Å (the mean rest wavelength of the strongest two components of the helium triplet) with a width of ±1.8 Å (corresponding to an RV range of ±50 km s^{-1}), with spectral uncertainties propagated in an analytical fashion.

3D hydrodynamic models

Our 3D hydrodynamic models made use of the Athena++ (magneto)hydrodynamics code (*54*), which uses an Eulerian algorithm with active and static mesh refinement capabilities. Our models simulated the properties of the interaction between the planetary outflow (with properties based on parameterized assumptions) and the stellar wind and the planet-star gravitational field [e.g., (*31*)]. We adopted a nearly isothermal ideal-gas equation of state with an adiabatic index $\gamma = 1.0001$ (allowing each of the stellar and planetary outflows to be nearly isothermal but with very different temperatures) and ignored any possible effects of stellar or planetary magnetic and radiation fields.

We solved the hydrodynamics equations in a rotating reference frame centered on the host star HAT-P-32 A. Our frame rotates with the planetary mean motion to minimize the orbital advection of planetary outflow across the coordinate mesh. We used a spherical-polar mesh that covers the full 4π of solid angle and extends in radius from HAT-P-32 A's stellar radius of $R_* \approx 9.5 \times 10^{10}$ cm [or 1.37 ± 0.03 $R_\odot$ as determined by (*20*)], to about 100 × R_* of 9 × 10^{12} cm. With a semimajor axis of 0.034 au ~5 × 10^{11} cm (*19*, *20*, *41*) or 5.3 R_*, the orbit of HAT-P-32 b is covered by this coordinate mesh. Our base mesh uses 144 × 96 × 192 zones in the *r*, θ, ∅ coordinate, with the planet placed at θ = π/2. To increase the resolution of simulations near the planet's orbit, we add static mesh refinement. Specifically, we refined an equatorial torus extending 2 × 10^{11} to 8 × 10^{11} cm in *r*, π/4 − 3π/4 in θ, and 0 − 2π in ∅ by one level above the base mesh or a factor of two higher spatial resolution. We also refined a box surrounding the planet location on the mesh by four levels of refinement (i.e., 16× higher spatial resolution than the base mesh) to capture the planet-scale outflow with sufficient resolution in our simulation.

We set our model parameters based on orbital properties (with *e* = 0) that have been derived for HAT-P-32 b (*19*, *21*). To model the planetary outflow, we used the hydrodynamic escape parameter

$$\lambda = \frac{GM_p}{R_p c_s^2} \quad (2)$$

where M_p is the planet's mass, R_p is the planet radius, and c_s is the sound speed of the outflow. We adopted λ = 8 for the planetary wind in our models, implying an outflow temperature of ≈5750 K. This is a free parameter of our current models, and we find that λ particularly affects the stream kinematics, as well as the inferred planetary mass loss rate (*55*). To model the much hotter (≈10^6 K), fast-expanding stellar wind, we adopted λ = 15 and replaced M_p and R_p to be the mass and radius of the host star, respectively, in the Eq. 2. The planetary mass loss rate in our model is 1.07 × 10^{12} g s^{-1} (≈1.7 × 10^{-14} $M_\odot$ $year^{-1}$). This implies a loss time scale for the planetary envelope of $M_p/\dot{M}_p \approx 3.8 \times 10^{10}$ year. The stellar mass loss rate in our model, ≈7 × 10^{-14} $M_\odot$ $year^{-1}$, is on the order of typical main sequence mass loss rates (*56*).

We postprocessed these snapshots by iterating to find the stellar and planetary outflow ionization states in the stellar radiation field. To construct the spectral energy distribution of the host star, we combined the published XUV spectrum of τ Boo (0 to 1200 Å) (*57*), which has the same spectral type as HAT-P-32 A, and the BT-Settl model spectrum (>1200 Å) with an effective temperature of 6300 K and logarithmic surface gravity of log(*g*) = 4.5 dex; we further scaled this spectrum based on the XUV flux estimates from (*21*). We then cast rays from the star through the domain to an observer. The full methodology is presented in (*31*).

Figure 4 demonstrates a slice of gas density through the simulation model domain centered on HAT-P-32 A, showing that an outflow from HAT-P-32 b extends nearly along the orbital path both leading and trailing the planet. This outflow is shaped by its interactions with the much-faster stellar wind (as is visible from unstable interfaces between the higher-density planetary outflow and the lower-density stellar wind). However, the primary force shaping the planetary outflow is the tidal gravity of the star-planet system, which is particularly strong for HAT-P-32 b because the planet is nearly filling its Roche lobe (*21*). As a result, the planetary outflow is slow-moving by comparison to the planet's orbital speed. The differential orbital frequency as a function of the distance from the star means that gas in the planetary outflow is advected into leading and trailing arms of the planet's upper atmosphere.

The consequences for the observable properties of excess helium absorption of this outflow geometry are marked. Figure 7 presents the number density of metastable helium and the RV of gas in the region surrounding the planet. Overlying contours show the cumulative, radial optical depth from the host star in the metastable helium line. These contours show that the columnar structure of planetary outflow maintains relatively high optical depth even at

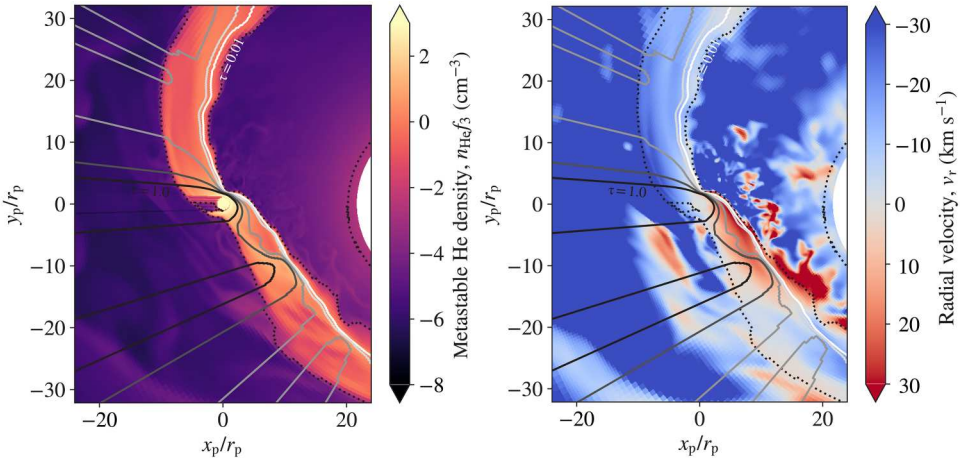

Fig. 7. Number density and RV of the metastable helium in 3D simulations. The left panel shows the showing number density of metastable helium (left) and and the right panel shows the RV in a postprocessed simulation snapshot (same as Fig. 4) . Contours show the cumulative radial optical depths of 0.01 to 1 in half-dex steps (light to dark). The dotted contour shows the surface of $n_{He}f_3 10^{-3}$ cm^{-3}. The extended tidal tails of mass loss in this HAT-P-32 Ab analog system imply significant optical depth of the planetary mass loss even far from the planet itself, in significant contrast to a more-spherical pattern of mass loss. Further, these tidal tails orbit the host star with little RV (or line-of-sight velocity for an observer) implying that their absorption signatures lie close to the stellar rest frame, which is in excellent agreement with observations (see Fig. 2).

large distances from the planet. This can be contrasted to a spherical outflow, in which the optical depth drops steeply with distance above the planetary surface. For the observable properties of HAT-P-32 b's transit, this means that the extended absorption in PRE and POST phases (e.g., Fig. 1) can be attributed to columns of planetary outflow that are strongly shaped by orbital advection into leading and trailing tails.

Figure 7 also shows the RV of material with the same overlying contours of optical depth. We see that on the leading arm, planetary material has a slight redshift, implying flow toward the host star, while material in the trailing arm is slightly blueshifted. The RVs of gas are low compared to the planet's orbital velocity (~170 km s^{-1}). The leading and trailing tails of the planet's escaping atmosphere, therefore, lie close to the stellar rest frame as most of its motion is along the orbit, perpendicular to an observer during transit. Several properties of the model affect the kinematics of the tidal tails of planetary mass loss. We find that one of the strongest effects is the characteristic temperature of the planetary outflow (controlled by the parameter λ in our models). Cooler tidal tails are shaped more strongly by the tidal potential and are broadened less by their own thermal expansion. This suggests that more sophisticated modeling that fully reproduces the EW light curve (Fig. 1) and kinematics as a function of phase (Fig. 2) will be very constraining about the planetary outflow's thermodynamics.

The PRE and POST tails of material need not share an identical temperature (as they currently do in our hydrodynamic models). We find that cooler POST tails better reproduce the redshifts observed several hours after mid-transit. In addition, it is important to highlight that there are physical processes not included in our models that could influence tidal tail kinematics. We have not included momentum deposition by the stellar radiation field on the outflow directly in our models, nor have we systematically varied the orbital eccentricity, the relative strength of the stellar wind, or the thermodynamics of the planetary outflow. Stellar wind and radiation pressure act similarly, applying a roughly r^{-2}-scaled radial pressure away from the star. Increasing these effects blueshifts the trailing tail and can erode the leading tail until the outflow forms a cometary morphology (*31*). Eccentricity introduces waves into the tails, perhaps including subtle RV signatures. Because these effects interact nonlinearly, sophisticated hydrodynamic simulations are needed to explore this phase space and to determine to what degree the observational constraints uniquely determine HAT-P-32 A + b's properties.

We also supplemented our 3D modeling with 1D hydrodynamic models [following (*58*, *59*)] of planetary outflows of varying temperatures, with otherwise equivalent assumptions. At identical temperatures and EW, these 1D models predict ~2× higher planetary mass loss rate because they neglect the compression of material into tidal tails. The 1D models also suggest that the best-fitting mass-loss rate scales as $\dot{M}_p \propto T$ (i.e., $\dot{M}_p \propto_p^1 \lambda_p^{-1}$, where T is the outflow temperature), thus giving an indication of how varying the uncertain planetary outflow thermodynamics affects the inferred planetary mass loss rate [also see (*55*)].

Supplementary Materials

This PDF file includes:
Figs. S1 to S4
Table S1
Legend for data S1
References

Other Supplementary Material for this manuscript includes the following:
Data S1

REFERENCES AND NOTES

1. T. Mazeh, T. Holczer, S. Faigler, Dearth of short-period Neptunian exoplanets: A desert in period-mass and period-radius planes. *Astron. Astrophys.* **589**, 78–81 (2016).
2. J. E. Owen, Y. Wu, Kepler planets: A tale of evaporation. *Astrophys. J.* **775**, 105 (2013).
3. E. D. Lopez, J. J. Fortney, The role of core mass in controlling evaporation: The kepler radius distribution and the Kepler-36 density dichotomy. *Astrophys. J.* **776**, 11 (2013).
4. J. E. Owen, Y. Wu, The evaporation valley in the Kepler planets. *Astrophys. J.* **847**, 29 (2017).
5. S. Ginzburg, H. E. Schlichting, R. Sari, Core-powered mass-loss and the radius distribution of small exoplanets. *Mon. Notices Royal Astron. Soc.* **476**, 759–765 (2018).
6. A. Gupta, H. E. Schlichting, Sculpting the valley in the radius distribution of small exoplanets as a by-product of planet formation: The core-powered mass-loss mechanism. *Mon. Notices Royal Astron. Soc.* **487**, 24–33 (2019).
7. A. Gupta, H. E. Schlichting, Signatures of the core-powered mass-loss mechanism in the exoplanet population: Dependence on stellar properties and observational predictions. *Mon. Notices Royal Astron. Soc.* **493**, 792–806 (2020).
8. R. O. P. Loyd, E. L. Shkolnik, A. C. Schneider, T. Richey-Yowell, T. S. Barman, S. Peacock, I. Pagano, Current population statistics do not favor photoevaporation over core-powered mass loss as the dominant cause of the exoplanet radius gap. *Astrophys. J.* **890**, 23 (2020).
9. J. G. Rogers, A. Gupta, J. E. Owen, H. E. Schlichting, Photoevaporation versus core-powered mass-loss: Model comparison with the 3D radius gap. *Mon. Notices Royal Astron. Soc.* **508**, 5886–5902 (2021).
10. J. J. Spake, D. K. Sing, T. M. Evans, A. Oklopčić, V. Bourrier, L. Kreidberg, B. V. Rackham, J. Irwin, D. Ehrenreich, A. Wyttenbach, H. R. Wakeford, Y. Zhou, K. L. Chubb, N. Nikolov, J. M. Goyal, G. W. Henry, M. H. Williamson, S. Blumenthal, D. R. Anderson, C. Hellier, D. Charbonneau, S. Udry, N. Madhusudhan, Helium in the eroding atmosphere of an exoplanet. *Nature* **557**, 68–70 (2018).
11. R. Allart, V. Bourrier, C. Lovis, D. Ehrenreich, J. J. Spake, A. Wyttenbach, L. Pino, F. Pepe, D. K. Sing, A. Lecavelier des Etangs, Spectrally resolved helium absorption from the extended atmosphere of a warm Neptune-mass exoplanet. *Science* **362**, 1384–1387 (2018).
12. L. Nortmann, E. Pallé, M. Salz, J. Sanz-Forcada, E. Nagel, F. J. Alonso-Floriano, S. Czesla, F. Yan, G. Chen, I. A. G. Snellen, M. Zechmeister, J. H. M. M. Schmitt, M. López-Puertas, N. Casasayas-Barris, F. F. Bauer, P. J. Amado, J. A. Caballero, S. Dreizler, T. Henning, M. Lampón, D. Montes, K. Molaverdikhani, A. Quirrenbach, A. Reiners, I. Ribas, A. Sánchez-López, P. C. Schneider, M. R. Zapatero Osorio, Ground-based detection of an extended helium atmosphere in the Saturn-mass exoplanet WASP-69b. *Science* **362**, 1388–1391 (2018).
13. S. Mahadevan, L. Ramsey, C. Bender, R. Terrien, J. T. Wright, S. Halverson, F. Hearty, M. Nelson, A. Burton, S. Redman, S. Osterman, S. Diddams, J. Kasting, M. Endl, R. Deshpande, The Habitable-zone Planet Finder: A stabilized fiber-fed NIR spectrograph for the Hobby-Eberly Telescope, in *Ground-Based and Airborne Instrumentation for Astronomy IV* (SPIE, 2012), vol. 8446, pp. 624–637.
14. S. Mahadevan, L. W. Ramsey, R. Terrien, S. Halverson, A. Roy, F. Hearty, E. Levi, G. K. Stefansson, P. Robertson, C. Bender, C. Schwab, M. Nelson, The Habitable-zone Planet Finder: A status update on the development of a stabilized fiber-fed near-infrared spectrograph for the for the Hobby-Eberly Telescope, in *Ground-Based and Airborne Instrumentation for Astronomy V* (SPIE, 2014), vol. 9147, pp. 543–552.
15. S. Mahadevan, T. Anderson, E. Balderrama, C. F. Bender, E. Bevins, S. Blakeslee, A. Cole, D. Conran, S. Diddams, A. Dykhouse, J. Darling, C. Fredrick, S. Halverson, F. Hearty, J. Jennings, K. Kaplan, S. Kanodia, E. Levi, E. Lubar, A. J. Metcalf, A. Monson, J. Ninan, C. Nitroy, L. Ramsey, P. Robertson, A. Roy, C. Schwab, M. Shetrone, R. Spencer, G. Stefansson, R. Terrien, J. Wright, The Habitable-zone Planet Finder: Engineering and commissioning on the Hobby Eberly telescope (conference presentation), in *Ground-based and Airborne Instrumentation for Astronomy VII* (SPIE, 2018), vol. 10702, p. 1070214.
16. L. W. Ramsey, M. T. Adams, T. G. Barnes, J. A. Booth, M. E. Cornell, J. R. Fowler, N. I. Gaffney, J. W. Glaspey, J. M. Good, G. J. Hill, P. W. Kelton, V. L. Krabbendam, L. Long, P. J. McQueen, F. B. Ray, R. L. Ricklefs, J. Sage, T. A. Sebring, W. J. Spiesman, M. Steiner, Early performance and present status of the Hobby-Eberly Telescope, in *Advanced Technology Optical/IR Telescopes VI* (SPIE, 1998), vol. 3352, p. 34–42.
17. M. Shetrone, M. E. Cornell, J. R. Fowler, N. Gaffney, B. Laws, J. Mader, C. Mason, S. Odewahn, B. Roman, S. Rostopchin, D. P. Schneider, J. Umbarger, A. Westfall, Ten year review of queue scheduling of the Hobby-Eberly Telescope. *Publ. Astron. Soc. Pac.* **119**, 556–566 (2007).

18. G. J. Hill, H. Lee, P. J. MacQueen, A. Kelz, N. Drory, B. L. Vattiat, J. M. Good, J. Ramsey, H. Kriel, T. Peterson, D. L. DePoy, K. Gebhardt, J. L. Marshall, S. E. Tuttle, S. M. Bauer, T. S. Chonis, M. H. Fabricius, C. Froning, M. Häuser, B. L. Indahl, T. Jahn, M. Landriau, R. Leck, F. Montesano, T. Prochaska, J. M. Snigula, G. Zeimann, R. Bryant, G. Damm, J. R. Fowler, S. Janowiecki, J. Martin, E. Mrozinski, S. Odewahn, S. Rostopchin, M. Shetrone, R. Spencer, E. M. Cooper, T. Armandroff, R. Bender, G. Dalton, U. Hopp, E. Komatsu, H. Nicklas, L. W. Ramsey, M. M. Roth, D. P. Schneider, C. Sneden, M. Steinmetz, The HETDEX instrumentation: Hobby-Eberly Telescope wide-field upgrade and VIRUS. *Astronom. J.* **162**, 298 (2021).
19. J. D. Hartman, G. Á. Bakos, G. Torres, D. W. Latham, G. Kovács, B. Béky, S. N. Quinn, T. Mazeh, A. Shporer, G. W. Marcy, A. W. Howard, D. A. Fischer, J. A. Johnson, G. A. Esquerdo, R. W. Noyes, D. D. Sasselov, R. P. Stefanik, J. M. Fernandez, T. Szklenár, J. Lázár, I. Papp, P. Sári, HAT-P-32b and HAT-P-33b: Two highly inflated hot Jupiters transiting high-jitter stars. *Astrophys. J.* **742**, 59–77 (2011).
20. Y.-H. Wang, S. Wang, T. C. Hinse, Z.-Y. Wu, A. B. Davis, Y. Hori, J.-N. Yoon, W. Han, J.-D. Nie, H.-G. Liu, H. Zhang, J.-L. Zhou, R. A. Wittenmyer, X.-Y. Peng, G. Laughlin, Transiting exoplanet monitoring project (TEMP). V. Transit follow up for HAT-P-9b, HAT-P-32b, and HAT-P-36b. *Astronom. J.* **157**, 82 (2019).
21. S. Czesla, M. Lampón, J. Sanz-Forcada, A. García Muñoz, M. López-Puertas, L. Nortmann, D. Yan, E. Nagel, F. Yan, J. H. M. M. Schmitt, J. Aceituno, P. J. Amado, J. A. Caballero, N. Casasayas-Barris, T. Henning, S. Khalafinejad, K. Molaverdikhani, D. Montes, E. Pallé, A. Reiners, P. C. Schneider, I. Ribas, A. Quirrenbach, M. R. Zapatero Osorio, M. Zechmeister, Hα and He I absorption in HAT-P-32 b observed with CARMENES - Detection of Roche lobe overflow and mass loss. *Astron. Astrophys.* **657**, 10.1051/0004-6361/202039919, (2021).
22. A. Quirrenbach, P. J. Amado, J. A. Caballero, R. Mundt, A. Reiners, I. Ribas, W. Seifert, M. Abril, J. Aceituno, F. J. Alonso-Floriano, M. Ammler-von Eiff, R. Antona Jiménez, H. Anwand-Heerwart, M. Azzaro, F. Bauer, D. Barrado, S. Becerril, V. J. S. Béjar, D. Benítez, Z. M. Berdiñas, M. C. Cárdenas, E. Casal, A. Claret, J. Colomé, M. Cortés-Contreras, S. Czesla, M. Doellinger, S. Dreizler, C. Feiz, M. Fernández, D. Galadí, M. C. Gálvez-Ortiz, A. García-Piquer, M. L. García-Vargas, R. Garrido, L. Gesa, V. Gómez Galera, E. González Álvarez, J. I. González Hernández, U. Grözinger, J. Guàrdia, E. W. Guenther, E. de Guindos, J. Gutiérrez-Soto, H. -J. Hagen, A. P. Hatzes, P. H. Hauschildt, J. Helmling, T. Henning, D. Hermann, L. Hernández Castaño, E. Herrero, D. Hidalgo, G. Holgado, A. Huber, K. F. Huber, S. Jeffers, V. Joergens, E. de Juan, M. Kehr, R. Klein, M. Kürster, A. Lamert, S. Lalitha, W. Laun, U. Lemke, R. Lenzen, M. López del Fresno, B. López Martí, J. López-Santiago, U. Mall, H. Mandel, E. L. Martín, S. Martín-Ruiz, H. Martínez-Rodríguez, C. J. Marvin, R. J. Mathar, E. Mirabet, D. Montes, R. Morales Muñoz, A. Moya, V. Naranjo, A. Ofir, R. Oreiro, E. Pallé, J. Panduro, V.-M. Passegger, A. Pérez-Calpena, D. Pérez Medialdea, M. Perger, M. Pluto, A. Ramón, R. Rebolo, P. Redondo, S. Reffert, S. Reinhardt, P. Rhode, H. -W. Rix, F. Rodler, E. Rodríguez, C. Rodríguez-López, E. Rodríguez-Pérez, R. -R. Rohloff, A. Rosich, E. Sánchez-Blanco, M. A. Sánchez Carrasco, J. Sanz-Forcada, L. F. Sarmiento, S. Schäfer, J. Schiller, C. Schmidt, J. H. M. M. Schmitt, E. Solano, O. Stahl, C. Storz, J. Stürmer, J. C. Suárez, R. G. Ulbrich, G. Veredas, K. Wagner, J. Winkler, M. R. Zapatero Osorio, M. Zechmeister, F. J. Abellán de Paco, G. Anglada-Escudé, C. del Burgo, A. Klutsch, J. L. Lizon, M. López-Morales, J. C. Morales, M. A. C. Perryman, S. M. Tulloch, W. Xu, CARMENES instrument overview, in *Ground-Based and Airborne Instrumentation for Astronomy V* (SPIE, 2014), vol. 9147, pp. 531–542.
23. J. P. Ninan, C. F. Bender, S. Mahadevan, E. B. Ford, A. J. Monson, K. F. Kaplan, R. C. Terrien, A. Roy, P. M. Robertson, S. Kanodia, G. K. Stefansson, The Habitable-zone Planet Finder: Improved flux image generation algorithms for H2RG up-the-ramp data, in *High Energy, Optical, and Infrared Detectors for Astronomy VIII* (SPIE, 2018), vol. 10709, pp. 694–704.
24. K. F. Kaplan, C. F. Bender, R. C. Terrien, J. Ninan, A. Roy, S. Mahadevan, The algorithms behind the HPF and NEID pipeline. *ASPCS* **523**, 567–570 (2019).
25. A. J. Metcalf, T. Anderson, C. F. Bender, S. Blakeslee, W. Brand, D. R. Carlson, W. D. Cochran, S. A. Diddams, M. Endl, C. Fredrick, S. Halverson, D. D. Hickstein, F. Hearty, J. Jennings, S. Kanodia, K. F. Kaplan, E. Levi, E. Lubar, S. Mahadevan, A. Monson, J. P. Ninan, C. Nitroy, S. Osterman, S. B. Papp, F. Quinlan, L. Ramsey, P. Robertson, A. Roy, C. Schwab, S. Sigurdsson, K. Srinivasan, G. Stefansson, D. A. Sterner, R. Terrien, A. Wolszczan, J. T. Wright, G. Ycas, Stellar spectroscopy in the near-infrared with a laser frequency comb. *Optica* **6**, 233–239 (2019).
26. M. Gully-Santiago, J. Luna, C. Morley, K. Kaplan, A. Ganesh, E. Sawczynec, J. Burke, D. Krolikowski, Astronomical échelle spectroscopy data analysis with muler. *J. Open Source Softw.* **7**, 4302 (2022).
27. J. E. Owen, F. C. Adams, Magnetically controlled mass-loss from extrasolar planets in close orbits. *Mon. Notices Royal Astron. Soc.* **444**, 3761–3779 (2014).
28. J. J. Spake, A. Oklopˇić, L. A. Hillenbrand, The posttransit tail of WASP-107b observed at 10830 Å. *Astron. J.* **162**, 284–292 (2021).
29. D. Ehrenreich, V. Bourrier, P. J. Wheatley, A. L. des Etangs, G. Hébrard, S. Udry, X. Bonfils, X. Delfosse, J. M. Désert, D. K. Sing, A. Vidal-Madjar, A giant comet-like cloud of hydrogen escaping the warm Neptune-mass exoplanet GJ 436b. *Nature* **522**, 459–461 (2015).
30. B. Lavie, D. Ehrenreich, V. Bourrier, A. Lecavelier des Etangs, A. Vidal-Madjar, X. Delfosse, A. G. Berna, K. Heng, N. Thomas, S. Udry, P. J. Wheatley, The long egress of GJ 436b's giant exosphere. *Astron. Astrophys.* **605**, L7 (2017).
31. M. MacLeod, A. Oklopˇić, Stellar wind confinement of evaporating exoplanet atmospheres and its signatures in 1083 nm observations. *Astrophys. J.* **926**, 226–238 (2022).
32. A. Oklopˇić, Helium absorption at 1083 nm from extended exoplanet atmospheres: Dependence on stellar radiation. *Astrophys. J.* **881**, 133–140 (2019).
33. I. Carleo, A. Youngblood, S. Redfield, N. C. Barris, T. R. Ayres, H. Vannier, L. Fossati, E. Palle, J. H. Livingston, A. F. Lanza, P. Niraula, J. D. Alvarado-Gómez, G. Chen, D. Gandolfi, E. W. Guenther, J. L. Linsky, E. Nagel, N. Narita, L. Nortmann, E. L. Shkolnik, M. Stangret, A multiwavelength look at the GJ 9827 system: No evidence of extended atmospheres in GJ 9827b and d from HST and CARMENES data. *Astron. J.* **161**, 136–147 (2021).
34. M. Zhang, H. A. Knutson, L. Wang, F. Dai, O. Barragán, Escaping helium from TOI 560.01, a young mini-Neptune. *Astron. J.* **163**, 67–81 (2022).
35. G. Hébrard, A. C. Cameron, D. J. A. Brown, R. F. Díaz, F. Faedi, B. Smalley, D. R. Anderson, D. Armstrong, S. C. C. Barros, J. Bento, F. Bouchy, A. P. Doyle, B. Enoch, Y. G. M. Chew, E. M. Hébrard, C. Hellier, M. Lendl, T. A. Lister, P. F. L. Maxted, J. McCormac, C. Moutou, D. Pollacco, D. Queloz, A. Santerne, I. Skillen, J. Southworth, J. Tregloan-Reed, A. H. M. J. Triaud, S. Udry, M. Vanhuysse, C. A. Watson, R. G. West, P. J. Wheatley, WASP-52b, WASP-58b, WASP-59b, and WASP-60b: Four new transiting close-in giant planets. *Astron. Astrophys.* **549**, 1–11 (2013).
36. P. P. Eggleton, Approximations to the radii of Roche lobes. *Astrophys. J.* **268**, 368–369 (1983).
37. K. Paragas, S. Vissapragada, H. A. Knutson, A. Oklopˇić, Y. Chachan, M. G.-M. Keon, F. Dai, S. Tinyanont, G. Vasisht, Metastable helium reveals an extended atmosphere for the gas giant HAT-P-18b. *Astrophys. J. Lett.* **909**, L10 (2021).
38. C. A. L. Bailer-Jones, J. Rybizki, M. Fouesneau, M. Demleitner, R. Andrae, Estimating distances from parallaxes. V. Geometric and photogeometric distances to 1.47 billion stars in Gaia early data release 3. *Astron. J.* **161**, 147–170 (2021).
39. D. J. A. Brown, Discrepancies between isochrone fitting and gyrochronology for exoplanet host stars? *Mon. Notices Royal Astron. Soc.* **442**, 1844–1862 (2014).
40. H. A. Knutson, B. J. Fulton, B. T. Montet, M. Kao, H. Ngo, A. W. Howard, J. R. Crepp, S. Hinkley, G. Á. Bakos, K. Batygin, J. A. Johnson, T. D. Morton, P. S. Muirhead, Friends of hot jupiters. I. A radial velocity search for massive, long-period companions to close-in gas giant planets. *Astrophys. J.* **785**, 126–148 (2014).
41. M. Zhao, J. G. O'Rourke, J. T. Wright, H. A. Knutson, A. Burrows, J. Fortney, H. Ngo, B. J. Fulton, C. Baranec, R. Riddle, N. M. Law, P. S. Muirhead, S. Hinkley, A. P. Showman, J. Curtis, R. Burruss, Characterization of the atmosphere of the hot Jupiter HAT-P-32Ab and the M-dwarf companion HAT-P-32B. *Astrophys. J.* **796**, 115–129 (2014).
42. J. J. Fortney, M. S. Marley, J. W. Barnes, Planetary radii across five orders of magnitude in mass and stellar insolation: Application to transits. *Astrophys. J.* **659**, 1661–1672 (2007).
43. S. Albrecht, J. N. Winn, J. A. Johnson, A. W. Howard, G. W. Marcy, R. P. Butler, P. Arriagada, J. D. Crane, S. A. Shectman, I. B. Thompson, T. Hirano, G. Bakos, J. D. Hartman, Obliquities of hot Jupiter host stars: Evidence for tidal interactions and primordial misalignments. *Astron. J.* **757**, 18–42 (2012).
44. E. R. Adams, A. K. Dupree, C. Kulesa, D. McCarthy, Adaptive optics images. II. 12 Kepler objects of interest and 15 confirmed transiting planets. *Astron. J.* **146**, 9 (2013).
45. H. Ngo, H. A. Knutson, S. Hinkley, J. R. Crepp, E. B. Bechter, K. Batygin, A. W. Howard, J. A. Johnson, T. D. Morton, P. S. Muirhead, Friends of hot Jupiters. II. No correspondence between hot-Jupiter spin-orbit misalignment and the incidence of directly imaged stellar companions. *Astrophys. J.* **800**, 138–159 (2015).
46. D. Krolikowski, "Exploring the formation and evolutionary pathways of young stars and planetary systems at high precision," thesis, University of Texas at Austin (2022).
47. E. Oliva, L. Origlia, S. Scuderi, S. Benatti, I. Carleo, E. Lapenna, A. Mucciarelli, C. Baffa, V. Biliotti, L. Carbonaro, G. Falcini, E. Giani, M. Iuzzolino, F. Massi, N. Sanna, M. Sozzi, A. Tozzi, A. Ghedina, F. Ghinassi, M. Lodi, A. Harutyunyan, M. P. I. Arcetri, I. Bologna, Inaf-Catania, I. Padova, U. Bologna, I. G. Galilei, Lines and continuum sky emission in the near infrared: Observational constraints from deep high spectral resolution spectra with GIANO-TNG. *Astron. Astrophys.* **581**, 10.1051/0004-6361/201526291, (2015).
48. Q. H. Tran, B. P. Bowler, W. D. Cochran, M. Endl, G. Stefánsson, S. Mahadevan, J. P. Ninan, C. F. Bender, S. Halverson, A. Roy, R. C. Terrien, The epoch of giant planet migration planet search program. I. Near-infrared radial velocity jitter of young sun-like stars. *Astron. J.* **161**, 173–189 (2021).
49. Astropy Collaboration, T. P. Robitaille, E. J. Tollerud, P. Greenfield, M. Droettboom, E. Bray, T. Aldcroft, M. Davis, A. Ginsburg, A. M. Price-Whelan, W. E. Kerzendorf, A. Conley, N. Crighton, K. Barbary, D. Muna, H. Ferguson, F. Grollier, M. M. Parikh, P. H. Nair, H. M. Günther, C. Deil, J. Woillez, S. Conseil, R. Kramer, J. E. H. Turner, L. Singer, R. Fox, B. A. Weaver, V. Zabalza, Z. I. Edwards, K. A. Bostroem, D. J. Burke, A. R. Casey, S. M. Crawford, N. Dencheva, J. Ely, T. Jenness, K. Labrie, P. L. Lim, F. Pierfederici, A. Pontzen, A. Ptak, B.

Refsdal, M. Servillat, O. Streicher, Astropy: A community Python package for astronomy. *Astron. Astrophys.* **558**, 33–41 (2013).

50. The Astropy Collaboration, A. M. Price-Whelan, B. M. Sipőcz, H. M. Günther, P. L. Lim, S. M. Crawford, S. Conseil, D. L. Shupe, M. W. Craig, N. Dencheva, A. Ginsburg, J. T. VanderPlas, L. D. Bradley, D. Pérez-Suárez, M. de Val-Borro; Primary Paper Contributors, T. L. Aldcroft, K. L. Cruz, T. P. Robitaille, E. J. Tollerud; Astropy Coordination Committee, C. Ardelean, T. Babej, Y. P. Bach, M. Bachetti, A. V. Bakanov, S. P. Bamford, G. Barentsen, P. Barmby, A. Baumbach, K. L. Berry, F. Biscani, M. Boquien, K. A. Bostroem, L. G. Bouma, G. B. Brammer, E. M. Bray, H. Breytenbach, H. Buddelmeijer, D. J. Burke, G. Calderone, J. L. C. Rodríguez, M. Cara, J. V. M. Cardoso, S. Cheedella, Y. Copin, L. Corrales, D. Crichton, D. D'Avella, C. Deil, É. Depagne, J. P. Dietrich, A. Donath, M. Droettboom, N. Earl, T. Erben, S. Fabbro, L. A. Ferreira, T. Finethy, R. T. Fox, L. H. Garrison, S. L. J. Gibbons, D. A. Goldstein, R. Gommers, J. P. Greco, P. Greenfield, A. M. Groener, F. Grollier, A. Hagen, P. Hirst, D. Homeier, A. J. Horton, G. Hosseinzadeh, L. Hu, J. S. Hunkeler, Ž. Ivezić, A. Jain, T. Jenness, G. Kanarek, S. Kendrew, N. S. Kern, W. E. Kerzendorf, A. Khvalko, J. King, D. Kirkby, A. M. Kulkarni, A. Kumar, A. Lee, D. Lenz, S. P. Littlefair, Z. Ma, D. M. Macleod, M. Mastropietro, C. McCully, S. Montagnac, B. M. Morris, M. Mueller, S. J. Mumford, D. Muna, N. A. Murphy, S. Nelson, G. H. Nguyen, J. P. Ninan, M. Nöthe, S. Ogaz, S. Oh, J. K. Parejko, N. Parley, S. Pascual, R. Patil, A. A. Patil, A. L. Plunkett, J. X. Prochaska, T. Rastogi, V. R. Janga, J. Sabater, P. Sakurikar, M. Seifert, L. E. Sherbert, H. Sherwood-Taylor, A. Y. Shih, J. Sick, M. T. Silbiger, S. Singanamalla, L. P. Singer, P. H. Sladen, K. A. Sooley, S. Sornarajah, O. Streicher, P. Teuben, S. W. Thomas, G. R. Tremblay, J. E. H. Turner, V. Terrón, M. H. van Kerkwijk, A. de la Vega, L. L. Watkins, B. A. Weaver, J. B. Whitmore, J. Woillez, V. Zabalza; Astropy Contributors, The astropy project: Building an open-science project and status of the v2.0 core package. *Astron. J.* **156**, 123–141 (2018).
51. M. Zechmeister, A. Reiners, P. J. Amado, M. Azzaro, F. F. Bauer, V. J. S. Béjar, J. A. Caballero, E. W. Guenther, H.-J. Hagen, S. V. Jeffers, A. Kaminski, M. Kürster, R. Launhardt, D. Montes, J. C. Morales, A. Quirrenbach, S. Reffert, I. Ribas, W. Seifert, L. Tal-Or, V. Wolthoff, Spectrum radial velocity analyser (SERVAL). High-precision radial velocities and two alternative spectral indicators. *Astron. Astrophys.* **609**, 12–24 (2018).
52. J. Martin, B. Fuhrmeister, M. Mittag, T. O. B. Schmidt, A. Hempelmann, J. N. González-Pérez, J. H. M. M. Schmitt, The Ca II infrared triplet's performance as an activity indicator compared to Ca II H and K. Empiricalrelations to convert Ca II infrared triplet measurements to common activity indices. *Astron. Astrophys.* **605**, 113–127 (2017).
53. M. K. Alam, M. López-Morales, N. Nikolov, D. K. Sing, G. W. Henry, C. Baxter, J. M. Désert, J. K. Barstow, T. Mikal-Evans, V. Bourrier, P. Lavvas, H. R. Wakeford, M. H. Williamson, J. Sanz-Forcada, L. A. Buchhave, O. Cohen, A. G. Muñoz, The Hubble space telescope PanCET program: An optical to infrared transmission spectrum of HAT-P-32Ab. *Astron. J.* **160**, 51–69 (2020).
54. J. M. Stone, K. Tomida, C. J. White, K. G. Felker, The Athena++ adaptive mesh refinement framework: Design and magnetohydrodynamic solvers. *Astrophys. J. Suppl. Ser.* **249**, 4–43 (2020).
55. D. Linssen, A. Oklopčić, M. MacLeod, Constraining planetary mass-loss rates by simulating Parker wind profiles with Cloudy. *Astron. Astrophys.* **667**, 54–67 (2022).
56. B. E. Wood, H.-R. Müller, G. P. Zank, J. L. Linsky, Measured mass-loss rates of solar-like stars as a function of age and activity. *Astrophys. J.* **574**, 412–425 (2002).
57. J. Sanz-Forcada, G. Micela, I. Ribas, A. M. T. Pollock, C. Eiroa, A. Velasco, E. Solano, D. García-Álvarez, Estimation of the XUV radiation onto close planets and their evaporation. *Astron. Astrophys.* **532**, 6–23 (2011).
58. A. Oklopčić, C. M. Hirata, A new window into escaping exoplanet atmospheres: 10830 Å line of helium. *Astrophys. J. Lett.* **855**, L11 (2018).
59. J. P. Ninan, G. Stefansson, S. Mahadevan, C. Bender, P. Robertson, L. Ramsey, R. Terrien, J. Wright, S. A. Diddams, S. Kanodia, W. Cochran, M. Endl, E. B. Ford, C. Fredrick, S. Halverson, F. Hearty, J. Jennings, K. Kaplan, E. Lubar, A. J. Metcalf, A. Monson, C. Nitroy, A. Roy, C. Schwab, Evidence for He I 10830 Å absorption during the transit of a warm Neptune around the M-dwarf GJ 3470 with the Habitable-zone Planet Finder. *Astrophys. J.* **894**, 97–105 (2020).
60. M. Zhang, H. A. Knutson, F. Dai, L. Wang, G. R. Ricker, R. P. Schwarz, C. Mann, K. Collins, Detection of atmospheric escape from four young mini-Neptunes. *Astron. J.* **165**, 62–77 (2023).
61. E. Gaidos, T. Hirano, R. A. Lee, H. Harakawa, K. Hodapp, S. Jacobson, T. Kotani, T. Kudo, T. Kurokawa, M. Kuzuhara, J. Nishikawa, M. Omiya, T. Serizawa, M. Tamura, A. Ueda, S. Vievard, Planet(esimal)s around stars with *TESS* (PAST) III: A search for triplet He I in the atmospheres of two 200 Myr-old planets. *Mon. Notices. Royal Astron. Soc.* **518**, 3777–3783 (2022).
62. A. W. Mann, A. Vanderburg, A. C. Rizzuto, A. L. Kraus, P. Berlind, A. Bieryla, M. L. Calkins, G. A. Esquerdo, D. W. Latham, G. N. Mace, N. R. Morris, S. N. Quinn, K. R. Sokal, R. P. Stefanik, Zodiacal exoplanets in time (ZEIT). VI. A three-planet system in the Hyades cluster including an Earth-sized planet. *Astron. J.* **155**, 4–14 (2018).
63. D. R. Ciardi, I. J. M. Crossfield, A. D. Feinstein, J. E. Schlieder, E. A. Petigura, T. J. David, M. Bristow, R. I. Patel, L. Arnold, B. Benneke, J. L. Christiansen, C. D. Dressing, B. J. Fulton, A. W. Howard, H. Isaacson, E. Sinukoff, B. Thackeray, K2-136: A binary system in the Hyades cluster hosting a Neptune-sized planet. *Astron. J.* **155**, 10–20 (2018).
64. E. Gaidos, T. Hirano, M. Omiya, M. Kuzuhara, T. Kotani, M. Tamura, H. Harakawa, T. Kudo, Zodiacal exoplanets in time (ZEIT). XIV. He I transit spectroscopy of the 650 Myr Hyades planet K2-136c. *Res. Notes AAS* **5**, 238 (2021).
65. J. Fernández, P. J. Wheatley, X-ray irradiation of three planets around Hyades star K2−136. *Astron. Notes* **343**, e210076 (2022).
66. O. Barragán, S. Aigrain, D. Kubyshkina, D. Gandolfi, J. Livingston, M. C. V. Fridlund, L. Fossati, J. Korth, H. Parviainen, L. Malavolta, E. Palle, H. J. Deeg, G. Nowak, V. M. Rajpaul, N. Zicher, G. Antoniciello, N. Narita, S. Albrecht, L. R. Bedin, J. Cabrera, W. D. Cochran, J. de Leon, P. Eigmüller, A. Fukui, V. Granata, S. Grziwa, E. Guenther, A. P. Hatzes, N. Kusakabe, D. W. Latham, M. Libralato, R. Luque, P. Montañés-Rodríguez, F. Murgas, D. Nardiello, I. Pagano, G. Piotto, C. M. Persson, S. Redfield, M. Tamura, Radial velocity confirmation of K2-100b: A young, highly irradiated, and low-density transiting hot Neptune. *Mon. Notices Royal Astron. Soc.* **490**, 698–708 (2019).
67. E. Gaidos, T. Hirano, A. W. Mann, D. A. Owens, T. A. Berger, K. France, A. Vanderburg, H. Harakawa, K. W. Hodapp, M. Ishizuka, S. Jacobson, M. Konishi, T. Kotani, T. Kudo, T. Kurokawa, M. Kuzuhara, J. Nishikawa, M. Omiya, T. Serizawa, M. Tamura, A. Ueda, Zodiacal exoplanets in time - X. The orbit and atmosphere of the young 'neptune desert'-dwelling planet K2-100b. *Mon. Notices Royal Astron. Soc.* **495**, 650–662 (2020).
68. T. J. David, E. A. Petigura, R. Luger, D. Foreman-Mackey, J. H. Livingston, E. E. Mamajek, L. A. Hillenbrand, Four newborn planets transiting the young solar analog V1298 tau. *Astrophys. J. Lett.* **885**, L12 (2019).
69. S. Vissapragada, G. Stefánsson, M. Greklek-McKeon, A. Oklopčić, H. A. Knutson, J. P. Ninan, S. Mahadevan, C. I. Cañas, Y. Chachan, W. D. Cochran, K. A. Collins, F. Dai, T. J. David, S. Halverson, S. L. Hawley, L. Hebb, S. Kanodia, A. F. Kowalski, J. H. Livingston, M. Maney, A. J. Metcalf, C. Morley, L. W. Ramsey, P. Robertson, A. Roy, J. Spake, C. Schwab, R. C. Terrien, S. Tinyanont, G. Vasisht, J. Wisniewski, A search for planetary metastable helium absorption in the V1298 tau system. *Astron. J.* **162**, 222–231 (2021).
70. K. Poppenhaeger, L. Ketzer, M. Mallonn, X-ray irradiation and evaporation of the four young planets around V1298 tau. *Mon. Notices Royal Astron. Soc.* **500**, 4560–4572 (2020).
71. M. Gillon, A. H. M. J. Triaud, B. O. Demory, E. Jehin, E. Agol, K. M. Deck, S. M. Lederer, J. de Wit, A. Burdanov, J. G. Ingalls, E. Bolmont, J. Leconte, S. N. Raymond, F. Selsis, M. Turbet, K. Barkaoui, A. Burgasser, M. R. Burleigh, S. J. Carey, A. Chaushev, C. M. Copperwheat, L. Delrez, C. S. Fernandes, D. L. Holdsworth, E. J. Kotze, V. van Grootel, Y. Almleaky, Z. Benkhaldoun, P. Magain, D. Queloz, Seven temperate terrestrial planets around the nearby ultracool dwarf star TRAPPIST-1. *Nature* **542**, 456–460 (2017).
72. P. J. Wheatley, T. Louden, V. Bourrier, D. Ehrenreich, M. Gillon, Strong XUV irradiation of the Earth-sized exoplanets orbiting the ultracool dwarf TRAPPIST-1. *Mon. Notices Royal Astron. Soc.* **465**, L74–L78 (2017).
73. V. Krishnamurthy, T. Hirano, G. Stefánsson, J. P. Ninan, S. Mahadevan, E. Gaidos, R. Kopparapu, B. Sato, Y. Hori, C. F. Bender, C. I. Cañas, S. A. Diddams, S. Halverson, H. Harakawa, S. Hawley, F. Hearty, L. Hebb, K. Hodapp, S. Jacobson, S. Kanodia, M. Konishi, T. Kotani, A. Kowalski, T. Kudo, T. Kurokawa, M. Kuzuhara, A. Lin, M. Maney, A. J. Metcalf, B. Morris, J. Nishikawa, M. Omiya, P. Robertson, A. Roy, C. Schwab, T. Serizawa, M. Tamura, A. Ueda, S. Vievard, J. Wisniewski, Nondetection of helium in the upper atmospheres of TRAPPIST-1b, e, and f. *Astron. J.* **162**, 82–89 (2021).
74. E. Agol, C. Dorn, S. L. Grimm, M. Turbet, E. Ducrot, L. Delrez, M. Gillon, B. O. Demory, A. Burdanov, K. Barkaoui, Z. Benkhaldoun, E. Bolmont, A. Burgasser, S. Carey, J. de Wit, D. Fabrycky, D. Foreman-Mackey, J. Haldemann, D. M. Hernandez, J. Ingalls, E. Jehin, Z. Langford, J. Leconte, S. M. Lederer, R. Luger, R. Malhotra, V. S. Meadows, B. M. Morris, F. J. Pozuelos, D. Queloz, S. N. Raymond, F. Selsis, M. Sestovic, A. H. M. J. Triaud, V. V. Grootel, Refining the transit-timing and photometric analysis of TRAPPIST-1: Masses, radii, densities, dynamics, and ephemerides. *Planet. Sci. J.* **2**, 1–38 (2021).
75. O. D. Turner, D. R. Anderson, K. Barkaoui, F. Bouchy, Z. Benkhaldoun, D. J. A. Brown, A. Burdanov, A. Collier Cameron, E. Ducrot, M. Gillon, C. Hellier, E. Jehin, M. Lendl, P. F. L. Maxted, L. D. Nielsen, F. Pepe, D. Pollacco, F. J. Pozuelos, D. Queloz, D. Ségransan, B. Smalley, A. H. M. J. Triaud, S. Udry, R. G. West, Three hot-Jupiters on the upper edge of the mass-radius distribution: WASP-177, WASP-181, and WASP-183. *Mon. Notices Royal Astron. Soc.* **485**, 5790–5799 (2019).
76. J. Kirk, L. A. dos Santos, M. López-Morales, M. K. Alam, A. Oklopčić, M. MacLeod, L. Zeng, G. Zhou, Keck/NIRSPEC studies of He I in the atmospheres of two inflated hot gas giants orbiting K dwarfs: WASP-52b and WASP-177b. *Astron. J.* **164**, 24–37 (2022).
77. D. Kasper, J. L. Bean, A. Oklopčić, I. Malsky, E. M. R. Kempton, J. M. Désert, L. A. Rogers, M. Mansfield, Nondetection of helium in the upper atmospheres of three sub-Neptune exoplanets. *Astron. J.* **160**, 258–270 (2020).
78. K. Rice, L. Malavolta, A. Mayo, A. Mortier, L. A. Buchhave, L. Affer, A. Vanderburg, M. Lopez-Morales, E. Poretti, L. Zeng, A. C. Cameron, M. Damasso, A. Coffinet, D. W. Latham, A. S.

Bonomo, F. Bouchy, D. Charbonneau, X. Dumusque, P. Figueira, A. F. Martinez Fiorenzano, R. D. Haywood, J. A. Johnson, E. Lopez, C. Lovis, M. Mayor, G. Micela, E. Molinari, V. Nascimbeni, C. Nava, F. Pepe, D. F. Phillips, G. Piotto, D. Sasselov, D. Ségransan, A. Sozzetti, S. Udry, C. Watson, Masses and radii for the three super-Earths orbiting GJ 9827, and implications for the composition of small exoplanets. *Mon. Notices Royal Astron. Soc.* **484**, 3731–3745 (2019).

79. T. G. Ellis, T. Boyajian, K. von Braun, R. Ligi, D. Mourard, D. Dragomir, G. H. Schaefer, C. D. Farrington, Directly determined properties of HD 97658 from interferometric observations. *Astron. J.* **162**, 118–126 (2021).
80. B.-O. Demory, M. Gillon, D. Deming, D. Valencia, S. Seager, B. Benneke, C. Lovis, P. Cubillos, J. Harrington, K. B. Stevenson, M. Mayor, F. Pepe, D. Queloz, D. Ségransan, S. Udry, Detection of atransit of the super-Earth 55 Cancri e with warm Spitzer. *Astron. Astrophys.* **533**, 114–120 (2011).
81. V. Bourrier, X. Dumusque, C. Dorn, G. W. Henry, N. Astudillo-Defru, J. Rey, B. Benneke, G. Hébrard, C. Lovis, B. O. Demory, C. Moutou, D. Ehrenreich, The 55 Cancri system reassessed. *Astron. Astrophys.* **619**, 1–18 (2018).
82. M. Zhang, H. A. Knutson, L. Wang, F. Dai, A. Oklopcic, R. Hu, No escaping helium from 55 Cnc e. *Astron. J.* **161**, 181–198 (2021).
83. B. S. Gaudi, K. G. Stassun, K. A. Collins, T. G. Beatty, G. Zhou, D. W. Latham, A. Bieryla, J. D. Eastman, R. J. Siverd, J. R. Crepp, E. J. Gonzales, D. J. Stevens, L. A. Buchhave, J. Pepper, M. C. Johnson, K. D. Colon, E. L. N. Jensen, J. E. Rodriguez, V. Bozza, S. C. Novati, G. D'Ago, M. T. Dumont, T. Ellis, C. Gaillard, H. Jang-Condell, D. H. Kasper, A. Fukui, J. Gregorio, A. Ito, J. F. Kielkopf, M. Manner, K. Matt, N. Narita, T. E. Oberst, P. A. Reed, G. Scarpetta, D. C. Stephens, R. R. Yeigh, R. Zambelli, B. J. Fulton, A. W. Howard, D. J. James, M. Penny, D. Bayliss, I. A. Curtis, D. L. DePoy, G. A. Esquerdo, A. Gould, M. D. Joner, R. B. Kuhn, J. Labadie-Bartz, M. B. Lund, J. L. Marshall, K. K. McLeod, R. W. Pogge, H. Relles, C. Stockdale, T. G. Tan, M. Trueblood, P. Trueblood, A giant planet undergoing extreme-ultraviolet irradiation by its hot massive-star host. *Nature* **546**, 514–518 (2017).
84. G. Torres, J. N. Winn, M. J. Holman, Improved parameters for extrasolar transiting planets. *Astrophys. J.* **677**, 1324–1342 (2008).
85. G. Maciejewski, A. Niedzielski, G. Nowak, E. Pallé, B. Tingley, R. Errmann, R. Neuhäuser, On the GJ 436 planetary system. *Acta Astron.* **64**, 323–335 (2014).
86. A. H. M. J. Triaud, M. Gillon, D. Ehrenreich, E. Herrero, M. Lendl, D. R. Anderson, A. Collier Cameron, L. Delrez, B. O. Demory, C. Hellier, K. Heng, E. Jehin, P. F. L. Maxted, D. Pollacco, D. Queloz, I. Ribas, B. Smalley, A. M. S. Smith, S. Udry, WASP-80b has a dayside within the T-dwarf range. *Mon. Notices Royal Astron. Soc.* **450**, 2279–2290 (2015).
87. L. Fossati, G. Guilluy, I. F. Shaikhislamov, I. Carleo, F. Borsa, A. S. Bonomo, P. Giacobbe, M. Rainer, C. Cecchi-Pestellini, M. L. Khodachenko, M. A. Efimov, M. S. Rumenskikh, I. B. Miroshnichenko, A. G. Berezutsky, V. Nascimbeni, M. Brogi, A. F. Lanza, L. Mancini, L. Affer, S. Benatti, K. Biazzo, A. Bignamini, D. Carosati, R. Claudi, R. Cosentino, E. Covino, S. Desidera, A. Fiorenzano, A. Harutyunyan, A. Maggio, L. Malavolta, J. Maldonado, G. Micela, E. Molinari, I. Pagano, M. Pedani, G. Piotto, E. Poretti, G. Scandariato, A. Sozzetti, H. Stoev, The GAPS Programme at TNG. XXXII. The revealing non-detection of metastable He I in the atmosphere of the hot Jupiter WASP-80b. *Astron. Astrophys.* **658**, 136–149 (2022).
88. L. A. dos Santos, D. Ehrenreich, V. Bourrier, R. Allart, G. King, M. Lendl, C. Lovis, S. Margheim, J. Mel'endez, J. Seidel, S. Sousa, Search for helium in the upper atmosphere of the hot Jupiter WASP-127 b using Gemini/Phoenix. *Astron. Astrophys.* **640**, 29–33 (2020).
89. K. W. F. Lam, F. Faedi, D. J. A. Brown, D. R. Anderson, L. Delrez, M. Gillon, G. Hébrard, M. Lendl, L. Mancini, J. Southworth, B. Smalley, A. H. M. Triaud, O. D. Turner, K. L. Hay, D. J. Armstrong, S. C. C. Barros, A. S. Bonomo, F. Bouchy, P. Boumis, A. C. Cameron, A. P. Doyle, C. Hellier, T. Henning, E. Jehin, G. King, J. Kirk, T. Louden, P. F. L. Maxted, J. J. M. Cormac, H. P. Osborn, E. Palle, F. Pepe, D. Pollacco, J. Prieto-Arranz, D. Queloz, J. Rey, D. Ségransan, S. Udry, S. Walker, R. G. West, P. J. Wheatley, From dense hot Jupiter to low-density Neptune: The discovery of WASP-127b, WASP-136b, and WASP-138b. *Astron. Astrophys.* **599**, A3 (2017).
90. J. V. Seidel, M. Lendl, V. Bourrier, D. Ehrenreich, R. Allart, S. G. Sousa, H. M. Cegla, X. Bonfils, U. Conod, A. Grandjean, A. Wyttenbach, N. Astudillo-Defru, D. Bayliss, K. Heng, B. Lavie, C. Lovis, C. Melo, F. Pepe, D. Ségransan, S. Udry, Hot exoplanet atmospheres resolved with transit spectroscopy (HEARTS). VI. Non-detection of sodium with HARPS on the bloated super-Neptune WASP-127b. *Astron. Astrophys.* **643**, A45–A54 (2020).
91. N. Casasayas-Barris, J. Orell-Miquel, M. Stangret, L. Nortmann, F. Yan, M. Oshagh, E. Palle, J. Sanz-Forcada, M. López-Puertas, E. Nagel, R. Luque, G. Morello, I. A. G. Snellen, M. Zechmeister, A. Quirrenbach, J. A. Caballero, I. Ribas, A. Reiners, P. J. Amado, G. Bergond, S. Czesla, T. Henning, S. Khalafinejad, K. Molaverdikhani, D. Montes, M. Perger, A. Sánchez-López, E. Sedaghati, CARMENES detection of the ca II infrared triplet and possible evidence of He I in the atmosphere of WASP-76b. *Astron. Astrophys.* **654**, A163–A182 (2021).
92. R. G. West, J.-M. Almenara, D. R. Anderson, F. Bouchy, D. J. A. Brown, A. C. Cameron, M. Deleuil, L. Delrez, A. P. Doyle, F. Faedi, A. Fumel, M. Gillon, G. Hebrard, C. Hellier, E. Jehin, M. Lendl, P. F. L. Maxted, F. Pepe, D. Pollacco, D. Queloz, D. Segransan, B. Smalley, A. M. S. Smith, A. H. M. J. Triaud, S. Udry, Three irradiated and bloated hot Jupiters: WASP-76b, WASP-82b, and WASP-90b. *Astron. Astrophys.* **585**, A126–A132 (2016).
93. J. D. Hartman, G. Á. Bakos, B. Sato, G. Torres, R. W. Noyes, D. W. Latham, G. Kovács, D. A. Fischer, A. W. Howard, J. A. Johnson, G. W. Marcy, L. A. Buchhave, G. Füresz, G. Perumpilly, B. Béky, R. P. Stefanik, D. D. Sasselov, G. A. Esquerdo, M. Everett, Z. Csubry, J. Lázár, I. Papp, P. Sári, HAT-P-18b and HAT-P-19b: Two low-density Saturn-mass planets transiting metal-rich K stars. *Astrophys. J.* **726**, 52–67 (2011).
94. O. Barragán, D. J. Armstrong, D. Gandolfi, I. Carleo, A. A. Vidotto, C. V. D'Angelo, A. Oklop˘ić, H. Isaacson, D. Oddo, K. Collins, M. Fridlund, S. G. Sousa, C. M. Persson, C. Hellier, S. Howell, A. Howard, S. Redfield, N. Eisner, I. Y. Georgieva, D. Dragomir, D. Bayliss, L. D. Nielsen, B. Klein, S. Aigrain, M. Zhang, J. Teske, J. D. Twicken, J. Jenkins, M. Esposito, V. Van Eylen, F. Rodler, V. Adibekyan, J. Alarcon, D. R. Anderson, J. M. A. Murphy, D. Barrado, S. C. C. Barros, B. Benneke, F. Bouchy, E. M. Bryant, P. Butler, J. Burt, J. Cabrera, S. Casewell, P. Chaturvedi, R. Cloutier, W. D. Cochran, J. Crane, I. Crossfield, N. Crouzet, K. I. Collins, F. Dai, H. J. Deeg, A. Deline, O. D. S. Demangeon, X. Dumusque, P. Figueira, E. Furlan, C. Gnilka, M. R. Goad, E. Goffo, F. Gutiérrez-Canales, A. Hadjigeorghiou, Z. Hartman, A. P. Hatzes, M. Harris, B. Henderson, T. Hirano, S. Hojjatpanah, S. Hoyer, P. Kabáth, J. Korth, J. Lillo-Box, R. Luque, M. Marmier, T. Mo˘nik, A. Muresan, F. Murgas, E. Nagel, H. L. M. Osborne, A. Osborn, H. P. Osborn, E. Palle, M. Raimbault, G. R. Ricker, R. A. Rubenzahl, C. Stockdale, N. C. Santos, N. Scott, R. P. Schwarz, S. Shectman, M. Raimbault, S. Seager, D. Ségransan, L. M. Serrano, M. Skarka, A. M. S. Smith, J. Šubjak, T. G. Tan, S. Udry, C. Watson, P. J. Wheatley, R. West, J. N. Winn, S. X. Wang, A. Wolfgang, C. Ziegler, The young HD 73583 (TOI-560) planetary system: Two 10-$M_{\oplus}$ mini-Neptunes transiting a 500-Myr-old, bright, and active K dwarf. *Mon. Notices Royal Astron. Soc.* **514**, 1606–1627 (2022).
95. K. G. Stassun, K. A. Collins, B. S. Gaudi, Accurate empirical radii and masses of planets and their host stars with *Gaia* parallaxes. *Astron. J.* **153**, 136–155 (2017).
96. F. J. Alonso-Floriano, I. Snellen, S. Czesla, F. Bauer, M. Salz, M. Lamp'on, L. Lara, E. Nagel, M. L'opez-Puertas, L. Nortmann, A. Sánchez-López, J. Sanz-Forcada, J. Caballero, A. Reiners, I. Ribas, A. Quirrenbach, P. Amado, J. Aceituno, G. Anglada-Escud'e, V. B'ejar, M. Brinkmöller, A. Hatzes, T. Henning, A. Kaminski, M. Kürster, F. Labarga, D. Montes, E. Pall'e, J. Schmitt, M. Z. Z. Osorio, He I λ 10 830 Å in the transmission spectrum of HD209458 b. *Astron. Astrophys.* **629**, 110–116 (2019).
97. H. P. Osborn, A. Bonfanti, D. Gandolfi, C. Hedges, A. Leleu, A. Fortier, D. Futyan, P. Gutermann, P. F. L. Maxted, L. Borsato, K. A. Collins, J. G. da Silva, Y. G. M. Chew, M. J. Hooton, M. Lendl, H. Parviainen, S. Salmon, N. Schanche, L. M. Serrano, S. G. Sousa, A. Tuson, S. Ulmer-Moll, V. Van Grootel, R. D. Wells, T. G. Wilson, Y. Alibert, R. Alonso, G. Anglada, J. Asquier, D. B. Y. Navascues, W. Baumjohann, T. Beck, W. Benz, F. Biondi, X. Bonfils, F. Bouchy, A. Brandeker, C. Broeg, T. Bárczy, S. C. C. Barros, J. Cabrera, S. Charnoz, A. C. Cameron, S. Csizmadia, M. B. Davies, M. Deleuil, L. Delrez, B.-O. Demory, D. Ehrenreich, A. Erikson, L. Fossati, M. Fridlund, M. Gillon, M. A. Gómez-Muñoz, M. Güdel, K. Heng, S. Hoyer, K. G. Isaak, L. Kiss, J. Laskar, A. L. D. Etangs, C. Lovis, D. Magrin, L. Malavolta, J. M. Cormac, V. Nascimbeni, G. Olofsson, R. Ottensamer, I. Pagano, E. Pallé, G. Peter, D. Piazza, G. Piotto, D. Pollacco, D. Queloz, R. Ragazzoni, N. Rando, H. Rauer, C. Reimers, I. Ribas, O. D. S. Demangeon, A. M. S. Smith, L. Sabin, N. Santos, G. Scandariato, U. Schroffenegger, R. P. Schwarz, A. Shporer, A. E. Simon, M. Steller, G. M. Szabó, D. Ségransan, N. Thomas, S. Udry, I. Walter, N. Walton, Uncovering the true periods of the young sub-Neptunes orbiting TOI-2076. *Astron. Astrophys.* **644**, 156–172 (2022).
98. M. Salz, S. Czesla, P. Schneider, E. Nagel, J. Schmitt, L. Nortmann, F. J. Alonso-Floriano, M. L'opez-Puertas, M. Lamp'on, F. Bauer, I. Snellen, E. Pall'e, J. Caballero, F. Yan, G. Chen, J. Sanz-Forcada, P. Amado, A. Quirrenbach, I. Ribas, A. Reiners, V. B'ejar, N. Casasayas-Barris, M. Cort'es-Contreras, S. Dreizler, E. Guenther, T. Henning, S. Jeffers, A. Kaminski, M. Kürster, M. Lafarga, L. Lara, K. Molaverdikhani, D. Montes, J. Morales, A. Sánchez-López, W. Seifert, M. Z. Z. Osorio, M. Zechmeister, Detection of He I λ10830 Å absorption on HD 189733 b with CARMENES high-resolution transmission spectroscopy. *Astron. Astrophys.* **620**, 97–109 (2018).
99. G. Guilluy, V. Andretta, F. Borsa, P. Giacobbe, A. Sozzetti, E. Covino, V. Bourrier, L. Fossati, A. S. Bonomo, M. Esposito, M. S. Giampapa, A. Harutyunyan, M. Rainer, M. Brogi, G. Bruno, R. Claudi, G. Frustagli, A. F. Lanza, L. Mancini, L. Pino, E. Poretti, G. Scandariato, L. Affer, C. Baffa, A. Baruffolo, S. Benatti, K. Biazzo, A. Bignamini, W. Boschin, I. Carleo, M. Cecconi, R. Cosentino, M. Damasso, S. Desidera, G. Falcini, A. F. M. Fiorenzano, A. Ghedina, E. González-Álvarez, J. Guerra, N. Hernandez, G. Leto, A. Maggio, L. Malavolta, J. Maldonado, G. Micela, E. Molinari, V. Nascimbeni, I. Pagano, M. Pedani, G. Piotto, A. Reiners, The GAPS programme at TNG. XXII. The GIARPS view of the extended helium atmosphere of HD 189733 b accounting for stellar activity. *Astron. Astrophys.* **639**, A49 (2020).
100. G. Á. Bakos, G. Torres, A. Pál, J. Hartman, G. Kovács, R. W. Noyes, D. W. Latham, D. D. Sasselov, B. Sipőcz, G. A. Esquerdo, D. A. Fischer, J. A. Johnson, G. W. Marcy, R. P. Butler, H. Isaacson, A. Howard, S. Vogt, G. Kovács, J. Fernandez, A. Moór, R. P. Stefanik, J. Lázár, I. Papp, P. Sári, HAT-P-11b: A super-Neptune planet transiting a bright K star in the Kepler field. *Astrophys. J.* **710**, 1724–1745 (2010).
101. S. W. Yee, E. A. Petigura, B. J. Fulton, H. A. Knutson, K. Batygin, G. Bakos, J. D. Hartman, L. A. Hirsch, A. W. Howard, H. Isaacson, M. R. Kosiarek, E. Sinukoff, L. M. Weiss, HAT-P-11:

Discovery of a second planet and a clue to understanding exoplanet obliquities. *Astron. J.* **155**, 255–267 (2018).

102. S. Awiphan, E. Kerins, S. Pichadee, S. Komonjinda, V. S. Dhillon, W. Rujopakarn, S. Poshyachinda, T. R. Marsh, D. E. Reichart, K. M. Ivarsen, J. B. Haislip, Transit timing variation and transmission spectroscopy analyses of the hot Neptune GJ3470b. *Mon. Notices Royal Astron. Soc.* **463**, 2574–2582 (2016).
103. E. Palle, L. Nortmann, N. Casasayas-Barris, M. Lampón, M. López-Puertas, J. A. Caballero, J. Sanz-Forcada, L. M. Lara, E. Nagel, F. Yan, F. J. Alonso-Floriano, P. J. Amado, G. Chen, C. Cifuentes, M. Cortés-Contreras, S. Czesla, K. Molaverdikhani, D. Montes, V. M. Passegger, A. Quirrenbach, A. Reiners, I. Ribas, A. Sánchez-López, A. Schweitzer, M. Stangret, M. R. Z. Osorio, M. Zechmeister, AHe I upper atmosphere around the warm Neptune GJ 3470 b. *Astron. Astrophys.* **638**, 61–68 (2020).
104. J. Orell-Miquel, F. Murgas, E. Pallé, M. Lampón, M. López-Puertas, J. Sanz-Forcada, E. Nagel, A. Kaminski, N. Casasayas-Barris, L. Nortmann, R. Luque, K. Molaverdikhani, E. Sedaghati, J. A. Caballero, P. J. Amado, G. Bergond, S. Czesla, A. P. Hatzes, T. Henning, S. Khalafinejad, D. Montes, G. Morello, A. Quirrenbach, A. Reiners, I. Ribas, A. Sánchez-López, A. Schweitzer, M. Stangret, F. Yan, M. R. Z. Osorio, A tentative detection of He I in the atmosphere of GJ 1214 b. *Astron. Astrophys.* **659**, 55–66 (2022).
105. D. J. M. Petit dit de la Roche, M. E. van den Ancker, P. A. Miles-Paez, An upper limit on the extended helium atmosphere of GJ 1214 b. *Res. Notes AAS* **4**, 231 (2020).
106. R. Cloutier, D. Charbonneau, D. Deming, X. Bonfils, N. Astudillo-Defru, A more precise mass for GJ 1214 b and the frequency of multiplanet systems around mid-M dwarfs. *Astron. J.* **162**, 174–188 (2021).
107. S. Vissapragada, H. A. Knutson, N. Jovanovic, C. K. Harada, A. Oklopˇcić, J. Eriksen, D. Mawet, M. A. Millar-Blanchaer, S. Tinyanont, G. Vasisht, Constraints on metastable helium in the atmospheres of WASP-69b and WASP-52b with ultranarrowband photometry. *Astron. J.* **159**, 278–290 (2020).
108. R. Allart, V. Bourrier, C. Lovis, D. Ehrenreich, J. Aceituno, A. Guijarro, F. Pepe, D. K. Sing, J. J. Spake, A. Wyttenbach, High-resolution confirmation of an extended helium atmosphere around WASP-107b. *Astron. Astrophys.* **623**, 58–63 (2019).
109. J. Kirk, M. K. Alam, M. López-Morales, L. Zeng, Confirmation of WASP-107b's extended helium atmosphere with keck II/NIRSPEC. *Astron. J.* **159**, 115–123 (2020).
110. T. Moˇnik, C. Hellier, D. R. Anderson, B. J. M. Clark, J. Southworth, Starspots on WASP-107 and pulsations of WASP-118. *Mon. Notices Royal Astron. Soc.* **469**, 1622–1629 (2017).
111. C. Piaulet, B. Benneke, R. A. Rubenzahl, A. W. Howard, E. J. Lee, D. Thorngren, R. Angus, M. Peterson, J. E. Schlieder, M. Werner, L. Kreidberg, T. Jaouni, I. J. M. Crossfield, D. R. Ciardi, E. A. Petigura, J. Livingston, C. D. Dressing, B. J. Fulton, C. Beichman, J. L. Christiansen, V. Gorjian, K. K. Hardegree-Ullman, J. Krick, E. Sinukoff, WASP-107b's density is even lower: A case study for the physics of planetary gas envelope accretion and orbital migration. *Astron. J.* **161**, 70–82 (2021).

Acknowledgments: These results are based on observations obtained with the Habitable-zone Planet Finder Spectrograph on the HET. The HET is a joint project of the University of Texas at Austin, the Pennsylvania State University, Ludwig-Maximilians-Universität München, and Georg-August Universität Gottingen. The HET is named in honor of its principal benefactors, W. P. Hobby and R. E. Eberly. The HET collaboration acknowledges the support and resources from the Texas Advanced Computing Center. We are grateful to the HET Resident Astronomers and Telescope Operators for valuable assistance in gathering our HPF data. **Funding:** This work was supported by NASA Exoplanets Research Program grant number 80NSSC20K0257 (to Z.Z., C.V.M., J.L., and M.G.-S.), Dutch Research Council NWO Veni Grant (to A.O.), National Science Foundation grant 2108801 (to W.D.C.), and NASA Hubble Fellowship grants HST-HF2-51522.001-A (to Z.Z.) and HST-HF2-51519.001-A (to G.S.). The HPF team was also supported by the NSF grants AST-1006676, AST-1126413, AST-1310875, AST-1310885, AST 2009889, AST 2009982, ATI 2009955, and AAG 2108512 and the Heising-Simons Foundation via grant 2017-0494. **Author contributions:** Data acquisition, proposal writing, and preparation of observations: J.L., C.V.M., M.G.-S., Q.H.T., J.P.N., S.M., D.M.K., W.D.C., B.P.B., M.E., G.S., B.M.T., and A.V. Data reduction: G.R.Z., M.G.-S., and Z.Z. Observational data analysis: Z.Z., C.V.M., and Q.H.T. Hydrodynamical simulations: M.M., A.O., and J.P.N. Paper writing and data visualization: Z.Z., C.V.M., M.M., A.O., M.G.-S., and Q.H.T. Paper review and editing: Z.Z., C.V.M., M.G.-S., M.M., A.O., Q.H.T., J.L., J.P.N., S.M., D.M.K., W.D.C., B.P.B., M.E., G.S., B.M.T., A.V., and G.R.Z. **Competing interests:** The authors declare that they have no competing interests. **Data and materials availability:** All data needed to evaluate the conclusions in the paper are present in the paper and/or the Supplementary Materials. Availability of software used in this work: The muler package is accessible at https://muler.readthedocs.io/en/latest/. In addition, the reduced HPF spectra, all measured spectral and physical properties, and our 3D hydrodynamic simulation results, as presented in this work, are all available on Zenodo: https://doi.org/10.5281/zenodo.7767042.

Submitted 17 November 2022
Accepted 1 May 2023
Published 7 June 2023
10.1126/sciadv.adf8736

GEOCHEMISTRY

Dominance of benthic fluxes in the oceanic beryllium budget and implications for paleo-denudation records

Kai Deng[1]*, Jörg Rickli[1], Tim Jesper Suhrhoff[1], Jianghui Du[1], Florian Scholz[2], Silke Severmann[3], Shouye Yang[4], James McManus[5], Derek Vance[1]

The ratio of atmosphere-derived ^{10}Be to continent-derived ^{9}Be in marine sediments has been used to probe the long-term relationship between continental denudation and climate. However, its application is complicated by uncertainty in ^{9}Be transfer through the land-ocean interface. The riverine dissolved load alone is insufficient to close the marine ^{9}Be budget, largely due to substantial removal of riverine ^{9}Be to continental margin sediments. We focus on the ultimate fate of this latter Be. We present sediment pore-water Be profiles from diverse continental margin environments to quantify the diagenetic Be release to the ocean. Our results suggest that pore-water Be cycling is mainly controlled by particulate supply and Mn-Fe cycling, leading to higher benthic fluxes on shelves. Benthic fluxes may help close the ^{9}Be budget and are at least comparable to, or higher (~2-fold) than, the riverine dissolved input. These observations demand a revised model framework, which considers the potentially dominant benthic source, to robustly interpret marine Be isotopic records.

INTRODUCTION

Earth's environment gradually moved from greenhouse conditions to an icehouse state in the Cenozoic, concurrent with a decline in atmospheric CO_2 concentrations (*1*, *2*). A long-standing hypothesis to explain these observations invokes enhanced removal of CO_2 from the atmosphere via increased silicate weathering. It is further posited that this weathering is driven by mountain uplift and erosion as inferred from an increase in oceanic isotope ratios of elements such as strontium (^{87}Sr/^{86}Sr) and lithium (^{7}Li/^{6}Li) (*3*, *4*). However, it is also well-established that a small excess of CO_2 output by silicate weathering (C sink) relative to volcanic degassing (C source) could potentially remove all atmospheric CO_2 in a few million years (*5*). Recent studies have sought to resolve this controversy in two ways, by invoking either CO_2 release from a compensatory source (*6*) or an increase in the weathering feedback strength without requiring a higher weathering flux (*7*, *8*).

In recent years, marine sedimentary records of beryllium isotopes (^{10}Be/^{9}Be) have been used as a tracer for continental denudation, which is the sum of chemical weathering and physical erosion (*9*, *10*). Since estimates are available for the past atmospheric delivery of ^{10}Be to the oceans (*11*), the ratio can, in principle, quantify fluxes of ^{9}Be delivered by rivers in dissolved and particulate forms (*10*). Compared to other weathering tracers mentioned above (*3*, *4*), which may mostly be sensitive to weathering style and/or the isotope composition of the source rather than weathering flux, the major potential advantage of ^{10}Be/^{9}Be lies in its direct link with the continental input flux of ^{9}Be (*8*, *12*). The discrepancy between proxy behaviors might help explain the inconsistency between the marked change in Sr-Li isotopes and relatively stable ^{10}Be/^{9}Be ratios. The latter proxy suggests a small variability in fluxes of chemical weathering and/or denudation in the late Cenozoic (*8*, *9*).

The promising applications of ^{10}Be/^{9}Be ratios are currently hampered by an incomplete understanding of the Be budget of the oceans, particularly the efficiency of ^{9}Be transmission through the continent-ocean interface (*13*, *14*). Recent modeling efforts have brought this uncertainty into the spotlight, emphasizing that different parametrizations of estuarine removal of dissolved ^{9}Be lead to contrasting expectations for the response of oceanic ^{10}Be/^{9}Be ratios to continental denudation (*15*, *16*). However, riverine dissolved ^{9}Be alone is insufficient to close the oceanic ^{9}Be budget (*14*, *16*). One potential missing source could be the early diagenetic release of particulate-bound reactive ^{9}Be deposited on continental margins (*10*, *14*). This benthic flux generated at the sediment-water interface is substantial for the marine budget of a number of other particle-reactive metals, such as iron (*17*) and rare earth elements (REE) (*18*).

A quantification of such benthic sedimentary fluxes is key to understanding the sensitivity of oceanic ^{10}Be/^{9}Be to changing continental denudation and/or weathering and the time scales on which the ocean responds to changes in continental inputs. However, direct constraints on benthic Be fluxes from marine pore-water data are extremely scarce (*19*) and still absent for continental shelves where most terrigenous sediment is deposited. Here, we present depth profiles of pore-water Be from different continental margins across variable water depth and redox conditions, which allow the derivation of a comprehensive quantitative constraint on this source. We seek to reveal the controls on pore-water Be concentrations and to quantify the benthic Be flux. We show that the benthic flux could be the major pathway by which ^{9}Be enters the dissolved pool of the oceans and provide an alternative interpretative framework for the small variability in Cenozoic Be isotopic records.

Sedimentary environment background

We studied stations in the East China Sea (depth: 6 to 46 m), the Baltic Sea (depth: 23 to 24 m), the Mexico margin (site: Soledad; depth: 542 m), and the California margin (sites: Catalina, San

[1]Institute of Geochemistry and Petrology, Department of Earth Sciences, ETH Zürich, Clausiusstrasse 25, 8092 Zürich, Switzerland. [2]GEOMAR Helmholtz Centre for Ocean Research Kiel, Wischhofstraße 1-3, 24148 Kiel, Germany. [3]Department of Marine and Coastal Sciences, Rutgers, The State University of New Jersey, New Brunswick, NJ 08901-8521, USA. [4]State Key Laboratory of Marine Geology, Tongji University, 200092 Shanghai, China. [5]Bigelow Laboratory for Ocean Sciences, 60 Bigelow Drive, East Boothbay, ME 04544, USA.
*Corresponding author. Email: kai.deng@erdw.ethz.ch

Clemente, and Patton Escarpment; depth: 1300 to 3707 m), covering a wide range of water depths from the continental shelf to the deep sea. These sites (Fig. 1 and table S1) are characterized by variable sedimentation rates (<0.1 to >10 mm/year) and redox conditions (oxic to anoxic), implying distinct diagenetic regimes.

The East China Sea shelf is one of the widest shelves worldwide, with a maximum width of >500 km and an area of ~5×10^5 km^2. It receives large amounts of terrestrial sediment, with sedimentation rates ranging from ~0.1 to >3 cm/year (*20*). The water column is dominantly oxic, with occasional occurrence of seasonal hypoxia (*21*). The Baltic Sea is one of the largest brackish water basins globally, and the studied Kiel Bight is a semi-enclosed basin in its southwest. It is at the other end of the redox scale, with anoxic and potentially sulfidic conditions commonly established at the sediment-water interface in summer through fall, that terminated in late fall by lateral advection of well-oxygenated water (*22*). Manganese and Fe shuttling takes place throughout the anoxic season. During the well-oxygenated season, terrigenous Mn and Fe oxides are also likely to be an important carrier phase for trace metals to the sediments (*23*). The major sediment source in the Kiel Bight is erosion of proximal coastal cliffs (*24*), resulting in a sedimentation rate of 0.2 to 0.9 cm/year (*25*). The Californian and Mexican margin sites encompass a range of redox situations broadly intermediate between the above two sites as well as a broad spectrum of particulate input. Soledad on the slope of the Mexico margin is characterized by anoxic conditions in bottom water and reduced particulate Mn supply to the sediments (*26*, *27*). The southern California margin sites (slope to deep sea) see bottom water conditions ranging from hypoxia to well oxygenated (bottom water O_2: 19 to 132 μmol/liter) and sediment accumulation rates ranging from 3 to 15 mg cm^{-2} $year^{-1}$ (*28*).

RESULTS

Pore-water Be and its controls

At each sampling station, pore-water samples were separated from core sediments at ~cm resolution for the preconcentration and determination of Be concentrations. A detailed description of the sampling and analysis is provided in Materials and Methods. Pore-water and bottom water Be concentrations, together with Mn and Fe concentrations, are presented in Fig. 2 and table S2. Pore-water Be concentrations ($[Be]_{diss}$) range from seawater-like values of ~20 pM to a maximum of ~1000 pM. At shallow depths (e.g., <5 cm), $[Be]_{diss}$ is commonly elevated compared to bottom water or near-interface pore-water (Fig. 2). This observation suggests that pore-water Be is released from sediments into overlying seawater. In general, pore-water $[Be]_{diss}$ reaches the highest values in the Baltic Sea (685 pM on average), intermediate values in the East China Sea (239 pM), and lowest values in the California (60 pM) and Mexico (46 pM) margins. At most stations, $[Be]_{diss}$ shows little variability at depth in contrast to its rapid rise just beneath the sediment-water interface.

Labile Be is mainly bound with reactive Mn-Fe oxyhydroxides in riverine and marine sediments (*29*, *30*). On the East China Sea shelf, the pore-water peak in $[Fe]_{diss}$ or $[Mn]_{diss}$ generally shallows with increasing water depth, together with a decrease in maximum concentration (Fig. 2). These features are also observed for $[Be]_{diss}$, suggesting a Be source linked to Mn-Fe mobilization through reduction. Likewise, $[Be]_{diss}$ and $[Mn]_{diss}$ show similar increases at shallow core depth (≤6 cm) in the Baltic Sea. However, the slight decrease in $[Mn]_{diss}$ at depth and overall low $[Fe]_{diss}$ point to sinks for both elements, such as Mn carbonate and Fe sulfide (*23*). These sinks do not appear to affect $[Be]_{diss}$.

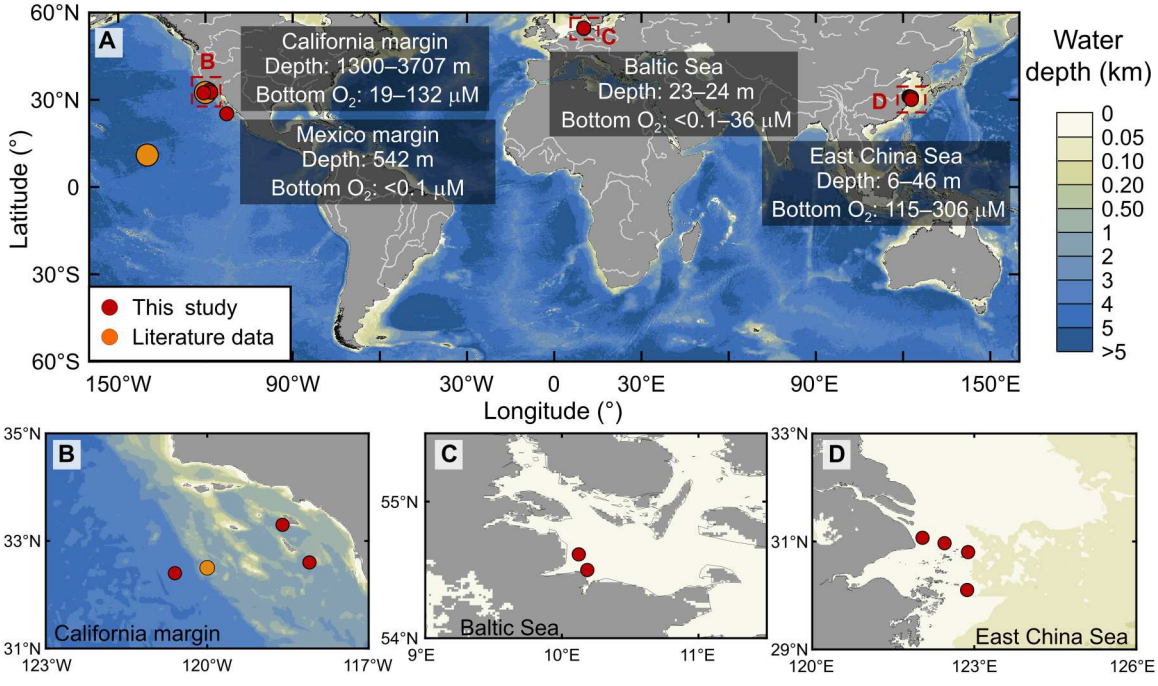

Fig. 1. Pore-water sampling stations. (**A**) An overview of all the stations with pore-water Be data. Basic information on each station is provided in table S1. Locations with literature pore-water Be data are also shown (*19*). Study regions with more than one sampling station are enlarged, including (**B**) the California margin, (**C**) the Baltic Sea, and (**D**) the East China Sea.

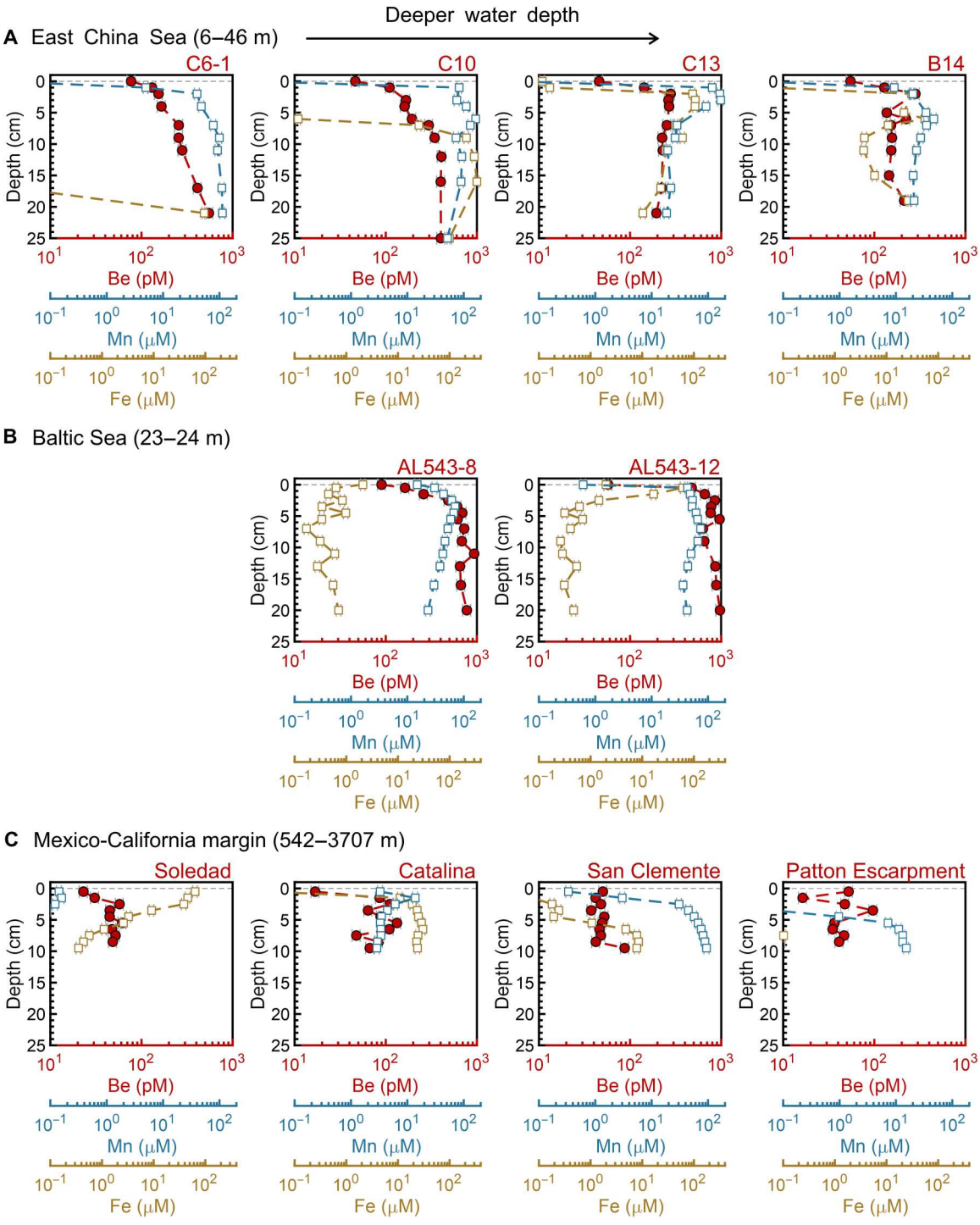

Fig. 2. Pore-water and bottom seawater Be, Mn, and Fe concentrations. Dissolved metal concentrations are shown for stations in (**A**) the East China Sea, (**B**) the Baltic Sea, and (**C**) the Mexico-California margin. Bottom water samples are plotted at a depth of 0 cm (gray dashed line). Note that the *x* axis is on a log scale.

For the Mexico-California margin sites, the depth profiles of $[Be]_{diss}$ do not correlate as closely with those of $[Mn]_{diss}$ or $[Fe]_{diss}$, perhaps because of contrasting cycling processes for Fe and Mn at these sites. For example, negligible $[Mn]_{diss}$ in Soledad is due to limited Mn oxide supply from the water column (*26*), while negligible $[Fe]_{diss}$ in Patton Escarpment is explained by a deep O_2 penetration depth and low organic carbon remineralization rate (*28*). Hence, changes in individual sources and sinks of each element may obscure the link between Be and Mn or Fe. Nevertheless, Fig. 3 illustrates a systematic relationship between pore-water Be and Mn during early diagenesis: $[Be]_{diss}$ remains at relatively low levels under low $[Mn]_{diss}$, while it strongly increases when reduction

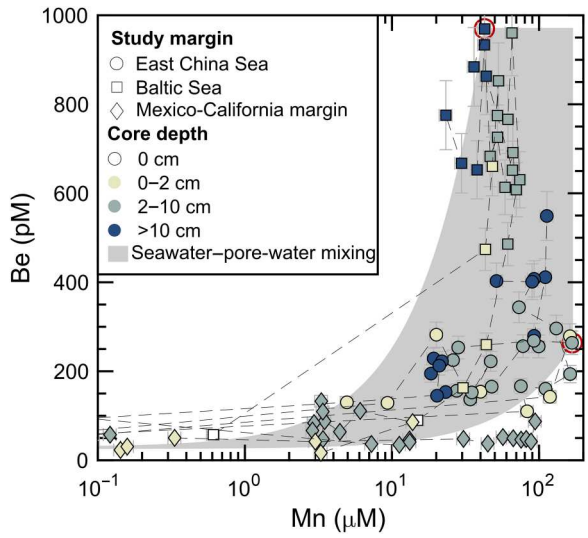

Fig. 3. Pore-water concentrations of Be versus Mn. Note that the *x* axis is on a log scale. The envelope of seawater–pore-water mixing is modeled using a seawater end-member, i.e., Pacific deep water (*55*, *56*), and two high $[Be]_{diss}$-$[Mn]_{diss}$ pore-water end-members that are potentially dominated by Mn reduction. Sources and sinks of Mn and Be do not entirely overlap. For example, formation of Mn carbonate could cause decrease in $[Mn]_{diss}$ (*23*) at high $[Be]_{diss}$. Hence, we include two scenarios using a pore-water sample with the highest $[Mn]_{diss}$ and another with the highest $[Be]_{diss}$ (red circles), leading to the lower and upper limits of the envelop, respectively.

of Mn oxides is prominent. Most samples fall within an envelope explained by mixing between a seawater end-member and two pore-water end-members whose sources are potentially located at the depth of Mn reduction.

Overall, $[Be]_{diss}$ is much lower on the continental slope and in the deep sea than on the shelf (Fig. 2). We suggest that abundant particle supply (*20*), in particular, Mn-Fe oxides (*23*), coupled to strong redox cycling in pore-water, could play a major role in the strong diagenetic Be release on the continental shelf.

Benthic Be fluxes in the oceans

We calculate the diffusive flux of Be across the sediment-water interface at each station (Fig. 4A), using Fick's first law and the pore-water $[Be]_{diss}$ gradient (details in Materials and Methods). Literature data from two deep-sea stations are included (*19*). The diffusive Be flux varies over two orders of magnitude, ranging from 0.8 pmol cm^{-2} $year^{-1}$ at the Mexico margin to 85.5 pmol cm^{-2} $year^{-1}$ in the Baltic Sea (AL543-12). If diffusive Be fluxes were strictly controlled of the oxidation-reduction potential of the sediment package, then they would be negatively correlated with bottom water O_2, but such correlation is insignificant in our dataset ($P > 0.1$; Fig. 4A). For example, in the Baltic Sea, the suboxic site shows a higher flux than the anoxic site, potentially because it is located within a submarine channel and may receive more terrestrial sediment (*31*). At the Mexico-California margins, the lower Be flux in anoxic Soledad is likely caused by limited Mn and Be supply from the water column (*26*). Nevertheless, any potential relationship between sediment supply and diffusive Be flux cannot easily be inferred from our dataset. For example, the diffusive Be fluxes show a small range (2.7 to 3.2 pmol cm^{-2} $year^{-1}$) at the three Californian margin sites despite a fivefold variability in sedimentation rates (*28*).

In brief, benthic Be fluxes on shelves are much higher than those on the slope and in the deep sea (Fig. 4A), consistent with the general spatial pattern of, e.g., benthic Mn fluxes (*32*). Furthermore, advection caused by bioirrigation and dynamic hydrological conditions, rather than diffusion, may dominate benthic fluxes of trace metals on shelves (*33*), suggesting that the actual fluxes could be even higher than diffusion-based estimates. Hence, our observations argue for an important role of continental shelves in the benthic Be source.

DISCUSSION

Updated framework of oceanic Be cycling

On the basis of pore-water data from this study and from the literature (*19*), a first-order estimate of the global benthic Be flux can be provided. We use benthic Be fluxes at a range of stations (table S3) for areal extrapolation at different water depth intervals. For global continental shelves (0 to 200 m), the studied East China Sea shelf, as one of the widest shelves worldwide (~2% of global shelf area), is adopted as the representative setting. When calculating the benthic Be flux on shelves, advection processes including bioirrigation and kinetic energy dissipation from, e.g., shear flow (*33*) need to be taken into account. Here, this is done by multiplying the change in $[Be]_{diss}$ across the sediment-water interface by the advective water exchange rate (v) determined around our study region using $^{224}Ra/^{228}Th$ disequilibria (Eqs. 3 and 4 and Materials and Methods) (*33*). The suggested shelf benthic Be flux for areal extrapolation is 140 ± 107 pmol cm^{-2} $year^{-1}$, much higher than the diffusion-based estimates at the same stations of the East China Sea shelf as expected (13.9 ± 4.2 pmol cm^{-2} $year^{-1}$; table S3). We consider this advection-based estimate to be reasonable, because the range of v on shelves used here (18 ± 13 m/year) agrees well with the range of the apparent pore-water exchange velocity across the sediment-water interface (2 to 34 m/year) calculated from several shelf settings in North America (*34*–*36*).

At deeper water depth, the global benthic flux on the slope and in the deep sea (water depth: 0.2 to 4 km) is calculated as the average diffusive flux at three nonanoxic stations (1300 to 3707 m) on the California margin (2.9 ± 0.3 pmol cm^{-2} $year^{-1}$; Fig. 4A). In addition, the global benthic flux in the abyssal basins (>4 km) is derived from the diffusive flux in the deep Pacific at 4910 m (1.4 ± 0.2 pmol cm^{-2} $year^{-1}$) (*19*). In general, the sedimentary (sedimentation rate) and diagenetic (related to organic carbon delivery/oxidation) environments at the selected stations are close to globally representative conditions at the corresponding depth intervals or fall within the representative parameter range (table S4). The calculation of a global-scale flux estimate based on areal extrapolation (*37*) is given in table S5. When only considering diffusion processes over the global scale as a conservative estimate, the total benthic Be input is calculated as $1.1 \pm 0.1 \times 10^7$ mol/year. In comparison, after accounting for advection processes on shelves, the global integrated benthic Be input reaches $4.5 \pm 2.9 \times 10^7$ mol/year. In particular, continental shelves with abundant terrestrial particle supply account for 84% of the total benthic source.

We revisit the oceanic Be budget based on these updated constraints on the benthic source (Fig. 4B; calculation details in table S5). The oceanic Be sources include riverine dissolved loads,

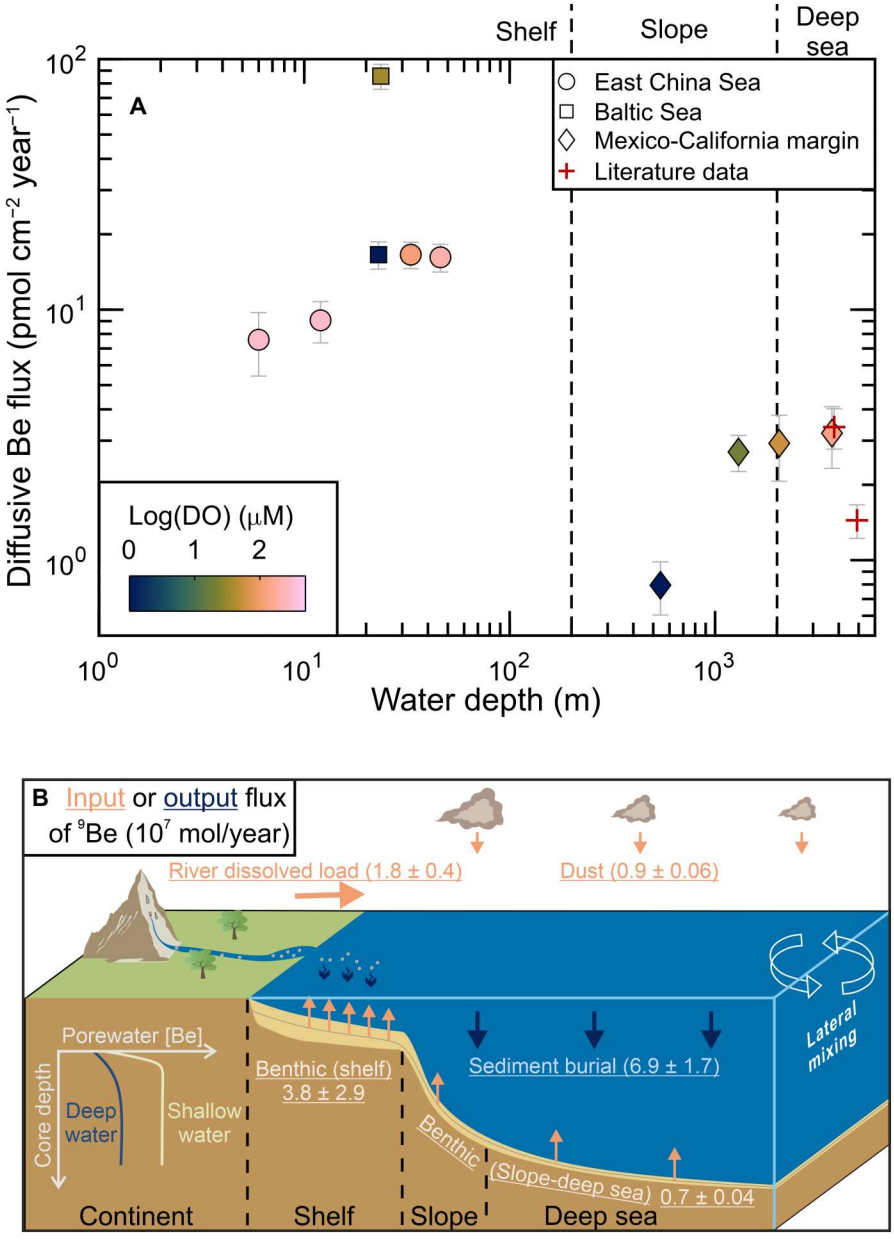

Fig. 4. Updated framework of oceanic Be cycling. (**A**) Diffusive sedimentary Be flux variation with water depth. The symbols are colored by bottom water O_2 (DO). Axes and color bars are on a log scale. Literature data (red crosses) are from (*19*). Details on flux calculations are provided in table S3. (**B**) First-order estimate of oceanic Be budget. The major sources are river dissolved load, eolian dust, and benthic flux, while the major sink is sediment burial. Inputs ($7.2 \pm 2.9 \times 10^7$ mol/year) and outputs ($6.9 \pm 1.7 \times 10^7$ mol/year) match within uncertainty. Calculation details and references are provided in table S5.

eolian dust, and benthic fluxes, while the major sink is scavenging onto marine particulates. The effective riverine input to the oceans ($1.8 \pm 0.4 \times 10^7$ mol/year) is calculated using compiled riverine dissolved Be flux data (table S6) and the average estuarine removal (56%) (*14*). The dust input ($0.9 \pm 0.06 \times 10^7$ mol/year) is estimated using the global dust flux (*38*), the Be concentration in dust same as that of the upper continent crust (*39*), and the soluble fraction (~9%) of dust Be (*13*). The diffusion-based benthic Be fluxes are of the same magnitude as the riverine input and would account for 28% of the total oceanic Be input. If advective fluxes on shelves are included as estimated above, then the benthic input becomes the largest source to the oceans (62% of the total input on average) and ~2-fold higher than the effective riverine dissolved input.

The sediment burial output of ^{9}Be ($6.9 \pm 1.7 \times 10^7$ mol/year) can be calculated (*40*) on the basis of global atmospheric ^{10}Be input (assuming a negligible continental ^{10}Be input; see the sensitivity test in the Supplementary Materials), the assumption of input-output balance for oceanic ^{10}Be, and the global average deep-sea ^{10}Be/^{9}Be (*10*, *41*). This estimate of oceanic ^{9}Be output, if valid, would result in an oceanic ^{9}Be residence time of 485 ± 120 year, which falls within the range for the ocean-wide scavenging residence time of Be (480

to 1250 years) estimated by other methods (*42*, *43*). Because the ^{9}Be sources ($7.2 \pm 2.9 \times 10^{7}$ mol/year in total) and the ^{9}Be sink are constrained by independent approaches, it is encouraging that they agree within uncertainty (<10% mismatch; Fig. 4B).

Given different scenarios for the benthic flux calculation and the uncertainty therein, we perform a sensitivity analysis on their effect on the resulting benthic ^{9}Be input and the ratio of benthic to riverine ^{9}Be input (fig. S2). The calculated benthic ^{9}Be flux through diffusion processes only (1.1×10^{7} mol/year) is equivalent to ~60% of the riverine dissolved input. This flux estimate is in itself substantial but not enough to close the oceanic ^{9}Be budget, which requires an input flux of $4.2 \pm 1.7 \times 10^{7}$ mol/year from sources other than rivers and dust according to the ^{9}Be burial output (table S5). In comparison, the benthic flux that takes advection on shelves into account ($4.5 \pm 2.9 \times 10^{7}$ mol/year) would meet the required missing source. Even when considering the large uncertainty propagated from estimates on water advection, the benthic flux is close to, or higher than, the riverine dissolved load (minimum ratio: 0.8; average ratio: 2.4) and accounts for 62 ± 16% of the total ^{9}Be input. In addition, a fraction of pore-water trace metals released via water advection might immediately be rescavenged near the sediment-water interface (*44*). It is difficult to quantify the effect of this process without in situ observations. However, on the basis of our constraints on ^{9}Be mass balance, a minimum benthic flux that could be affected by rescavenging and still meet the total ^{9}Be output within uncertainty (lower bound: 5.2×10^{7} mol/year; table S5) is 2.4×10^{7} mol/year. Even in this case, the benthic flux that ultimately enters the ocean is 130% of the riverine dissolved load and 47% of the total input (fig. S2), emphasizing its potential control on oceanic Be cycling.

Implications for the Cenozoic oceanic Be isotopic records

The updated framework for the oceanic Be budget (Fig. 4B) is valuable for the interpretation of marine isotope records. Recent debate has centered on the uncertainties in the riverine dissolved input and its estuarine removal (*15*, *16*). However, in the budget presented above, this riverine dissolved source is not the most important and may not control variability in paleo-records. Secular records are here predicted to respond more to the benthic source, either in a diffusion-only scenario or more plausibly in a scenario including advection processes on shelves. In addition, because pore-water Be only reflects a minor fraction (<0.1%) of the sediment reactive pool (e.g., ~20% of bulk sediment Be) (*10*), the benthic source has the potential to change with time in response to sedimentary processes. Key factors might include (i) changing pore-water Mn-Fe redox cycling, potentially controlled by organic carbon delivery (*32*), and perhaps (ii) changing sediment delivery (*10*). Both processes are likely dynamic on continental shelves and would respond to environmental changes (e.g., sea-level fluctuation), although the relative importance of each process is still to be established.

Late Cenozoic ^{10}Be/^{9}Be records show minor temporal variability (relative SD of ocean ^{9}Be input: 20 to 30%) and have been interpreted in terms of a relatively stable rate of continental denudation and/or weathering (*8*–*10*). However, because the riverine dissolved input is unlikely to be a major ^{9}Be source, we suggest that there are alternative views of the paleo-isotope records. For example, if the benthic source is kept constant at 4.5×10^{7} mol/year, then a ~2-fold increase in denudation rate in the late Cenozoic [inferred from, e.g., globally compiled thermochronometric age data (*45*) and modeling results (*8*) based on C-Li-Be-S-O data], together with the assumption of a linear relationship between effective riverine dissolved input and denudation rate (*10*), would lead to an increase of less than 20% in the total ^{9}Be input, consistent with the minor paleo-record variability. Moreover, a potential decrease in the benthic source resulting from the sea-level fall and smaller shelf area in the late Cenozoic (*46*) could counterbalance an increase in riverine dissolved input. Overall, the realization of a substantial benthic flux of Be implies a more indirect and complex response of oceanic ^{9}Be to continental denudation fluxes than previously assumed (*15*, *16*). The paleo-records of oceanic ^{10}Be/^{9}Be may not mimic the evolution of one single source. Instead, individual sources—benthic processes, rivers, and dust—could show different responses to climatic-tectonic factors, with their integrated effect potentially resulting in the observed small oceanic ^{10}Be/^{9}Be variability back through time (*9*).

Overall, our marine pore-water Be results provide direct evidence for a benthic Be flux to overlying seawater over the full depth range of the ocean basins (shelf-slope-deep sea). This benthic source provides a resolution to the oceanic Be imbalance, and it may dominate the present-day oceanic input. More marine pore-water Be data, especially on advection-dominated continental shelves, will still be required to refine our proposed Be budget and reduce the flux uncertainty. On the basis of this updated framework for the oceanic Be budget, we propose that oceanic Be cycling may be governed "bottom-up" (benthic process) rather than "top-down" (river or dust) (*47*). Hence, the hypothesis of a dominant riverine dissolved Be input to the oceans needs to be revisited (*15*). Given the strong cycling of pore-water Be on shelves and distinct Be isotope ratios of marine and continental sources, Be isotopes may have the potential to distinguish between the two types of reactive pools in marine sediments, allowing the investigation of boundary exchange processes in the modern ocean (*48*, *49*). For a robust interpretation of open-ocean paleo-isotopic records, a revised model framework considering the potentially dominant benthic source is, however, still required.

MATERIALS AND METHODS

Details on pore-water Be separation and determination

At each sampling station, sediment cores (10 to 25 cm) were retrieved using multi- or mini-corers. Overlying bottom water was first drained and filtered. Pore-water was separated using methods previously described in detail (*31*, *50*) at ~cm resolution, either by centrifuging sliced core sediment under anaerobic conditions followed by filtration (Baltic Sea samples: 0.2-μm filters and Mexico-California margin samples: 0.45-μm filters) or by in situ extraction via precleaned Rhizon samplers (East China Sea samples: 0.15-μm filters). Water samples were acidified for storage (pH ≤ 2).

Separation and determination of Be were performed at ETH Zürich. Beryllium measurement in pore-water samples is analytically challenging due to the low concentrations (picomol/liter level) and the small available sample volumes (e.g., several milliliters). We developed a procedure that can separate three components, which are, salt matrix, Be, and other trace metals such as REE on the same sample, optimizing the usage of precious pore-water samples. To do so, we coupled a well-established REE

preconcentration protocol (*50*, *51*) with an additional procedure for the preconcentration of Be from the remaining seawater matrix (*14*, *52*).

About 5 to 20 ml of filtered and acidified pore- or seawater was used to preconcentrate most trace metals (called TM fraction) using ethylenediaminetriacetic acid chelating resin, i.e., NOBIAS PA1 (*51*). Concentrated ammonium acetate buffer was added to each sample to reach an acetic acid concentration of 0.1 M, and the sample pH was adjusted to 5.5 to 6.0 using concentrated ammonia and HCl. Subsequently, samples were loaded onto pre-cleaned and preconditioned NOBIAS columns with a resin bed of ~100 μl, and the matrix cations were eluted from the column with 16 to 20 ml of 30 mM ammonium acetate buffer. The loaded sample and the matrix-eluting buffer solutions were collected as the B fraction. Beryllium is overwhelmingly in this fraction (> ~95%) (*51*), as it is commonly not retained by the resin at a pH of 5.5 to 6.0. Trace metals including REE (TM fraction) were lastly eluted from the resin in 4 ml of 1 M HCl.

We added $FeCl_3$ in concentrated HCl immediately to the B fractions to lower the pH to <2, and the samples were shaken for some time to reach equilibrium. Beryllium was then coprecipitated with Fe hydroxides at a pH of 7.5 to 8.2. After >12 hours with mild shaking, the precipitates were separated from the supernatants by centrifugation and rinsed twice with pH-adjusted Milli-Q water (pH = ~8). Beryllium was separated from Fe using anion resin (AG MP-1, 1-ml resin bed), and the dried B fraction was oxidized using 14.5 M HNO_3 and 30 volume % H_2O_2. An additional purification step using cation resin (AG 50W-X8, 0.8-ml resin bed) was applied (*53*) to further reduce remaining matrix cations such as Ca and Mg in the B fraction.

Beryllium concentrations of the B fractions were measured in 0.5 to 1 ml of 2% HNO_3 doped with 1 part per billion of indium (as an internal standard) on a Thermo Fisher Element XR [inductively coupled plasma mass spectrometry (ICP-MS)] in low-resolution mode. Given the low Be concentrations, the ICP-MS was coupled with a desolvating sample introduction system (Aridus 1) to boost instrument sensitivity and to increase the signal-to-noise ratio. The intensity data were corrected for machine blank and machine drift. Final Be concentrations were also corrected for procedural blanks of the corresponding batches, which reflect the Be accumulated during chemical processing and account for ~2% of the average [Be] of all samples (0.05 ± 0.05 parts per trillion, 1 SD; n = 16; the processed volume is the same as the sample volume of the given batch). Note that the TM fractions were also measured for Be concentrations using an ICP-MS setup as described in (*50*) to check whether a minor amount of Be was retained on the NOBIAS PA1 resin. When this fraction of Be was not negligible (accounting for ~6% of total [Be] on average), it was added to the Be measurement of the B fraction to derive a final Be concentration.

An in-house seawater standard Jstd-1 of known Be concentration (1 nM) (*14*) was processed in each sample batch to assess accuracy and precision. The total Be amount of each standard processed (from 5 to 10 ml of solution) is similar to that of the pore-water samples with high Be concentrations. The average Be yield of this standard was 95 ± 8% (n = 11, 1 SD). Hence, we propagated a relative uncertainty of 10% for all pore-water Be measurements.

In addition, an aliquot of each original pore-water sample was diluted ~40 times for the determination of Fe and Mn concentrations. Accuracy and precision were assessed using river standard SLRS-6 from the National Research Council Canada. Repeat measurements of SLRS-6 show an SD of <10% and also agree with certified values within ~10%. All element concentrations were measured using a Thermo Fisher Element XR at ETH Zürich, except Mn data in the Baltic Sea that were measured at GEOMAR (Germany) using ICP optical emission spectrometry (VARIAN 720-ES). Note that pore-water Fe and Mn data from the stations in the East China Sea were published before (*50*).

Calculation of benthic Be flux

Early diagenetic reactions can produce a $[Be]_{diss}$ gradient in sediment pore-waters, which is used for quantifying the diffusive Be flux ($J_{Be-diff}$) following Fick's first law of diffusion (*36*)

$$J_{Be-diff} = \varphi \times D_{Be}^{sed} \times \frac{\partial C_{Be}}{\partial z} \quad (1)$$

where $\frac{\partial C_{Be}}{\partial z}$ is the maximum concentration gradient in Be from shallow pore-water to bottom water (mol liter^{-1} cm^{-1}) in the pore-water profile, φ is the porosity (assuming as a constant of 0.9) (*19*, *54*), and D_{Be}^{sed} is the effective diffusion coefficient of Be in sediments (cm^2/s). D_{Be}^{sed} is calculated using the diffusion coefficient of Be in seawater (D_{Be}^{sw} in cm^2/s) and tortuosity (θ^2; estimated from porosity as given in the denominator of Eq. 2) (*36*)

$$D_{Be}^{sed} = \frac{D_{Be}^{sw}}{1 - \ln(\varphi^2)} \quad (2)$$

The empirical relationship between D_{Be}^{sw} and bottom water temperature (T in degrees Celsius) is provided by Boudreau (*36*), i.e., $D_{Be}^{sw} = (2.57 + 0.14\ T) \times 10^{-6}$ cm^2/s (R^2 = 0.99), and applied here, and site-specific D_{Be}^{sed} is provided in table S3. Diffusive Be fluxes from this study and the literature are provided in table S3.

In an advection-dominated setting, additional processes, e.g., bioirrigation and shear flow, can dominate solute exchange across the sediment-water interface. The advection-based Be flux (J_{Be-add}) is then calculated by the equation modified from (*33*)

$$J_{Be-add} = \nu \times \Delta[Be] \quad (3)$$

where Δ[Be] is the concentration difference between uppermost pore-water (1 cm) and bottom seawater, and ν is the interfacial water exchange rate (in m^3 m^{-2} d^{-1}). An exponential relationship between water depth (Z in meters) and ν determined from $^{224}Ra/^{228}Th$ disequilibria was proposed in China coastal seas (*33*). We here reprocessed the literature data (*33*) to generate a data fit and an estimate of its uncertainty (Eq. 4 and fig. S1).

$$\nu = 0.049 + 0.856e^{-0.134Z} \quad (4)$$

The coefficient of determination (R^2) of the fit is 0.97, and the root mean square error is 0.030. To estimate the advective Be flux on the shelf, we first calculated the mean gradient in $[Be]_{diss}$ at the sediment-water interface from the East China Sea stations at a water depth of ≥12 m, where pore-water depth patterns of Be (Fig. 2) and REE (*50*) are similar. We then multiplied this gradient with the advective water flux (0.049 ± 0.036 m^3 m^{-2} d^{-1}) derived from Eq. 4 for the global average shelf depth (65 m) (*37*), which is similar to the average depth of the East China Sea shelf (72 m). Overall, ν is relatively stable at ~0.05 m^3 m^{-2} d^{-1} when Z is >40 m.

Supplementary Materials

This PDF file includes:

Supplementary Text
Figs. S1 and S2
Tables S1 to S6
References

REFERENCES AND NOTES

1. J. W. B. Rae, Y. G. Zhang, X. Liu, G. L. Foster, H. M. Stoll, R. D. M. Whiteford, Atmospheric CO_2 over the past 66 million years from marine archives. *Annu. Rev. Earth Planet. Sci.* **49**, 609–641 (2021).
2. J. Zachos, M. Pagani, L. Sloan, E. Thomas, K. Billups, Trends, rhythms, and aberrations in global climate 65 Ma to present. *Science* **292**, 686–693 (2001).
3. M. E. Raymo, W. F. Ruddiman, Tectonic forcing of Late Cenozoic climate. *Nature* **359**, 117–122 (1992).
4. S. Misra, P. N. Froelich, Lithium isotope history of Cenozoic seawater: Changes in silicate weathering and reverse weathering. *Science* **335**, 818–823 (2012).
5. R. A. Berner, K. Caldeira, The need for mass balance and feedback in the geochemical carbon cycle. *Geology* **25**, 955–956 (1997).
6. M. A. Torres, A. J. West, G. Li, Sulphide oxidation and carbonate dissolution as a source of CO_2 over geological timescales. *Nature* **507**, 346–349 (2014).
7. J. K. Caves, A. B. Jost, K. V. Lau, K. Maher, Cenozoic carbon cycle imbalances and a variable weathering feedback. *Earth Planet. Sci. Lett.* **450**, 152–163 (2016).
8. J. K. Caves, D. E. Ibarra, F. von Blanckenburg, Neogene cooling driven by land surface reactivity rather than increased weathering fluxes. *Nature* **571**, 99–102 (2019).
9. J. K. Willenbring, F. von Blanckenburg, Long-term stability of global erosion rates and weathering during late-Cenozoic cooling. *Nature* **465**, 211–214 (2010).
10. F. von Blanckenburg, J. Bouchez, River fluxes to the sea from the ocean's $^{10}Be/^{9}Be$ ratio. *Earth Planet. Sci. Lett.* **387**, 34–43 (2014).
11. K. Deng, H. Wittmann, F. von Blanckenburg, The depositional flux of meteoric cosmogenic ^{10}Be from modeling and observation. *Earth Planet. Sci. Lett.* **550**, 116530 (2020).
12. F. von Blanckenburg, J. Bouchez, D. E. Ibarra, K. Maher, Stable runoff and weathering fluxes into the oceans over Quaternary climate cycles. *Nat. Geosci.* **8**, 538–542 (2015).
13. E. T. Brown, C. I. Measures, J. M. Edmond, D. L. Bourlès, G. M. Raisbeck, F. Yiou, Continental inputs of beryllium to the oceans. *Earth Planet. Sci. Lett.* **114**, 101–111 (1992).
14. T. J. Suhrhoff, J. Rickli, K. Crocket, E. Bura-Nakic, D. Vance, Behavior of beryllium in the weathering environment and its delivery to the ocean. *Geochim. Cosmochim. Acta* **265**, 48–68 (2019).
15. S. Li, S. L. Goldstein, M. E. Raymo, Neogene continental denudation and the beryllium conundrum. *Proc. Natl. Acad. Sci. U.S.A.* **118**, e2026456118 (2021).
16. F. von Blanckenburg, J. Bouchez, J. K. Willenbring, D. E. Ibarra, J. K. C. Rugenstein, There is no Neogene denudation conundrum. *Proc. Natl. Acad. Sci. U.S.A.* **119**, e2202387119 (2022).
17. V. A. Elrod, W. M. Berelson, K. H. Coale, K. S. Johnson, The flux of iron from continental shelf sediments: A missing source for global budgets. *Geophys. Res. Lett.* **31**, L12307 (2004).
18. A. N. Abbott, B. A. Haley, J. McManus, C. E. Reimers, The sedimentary flux of dissolved rare earth elements to the ocean. *Geochim. Cosmochim. Acta* **154**, 186–200 (2015).
19. D. L. Bourlès, G. Klinkhammer, A. C. Campbell, C. I. Measures, E. T. Brown, J. M. Edmond, Beryllium in marine pore waters: geochemical and geochronological implications. *Nature* **341**, 731–733 (1989).
20. J. P. Liu, A. C. Li, K. H. Xu, D. M. Velozzi, Z. S. Yang, J. D. Milliman, D. J. DeMaster, Sedimentary features of the Yangtze River-derived along-shelf clinoform deposit in the East China Sea. *Cont. Shelf Res.* **26**, 2141–2156 (2006).
21. J. Zhu, Z. Zhu, J. Lin, H. Wu, J. Zhang, Distribution of hypoxia and pycnocline off the Changjiang Estuary, China. *J. Mar. Sys.* **154**, 28–40 (2016).
22. S. T. Lennartz, A. Lehmann, J. Herrford, F. Malien, H. P. Hansen, H. Biester, H. W. Bange, Long-term trends at the Boknis Eck time series station (Baltic Sea), 1957–2013: Does climate change counteract the decline in eutrophication? *Biogeosciences* **11**, 6323–6339 (2014).
23. F. Scholz, J. McManus, S. Sommer, The manganese and iron shuttle in a modern euxinic basin and implications for molybdenum cycling at euxinic ocean margins. *Chem. Geol.* **355**, 56–68 (2013).
24. E. Seibold, N. Exon, M. Hartmann, F.-C. Kögler, H. Krumm, G. Lutze, R. Newton, F. Werner, Marine geology of Kiel bay, in *Sedimentology of Parts of Central Europe, Guidebook VIII International Sedimentology Congress* (Kramer, 1971).
25. C. A. Nittrouer, G. R. Lopez, L. Donelson Wright, S. J. Bentley, A. F. D'Andrea, C. T. Friedrichs, N. I. Craig, C. K. Sommerfield, Oceanographic processes and the preservation of sedimentary structure in Eckernförde Bay, Baltic Sea. *Cont. Shelf Res.* **18**, 1689–1714 (1998).
26. J. McManus, W. M. Berelson, S. Severmann, R. L. Poulson, D. E. Hammond, G. P. Klinkhammer, C. Holm, Molybdenum and uranium geochemistry in continental margin sediments: Paleoproxy potential. *Geochim. Cosmochim. Acta* **70**, 4643–4662 (2006).
27. S. Bruggmann, S. Severmann, J. McManus, Geochemical conditions regulating chromium preservation in marine sediments. *Geochim. Cosmochim. Acta* **348**, 239–257 (2023).
28. W. M. Berelson, J. McManus, K. H. Coale, K. S. Johnson, T. Kilgore, D. Burdige, C. Pilskaln, Biogenic matter diagenesis on the sea floor: A comparison between two continental margin transects. *J. Mar. Res.* **54**, 731–762 (1996).
29. D. Bourlès, G. M. Raisbeck, F. Yiou, ^{10}Be and ^{9}Be in marine sediments and their potential for dating. *Geochim. Cosmochim. Acta* **53**, 443–452 (1989).
30. H. Wittmann, F. von Blanckenburg, J. Bouchez, N. Dannhaus, R. Naumann, M. Christl, J. Gaillardet, The dependence of meteoric ^{10}Be concentrations on particle size in Amazon River bed sediment and the extraction of reactive $^{10}Be/^{9}Be$ ratios. *Chem. Geol.* **318–319**, 126–138 (2012).
31. F. Scholz, J. Cheng, Z. Zhang, P. Vosteen, C. Siebert, M. Frank, Benthic-pelagic coupling and isotopic fractionation of barium in Kiel Bight, SW Baltic Sea. *Front. Mar. Sci.* **10**, 1101095 (2023).
32. J. McManus, W. M. Berelson, S. Severmann, K. S. Johnson, D. E. Hammond, M. Roy, K. H. Coale, Benthic manganese fluxes along the Oregon-California continental shelf and slope. *Cont. Shelf Res.* **43**, 71–85 (2012).
33. X. Shi, L. Wei, Q. Hong, L. Liu, Y. Wang, X. Shi, Y. Ye, P. Cai, Large benthic fluxes of dissolved iron in China coastal seas revealed by $^{224}Ra/^{228}Th$ disequilibria. *Geochim. Cosmochim. Acta* **260**, 49–61 (2019).
34. D. E. Hammond, C. Fuller, in *The use of radon-222 to estimate benthic exchange and atmospheric exchange rates in San Francisco Bay* (American Association for the Advancement of Science-Pacific Division, 1979).
35. D. Archer, A. Devol, Benthic oxygen fluxes on the Washington shelf and slope: A comparison of in situ microelectrode and chamber flux measurements. *Limnol. Oceanogr.* **37**, 614–629 (1992).
36. B. P. Boudreau, in *Diagenetic Models and Their Implementation* (Springer, Berlin, 1997), vol. 410.
37. B. Eakins, G. Sharman, Hypsographic curve of Earth's surface from ETOPO1 (NOAA National Geophysical Data Center, Boulder, CO, 2012).
38. T. D. Jickells, Z. S. An, K. K. Andersen, A. R. Baker, G. Bergametti, N. Brooks, J. J. Cao, P. W. Boyd, R. A. Duce, K. A. Hunter, H. Kawahata, N. Kubilay, J. laRoche, P. S. Liss, N. Mahowald, J. M. Prospero, A. J. Ridgwell, I. Tegen, R. Torres, Global iron connections between desert dust, ocean biogeochemistry, and climate. *Science* **308**, 67–71 (2005).
39. R. L. Rudnick, S. Gao, 3.01 - Composition of the Continental Crust A2 - Holland, Heinrich D, in *Treatise on Geochemistry*, K. K. Turekian, Ed. (Pergamon, Oxford, 2003), pp. 1–64.
40. F. von Blanckenburg, R. K. O'Nions, N. S. Belshaw, A. Gibb, J. R. Hein, Global distribution of beryllium isotopes in deep ocean water as derived from Fe Mn crusts. *Earth Planet. Sci. Lett.* **141**, 213–226 (1996).
41. U. Heikkilä, F. von Blanckenburg, The global distribution of Holocene meteoric 10Be fluxes from atmospheric models. Distribution maps for terrestrial Earths surface applications (GFZ Data Services, GFZ Potsdam, Germany, 2015).
42. T. L. Ku, M. Kusakabe, C. I. Measures, J. R. Southon, G. Cusimano, J. S. Vogel, D. E. Nelson, S. Nakaya, Beryllium isotope distribution in the western North Atlantic: A comparison to the Pacific. *Deep Sea Res. Part A Oceanogr. Res. Papers* **37**, 795–808 (1990).
43. R. F. Anderson, Y. Lao, W. S. Broecker, S. E. Trumbore, H. J. Hofmann, W. Wolfli, Boundary scavenging in the Pacific Ocean: A comparison of ^{10}Be and ^{231}Pa. *Earth Planet. Sci. Lett.* **96**, 287–304 (1990).
44. G. M. Patton, R. Francois, D. Weis, E. Hathorne, M. Gutjahr, M. Frank, K. Gordon, An experimental investigation of the acquisition of Nd by authigenic phases of marine sediments. *Geochim. Cosmochim. Acta* **301**, 1–29 (2021).
45. F. Herman, D. Seward, P. G. Valla, A. Carter, B. Kohn, S. D. Willett, T. A. Ehlers, Worldwide acceleration of mountain erosion under a cooling climate. *Nature* **504**, 423–426 (2013).
46. K. G. Miller, M. A. Kominz, J. V. Browning, J. D. Wright, G. S. Mountain, M. E. Katz, P. J. Sugarman, B. S. Cramer, N. Christie-Blick, S. F. Pekar, The Phanerozoic record of global sea-level change. *Science* **310**, 1293–1298 (2005).
47. B. A. Haley, J. Du, A. N. Abbott, J. McManus, The impact of benthic processes on rare earth element and neodymium isotope distributions in the oceans. *Front. Mar. Sci.* **4**, 426 (2017).
48. A. Bernhardt, M. Oelze, J. Bouchez, F. von Blanckenburg, M. Mohtadi, M. Christl, H. Wittmann, $^{10}Be/^{9}Be$ ratios reveal marine authigenic clay formation. *Geophys. Res. Lett.* **47**, e2019GL086061 (2020).

49. H. Wittmann, F. von Blanckenburg, M. Mohtadi, M. Christl, A. Bernhardt, The competition between coastal trace metal fluxes and oceanic mixing from the $^{10}Be/^{9}Be$ ratio: Implications for sedimentary records. *Geophys. Res. Lett.* **44**, 8443–8452 (2017).
50. K. Deng, S. Yang, J. Du, E. Lian, D. Vance, Dominance of benthic flux of REEs on continental shelves: Implications for oceanic budgets. *Geochem. Perspect. Lett.* **22**, 26–30 (2022).
51. Y. Sohrin, S. Urushihara, S. Nakatsuka, T. Kono, E. Higo, T. Minami, K. Norisuye, S. Umetani, Multielemental determination of GEOTRACES key trace metals in seawater by ICPMS after preconcentration using an ethylenediaminetriacetic acid chelating resin. *Anal. Chem.* **80**, 6267–6273 (2008).
52. M. Frank, D. Porcelli, P. Andersson, M. Baskaran, G. Björk, P. W. Kubik, B. Hattendorf, D. Guenther, The dissolved Beryllium isotope composition of the Arctic Ocean. *Geochim. Cosmochim. Acta* **73**, 6114–6133 (2009).
53. T. J. Suhrhoff, J. Rickli, M. Christl, E. G. Vologina, V. Pham, M. Belhadj, E. V. Sklyarov, C. Jeandel, D. Vance, Source to sink analysis of weathering fluxes in Lake Baikal and its watershed based on riverine fluxes, elemental lake budgets, REE patterns, and radiogenic (Nd, Sr) and $^{10}Be/^{9}Be$ isotopes. *Geochim. Cosmochim. Acta* **321**, 133–154 (2022).
54. J. McManus, W. M. Berelson, G. P. Klinkhammer, D. E. Hammond, C. Holm, Authigenic uranium: Relationship to oxygen penetration depth and organic carbon rain. *Geochim. Cosmochim. Acta* **69**, 95–108 (2005).
55. M. Kusakabe, T. L. Ku, J. R. Southon, J. S. Vogel, D. E. Nelson, C. I. Measures, Y. Nozaki, Distribution of ^{10}Be and ^{9}Be in the Pacific Ocean. *Earth Planet. Sci. Lett.* **82**, 231–240 (1987).
56. P. J. Statham, P. A. Yeats, W. M. Landing, Manganese in the eastern Atlantic Ocean: Processes influencing deep and surface water distributions. *Mar. Chem.* **61**, 55–68 (1998).
57. J. D. Milliman, K. L. Farnsworth, in *River Discharge to the Coastal Ocean – a Global Synthesis* (Cambridge Univ. Press, 2011).
58. B. Campforts, V. Vanacker, J. Vanderborght, S. Baken, E. Smolders, G. Govers, Simulating the mobility of meteoric ^{10}Be in the landscape through a coupled soil-hillslope model (Be2D). *Earth Planet. Sci. Lett.* **439**, 143–157 (2016).
59. J. Gaillardet, J. Viers, B. Dupré, Trace Elements in River Waters, in *Treatise on Geochemistry*, H. D. Holland, K. K. Turekian, Eds. (Elsevier, Oxford, ed. 2, 2014), pp. 195–235.
60. C. Shen, J. Beer, P. Kubik, W. Sun, T. Liu, K. Liu, ^{10}Be in desert sands, falling dust and loess in China. *Nucl. Instrum. Methods Phys. Res., Sect. B* **268**, 1050–1053 (2010).
61. F. von Blanckenburg, J. Bouchez, H. Wittmann, Earth surface erosion and weathering from the ^{10}Be (meteoric)/^{9}Be ratio. *Earth Planet. Sci. Lett.* **351**–**352**, 295–305 (2012).
62. C.-T. A. Chen, Chemical and physical fronts in the Bohai, Yellow and East China seas. *J. Mar. Sys.* **78**, 394–410 (2009).
63. J. J. Middelburg, K. Soetaert, P. M. J. Herman, Empirical relationships for use in global diagenetic models. *Deep Sea Res. Part I* **44**, 327–344 (1997).
64. K. M. Costa, C. T. Hayes, R. F. Anderson, F. J. Pavia, A. Bausch, F. Deng, J.-C. Dutay, W. Geibert, C. Heinze, G. Henderson, C. Hillaire-Marcel, S. Hoffmann, S. L. Jaccard, A. W. Jacobel, S. S. Kienast, L. Kipp, P. Lerner, J. Lippold, D. Lund, F. Marcantonio, D. McGee, J. F. McManus, F. Mekik, J. L. Middleton, L. Missiaen, C. Not, S. Pichat, L. F. Robinson, G. H. Rowland, M. Roy-Barman, A. Tagliabue, A. Torfstein, G. Winckler, Y. Zhou, ^{230}Th normalization: New insights on an essential tool for quantifying sedimentary fluxes in the modern and quaternary ocean. *Paleoceanogr. Paleoclimatol.* **35**, e2019PA003820 (2020).
65. B. Deng, J. Zhang, Y. Wu, Recent sediment accumulation and carbon burial in the East China Sea. *Global Biogeochem. Cycles* **20**, GB3014 (2006).
66. S. Emerson, V. Grundmanis, D. Graham, Carbonate chemistry in marine pore waters: MANOP sites C and S. *Earth Planet. Sci. Lett.* **61**, 220–232 (1982).
67. D. J. Burdige, Preservation of organic matter in marine sediments: Controls, mechanisms, and an imbalance in sediment organic carbon budgets? *Chem. Rev.* **107**, 467–485 (2007).
68. G. Song, S. Liu, Z. Zhu, W. Zhai, C. Zhu, J. Zhang, Sediment oxygen consumption and benthic organic carbon mineralization on the continental shelves of the East China Sea and the Yellow Sea. *Deep Sea Res. Part II* **124**, 53–63 (2016).
69. W. M. Berelson, D. E. Hammond, D. O'Neill, X. m. Xu, C. Chin, J. Zukin, Benthic fluxes and pore water studies from sediments of the central equatorial north Pacific: Nutrient diagenesis. *Geochim. Cosmochim. Acta* **54**, 3001–3012 (1990).
70. D. Kadko, A multitracer approach to the study of erosion in the northeast equatorial Pacific. *Earth Planet. Sci. Lett.* **63**, 13–33 (1983).
71. N. M. Mahowald, A. R. Baker, G. Bergametti, N. Brooks, R. A. Duce, T. D. Jickells, N. Kubilay, J. M. Prospero, I. Tegen, Atmospheric global dust cycle and iron inputs to the ocean. *Global Biogeochem. Cycles* **19**, GB4025 (2005).
72. C. I. Measures, J. M. Edmond, The geochemical cycle of ^{9}Be: A reconnaissance. *Earth Planet. Sci. Lett.* **66**, 101–110 (1983).
73. E. T. Brown, J. M. Edmond, G. M. Raisbeck, D. L. Bourlès, F. Yiou, C. I. Measures, Beryllium isotope geochemistry in tropical river basins. *Geochim. Cosmochim. Acta* **56**, 1607–1624 (1992).
74. W. Kong, L. Zhou, G. Aumaître, D. Bourlès, K. Keddadouche, Dissolved and particulate beryllium isotopes in the Pearl River estuary: Their geochemical behavior in estuarine water and potential contributions from anthropogenic sources. *Front. Mar. Sci.* **8**, 689890 (2021).
75. M. Kusakabe, T. L. Ku, J. R. Southon, L. Shao, J. S. Vogel, D. E. Nelson, S. Nakaya, G. L. Cusimano, Be isotopes in rivers/estuaries and their oceanic budgets. *Earth Planet. Sci. Lett.* **102**, 265–276 (1991).
76. C. Neal, Dissolved and acid available particulate beryllium in eastern UK surface waters. *Sci. Total Environ.* **314**–**316**, 185–208 (2003).
77. C. Neal, Dissolved beryllium in rainfall, stream and shallow groundwaters in the Upper River Severn catchments, Plynlimon, mid Wales. *Sci. Total Environ.* **314**–**316**, 171–184 (2003).
78. M. E. Åström, C. Yu, P. Peltola, J. K. Reynolds, P. Österholm, M. I. Nystrand, A. Augustsson, J. J. Virtasalo, L. Nordmyr, A. E. K. Ojala, Sources, transport and sinks of beryllium in a coastal landscape affected by acidic soils. *Geochim. Cosmochim. Acta* **232**, 288–302 (2018).

Acknowledgments: K.D. thanks A. Corey for the help with lab work. Participants of RV Alkor Cruise AL543 are thanked for their contribution to the sampling. **Funding:** This work was supported by ETH Zürich Postdoctoral Fellowship 20-1 FEL-24 (K.D.); National Key R&D Program of China (no. 2022YFF0800504); National Natural Science Foundation of China (nos. 42230410 and 42006059); German Research Foundation (DFG), Emmy-Noether-Nachwuchsforschergruppe ICONOX (F.S.); and U.S. National Science Foundation (no. OC-1657690 to S.S. and no. OC-1657832 to J.M.). **Author contributions:** Conceptualization: K.D. and D.V. Methodology: K.D., J.R., T.J.S., and J.D. Investigation: K.D. Resources: S.S., J.M., F.S., and S.Y. Visualization: K.D. Supervision: D.V. Funding acquisition: D.V. and K.D. Writing (original draft): K.D. Writing (review and editing): D.V., J.R., T.J.S., J.D., F.S., S.Y., and J.M. **Competing interests:** The authors declare that they have no competing interests. **Data and materials availability:** All data needed to evaluate the conclusions in the paper are present in the paper and/or the Supplementary Materials.

Submitted 22 December 2022
Accepted 5 May 2023
Published 7 June 2023
10.1126/sciadv.adg3702

PLANETARY SCIENCE

Origin of biological homochirality by crystallization of an RNA precursor on a magnetic surface

S. Furkan Ozturk[1]*, Ziwei Liu[2], John D. Sutherland[2], Dimitar D. Sasselov[3]

Homochirality is a signature of life on Earth, yet its origins remain an unsolved puzzle. Achieving homochirality is essential for a high-yielding prebiotic network capable of producing functional polymers like RNA and peptides on a persistent basis. Because of the chiral-induced spin selectivity effect, which established a strong coupling between electron spin and molecular chirality, magnetic surfaces can act as chiral agents and be templates for the enantioselective crystallization of chiral molecules. Here, we studied the spin-selective crystallization of racemic ribo-aminooxazoline (RAO), an RNA precursor, on magnetite (Fe_3O_4) surfaces, achieving an unprecedented enantiomeric excess (ee) of about 60%. Following the initial enrichment, we then obtained homochiral (100% ee) crystals of RAO after a subsequent crystallization. Our results demonstrate a prebiotically plausible way of achieving system-level homochirality from completely racemic starting materials, in a shallow-lake environment on early Earth where sedimentary magnetite deposits are expected to be common.

INTRODUCTION

Understanding the origins of biomolecular homochirality is essential for understanding the origins of life, and the origin of homochirality remains a long-standing mystery since Pasteur (*1*) found the molecular asymmetry of organic compounds in 1848. Achieving a homochiral state early in the prebiotic synthesis of the monomers would be very beneficial for successful polymerization and the overall robustness of the entire synthetic network (*2*, *3*). The prebiotic need for high yields combined with high selectivity requires a persistent and well-matched pair of a chiral symmetry-breaking agent and an amplification mechanism.

Multiple studies [see (*4*, *5*) for review] have identified ways to induce an initial chiral imbalance, by a symmetry-breaking agent, like parity-violating energy difference (*6*), selective adsorption on surfaces (*7*), conglomerate resolution (*8*, *9*), circularly polarized light (*10*), and longitudinally spin-polarized electrons and muons (e.g., in cosmic ray showers) (*11*, *12*). Others have focused on the amplification of such initial imbalance to reach homochirality [see (*13*, *14*) for review]. A few studies (e.g., Viedma ripening) have realized a spontaneous symmetry breaking in racemizing compounds, followed by amplification by means of conglomerate crystallization to reach homochirality (*15*, *16*). Blackmond and colleagues realized that reaching homochirality in a single compound per se is not sufficient to reach system-level homochirality and studied the interchange of enantiomeric excess (ee) between amino acids and sugars (*17*–*19*). However, no studies have shown a way to pair a nondestructive chiral agent with a chiral amplification scheme to achieve a persistent, system-level homochiral state, especially in prebiotically relevant chemistry.

One of the central molecules for prebiotic synthetic networks emerged in 1970 from the work of Sanchez and Orgel (*20*), who identified the aminooxazolines (ribo, arabino, xylo, and lyxo) as organic intermediates useful for the synthesis of a wide variety of nucleotides, the monomers of nucleic acids (RNA and DNA). Later studies by Sutherland's group (*21*, *22*) culminated in the prebiotic synthesis of pyrimidine nucleotides (*23*) with aminooxazolines as the precursors and the consequent development of an entire synthetic network for nucleotides and amino acids (*24*). Follow-up studies highlighted ribo-aminooxazoline (RAO) as a key compound to resolve the origin of homochirality due to its centrality in the synthesis of nucleotides and crystallization properties (*22*, *25*–*27*). Hein *et al.* (*17*) further emphasized the importance of RAO and obtained enantiopure RAO crystals directly from glyceraldehyde by kinetic resolution of the latter with enantioenriched proline. However, the search for a prebiotically plausible mechanism that can both induce and amplify a chiral bias in an RNA precursor from a fully racemic starting material has remained to be an open problem.

Biological systems comprise many homochiral molecules. In principle, such a state could be achieved by separately resolving each individual chiral compound. However, a more attractive solution would be to establish the homochirality in a compound from which propagation of homochirality to the whole system could occur. Emergence of homochirality at the stage of RAO sets the stage for the propagation of homochirality through RNA to peptides and thence through enantioselective catalysis to metabolites.

In our recent work, we proposed a symmetry-breaking agent that can trigger such an amplification in the reduction reactions, leading up to the production of the chiral 3-carbon sugar glyceraldahyde (itself the precursor to RAO). Our proposed mechanism uses the strong coupling between the electron spin and molecular chirality as established by the chiral-induced spin selectivity (CISS) effect (*28*). We identified evaporative lakes with authigenic iron-oxide sediments as prebiotically plausible settings (*29*), in which enantioselective reduction reactions can occur close to the magnetized surface by spin-polarized photoelectrons released from the magnetite by solar ultraviolet (UV) light.

In this work, we demonstrate that the spin-polarized surfaces themselves can function as chiral agents, breaking the chiral symmetry in a further expansion of the role of the CISS effect (*30*–*32*). The simultaneous conglomerate crystallization provides the

[1]Department of Physics, Harvard University, Cambridge, MA 02138, USA. [2]MRC Laboratory of Molecular Biology, Cambridge Biomedical Campus, Cambridge CB2 0QH, UK. [3]Department of Astronomy, Harvard University, Cambridge, MA 02138, USA.
*Corresponding author. Email: sukrufurkanozturk@g.harvard.edu

amplification of the induced ee at the surface, necessary to reach a homochiral state (Fig. 1). Here, we report the spin-selective homochiral crystallization of a ribonucleotide precursor, RAO, on magnetite surfaces, from its completely racemic solution (Figs. 2 and 3).

Homochirality of RNA and the central role of RAO

RNA is thought to have played two major roles in the origin of life. The sequence of the nucleobases attached to the sugar phosphate backbone constitutes genetic information that can be passed from generation to generation by replication via a complementary strand through Watson-Crick base pairing. The sequence of an RNA also dictates its shape, and it is the adoption of a wide variety of shapes that endows RNA with its catalytic ability. Enantiomeric purity of the nucleotide components of RNA is crucial to both its roles. Replication via a complementary strand proceeds by way of an A-form duplex, and this is not possible if the nucleotide components deviate significantly from enantiomeric purity. Incorporation of a nucleotide of opposite handedness into an RNA strand changes its shape, and this might endow a different or improved catalytic ability, but the chirality switch cannot be passed to subsequent generations by replication, so the potentially beneficial change is nonhereditable. Establishing a mechanism whereby the nucleotide building blocks of RNA might have been synthesized enantiomerically pure is thus crucial to understanding how Earth's RNA-based life originated. Peptides too depend on the enantiomeric purity of their component amino acids. In extant biology, the correlation of D-ribonucleotides with L-amino acids is established in two principal ways. Ribonucleotides and chiral amino acids are biosynthesized with high stereoselectivity, and L-amino acids are attached to transfer RNA (tRNA) composed of D-ribonucleotides by stereoselective aminoacyl-tRNA synthetases. The idiosyncratic behavior of amino acids makes the synthesis of all L-amino acids under early Earth conditions a daunting challenge, but recent findings suggest that this hurdle might be side-stepped. Prebiotically plausible chemical means of attaching amino acids to tRNA analogs have been found and proceed with high-level control of relative stereochemistry. Thus, for example, the L- over D-stereoselectivity for attachment of alanine to a tRNA acceptor stem mimic composed of D-ribonucleotides is of the order of 10:1 (*33*). This suggests that the overall homochirality problem of prebiotic chemistry might be reduced to the problem of making ribonucleotides in enantiopure form; racemic amino acids might suffice.

RAO emerged as a potentially important ribonucleotide precursor more than 50 years ago, but there remained several issues to be dealt with before its true potential was realized. Sanchez and Orgel (*20*) showed that RAO (which they synthesized from ribose and cyanamide) was a highly crystalline compound that underwent reaction with cyanoacetylene to generate α-cytidine, but subsequent conversion to the natural β-anomer was very inefficient. Furthermore, the synthesis of ribose is one of the persistent challenges of prebiotic chemistry; although the formose reaction is now very well understood, it still cannot be controlled to produce more than a trace of ribose as part of a complex mixture. Nevertheless, the attractiveness of RAO prompted further research, and Springsteen and Joyce (*21*) showed that it could be sequestered from simpler mixtures of sugars than those made by the formose reaction by reaction with cyanamide followed by crystallization. Joyce also reported more on the crystallization behavior of RAO and showed that it crystallized in the chiral $P2_12_12_1$ space group and that crystals grown from solutions of *rac*-RAO were composed of twinned clusters with individually homochiral domains. The problem with the provenance of ribose was solved when Sutherland and colleagues showed RAO could be obtained, along with lesser amounts of the other pentose aminooxazolines, by reaction of glyceraldehyde

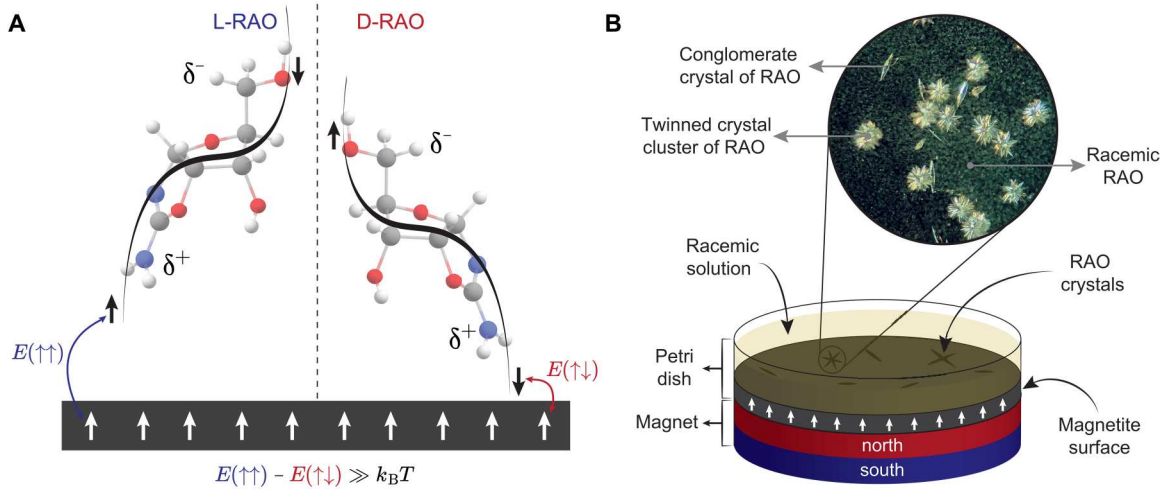

Fig. 1. The mechanism of spin-selective crystallization due to the CISS effect and the experimental setup. (**A**) As molecules approach a surface, they transiently acquire an induced charge polarization. Because of the CISS effect, transient charge polarization of a chiral molecule is accompanied by spin polarization. The spin state associated with the charge poles is determined by the handedness of the chiral molecule. Because the magnetic surface itself is spin-polarized, it kinetically favors (akin to a seed crystal) the enantiomer whose transient spin state results in a lower-energy spin-exchange interaction. The lower-energy overlap with the magnetic surface is singlet-like (red, ↑↓) and the higher-energy overlap is triplet-like (blue, ↑↑). The energy difference between these two configurations is higher than the room temperature, k_BT; therefore, the effect robustly manifests itself. (**B**) Schematic of the setup used in the crystallization experiments and a sample microscope image of the RAO crystals on a magnetite surface from a direct crystallization experiment. The image shows the magnetite surface as the black background and the needle-shaped conglomerate crystals of RAO formed on the surface, as well as the twinned crystals with stochastically arranged needles of D- and L-RAO, and racemic RAO in the form of a flaky powder suspended in the water column above the surface.

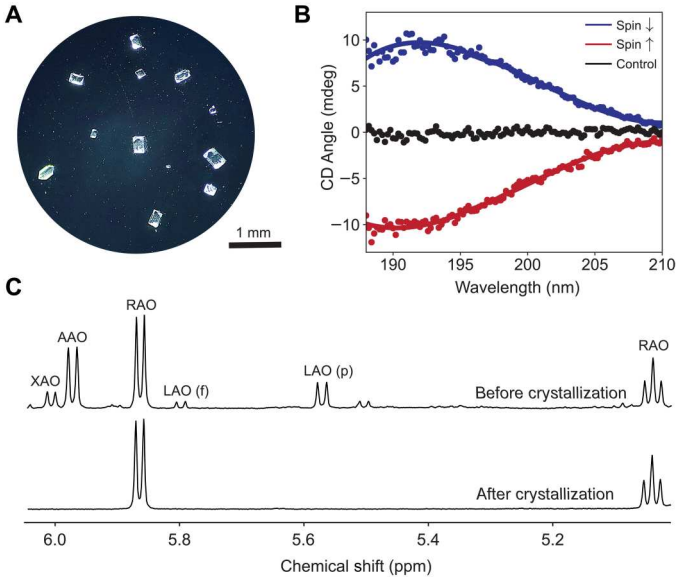

Fig. 2. Stereoselective and enantioselective crystallization of RAO. (**A**) A microscope image of the nearly enantiopure RAO crystals formed on a magnetite surface from their racemic solution. (**B**) Circular dichroism (CD) spectra of the crystals formed on the magnetite surface. The red (blue) spectrum corresponds to D-RAO (L-RAO) crystals formed when the magnetite surface is magnetized parallel (antiparallel) to the surface normal. Both spectra are obtained when racemic RAO is recrystallized, and they show a cumulative ee of about 60% for the whole surface. The black spectrum corresponds to crystallization on a nonmagnetic, silicon surface in the presence of a magnetic field, and it shows no selectivity. The latter control experiment shows that the enantioselective effect is due to the spin-exchange interaction, not due to the applied magnetic field. (**C**) ^{1}H nuclear magnetic resonance (NMR) spectrum (400 MHz; H_2O/D_2O, 90:10) before and after the direct crystallization of RAO. Before the crystallization, the solution is a mixture of four aminoxazolines: RAO/AAO/LAO (f for furanose and p for pyranose)/XAO (42:30:18:10). After the crystallization, the redissolved crystals only contain RAO within the limits of ^{1}H NMR detection. Thereby, mere crystallization on the magnetic surface stereoselectively and enantioselectively purifies RAO. ppm, parts per million.

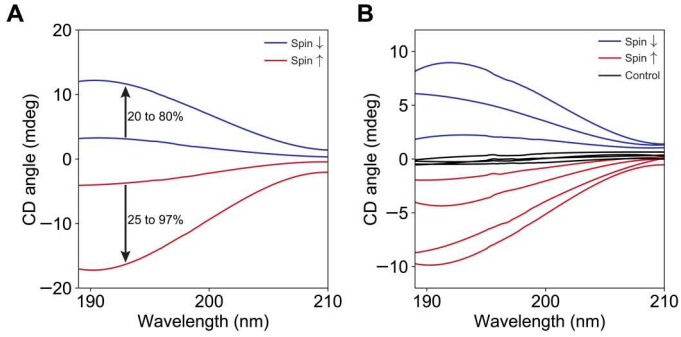

Fig. 3. Recrystallization of enantioenriched and racemic RAO on magnetite. (**A**) When we crystallized enantioenriched solutions of RAO, we observed a marked increase in the enantiomeric excess (ee), and, from about 25%, ee we could reach a homochirality state. The 25% enriched D-RAO (red) is crystallized on an up-spin magnetite, and we obtained homochiral D-RAO. Similarly, 20% enriched L-RAO (blue) is crystallized on a down-spin magnetite, and we obtained nearly homochiral (80%) L-RAO. (**B**) Repeated recrystallization of racemic RAO is done to accumulate statistics. DL-RAO is crystallized on up- and down-spin magnetite. Red curves correspond to up-spin and blue curves to down-spin. Black lines are the control experiments done on a silicon surface in the presence of the magnetic field. The ee for the down-spin experiments is calculated to be 59, 36, and 18 (mean, 38%). The ee for the up-spin experiments is calculated to be −10, −22, −41, and −54 (mean, −32%). The ee for the control experiments is calculated to be 5.5, 0.9, 0.6, and −3.4 (mean, 0.9%). We estimate an error of ±5% for the ee calculations.

with 2-aminooxazole, the latter itself deriving from the reaction of glycolaldehyde with cyanamide (*22*). The same group also found that nonracemic solutions of RAO gave rise to crystals with increased ees, and, above a threshold ee, enantiopure crystals were obtained. This behavior is consistent with a conglomerate susceptible to twinning. The conglomerate nature of RAO was lastly proven by Powner (*34*). Then, high-yielding prebiotic syntheses of ribonucleotides from aminooxazolines were reported by Sutherland and colleagues. First, it was shown that arabino-aminooxazoline could be elaborated to pyrimidine nucleoside cyclic phosphates (*23*); then, it was shown that RAO could be converted to pyrimidine nucleotides by a reaction sequence involving a photochemical inversion of the anomeric stereocenter (*25*). In the meantime, Blackmond and colleagues had shown that enantiomerically enriched proline could participate in the reaction of 2-AO with glyceraldehyde and give enantiopure RAO after crystallization (*17*). What has remained elusive, however, is how racemic compounds could give rise to enantiopure RAO purely by means of a process controlled only by the environment.

CISS and spin-selective chemistry

The CISS effect has established a robust coupling of electron spin to molecular chirality. The initial experiments have shown that the electron transfer through a chiral monolayer is spin-dependent and that the preferentially transferred spin state depends on the handedness of the monolayer (*35*, *36*). The experiments have achieved near-perfect spin filtering at room temperature, showing the robustness of the coupling (*37*). Later work has proved that the coupling established by the CISS effect can be manifested in various ways from spintronic applications to long-range electron transfer in biology (*38*–*40*). More recent studies have shown that spin-selective behavior exists for freely diffusing molecules near magnetic surfaces (*41*, *42*) and even for achiral reagents (*43*, *44*). These studies have motivated us to consider the spin-selective processes near magnetic surfaces due to the CISS effect to impose a chiral bias on prebiotic chemistry.

Recently, we proposed closed-basin evaporative lakes with authigenic ferrimagnetic sediments (e.g., magnetite and greigite) as plausible prebiotic environments in which enantiospecific processes can be carried out because of the CISS effect (*28*). Our mechanism used UV-ejected photoelectrons from magnetite surfaces as chiral agents in reductive synthesis because of the helical character of such electrons in the close vicinity of the magnetic surface [figure 1 of (*28*)]. We proposed that these helical electrons can achieve kinetic resolution in the reduction of chiral molecules for which the reaction rates for enantiomers differ by $\exp\left(\frac{2H_{SO}}{k_B T}\right)$. Here, H_{SO} is defined as the effective coupling due to a combination of spin-orbit and spin-exchange interactions of a chiral molecule with an electron, k_B is the Boltzmann constant, and T is the temperature [figure 2 of (*28*)]. As a suitable chemistry to apply our idea, we proposed cyanosulfidic chemistry that uses photoejected hydrated electrons to drive the reductive synthesis of sugars (*24*, *45*). In particular, we focused our attention on the spin-selective reduction of the cyanohydrin of

glycolaldehyde that is producing glyceraldehyde, the first chiral sugar, and an RNA precursor, after the hydrolysis of the resultant imine. Although this proposed reduction is still a worthy experiment, the isomerization of glyceraldehyde to dihydroxyacetone and the cyanide liberating equilibrium of the reagent cyanohydrin make it a harder reaction to study. Moreover, freely diffusing molecules with a single chiral center are likely to display less enantioselective behavior due to the reduced coupling of the electron spin to the molecular frame. Therefore, in this work, we studied the crystallization of the stable RNA precursor, RAO, as a static process with higher selectivity, on a magnetic surface.

We should emphasize that, if realized, enantioselective synthesis of glyceraldehyde reinforces the spin-selective crystallization of RAO as glyceraldehyde's chirality directly determines the chirality of RAO as can be seen in the blue box in Fig. 4B. However, the crystallization process does not rely on starting from an enantioenriched solution of RAO; therefore, our results presented here are self-sufficient to achieve a homochiral RNA world.

Magnetic surfaces as chiral agents

Magnetic surfaces themselves can be chiral agents due to the CISS effect, and surface processes such as crystallization or adsorption on a magnetic surface can be enantioselective. As demonstrated by the early CISS experiments, electron flow from a surface through a chiral monolayer is spin-dependent. The same effect manifests itself when a chiral molecule acquires an induced charge polarization because the latter is nothing but a transient electron flow inside a chiral potential. In addition, because of the CISS effect, charge polarization is accompanied by spin polarization. This transient, induced charge polarization can be due to intermolecular interactions among chiral molecules or between a chiral molecule and a surface (*39*, *46*).

When a chiral molecule approaches a surface, the electron density of the molecule redistributes itself, which gives rise to an induced charge dipole. In addition, for a chiral molecule, this transient electron flow is spin-dependent due to the CISS effect and gives rise to a transient spin polarization as shown in Fig. 1A. This spin polarization is realized along the chiral molecular axis, and it is dependent on the handedness of the chiral molecule. In Fig. 1A, the right-handed (D) enantiomer has the minority spin (↓) on its positively charged pole (δ^+), whereas the left-handed (L) one has the majority spin (↑). This is how the chiral symmetry is broken by a magnetic surface, which is itself spin-polarized: The spin-exchange interaction between the surface electron spins and the transiently spin-polarized chiral molecules is higher or lower depending on the handedness of the molecule. The favorable, lower energy interaction with the surface corresponds to a singlet-like (↑↓), and the penalized, higher energy interaction corresponds to a triplet-like (↑↑) overlap of the spins. Therefore, a spin-polarized surface kinetically traps an enantiomer based on its spin polarization and breaks the chiral symmetry. In other words, a magnetized surface can be considered as a crystal seed, breaking the chiral symmetry by promoting the crystallization of one enantiomer. However, it should be noted that this is a kinetic entrainment–like phenomenon and not a thermodynamic effect. Therefore, if all molecules are allowed to crystallize, then the enantioselective effect cannot be observed.

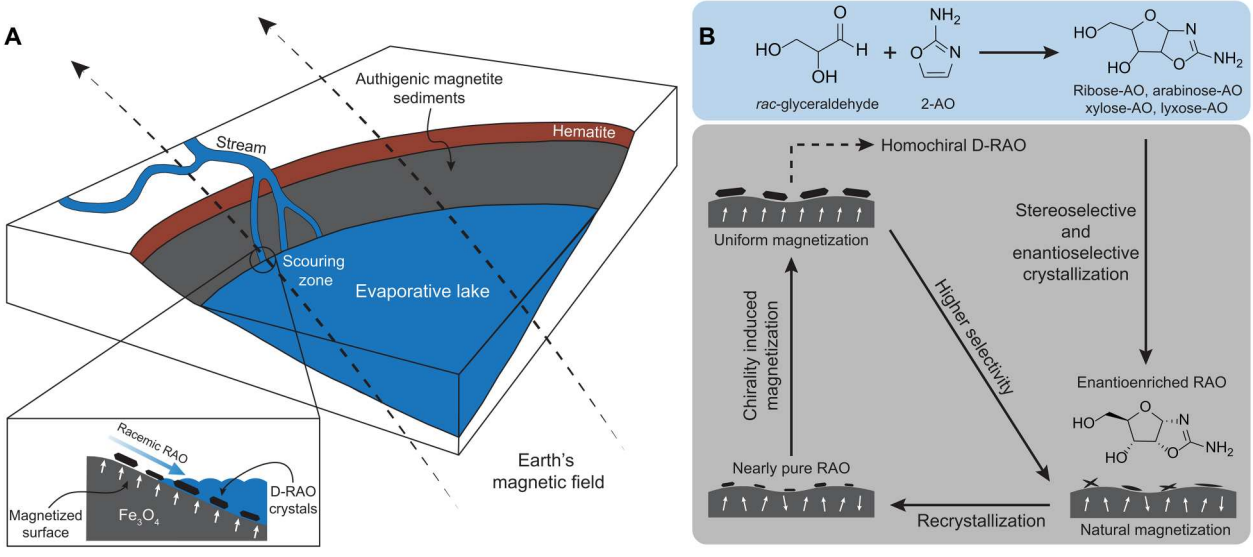

Fig. 4. An evaporative lake with magnetic sediments can accommodate spin-selective processes between an RNA precursor and a magnetized surface. (**A**) An evaporative lake contains authigenic magnetite sediments magnetized by the Earth's magnetic field. An incoming stream with racemic aminooxazolines scours the muddy material off the surface. As the lake evaporates, D-RAO selectively crystallizes on the magnetic surface. (**B**) An incoming stream carries the reaction products of racemic glyceraldehyde and 2-aminooxazole: racemic RAO, AAO, XAO, and LAO. Initially, the magnetic sediments are authigenically magnetized and carry a bias along the Earth's field. This natural bias enables the enantioselective crystallization of RAO, which also sterically purifies RAO from the mixture of aminooxazolines. After a small enantiomeric imbalance is induced, sporadic water flow redissolves the RAO crystals, and, in a subsequent dry phase, RAO recrystallizes on the surface with higher enantiomeric excess (ee). As these nearly pure conglomerate crystals accumulate more material, they cover a larger area of the surface and flip the spin of magnetic domains along the chiral molecular axis. This chirality-induced magnetization process increases the magnetization of the surface and allows for a positive feedback loop between the magnetic surface and the chiral crystals. As a result, the surface with higher magnetization induces higher ee for the upcoming crystallizations, and, eventually, enantiopure D-RAO is obtained.

Enantioselective behavior on magnetic surfaces due to the CISS effect has been demonstrated with the adsorption of chiral molecules like double-stranded DNA and L-cysteine on magnetized ferromagnetic films (*30*). Moreover, enantioseparation on magnetic surfaces by conglomerate crystallization has been realized by Tassinari *et al.* (*31*) with a moderate ee. This pioneering study lays the groundwork for our current research, as we use the same effect with a higher efficiency while also ensuring its relevance to prebiotic conditions. Therefore, we use magnetite (Fe_3O_4) surfaces available on early Earth and stable under ambient conditions and work with a compound (i.e., RAO) central to the synthesis of RNA, from which the propagation of homochirality to the entire prebiotic network is possible.

Naturally, the CISS-driven interaction between chiral molecules and magnetic surfaces work both ways around: A chiral molecule can also selectively spin polarize a magnetic surface and the direction of this polarization is determined by the handedness of the chiral molecule. This effect has also been demonstrated by the chirally selective magnetization switching in a ferromagnet upon the adsorption of chiral molecules (*47*). In that work, Ben Dor *et al.* (*47*) have shown that chiral molecules can robustly affect the magnetization of surfaces due to the long-range spin-exchange interaction. Chirality-induced magnetization switching combined with the presented results pave the way for positive feedback between chiral molecules and magnetic surfaces that can purify the magnetization of the iron-oxide sediments and thus promote the homochiral crystallization of RAO.

Feedback between the magnetic surface and RAO

Using the CISS-based interaction between magnetic surfaces and chiral molecules, it is possible to envision a positive feedback loop between the magnetite surfaces and RAO in a prebiotic setting as shown in Fig. 4B.

Magnetite is the most abundant natural magnetic mineral on Earth, as well as the strongest one (*48*, *49*). In a wide range of natural depositional environments, authigenic magnetite sediments form and magnetize under the Earth′s field, resulting in a chemical remanent magnetization (*50*). Sediments that acquired a chemical remanence after the most recent geomagnetic reversal are expected to have a statistically uniform remnant magnetization on a hemisphere scale within a shallow depth interval (*51*). This initial natural bias of the magnetic domains can break the chiral symmetry if racemic RAO crystallizes on the magnetic surface. However, because of the imperfect alignment of the magnetic domains, the first crystallization attempt can only induce a small enantiomeric imbalance. However, after the enriched crystals are dissolved due to a sporadic water flow and recrystallize on the magnetic surface again, the selectivity will be higher due to the asymmetric crystallization of RAO (*22*) and further magnetic seeding due to the CISS effect (Fig. 4). When these nearly pure RAO conglomerates grow on the surface, they can simultaneously interact with the surface spins and switch the magnetization of the surface. This process can purify the magnetic domains along the chiral molecular axis of RAO. In addition, because these sedimentary rocks are no longer small superparamagnetic particles, this CISS-induced magnetic diagenesis can permanently lock the surface spins along one direction, unless a large (much larger than Earth′s field) coercive field is applied. When the surface spins are locked once and for all, they can induce efficient enantioselectivity for the upcoming crystallizations and the magnetized surface can separate homochiral RAO crystals in just a few cycles.

This feedback mechanism can be more effectively realized over a small area such as the scouring zone of an incoming stream as shown in Fig. 4A. At the scouring zone, the authigenic magnetic sediments are exposed, wet-dry cycles are more frequently realized (like a shore), and an incoming stream can constantly feed the surface with racemic RAO. With the described feedback mechanism, magnetized magnetite sediments at the scouring zone can filter out homochiral RAO crystals from the incoming racemic stream.

RESULTS

We have studied the crystallization of RAO from its racemic solution on magnetite surfaces. We fabricated the magnetite surfaces as thin films (200 nm) on silicon substrates following the procedure by Jubb and Allen (*52*) (see also section S5). We used electron beam evaporation to deposit 100-nm iron on silicon (100) surface and then heated the sample at 175°C for 4 hours to promote the oxidation of iron, producing a magnetite film of about 200 nm. We characterized the samples by Fourier transform infrared spectroscopy and confirmed the complete conversion of iron to magnetite (fig. S5). We further analyzed the surface roughness and magnetic properties of the samples by atomic force microscopy (AFM) and superconducting quantum interference device (section S6). We placed the magnetite surfaces horizontally in a petri dish and placed a magnet just below the surface as shown in Fig. 1B. We used the magnet to spin-polarize the magnetite surface and measured the magnetic field to be 325 mT at the surface location. It is important to place the magnet such that the magnetization direction is parallel to the surface normal to maximize the helical character of the surface electrons.

The ^{1}H nuclear magnetic resonance (NMR) spectra confirmed the stereoselective crystallization of RAO, as has been previously reported (*21*, *22*). Having identified the composition of the crystals by NMR, we measured the chiro-optical properties by circular dichroism (CD) spectroscopy. We obtained a nonzero CD signal for the individual needle-shaped crystals of RAO; however, the rosette-shaped crystals did not consistently give a CD signal. We further analyzed the rosette-shaped crystals by x-ray crystallography and found that the individual arms of the rosettes contain only one enantiomer yet the crystal as a whole is racemic. Therefore, we found that the rosettes formed because of the twinning of needle-shaped homochiral domains. When we analyzed rosettes with less homochiral domains, we obtained a nonzero CD signal with a randomly varying sign. However, the rosettes with more branching did not give a CD signal. We also did a control experiment by crystallizing the enantiopure compound and still observed the formation of rosette-shaped crystals. Therefore, we concluded that the twinned, rosette-shaped crystals formed because of a stochastic arrangement of homochiral domains. Because this stochastic twinning occurs on an existing crystal face, it nullifies the enantioselection seeded by the magnetic surface. For the experiments in which we primarily obtained needles on the surface (fig. S12), we observed a surface-wide ee (in addition to the ee of the individual crystals); however, for most of the cases, we could not consistently avoid the formation of the twinned crystals. Therefore, we did not observe consistent selectivity for direct crystallization experiments on magnetite

surfaces. However, if the rosette formation can be avoided by the change of conditions, such as concentration, buffer, or pH, then it should be possible to observe selectivity for direct crystallization.

We proceeded with the recrystallization of RAO. We synthesized racemic RAO by the reaction of D- and L-ribose with cyanamide on a large scale. We confirmed that synthesized RAO is fully racemic with a CD measurement before the crystallization experiments (fig. S18). We then prepared a 65 mM solution of the racemic RAO in pure water and placed it on the magnetized magnetite surface. We followed the same crystallization procedure described above and obtained diamond-shaped crystals on the magnetite surface as shown in Fig. 2A. We collected the crystals with tweezers, dissolved them in pure water, and obtained their CD spectra: first individually and after for the whole surface. We confirmed that diamond-shaped crystals of RAO are individually homochiral by CD and x-ray diffraction measurements. These diamond-shaped crystals and the individual needle-shaped ones both gave identical x-ray diffraction patterns, and they all belong to the $P2_12_12_1$ chiral space group. However, with the diamond-shaped crystals, we did not observe twinning when the crystallization is stopped soon after the crystals are observed. When we waited longer, as the crystals grew in size, we observed that a crystal face became a seed for the other enantiomer. However, these twinned crystals mostly contained two to three macroscopic, homochiral domains unlike the rosettes containing many arms, for which each arm is an individual, homochiral domain. In addition, for the recrystallization experiments, twinned diamond crystals appeared well after the individual diamonds were formed and visible; therefore, we could stop the experiment before the twinning started to take over. However, for the direct crystallization experiments, rosettes appeared almost simultaneously with the needles so there was no slow progression of the twinning that we could control.

Having confirmed that diamond-shaped crystals are individually homochiral, we dissolved all the crystals on the magnetite surface together in water and obtained the CD spectrum for the whole surface. To our delight, not only the individual crystals showed optical activity but also the entire surface did. As the smoking gun of the CISS-driven phenomenon, when we reversed the magnetic field direction (therefore, the spin state of the surface electrons), the observed CD signal reversed in sign. As shown in Fig. 2B, left-handed RAO crystals (blue curve) dominated the down-spin (↓, south pole) surface and the right-handed ones dominated the up-spin (↑, north pole) surface. We obtained an ee of about 60% for the entire surface, for both spin directions starting from a completely racemic solution of RAO. (Check section S8.3 on how the ee is calculated.) For this step, it was crucial to collect the crystals early, as the enantioselectivity of the magnetic surface is a kinetic entrainment effect, and, beyond a certain point, ee decreased with the increasing crystallization yields and due to enantiomorphous twinning. Crystals were usually visible after several hours, and we collected them after about 6 hours to a day. We collected 48 and 16 individual crystals for the up-spin and down-spin experiments, respectively, for the data shown in Fig. 2B. Because of the high number of crystals and the repeatability of the results (Fig. 3B), we can rule out the presence of a net ee due to statistical fluctuations of homochiral crystals.

We investigated the reason why recrystallization of RAO gives crystals with different morphology (diamond-shaped) compared to direct crystallization of the reaction products of glyceraldehyde and 2-aminooxazole (needle-shaped) and crystallized RAO with added aminooxazolines [arabino-AO (AAO), lyxo-AO (LAO), and xylo-AO (XAO)] one by one. We found that, in the presence of XAO, RAO crystallizes as needle-shaped crystals, whereas AAO and LAO do not visibly modify the crystallization habit of RAO. Moreover, we observed a concentration-dependent formation of the rosette-shaped twinned crystals only when RAO is crystallized in the presence of XAO (fig. S26). At higher concentrations, when XAO is present in the solution, RAO forms rosette-shaped crystals, and the crystal morphology is altered by the relative amount of XAO (fig. S26); therefore, we conclude that XAO is a crystal habit modifier for RAO [see scheme 1 of (*53*)]. We also found that, at higher relative concentrations (e.g., 1:1), XAO is embedded in the crystal lattice structure of RAO as an impurity with 4.8(4)% abundance, as detected by x-ray diffraction analysis (fig. S31). Last, we found that XAO affected the RAO crystallization only when the relative stereochemistries matched (e.g., D-RAO with D-XAO); we did not observe any effect of XAO when we crystallized L-RAO with D-XAO. These findings show the necessity of recrystallization to observe enantioenrichment to enantiopurity, as, by removing XAO from the solution, racemizing stochastic twinning is circumvented.

As a control experiment, we recrystallized RAO on a nonmagnetic, silicon surface in the presence of a magnetic field of the same strength, and we collected the crystals from the nonmagnetic surface and obtained the black spectra in Fig. 2B. As seen, the surface with no net spin polarization does not induce any enantioselectivity in the presence of a magnetic field, as shown by Pasteur (*1*). The control experiment confirms that the observed selectivity is not due to the magnetic field but due to the spin-exchange interaction. The control experiments on the nonmagnetic surface and the consistent flipping of the ee (Fig. 3B) with the flipping magnetic pole direction ensure that the obtained ee is physical and not due to the contamination of surfaces with chiral impurities.

We repeated the recrystallization experiment on magnetite for both pole directions multiple times and found that, on average, we can get around 35% ee for the entire magnetite surface. We then considered this value as a typical outcome from a racemic solution and then crystallized the enriched crystals on the magnetic surface one more time. We found that, above a starting ee of about 25%, we can obtain completely enantiopure crystals (Fig. 3A). Therefore, in just two crystallization steps on the magnetic surface, we could achieve homochirality from a completely racemic mixture.

DISCUSSION

We have demonstrated an efficient mechanism to resolve racemic RAO, an important RNA precursor, on a prebiotically available mineral surface, magnetite (Fe_3O_4), and obtained homochiral crystals of RAO in two crystallization steps.

Our mechanism features the two requisites to reach homochirality: chiral symmetry breaking by the magnetic surface due to the CISS effect and self-amplification by conglomerate crystallization. The symmetry breaking by magnetic surfaces is prebiotically plausible, nondestructive, and robust at room temperature and in solution. Although the demonstrated symmetry breaking is a surface effect [two-dimensional (2D)], conglomerate crystallization allows for the extension into the bulk (3D). Therefore, the attained

selectivity at the surface level can be seamlessly carried into the bulk of the solution.

Our mechanism requires a well-defined magnetic surface (fig. S10), and the crystallization on colloidal magnetic particles is not enantioselective. A detailed discussion on this can be found in section S7.1. In light of this fact, we consider sedimentary rock surfaces similar to those found in the Gale crater (*54*), as opposed to colloidal muds, as likely sites to realize our mechanism. In these environments, magnetite is present as inclusions in silica-based rocks (magnetite-silica facies) and is highly magnetic, especially as single-domain particles (*49*, *54*). In such a setting, we envision a kinetically favored crystallization of RAO on magnetized magnetite inclusions.

With the feedback effect that we suggested, our mechanism offers a persistent and deterministic chiral bias to prebiotic chemistry as opposed to a singular and stochastic trigger (e.g., spontaneous symmetry breaking). The advantage of this over a spontaneous one is that, at various stages of prebiotic chemistry, the same chiral bias is present in the environment in a persistent basis, reinforcing the previously attained ee. In addition, by combining the symmetry breaking with a well-matched, simultaneous amplification, we have shown a direct way to reach the homochiral state from a completely racemic starting point.

The mechanism is a kinetic entrainment–like effect, and the magnetic surface acts as a chiral seed based on its magnetization direction. Because of the kinetic nature of the effect beyond a certain point, enantioselectivity will decrease with increasing crystallization yields, as the system approaches to the thermodynamic equilibrium. Because of this, the mechanism can benefit from the presence of flow as previously considered by Ritson *et al.* (*55*). As such, we can conceive of the enantioselective crystallization of RAO on the scouring zone of an evaporative lake by an incoming stream carrying the racemic solution of sugar aminooxazolines. In this scenario, the crystallization takes place on the shallow shores of the magnetite lake, which can undergo multiple wet-dry cycles, allowing several crystallization-dissolution cycles of RAO. The flow also scours the soft, muddy material off the surface and exposes the authigenic magnetite sediments on which enantioselective processes can take place. Moreover, while the flow feeds the magnetic surface with a racemic solution of RAO, it simultaneously washes the other enantiomer in the solution and the racemic powder suspended in the bulk away from the zone and allows for higher enantioselectivity.

It seems more convenient to conceive of the feedback loop that we propose on a smaller region rather than the whole surface of the lakebed. With selective crystallization and magnetization cycles, the spin purity of the magnetic surface around the scouring zone can be locked with less material, and this small bottleneck region over which the material flows can act as a chiral filter for the incoming RAO. Nevertheless, achieving our enantioseparation mechanism is not a fine-tuned geochemical scenario, and one can come up with other (or more refined) prebiotically plausible scenarios compatible with this process. We, therefore, emphasize the robustness and the strength of our mechanism rather than the specific geochemical scenario that can accommodate the enantioseperation process.

The efficiency of the enantioseparation by magnetic surfaces is concentration-dependent, and it works best around or below the solubility limit of the compound. At higher concentrations, the selectivity goes down as the eutectic equilibrium forces the crystallization. Therefore, the slower the crystallization process and the lower the concentration, the higher the enantioselectivity. The low solubility of RAO in water allowed for obtaining its crystals at low concentrations; therefore, we could achieve high enantioselectivity in just one crystallization in comparison to the previous work by Tassinari *et al.* (*31*) with highly soluble amino acids in water. Our results can be further improved if the magnetic surface is placed vertically such that the crystals forming in the bulk do not fall on the magnetic surface and reduce the selectivity, as demonstrated by Bhowmick *et al.* (*32*).

In addition, we used magnetite as the magnetic substrate with near-unity spin polarization at its Fermi level (*56*) in comparison to commonly used Ni/Au substrates with lower intrinsic spin polarization (around 20%) and protective gold layer further reducing the spin polarization (*31*, *32*). Therefore, we have shown that magnetite surfaces can be used effectively in the CISS experiments due to their optimal spin polarization properties.

Similar to the previous work by Tassinari *et al.* (*31*), we used magnetic substrates to resolve chiral compounds, yet our work is constrained by prebiotic relevance, and our results differ from theirs in multiple aspects. First, we obtain higher ee′s and achieve homochirality due to the low solubility of RAO in water and high spin polarization of magnetite. Because of the high solubility of conglomerate-forming amino acids in water, Tassinari *et al.* (*31*) used supersaturated solutions prepared at 80°C, resulting in lower ee′s. In contrast to this, RAO is poorly soluble (~0.01 g/ml) in water, and its conglomerate crystallization does not require supersaturation or extreme conditions that are prebiotically implausible. In addition, they achieve the selective crystallization of racemic amino acids from their aqueous solutions only by asparagine as they could not resolve racemic threonine, and glutamic acid is resolved as its hydrochloric acid (HCl) salt in high concentrations of HCl. This harsh condition is prebiotically unlikely, and HCl is known to dissolve magnetite, creating iron chlorides. Therefore, the pioneering work by Tassinari *et al.* (*31*) establishes the feasibility of the enantioseperation mechanism using magnetic substrates however does not account for the origin of biological homochirality.

Although we used stronger magnetic fields to spin-polarize the magnetite surfaces than what was likely available on early Earth, similar spin polarizations under weak fields can be achieved if magnetite forms as small (~100 nm in diameter) superparamagnetic particles. Such authigenic magnetite particles have been shown to have remanent magnetizations of above 10 kA/m even when they form under weak magnetic fields (0.1 mT ≈0.08 kA/m) comparable to the Earth′s (*49*). Because our mechanism is based on spin-exchange interaction rather than a magnetic field effect, the figure of merit is not the magnetic field strength but the degree of spin alignment (magnetization) at the active surface. Hence, one should pay attention to the prebiotically relevant remanent magnetizations available in natural magnetic minerals rather than early Earth′s magnetic field strength. Having said that, with the described feedback mechanism between the chiral molecules and the magnetic surface, even higher magnetizations can be realized.

RAO is not just like any chiral compound; it has a central role in the synthesis of ribonucleotides, and its chirality directly determines the chirality of RNA. The attained homochirality at RNA can then be spread to peptides by the stereoselective binding of amino acids to the tRNA analogs (*33*). Moreover, RAO is very stable against isomerization unlike sugars like ribose or glyceraldehyde as well as against thermal degradation and UV damage. Therefore, it is a very suitable molecule to lock the chirality in prebiotic chemistry.

Combining this with the fact that it crystallizes as a conglomerate, RAO is an ideal molecule to apply the described enantioseparation mechanism. However, as shown by Tassinari *et al.* (*31*), the mechanism is versatile and applicable to other chiral molecules forming conglomerate crystals (e.g., asparagine).

MATERIALS AND METHODS

Reagents and solvents were obtained from Acros Organics, Santa Cruz Biotechnology, and Sigma-Aldrich and were used without further purification unless otherwise specified. We performed all of the experiments under ambient conditions unless otherwise specified.

Method for synthesizing RAO, AAO, XAO, and LAO

Ribo-, arabino-, xylo-, and lyxo-aminooxazolines were synthesized by the reaction of two equivalents of cyanamide with one equivalent of the corresponding aldopentose sugar. Cyanamide (5 g, 0.12 mol, 2 eq) was added to a solution of sugar (9 g, 0.06 mol, 1 eq) in aqueous ammonia (3.5%, 10 ml). Then, the resultant mixture was swirled at room temperature, and all solid material was dissolved. After 30 min, the solution was maintained at 60°C for another hour. The reaction mixture was then cooled to room temperature, and methanol (10 ml) was added to promote crystallization. After 16 hours at 4°C, the crystals were collected by filtration, washed with ice-cold methanol (20 ml), and dried under vacuum.

We separately purchased the L and D sugars and synthesized the L and D aminooxazolines in large amounts (gram level for each enantiomer). We then weighed the enantiomer on the scale, ground them into powder, and mixed them in equal amounts to make the racemic pentose aminooxazolines. We confirmed that the aminooxazolines are racemic by CD measurements.

Method for fabricating magnetite surfaces

We fabricated the magnetite films by evaporating a 100-nm iron layer on 0.625-mm-thick silicon (100) wafers using electron beam evaporation under a high vacuum of 5×10^{-6} torr. Following the evaporation, we baked the samples at 175°C for 4 hours in the air and promoted the oxidation of iron (Fe) to magnetite (Fe_3O_4). We then cleaned the sample surfaces with acetone and subsequently in ethanol before every experiment.

Method for crystallization experiments

For the direct crystallization experiments, we prepared a 0.5:0.5 M solution of racemic glyceraldehyde and 2-aminooxazole in 2 ml of water. We incubated the solution at 40°C for 12 hours and obtained a yellow-brown solution of aminooxazoles. For the recrystallization experiments, we prepared a 65 mM solution of racemic RAO in 2 ml of water.

We placed the magnetite surfaces horizontally in a polystyrene petri dish (35 mm by 10 mm) on a magnet such that the surface normal is parallel to the magnetization direction. The magnetic field strength at the sample position was measured to be 325 mT with a Hall probe. We then filled the petri dish with the incubated solution and made sure that the magnetite surface is covered with the liquid. We then placed the setup in the fridge kept at 12°C and waited until the first crystals appear. This process can take several hours to a few days. Afterward, we slowly filtered out the mother liquid and washed three times the surface and crystals with pure water such that the racemic liquid is washed away. We then collected the crystals with tweezers under a stereomicroscope. We discarded the crystals formed on the plastic surface of the petri dish and on the rough edges of the silicon substrate and collected the rest formed on the magnetite surface. We fully dissolved all of the collected crystals in pure water and analyzed the solution.

Method for CD measurements

We took the CD measurements in a quartz cuvette after diluting the solution in 2 ml of water until the UV/visible (Vis) absorption peak is below optical density of 1 for accurate measurements. We used the Jasco J-815 Circular Dichroism Spectropolarimeter with an active temperature control connected to a water bath with a temperature set to 20°C. The temperature feedback is performed by a Jasco PFD-425S/15 controller with a Peltier control unit. Before the measurements, we took a baseline measurement of the water and cuvette background. We simultaneously measured the CD and UV/Vis absorption of the sample together with the photomultiplier voltage to ensure that the spectrometer is not operating beyond its specified voltage range of 600 units. We took the measurements in the 185- to 210-nm wavelength range and used the auto-baseline subtraction feature. We used a data pitch of 0.2 nm, a bandwidth of 1 nm, a data integration time of 1 s, and a scanning speed of 20 nm/min. We averaged each measurement five times. We normalized the CD signal amplitude on the basis of the UV/Vis absorption and calculated the ee using the calibration procedure described in section S9 (*57*–*62*).

Supplementary Materials

This PDF file includes:

Materials and Methods
Sections S1 to S11
Figs. S1 to S32
Tables S1 to S11
Legend for movie S1
Legends for data S1 to S3

Other Supplementary Material for this manuscript includes the following:

Movie S1
Data S1 to S3

REFERENCES AND NOTES

1. L. Pasteur, On the relationships between the crystalline form, chemical composition and the direction of optical rotation. *Annales Chimie Phys.* **24**, 442–459 (1848).
2. G. Joyce, G. Visser, C. Van Boeckel, J. Van Boom, L. Orgel, J. VanWestrenen, Chiral selection in poly(C)-directed synthesis of oligo(G). *Nature* **310**, 602–604 (1984).
3. D. G. Blackmond, The origin of biological homochirality. *Cold Spring Harb. Perspect. Biol.* **2**, a002147 (2010).
4. W. Bonner, Chirality and life. *Orig. Life Evol. Biosph.* **25**, 175–190 (1995).
5. Q. Sallembien, L. Bouteiller, J. Crassous, M. Raynal, Possible chemical and physical scenarios towards biological homochirality. *Chem. Soc. Rev.* **51**, 3436–3476 (2022).
6. Y. Yamagata, A hypothesis for the asymmetric appearance of biomolecules on earth. *J. Theor. Biol.* **11**, 495–498 (1966).
7. I. Weissbuch, M. Lahav, Crystalline architectures as templates of relevance to the origins of homochirality. *Chem. Rev.* **111**, 3236–3267 (2011).
8. L. Addadi, Z. Berkovitch-Yellin, N. Domb, E. Gati, M. Lahav, L. Leiserowitz, Resolution of conglomerates by stereoselective habit modifications. *Nature* **296**, 21–26 (1982).
9. D. K. Kondepudi, R. J. Kaufman, N. Singh, Chiral symmetry breaking in sodium chlorate crystallization. *Science* **250**, 975–976 (1990).
10. P. De Marcellus, C. Meinert, M. Nuevo, J.-J. Filippi, G. Danger, D. Deboffle, L. Nahon, L. L. S. d'Hendecourt, U. J. Meierhenrich, Non-racemic amino acid production by ultraviolet

irradiation of achiral interstellar ice analogs with circularly polarized light. *Astrophys. J. Lett.* **727**, L27 (2011).
11. R. Rosenberg, M. A. Haija, P. Ryan, Chiral-selective chemistry induced by spin-polarized secondary electrons from a magnetic substrate. *Phys. Rev. Lett.* **101**, 178301 (2008).
12. N. Globus, R. D. Blandford, The chiral puzzle of life. *Astrophys. J. Lett.* **895**, L11 (2020).
13. D. G. Blackmond, Autocatalytic models for the origin of biological homochirality. *Chem. Rev.* **120**, 4831–4847 (2019).
14. D. G. Blackmond, The origin of biological homochirality. *Cold Spring Harb. Perspect. Biol.* **11**, a032540 (2019).
15. C. Viedma, Complete chiral purity induced by nonlinear autocatalysis and recycling. *Phys. Rev. Lett.* **94**, 065504 (2005).
16. D. B. Amabilino, R. M. Kellogg, Spontaneous deracemization. *Israel J. Chem.* **51**, 1034–1040 (2011).
17. J. E. Hein, E. Tse, D. G. Blackmond, A route to enantiopure RNA precursors from nearly racemic starting materials. *Nat. Chem.* **3**, 704–706 (2011).
18. J. E. Hein, D. G. Blackmond, On the origin of single chirality of amino acids and sugars in biogenesis. *Acc. Chem. Res.* **45**, 2045–2054 (2012).
19. L. Legnani, A. Daru, A. X. Jones, D. G. Blackmond, Mechanistic insight into the origin of stereoselectivity in the ribose-mediated strecker synthesis of alanine. *J. Am. Chem. Soc.* **143**, 7852–7858 (2021).
20. R. A. Sanchez, L. E. Orgel, Studies in prebiotic synthesis. V. Synthesis and photoanomerization of pyrimidine nucleosides. *J. Mol. Biol.* **47**, 531–543 (1970).
21. G. Springsteen, G. F. Joyce, Selective derivatization and sequestration of ribose from a prebiotic mix. *J. Am. Chem. Soc.* **126**, 9578–9583 (2004).
22. C. Anastasi, M. A. Crowe, M. W. Powner, J. D. Sutherland, Direct assembly of nucleoside precursors from two- and three-carbon units. *Angew. Chem. Int. Ed.* **45**, 6176–6179 (2006).
23. M. W. Powner, B. Gerland, J. D. Sutherland, Synthesis of activated pyrimidine ribonucleotides in prebiotically plausible conditions. *Nature* **459**, 239–242 (2009).
24. B. H. Patel, C. Percivalle, D. J. Ritson, C. D. Duffy, J. D. Sutherland, Common origins of RNA, protein and lipid precursors in a cyanosulfidic protometabolism. *Nat. Chem.* **7**, 301–307 (2015).
25. J. Xu, M. Tsanakopoulou, C. J. Magnani, R. Szabla, J. E. Šponer, J. Šponer, R. W. Góra, J. D. Sutherland, A prebiotically plausible synthesis of pyrimidine β-ribonucleosides and their phosphate derivatives involving photoanomerization. *Nat. Chem.* **9**, 303–309 (2017).
26. J. Xu, V. Chmela, N. J. Green, D. A. Russell, M. J. Janicki, R. W. Góra, R. Szabla, A. D. Bond, J. D. Sutherland, Selective prebiotic formation of RNA pyrimidine and DNA purine nucleosides. *Nature* **582**, 60–66 (2020).
27. J. Xu, N. J. Green, D. A. Russell, Z. Liu, J. D. Sutherland, Prebiotic photochemical coproduction of purine ribo- and deoxyribonucleosides. *J. Am. Chem. Soc.* **143**, 14482–14486 (2021).
28. S. F. Ozturk, D. D. Sasselov, On the origins of life's homochirality: Inducing enantiomeric excess with spin-polarized electrons. *Proc. Natl. Acad. Sci. U.S.A.* **119**, e2204765119 (2022).
29. D. D. Sasselov, J. P. Grotzinger, J. D. Sutherland, The origin of life as a planetary phenomenon. *Sci. Adv.* **6**, eaax3419 (2020).
30. K. Banerjee-Ghosh, O. Ben Dor, F. Tassinari, E. Capua, S. Yochelis, A. Capua, S.-H. Yang, S. S. Parkin, S. Sarkar, L. Kronik, L. T. Baczewski, R. Naaman, Y. Paltiel, Separation of enantiomers by their enantiospecific interaction with achiral magnetic substrates. *Science* **360**, 1331–1334 (2018).
31. F. Tassinari, J. Steidel, S. Paltiel, C. Fontanesi, M. Lahav, Y. Paltiel, R. Naaman, Enantioseparation by crystallization using magnetic substrates. *Chem. Sci.* **10**, 5246–5250 (2019).
32. D. Bhowmick, Y. Sang, K. Santra, M. Halbauer, E. Capua, Y. Paltiel, R. Naaman, F. Tassinari, Simultaneous high-purity enantiomeric resolution of conglomerates using magnetic substrates. *Cryst. Growth Des.* **21**, 2925–2931 (2021).
33. L.-F. Wu, M. Su, Z. Liu, S. J. Bjork, J. D. Sutherland, Interstrand aminoacyl transfer in a tRNA acceptor stem-overhang mimic. *J. Am. Chem. Soc.* **143**, 11836–11842 (2021).
34. S. Islam, M. W. Powner, Prebiotic systems chemistry: Complexity overcoming clutter. *Chem* **2**, 470–501 (2017).
35. K. Ray, S. Ananthavel, D. Waldeck, R. Naaman, Asymmetric scattering of polarized electrons by organized organic films of chiral molecules. *Science* **283**, 814–816 (1999).
36. B. Göhler, V. Hamelbeck, T. Markus, M. Kettner, G. Hanne, Z. Vager, R. Naaman, H. Zacharias, Spin selectivity in electron transmission through self-assembled monolayers of double-stranded DNA. *Science* **331**, 894–897 (2011).
37. R. Naaman, D. H. Waldeck, Chiral-induced spin selectivity effect. *J. Phys. Chem. Lett.* **3**, 2178–2187 (2012).
38. R. Naaman, Y. Paltiel, D. H. Waldeck, Chiral induced spin selectivity and its implications for biological functions. *Annu. Rev. Biophys.* **51**, 99–114 (2022).
39. K. Michaeli, N. Kantor-Uriel, R. Naaman, D. H. Waldeck, The electron's spin and molecular chirality – how are they related and how do they affect life processes? *Chem. Soc. Rev.* **45**, 6478–6487 (2016).
40. R. Naaman, D. H. Waldeck, Spintronics and chirality: Spin selectivity in electron transport through chiral molecules. *Annu. Rev. Phys. Chem.* **66**, 263–281 (2015).
41. T. S. Metzger, S. Mishra, B. P. Bloom, N. Goren, A. Neubauer, G. Shmul, J. Wei, S. Yochelis, F. Tassinari, C. Fontanesi, D. H. Waldeck, Y. Paltiel, R. Naaman, The electron spin as a chiral reagent. *Angewandte Chemie* **132**, 1670–1675 (2020).
42. B. P. Bloom, Y. Lu, T. Metzger, S. Yochelis, Y. Paltiel, C. Fontanesi, S. Mishra, F. Tassinari, R. Naaman, D. H. Waldeck, Asymmetric reactions induced by electron spin polarization. *Phys. Chem. Chem. Phys.* **22**, 21570–21582 (2020).
43. T. S. Metzger, R. Siam, Y. Kolodny, N. Goren, N. Sukenik, S. Yochelis, R. Abu-Reziq, D. Avnir, Y. Paltiel, Dynamic spin-controlled enantioselective catalytic chiral reactions. *J. Phys. Chem. Lett.* **12**, 5469–5472 (2021).
44. D. K. Bhowmick, T. K. Das, K. Santra, A. K. Mondal, F. Tassinari, R. Schwarz, C. E. Diesendruck, R. Naaman, Spin-induced asymmetry reaction—The formation of asymmetric carbon by electropolymerization. *Sci. Adv.* **8**, eabq2727 (2022).
45. J. Xu, D. J. Ritson, S. Ranjan, Z. R. Todd, D. D. Sasselov, J. D. Sutherland, Photochemical reductive homologation of hydrogen cyanide using sulfite and ferrocyanide. *Chem. Commun.* **54**, 5566–5569 (2018).
46. R. Naaman, Y. Paltiel, D. H. Waldeck, Chiral molecules and the electron spin. *Nat. Rev. Chem.* **3**, 250–260 (2019).
47. O. Ben Dor, S. Yochelis, A. Radko, K. Vankayala, E. Capua, A. Capua, S.-H. Yang, L. T. Baczewski, S. S. P. Parkin, R. Naaman, Y. Paltiel, Magnetization switching in ferromagnets by adsorbed chiral molecules without current or external magnetic field. *Nat. Commun.* **8**, 14567 (2017).
48. R. J. Harrison, R. E. Dunin-Borkowski, A. Putnis, Direct imaging of nanoscale magnetic interactions in minerals. *Proc. Natl. Acad. Sci. U.S.A.* **99**, 16556–16561 (2002).
49. D. J. Dunlop, J. Arkani-Hamed, Magnetic minerals in the Martian crust. *J. Geophys. Res. Planets* **110**, 1–11 (2005).
50. D. J. Dunlop, O. Ozdemir, *Rock Magnetism: Fundamentals and Frontiers* (Cambridge Studies in Magnetism, Cambridge Univ. Press, 1997).
51. R. Karlin, M. Lyle, G. R. Heath, Authigenic magnetite formation in suboxic marine sediments. *Nature* **326**, 490–493 (1987).
52. A. M. Jubb, H. C. Allen, Vibrational spectroscopic characterization of hematite, maghemite, and magnetite thin films produced by vapor deposition. *ACS Appl. Mater. Interfaces* **2**, 2804–2812 (2010).
53. I. Weissbuch, R. Popovitz-Biro, M. Lahav, L. Leiserowitz, Rehovot, Understanding and control of nucleation, growth, habit, dissolution and structure of two- and three-dimensional crystals using `tailor-made' auxiliaries. *Acta Crystallogr. Sec. B Struct. Sci.* **51**, 115–148 (1995).
54. J. Hurowitz, J. Grotzinger, W. Fischer, S. McLennan, R. E. Milliken, N. Stein, A. R. Vasavada, D. F. Blake, E. Dehouck, J. L. Eigenbrode, A. G. Fairén, J. Frydenvang, R. Gellert, J. A. Grant, S. Gupta, K. E. Herkenhoff, D. W. Ming, E. B. Rampe, M. E. Schmidt, K. L. Siebach, K. Stack-Morgan, D. Y. Sumner, R. C. Wiens, Redox stratification of an ancient lake in Gale crater, Mars. *Science* **356**, eaah6849 (2017).
55. D. J. Ritson, C. Battilocchio, S. V. Ley, J. D. Sutherland, Mimicking the surface and prebiotic chemistry of early Earth using flow chemistry. *Nat. Commun.* **9**, 1821 (2018).
56. M. Schmitt, O. Kirilmaz, S. Chernov, S. Babenkov, D. Vasilyev, O. Fedchenko, K. Medjanik, Y. Matveyev, A. Gloskovskii, C. Schlueter, A. Winkelmann, L. Dudy, H. J. Elmers, G. Schönhense, M. Sing, R. Claessen, Bulk spin polarization of magnetite from spin-resolved hard x-ray photoelectron spectroscopy. *Phys. Rev. B* **104**, 045129 (2021).
57. T. D. Glotch, G. R. Rossman, Mid-infrared reflectance spectra and optical constants of six iron oxide/oxyhydroxide phases. *Icarus* **204**, 663–671 (2009).
58. I. Bruker, *Madison: Bruker AXS Inc* (2015).
59. L. Krause, R. Herbst-Irmer, G. M. Sheldrick, D. Stalke, Comparison of silver and molybdenum microfocus X-ray sources for single-crystal structure determination. *J. Appl. Cryst.* **48**, 3–10 (2015).
60. G. M. Sheldrick, Crystal structure refinement withSHELXL. *Acta Crystallogr. A Struct. Chem* **71**, 3–8 (2015).
61. O. V. Dolomanov, L. J. Bourhis, R. J. Gildea, J. A. Howard, H. Puschmann, *OLEX2*: A complete structure solution, refinement and analysis program. *J. Appl. Cryst.* **42**, 339–341 (2009).
62. D. Studio, *Accelrys [2.1]* (2008).

Acknowledgments: We thank O. Ben Dor, D. Bhowmick, D. Blackmond, R. Fu, S. Mojzsis, R. Naaman, and J. Szostak for helpful discussions, suggestions, and feedback. We thank V. Loi for the AFM measurements. We acknowledge the Center for Macromolecular Interactions at Harvard Medical School for the use of the CD spectrometer and K. L. Arnett for assistance. We acknowledge the Center for Nanoscale Systems (CNS) and the National Science Foundation's

(NSF) National Nanotechnology Coordinated Infrastructure (NNCI) for the use of the Sharon EE-3 E-Beam Evaporator. We acknowledge the Laukien-Purcell Instrumentation Center for the use of the NMR facility and D. Cui for the assistance. We acknowledge Harvard X-ray Laboratory supported by the Major Research Instrumentation (MRI) Program of the NSF under award number 2216066 and S.-L. Zheng for help with the x-ray data collection and structure determination. We also acknowledge other members of the Simons Collaboration on the Origins of Life and the Harvard Origins of Life Initiative for fruitful discussions that shaped the ideas behind this work. **Funding:** This work was supported by a grant from the Simons Foundation (290360) to D.D.S. The Harvard X-ray Laboratory is supported by the Major Research Instrumentation (MRI) Program of the NSF under award number 2216066. **Author contributions:** S.F.O., J.D.S., and D.D.S. designed the research. S.F.O. performed the crystallization experiments and collected and analyzed the data. Z.L. synthesized the aminooxazolines. S.F.O., J.D.S., and D.D.S. wrote the paper. **Competing interests:** The authors declare that they have no competing interests. **Data and materials availability:** All data needed to evaluate the conclusions in the paper are present in the paper and/or the Supplementary Materials.

Submitted 24 January 2023
Accepted 3 May 2023
Published 7 June 2023
10.1126/sciadv.adg8274

PLANETARY SCIENCE

Complex organosulfur molecules on comet 67P: Evidence from the ROSINA measurements and insights from laboratory simulations

Ahmed Mahjoub[1,2]*, Kathrin Altwegg[3], Michael J. Poston[4], Martin Rubin[3], Robert Hodyss[1], Mathieu Choukroun[1], Bethany L. Ehlmann[5], Nora Hänni[3], Michael E. Brown[5], Jordana Blacksberg[1], John M. Eiler[5], Kevin P. Hand[1]

The ROSINA (Rosetta Orbiter Spectrometer for Ion and Neutral Analysis) instrument aboard the Rosetta mission revolutionized our understanding of cometary material composition. One of Rosetta's key findings is the complexity of the composition of comet 67P/Churyumov-Gerasimenko. Here, we used ROSINA data to analyze dust particles that were volatilized during a dust event in September 2016 and report the detection of large organosulfur species and an increase in the abundances of sulfurous species previously detected in the coma. Our data support the presence of complex sulfur-bearing organics on the surface of the comet. In addition, we conducted laboratory simulations that show that this material may have formed from chemical reactions that were initiated by the irradiation of mixed ices containing H_2S. Our findings highlight the importance of sulfur chemistry in cometary and precometary materials and the possibility of characterizing organosulfur materials in other comets and small icy bodies using the James Webb Space Telescope.

INTRODUCTION

The Rosetta mission's visit to the comet 67P revealed a remarkable diversity of organic molecules in the comet's materials (*1*). During the Rosetta mission, organics were detected by the remote sensing instrument VIRTIS (Visible and Infrared Thermal Imaging Spectrometer) (*2*) as well as in situ instruments, including ROSINA (Rosetta Orbiter Spectrometer for Ion and Neutral Analysis) (*3*), Ptolemy (*4*), and COSAC (Cometary Sampling and Composition experiment) (*5*). ROSINA measurements substantially improved our understanding of the complex organic chemistry in the cometary materials, and ROSINA measurements during enhanced dust emission events offered insights into the composition of the semivolatile phases of the comet 67P. These phases can be regarded as a bridge between the gas phase composition of the comet coma and the nonvolatile refractory organics. Measurements from such events have already proven to be very informative, leading to the detection of complex organic molecules (*6*), the detection of ammonium salts (*7*), and, more recently, the detection of high abundance of ammonium hydrosulfide salt NH_4^+ SH^- (*8*).

Reactions on the surfaces of icy grains are believed to play a pivotal role in the chemistry of dense molecular clouds and solar nebulae (*9*). These reactions are mainly initiated by ultraviolet (UV) photons (either external or from the young star) or by bombardment by energetic particles. Hence, analysis of the cometary materials could enhance our understanding of this grain-surface photo- and radiolytic chemistry. Laboratory simulations of this chemical processing are needed to decipher the link between cometary molecules detected by Rosetta and the reservoirs from which comets are formed. Growing evidence suggests that H_2S was a highly abundant molecule in the presolar nebula (*8*, *10*). The Rosetta mission to comet 67P demonstrated that H_2S is the fifth most abundant molecule in the coma after H_2O, CO, CO_2, and O_2 (*10*). A recently published analysis of ROSINA-DFMS (Double Focusing Mass Spectrometer) data during multiple dust events shows a very high abundance of NH_3 and H_2S, believed to result from the decomposition of ammonium hydrosulfide (*8*). During some of these dust events, H_2S and NH_3 were more abundant than even water (*8*). Despite the importance of H_2S and the potential of sulfur chemistry to considerably affect the chemical reactivity in mixed ices, little has been published exploring this chemistry. We recently demonstrated that H_2S could markedly affect the chemistry (*11*, *12*) and spectroscopy (*13*, *14*) of mixed ices relevant to small icy bodies—particularly Kuiper belt objects (KBOs) and Jupiter Trojans (*15*). Sulfur chemistry could also play an important role in prebiotic chemistry and abiotic synthesis of biomolecules such as amino acids (*16*).

Here, we discuss data from Rosetta/ROSINA measurements obtained during an event of enhanced dust impacts into the instrument and interpret these data as showing the presence of large organosulfur molecules with low volatility embedded in the dust grains in comet 67P. We also report laboratory simulations of organic chemistry initiated by irradiation of simple ice mixtures with and without H_2S. This laboratory work shows that sulfur dominates the chemistry when H_2S is included and points toward a possible ice-chemistry origin of the diversity of sulfur-bearing species detected in the cometary material.

RESULTS

The dust event

In the last few weeks of the mission before landing on the comet, Rosetta flew elliptical orbits with the pericenter altitude gradually

[1]Jet Propulsion Laboratory, California Institute of Technology, Pasadena, CA 91109, USA. [2]Space Science Institute, 4765 Walnut St, Suite B, Boulder, CO 80301, USA. [3]Physikalisches Institut, University of Bern, Bern, Switzerland. [4]SWRI, San Antonio, TX 78238, USA. [5]Division of Planetary and Space Sciences, Caltech, Pasadena, CA 91125, USA.
*Corresponding author. Email: amahjoub@spacescience.org

lowered (and the apocenter altitude increased, keeping the size of the ellipse constant). On 5 September 2016, around 22:00 UTC, the spacecraft reached its closest distance from the comet, 3.9 km from the comet center (approximately 1.9 km above the surface). Shortly before that, Rosetta was most probably hit by a chunk of ice and dust, showing high-density gas peaks for more than 3 hours in the vicinity of the ROSINA-COPS [COmetary Pressure Sensor; more details about ROSINA instruments can be found in the study by Balsiger *et al.* (*17*)] nude gauge with its field of view of 340°. Around 19:00 UTC, the nude gauge was saturated. The COPS ram gauge, measuring ram pressure and pointing toward the comet, showed large pressure spikes around 18:00 UTC, most likely dust-ice grains entering the equilibrium chamber and sublimating inside the gauge. The ROSINA-DFMS also registered the event. The data from the ROSINA-COPS were very reproducible, suggesting very stable outgassing before the dust event took place around 18:00 UTC. During the event, the total density, as measured by ROSINA-COPS, increased by about one order of magnitude; shortly after 20:00 UTC, the density returned to normal values. More details about the dust event are given in the references (*7*, *18*).

ROSINA measurements of sulfur-rich organics

Figure 1 shows the abundances of various sulfur-bearing molecules before and after the dust event. Samples of mass spectra from which these abundances were determined are given in the Supplementary Materials (figs. S2 to S6). Abundances are given in arbitrary units but corrected for instrumental effects (mass-dependent sensitivity). The ROSINA-DFMS instrument had previously detected multiple sulfurous molecules in the undisturbed coma of comet 67P, as reported by Calmonte *et al.* (*19*); ROSINA's high mass resolution enabled precise molecular assignments. However, during the dust event (on 5 September 2016), ROSINA-DFMS measured an increase by a factor between 10 and 100 for many of these molecules, compared to the abundance just before the event around 17:00. S_2, S_3, and H_2S increased in abundance by a factor of 100, 10, and 100, respectively. Sulfur dioxide (SO_2) also increased by about two orders of magnitude. SO has an abundance during the event comparable to that of SO_2; however, its abundance right before the event could not be determined because of corruption of the spectrum. Carbonyl sulfide (COS) and carbon disulfide (CS_2) are the only species that did not increase during the dust event. These molecules are much more volatile than the other S species considered here, which could explain the depletion of these two molecules.

Hereafter, we focus on the plethora of sulfurous molecules that are not detected in the undisturbed coma but detected by the ROSINA-DFMS instrument during the dust event that establish the presence of semivolatile organo-sulfurous molecules on the surface of comet 67P. These are mainly heavy molecules (or fragments due to dissociation of larger molecules) that are not volatile enough to be detected in the gas phase. Their detectability was enhanced during the dust event because of volatilization upon impact with the Rosetta spacecraft and sublimation inside ROSINA, which was warmer than the comet. During the dust event, particles entered the instrument's ion source at 273 K (*18*). Semivolatile molecules

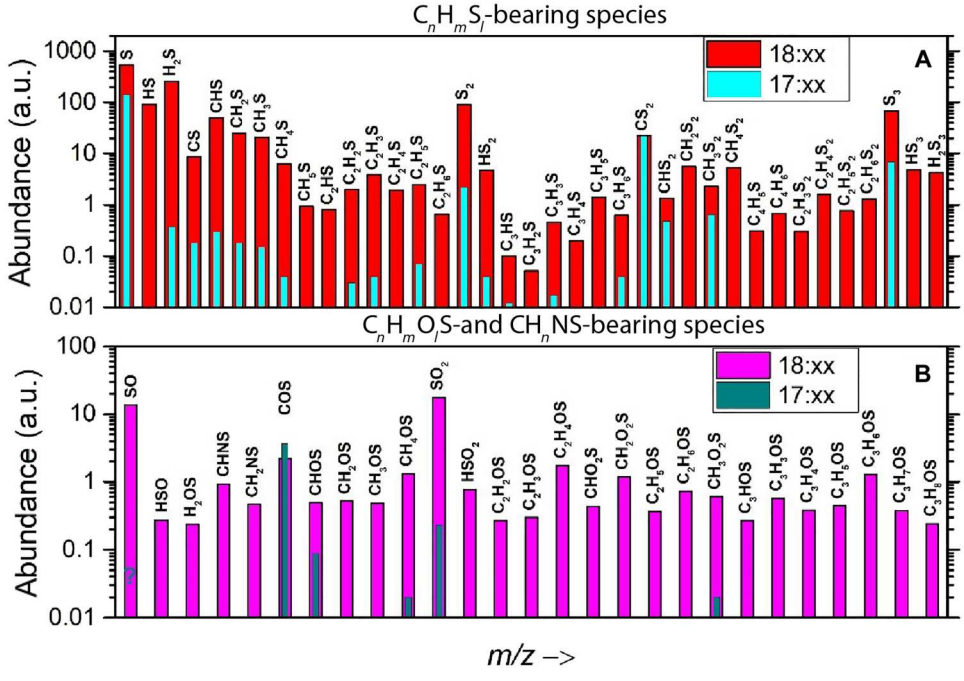

Fig. 1. Sulfur-bearing species detected by ROSINA (Rosetta Orbiter Spectrometer for Ion and Neutral Analysis)–DFMS (Double Focusing Mass Spectrometer) before and during the dust event on 5 September 2016, ~2 km above the nucleus surface. 17:xx denotes measurements made before the dust impact between 17:15 and 17:55 UTC (depending on mass), and 18:xx denotes measurements during the dust impact (18:09 to 18:50). (**A**) $C_nH_mS_l$ bearing species, $n = 0$ to 4; $m = 0$ to 6, $l = 1$ to 2. (**B**) $C_nH_mO_lS$- and CH_nNS-bearing species, $n = 0$ to 3; $m = 0$ to 6, $l = 1$ to 2. Species are ordered by mass/charge ratio (m/z) but not spaced accordingly (x axis not linear). The value, pre-event, for SO could not be derived as the spectrum is corrupted. Abundances are given in arbitrary units (a.u.) but corrected for instrumental effects (mass-dependent sensitivity). Caution: During the impact, coma background densities decreased over the 40 min needed to cover the mass range. Higher masses are therefore underestimated compared to low masses.

sublimated slowly over the course of many hours at this temperature.

Detected S-bearing species can be categorized into three families: $C_nH_mS_l$-bearing molecules with elemental abundances (n = 0 to 4; m = 0 to 6, l = 1 and 2), $C_nH_mO_lS$ (n = 0 to 3; m = 0 to 6, l = 1 to 2) and CH_nNS (n = 1 to 2). Among the $C_nH_mS_l$ family, only CH_4S and C_2H_6S had previously been detected in the coma (*19*). During the dust event, more complex species with up to four carbon atoms were identified. For n = 1 (one carbon atom) detected species are CS, CHS, CH_2S, CH_3S, CH_4S, and CH_5S. CH_4S had previously been detected in the coma and was assigned as methanethiol (CH_3SH) because the fragments and protonated species expected from impact ionization (CH_3S and CH_3SH_2) were also detected. CH_2S could be assigned to thioformaldehyde, which could exist in the cometary material as a monomer or as a result of dissociation of a larger polymer (thioformaldehyde is known to be unstable at room temperature and to quickly polymerize). This interpretation is supported by the detection of the thioformaldehyde dimer ($2{\bullet}CH_2S$) in the n = 2 family (see Fig. 1).

For $C_nH_mS_l$ with n and/or l greater than 1, species containing up to four carbon atoms were observed with notable abundances, while in the undisturbed coma, only $C_2H_6S_2$ was observed. These species could be products of dissociation of larger polymers that are not stable at T = 273 K, and some of them could also be products of fragmentation by electron impact inside the mass spectrometer. For the family $C_nH_mO_lS$, only COS has been detected in the undisturbed coma. During the dust event, multiple species were detected within this family. Most of these species contain only one oxygen atom (C_nH_mOS) with up to three carbon atoms. These species resemble hydrocarbons substituted with an OS group. Each of these species could correspond to a large variety of isomers, and their fragmentation patterns are complex; therefore, it is hard to disentangle the parent molecules from the daughter species produced by dissociative reactions. Another important result from the ROSINA data is the detection of CH_nNS in the coma of comet 67P. While NS was tentatively detected by Calmonte *et al.* (*19*), CHNS and CH_2NS are the first species containing C, N, and S atoms to be detected.

Laboratory simulations

The ROSINA-DFMS data recorded during the dust event and presented above indicate a sulfur chemistry more complex and diverse than previously anticipated from the measurements in the undisturbed coma (*19*). The variety of sulfur-bearing molecules detected in the cometary material by the ROSINA instrument is believed to be a result of ice chemistry involving H_2S (*20*). To investigate the effect of H_2S on this chemistry, we performed electron irradiation experiments on ice mixtures with and without H_2S. Details about the protocols and apparatus used for this laboratory simulation are summarized in Materials and Methods below. Briefly, the setup is a high-vacuum stainless steel chamber that reaches a pressure of approximately 1×10^{-8} torr. The ices were deposited on a gold substrate attached to the cold finger of a helium cryostat using a gas manifold to prepare gas mixtures. An electron gun was mounted on the chamber perpendicular to the substrate, and a Faraday cup was used to monitor the electron beam current. The chemical evolution of the samples was monitored using a Fourier transform infrared (FTIR) spectrometer.

Two ice samples "without sulfur" $CH_3OH{:}NH_3{:}H_2O$ (3:3:1) and "with sulfur" $CH_3OH{:}NH_3{:}H_2S{:}H_2O$ (3:3:3:1) were deposited under vacuum at T = 50 K and irradiated with a 10-keV electron gun. Both samples were irradiated for 20 hours with a beam current of 0.5 μA corresponding to a total fluence of electron energy $\sim 2 \times 10^{21}$ eV cm^{-2}. After irradiation, both samples were warmed up to 120 K at a rate of 0.5 K min^{-1} and held there for one additional hour under continued electron irradiation. Both samples were then warmed to room temperature at a rate of 0.5 K min^{-1}. The gases sublimating from the irradiated ices were detected with a Stanford Research System RGA (Residual Gas Analyzer) 200 quadrupole mass spectrometer, operated with 70-eV electron impact ionization and mass resolution <0.5 amu. The refractory thin films remaining after warming to room temperature were characterized by infrared (IR) spectroscopy. The ice mixtures presented here are depleted in water compared to the composition of comets and protoplanetary disks and interstellar ices. This was necessary to increase the detectability of minor irradiation products that would otherwise be hard to detect at very low abundances. A separate test was conducted with a more representative mixture of $CH_3OH{:}NH_3{:}H_2S{:}H_2O$ (10:1:1:100), and the results presented and discussed in the Supplementary Materials.

Our laboratory simulations investigate the sulfur chemistry triggered by energetic processing of ice grains in the presolar nebula. According to Ciesla and Sandford (*21*), these grains are exposed to temperatures ranging from 30 K to approximately 120 K, based on their dynamical evolution. We conducted our irradiation experiment under temperatures within this range. Our working pressure is also relevant to the outer solar nebula, estimated to be $<10^{-6}$ bar (*22*). To initiate the radiolytic chemistry, we used 10-keV electrons. At this electron energy, the penetration depth is approximately 2.6 μm (into water ice), which is close to the thickness of our ice films (~2 μm) and ensures that most of the beam energy is deposited in the film. The total fluence received by irradiated samples is $\sim 2 \times 10^{21}$ eV cm^{-2}, corresponding to a dose of 600 eV/16 amu. This irradiation dose is scalable to an irradiation time in the presolar nebula between 3.7 and 37 million years (Ma) (see details in Materials and Methods). It is worth noting that UV (*23*), x-ray (*24*), and ion (*25*) irradiations, among other sources, likely played a role in the processing of icy grains in the presolar nebula. We intend to carry out further studies to compare the impact of different energy sources on the sulfur chemistry.

Figure 2 shows a comparison between the mass spectra at T = 275 K of species desorbed from the "with sulfur" and the "without sulfur" irradiated ices. The two spectra are quite different especially at high mass/charge ratio (m/z), indicating the important role of sulfur chemistry. The spectrum of the "with sulfur" sample displays multiple additional peaks clearly undetected in the sample "without sulfur." This implies that these species are sulfur-bearing molecules. These additional peaks dominate the mass spectrum of the "with sulfur" sample, indicating a very rich sulfur chemistry. This was confirmed by IR spectroscopy of the residues left at room temperature, as discussed later. Note that the mass resolution of our mass spectrometer is much lower than the ROSINA-DFMS instrument and could not resolve the different species that might contribute to the signal at each m/z. The assignment of peaks displayed in Fig. 2 is limited to species confirmed by IR spectroscopy (*11*) or by Temperature Programmed Desorption (TPD) verification of fragmentation patterns (*12*).

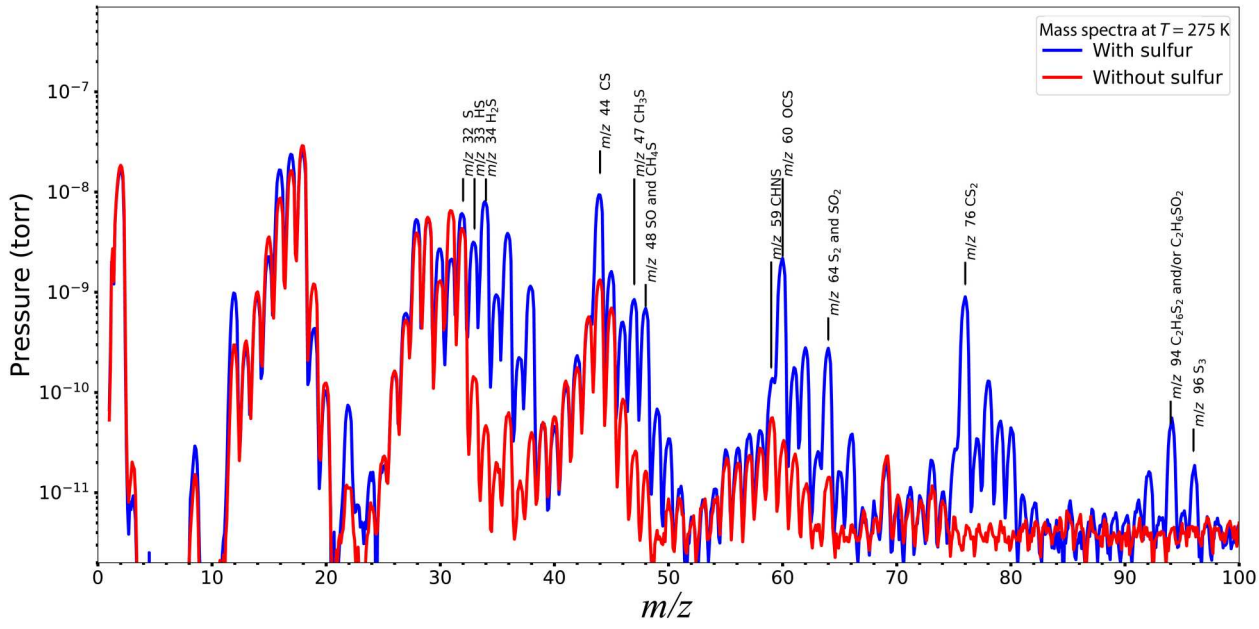

Fig. 2. Comparison between mass spectra of species desorbed from "with sulfur" (blue) and "without sulfur" (red) irradiated ice mixtures in the laboratory experiments. Both spectra are recorded at $T = 275$ K, and both samples received similar irradiation doses. *m/z*, mass/charge ratio.

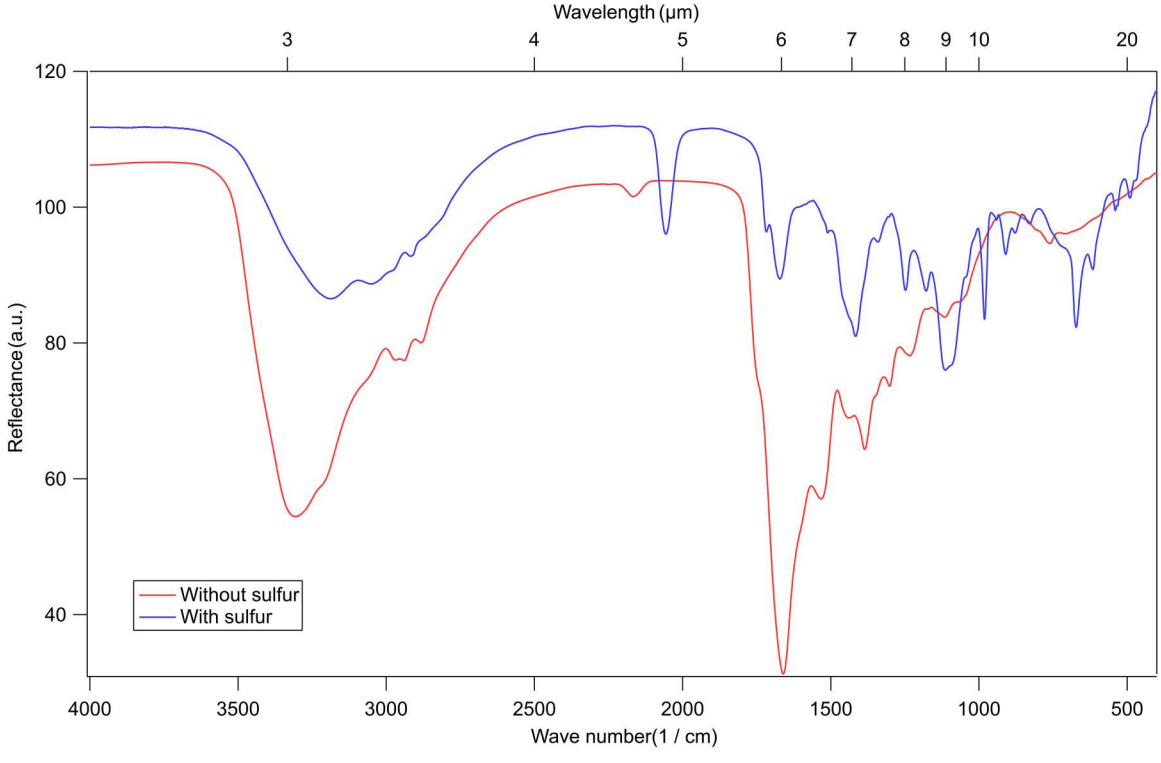

Fig. 3. Comparison between the infrared (IR) spectra of "without sulfur" residue (red spectrum) and "with sulfur" residue samples (blue spectrum). Both samples were produced by irradiating ice films with a 10-keV electron beam for 20 hours at 50 K. This irradiation time is equivalent to a total fluence of 2×10^{21} eV cm^{-2}. Initial ices are made of CH_3OH:NH_3:H_2S:H_2O (3:3:3:1) ("with sulfur") and CH_3OH:NH_3:H_2O (3:3:1) ("without sulfur"). a.u., arbitrary units.

Table 1. List of sulfur-bearing species detected by ROSINA (Rosetta Orbiter Spectrometer for Ion and Neutral Analysis)–DFMS (Double Focusing Mass Spectrometer) instrument with abundance > 1 arbitrary units (a.u.) compared to detections in mass spectra from the laboratory experiment. Because of the fragmentation inside the ROSINA-DFMS instrument, many of the species detected could be fragments of larger parent molecules (see discussion in the ROSINA data paragraph). *m/z*, mass/charge ratio

Detection by ROSINA (abundance >1 a.u.)	Detection in laboratory	Detection by ROSINA (abundance >1 a.u.)	Detection in laboratory
CS (*m/z* 44)	Confirmed by IR	CH_2S_2 (*m/z* 78)	Assignment cannot be confirmed
CSH (*m/z* 45)	Assignment cannot be confirmed	CH_4S_2 (*m/z* 80)	Assignment cannot be confirmed
CH_2S (*m/z* 46)	Assignment cannot be confirmed	$C_2H_6S_2$ (*m/z* 94)	Confirmed by TPD
CH_3S (*m/z* 47)	Confirmed by fragment patterns	S_3 (*m/z* 96)	Confirmed by TPD
CH_4S (*m/z* 48)	Confirmed by fragment patterns	SO (*m/z* 48)	Confirmed by IR
C_2H_2S (*m/z* 58)	Assignment cannot be confirmed	CHNS (*m/z* 59)	Confirmed by comparison with NIST data
C_2H_3S (*m/z* 59)	Assignment cannot be confirmed	COS (*m/z* 60)	Confirmed by IR
C_2H_4S (*m/z* 60)	Assignment cannot be confirmed	CH_4OS (*m/z* 64)	Assignment cannot be confirmed
C_2H_5S (*m/z* 61)	Assignment cannot be confirmed	SO_2 (*m/z* 64)	Confirmed by IR
S_2 (*m/z* 64)	Confirmed by TPD	C_2H_4OS (*m/z* 61)	Assignment cannot be confirmed
C_3H_5S (*m/z* 73)	Assignment cannot be confirmed	CH_2O_2S (*m/z* 78)	Assignment cannot be confirmed
CS_2 (*m/z* 76)	Confirmed by IR	C_3H_6OS (*m/z* 90)	Assignment cannot be confirmed
CHS_2 (*m/z* 77)	Assignment cannot be confirmed		

We focus our comparison of the mass spectra between the ROSINA data and the laboratory measurements on S-bearing species with an abundance >1 a.u. ($\sim^1/_{200}$ the abundance of H_2S) (Table 1). For all these species, a peak was observed in the mass spectrum of the laboratory "with sulfur" sample, but the assignment could not be confirmed for all of them. In the Supplementary Materials, we discuss the possible contributors of each peak based on the National Institute of Standards and Technology (NIST) database for mass spectra of sulfur-bearing molecules. Many of the molecules, such as COS, SO_2, CS, and CS_2 (*11*), have previously been confirmed in the IR spectrum of the irradiated ice mixtures. Sulfur allotropes have also been confirmed by TPD measurements (*12*). Among the 25 species detected by ROSINA and listed in Table 1, we are able to confirm the production of 11 molecules in our laboratory simulation. The species C_2H_nS (n = 2 to 5) are probably fragments of $C_2H_6S_2$ that was previously detected, and it is likely that these species contributed to the mass spectrum, but we cannot confirm the detection of these species. Although we cannot firmly confirm the production of all sulfurous species detected by ROSINA, our laboratory work can reproduce the three families of S-bearing molecules found in comet 67P (see Fig. 1).

At room temperature, organic residues remained on the gold substrates for both samples. These organic refractory materials are proposed as analogs of the refractory organics in cometary materials. The COSIMA (COmetary Secondary Mass Analyzer) instrument has provided insight into the characterization of refractory organics in particles from comet 67P, revealing the detection of high–molecular weight organic matter (*26*). In addition, the detection of sulfur atoms (as well as possibly S_2 and S_3 allotropes) in these particles has also been confirmed by COSIMA (*27*). However, it has been challenging to determine the source of sulfur, as it could have been derived from either organics, minerals, or a combination of both. The semivolatile organics such the one detected by Hänni *et al.* (*6*) and the S-bearing molecules reported here are believed to be a link between the gas phase and the refractory organics in comet 67P as measured by COSIMA. Consequently, we also characterized the residues produced in our laboratory samples "with sulfur" and "without sulfur" using IR spectroscopy (Fig. 3; table S1 summarizes all bands observed in both samples with tentative assignments to particular vibrational modes).

Comparison between these two spectra shows a clear difference over the entire spectrum, suggesting a marked change in the chemical composition of the residue when H_2S participates in the reaction chemistry. The strong NH and OH bands at 3200 and 3300 cm^{-1} as well as the CN and CO bands around 1600 and 2200 cm^{-1} were clearly decreased in the "with sulfur" sample compared to the "without sulfur" sample; the same decrease is also observed for bands around 3000 cm^{-1}, assigned to CH stretching modes. For example, the C═O absorption band at 1660 cm^{-1} is three times deeper in the "without sulfur" sample, while the broad band between 3000 and 3200 cm^{-1} is two times deeper. The shape of this band around 3100 cm^{-1} is also different between the two samples, with the center shifted to higher wave numbers by 110 cm^{-1} in the "with sulfur" residue. The decrease of CO, CN, CH_x, NH_x, and OH strongly implies a depression of carbon-, nitrogen- and oxygen-containing compounds in the residue when H_2S is added to the ice composition.

A clear difference between the two spectra is the strong band at 2057 cm^{-1} in the "with sulfur" sample that is totally absent in the "without sulfur" sample. This band is correlated to sulfur and could be tentatively assigned to the N═C═S group. This band may be a good probe for the sulfur residue, although CO_3 also has a weak absorption feature at this wavelength. In the fingerprint region, the "with sulfur" residue displays strong bands between 500 and 700 cm^{-1} and between 1000 and 1500 cm^{-1}, which are not observed in the "without sulfur" sample. These absorption features are

assigned to sulfur containing CS, SO, and SS vibrational modes. A group of these features is compatible with polymers of CH_2S (thioformaldehyde): Bands at 670, 986, 1247, and 1446 cm^{-1} are compatible with the strongest bands of CH_2S dimer and trimer (*28*). Also, weak bands observed at 477 and 876 cm^{-1} are in good agreement with symmetric and asymmetric SS stretching modes in H_2S_x species as measured by IR spectroscopy for H_2S_3 and H_2S_4 (*29*). The vibrational modes SS and CS usually result in weak absorption bands below 900 cm^{-1} (*30*).

The magnitude of the observed bands in the spectrum of the "with sulfur" sample suggests that molecules/functional groups rich in sulfur dominate the composition of the residue "with sulfur." One hypothesis to explain the impact of H_2S on the chemistry of the ice samples is the difference in dissociation energies among H_2S, water, and methanol. The dissociation energy of the SH bond in H_2S [376.2 kJ/mol (*31*)] is substantially lower than those of the OH bond for water [492.6 kJ/mol (*31*)] or methanol (463 kJ/mol). The rapid dissociation of H_2S compared to methanol and water will produce a high concentration of radical HS and free sulfur atoms compared to the concentrations of OH and O produced by dissociation of water and methanol. These reactive sulfur-bearing radicals, present at high concentration quickly after the beginning of irradiation, will react with CO and CH_3 and CH_2 radicals produced by dissociation of methanol. This could affect the chemistry in the ice films and enhance the production of molecules rich in CS, OS and SS bonds.

DISCUSSIONS

These results show that the effect of H_2S on the refractory residue is important and should be considered in the characterization of organic heteropolymers in small icy bodies and interstellar icy grains. The similarity between the large, low-volatility sulfur-containing molecules detected in the 67P cometary dust grains and those produced in our laboratory experiments suggests that H_2S ice chemistry is likely responsible for the observed species. However, it is worth noting that other pathways could also contribute to the formation of organosulfur compounds in both the diffuse interstellar medium and the solar nebula. For instance, laboratory simulations have shown that a variety of sulfur-bearing organic compounds are formed by sulfur ion bombardment of astrophysical ices containing carbon, oxygen, and nitrogen sources (*32*, *33*). The residue from these experiments contained more than 9000 molecules, and 12% of them contain sulfur atoms. The range of masses detected in those studies is $m/z > 147$ Da, which preclude their comparison to the sulfurous species detected by ROSINA-DFMS during the dust event in the range $m/z < 100$ Da.

Our work supports the hypothesis that organosulfur residues could be an important reservoir for sulfur in molecular clouds (*23*). The abundance of gaseous sulfur in dense clouds and circumstellar regions is only a small fraction (0.3 to 0.1%) of its cosmic abundance, a discrepancy that is known as The Sulfur Depletion Puzzle (*34*, *35*), while in diffuse clouds, the sulfur abundance agrees with the cosmic abundance (*36*). The fact that sulfur-containing organic heteropolymers are not volatile means that they cannot be detected with ground-based submillimeter telescopic observations. While a paucity of production rates for sulfur residues have hindered evaluation of the S sink in the modeling of the hot molecular cores (*37*), the results from ion irradiation experiments (*25*), this work, and recent gas-grain astrochemical modeling (*37*) indicate that organosulfur molecules made of CNOH atoms mixed with S could be the main sink for sulfur in the dense clouds. We also suggest that organic sulfurous species should be considered in accounting for some of the 89 ± 8% of elemental sulfur in refractory form, estimated for disks from the accretion-contaminated photospheres of stars, in addition to a hypothesized sulfide mineral sink (*38*).

Tracing organosulfur molecules in meteoritic materials also points to a potential key role for H_2S ice. Recent samples returned by the Hayabusa-2 mission from asteroid Ryugu have revealed the presence of a wide range of sulfur-bearing species (*39*). Molecules containing CHS, CHOS, and CHONS functional groups have been detected in the soluble organic matter, and the estimated total sulfur bulk composition is approximately 3.3 weight %, corresponding to a C/S ratio of ~1.15. Organosulfur molecules have also been detected in the insoluble organic matter of Murchison and Allende meteorites, even though the chemistry creating these species is not known (*40*). A carbon-rich clast with exceptionally high sulfur was found in a carbonaceous chondrite meteorite and may have originated from a comet containing H_2S ice (*41*), and Vacher *et al.* (*42*) identified sulfur isotope anomalies in unique minerals within a primitive carbonaceous chondrite, which they hypothesized may have resulted from UV irradiation of H_2S ice in the solar nebula, subsequently incorporated into the parent asteroid of the meteorite.

The James Webb Space Telescope (JWST) is expected to substantially increase our understanding of the chemistry of the solar system (*43*) including comets (*44*), asteroids (*45*), and KBOs. The large wavelength coverage of 0.6 to 28.5 μm and the high sensitivity (10× to 100× that of current facilities) will help reveal the composition of a considerable number of small icy bodies and the similarities and differences between their compositions. This in turn will enable the evaluation of hypotheses about the formation and evolution of the solar system. Sulfur chemistry is particularly interesting in this context and could provide a rich source of knowledge about the formation and evolution of the solar system. For example, Wong and Brown (*46*) demonstrated that the sublimation line of H_2S is located within the belt of primordial planetesimals. Therefore, these objects would have been divided into two groups: those that retained H_2S for enough time to develop a sulfur-containing organic crust and those that did not. The clear effect of adding H_2S to the irradiation chemistry of mixed ices of simple molecules and the very pronounced difference between the spectra of "with sulfur" and "without sulfur" residue samples (Fig. 3) open an opportunity to distinguish H_2S retention in a wide range of small icy bodies. The high resolving power of the MIRI (Mid-infrared Instrument) of JWST ($2200 < \lambda/\Delta\lambda < 3500$) will enable detailed characterization of the surface composition. The NIRSpec (Near Infrared Spectrograph) instrument with its 0.6- to 5.0-μm spectral range and its high resolving power will provide access to measurements of the interesting 3.2-μm region as well as the 1.8-μm feature that is present only in the "with sulfur" sample (*14*). All these absorption features provide a fingerprint of the sulfur chemistry that make it highly discernable from other materials expected in comets and other small icy bodies surfaces such as water ice and minerals.

In conclusion, the fate of sulfur in the building blocks of the solar system and its incorporation into various small bodies is still not fully understood. However, it holds the potential to provide

answers regarding the origin and evolution of these small bodies and test the links between them.

MATERIALS AND METHODS

Laboratory simulations

Electron irradiation experiments were carried out in the Ocean Worlds Lab (http://oceanworldslab.jpl.nasa.gov). A detailed description of the facilities and the capabilities of this laboratory can be found in (*47*). The experimental setup consists of a high-vacuum stainless steel chamber pumped by a Varian Turbo pump and backed by oil-free pumps (pressure after overnight pumping about 1×10^{-8} torr). The ices were vapor-deposited on a substrate attached to the cold finger of a closed-cycle helium cryostat (ARS model DE-204). An attached gas manifold was used to prepare gas mixtures before deposition. The ice films were grown by leaking the gas mixture onto the mirror substrate at a controlled rate through capillary tubes just above the sample, forming ices on the substrate, which was held at 50 K. Two different ice mixtures are considered in this study, and they were made from two different gas mixtures: "without sulfur" CH_3OH:NH_3:H_2O (3:3:1) and "with sulfur" CH_3OH:NH_3:H_2S:H_2O (3:3:3:1). The composition of the ice films could be slightly different because of the different sticking efficiency of each type of molecule in the mixture.

High-energy electrons (10 keV) were directed at the ice with a typical beam current of 0.5 μA. All studied ices were subjected to the same fluence of electron energy $\sim 2 \times 10^{21}$ eV cm^{-2}. Radiation fluences were scaled to the outer solar system based on the electron flux at 1 au, which was deduced from values given by Bennett *et al.* (*48*). We found that the total fluence received by our ice samples corresponds to a time scale of 0.2 Ma for an object at 5 au and 1.8 Ma at 15 au. This energy could also be scaled to energy received by icy grains in presolar nebula using the cosmic ray flux as reported by Yeghikyan (*49*). We found an irradiation time between 3.7 and 37 Ma depending on the density of the nebula. The processes simulated here are processes in the presolar nebula.

After irradiation for 20 hours at 50 K, samples were warmed to 120 K at a rate of 0.5 K min^{-1} and held there for one additional hour under continued electron irradiation. After the electron irradiation was concluded, the samples were warmed at a rate of 0.5 K min^{-1} to 300 K. The resulting residue films were characterized at room temperature by specular reflectance spectroscopy, using an FTIR spectrometer.

ROSINA-DFMS data analysis

Details on data analysis methods for ROSINA-DFMS are given in (*3*, *19*). ROSINA-DFMS steps through integer masses with an integration time of 20 s per mass. The neutral molecules are ionized by 45-eV electrons, which leads to parent ions as well as fragment ions. The detector has two times 512 anodes, which register the incoming ions. The peak shape on the detector can be described very well by a double Gaussian, whereby the second Gaussian has a width about three times the width of the first one and the amplitude is <10% of the peak amplitude. For small peaks, the smaller Gaussian is often not seen. The width is not dependent on the location on the detector as long as it is relatively close to the center. This means that if we have several peaks, we can use the same width for all of them. Once species have been identified, we also know their exact masses. This allows the disentanglement of even several masses close together with high confidence. Figures S2 to S6 show five representative spectra for CHNS (m/z 59), C_3H_6S (m/z 62), S_2 (m/z 64), C_3H_6OS (m/z 78), and S_3 (m/z 96). Given are spectra from before the impact (blue) and after the impact (black). Because at that time, the pressure inside the ion source of ROSINA-DFMS was still changing rapidly, peak heights cannot easily be compared between masses. An example for the Gaussian fits is given in fig. S1 for m/z = 59 where we fit five masses, all with the same width. In this case, the second Gaussian is mostly unimportant as it affects only the tails of the peaks. From such fits, we obtain the peak heights and the peak areas. For the other spectra, we do not plot the fits for readability reasons. In the present analysis, we use peak height in arbitrary units and correct them for the mass (energy)–dependent sensitivity of the instrument.

Supplementary Materials

This PDF file includes:

Supplementary Text
Table S1
Figs. S1 to S7

REFERENCES AND NOTES

1. E. Quirico, L. V. Moroz, B. Schmitt, G. Arnold, M. Faure, P. Beck, L. Bonal, M. Ciarniello, F. Capaccioni, G. Filacchione, S. Erard, C. Leyrat, D. Bockelée-Morvan, A. Zinzi, E. Palomba, P. Drossart, F. Tosi, M. T. Capria, M. C. De Sanctis, A. Raponi, S. Fonti, F. Mancarella, V. Orofino, A. Barucci, M. I. Blecka, R. Carlson, D. Despan, A. Faure, S. Fornasier, M. S. Gudipati, A. Longobardo, K. Markus, V. Mennella, F. Merlin, G. Piccioni, B. Rousseau, F. Taylor, Refractory and semi-volatile organics at the surface of comet 67P/Churyumov-Gerasimenko: Insights from the VIRTIS/Rosetta imaging spectrometer. *Icarus* **272**, 32–47 (2016).
2. F. Capaccioni, A. Coradini, G. Filacchione, S. Erard, G. Arnold, P. Drossart, M. C. D. Sanctis, D. Bockelee-Morvan, M. T. Capria, F. Tosi, C. Leyrat, B. Schmitt, E. Quirico, P. Cerroni, V. Mennella, A. Raponi, M. Ciarniello, T. McCord, L. Moroz, E. Palomba, E. Ammannito, M. A. Barucci, G. Bellucci, J. Benkhoff, J. P. Bibring, A. Blanco, M. Blecka, R. Carlson, U. Carsenty, L. Colangeli, M. Combes, M. Combi, J. Crovisier, T. Encrenaz, C. Federico, U. Fink, S. Fonti, W. H. Ip, P. Irwin, R. Jaumann, E. Kuehrt, Y. Langevin, G. Magni, S. Mottola, V. Orofino, P. Palumbo, G. Piccioni, U. Schade, F. Taylor, D. Tiphene, G. P. Tozzi, P. Beck, N. Biver, L. Bonal, J.-P. Combe, D. Despan, E. Flamini, S. Fornasier, A. Frigeri, D. Grassi, M. Gudipati, A. Longobardo, K. Markus, F. Merlin, R. Orosei, G. Rinaldi, K. Stephan, M. Cartacci, A. Cicchetti, S. Giuppi, Y. Hello, F. Henry, S. Jacquinod, R. Noschese, G. Peter, R. Politi, J. M. Reess, A. Semery, The organic-rich surface of comet 67P/Churyumov-Gerasimenko as seen by VIRTIS/Rosetta. *Science* **347**, aaa0628 (2015).
3. L. Le Roy, K. Altwegg, H. Balsiger, J.-J. Berthelier, A. Bieler, C. Briois, U. Calmonte, M. R. Combi, J. De Keyser, F. Dhooghe, B. Fiethe, S. A. Fuselier, S. Gasc, T. I. Gombosi, M. Hässig, A. Jäckel, M. Rubin, C.-Y. Tzou, Inventory of the volatiles on comet 67P/Churyumov-Gerasimenko from Rosetta/ROSINA. *Astron. Astrophys.* **583**, A1 (2015).
4. I. P. Wright, S. Sheridan, S. J. Barber, G. H. Morgan, D. J. Andrews, A. D. Morse, CHO-bearing organic compounds at the surface of 67P/Churyumov-Gerasimenko revealed by Ptolemy. *Science* **349**, aab0673 (2015).
5. F. Goesmann, H. Rosenbauer, J. H. Bredehöft, M. Cabane, P. Ehrenfreund, T. Gautier, C. Giri, H. Krüger, L. L. Roy, A. J. MacDermott, S. McKenna-Lawlor, U. J. Meierhenrich, G. M. Muñoz Caro, F. Raulin, R. Roll, A. Steele, H. Steininger, R. Sternberg, C. Szopa, W. Thiemann, S. Ulamec, Organic compounds on comet 67P/Churyumov-Gerasimenko revealed by COSAC mass spectrometry. *Science* **349**, aab0689 (2015).
6. N. Hänni, K. Altwegg, M. Combi, S. A. Fuselier, J. De Keyser, M. Rubin, S. F. Wampfler, Identification and characterization of a new ensemble of cometary organic molecules. *Nat. Commun.* **13**, 3639 (2022).
7. K. Altwegg, H. Balsiger, N. Hänni, M. Rubin, M. Schuhmann, I. Schroeder, T. Sémon, S. Wampfler, J.-J. Berthelier, C. Briois, M. Combi, T. I. Gombosi, H. Cottin, J. De Keyser, F. Dhooghe, B. Fiethe, S. A. Fuselier, Evidence of ammonium salts in comet 67P as explanation for the nitrogen depletion in cometary comae. *Nat. Astron.* **4**, 533–540 (2020).
8. K. Altwegg, M. Combi, S. A. Fuselier, N. Hänni, J. De Keyser, A. Mahjoub, D. R. Müller, B. Pestoni, M. Rubin, S. F. Wampfler, Abundant ammonium hydrosulphide embedded in cometary dust grains. *Mon. Not. R. Astron. Soc.* **516**, 3900–3910 (2022).

9. E. F. van Dishoeck, G. A. Blake, Chemical evolution of star-forming regions. *Annu. Rev. Astron. Astrophys.* **36**, 317–368 (1998).
10. M. Rubin, K. Altwegg, H. Balsiger, J.-J. Berthelier, M. R. Combi, J. De Keyser, M. Drozdovskaya, B. Fiethe, S. A. Fuselier, S. Gasc, T. I. Gombosi, N. Hänni, K. C. Hansen, U. Mall, H. Rème, I. R. H. G. Schroeder, M. Schuhmann, T. Sémon, J. H. Waite, S. F. Wampfler, P. Wurz, Elemental and molecular abundances in comet 67P/Churyumov-Gerasimenko. *Mon. Not. R. Astron. Soc.* **489**, 594–607 (2019).
11. A. Mahjoub, M. J. Poston, K. P. Hand, M. E. Brown, R. Hodyss, J. Blacksberg, J. M. Eiler, R. W. Carlson, B. L. Ehlmann, M. Choukroun, Electron irradiation and thermal processing of mixed-ices of potential relevance to Jupiter Trojan asteroids. *Astrophys. J.* **820**, 141 (2016).
12. A. Mahjoub, M. J. Poston, J. Blacksberg, J. M. Eiler, M. E. Brown, B. L. Ehlmann, R. Hodyss, K. P. Hand, R. Carlson, M. Choukroun, Production of sulfur allotropes in electron irradiated Jupiter trojans ice analogs. *Astrophys. J.* **846**, 148 (2017).
13. M. J. Poston, A. Mahjoub, B. L. Ehlmann, J. Blacksberg, M. E. Brown, R. W. Carlson, J. M. Eiler, K. P. Hand, R. Hodyss, I. Wong, Visible near-infrared spectral evolution of irradiated mixed ices and application to kuiper belt objects and Jupiter trojans. *Astrophys. J.* **856**, 124 (2018).
14. A. Mahjoub, M. E. Brown, M. J. Poston, R. Hodyss, B. L. Ehlmann, J. Blacksberg, M. Choukroun, J. M. Eiler, K. P. Hand, Effect of H2S on the near-infrared spectrum of irradiation residue and applications to the kuiper belt object (486958) arrokoth. *Astrophys. J. Lett.* **914**, L31 (2021).
15. I. Wong, M. E. Brown, J. Blacksberg, B. L. Ehlmann, A. Mahjoub, Hubble ultraviolet spectroscopy of Jupiter trojans. *Astron. J.* **157**, 161 (2019).
16. E. T. Parker, H. J. Cleaves, J. P. Dworkin, D. P. Glavin, M. Callahan, A. Aubrey, A. Lazcano, J. L. Bada, Primordial synthesis of amines and amino acids in a 1958 Miller H2S-rich spark discharge experiment. *Proc. Natl. Acad. Sci. U.S.A.* **108**, 5526–5531 (2011).
17. H. Balsiger, K. Altwegg, P. Bochsler, P. Eberhardt, J. Fischer, S. Graf, A. Jäckel, E. Kopp, U. Langer, M. Mildner, J. Müller, T. Riesen, M. Rubin, S. Scherer, P. Wurz, S. Wüthrich, E. Arijs, S. Delanoye, J. D. Keyser, E. Neefs, D. Nevejans, H. Rème, C. Aoustin, C. Mazelle, J.-L. Médale, J. A. Sauvaud, J.-J. Berthelier, J.-L. Bertaux, L. Duvet, J.-M. Illiano, S. A. Fuselier, A. G. Ghielmetti, T. Magoncelli, E. G. Shelley, A. Korth, K. Heerlein, H. Lauche, S. Livi, A. Loose, U. Mall, B. Wilken, F. Gliem, B. Fiethe, T. I. Gombosi, B. Block, G. R. Carignan, L. A. Fisk, J. H. Waite, D. T. Young, H. Wollnik, Rosina – Rosetta orbiter spectrometer for ion and neutral analysis. *Space Sci. Rev.* **128**, 745–801 (2007).
18. K. Altwegg, H. Balsiger, J. J. Berthelier, A. Bieler, U. Calmonte, S. A. Fuselier, F. Goesmann, S. Gasc, T. I. Gombosi, L. Le Roy, J. de Keyser, A. Morse, M. Rubin, M. Schuhmann, M. G. G. T. Taylor, C.-Y. Tzou, I. Wright, Organics in comet 67P – a first comparative analysis of mass spectra from ROSINA–DFMS, COSAC and Ptolemy. *Mon. Not. R. Astron. Soc.* **469**, S130–S141 (2017).
19. U. Calmonte, K. Altwegg, H. Balsiger, J. J. Berthelier, A. Bieler, G. Cessateur, F. Dhooghe, E. F. van Dishoeck, B. Fiethe, S. A. Fuselier, S. Gasc, T. I. Gombosi, M. Hässig, L. Le Roy, M. Rubin, T. Sémon, C.-Y. Tzou, S. F. Wampfler, Sulphur-bearing species in the coma of comet 67P/Churyumov–Gerasimenko. *Mon. Not. R. Astron. Soc.* **462**, S253–S273 (2016).
20. U. Calmonte, K. Altwegg, H. Balsiger, J.-J. Berthelier, A. Bieler, J. De Keyser, B. Fiethe, S. A. Fuselier, S. Gasc, T. I. Gombosi, L. Le Roy, M. Rubin, T. Sémon, C.-Y. Tzou, S. F. Wampfler, Sulphur isotope mass-independent fractionation observed in comet 67P/Churyumov-–Gerasimenko by Rosetta/ROSINA. *Mon. Not. R. Astron. Soc.* **469**, S787–S803 (2017).
21. F. J. Ciesla, S. A. Sandford, Organic synthesis via irradiation and warming of ice grains in the solar nebula. *Science* **336**, 452–454 (2012).
22. J. A. Wood, Pressure and temperature profiles in the solar nebula. *Space Sci. Rev.* **92**, 87–93 (2000).
23. A. Jiménez-Escobar, G. M. Muñoz Caro, Y.-J. Chen, Sulphur depletion in dense clouds and circumstellar regions. Organic products made from UV photoprocessing of realistic ice analogs containing H2S. *Mon. Not. R. Astron. Soc.* **443**, 343–354 (2014).
24. A. Jiménez-Escobar, G. M. Muñoz Caro, A. Ciaravella, C. Cecchi-Pestellini, R. Candia, G. Micela, Soft X-ray irradiation of H_2S ice and the presence of S_2 in comets. *Astrophys. J. Lett.* **751**, L40 (2012).
25. M. Garozzo, D. Fulvio, Z. Kanuchova, M. E. Palumbo, G. Strazzulla, The fate of S-bearing species after ion irradiation of interstellar icy grain mantles. *Astron. Astrophys.* **509**, A67 (2010).
26. N. Fray, A. Bardyn, H. Cottin, K. Altwegg, D. Baklouti, C. Briois, L. Colangeli, C. Engrand, H. Fischer, A. Glasmachers, E. Grün, G. Haerendel, H. Henkel, H. Höfner, K. Hornung, E. K. Jessberger, A. Koch, H. Krüger, Y. Langevin, H. Lehto, K. Lehto, L. Le Roy, S. Merouane, P. Modica, F.-R. Orthous-Daunay, J. Paquette, F. Raulin, J. Rynö, R. Schulz, J. Silén, S. Siljeström, W. Steiger, O. Stenzel, T. Stephan, L. Thirkell, R. Thomas, K. Torkar, K. Varmuza, K.-P. Wanczek, B. Zaprudin, J. Kissel, M. Hilchenbach, High-molecular-weight organic matter in the particles of comet 67P/Churyumov–Gerasimenko. *Nature* **538**, 72–74 (2016).
27. J. A. Paquette, K. Hornung, O. J. Stenzel, J. Rynö, J. Silen, J. Kissel, M. Hilchenbach, The $^{34}S/^{32}S$ isotopic ratio measured in the dust of comet 67P/Churyumov-Gerasimenko by Rosetta/COSIMA. *Mon. Not. R. Astron. Soc.* **469**, S230–S237 (2017).
28. P. Klaboe, The vibrational spectra of 1,4-dithiane and 1,3,5-trithiane. *Spectrochim. Acta A* **25**, 1437–1447 (1969).
29. H. Wieser, P. J. Krueger, E. Muller, J. B. Hyne, Vibrational spectra and a force field for H2S3 and H2S4. *Can. J. Chem.* **47**, 1633–1637 (1969).
30. C. N. R. Rao, R. Venkataraghavan, T. R. Kasturi, Contribution to the infrared spectra of organosulphur compounds. *Can. J. Chem.* **42**, 36–42 (1964).
31. L. R. Peebles, P. Marshall, High-accuracy coupled-cluster computations of bond dissociation energies in SH, H2S, and H2O. *J. Chem. Phys.* **117**, 3132–3138 (2002).
32. A. Ruf, A. Bouquet, P. Boduch, P. Schmitt-Kopplin, V. Vinogradoff, F. Duvernay, R. G. Urso, R. Brunetto, L. Le Sergeant d'Hendecourt, O. Mousis, G. Danger, Organosulfur compounds formed by sulfur ion bombardment of astrophysical ice analogs: Implications for moons, comets, and kuiper belt objects. *Astrophys. J. Lett.* **885**, L40 (2019).
33. A. Ruf, A. Bouquet, P. Schmitt-Kopplin, P. Boduch, O. Mousis, G. Danger, Sulfur ion irradiation experiments simulating space weathering of solar system body surfaces. *Astron. Astrophys.* **655**, A74 (2021).
34. A. Tieftrunk, G. Pineau des Forets, P. Schilke, C. M. Walmsley, SO and H_2S in low density molecular clouds. *Astron. Astrophys.* **289**, 579–596 (1994).
35. D. P. Ruffle, T. W. Hartquist, P. Caselli, D. A. Williams, The sulphur depletion problem. *Mon. Not. R. Astron. Soc.* **306**, 691–695 (1999).
36. E. B. JENKINS, A unified representation of gas-phase element depletions in the interstellar medium. *Astrophys. J.* **700**, 1299–1348 (2009).
37. P. M. Woods, A. Occhiogrosso, S. Viti, Z. Kaňuchová, M. E. Palumbo, S. D. Price, A new study of an old sink of sulphur in hot molecular cores: The sulphur residue. *Mon. Not. R. Astron. Soc.* **450**, 1256–1267 (2015).
38. M. Kama, O. Shorttle, A. S. Jermyn, C. P. Folsom, K. Furuya, E. A. Bergin, C. Walsh, L. Keller, Abundant refractory sulfur in protoplanetary disks. *Astrophys. J.* **885**, 114 (2019).
39. H. Naraoka, Y. Takano, J. P. Dworkin, Y. Oba, K. Hamase, A. Furusho, N. O. Ogawa, M. Hashiguchi, K. Fukushima, D. Aoki, P. Schmitt-Kopplin, J. C. Aponte, E. T. Parker, D. P. Glavin, H. L. McLain, J. E. Elsila, H. V. Graham, J. M. Eiler, F.-R. Orthous-Daunay, C. Wolters, J. Isa, V. Vuitton, R. Thissen, S. Sakai, T. Yoshimura, T. Koga, N. Ohkouchi, Y. Chikaraishi, H. Sugahara, H. Mita, Y. Furukawa, N. Hertkorn, A. Ruf, H. Yurimoto, T. Nakamura, T. Noguchi, R. Okazaki, H. Yabuta, K. Sakamoto, S. Tachibana, H. C. Connolly, D. S. Lauretta, M. Abe, T. Yada, M. Nishimura, K. Yogata, A. Nakato, M. Yoshitake, A. Suzuki, A. Miyazaki, S. Furuya, K. Hatakeda, H. Soejima, Y. Hitomi, K. Kumagai, T. Usui, T. Hayashi, D. Yamamoto, R. Fukai, K. Kitazato, S. Sugita, N. Namiki, M. Arakawa, H. Ikeda, M. Ishiguro, N. Hirata, K. Wada, Y. Ishihara, R. Noguchi, T. Morota, N. Sakatani, K. Matsumoto, H. Senshu, R. Honda, E. Tatsumi, Y. Yokota, C. Honda, T. Michikami, M. Matsuoka, A. Miura, H. Noda, T. Yamada, K. Yoshihara, K. Kawahara, M. Ozaki, Y. Iijima, H. Yano, M. Hayakawa, T. Iwata, R. Tsukizaki, H. Sawada, S. Hosoda, K. Ogawa, C. Okamoto, N. Hirata, K. Shirai, Y. Shimaki, M. Yamada, T. Okada, Y. Yamamoto, H. Takeuchi, A. Fujii, Y. Takei, K. Yoshikawa, Y. Mimasu, G. Ono, N. Ogawa, S. Kikuchi, S. Nakazawa, F. Terui, S. Tanaka, T. Saiki, M. Yoshikawa, S. Watanabe, Y. Tsuda, Soluble organic molecules in samples of the carbonaceous asteroid (162173) Ryugu. *Science* **379**, eabn9033 (2023).
40. A. Zherebker, Y. Kostyukevich, D. S. Volkov, R. G. Chumakov, L. Friederici, C. P. Rüger, A. Kononikhin, O. Kharybin, A. Korochantsev, R. Zimmermann, I. V. Perminova, E. Nikolaev, Speciation of organosulfur compounds in carbonaceous chondrites. *Sci. Rep.* **11**, 7410 (2021).
41. L. R. Nittler, R. M. Stroud, J. M. Trigo-Rodríguez, B. T. De Gregorio, C. M. O. Alexander, J. Davidson, C. E. Moyano-Cambero, S. Tanbakouei, A cometary building block in a primitive asteroidal meteorite. *Nat. Astron.* **3**, 659–666 (2019).
42. L. G. Vacher, R. C. Ogliore, C. Jones, N. Liu, D. A. Fike, Cosmic symplectite recorded irradiation by nearby massive stars in the solar system's parent molecular cloud. *Geochim. Cosmochim. Acta* **309**, 135–150 (2021).
43. S. N. Milam, J. A. Stansberry, G. Sonneborn, C. Thomas, The *James Webb Space Telescope's* plan for operations and instrument capabilities for observations in the solar system. *Publ. Astron. Soc. Pac.* **128**, 018001 (2016).
44. M. S. P. Kelley, C. E. Woodward, D. Bodewits, T. L. Farnham, M. S. Gudipati, D. E. Harker, D. C. Hines, M. M. Knight, L. Kolokolova, A. Li, I. de Pater, S. Protopapa, R. W. Russell, M. L. Sitko, D. H. Wooden, Cometary Science with the *James Webb Space Telescope*. *Publ. Astron. Soc. Pac.* **128**, 018009 (2016).
45. A. S. Rivkin, F. Marchis, J. A. Stansberry, D. Takir, C. Thomas, Asteroids and the *James Webb Space Telescope*. *Publ. Astron. Soc. Pac.* **128**, 018003 (2016).
46. I. Wong, M. E. Brown, A hypothesis for the color bimodality of Jupiter trojans. *Astron. J.* **152**, 90 (2016).
47. K. P. Hand, R. W. Carlson, H2O2 production by high-energy electrons on icy satellites as a function of surface temperature and electron flux. *Icarus* **215**, 226–233 (2011).
48. C. J. Bennett, C. Pirim, T. M. Orlando, Space-weathering of solar system bodies: A laboratory perspective. *Chem. Rev.* **113**, 9086–9150 (2013).

49. A. G. Yeghikyan, Irradiation of dust in molecular clouds. II. Doses produced by cosmic rays. *Astrophysics* **54**, 87–99 (2011).

Acknowledgments: This work has been conducted at the JPL, Caltech, under a contract with the National Aeronautics and Space Administration (NASA), and at the Caltech Division of Geological and Planetary Sciences. ROSINA would not have produced such outstanding results without the work of the many engineers, technicians, and scientists involved in the mission, in the Rosetta spacecraft team, and in the ROSINA instrument team over the past 20 years, whose contributions are acknowledged. Rosetta is an ESA mission with contributions from its member states and NASA. We acknowledge herewith the work of the whole ESA Rosetta team. We would like to thank anonymous reviewers for valuable comments. **Funding:** This work has been supported in part by the NASA/RDAP program (80NM0018F0612) and by the Keck Institute for Space Studies (KISS). Part of this work was supported by NASA/DDAP program under grant no. 80NSSC21K1015. **Author contributions:** A.M. wrote the manuscript. A.M. and M.J.P. led the work on laboratory simulations and analyzed the data from laboratory measurements. K.A., M.R., and N.H. analyzed the data from ROSINA-DFMS measurements. K.P.H. built and developed the experimental setup used on laboratory simulations and supervised the experimental work. M.E.B., J.M.E., and J.B. supervised the work. B.L.E., R.H., and J.B. participated in the laboratory work. All authors participated in the interpretation of the results and read and commented on the manuscript. **Competing interests:** The authors declare that they have no competing interests. **Data and materials availability:** The datasets analyzed during the current study together with a user manual for data analysis are available in the ESA-PSA archive (www.cosmos.esa.int/web/psa/rosetta) or the NASA PDS archive (https://pdssbn.astro.umd.edu/data_sb/missions/rosetta/index.html). Laboratory simulations data are available at Dryad (https://datadryad.org/stash/share/q3OXw5x2Xlgze7zZ_ss8_-U54pUOzzZFttVrpm8gUzo). All data needed to evaluate the conclusions in the paper are present in the paper and/or the Supplementary Materials.

Submitted 7 February 2023
Accepted 1 May 2023
Published 7 June 2023
10.1126/sciadv.adh0394

SPACE SCIENCES

A structured jet explains the extreme GRB 221009A

Brendan O'Connor[1,2,3,4]*†, Eleonora Troja[5,6]*†, Geoffrey Ryan[7], Paz Beniamini[8,9], Hendrik van Eerten[10], Jonathan Granot[8,9,1], Simone Dichiara[11], Roberto Ricci[12,13], Vladimir Lipunov[14], James H. Gillanders[5], Ramandeep Gill[15], Michael Moss[1], Shreya Anand[16], Igor Andreoni[17,3,4], Rosa L. Becerra[18], David A. H. Buckley[19,20], Nathaniel R. Butler[21], Stephen B. Cenko[4,17], Aristarkh Chasovnikov[14], Joseph Durbak[3,4], Carlos Francile[22,23], Erica Hammerstein[3], Alexander J. van der Horst[1], Mansi M. Kasliwal[16], Chryssa Kouveliotou[12], Alexander S. Kutyrev[3,4], William H. Lee[24], Gokul P. Srinivasaragavan[3], Vladislav Topolev[14], Alan M. Watson[14], Yuhan Yang[5], Kirill Zhirkov[14]

Long-duration gamma-ray bursts (GRBs) are powerful cosmic explosions, signaling the death of massive stars. Among them, GRB 221009A is by far the brightest burst ever observed. Because of its enormous energy ($E_{iso} \approx 10^{55}$ erg) and proximity ($z \approx 0.15$), GRB 221009A is an exceptionally rare event that pushes the limits of our theories. We present multiwavelength observations covering the first 3 months of its afterglow evolution. The x-ray brightness decays as a power law with slope $\approx t^{-1.66}$, which is not consistent with standard predictions for jetted emission. We attribute this behavior to a shallow energy profile of the relativistic jet. A similar trend is observed in other energetic GRBs, suggesting that the most extreme explosions may be powered by structured jets launched by a common central engine.

INTRODUCTION

Gamma-ray bursts (GRBs) are sudden and brief flashes of high-energy radiation. Those lasting longer than a couple of seconds generally signal the death of very massive, rapidly rotating stars. With typical durations of 1 to 100 s (*1*) and isotropic-equivalent luminosities of 10^{50} to 10^{54} erg s^{-1} (*2*), they are considered one of the most energetic explosions in the Universe. When their intense radiation reaches us, it is attenuated by the large distance scale it has traveled, ≈16 Gpc for the median GRB redshift $z \sim 2$ (*3*). Moreover, most of the flux above gigaelectronvolt energies is suppressed by interactions with the extragalactic background light (*4*). Therefore, as observed at Earth, GRBs display fluences in the range 10^{-7} to 10^{-4} erg cm^{-2} (*1*) and spectra up to the megaelectron volt or, less frequently, gigaelectronvolt range (*5*).

On 9 October 2022 at 13:16:59 UT (hereafter referred to as T_0), the Gamma-ray Burst Monitor (GBM) aboard Fermi (*6*), among other high-energy satellites [Konus-Wind, SRG, and GRBAlpha; (*7*, *8*)], detected an unprecedented, extremely bright burst lasting hundreds of seconds. This burst, dubbed GRB 221009A, is the brightest GRB ever detected in nearly 55 years of operating gamma-ray observatories, with an observed fluence of $\approx 5 \times 10^{-2}$ erg cm^{-2} in the 20-keV to 10-MeV band, more than an order of magnitude brighter than GRB 840304 and GRB 130427A (*9*), the previous record holders (Fig. 1). Its high-energy radiation was so intense that it disturbed Earth's ionosphere (*10*).

The prompt gamma-ray phase was followed by longer-lived, nonthermal afterglow radiation, visible across nearly 19 decades in energy, from low-frequency radio up to the teraelectronvolt range, corresponding to the highest energy photon (18 TeV) ever detected from a GRB (*11*). The afterglow phase was exceptionally bright at all frequencies and at all times, surpassing the population of x-ray afterglows by over an order of magnitude (Fig. 1) and causing the Neil Gehrels Swift Observatory to send a trigger alert nearly an hour (T_0 + 55 min) after the initial gamma rays were detected for the first time (*12*).

The extraordinary properties of this GRB are only partially explained by its proximity to us. At a redshift of $z = 0.1505$ (*13*), its luminosity distance is ≈ 720 Mpc (*14*), a factor of $\gtrsim$20 closer than the average GRB. However, even after correcting for distance effects, GRB 221009A remains one of the most luminous explosions to date, pushing the limits of our understanding in terms of both GRB

[1]Department of Physics, The George Washington University, 725 21st Street NW, Washington, DC 20052, USA. [2]Astronomy, Physics and Statistics Institute of Sciences (APSIS), Washington, DC 20052, USA. [3]Department of Astronomy, University of Maryland, College Park, MD 20742-4111, USA. [4]Astrophysics Science Division, NASA Goddard Space Flight Center, 8800 Greenbelt Rd, Greenbelt, MD 20771, USA. [5]Department of Physics, University of Rome "Tor Vergata", via della Ricerca Scientifica 1, I-00133 Rome, Italy. [6]INAF - Istituto di Astrofisica e Planetologia Spaziali, via Fosso del Cavaliere 100, 00133 Rome, Italy. [7]Perimeter Institute for Theoretical Physics, 31 Caroline St. N., Waterloo, ON N2L 2Y5, Canada. [8]Department of Natural Sciences, The Open University of Israel, P.O. Box 808, Ra'anana 4353701, Israel. [9]Astrophysics Research Center of the Open university (ARCO), P.O. Box 808, Ra'anana 4353701, Israel. [10]Physics Department, University of Bath, Claverton Down, Bath BA2 7AY, UK. [11]The Pennsylvania State University, 525 Davey Lab, University Park, PA 16802, USA. [12]Istituto Nazionale di Ricerca Metrologica, I-10135 Torino, Italy. [13]INAF - Istituto di Radioastronomia, via Gobetti 101, I-40129 Bologna, Italy. [14]Sternberg Astronomical Institute, Lomonosov Moscow State University, Universitetsky pr. 13, 119234 Moscow, Russia. [15]Instituto de Radioastronomía y Astrofísica, Universidad Nacional Autónoma de México, Antigua Carretera. a Pátzcuaro #8701, Ex-Hda. San José de la Huerta, Morelia, Michoacán, C.P. 58089, México. [16]Division of Physics, Mathematics and Astronomy, California Institute of Technology, Pasadena, CA 91125, USA. [17]Joint Space-Science Institute, University of Maryland, College Park, MD 20742, USA. [18]Instituto de Ciencias Nucleares, Universidad Nacional Autónoma de México, 04510 México, CDMX, Mexico. [19]Department of Astronomy, University of Cape Town, Private Bag X3, Rondebosch 7701, South Africa. [20]South African Astronomical Observatory, PO Box 9, 7935 Observatory, Cape Town, South Africa. [21]School of Earth and Space Exploration, Arizona State University, Tempe, AZ 85287, USA. [22]Observatorio Astronomico Felix Aguilar (OAFA), San Juan 5400, Argentina. [23]Facultad de Ciencias Exactas Fisicas y Naturales, San Juan National University, San Juan 5400, Argentina. [24]Instituto de Astronomía, Universidad Nacional Autónoma de México, 04510 México, CDMX, Mexico.
*Corresponding author. Email: oconnorb@gwmail.gwu.edu (B.O.); eleonora.troja@uniroma2.it (E.T.)
†These authors contributed equally to this work.

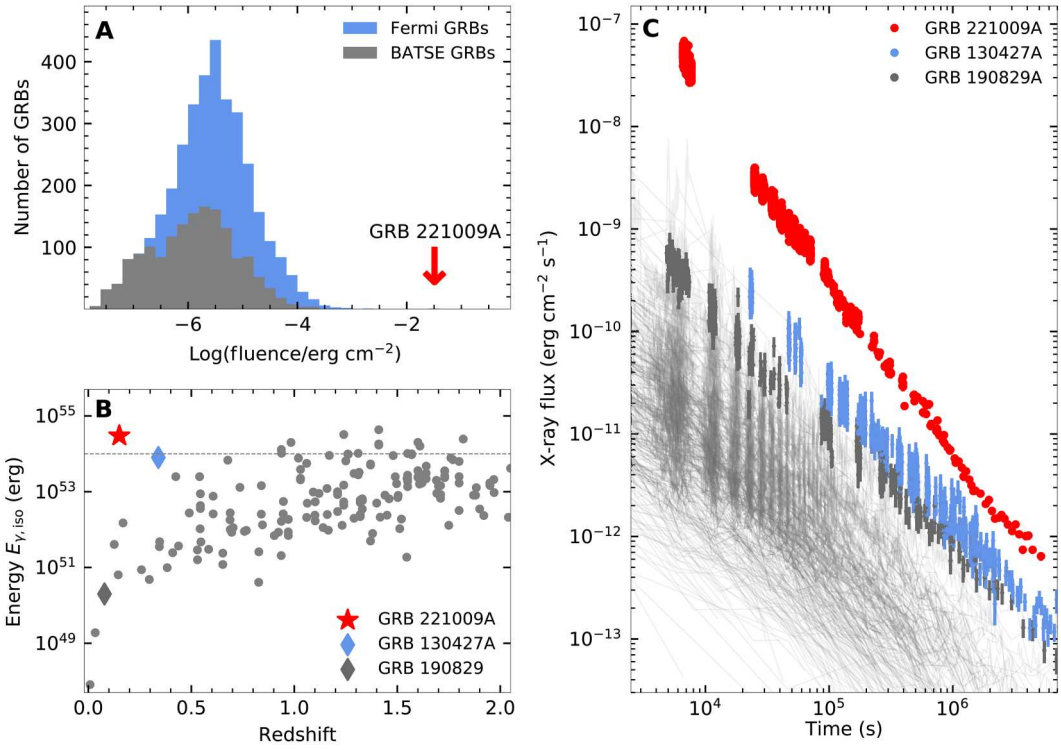

Fig. 1. The extreme brightness of GRB 221009A. (**A**) Top left: Histogram of gamma-ray fluence for Fermi (blue; 10 to 1000 keV) and BATSE (gray; 50 to 300 keV) GRBs compared to GRB 221009A. (**B**) Bottom left: Isotropic-equivalent gamma-ray energy (1 keV to 10 MeV) versus redshift for a sample of long-duration GRBs compiled from (*44*, *64*). (**C**) Right: Observed x-ray afterglow light curves in the Swift XRT (03 to 10 keV) energy band for a sample of long-duration GRBs. GRB 221009A is the brightest x-ray afterglow ever observed.

energetics and the rate of events. Its isotropic-equivalent gamma-ray energy, $E_{\gamma,iso} \gtrsim 3 \times 10^{54}$ erg measured over the 20-keV to 10-MeV energy range (*15*), is at the top of the GRB energy distribution (Fig. 1) and only sets a lower limit to the total (isotropic-equivalent) energy release. By including the blast-wave kinetic energy that is converted into afterglow radiation, as well as the contribution of the teraelectronvolt component, the isotropic-equivalent energy budget would easily surpass 10^{55} erg, corresponding to $\gtrsim 5\ M_\odot c^2$. According to the GRB luminosity function (*2*), an event as bright as GRB 221009A occurs this close to Earth less than once in a century. If we factor in its long duration and total energy release, then our chance to observe a similar event is 1 in ≈ 1000 years (see Materials and Methods). The detection of GRB 221009A and other extraordinary events, such as GRB 130427A (*9*), seems therefore at odds with our basic expectations of how frequent the most energetic explosions are in the nearby Universe.

A key element for calculating the true energy release and rate of events is the geometry of the relativistic outflow. The outflow's angular structure and collimation leave clear imprints in GRB afterglow light curves (*16*–*19*), and, therefore, we can constrain these properties through our multiwavelength campaign. In particular, if the outflow is collimated into narrow sharp-edged jets, then we should observe the afterglow flux rapidly falling off after the time of the "jet break," i.e., when the inverse of the Lorentz factor of the outflow becomes comparable to the jet's half-opening angle θ_j (*19*, *20*). To search for the signature of collimation, we turn to the x-ray afterglow, which is unaffected by other components [e.g., supernova and reverse shock (RS)] and probes the nonthermal emission from electrons accelerated by the forward shock (FS), driven by the outflow into the surrounding medium (*21*).

RESULTS

The x-ray light curve features an initial power-law decay index of $\alpha_{X,1} = -152 \pm 0.01$, steepening to $\alpha_{X,2} = -1.66 \pm 001$ after $t_{b,X} = 0.82 \pm 0.07$ days (see Fig. 2). The x-ray spectrum is well described by an absorbed power law with a time-variable spectral index, ranging from -0.65 ± 0.02 measured by Swift at 1 hour to -1.10 ± 0.17 measured by NuSTAR at 32 days. According to standard models of GRB jets (*21*, *22*), this progressive softening is consistent with the passage of the cooling frequency ν_c of the synchrotron spectrum. Therefore, the x-ray spectral shape can be used to constrain the density profile of the circumburst medium as $\rho(r) \propto r^{-k}$ where $k < 4/3$ (such that ν_c decreases with time) and the energy distribution of the shock-accelerated electrons as $N(E) \propto E^{-p}$ where $p \approx 2.2$ to 2.4. This value matches the spectral measurements of the early high-energy emission (*23*, *24*), suggesting that the synchrotron component extends to the gigaelectronvolt range. Thus, we can use the high energy flux, assuming that it is afterglow-dominated, as a proxy for the blast-wave kinetic energy (*25*), obtaining $E_{K,iso} \approx 10^{55}$ $(1 + Y)$ erg, where Y is the Compton parameter of the gigaelectronvolt-emitting electrons. A similarly high value is obtained by assuming a typical gamma-ray efficiency $\eta_\gamma \approx 20\%$.

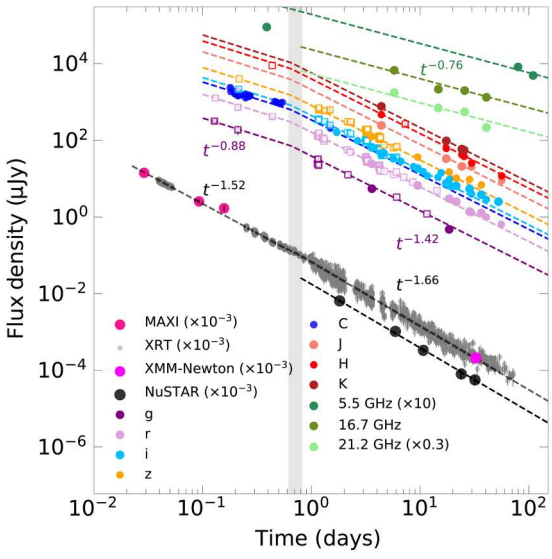

Fig. 2. Multiwavelength light curve of GRB 221009A. The XRT and XMM-Newton data represent the x-ray flux density at 1 keV, whereas the flux density from the NuSTAR observations is reported at 5 keV. OIR data represented as empty squares were compiled from General Coordinates Network circulars, whereas filled circles are data analyzed in this work. The OIR data are not corrected for Galactic extinction.

In the standard model, the GRB jet has a constant energy profile within its core of angular size θ_j. The energy then declines rapidly or goes to zero at angles beyond θ_j. The prediction for the post–jet-break decay is $t^{-p} \approx t^{-2.2}$, which is inconsistent with the x-ray slope of −1.66 measured after $t_{b,X}$. If $t_{b,X}$ is not the jet-break time t_j, then the uninterrupted power-law decay of the x-ray emission sets a lower limit $t_j > 80$ days for the jet-break time. The resulting limit on the jet opening angle, $\theta_j \gtrsim 15°$, pushes the total collimation-corrected energy release to $E_K \gtrsim 4 \times 10^{53}\ (t_j/80\ \text{days})^{0.75}$ erg (see Materials and Methods), leading to an energy crisis for most models of GRB central engines (*26*, *27*). However, at the time of the x-ray temporal break, the optical and infrared (hereafter, OIR) light curves are also seen to steepen. The OIR emission displays an initial shallow decay with $\alpha_{OIR,1} = -0.88 \pm 0.05$, which steepens to $\alpha_{OIR,2} = -1.42 \pm 0.11$ at around $t_{b,OIR} = -0.63 \pm 0.13$ days (Fig. 2). The achromatic steepening of the x-ray and OIR light curves provides a strong indication of a geometrical effect, such as a jet break (*19*, *20*), although the observed post-break decay rates are shallower than theoretical predictions. If GRB 221009A was followed by a supernova, like most long GRBs are, then the supernova contribution could cause an apparent flattening of the OIR light curve and mask the jet break. By assuming that a SN 1998bw–like transient contributes to the OIR emission, an afterglow decay rate as steep as −1.5 is consistent with the optical and near-IR data. This is close to the observed x-ray slopes, yet too shallow for a post–jet-break phase.

Additional evidence for geometrical effects comes from the late-time radio observations, which tend to favor a collimated outflow. The x-ray flux at 1 hour sets a lower limit of ≳10 mJy to the FS peak flux. As the shock cools down and passes from the x-rays to the radio band, the peak brightness remains constant in a uniform medium (*28*) or slowly decreases as $F_{\nu,\max} \propto t^{-\alpha_k}$, with $\alpha_k < 1/4$ in a stratified environment with $k < 4/3$. Either behavior would violate the observed radio limits of 0.4 mJy at 80 days unless the assumption of spherical symmetry breaks down, causing the peak flux to decrease more rapidly (*20*).

These different and apparently discordant observations can be reconciled if the afterglow emission is powered by a structured jet with a shallow angular energy profile (*29*–*31*), composed by an inner component of angular size θ_b with a shallow energy profile $dE_K/d\Omega \propto \theta^{-a_1}$ and a slightly steeper lateral structure at $\theta > \theta_b$ with $dE_K/d\Omega \propto \theta^{-a_2}$, where $a_1 < a_2 < 2$ (see Fig. 3). This profile is motivated by the lack of a sharp jet break feature in the x-ray and OIR light curves and the energy crisis that would be implied for a jet with a steeper angular profile. Similar shallow angular profiles are seen in simulations of relativistic jets expanding in complex media (*32*).

A structured jet can account for the achromatic temporal break visible at x-ray and OIR wavelengths and explain their post-break slopes as emission from the lateral structure as it comes into view. For $a_1 \sim 0.75$, $a_2 \sim 1.15$, and a transition at $\theta_b \sim 3°$, this model yields

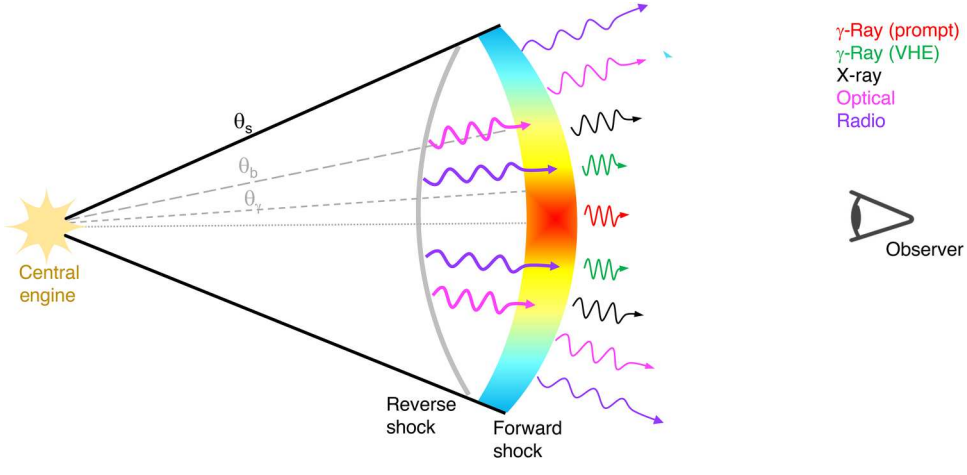

Fig. 3. Schematic of the structured jet for GRB 221009A. Emission from the FS and RS are produced by the jet out to its truncation angle θ_s. The angular structure of the jet, $E_K/d\Omega \propto \theta^{-a}$, breaks slightly at θ_b, transitioning from a slope $a_1 \sim 0.75$ to $a_2 \sim 1.15$. The prompt gamma rays may be radiated from the central narrow core of aperture θ_γ, whereas the afterglow and very-high energy (VHE) gamma-rays could come from a wider angular structure.

initial temporal slopes of $\alpha_{OIR,1} = -1.3$ and $\alpha_{X,1} = -1.55$ that transition to $\alpha_{OIR,2} = -1.47$ and $\alpha_{X,2} = -1.67$ after ~0.8 days. Although this does not capture the complexity of the early-time afterglow evolution, it provides a good description of the full x-ray light curve and the OIR dataset from 0.8 to 80 days (Fig. 4). Over this time period, the low-frequency radio counterpart is dominated by synchrotron emission from the ejecta decelerated by the RS. Emission from the RS is likely contributing to the optical light curve at $t < 0.8$ days, and responsible for its early shallow decay. The evolution of this component, however, does not follow standard prescriptions.

DISCUSSION

The main advantage of the structured jet model is that it eases up the energetic requirements relative to the uniform jet, leading to $E_K \lesssim 8 \times 10^{52}$ $(t_j/80 \text{ days})^{0.37}$ erg (see Materials and Methods), where t_j is the observed time when the jet edges become visible, causing a final steepening of the light curve (if still relativistic). Causal contact across the full jet surface will only be established once the jet edges are already subrelativistic, leaving no room for strong jet spreading before the observed x-ray light curve behavior segues into a nonrelativistic slope $t^{(4-3p)/2}$ (*33*) that resembles the pre-transition slope. In the structured jet model, the collimation-corrected energy remains at the boundary of the energy budget for a magnetar central engine ($<10^{53}$ erg for a rapidly rotating supramassive neutron star), requiring an unrealistically high efficiency inconverting the magnetar's rotational output into gamma rays and blast-wave kinetic energy. The massive energy required to power GRB 221009A is consistent with a magneto-hydrodynamical process (*34*), extracting rotational energy from a rapidly spinning ($a = 0.9$) stellar mass (~5 $M_\odot$) black hole (*35*).

The shallow structured jet model helps explain the lack of prominent jet breaks in some long GRBs (*36*). In particular, the family of bright bursts with very high-energy emission, including events like GRB 130427A, GRB 180720B, GRB 190114C, and GRB 190829A, shares the common property of long-lasting afterglows (Fig. 5) with late-time temporal decay indices between 1.4 and 1.7 (*37*–*39*), similar to GRB 221009A. A shallow angular structure may thus be a frequent feature of the most violent explosions. However, none of these bursts reached the high energy of GRB 221009A, which provides compelling evidence for revising the standard jet model in a massive star explosion.

A structured jet profile also affects the rate calculation. For GRB 221009A, we infer an angular size, $\theta_s \gtrsim 0.4$ rad (see Materials and Methods), larger than that of the general GRB population, $\theta_j \approx 0.1$ rad. This would naively suggest that a similar event is $(\theta_s/\theta_j)^2 \approx 16$ times more likely to be detected than a regular GRB. If the intrinsic rate of highly energetic GRBs is significantly lower than the rate of typical GRBs, then the larger solid angle of the jet can explain the detection of GRB 221009A. However, this interpretation is not supported by the small viewing angle, $\theta_{obs} \lesssim 0.01$ rad, inferred from afterglow observations. Alternatively, if the rate of highly energetic GRBs is comparable to the rate of standard GRBs, then the large angular size of GRB 221009A is not consistent with the low rate of observed events (Fig. 1). A natural explanation for this contradiction is that the prompt gamma-ray radiation is produced only within a narrow range of the GRB jet ($\theta_\gamma \ll \theta_s$) (*40*), due to a reduction in Lorentz factor Γ with angle.

This leads to an increased opacity to photon-photon annihilation, which, in turn, can suppress the emission beyond a critical value (*41*), and, for a wide range of dissipation and emission mechanism models, a smaller Lorentz factor also leads to a reduction in the gamma-ray production. One example is a decrease in the dissipation radius $R_d \propto \Gamma^2$ at which the gamma rays are emitted. Even a

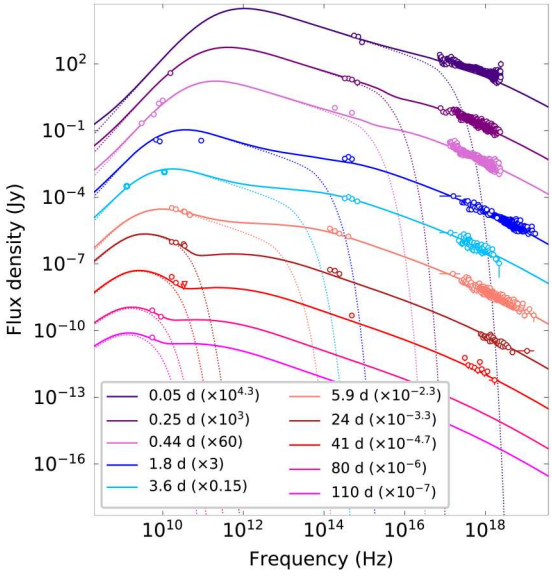

Fig. 4. Afterglow spectral evolution. Multiepoch broad-band spectral energy distributions (SEDs) of GRB 221009A modeled by the combination (solid line) of FS and RS (dotted line); see Materials and Methods. The data are corrected for extinction and absorption.

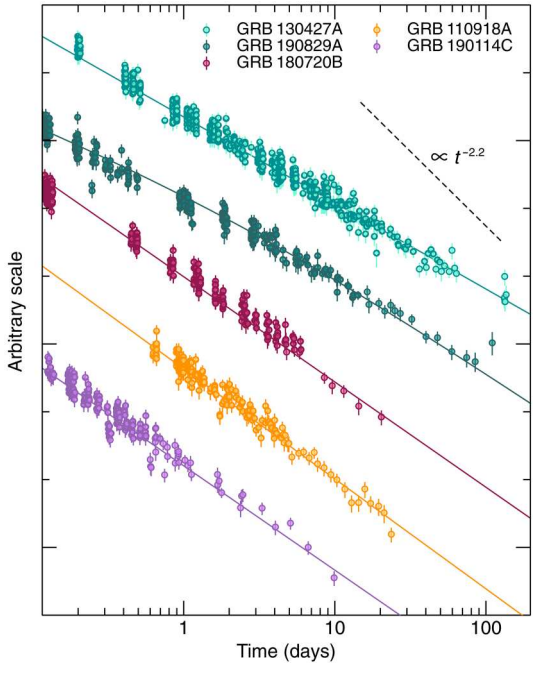

Fig. 5. Long-lived x-ray light curves of bright GRBs. A sample of bright long GRBs without a canonical jet break to late times is shown. For comparison, the dashed line shows the predicted late-time decay for a sharp-edged uniform jet.

small reduction in Lorentz factor can lead the dissipation radius to be smaller than the photospheric radius, which decreases with Lorentz factor, trapping the gamma-ray radiation for angles away from the core. This would lower the total energy released in gamma rays by a factor $(\theta_s/\theta_\gamma) \gtrsim 20$ but still require a substantial radiative efficiency along the sight line, $\eta_\gamma(\theta_{obs}) \gtrsim 20\%$.

The suppression of gamma-ray emission above θ_γ would cause observers at $\theta_{obs} > \theta_\gamma$ not to detect the prompt GRB emission and instead possibly identify such an event as an "orphan" afterglow. This may lead to a population of luminous orphan afterglows, which could be searched for in various transient surveys (*42*). The predicted rate of orphan afterglows differs by orders of magnitude between different jet models. However, as the jet angular structure shapes the early afterglow evolution (*17*), search strategies calibrated on a uniform jet model may not efficiently recover all the possible events. To constrain the rate of GRB 221009A–like transients and their gamma-ray beaming factor, transient classification schemes should be fine-tuned to a wide range of angular energy profiles.

MATERIALS AND METHODS

Energetics and rates

GRB 221009A triggered Fermi/GBM (*6*) on 2022-10-09 at 13:16:59 UT. The GRB displayed an initial short pulse (~40 s) followed by a period of apparent quiescence and then a main emission episode consisting of two bright peaks, at T_0 + 225 s and T_0 + 260 s, respectively. A third, weaker peak is visible at T_0 + 520 s.

Because of the GRB's immense brightness, the majority of satellites were saturated during the main emission episode. This prevents us from carrying out standard analysis without careful corrections (*6*, *7*, *43*). However, the burst fluence can be constrained using the Konus-Wind spectrum at the onset of the main pulse (T_0 + 180 to 200 s). This is described by a band function with $\alpha = -109$, $\beta = 2.6$, and peak energy $E_p \approx 1$ MeV. By applying this model to the entire GRB prompt phase, a fluence of $\sim 5.2 \times 10^{-2}$ erg cm^{-2} (20 keV to 10 MeV) (*15*) was derived between 0 and 700 s after the initial trigger. As the spectrum of the brightest peaks is likely harder than the spectrum at the onset, this value places a conservative lower bound to the true GRB fluence and already makes GRB 221009A the brightest GRB ever detected by over an order of magnitude (Table 1). On the basis of the fluence distribution of Fermi bursts (*1*), the expected probability of observing a similar event is less than 1 in 1000 years for a spatially homogeneous GRB population in Euclidean space (Fig. 6).

Table 1. Historical bright GRBs.

GRB	Observatory	Fluence (erg cm^{-2})	Energy band	Reference
840304	PVO, ICE, Vela 5B	2.8×10^{-3}	5 keV to 3 MeV	(*66*)
130427A	Fermi, Swift	2.5×10^{-3}	10 keV to 1 MeV	(*9*)
830801B	SIGNE 2 MP9	2.0×10^{-3}	30 keV to 7.5 MeV	(*67*)
850624	PVO	2.0×10^{-3}	5 keV to 3 MeV	(*68*)
940703A	BATSE, GRANAT, ULYSSES	1.6×10^{-3}	100 keV to 1 MeV	(*69*)

At the redshift of $z = 0.1505$ (*13*), the observed fluence corresponds to an isotropic-equivalent energy of $E_{\gamma,iso} \gtrsim 3 \times 10^{54}$ erg (1 keV to 10 MeV), among a short list of the most energetic GRBs to date (*44*) and very similar to GRB 160625B (*45*). Highly energetic ($\gtrsim 10^{54}$) GRBs are intrinsically rare events. Swift has detected approximately 11 of them during its entire lifetime (*46*). As expected, most are in the redshift range $1 \lesssim z \lesssim 3$, where the star formation (hence, the GRB rate) peaks. Assuming a constant GRB formation rate over this redshift interval, we compute an all-sky volumetric rate of energetic GRBs

$$R_z \approx \frac{N_{54}}{V} \frac{4\pi}{f_z \Omega_{BAT}} \frac{1}{\varepsilon T} = 0.014^{+0007}_{-0006}\ \mathrm{Gpc}^{-3}\ \mathrm{year}^{-1} \quad (1)$$

where $N_{54} \approx 8$ is the number of very energetic events detected within $1 \lesssim z \lesssim 3$, the available volume is $V = \int_1^3 \frac{dV}{dz} \frac{dz}{1+z} \approx 300$ Gpc^{-3}, where $\frac{dV}{dz}$ is the comoving volume element (*14*), $T \approx 18$ years is the current lifetime of the Swift mission, $\varepsilon \approx 78\%$ is the duty cycle, and $\Omega_{BAT} \approx 2.2$ sr is the field of view of the Swift Burst Alert Telescope (BAT) with partial coding > 10%. As these are very energetic events, we use an efficiency $f_z \approx 0.8$ for obtaining a redshift measurement.

If we assume that the GRB rate scales as the star formation rate (*47*), then the local rate of events is at least a factor of 10 lower, $R_{local} \approx 0.001$ Gpc^{-3} year^{-1}, and the probability of seeing a GRB as energetic as GRB 221009A within $z < 0.15$ is only 1 in 1000 years. Growing evidence shows that metallicity has a primary role in

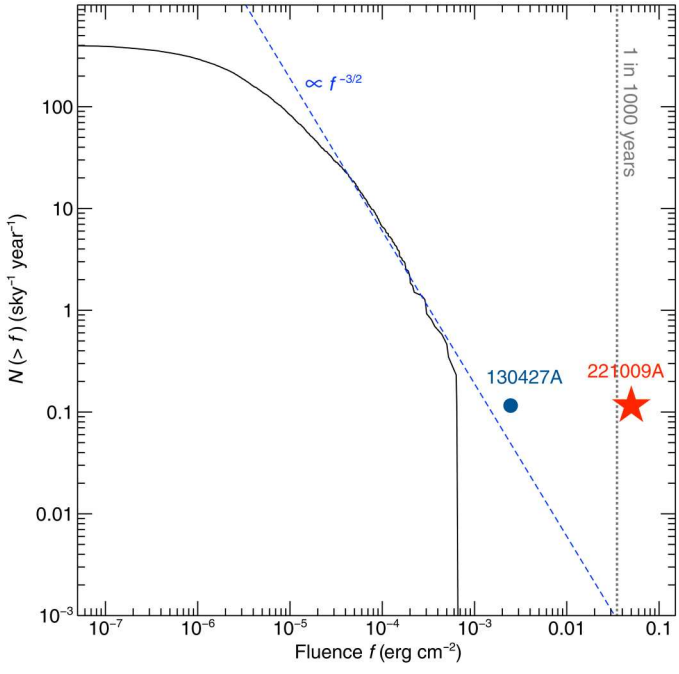

Fig. 6. Fluence distribution of Fermi GRBs. We have normalized the number of bursts for the mission lifetime, its duty cycle, and field of view (*1*). At large fluences ($S \gtrsim 5 \times 10^{-5}$ erg cm^{-2}) the distribution has a slope consistent with the Euclidean one (−3/2), also shown for comparison (dashed line). The two most fluent GRBs are GRB 130427A (circle) and GRB 221009A (star).

driving the GRB formation, and this could further lower the local rate by a factor ≈ 2.

A similar conclusion is reached by comparing GRB 221009A to the distribution of isotropic-equivalent GRB luminosities (*2*). Using the burst peak photon flux (10 to 1000 keV) from the preliminary GBM analysis, 2385 ± 3 photons s^{-1} cm^{-2} (*48*), and the Konus-Wind spectral parameters reported above, we derive a peak gamma-ray luminosity of $L_{\gamma,\,iso} \approx 9 \times 10^{52}$ erg s^{-1}. In the simplest scenario, not including an evolution of the GRB rate with redshift or metallicity, we find that less than ≈ 0.1% of GRBs have luminosities comparable to GRB 221009A, which translates in an all-sky rate of once in a decade across the visible Universe. For a local GRB rate in the range 0.3 to 2 Gpc^{-3} $year^{-1}$, we derive that the rate of events as luminous as GRB 221009A is one every 300 to 1100 years within $z \lesssim 0.15$. These independent analyses confirm that, due to its brightness and proximity to Earth, GRB 221009A is an exceptionally rare event.

Afterglow temporal evolution

We model the afterglow light curves with a series of power-law segments, $F_\nu \propto t^\alpha$. In the x-ray band, our best fit model (χ^2/df ≈ 1.3 for 1679 df) is a broken power law with initial decay index $\alpha_{X,1} = -1.52 \pm 0.01$, steepening to $\alpha_{X,2} = -1.66 \pm 0.01$ after $t_{break,X} = 0.82 \pm 0.07$ days. A single power-law slope provides a significantly worse description of the data (χ^2/df ≈ 2.1).

The OIR light curve, combining the grizJHK and the MASTER *C* filters, displays an initial power-law decay of $\alpha_{OIR,1} = -0.88 \pm 0.05$, which steepens to $\alpha_{OIR,2} = -1.42 \pm 0.11$ at around $t_{break,OIR} = 0.63 \pm 0.13$ days (χ^2/df ≈ 1.3 for 95 df). At times $t > 10$ days, a slight deviation from this power law is observed (Fig. 2), possibly caused by the contribution from a supernova (*49*) or the underlying host galaxy. By performing a joint fit to the x-ray and OIR light curves, we derive a break time of $t_{break,XOIR} = 0.79 \pm 0.04$ days (χ^2/df ≈ 1.3 for 1775 df). This joint fit results in a slightly steeper initial OIR decay of $\alpha_{OIR,1} = -0.92 \pm 0.04$, whereas the other best-fit slopes remain consistent with our previous values.

The afterglow behavior at radio energies is markedly different, suggesting that its evolution is decoupled from the higher energy data. Our dataset starts 6 days after the GRB trigger and follows the afterglow evolution up to 110 days in multiple frequencies. During the time interval of 6 to 41 days, we derive a power-law decay with slope −0.76 ± 0.08 at 16.7 GHz (Fig. 2), much shallower than the simultaneous OIR and x-ray light curves. A consistent behavior is observed at 21.2 GHz, whereas higher (>30-GHz) frequencies show a possible chromatic steepening after ≈30 days. A comparison with the lower frequency data (5.5 GHz) shows that the simple power-law model overpredicts the radio flux at $t \lesssim 1$ day, requiring the presence of a temporal break at early times.

Afterglow spectral properties

X-rays

We model the afterglow spectra in each energy band (x-ray, OIR, and radio) using a simple power-law function, $F_\nu \propto \nu^\beta$. The best fit was found by minimizing the Cash statistic within XSPEC v12.12.0. The effects of absorption were included using the XSPEC model tbabs*ztbabs*pow with fixed redshift $z = 0.1505$. The GRB sight line intercepts dense clouds along the Galactic plane, as shown by the bright dust scattering echoes at x-ray energies (*12*). We probed the absorbing column in the GRB direction by extracting multiple spectra of the ring located 6 arcmin from the GRB position at T_0 + 1.2 days (ObsID: 01126853005). They are well described by a power law with photon index $\Gamma = 4.3^{+0.6}_{-0.5}$ and an absorbing column of $N_H = 2.1^{+0.2}_{-0.6} \times 10^{22}$ cm^{-2}. We used the latter value as our estimate of the Galactic hydrogen column density.

The soft x-ray spectra (0.3 to 10 keV) display an initial hard spectral index of $\beta_X = -0.65 \pm 0.02$ at 1 hour, which is seen to soften with time to $\beta_X = -0.85 \pm 0.03$ at 5 hours and $\beta_X = -0.92 \pm 0.01$ at 32 days. A similar trend is measured in the NuSTAR data (3 to 79 keV), which also display a spectral softening between −0.81 ± 0.01 at 1.8 days and −1.10 ± 0.17 at 32 days. The latter value is consistent with the initial spectral index, $\beta_{BAT} = -1.08 \pm 0.03$, determined by Swift BAT (*12*).

Optical and infrared

The OIR data were modeled within XSPEC using the model redden*zdust*pow with fixed redshift $z = 0.1505$. Using a Galactic extinction of $E(B-V) = 1.32$ mag (*50*), we derive a negligible intrinsic extinction $E(B-V)_z < 0.1$ mag at the 3σ confidence level, a spectral index $\beta_{OIR} = -0.53 \pm 0.10$ between 0.2 and 0.5 days, and a steeper index $\beta_{OIR} = -0.68 \pm 0.05$ after 1.7 days (see Fig. 7). These values are consistent with the spectral index of the early (∼1 hour) x-ray afterglow.

Radio

Our dataset spans the frequency range between 5.5 and 47 GHz. Our second epoch (14.7 days after burst) was not included in the spectral analysis due to the large systematic uncertainty at higher frequencies. As shown in Fig. 7, the spectra at 5.8 and 25.7 days can be described by a power law with spectral index $\beta_R = -0.53 \pm 0.17$. There is possible evidence for a turnover of the radio spectrum at 40.7 days, suggesting that the component powering the low-frequency radio emission is not contributing to the optical and x-ray flux.

Theoretical modeling

Standard jet model

We began by exploring the simple scenario of a relativistic fireball (*21*, *22*, *28*, *51*) propagating into an ambient medium with density of the form $\rho_{ext}(r) = A\, r^{-k}$. The shock-accelerated electrons have an energy distribution of the form $N(E) \propto E^{-p}$ and cool via synchrotron radiation with a broadband spectrum described by three break frequencies: the cooling frequency ν_c, the characteristic frequency ν_m, and the self-absorption frequency ν_a. We focus mainly on the properties of the x-ray and OIR afterglow, as our analysis shows that the radio emission is dominated by a different component.

Our observational constraints include (i) the notable spectral evolution of the optical and x-ray emission during the first 24 hours since the GRB and (ii) the nearly achromatic steepening of the optical and x-ray light curves at around 0.8 days. A simple explanation for the spectral and temporal evolution of the x-ray counterpart is the passage of the cooling break. The observed change in x-ray spectral index, $\Delta\beta_X = -0.46 \pm 0.07$ between 0.05 and 40 days, points to a decreasing cooling break. The synchrotron cooling frequency is expected to change with time as $\nu_c \propto t^{\frac{3k-4}{2k-8}}$. This constraint implies $k < 4/3$ and rules out a wind-like environment with density profile $k = 2$ or steeper. However, if $\nu_c \lesssim \nu_X$ at 1 day, the x-ray temporal slope after the break, $\alpha_X = -1.66$, would require a steep $p = (2 - 4\alpha_X)3 \approx 2.88$, hence a soft spectral index $\beta_X = p/2 \approx 1.4$ inconsistent with the observed spectral shape by ≈5σ.

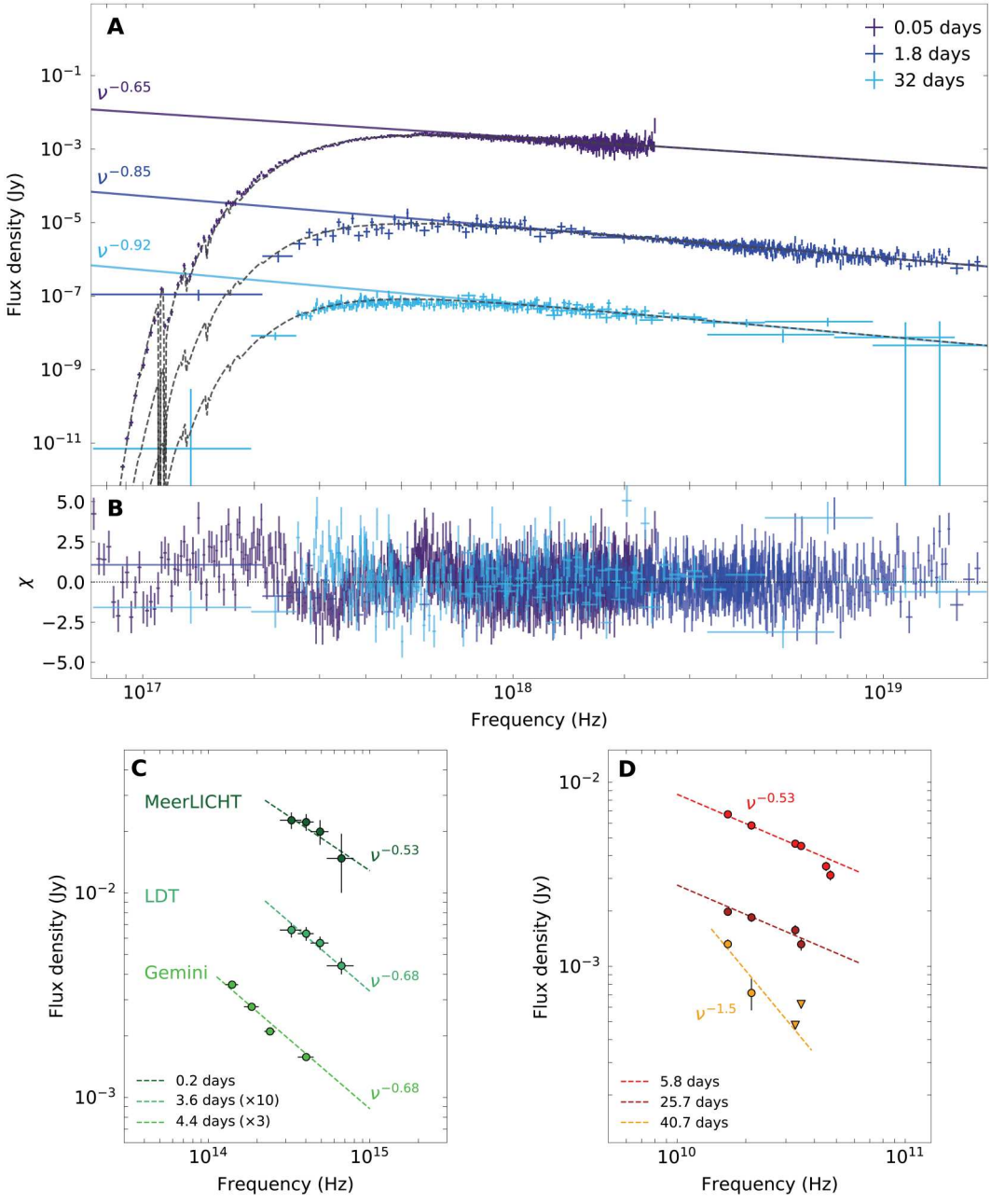

Fig. 7. Multiepoch spectra and SEDs of GRB 221009A. (**A**) Top: X-ray spectra of GRB 221009A fit an absorbed power-law model: Swift at 0.05 days, Swift and NuSTAR at 1.8 days, and XMM-Newton and NuSTAR at 32 days. (**B**) Middle: Residuals of the x-ray spectral fits. (**C**) Bottom left: Spectral energy distributions of the OIR data fit with a simple power-law model. The OIR data have been corrected for Galactic extinction $E(B-V) = 1.32$ mag (*50*). (**D**) Bottom right: Spectral energy distributions of the radio data (16.7 to 47 GHz).

A possible solution could be to include a time-dependent evolution of the shock microphysical parameters (*52*–*54*): ε_e is the fraction of the burst kinetic energy E_K in electrons and ε_B is the fraction in magnetic fields. To explain the slope of the x-ray light curve after the break, we require that the time dependence of the microphysical parameters adds an additional $t^{-0.51}$ to the temporal decay above ν_c (assuming $p = 2.2$). As the flux above ν_c has a very shallow dependence on ε_B ($\propto_B^{1/20}$ for $p = 2.2$), it is more practical to consider a time evolution of ε_e. We find that $\varepsilon_e \propto t^{-0.425}$ would not only reproduce the x-ray temporal slope but also drive a fast evolution of the spectral peak toward lower frequencies, $\nu_m \propto t^{-235}$, severely overpredicting the observed radio flux. Moreover, it does not account for the nearly simultaneous steepening of the optical emission. We therefore conclude that the passage of the cooling break across the x-ray band can explain some of the observed properties (e.g., the spectral softening) but does not entirely account for the steep temporal decay.

A straightforward explanation for the nearly achromatic temporal break at 0.8 days is a geometrical effect (*19*, *20*). The beamed geometry of the outflow causes the afterglow to decay at a faster rate once the jet edges become visible, with a change in temporal slope of $\Delta\alpha = (3 - k)/(4 - k)$ in the absence of lateral spreading, for a uniform sharp-edged (or "top-hat") jet. To be consistent with the x-ray measurements of $\Delta\alpha_X = 0.14 \pm 0.02$, this model requires a steep density profile $k \approx 2.8$ in disagreement with the limit $k < 4/3$ derived above.

If the temporal break at 0.8 days is not due to the collimation of the GRB outflow, then the required energetics to power the burst are challenging to reproduce. The x-ray light curve evolves as a power law up to at least 80 days after the trigger (at the time of writing).

Therefore, we can put an observational lower limit on $t_j > 80$ days, which leads to a lower limit on both the jet opening angle θ_j and the collimation-corrected energy of the GRB. Assuming $k = 0$ (uniform medium) and a redshift $z = 0.1505$, we derive

$$E_K > 4 \times 10^{53}\ \mathrm{erg} \left(\frac{t_j}{80\ \mathrm{days}}\right)^{3/4} \left(\frac{1+z}{1.15}\right)^{-3/4} \left(\frac{E_{K,\mathrm{iso}}}{10^{55}\ \mathrm{erg}}\right)^{3/4} \left(\frac{n}{1\ \mathrm{cm}^{-3}}\right)^{1/4} \quad (2)$$

where n is the circumburst density for a uniform medium. Such a high beaming corrected energy would be an outlier in the GRB energy distribution (Fig. 8) (*35*).

A structured jet

The standard assumption that GRB jets have a constant energy $dE_K/d\Omega$ within the core of the jet is likely an oversimplification, and a structured jet naturally arises as the GRB breaks out of its stellar environment (*32*, *55*). Here, we consider a GRB jet with a broken power-law structure (Fig. 3) defined by

$$\frac{dE_K}{d\Omega} \propto \begin{cases} \theta^{-a1} & \text{for } \theta < \theta_b \\ \theta^{-a2} & \text{for } \theta_b < \theta < \theta_s \\ \theta^{-a3} & \text{for } \theta > \theta_s \end{cases} \quad (3)$$

where $a_1 < a_2 < 2$, $a_3 \to \infty$, and an observer angle $\theta_{obs} < \theta_b$. This jet is therefore composed of an initial shallow slope followed by a steeper lateral profile that becomes visible when $\Gamma \approx \theta_b^{-1}$, where θ_b is the width of the initial shallow profile. In this case, the flux and frequency evolution is dictated by the lateral structure, leading to a shallow angular structure dominated emission (sASDE) phase [see tables 1 and 2 of (*29*)]. The flux evolution is initially the same as for a spherical outflow with an isotropic-equivalent energy corresponding to the value along the line of sight. This lasts up to a time, t_{sph}, when the Lorentz factor along the line of sight has decelerated to θ_{obs}^{-1}. At this point, the lateral structure becomes visible and the sASDE phase begins. In this regime, the flux in an interstellar medium environment is determined by

$$F_\nu \propto \begin{cases} t^{\frac{3(a+2p-2)}{(a-8)}} & \text{for } \nu_m < \nu < \nu_c \\ t^{\frac{2(a+3p-2)}{a-8}} & \text{for } \nu_c < \nu \end{cases} \quad (4)$$

This phase lasts until $t_b \approx 0.8$ days, which is the time at which $\Gamma = \theta_b^{-1}$. For $t > t_b$, the flux evolves in a similar way (i.e., governed by Eq. 4) but with $a_1 \to a_2$. For angles $\theta > \theta_s$, a steep jet break is expected at late times ($t_j > 80$ days) if the jet is still relativistic (*33*, *56*).

We consider a scenario where $t_{sph} < 1$ hour, such that the temporal decay is provided by Eq. 4 for the entire time period of our observations (0.05 to 80 days). We find a solution for $p = 2.2$, $k = 0$, $a_1 = 0.75$, and $a_2 = 1.15$, which yields an initial pre-break slope of $\alpha_{X,1} = 1.55$ that steepens to $\alpha_{X,2} = -1.67$ after ~ 0.8 days, assuming that $\nu_c < \nu_X$. The OIR slope after the break is $\alpha_{OIR,2} = -1.47$ for $\nu_m < \nu_{OIR} < \nu_c$, while the early OIR data (<1 day) are dominated by emission from a different component, likely an RS.

Motivated by this solution, we modeled the afterglow spectral energy distributions from radio to x-ray wavelengths with a phenomenological model combining two components, an FS and an RS. The FS closure relations are governed by the jet structure (Eq. 4).

The RS evolution in a structured outflow has not been sufficiently developed yet for inclusion in our study. We therefore adopt standard prescriptions of a thin-shell model parameterized by the power-law index g of the Lorentz factor distribution with radius $\Gamma \propto R^{-g}$ (*57*). Each component was allowed to have an independent electron spectral slope p and was parameterized by the locations of ν_a, ν_m, and ν_c at a reference time of 1 day as well as the peak flux $F_{\nu,max}$ at that time. The best fit was obtained by simple χ^2 minimization on the extinction-corrected afterglow data (Fig. 4).

We find that the FS reproduces the full x-ray light curve and the OIR data after 0.8 days (Fig. 4). In this model, the cooling break $\nu_{c,FS}$ moves through the x-ray band, producing the observed spectral softening. The injection frequency $\nu_{m,FS}$ is constrained to be close to the soft x-ray band at early times, as otherwise the FS severely overpredicts the radio emission at later times (>14 days). A jet model with a single slope for the power-law energy distribution $dE_K/d\Omega \propto \theta^{-a}$ with $a \approx 1$ can reproduce these observations. However, a broken power-law energy structure is well motivated by simulations (*32*) of GRB jets, which display an evolution of the jet's angular energy distribution from shallower to steeper slopes. For a jet with structure

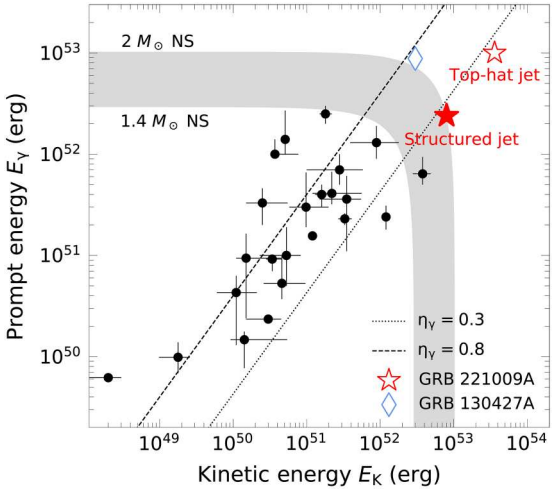

Fig. 8. Collimation corrected kinetic energy E_K versus prompt gamma-ray energy E_γ. We have displayed a sample of long GRBs from the literature (*35*, *38*). The empty red star displays the lowerlimit to the energy of GRB 221009A in the top-hat jet scenario and the filled red star in the structured jet case. The gray-shaded regions show a range of allowed values for magnetar central engines based on the mass of the neutron star (NS) (*26*, *65*). The black lines show a gamma-ray efficiency of $\eta_\gamma = 30$ to 80%.

given by $a_1 \approx 0.75$ and $a_2 \approx 1.15$, we derive $\nu_{c,FS} \approx 1.7 \times 10^{18}$ Hz, $\nu_{m,FS} \approx 3.6 \times 10^{14}$ Hz, $F_{\nu,max,FS} \approx 5.9$ mJy, and $p \approx 2.25$. The self-absorption frequency $\nu_{a,FS} \lesssim 10^{10}$ Hz remains unconstrained.

Afterglow modeling depends on a large number of physical parameters, larger than the number of observed constraints. Many values of the physical parameters, varying over orders of magnitude, will produce nearly identical afterglow emission. Using fiducial values of $E_{K,iso} = 10^{55}$ erg, $n = 1$ cm^{-3}, and $\theta_{obs} = 0.01$ rad and inverting the values of $F_{\nu,max,FS}$, $\nu_{m,FS}$, and $\nu_{c,FS}$, we find a solution for $\varepsilon_e = 0.17$, $\varepsilon_B = 4.4 \times 10^{-6}$, and an electron participation fraction $\xi_N = 0.015$.

As expected, we find that the standard thin-shell RS is not capable of reproducing the phenomenology of a structured outflow. Even for large values of the parameter $g \gtrsim 3$, this model cannot account for the early optical emission and, at the same time, reproduce the shallow decay of the radio afterglow (Fig. 9). To capture this behavior, we require at least two separate RS components (Fig. 4), with the first RS dominating at <10 days capable of explaining the early radio and OIR data. Alternatively, ad hoc solutions such as energy injection and/or variability of the shock microphysics may be introduced to slow down the RS evolution.

Similar challenges were encountered in the modeling of other bright GRBs (*58*). For example, a two component model was explored in the case of GRB 030329A (*40*), GRB 130427A (*59*), and GRB 190829A (*37*, *60*), whereas time-evolving microphysics were favored in the case of GRB 190114C (*39*). GRB 221009A adds to the growing sample of bursts deviating from the basic RS scenario and motivates further extension of the standard model by incorporating a broader set of jet angular structures.

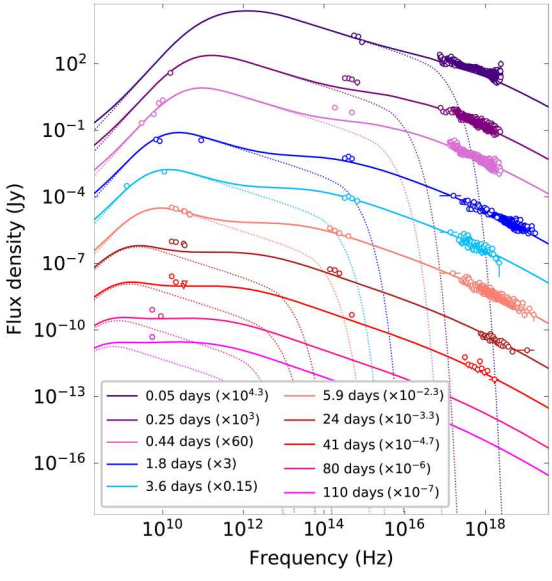

Fig. 9. Multiepoch broad-band SEDs of GRB 221009A. We have modeled the data by the combination (solid line) of an FS and an RS (dotted line). A single RS evolved following the thin-shell closure relations (*57*) cannot reproduce the early optical and late radio emission. The data are corrected for extinction and absorption.

Implications of a structured jet

Energetics

An advantage of the shallow structured jet scenario suggested above is that it reduces the energy requirements compared to steep jet models. The viewing angle to the burst θ_{obs} is directly related to the earliest time, t_{sph}, at which the afterglow begins evolving according to the inner (shallow) slope of the energy profile (i.e., $E_{K,iso} \propto \theta^{-a_1}$; see Eq. 4) and can be expressed as

$$\theta_{obs} = \left(\frac{(3-k)E_{K,iso}(\theta_{obs})}{4\pi A\ 2^{3-k}c^{5-k}}\right)^{\frac{1}{2k-8}} t_{sph}^{\frac{3-k}{8-2k}} \quad (5)$$

which, for $k = 0$ (as favored by the spectral evolution), implies $\theta_{obs} \lesssim 0.016$ rad for $t_{sph} < 0.05$ days. For a shallow structured jet, the maximum polar angle of the jet viewable to an observer at θ_{obs} evolves in time according to

$$\theta(t) = \theta_{obs}\begin{cases} (t/t_{sph})^{\frac{3-k}{8-2k-a_1}} \text{ for } t_{sph} < t < t_b \\ (t_b/t_{sph})^{\frac{3-k}{8-2k-a_1}}(t/t_b)^{\frac{3-k}{8-2k-a2}} \text{ for } t > t_b \end{cases} \quad (6)$$

where we adopt $a_1 = 0.75$ and $a_2 = 1.15$. This is related to the angle θ_b below which $E_{K,iso}$ evolves as θ^{-a_1} and above which as θ^{-a_2}. Therefore, θ_b can be expressed as

$$\theta_b = \left(\frac{(3-k)E_{K,iso}(\theta_{obs})}{4\pi A\ 2^{3-k}c^{5-k}}\right)^{\frac{1}{2k-8+a_1}} t_b^{\frac{3-k}{8-2k-a_1}} \theta_{obs}^{\frac{a_1}{8-2k-a_1}}$$
$$= 0.057 \text{ rad}\left(\frac{E_{K,iso}}{10^{55}\text{ erg}}\right)^{-0.14}\left(\frac{n}{1\text{ cm}^{-3}}\right)^{0.14}\left(\frac{\theta_{obs}}{0.01}\right)^{-0.10}\left(\frac{t_b}{0.8\text{ days}}\right)^{0.4}\left(\frac{1+z}{115}\right)^{-0.4} \quad (7)$$

As we do not observe a steep break (i.e., traditional jet break with $F_\nu \propto t^{-p}$) in the light curve out to $t_j > 80$ days, we can set a lower limit to the opening angle θ_s (see Eq. 3) out to which the relation $E_{K,iso} \propto \theta^{-a_2}$ extends. This, in turn, allows us to derive a lower limit to the collimation-corrected kinetic energy in the jet E_K. Using θ_{obs} and θ_b, these relations are provided by

$$\theta_s > \theta(t) = \theta_b\left(\frac{t_j}{t_b}\right)^{\frac{3-k}{8-2k-a_2}} \quad (8)$$

$$E_K = \frac{a_3 - a_2}{(2-a_2)(a_3-2)}\,\theta(t)^2 E_{K,iso}\,(\theta_{obs})\left(\frac{\theta_b}{\theta_{obs}}\right)^{-a_1}\left(\frac{\theta(t)}{\theta_b}\right)^{-a_2} \quad (9)$$

which, for $\theta(t) = \theta_s$, $k = 0$, $a_1 = 0.75$, $a_2 = 1.15$, and $a_3 \to \infty$, becomes

$$\theta_s > 0.4 \text{ rad}\left(\frac{E_{K,iso}}{10^{55}\text{ erg}}\right)^{-0.14}\left(\frac{n}{1\text{ cm}^{-3}}\right)^{0.14}\left(\frac{\theta_{obs}}{0.01}\right)^{-0.10}$$
$$\left(\frac{t_b}{0.8\text{ days}}\right)^{-0.04}\left(\frac{1+z}{1.15}\right)^{0.04}\left(\frac{t_j}{80\text{ days}}\right)^{0.44} \quad (10)$$

$$E_K = 8\times 10^{52}\left(\frac{E_{K,iso}}{10^{55}\text{ erg}}\right)^{0.83}\left(\frac{n}{1\text{ cm}^{-3}}\right)^{0.17}\left(\frac{\theta_{obs}}{0.01}\right)^{062}\left(\frac{t_b}{0.8\text{ days}}\right)^{0.14}$$
$$\left(\frac{t_j}{80\text{ days}}\right)^{0.37}\left(\frac{1+z}{1.15}\right)^{-0.51} \quad (11)$$

Formally, this limit decreases for smaller viewing angles θ_{obs}. However, considering that t_{sph} has to be greater than the prompt duration of the GRB, θ_{obs} cannot decrease by much. The required energy is reduced compared to the standard jet case (4×10^{53} erg). Furthermore, the energy has a shallower dependence on the time of the steep jet break $t_j^{0.37}$ compared to $t_j^{3/4}$ for a top-hat jet. In other words, as the length of time over which we do not observe a steep jet break increases, the more energetically favorable the structured jet model becomes.

A structured jet with extended wings will take even longer to establish causal contact across the jet surface than a top-hat jet, which can help to explain the lack of post–jet break dynamics observed for GRB 221009A and similar events. In the central engine frame, a relativistic sound wave traveling along the jet surface between edge and tip will move along with velocity $\beta_\theta = 1/(2\Gamma)$ for a jet with local shock Lorentz factor Γ. If $\Gamma \propto \theta^{-a_1/2}$, then causal contact out to angle θ will occur once $\Gamma(\theta) = (1 - a_1/2)/(3\theta) \lesssim 1$ (for example, $\theta = 0.4$ rad, $a_1 = 0.75$, $\Gamma = 0.52 < 1$ shows a clear breakdown of the assumption of relativistic dynamics; a steepening to a jet structure slope a_2 at intermediate angle would lead to an even lower Γ). The nonrelativistic light curve slope above the cooling break (e.g., in the x-rays) is given by $t^{(4-3p)/2}$, which can be very similar to the relativistic slope of a shallow structured jet.

Rate of events

We have demonstrated that GRB 221009A stands out compared to other long-duration GRBs in terms of its both energetics and close proximity. The shallow flux decay in the x-ray and OIR until very late times is interpreted as evidence for a shallow jet structure. We therefore suggest that GRB 221009A and other nearby GRBs without steep jet breaks (GRB 130427A, GRB 180720B, GRB 190114C, and GRB 190829A) imply the existence of a subclass of energetic GRBs with shallow jet structures.

This subclass, due to their shallow angular profiles, has a different effective beaming compared to the typical GRB population, which affects their observed rate. On the one hand, the large inferred value of $\theta_s \approx 0.4$ rad derived for GRB 221009A in Eq. 10 is larger than typical opening angles derived for long GRBs, i.e., $\theta_j \approx 0.1$ rad, where jet breaks are easier to observe for energetic and narrow jets. This would suggest that even a relatively small intrinsic rate associated with the subpopulation of shallow jets might be overrepresented in the observed data, approximately by a factor of $(\theta_s/\theta_j)^2 \approx 16$. However, the low derived value of the viewing angle to GRB 221009A, $\theta_{obs} \lesssim 0.016$ rad (Eq. 5), is in tension with this suggestion. In particular, because of the larger solid angles associated with greater viewing angles, for each burst like GRB 221009A that is viewed from $\lesssim\theta_{obs}$, there should be (on average) ~ 625 GRBs viewed from $\lesssim \theta_s$. If we take a shallow angular profile of the kinetic energy, $E_{K,iso} \propto \theta^{-a}$ with $a \approx 0.9$ between θ_{obs} and θ_s, then bursts viewed from $\sim\theta_s$ might be expected to have a gamma-ray fluence that is roughly 20 times smaller than that of GRB 221009A. In other words, if the observed rate of GRB 221009A is about 1 in 1000 years, then, roughly once in 1.5 year, we should be detecting bursts that are ~20 times less fluent. As shown in Figs. 1 and 6, this is clearly in contradiction with Fermi and BATSE observations. This suggests that, even if GRB 221009A–like jets have shallow profiles extending up to large latitudes, their gamma-ray production might be restricted to a much narrower range (up to some $\theta_\gamma \ll \theta_s$). Such a possibility is expected if there is even a relatively small reduction in the bulk Lorentz factor of the outflows with θ (*61*). Beniamini and Nakar (*61*) have argued that this is a limiting factor in the detectability of long GRBs based on various observational lines of evidence. To conclude, the intrinsic rate of GRB 221009A–like jets is strongly dependent on the effective opening angle for gamma-ray production, and, with only one well-constrained event of this type, the intrinsic rate of such bursts remains largely unconstrained. Nonetheless, if $\theta_\gamma \ll \theta_s$ as suggested by the discussion above, then there should be a large population of similar jets that would have produced little or no gamma rays, despite having been viewed from $\theta < \theta_s$ and, therefore, corresponded to very bright and initially fast evolving afterglows in all wavelengths. The existence of these on-axis orphan afterglows of shallow jets can be constrained using transient surveys (*62*).

Assuming that the prompt GRB emission is produced in an optically thin region of the outflow, the dissipation radius inferred from the prompt emission variability timescale t can be compared to the photospheric radius to place a constraint on the minimum outflow Lorentz factor placing emission beyond the photospheric radius. Following (*63*), this requirement translates to $\Gamma \gtrsim 505(E/10^{55}\ \mathrm{erg})^{1/5}\ (\delta t/0.1\ \mathrm{s})^{-2/5}$ for a jet of isotropic-equivalent energy E. The atypical jet structure inferred for GRB 221009A, with a very narrow core (a tip) embedded within shallow power-law profile, implies a far smaller jet surface area detectable in prompt emission. Assuming an inner jet Lorentz factor profile $\Gamma = \Gamma_{tip}(\theta/\theta_j)^{-a_1/2}$ and $a_1 = 0.9$, we find a maximum observer angle $\theta_\gamma \sim 0.043(\theta_j/10^{-2})(E/10^{55}\ \mathrm{erg})^{-0.74}(\delta t/0.1\ \mathrm{s})^{1.5}(\Gamma_{tip}/750)^{3.7}$ rad, assuming that the tip (i.e., the region of the jet at $\theta < \theta_\gamma$) is sufficiently fast in the first place. Thus, even if shallow power-law jets with narrow cores were intrinsically equally likely as "typical" top-hat jets with $\theta_j \sim 0.1$ rad, this already renders them about five times as rare. The intrinsic likelihood of producing a jet with a narrow core and shallow power-law structure further affects their expected rate, as do the energetics and initial baryon loading of the jet.

Supplementary Materials

This PDF file includes:

Supplementary Text
Tables S1 to S5
References

REFERENCES AND NOTES

1. A. von Kienlin, C. A. Meegan, W. S. Paciesas, P. N. Bhat, E. Bissaldi, M. S. Briggs, E. Burns, W. H. Cleveland, M. H. Gibby, M. M. Giles, A. Goldstein, R. Hamburg, C. M. Hui, D. Kocevski, B. Mailyan, C. Malacaria, S. Poolakkil, R. D. Preece, O. J. Roberts, P. Veres, C. A. Wilson-Hodge, The fourth fermi-GBM gamma-ray burst catalog: A decade of data. *Astrophys. J.* **893**, 46 (2020).
2. R. Salvaterra, S. Campana, S. D. Vergani, S. Covino, P. D'Avanzo, D. Fugazza, G. Ghirlanda, G. Ghisellini, A. Melandri, L. Nava, B. Sbarufatti, H. Flores, S. Piranomonte, G. Tagliaferri, A complete sample of bright Swift long gamma-ray bursts. I. Sample presentation, luminosity function and evolution. *Astrophys. J.* **749**, 68 (2012).
3. J. Hjorth, D. Malesani, P. Jakobsson, A. O. Jaunsen, J. P. U. Fynbo, J. Gorosabel, T. Krühler, A. J. Levan, M. J. Michałowski, B. Milvang-Jensen, P. Møller, S. Schulze, N. R. Tanvir, D. Watson, The optically unbiased gamma-ray burst host (TOUGH) survey. I. Survey design and catalogs. *Astrophys. J.* **756**, 187 (2012).
4. A. Franceschini, G. Rodighiero, M. Vaccari, Extragalactic optical-infrared background radiation, its time evolution and the cosmic photon-photon opacity. *Astron. Astrophys.* **487**, 837–852 (2008).
5. M. Ajello, M. Arimoto, M. Axelsson, L. Baldini, G. Barbiellini, D. Bastieri, R. Bellazzini, P. N. Bhat, E. Bissaldi, R. D. Blandford, R. Bonino, J. Bonnell, E. Bottacini, J. Bregeon, P. Bruel, R. Buehler, R. A. Cameron, R. Caputo, P. A. Caraveo, E. Cavazzuti, S. Chen, C. C. Cheung, G. Chiaro, S. Ciprini, D. Costantin, M. Crnogorcevic, S. Cutini, M. Dainotti, F. D'Ammando, P. d. I.

Torre Luque, F. Palma, A. Desai, R. Desiante, N. D. Lalla, L. D. Venere, F. F. Dirirsa, S. J. Fegan, A. Franckowiak, Y. Fukazawa, S. Funk, P. Fusco, F. Gargano, D. Gasparrini, N. Giglietto, F. Giordano, M. Giroletti, D. Green, I. A. Grenier, J. E. Grove, S. Guiriec, E. Hays, J. W. Hewitt, D. Horan, G. Jóhannesson, D. Kocevski, M. Kuss, L. Latronico, J. Li, F. Longo, F. Loparco, M. N. Lovellette, P. Lubrano, S. Maldera, A. Manfreda, G. Martí-Devesa, M. N. Mazziotta, I. Mereu, M. Meyer, P. F. Michelson, N. Mirabal, W. Mitthumsiri, T. Mizuno, M. E. Monzani, E. Moretti, A. Morselli, I. V. Moskalenko, M. Negro, E. Nuss, M. Ohno, N. Omodei, M. Orienti, E. Orlando, M. Palatiello, V. S. Paliya, D. Paneque, M. Persic, M. Pesce-Rollins, V. Petrosian, F. Piron, S. Poolakkil, H. Poon, T. A. Porter, G. Principe, J. L. Racusin, S. Rainò, R. Rando, M. Razzano, S. Razzaque, A. Reimer, O. Reimer, T. Reposeur, F. Ryde, D. Serini, C. Sgrò, E. J. Siskind, E. Sonbas, G. Spandre, P. Spinelli, D. J. Suson, H. Tajima, M. Takahashi, D. Tak, J. B. Thayer, D. F. Torres, E. Troja, J. Valverde, P. Veres, G. Vianello, A. von Kienlin, K. Wood, M. Yassine, S. Zhu, S. Zimmer, A decade of gamma-ray bursts observed by Fermi-LAT: The second GRB catalog. *Astrophys. J.* **878**, 52 (2019).

6. S. Lesage, P. Veres, M. S. Briggs, A. Goldstein, D. Kocevski, E. Burns, C. A. Wilson-Hodge, P. N. Bhat, D. Huppenkothen, C. L. Fryer, R. Hamburg, J. Racusin, E. Bissaldi, W. H. Cleveland, S. Dalessi, C. Fletcher, M. M. Giles, B. A. Hristov, C. M. Hui, B. Mailyan, S. Poolakkil, O. J. Roberts, A. von Kienlin, J. Wood, M. Ajello, M. Arimoto, L. Baldini, J. Ballet, M. G. Baring, D. Bastieri, J. Becerra Gonzalez, R. Bellazzini, E. Bissaldi, R. D. Blandford, R. Bonino, P. Bruel, S. Buson, R. A. Cameron, R. Caputo, P. A. Caraveo, E. Cavazzuti, G. Chiaro, N. Cibrario, S. Ciprini, P. Cristarella Orestano, M. Crnogorcevic, A. Cuoco, S. Cutini, F. DAmmando, S. De Gaetano, N. Di Lalla, L. Di Venere, A. Dominguez, S. J. Fegan, E. C. Ferrara, H. Fleischhack, Y. Fukazawa, S. Funk, P. Fusco, G. Galanti, V. Gammaldi, F. Gargano, C. Gasbarra, D. Gasparrini, S. Germani, F. Giacchino, N. Giglietto, R. Gill, M. Giroletti, J. Granot, D. Green, I. A. Grenier, S. Guiriec, M. Gustafsson, E. Hays, J. W. Hewitt, D. Horan, X. Hou, M. Kuss, L. Latronico, A. Laviron, M. Lemoine-Goumard, J. Li, I. Liodakis, F. Longo, F. Loparco, L. Lorusso, M. N. Lovellette, P. Lubrano, S. Maldera, A. Manfreda, G. Marti-Devesa, M. N. Mazziotta, J. E. Mc Enery, I. Mereu, M. Meyer, P. F. Michelson, T. Mizuno, M. E. Monzani, A. Morselli et al., Fermi-GBM discovery of GRB 221009A: An extraordinarily bright GRB from onset to afterglow. arXiv:2303.14172 [astro-ph.HE] (2023).
7. D. Frederiks, D. Svinkin, A. L. Lysenko, S. Molkov, A. Tsvetkova, M. Ulanov, A. Ridnaia, A. A. Lutovinov, I. Lapshov, A. Tkachenko, V. Levin, Properties of the extremely energetic GRB-0.5ex~221009A from Konus-WIND and SRG/ART-XC observations. arXiv:2302.13383 [astro-ph.HE] (2023).
8. J. Ripa, H. Takahashi, Y. Fukazawa, N. Werner, F. Munz, A. Pal, M. Ohno, M. Dafcikova, L. Meszaros, B. Csak, N. Husarikova, M. Kolar, G. Galgoczi, J.-P. Breuer, F. Hroch, J. Hudec, J. Kapus, M. Frajt, M. Rezenov, R. Laszlo, M. Koleda, M. Smelko, P. Hanak, P. Lipovsky, T. Urbanec, M. Kasal, A. Povalac, Y. Uchida, H. Poon, H. Matake, K. Nakazawa, N. Uchida, T. Bozoki, G. Dalya, T. Enoto, Z. Frei, G. Friss, Y. Ichinohe, K. Kapas, L. L. Kiss, T. Mizuno, H. Odaka, J. Takatsy, M. Topinka, K. Torigoe, The peak-flux of GRB 221009A measured with GRBAlpha. arXiv:2302.10047 [astro-ph.HE] (2023).
9. M. Ackermann, M. Ajello, K. Asano, W. B. Atwood, M. Axelsson, L. Baldini, J. Ballet, G. Barbiellini, M. G. Baring, D. Bastieri, K. Bechtol, R. Bellazzini, E. Bissaldi, E. Bonamente, J. Bregeon, M. Brigida, P. Bruel, R. Buehler, J. M. Burgess, S. Buson, G. A. Caliandro, R. A. Cameron, P. A. Caraveo, C. Cecchi, V. Chaplin, E. Charles, A. Chekhtman, C. C. Cheung, J. Chiang, G. Chiaro, S. Ciprini, R. Claus, W. Cleveland, J. Cohen-Tanugi, A. Collazzi, L. R. Cominsky, V. Connaughton, J. Conrad, S. Cutini, F. D'Ammando, A. de Angelis, M. DeKlotz, F. de Palma, C. D. Dermer, R. Desiante, A. Diekmann, L. di Venere, P. S. Drell, A. Drlica-Wagner, C. Favuzzi, S. J. Fegan, E. C. Ferrara, J. Finke, G. Fitzpatrick, W. B. Focke, A. Franckowiak, Y. Fukazawa, S. Funk, P. Fusco, F. Gargano, N. Gehrels, S. Germani, M. Gibby, N. Giglietto, M. Giles, F. Giordano, M. Giroletti, G. Godfrey, J. Granot, I. A. Grenier, J. E. Grove, D. Gruber, S. Guiriec, D. Hadasch, Y. Hanabata, A. K. Harding, M. Hayashida, E. Hays, D. Horan, R. E. Hughes, Y. Inoue, T. Jogler, G. Jóhannesson, W. N. Johnson, T. Kawano, J. Knödlseder, D. Kocevski, M. Kuss, J. Lande, S. Larsson, L. Latronico, F. Longo, F. Loparco, M. N. Lovellette, P. Lubrano, M. Mayer, M. N. Mazziotta, J. E. McEnery, P. F. Michelson, T. Mizuno, A. A. Moiseev, M. E. Monzani, E. Moretti, A. Morselli, I. V. Moskalenko, S. Murgia, R. Nemmen, E. Nuss, M. Ohno, T. Ohsugi, A. Okumura, N. Omodei, M. Orienti, D. Paneque, V. Pelassa, J. S. Perkins, M. Pesce-Rollins, V. Petrosian, F. Piron, G. Pivato, T. A. Porter, J. L. Racusin, S. Rainò, R. Rando, M. Razzano, S. Razzaque, A. Reimer, O. Reimer, S. Ritz, M. Roth, F. Ryde, A. Sartori, P. M. S. Parkinson, J. D. Scargle, A. Schulz, C. Sgrò, E. J. Siskind, E. Sonbas, G. Spandre, P. Spinelli, H. Tajima, H. Takahashi, J. G. Thayer, J. B. Thayer, D. J. Thompson, L. Tibaldo, M. Tinivella, D. F. Torres, G. Tosti, E. Troja, T. L. Usher, J. Vandenbroucke, V. Vasileiou, G. Vianello, V. Vitale, B. L. Winer, K. S. Wood, R. Yamazaki, G. Younes, H. F. Yu, S. J. Zhu, P. N. Bhat, M. S. Briggs, D. Byrne, S. Foley, A. Goldstein, P. Jenke, R. M. Kippen, C. Kouveliotou, S. McBreen, C. Meegan, W. S. Paciesas, R. Preece, A. Rau, D. Tierney, A. J. van der Horst, A. von Kienlin, C. Wilson-Hodge, S. Xiong, G. Cusumano, V. la Parola, J. R. Cummings, Fermi-LAT observations of the gamma-ray burst GRB 130427A. *Science* **343**, 42–47 (2014).
10. L. A. Hayes, P. T. Gallagher, A significant sudden ionospheric disturbance associated with gamma-ray burst GRB 221009A. *Res. Notes Am. Astron. Soc.* **6**, 222 (2022).
11. Y. Huang, S. Hu, S. Chen, M. Zha, C. Liu, Z. Yao, Z. Cao; The Lhaaso Experiment, LHAASO observed GRB 221009A with more than 5000 VHE photons up to around 18 TeV. *GRB Coord. Netw.* **32677**, 1 (2022).
12. M. A. Williams, J. A. Kennea, S. Dichiara, K. Kobayashi, W. B. Iwakiri, A. P. Beardmore, P. A. Evans, S. Heinz, A. Lien, S. R. Oates, H. Negoro, S. Bradley Cenko, D. J. K. Buisson, D. H. Hartmann, G. K. Jaisawal, N. P. M. Kuin, S. Lesage, K. L. Page, T. Parsotan, D. R. Pasham, B. Sbarufatti, M. H. Siegel, S. Sugita, G. Younes, E. Ambrosi, Z. Arzoumanian, M. G. Bernardini, S. Campana, M. Capalbi, R. Caputo, A. D'Ai, P. D'Avanzo, V. D'Elia, M. De Pasquale, R. A. J. Eyles-Ferris, E. Ferrara, K. C. Gendreau, J. D. Gropp, N. Kawai, N. Klingler, S. Laha, A. Melandri, T. Mihara, M. Moss, P. O.'B, J. P. Osborne, D. M. Palmer, M. Perri, M. Serino, E. Sonbas, M. Stamatikos, R. Starling, G. Tagliaferri, A. Tohuvavohu, S. Zane, H. Ziaeepour, GRB 221009A: Discovery of an exceptionally rare nearby and energetic gamma-ray burst. arXiv:2302.03642 [astro-ph.HE] (2023).
13. D. B. Malesani, A. J. Levan, L. Izzo, A. de Ugarte Postigo, G. Ghirlanda, K. E. Heintz, D. A. Kann, G. P. Lamb, J. Palmerio, O. S. Salafia, R. Salvaterra, N. R. Tanvir, J. F. Agüí Fernández, S. Campana, A. A. Chrimes, P. D'Avanzo, V. D'Elia, M. Della Valle, M. De Pasquale, J. P. U. Fynbo, N. Gaspari, B. P. Gompertz, D. H. Hartmann, J. Hjorth, P. Jakobsson, E. Palazzi, E. Pian, G. Pugliese, M. E. Ravasio, A. Rossi, A. Saccardi, P. Schady, B. Schneider, J. Sollerman, R. L. C. Starling, C. C. Thöne, A. J. van der Horst, S. D. Vergani, D. Watson, K. Wiersema, D. Xu, T. Zafar, The brightest GRB ever detected: GRB 221009A as a highly luminous event at z = 0.151. arXiv:2302.07891 [astro-ph.HE] (2023).
14. W. L. Freedman, Measurements of the hubble constant: Tensions in perspective. *Astrophys. J.* **919**, 16 (2021).
15. D. Frederiks, A. Lysenko, A. Ridnaia, D. Svinkin, A. Tsvetkova, M. Ulanov, T. Cline; Konus-Wind Team, Konus-Wind detection of GRB 221009A. *GRB Coord. Netw.* **32668**, 1 (2022).
16. P. Beniamini, J. Granot, R. Gill, Afterglow light curves from misaligned structured jets. *Mon. Notices Royal Astron. Soc.* **493**, 3521–3534 (2020).
17. G. Ryan, H. van Eerten, L. Piro, E. Troja, Gamma-ray burst afterglows in the multimessenger era: Numerical models and closure relations. *Astrophys. J.* **896**, 166 (2020).
18. H. van Eerten, A. MacFadyen, Gamma-ray burst afterglow light curves from a Lorentz-boosted simulation frame and the shape of the jet break. *Astrophys. J.* **767**, 141 (2013).
19. J. E. Rhoads, The dynamics and light curves of beamed gamma-ray burst afterglows. *Astrophys. J.* **525**, 737–749 (1999).
20. R. Sari, T. Piran, J. P. Halpern, Jets in gamma-ray bursts. *Astrophys. J.* **519**, L17–L20 (1999).
21. P. Mészáros, M. J. Rees, Optical and long-wavelength afterglow from gamma-ray bursts. *Astrophys. J.* **476**, 232–237 (1997).
22. R. Sari, T. Piran, R. Narayan, Spectra and light curves of gamma-ray burst afterglows. *Astrophys. J.* **497**, L17–L20 (1998).
23. R. Pillera, E. Bissaldi, N. Omodei, G. La Mura, F. Longo; Fermi-LAT team, GRB 221009A: Fermi-LAT refined analysis. *GRB Coord. Netw.* **32658**, 1 (2022).
24. A. Ursi, G. Panebianco, C. Pittori, F. Verrecchia, F. Longo, N. Parmiggiani, M. Tavani, A. Argan, M. Cardillo, C. Casentini, Y. Evangelista, L. Foffano, E. Menegoni, G. Piano, F. Lucarelli, A. Addis, L. Baroncelli, A. Bulgarelli, A. di Piano, V. Fioretti, F. Fuschino, M. Romani, M. Marisaldi, M. Pilia, A. Trois, I. Donnarumma, A. Giuliani, P. Tempesta; Agile Team, GRB 221009A (Swift J1913.1+1946): AGILE/MCAL detection. *GRB Coord. Netw.* **32650**, 1 (2022).
25. P. Beniamini, L. Nava, R. B. Duran, T. Piran, Energies of GRB blast waves and prompt efficiencies as implied by modelling of X-ray and GeV afterglows. *Mon. Notices Royal Astron. Soc.* **454**, 1073–1085 (2015).
26. V. V. Usov, Millisecond pulsars with extremely strong magnetic fields as a cosmological source of γ-ray bursts. *Nature* **357**, 472–474 (1992).
27. R. Narayan, T. Piran, P. Kumar, Accretion models of gamma-ray bursts. *Astrophys. J.* **557**, 949–957 (2001).
28. J. Granot, R. Sari, The shape of spectral breaks in gamma-ray burst afterglows. *Astrophys. J.* **568**, 820–829 (2002).
29. P. Beniamini, R. Gill, J. Granot, Robust features of off-axis gamma-ray burst afterglow light curves. *Mon. Notices Royal Astron. Soc.* **515**, 555–570 (2022).
30. G. P. Lamb, D. A. Kann, J. J. Fernández, I. Mandel, A. J. Levan, N. R. Tanvir, GRB jet structure and the jet break. *Mon. Notices Royal Astron. Soc.* **506**, 4163–4174 (2021).
31. E. M. Rossi, D. Lazzati, J. D. Salmonson, G. Ghisellini, The polarization of afterglow emission reveals γ-ray bursts jet structure. *Mon. Notices Royal Astron. Soc.* **354**, 86–100 (2004).
32. O. Gottlieb, E. Nakar, O. Bromberg, The structure of hydrodynamic γ-ray burst jets. *Mon. Notices Royal Astron. Soc.* **500**, 3511–3526 (2020).
33. H. J. van Eerten, A. I. MacFadyen, Gamma-ray burst afterglow scaling relations for the full blast wave evolution. *Astrophys. J.* **747**, L30 (2012).
34. R. D. Blandford, R. L. Znajek, Electromagnetic extraction of energy from Kerr black holes. *Mon. Notices Royal Astron. Soc.* **179**, 433–456 (1977).
35. S. B. Cenko, D. A. Frail, F. A. Harrison, J. B. Haislip, D. E. Reichart, N. R. Butler, B. E. Cobb, A. Cucchiara, E. Berger, J. S. Bloom, P. Chandra, D. B. Fox, D. A. Perley, J. X. Prochaska, A. V. Filippenko, K. Glazebrook, K. M. Ivarsen, M. M. Kasliwal, S. R. Kulkarni, A. P. LaCluyze, S.

Lopez, A. N. Morgan, M. Pettini, V. R. Rana, Afterglow observations offer milarge area telescope gamma-ray bursts and the emerging class of hyper-energetic events. *Astrophys. J.* **732**, 29 (2011).
36. J. L. Racusin, E. W. Liang, D. N. Burrows, A. Falcone, T. Sakamoto, B. B. Zhang, B. Zhang, P. Evans, J. Osborne, Jet breaks and energetics of swift gamma-ray burst x-ray afterglows. *Astrophys. J.* **698**, 43–74 (2009).
37. S. Dichiara, E. Troja, V. Lipunov, R. Ricci, S. R. Oates, N. R. Butler, E. Liuzzo, G. Ryan, B. O'Connor, S. B. Cenko, R. G. Cosentino, A. Y. Lien, E. Gorbovskoy, N. Tyurina, P. Balanutsa, D. Vlasenko, I. Gorbunov, R. Podesta, F. Podesta, R. Rebolo, M. Serra, D. A. H. Buckley, The early afterglow of GRB 190829A. *Mon. Notices Royal Astron. Soc.* **512**, 2337–2349 (2022).
38. M. De Pasquale, M. J. Page, D. A. Kann, S. R. Oates, S. Schulze, B. Zhang, Z. Cano, B. Gendre, D. Malesani, A. Rossi, E. Troja, L. Piro, M. Boër, G. Stratta, N. Gehrels, The 80 Ms follow-up of the X-ray afterglow of GRB 130427A challenges the standard forward shock model. *Mon. Notices Royal Astron. Soc.* **462**, 1111–1122 (2016).
39. K. Misra, L. Resmi, D. A. Kann, M. Marongiu, A. Moin, S. Klose, G. Bernardi, A. de Ugarte Postigo, V. K. Jaiswal, S. Schulze, D. A. Perley, A. Ghosh, Dimple, H. Kumar, R. Gupta, M. J. Michałowski, S. Martín, A. Cockeram, S. V. Cherukuri, V. Bhalerao, G. E. Anderson, S. B. Pandey, G. C. Anupama, C. C. Thöne, S. Barway, M. H. Wieringa, J. P. U. Fynbo, N. Habeeb, Low frequency view of GRB 190114C reveals time varying shock micro-physics. *Mon. Notices Royal Astron. Soc.* **504**, 5685–5701 (2021).
40. E. Berger, S. R. Kulkarni, G. Pooley, D. A. Frail, V. McIntyre, R. M. Wark, R. Sari, A. M. Soderberg, D. W. Fox, S. Yost, P. A. Price, A common origin for cosmic explosions inferred from calorimetry of GRB030329. *Nature* **426**, 154–157 (2003).
41. Y. Lithwick, R. Sari, Lower limits on Lorentz factors in gamma-ray bursts. *Astrophys. J.* **555**, 540–545 (2001).
42. S. B. Cenko, S. R. Kulkarni, A. Horesh, A. Corsi, D. B. Fox, J. Carpenter, D. A. Frail, P. E. Nugent, D. A. Perley, D. Gruber, A. Gal-Yam, P. J. Groot, G. Hallinan, E. O. Ofek, A. Rau, C. L. MacLeod, A. A. Miller, J. S. Bloom, A. V. Filippenko, M. M. Kasliwal, N. M. Law, A. N. Morgan, D. Poleishook, D. Poznanski, R. M. Quimby, B. Sesar, K. J. Shen, J. M. Silverman, A. Sternberg, Discovery of a cosmological, relativistic outburst via its rapidly fading optical emission. *Astrophys. J.* **769**, 130 (2013).
43. Z.-H. An, S. Antier, X.-Z. Bi, Q.-C. Bu, C. Cai, X.-L. Cao, A.-E. Camisasca, Z. Chang, G. Chen, L. Chen, T.-X. Chen, W. Chen, Y.-B. Chen, Y. Chen, Y.-P. Chen, M. W. Coughlin, W.-W. Cui, Z.-G. Dai, T. Hussenot-Desenonges, Y.-Q. Du, Y.-Y. Du, Y.-F. Du, C.-C. Fan, F. Frontera, H. Gao, M. Gao, M.-Y. Ge, K. Gong, Y.-D. Gu, J. Guan, D.-Y. Guo, Z.-W. Guo, C. Guidorzi, D.-W. Han, J.-J. He, J.-W. He, D.-J. Hou, Y. Huang, J. Huo, Z. Ji, S.-M. Jia, W.-C. Jiang, D. A. Kann, A. Klotz, L.-D. Kong, L. Lan, A. Li, B. Li, C.-Y. Li, C.-K. Li, G. Li, M.-S. Li, T.-P. Li, W. Li, X.-B. Li, X.-Q. Li, X.-F. Li, Y.-G. Li, Z.-W. Li, J. Liang, X.-H. Liang, J.-Y. Liao, L. Lin, C.-Z. Liu, H.-X. Liu, H.-W. Liu, J.-C. Liu, X.-J. Liu, Y.-Q. Liu, Y.-R. Liu, F.-J. Lu, H. Lu, X.-F. Lu, Q. Luo, T. Luo, B.-Y. Ma, F.-L. Ma, R.-C. Ma, X. Ma, R. Maccary, J.-R. Mao, B. Meng, J.-Y. Nie, M. Orlandini, G. Ou, J.-Q. Peng, W.-X. Peng, R. Qiao, J.-L. Qu, X.-Q. Ren, J.-Y. Shi, Q. Shi, L.-M. Song, X.-Y. Song, J. Su, G.-X. Sun, L. Sun, X.-L. Sun, W.-J. Tan, Y. Tan et al., Insight-HXMT and GECAM-C observations of the brightest-of-all-time GRB 221009A. arXiv:2303.01203 [astro-ph.HE] (2023).
44. J. L. Atteia, V. Heussaff, J. P. Dezalay, A. Klotz, D. Turpin, A. E. Tsvetkova, D. D. Frederiks, Y. Zolnierowski, F. Daigne, R. Mochkovitch, The maximum isotropic energy of gamma-ray bursts. *Astrophys. J.* **837**, 119 (2017).
45. E. Troja, V. M. Lipunov, C. G. Mundell, N. R. Butler, A. M. Watson, S. Kobayashi, S. B. Cenko, F. E. Marshall, R. Ricci, A. Fruchter, M. H. Wieringa, E. S. Gorbovskoy, V. Kornilov, A. Kutyrev, W. H. Lee, V. Toy, N. V. Tyurina, N. M. Budnev, D. A. H. Buckley, J. González, O. Gress, A. Horesh, M. I. Panasyuk, J. X. Prochaska, E. Ramirez-Ruiz, R. Rebolo Lopez, M. G. Richer, C. Roman-Zuniga, M. Serra-Ricart, V. Yurkov, N. Gehrels, Significant and variable linear polarization during the prompt optical flash of GRB 160625B. *Nature* **547**, 425–427 (2017).
46. P. Y. Minaev, A. S. Pozanenko, The $E_{p,i}$–E_{iso} correlation: Type I gamma-ray bursts and the new classification method. *Mon. Notices Royal Astron. Soc.* **492**, 1919–1936 (2020).
47. A. M. Hopkins, J. F. Beacom, On the normalization of the cosmic star formation history. *Astrophys. J.* **651**, 142–154 (2006).
48. S. Lesage, P. Veres, O. J. Roberts, E. Burns, E. Bissaldi; Fermi GBM Team, GRB 221009A: Fermi GBM observation. *GRB Coord. Netw.* **32642**, 1 (2022).
49. G. P. Srinivasaragavan, B. O' Connor, S. B. Cenko, A. J. Dittmann, S. Yang, J. Sollerman, G. C. Anupama, S. Barway, V. Bhalerao, H. Kumar, V. Swain, E. Hammerstein, I. Holt, S. Anand, I. Andreoni, M. W. Coughlin, S. Dichiara, A. Gal-Yam, M. C. Miller, J. Soon, R. Soria, J. Durbak, J. H. Gillanders, S. Laha, A. M. Moore, F. Ragosta, E. Troja, A sensitive search for supernova emission associated with the extremely energetic and nearby GRB 221009A. arXiv:2303.12849 [astro-ph.HE] (2023).
50. E. F. Schlafly, D. P. Finkbeiner, Measuring reddening with sloan digital sky survey stellar spectra and recalibrating SFD. *Astrophys. J.* **737**, 103 (2011).
51. R. A. M. J. Wijers, T. J. Galama, Physical parameters of GRB 970508 and GRB 971214 from their afterglow synchrotron emission. *Astrophys. J.* **523**, 177–186 (1999).
52. R. Filgas, J. Greiner, P. Schady, T. Krühler, A. C. Updike, S. Klose, M. Nardini, D. A. Kann, A. Rossi, V. Sudilovsky, P. M. J. Afonso, C. Clemens, J. Elliott, A. Nicuesa Guelbenzu, F. Olivares, A. Rau, GRB 091127: The cooling break race on magnetic fuel. *Astron. Astrophys.* **535**, A57 (2011).
53. E. Troja, T. Sakamoto, C. Guidorzi, J. P. Norris, A. Panaitescu, S. Kobayashi, N. Omodei, J. C. Brown, D. N. Burrows, P. A. Evans, N. Gehrels, F. E. Marshall, N. Mawson, A. Melandri, C. G. Mundell, S. R. Oates, V. Pal'shin, R. D. Preece, J. L. Racusin, I. A. Steele, N. R. Tanvir, V. Vasileiou, C. Wilson-Hodge, K. Yamaoka, Broadband study of GRB 091127: A sub-energetic burst at higher redshift? *Astrophys. J.* **761**, 50 (2012).
54. A. Maselli, A. Melandri, L. Nava, C. G. Mundell, N. Kawai, S. Campana, S. Covino, J. R. Cummings, G. Cusumano, P. A. Evans, G. Ghirlanda, G. Ghisellini, C. Guidorzi, S. Kobayashi, P. Kuin, V. la Parola, V. Mangano, S. Oates, T. Sakamoto, M. Serino, F. Virgili, B. B. Zhang, S. Barthelmy, A. Beardmore, M. G. Bernardini, D. Bersier, D. Burrows, G. Calderone, M. Capalbi, J. Chiang, P. D'Avanzo, V. D'Elia, M. de Pasquale, D. Fugazza, N. Gehrels, A. Gomboc, R. Harrison, H. Hanayama, J. Japelj, J. Kennea, D. Kopac, C. Kouveliotou, D. Kuroda, A. Levan, D. Malesani, F. Marshall, J. Nousek, P. O'Brien, J. P. Osborne, C. Pagani, K. L. Page, M. Page, M. Perri, T. Pritchard, P. Romano, Y. Saito, B. Sbarufatti, R. Salvaterra, I. Steele, N. Tanvir, G. Vianello, B. Wiegand, K. Wiersema, Y. Yatsu, T. Yoshii, G. Tagliaferri, GRB 130427A: A nearby ordinary monster. *Science* **343**, 48–51 (2014).
55. O. Gottlieb, M. Liska, A. Tchekhovskoy, O. Bromberg, A. Lalakos, D. Giannios, P. Mösta, Black hole to PHOTOsphere: 3D GRMHD simulations of collapsars reveal wobbling and hybrid composition jets. *Astrophys. J.* **933**, L9 (2022).
56. D. A. Frail, E. Waxman, S. R. Kulkarni, A 450 day light curve of the radio afterglow of GRB 970508: Fireball calorimetry. *Astrophys. J.* **537**, 191–204 (2000).
57. S. Kobayashi, Light curves of gamma-ray burst optical flashes. *Astrophys. J.* **545**, 807–812 (2000).
58. T. Kangas, A. S. Fruchter, The late-time radio behavior of gamma-ray burst afterglows: Testing the standard model. *Astrophys. J.* **911**, 14 (2021).
59. A. J. van der Horst, Z. Paragi, A. G. de Bruyn, J. Granot, C. Kouveliotou, K. Wiersema, R. L. C. Starling, P. A. Curran, R. A. M. J. Wijers, A. Rowlinson, G. A. Anderson, R. P. Fender, J. Yang, R. G. Strom, A comprehensive radio view of the extremely bright gamma-ray burst 130427A. *Mon. Notices Royal Astron. Soc.* **444**, 3151–3163 (2014).
60. Y. Sato, K. Obayashi, R. Yamazaki, K. Murase, Y. Ohira, Off-axis jet scenario for early afterglow emission of low-luminosity gamma-ray burst GRB 190829A. *Mon. Notices Royal Astron. Soc.* **504**, 5647–5655 (2021).
61. P. Beniamini, E. Nakar, Observational constraints on the structure of gamma-ray burst jets. *Mon. Notices Royal Astron. Soc.* **482**, 5430–5440 (2019).
62. E. Nakar, T. Piran, On-axis orphan afterglows. *New Astron.* **8**, 141–153 (2003).
63. G. P. Lamb, S. Kobayashi, Low-Γ jets from compact stellar mergers: Candidate electromagnetic counterparts to gravitational wave sources. *Astrophys. J.* **829**, 112 (2016).
64. A. Lien, T. Sakamoto, S. D. Barthelmy, W. H. Baumgartner, J. K. Cannizzo, K. Chen, N. R. Collins, J. R. Cummings, N. Gehrels, H. A. Krimm, C. B. Markwardt, D. M. Palmer, M. Stamatikos, E. Troja, T. N. Ukwatta, The third swift burst alert telescope gamma-ray burst catalog. *Astrophys. J.* **829**, 7 (2016).
65. T. A. Thompson, P. Chang, E. Quataert, Magnetar spin-down, hyperenergetic supernovae, and gamma-ray bursts. *Astrophys. J.* **611**, 380–393 (2004).
66. R. W. Klebesadel, J. G. Laros, E. E. Fenimore, The Unusual Gamma-Ray Burst of March 4, 1984. *Bull. Am. Astron. Soc.* **16**, 1016 (1984).
67. A. V. Kuznetsov, R. A. Syunyaev, O. V. Terekhov, L. A. Yakubtsev, C. Barat, B. Boer, K. Hurley, M. Niel, G. Vedrenne, SIGNE:2 MP9 data for the powerful gamma-ray burst of 1983AUG1. *Soviet Astron. Lett.* **12**, 315–318 (1986).
68. K.-W. Chuang, "Identification and analysis of cosmic gamma ray bursts from Pioneer Venus Orbiter," thesis, University of California, Riverside, CA (1990).
69. A. Y. Tkachenko, O. V. Terekhov, R. A. Sunyaev, A. V. Kuznetsov, C. Barat, J. P. Dezalay, G. Vedrenne, R. Talon, A catalog of cosmic gamma-ray bursts recorded by PHEBUS/Granat: January 1993-September 1994. *Astron. Lett.* **24**, 722–741 (1998).
70. V. Lipunov, V. Kornilov, E. Gorbovskoy, N. Shatskij, D. Kuvshinov, N. Tyurina, A. Belinski, A. Krylov, P. Balanutsa, V. Chazov, A. Kuznetsov, P. Kortunov, A. Sankovich, A. Tlatov, A. Parkhomenko, V. Krushinsky, I. Zalozhnyh, A. Popov, T. Kopytova, K. Ivanov, S. Yazev, V. Yurkov, Master robotic net. *Adv. Astron.* **2010**, 349171 (2010).
71. E. Bertin, S. Arnouts, SExtractor: Software for source extraction. *Astron. Astrophys.* **117**, 393–404 (1996).
72. M. F. Skrutskie, R. M. Cutri, R. Stiening, M. D. Weinberg, S. Schneider, J. M. Carpenter, C. Beichman, R. Capps, T. Chester, J. Elias, J. Huchra, J. Liebert, C. Lonsdale, D. G. Monet, S. Price, P. Seitzer, T. Jarrett, J. D. Kirkpatrick, J. E. Gizis, E. Howard, T. Evans, J. Fowler, L. Fullmer, R. Hurt, R. Light, E. L. Kopan, K. A. Marsh, H. L. McCallon, R. Tam, S. Van Dyk, S. Wheelock, The two micron all sky survey (2MASS). *Astron. J.* **131**, 1163–1183 (2006).
73. B. O'Connor, E. Troja, S. Dichiara, P. Beniamini, S. B. Cenko, C. Kouveliotou, J. B. González, J. Durbak, P. Gatkine, A. Kutyrev, T. Sakamoto, R. Sánchez-Ramírez, S. Veilleux, A deep survey of short GRB host galaxies over z∼ 0–2: Implications for offsets, redshifts, and environments. *Mon. Notices Royal Astron. Soc.* **515**, 4890–4928 (2022).

74. S. Belkin, V. Kim, A. Pozanenko, M. Krugov, Y. Aimuratov, N. Pankov; GRB IKI FuN, GRB 221009A: Continued Assy optical afterglow observations, possible SN evidence. *GRB Coord. Netw.* **32769**, 1 (2022).
75. S. Belkin, S. Nazarov, A. Pozanenko, N. Pankov; GRB IKI FuN, GRB 221009A: Sintez-Newton/CrAO optical observations. *GRB Coord. Netw.* **32684**, 1 (2022).
76. I. Bikmaev, I. Khamitov, E. Irtuganov, M. Gorbachev, N. Sakhibullin, R. Burenin, GRB221009A: RTT-150 optical observations. *GRB Coord. Netw.* **32752**, 1 (2022).
77. R. Brivio, M. Ferro, P. D'Avanzo, D. Fugazza, A. Melandri, S. Covino; REM Team, GRB 221009A: REM optical and NIR detection of the afterglow. *GRB Coord. Netw.* **32652**, 1 (2022).
78. P. D'Avanzo, M. Ferro, R. Brivio, M. G. Bernardini, D. Fugazza, S. Campana, S. Covino, V. D'Elia, M. De Pasquale, D. B. Malesani, A. Melandri, E. Palazzi, S. Piranomonte, A. Rossi, B. Sbarufatti, G. Tagliaferri; REM Team; CIBO Collaboration, GRB 221009A: Continued REM optical/NIR observations and evidence for an achromatic steepening in the afterglow light curve. *GRB Coord. Netw.* **32755**, 1 (2022).
79. S. de Wet, P. J. Groot; Meerlicht Consortium, GRB 221009A (Swift J1913.1+1946): Meer-LICHT observations. *GRB Coord. Netw.* **32646**, 1 (2022).
80. M. Ferro, R. Brivio, P. D'Avanzo, S. Piranomonte, V. Lorenzi, G. Mainella; CIBO Collaboration, GRB 221009A: TNG NIR detection. *GRB Coord. Netw.* **32804**, 1 (2022).
81. P. J. Groot, P. M. Vreeswijk, R. Ter Horst, S. D. Bloemen, P. G. Jonker, S. de Wet, D. B. Malesani, D. Pieterse; BlackGEM Consortium, GRB 221009A: BlackGEM optical observations. *GRB Coord. Netw.* **32678**, 1 (2022).
82. R. Gupta, A. K. Ror, S. B. Pandey, A. Aryan, A. Ghosh, K. Misra, GRB 221009A: 1.3m DFOT optical observations. *GRB Coord. Netw.* **32811**, 1 (2022).
83. M. Huber, A. Schultz, K. C. Chambers, K. W. Smith, M. Fulton, S. J. Smartt, T. W. Chen, M. Nicholl, D. R. Young, L. J. Shingles, S. Srivastav, S. Sim, T. de Boer, J. Bulger, J. Fairlamb, C. C. Lin, T. Lowe, E. Magnier, R. J. Wainscoat, H. Gao, C. Stubbs, A. Rest, GRB 221009A: Pan-STARRS optical photometry. *GRB Coord. Netw.* **32758**, 1 (2022).
84. V. Kim, M. Krugov, A. Pozanenko, Y. Aimuratov, S. Belkin, N. Pankov; G. IKI FuN, GRB 221009A/Swift J1913.1+1946: Assy optical afterglow observation. *GRB Coord. Netw.* **32670**, 1 (2022).
85. H. Kumar, V. Swain, G. Waratkar, K. Angail, V. Bhalerao, G. C. Anupama, S. Barway; GIT Team, GRB 221009A / Swift J1913.1+1946: GIT detection of the optical afterglow. *GRB Coord. Netw.* **32662**, 1 (2022).
86. K. Pellegrin, K. Rumstay, D. Hartmann, GRB 221009A: SARA-RM 1m optical afterglow detection. *GRB Coord. Netw.* **32852**, 1 (2022).
87. Y. Rajabov, T. Sadibekova, Y. Tillayev, C. Rinner, Z. Benkhaldoun, X. F. Wang, J. Zhu, X. Y. Zeng, L. T. Wang, A. Iskandar, A. M. Fouad, A. Shokry, A. Takey, M. Soliman, P. Hello, T. Hussenot, M. Boer, A. de Ugarte Postigo, S. Antier, D. A. Kann, E. Burns, A. Simon, A. Baransky, L. Abe, P. Bendjoya, J. P. Rivet, D. Vernet, S. Brunier, R. Inasaridze, R. Natsvlishvili, N. Kochiashvili, S. Beradze, V. Aivazyan, G. Kapanadze, O. Burkhonov, J. G. Ducoin, S. Ehgamberdiev, A. Klotz, I. Tosta, E. Melo; GRANDMA Collaboration, GRB 221009A: GRANDMA observations. *GRB Coord. Netw.* **32795**, 1 (2022).
88. A. Rossi, E. Maiorano, D. B. Malesani; CIBO Collaboration, F. Cusano, D. Paris, GRB221009A: LBT optical imaging. *GRB Coord. Netw.* **32809**, 1 (2022).
89. B. Schneider, C. Adami, E. Le Floc'h, D. Turpin, D. Götz, S. D. Vergani, A. Saccardi, S. Basa, A. Le Van Suu; a larger Collaboration, GRB 221009A: OHP optical observations. *GRB Coord. Netw.* **32753**, 1 (2022).
90. M. Shrestha, K. Bostroem, D. Sand, K. D. Alexander, J. Andrews, J. Pearson, G. Hosseinzadeh, N. Smith, D. A. Howell, C. McCully, M. Newsome, E. Padilla Gonzalez, C. Pellegrino, G. Terreran, J. Farah; Global Supernova Project Collaboration, GRB 221009A: Faulkes Telescope North continued optical afterglow follow-up. *GRB Coord. Netw.* **32771**, 1 (2022).
91. K. Kobayashi, H. Negoro, M. Nakajima, M. Tanaka, Y. Soejima, T. Mihara, T. Kawamuro, S. Yamada, T. Tamagawa, M. Matsuoka, T. Sakamoto, M. Serino, S. Sugita, H. Hiramatsu, A. Yoshida, Y. Tsuboi, W. Iwakiri, J. Kohara, M. Shidatsu, M. Iwasaki, N. Kawai, M. Niwano, R. Hosokawa, Y. Imai, N. Ito, Y. Takamatsu, S. Nakahira, S. Ueno, H. Tomida, M. Ishikawa, T. Kurihara, Y. Ueda, S. Ogawa, K. Setoguchi, T. Yoshitake, K. Inaba, M. Yamauchi, T. Sato, R. Hatsuda, R. Fukuoka, Y. Hagiwara, Y. Umeki, K. Yamaoka, Y. Kawakubo, M. Sugizaki, MAXI/GSC refined analysis of the bright X-ray afterglow of GRB 221009A/Swift J1913.1+1946. *Astronomer's Telegram* **15677**, 1 (2022).
92. J. Vinko, A. Bodi, A. Pal, L. Kriskovics, R. Szakats, K. Vida, GRB221009A: Optical afterglow measurements from Konkoly observatory. *GRB Coord. Netw.* **32709**, 1 (2022).
93. R. J. Sault, P. J. Teuben, M. C. H. Wright, *Astronomical Data Analysis Software and Systems IV*, vol. 77 of *Astronomical Society of the Pacific Conference Series*, R. A. Shaw, H. E. Payne, J. J. E. Hayes, eds. (Astronomical Society of the Pacific, 1995), p. 433.
94. J. Bright, L. Rhodes, R. Fender, W. Farah, A. Pollak, A. Siemion, GRB 221009A/Swift J1913.1+1946: AMI-LA observations. *GRB Coord. Netw.* **32653**, 1 (2022).
95. W. Farah, J. Bright, A. Pollak, A. Siemion, D. DeBoer, R. Fender, L. Rhodes, I. Heywood, GRB221009A/Swift J1913.1+1946: ATA follow-up observations. *GRB Coord. Netw.* **32655**, 1 (2022).

Acknowledgments: B.O. acknowledges useful discussions with O. Fox, T. Jacovich, and S. Chastain and thanks J. Bauer and Q. Ye for assistance obtaining the Lowell Discovery Telescope (LDT) observations. We acknowledge the ATCA staff, particularly M. Wieringa, for helpful discussions. I.A. is a Neil Gehrels Fellow. **Funding:** This work was supported by the European Research Council through the Consolidator grant BHianca (grant agreement ID 101002761) and by the National Science Foundation (under award number 12850). The development of afterglow models used in this work was partially supported by the European Union Horizon 2020 Programme under the AHEAD2020 project (grant agreement number 871158). P.B.'s research was supported by a grant (number 2020747) from the United States–Israel Binational Science Foundation (BSF), Jerusalem, Israel. J.G.'s research was supported by the Israel Science Foundation–National Natural Science Foundation of China joint research program under grant number 3296/19. R.G. acknowledges financial support from the UNAM-DGAPA-PAPIIT IA105823 grant, Mexico. Research at Perimeter Institute is supported, in part, by the Government of Canada through the Department of Innovation, Science and Economic Development and by the Province of Ontario through the Ministry of Colleges and Universities. The material is based on work supported by NASA under award number 80GSFC21M0002, and based on observations obtained with MASTER, which is supported by the Development Program of Lomonosov MSU and the UNU Astrophysical Complex of MSU-ISU (agreement EB-075-15-2021-675). **Author contributions:** B.O. was lead on this project and organized the team, performed the multiwavelength data analysis, and contributed to the interpretation of results and writing of the manuscript. E.T. formulated the project, contributed to the interpretation of the dataset and writing of the manuscript, and provided feedback on the analysis techniques. E.T. and S.D. contributed to the analysis and interpretation of the x-ray data. G.R., P.B., H.v.E., J.G., R.G., and A.J.v.d.H. contributed to the theoretical interpretation and the writing of the manuscript. P.B. proposed the structured jet model. G.R. performed the modeling of the dataset with assistance from H.v.E. and R.G. S.D., J.G., and M.M. assisted in editing the manuscript. R.R. analyzed the radio data. V.L., D.A.H.B., A.C., C.F., V.T., and K.Z. acquired, reduced, and analyzed the MASTER data. S.A. and M.M.K. acquired and reduced the P200 data. R.L.B., N.R.B., W.H.L., and A.M.W. acquired, reduced, and analyzed the COATLI data. B.O., S.B.C., J.D., E.H., I.A., A.S.K., and G.P.S. acquired and reduced the LDT data. B.O. acquired, reduced, and analyzed the Gemini data. Y.Y. compiled the list of bright historical long GRBs. All authors provided feedback on the manuscript. **Competing interests:** The authors declare that they have no competing interests. **Data and materials availability:** All data needed to evaluate the conclusions in the paper are present in the paper and/or the Supplementary Materials.

Submitted 5 April 2023
Accepted 2 May 2023
Published 7 June 2023
10.1126/sciadv.adi1405

MATERIALS SCIENCE

Systematic modification of functionality in disordered elastic networks through free energy surface tailoring

Dan Mendels[1]*†, Fabian Byléhn[1], Timothy W. Sirk[2], Juan J. de Pablo[1]*

A combined machine learning–physics–based approach is explored for molecular and materials engineering. Specifically, collective variables, akin to those used in enhanced sampled simulations, are constructed using a machine learning model trained on data gathered from a single system. Through the constructed collective variables, it becomes possible to identify critical molecular interactions in the considered system, the modulation of which enables a systematic tailoring of the system's free energy landscape. To explore the efficacy of the proposed approach, we use it to engineer allosteric regulation and uniaxial strain fluctuations in a complex disordered elastic network. Its successful application in these two cases provides insights regarding how functionality is governed in systems characterized by extensive connectivity and points to its potential for design of complex molecular systems.

INTRODUCTION

Progress in the manufacturing and characterization of complex molecular and material systems is often hampered by the complexity of such systems and the enormity of the available design space. Engineering systems at molecular length scales remains a challenging, costly, and time-consuming endeavor. There is a need for new design and optimization methods that can, on the one hand, harness the underlying complexity and, on the other, identify the regions in design space that are most likely to provide fruitful solutions for a given problem.

Several promising strategies for devising such methods revolve around the use of machine learning and particularly its application to large libraries of data associated with sets of diverse systems corresponding to design problems being considered. Given the increasing amounts of data being generated through experiments and simulations, the use of machine learning for molecular and materials design in this way continues to grow (*1*–*11*). There are, however, limitations to such approaches' effectiveness. These include (i) the volume of training data that is required, (ii) the inability to interpret certain outcomes given the black-box nature of many AI-based algorithms, and (iii) the limited applicability of the constructed models beyond the underlying training domain. While overcoming these issues is a matter of ongoing research within the field of machine learning at large, we have recently proposed a machine learning–based method designed to circumvent them. The method, referred to as collective variables for free energy surface tailoring (CV-FEST), does so by (i) using the considerable amount of data generated in simulations or experiments of a single system and by (ii) relying on the powerful ability of certain machine learning algorithms to generate insightful dimensionally reduced representations of complex high-dimensional data.

Specifically, CV-FEST relies on the notion that the functionality of many systems can often be characterized using a dimensionally reduced representation of their free energy surfaces (FES) within a space spanned by a set of collective variables (CVs). Such a depiction serves two interconnected objectives: (i) It provides insight into the mechanisms underlying the functionality of a considered system, and (ii) it allows to condense the most essential information about such a system into a small number of parameters that can be tuned with the aid of optimization algorithms [e.g., (*12*–*17*)] for design purposes.

In (*18*), we focused on analyzing and modifying the functionality of systems that consist of relatively small numbers of degrees of freedom, e.g., a small peptide. Here, we focus on a system of much higher complexity and focus on the question of whether its underlying FES can be manipulated at will. Specifically, we consider an elastic network consisting of roughly 1000 harmonic bonds. Elastic networks have become a subject of increasing interest in recent years given their functional similarities to proteins (*19*, *20*) and their ability to exhibit metamaterial qualities (*21*, *22*). In addition, elastic networks form a natural framework for studying network structure and behavior in the physical realm, potentially providing new and general perspectives on network behavior (*23*, *24*).

For concreteness, we consider a two-dimensional disordered network consisting of identical beads connected by harmonic bonds of identical elastic modulus (see Fig. 1 for illustration). We focus on two properties of the network. The first, allosteric regulation, is analogous to that found in proteins, in which the conformation of a target site (referred to as the active site) in the network is regulated by the conformation of a different, distant site in the network (referred to as the allosteric site). The second functionality examined here is the network's uniaxial mechanical behavior, as manifested by its uniaxial strain fluctuations. We find that using CV-FEST, we are able to modify these two network characteristics in a simple and tractable manner by systemically tailoring the FES associated with them.

[1]Pritzker School of Molecular Engineering, University of Chicago, 5640 S. Ellis Avenue, Chicago, IL 60637 USA. [2]Polymers Branch, U.S. CCDC Army Research Laboratory, Aberdeen Proving Ground, MD 21005, USA.
*Corresponding author. Email: depablo@uchicago.edu (J.J.d.P.); danmendels@technion.ac.il (D.M.)
†Present address: Department of Chemical Engineering, Technion–Israel Institute of Technology, Haifa, 32000 Israel.

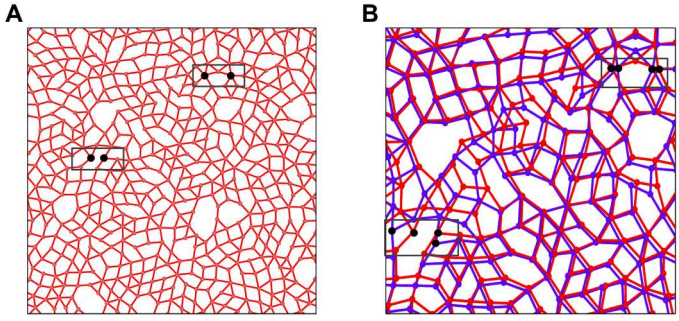

Fig. 1. Illustration of a simulated network from which 12 bonds were removed to embed allosteric response between the indicated sites. (**A**) The source (top) and target (bottom) beads are represented by the black circles. (**B**) Magnified view of the network in its activated state (in blue) overlayed with the network in its inactivated state (in red). The source beads are pinched toward one another in the activated state leading to the distancing of the target beads from one another.

CVs for free energy tailoring

As described above, CV-FEST relies on the idea that the functionality of many systems in nature can be captured using a dimensionally reduced representation of their FES within a space spanned by a set of CVs. The CVs describe the relevant modes of behavior of a system, similar to the role they play in enhanced sampling methods such as umbrella sampling (*25*), metadynamics (*26*), and adaptive biasing force (*27*), which are used to accelerate the sampling of systems for which the characteristic time scales lie beyond the reach of ordinary simulations. Generally speaking, CVs are functions of the system′s atomic coordinates s(**R**) and can be defined through the following relations

$$P(\mathrm{s}) = \int d\mathbf{R}\delta[\mathrm{s}-\mathrm{s}(\mathbf{R})]P(\mathbf{R}) \tag{1}$$

where P(s) is the system probability to hold a set of CV values s, and P(**R**) is the Boltzmann probability and is Dirac′s delta function. A system′s FES with respect to the used set of CVs then follows

$$F(\mathrm{s}) = -\frac{1}{\beta}\log P(\mathrm{s}) \tag{2}$$

where $\beta = 1/k_{\mathrm{B}}T$ and k_{B} is Boltzmann′s constant and T is the temperature.

While the construction of adequate CVs in the context of enhanced sampling can be challenging, once achieved, CVs encode the physical essence of the processes that determine a system′s behavior at long time scales. This renders them potentially useful tools for engineering. While traditionally the construction of CVs was deemed to require a certain degree of expertise regarding the system being studied, new machine learning–based methods for this task have been introduced in recent years (*28*–*34*). CV-FEST uses harmonic linear discriminant analysis (HLDA) (*29*, *35*–*38*), given its ease of use and straightforward interpretation. HLDA constructs CVs as linear weighted sums of descriptors and requires as input a limited amount of information, which can be collected via short simulations in states relevant to the processes being considered. Given their linear form, the interpretation of the HLDA CVs is straightforward; descriptors attaining larger weights in absolute value are deemed to be associated with the forces that encompass higher physicochemical importance with respect to the relevant behavior or process. The HLDA CV descriptor hierarchy can thus be used to identify the set of forces and interactions in a system that can be tuned for the purposes of tailoring its FES and modifying its functionality in desirable ways.

While HLDA was originally designed to construct CVs that correspond to rare transitions occurring between metastable states (*29*, *35*), its applicability has since been shown to extend also to cases in which the input data are collected in unstable states (*39*). In what follows, we take advantage of this aspect of the method. The application of HLDA requires that a list of system descriptors d_i be identified as an input, e.g., distances between beads, bond angles, or more complex variables such as the enthalpy or entropy of a system (*40*, *41*). In the current context, however, we limit the type of descriptors to those which directly correspond to tunable force potentials of the system, namely, the system′s bond potentials.

Once a descriptor set is assembled, HLDA requires as input the expectation value vectors Σ_I and covariance matrices μ_I with respect to the predefined descriptor space, corresponding to each of the states $I \in M$ associated with the relevant processes. The computation of the elements can be carried out using data collected in short unbiased simulations of each of the relevant states. To construct the CVs, HLDA estimates the directions **W** in the N_d dimensional descriptor space on which the projections of the collected training distributions are best separated. This is done through the maximization of the ratio between the training data, the so-called between-class $\mathbf{S}_b$ and within-class $\mathbf{S}_w$ scatter matrices, and can be written as

$$\mathcal{J}(\mathbf{W}) = \frac{\mathbf{W}^T\mathbf{S}_b\mathbf{W}}{\mathbf{W}^T\mathbf{S}_w\mathbf{W}} \tag{3}$$

with

$$\mathbf{S}_b = (\boldsymbol{\mu}_I - \overline{\boldsymbol{\mu}})\,(\overline{\boldsymbol{\mu}} - \boldsymbol{\mu}_I)^T \tag{4}$$

where $\boldsymbol{\mu}_I$ are the expectation value vectors of the Ith metastable state, and $\overline{\boldsymbol{\mu}}$ is the overall mean of the distributions, i.e., $\overline{\boldsymbol{\mu}} = 1/M \sum_{I=1}^{M}$, and with

$$\mathbf{S}_w = \frac{1}{\sum_1^1 + \sum_2^1 + \cdots + \sum_M^1} \tag{5}$$

Given the normalization $\mathbf{W}^T\mathbf{S}_w\mathbf{W}$= 1, Eq. 3 can be shown to be equivalent to solving the eigenvalue equation (*35*)

$$\mathbf{S}_w^{-1}\mathbf{S}_b\mathbf{W} = \lambda\mathbf{W} \tag{6}$$

The eigenvectors of Eq. 6 associated with the largest M-1 eigenvalues define the directions in the N_d space along which the distributions obtained from the M sampled states overlap the least and thus constitute the CVs that correspond to the transitions of interest. Using these CVs, we can now systematically tailor the system FES and modify its functionality in a purposeful manner. To do that, the leading descriptors of each of the constructed CVs are identified and their corresponding interaction potentials are changed. The modification of the force potentials is guided by inspection of their functional form relative to the system′s overall FES (e.g., augmenting force potentials which have minima within a metastable state which is sought to be further stabilized) (*18*).

RESULTS

Allosteric response

The first network functionality we focus on is that of allosteric regulation. The term allosteric regulation originates from the study of proteins, referring to the alteration of the activity of a site in the protein (e.g., its ability to have a ligand bind to it) through the binding of an effector molecule to another distal site in it, i.e., the allosteric site. Allosteric regulation plays an important role in many biological processes, such as transcriptional regulation and metabolism, and is rooted in the fundamental physical properties of macromolecular systems. Its underlying mechanisms are still poorly understood and hence it constitutes a central theme of present research in the field of biology (*42*, *43*).

In the considered network, we simulate the binding of an effector molecule to an allosteric site as the pinching of two neighboring nonbonded beads toward each other. We refer to these two beads as the source beads (represented by blue circles in Fig. 1A) of the considered allosteric process. Correspondingly, a pair of target beads is defined at a different location in the network, representing the active site (also represented by blue circles in Fig. 1A). The allosteric activation of the target beads, defined as their distancing from one another in response to the pinching of the source beads, is embedded into the network using the "tuning by pruning" algorithm introduced in (*20*) (see Methods for more details). Thus, when the source beads are at their relaxed positions, the distance between the target beads assumes its initial value, and the active site is in its inactivated state. However, when the source beads are pinched beyond a threshold, the target beads respond by distancing from one another, and the active site is deemed to be activated. We consider an additional third state of the system, corresponding to the phenomenon of negative cooperativity (*44*). A scenario is considered in which the binding of a ligand to a site neighboring the allosteric site inhibits the binding of the effector molecule, for example, by steric repulsion. We simulate this scenario as a state of the network in which the source beads are stretched away from one another, thus inhibiting their ability to arrive to the pinched active state. The system in practice can thus be in one of three states: the inactivated, activated, or inhibited state.

To explore our ability to systematically tailor the system's FES associated with its allosteric behavior, we start by defining a descriptor set for the problem at hand. In this case, we opt for a descriptor set composed of all the network bond distances. Next, we run short simulations in the three different states of the system at finite temperature, constraining the source beads to their respective positions at each state. Before calculating the HLDA CVs, to prevent the skewing of the obtained results (and following a common practice in the context of many machine learning algorithms), we compute the correlation matrices corresponding to each of the collected distributions and omit descriptors that exhibit correlations greater than 0.9 (in absolute value) to others in the set. Last, using the data collected in the simulations, we calculate the expectation values μ_I and covariance matrices Σ_I associated with each of the states and, using Eq. 6, compute the HLDA CVs corresponding to the three-state system. The weight distribution corresponding to the first eigenvector is presented in the inset of Fig. 2C.

While the HLDA eigenvectors corresponding to the top two eigenvalues provide good separation between the predefined states, to augment our ability to tailor the system's FES, before selecting the top weighted descriptors, we apply a two-dimensional rotation to the plane spanned by the two HLDA CVs. This is implemented in such a way that states A and B are best separated with respect to the direction corresponding to the rotated $HLDA_1$, while states B and C are best separated with respect to the direction corresponding to the rotated $HLDA_2$ (see fig. S1 in the Supplementary Materials for illustration). In analogy to the concept of normal modes, applying the described rotation allows us to substantially decouple the effects induced by the modification of bonds associated with $HLDA_1$ on the FES associated with those induced by the modification of the bonds involved in $HLDA_2$. In essence, modifying bonds associated with $HLDA_1$ predominantly affect the free energy difference between states A and B, whereas modifying bonds associated with $HLDA_2$ predominantly affects the free energy difference between states A and C, as can be seen in Fig. 2A. Given the linearity of HLDA, the resulting CVs tend to be dominated by the descriptors associated with the largest weights in the CV, rendering the weight distribution of the lower weighted descriptors potentially less accurate. To circumvent this issue, we apply HLDA iteratively, whereby after each iteration (and rotation), the top five weighted descriptors (in absolute value) of each of the two constructed CVs are selected and removed from the descriptor list for subsequent iterations. The top bonds selected in this way are highlighted in Fig. 3A. As can be seen, both bond sets corresponding to the two HLDA CVs form distinct patterns, reflecting their functional significance.

To test our ability to tailor the FES corresponding to the allosteric and cooperative behaviors of the system, we alter the bond coefficient of the selected bonds and then compute the FES. Given the large differences in free energy between the considered states, the computation of the system's FES requires the use of an enhanced sampling approach. Here, we use well-tempered metadynamics (*45*), using the distance between the source beads d_s as the biasing CV for simulations. (See Methods for details and fig. S3 for an example of the time-dependent behavior of the source and target nodes in such simulations). Upon convergence of the well-tempered metadynamics runs, we compute the FES of the system using Eq. 9. Figure 2A presents the FES computed in this way for several realizations of the system. One can appreciate that altering the bond coefficient of the selected bonds gives rise to substantial changes in the system's FES. In contrast, similar alterations of randomly selected bonds do not lead to noticeable changes of the FES. It can also be seen that altering the bonds associated with $HLDA_1$ mainly affects the FES branch corresponding to the $A \leftrightarrow B$ transition, while altering those associated with $HLDA_2$ predominantly affects the FES branch corresponding to the $B \leftrightarrow C$ transition.

An examination of the effects of altering the bond coefficient of the top 10 bonds corresponding to $HLDA_1$ reveals that one can systematically modify the extent to which the source nodes need to be pinched to initiate the "activation" of the target beads. Figure 2C illustrates this feature by showing the dependence of the distance d_s for which the allosteric response is initiated as a function of the bond coefficient of the top 10 $HLDA_1$ bonds. Our results show that as the selected bonds are weakened, the source beads need to be brought closer to one another for allosteric activation to occur and vice versa. One can envision inducing similar effects in real proteins; by systemically softening the environment of an allosteric site, one could alter the types of molecules (e.g., different dimensions or interactions with the allosteric site) that would lead to its activation. We find that we obtain such an effect, albeit to a slightly lesser

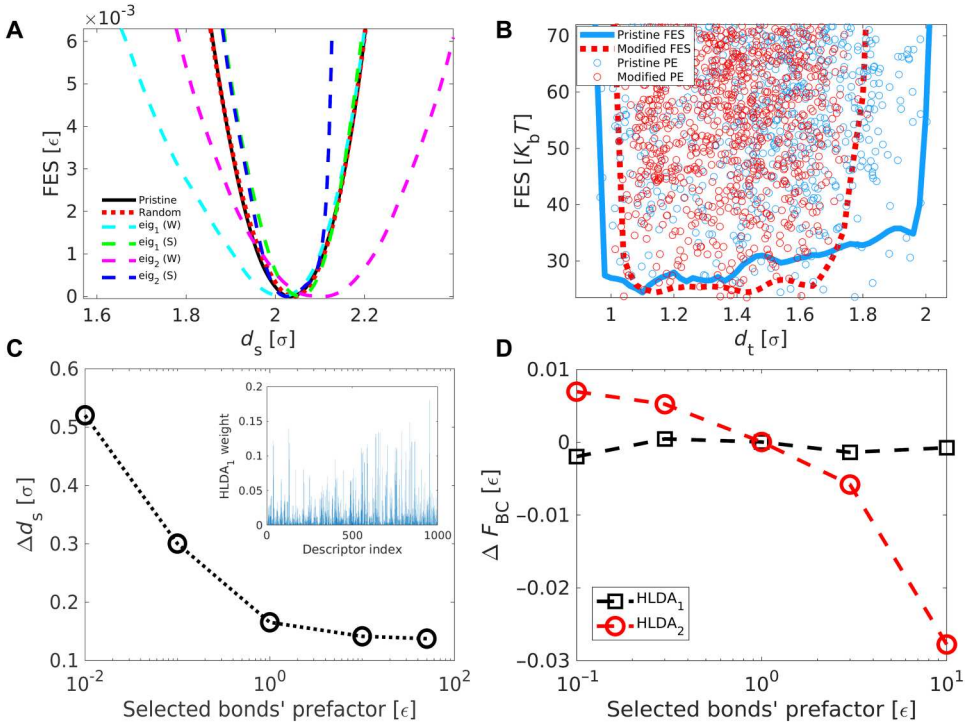

Fig. 2. Systematic modifications of the system's allosteric response. (**A**) FES with different realizations of the allosteric network as a function of the distance between the source nodes. FES of the pristine network (solid line) and FES obtained after 30 random bonds are strengthened to 50ϵ (dotted line). Also shown: FES obtained of networks in which the 10 highest weighted bonds of either $HLDA_1$ or $HLDA_2$ are either strengthened (S) to 50ϵ or weakened (W) to 0.1ϵ (dashed lines). (**B**) Potential energy distributions and reweighted FES as a function of d_t calculated using the methodology of (*60*). The pristine network can reach the fully activated state at $d_t > 17\sigma$, while this state is not accessible to the network in which the bonds ranked 12 to 27 in the $HLDA_1$ weight hierarchy are weakened. (**C**) Minimal pinching length for which activation of the target beads is initiated as a function of the bond coefficient of the 10 highest weighted $HLDA_1$ bonds. Inset: Absolute value of the weight distribution of $HLDA_1$, generated in the first iteration of the calculation. (**D**) ΔF_{BC} (calculated using equation S10), the free energy difference between state C (the stretched state), $d_s = 2.19\sigma$, and the pinched state (defined as the point at which activation of the target site is initiated) as a function of the bond coefficient of the targeted bonds.

extent, also by modifying only the top ranked $HLDA_1$ bond as shown in fig. S5.

While altering the top bonds associated with $HLDA_1$ has a significant effect on the distance d_S for which the allosteric response is initiated, we find that it induces a more modest effect on the free energy difference between states A and B and consequently also on that between states B and C. In contrast, however, modifying the bonds associated with $HLDA_2$ leads to large changes in the free energy difference between states B and C, thereby allowing us to easily alter this free energy difference between the activated and inhibited states, as shown in Fig. 2D.

By repeating the bond selection procedure for several iterations, we find that we can reveal segments that compose the primary channel of mechanical communication between the allosteric and active sites. The corresponding bonds, placed in positions 12 to 27 in the hierarchy of $HLDA_1$, are highlighted in Fig. 3B. Specifically, we find that weakening this set of bonds limits the communication between the sites, precluding the activation of the active site, as illustrated in fig. S4. Figure 2B illustrates this point further by presenting the FES corresponding to the distance between the target beads, plotted for the pristine system and the modified system. It can be seen that the fully activated region corresponding to $d_t > 1.7\sigma$ is inaccessible in the case of the modified system. Considering again the analogy to proteins, it would be intriguing to explore if the proposed methodology would be able to help shed light on the prominent question of how communication occurs between allosteric and active sites.

Uniaxial strain fluctuations

To complement the analysis of the network's allosteric behavior, we apply CV-FEST also to a comparably more global attribute of the network, namely, its uniaxial strain fluctuations (*46*). The network is constructed in the same manner as before. As in the previous case, to systematically modify the behavior of the network, we start by collecting training data. We do this by running a slow uniaxial compression simulation at constant temperature and constant lateral dimension. The network is deformed in the x direction to a strain of $\delta L_x/L_x = 0.0075$. To construct the HLDA CV that corresponds to the network's strain fluctuations in the x direction, we use data collected in two short segments of the compression simulation. The first, taken from the beginning of the simulation when the network is nearly relaxed, and the second from the end of the simulation when the network is nearly fully deformed.

Defining the 1007 distances corresponding to all of the network's bonds as our descriptor set and calculating the relaxed and compressed states' expectation vectors and covariance matrices, we apply Eq. 6 to obtain the HLDA CV. As previously done, to circumvent the limitation imposed by the linearity of HLDA, we apply it iteratively, whereby the descriptors attaining the three largest weights in absolute value at each iteration are selected and

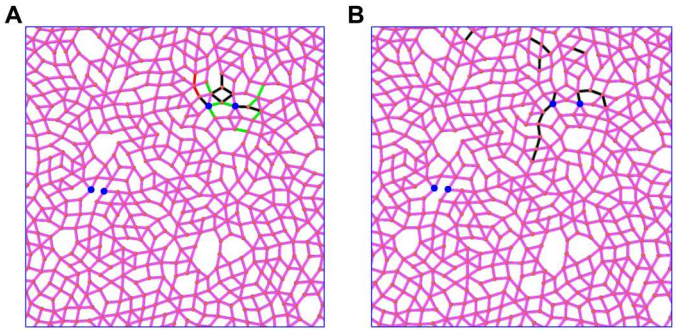

Fig. 3. Depiction of the highest weighted HLDA bonds. (**A**) Depiction of the 10 highest HLDA CVs weighted bonds in absolute value. The top bonds corresponding to $HLDA_1$ are shown in black, and the top bonds corresponding to $HLDA_2$ are shown in green. The top bonds corresponding to both $HLDA_1$ and $HLDA_2$ are red. (**B**) Depiction of the bonds ranked 12 to 27 in the weight hierarchy of $HLDA_1$. Decreasing the bond coefficient of these bonds inhibits the activation of the active site.

removed from the descriptor set used in the iterations to follow. Figures 4 (A and B) highlight, respectively, the top ~1% and top ~6% of bonds selected in this manner. The selected bonds are distributed fairly homogeneously across the network, in contrast to the allosteric case. Such bonds appear to be organized in small clusters, consisting of two to six bonds each.

To modify the FES corresponding to the network's uniaxial strain fluctuations, we systematically alter the bond coefficient of the selected bonds. To quantify the resulting behavior, we simulate the network under constant temperature and constant pressure, applying the Parrinello-Rahman barostat (*47*, *48*) in the x direction of the simulation cell, keeping the simulation cell edge in the perpendicular direction, L_y, constant. From these simulations, we compute the probability density $P(L_x)$ and, using Eq. 1, $F(Lx)$, the corresponding FES of the network (*49*).

Figure 4B exhibits the FES of the pristine and modified networks. Altering the bonds selected by CV-FEST gives rise to substantially greater changes in the system's FES compared to the case in which randomly selected bonds are altered. This is particularly apparent when less than 1% (i.e., nine bonds) of the network's bonds are altered. In that case, CV-FEST is able to select strategically important bonds of the network, whereas a random selection yields no apparent change of the system's FES. This stark difference illustrates the importance of the critical bonds' positions in the network, given that all the bonds in the pristine network have the same elastic modulus. Examining the FES of the different networks, we find that altering the bond coefficient of the selected bonds leads to three different effects. The first is a modification of the steepness of the FES. The second is a change of the functional form of the FES, namely, the extent to which it deviates from a parabola (as would be expected for entropic contributions to the system's elasticity). The third is a shift of the minimum. These three differences are further illustrated in figs. S6 and S7 in which the FES of the different networks are aligned and in fig. S8, which illustrates how the stress-strain curves and Young's modulus of the system are changed given the underlying modifications. The ability to modify the FES of the network in these ways points to the promise of using CV-FEST to engineer systems that exhibit targeted, desirable mechanical properties.

DISCUSSION

We have studied the ability to systematically tailor the FES of a disordered elastic network with respect to allosteric regulation and uniaxial strain fluctuations at finite temperature and pressure conditions. We find that CV-FEST is capable of (i) identifying the important bonds in the network with respect to each of these functionalities and (ii) by altering these bonds' stiffness, of tailoring in a tractable way the system's FES and the corresponding functional behavior.

Given the complex interconnected nature of the networks, CV-FEST's demonstrated capabilities offer potential as a tool for design and analysis of complex systems in general, including systems such as proteins, macromolecules, and materials. In this context, it is also worthwhile mentioning the interesting works of (*50*, *51*) which also use contrastive machine learning methodologies for network design. While these works focus on continuous, simultaneous and

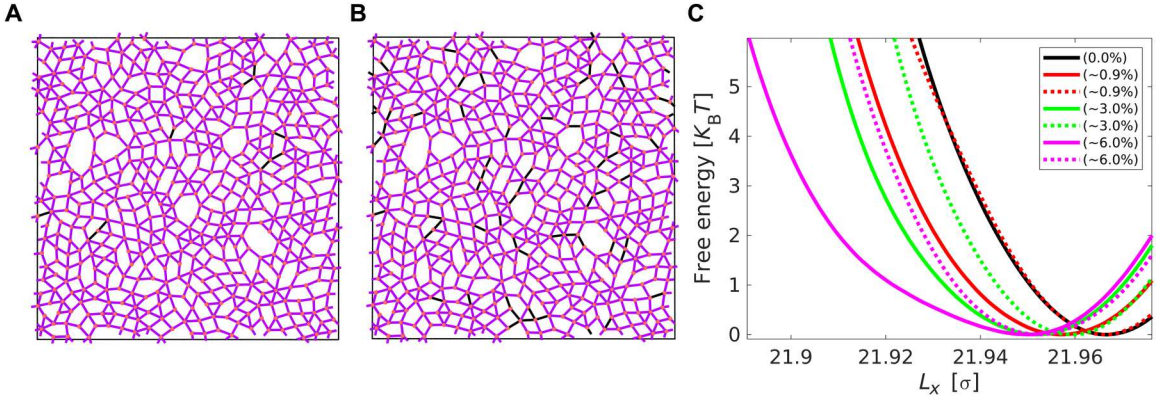

Fig. 4. Systematic modifications of the system's uniaxial strain fluctuations. (**A**) Illustration of the simulated network with the top 9 (~1%) HLDA bonds highlighted in dark blue and (**B**) with the top 60 (~6%) HLDA bonds highlighted in dark blue. (**C**) The computed FES of the simulated pristine network as function of L_x (solid black) along with the FES of modified realizations of the network in which the bond coefficient of the highest weighted HLDA bonds was reduced to $0.01\epsilon/\sigma^2$ (solid lines) or in which the bond coefficient of randomly selected bonds was reduced to $0.01\epsilon/\sigma^2$ (dotted lines). In parenthesis, the percentage of bonds that was modified in the network in each case.

incremental modifications of all the forces in a considered network and hence are less suitable for more realistic systems such as proteins and materials, investigating the potential for combining their proposed methods with the approach introduced here could prove to be an interesting direction for future research. Last, considering that CV-FEST relies solely on kinematic information for its input, it would be interesting to explore its direct applicability to macroscopic mechanical experimental systems (*21*, *52*) for which such information is relatively easily obtained. In the case of microscopic systems, we envision the use of CV-FEST to come to fruition in the context of combined experimental-simulation studies of macromolecular systems such as biomolecules and complex materials such as polymer networks.

METHODS

Network construction

Construction of the networks followed the protocol put forward in (*20*). Briefly, two-dimensional configurations of soft disks placed in a simulation cell with periodic boundary conditions and allowed to relax to a local energy minimum using a standard jamming algorithm (*53*). The network is then constructed by placing nodes at the center of each disk and by linking nodes corresponding to disks which overlap in the resulting configuration. To implement the elastic networks, beads of identical mass are placed at every node position in the network, and links are replaced by harmonic bonds with an elastic energy of the form

$$V(\mathbf{r}_{ij}) = \frac{K_{ij}}{(\mathbf{r}_{ij}^0)^2}\,(\mathbf{r}_{ij} - \mathbf{r}_{ij}^0)^2 \tag{7}$$

where K_{ij} is the bond coefficient corresponding to the bond between the i and j beads and is set initially to 1 for all bonds in the network; $\mathbf{r}_{ij}^0$ is the rest length of the bond, and $\mathbf{r}_{ij}$ is the distance between the beads.

Embedding allosteric response into the network

Allosteric response is embedded into the network by randomly selecting two pairs of neighboring nonbonded beads, referred to as the source beads and target beads (see Fig. 1). The target beads are chosen to be spatially distant from the source beads to achieve the long-range effect that characterizes allostery.

The allosteric effect is defined as an imposed change of the distance between the target beads given a change in the distance between the source beads. To optimize the network such that this effect will emerge, a tuning-by-pruning of bonds strategy is used with the objective to minimize the fitness function of Eq. 8, which measures the difference between the desired target beads' response and the actual response (*20*, *54*). Namely, the ratio of the target strain to the source strain, $\eta = \Delta d_t/\Delta d_s$, is measured and compared to the desired ratio η^*, set to 5, rendering the fitness function to be

$$\Delta^2 = (\eta/\eta^* - 1)^2 \tag{8}$$

To compute Eq. 8, the source beads are "pinched" to 50% of their initial distance and frozen at their new positions, after which a second minimization of network energy is carried out and the ratio η is calculated. The optimization procedure was applied iteratively, whereby at each iteration, Δ^2 resulting from a trial removal of each bond in the network was computed. A greedy algorithm was followed in which the bond the removal of which lead to the largest decrease in Δ^2 with respect to its previous value was permanently deleted. To keep local stability, however, the bond is deleted only if all the beads it was connected to were connected to at least three remaining bonds (*55*). Otherwise, the bond that created the next-largest decrease in Δ^2 is permanently deleted, given that it satisfied this constraint and so on. This iterative process is continued until the desired strain ratio (Eq. 8) is attained. The energy minimization of the network was performed using LAMMPS (*56*).

Dynamic simulations of the allosteric network

All simulations were run with LAMMPS (*56*) patched with PLUMED2.6 (*57*). The network consisted of 499 beads and 999 bonds. For simulations run at $T = 8.6 \cdot 10^{-6}$, all beads had a mass of $M = m$ with the exception of the source beads which had a mass of $M_s = 1000\ m$. For the sake of preventing the destabilization of the network, for well-tempered metadynamics, simulations run at $T = 4.3 \cdot 10^{-5}$ all beads had a mass of $M = 100\ m$ with the exception of the source beads which had a mass of $M_s = 1000\ m$. All simulations were initially energetically relaxed at zero pressure and subsequently run at a constant temperature using a Langevin thermostat (*58*) with a damping parameter of 1 and a time step of 0001. In the unbiased training simulations, the source bead positions were constrained in the allosteric activated state B, $d_s = 1.87\sigma$, and the trap state C, $d_s = 2.1\sigma$, to keep the network from relaxing back to the inactivated state A. The FES of the system was computed using Eq. 9

$$F(\mathrm{s}) = \frac{\gamma}{1-\gamma}V(s) \tag{9}$$

where $V(\mathrm{s})$ is the bias potential deposited in the well-tempered metadynamics simulations, and γ is the so-called bias factor. Well-tempered metadynamics simulations were run with a bias factor of $\gamma = 180$, a hill height of 0.0001ϵ, and a hill width of 0.01σ.

Probing uniaxial fluctuations

Simulations were run with LAMMPS (*56*) patched with PLUMED2.6 (*57*). The network consisted of 499 beads and 1007 bonds. All beads had a mass m. Training simulations, in which the networks were slightly compressed in the x direction, were run at constant temperature $T = 8.6 \cdot 10^{-6}$ (with $k_B = 1$) using a Langevin thermostat (*58*) with a damping parameter of 1 and a time step of 0.01τ. Compression was executed using a constant deformation rate of $10^{-7}\tau^{-1}$. The FESs of the networks were measured in constant pressure simulations run at zero pressure, using a Parrinello-Rahman barostat (*48*, *59*) applied in the x direction, corresponding to the direction of compression in the training simulations. The simulation box side in the y direction was kept constant in all simulations.

Supplementary Materials

This PDF file includes:

Figs. S1 to S9

REFERENCES AND NOTES

1. A. Agrawal, A. Choudhary, Perspective: Materials informatics and big data: Realization of the "fourth paradigm" of science in materials science. *APL Mater.* **4**, 053208 (2016).

2. B. Meredig, A. Agrawal, S. Kirklin, J. E. Saal, J. W. Doak, A. Thompson, K. Zhang, A. Choudhary, C. Wolverton, Combinatorial screening for new materials in unconstrained composition space with machine learning. *Phys. Rev. B* **89**, 094104 (2014).
3. Z. Yang, X. Li, L. Catherine Brinson, A. N. Choudhary, W. Chen, A. Agrawal, Microstructural materials design via deep adversarial learning methodology. *J. Mech. Des.* **140**, 111416 (2018).
4. M. A. Webb, N. E. Jackson, P. S. Gil, J. J. de Pablo, Targeted sequence design within the coarse-grained polymer genome. *Sci. Adv.* **6**, eabc6216 (2020).
5. Z. Liu, D. Zhu, S. P. Rodrigues, K.-T. Lee, W. Cai, Generative model for the inverse design of metasurfaces. *Nano Lett.* **18**, 6570–6576 (2018).
6. Y. Mao, Q. He, X. Zhao, Designing complex architectured materials with generative adversarial networks. *Sci. Adv.* **6**, eaaz4169 (2020).
7. B. Kim, S. Lee, J. Kim, Inverse design of porous materials using artificial neural networks. *Sci. Adv.* **6**, eaax9324 (2020).
8. K. Swanson, S. Trivedi, J. Lequieu, K. Swanson, R. Kondor, Deep learning for automated classification and characterization of amorphous materials. *SoftMatter* **16**, 435–446 (2020).
9. J. M. Stokes, K. Yang, K. Swanson, W. Jin, A. Cubillos-Ruiz, N. M. Donghia, C. R. MacNair, S. French, L. A. Carfrae, Z. Bloom-Ackermann, V. M. Tran, A. Chiappino-Pepe, A. H. Badran, I. W. Andrews, E. J. Chory, G. M. Church, E. D. Brown, T. S. Jaakkola, R. Barzilay, J. J. Collins, A deep learning approach to antibiotic discovery. *Cell* **180**, 688–702.e13 (2020).
10. C. Shen, M. Krenn, S. Eppel, A. Aspuru-Guzik, Deep molecular dreaming: Inverse machine learning for *de-novo* molecular design and interpretability with surjective representations. *Mach. Learn. Sci. Technol.* **2**, 03LT02 (2021).
11. R. Gómez-Bombarelli, J. N. Wei, D. Duvenaud, J. M. Hernández-Lobato, B. Sánchez-Lengeling, D. Sheberla, J. Aguilera-Iparraguirre, T. D. Hirzel, R. P. Adams, A. Aspuru-Guzik, Automatic chemical design using a data-driven continuous representation of molecules. *ACS Central Sci.* **4**, 268–276 (2018).
12. A. W. Long, A. L. Ferguson, Rational design of patchy colloids via landscape engineering. *Mol. Syst. Des. Eng.* **3**, 49–65 (2018).
13. A. D. White, G. A. Voth, Efficient and minimal method to bias molecular simulations with experimental data. *J. Chem. Theory Comput.* **10**, 3023–3030 (2014).
14. D. B. Amirkulova, A. D. White, Recent advances in maximum entropy biasing techniques for molecular dynamics. *Mol. Simul.* **45**, 1285–1294 (2019).
15. A. Gil-Ley, S. Bottaro, G. Bussi, Empirical corrections to the amber RNA force field with target metadynamics. *J. Chem. Theory Comput.* **12**, 2790–2798 (2016).
16. F. Marinelli, J. D. Faraldo-Gómez, Ensemble-biased metadynamics: A molecular simulation method to sample experimental distributions. *Biophys. J.* **108**, 2779–2782 (2015).
17. A. Cesari, S. Reißer, G. Bussi, Using the maximum entropy principle to combine simulations and solution experiments. *Comput. Secur.* **6**, 15 (2018).
18. D. Mendels, J. J. de Pablo, Collective variables for free energy surface tailoring: Understanding and modifying functionality in systems dominated by rare events. *J. Phys. Chem. Lett.* **13**, 2830–2837 (2022).
19. I. Bahar, T. R. Lezon, L.-W. Yang, E. Eyal, Global dynamics of proteins: Bridging between structure and function. *Annu. Rev. Bophys.* **39**, 23–42 (2010).
20. J. W. Rocks, N. Pashine, I. Bischofberger, C. P. Goodrich, A. J. Liu, S. R. Nagel, Designing allostery-inspired response in mechanical networks. *Proc. Natl. Acad. Sci. U.S.A.* **114**, 2520–2525 (2017).
21. D. R. Reid, N. Pashine, J. M. Wozniak, H. M. Jaeger, A. J. Liu, S. R. Nagel, J. J. de Pablo, Auxetic metamaterials from disordered networks. *Proc. Natl. Acad. Sci. U.S.A.* **115**, E1384–E1390 (2018).
22. D. Hexner, A. J. Liu, S. R. Nagel, Periodic training of creeping solids. *Proc. Natl. Acad. Sci. U.S.A.* **117**, 31690–31695 (2020).
23. R. Albert, A.-L. Barabási, Statistical mechanics of complex networks. *Rev. Mod. Phys.* **74**, 47–97 (2002).
24. Y.-Y. Liu, A.-L. Barabási, Control principles of complex systems. *Rev. Mod. Phys.* **88**, 035006 (2016).
25. G. M. Torrie, J. P. Valleau, Nonphysical sampling distributions in Monte Carlo free-energy estimation: Umbrella sampling. *J. Comput. Phys.* **23**, 187–199 (1977).
26. A. Laio, M. Parrinello, Escaping free-energy minima. *Proc. Natl. Acad. Sci. U.S.A.* **99**, 12562–12566 (2002).
27. E. Darve, A. Pohorille, Calculating free energies using average force. *J. Chem. Phys.* **115**, 9169–9183 (2001).
28. J. M. L. Ribeiro, P. Bravo, Y. Wang, P. Tiwary, Reweighted autoencoded variational bayes for enhanced sampling (rave). *J. Chem. Phys.* **149**, 072301 (2018).
29. D. Mendels, G. Piccini, M. Parrinello, Collective variables from local fluctuations. *J. Phys. Chem. Lett.* **9**, 2776–2781 (2018).
30. L. Bonati, V. Rizzi, M. Parrinello, Data-driven collective variables for enhanced sampling. *J. Phys. Chem. Lett.* **11**, 2998–3004 (2020).
31. W. Chen, A. R. Tan, A. L. Ferguson, Collective variable discovery and enhanced sampling using autoencoders: Innovations in network architecture and error function design. *J. Chem. Phys.* **149**, 072312 (2018).
32. C. Wehmeyer, F. Noé, Time-lagged autoencoders: Deep learning of slow collective variables for molecular kinetics. *J. Chem. Phys.* **148**, 241703 (2018).
33. M. M. Sultan, V. S. Pande, Automated design of collective variables using supervised machine learning. *J. Chem. Phys.* **149**, 094106 (2018).
34. J. McCarty, M. Parrinello, A variational conformational dynamics approach to the selection of collective variables in metadynamics. *J. Chem. Phys.* **147**, 204109 (2017).
35. G. Piccini, D. Mendels, M. Parrinello, Metadynamics with discriminants: A tool for understanding chemistry. *J. Chem. Theory Comput.* **14**, 5040–5044 (2018).
36. D. Mendels, G. Piccini, Z. F. Brotzakis, Y. I. Yang, M. Parrinello, Folding a small protein using harmonic linear discriminant analysis. *J. Chem. Phys.* **149**, 194113 (2018).
37. V. Rizzi, D. Mendels, E. Sicilia, M. Parrinello, Blind search for complex chemical pathways using harmonic linear discriminant analysis. *J. Chem. Theory Comput.* **15**, 4507–4515 (2019).
38. Y.-Y. Zhang, H. Niu, G. Piccini, D. Mendels, M. Parrinello, Improving collective variables: The case of crystallization. *J. Chem. Phys.* **150**, 094509 (2019).
39. Z. F. Brotzakis, D. Mendels, M. Parrinello, Augmented harmonic linear discriminant analysis. arXiv 1902.08854 (2019).
40. P. M. Piaggi, O. Valsson, M. Parrinello, Enhancing entropy and enthalpy fluctuations to drive crystallization in atomistic simulations. *Phys. Rev. Lett.* **119**, 015701 (2017).
41. D. Mendels, J. McCarty, P. M. Piaggi, M. Parrinello, Searching for entropically stabilized phases: The case of silver iodide. *J. Phys. Chem. C* **122**, 1786–1790 (2018).
42. S. J. Wodak, E. Paci, N. V. Dokholyan, I. N. Berezovsky, A. Horovitz, J. Li, V. J. Hilser, I. Bahar, J. Karanicolas, G. Stock, P. Hamm, R. H. Stote, J. Eberhardt, Y. Chebaro, A. Dejaegere, M. Cecchini, J. P. Changeux, P. G. Bolhuis, J. Vreede, P. Faccioli, S. Orioli, R. Ravasio, L. Yan, C. Brito, M. Wyart, P. Gkeka, I. Rivalta, G. Palermo, J. A. McCammon, J. Panecka-Hofman, R. C. Wade, A. di Pizio, M. Y. Niv, R. Nussinov, C. J. Tsai, H. Jang, D. Padhorny, D. Kozakov, T. McLeish, Allostery in its many disguises: From theory to applications. *Structure* **27**, 566–578 (2019).
43. A. J. Faure, J. Domingo, J. M. Schmiedel, C. Hidalgo-Carcedo, G. Diss, B. Lehner, Mapping the energetic and allosteric landscapes of protein binding domains. *Nature* **604**, 175–183 (2022).
44. C. A. Hunter, H. L. Anderson, What is cooperativity? *Angew. Chem. Int. Ed.* **48**, 7488–7499 (2009).
45. A. Barducci, G. Bussi, M. Parrinello, Well-tempered metadynamics: A smoothly converging and tunable free-energy method. *Phys. Rev. Lett.* **100**, 020603 (2008).
46. M. Parrinello, A. Rahman, Strain fluctuations and elastic constants. *J. Chem. Phys.* **76**, 2662–2666 (1982).
47. M. Parrinello, A. Rahman, Polymorphic transitions in single crystals: A new molecular dynamics method. *J. Appl. Phys.* **52**, 7182–7190 (1981).
48. G. J. Martyna, D. J. Tobias, M. L. Klein, Constant pressure molecular dynamics algorithms. *J. Chem. Phys.* **101**, 4177–4189 (1994).
49. R. Martoňák, A. Laio, M. Parrinello, Predicting crystal structures: The parrinello-rahman method revisited. *Phys. Rev. Lett.* **90**, 075503 (2003).
50. B. Scellier, Y. Bengio, Equilibrium propagation: Bridging the gap between energy-based models and backpropagation. *Front. Comput. Neurosci.* **11**, 24 (2017).
51. M. Stern, D. Hexner, J. W. Rocks, A. J. Liu, Supervised learning in physical networks: From machine learning to learning machines. *Phys. Rev. X* **11**, 021045 (2021).
52. N. Pashine, D. Hexner, A. J. Liu, S. R. Nagel, Directed aging, memory, and nature's greed. *Sci. Adv.* **5**, eaax4215 (2019).
53. A. J. Liu, S. R. Nagel, The jamming transition and the marginally jammed solid. *Annu. Rev. Condens. Matter Phys.* **1**, 347–369 (2010).
54. J. W. Rocks, H. Ronellenfitsch, A. J. Liu, S. R. Nagel, E. Katifori, Limits of multifunctionality in tunable networks. *Proc. Natl. Acad. Sci. U.S.A.* **116**, 2506–2511 (2019).
55. C. P. Goodrich, A. J. Liu, S. R. Nagel, The principle of independent bond-level response: Tuning by pruning to exploit disorder for global behavior. *Phys. Rev. Lett.* **114**, 225501 (2015).
56. S. Plimpton, Fast parallel algorithms for short-range molecular dynamics. *J. Comput. Phys.* **117**, 1–19 (1995).
57. G. A. Tribello, M. Bonomi, D. Branduardi, C. Camilloni, G. Bussi, PLUMED 2: New feathers for an old bird. *Comput. Phys. Commun.* **185**, 604–613 (2014).
58. T. Schneider, E. Stoll, Molecular-dynamics study of a three-dimensional one-component model for distortive phase transitions. *Phys. Rev. B* **17**, 1302–1322 (1978).
59. M. Parrinello, A. Rahman, Crystal structure and pair potentials: A molecular-dynamics study. *Phys. Rev. Lett.* **45**, 1196–1199 (1980).

60. P. Tiwary, M. Parrinello, A time-independent free energy estimator for metadynamics. *J. Phys. Chem. B* **119**, 736–742 (2015).

Acknowledgments

Funding: This work is supported by the Department of Energy, Basic Energy Sciences, through the Midwest Center for Computational Materials (MiCCoM). Additional support for a collaboration on materials design for impact mitigation between the Army Research Laboratory and the University of Chicago was provided by the Center for Hierarchical Materials Design (CHiMaD), supported by NIST. **Author contributions:** D.M., J.J.d.P., and T.W.S. designed the research. D.M. and F.B. performed the research, and D.M. and J.J.D.P. wrote the manuscript. **Competing interests:** The authors declare that they have no competing interests. **Data and materials availability:** All data needed to evaluate the conclusions in the paper are present in the paper and/or the Supplementary Materials.

Submitted 14 November 2022
Accepted 1 May 2023
Published 7 June 2023
10.1126/sciadv.adf7541

MATERIALS SCIENCE

A CMOS-based highly scalable flexible neural electrode interface

Eric T. Zhao[1], Jacob M. Hull[2], Nofar Mintz Hemed[3], Hasan Uluşan[4], Julian Bartram[4], Anqi Zhang[1], Pingyu Wang[3], Albert Pham[3], Silvia Ronchi[4], John R. Huguenard[2], Andreas Hierlemann[4], Nicholas A. Melosh[3]*

Perception, thoughts, and actions are encoded by the coordinated activity of large neuronal populations spread over large areas. However, existing electrophysiological devices are limited by their scalability in capturing this cortex-wide activity. Here, we developed an electrode connector based on an ultra-conformable thin-film electrode array that self-assembles onto silicon microelectrode arrays enabling multithousand channel counts at a millimeter scale. The interconnects are formed using microfabricated electrode pads suspended by thin support arms, termed Flex2Chip. Capillary-assisted assembly drives the pads to deform toward the chip surface, and van der Waals forces maintain this deformation, establishing Ohmic contact. Flex2Chip arrays successfully measured extracellular action potentials ex vivo and resolved micrometer scale seizure propagation trajectories in epileptic mice. We find that seizure dynamics in absence epilepsy in the *Scn8a*$^{+/-}$ model do not have constant propagation trajectories.

INTRODUCTION

Perception, thoughts, and actions involve the coordinated activity of large populations of neurons in multiple regions of the brain (*1*–*3*). Nonpenetrative, subdural ECoG grids laid on top of the brain surface are the gold standard for recording population-level activity, measured from the local field potential (LFP). Neurophysiological recordings with ECoG grids have been successfully used for speech synthesis (*4*, *5*), reproduction of arm movements (*6*), and spatial localization of ictal onset zones (*7*). They have also been used to characterize cortical traveling waves (*8*), which have been shown to modulate perceptual sensitivity (*9*). Hence, ECoG grids are a favorable modality for brain-computer interface applications, localization of epileptic foci for clinical epilepsy diagnosis and targeted tissue resection, and as a basic science tool.

Ultraconformable thin-film flexible devices that can conform to the curvilinear surface of the brain are a promising technology to capture cortex-wide spatiotemporal dynamics (*10*–*12*). Microfabrication and advanced lithography methods have enabled the creation of thin-film arrays with hundreds to thousands of recording sites (*13*, *14*). However, the key bottleneck lies not in the fabrication of these devices but in the connectorization between each electrode and the external circuitry. Because of the bulkiness of existing connectorization methods such as wire bonding, anisotropic conductive film (*15*), and ultrasonic-on-bump bonding (*16*), current implementations of multithousand channel count, passive thin-film neural interfaces are highly complex, bulky, and unscalable. Examples include the stacking of 16 application-specific integrated circuits (ASICs) on eight circuit boards to achieve 1024 channels (*17*, *18*), modularization of 12 ASICs on a single circuit board for 3072 channels (*19*), and the use of 2 central processing unit sockets, 2 circuit boards, and 32 ASICs for 2048 channels (*11*).

Consequently, the field has focused on adapting this technology for active, multiplexed thin-film arrays that monolithically integrate the recording electrodes with amplifiers and analog-to-digital converters, bypassing the one electrode per input/output (I/O) limit (*12*, *20*). However, these active thin-film arrays suffer from increased noise, subkilohertz sampling rates, lower channel counts, and substantially increased device size due to the difficulty in fabricating high-mobility, high mechanical flexibility, and small-size flexible transistors (*21*). On the other hand, silicon-based large-scale complementary metal-oxide semiconductor microelectrode arrays (CMOS-MEAs) have built on decades of development in active pixel sensors, traditionally used in cameras, to provide excellent signal-to-noise ratio, high sampling rates, and scalability up to tens of thousands of channels at high densities (*22*–*24*). However, their rigid form factor is incompatible for interfacing with the brain surface.

Here, we sought to combine the scalability and exceptional performance of CMOS-MEAs with the ultraconformable form factor of flexible devices. We achieve this by developing a scalable, high-density connectorization strategy, which can form thousands of interconnections between the electrode pads on the flexible device and the pixels on the CMOS-MEA at a high density. The flexible device extends out from the CMOS-MEA through long leads, converging at the distal end as an array that interfaces with the brain (Fig. 1A).

We design a microstructure, termed Flex2Chip, which consists of microfabricated 1-μm-thick and 2-μm-wide supporting arms suspending each individual electrode pad. We leverage the ultra-compliant nature of the supporting arms to allow capillary and van der Waals forces to deform the pad to establish mechanical and electrical contact with the underlying pixels (Fig. 1B). This Flex2Chip interconnection is self-assembled and does not require any equipment or lithographic postprocessing to facilitate electrical connectivity. After assembly, the device could be encapsulated with silicone at high yield to provide mechanical robustness. We demonstrate a 2200-channel device with a connection interface area of 3.85

[1]Department of Chemical Engineering, Stanford University, Stanford, CA, USA. [2]Department of Neurology, Stanford University, Stanford, CA, USA. [3]Department of Materials Science and Engineering, Stanford University, Stanford, CA, USA. [4]Department of Biosystems Engineering, ETH Zürich, Basel, Switzerland.
*Corresponding author. Email: nmelosh@stanford.edu

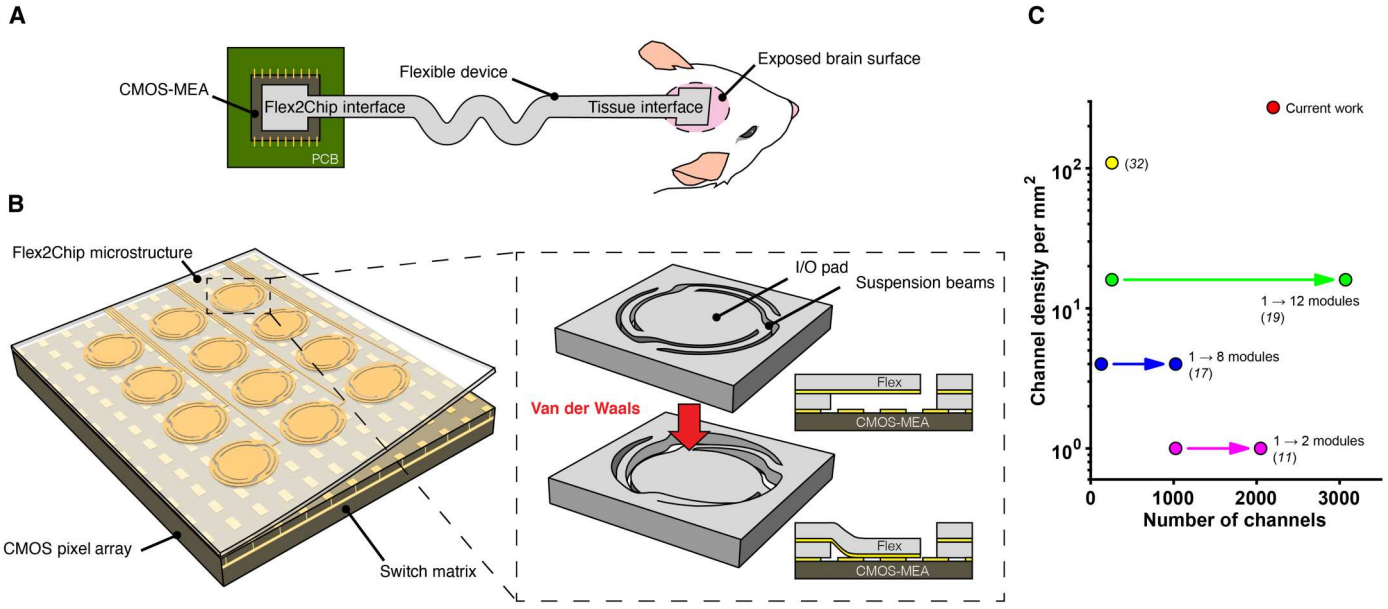

Fig. 1. Flex2Chip design. (**A**) Schematic of the flexible device. At the chip interface, Flex2Chip microstructures enable multithousand ohmic interconnections to a CMOS-MEA. At the tissue interface, the device terminates as an electrode array for high density recording. (**B**) Flex2Chip interface consists of an array of deformable Flex2Chip microstructures, integrated with the underlying CMOS-MEA. The Flex2Chip microstructures consist of three suspended beams and an I/O pad. Capillary forces deform the I/O pad to contact the CMOS pixels, upon which van der Waals forces become significant to establish structural and electrical contact. (**C**) Current approaches to multithousand channel counts rely on the modularization of multiple ASICs and circuit boards. The Flex2Chip structures facilitate 2200 individual ohmic connections to a single ASIC with an area of 3.5 mm by 2.1 mm, yielding a channel density of 272 channels/mm^2.

mm by 2.1 mm, 17 times denser than that of current multithousand-channel devices (Fig. 1C). Our method could achieve multithousand-channel counts without relying on the modularization of multiple ASICs and circuit boards.

We further show the utility of our devices in neuroscience and biologically relevant applications. We validate that our device can record extracellular action potentials with a high signal-to-noise ratio in acute ex vivo cerebellar slices. Last, we demonstrate the efficacy of our device and its potential clinical utility through the detection and characterization of submillimeter traveling waves during absence seizures on the cortical surface of awake and behaving epileptic mice. Here, our high-density flexible probes combined with the temporal resolution of the CMOS-MEA enabled the observation of highly variable propagation trajectories at micrometer scales even across the duration of a single spike-and-wave discharge (SWD).

RESULTS

System design and connectorization for the Flex2Chip devices and microstructures

The Flex2Chip devices were fabricated using standard microfabrication procedures (Materials and Methods). The devices consist of a 2200-channel array of 1-μm-wide and 100-nm-thick platinum leads at a 2-μm pitch, sandwiched between two 1-μm-thick polyimide sheets that serve as substrate and dielectric layers (Fig. 1A). At the Flex2Chip interface, these leads branch out to an array of I/O pads, which interface with the CMOS-MEA (Fig. 1B and fig. S1A). At the tissue interface, the leads branch out into an array of recording/stimulation pads (fig. S1, B and C).

At the Flex2Chip interface, the dielectric layer is etched so that the conductive I/O pad is exposed. However, the pad is recessed by 1 μm and unable to directly contact external circuitry. Unlike previous approaches, which rely on the addition of external components, e.g., gold wires for wire bonding and microparticles for anisotropic conductive films, we instead modified the I/O pad itself to facilitate connectorization.

Here, we developed a microstructure on the I/O pad, termed Flex2Chip, enabling the pad to deform downward to mate with contact pads on external circuitry. The Flex2Chip consists of a 35-μm-diameter I/O pad suspended by three suspension beams, 2-μm wide and 10-μm long (Fig. 1B, inset top, and fig. S2). The conductive leads run from the I/O pad, across the suspension beams, and onto the main substrate.

The low-bending stiffness and flexibility of the suspension beams permit the I/O pad to deform relative to the flexible device and toward the underlying pixel on the CMOS array under capillary forces (see the section below) until the platinum electrodes make physical and electrical contact with the gold-plated pixels, upon which van der Waals forces hold the microstructure in its collapsed configuration (Fig. 1B, inset bottom).

We included three suspension beams that mechanically prevent the pad from twisting or flipping over during handling and assembly. The interelectrode pitch was set at 50 μm (Fig. 2, A and B, and fig. S2D), greater than the pixel pitch, so that adjacent pads will not be shorted (*22*, *25*, *26*). This simplifies assembly, allowing rotational and translational degrees of freedom.

At the tissue interface, the leads fan out to an array of recording/stimulation pads (fig. S1C). The distal end geometry can be freely customized for the specific biological system of interest. For

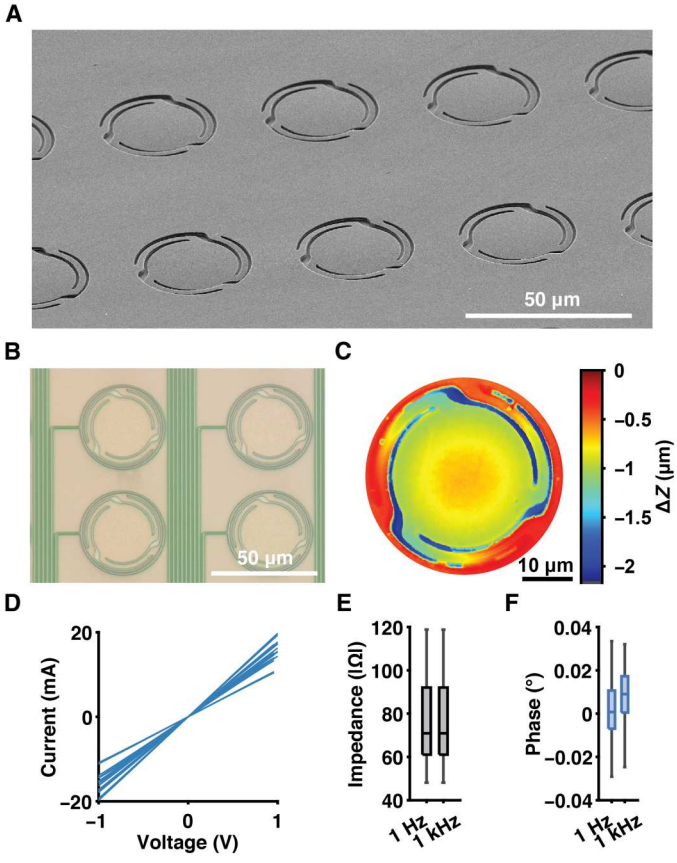

Fig. 2. Flex2Chip structure and electrical characteristics. (**A**) SEM image of the Flex2Chip device laid on top of a planar glass surface. A slight deformation of the 40-µm-diameter I/O pad toward the underlying surface enabled by the suspension beams can be observed. (**B**) Each Flex2Chip microstructure is routed by a 1-µm-wide trace toward the distal end of the device, terminated by a recording/stimulation pad. (**C**) Optical profilometer measurement confirms that the Flex2Chip I/O pad has fully deformed by 1 µm to contact the underlying surface and that van der Waals forces are sufficient to hold the structure in its deformed configuration, which facilitates stable mechanical contact. (**D**) Contact is ohmic, as seen in the resistive behavior of the *I-V* curve (n = 18). (**E**) Impedance magnitude of the Flex2Chip interface is 76.7 ± 20.0 and 76.7 ± 20 ohm at 1 and 1000 Hz, respectively (n = 64). (**F**) Phase of the Flex2Chip interface is 0.00° ± 0.01° and 0.01° ± 0.01° at 1 and 1000 Hz, respectively (n = 64).

example, we can have a contiguous sheet for ECoG grids or shanks for intracortical insertion (*18*).

Microstructure deformation assisted by capillary assembly

We leverage the flexibility of the Flex2Chip microstructures to establish connectorization between the I/O pad and CMOS-MEA pixel. This deformation is achieved under the action of capillary and van der Waals forces, which operate at micrometer- and nanometer-length scales, respectively. When the flexible device is placed on the CMOS-MEA, the I/O pad is 1 µm away from the underlying pixel (the thickness of the dielectric layer) (Fig. 1B, inset top). We initiate the microstructure deformation by applying a thin layer of isopropyl alcohol (IPA) between the device and CMOS-MEA. The capillary force of the liquid bridge formed between the I/O pad, and the pixel "pulls" the pad toward the pixel as the solvent evaporates. After the IPA fully evaporates and the pad reaches its fully collapsed structure, van der Waals forces become significant enough to hold the microstructure in its collapsed configuration (Fig. 1B, inset bottom).

We characterized this deflection by assembling a device on a CMOS-MEA phantom. Optical profilometry of the Flex2Chip microstructures showed that the structures have fully deformed and contacted the underlying chip (Fig. 2C). The deformation was observed to be uniformly distributed across the three suspension beams, and the I/O pad was uniformly displaced by 1 µm relative to the bulk device. The center of the I/O pad was slightly curved upward, indicative of residual stress from the device fabrication. Scanning electron microscopy (SEM) images also support the optical profilometer results, with a slight deformation visible despite its 1:40 aspect ratio (Fig. 2A).

The electrical characteristics of the Flex2Chip microstructure interface were evaluated to assess the quality of electrical contact and whether stray capacitance was introduced, which may affect the quality of the recording, electrical stimulation, or electrochemical measurements. Here, we shorted the distal end of the Flex2Chip device to a gallium droplet as a liquid contact. The current-voltage characteristic curve [current-voltage relation (I-V)] exhibits a clear linear relationship, characteristic of Ohmic resistors, with a resistance of 66.5 ± 12.9 ohm (Fig. 2D and fig. S3A). Furthermore, impedance spectroscopy indicated an ohmic connection between the microstructure and chip, with an average phase of 0.00° ± 0.01° and 0.01° ± 0.01° at 10 and 1000 Hz, respectively (Fig. 2, E and F, and fig. S3B). This finding confirmed that there is no capacitive impedance at the physiological frequencies of interest. Impedance contributions included cumulative contributions from the Flex2Chip interface and trace resistances but were insignificant compared to electrode-electrolyte impedance.

Electrical performance through CMOS-MEA

Having confirmed the quality of the mechanical and electrical contact of our Flex2Chip structures, we sought to characterize the electrode yield and recording quality of our device using a CMOS-MEA recording chip. Here, we fabricated a 720- and 2200-channel Flex2Chip array (figs. S1A and S5A). The I/O pads are distributed across a 3.85 mm–by–2.10 mm area, the active dimensions of the CMOS-MEA (MaxWell Biosystems Inc., Zurich, Switzerland), which has 26,400 active pixel sensors at a pitch of 17.5 µm. As our interelectrode pitch is greater than the pixel pitch, no alignment is needed during assembly.

We evaluated the connectivity yield of the device by applying a sinusoidal waveform across all the electrodes. We submerged the distal end of the device (figs. S1, B and C, and S5, B and C) in a phosphate-buffered saline (PBS) bath along with a Pt reference electrode. We applied a sinusoidal waveform at 1 kHz at the reference electrode and scanned the response of each of the 26,400 active pixel sensors. The pixels that were connected to our Flex2Chip microstructure subsequently then recorded the resulting waveform (Fig. 3A). By cross-referencing with the geometry of the flexible array (Fig. 3B), the position of each microstructure on the CMOS-MEA was localized. As the CMOS-MEA can only measure from 1024 channels simultaneously, we programmed the switch matrix to select only the pixels that corresponded to the individual microstructures to record from.

We then deposited platinum black (Pt black) on the electrode pads to reduce the signal attenuation, Johnson-Nyquist noise, and

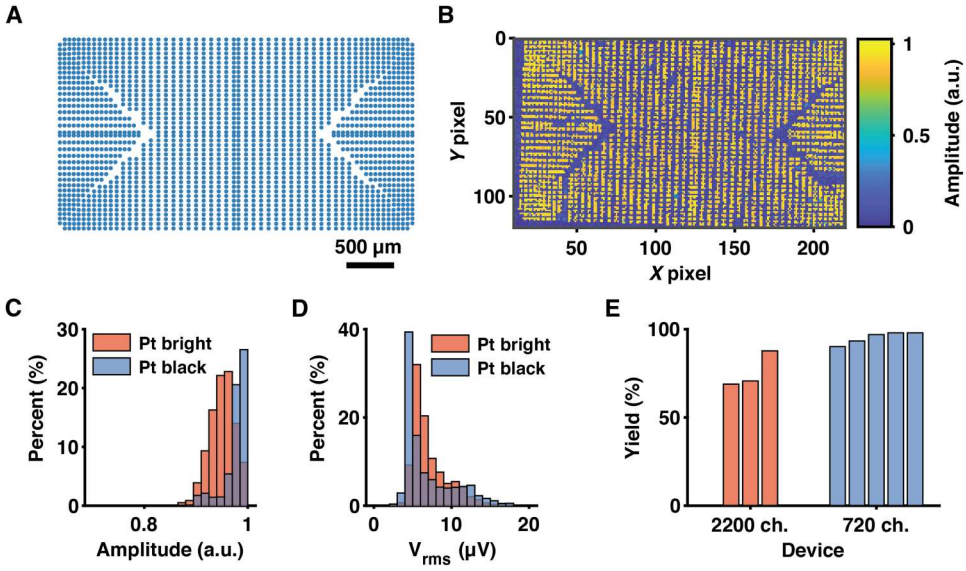

Fig. 3. Connectivity to the CMOS-MEA. (**A**) Flex2Chip pad layout. The traces are routed out on all four sides to maximize the pad density interfacing with the CMOS-MEA, as seen in fig. S5A. (**B**) Heatmap of the relative signal amplitude measured by each pixel in the CMOS-MEA. The signal is generated through the reference electrode in a saline bath by an external function generator. (**C**) Histogram of the relative signal amplitude of the pixels connected to the Flex2Chip microstructures. Bright platinum electrodes detected 0.95 ± 0.03, and platinum black–coated electrodes detected 0.99 ± 0.03 with respect to the full-scale injected signal, indicative of minimal attenuation. (**D**) Histogram of the RMS noise was 7.13 ± 2.33 μV for bright platinum and 6.93 ± 3.31 μV for platinum black electrodes. (**E**) Average connectivity yield of the 2200-channel device and 720-channel device was 75.7 and 95.3%, respectively. a.u., arbitrary units.

interelectrode cross-talk (*27*). Here, we leveraged the stimulation units of the CMOS-MEA for voltage-controlled electrochemical deposition at −0.5 V at the working electrode for 40 s. With bare platinum (Pt bright), the pixels detected 0.95 ± 0.03 of the injected sine wave signal, a 5% attenuation. This was further reduced by Pt black, which detected 0.99 ± 0.03 with respect to the full-scale injected signal (Fig. 3C). The root mean square (RMS) noise was also low, with platinum bright 7.13 ± 2.33 μV and platinum black 6.93 ± 3.31 μV, minimally higher than that of the bare pixels 5.00 ± 1.50 μV (*25*).

The developed connectorization methodology is also highly reliable with an average connectivity yield of 95.3 ± 3.42 and 75.7 ± 10.4% for a 720-channel and a 2200-channel device, respectively (Fig. 3E). The ultralow footprint of the device is highlighted with a 720-channel device for in vivo recordings as shown in fig. S2C. We also assessed the stability of the interconnection in an incubator over a month (37°C, 97% humidity, Heracell 150i, Thermo Fisher Scientific Inc., MA, USA). The yield is virtually unchanged, decreasing from 709 to 705 of 720 channels (fig. S3D), with no decrease in the sensitivity (0.99 ± 0.03) (fig. S3E).

Encapsulation

Although ohmic connectivity was established, the connection interface is only held with van der Waals forces and is delicate to external mechanical forces. The interface can be secured by applying a liquid silicone elastomer (KwikSil), which upon curing, seals the pads in place and provides a mechanically robust encapsulation layer. This encapsulation method minimally affects the channel yield, with a decrease of 9.38 ± 14.6% (fig. S4A).

The encapsulated interface was robust and could withstand a tensile force of 268 ± 6.65 mN before breakage and loss of electrical connectivity (fig. S4B). The failure occurred along the interconnect lead rather than the device itself. This is more than sufficient for a head-mounted device as in a chronic animal setup, slack in the lead cable would be introduced to mitigate any tensile forces that the device will experience between the brain and skull. Last, the electrical performance was not affected, with no statistically significant differences in the impedance or phase after encapsulation (fig. S4, C to F).

Multisite brain slice electrophysiology

Having prepared our Flex2Chip device, we then tested its ability to record neural activity in an ex vivo preparation of an acute cerebellar brain slice. Here, we used a 720-channel device, where the recording end covers an area of 3.6 mm by 1.62 mm with 90-μm pitch (30 × 24 array) with 20-μm-diameter electrode pads (fig. S5, C and D). The dimensions and channel count of the device were chosen to match the size of the tissue slice. The 720-channel device was attached to a 6-mm-diameter stainless steel ring, and the weighted construct was placed on top of the slice (fig. S6). The device was fenestrated with 60 μm–by–80 μm holes between each electrode to allow sufficient nutrient and oxygen diffusion to keep the slice healthy for the duration of the experiment. As seen in the bright-field microscopy image in Fig. 4A, the neurons were on the same focal plane as the device, indicating good contact.

We observed spontaneous spiking activity and isolated 36 individual units from various spatial locations of the slice (Fig. 4, B and C). Units were well isolated as indicated by interspike interval (ISI) violations within the refractory period (±1.5 ms) below 0.1. The clearly defined peaks in the autocorrelograms demonstrate regular firing behavior typical of cerebellar Purkinje cells (*28*). With an electrode pitch of 90 μm, we successfully detected the same neuron across multiple electrodes so that we were able to establish a neural footprint, that is, the spike-triggered average electrical

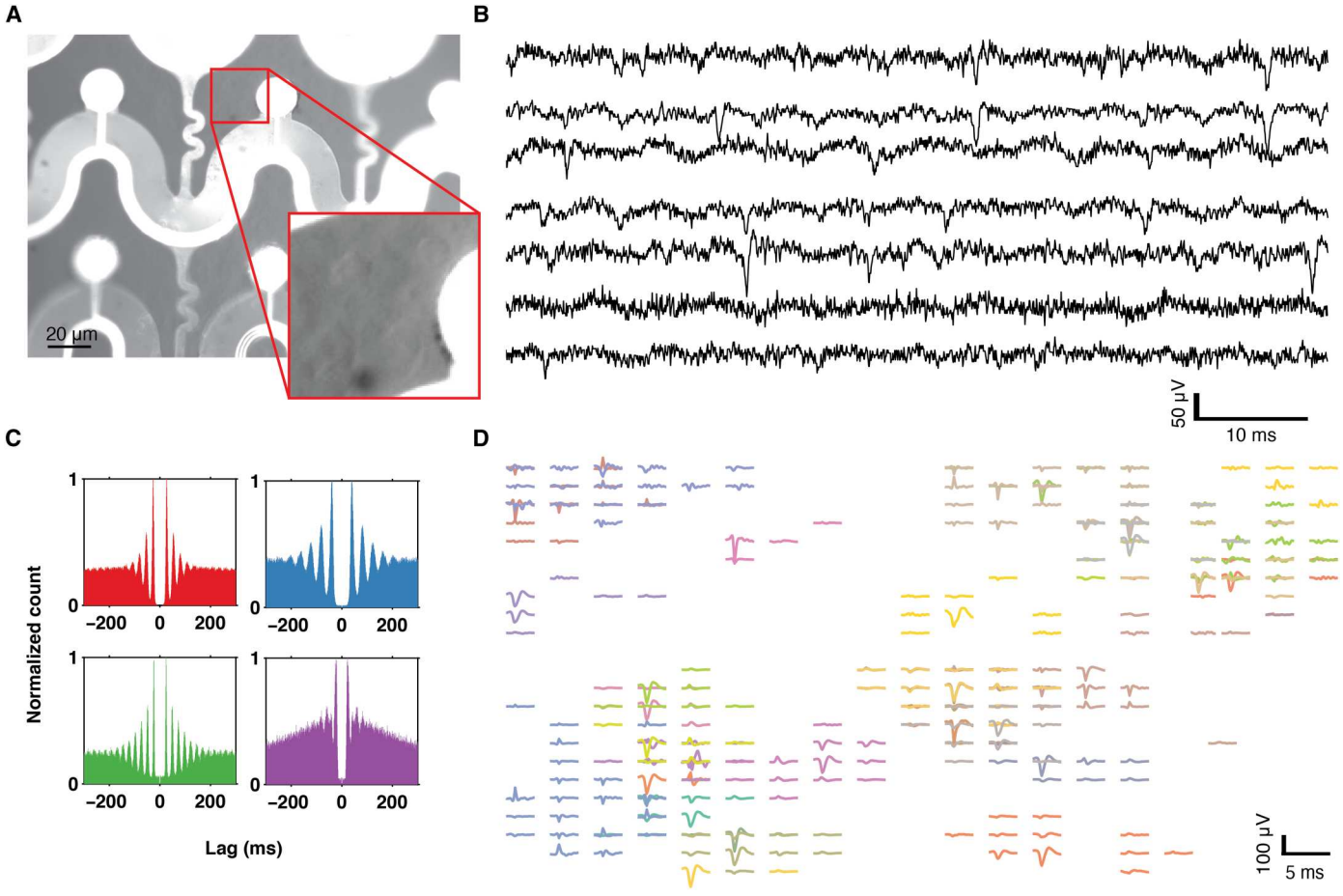

Fig. 4. In vitro cerebellar slice recordings. (**A**) Microscopy of the fenestrated 720-channel device. The device and the cerebellar cells were in the same focal plane. The inset has adjusted brightness and contrast highlighting the cerebellar cells. (**B**) Representative traces off the 720-channel device with a 50-Hz notch filter. (**C**) Spike autocorrelograms of cerebellar cells exhibiting regular firing behavior, spanning ±300 ms and a bin size of 5 ms. The peaks show that the spiking activity occurred at a regular period characteristic of Purkinje cells. (**D**) Spike-triggered average waveform of individually sorted units plotted spatially across the electrodes.

potential distribution across electrodes for a specific unit (Fig. 4D). For multiple neurons, we detected both negative and positive amplitude spikes, indicative of the signal originating from the axon initial segment (negative), and dendritic branches (positive) (*29*). This system thus provides a simple, small form-factor method of recording from hundreds to thousands of electrode sites while retaining high-quality recordings and single-spike level sensitivity.

Seizure recordings in awake and behaving mice

We next evaluated the performance of the device in a real-world application as an ECoG grid to track the dynamics of seizure propagation with micrometer precision by placing it on the cortical surface of an epileptic mouse (Fig. 5A). Here, we fabricated a 504-channel device with an active area of 760 μm by 760 μm with 20-μm-diameter electrode pads (Fig. 5B and fig. S5B), customized to record from a 2-mm-diameter craniotomy window above the sensorimotor cortex. The total channel count in this case was constrained simply by the size of the craniotomy. To differentiate local activity at each recording site from volume conducted signals, we used the analytic signal method, which can identify localized instantaneous frequency and phase information (Fig. 5C). The recordings were performed acutely within 2 hours of the device placement onto the exposed motor and somatosensory cortex. Mice were allowed to run voluntarily on a cylindrical treadmill in a head-strained condition while recording with the device and CMOS-MEA.

The transgenic mouse model *Scn8a*$^{+/-}$ exhibits spontaneous absence epilepsy, characterized by brief periods of unconsciousness and lapse in motor function that have a distinct 7-Hz SWD (*30*). Our single-channel measurements showed the stereotypical 7-Hz SWD with a shift toward low-frequency band power across the duration of a single seizure (Fig. 5D).

We computed the instantaneous phase of the LFP signal to characterize the spatiotemporal propagating wave dynamics that occurs during seizures (*31*). Here, we used the generalized phase (GP), an updated approach of the analytic signal to enable the analysis of wideband signals (*9*). We chose this approach to sufficiently capture the multiple frequency bands associated with the SWD as shown in the spectrogram in Fig. 5D. In short, the GP captures the phase of the largest fluctuation on the recording electrode at any moment in time without distortions due to large low-frequency intrusions or smaller high-frequency inclusions (Fig. 5E). We applied this method to the LFP signal pretreated with a wide bandpass (5 to 40 Hz; eighth-order zero-phase Butterworth filter).

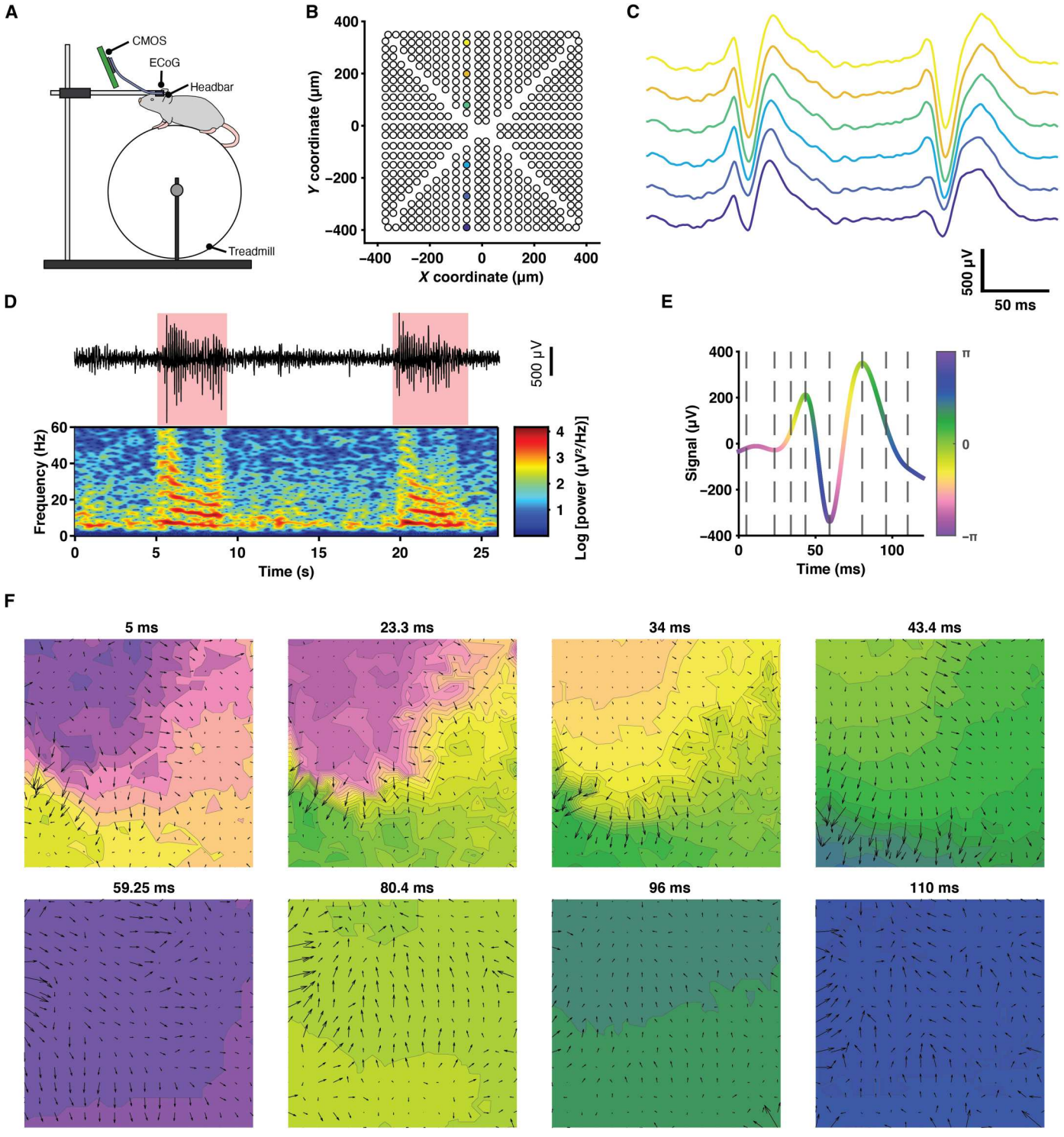

Fig. 5. In vivo recording in an awake and moving mouse. (**A**) Schematic of a head-fixed epileptic mouse on a treadmill. A 2-mm-diameter craniotomy exposes the cortex upon which a 504-channel ECoG array spanning 0.76 mm by 0.76 mm is laid. (**B** and **C**) ECoG electrode layout and representative traces showing SWDs during a seizure, color-coded to match their respective positions. (**D**) Top: Representative trace of a single channel with two seizures highlighted in red. Bottom: Corresponding spectrogram showing the decrease in the frequency band across the duration of the seizure, characteristic of absence epilepsy. (**E**) Representative trace color-coded according to the instantaneous phase of the signal. (**F**) Heatmap of the instantaneous phase across the electrode arrays during a single SWD. Each frame corresponds to a dotted line in Fig. 3E.

Figure 5F shows snapshots of the spatial variation of the phase throughout the time course of a single SWD. Here, we observed complex traveling wave behavior that constantly shifted in direction and velocity, even across the duration of a single spike SWD. Movie S1 shows a video of the phase evolution across multiple SWDs. Seizure propagation patterns were notably different with time through the seizure, demonstrating that seizure dynamics in absence epilepsy in this model do not have constant propagation trajectories or site of onset. More studies must be conducted to elucidate the origins of this variation. Our high channel density combined with a large area of recording along the cortical surface has allowed an unprecedented level of detail into seizure dynamics at micrometer-level precision.

DISCUSSION

Flex2Chip introduces a facile system design and connectorization method which increases the channel density of ultraconformable, thin-film, flexible devices by 17 times in comparison to state-of-the-art devices. This enables multithousand channel counts on a single ASIC, unlike current approaches, which rely on the modularization of multiple ASICs and circuit boards (*11*, *17*, *19*, *32*). The assembly method is simple, consisting of placing the device on a CMOS-MEA with a thin layer of IPA. As the IPA dries, the microstructures self-assemble in their collapsed configuration. The connectorization does not require specialized equipment as needed for wire bonding, anisotropic conductive film (*15*), or ultrasonic-on-bump bonding (*16*).

Here, the key limitation to pad density is not the interconnection interfacial area but the routing of the traces. Although we demonstrate that we can form interconnections with a pitch of 50 μm with a theoretical density of 400 channels/mm^2, the density for our 2200-channel devices is 272 channels/mm^2 even with 1-μm-wide traces with 1-μm spacing. The input-referred noise level in the action potential range (300 Hz to 10 kHz) is 6.93 ± 3.30 μV_{rms}, comparable to that of monolithic silicon probes such as the Neuropixels 2.0 (8.2 μV_{rms}) (*33*).

The bonding methodology is agnostic to the chip, and rapid progress in their functionality—such as the addition of fast scan cyclic voltammetry, impedance spectroscopy, stimulation artifact suppression units, etc.—can be facilely extended to the polymer device (*34*). Furthermore, it is also agnostic to downstream geometry, as shown here with both acute brain slice and in vivo cortical recordings. The developed technology can be easily used to extend the work on cutting-edge chronic intracortical and organoid recordings with mesh electronics (*35*–*37*). Improvements to miniaturize the CMOS-MEA onto a headstage for freely behaving mice experiments are already on the way.

MATERIALS AND METHODS

Flex2Chip device fabrication

The devices were fabricated using standard microfabrication processes. The fabrication steps are as follows: (i) A 4-inch silicon wafer (P-type silicon, 0.1 to 0.9 ohm/cm; Silicon Valley Microelectronics Inc., CA, USA) was cleaned with O_2 plasma [27.6 standard cubic centimeter per minute (sccm), 50 W, 300 mtorr, 1 min; PE II-A, Technics, CA, USA]. (ii) Alignment marks were patterned on the wafer. First, the wafer was dehydrated at 150°C and primed with hexamethyldisilazane (YES LP-III, Yield Engineering Systems, USA). Second, a 0.7-μm-thick layer of positive photoresist (I Line SPR 955 CM-0.7, Dow, MI, USA) was spin-coated on the wafer (1700 rpm, 30 s) and baked (90°C, 120 s). Third, the alignment marks were exposed (150 mW/cm^2; PAS 5500/60, ASML, Veldhoven, The Netherlands). Fourth, after exposure, the resist was baked (90 s), developed with MF-26A (60 s, Dow, MI, USA), rinsed with water, and hard-baked (110°C, 60 s). Fifth, the alignment marks were etched 120-nm deep into SiO_2 (100 sccm CF_4, 2 sccm O_2, 500 W, 250 mtorr, 40 s; P5000, Applied Materials, CA, USA). Last, the photoresist was stripped using a microwave plasma system (LoLamp, 45 s; Aura Asher, Gasonics, CA, USA). (iii) A 250-nm-thick Ni sacrificial layer was deposited with electron beam evaporation (2.5 Å/s, 6×10^{-7} torr; ES26C, Innotec, MI, USA). (iv) A 1-μm-thick layer of polyimide (PI2610, Dupont, DE, USA) forming the substrate base was spin-coated (3000 rpm, 60 s), soft-baked (90°C, 3 min), and finally hard-baked in an inert N_2 atmosphere (325°C, 30 min, 2°C/min ramp; Blue-M, PA, USA). (v) A metallic layer, which forms the electrodes, interconnects, and bonding pads, was then deposited. First, a 200-nm-thick liftoff layer (Microposit LOL 2000, Dow, MI, USA) was spin-coated (3000 rpm, 60 s) and baked (200°C, 7 min). Second, positive photoresist was patterned as described above. Third, the photoresist was descummed with O_2 plasma (27.6 sccm, 50 W, 300 mtorr, 2.5 min; PE II-A, Technics, CA, USA). Fourth, a 10-nm-thick Cr and 100-nm-thick Pt layer were deposited with electron beam evaporation (1 Å/s, 6×10^{-7} torr; ES26C, Innotec, MI, USA). Last, the photoresist was lifted off overnight (Microposit Remover 1165, Dow, MI, USA). (vi) A 1-μm-thick layer of polyimide, which formed the insulating layer, was spin-coated as described above. (vii) A negative mask, which defined the shape of the device and the exposure of the electrode pads, was deposited. First, positive photoresist was patterned and descummed as described above. Second, a 50-nm-thick Ni layer was deposited with electron beam evaporation (1 Å/s, 6×10^{-7} torr; ES26C, Innotec, MI, USA). Third, the photoresist was lifted off as described above. Fourth, the unprotected polyimide was then etched with O_2 plasma (60 sccm O_2, 400 W, 200 mtorr, 100 s; P5000, Applied Materials, CA, USA). (viii) Last, the Si wafer was transferred to an Ni etchant solution (40% $FeCl_3$:39% HCl:H_2O = 1:1:20) to remove the sacrificial Ni layer and negative mask and to release the device from the Si wafer.

CMOS-MEA modifications

The CMOS-MEA (MaxWell Biosystems, Zurich, Switzerland) has 26,400 pixels, 1024 of which can be arbitrarily chosen to record from simultaneously at 20 kHz (*23*). The bare die was wire-bonded to custom printed circuit boards (PCBs) (3100 Plus, ESEC, Cham, Switzerland). The wirebonds were then encapsulated with epoxy (353ND-T, Epoxy Technology, MA, USA). Here, the pixels were recessed by a 1.2-μm-thick layer of SiO_2 and SiN_x. To elevate the pixel, Au was electrochemically deposited (60 s, 1.5 V, NB Semiplate AU 100 AS, Microchemicals, Ulm, Germany) using a Pt counter electrode.

Flex2Chip device assembly

For the device assembly, it is critical to minimize the number of particles to maximize the connectivity yield. The assembly of the device onto the CMOS-MEA is as follows. (i) The CMOS-MEA was transferred to a bath of submicrometer-filtered IPA (Millipore Sigma,

MA, USA, PX1838), cleaned by ultrasonication for 30 s, and blown dry. (ii) A thin layer of IPA was applied using a pipette on the surface of the CMOS-MEA to form a stable liquid film, and the device was then placed on top with a pair of paintbrushes. The capillary forces from the liquid bridge acts to pull the bulk device flat, preventing the buckling of the device during transfer and manipulation. Furthermore, the liquid film also reduces the friction coefficient between the CMOS-MEA and device when sheared, enabling sliding without damaging the device. Paintbrushes were chosen as opposed to forceps as their softness prevents scratching of the device during manipulation and provides a mechanical spring–like buffer between the hand and device. As a result, once the device is placed on top of the CMOS-MEA, the paintbrushes can be used to gently drag the device into approximate alignment on top of the active region of the chip. Subsequently, as the IPA dries, the pads are then self-assembled onto the pixels. (iii) The device was then sterilized in 70% ethanol solution for 1 hour and exposed to ultraviolet for 3 min.

Electrical characterization

Impedance and *I-V* curve measurements were conducted on a CMOS-MEA phantom using a potentiostat (SP-200, BioLogic, Seyssinet-Pariset, France). The distal end of the device was shorted to a gallium droplet to ensure ohmic contact to probe the Flex2Chip interface at the proximal end. Connectivity, noise, and signal attenuation measurements were conducted on the CMOS-MEA, as described by previous work (*23*). The distal end of the device was immersed in a PBS bath (Thermo Fisher Scientific, MA, USA, 10010-023) along with a Pt counter electrode. For connectivity and signal attenuation measurements, the gain of the amplifiers was set to 24, and a 1-kHz 5-mV sine wave was injected at the counter electrode. Pixels connected to Flex2Chip microstructures would then record the sinusoidal waveform, and the corresponding pad could then be mapped. The attenuation was calculated to be the ratio between the measured and injected signal. Pt black coating (100 mM hexachloroplatinic acid, Millipore Sigma, MA, USA, 206083) was electrochemically deposited (0.5 V, 30 s) under mechanical agitation to lower the electrode-electrolyte impedance.

Device encapsulation

The devices could be encapsulated by applying a liquid silicone elastomer (KwikSil, World Precision Instruments Inc., FL, USA) over the Flex2Chip interface. The silicone elastomer was cured after 10 min, after which the connectivity and mechanically robustness were subsequently assessed.

The tensile forces were measured by mounting one end of the device on a z stage and the other on a weighing balance (PM4000, Mettler Toledo, OH, USA). At the weighing balance, glass slides were attached to the device as miniature weights. The device was then lifted stepwise by the z stage, which gradually lifts the glass slides off the weighing balance. The tensile force experienced by the device was calculated from the decrease in weight at the balance as the glass slides are increasingly supported by the flexible device. At fixed intervals, a current (20 μA) was applied for 5 s, and the average voltage was used to measure the resistance of the interconnect. The measurements were conducted on a CMOS-MEA phantom to probe the interface with a potentiostat (SP-200, BioLogic, Seyssinet-Pariset, France).

Brain slice preparation

All use of mice and experimental protocols were approved by the Basel Stadt veterinary office according to Swiss federal laws on animal welfare. Wild-type mice (male, postnatal day 14, C57BL/6JRj, Janvier Labs) were decapitated under isoflurane anesthesia, and the brains were removed and immersed into ice-cold carbogen-bubbled (95% O_2 + 5% CO_2) artificial cerebrospinal fluid (ACSF) solution containing 125 mM NaCl, 2.5 mM KCl, 25 mM glucose, 1.25 mM NaH_2PO_4, 25 mM $NaHCO_3$, 2 mM $CaCl_2$, and 1 mM $MgCl_2$. The cerebellum was dissected and glued on the cutting stage of a vibratome (VT1200S, Leica, Wetzlar, Germany). Sagittal cerebellar slices with a thickness of 380 μm were obtained. Slices were then maintained in ACSF at room temperature until use.

A 6-mm-diameter stainless steel ring was bonded to a 720-channel device using cyanoacrylate adhesive (Pattex, Henkel, Aachen, Germany), where the exposed platinum electrodes were facing away from the ring. The construct was placed on the acute slice and held in place with the stainless steel ring. The tissue was continuously perfused with carbogen-bubbled ACSF at 33° to 36°C to maintain cell viability.

In vivo preparation

Mice with the heterozygous loss of function mutation in *Scn8a* [male, 12 weeks old, C3HeB/FeJ-Scn8amed/J, the Jackson Laboratory, stock no. 003798 (*38*)], referred to here as *Scn8a*$^{+/-}$, were the vertebrate animal subjects used for in vivo measurements. All procedures performed on the mice were approved by Stanford University's Administrative Panel on Laboratory Animal Care (protocol no. 12363). The animal care and use programs at Stanford University meet the requirements of all federal and state regulations governing the humane care and use of laboratory animals, including the United States Department of Agriculture Animal Welfare Act and the Public Health Service Policy on Humane Care and Use of Laboratory Animals. The laboratory animal care program at Stanford is accredited by the Association for the Assessment and Accreditation of Laboratory Animal Care. All mice were maintained on a reverse 12-hour dark/12-hour light cycle (temperature: 20° to 25°C; humidity: 50 to 65%) in the Stanford University's Veterinary Service Center and fed with food and water ad libitum as appropriate. All experiments occurred during their active cycle.

Surgery

Anesthesia was induced with isoflurane (4%; maintained at 1.5%) followed by injection of carprofen (2 mg/kg). Fiducial marks were marked on the skull at the following coordinates from bregma: anteroposterior, −0.85 mm; mediolateral, 2.5 mm. A self-tapping bone screw (Fine Science Tools, CA, USA, 19010-10) was set in the skull over the cerebellum. A stainless steel headbar was cemented onto the skull using dental cement (C&B Metabond, Parkell, NY, USA). After headbar implantation, mice were habituated to run on a treadmill for 7 days. In a second surgical procedure, a 2-mm-diameter craniotomy was then made over the fiducial mark and covered with KwikCast (World Precision Instruments, FL, USA). The mouse then recovered overnight before the recording session.

Electrophysiological recording

Once mounted on the treadmill, the KwikCast above the craniotomy was removed, and the well was filled with saline (0.9% NaCl).

The ECoG device was lain on the surface of the cortex, and the saline was wicked away to allow sufficient contact between the device and cortex. KwikCast was then reapplied. The CMOS-MEA counter electrode operates at a reference voltage of 1.65 V. Consequently, the animal was isolated from the ground by connecting the reference of the chip to a skull screw. Recording then lasted for 40 min.

Spike sorting

Data analysis was performed using custom software written in Python 3.9.0 and MATLAB 2019b (MathWorks, MA, USA). Automatic spike sorting was performed using Kilosort 3 (https://github.com/MouseLand/Kilosort) (*33*, *39*). Subsequently, using the ecephys spike sorting pipeline (https://github.com/AllenInstitute/ecephys_spike_sorting), double counted spikes were removed from each cluster (within ±0.16 ms), and the ISI violations within the refractory period (± 1.5 ms) were calculated. Units were only classified as good if the number of spikes was greater than 100, the ISI violations were less than 0.1, and if Kilosort 3 originally labeled the spike as "good." Last, clusters were inspected and curated in Phy (https://github.com/cortex-lab/phy).

Supplementary Materials

This PDF file includes:
Figs. S1 to S6
Legend for movie S1

Other Supplementary Material for this manuscript includes the following:
Movie S1

View/request a protocol for this paper from *Bio-protocol*.

REFERENCES AND NOTES

1. J. F. Hipp, D. J. Hawellek, M. Corbetta, M. Siegel, A. K. Engel, Large-scale cortical correlation structure of spontaneous oscillatory activity. *Nat. Neurosci.* **15**, 884–890 (2012).
2. L. Huber, E. S. Finn, D. A. Handwerker, M. Bönstrup, D. R. Glen, S. Kashyap, D. Ivanov, N. Petridou, S. Marrett, J. Goense, B. A. Poser, P. A. Bandettini, Sub-millimeter fMRI reveals multiple topographical digit representations that form action maps in human motor cortex. *Neuroimage* **208**, 116463 (2020).
3. Y. Yang, M. R. DeWeese, G. H. Otazu, A. M. Zador, Millisecond-scale differences in neural activity in auditory cortex can drive decisions. *Nat. Neurosci.* **11**, 1262–1263 (2008).
4. D. A. Moses, S. L. Metzger, J. R. Liu, G. K. Anumanchipalli, J. G. Makin, P. F. Sun, J. Chartier, M. E. Dougherty, P. M. Liu, G. M. Abrams, A. Tu-Chan, K. Ganguly, E. F. Chang, Neuroprosthesis for decoding speech in a paralyzed person with anarthria. *N. Engl. J. Med.* **385**, 217–227 (2021).
5. G. K. Anumanchipalli, J. Chartier, E. F. Chang, Speech synthesis from neural decoding of spoken sentences. *Nature* **568**, 493–498 (2019).
6. G. Hotson, D. P. McMullen, M. S. Fifer, M. S. Johannes, K. D. Katyal, M. P. Para, R. Armiger, W. S. Anderson, N. V. Thakor, B. A. Wester, N. E. Crone, Individual finger control of a modular prosthetic limb using high-density electrocorticography in a human subject. *J. Neural Eng.* **13**, 026017 (2016).
7. E. Boran, G. Ramantani, N. Krayenbühl, M. Schreiber, K. König, T. Fedele, J. Sarnthein, High-density ECoG improves the detection of high frequency oscillations that predict seizure outcome. *Clin. Neurophysiol.* **130**, 1882–1888 (2019).
8. L. Muller, G. Piantoni, D. Koller, S. S. Cash, E. Halgren, T. J. Sejnowski, Rotating waves during human sleep spindles organize global patterns of activity that repeat precisely through the night. *eLife* **5**, e17267 (2016).
9. Z. W. Davis, L. Muller, J. Martinez-Trujillo, T. Sejnowski, J. H. Reynolds, Spontaneous traveling cortical waves gate perception in behaving primates. *Nature* **587**, 432–436 (2020).
10. D. Khodagholy, J. N. Gelinas, T. Thesen, W. Doyle, O. Devinsky, G. G. Malliaras, G. Buzsáki, NeuroGrid: Recording action potentials from the surface of the brain. *Nat. Neurosci.* **18**, 310–315 (2015).
11. Y. Tchoe, A. M. Bourhis, D. R. Cleary, B. Stedelin, J. Lee, K. J. Tonsfeldt, E. C. Brown, D. A. Siler, A. C. Paulk, J. C. Yang, H. Oh, Y. G. Ro, K. Lee, S. M. Russman, M. Ganji, I. Galton, S. Ben-Haim, A. M. Raslan, S. A. Dayeh, Human brain mapping with multithousand-channel PtNRGrids resolves spatiotemporal dynamics. *Sci. Transl. Med.* **14**, eabj1441 (2022).
12. C.-H. Chiang, S. M. Won, A. L. Orsborn, K. J. Yu, M. Trumpis, B. Bent, C. Wang, Y. Xue, S. Min, V. Woods, C. Yu, B. H. Kim, S. B. Kim, R. Huq, J. Li, K. J. Seo, F. Vitale, A. Richardson, H. Fang, Y. Huang, K. Shepard, B. Pesaran, J. A. Rogers, J. Viventi, Development of a neural interface for high-definition, long-term recording in rodents and nonhuman primates. *Sci. Transl. Med.* **12**, eaay4682 (2020).
13. K. Scholten, C. E. Larson, H. Xu, D. Song, E. Meng, A 512-channel multi-layer polymer-based neural probe array. *J. Microelectromechanical Syst.* **29**, 1054–1058 (2020).
14. S. Guan, J. Wang, X. Gu, Y. Zhao, R. Hou, H. Fan, L. Zou, L. Gao, M. Du, C. Li, Y. Fang, Elastocapillary self-assembled neurotassels for stable neural activity recordings. *Sci. Adv.* **5**, eaav2842 (2019).
15. P. Ledochowitsch, R. J. Félus, R. R. Gibboni, A. Miyakawa, S. Bao, M. M. Maharbiz, Fabrication and testing of a large area, high density, parylene MEMS μECoG array, in *2011 IEEE 24th International Conference on Micro Electro Mechanical Systems* (2011), pp. 1031–1034.
16. J. J. Yoo, E. Meng, Bonding methods for chip integration with parylene devices. *J. Micromechanics Microengineering* **31**, 045011 (2021).
17. Z. Zhao, H. Zhu, X. Li, L. Sun, F. He, J. E. Chung, D. F. Liu, L. Frank, L. Luan, C. Xie, Ultraflexible electrode arrays for months-long high-density electrophysiological mapping of thousands of neurons in rodents. *Nat. Biomed. Eng.* **7**, 520–532 (2023).
18. J. E. Chung, H. R. Joo, J. L. Fan, D. F. Liu, A. H. Barnett, S. Chen, C. Geaghan-Breiner, M. P. Karlsson, M. Karlsson, K. Y. Lee, H. Liang, J. F. Magland, J. A. Pebbles, A. C. Tooker, L. F. Greengard, V. M. Tolosa, L. M. Frank, High-density, long-lasting, and multi-region electrophysiological recordings using polymer electrode arrays. *Neuron* **101**, 21–31.e5 (2019).
19. E. Musk; Neuralink, An integrated brain-machine interface platform with thousands of channels. *J. Med. Internet Res.* **21**, e16194 (2019).
20. J. Viventi, D.-H. Kim, L. Vigeland, E. S. Frechette, J. A. Blanco, Y.-S. Kim, A. E. Avrin, V. R. Tiruvadi, S.-W. Hwang, A. C. Vanleer, D. F. Wulsin, K. Davis, C. E. Gelber, L. Palmer, J. Van der Spiegel, J. Wu, J. Xiao, Y. Huang, D. Contreras, J. A. Rogers, B. Litt, Flexible, foldable, actively multiplexed, high-density electrode array for mapping brain activity in vivo. *Nat. Neurosci.* **14**, 1599–1605 (2011).
21. J.-H. Seo, T. Ling, S. Gong, W. Zhou, A. L. Ma, L. J. Guo, Z. Ma, Fast flexible transistors with a nanotrench structure. *Sci. Rep.* **6**, 24771 (2016).
22. K. Sahasrabuddhe, A. A. Khan, A. P. Singh, T. M. Stern, Y. Ng, A. Tadić, P. Orel, C. LaReau, D. Pouzzner, K. Nishimura, K. M. Boergens, S. Shivakumar, M. S. Hopper, B. Kerr, M.-E. S. Hanna, R. J. Edgington, I. McNamara, D. Fell, P. Gao, A. Babaie-Fishani, S. Veijalainen, A. V. Klekachev, A. M. Stuckey, B. Luyssaert, T. D. Y. Kozai, C. Xie, V. Gilja, B. Dierickx, Y. Kong, M. Straka, H. S. Sohal, M. R. Angle, The Argo: A high channel count recording system for neural recording in vivo. *J. Neural Eng.* **18**, 015002 (2021).
23. M. Ballini, J. Müller, P. Livi, Y. Chen, U. Frey, A. Stettler, A. Shadmani, V. Viswam, I. L. Jones, D. Jäckel, M. Radivojevic, M. K. Lewandowska, W. Gong, M. Fiscella, D. J. Bakkum, F. Heer, A. Hierlemann, A 1024-channel CMOS microelectrode array with 26,400 electrodes for recording and stimulation of electrogenic cells in vitro. *IEEE J. Solid-State Circuits.* **49**, 2705–2719 (2014).
24. B. Miccoli, C. M. Lopez, E. Goikoetxea, J. Putzeys, M. Sekeri, O. Krylychkina, S.-W. Chang, A. Firrincieli, A. Andrei, V. Reumers, D. Braeken, High-density electrical recording and impedance imaging with a multi-modal CMOS multi-electrode array chip. *Front. Neurosci.* **13**, 641 (2019).
25. A. Obaid, M.-E. Hanna, Y.-W. Wu, M. Kollo, R. Racz, M. R. Angle, J. Müller, N. Brackbill, W. Wray, F. Franke, E. J. Chichilnisky, A. Hierlemann, J. B. Ding, A. T. Schaefer, N. A. Melosh, Massively parallel microwire arrays integrated with CMOS chips for neural recording. *Sci. Adv.* **6**, eaay2789 (2020).
26. M. Kollo, R. R. Racz, M.-E. S. Hanna, A. M. Obaid, M. R. Angle, W. Wray, Y. Kong, A. Hierlemann, J. Müller, N. A. Melosh, A. T. Schaefer, CHIME: CMOS-hosted in vivo microelectrodes for massively scalable neuronal recordings. *Neuroscience* **14**, 834 (2020).
27. Y. Qiang, W. Gu, Z. Liu, S. Liang, J. H. Ryu, K. J. Seo, W. Liu, H. Fang, Crosstalk in polymer microelectrode arrays. *Nano Res.* **14**, 3240–3247 (2021).
28. J. Mordel, D. Karnas, P. Pévet, P. Isope, E. Challet, H. Meissl, The output signal of purkinje cells of the cerebellum and circadian rhythmicity. *PLOS ONE* **8**, e58457 (2013).
29. D. J. Bakkum, M. E. J. Obien, M. Radivojevic, D. Jäckel, U. Frey, H. Takahashi, A. Hierlemann, The axon initial segment is the dominant contributor to the neuron's extracellular electrical potential landscape. *Adv. Biosyst.* **3**, 1800308 (2019).

30. C. D. Makinson, B. S. Tanaka, J. M. Sorokin, J. C. Wong, C. A. Christian, A. L. Goldin, A. Escayg, J. R. Huguenard, Regulation of thalamic and cortical network synchrony by Scn8a. *Neuron* **93**, 1165–1179.e6 (2017).
31. D. Gabor, Theory of communication. Part 1: The analysis of information. *J. Inst. Electr. Eng.* **3**, 429–441 (1946).
32. S.-Y. Park, K. Na, M. Vöröslakos, H. Song, N. Slager, S. Oh, J. Seymour, G. Buzsáki, E. Yoon, A miniaturized 256-channel neural recording interface with area-efficient hybrid integration of flexible probes and CMOS integrated circuits. *IEEE Trans. Biomed. Eng.* **69**, 334–346 (2022).
33. N. A. Steinmetz, C. Aydin, A. Lebedeva, M. Okun, M. Pachitariu, M. Bauza, M. Beau, J. Bhagat, C. Böhm, M. Broux, S. Chen, J. Colonell, R. J. Gardner, B. Karsh, F. Kloosterman, D. Kostadinov, C. Mora-Lopez, J. O'Callaghan, J. Park, J. Putzeys, B. Sauerbrei, R. J. J. van Daal, A. Z. Vollan, S. Wang, M. Welkenhuysen, Z. Ye, J. T. Dudman, B. Dutta, A. W. Hantman, K. D. Harris, A. K. Lee, E. I. Moser, J. O'Keefe, A. Renart, K. Svoboda, M. Häusser, S. Haesler, M. Carandini, T. D. Harris, Neuropixels 2.0: A miniaturized high-density probe for stable, long-term brain recordings. *Science* **372**, eabf4588 (2021).
34. J. Dragas, V. Viswam, A. Shadmani, Y. Chen, R. Bounik, A. Stettler, M. Radivojevic, S. Geissler, M. Obien, J. Müller, A. Hierlemann, A multi-functional microelectrode array featuring 59760 electrodes, 2048 electrophysiology channels, stimulation, impedance measurement and neurotransmitter detection channels. *IEEE J. Solid-State Circuits* **52**, 1576–1590 (2017).
35. X. Yang, T. Zhou, T. J. Zwang, G. Hong, Y. Zhao, R. D. Viveros, T.-M. Fu, T. Gao, C. M. Lieber, Bioinspired neuron-like electronics. *Nat. Mater.* **18**, 510–517 (2019).
36. S. Zhao, X. Tang, S. Partarrieu, S. Guo, R. Liu, J. Lee, Z. Lin, J. Liu, Tracking neural activity from the same cells during the entire adult life of mice. *Nat. Neurosci.* **26**, 696–710 (2021).
37. P. Le Floch, Q. Li, Z. Lin, S. Zhao, R. Liu, K. Tasnim, H. Jiang, J. Liu, Stretchable mesh nanoelectronics for 3D single-cell chronic electrophysiology from developing brain organoids. *Adv. Mater.* **34**, 2106829 (2022).
38. D. C. Kohrman, J. B. Harris, M. H. Meisler, Mutation detection in the *med* and *med*^{J} Alleles of the sodium channel *Scn8a*: Unusual splicing due to a minor class AT-AC intron*. *J. Biol. Chem.* **271**, 17576–17581 (1996).
39. M. Pachitariu, N. A. Steinmetz, S. N. Kadir, M. Carandini, K. D. Harris, Fast and accurate spike sorting of high-channel count probes with KiloSort, in *Advances in Neural Information Processing Systems* (Curran Associates Inc., 2016), vol. 29; https://proceedings.neurips.cc/paper/2016/hash/1145a30ff80745b56fb0cecf65305017-Abstract.html.

Acknowledgments
Funding: Research at Stanford was supported by the Wu Tsai Institute Big Ideas program. E.T.Z. was supported by the Bio-X Stanford Interdisciplinary Fellowship and Croucher Scholarship. Part of this work was performed at the Stanford Nanofabrication Facility (SNF), supported by the National Science Foundation under award ECCS-2026822. The CMOS-MEA work was supported by the European Union under the ERC advanced grant "neuroXscales" (contract 694829). **Author contributions:** E.T.Z. and N.A.M. conceived the experiments. E.T.Z. and P.W. fabricated the devices. E.T.Z. and A.P. developed the assembly process. E.T.Z., N.M.H., H.U., and A.Z. characterized the devices. H.U., S.R., and E.T.Z. prepared the CMOS-MEAs. J.M.H. and E.T.Z. performed experiments in rodents and analyzed the data. J.B. and E.T.Z. performed experiments on cerebellar slices and analyzed the data. N.A.M., A.H., and J.R.H. supervised the work. E.T.Z. and N.A.M. wrote the manuscript with contribution from all the authors. Cartoons in Fig. 1A were created with BioRender.com. **Competing interests:** N.A.M. is a cofounder in Paradromics Inc., a company developing scalable electrophysiology. S.R. is now employed at MaxWell Biosystems AG, a company that fabricates and commercializes high-density microelectrode arrays. The authors declare that they have no other competing interests. **Data and materials availability:** All data needed to evaluate the conclusions in the paper are present in the paper and/or the Supplementary Materials.

Submitted 22 November 2022
Accepted 3 May 2023
Published 7 June 2023
10.1126/sciadv.adf9524

MATERIALS SCIENCE

Holistic energy landscape management in 2D/3D heterojunction via molecular engineering for efficient perovskite solar cells

Ke Ma[1]†, Jiaonan Sun[1]†, Harindi R. Atapattu[2], Bryon W. Larson[3], Hanjun Yang[1,4], Dewei Sun[4], Ke Chen[4], Kang Wang[1], Yoonho Lee[1], Yuanhao Tang[1], Anika Bhoopalam[1], Libai Huang[4], Kenneth R. Graham[2], Jianguo Mei[4], Letian Dou[1,5]*

Constructing two-dimensional (2D) perovskite atop of 3D with energy landscape management is still a challenge in perovskite photovoltaics. Here, we report a strategy through designing a series of π-conjugated organic cations to construct stable 2D perovskites and to realize delicate energy level tunability at 2D/3D heterojunctions. As a result, the hole transfer energy barriers can be reduced both at heterojunctions and within 2D structures, and the preferable work function shift reduces charge accumulation at interface. Leveraging these insights and also benefitted from the superior interface contact between conjugated cations and poly(triarylamine) (PTAA) hole transporting layer, a solar cell with power conversion efficiency of 24.6% has been achieved, which is the highest among PTAA-based n-i-p devices to the best of our knowledge. The devices exhibit greatly enhanced stability and reproducibility. This approach is generic to several hole transporting materials, offering opportunities to realize high efficiency without using the unstable Spiro-OMeTAD.

INTRODUCTION

Perovskite solar cells (PSCs) have emerged as a strong candidate for future photovoltaic technology (*1*–*4*). However, achieving high efficiency together with long-term stability is still a challenge (*5*–*7*). More recently, the strategy of constructing two-dimensional/three-dimensional (2D/3D) heterostructures to passivate interface defects and improve stability has contributed to some of high-efficiency devices, including the record-performing PSCs (*8*–*14*). These studies have also revealed that energy level alignment at the 2D/3D heterojunction is crucial for efficient charge transfer (*15*, *16*). However, the methods of managing energy level alignment are limited to phase control of 2D perovskites (i.e., the thickness of the inorganic layers), owing to the insignificant contribution of conventional organic ligands to the density of states at the band edges in 2D perovskites (*17*).

Here, we developed a series of bulky semiconducting ligands with tunable energy levels that can form stable 2D perovskites (Fig. 1A). These π-conjugated ligands provide an opportunity for manipulating energy level alignment at 2D/3D heterojunctions through rational design of organic cations, thereby allowing more efficient hole extraction and reducing interface charge accumulation (*18*). Furthermore, the reduced energy level offset between the valence band maximum (VBM) of inorganic sheets and the highest occupied molecular orbital (HOMO) of conjugated organic layers in 2D perovskites, as well as preferable ligand packing geometry, allows more efficient hole transfer through the out-of-plane direction (*19*, *20*). This holistic energy landscape management of 2D/3D heterojunction in PSCs, together with the improved interface quality between perovskite and polymeric hole transporting layer (HTL) via π-conjugated ligands, enabled the demonstration of a remarkable power conversion efficiency (PCE) of 24.6% for poly(triarylamine) (PTAA)–based devices with n-i-p structure. The fine-tuned conjugated ligands allow more stable 2D structures and suppress interlayer ion migration, which result in improved photostability and thermal stability.

RESULTS

2D perovskite structures and properties

Our general design strategy of the ligands is tethering an ammonium anchoring group to one end of a conjugated quaterthiophene unit (*18*, *21*) and having halogen substitution on the opposite end thiophene to manipulate the HOMO levels of the molecules (*22*). The chemical structures of the synthesized organic ligands feature different substituting groups, namely, F4Tm, Cl4Tm, and Br4Tm, all of which are derived from 4Tm (Fig. 1B). The synthesis of halogen-4Tm was based on electrophilic halogenation reactions to add functional groups and Stille coupling reaction to connect all the thiophene moieties together (details of synthesis in the Supplementary Materials). All ligands were converted to iodide salts through reactions with hydroiodic acid. The halogen substituent acts as an electron-withdrawing group that deepens the HOMO level of the ligands, from −5.21 eV for 4Tm to −5.25, −5.26, and −5.25 eV for F4Tm, Cl4Tm, and B4Tm ligands, respectively (fig. S1 and table S1).

Within the 2D perovskite structures formed with these ligands, type II band alignments are formed, because of the small bandgaps and shallow HOMO levels of the conjugated ligands (Fig. 1C). The type II alignment results in quenched photoluminescence observed from these 2D perovskite thin films (fig. S2). Unlike the conventional wide-bandgap ligands that usually form type I artificial quantum

[1]Davidson School of Chemical Engineering, Purdue University, West Lafayette, IN 47907, USA. [2]Department of Chemistry, University of Kentucky, Lexington, KY 40506, USA. [3]Chemistry and Nanoscience Center, National Renewable Energy Laboratory, Golden, CO 80401, USA. [4]Department of Chemistry, Purdue University, West Lafayette, IN 47907, USA. [5]Birck Nanotechnology Center, Purdue University, West Lafayette, IN 47907, USA.
*Corresponding author. Email: dou10@purdue.edu
†These authors contributed equally to this work.

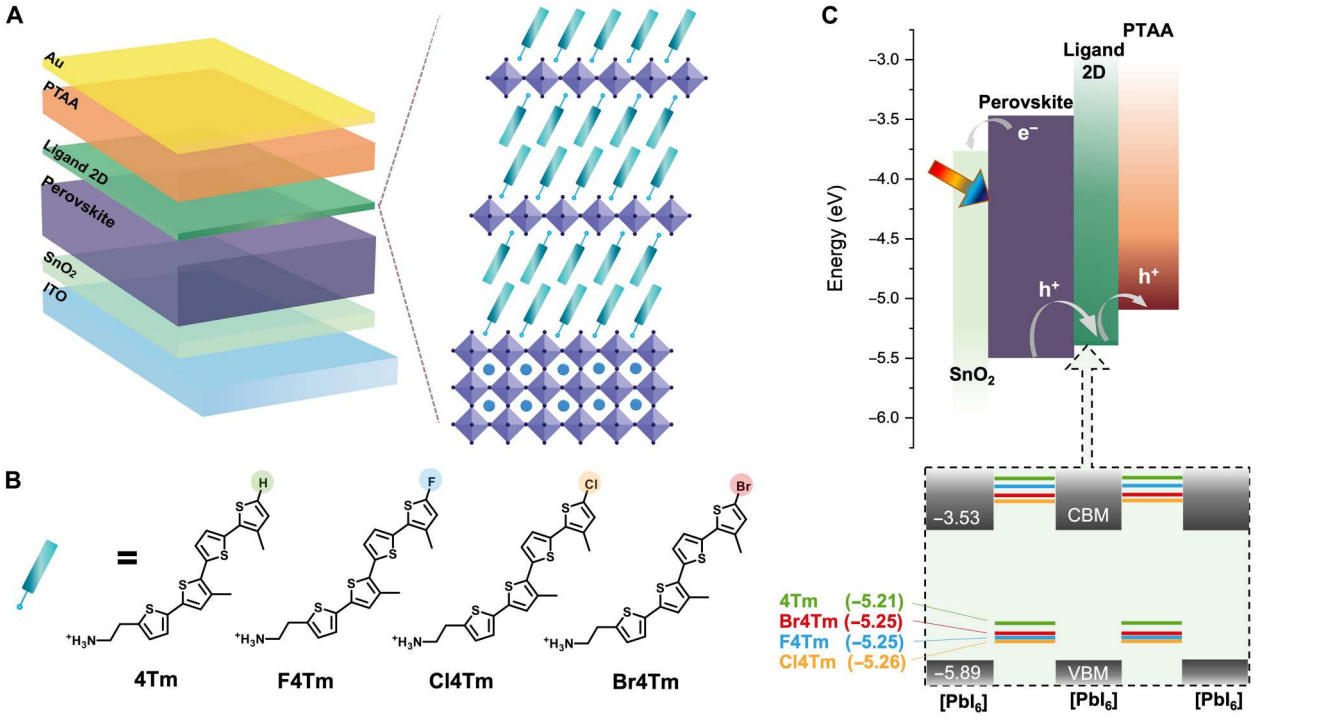

Fig. 1. Device structure and conjugated ligands design. (**A**) Schematic of device structure used in this work with a 2D perovskite layer atop of 3D perovskite. (**B**) Chemical structures of the designed conjugated molecules in the form of ammonium cations. (**C**) The schematic of band alignment of device treated with conjugated ligands. The bottom shows the band alignments within the 2D perovskite structures formed with different conjugated ligands. The energy diagram is plotted as a schematic illustration, while the accurate energy levels are labeled in the plot. CBM, conduction band minimum; ITO, indium tin oxide.

wells in 2D perovskites and generate energy barriers for out-of-plane charge transfer, the shallow HOMO levels of conjugated ligands reduce the energy barriers for hole transfer. However, the shallow HOMO level of 4Tm creates a reverse energy level offset with inorganic layers in 2D perovskites, which, in turn, can potentially trap holes. The halogen-4Tm reduces the energy level offsets, suggesting minimal energy barriers and a decreased probability of hole trapping, which, in principle, could facilitate out-of-plane hole transport within 2D perovskite structures.

Besides the energy level alignment, a strong dependence between crystal structures and electronic properties also exists in 2D perovskites (*23*, *24*). Therefore, we characterized 2D perovskites through thin-film x-ray diffraction (XRD) and single-crystal analysis to gain insights from their crystal structures. The 2D perovskite thin films can be obtained by one-step spin coating followed by thermal annealing. The XRD patterns with characteristic planes—(001), (002), (003), etc.—are different from the XRD patterns of the aggregated ligands (fig. S3), confirming the formation of layered 2D structures (Fig. 2A). The absorption spectra exhibited distinctive exitonic peaks at around 512 nm, further supporting the formation of n = 1 2D Ruddlesden-Popper phase perovskites (fig. S4). The corresponding d-spacings of $(4Tm)_2PbI_4$, $(F4Tm)_2PbI_4$, $(Cl4Tm)_2PbI_4$, and $(Br4Tm)_2PbI_4$ were calculated as 3.18, 3.28, 3.28, and 3.37 nm from the 2θ of (001) planes at 2.78°, 2.69°, 2.68°, and 2.62°, respectively, which are correlated with the increased atomic radius of H, F, Cl, and Br. Note that, although fluorine has a smaller atomic radius than chlorine, $(F4Tm)_2PbI_4$ and $(Cl4Tm)_2PbI_4$ share similar interlayer distances, which is likely due to the interplay between atomic versus electrostatic attractive and repulsive forces.

To gauge the effect of molecular configuration on intermolecular packing, we further examined the single crystals of 2D perovskites formed with different ligands (Fig. 2, B to D). Single crystals of $(Cl4Tm)_2PbI_4$ were obtained by slow-cooling method, while solvent diffusion method was applied to grow crystals of $(Br4Tm)_2PbI_4$ (details in the Supplementary Materials). For F4TmI, suitable crystal specimens for accurate single-crystal structure determination proved challenging and resulted in high R-factors, although several attempts have been made, which is probably due to the weak interactions between F4Tm layers (fig. S5). The average in-plane Pb—I—Pb bond angle is 151.6° and the Pb—I bond length is 3.17 Å (horizontal) in $(Cl4Tm)_2PbI_4$. We observed a small distance of 3.2 Å between alternating Cl—Cl atoms within two Cl4Tm layers, which indicates the existence of weak halogen interaction (considering the 1.75-Å van der Waals radius of a single chlorine atom) and could contribute to the stabilization of the structure. The $(Br4Tm)_2PbI_4$ single-crystal structure was resolved with chloroform solvent molecules trapped between the ligand layers, from which Br—Cl halogen interaction between Br4Tm and chloroform were observed because of the shortened interatom distance. Because of solvent intercalation, the inorganic lattice of $(Br4Tm)_2PbI_4$ has less distortion compared with $(Cl4Tm)_2PbI_4$, with the average in-plane Pb—I—Pb bond angle as 152.6° and Pb—I bond length as 3.14 Å (horizontal). However, part of the conjugated ligand molecules in $(Br4Tm)_2PbI_4$ crystal structure exhibit more distortion compared to $(Cl4Tm)_2PbI_4$, which could increase the formation barrier of this 2D structure (*25*).

To understand the relationship between crystal structures and the electronic properties, we applied time-resolved microwave

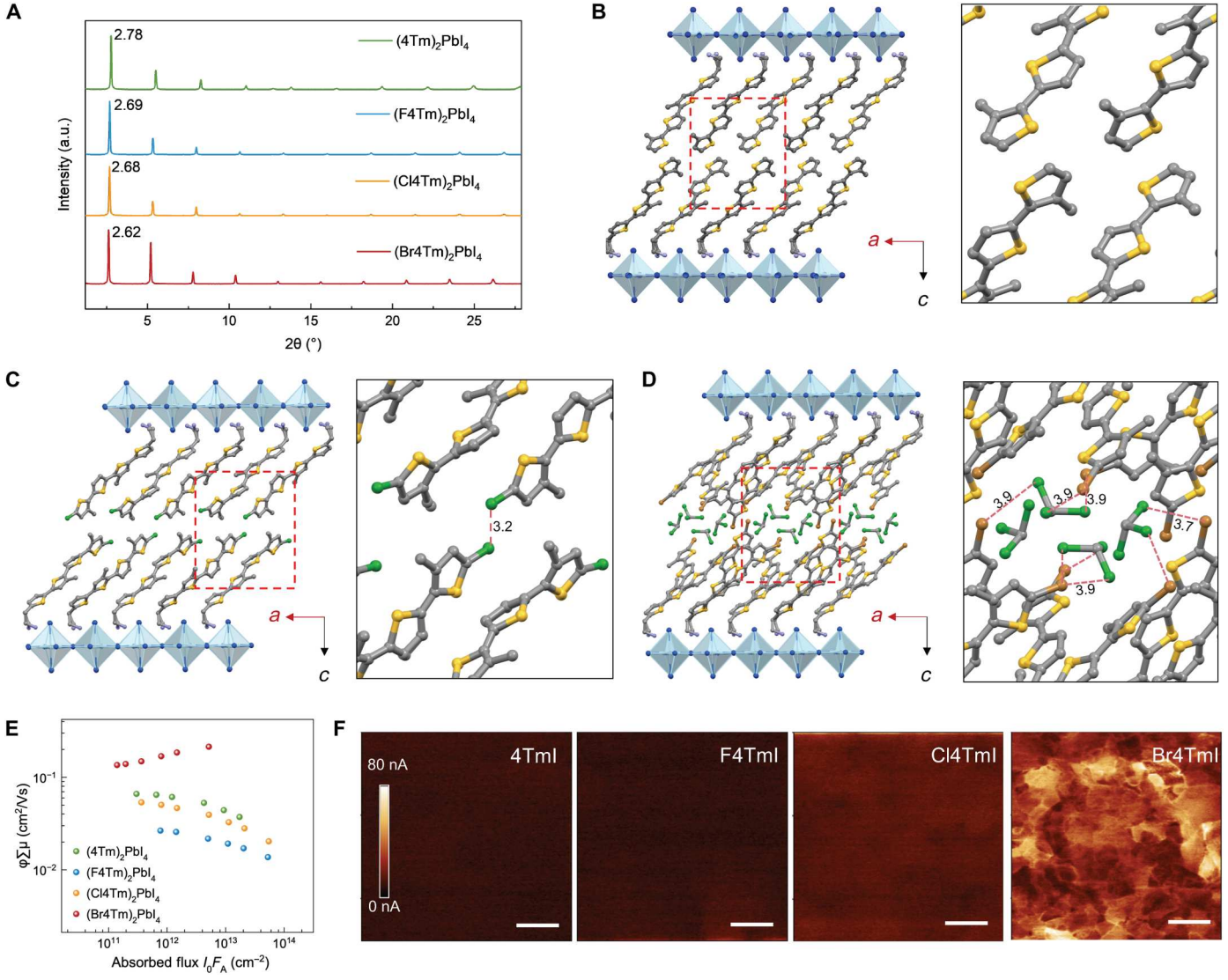

Fig. 2. Structure and conductivity of 2D perovskites. (**A**) XRD of 2D perovskite (n = 1) thin films. (**B** to **D**) Single-crystal structures of 2D perovskites with different ligands. (B) $(4Tm)_2PbI_4$. (C) $(Cl4Tm)_2PbI_4$. (D) $(Br4Tm)_2PbI_4$. The right panels of (B), (C) and (D) present the zoom-in images of ligand interactions. (**E**) TRMC comparison of out-of-plane charge transport in n = 1 2D perovskite thin films. ϕ is the carrier generation yield and μ is the mobility for carriers. (**F**) Conductive atomic force microscopy (cAFM) of 2D perovskite thin films formed with different ligands. Scale bars, 1 μm. a.u., arbitrary units.

conductivity (TRMC) measurements to characterize the out-of-plane carrier transport in 2D perovskite thin films (Fig. 2E) (*13*, *26*). The $(Br4Tm)_2PbI_4$ sample has the highest yield-mobility product, which is a factor of 2 to 4 larger than that of $(Cl4Tm)_2PbI_4$ and $(4Tm)_2PbI_4$. However, the $(F4Tm)_2PbI_4$ sample exhibits obviously lower mobility, which could be correlated with the difficulty of achieving high-quality $(F4Tm)_2PbI_4$ single crystal and the repulsion between fluorine atoms. We also performed conductive atomic force microscopy (cAFM) to examine the spatial distribution of the current path in these thin films (Fig. 2F). In agreement with the TRMC results, the $(F4Tm)_2PbI_4$ sample exhibits the lowest conductivity, while the $(Br4Tm)_2PbI_4$ sample preserves the highest conductivity. The higher out-of-plane conductivity of the $(Br4Tm)_2PbI_4$ thin film than the Cl4TmI sample has also been confirmed with single-crystal conductivity (fig. S6). The single-crystal structures show that the outer thiophenes in $(Cl4Tm)_2PbI_4$ crystals favor in-plane edge-to-edge arrangement between the neighboring Cl4Tm layers, similar to 4Tm samples, which may not support efficient charge transfer (fig. S7). In contrast, the $(Br4Tm)_2PbI_4$ crystal exhibits face-to-face ligand packing geometry, thus exhibiting higher out-of-plane conductivity (*23*, *25*, *27*, *28*). However, the cAFM images reveal that $(Br4Tm)_2PbI_4$ thin film, although having higher conductivity, has greater heterogeneity in the current path distribution, which may result from the nonuniform crystallinity and the potential higher formation energy of this 2D structure.

2D/3D heterostructure formation and characterization

We then investigated the formation of 2D/3D heterostructures on the surface of 3D perovskites for photovoltaic devices. The 2D structures were formed by means of coating the corresponding ligand

solution on the surface of 3D perovskite, followed by thermal annealing. To enhance the 2D perovskite signal for XRD characterization, we extended the reaction time between 3D perovskite and the ligands by dropping the ligand solutions and waiting for 60 s before spinning. The thin-film XRD suggests that $n = 1$ 2D structures form with all the investigated ligands, as evidenced by the diffraction peaks at low angles (<10°) (Fig. 3A), which match with the peaks from pure 2D perovskite thin films. The minor shift of the low-angle peaks from pure 2D perovskites to the 2D/3D heterostructures may be induced by the slight lattice distortion caused by 2D/3D interfacial strain. Only the $n = 1$ phase is formed on the surface with horizontal orientation, while high-n number phases are absent for all ligands investigated. We ascribe the stability of 2D structures, the rigidity of the ligands, and their unlikely penetration into the 3D structure due to steric bulk, all as factors that prevent formation of other phases during the treatment. The exclusive formation of $n = 1$ phase in 2D/3D junctions distinguishes these ligands from conventional small ligands and eliminates the influence of phase impurity in the surface characterizations. The AFM images indicate the unchanged surface morphology of perovskite with short-time ligand treatment (fig. S8). The x-ray photoelectron spectroscopy (XPS) conducted on ligand-treated 3D perovskite thin films demonstrates the existence of oligothiophene ligands on the 3D perovskite surface from the peaks of S 2p at 164 eV (fig. S9). Moreover, the characteristic peaks of F 1s (687 eV), Cl 2p (202 eV), and Br 3d (71 eV) show up in the XPS results of F4TmI, Cl4TmI, and Br4TmI thin films, respectively, which belong to the terminal substituents of the corresponding ligands.

We proposed to modulate the surface potential and 2D/3D band alignment via rational design of ligand molecular configurations. Through ultraviolet photoelectron spectroscopy (UPS) measurements (Fig. 3B), we verified that ligand treatment upshifts the VBM in comparing with the control film (untreated), based on the aligned Fermi level, which is induced by the shallower HOMO levels of the conjugated ligands (fig. S10 and table S2). The upshifted VBM generates a more p-type surface, which is expected to facilitate efficient hole transfer from perovskite to PTAA (with a reported HOMO at −5.2 eV) (*21*). The shallow HOMO levels of these conjugated ligands also allow them to directly extract holes from 3D perovskites, which is verified by time-resolved photoluminescence (TRPL) measurement with a biexponential decay and fast hole extraction process within 20 ns (fig. S11).

The work functions (WFs) have also been extracted from UPS measurements, which show notable differences between 4TmI and halogen-4TmI treatment. The 4TmI treatment notably reduces WF to 3.82 eV from the 4.22 eV of the control film. In contrast, the reduction of WF is smaller when halogen substitutions are introduced, showing less than 0.1-eV changes (Fig. 3B and table S2). Kelvin probe force microscopy (KPFM) measurements revealed WF distribution differences at the ligand-treated surfaces (Fig. 3C). The average WF of 4TmI-treated surface reduced to 4.18 eV from 4.76 eV for the control film, while the change of WF of the halogen-4TmI–treated surface was negligible (Fig. 3D), which is in accordance with the trend observed in UPS analysis.

The band alignment formed with 4TmI surface treatment showed that the perovskite surface has shallower VBM compared with the bulk material, but a negative ΔWF could generate a

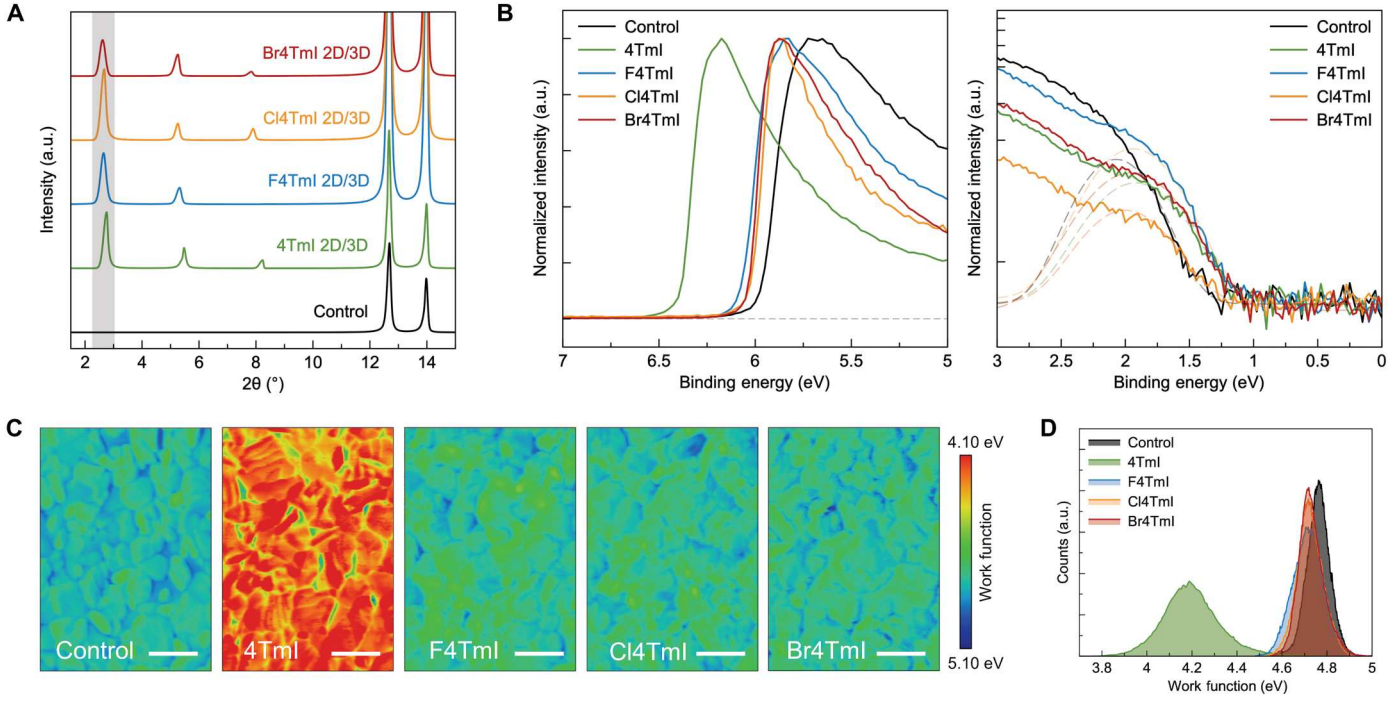

Fig. 3. Formation of 2D/3D heterojunction and surface energetic characterization. (**A**) XRD patterns of 3D perovskite thin films without and with surface treatment. (**B**) Ultraviolet photoelectron spectroscopy (UPS) results of various surface treatments. Left: Secondary cut-off region; right: on-set region (light source of 10.2 eV). (**C**) Kelvin probe force microscopy (KPFM) surface potential maps of perovskite thin films with different surface treatments. Scale bars, 2 μm. (**D**) Work function distribution extracted from KPFM results.

potential well at the interface of the 2D/3D heterostructure and trap the electrons (fig. S11). Unlike the downshifted VBM of other 2D/3D heterostructures formed with wide-bandgap ligands, the hole transfer benefits from the upshifted VBM of perovskite surface with conjugated ligands. However, the trapped and accumulated electrons at perovskite/HTL interface can cause charge trapping–induced defects (*4*, *29*). In comparison, the 2D/3D heterostructures formed with halogen-4TmI cause minimum WF shift, thus being unlikely to create a deep potential well at interfaces. The reduced charge-trapping defects in halogen-4TmI–treated films are evidenced by the enhanced photoluminescence (PL) intensities with a film structure of glass/3D perovskite/2D perovskite (fig. S12). The reduced bimolecular recombination was further affirmed with intensity-dependent photoconductivity transient characterization from TRMC measurements (fig. S13).

In addition, benefitted from the exceptional out-of-plane transport of the $n = 1$ 2D perovskite structures containing Cl4TmI and Br4TmI, the coverage of 2D perovskite atop of 3D thin films does not decrease the carrier mobility (fig. S14), which further indicates that the enhanced out-of-plane charge transport in 2D perovskites is critical to reduce charge transfer barriers at the 2D/3D heterojunction. The cAFM results even suggest slightly higher conductivity in Cl4TmI-treated films than that in Br4TmI samples (fig. S15), which we attribute to the different formation energy of 2D/3D heterojunction with different ligands.

Carrier dynamics and device performance

We investigated the impact of these 2D/3D heterostructures on the photovoltaic performance by fabricating the PSCs using an n-i-p device architecture, ITO/SnO_2/perovskite/PTAA/Au, with different surface ligand treatments. In agreement with our analysis, the Cl4TmI and Br4TmI surface treatment results in remarkably enhanced PCE, which outperformed the devices treated with 4TmI and F4TmI. A typical set of *J-V* curves of devices fabricated with different ligands is shown in Fig. 4A. The nonideal energy alignment of 4TmI and the unstable 2D crystal structure and low conductivity of $(F4Tm)_2PbI_4$ are the limiting factors of these two ligands. Comparing with Cl4TmI, slightly less improvement with Br4TmI treatment was achieved, which could correspond to the different conductivity of the 2D/3D heterostructure formed with Cl4TmI and Br4TmI, as well as the heterogeneity of conductivity distribution in $(Br4Tm)_2PbI_4$ thin film. To verify the reproducibility of the results, we provide the statistics for at least 38 devices of each condition (Fig. 4B and fig. S16). Furthermore, we compared our conjugated ligands to the devices passivated with butylammonium iodide and phenethylammonium iodide (fig. S17). Neither of these commonly used ligands was able to produce comparable PCEs as Cl4TmI and Br4TmI, which suggests the critical role of the semiconducting ligands in 2D/3D heterostructures. In addition to the $FA_{0.9}MA_{0.05}Cs_{0.05}PbI_3$ perovskite composition, we also investigated the effect of Cl4TmI surface treatment on PSCs with a composition of double halide ($FA_{0.88}MA_{0.07}Cs_{0.05}PbI_{2.89}Br_{0.11}$) and also found an increase in PCE (fig. S18).

Note that we focused on PTAA doped with a hydrophobic Lewis acid as HTL, because it is considered as a more stable hole transporting material than Spiro-OMeTAD and does not need lithium salt for efficient doping, which eliminates a degrading factor of $FAPbI_3$. In addition, PTAA is known to be less sensitive to processing conditions with no air aging requirement and leads to devices with better reproducibility. However, the limiting factor of the application of PTAA is the interface quality with perovskite, leading to low PCE values in conventional devices (*30*). Here, the designed conjugated ligands increase the hydrophobicity of perovskite surface (fig. S19), forming perfect atomic registry to the perovskite lattice, and share similar aromaticity and improve the interface contact between perovskite and PTAA. This critical interface supports efficient hole transfer and results in increased open circuit voltage (V_{OC}) and fill factor (*FF*). With further optimization of ligand concentrations and passivation procedures (figs. S20 to S23), and together with an antireflection layer coating, a champion device with a PCE of 24.63% was achieved through Cl4TmI treatment (V_{OC} = 1.125 V, *FF* = 84.32%, short circuit current density (J_{SC}) = 25.96 mA/cm^2) with small hysteresis comparing with control device (Fig. 4C and fig. S24), which is the highest reported PCE among PTAA-based PSCs to the best of our knowledge (*31*–*33*). A stabilized power output of 24.45% was also measured at maximum power point (Fig. 4C), and the external quantum efficiency (EQE) spectrum was confirmed with an integrated J_{SC} of 25.5 mA/cm^2 (fig. S25). The reproducibility of PTAA-based devices with our strategy has also been demonstrated by showing the small deviation from person-to-person variations of four different researchers (fig. S26).

We further conducted space-charge–limited current (SCLC) to probe the hole mobilities in the hole-only devices (Fig. 4D). Devices treated with different conjugated ligands all exhibit almost two orders of magnitude increase in hole mobility compared with the control device, which highlights the critical role of interface treatment in improving the interface contact between perovskite and PTAA and enhancing charge transport efficiency (table S3) (*34*, *35*). Note that, although the F4TmI-treated perovskite thin film exhibits lower mobility than the control film by TRMC, the F4TmI device still shows higher hole mobility than the control device, further supporting the notion that the PTAA/perovskite interface is the major bottleneck at the device level. In addition, the trap densities extracted from the trap-filled limit voltage (V_{TFL}) in SCLC plots indicate reduced defect density in ligand-treated devices (table S3) (*36*). TRPL measurements on samples with a structure of glass/perovskite/ligand/PTAA were used to assess the defect densities at interfaces and the charge extraction processes (Fig. 4E and table S4). Ligand-treated films, benefitting from the gradient energy level alignment, exhibit faster charge extraction, as indicated by the fast decay of PL at initial stage. In the second stage of the biexponential decay, the PL lifetime is dominated by defect-induced monomolecular recombination. The lifetime of Cl4TmI-treated perovskite is 20.65 ns, two times higher than the 9.34 ns of the control sample that is correlated with the decreased defect density and increased V_{OC} with surface passivation (*37*, *38*). The suppressed mobile ions in Cl4TmI-treated devices were further evidenced by the capacitance-frequency profiles of the device compared with the control device (fig. S27). The decreased capacitance at a low-frequency region (<100 Hz) in the Cl4TmI-treated device reveals less-mobile ion response, which is correlated with the suppressed defect density at the surface (*39*). The tuned energy level alignment of perovskite surface not only results in efficient charge transfer but also affects the built-in potential (V_{bi}). The Mott-Schottky plot analysis of ligand-treated devices reveals higher V_{bi} compared with that of control device, which is induced by the proper band alignment and the efficient hole extraction, among which Cl4TmI device exhibits

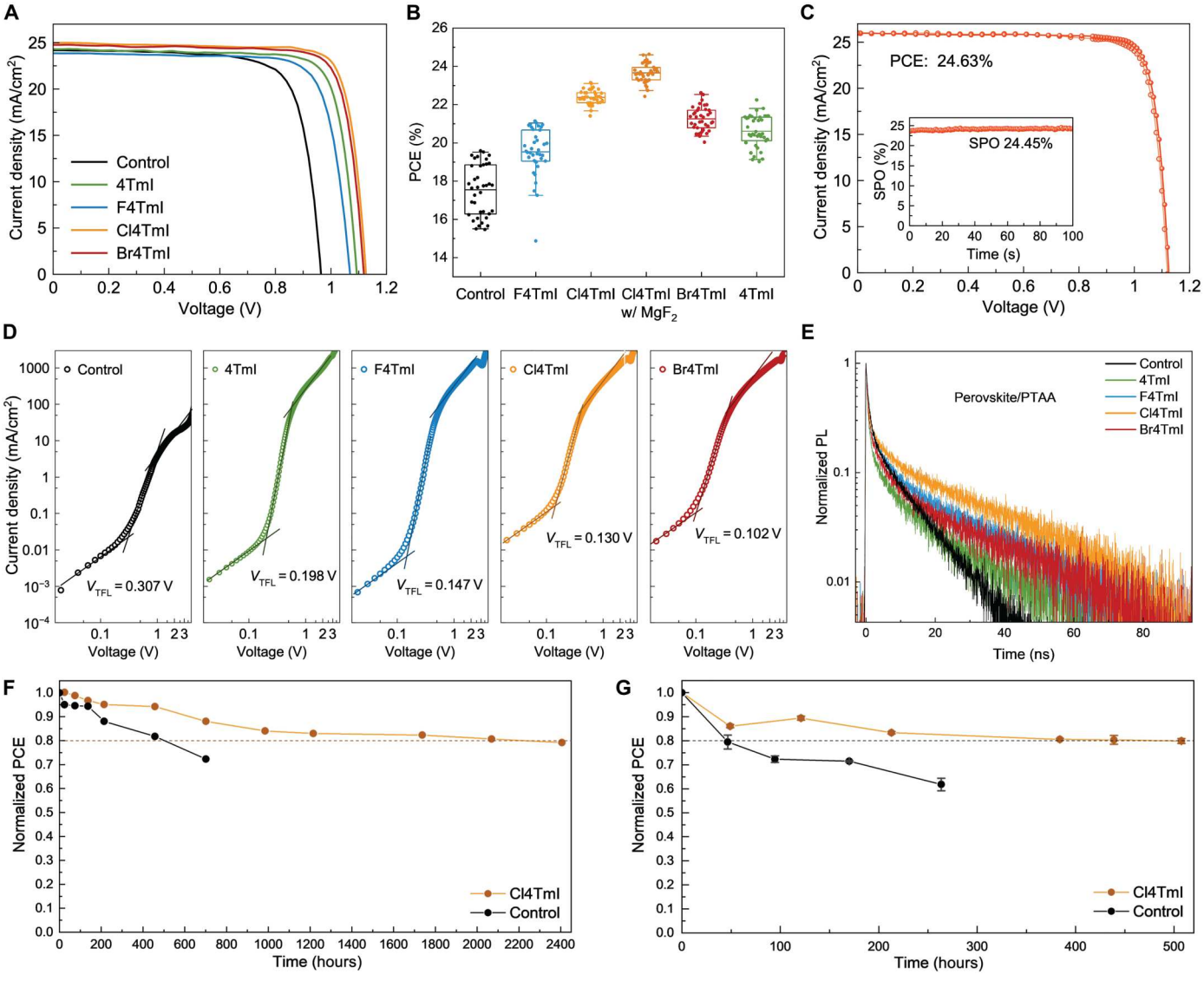

Fig. 4. Device performance and carrier dynamics. (**A**) *J-V* characteristics of PSCs based on different surface treatments. (**B**) Statistics showing the PCE distribution of the devices with different treatments. (**C**) *J-V* characteristic of the champion device with reverse (solid dot) and forward (open dot) scans. Inset: SPO (stabilized power output) of the corresponding device. (**D**) Space-charge–limited current (SCLC) characteristics of the hole-only devices treated with different ligands. (**E**) TRPL spectra of the glass/perovskite/PTAA films with different ligand treatments between perovskite and PTAA. (**F**) Long-term stability of PSCs tested at 65°C under N_2 environment. The initial PCE of Cl4Tm and control devices are 20.9 and 17.5%, respectively. (**G**) Photostability tracking under the open-circuit condition of PSCs without and with Cl4TmI treatment. The measurement was performed in the N_2-filled glovebox with encapsulation. The initial PCE of Cl4TmI and control devices are 21.3 and 18.3%, respectively.

the highest V_{bi} (fig. S28 and table S5). In addition, the improved energy level alignment also reduces the energy barriers for charge injection when the device is operated as a light-emitting diode (LED) and results in an electroluminescence EQE of 4.6% (fig. S29). This strategy is generically applicable to multiple small molecular and polymeric HTL materials with remarkably improved performance (fig. S30), representing a critical design element for future PSC interfacial engineering.

Last, we tracked the thermal stability of the unencapsulated devices at 65°C under N_2 environment (Fig. 4F). The device treated with Cl4TmI maintained 80% of its initial efficiency after 2220 hours of heating, while the PCE of the control device dropped by 20% within 640 hours, showing only one-third of T_{80} lifetime compared with the Cl4TmI-treated device. The improved thermal stability is benefitted from the inhibition of ion migration at interface with the 2D layer modification, characterized with time-of-flight secondary ion mass spectrometry (TOF-SIMS) (fig. S31). We also checked the photostability of the encapsulated device under continuous illumination at an open-circuit condition in N_2 environment (Fig. 4G). The photogenerated charge carriers are unextractable under an open-circuit condition and can accumulate at interfaces, accelerating the degradation process. The Cl4TmI-treated device exhibits 20% relative efficiency drop after 507 hours, while the control device decreased to 80% of its initial efficiency within 50 hours. In addition, the Cl4TmI-treated device maintained 80% of its initial PCE after 496 hours of continuous

operation under illumination using maximum power point tracking under N_2 environment with temperature around 45°C (fig. S32).

DISCUSSION

We present the pivotal role of organic molecular design in holistically manipulating the physical and energy landscapes to reduce charge transfer barriers and defects at 3D/2D/HTL heterointerfaces. The synergistic impact of tunable energy levels and molecular packing geometry of conjugated ligands in 2D structures facilitates efficient out-of-plane charge transport in 2D perovskites, while the manageable energy alignment at 2D/3D heterojunction supports charge extraction in device level. Our strategy of molecular engineering enabled us to demonstrate a remarkable PCE of 24.6% for n-i-p PSCs based on PTAA HTLs, addressing long-standing interfacial issues in PTAA-based devices.

MATERIALS AND METHODS

Materials

SnO_2 (15% colloidal solution) was purchased from Alfa Aesar. PTAA was purchased from 1-Material. 4-Isopropyl-4′-methyldiphenyliodonium tetrakis(pentafluorophenyl)borate (TPFB) was purchased from TCI. PbI_2 (99.9999% perovskite grade), CsI, KOH, polyethylenimine (80% ethoxylated solution) (PEIE), 2,5-bis(tributylstannyl)thiophene, 2-bromo-3-methylthiophene, tris(dibenzylideneacetone)dipalla-dium(0), tri(*o*-tolyl)phosphine, *n*-butyl lithium, *N*-fluorobenzenesulfonimide, tetrabutylammonium hexafluorophosphate ($TBAPF_6$), lithium diisopropylamide, and tributyltin chloride were purchased from Sigma-Aldrich. Formamidinium iodide, methylammonium iodide, methylammonium chloride, and methylammonium bromide were purchased from Greatcell Solar. Chlorobenzene, dimethylformamide (DMF), dimethyl sulfoxide (DMSO), and iso-propanol (IPA) are all anhydrous and were purchased from Sigma-Aldrich.

2D perovskite single-crystal growth

The $(Cl4Tm)_2PbI_4$ single crystal was obtained by slow cooling method. Two milligrams of Cl4TmI, 5 mg of PbI_2, 200 μl of 57 wt % (weight %) of hydroiodic acid (HI) solution, and 100 μl of H_3PO_2 were added to 1 ml of ethanol. The mixture was heated at 100°C until dissolved and then the solution was slowly cooled to room temperature over the course of 60 hours. By filtration and ethanol wash, orange needle–like single crystals were collected.

The $(Br4Tm)_2PbI_4$ single crystal was obtained by solvent diffusion method. A total of 0.01 M Br4TmI and 0.005 M PbI_2 were dissolved in gamma-butyrolactone at 70°C overnight. After dissolution, 0.1 ml of the precursor solution in a small vial was placed in a large vial with 3 ml of chloroform as antisolvent. Orange plate–like crystals precipitated out after 3 days. The crystallization process was conducted at room temperature in atmosphere.

2D perovskite film fabrication

Glass slides were cleaned using soap water, water, acetone, and isopropanol for 15 min in ultrasonic bath; dried with a nitrogen gun; and then were used as substrates for 2D perovskite thin-film fabrication. The clean substrates were treated with UV Ozone cleaner for 20 min before use. The precursor solution (200 μl) for spin-coating was prepared by dissolving 0.2 M ligands and 0.1 M PbI_2 in dry DMF/DMSO (in 4/1 ratio) at 70°C. For spin-coating, 20 μl of precursor solution was used with a spin speed at 2000 rpm for 30 s. In the end, as-prepared thin films were transfer to a heating plate to anneal at 100° to 200°C for 10 min. The above precursor solution preparation, spin,-coating and thermal annealing processes were conducted in a N_2 glove box.

PSC fabrication

The ITO/glass substrates were cleaned extensively with deionized water, acetone, and isopropanol. The cleaned substrates were UVO treated for 30 min before using. SnO_2 (15 wt%) stock solution was diluted with IPA:H_2O (v/v = 1:1) to 2.14%, and then 0.61% polyethylenimine ethoxylated (PEIE) solution was added to the SnO_2 solution. The SnO_2 solution was spun-coated onto the ITO substrate at 3000 rpm, followed by annealing at 150°C for 30 min. After UVO treating the SnO_2 surface for 10 min, 10 mM KOH solution was coated on to the substrate at 3000 rpm, followed by another annealing at 150°C for 30 min. The SnO_2 substrates were UVO treated for 10 min before transferred into the glovebox to conduct the following process. The perovskite film was coated on SnO_2 substrate with a two-step method. In the first step, the PbI_2 solution (691.5 mg of PbI_2, 19.5 mg of CsI, 900 μl of DMF, and 100 μl of DMSO) was spun-coated onto the substrate at 1500 rpm for 30 s, followed by annealing at 70°C for 1 min. After cooling down, the cation solution (90 mg of FAI, 5 mg of MAI, 10.8 mg of MACl, and 1 ml of IPA) was coated on the PbI_2 film at 1500 rpm for 30 s, followed by annealing at 150°C for 15 min under ambient environment (50 to 70% relative humidity). For $FA_{0.88}MA_{0.07}Cs_{0.05}PbI_{2.89}Br_{0.11}$ devices, the composition of cation solution changed to 90 mg of FAI, 3.2 mg of MABr, and 10.8 mg of MACl in 1 ml of IPA. The perovskite film was then transferred back to an N_2-filled glovebox for ligand and HTL coating. The conjugated ligands were dissolved in a mixture of chlorobenzene and isopropanol (9:1 v/v) with a concentration of 0.5 mg/ml. Because of the properties of oligothiophene ammonia iodide salt, a mixture of polar solvent and nonpolar solvent was selected for better solubility. The concentration of the ligand solution was optimized on the basis of its solubility and influence on device performance. For ligand-treated devices, the ligand solution was coated on perovskite surface at 4000 rpm, followed by annealing at 100°C for 2 min. PTAA HTL was prepared in chlorobenzene solution (30 mg/ml), doped with 11% TPFB. The doped PTAA solution was stirred at 45°C overnight to ensure full dissolving and doping of PTAA. TPFB, a hydrophobic Lewis acid, is selected here as the dopant to avoid the incorporation of small mobile Li^+ into the system while maintaining the hole mobility of PTAA. PTAA solution was spun on perovskite film at 4000 rpm for 30 s, followed by annealing at 80°C for 5 min. Last, 90 nm of gold was evaporated onto the device with shadow mask to determine the device area. For champion devices, 105 nm of MgF_2 was evaporated on to the glass substrate as an antireflection layer. Four pixels are made on each device substrates, and more than 10 batches of devices were fabricated to confirm the reproducibility.

Chemical characterization

NMR spectra were collected using a Bruker AV-III-400-MHz spectrometer. The cyclic voltammetry was completed with a CHI660 electrochemical analyzer. The working electrode is a glassy carbon, and the counter electrode is a Pt wire. Ag/AgCl is the

reference electrode, and the electrolyte is 0.1 M $TBAPF_6$, 1 mM ligand in dry dichloromethane. The measurement was conducted at a scan rate of 40 mV/s under a N_2-purged environment. Ferrocene was added to the electrolyte to calibrate the reference electrode.

Thin film characterization

The 2D/3D thin films used for characterizations were prepared with the same methods used in device fabrication, unless otherwise noted. The thin-film XRD patterns were characterized with a Rigaku Smart Lab equipped with a Cu Kα source (λ = 1.54056 Å). The 2D layer formed on top of 3D thin films used for XRD characterization was prepared by allowing the ligand solution (0.5 mg/ml) to stay on the surface of 3D thin films for an extended time before spun off. Steady-state PL spectra were measured using a SpectraPro HRS-300. TRPL spectra were collected using a time-correlated single-photon counting apparatus (PicoQuant) with a picosecond pulsed laser at 447 nm as the excitation source. The water contact angle image was captured with Ramé-hart Model 200. Fractional absorptance was measured inside a Cary 6000i integrating sphere center-mounted sample holder to account for diffuse and specular scatter off the film and quartz substrate independently from absorption of photons by each film.

All TRMC measurements on the 3D/2D perovskite films were recorded at 650-nm excitation, over one order of magnitude in excitation power at the lowest fluence limit, while continuously purging the microwave cavity with dry nitrogen. For the n = 1 2D perovskite films, 512 nm was used as the excitation wavelength, with over two orders of magnitude in power. The pulse width of the 10-Hz excitation beam is approximately 5 ns, and photoconductivity transients were recorded over a 500-ns time window for all samples. Fractional absorptance was used to quantify the TRMC yield-mobility product data.

The UPS characterization was conducted with an H Lyman-α photon source (E-LUX 121), which emits photon energy of 10.2 eV, and the electrons were detected with a 5.85-eV pass energy using a multichannel plate detector and a hemispherical electron energy analyzer while the perovskite samples were biased at −5 V. The XPS measurements were performed with the same PHI 5600 ultrahigh vacuum system and used an Al Kα source (1486.6 eV; PHI 04-548 dual-anode x-ray source) for excitation.

Both the KPFM and cAFM images were obtained using the Asylum Research Cypher ES Environmental AFM in the air. The samples for KPFM and cAFM measurements were prepared on ITO/glass substrates as conductive substrates, and the AFM tips used during the measurement were Ti/Pt-coated AC240TM-R3 tips (Oxford Instruments). All the KPFM measurements were conducted with the same tip and repetitively checked with another tip. In addition, during each KPFM measurement, the perovskite sample was electrically grounded with a conductive sample holder, which allows the surface potential of all the samples having the same zero point. For cAFM, all the measurements were conducted in the dark. Both the 2D thin-film samples and 2D single-crystal samples were biased at 3 V, while the 3D perovskite thin films treated with different ligands were biased at 0.8 V. The 2D single-crystal samples were transferred on to the substrates through tape-peeling method.

Positive high–mass resolution depth profile was performed using a TOF-SIMS NCS instrument, which combines a TOF.SIMS5 instrument (ION-TOF GmbH, Münster, Germany) and an in situ scanning probe microscope (NanoScan, Switzerland) at the Shared Equipment Authority from Rice University.

Device characterization

The *J-V* curve characteristics were performed with simulated AM1.5G irradiation (100 mW/cm^2), produced by a Xenon lamp–based solar simulator (Enlitech, SS-F5-3A). The light intensity was calibrated with Si reference cell certified by National Renewable Energy Laboratory (NREL). The active area was defined by Au electrode and was measured under a microscope (around 0.05 cm^2). The voltage scan was conducted under both reverse scan (1.2 to −0.1 V) and forward scan (−0.1 to 1.2 V). The voltage step is 40 mV from −0.1 to 0.8 V and 10 mV from 0.8 to 1.2 V. The devices were measured in a nitrogen-filled glovebox. The EQE results were collected at zero bias under an ambient environment on a home-built equipment using a preamplifier and a lock-in amplifier at a chopper frequency of around 161 Hz. The light source was calibrated with a reference Si (818-UV-L) diode. The SCLC characterization was performed with hole-only devices (ITO/PEDOT:PSS/perovskite/PTAA/Au), and the voltage was scanned from 0 to 5 V with step size of 20 mV under a dark condition. The hole mobilities were calculated by fitting the curve using Mott-Gurney law in Child's regime with the following equation

$$J = \frac{9\varepsilon_0\varepsilon_r\mu V^2}{8L^3}$$

where ε_0 is the vacuum permittivity, ε_r (i.e., 25) is the relative dielectric constant, μ is the charge mobility, V is the applied voltage, L is the thickness of perovskite (700 nm), and J is the current density.

The defect density was calculated on the basis of the following equation

$$\frac{N_t = 2\varepsilon_0\varepsilon_r V_{TFL}}{qL^2}$$

where V_{TFL} is the onset voltage of the trap filled limit region and q is the elemental charge.

The capacitance-frequency measurements were performed at a frequency range of 1000 kHz to 100 mHz using a VersaSTAT electrochemical workstation (Ametek). The devices were measured with zero direct voltage bias and a sinusoidal perturbation of 20 mV. The Mott-Schottky analysis was performed on the same equipment at fixed frequency (10 kHz) with a scan from 0 to 1.2 V.

Device stability measurement

For maximum power point stability test, the unencapsulated devices were exposed under continuous LED light source under N_2 environment. The devices were biased with a voltage corresponding to their maximum power point, and the current was continuously tracked. For open-circuit stability test, the encapsulated devices were exposed under continuous LED light source under N_2 environment. All the stability tests were performed without temperature control, and the device temperature was around 45°C. For thermal stability test, the devices were located on a hot plate with designated temperature under N_2 environment.

Supplementary Materials

This PDF file includes:

Supplementary Text

Figs. S1 to S32
Tables S1 to S7
References

REFERENCES AND NOTES

1. M. Grätzel, The rise of highly efficient and stable perovskite solar cells. *Acc. Chem. Res.* **50**, 487–491 (2017).
2. H. Min, D. Y. Lee, J. Kim, G. Kim, K. S. Lee, J. Kim, M. J. Paik, Y. K. Kim, K. S. Kim, M. G. Kim, T. J. Shin, S. I. Seok, Perovskite solar cells with atomically coherent interlayers on SnO_2 electrodes. *Nature* **598**, 444–450 (2021).
3. Y. Zhao, Z. Qu, S. Yu, T. Shen, H. Deng, X. Chu, X. Peng, Y. Yuan, X. Zhang, J. You, Inactive $(PbI_2)_2RbCl$ stabilizes perovskite films for efficient solar cells. *Science* **377**, 531–534 (2022).
4. S. Tan, T. Huang, I. Yavuz, R. Wang, T. W. Yoon, M. Xu, Q. Xing, K. Park, D.-K. Lee, C.-H. Chen, R. Zheng, T. Yoon, Y. Zhao, H.-C. Wang, D. Meng, J. Xue, Y. J. Song, X. Pan, N.-G. Park, J.-W. Lee, Y. Yang, Stability-limiting heterointerfaces of perovskite photovoltaics. *Nature* **605**, 268–273 (2022).
5. Y. Wang, I. Ahmad, T. Leung, J. Lin, W. Chen, F. Liu, A. M. C. Ng, Y. Zhang, A. B. Djurišić, Encapsulation and stability testing of perovskite solar cells for real life applications. *ACS Mater. Au.* **2**, 215–236 (2022).
6. R. Wang, M. Mujahid, Y. Duan, Z. K. Wang, J. Xue, Y. Yang, A review of perovskites solar cell stability. *Adv. Funct. Mater.* **29**, 1808843 (2019).
7. Q. Jiang, J. Tong, Y. Xian, R. A. Kerner, S. P. Dunfield, C. Xiao, R. A. Scheidt, D. Kuciauskas, X. Wang, M. P. Hautzinger, R. Tirawat, M. C. Beard, D. P. Fenning, J. J. Berry, B. W. Larson, Y. Yan, K. Zhu, Surface reaction for efficient and stable inverted perovskite solar cells. *Nature* **611**, 278–283 (2022).
8. Q. Jiang, Y. Zhao, X. Zhang, X. Yang, Y. Chen, Z. Chu, Q. Ye, X. Li, Z. Yin, J. You, Surface passivation of perovskite film for efficient solar cells. *Nat. Photonics* **13**, 460–466 (2019).
9. Z. Wang, Q. Lin, F. P. Chmiel, N. Sakai, L. M. Herz, H. J. Snaith, Efficient ambient-air-stable solar cells with 2D–3D heterostructured butylammonium-caesium-formamidinium lead halide perovskites. *Nat. Energy* **2**, 17135 (2017).
10. Y.-W. Jang, S. Lee, K. M. Yeom, K. Jeong, K. Choi, M. Choi, J. H. Noh, Intact 2D/3D halide junction perovskite solar cells via solid-phase in-plane growth. *Nat. Energy* **6**, 63–71 (2021).
11. F. Zhang, H. Lu, J. Tong, J. J. Berry, M. C. Beard, K. Zhu, Advances in two-dimensional organic-inorganic hybrid perovskites. *Energ. Environ. Sci.* **13**, 1154–1186 (2020).
12. J. J. Yoo, G. Seo, M. R. Chua, T. G. Park, Y. Lu, F. Rotermund, Y.-K. Kim, C. S. Moon, N. J. Jeon, J.-P. Correa-Baena, V. Bulović, S. S. Shin, M. G. Bawendi, J. Seo, Efficient perovskite solar cells via improved carrier management. *Nature* **590**, 587–593 (2021).
13. F. Zhang, S. Y. Park, C. Yao, H. Lu, S. P. Dunfield, C. Xiao, S. Uli˘ná, X. Zhao, L. D. Hill, X. Chen, X. Wang, L. E. Mundt, K. H. Stone, L. T. Schelhas, G. Teeter, S. Parkin, E. L. Ratcliff, Y.-L. Loo, J. J. Berry, M. C. Beard, Y. Yan, B. W. Larson, K. Zhu, Metastable Dion-Jacobson 2D structure enables efficient and stable perovskite solar cells. *Science* **375**, 71–76 (2022).
14. S. Sidhik, Y. Wang, M. De Siena, R. Asadpour, A. J. Torma, T. Terlier, K. Ho, W. Li, A. B. Puthirath, X. Shuai, A. Agrawal, B. Traore, M. Jones, R. Giridharagopal, P. M. Ajayan, J. Strzalka, D. S. Ginger, C. Katan, M. A. Alam, J. Even, M. G. Kanatzidis, A. D. Mohite, Deterministic fabrication of 3D/2D perovskite bilayer stacks for durable and efficient solar cells. *Science* **377**, 1425–1430 (2022).
15. H. Chen, S. Teale, B. Chen, Y. Hou, L. Grater, T. Zhu, K. Bertens, S. M. Park, H. R. Atapattu, Y. Gao, M. Wei, A. K. Johnston, Q. Zhou, K. Xu, D. Yu, C. Han, T. Cui, E. H. Jung, C. Zhou, W. Zhou, A. H. Proppe, S. Hoogland, F. Laquai, T. Filleter, K. R. Graham, Z. Ning, E. H. Sargent, Quantum-size-tuned heterostructures enable efficient and stable inverted perovskite solar cells. *Nat. Photonics* **16**, 352–358 (2022).
16. R. Azmi, E. Ugur, A. Seitkhan, F. Aljamaan, A. S. Subbiah, J. Liu, G. T. Harrison, M. I. Nugraha, M. K. Eswaran, M. Babics, Y. Chen, F. Xu, T. G. Allen, A. U. Rehman, C.-L. Wang, T. D. Anthopoulos, U. Schwingenschlögl, M. De Bastiani, E. Aydin, S. De Wolf, Damp heat–stable perovskite solar cells with tailored-dimensionality 2D/3D heterojunctions. *Science* **376**, 73–77 (2022).
17. J. Xue, R. Wang, X. Chen, C. Yao, X. Jin, K.-L. Wang, W. Huang, T. Huang, Y. Zhao, Y. Zhai, D. Meng, S. Tan, R. Liu, Z.-K. Wang, C. Zhu, K. Zhu, M. C. Beard, Y. Yan, Y. Yang, Reconfiguring the band-edge states of photovoltaic perovskites by conjugated organic cations. *Science* **371**, 636–640 (2021).
18. Y. Gao, E. Shi, S. Deng, S. B. Shiring, J. M. Snaider, C. Liang, B. Yuan, R. Song, S. M. Janke, A. Liebman-Peláez, P. Yoo, M. Zeller, B. W. Boudouris, P. Liao, C. Zhu, V. Blum, Y. Yu, B. M. Savoie, L. Huang, L. Dou, Molecular engineering of organic–inorganic hybrid perovskites quantum wells. *Nat. Chem.* **11**, 1151–1157 (2019).
19. H. Tsai, R. Asadpour, J.-C. Blancon, C. C. Stoumpos, J. Even, P. M. Ajayan, M. G. Kanatzidis, M. A. Alam, A. D. Mohite, W. Nie, Design principles for electronic charge transport in solution-processed vertically stacked 2D perovskite quantum wells. *Nat. Commun.* **9**, 2130 (2018).
20. T. He, S. Li, Y. Jiang, C. Qin, M. Cui, L. Qiao, H. Xu, J. Yang, R. Long, H. Wang, M. Yuan, Reduced-dimensional perovskite photovoltaics with homogeneous energy landscape. *Nat. Commun.* **11**, 1672 (2020).
21. K. Ma, H. R. Atapattu, Q. Zhao, Y. Gao, B. P. Finkenauer, K. Wang, K. Chen, S. M. Park, A. H. Coffey, C. Zhu, L. Huang, K. R. Graham, J. Mei, L. Dou, Multifunctional conjugated ligand engineering for stable and efficient perovskite solar cells. *Adv. Mater.* **33**, 2100791 (2021).
22. A. Bala, V. Kumar, Effects of Cl and F substitution in phenylethylammonium spacer cations on stability, structure, and optical properties of 2D–3D ruddlesden–Popper perovskite layers. *ACS Appl. Energy Mater.* **4**, 1860–1867 (2021).
23. J. V. Passarelli, D. J. Fairfield, N. A. Sather, M. P. Hendricks, H. Sai, C. L. Stern, S. I. Stupp, Enhanced out-of-plane conductivity and photovoltaic performance in n = 1 layered perovskites through organic cation design. *J. Am. Chem. Soc.* **140**, 7313–7323 (2018).
24. G. Liu, X.-X. Xu, S. Xu, L. Zhang, H. Xu, L. Zhu, X. Zhang, H. Zheng, X. Pan, Passivation effect of halogenated benzylammonium as a second spacer cation for improved photovoltaic performance of quasi-2D perovskite solar cells. *J. Mater. Chem. A* **8**, 5900–5906 (2020).
25. J. Hu, I. W. H. Oswald, S. J. Stuard, M. M. Nahid, N. Zhou, O. F. Williams, Z. Guo, L. Yan, H. Hu, Z. Chen, X. Xiao, Y. Lin, Z. Yang, J. Huang, A. M. Moran, H. Ade, J. R. Neilson, W. You, Synthetic control over orientational degeneracy of spacer cations enhances solar cell efficiency in two-dimensional perovskites. *Nat. Commun.* **10**, 1276 (2019).
26. D. Kim, H. J. Jung, I. J. Park, B. W. Larson, S. P. Dunfield, C. Xiao, J. Kim, J. Tong, P. Boonmongkolras, S. G. Ji, F. Zhang, S. R. Pae, M. Kim, S. B. Kang, V. Dravid, J. J. Berry, J. Y. Kim, K. Zhu, D. H. Kim, B. Shin, Efficient, stable silicon tandem cells enabled by anion-engineered wide-bandgap perovskites. *Science* **368**, 155–160 (2020).
27. Y. Gao, Z. Wei, P. Yoo, E. Shi, M. Zeller, C. Zhu, P. Liao, L. Dou, Highly stable lead-free perovskite field-effect transistors incorporating linear π-conjugated organic ligands. *J. Am. Chem. Soc.* **141**, 15577–15585 (2019).
28. A. H. Proppe, R. Quintero-Bermudez, H. Tan, O. Voznyy, S. O. Kelley, E. H. Sargent, Synthetic control over quantum well width distribution and carrier migration in low-dimensional perovskite photovoltaics. *J. Am. Chem. Soc.* **140**, 2890–2896 (2018).
29. M. Daboczi, S. R. Ratnasingham, L. Mohan, C. Pu, I. Hamilton, Y.-C. Chin, M. A. Mclachlan, J.-S. Kim, Optimal interfacial band bending achieved by fine energy level tuning in mixed-halide perovskite solar cells. *ACS Energy Lett.* **6**, 3970–3981 (2021).
30. Y. Zhao, T. Heumueller, J. Zhang, J. Luo, O. Kasian, S. Langner, C. Kupfer, B. Liu, Y. Zhong, J. Elia, A. Osvet, J. Wu, C. Liu, Z. Wan, C. Jia, N. Li, J. Hauch, C. J. Brabec, A bilayer conducting polymer structure for planar perovskite solar cells with over 1,400 hours operational stability at elevated temperatures. *Nat. Energy* **7**, 144–152 (2022).
31. Y. Wang, L. Duan, Z. Hameiri, M. Zhang, X. Liu, Y. Bai, X. Hao, PTAA as efficient hole transport materials in perovskite solar cells: A review. *Sol. RRL* **6**, 2200234 (2022).
32. F. M. Rombach, S. A. Haque, T. J. Macdonald, Lessons learned from spiro-OMeTAD and PTAA in perovskite solar cells. *Energ. Environ. Sci.* **14**, 5161–5190 (2021).
33. W. S. Yang, B. W. Park, E. H. Jung, N. J. Jeon, Y. C. Kim, D. U. Lee, S. S. Shin, J. Seo, E. K. Kim, J. H. Noh, S. I. Seok, Iodide management in formamidinium-lead-halide-based perovskite layers for efficient solar cells. *Science* **356**, 1376–1379 (2017).
34. M. Jeong, I. W. Choi, E. M. Go, Y. Cho, M. Kim, B. Lee, S. Jeong, Y. Jo, H. W. Choi, J. Lee, J.-H. Bae, S. K. Kwak, D. S. Kim, C. Yang, Stable perovskite solar cells with efficiency exceeding 24.8% and 0.3-V voltage loss. *Science* **369**, 1615–1620 (2020).
35. H. Ren, S. Yu, L. Chao, Y. Xia, Y. Sun, S. Zuo, F. Li, T. Niu, Y. Yang, H. Ju, B. Li, H. Du, X. Gao, J. Zhang, J. Wang, L. Zhang, Y. Chen, W. Huang, Efficient and stable Ruddlesden–Popper perovskite solar cell with tailored interlayer molecular interaction. *Nat. Photonics* **14**, 154–163 (2020).
36. Z. Liu, L. Qiu, L. K. Ono, S. He, Z. Hu, M. Jiang, G. Tong, Z. Wu, Y. Jiang, D.-Y. Son, Y. Dang, S. Kazaoui, Y. Qi, A holistic approach to interface stabilization for efficient perovskite solar modules with over 2,000-hour operational stability. *Nat. Energy* **5**, 596–604 (2020).
37. M. Stolterfoht, C. M. Wolff, J. A. Márquez, S. Zhang, C. J. Hages, D. Rothhardt, S. Albrecht, P. L. Burn, P. Meredith, T. Unold, D. Neher, Visualization and suppression of interfacial recombination for high-efficiency large-area pin perovskite solar cells. *Nat. Energy* **3**, 847–854 (2018).
38. J. Wang, W. Fu, S. Jariwala, I. Sinha, A. K.-Y. Jen, D. S. Ginger, Reducing surface recombination velocities at the electrical contacts will improve perovskite photovoltaics. *ACS Energy Lett.* **4**, 222–227 (2019).
39. Z. Ni, H. Jiao, C. Fei, H. Gu, S. Xu, Z. Yu, G. Yang, Y. Deng, Q. Jiang, Y. Liu, Y. Yan, J. Huang, Evolution of defects during the degradation of metal halide perovskite solar cells under reverse bias and illumination. *Nat. Energy* **7**, 65–73 (2022).
40. L. J. Farrugia, WinGX and ORTEP for Windows: An update. *J. Appl. Cryst.* **45**, 849–854 (2012).
41. C. B. Hübschle, G. M. Sheldrick, B. Dittrich, ShelXle: A Qt graphical user interface for SHELXL. *J. Appl. Cryst.* **44**, 1281–1284 (2011).

42. G. M. Sheldrick, Crystal structure refinement with SHELXL. *Acta Crystallogr. C* **71**, 3–8 (2015).
43. G. M. Sheldrick, SHELXT–integrated space-group and crystal-structure determination. *Acta Crystallogr. Sect. A* **71**, 3–8 (2015).

Acknowledgments: We thank K. Zhu for experimental help and M. Zeller for single-crystal analysis. We also thank T. Terlier for TOF-SIMS characterization. **Funding:** This material is based on work supported by the U.S. Department of Energy's Office of Energy Efficiency and Renewable Energy (EERE) under Solar Energy Technologies Office Award DE-EE0009519. K.M. acknowledges the financial support from Lillian Gilbreth Postdoctoral Fellowships. H.R.A. and K.R.G. acknowledge funding from the Office of Science of the U.S. Department of Energy for supporting the UPS and XPS measurements under award number DE-SC0018208. D.S. and L.H. acknowledge funding from the Office of Science of the U.S. Department of Energy for supporting the time-resolved TA and PL measurements under award number DE-SC0022082. The work was partially supported by the U.S. Department of Energy under contract number DE-AC36-08GO28308 with Alliance for Sustainable Energy, Limited Liability Company (LLC), the Manager and Operator of the National Renewable Energy Laboratory. TRMC measurements and optical characterizations were supported by the De-Risking Halide Perovskite Solar Cells program of the National Center for Photovoltaics from DE-FOA-0002064 and DE-EE0008790, funded by the U.S. Department of Energy, Office of Energy Efficiency and Renewable Energy, Solar Energy Technologies Office. The views expressed in the article do not necessarily represent the views of the DOE or the U.S. government. **Author contributions:** Conceptualization: L.D., K.M., and J.S. Organic chemical synthesis: J.S. Device fabrication and general characterization: K.M., J.S., Y.T., and A.B. UPS/XPS measurement and analysis: H.R.A. and K.R.G. TRMC measurement: B.W.L. TRPL measurement and analysis: D.S. and H.Y. Cyclic voltammetry: K.C. LED measurement: K.W. Contact angle measurement: Y.L. Supervision: L.D., J.M., and L.H. Writing—original draft: K.M., J.S., and L.D. Writing—review and editing: all authors **Competing interests:** An application has been made for a provisional patent (U.S. patent application number 70055-01) related to the subject matter of this manuscript, and the authorship include L.D., K.M., and J.S. The authors declare that they have no other competing interests. **Data and materials availability:** All data needed to evaluate the conclusions in the paper are present in the paper and/or the Supplementary Materials.

Submitted 25 November 2022
Accepted 1 May 2023
Published 7 June 2023
10.1126/sciadv.adg0032

ENGINEERING

In situ sensing physiological properties of biological tissues using wireless miniature soft robots

Chunxiang Wang[1,2†], Yingdan Wu[1†], Xiaoguang Dong[3*†], Milena Armacki[4], Metin Sitti[1,2,5*]

Implanted electronic sensors, compared with conventional medical imaging, allow monitoring of advanced physiological properties of soft biological tissues continuously, such as adhesion, pH, viscoelasticity, and biomarkers for disease diagnosis. However, they are typically invasive, requiring being deployed by surgery, and frequently cause inflammation. Here we propose a minimally invasive method of using wireless miniature soft robots to in situ sense the physiological properties of tissues. By controlling robot-tissue interaction using external magnetic fields, visualized by medical imaging, we can recover tissue properties precisely from the robot shape and magnetic fields. We demonstrate that the robot can traverse tissues with multimodal locomotion and sense the adhesion, pH, and viscoelasticity on porcine and mice gastrointestinal tissues ex vivo, tracked by x-ray or ultrasound imaging. With the unprecedented capability of sensing tissue physiological properties with minimal invasion and high resolution deep inside our body, this technology can potentially enable critical applications in both basic research and clinical practice.

INTRODUCTION

Sensing the physiological properties of soft biological tissues is important to understand the development of tissues and help diagnose and treat diseases. The biomechanical and biochemical physiological properties, such as electrophysiologic, metabolism, circulation, thermal properties, and organ mechanics, across a variety of developmental stages in organs and organisms are key to understanding the role of various forces in shaping life (*1*) associated with growth, aging, regeneration, and wound healing (*2*, *3*). Moreover, the biomechanical and biochemical properties of tissues and organs also have a strong correlation with the development of diseases (*4*, *5*). Sensing the physiological properties of soft tissues deep inside the human body directly and accurately could thus help monitor and understand disease development, as well as provide feedback to therapy.

Methods of using medical imaging tools have been developed to sense the mechanical properties of soft tissues. Optical coherence elastography can sense the elastic property of soft tissues with a spatial resolution at the submillimeter level (*6*) by combining light transmission and photophysical interactions but has a limited penetration depth of up to several millimeters. Ultrasonic elastography (UE) (*7*, *8*) and magnetic resonance elastography (MRE) (*9*, *10*) have a larger penetration depth (>10 cm), as well as relatively good spatial (0.3 to 0.8 mm) and temporal (several seconds) resolutions, but can only measure elasticity. Recent works on ultrasonic transducers (*11*–*13*) attached to the human skin can perform sensing at a spatial resolution of hundreds of micrometers, which is promising for realizing deep (~4 cm) tissue sensing of blood flow and elasticity. Despite these recent advances, there are still limitations of using pure medical imaging to sense advanced physiological properties of tissues. For example, they could only sense the elastic properties of tissues. Moreover, UE typically has a relatively low signal-to-noise ratio (SNR), while MRE cannot be performed on patients with implantable devices and obesity.

On the other hand, flexible and stretchable electronic devices have been used to sense various physiological properties of soft biological tissues on the human skin (*4*, *5*). Passive and active vibration sensors based on resonators on the skin, such as piezoelectric actuators (*14*) and magnetic actuators based on Lorenz forces (*15*), can sense the elastic properties of soft tissues, but these methods can only sense physiological signals limited to a few millimeters close to the epidermis, limiting their application for deep tissue sensing. Other flexible sensors implanted inside the organs can sense deep tissue properties but require open surgery for implantation and may potentially cause inflammation (*16*). For example, existing devices for measuring the pH of tissues, such as electrical impedance spectroscopy (*17*), are typically wired and rely on endoscope delivery, which is more invasive, and lack the mobility to be easily relocated. Ingestible robotic capsule endoscopes (*18*–*20*) with various active locomotion have been shown to sense the physiological properties of the gut in the gastrointestinal (GI) tract. However, they typically have a larger size at the centimeter scale due to the difficulty of scaling down power and communication modules, which limits their access to narrow areas with collapsed tissues and makes them potentially lead to obstruction (*19*).

Here, we propose a framework combining wireless soft robots and medical imaging to sense advanced physiological properties of tissues, including adhesion, pH, and viscoelasticity deep inside the organs. The millimeter-scale soft robots, actuated by magnetic fields remotely, can attach to and detach from the surface of soft tissues in a controlled manner and interact with soft tissues using their static and dynamic body shapes while being monitored and tracked by medical imaging, such as ultrasound and x-ray medical imaging. Compared with previously reported implanted electronic sensors (*14*, *21*), magnetic microdevices (*22*, *23*), and capsule endoscopes (*18*–*20*) for sensing the properties of tissues (*20*, *21*), the

[1]Physical Intelligence Department, Max Planck Institute for Intelligent Systems, Stuttgart 70569, Germany. [2]Institute for Biomedical Engineering, ETH Zürich, Zürich 8092, Switzerland. [3]Department of Mechanical Engineering, Vanderbilt University, Nashville, TN 37235, USA. [4]University Hospital Ulm, Ulm 89081, Germany. [5]School of Medicine and College of Engineering, Koç University, Istanbul 34450, Turkey.
*Corresponding author. Email: xiaoguang.dong@vanderbilt.edu (X.D.); sitti@is.mpg.de (M.S.)
†These authors contributed equally to this work.

untethered multimodal locomotion capability of our wireless soft robot could enable access to enclosed and confined spaces with minimal invasion. Our method could potentially sense the physiological properties of tissues, such as adhesion, pH, and viscoelasticity, which are challenging to be sensed using conventional medical imaging tools, electronic sensors, and other existing medical devices.

RESULTS

Sensing mechanism

Our proposed sensing framework is composed of three key components: a wirelessly actuated soft robot; a medical imaging module, such as ultrasound imaging or x-ray fluoroscopy machines, for tracking the robot shape; and the targeted soft tissue (Fig. 1A). The robot soft body shape is precisely controlled by external magnetic fields generated by a customized magnetic actuation system (figs. S1 and S2). As shown in Fig. 1B, the robot has multiple locomotion modes, including walking and climbing on soft tissue surfaces, crawling in narrow crevices, and swimming inside liquids, to navigate through complex terrains and attach to soft tissue surfaces by a bioadhesive patch bonded to the robot body, which is controlled by different external magnetic fields (*24*). Two types of robot-tissue interaction are reported, which are static and dynamic interactions. In the static interaction, the robot body interacts with the soft tissue in a static manner, where the damping force is negligible, as showcased with a buckling-based motion in Fig. 1C. In the dynamic interaction, the robot constantly experiences a time-varying magnetic field, resulting in a dynamic deformation of the tissue surface, which depends on both the magnitude and frequency of the external magnetic fields. Figure 1D shows that the robot can attach its whole body to the soft tissue surface and perform an undulating motion.

To show the fundamental mechanisms of sensing soft tissue physiological properties, we develop a wireless soft millirobot by bonding bioadhesive patches on the robot body. Our control strategies allow the robot to interact with soft tissues for in situ sensing, where we implemented our previously reported switchable tissue adhesion mechanism (*24*) on this robot. As shown in Fig. 2A, the robot has a magnetoelastic soft body, two ring-shaped footpads, and an adhesive patch bonded to the body surface. The robot (length, L; width, w; thickness, t) has magnetization magnitude and phase profiles $\mathbf{M}(s)$ and $\phi(s)$ ($s \in [0, L]$, s: material coordinate) shown in Fig. 2B, which allows it to realize desired multimodal locomotion,

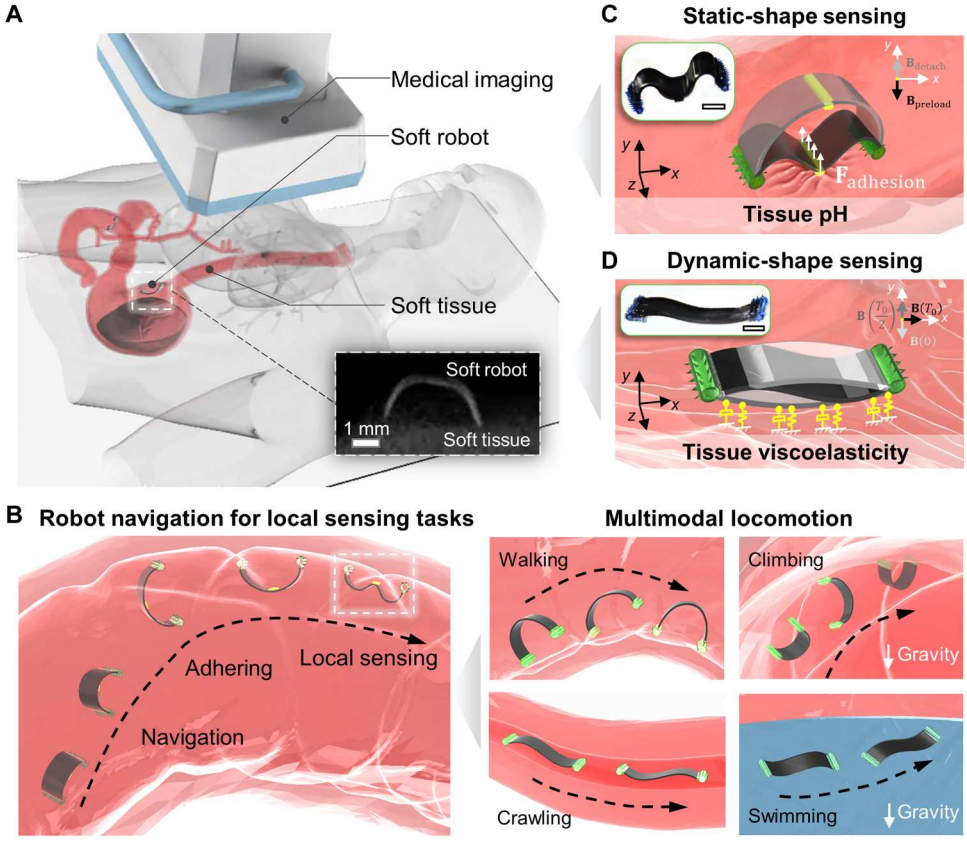

Fig. 1. Concept of in situ sensing the physiological properties of soft tissues by a wireless miniature soft robot. (**A**) Concept of wireless miniature soft robots for sensing soft tissue properties in the gastrointestinal (GI) tract. The inner x-ray image presents an example of the visualized robot body and porcine small intestine tissue. (**B**) Schematics of the overall sensing mechanism using a wireless miniature soft robot with multimodal locomotion capability. Left: Process of delivering the robot, robot navigation, and performing local sensing task. Right: Multimodal locomotion modes of the robot, including walking and climbing on tissue surfaces, crawling in tubular channels, and swimming in fluids. (**C**) Sensing soft tissue properties by static robot-tissue interactions, showcased by sensing tissue adhesion and pH values. The subplot illustrates the real robot. (**D**) Sensing tissue properties by dynamic robot-tissue interactions showcased by sensing tissue viscoelastic property. The subplot shows the real robot. In all figures, scale bars are 1 mm.

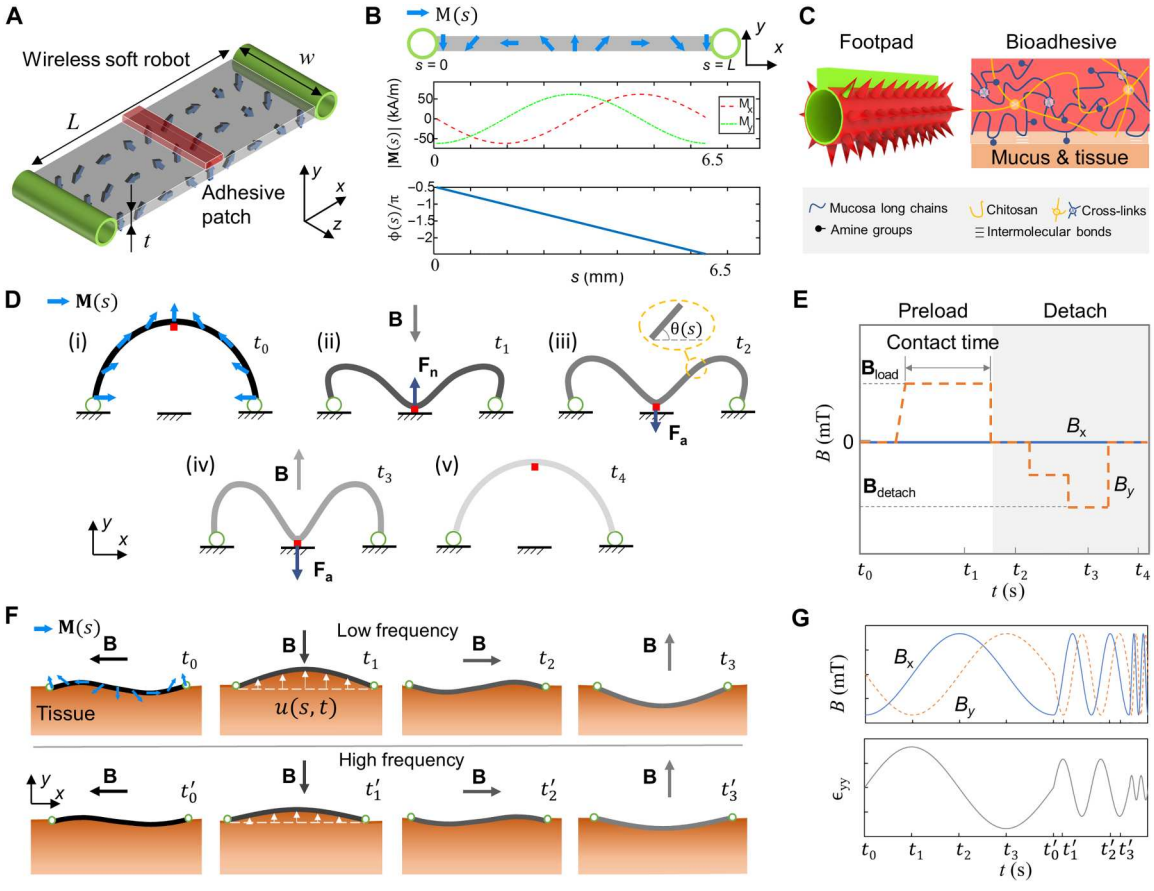

Fig. 2. Mechanism of sensing the physiological properties of soft tissues in situ by a wireless miniature soft robot. (**A**) Schematics of the robot design for sensing robot-tissue adhesion. The size of the adhesive patch could be adjusted during fabrication to allow two different attaching modes [partial contact in (D) or full contact in (F)] when contacting soft tissues. The finalized robot size is 6.5 mm × 2 mm × 15 mm ($L \times w \times t$). (**B**) Magnetization profile of the soft robot. The blue arrows indicate the magnetization profile **M**(s) of the robot body. (**C**) Robot footpad design with microspikes and chitosan-based bioadhesives (*27*) for multimodal locomotion. (**D**) Schematics of the buckling-based motion of the robot when interacting with soft tissues for adhesion sensing. (**E**) Time-varying magnetic field for inducing the buckling motion of the robot when interacting with soft tissues. $\mathbf{B}_{load}$ denotes the magnetic field applied to load the adhesive patch into contact with the substrate. $\mathbf{B}_{detach}$ represents the magnetic field required to detach the adhesive patch from the substrate. The magnetic fields at time stamps t_1 to t_4 are corresponding to those shown in (D). (**F**) Illustration of the deformation of the robot and tissue in a period when the robot is actuated by a rotating magnetic field of the constant magnitude at various frequencies (top, low frequency; bottom, high frequency). (**G**) Magnetic field waveforms for inducing the dynamic shapes of the robot. The time frames correspond to their counterparts in (F). ε_{yy} represents the material strain at the location of s = 3.25 mm at the robot-material interface.

including climbing, crawling, and swimming (*24*). The robot footpads have microspikes coated with hydrogel and tough bioadhesives made of chitosan, as shown in Fig. 2C, so that it can attach to and detach from tissue surfaces controlled by external magnetic fields. The conical microspikes ensure large friction on tissue surfaces, while the biocompatible chitosan-based bioadhesive, capable of cross-linking with the mucus layer, provides large adhesion (*24*).

Two fundamental mechanisms have been proposed for sensing the physiological properties of tissues in situ. First, the robot can use buckling-based static shapes to sense robot-tissue adhesion (Fig. 2D). Such adhesion measurement can also be used for sensing various mechanical properties of tissues, such as pH and temperature, by using stimuli-responsive adhesives (*25*). A remote magnetic field (Fig. 2E) is controlled to induce the buckling motion by the distributed magnetic torque along the robot body, which will be discussed in detail in the next section. The fundamental principle is that when the robot's two footpads attach to a soft tissue surface (Fig. 2D, i), a magnetic field **B** perpendicular to the tissue surface in the negative y direction will induce the deformation of the robot body toward the tissue surface (Fig. 2D, ii). The adhesive patch will be loaded to the tissue surface due to a buckling effect (*26*). After removing the magnetic field, the robot will maintain the buckled shape due to the patch-tissue adhesion (Fig. 2D, iii). Gradually increasing the magnetic field in the positive y direction (Fig. 2D, iv) will result in a distributed magnetic torque to detach the adhesive patch from the tissue surface once the **B** field reaches a threshold value (Fig. 2D, v). Moreover, the patch-tissue adhesion can be estimated using the robot body shape and the input magnetic field based on a magnetoelastic model using the Euler-Bernoulli Beam theory (see the "Estimating robot-tissue adhesion" section in note S1). As illustrated in Fig. 2D, the static shape of the robot body is described by $\theta(s)$ and $\frac{\partial\theta}{\partial s}$, which are the slope angle and curvature of the robot body at a specific location $s \in [0, L]$, respectively. The robot shape data can be obtained by optical imaging in vitro

and medical imaging in vivo, while the input magnetic field can be obtained from the calibrated magnetic actuation system (fig. S1).

In addition, our robot can also adhere to and dynamically interact with soft tissues to sense their viscoelastic properties under a periodic magnetic field waveform (Fig. 2F). For example, Fig. 2G shows rotating magnetic fields with a constant magnitude at various frequencies. The tissue viscoelastic properties can be estimated from the tissue normal strain ε_{yy}^{t} (or the tissue normal displacement u_y^t) and the tissue normal stress σ_{yy}^{t} at the robot-tissue interface. At the robot-tissue interface, we have $\sigma_{yy}^{t} = -\sigma_{yy}^{r}$ and $u_y^t = u_y^r$, where σ_{yy}^{r} and u_y^r are the robot's normal stress and displacement, respectively. We can further use the dynamic shape of the robot to approximate the tissue strain and stress using a magnetoelastic model. Given a specific robot, we assume that the normal stress of the soft tissue is proportional to the external magnetic field with a scaling factor k_y assuming small deflections. When subjected to a rotating magnetic field with a frequency of $f = \omega/2\pi$, σ_{yy}^{r} can be estimated from the magnetic field given by $\sigma_{yy}^{r} = k_y[\mathbf{M}(s), K_r]B(\omega t)$, where k_y is a function of the bulk modulus K_r and the magnetization profile $M(s)$ of the robot, independent of the external magnetic field and the soft tissue properties. Therefore, if we perform the frequency sweeping for the function $\varepsilon_{yy}^{t}(\omega t)/B_y(\omega t)$ by varying ω, we can estimate the storage and loss moduli of the tissue E' and E'' using the low- and high-frequency parts of the frequency response described in the "Estimating tissue viscoelastic properties" section in note S2.

Sensing robot-tissue adhesion using static robot-body shapes

In Fig. 3 and movie S2, we present the robot design, characterization, sensing mechanism, and validation results for sensing robot-tissue adhesion and, therein, the tissue pH values at a specific location. A 2 mm × 0.5 mm × 0.35 mm adhesive patch coated with pH-sensitive bioadhesives is bonded at the middle of the robot body (Fig. 3A). The patch is composed of three layers: a layer of elastomer (thickness: 0.1 mm), a thin layer of coated hydrogel (thickness: 0.05 mm), and a layer of pH-sensitive bio-adhesive (thickness: 0.2 mm). The hydrogel layer serves as a dissipative matrix material for tough adhesives (*27*) as well as a bonding material between the elastomer patch and bioadhesive. The pH-sensitive bioadhesive layer combines both the chitosan-based bioadhesive for tough adhesion to mucus-covered tissues via cross-linking (*27*) and the catechol-boronate–based hydrogel adhesive for pH-responsive adhesion via amine-borate complexation (see the "Fabrication of the adhesive patch for sensing adhesion and pH" section in Materials and Methods) (*28*, *29*).

We quantify the pH-sensitive adhesion to tissue surfaces of the adhesive patch in Fig. 3 (B and C). Figure 3B compares the adhesion of the adhesive patch on ex vivo porcine stomach and small intestine tissue surfaces with different pH values. Standard phosphate-buffered saline (PBS) buffer solutions with different pH values are added to the same tissue surfaces to achieve the desired pH values, validated by a pH indicator. With a preload of 0.5 mN in a customized adhesion measurement setup (fig. S3 and movie S2), we perform a systematic measurement of the patch-tissue adhesion. The adhesive patch shows adhesion of 1.08 ± 0.07 mN on an acidic porcine stomach surface with pH 1 but only 0.54 ± 0.06 mN on the same porcine stomach surface with pH 3. Furthermore, the adhesive patch shows the adhesion of 0.56 ± 0.04 mN on the porcine small intestine surface with pH 5, while only 0.23 ± 0.09 mN on the same porcine small intestine surface with pH 7.4.

In Fig. 3C, we further prove that the patch-tissue adhesion is almost linearly dependent on the pH of the tissue surface so that the patch-tissue adhesion can be used to sense pH assuming similar surface conditions. First, the pH-responsive properties of the adhesive patch can be designed to sense a wide range of pH values. For example, the adhesion decreases from 1.08 ± 0.07 to 0.31 ± 0.12 mN on the porcine stomach tissue surfaces when the pH increases from 1 to 5. This pH range can cover most of the possible cases in the stomach. For example, the average pH is about 5.4 ± 2.1 in patients with gastric cancer, 3.0 ± 2.2 for gastritis, 2.4 ± 1.9 for gastric ulcers, 1.3 ± 0.6 for duodenal ulcers, and 1.7 ± 0.2 for normal subjects (*30*). Meanwhile, the adhesion decreases from 0.58 ± 0.03 to 0.11 ± 0.05 mN on porcine small intestine tissue surfaces when a pH increases from 4 to 8. In addition, our pH-responsive adhesive patch shows a comparable sensitivity of 1 pH unit like the commercial pH-indicator strips pH 2.0 to 9.0 (MQuant 1.09502, Sigma-Aldrich Inc.) with a sensing range from 1 to 8.

Figure 3D shows the design of the robot for achieving both desired climbing locomotion and the adhesion sensing function. To achieve both climbing locomotion and deployment for sensing, we optimize the robot body design with a key design parameter—the thickness-to-length ratio (TLR), which compromises the climbing locomotion and the buckling-based attachment to tissues. With a relatively small TLR, the robot can be deployed with a buckling motion easily due to a relatively small bending stiffness, but the robot has degraded climbing locomotion due to insufficient net magnetic torque (fig. S4). We perform a systematic parameter sweeping of the TLR from 0.018 to 0.033 (body thickness: 0.15 mm) to optimize the TLR for both the robot climbing locomotion and the buckling-based attachment to tissues. We find that a TLR of 0.023 (body length: 6.5 mm) allows a sufficient climbing ability with a wide range of reachability quantified by the ratio of the distance between the footpads to the length of the robot body (0.3 to 0.5) while using a relatively small actuation magnetic field (<20 mT). The robot with a TLR of 0.023 also allows easy deployment, as showcased in Fig. 3E and movie S1.

Figure 4A shows the schematics of estimating the robot-tissue adhesion using a magnetoelastic model. Given the robot static shapes parameterized by $\theta(s)$, $\frac{\partial\theta(s)}{\partial s}$, and the external magnetic field $\mathbf{B}$, we can estimate the patch-tissue adhesion. Figure 4B illustrates the free-body diagram of the robot under a "pinned-fixed-pinned" boundary condition, where the adhesion $\mathbf{F}_a$ between the adhesive patch and the tissue surface is balanced by the reaction forces $\mathbf{F_1}$ and $\mathbf{F_2}$ in addition to the robot body weight. As shown in Fig. 4C, $\mathbf{F_1}$, $\mathbf{F_2}$, and $\mathbf{F_a}$ can be estimated by solving the moment and force balance equations based on the Euler-Bernoulli beam theory (see "Estimating robot-tissue adhesion" section in note S1). As an example, Fig. 4D illustrates the sensing process of the robot-material adhesion $\mathbf{F}_a$ on a substrate surface of Ecoflex-0030 silicone rubber (1:1 weight ratio). In this process, the robot is first loaded for attachment with an external magnetic field of 13.4 mT for 5 s in the $+y$ axis. Then, an external magnetic field in the $-y$ axis is applied from 0 mT with a magnitude interval of 2.7 mT and a time interval of 2.5 s until the robot is detached from the surface. Note that our method

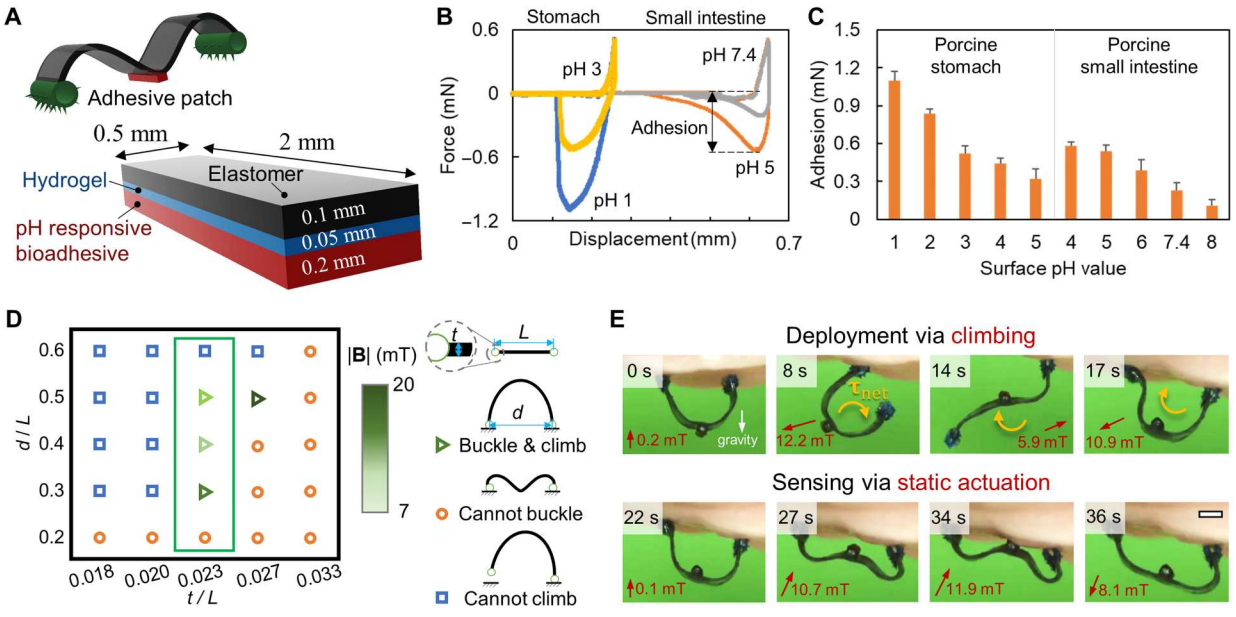

Fig. 3. Sensing the adhesion and pH of soft tissues using a wireless miniature soft robot integrated with a pH-responsive adhesive patch. (**A**) Design of the soft robot with a pH-responsive bioadhesive patch. (**B**) Normal force between the adhesive patch and the soft tissues as a function of the displacement. The adhesion is quantified using the maximum pull-off force (negative normal force) as denoted in the plot. Soft tissue: porcine stomach and porcine small intestine. (**C**) pH-responsive properties of the adhesive patch on porcine stomach and small intestine tissues. (**D**) Feasible robot thickness-to-length ratio (TLR) for realizing both the climbing locomotion and the buckling-based deployment. *t*, *L*, and *d* are the robot body thickness, body length, and the distance between the footpads when buckling, respectively. The selected robot geometry design is marked by the green box. A small *d*/*L* disables the buckling due to the large curvature of the robot body and consequently a large bending stiffness, while a large *d*/*L* hampers the climbing mobility because of the insufficient net magnetic torque. (**E**) Climbing-based deployment of the robot to the targeted position and the buckling-based sensing of the robot adhesive patch to the soft tissue surfaces. Scale bar, 1 mm. In all figures, the error bar represents the SD for $n = 5$ measurements. The measurements involved a pH-responsive bioadhesive patch per sample, with *n* indicating the number of samples.

yields consistent adhesion estimation results for over five repetitions with an average relative SD of 4.4%, as shown in fig. S5.

To further verify our sensing method, we compare the estimated adhesion using the soft robot on various synthetic substrate surfaces with the adhesion measured by a high-precision force sensor in a customized adhesion measurement setup (fig. S3). Figure 4E compares the estimated adhesion and the reference adhesion for synthetic surfaces with various adhesion properties. For the adhesion range from 0.13 ± 0.02 to 0.82 ± 0.02 mN, the estimated results from the proposed sensing method match the reference adhesion with relative errors all less than 12%, as shown in Fig. 4E and movie S2. The proposed method is also applicable to a substrate surface with relatively large curvatures. We perform the sensing experiments on the convex, flat, and concave surfaces with a curvature of −250, −150, 0, 150, and 250 m^{-1} covered by the 2-mm-thick Ecoflex-0030 silicone rubber sheets (1:1 weight ratio). The relative errors between the estimated adhesion on curved surfaces and the measured force are less than 2.6% (Fig. 4F). In summary, the proposed sensing method can estimate the robot-substrate adhesion with a relative error less than 20% for a wide range of adhesion from 0.13 ± 0.02 to 0.82 ± 0.02 mN and various curvatures from −250 to 250 m^{-1}.

To further quantify the performance of sensing robot-tissue adhesion and therein the pH values, we use the robot to sense adhesion on various tissue surfaces with different pH values. Figure 4G compares the estimated adhesion by the proposed method and the reference adhesion measured by a high-precision force sensor (fig. S3) on tissues, including rat stomach, porcine stomach, and porcine small intestine (see fig. S6 for more detailed comparisons for the same tissues covered by PBS solutions of various pH values). The relative errors in adhesion between the estimation and the measured values for all three tissues are less than 10%. Therefore, the proposed method could potentially enable minimally invasive sensing of the tissue adhesion and pH at a hard-to-reach spot inside the human body with the aid of medical imaging devices.

Sensing viscoelasticity of soft tissues using dynamic robot-body motion

In Fig. 5, we present the design of the soft robot to sense tissue viscoelastic properties with dynamic robot-body motion. To maintain the robot-tissue attachment during the dynamic interactions, a 6.5 mm × 2 mm adhesive patch is bonded to the robot body (Fig. 5A). The adhesive patch is fabricated by coating the robot body with hydrogel and bioadhesive sequentially with a total thickness of about 0.05 mm (see the "Fabrication of the adhesive patch for sensing tissue viscoelasticity" section in Materials and Methods). The adhesive layer bonds the robot and tissue surfaces together while having a minimal effect on the robot-tissue dynamic interactions. We further show that the adhesion strength between the robot and tissue surfaces can be adjusted by the contact time in Fig. 5B. The adhesion between the bioadhesive patch and the porcine small intestine tissue is a function of the contact time, characterized by a customized setup with a preload of 0.1 mN (fig. S3). The bonding process involves the intermolecular interaction and cross-linking between the bioadhesive and the mucus, which is time dependent (*29*). When the bonding is sufficiently formed (after 1 min), the

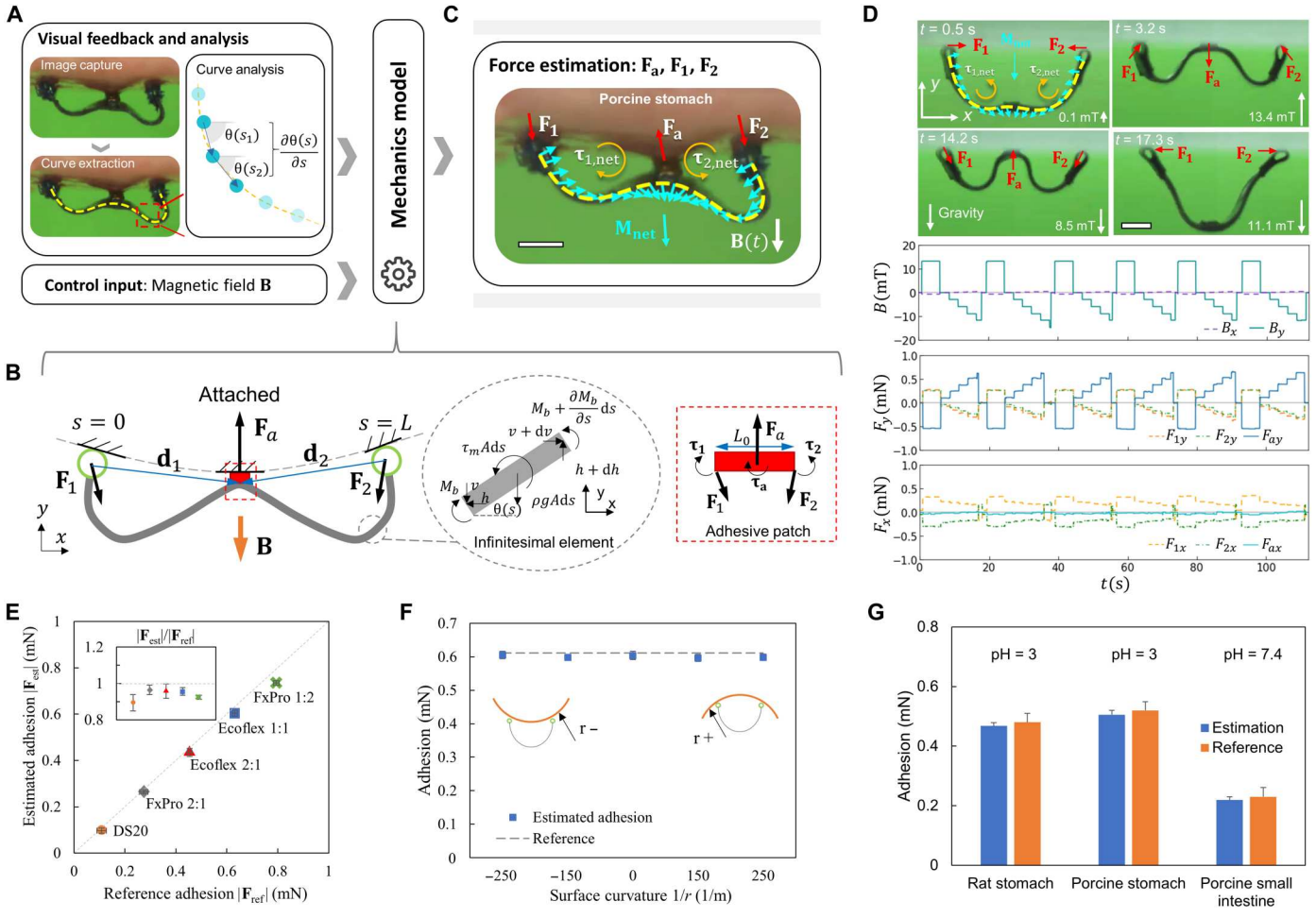

Fig. 4. Quantification of the performance of sensing robot-tissue adhesion and therein the pH. (**A**) Schematics of the overall sensing mechanism. The robot shape is assumed to be known and described by functions θ(*s*) and $\frac{\partial\theta(s)}{\partial s}$. The magnetic field input is assumed to be known as **B**(*t*). (**B**) Schematics of the robot-tissue interaction model. (**C**) Schematics of the distributed torque and force applied to the robot body. (**D**) Top: Snapshots of the robot at rest, the robot loaded for attachment, the robot to be detached, and the robot just detached (movie S2). Bottom: Magnetic field input signals and the estimated forces. The proposed method yields consistent adhesion estimation results for over five repetitions with an average relative SD of 4.4%. Synthetic substrate material: FxPro 1:2 (Dragon Skin FX Pro/1 Silicone Rubber; mixture ratio, part A:part B = 1:2 by weight, Smooth-On Inc.). (**E**) Comparison of the estimated and real robot-tissue adhesion on synthetic materials (see "Preparation of synthetic materials for adhesion measurements" section in Materials and Methods). (**F**) Estimated adhesion on curved surfaces of synthetic materials. Estimated adhesion lies within the range of 0.596 to 0.606 mN compared to the measured adhesion of 0.612 ± 0.020 mN. *r* is the curvature radius. Material: Ecoflex 0030 silicone rubber with a weight ratio of 1:1 (Smooth-On Inc.). (**G**) Estimated robot-tissue adhesion on different animal soft tissue surfaces. In all figures, scale bars are 1 mm. Error bars indicate the SD for *n* = 5 measurements. For the estimation data, the measurements involved a robot per sample, with *n* indicating the number of samples. For the reference data, *n* is the number of samples measured by the setup in fig. S3.

adhesion per unit area is around 509 ± 47 N/m^2 and large enough to maintain the robot-tissue attachment. In addition, the adhesion per unit area is still within 574 ± 83 N/m^2 as the contact time reaches 10 min, enabling the on-demand detachment under magnetic actuation.

Figure 5C shows the robot attachment, sensing, and detachment behaviors for sensing tissue viscoelasticity. First, the robot is deployed and adheres its bioadhesive side to the targeted tissue area with the whole-body torque generated by the nonzero net magnetic torque $\boldsymbol{\tau}_{\mathbf{net}}$. Then, the robot is actuated to sense tissue viscoelasticity under a rotating magnetic field (magnitude: 7.5 mT). When the sensing process is completed, the robot body is detached from the tissue surface under a magnetic field with a relatively large magnitude (~26 mT). Figure 5D shows the minimum magnetic field needed for the detachment as a function of the contact time when the robot is attached to the porcine small intestine tissue. A more detailed illustration of the robot dynamic motion under a rotating magnetic field is presented in Fig. 5E and movie S3, where the robot undulates when attaching to an agarose gel [0.3 weight % (wt %)] back layer under a rotating magnetic field (24 mT, 0.1 Hz).

We further demonstrate the method to estimate the tissue storage modulus E' and the loss modulus E'' using a frequency sweeping method based on the mechanical model in Fig. 6A. On the one hand, E' is estimated under a low-frequency (0.1 Hz) rotating magnetic field. In this case, the robot deformation magnitude is only dependent on E' and the effect of E'' is negligible. As illustrated in Fig. 6B, the robot shows distinct deformation magnitudes when interacting with materials of different E' upon applying the same

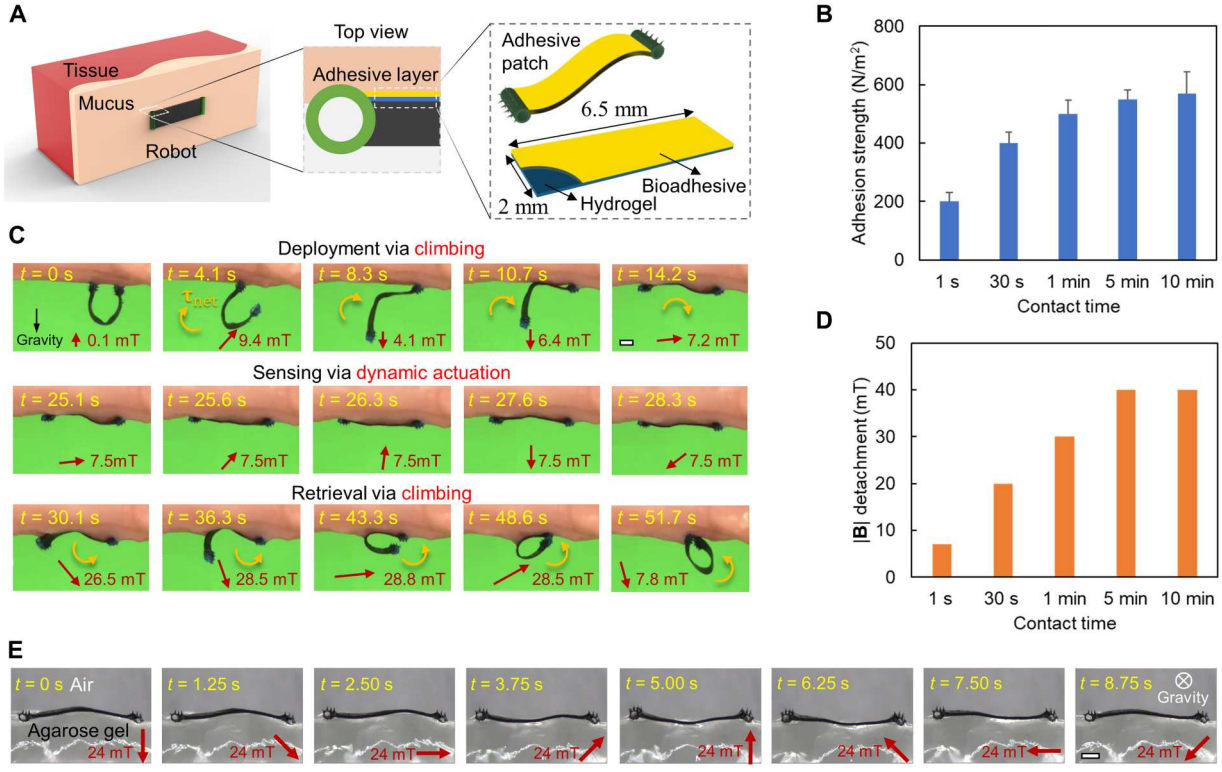

Fig. 5. Sensing the viscoelasticity of soft tissues using a wireless soft robot integrated with a bioadhesive patch. (**A**) Bioadhesive patch design. The adhesive patch is made of a hydrogel layer coated with bioadhesives. (**B**) Adhesion between the robot adhesive patch and the soft tissues as a function of the contact time. The soft tissue is from the porcine small intestine. Error bars indicate the SD for $n = 5$ measurements. The measurements involved a robot adhesive patch per sample, with n indicating the number of samples. (**C**) Video snapshots (movie S1) of the deployment, sensing, and retrieval process of the soft robot on the porcine small intestine surfaces. (**D**) Magnitude of the applied rotating magnetic field for detaching the adhesive patch from soft tissues as a function of the contact time. The soft tissue is from the porcine small intestine. (**E**) Video snapshots (movie S3) of the robot dynamic shape when interacting with the agarose gel (0.3 wt %) under a rotating magnetic field with a magnitude of 24 mT and a frequency of 0.1 Hz. In all figures, scale bars are 1 mm.

low-frequency magnetic field (20 mT, 0.1 Hz). The average material strain $\overline{\varepsilon_{yy}}$ at the robot-material interface, calculated by $\overline{\varepsilon_{yy}} = \int_{0.3L}^{0.7L} \varepsilon_{yy}(s)ds/0.4L$ (L = 6.5 mm; see Fig. 6B, i, and fig. S7), varies significantly with the amplitude of 0.19 and 0.11 for E' = 3.2 ± 0.3 kPa and 6.2 ± 0.5 kPa, respectively.

On the other hand, E'' is estimated from the robot deformation magnitude change by sweeping the rotating magnetic field at different frequencies. As shown in Fig. 6C, the robot deforms less for the same material when the actuation frequency increases, and the $\overline{\varepsilon_{yy}}$ amplitude drops from 0.23 to 0.08 under the actuation frequency of 1.9 and 14.2 Hz. In our method, the scaling factors k and k_τ, independent of materials, are first calibrated using synthetic materials to obtain the function E' $(\overline{\varepsilon_{yy}}/B_y)$ and E'' $(\overline{\varepsilon_{yy}}/B_y)$, which are further used to estimate E' and E'' of tissues (see the "Estimating tissue viscoelastic properties" section in note S2). First, E' $(\overline{\varepsilon_{yy}}/B_y)$ is estimated under the actuation frequency of 0.1 Hz. In Fig. 6D, we use the agarose and gelatin gels as the training and validation materials to obtain the fitted function $\overline{\varepsilon_{yy}}/B_y = 54.128(E')^{-1.067}$. In this function, k is calibrated as 54.128 Pa/mT, and the index value −1.067 is close to −1, which validates that E'' has a negligible effect on the estimation of E' under the 0.1-Hz actuation. It is notable that the E' of the experiment synthetic materials ranges from 1.9 ± 0.2 kPa to 51.2 ± 0.6 kPa, which covers the stiffness range of most soft tissues (*31*). After E' is estimated, the frequency sweeping method is used to compute the time constant τ, as shown in the subplot of Fig. 6E. Further, k_τ, the ratio of τ to E'/E'', is calibrated with the agarose-based viscoelastic gel and further validated by the gelatin-based gel and chicken breast tissue (k_τ = 0.0703 s; Fig. 6E), through which E'' is obtained on the basis of the estimated E' and τ. Last, the healthy porcine GI tissues are adopted to test the viscoelasticity sensing method ex vivo. Figure 6 (F and G) shows that the estimated E' and E'' of the tissues match the reference moduli characterized by the rheometer. The relative errors are within 8% for E' and 12% for E'', as shown in the subplots of Fig. 6 (F and G). Notably, the degree of robot deformation can be controlled by adjusting the magnetic field. This helps minimize the effect of sample boundary conditions on the robot deformation, particularly when the material thickness is small (see fig. S8), and ε_{yy} in the robot coordinate system is adopted for the calibration process (see fig. S9).

Our robot also has the potential to achieve distributed sensing due to the continuous stress imposed on the contact interface along the robot body. The method can be potentially used for disease location sensing during its development, such as cystic fibrosis in lungs (*32*). As illustrated in Fig. 6H (i) and movie S3, the robot contacts the stiff cylinder and is actuated by the rotating magnetic field, during which the robot deformation difference with and without a stiff cylinder can indicate the cylinder location in Fig. 6H (ii). Correspondingly, the material deforms less at the

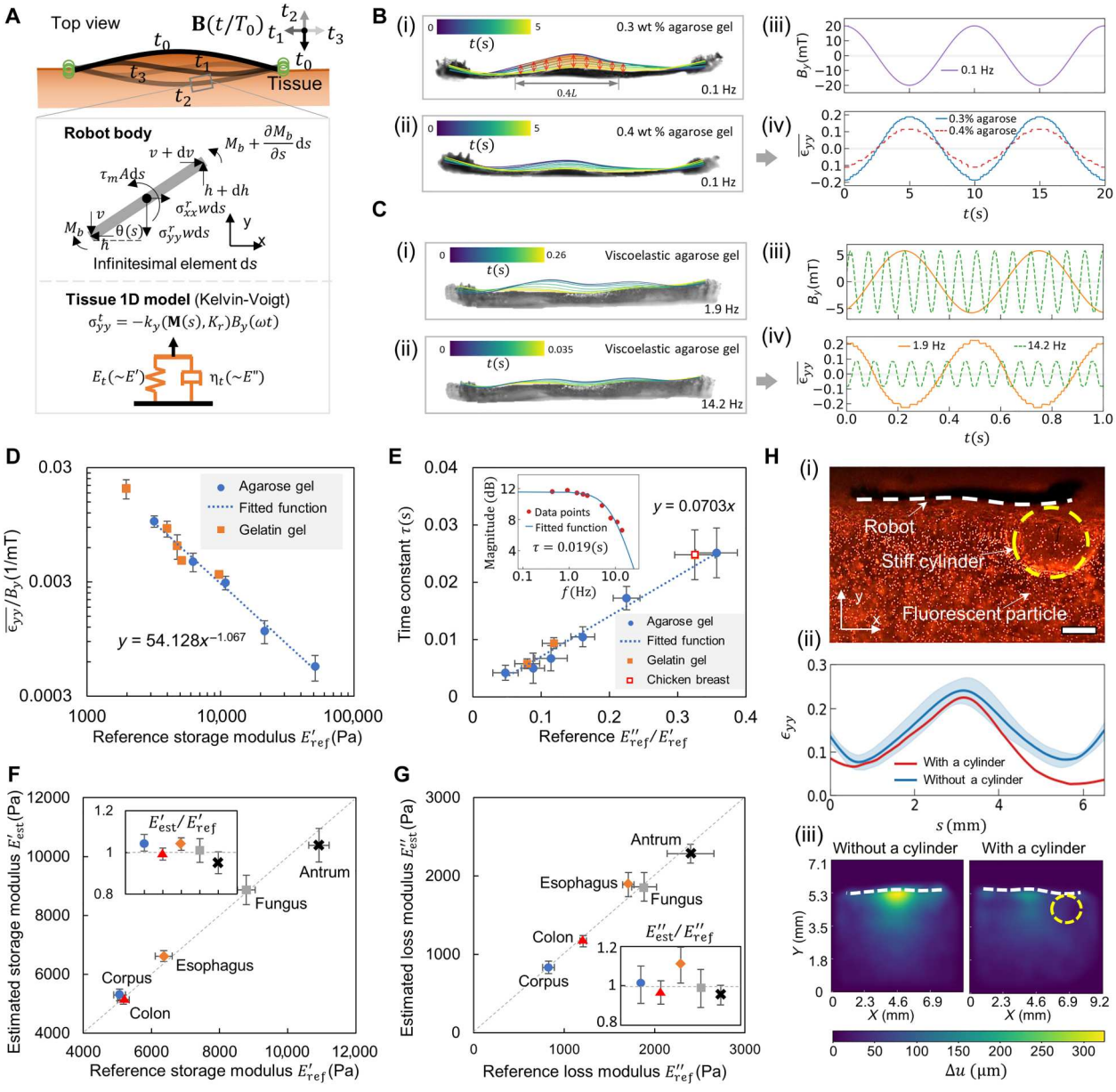

Fig. 6. Quantification of the performance of sensing viscoelasticity. (**A**) Illustration of the mechanic model for the dynamic robot-material interaction. (**B**) (i and ii) Robot dynamic shape when interacting with different synthetic materials. Material: 0.3 and 0.4 wt % agarose gel with E' = 3.2 ± 0.3 and 6.2 ± 0.5 kPa, respectively. (iii and iv) Applied magnetic field waveform and the measured normal strain $\overline{\varepsilon_{yy}}$ at the robot-material boundary. $\overline{\varepsilon_{yy}} = \int_{0.3L}^{0.7L} \varepsilon_{yy}(s)ds/0.4L$ (L = 6.5 mm), as the middle part of the robot body has the largest signal-to-noise ratio (SNR) (see fig. S5). (**C**) (i and ii) Robot dynamic shape subject to rotating magnetic fields of different frequencies. (iii and iv) B_y and $\overline{\varepsilon_{yy}}$ at the robot-material boundary. Material: 70-0.3 agarose-based gel (weight ratio, sucrose:water:agarose = 70:30:0.3) with E'' = 439.1 ± 46.8 Pa. (**D**) Correlation between $\overline{\varepsilon_{yy}}/B_y$ and the reference storage modulus E'_{ref} of different synthetic gels. (**E**) Correlation between the measured time constant τ and the ratio of the characterized loss modulus E''_{ref} and storage modulus E'_{ref}. Subplot: frequency response of the robot normal deformation [magnitude: 20log($\overline{\varepsilon_{yy}}/B_y$)]. (**F** and **G**) Comparison of the estimated and real (F) E' and (G) E'' of different porcine tissues. (**H**) Sensing simulated disease spots spatially. (i) Fluorescence image of a tested sample. A stiff cylinder of 1.0 wt % agarose gel (E' = 51.2 ± 0.6 kPa; diameter, 2 mm) is embedded inside the 0.3 wt % agarose gel (E' = 3.2 ± 0.3 kPa). (ii) Comparison of the robot deformation with and without a cylinder. (iii) Comparison of the material maximum displacement distribution with and without a cylinder. Scale bar, 1 mm. In all figures, error bars represent the SD of n = 5 measurements. For the estimation data, the measurements involved a robot per sample, with n indicating the number of samples. For the reference data, n is the number of samples measured by the rheometer (Discovery HR-2, TA Instruments).

cylinder location (Fig. 6H, iii). In fig. S10, the location and diameter of the cylinder are adjusted to simulate different occasions, and the corresponding robot and material deformation are shown in figs. S11 and S12. By analyzing the robot deformation, the cylinder location and its influence on the surrounding area can be quantified (fig. S13).

Sensing soft tissue mechanics ex vivo for organs with diseases

To show the potential of using our robot to monitor and understand the biomechanics of soft tissues with diseases, we present ex vivo sensing tissue pH and viscoelastic properties of soft tissues using our robot together with x-ray imaging in Fig. 7 and movies S4 and S5. The robot is first deployed into the diseased area of the mouse models and then actuated by the external magnetic field to implement the sensing functions, as shown in Fig. 7A. An x-ray cabinet imaging tool tracks the robot and surrounding soft tissues during the sensing processes. Figure 7 (B and C) shows that the static and dynamic robot-body shapes can be distinguished from the soft tissues in the x-ray images. For dynamic shape-based sensing, this framerate can allow sensing the storage modulus E' of soft materials and the loss modulus E'' of the soft material with a cutoff frequency up to 7 Hz based on the Nyquist sampling criterion. The x-ray imaging device has a framerate of 30 frames per second (FPS), which is sufficiently fast for imaging robot-body dynamic motion with a frequency of less than 10 Hz. Notably, the x-ray radiation dose in our experiment is under 410 μSv/hour (see the "x-ray medical imaging" section in Materials and Methods),

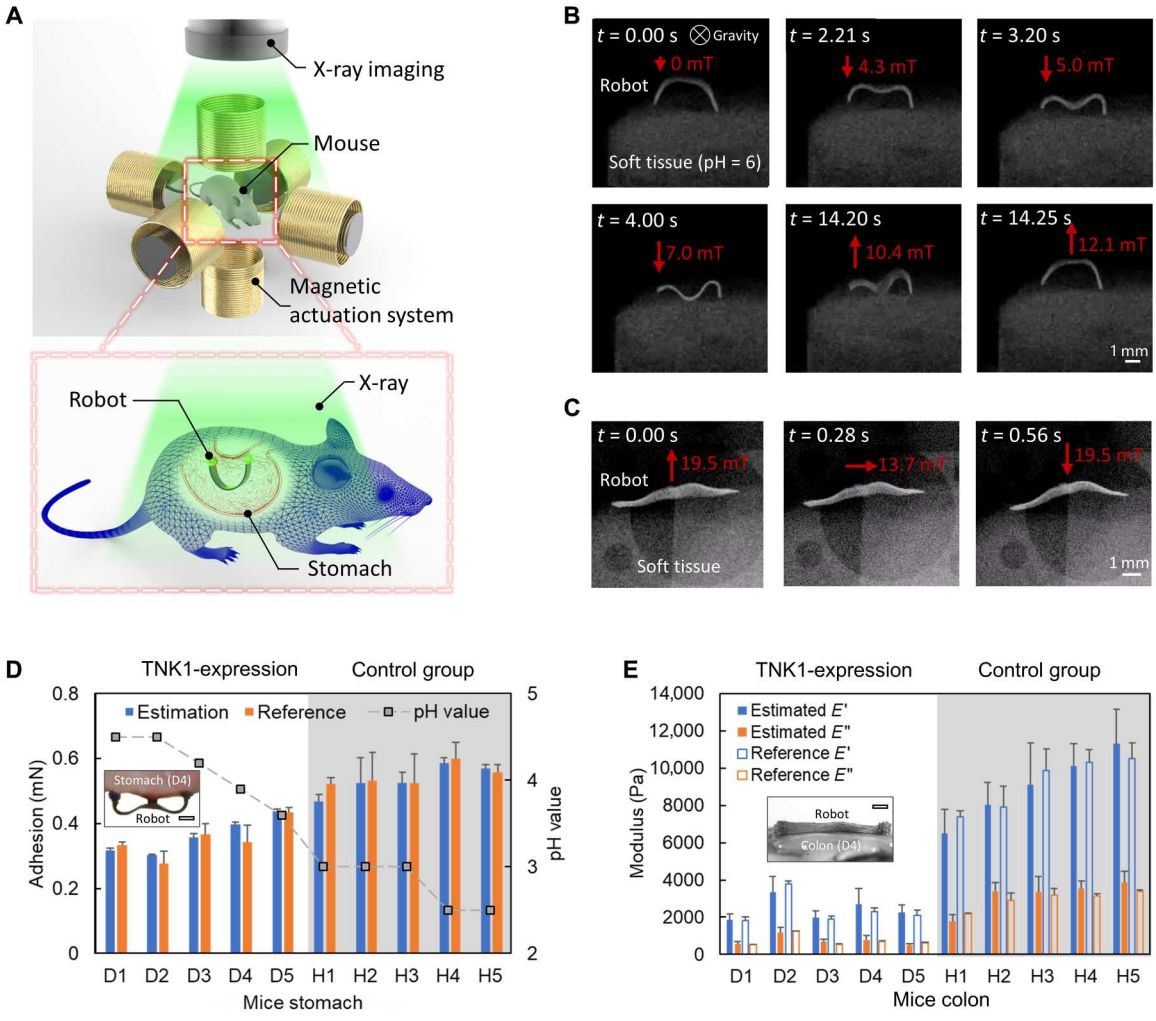

Fig. 7. Demonstration of measuring the physiological properties of soft tissues in an ex vivo intestinal disease model using x-ray medical imaging. (**A**) Schematics of sensing the tissue physiological properties in ex vivo disease model under x-ray medical imaging. (**B**) Video snapshots (movie S4) of sensing the pH of the tissue by the robot with the pH-responsive bioadhesive patch under x-ray cabinet imaging. (**C**) Video snapshots (movie S5) of sensing the viscoelastic properties of the tissue by a soft robot with the bioadhesive patch attached to one side of the whole robot body visualized by x-ray cabinet imaging. (**D**) Sensed adhesion between the soft robot and stomach tissue of mice with and without the thirty-eight–negative kinase 1 (TNK1) expression–related disease (*34*). The subfigure shows sensing adhesion on mice stomach tissues (D4) ex vivo. (**E**) Sensed viscoelastic properties of colon tissue of mice with and without the TNK1 expression–related disease. The subfigure indicates sensing viscoelasticity on mice colon tissues (D4) ex vivo. In all figures, error bars represent the SD. For the estimation data, $n = 3$ tissue samples were prepared, with a robot attached per sample. For the reference data, $n = 5$ tissue samples were measured by the customized setup (fig. S3) for adhesion or the rheometer (Discovery HR-2, TA Instruments) for viscoelastic properties. Scale bars, 1 mm.

which is safe for live animal experiments (*33*). In addition, we also show that ultrasound imaging can be used for tracking the robot body shape to sense tissue viscoelastic properties with a framerate of up to 30 FPS (fig. S14).

Further, mice with forced expression of thirty-eight–negative kinase 1 (TNK1), which exhibit impaired intestinal barrier (*34*), and healthy wild-type littermates are used to showcase the proposed methods for sensing pH and viscoelasticity to diagnose diseases. Regulation of apoptosis and immunomodulatory functions have been ascribed to TNK1, which is a promising target during multiorgan dysfunction syndrome to prevent damage in several organs, especially the gut. Because of the TNK1 expression, the normal intestinal architecture is perturbed. In addition, the basal pH in the stomach of the TNK1-expression mouse is higher than that of a mouse from the healthy control group (fig. S15) since the diseased mice are fasted because of abnormal intestinal activities (*34*).

Figure 7D compares the robot-tissue adhesion estimated by the proposed method, the reference data measured by the high-precision force sensor, and the pH value measured by the pH indicator of the mice stomach tissues with (H1 to H5) and without a TNK1 expression–related intestinal disorder/disease (D1 to D5). Despite the deviations among individuals from the same group, the TNK1-expression disease shows high relevance with the estimated adhesion results, which also matches the reference results and the corresponding pH values. The proposed adhesion sensing method shows its ability to indicate the difference in adhesion or pH of the ex vivo tissues, with 0.32 ± 0.01 mN to 0.44 ± 0.01 mN for TNK1 expression–diseased mice compared to 0.47 ± 0.02 mN to 0.59 ± 0.02 mN for healthy mice, potentially serving as a minimally invasive tool for detecting diseases.

Figure 7E compares the storage and loss moduli estimated using our method and the reference data characterized by a rheometer of the colon tissues of mice with (H1 to H5) and without a TNK1 expression–related disease (D1 to D5). The estimated storage and loss moduli for the TNK1-expression mice range from 1.9 ± 0.3 to 3.4 ± 0.8 kPa and 0.5 ± 0.1 to 1.2 ± 0.3 kPa, respectively, whereas the estimated storage and loss moduli for the healthy mice are from 6.5 ± 1.3 to 11.3 ± 1.8 kPa and 1.8 ± 0.4 to 3.8 ± 0.6 kPa, respectively. The estimated results are consistent with the reference data measured by the rheometer and can indicate the abnormal viscoelastic properties of the tissues.

DISCUSSION

We have reported a generic framework to sense the physiological properties of soft tissues using wireless miniature soft robots and medical imaging. A fundamental magnetic-mechanical model is developed to recover the mechanical properties of soft tissues, such as adhesion and viscoelasticity, with the tracked robot shape changes using medical imaging. This framework has been showcased with two example applications. One is a soft robot with an integrated pH-responsive adhesive patch for sensing robot-tissue adhesion and therein the correlated pH values using a buckling motion. The other one is a soft robot with an integrated adhesive patch that can be deployed on soft tissue surfaces and measure the viscoelasticity of soft tissues using a dynamic undulating motion. We have performed systematic experiments on synthetic materials and ex vivo soft tissues and validated the sensing mechanisms by comparing them with direct and high-precision measurements of the synthetic materials and biological soft tissues. Last, we have demonstrated the feasibility of sensing the mechanics of soft tissues in mice with diseases as a tool for diagnostics and monitoring GI tract diseases.

Compared with other implantable magnetic and electric devices where the components are embedded inside the tissues (*22*, *23*), our device can traverse complex soft and wet tissues to provide minimally invasive sensing ability to a wide range of tissue properties. Our robots can bond to the surfaces of soft tissues on demand and sense the advanced physiological properties of soft tissues. The deployment of the robot can be realized by a soft-body self-deformation or using an existing medical device, such as an endoscope. On the other hand, existing miniature robots have only shown simple in vitro sensing of temperature using thermally responsive liquid elastomer materials on a magnetic body (*35*). Our soft robot–based approach can locally sense the tissue biomechanics in vivo, where the medical imaging signals are amplified by the body shapes, allowing sensing various physiological properties of soft tissues. In addition, our method can potentially achieve a higher SNR compared with UE. The SNR of the basic UE is below 6 (*36*) and can be improved to up to 14 with the optimization algorithms (*37*, *38*), while the SNR of our method can reach 39 because of the high contrast between the robot and the sensed materials under x-ray imaging (see the "Calculating the signal-to-noise ratio" section in note S3).

The biocompatibility of our soft robot can be ensured by coating a thin layer of biocompatible materials such as polydimethylsiloxane (PDMS) (*39*) or parylene C (*40*) to prevent the toxic NdFeB particles from contacting the tissues. We will investigate the biocompatibility before and after coating with the standard cell survival test in the future. In addition, our soft robot–based sensing may be affected by the fluid flow but might be compensated with faster medical imaging and integrating the robot-fluid interaction into the mechanical model, which will be explored in future work. Moreover, despite that the multistep fabrication process can result in a variance of the robot properties (fig. S16), the current experimental results show acceptable deviation in the measured properties of the tissues using five different robots. However, we can always calibrate the robot properties for better accuracy before using the robot for sensing.

Our demonstrated sensing mechanisms can potentially be used for sensing peptic ulcers (*41*) in the GI tract, where the pH level changes markedly compared with normal tissues, as well as pulmonary fibrosis (*42*) and cancer (*43*), where the viscoelastic properties have changed substantially when the disease is developing. It should be noted that it is indeed difficult for our robot to detect a sudden change in the pH value, which generally takes about 30 s to sense the pH with our robot. However, the pH of the surfaces in the GI tract does not change rapidly (*44*). We can improve the sensing speed by integrating more sensitive bioadhesives, such as optimizing the concentration of the amine groups and borate ester groups in the bioadhesives (*28*, *29*) or increasing the surface area to volume ratio by incorporating microstructures into the adhesive patch design (*45*), in the future.

The proposed framework of using wirelessly actuated miniature robots to interact with soft tissue surfaces while monitoring their shape deformation using medical imaging thus opens a door for monitoring and understanding tissue biomechanics in vivo during disease development as well as providing feedback

information for the applied therapeutic solutions. Our method thus adds unprecedented capabilities to available minimally invasive sensing methods and medical devices, potentially enabling versatile applications in both basic research and clinical practice.

MATERIALS AND METHODS

Fabrication of the soft millirobot

As shown in fig. S17A, the footpads were made of PDMS (Sylgard 184, Dow Inc.) with a weight ratio of 20:1 between the monomer to the cross-linker using a two-step molding method. A spike mold was prepared using a two-photon polymerization (2PP) three-dimensional (3D) printer (Photonic Professional GT, Nanoscribe GmbH) with a rigid commercial photo resin (IP-S, Nanoscribe GmbH). The spike mold has 9 × 7 conical spike arrays of 200 μm in height, 100 μm in diameter, 200 μm in spacing, and a 2 mm × 1.5 mm × 60 μm backing layer. We pipetted the benzophenone solution (20 wt % in ethanol, Sigma-Aldrich Inc.) over the micro-spike patch as the hydrophobic photoinitiator and coated the patch with the poly(ethylene glycol) diacrylate (PEGDA; Sigma-Aldrich Inc.) as a dissipative hydrogel layer and a chitosan-based bioadhesive as the tough adhesive for tissue surfaces sequentially. The bioadhesive for the footpads was prepared by dissolving the chitosan (high molecular weight, Sigma-Aldrich Inc.) as a bridging polymer and the unsulfated *N*-hydroxysuccinimide (98%, Sigma-Aldrich Inc.) as a coupling reagent (12 mg/ml) into the compound MES buffer (Sigma-Aldrich Inc.) at the weight ratio of 2.0 and 0.12%, respectively. The robot body was fabricated with the procedure shown in fig. S17B. First, Ecoflex 00-30 silicone rubber (mixture ratio, part A:part B = 1:1 by weight, Smooth-On Inc.) and NdFeB microparticles (average diameter, 5 μm; MQFP-15-7, Neo Magnequench) were mixed at a 1:2 ratio by weight and then poured onto apoly(-methyl methacrylate) substrate with 150-μm-thick spacers, against which a razor blade was scraped for the control of the sheet thickness. The scraped mixture was cured at 90°C on a hot plate for 30 min. The cured sheet was then cut into a 4 mm × 2 mm rectangular sheet using a laser machine (LPKF ProtoLaser U3, LPKF Laser & Electronics AG). The material has a density of 2.5 g/cm^3 and a Young's modulus of 163 ± 5 kPa measured by a tensile testing machine (5940 series, Instron GmbH). In fig. S17C, the footpads were bonded with the robot body with Ecoflex 00-30 silicone rubber (mixture ratio, part A:part B = 1:1 by weight, Smooth-On Inc.).

Fabrication of the adhesive patch for sensing adhesion and pH

The adhesive patch for sensing dry adhesion had a back layer of Ecoflex-0030 silicone rubber. It was cut into a 0.5 mm × 2 mm × 100 μm rectangular sheet prepared using a laser machine (LPKF ProtoLaser U3, LPKF Laser & Electronics AG). The sheet was bonded to the middle part of the robot body using uncured Ecoflex-0030 as glue. The adhesive patch used for sensing tissue adhesion consists of three layers: the 100-μm-thick elastomer, the dissipative hydrogel, and the pH-responsive bioadhesive. The elastomer layer was prepared the same way as the used dry adhesive patch. Then, we pipetted the benzophenone solution (20 wt % in ethanol) over the patch as the hydrophobic photoinitiator and coated the patch with PEGDA as a dissipative hydrogel layer. To prepare the pH-responsive bioadhesive, 5,5′,6,6′-tetrahydroxy-3,3,3′,3′-tetramethyl-1,1′-spirobiindane (Sigma-Aldrich Inc.), boric acid (Sigma-Aldrich Inc.), and sodium hydroxide (Sigma-Aldrich Inc.) were dissolved into deionized water with a concentration of 0.11, 0.022, and 0.02 g/ml, respectively, in the final solution. The mixture was stirred at 90°C for 8 hours for reaction and then filtrated with a 0.2-μm sterile syringe filter. Polyvinyl alcohol (molecular weight, 89,000 to 98,000, 99+% hydrolyzed; Sigma-Aldrich Inc.) and the chitosan-based bioadhesive solution were added to the solution at a weight ratio of 1:3:4 and then stirred at 90°C for 1 hour. The mixture solution (~0.2 μl) was pipetted over the hydrogel layer of the patch. The characterization result of the pH-responsive bioadhesives was shown in fig. S18.

Fabrication of the adhesive patch for sensing tissue viscoelasticity

Benzophenone solution (20 wt % in ethanol) was pipetted over the robot body to initiate the surface bonding to hydrogels by serving as the hydrophobic photoinitiator. PEGDA was poured onto the robot body and then degassed for 30 min. After curing in a 365-nm ultraviolet chamber (ELG100S, Dinies Technologies GmbH) for 6 min, the coated robot body was washed using deionized water to remove the unreacted chemicals. The chitosan-based bioadhesive was then applied to the robot body surface by dip coating.

Preparation of synthetic materials for adhesion measurements

The synthetic materials used for adhesion characterization included Dragon Skin 0020 (Smooth-On Inc.), Dragon Skin FxPro (Smooth-On Inc.), and Ecoflex 0030 (Smooth-On Inc.). The corresponding monomer and cross-linker were mixed at the ratio denoted as the prefix of the name of the surface and degassed for 5 min. The mixture of 2 ml was then poured into a small petri dish and cured at 60°C for 10 min. A 2-mm-thick rectangular sheet (size: 10 mm × 5 mm) was cut for adhesion tests. In addition, the 3D phantom models with surfaces of various curvatures were prepared using a 3D printer (Form 3, Formlabs Inc.) with the photo resin Clear V4 (Formlabs Inc.). Then, the Ecoflex 0030 rubber was applied to the surfaces by dip coating. The tested materials included Ecoflex 0030 with weight ratios of 1:1 and 2:1, Dragon Skin FxPro with weight ratios of 1:2 and 2:1, and Dragon Skin 0020 with a weight ratio of 1:1.

Preparation of synthetic materials for viscoelasticity measurements

The agarose gel samples were prepared in the following steps. First, agarose powder (BioReagents A9539, Sigma-Aldrich Co.) was mixed with deionized water, after which the mixture was continuously heated and stirred at 90°C until all the powder was dissolved. Then, the solution was boiled for another 5 min, poured into a 3D-printed container (photo resin Clear V4, Formlabs Inc.) with a dimension of 25 mm × 10 mm × 10 mm (length × width × thickness), and then cooled at room temperature 24°C for about 30 min. Subsequently, the robot with the bioadhesive was attached to the gel. The same procedure was repeated for preparing agarose gel samples with varying thicknesses using different containers. The agarose gels with weight ratios of 0.3, 0.4, 0.5, 0.6, and 1.0 wt % were prepared. The gelatin powder from porcine skin (~300 g Bloom, Type A, Sigma-Aldrich Co.) was mixed with deionized water and then stirred at 90°C. After the gelatin powder was fully

dissolved, the solution was cooled down at 60°C for 20 min and congealed when immersed in ice water. Thereafter, the robot was attached to the gelatin gel. The gelatin gels with weight ratios of 3.0, 4.0, and 5.0 wt % were prepared.

Sucrose was used for the preparation of viscoelastic samples (*46*). The sucrose powder (S9378, Sigma-Aldrich Co.) was added to the deionized water, and the mixture was heated and stirred at 90°C until all the powder was dissolved. Then, the gels were made through the same procedures above. For example, 60-0.3 agarose-based gel (weight ratio, sucrose:water:agarose, 60:40:0.3) was used for testing the material viscoelasticity in Fig. 6C. Likewise, 50-0.3, 60-0.2, 60-0.4, and 70-0.3 agarose-based gels and 50-3 and 60-3 gelatin-based gels were used. Fluorescent red polyethylene microspheres (UVPMS-BR-1.090 27-32 μm, Cospheric Co.) were adopted to visualize the deformation of the material under a fluorescent microscope (Leica M165 FC, Leica Microsystems). The mixture of the fluorescent microspheres (diameter: 27 to 32 μm) and surfactants Polysorbate 80 (P1754, Sigma-Aldrich Co.) was added to the agarose gel solution and stirred at room temperature for at least 2 min, after which the mixture was cooled for more than 30 min. The soft agarose gel sample with a rigid cylinder embedded was prepared using the following steps. First, the 1.0 wt % agarose gel solution was poured into the negative cylinder mold, whose one end was sealed by plastic tape. Then, the tape was removed, and the cured cylinder was extracted and placed on the bottom of the container. Afterward, the 0.3 wt % agarose gel solution was poured into it, and the mixture cooled at about 24°C for more than 30 min. If the cylinder needed to be at a distance from the robot, the agarose gel with a given thickness was attached to the cylinder side with the 0.3 wt % agarose gel solution. Last, the robot was attached to the desired position with the abovementioned method.

Adhesion measurements

The adhesion measurement using the robot was conducted in the electromagnetic actuation setup, as shown in fig. S1. To make the measurement consistent for each test, a sequence of external magnetic field waveforms were designed and preprogrammed using LabVIEW (National Instruments Inc.). As shown in Fig. 4D, the procedures include three steps. First, we increased the magnetic field B_y from 0 to 10 mT rapidly to load the adhesive patch for attachment (snapshot at a time interval of 2.5 s) and maintained it for 5 s. Second, we increased the magnetic field B_y in a step-wise waveform from 0 mT up to 20 mT in the negative y direction with an interval of 2 mT while maintaining the magnetic field value at each step for 2.5 s to detach the adhesive patch (snapshot at a time interval of 14.2 s). Last, the measurement cycle was completed until the adhesive patch was completely detached from the tissue (snapshot at a time interval of 17.3 s). The procedures were repeated for at least five times to reduce the measurement errors.

The adhesion measurements to obtain ground-truth data were conducted in a customized experimental setup, as reported in our previous work (*24*). The adhesive patches, including the dry adhesive patch and the pH-responsive adhesive patch, were prepared in the same way as described in the "Fabrication of the adhesive patch for sensing adhesion and pH" section, except that the patches were cropped into 1 mm × 1 mm square sheets. They were attached to a 3D-printed tip and aligned to the substrate, as shown in fig. S3B. The tissue samples were prepared for every 10 tests (within 5 min) from the fresh animal organs to avoid the dehydration of the tissues. The approaching and retracting speeds of the probe were both set to 20 μm/s. The preload and contact time were set to 0.5 mN and 3 s, respectively.

Viscoelasticity measurements

The soft robot attached to a tissue sample was actuated by a rotating magnetic field of different frequencies generated by the Halbach array, as shown in fig. S2. A translational motorized stage (LTS300/M, Thorlabs Inc.) mounted on the vertical stage (DIN 12897, Bochem Instrumente GmbH) was used to control the position of the Halbach array in the x and z axes, while a stepper motor (535-0372, RS Components GmbH) or DC motor (242478, Maxon Co.) was used to rotate the Halbach array.

To measure the viscoelasticity of the material, the prepared sample was first placed under the field of view of the microscope. The motorized stage moved the Halbach array to ensure that the robot was located at the center of the array. Then, the motor started rotating at a given frequency. The Halbach array was rotated at 0.1 Hz for sensing the material elasticity. Subsequently, the robot was actuated by sweeping the magnetic field from 0.3 to 15 Hz to measure the material viscoelasticity. The magnetic field magnitude was adjusted by using different Halbach arrays and changing the z distance from the robot to the array. The robot showed sufficient large deformation for visualization while not detaching from the material. The whole process was recorded with a high-speed camera (mmDK-2740, Dantec Dynamics A/S Inc.) at a sampling rate of 400 FPS. Five material samples were prepared for each type of material. Five soft robot samples were used for each material sample. The viscoelasticity of the samples was characterized using the oscillation frequency module on a rheometer (Discovery HR-2, TA Instruments). The constant strain was set to 0.1%. The frequency varied from 0.1 to 100 rad/s with five test points between 1 and 10 in a log scale. The gel and tissue samples were prepared as 2-mm-thick circular plates with a diameter of 20 mm. The storage and loss moduli used as the ground truth data for quantifying the sensing accuracy of our soft robot–based method are the mean values of those measured at the frequency of 0.1 Hz.

Robot shape tracking and analysis

The robot shape tracking was achieved by extracting its edge or segmenting the image plus centerline extraction at each frame, during which the robot footpads were also tracked. A range of discrete points were sampled at the same interval from the extracted centerline or edge and further used to fit the B-spline to represent the robot curve. All the procedures were accomplished by a customized python code, which is available on GitHub (https://github.com/wchunxiang/biomechanics-estimation).

Visualization and analysis of surface material deformation

Digital image correlation implemented with a customized python code was used to compute the displacement field of the material, whose deformation was visualized by fluorescent particles. On the basis of the assumption that there was no flip between the robot body and the tested material, the displacement of the tracked particles and the robot were combined to compute the strain field. The displacement in the x and y axes of the point $[x_0^{(i)}, y_0^{(i)}]$ in the displacement field were calculated by $u_x[x_0^{(i)}, y_0^{(i)}, t = j] = x_j^{(i)} - x_0^{(i)}$ and $u_y[x_0^{(i)}, y_0^{(i)}, t = j] = y_j^{(i)} - y_0^{(i)}$, where $[x_j^{(i)}, y_j^{(i)}]$ was the position

of the ith particle or robot curve point in the jth frame and $[x_0^{(i)}, y_0^{(i)}]$ was the original position of the tracked particle or robot curve point with no magnetic field actuation. Further, the discrete field points were processed by linear interpolation and data smoothing to obtain the displacement field, as shown in fig. S19 and movie S3. In Fig. 6H and fig. S12, the value of the maximum displacement field $\Delta u(x, y)$ at position (x, y) was calculated by

$$\Delta u(x,y) = \sqrt{\{\max[u_x(x,y,t)] - \min[u_x(x,y,t)]\}^2 + \{\max[u_y(x,y,t)] - \min[u_y(x,y,t)]\}^2} \quad (1)$$

The wavelet transform used for the analysis of the effect of the cylinder inside the homogeneous bulk material was based on the default function cwt (Continuous 1-D wavelet transform) of the SciPy package (*47*).

Correction of the robot curve misalignment for viscoelasticity sensing

As illustrated in fig. S9, the error in the extracted robot shape due to the misalignment between the imaging coordinate system xyz and the robot-tissue coordinate system $x'y'z'$ about the x axis can be corrected using the following equation

$$\begin{bmatrix} x \\ y \\ z \\ 1 \end{bmatrix} = \begin{bmatrix} 1 & 0 & 0 & x_0 \\ 0 & \cos(\varphi) & -\sin(\varphi) & y_0 \\ 0 & \sin(\varphi) & \cos(\varphi) & z_0 \\ 0 & 0 & 0 & 1 \end{bmatrix} \begin{bmatrix} x' \\ y' \\ z' \\ 1 \end{bmatrix} \quad (2)$$

where (x_0, y_0, z_0) is the origin coordinate of $x'y'z'$ in xyz and φ is the misalignment angle about the x axis, $\varphi = \arcsin[(l - t)/w]$. Here, l is the nominal thickness of the robot, and t and w are the real thickness and width of the robot body. Assuming that the robot only deforms in the $x'y'$ plane during the actuation, the real robot displacement u'_y can be obtained using the correction, $u'_y = u_y/\cos(\varphi)$, where u_y is the detected robot displacement in the imaging coordinate system.

X-ray medical imaging

An x-ray imaging device (XPERT 80, KUBTEC, Stratford CT) was used to visualize the robot shape changes on tissues. As illustrated in fig. S20A, sensing adhesion under x-ray imaging was achieved by adjusting the position and orientation of the permanent magnet. With the Halbach array mounted on a rotary motion stage in fig. S20B, the robot motion for viscoelasticity sensing was clearly demonstrated in movie S5. The x-ray accelerating voltage was set to 65 kV during the experiments, and the video was recorded at 30 FPS. The x-ray dose was measured with the radiation meter (RM-400, Voltcraft GmbH) under the α + γ + β mode for the x-ray accelerating voltage 65 kV and current 86 μA.

Preparation of animal organs

The porcine organs in the GI tract, including the small intestine, stomach, and chicken breast, were from the local food factory in Stuttgart, Germany. The rat stomachs were from the Anatomy and Cell Biology Laboratory in University of Ulm, Germany. The organs were minimally cleaned by emptying the organ while minimizing the surface damage. The tissues used for tests and characterization were within 24 hours and stored in a refrigerator at 2°C. The organs were cut into blocks with a size of 25 mm × 15 mm (width × height) and a thickness of 6.4 ± 1.4 mm. Then, the robot was attached to the surface to sense viscoelasticity. For viscoelasticity characterization, the organs were cut into circular plates with a radius of 10 mm and a thickness of 5 mm. For the adhesion tests, the organs were cut and attached to a glass slide. Then, the robot was put on the tissue to test the adhesion property.

Preparation of mice with TNK1 expression–related intestinal disorder or disease model

The expression of TNK1 in 8-week-old *Tnk1*-knockin mice (*Rosa26rtTA/+*, *Hprt MycTnk1tg*) was induced by the single intraperitoneal injection of doxycycline (50 μg/g). The control group of healthy mice was treated with the intraperitoneal injection of the same volume of saline solution (0.9% NaCl). Twenty-four hours after the injection, the mice were sacrificed and dissected. Genetic modification of TNK1-knockin mice was verified by genotyping. To prepare the tissues for the viscoelasticity tests, the colon and the intestinal organs behind it were cut out, and the robot was attached to the internal surface of the opened colon. To prepare the tissues for the adhesion tests, the stomach was opened and minimally cleaned by emptying the inner stuff. All tests were completed within 3 hours.

Supplementary Materials

This PDF file includes:
Notes S1 to S3
Figs. S1 to S23
Legends for movies S1 to S5
References

Other Supplementary Material for this manuscript includes the following:
Movies S1 to S5

REFERENCES AND NOTES

1. A. J. Thompson, E. K. Pillai, I. B. Dimov, S. K. Foster, C. E. Holt, K. Franze, Rapid changes in tissue mechanics regulate cell behaviour in the developing embryonic brain. *eLife* **8**, e39356 (2019).
2. A. Dance, The secret forces that squeeze and pull life into shape. *Nature* **589**, 186–188 (2021).
3. N. F. Läubli, J. T. Burri, J. Marquard, H. Vogler, G. Mosca, N. Vertti-Quintero, N. Shamsudhin, A. deMello, U. Grossniklaus, D. Ahmed, B. J. Nelson, 3D mechanical characterization of single cells and small organisms using acoustic manipulation and force microscopy. *Nat. Commun.* **12**, 2583 (2021).
4. M. Lin, H. Hu, S. Zhou, S. Xu, Soft wearable devices for deep-tissue sensing. *Nat. Rev. Mater.* **7**, 850–869 (2022).
5. E. Song, Y. Huang, N. Huang, Y. Mei, X. Yu, J. A. Rogers, Recent advances in microsystem approaches for mechanical characterization of soft biological tissues. *Microsyst. Nanoeng.* **8**, 77 (2022).
6. K. M. Kennedy, L. Chin, R. A. McLaughlin, B. Latham, C. M. Saunders, D. D. Sampson, B. F. Kennedy, Quantitative micro-elastography: Imaging of tissue elasticity using compression optical coherence elastography. *Sci. Rep.* **5**, 15538 (2015).
7. R. M. S. Sigrist, J. Liau, A. El Kaffas, M. C. Chammas, J. K. Willmann, Ultrasound elastography: Review of techniques and clinical applications. *Theranostics* **7**, 1303–1329 (2017).
8. K. K. Shung, *Diagnostic Ultrasound: Imaging and Blood Flow Measurements* (CRC Press, 2005).
9. G. Low, S. A. Kruse, D. J. Lomas, General review of magnetic resonance elastography. *World J. Radiol.* **8**, 59–72 (2016).
10. F. Schrank, C. Warmuth, S. Görner, T. Meyer, H. Tzschätzsch, J. Guo, Y. O. Uca, T. Elgeti, J. Braun, I. Sack, Real-time MR elastography for viscoelasticity quantification in skeletal muscle during dynamic exercises. *Magn. Reson. Med.* **84**, 103–114 (2020).
11. H. Hu, X. Zhu, C. Wang, L. Zhang, X. Li, S. Lee, Z. Huang, R. Chen, Z. Chen, C. Wang, Y. Gu, Y. Chen, Y. Lei, T. Zhang, N. H. Kim, Y. Guo, Y. Teng, W. Zhou, Y. Li, A. Nomoto, S. Sternini,

Q. Zhou, M. Pharr, F. L. di Scalea, S. Xu, Stretchable ultrasonic transducer arrays for three-dimensional imaging on complex surfaces. *Sci. Adv.* **4**, eaar3979 (2018).
12. C. Wang, X. Li, H. Hu, L. Zhang, Z. Huang, M. Lin, Z. Zhang, Z. Yin, B. Huang, H. Gong, S. Bhaskaran, Y. Gu, M. Makihata, Y. Guo, Y. Lei, Y. Chen, C. Wang, Y. Li, T. Zhang, Z. Chen, A. P. Pisano, L. Zhang, Q. Zhou, S. Xu, Monitoring of the central blood pressure waveform via a conformal ultrasonic device. *Nat. Biomed. Eng.* **2**, 687–695 (2018).
13. C. Wang, X. Chen, L. Wang, M. Makihata, H.-C. Liu, T. Zhou, X. Zhao, Bioadhesive ultrasound for long-term continuous imaging of diverse organs. *Science* **377**, 517–523 (2022).
14. X. Yu, H. Wang, X. Ning, R. Sun, H. Albadawi, M. Salomao, A. C. Silva, Y. Yu, L. Tian, A. Koh, C. M. Lee, A. Chempakasseril, P. Tian, M. Pharr, J. Yuan, Y. Huang, R. Oklu, J. A. Rogers, Needle-shaped ultrathin piezoelectric microsystem for guided tissue targeting via mechanical sensing. *Nat. Biomed. Eng.* **2**, 165–172 (2018).
15. E. Song, Z. Xie, W. Bai, H. Luan, B. Ji, X. Ning, Y. Xia, J. M. Baek, Y. Lee, R. Avila, H.-Y. Chen, J.-H. Kim, S. Madhvapathy, K. Yao, D. Li, J. Zhou, M. Han, S. M. Won, X. Zhang, D. J. Myers, Y. Mei, X. Guo, S. Xu, J.-K. Chang, X. Yu, Y. Huang, J. A. Rogers, Miniaturized electromechanical devices for the characterization of the biomechanics of deep tissue. *Nat. Biomed. Eng.* **5**, 759–771 (2021).
16. J. Shin, Y. Yan, W. Bai, Y. Xue, P. Gamble, L. Tian, I. Kandela, C. R. Haney, W. Spees, Y. Lee, M. Choi, J. Ko, H. Ryu, J. K. Chang, M. Pezhouh, S. K. Kang, S. M. Won, K. J. Yu, J. Zhao, Y. K. Lee, M. MacEwan, S. K. Song, Y. Huang, W. Z. Ray, J. A. Rogers, Bioresorbable pressure sensors protected with thermally grown silicon dioxide for the monitoring of chronic diseases and healing processes. *Nat. Biomed. Eng.* **3**, 37–46 (2019).
17. A. J. Bredenoord, Impedance-pH monitoring: New standard for measuring gastro-oesophageal reflux. *Neurogastroenterol. Motil.* **20**, 434–439 (2008).
18. G. Ciuti, R. Caliò, D. Camboni, L. Neri, F. Bianchi, A. Arezzo, A. Koulaouzidis, S. Schostek, D. Stoyanov, C. M. Oddo, B. Magnani, A. Menciassi, M. Morino, M. O. Schurr, P. Dario, Frontiers of robotic endoscopic capsules: A review. *J. Microbio Robot.* **11**, 1–18 (2016).
19. J. Min, Y. Yang, Z. Wu, W. Gao, Robotics in the gut. *Adv. Ther.* **3**, 1900125 (2020).
20. N. Shamsudhin, V. I. Zverev, H. Keller, S. Pane, P. W. Egolf, B. J. Nelson, A. M. Tishin, Magnetically guided capsule endoscopy. *Med. Phys.* **44**, e91–e111 (2017).
21. S. Baltsavias, W. Van Treuren, M. J. Weber, J. Charthad, S. Baker, J. L. Sonnenburg, A. Arbabian, In vivo wireless sensors for gut microbiome redox monitoring. *IEEE Trans. Biomed. Eng.* **67**, 1821–1830 (2020).
22. F. Serwane, A. Mongera, P. Rowghanian, D. A. Kealhofer, A. A. Lucio, Z. M. Hockenbery, O. Campàs, In vivo quantification of spatially varying mechanical properties in developing tissues. *Nat. Methods* **14**, 181–186 (2016).
23. F. E. Uslu, C. D. Davidson, E. Mailand, N. Bouklas, B. M. Baker, M. S. Sakar, Engineered extracellular matrices with integrated wireless microactuators to study mechanobiology. *Adv. Mater.* **33**, 2102641 (2021).
24. Y. Wu, X. Dong, J. K. Kim, C. Wang, M. Sitti, Wireless soft millirobots for climbing three-dimensional surfaces in confined spaces. *Sci. Adv.* **8**, eabn3431 (2022).
25. N. D. Blelloch, H. J. Yarbrough, K. A. Mirica, Stimuli-responsive temporary adhesives: Enabling debonding on demand through strategic molecular design. *Chem. Sci.* **12**, 15183–15205 (2021).
26. D. Yan, M. Pezzulla, L. Cruveiller, A. Abbasi, P. M. Reis, Magneto-active elastic shells with tunable buckling strength. *Nat. Commun.* **12**, 2831 (2021).
27. J. Li, A. D. Celiz, J. Yang, Q. Yang, I. Wamala, W. Whyte, B. R. Seo, N. V. Vasilyev, J. J. Vlassak, Z. Suo, D. J. Mooney, Tough adhesives for diverse wet surfaces. *Science* **357**, 378–381 (2017).
28. J. Huang, Y. Liu, Y. Yang, Z. Zhou, J. Mao, T. Wu, J. Liu, Q. Cai, C. Peng, Y. Xu, B. Zeng, W. Luo, G. Chen, C. Yuan, L. Dai, Electrically programmable adhesive hydrogels for climbing robots. *Sci. Robot.* **6**, eabe1858 (2021).
29. M. S. Akram Bhuiyan, J. D. Roland, B. Liu, M. Reaume, Z. Zhang, J. D. Kelley, B. P. Lee, In situ deactivation of catechol-containing adhesive using electrochemistry. *J. Am. Chem. Soc.* **142**, 4631–4638 (2020).
30. T. Machida, A study of intragastric pH in patients with peptic ulcer-with special reference to the clinical significance of basal pH value. *Gastroenterol. Jpn.* **16**, 447–458 (1981).
31. A. M. Handorf, Y. Zhou, M. A. Halanski, W.-J. Li, Tissue stiffness dictates development, homeostasis, and disease progression. *Organogenesis* **11**, 1–15 (2015).
32. D. A. Stoltz, D. K. Meyerholz, M. J. Welsh, Origins of cystic fibrosis lung disease. *N. Engl. J. Med.* **372**, 351–362 (2015).
33. N. Miyahara, T. Kokubo, Y. Hara, A. Yamada, T. Koike, Y. Arai, Evaluation of X-ray doses and their corresponding biological effects on experimental animals in cone-beam micro-CT scans (R-mCT2). *Radiol. Phys. Technol.* **9**, 60–68 (2016).
34. M. Armacki, A. K. Trugenberger, A. K. Ellwanger, T. Eiseler, C. Schwerdt, L. Bettac, D. Langgartner, N. Azoitei, R. Halbgebauer, R. Groß, T. Barth, A. Lechel, B. M. Walter, J. M. Kraus, C. Wiegreffe, J. Grimm, A. Scheffold, M. R. Schneider, K. Peuker, S. Zeißig, S. Britsch, S. Rose-John, S. Vettorazzi, E. Wolf, A. Tannapfel, K. Steinestel, S. O. Reber, P. Walther, H. A. Kestler, P. Radermacher, T. F. E. Barth, M. Huber-Lang, A. Kleger, T. Seufferlein, Thirty-eight-negative kinase 1 mediates trauma-induced intestinal injury and multi-organ failure. *J. Clin. Investig.* **128**, 5056–5072 (2018).
35. J. Zhang, Y. Guo, W. Hu, R. H. Soon, Z. S. Davidson, M. Sitti, Liquid crystal elastomer-based magnetic composite films for reconfigurable shape-morphing soft miniature machines. *Adv. Mater.* **33**, 2006191 (2021).
36. A. Thitaikumar, T. A. Krouskop, J. Ophir, Signal-to-noise ratio, contrast-to-noise ratio and their trade-offs with resolution in axial-shear strain elastography. *Phys. Med. Biol.* **52**, 13–28 (2007).
37. R. Delaunay, Y. Hu, T. Vercauteren, in *Medical Image Computing and Computer Assisted Intervention–MICCAI 2020* (Springer, 2020), pp. 573–582.
38. M. Mirzaei, A. Asif, H. Rivaz, Combining total variation regularization with window-based time delay estimation in ultrasound elastography. *IEEE Trans. Med. Imaging* **38**, 2744–2754 (2019).
39. S.-J. Kim, D.-S. Lee, I.-G. Kim, D.-W. Sohn, J.-Y. Park, B.-K. Choi, S.-W. Kim, Evaluation of the biocompatibility of a coating material for an implantable bladder volume sensor. *Kaohsiung J. Med. Sci.* **28**, 123–129 (2012).
40. H.-J. Chung, A. M. Parsons, L. Zheng, Magnetically controlled soft robotics utilizing elastomers and gels in actuation: A review. *Adv. Intell. Syst.* **3**, 2000186 (2021).
41. D. Armstrong, Review article: Gastric pH—The most relevant predictor of benefit in reflux disease? *Aliment. Pharmacol. Ther.* **20**, 19–26 (2004).
42. T. Ebihara, N. Venkatesan, R. Tananka, M. S. Ludwig, Changes in extracellular matrix and tissue viscoelasticity in bleomycin-induced lung fibrosis. *Am. J. Respir. Crit. Care Med.* **162**, 1569–1576 (2000).
43. H. T. Nia, L. L. Munn, R. K. Jain, Physical traits of cancer. *Science* **370**, eaaz0868 (2020).
44. H. S. Merki, C. J. Fimmel, R. P. Walt, K. Harre, J. Röhmel, L. Witzel, Pattern of 24 hour intragastric acidity in active duodenal ulcer disease and in healthy controls. *Gut* **29**, 1583–1587 (1988).
45. A. R. Narkar, C. Kendrick, K. Bellur, T. Leftwich, Z. Zhang, B. P. Lee, Rapidly responsive smart adhesive-coated micropillars utilizing catechol–boronate complexation chemistry. *Soft Matter* **15**, 5474–5482 (2019).
46. S. Maurer, A. Junghans, T. A. Vilgis, Impact of xanthan gum, sucrose and fructose on the viscoelastic properties of agarose hydrogels. *Food Hydrocoll.* **29**, 298–307 (2012).
47. P. Virtanen, R. Gommers, T. E. Oliphant, M. Haberland, T. Reddy, D. Cournapeau, E. Burovski, P. Peterson, W. Weckesser, J. Bright, S. J. van der Walt, M. Brett, J. Wilson, K. J. Millman, N. Mayorov, A. R. J. Nelson, E. Jones, R. Kern, E. Larson, C. J. Carey, I. Polat, Y. Feng, E. W. Moore, J. VanderPlas, D. Laxalde, J. Perktold, R. Cimrman, I. Henriksen, E. A. Quintero, C. R. Harris, A. M. Archibald, A. H. Ribeiro, F. Pedregosa, P. van Mulbregt; SciPy 1.0 Contributors, SciPy 1.0: Fundamental algorithms for scientific computing in Python. *Nat. Methods* **17**, 261–272 (2020).
48. J. Nocedal, S. J. Wright, *Numerical Optimization* (Springer, 1999).
49. Y. Kim, H. Yuk, R. Zhao, S. A. Chester, X. Zhao, Printing ferromagnetic domains for untethered fast-transforming soft materials. *Nature* **558**, 274–279 (2018).
50. K. L. Johnson, *Contact Mechanics* (Cambridge Univ. Press, 1987).

Acknowledgments
Funding: This work was funded by the Max Planck Society, European Research Council (ERC) Advanced Grant SoMMoR project with grant no. 834531, German Research Foundation (DFG) Soft Material Robotic Systems (SPP 2100) Program with grant no. 2197/5-1, and the Max Planck Queensland Center. Y.W. thanks the Alexander von Humboldt Foundation for financial support.
Author contributions: X.D., C.W., Y.W., and M.S. conceived the idea and designed the research. C.W., Y.W., and X.D. carried out the experiments and analyzed the data with the assistance from M.A. X.D. developed the theory. M.S. and X.D. supervised the research. C.W., Y.W., and X.D. wrote the manuscript with input from all authors. All authors discussed the results and commented on or edited the manuscript. **Competing interests:** X.D., Y.W., C.W., and M.S. are coinventors on a pending patent application related to this work to be filed at the European Patent Office. The authors declare that they have no other competing interests. **Data and materials availability:** All data needed to evaluate the conclusions in the paper are present in the paper and/or the Supplementary Materials.

Submitted 20 December 2022
Accepted 2 May 2023
Published 7 June 2023
10.1126/sciadv.adg3988

APPLIED PHYSICS

Ultrafast dynamic machine vision with spatiotemporal photonic computing

Tiankuang Zhou[1,2,3,4]†, Wei Wu[1]†, Jinzhi Zhang[1,4], Shaoliang Yu[5], Lu Fang[1,3,6]*

Ultrafast dynamic machine vision in the optical domain can provide unprecedented perspectives for high-performance computing. However, owing to the limited degrees of freedom, existing photonic computing approaches rely on the memory's slow read/write operations to implement dynamic processing. Here, we propose a spatiotemporal photonic computing architecture to match the highly parallel spatial computing with high-speed temporal computing and achieve a three-dimensional spatiotemporal plane. A unified training framework is devised to optimize the physical system and the network model. The photonic processing speed of the benchmark video dataset is increased by 40-fold on a space-multiplexed system with 35-fold fewer parameters. A wavelength-multiplexed system realizes all-optical nonlinear computing of dynamic light field with a frame time of 3.57 nanoseconds. The proposed architecture paves the way for ultrafast advanced machine vision free from the limits of memory wall and will find applications in unmanned systems, autonomous driving, ultrafast science, etc.

INTRODUCTION

Processing dynamic light fields at high speed has proven to be of vital importance in visual computing and scientific discovery. With the development of artificial neural networks (*1*, *2*), machine learning–based electronic visual computing has achieved excellent performances in various applications (*3*, *4*). The rapid implementation of dynamic visual computing such as tracking, detection, and recognition has become vital in time-varying scenarios, including autonomous driving (*5*) and intelligent robots (*6*). Unfortunately, the integration density of silicon transistors gradually approaches physical limits, thereby saturating the computational speed of electronic computers and electronic visual computing (*7*, *8*). Besides visual computing, studying ultrafast light fields is also crucial for scientific research. Repetitive probing and continuous imaging support recording transient processes down to the nanosecond and picosecond levels (*9*–*11*). However, the reconstruction and analysis of ultrafast visual dynamics require digital transferring and postprocessing with electronic computers, which precludes real-time analysis and feedback control of the ultrafast phenomena (*12*).

Endowed with low-loss, parallel, ultrafast, and clock-free light propagation, photonic computing has been heralded as a prospective solution to alleviate the limitations of electronic computing and expedite light-field processing (*13*–*17*). Recently, researchers have validated the advantages of photonic computing in performing high-speed linear matrix operations with coherent photonic integrated circuits (*18*, *19*), on-chip resonators (*20*), diffractive optical processors (*21*–*25*), photonic phase-change materials (*26*–*28*), dispersive optical delay lines (*29*), etc. It has also been demonstrated that light can be used for ubiquitous computing, including nonlinear neuron activation (*30*), nondeterministic polynomial-time hard (NP-hard) optimization (*31*, *32*), equation solving (*33*), and integration as well as differentiation (*34*–*36*). On the basis of the linear and nonlinear optical computing paradigms, photonic neural networks have been constructed for machine vision tasks such as edge detection (*37*), image classification (*25*, *38*), saliency detection (*22*), and human action recognition (*25*, *39*). Despite recent advances, state-of-the-art photonic computing methods are incapable of processing ultrafast dynamic light fields. Currently, to process spatiotemporal light fields, dynamic inputs are usually computed sequentially in the spatial domain, while the spatial output at different time steps needs to be transmitted, stored, and further processed with digital electronics (*25*, *39*). Although such a procedure exploits the advantage of high spatial parallelism of light propagation, digital transmission and read/write operations of memory pose severe limitations to inference speed, which impairs the merit of photonics for high-speed computing.

The incorporation of spatial and temporal photonic computing to eliminate the digital bottlenecks is promising for ultrafast light-field processing. This is because the spatiotemporal manipulation of light fields can overcome the limitations of spatial-only modulation (*40*, *41*). Temporal information preprocessing with nonlinear reservoirs has been applied in vowel recognition (*42*), serial data classification (*43*), time-series prediction (*44*), etc. In addition, multimode fiber has also been used to build a nonlinear reservoir for single-image classification (*45*). However, these solutions apply only to spatial or temporal data. The limited degree of freedoms (DOFs) render these approaches ineffective in processing high-dimensional light fields. Another approach, that is, computational imaging, exploits the dimensional advantages of light and realizes high-speed imaging. For example, single-pixel imaging encodes the spatial data in the temporal dimension for fast and compressed imaging (*46*). The time-stretched serial time-encoded amplified imaging uses a dispersed supercontinuum laser pulse to spectrally capture and record the serialized image contents (*9*). However, without a computational model, these computational imaging

[1]Department of Electronic Engineering, Tsinghua University, Beijing 100084, China. [2]Department of Automation, Tsinghua University, Beijing 100084, China. [3]Beijing National Research Center for Information Science and Technology, Tsinghua University, Beijing 100084, China. [4]Shenzhen International Graduate School, Tsinghua University, Shenzhen 518071, China. [5]Research Center for Intelligent Optoelectronic Computing, Zhejiang Laboratory, Hangzhou 311100, China. [6]Institute for Brain and Cognitive Sciences, Tsinghua University, Beijing 100084, China.
*Corresponding author. Email: fanglu@tsinghua.edu.cn
†These authors contributed equally to this work.

methods only record the data and are unable to effectively compute and make decisions. Thus far, a general parametric photonic computing solution to process spatiotemporal light fields at high speed is still lacking, which restricts the rapid implementation of advanced machine vision architecture and real-time analysis of ultrafast visual dynamics. Technically, (i) owing to the inherent dimension mismatch of the spatial and temporal light fields, computing and converting between highly parallel spatial light fields and high-speed temporal optical dynamics remain challenging. (ii) The DOFs of spatial and temporal computing are limited; thus, there is a gap between the existing photonic computing methods and full-space spatiotemporal computing.

In this study, we propose and implement a spatiotemporal photonic computing (STPC) architecture for ultrafast dynamic machine vision. By co-optimizing a general STPC unit, the STPC extracts spatiotemporal information and makes predictions based on time-varying light fields. In essence, the STPC architecture comprises the spatial computing module, the spatiotemporal multiplexing module, and the temporal computing module. Specifically, (i) a spatial computing module involves a spatial modulator that performs per-point multiplication, convolution, etc. (ii) To effectively compute and convert between spatial and temporal optical dynamics, we devise spatial multiplexing (SMUX) and wavelength multiplexing (WMUX) modules to match the highly parallel spatial outputs and high-speed temporal inputs while adequately preserving content information. Spatial content is thus processed and mapped to parallel sequences of temporal dynamics spatially and spectrally, leading to the generation of a temporal computing–compatible spatiotemporal feature space. (iii) In the temporal computing module, to store and merge the fast-changing optical signals, an analog temporal buffer is constructed such that the information can be delayed and reproduced in the optical domain. Temporal matrix-vector multiplication (MVM) is then performed to build weighted connections in the time domain, which is co-designed with spatial computing modules to implement comprehensive computing in the entire spatiotemporal plane. The STPC architecture is enhanced with an experimental system learning method, which can optimize the parametric physical system along with the computational model and improves the accuracy of STPC by more than 80%. The experiments of the SMUX-STPC network showed superior performance on spiking sequence classification, human action recognition, and object motion tracking tasks. Compared with existing photonic computing methods, the SMUX-STPC system increases parameter efficiency and reduces inference time by more than one order of magnitude. A two-layer all-optical WMUX-STPC network with multivariate nonlinear activation function recognizes the ultrafast flashing sequences with nanoseconds frame time, free of memory read/write latencies. The STPC architecture bolsters high-performance photonic neural networks and enables real-time analysis of dynamic visual scenes beyond nanosecond time scales.

RESULTS

STPC architecture

The STPC architecture is illustrated in Fig. 1A. Millisecond-to-nanosecond time-varying light fields from a dynamic scene propagates into the STPC network, which consists of cascaded blocks of STPC units, each with a spatial module and a temporal module connected by a multiplexing module. Through combinations of spatial and temporal operations, the STPC unit extracts information from the high-dimensional dynamic light fields and infers semantic information from the contents of the scene. The core STPC system is shown in the left panel of Fig. 1B, with the network model displayed on the right. The unfolded system is shown in Fig. 1C. Each STPC unit transforms the spatiotemporal input $x_i(s, t)$ to the output $y(s, t)$, where s, t are the spatial and temporal coordinates, respectively. The output $y(s, t)$ is subsequently activated nonlinearly and fed into the next layer. There are three main procedures in each spatiotemporal (ST) layer: (i) spatial modulation in the spatial computing module, (ii) spatiotemporal multiplexing, and (iii) MVM in the temporal computing module. The input spatiotemporal light field x_i is a three-dimensional (3D, two spatial dimensions and one temporal dimension) stack. In the spatial computing module, $x_i(s, t)$ is weighted with a spatial light modulator, such as a digital micromirror device (DMD), or a liquid crystal on silicon–based spatial light modulator to perform amplitude and/or phase modulation, that is

$$x_{st}(s, t) = w_s(s, t)x_i(s, t) \tag{1}$$

As shown in Fig. 1 (B and C), during the period of each input temporal slice, $x_i(s, t)$ is sequentially modulated K times, such that the effective number of temporal slices in $x_{st}(s, t)$ is K times that of $x_i(s, t)$. Although we used element-wise weighting in spatial computing, it can also be generalized to other spatial computing models, such as convolution (*47*) and diffractive processing (*25*).

The spatially weighted results $x_{st}(s, t)$ are then fed into the temporal channels. When spatial outputs transition into temporal channels, the mode diversity decreases drastically. Thus, directly coupling the spatial contents into the single-mode temporal channel leads to the loss of most of the information. Thus, we propose SMUX STPCs and WMUX STPCs to increase the information capacity (*48*), which coordinates between highly parallel spatial and high-speed temporal modules

$$o(u, t) = \int T(u, s)x_{st}(s, t)ds \tag{2}$$

where $T(u, s)$ is the spatial-to-temporal transfer function, and u is in the multiplexing dimension, which is the space and wavelength for SMUX and WMUX, respectively. The details of SMUX and WMUX are presented in Fig. 2B.

The temporal module then takes in the multiplexing outputs $o(u, t)$, where a temporal MVM is constructed. Discretizing the time, the temporal operations can be formulated as

$$y(u, k\Delta\tau) = \Sigma_i\ w_t(k\Delta\tau, i\Delta t)o(u, i\Delta t) \tag{3}$$

Specifically, temporal modulation is conducted to weigh the temporal inputs with an intensity modulator (MOD), producing $w_t(k\Delta\tau, i\Delta t)o(u, i\Delta t)$, with $\Delta\tau$ denoting the output sampling period and Δt indicating the recurrent period in the temporal buffer. The temporal buffer, constructed through waveguide extension and recurrent coupler (CL) connection, offers picosecond to millisecond buffering and merging of temporal signals. With i = 1,2,3, ..., M and k = 1,2,3, ..., N, Eq. 3 essentially formulates the multiplication between an $M \times 1$ vector and an $N \times M$ matrix. An implementation of linear MVM and the extension to nonlinear MVM are presented in Fig. 2C. The dynamic light field $y(u, t)$ is then nonlinearly activated using nonlinear optical effects such as the

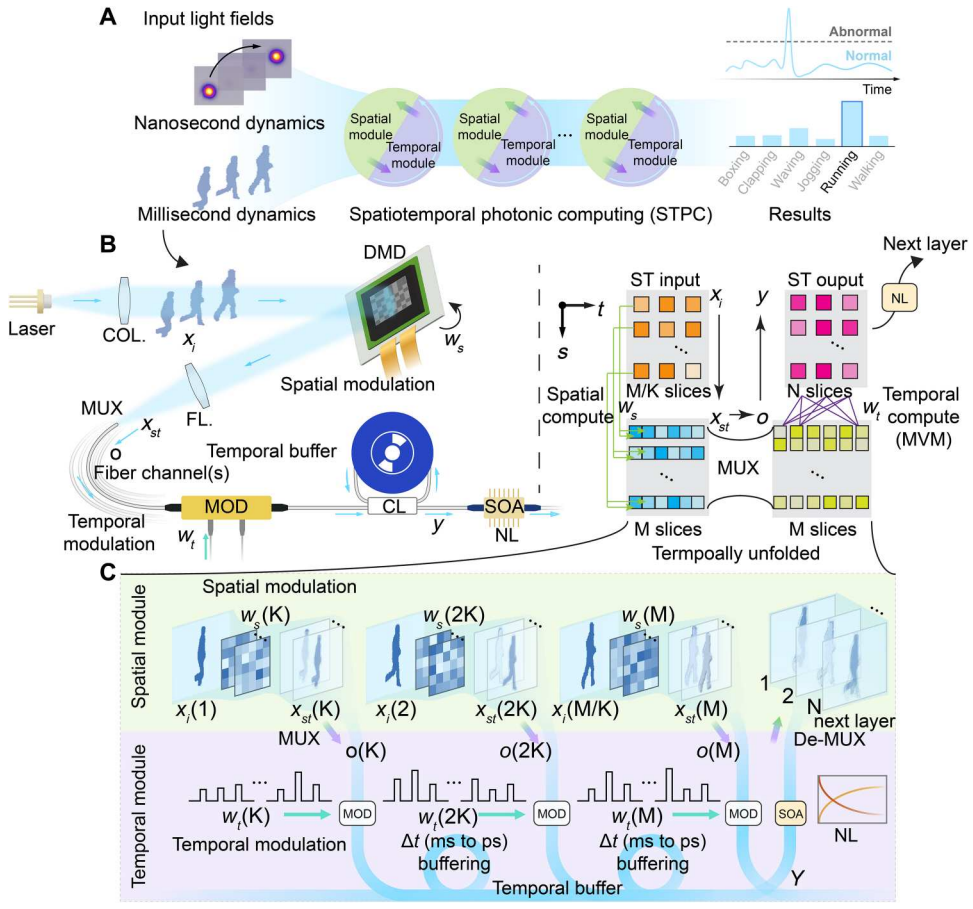

Fig. 1. STPC for ultrafast dynamic light-field processing. (**A**) STPC architecture. Dynamic scene encoded on spatiotemporal light fields enters the STPC network consisting of STPC units. Each unit contains a spatial module and a temporal module connected by a multiplexing module. Decision-making is finally executed by the last STPC unit. (**B**) Core system of the STPC unit (left) and the corresponding network model (right). The input spatiotemporal light field x_i is modeled as a 3D (two spatial dimensions and one temporal dimension) stack. In the spatial module, a DMD performs spatial modulations and expands the stack in the time dimension. Spatial output x_{st} is spatially/spectrally multiplexed (MUX) into the temporal module (o). Through temporal modulations in the modulators (MOD) and buffering in the recurrent buffer, the temporal module performs weighted connection (MVM) in the time domain and produces the output y, which is activated by photonic nonlinearity (NL) and fed to the next layer. (**C**) Unfolded system of an STPC unit in time. The *M*/*K* spatiotemporal input slices are expanded *K* times in the spatial module, producing M output slices. The *M* slices are sequentially computed and recurrently merged in the $N \times M$ temporal MVM to produce the *N* final output slices. COL, collimator; FL, focusing lens; CL, 2 × 2 fiber coupler; SOA, semiconductor amplifier.

saturable gain effect of a semiconductor optical amplifier (SOA) and demultiplexed back into the spatiotemporal domain, which is fed into the subsequent ST computing units for further processing. Last, the characteristics of the light field are inferred, including the type of action and (non-)normality of the transient pattern.

Figure 2A shows the dimensionality of photonic computing. As shown in the left panel of Fig. 2A, basic spatial and temporal photonic computing modules are afflicted with (i) dimension mismatch and (ii) gap in the spatiotemporal plane. Electronic digital computing (EDC) can help alleviate these dimension issues; however, it also induces speed bottlenecks due to the read/write operations of the memory. STPC resolves these two issues in two ways, respectively. First, as shown in the middle panel of Fig. 2A, directly coupling the spatial light fields into the temporal channels would shrink the spatial information diversity (shaded arrow). The lost information could be recovered by stretching the shrunken spatial dimension and modulating the light field in the temporal dimension in SMUX-STPC. In the WMUX-STPC, the spatial dimension is rotated to the wavelength dimension such that the information can be accommodated in the temporal channel with a large optical bandwidth. Second, the photonic computing DOFs are limited. As shown in the left panel of Fig. 2A, a single spatial computing module (green ellipsoid) or temporal computing module (purple ellipsoid) could only process a temporal slice or a spatial slice, respectively, thus a gap between the single modules (inner dashed ellipsoid in the right panel of Fig. 2A) and the full ST plane (external dashed ellipsoid in the right panel of Fig. 2A). In this work, we propose the temporal MVM to connect the outputs from spatial computing modules at different time steps so that the computing DOFs are extended to the full spatiotemporal plane. With matched dimensions and fulfilled spatiotemporal plane, the STPC architecture can process dynamic light fields without memory read/write latency.

Figure 2B depicts the implementation of the SMUX and WMUX in the STPC. In SMUX-STPC, the input space is divided into subregions Ω_j, and the spatial features in each division are collectively

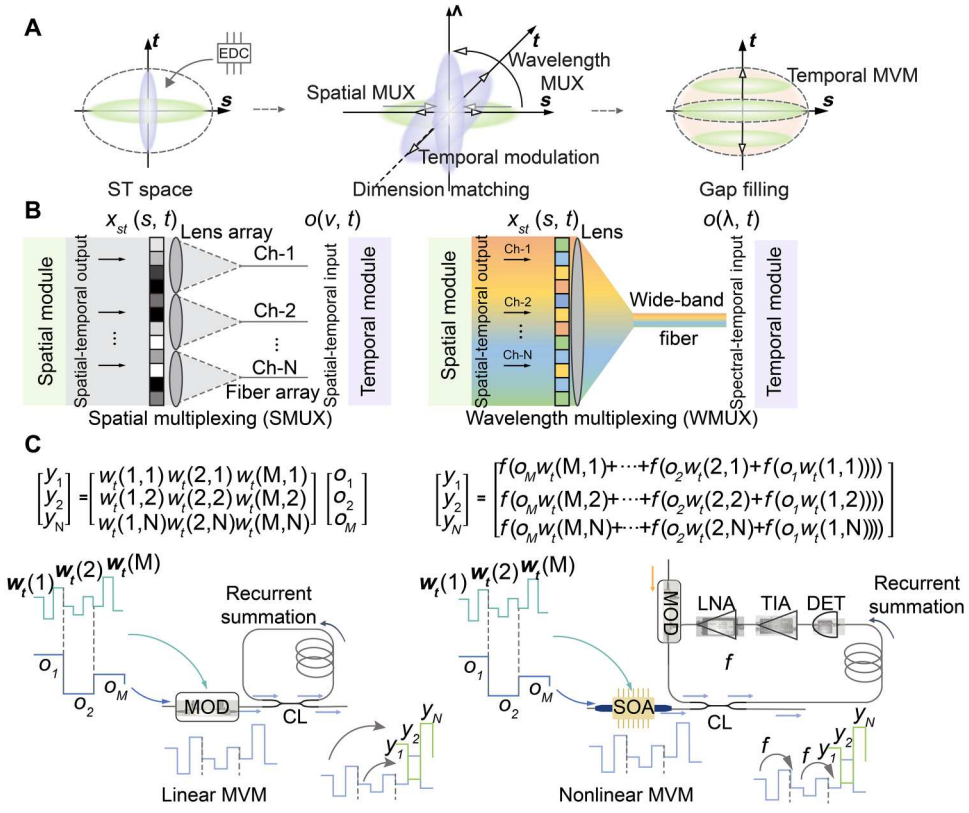

Fig. 2. Implementation of multiplexing modules and temporal MVMs. (**A**) Dimensionality of STPC. Left: Basic spatial and temporal modules with dimension mismatch and a gap in the spatiotemporal plane, which is usually alleviated with an EDC at the expense of speed bottlenecks. In the STPC, the spatiotemporal dimension mismatch is resolved with multiplexing techniques (middle), and the spatiotemporal gap is filled using the temporal MVM unit (right). (**B**) Implementation of spatial and wavelength multiplexing techniques that coordinate between spatial and temporal modules. In space-multiplexed (SMUX) STPC, the high-resolution output from the spatial module is divided into subdivisions. Light in each division is coupled into separate temporal fiber channels through a lens array. In wavelength-multiplexed (WMUX) STPC, spatial light is encoded on different wavelengths, and the multiwavelength optical signal is fed into a wide-band fiber channel. (**C**) Implementation of the linear (left) and nonlinear (right) MVM. Left: Each multiplier in the vector is multiplied by a column of multiplicands in the temporal modulator. The multiplied signals are then looped in the temporal buffer and recurrently added. Right: A nonlinear temporal MVM. The SOA performs temporal weighting. The detector (DET), amplifiers (transimpedance amplifier, TIA; voltage amplifier, LNA), and modulator (MOD) construct an OEO loop, which nonlinearly transforms the inputs in the temporal buffer. CL, 2 × 2 fiber coupler.

coupled into a single-mode-fiber channel through the focusing lens, that is, $o(j, t) = \int_{\Omega_j} T(j, s)x_{st}(s, t)ds$, with $T(j, s)$ being the coupling coefficients from spatial location s to the jth temporal channel. The SMUX and high-speed modulation implemented by millions-of-pixel spatial light modulators convert spatial information spatiotemporally. The higher modulation rate and the more spatial channels, the more retained information. With a fixed modulation speed and spatial channel number, there is a trade-off between the processing time and the amount of information retained. In WMUX-STPC, the spatial features are encoded onto different wavelengths and multiplexed into a single temporal channel, that is, spatial-to-temporal transfer function $T(j, s) = \delta(s - s_j)T(s)$, and $o(j, t) = \int \delta(s - s_j)T(s)x_{st}(s, t)ds$, with $\delta(s - s_j)$ being the Kronecker delta function that encodes the spatial features at s_j onto wavelength j and $T(s)$ being the spatial coupling coefficient. With WMUX, abundant spatial contents can be conserved spectrally so that it supports the processing of ultrafast dynamics without additional high-speed spatial modulators.

Figure 2C illustrates the mathematical model of the temporal MVM, including the linear (left) and nonlinear (right) implementations. Denote the buffer transfer function as $f(\cdot)$, the general form of the temporal MVM can be formulated as $y(u, k) = f\{o_M w_t(k, M) + ... + f[w_t(k,2)o_2 + f[w_t(k,1)o_1)]\}$ (k = 1, 2, ..., N). In the linear implementation, the fiber loop is used as the buffer; thus, $f(x) = x$. The input series o_1, o_2, ..., o_M is multiplied by vectors $\boldsymbol{w_t}(1)$, $\boldsymbol{w_t}(2)$, ..., $\boldsymbol{w_t}(M)$ $\{\boldsymbol{w_t}(j) = [w_t(j,1), w_t(j,2), ..., w_t(j, N)]^T\}$, respectively, with the intensity MOD, forming $o_1\boldsymbol{w_t}(1)$, $o_2\boldsymbol{w_t}(2)$, ...$o_M\boldsymbol{w_t}(M)$ injected into the temporal buffer. Each time light cycles through the temporal buffer, the signal is recurrently merged, such that the output sums to $\boldsymbol{y} = o_1\boldsymbol{w_t}(1) + o_2\boldsymbol{w_t}(2) + ... + o_M\boldsymbol{w_t}(M)$. The linear matrix multiplication performs coherent summation and thus supports complex matrix elements at a single wavelength. For signals at different wavelengths, the light intensities are summed so that the matrix elements are nonnegative real values. A nonlinear implementation of the temporal MVM is also shown in the right panel of Fig. 2C. The temporal weighting is performed by modulating the injection current of the SOA. In the recurrent buffer, an optical-electrical-optical (OEO) converter is constructed with a photodiode (PD), a transimpedance amplifier (TIA), a voltage amplifier [low-noise voltage amplifier (LNA)], and an

intensity MOD. Thus, the temporal transfer function $f(\cdot)$ exhibits nonlinear behavior that is programmable by tuning the bias of the intensity modulator. When the intensity modulator is biased at its minimal output (the NULL point), $f(x) = a \cdot \sin(b \cdot x)^2$, where a and b are system parameters depending on the input power and the loop gain coefficient. As nonlinear matrix multiplications are computed in terms of intensity, the elements of the nonlinear matrix elements are nonnegative as well. In addition, as the nonlinear buffer features a sinusoidal transfer function here, the matrix elements are thus nested in the sinusoidal function. In general, the proposed temporal MVM is a temporally reconfigurable recurrent neural network (*49*).

SMUX STPC network for high-speed dynamic scene analysis

Figure 3A illustrates the learning process of the STPC physical experiments, including model training and system learning. The entire system consists of three parts: datasets with input and target pairs, an experimental system, and the experimental outputs. The experimental system contains the model parameters and system parameters. The model parameters include the weights of the STPC, which primarily involve the spatial computing masks and the temporal modulation weights. The system parameters characterize the transfer function of the experimental physical system with spatial and temporal modules that can be initially calibrated with random inputs. Given the training input and target pairs, we pretrain the system using the calibrated system parameters until convergence. Owing to the bias and noise in the calibration data, the experimental results deviate from the simulation. Here,

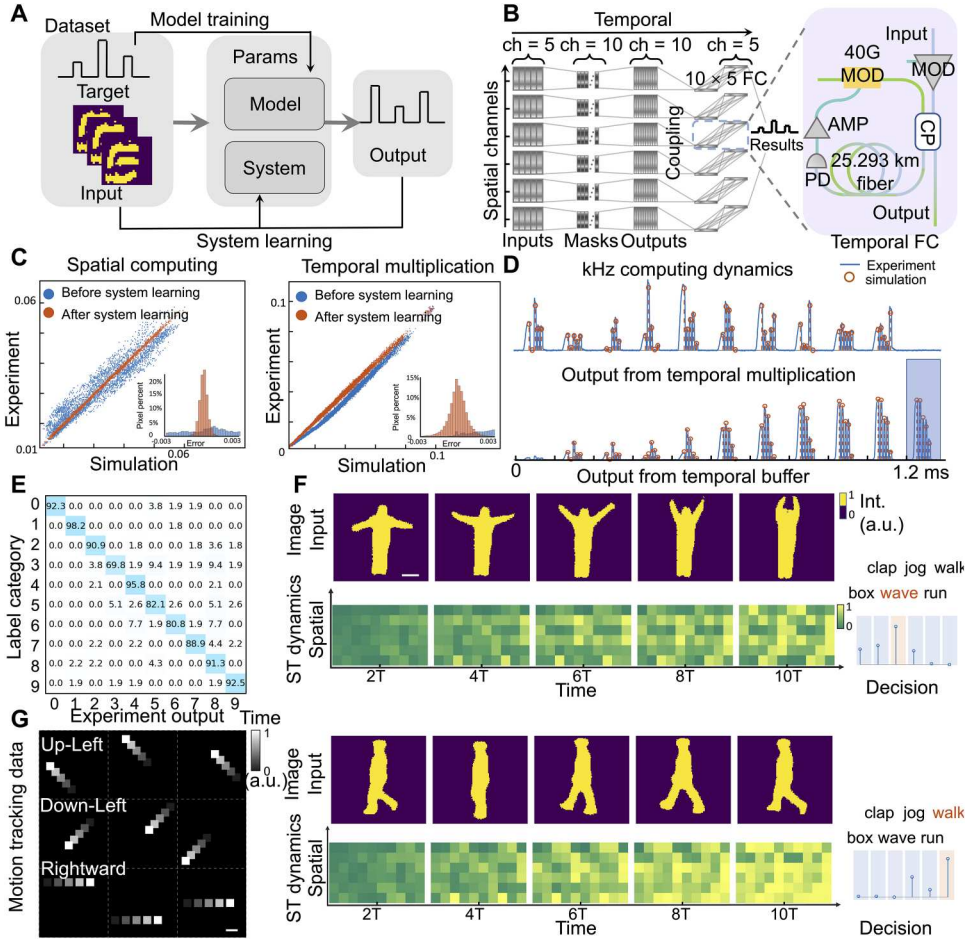

Fig. 3. Space-multiplexed (SMUX) STPC network for high-speed dynamic scene analysis. (**A**) Model training and system learning. The experimental system contains model parameters and system parameters. The model parameters configured in the STPC are learned with training input and target pairs, while the system parameters characterizing the transfer function of the physical system are learned with the experimental inputs and outputs to improve the system modeling fidelity. (**B**) An SMUX-STPC network consisting of six spatial divisions was designed to recognize high-speed video dynamics. Each division was spatially and temporally computed to infer the final results. (**C**) Spatial computing and temporal multiplication accuracy before (blue) and after (orange) system learning on spiking handwritten digits classification experiment. Inset shows the error distribution before and after system learning. (**D**) Kilohertz computing dynamics of the STPC system. The outputs from temporal multiplication were fed into and merged in the temporal buffer. The orange circles represent the simulation results, while the green line plots represent the experimental outputs. (**E**) Experimental confusion matrix of spiking handwritten digits classification. (**F**) Two samples from the human action recognition experiment. The first and the third rows show the input frames to the STPC network. The second and fourth rows show the spatiotemporal dynamics in the temporal buffer along with the final decision. (**G**) Examples in motion tracking dataset. Square objects were configured to move in three directions, up-left, down-left, and rightward. Scale bars, 1 mm. PD, photodiode; MOD, modulator; AMP, amplifier; CP, coupler; a.u., arbitrary units.

we devise a system learning process to finely train the system parameters when the model parameters are fixed and the system parameters are updated to fit the experimental output with higher precision. After completing the system learning process, the system corresponds better with the numerical prediction, and we use the refined system parameters for the final training of the model parameters, which are subsequently used for the experiments.

The proposed spatiotemporal architecture was validated using an SMUX-STPC network consisting of six SMUX divisions configured to recognize high-speed dynamics (Fig. 3B). In each division, every frame in the five-frame sequence is modulated with two spatial masks on the DMD working at a frame rate of 8024 frames per second (fps). Each spatial computing produced a temporal stack of 10 frames, summing to a spatiotemporal stack of dimension 6 × 10. The 6 × 10 outputs were then coupled into temporal channels. In the temporal module, multiplications were performed in a SOA by modulating its injection current. An OEO loop was constructed with a 25.293-km fiber ring, amplifiers (AMP, including a TIA and a low-noise amplifier), and intensity MOD to buffer and relay the inputs. Through the 10 × 5 temporal MVM in the temporal module, the 6 × 10 spatiotemporal outputs from the spatial module were transformed to a spatiotemporal stack of size 6 × 5, which was combined for the final inference results (details are provided in Materials and Methods).

Furthermore, the STPC network was experimentally tested on the dynamic version of the benchmarking handwritten digits classification task using the neuromorphic Modified National Institute of Standards and Technology database (N-MNIST) (*50*), which includes 10 classes of temporal spiking events. Each sample was preprocessed into a sequence of five spiking maps with a resolution of 541 × 541 DMD pixels (details are provided in Materials and Methods). To calibrate the system parameters, we first calibrated the DMD, SOA, and temporal buffer and used these measured transfer functions for the system simulation during the pre-training process (details of system calibration are provided in Materials and Methods). However, owing to the difference between the distributions of the calibration and dataset inputs, as well as the measurement noise present in the calibration process, the experimental outputs on 61 randomly selected training sequences obviously deviated from the simulations, as is shown by the blue data points in Fig. 3C. We further used these 61 randomly selected training sequences as the system learning subset to finely adjust the coupling matrix of the DMD and the system parameters of the SOA with the input data and the measured output. During system learning, the system parameters were updated using the gradient descent training method, targeting the captured experimental results (details are provided in Materials and Methods). After system learning and additional training, the experimental measurements corresponded better with the expected results (orange data points in Fig. 3C), and the relative error of spatial computing and temporal multiplication decreased from 12.05 to 1.20% and from 17.48 to 2.91%, that is, by 90.04 and 83.35%, respectively.

Figure 3D shows the evolution of the temporal buffer in temporal computing. In the first row, the output from temporal multiplication is displayed, which contains 10 coupled inputs, each weighted five times by SOA. In the temporal buffer, at each time step, the input light was merged with the buffered light in the temporal buffer. The merged light then passed through the buffer transfer function. There were 10 cycles of buffer and merge. At time step 11, the output was produced (shaded box). The constructed temporal buffer performed a 10 × 5 full connection at a frame rate of 8024 fps. The 6 × 5 spatiotemporal outputs were then spatially computed to classify the objects as one of the 10 digits. In the experiment, before system learning, the experimental accuracy degraded to 53.03% on the selected system learning subset, far below the training accuracy of 98.49%. After the system learning, we randomly selected 500 testing sequences from the testing set to evaluate the blind testing accuracy. The overall experimental accuracy was 88.4%, which agreed well with the simulation testing accuracy of 92.1%. The confusion matrix is shown in Fig. 3E. More than half of the categories were classified with more than 90% accuracy.

To further validate the capability of SMUX-STPC to recognize high-speed dynamic motion, we experimented with the KTH human-action video dataset (*51*). The dataset contained videos of six different actions, namely, boxing, clapping, waving, jogging, running, and walking, performed by 25 subjects. Videos were further decomposed into sequences of training and testing datasets and were fed into the constructed SMUX-STPC for recognition, with each input sequence consisting of five frames (details of preprocessing in Materials and Methods). On the basis of the content of the five-frame inputs, the STPC network determined the category. Figure 3G shows two inputs, "waving" and "walking," and the corresponding spatiotemporal dynamics. For these two different classes, the spatiotemporal outputs in the first temporal step were highly similar, suggesting that single-frame images have limited diversity and that human action recognition based on a single image frame is challenging. As more frames were fed into the system, the unique features of the different motions began to accumulate. Even with the same STPC architecture, the recognition performances with dynamic inputs (five frames) outperform those of single-frame inputs by more the 10% (fig. S16), which implies the importance of the STPC architecture in dynamic light-field processing. After system learning, the experimental sequence accuracy increased from 48.49 to 80.45%, approaching a simulated accuracy of 86.81%. We also calculated the video accuracy voted by the winner-takes-all policy for all the frames of the same video. The experimental video accuracy of the STPC was 90.74% (successfully classified 49 of the 54 testing videos), which is the same as simulation video accuracy. The confusion matrix and video classification results are shown in fig. S4.

The high-speed SMUX-STPC network will revolutionize video-based real-world applications, for example, biological research (*52*). In biology, tracking cell movements is a fundamental procedure that helps with analyzing tissue development and diseases (*53*). To study the potential of SMUX-STPC on this problem, we constructed a motion tracking dataset comprising 704 cell-like square objects moving in three directions, up-left, down-left, and rightward (Materials and Methods). The examples from the dataset are shown in Fig. 3G. An SMUX-STPC network with spatial outputs of size 8 × 10 and temporal outputs of size 8 × 5 was trained to classify the object as one of the three categories. With sufficient spatial and temporal connections, the SMUX-STPC successfully classified the testing dataset with 100% accuracy in the experiment, corresponding well with the simulation. The complete testing datasets and the spatiotemporal dynamics are shown in movie S1.

We compare the SMUX-STPC system with a state-of-the-art photonic video processor (*25*) performing the same tasks on the

KTH and motion tracking dataset. The results are shown in fig. S14 and section S1. Endowed with adequate trainable spatial and temporal connections, the SMUX-STPC architecture has competitive performances compared with the previously reported diffractive processor with 0.27 million parameters and five recurrent blocks while containing only 6.20- and 7.60-kilobyte parameters for the KTH recognition and motion tracking tasks, respectively, thus reducing the number of parameters by more than 35-fold compared with the 0.27-million-parameter benchmark. Furthermore, free from the limit of digital latency, the STPC system works at a frequency of 8024 Hz. With 10 spatial computes for the final inference, it has thus a speed of 802.4 sequences per second, which effectively increases the processing rate by more than 40 times compared with ~20 fps state-of-the-art speed (*25*, *39*). The details of the system evaluations are provided in section S1.

WMUX all-optical nonlinear STPC network for nanosecond dynamic light-field analysis

When the spatial inputs are encoded on different wavelengths, making use of a large spectral bandwidth, multiwavelength inputs can be multiplexed into the temporal channel without sacrificing spatial information. Thus, the structure of the WMUX-STPC is appropriate for processing ultrahigh-speed visual dynamics. To enable ultrafast spatiotemporal computing, a two-layer all-optical nonlinear WMUX-STPC network was constructed, as shown in Fig. 4A. In the spatial computing module, the spatial content was processed at the speed of light using a static spatial modulation mask on DMD. Subsequently, the spatial contents were squeezed into a single temporal fiber channel, and the weighted connection was temporally implemented with a 40-GHz modulator and a 0.6-m optical fiber buffer. All-optical nonlinearity between the two layers was realized through the nonlinear gain process of the stimulated emission. The details of the wavelength-multiplexed full connection are shown in Fig. 4B. The temporal dynamics were weighted and recurrently added in the all-optical buffer. At each time step, the spatial content was squeezed spatially and conserved spectrally. Thus, the spatial contents were computed in parallel by using the wideband optical modulators. Figure 4C illustrates the all-optical nonlinearity from the stimulated emission process of the SOA. The gain coefficient of the SOA is dependent on the input power and decreases with the increase of the input power. For self-gain modulation with input and output signals of the same wavelength, an increase in the input power leads to an increase in the output power but a decrease in the gain coefficient. For the multispectral inputs, an increased input power at one wavelength lowers the total gain of the SOA, resulting in a decrease in the output power at other wavelengths. In this work, self-gain modulation and cross-gain modulation effects are combined to construct a multivariate nonlinear neuron activation function, $z_{\lambda_i} = g(y_{\lambda_1}, \ldots y_{\lambda_N})$, where y_{λ_i} is the input power at wavelength λ_i, and z_{λ_i} is the output power at wavelength λ_i. Figure 4D shows the measured gain versus the input power, in which a highly nonlinear region was used in our experiment. We swept the input power of Ch1 and Ch2 and measured the output power of Ch1 (with Ch2 as the control channel). A gain coefficient dependent on the total input power was clearly observed (section S2). The self-modulation and cross-modulation effects of each wavelength channel were measured. The results are shown in the right panel of Fig. 4D. When increasing the input power of one wavelength, the output power at the corresponding channel will increase nonlinearly (top right panel in Fig. 4D), while the output at other channels will decrease nonlinearly (bottom right panel in Fig. 4D), as a result of the decreased total gain. Previously reported optical nonlinear neuron activation function models were univariate; that is, the output of a specific channel depends solely on its own input (*30*). Here, we develop a novel multivariate optical nonlinear activation function for multivariate STPC by modeling the self and mutual nonlinearity across multispectral channels.

We experimentally configured a high-speed dynamic scene consisting of two spherical objects flashing on and off at a nanosecond time scale (3.57 ns per frame) to validate the performance of the proposed method for high-speed processing. A dataset containing sequences of two objects with two different flashing orders was constructed (object 1 flashes first and object 2 flashes first). Every sequence comprises three frames, wherein one object flashes in a frame slot. There are 180 training data and 60 testing data, each with different flashing intensities. Experimentally, owing to the limited frame rate of existing cameras, it is difficult to capture the frequently and continuously flashing pattern and to discriminate the flashing order. As shown in Fig. 4E, dynamic datasets were slowed down and monitored using an InGaAs camera. A two-layer WMUX-STPC model was used to recognize the dynamics based on the previously calibrated parameters. Specifically, in each frame, the spatial input content was encoded on two different wavelengths. The spatial inputs were spatially weighted in amplitude using DMD. Thereafter, the signal was squeezed into one fiber channel by WMUX. In the temporal channel, the 3×2 and 2×2 temporal weighted connections were implemented with an intensity modulator and temporal buffer at layer 1 and layer 2 of the WMUX-STPC network. The multispectral output from the first layer entered the SOA and was activated nonlinearly, and the subsequent output was finally demultiplexed by a DWDM multiplexer and fed into the second spatiotemporal layer for the inference of the final computing results (details of the system are illustrated in Materials and Methods).

The sequences of the datasets were projected onto a two-dimensional (2D) manifold using principal components analysis (PCA; details in Materials and Methods) (right panel of Fig. 4E). The data from the two categories were distributed in three clusters and overlapped with each other, which are not linearly separable. The task is challenging because accurately identifying the category requires simultaneously determining the spatial location and temporal flashing order of the two objects. The output dynamics of class 1 (the third row of Fig. 4E) and class 2 (the sixth row of Fig. 4E) from the first layer of WMUX-STPC is visualized in Fig. 4F, the frame time is 3.57 ns, and the temporal weighting slots have a duration of 1.78 ns. Figure 4G shows the nonlinear activation outputs of the testing datasets. The output levels at different wavelengths are plotted against the input of their respective wavelengths (top) and total input (bottom). The multiwavelength input-output transfer function is highly nonlinear, as the output power levels depend on both the input power at the respective wavelength and the total input power (Fig. 4D). With a nonlinear multilayer architecture, the WMUX-STPC network successfully classified the entire testing dataset, which is consistent with the simulation. Comparatively, a one-layer WMUX-STPC network achieved only 84.4% testing accuracy (section S1 and fig. S15). The experimental results are shown in Fig. 4H. By setting an appropriate threshold (dashed line), the first half (class 1) and the second half (class 2)

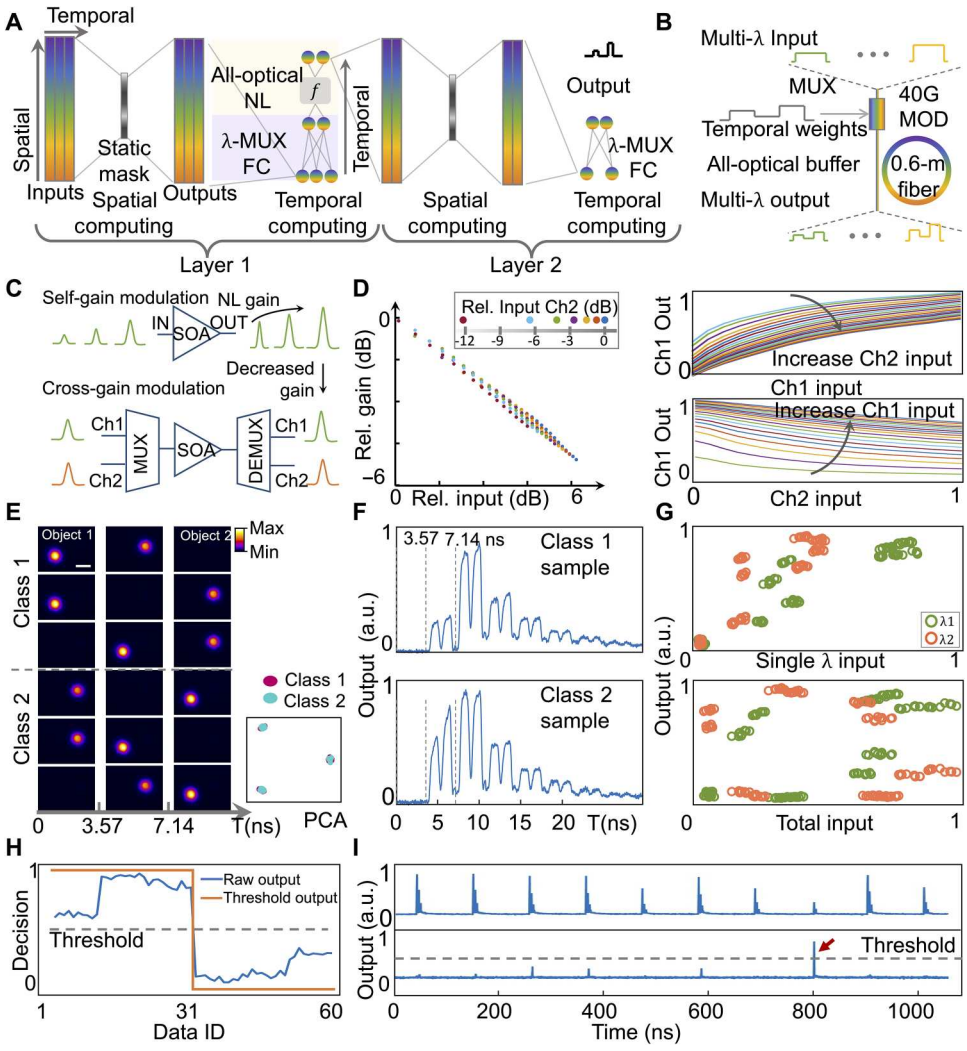

Fig. 4. Wavelength-multiplexed (WMUX) all-optical nonlinear STPC network for nanosecond dynamic light-field analysis. (**A**) Wavelength-multiplexed STPC network. The spatial light field was encoded on wavelengths and multiplexed (MUX) into a temporal channel. Different wavelength channels shared the multiplication weights and were recurrently added. Between layers, an all-optical nonlinear module took in the multispectral inputs, and the outputs were demultiplexed spatially after nonlinear activation. (**B**) Implementation of wavelength-multiplexed full connection. The multispectral spatial outputs were multiplexed into the temporal channel and modulated with a 40-GHz intensity modulator (MOD) and recurrently added in the temporal buffer consisting of a 0.6-m fiber ring. (**C**) Spectral nonlinearity of SOA, with nonlinear self-gain modulation and cross-gain modulation. (**D**) Left: Measured highly nonlinear region of SOA. Data points with the same color denote the same control power. Right: Measurement of self-gain modulation (top) and cross-gain modulation (bottom). (**E**) Slow motion of the ultrafast dataset captured by an InGaAs camera. Right: Low-dimensional manifold of the dataset, with PCA. (**F**) Layer 1 output temporal dynamics of class 1 and class 2 samples, with a 3.57-ns frame time. (**G**) Nonlinear activation. Outputs of different wavelengths as a function of the respective input (top) and as a function of total input (bottom). (**H**) Final output and classification results of the whole dataset. (**I**) Monitoring the continuous high-speed dynamics with a 10-MHz frame rate and a 3.57-ns frame time. Top: Temporal buffer output. Bottom: Output with a selection window. Scale bar, 3 mm.

of the dataset are clearly distinguished. The complete experimental results are presented in fig. S10. The system was then configured to operate in continuous mode. The input sequences flashed at a high repetition rate of up to 10 MHz. Among the continuous series, only one of the sequences flashed differently, and the WMUX-STPC network successfully determined the outliers. This shows that the all-optical WMUX-STPC network is capable of real-time processing with a response time at the nanosecond level. The final output can be used for real-time feedback control of the system.

Nanosecond real-time processing is already competitive against state-of-the-art specially designed electronic systems, including event cameras and field-programmable gate arrays (FPGAs) with at least nanoseconds cycle time (section S1). To further increase the processing speed of the system, the round-trip delay of the temporal buffer in the WMUX-STPC can be minimized on a photonic integrated circuit platform. Through simulation on a low-loss silicon-nitride-on-insulator photonic platform, we numerically validated that a ring resonator with a 1.4-mm ring length would reduce the delay time to 10 ps (section S3). We also extracted matrix multiplication operations of similar dimensions and executed them on a standard central processing unit (CPU) and graphics processing unit (GPU) system. Each read-compute-write cycle consumes at

least 4 and 20 μs on average (section S1). In summary, the proposed WMUX-STPC is three to five orders of magnitude faster than the CPU- and GPU-based general-purpose system and is also competitive against the specially optimized electronic system.

DISCUSSION

In this study, an STPC architecture is proposed and experimentally demonstrated for ultrafast dynamic machine vision. By codesigning the multiplexed spatiotemporal computing architecture and colearning the parametric physical system with the neural network model, fast and precise computing on spatially and temporally varying light fields becomes possible. The STPC comprehensively extracts content information in high-dimensional optical feature space and is free of the digital burden of transmission and storage; thus, it is promising for the high-speed analysis of complex visual scenes. We experimentally validated that the SMUX-STPC network can process daily visual scenes with similar performance to that of existing methods while having over an orders of magnitude improvement in speed and parameter efficiency. In addition, the WMUX-STPC network supports ultrahigh-speed photonic machine vision with multiwavelength inputs and permits discerning visual dynamics with frame times of nanoseconds to picoseconds. The introduction of multivariate all-optical nonlinearity effectively enhances the performances of the STPC network on linearly inseparable problems.

The SMUX-STPC system uses a high-speed modulator to stretch the spatial information in the temporal dimension; thus, a higher modulation speed can increase the inference speed and contribute to better information extraction. Currently, the upper speed limit of the DMD is tens of kilohertz, with millions of modulation pixels. With the advancement of high-speed spatial light modulators (*54*–*56*), the speed of SMUX-STPC would be further accelerated. Moreover, in the WMUX-STPC system, to increase the spatial resolution, the continuous wave (CW) laser sources can be upgraded with a supercontinuum source to allow for continuous sampling in the spatial optical domain (*9*). In the future, multimode fibers could also be used to enlarge the capacity of the temporal channels and provide alternative forms of nonlinearity (*45*). To scale up the STPC networks, the loop number in an all-optical buffer can be optimized by adjusting the coupling coefficients of the coupler (fig. S17). The noise induced by the amplifiers may be further controlled with quantization of analog-to-digital converters and digital-to-analog converters.

In state-of-the-art electronic computers, memory access is associated with latencies of more than 100 ns (*57*), which precludes real-time processing of dynamic events at the nanosecond time scale and inhibits the ultrafast implementation of artificial neural networks, as sequential data dependencies in the neural network architecture result in frequent read/write operations (*58*). The memory dependencies also block the access of existing photonic computing techniques to the full potential of light (a discussion of existing methods is provided in section S5). The STPC architecture eliminates the memory read/write burden by codesigning the computing, interfacing, and buffering modules in the spatiotemporal computational domain. Furthermore, with recent advancements in hundreds-of-gigahertz optical modulators and detectors (*59*–*61*), low-loss photonic integrated circuits, and ~100-GHz high-speed waveform generators, the temporal resolution of the STPC is expected to reach ~10 ps. The capability of high-speed and consecutive computing not only accelerates neural network computing but also underpins real-time analysis of nonrepetitive transient visual phenomena (*62*, *63*), thereby enabling in situ feedback control of light-field dynamics over gigahertz frequency. The STPC architecture broadens the scope of photonic computing, paving the way for ultrafast advanced machine learning and transient experimental control in the optical domain.

MATERIALS AND METHODS

Experimental system

In the spatial module of the SMUX-STPC system, the temporal free-space input stack was processed using a high-speed DMD (DLP9500, Texas Instruments DLP). The output from the spatial module was then downsampled by being focused through a focusing lens and coupled into a single-mode fiber. In this manner, free-space inputs were spatially squeezed and extended temporally with high-speed spatial modulation and converted to guided-wave dynamics in the fiber. The polarization of light in the fiber was controlled with a polarization controller to align with the slow axis of the SOA (Thorlabs S9FC1004P) input. By modulating the injection current of the SOA, its gain coefficient was varied, and the input guided-wave dynamic sequence was temporally weighted. A quarter of the emitted light from the SOA is split out with a 1 × 2 fiber coupler and monitored by a photodiode (PD-1, Thorlabs DET08CFC/M). The remainder of the light entered the temporal buffer constructed by an OEO loop through a 2 × 2 fiber coupler. Within the temporal buffer, the light passed through the 25.293-km fiber as a temporal delay line. The delayed optical output was then detected by a photodiode (PD-2), and the photocurrent was amplified by a TIA (FEMTO DHPCA-100) and a low-noise voltage amplifier (LNA, AMI 351A-1-50-NI). The amplified electrical signal drove the intensity modulator (Thorlabs LN05S-FC), and the temporal dynamics were converted back to the optical domain with different wavelengths from those of the spatial module (1550 and 1568 nm, respectively), which was subsequently fed back to the input of the buffer. The round-trip delay of the entire temporal buffer is approximately 124.6 μs, which matches the 8024-Hz spatial computing frequency. In the fiber coupler, the recurrent signal was incoherently merged with the input signal from the spatial module. The temporal module effectively performed weighted connections, and the final outputs from the buffer were monitored using a photodiode outside the buffer (PD-3). The details of the system are shown in fig. S1.

In an all-optical nonlinear WMUX-STPC system, the dynamic input scene was encoded on multiwavelength inputs to the DMD. In the experiment, we used laser beam spots at 1550.12 and 1550.92 nm to simulate two spherical objects. The on-and-off states of the objects were controlled with 10-GHz electro-optical modulators. The inputs were spatially weighted on the DMD, squeezed into a single fiber, and amplified by an erbium-doped fiber amplifier (EDFA; Amonics AEDFA-PA-35). The spatial computing outputs from the EDFA were N_λ 3 × 1 vectors with three timeslots and N_λ wavelengths. Each entry of the vector corresponded to a time duration of 3.57 ns. Then, the multiwavelength temporal inputs were modulated with a 40-GHz broadband modulator with a pulse width of 1.78 ns. The recurrent temporal connection was performed in an all-optical buffer consisting of an all-pass ring resonator with a

fiber ring of around 0.6-m length. The weighted optical connection parallelly implemented N_λ MVM on the 3 × 1 vectors with a 3 × 2 weight matrix. The outputs from the buffer were then selected with a high-speed modulator and were nonlinearly activated by the SOA (Thorlabs S9FC1004P) and demultiplexed before being injected into the second layer. The second layer performed a weighted connection, and the outputs were N_λ 2 × 1 vectors. With the detection of a PD, outputs of different wavelengths were summed, producing the final output of size 1 × 2, with the largest entry denoting the categories of the test sample. The high-speed system was controlled with a 5-GHz-bandwidth arbitrary wave generator (RIGOL DG70004) with 10-GHz drivers. The high-speed outputs were captured using a 10-GHz oscilloscope (Tektronix MSO64B). The details of the system are shown in fig. S2.

Dataset and preprocessing

N-MNIST dataset

The N-MNIST dataset (*50*) contains neuromorphic forms of handwritten digits captured by event cameras. It consists of 60,000 training samples and 10,000 testing samples. Each original sample is a spiking event series of ~5000 in length, with each entry in the series denoting the spiking position. The spiking events were first uniformly divided into 13 short image frames. For each frame, the spiking positions were grouped in a 2D plane and converted into a binary image with a resolution of 34 × 34. In the experiments, we selected the first five of the processed binary images and cropped 26 × 26 pixels from the center of the image, which were up-sampled to 541 × 541 and used for the evaluation in the experiments.

KTH human action dataset

The KTH dataset (*51*) contains 600 videos with a spatial resolution of 160 × 120, including six different types of natural actions (boxing, handclapping, handwaving, jogging, running, and walking) performed by 25 subjects in four different scenes. The same preprocessing method as (*25*) was used to extract the silhouette to accommodate the DMD used in the system. In the experiment, the first scene was selected for comparison with the existing methods, and the spatial resolution was rescaled to 541 × 541. Videos were divided into subsequences with a length of five and split into training and testing sets. The training set had 16 subjects, including 7680 subsequences, while the testing set had 9 subjects, including 2160 subsequences.

Motion tracking dataset

To validate a potential real-world use of the STPC network, we constructed a motion tracking dataset emulating the cell motion and performed the tracking task with it. The dataset contains 704 samples (674 for training and 30 for testing) moving in three directions, up-left, down-left, and rightward. Each sample contains five frames, where a 63 × 63 square object was randomly placed in the 541 × 541 grid initially and then moved toward one of the three directions. The interframe stepping distance is set to be 83 pixels for the rightward direction and 59 pixels for the up-left and down-left directions.

Flashing object dataset

The flashing object dataset constructed for nanosecond dynamic recognition contains two spherical objects flashing at different time steps. The dataset contains three frames, with the frame time being 3.57 ns, and one object flashes at a single frame. Examples of the six flashing patterns are shown in Fig. 4E. The relative flashing intensity of each object was randomly sampled from the range of 5.4 mW to 6.0 mW. The entire dataset contains 180 training data and 60 testing data. As shown in Fig. 4E, PCA (*64*) was performed on the testing dataset. Specifically, singular value decomposition was calculated on the basis of the centered dataset to obtain the projection matrix with which the data were projected onto a low-dimensional space.

Calibration of STPC units

In the SMUX-STPC system, the spatial computing modules can be numerically modeled as $o = |\boldsymbol{t}_s^T(\boldsymbol{w}_s\boldsymbol{x}_i) + b_0|^2$, where $\boldsymbol{x}_i$ denotes the input light fields, $\boldsymbol{w}_s$ denotes the spatial weights, $\boldsymbol{t}_s$ denotes the coupling coefficients, b_0 denotes the background, and o denotes the intensity of the light fields coupled to the optical fiber. In the experiment, $\boldsymbol{t}_s$, $\boldsymbol{w}_s$, and $\boldsymbol{x}_i$ had an effective dimension of 676 × 1. To calibrate the spatial coupling coefficient $\boldsymbol{t}_s$, 3300 random binary spatial masks representing $\boldsymbol{w}_s\boldsymbol{x}$ were projected onto the DMD. Each pixel value in the mask was drawn from independent and identically distributed Bernoulli distribution. The proportion of DMD pixels being in the "on" state varied from 30 to 57%. A neural network of the same form as the numerical model was then constructed. The collected ($\boldsymbol{w}_s\boldsymbol{x}$,$o$) pairs were fed into the constructed network to train the coefficient $\boldsymbol{t}_s$. The learning batch size was set to 16; the learning rate was set to 0.000005, and the learning rate decayed by 1% every 5000 iterations. In addition, the network was trained using Adam optimizer (*65*). The training error decreased to less than 5% after 15 epochs of training. Figure S5 shows the convergence curve, converged phase, and amplitude of $\boldsymbol{t}_s$.

The transfer function of the SOA is formulated as $o' = o \cdot w_t(o, v)$, where o is the input to the SOA, v is the modulation voltage, and o' is the output power. We swept the input-output relation of the SOA with different levels of input intensity o from 0 to 30 μW and swept the voltage v from 0 to 5 V. These points were selected as markers for the calibration of the function $o' = \varphi(o, v_t)$, from which the complete function could be interpolated. The results are presented in fig. S6. For each control voltage level, the input gain coefficient decreased with an increase in the input power, which is a manifestation of the nonlinear saturable gain effects of the SOA.

In the experiment, the modulator was biased toward the NULL point. The characteristics of the temporal buffer can be modeled as $o''_t = a \cdot \sin[b \cdot (o''_{t-1} + o'_t)]^2$, where o'_t is the input intensity at time t, o''_{t-1} is the precedent recurrent intensity, and o''_t is the current recurrent density at time t. In addition, a and b are the system parameters dependent on the driving laser power and amplifier gain coefficient, respectively. The system was calibrated by projecting light pulses onto a temporal buffer and measuring the decay dynamics of the cavity. The decay dynamics were then fitted to the transfer formula to obtain parameters a and b. Details of the calibration dynamics and the fitting results are shown in fig. S7.

In the WMUX-STPC system, the transfer dynamics of the spatial computing module are modeled as $o = t_s(\boldsymbol{x}_i, \boldsymbol{w}_s)$, where $\boldsymbol{x}_i$,o,$\boldsymbol{w}_s$ are the input light fields, output light, and spatial weights, respectively. Specifically, under different $\boldsymbol{w}_s$ levels, we swept the input light field $\boldsymbol{x}_i$ and measured the output intensity o. The measurement triplets ($\boldsymbol{x}_i$,o,$\boldsymbol{w}_s$) were further used for fitting the function $o = t_s(\boldsymbol{x}_i, \boldsymbol{w}_s)$. The transfer characteristics of object 1 and object 2 are shown in fig. S8. Then, wideband multiplication was also validated. The wavelength of the input light varied from 1528 to 1566 nm, and the transmission coefficient was measured against the modulating voltages. Specifically, we measured the high-speed modulating characteristics

at 1550.12 nm with 1.78-ns short pulses with amplitude varying between 0 and 2.1 V. In addition, the modulation output can be formulated as $w_t(v)$ and $o' = o \cdot w_t(v)$. The measurements are shown in fig. S9. Last, the nonlinear transfer function of the SOA was calibrated by measuring the self-gain modulation and cross-gain modulation nonlinearity. We denote the input intensity of different wavelengths with y_{λ_1}, y_{λ_2}, ..., y_{λ_N}. The input intensity was swept from 0 to the maximal intensity (6 mW), and the outputs z_{λ_1}, z_{λ_2}, ..., z_{λ_N} were measured. In the experiments, we measured the transfer function of two wavelengths, $z_{\lambda_1} = g(y_{\lambda_1}, y_{\lambda_2})$ and $z_{\lambda_2} = g(y_{\lambda_2}, y_{\lambda_1})$. The results are shown in Fig. 4D.

Neural network architectures and training methods

In the SMUX-STPC network, after calibration of the spatial computing module, temporal modulation module, and temporal buffer, the calibrated system parameters were used for pretraining the experimental system. In each of P spatial channels, the input image sequence consists of M/K frames, and each frame is spatially modulated by K spatial masks. The M spatial outputs are then coupled into the temporal buffer for spatiotemporal computing, forming temporal inputs $o_j = |\boldsymbol{t}_s^T(\boldsymbol{x_i} \cdot \boldsymbol{w}_{s,j}) + b_0|^2$, where j = 1,2,3, ..., M and $\boldsymbol{w}_{s,j}$ is the jth trainable spatial weight mask. Each value in the M outputs is modulated by N temporal voltage weights in the temporal computing module, $v_{j,k}$, k = 1,2,3, ...N, and the inputs to the temporal buffer are $o'_{j,k} = \varphi(o_j, v_{j,k})$. In the temporal buffer, the dynamics is $o''_{j,k} = a \cdot \sin[b \cdot (o''_{j-1,k} + o'_{j,k})]^2$. In spiking sequence classification and human action recognition experiments, M, N, K, and P were set to 10, 5, 2, and 6, respectively. Through the first ST unit, we obtained 6 × 5 spatiotemporal outputs $y_k = o''_{M,k}$, which were demultiplexed to a second ST unit simulated with an electronic linear layer, producing 10 × 1 and 6 × 1 output vectors, respectively, for final classification. In the motion tracking experiment, P was set to 8, and the output dimension was set to 3 × 1, while the other parameters were set the same as in the other two experiments. The source code of the numerical simulation was written in Python 3.7 using the PyTorch package on the Windows 10 platform with an Nvidia GeForce RTX 3070 GPU. During the training, the cross-entropy loss was used, and regularization terms were used to enhance the stability of the system and to maximize the signal-to-noise ratio in the experiments (details of training loss are presented in section S4). Adam optimizer was used for the training, and the training batch size was set to 16. In addition, the spatial learning rate was set to 0.01, and the temporal learning rate was set to 0.0001. Furthermore, training on the N-MNIST, KTH, and motion tracking datasets required 200, 100, and 2000 epochs, respectively, to converge.

In the WMUX-STPC network, the input sequential light field is the triplet $(\boldsymbol{x}_{i_{t_0}}, \boldsymbol{x}_{i_{t_1}}, \boldsymbol{x}_{i_{t_2}})$. $\boldsymbol{x}_{i_t}$ was fed into the spatial transfer function $o_t = t_s(\boldsymbol{x}_{i_t}, \boldsymbol{w}_s)$, and the input light fields at different time slots share the same spatial weight $\boldsymbol{w}_s$. The output triplet $(o_{t_0}, o_{t_1}, o_{t_2})$ was then fed into the temporal multiplication unit (intensity modulator); thus, $o' = o \cdot w_t(v)$, and the output o' from the temporal multiplication unit was recurrently added in the temporal buffer. The temporal output y was fed to the nonlinear activation function $g(y_1, y_2)$. The final two outputs at wavelengths λ_1 and λ_2 were demultiplexed and fed to the second layer. In this manner, the first layer implements 3 × 2 temporal nonlinear computing, while the second layer implements 2 × 2 temporal computing without nonlinear activation. The final outputs were used to determine the category of dynamics. In the network training, the cross-entropy loss was used with the Adam optimizer (regularization loss is presented in section S4), with a learning rate of 0.0005, on the same platform as that of the SMUX-STPC network. The training took 200 epochs to converge.

Experimental system learning

In the experiment, the calibrated parameters were dependent on the calibration data. Owing to the discrepancy between the inference inputs and random calibration inputs, as well as the presence of system noise in the calibration, the accuracy of the calibrated transfer matrix is biased to the distribution of the calibration data; consequently, the system computing accuracy may not be the best for the inference inputs.

To enhance the system modeling accuracy, instead of simply using calibrated system parameters for the final experiments, we used a further step to learn the system parameters with trainable functions, which we termed system learning. From the perspective of machine learning, we regard the parameters that characterize the experimental system as variables that are trainable and, together with the model parameters (weights in the ST modules of STPC), comprise the entire set of parameters. As a result, the pretraining step is the process of learning the neural network model parameters, and the system learning is the process of learning the experimental system parameters. These two steps can be iteratively performed to asymptotically approach the best computational neural network model and most accurate system model collaboratively. Compared with existing photonic neural network training methods that update only the model parameters during the learning process (*25*, *66*–*68*), the proposed system learning method constructed a unified trainable framework with both the experimental system parameters and computational model parameters, thus exploring the complete parametric space and achieving optimal convergence. A flowchart of the learning process of STPC is shown in fig. S3.

After pretraining, we extracted a subset of the training data and measured the experimental output to fine-train the system parameters. Specifically, we extracted a small portion of the training data (61 in spiking sequence classification, 42 in human action recognition, and 66 in motion tracking) as the system learning subset and measured the outputs from the spatial modules and the temporal multiplication modules. In spatial computing, the output $\tilde{o}_j = |\boldsymbol{t}_s^T(\boldsymbol{x_i} \cdot \boldsymbol{w}_{s,j}) + b_0|^2$ is collected (the experimental measurements are denoted with a tilde), and we used the $(\tilde{o}_i, \boldsymbol{x_i})$ pair to finely train the parameters $(\boldsymbol{t_s}, b_0)$. During the training, the learning rate was set to 0.000005, which decayed by 1% every 5000 iterations, and the batch size was set to 16. In addition, the training process converged after 500 epochs (fig. S5). We also collected SOA input and output pairs with experimental inputs $\tilde{o}' = \varphi(\tilde{o}, \tilde{v}_t)$. We used the $(\tilde{o}', \tilde{o}, \tilde{v}_t)$ triads to train the SOA calibrated markers with a learning rate of 0.0001 combined with a decay rate of 10% every 5000 iterations. The training process converged after 60 epochs (fig. S6). Furthermore, the system parameters from system learning were used for further training of the model parameters for 20 epochs, with the learning rate set to 0.0001. Last, the converged parameters were deployed in the experimental system.

Supplementary Materials

This PDF file includes:
Sections S1 to S5
Figs. S1 to S17
Table S1
Legend for movie S1
References

Other Supplementary Material for this manuscript includes the following:
Movie S1

REFERENCES AND NOTES

1. Y. LeCun, Y. Bengio, G. Hinton, Deep learning. *Nature* **521**, 436–444 (2015).
2. R. Szeliski, *Computer Vision: Algorithms and Applications* (Springer Nature, 2022).
3. A. Krizhevsky, I. Sutskever, G. E. Hinton, Imagenet classification with deep convolutional neural networks. *Adv. Neural. Inf. Process. Syst.* **25**, 1097–1105 (2012).
4. O. Ronneberger, P. Fischer, T. Brox, U-net: Convolutional networks for biomedical image segmentation, paper presented at the 18th International Conference on Medical image computing and computer-assisted intervention (MICCAI 2015), Munich, Germany, 5 to 9 October 2015, pp. 234–241.
5. J. Janai, F. Güney, A. Behl, A. Geiger, Computer vision for autonomous vehicles: Problems, datasets and state of the art. *Found. Trends. Comput. Graph. Vis.* **12**, 1–308 (2020).
6. A. Geiger, P. Lenz, C. Stiller, R. Urtasun, Vision meets robotics: The kitti dataset. *Int. J. Robot. Res.* **32**, 1231–1237 (2013).
7. G. E. Moore, Cramming more components onto integrated circuits. *Proc. IEEE* **86**, 82–85 (1998).
8. M. M. Waldrop, The chips are down for Moore's law. *Nature* **530**, 144–147 (2016).
9. K. Goda, K. Tsia, B. Jalali, Serial time-encoded amplified imaging for real-time observation of fast dynamic phenomena. *Nature* **458**, 1145–1149 (2009).
10. J. Liang, C. Ma, L. Zhu, Y. Chen, L. Gao, L. V. Wang, Single-shot real-time video recording of a photonic Mach cone induced by a scattered light pulse. *Sci. Adv.* **3**, e1601814 (2017).
11. M. Wagner, Z. Fei, A. S. McLeod, A. S. Rodin, W. Bao, E. G. Iwinski, Z. Zhao, M. Goldflam, M. Liu, G. Dominguez, M. Thiemens, M. M. Fogler, A. H. Castro Neto, C. N. Lau, S. Amarie, F. Keilmann, D. N. Basov, Ultrafast and nanoscale plasmonic phenomena in exfoliated graphene revealed by infrared pump–probe nanoscopy. *Nano Lett.* **14**, 894–900 (2014).
12. C. Brif, R. Chakrabarti, H. Rabitz, Control of quantum phenomena: Past, present and future. *New J. Phys.* **12**, 075008 (2010).
13. D. A. Miller, Attojoule optoelectronics for low-energy information processing and communications. *J. Light. Technol.* **35**, 346–396 (2017).
14. B. J. Shastri, A. N. Tait, T. Ferreira de Lima, M. A. Nahmias, H.-T. Peng, P. R. Prucnal, Principles of neuromorphic photonics. *Unconv. Comput.*, 83–118 (2018).
15. Q. Zhang, H. Yu, M. Barbiero, B. Wang, M. Gu, Artificial neural networks enabled by nanophotonics. *Light Sci. Appl.* **8**, 42 (2019).
16. G. Wetzstein, A. Ozcan, S. Gigan, S. Fan, D. Englund, M. Solja˘ić, C. Denz, D. A. Miller, D. Psaltis, Inference in artificial intelligence with deep optics and photonics. *Nature* **588**, 39–47 (2020).
17. B. J. Shastri, A. N. Tait, T. Ferreira de Lima, W. H. P. Pernice, H. Bhaskaran, C. D. Wright, P. R. Prucnal, Photonics for artificial intelligence and neuromorphic computing. *Nat. Photonics* **15**, 102–114 (2021).
18. Y. Shen, N. C. Harris, S. Skirlo, M. Prabhu, T. Baehr-Jones, M. Hochberg, X. Sun, S. Zhao, H. Larochelle, D. Englund, M. Solja˘ić, Deep learning with coherent nanophotonic circuits. *Nat. Photonics* **11**, 441–446 (2017).
19. D. Pérez, I. Gasulla, L. Crudgington, D. J. Thomson, A. Z. Khokhar, K. Li, W. Cao, G. Z. Mashanovich, J. Capmany, Multipurpose silicon photonics signal processor core. *Nat. Commun.* **8**, 636 (2017).
20. A. N. Tait, T. F. de Lima, E. Zhou, A. X. Wu, M. A. Nahmias, B. J. Shastri, P. R. Prucnal, Neuromorphic photonic networks using silicon photonic weight banks. *Sci. Rep.* **7**, 7430 (2017).
21. X. Lin, Y. Rivenson, N. T. Yardimci, M. Veli, Y. Luo, M. Jarrahi, A. Ozcan, All-optical machine learning using diffractive deep neural networks. *Science* **361**, 1004–1008 (2018).
22. T. Yan, J. Wu, T. Zhou, H. Xie, F. Xu, J. Fan, L. Fang, X. Lin, Q. Dai, Fourier-space diffractive deep neural network. *Phys. Rev. Lett.* **123**, 023901 (2019).
23. Y. Luo, D. Mengu, N. T. Yardimci, Y. Rivenson, M. Veli, M. Jarrahi, A. Ozcan, Design of task-specific optical systems using broadband diffractive neural networks. *Light Sci. Appl.* **8**, 112 (2019).
24. T. Zhou, L. Fang, T. Yan, J. Wu, Y. Li, J. Fan, H. Wu, X. Lin, Q. Dai, In situ optical backpropagation training of diffractive optical neural networks. *Photonics Res.* **8**, 940–953 (2020).
25. T. Zhou, X. Lin, J. Wu, Y. Chen, H. Xie, Y. Li, J. Fan, H. Wu, L. Fang, Q. Dai, Large-scale neuromorphic optoelectronic computing with a reconfigurable diffractive processing unit. *Nat. Photonics* **15**, 367–373 (2021).
26. J. Feldmann, M. Stegmaier, N. Gruhler, C. Ríos, H. Bhaskaran, C. D. Wright, W. H. P. Pernice, Calculating with light using a chip-scale all-optical abacus. *Nat. Commun.* **8**, 1256 (2017).
27. C. Ríos, N. Youngblood, Z. Cheng, M. Le Gallo, W. H. P. Pernice, C. D. Wright, A. Sebastian, H. Bhaskaran, In-memory computing on a photonic platform. *Sci. Adv.* **5**, eaau5759 (2019).
28. J. Feldmann, N. Youngblood, M. Karpov, H. Gehring, X. Li, M. Stappers, M. Le Gallo, X. Fu, A. Lukashchuk, A. S. Raja, J. Liu, C. D. Wright, A. Sebastian, T. J. Kippenberg, W. H. P. Pernice, H. Bhaskaran, Parallel convolutional processing using an integrated photonic tensor core. *Nature* **589**, 52–58 (2021).
29. X. Xu, M. Tan, B. Corcoran, J. Wu, A. Boes, T. G. Nguyen, S. T. Chu, B. E. Little, D. G. Hicks, R. Morandotti, 11 TOPS photonic convolutional accelerator for optical neural networks. *Nature* **589**, 44–51 (2021).
30. Y. Zuo, B. Li, Y. Zhao, Y. Jiang, Y.-C. Chen, P. Chen, G.-B. Jo, J. Liu, S. Du, All-optical neural network with nonlinear activation functions. *Optica* **6**, 1132–1137 (2019).
31. P. L. McMahon, A. Marandi, Y. Haribara, R. Hamerly, C. Langrock, S. Tamate, T. Inagaki, H. Takesue, S. Utsunomiya, K. Aihara, R. L. Byer, M. M. Fejer, H. Mabuchi, Y. Yamamoto, A fully programmable 100-spin coherent Ising machine with all-to-all connections. *Science* **354**, 614–617 (2016).
32. C. Roques-Carmes, Y. Shen, C. Zanoci, M. Prabhu, F. Atieh, L. Jing, T. Dub˘ek, C. Mao, M. R. Johnson, V. Čeperić, Heuristic recurrent algorithms for photonic Ising machines. *Nat. Commun.* **11**, 249 (2020).
33. N. Mohammadi Estakhri, B. Edwards, N. Engheta, Inverse-designed metastructures that solve equations. *Science* **363**, 1333–1338 (2019).
34. M. Ferrera, Y. Park, L. Razzari, B. E. Little, S. T. Chu, R. Morandotti, D. J. Moss, J. Azaña, On-chip CMOS-compatible all-optical integrator. *Nat. Commun.* **1**, 29 (2010).
35. A. Silva, F. Monticone, G. Castaldi, V. Galdi, A. Alù, N. Engheta, Performing mathematical operations with metamaterials. *Science* **343**, 160–163 (2014).
36. W. Liu, M. Li, R. S. Guzzon, E. J. Norberg, J. S. Parker, M. Lu, L. A. Coldren, J. Yao, A fully reconfigurable photonic integrated signal processor. *Nat. Photonics* **10**, 190–195 (2016).
37. T. Zhu, Y. Zhou, Y. Lou, H. Ye, M. Qiu, Z. Ruan, S. Fan, Plasmonic computing of spatial differentiation. *Nat. Commun.* **8**, 15391 (2017).
38. F. Ashtiani, A. J. Geers, F. Aflatouni, An on-chip photonic deep neural network for image classification. *Nature* **606**, 501–506 (2022).
39. P. Antonik, N. Marsal, D. Brunner, D. Rontani, Human action recognition with a large-scale brain-inspired photonic computer. *Nat. Mach. Intell.* **1**, 530–537 (2019).
40. A. M. Shaltout, V. M. Shalaev, M. L. Brongersma, Spatiotemporal light control with active metasurfaces. *Science* **364**, eaat3100 (2019).
41. D. Cruz-Delgado, S. Yerolatsitis, N. K. Fontaine, D. N. Christodoulides, R. Amezcua-Correa, M. A. Bandres, Synthesis of ultrafast wavepackets with tailored spatiotemporal properties. *Nat. Photonics* **16**, 686–691 (2022).
42. L. Larger, A. Baylón-Fuentes, R. Martinenghi, V. S. Udaltsov, Y. K. Chembo, M. Jacquot, High-speed photonic reservoir computing using a time-delay-based architecture: Million words per second classification. *Phys. Rev. X* **7**, 011015 (2017).
43. K. Vandoorne, P. Mechet, T. Van Vaerenbergh, M. Fiers, G. Morthier, D. Verstraeten, B. Schrauwen, J. Dambre, P. Bienstman, Experimental demonstration of reservoir computing on a silicon photonics chip. *Nat. Commun.* **5**, 3541 (2014).
44. D. Brunner, M. C. Soriano, C. R. Mirasso, I. Fischer, Parallel photonic information processing at gigabyte per second data rates using transient states. *Nat. Commun.* **4**, 1364 (2013).
45. U. Teğin, M. Yıldırım, İ. Oğuz, C. Moser, D. Psaltis, Scalable optical learning operator. *Nat. Comput. Sci.* **1**, 542–549 (2021).
46. M. P. Edgar, G. M. Gibson, M. J. Padgett, Principles and prospects for single-pixel imaging. *Nat. Photonics* **13**, 13–20 (2019).
47. J. Chang, V. Sitzmann, X. Dun, W. Heidrich, G. Wetzstein, Hybrid optical-electronic convolutional neural networks with optimized diffractive optics for image classification. *Sci. Rep.* **8**, 12324 (2018).
48. P. J. Winzer, Making spatial multiplexing a reality. *Nat. Photonics* **8**, 345–348 (2014).
49. T. Mikolov, M. Karafiát, L. Burget, J. Cernocký, S. Khudanpur, Recurrent neural network based language model. INTERSPEECH 2010, 11th Annual Conference of the International Speech Communication Association, Makuhari, Chiba, Japan, 2010 September 26–30, pp. 1045–1048.
50. G. Orchard, A. Jayawant, G. K. Cohen, N. Thakor, Converting static image datasets to spiking neuromorphic datasets using saccades. *Front. Neurosci.* **9**, 437 (2015).
51. C. Schuldt, I. Laptev, B. Caputo, Recognizing human actions: A local SVM approach. *Proceedings of the 17th International Conference on Pattern Recognition, 2004. ICPR 2004.* (2004), pp. 32–36.

52. T. Wang, M. M. Sohoni, L. G. Wright, M. M. Stein, S.-Y. Ma, T. Onodera, M. G. Anderson, P. L. McMahon, Image sensing with multilayer, nonlinear optical neural networks. *Nat. Photonics* **18**, 1–8 (2022).
53. V. Ulman, M. Maška, K. E. G. Magnusson, O. Ronneberger, C. Haubold, N. Harder, P. Matula, P. Matula, D. Svoboda, M. Radojevic, I. Smal, K. Rohr, J. Jaldén, H. M. Blau, O. Dzyubachyk, B. Lelieveldt, P. Xiao, Y. Li, S.-Y. Cho, A. C. Dufour, J.-C. Olivo-Marin, C. C. Reyes-Aldasoro, J. A. Solis-Lemus, R. Bensch, T. Brox, J. Stegmaier, R. Mikut, S. Wolf, F. A. Hamprecht, T. Esteves, P. Quelhas, Ö. Demirel, L. Malmström, F. Jug, P. Tomancak, E. Meijering, A. Muñoz-Barrutia, M. Kozubek, C. Ortiz-de-Solorzano, An objective comparison of cell-tracking algorithms. *Nat. Methods* **14**, 1141–1152 (2017).
54. Y.-W. Huang, H. W. H. Lee, R. Sokhoyan, R. A. Pala, K. Thyagarajan, S. Han, D. P. Tsai, H. A. Atwater, Gate-tunable conducting oxide metasurfaces. *Nano Lett.* **16**, 5319–5325 (2016).
55. A. Forouzmand, M. M. Salary, G. K. Shirmanesh, R. Sokhoyan, H. A. Atwater, H. Mosallaei, Tunable all-dielectric metasurface for phase modulation of the reflected and transmitted light via permittivity tuning of indium tin oxide. *Nanophotonics* **8**, 415–427 (2019).
56. G. K. Shirmanesh, R. Sokhoyan, P. C. Wu, H. A. Atwater, Electro-optically tunable multifunctional metasurfaces. *ACS Nano* **14**, 6912–6920 (2020).
57. C. Scott. 2020. "Latency Numbers Every Programmer Should Know.";https://people.eecs.berkeley.edu/~rcs/research/interactive_latency.html.
58. C. Li, Y. Yang, M. Feng, S. Chakradhar, H. Zhou, Optimizing memory efficiency for deep convolutional neural networks on GPUs. *SC'16: Proceedings of the International Conference for High Performance Computing, Networking, Storage and Analysis* (2016), pp. 633–644.
59. C. Haffner, W. Heni, Y. Fedoryshyn, J. Niegemann, A. Melikyan, D. L. Elder, B. Baeuerle, Y. Salamin, A. Josten, U. Koch, C. Hoessbacher, F. Ducry, L. Juchli, A. Emboras, D. Hillerkuss, M. Kohl, L. R. Dalton, C. Hafner, J. Leuthold, All-plasmonic Mach–Zehnder modulator enabling optical high-speed communication at the microscale. *Nat. Photonics* **9**, 525–528 (2015).
60. M. Burla, C. Hoessbacher, W. Heni, C. Haffner, Y. Fedoryshyn, D. Werner, T. Watanabe, H. Massler, D. L. Elder, L. R. Dalton, J. Leuthold, 500 GHz plasmonic Mach-Zehnder modulator enabling sub-THz microwave photonics. *APL Photonics* **4**, 056106 (2019).
61. S. Lischke, A. Peczek, J. S. Morgan, K. Sun, D. Steckler, Y. Yamamoto, F. Korndörfer, C. Mai, S. Marschmeyer, M. Fraschke, A. Krüger, A. Beling, L. Zimmermann, Ultra-fast germanium photodiode with 3-dB bandwidth of 265 GHz. *Nat. Photonics* **15**, 925–931 (2021).
62. D. R. Solli, C. Ropers, P. Koonath, B. Jalali, Optical rogue waves. *Nature* **450**, 1054–1057 (2007).
63. L. Gao, J. Liang, C. Li, L. V. Wang, Single-shot compressed ultrafast photography at one hundred billion frames per second. *Nature* **516**, 74–77 (2014).
64. H. Abdi, L. J. Williams, Principal component analysis. *Wiley Interdiscip. Rev. Comput. Stat.* **2**, 433–459 (2010).
65. D. P. Kingma, J. Ba, Adam: A method for stochastic optimization. arXiv:1412.6980 [cs.LG] (22 December 2014).
66. L. G. Wright, T. Onodera, M. M. Stein, T. Wang, D. T. Schachter, Z. Hu, P. L. McMahon, Deep physical neural networks trained with backpropagation. *Nature* **601**, 549–555 (2022).
67. R. C. Frye, E. A. Rietman, C. C. Wong, Back-propagation learning and nonidealities in analog neural network hardware. *IEEE Trans. Neural Netw.* **2**, 110–117 (1991).
68. J. Spall, X. Guo, A. I. Lvovsky, Hybrid training of optical neural networks. *Optica* **9**, 803–811 (2022).
69. C. Brandli, R. Berner, M. Yang, S.-C. Liu, T. Delbruck, A 240 × 180 130 db 3 μs latency global shutter spatiotemporal vision sensor. *IEEE J. Solid-State Circuits* **49**, 2333–2341 (2014).
70. Xilinx. 2020. "Kintex UltraScale FPGAs Data Sheet: DC and AC Switching Characteristics"; https://docs.xilinx.com/v/u/en-US/ds892-kintex-ultrascale-data-sheet.
71. M. Al-Ashrafy, A. Salem, W. Anis, An efficient implementation of floating point multiplier. *2011 Saudi International Electronics, Communications and Photonics Conference (SIECPC)* (2011), pp. 1–5.
72. L. Mennel, J. Symonowicz, S. Wachter, D. K. Polyushkin, A. J. Molina-Mendoza, T. Mueller, Ultrafast machine vision with 2D material neural network image sensors. *Nature* **579**, 62–66 (2020).
73. G. P. Agrawal, *Fiber-Optic Communication Systems* (John Wiley & Sons, 2012).
74. M. J. Connelly, Wideband semiconductor optical amplifier steady-state numerical model. *IEEE J. Quantum Electron.* **37**, 439–447 (2001).
75. K. Luke, Y. Okawachi, M. R. Lamont, A. L. Gaeta, M. Lipson, Broadband mid-infrared frequency comb generation in a Si_3N_4 microresonator. *Opt. Lett.* **40**, 4823–4826 (2015).
76. Y. Lecun, L. Bottou, Y. Bengio, P. Haffner, Gradient-based learning applied to document recognition. *Proc. IEEE* **86**, 2278–2324 (1998).

Acknowledgments

Funding: This work was supported in part by the Natural Science Foundation of China (NSFC) under contract nos. 62125106, 61860206003, and 62088102; in part by the Ministry of Science and Technology of China under contract no. 2021ZD0109901; and in part by the Beijing National Research Center for Information Science and Technology (BNRist) under grant no. BNR2020RC01002. **Author contributions:** L.F. initiated the project. L.F. and T.Z. conceived the original idea. W.W., J.Z., and T.Z. performed numerical simulations. T.Z. and W.W. constructed the experimental system and conducted the experiments. L.F., T.Z., W.W., and S.Y. analyzed the results and prepared the manuscript. **Competing interests:** The authors declare that they have no competing interests. **Data and materials availability:** All data needed to evaluate the conclusions in the paper are present in the paper and/or the Supplementary Materials. The software code for the neural network model and experimental control may be found online at https://doi.org/10.5281/zenodo.7749015.

Submitted 23 December 2022
Accepted 2 May 2023
Published 7 June 2023
10.1126/sciadv.adg4391

MATERIALS SCIENCE

In-plane anisotropy of graphene by strong interlayer interactions with van der Waals epitaxially grown MoO_3

Hangyel Kim[1], Jong Hun Kim[1,2], Jungcheol Kim[3], Jejune Park[4], Kwanghee Park[5,6], Ji-Hwan Baek[1], June-Chul Shin[1], Hyeongseok Lee[1], Jangyup Son[7,8], Sunmin Ryu[5], Young-Woo Son[4], Hyeonsik Cheong[3], Gwan-Hyoung Lee[1]*

van der Waals (vdW) epitaxy can be used to grow epilayers with different symmetries on graphene, thereby imparting unprecedented properties in graphene owing to formation of anisotropic superlattices and strong interlayer interactions. Here, we report in-plane anisotropy in graphene by vdW epitaxially grown molybdenum trioxide layers with an elongated superlattice. The grown molybdenum trioxide layers led to high p-doping of the underlying graphene up to $p = 1.94 \times 10^{13}$ cm^{-2} regardless of the thickness of molybdenum trioxide, maintaining a high carrier mobility of 8155 cm^2 V^{-1} s^{-1}. Molybdenum trioxide–induced compressive strain in graphene increased up to −0.6% with increasing molybdenum trioxide thickness. The asymmetrical band distortion of molybdenum trioxide–deposited graphene at the Fermi level led to in-plane electrical anisotropy with a high conductance ratio of 1.43 owing to the strong interlayer interaction of molybdenum trioxide–graphene. Our study presents a symmetry engineering method to induce anisotropy in symmetric two-dimensional (2D) materials via the formation of asymmetric superlattices with epitaxially grown 2D layers.

INTRODUCTION

van der Waals (vdW) epitaxy is a widely used technique for fabricating two-dimensional (2D) epitaxial layers on a variety of growth templates with crystallographic alignment (*1*–*3*). The major advantages of vdW epitaxy originate from the dangling bond–free interface and relatively weak vdW interactions between the epilayers and growth templates (*4*), enabling the growth of epilayers with a remarkable mismatch of lattice (*5*) and symmetry (*6*–*8*) without substantial interfacial strain or misfit dislocations. The interlayer interaction is of particular importance in vdW epitaxy with symmetry mismatch due to the formation of anisotropic superlattices (*9*–*12*) and directional strain during a cooling procedure (*13*).

Here, we report the in-plane anisotropy in graphene induced by the strong interlayer interaction with vdW epitaxially grown α-MoO_3. The strong interlayer interaction at the vdW interface helped modulate the mechanical and electrical properties of monolayer graphene. The epilayer and graphene template with different thermal expansion coefficients (TECs) exerted a high compressive strain on graphene, which increased up to −0.6% with increasing MoO_3 thickness. Meanwhile, the graphene was highly p-doped ($p = 1.94 \times 10^{13}$ cm^{-2}) by the charge transfer from MoO_3 regardless of the MoO_3 thickness. Notably, MoO_3-deposited graphene exhibited in-plane anisotropy (conductance ratio of 1.43) in the electrical conductance owing to the crystal orientation–related periodic potentials by MoO_3, maintaining a high carrier mobility of 8155 cm^2 V^{-1} s^{-1}. Our study shows that vdW epitaxial interface can induce the strong interlayer interaction and in-plane anisotropy, which can be used to modulate the crystal orientation–dependent properties of 2D materials.

RESULTS

Crystal structure of MoO_3/graphene heterostructure

To investigate the interlayer interaction at a symmetry-mismatched epitaxial interface, we used orthorhombic α-MoO_3 (*Pnma* space group) with in-plane anisotropic mechanical, electrical, and optical properties (*14*–*18*). MoO_3 layers comprising MoO_6 octahedral double layers ($a = 3.96$ Å and $c = 3.70$ Å) were stacked along the *b* axis with weak vdW forces (*14*, *19*–*22*). MoO_3 was grown on exfoliated graphene by the thermal evaporation of the Mo film in the air (see Materials and Methods) (*23*). Figure 1A shows MoO_3-grown monolayer graphene (MoO_3/Gr). Figure 1B shows the Raman spectra of the as-exfoliated graphene and MoO_3/Gr samples. Two main Raman peaks of MoO_3 can be observed at ~817 and ~ 995 cm^{-1}, corresponding to the stretching modes of doubly coordinated oxygen along the *a* axis (*24*, *25*). The absence of D peak, an indicator of defects in graphene, implies that there was no recognizable damage in graphene during MoO_3 growth (*26*, *27*). However, G and 2D peaks, which are sensitive to doping and strain, shifted markedly after the deposition of MoO_3. This indicates that the deposited MoO_3 induced doping and strain in the underlying graphene. This is discussed later in the paper. The morphology and thickness of MoO_3 were measured using atomic force microscopy (AFM), as shown in Fig. 1 (C and D). The graphene was fully covered by bilayer MoO_3 (2L-MoO_3) with a few thick islands, as reported previously (fig. S1) (*23*, *28*). The MoO_3 surface was clean and flat without contamination or damage. The height profile in Fig. 1D (from the white dashed line in Fig. 1C) shows that the thickness of

[1]Department of Materials Science and Engineering, Seoul National University, Seoul 08826, South Korea. [2]Department of Physics, Inha University, Incheon 22212, South Korea. [3]Department of Physics, Sogang University, Seoul 04107, South Korea. [4]School of Computational Sciences, Korea Institute for Advanced Study, Seoul 02455, South Korea. [5]Department of Chemistry, Pohang University of Science and Technology, Pohang 37673, South Korea. [6]Korea Research Institute of Standards and Science, Daejeon 34113, South Korea. [7]Functional Composite Materials Research Center, Korea Institute of Science and Technology (KIST), Jeonbuk 55324, South Korea. [8]Division of Nano and Information Technology, KIST School University of Science and Technology (UST), Jeonbuk 55324, South Korea.
*Corresponding author. Email: gwanlee@snu.ac.kr

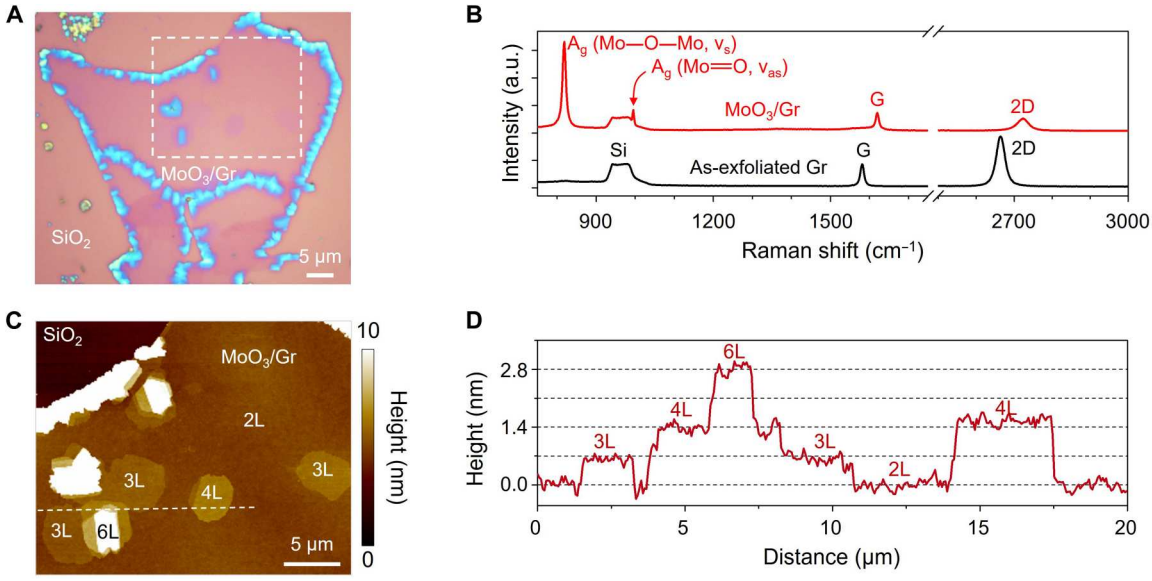

Fig. 1. vdW epitaxial growth of MoO_3 on monolayer graphene. (**A**) Optical microscope image of MoO_3/Gr. (**B**) Raman spectra of as-exfoliated Gr (black) and MoO_3/Gr (red). The notable features after MoO_3 growth are the emergence of MoO_3 Raman peaks at ~820 and ~990 cm^{-1}, blueshift in the G and 2D peaks, and absence of D peak. a.u., arbitrary units. (**C**) AFM image of MoO_3/Gr of the dashed area in (A). (**D**) AFM height profile along the white dashed line in (C). The heights of MoO_3 islands correspond to multiple layers of MoO_3 (~0.7 nm)

the monolayer MoO_3 corresponds to half of the unit cell (~0.7 nm) (*14*, *19*–*22*).

Epitaxial relationship between MoO_3 and graphene

To reveal the crystal structures and epitaxial relationship between MoO_3 and Gr, we used spherical aberration-corrected transmission electron microscopy (Cs-TEM). The TEM image in Fig. 2A shows MoO_3/Gr transferred onto a TEM grid with holes, where 2L-MoO_3 is partially grown on the graphene. The high-resolution TEM image in Fig. 2B confirms the epitaxial growth of crystalline MoO_3 on the graphene. The diffraction pattern obtained by fast Fourier transform (FFT), shown in the inset of Fig. 2B, verifies that the rhombic pattern (blue dashed line) of MoO_3 is aligned with the hexagonal pattern (orange dashed line) of graphene. The (200) plane of MoO_3 is parallel to the $(1\bar{1}00)$ plane of graphene (*29*, *30*). The FFT-filtered TEM images of graphene (left) and MoO_3 (right) in Fig. 2C, obtained from each diffraction pattern, clearly show the growth of rectangular MoO_3 unit cells with lattice parameters of 3.97 and 3.75 Å on the graphene with an epitaxial relationship: *a* and *c* axes of MoO_3 are parallel to the armchair (*ac*) and zigzag (*zz*) directions of graphene, respectively. The atomic model in Fig. 2D shows the formation of a superlattice (indicated by yellow dashed lines) in the MoO_3/Gr heterostructure with an epitaxial relationship. The long superlattice unit cell in MoO_3/Gr can induce distinct periodicities along two directions of *ac* and *zz* in graphene (*9*–*12*).

Modulation of doping and strain in graphene by MoO_3 epilayer

To investigate the interlayer interaction between MoO_3 and graphene, we measured the Raman spectra of the graphene regions covered by MoO_3 islands of different thicknesses (1L to 5L), as shown in Fig. 3A. For comparison, the Raman spectra of the as-exfoliated graphene (gray) and uncovered graphene (black) are also shown in Fig. 3A. The uncovered graphene is the region with no deposition of MoO_3 after epitaxial growth. Although the uncovered graphene had no MoO_3, there was a blue shift in the G and 2D peaks owing to the annealing effect (*31*). Notably, the MoO_3/Gr region showed a marked blue shift in the G and 2D peaks compared to the as-exfoliated and uncovered graphene. Furthermore, the two peaks substantially blue-shifted with increasing MoO_3 thickness. The marked shifts in the Raman peaks indicate a strong interlayer interaction between the MoO_3 epilayers and graphene, leading to considerable doping and strain in graphene depending on the MoO_3 thickness (*26*, *27*).

To separately measure the doping concentration (p) and strain (ε) of MoO_3/Gr, we marked the positions of the G (ω_G) and 2D (ω_{2D}) peaks in the correlation plot of Fig. 3B. The doping and strain of graphene can be quantified by projecting ω_G and ω_{2D} to the doping concentration (magenta) and strain axes (gray), respectively (fig. S2) (*32*). As shown in Fig. 3B, the uncovered graphene is p-doped ($p = 7.8 \times 10^{12}$ cm^{-2}) with a small compressive strain of −0.07% after the MoO_3 growth process, which is due to the conformal contact of graphene on the SiO_2 substrate by annealing under ambient condition (*31*, *33*, *34*). In the case of MoO_3/Gr, the graphene is highly p-doped ($p = 1.94 \times 10^{13}$ cm^{-2}) regardless of the MoO_3 thickness, while the compressive strain increases with the number of MoO_3 layers. Different MoO_3 thickness dependence of the doping concentration and strain can be clearly visualized in Fig. 3 (C to E). Although MoO_3 regions of different thicknesses were deposited on the graphene, as shown in the AFM image of Fig. 3C, the p-doping concentration of the graphene measured by the Raman peaks was maintained irrespective of the number of MoO_3 layers, as shown in Fig. 3D. Meanwhile, thicker MoO_3 epilayers resulted in a higher compressive strain, as shown in Fig. 3E.

To clearly show the MoO_3 thickness dependence of doping and strain in graphene, we plotted the doping concentration and

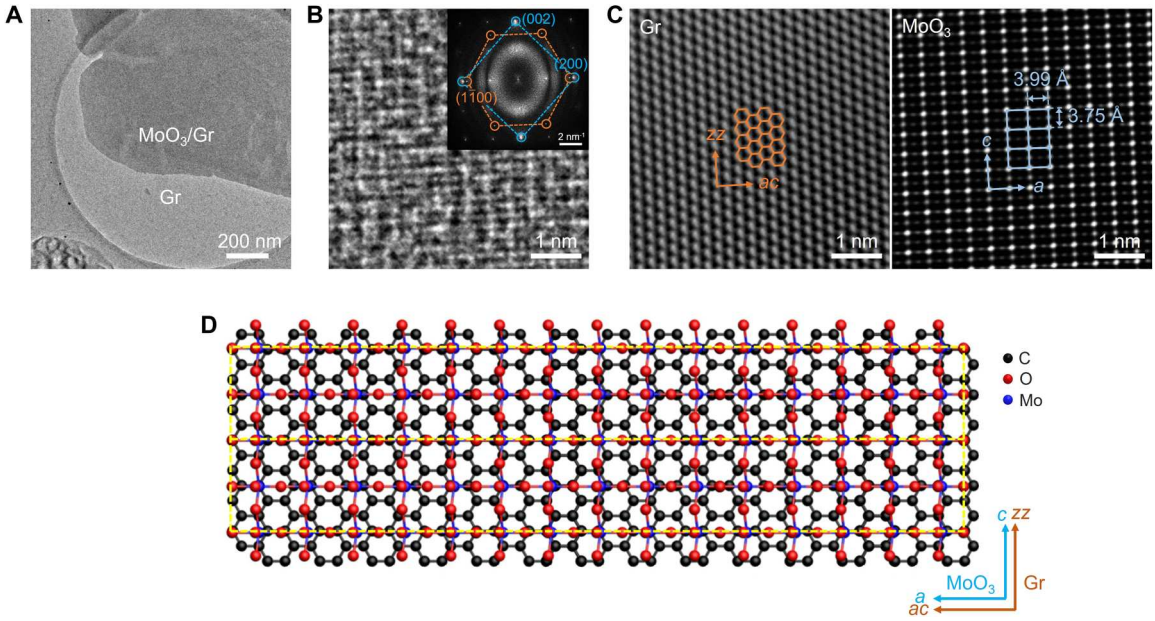

Fig. 2. Epitaxial relationship between MoO_3 epilayers and monolayer graphene growth template. (**A**) Low-magnification TEM image of MoO_3/Gr. (**B**) High-resolution TEM image of MoO_3/Gr. The inset shows the corresponding FFT image. Only a single set of rhombus pattern indicates the growth of single-crystal MoO_3 (blue). In addition, the perfect alignment of MoO_3 and graphene (orange) patterns demonstrates the epitaxial growth of MoO_3 on monolayer graphene. (**C**) FFT-filtered images of graphene (left) and MoO_3 (right). (**D**) Schematic of MoO_3/Gr superlattices (yellow dashed boxes) based on their epitaxial relationship. The periodicity along the horizontal direction (*a* axis of MoO_3 and *ac* direction of graphene) is approximately eight times greater than that along the vertical direction (*c* axis of MoO_3 and *zz* direction of graphene).

compressive strain as a function of the MoO_3 thickness in Fig. 3 (F and G), respectively. The p-doping concentration of 1L-MoO_3/Gr was almost twice higher than that of the uncovered graphene and almost invariant for 1L-MoO_3 to 5L-MoO_3 (Fig. 3F). This indicates that a high p-doping concentration of graphene can be achieved using only monolayer MoO_3. This is attributed to the efficient charge transfer between MoO_3 and graphene by the large and thickness-insensitive work function of MoO_3 (*28*, *35*–*37*). In contrast, the compressive strain of MoO_3/Gr clearly shows a dependency on the MoO_3 thickness (Fig. 3G). The compressive strain exerted on graphene by MoO_3 is due to the difference in the TECs between MoO_3 and graphene (*14*, *38*, *39*) as well as the high lateral stiffness and friction of MoO_3 (*28*, *40*, *41*). The strain of graphene increased, and the increment gradually decreased with the number of MoO_3 layers. This may be due to the formation of a more rigid MoO_3 structure with increasing thickness. Both the doping and strain of graphene induced by the MoO_3 epilayer indicate a strong interlayer interaction between MoO_3 and graphene with an epitaxial relationship.

In-plane anisotropy of MoO_3/Gr

The formation of an elongated superlattice and strong interlayer interaction at the MoO_3-Gr heterointerface can induce crystal orientation–dependent modulation of the properties of graphene. To verify the orientation-dependent structural modulation, we measured the angle-resolved polarized Raman spectra of MoO_3/Gr by rotating an analyzer (θ_{out}) at a fixed polarizer (θ_{in}) (see Materials and Methods for detailed information on angle-resolved polarized Raman spectroscopy). Figure 4A shows the G peaks of 3L-MoO_3/Gr measured at four specific angles. The G peaks were deconvoluted into two peaks of G^+ (red area) at 1621.7 cm^{-1} and G^- (blue area) at 1623.2 cm^{-1}, which have eigenvectors parallel and orthogonal to the strain direction, respectively (fig. S3) (*42*–*44*). The intensities of these peaks vary as a function of θ_{out}, resulting in a periodic shift in the convoluted G peak, as shown in the contour plot in Fig. 4B. The peak intensities of G^+ (red circles) and G^- (blue circles) are plotted in polar coordinates in Fig. 4C. They show well-defined $\cos^2 \theta_{out}$ patterns that repel each other in accordance with theoretical predictions (solid lines in Fig. 4C), indicating the presence of a uniaxial strain in graphene (*42*–*44*). Therefore, our observations from the polarized Raman spectra show that the vdW epitaxially grown MoO_3 generates an anisotropic strain in graphene (*13*, *14*, *38*, *39*).

We also measured the angle-resolved electrical transport in the 1L-MoO_3/Gr device. The inset of Fig. 4D shows a device in which multiple electrodes of different angles are deposited around the 1L-MoO_3 island. Figure 4D shows the transfer curves (I_{DS}-V_G) measured with different electrodes at specific angles, indicating a highly p-doped MoO_3/Gr, as observed in the Raman measurement. In addition, the current levels and slopes of the transfer curves strongly depend on the measured orientation. Figure 4 (E to G) shows the p-doping concentration at V_G = 0 V, conductance (G), and field-effect mobility (μ_{FE}) of MoO_3/Gr in polar coordinates. The p-doping concentration was calculated using the equation $p = \frac{\varepsilon_0 \varepsilon_r V_{CNP}}{e\, t_{ox}}$, where ε_0, ε_r, V_{CNP}, e, and t_{ox} are the vacuum permittivity, relative permittivity of SiO_2, charge neutrality point of the MoO_3/Gr device, elemental charge, and thickness of SiO_2, respectively. The doping level showed no orientation dependence because the doping of graphene was generated by the charge transfer between MoO_3 and graphene (Fig. 4E). In contrast, both

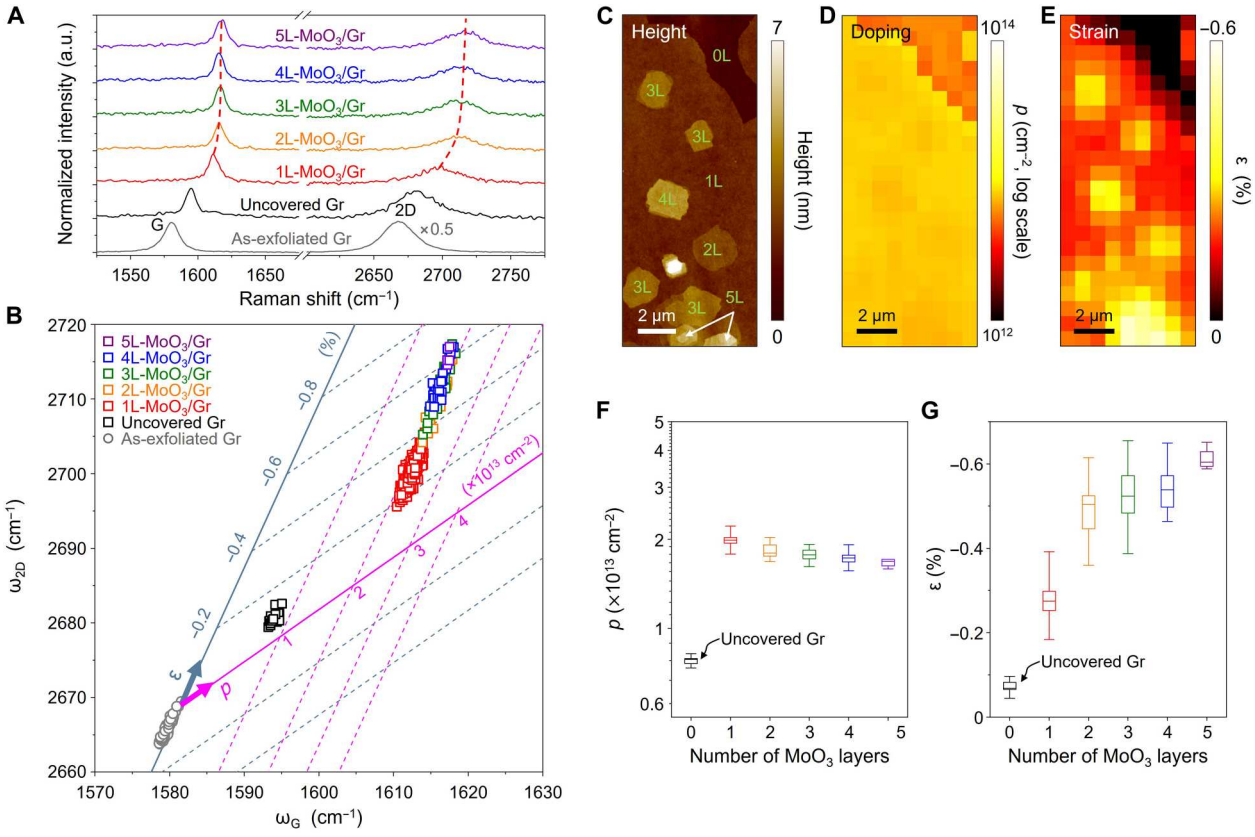

Fig. 3. Hole concentration and strain in the MoO_3-grown graphene. (**A**) Raman spectra of the as-exfoliated Gr (gray), uncovered Gr (black), and MoO_3/Gr with various MoO_3 thicknesses (rainbow colored, red to purple with increasing MoO_3 thickness). For MoO_3/Gr, the apexes of the G and 2D peaks are connected by dashed lines for visual guidance. (**B**) Correlation plot of the $\omega_{2D} - \omega_G$ for the samples shown in (A). (**C**) AFM image of MoO_3/Gr with various MoO_3 thicknesses. (**D** and **E**) Mapping images of doping and strain of MoO_3/Gr, respectively. The strain shows distinctive difference depending on the MoO_3 thickness, whereas doping exhibits a difference depending only on the presence of MoO_3 epilayers. (**F** and **G**) Plots of hole concentration and strain as a function of the number of MoO_3 layers.

conductance and μ_{FE} exhibit anisotropy with 180° periodicity, as shown in Fig. 4 (F and G), respectively. Anisotropy conductance ratio (G_{max}/G_{min}) was 1.43 at V_G = 0 V, which is comparable to that of a representative in-plane anisotropic 2D material, black phosphorus (~1.5) (*45*–*47*). Similarly, μ_{FE} of MoO_3/Gr showed a large anisotropy ratio ($\mu_{FE,max}/\mu_{FE,min}$) of 1.77, maintaining a high mobility of 8155 $cm^2\ V^{-1}\ s^{-1}$ at $p = 1 \times 10^{12}\ cm^{-2}$. This result shows that in-plane electrical anisotropy can be achieved by epitaxially grown MoO_3 even in symmetrical graphene with isotropic Dirac cones at K and K' points of the Brillouin zone (BZ) (*48*, *49*). The insulating properties of MoO_3 indicate no electrical contribution to the conductivity of MoO_3/Gr (fig. S4). Note that the vdW epitaxially grown MoO_3 led to a high p-doping concentration of graphene without substantial degradation in the carrier mobility. As a result, MoO_3/Gr shows low sheet resistance of ~133 ohms per square (figs. S5 and S6). Although the contact resistance of the MoO_3/Gr is reduced by doping compared to graphene device, influence of contacts on the conductivity of MoO_3/Gr was excluded because of small values (fig. S7).

Anisotropic distortion of graphene band structure by MoO_3 epilayer

To clarify the origin of the unconventional conductance anisotropy of MoO_3/Gr, we performed first-principles calculations based on density functional theory (DFT). Anisotropic periodic potentials on graphene cause anisotropic deformation of its band structure (*50*, *51*). Accordingly, we expected that the epitaxially grown MoO_3 layers would create anisotropic periodic potentials in graphene in close contact. The formation of a rectangular superlattice and uniaxial compressive strain, which was experimentally observed in MoO_3/Gr, can induce atomic-scale corrugation in monolayer graphene. Therefore, the MoO_3 epilayers can exert anisotropic periodic potentials on corrugated graphene, leading to an anisotropic deformation of the band structure in graphene.

To verify our hypothesis, we constructed a MoO_3/Gr heterostructure by considering the strain induced by thermal expansion. The optimized lattice constants were 2.47 Å for monolayer graphene, and a = 3.96 Å and c = 3.70 Å for MoO_3 monolayer. As observed in the TEM images in Fig. 2, the a and c axes of MoO_3 are aligned with the ac and zz directions of graphene, respectively. A MoO_3/Gr heterostructure with supercells of MoO_3 ($16 \times a + 2 \times c$) and graphene ($15 \times ac + 3 \times zz$) was constructed by minimizing the mismatch between the lattice parameters of MoO_3 and graphene and by applying orientation dependent TECs for MoO_3 and graphene (*14*, *39*). In the constructed MoO_3/Gr heterostructure, the graphene had anisotropic compressive strains of 1.2 and 0.2% along the ac and zz directions under the constraints of the MoO_3 lattice, respectively. Figure 5A shows the out-of-plane deformation

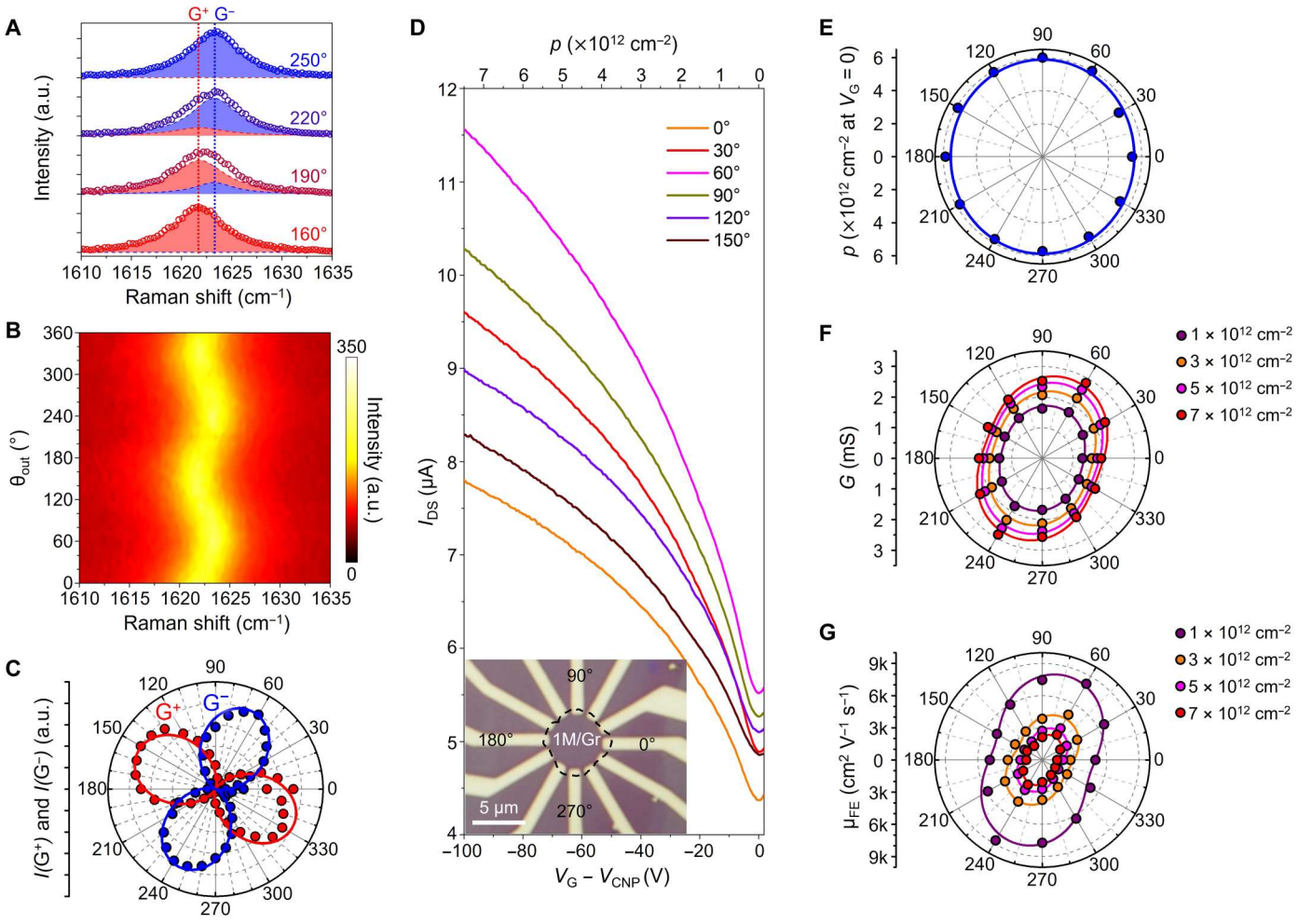

Fig. 4. Anisotropy in graphene induced by MoO_3 epilayers. (**A**) Fitting results of four representative angle-resolved polarized Raman spectra. The measured data are represented by the hollow circles, while the red and blue shaded areas correspond to the fitted results of the G^+ and G^- peaks, respectively. The peak positions of G^+ and G^- are indicated by the red and blue dotted lines, respectively. (**B**) Contour plot of the angle-resolved polarized Raman spectra of G peak as function of analyzer angle (θ_{out}). (**C**) Intensities of G^+ (red) and G^- (blue) peaks plotted in the polar coordinate. Spheres correspond to the intensities, and solid lines correspond to the results fitted to the theoretical expectation (*42*, *43*). (**D**) Orientation-dependent transfer characteristics of MoO_3/Gr electric device. The inset shows an optical image of the MoO_3/Gr electric device. (**E** to **G**) Polar coordinate plots of the hole concentration at zero-gate voltage (E), conductance (F), and field-effect mobility (G) of the MoO_3/Gr device in (D), respectively. Conductance and field-effect mobility are measured under various carrier concentrations, which are represented with different colors.

of graphene in contact with epitaxially grown 1L-MoO_3. Within the superlattice (indicated by a black box), the MoO_3-deposited graphene was corrugated with a maximum out-of-plane displacement of 0.09 Å. The carbon atoms that were aligned (misaligned) with the terminal oxygen atoms of MoO_3 were relocated below (above) the mass center of the graphene layer. The upward and downward displacements of the carbon atoms in graphene are indicated in red and blue, respectively. Because of the atomic arrangement, graphene exhibited a 1D-like corrugation parallel to the *zz* direction, and the periodicity of the corrugation corresponded to the length of the superlattice.

The directional corrugation of graphene results in periodic potentials on graphene depending on the distance between MoO_3 and graphene. In the supercell geometry, the electronic energy bands fold into small BZ of the cell so that the modifications of Dirac energy bands of graphene are hardly noticeable. To avoid this, we projected or unfolded the dense energy bands in the supercell BZ into the original BZ of graphene (*52*–*54*). Figure 5B shows the unfolded energy bands of the optimized MoO_3/graphene heterostructure (fire contour) along two directions of *x* (*ac*) and *y* (*zz*), shown in Fig. 5A, projected onto the graphene layer. The Fermi level (E_F; gray dashed lines) is downshifted by ~0.7 eV below the Dirac point of graphene, which supports our experimental observation of high p-doping concentration of graphene by the deposition of MoO_3. We also compared the band structures of the isolated graphene layer (green dashed lines), which had the same compressive strain as the MoO_3/graphene heterostructure. We noted that the apparent gapful (gapless) Dirac point along q_x (q_y) direction in Fig. 5B is caused by strain induced shift of Dirac point along q_y direction. The effective band structure along the *y* axis on the right side of Fig. 5B is strongly altered at certain energy ranges, while that along the *x* axis on the left side of Fig. 5B is similar to that of isolated graphene (white dashed boxes). Around the Fermi level, band splitting is noticeable, indicating strong hybridization with the MoO_3

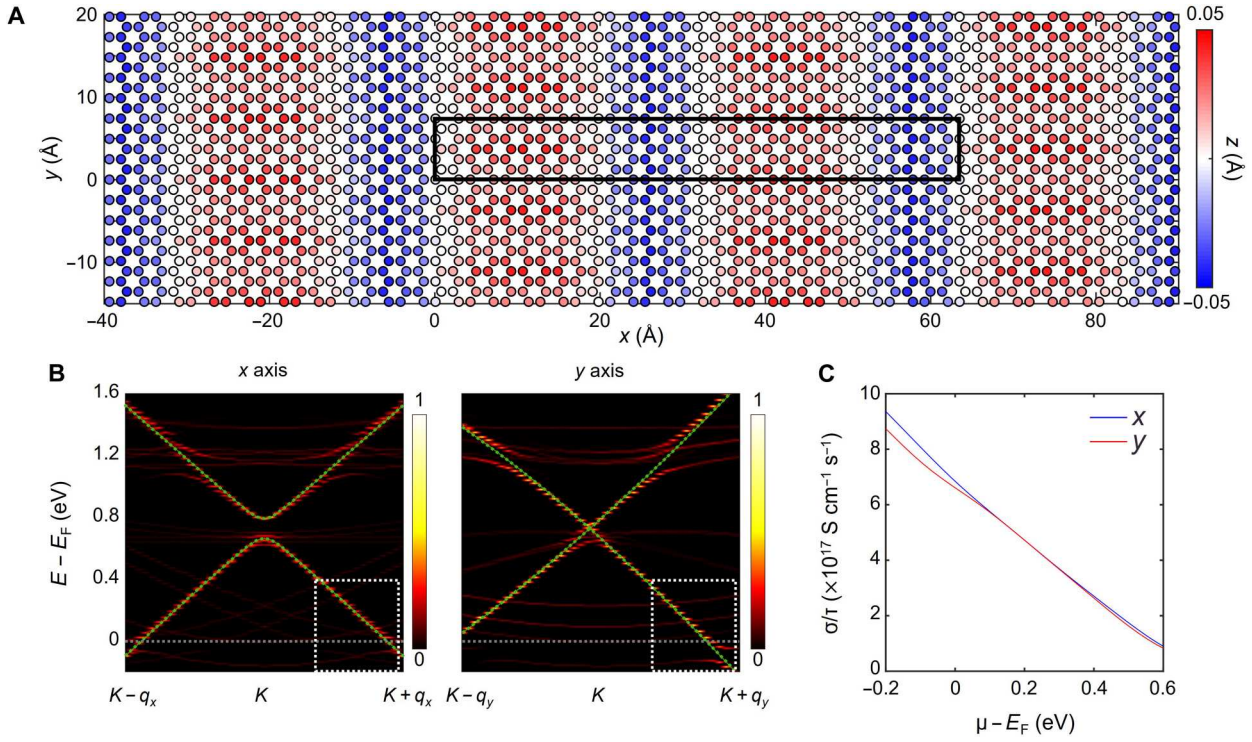

Fig. 5. Anisotropic band distortion in MoO_3/Gr. (**A**) Out-of-plane deformation of graphene for optimized MoO_3/Gr heterostructure. Blue (red) color represents the displacement of carbon atoms below (above) the center of mass of the graphene layer. (**B**) Unfolded energy bands of the MoO_3/Gr heterostructure, projected onto the graphene layer, along the *x* axis (left) and *y* axis (right) in the vicinity of the *K* point. The gray dashed lines represent the Fermi level of MoO_3/Gr. The green dashed lines indicate the band structure of isolated graphene with the same compressive strain as that in the heterostructure, 1.2% along the *ac* direction and 0.2% along the *zz* direction. The color scale indicates the *k*-dependent spectral weight for the primitive BZ of the graphene layer. (**C**) Calculated in-plane electrical conductivities using the unfolded spectral functions projected on graphene at 300 K along the *x* and *y* axes.

layer. It is estimated that the directional electronic difference shown in Fig. 5B induces anisotropy in the electrical transport properties of the MoO_3/graphene heterostructure.

On the basis of these band structures, the conductivities (σ) along the *x* and *y* axes could be estimated using the Boltzmann transport equation under a simple constant relaxation time (τ) approximation (*55*). Considering the crystal symmetry of the current system, the resulting conductivity along α(=x,y) direction (σ_α) is given by

$$\sigma_\alpha(\mu, T) = \frac{e^2\tau}{8\pi^3}\int\int\sum_n [\mathbf{v}^\alpha_{n,\mathbf{k}}]^2 \delta(\varepsilon - \varepsilon_{n,\mathbf{k}}) \times \left[-\frac{\partial f(\varepsilon, \mu, T)}{\partial \varepsilon}\right] d\mathbf{k}d\varepsilon \quad (1)$$

where $\mathbf{v}^\alpha_{n,\mathbf{k}}$, $\varepsilon_{n,\mathbf{k}}$, τ, and *f* are the α-directional component of **k**-dependent group velocity, energy of the *n*th band, relaxation time (considered a constant for simplicity), and Fermi distribution function as a function of the energy (ε), chemical potential (μ), and temperature (T), respectively. As shown in Fig. 5C, the electrical conductivity along the *y* axis is lower than that along the *x* axis around the Fermi level, consistent with our experimental results. Although the simulation results partly support observed anisotropic conductance originated from structural disparities for two orthogonal directions, the obtained anisotropy is still smaller than the measurement. We may consider further detailed characteristics reflecting actual experiment situations, such as larger supercell geometries and different scattering times along the direction, to improve the simulation results later.

DISCUSSION

In conclusion, we systemically investigated the interlayer interaction between MoO_3 epilayers and monolayer graphene growth templates in the symmetry-mismatched epitaxy. Our results demonstrated that the extreme modulation of doping and strain in graphene was generated by the strong interlayer interaction with the MoO_3 epilayers. First, the hole concentration in graphene could be markedly increased by the deposition of a single layer of MoO_3. Our results were comparable with those obtained using other similar doping methods (deposition of a charge-transfer layer on graphene) (*56*, *57*). In addition, by modulating the thickness of the MoO_3 epilayers, the strain exerted on graphene could be controlled, preserving a high hole concentration. Furthermore, the directional deformation of the graphene band structure leads to anisotropy in the electrical conductance of symmetric graphene. Overall, our work shows that the strong interlayer interaction between vdW epitaxially grown 2D oxides and 2D materials can be used as an approach for symmetry engineering of 2D materials, while preserving their outstanding electrical properties. Our findings have promising applications in optoelectronic devices that require optical and electrical anisotropy.

MATERIALS AND METHODS

Sample preparation

A MoO_3/graphene heterostructure was prepared using our previously reported methods (*23*). As the Mo source, a 100-nm-thick Mo film was deposited on a SiO_2 (285 nm)/Si substrate using an e-beam evaporator or a DC magnetron sputter. The quality and morphology of MoO_3 were irrelevant to the metal deposition method. As the target substrate, graphene was mechanically exfoliated on another SiO_2/Si substrate. Only monolayer graphene flakes were selected and used as target templates after their thicknesses were identified using Raman spectroscopy. To synthesize MoO_3 on monolayer graphene, the Mo film was placed on a preheated heater (525°C), and, shortly after, the target substrate was located 0.5 mm above the Mo film upside down. The Mo film was oxidized and sublimated into MoO_x and condensed on the graphene-exfoliated substrate because of the temperature difference between the source and target substrates. After 10 min, the target substrate was immediately removed from the heater. The thickness and coverage of MoO_3 could be roughly controlled by varying the deposition time.

Raman spectroscopy

Raman spectra were acquired using a Raman spectroscope (Renishaw Raman, inVia Reflex Confocal Raman Microscope, 532 nm, 600 gratings). Angle-resolved polarized Raman measurements were performed using a home-built confocal micro-Raman system with excitation sources of the 2.33 eV (532 nm) line from a diode-pumped solid-state laser. A 50× objective lens (0.8 numerical aperture) was used to focus the laser beam onto the sample and collect the scattered light (backscattering geometry). The Raman signal was dispersed using a Jobin-Yvon HORIBA iHR550 spectrometer (2400 grooves mm^{-1}) and detected by a liquid nitrogen–cooled back-illuminated charge-coupled device detector. The laser power was kept below 0.1 mW. The polarizer was fixed at constant angle (θ_{in}), and the analyzer angle (θ_{out}) was rotated to select specific polarization of the scattered light. An achromatic half-wave plate was placed in front of the spectrometer to keep the polarization direction of the signal entering the spectrometer constant with respect to the groove direction of the grating.

Transmission electron microscopy

MoO_3/Gr was transferred to a holey carbon Au TEM grid using a poly(methyl methacrylate) (PMMA)–based transfer method. PMMA was spin-coated on the SiO_2/Si substrate where MoO_3/Gr was located and immersed in a 2 weight % KOH solution after scouring the edges of the substrate. The PMMA/MoO_3/Gr film floated on the solution because SiO_2 was etched by KOH. The film was rinsed with deionized water several times and transferred onto a holey carbon Au TEM grid, and PMMA was removed by placing the TEM grid in acetone overnight. High-resolution TEM images were captured using a Cs-TEM (JEOL JEM-ARM 200F Cs-TEM).

Atomic force microscopy

AFM images were measured using NX-10 (Park Systems). Both contact and noncontact modes were performed considering the status of the samples and environment.

Device fabrication and electrical measurements

e-beam lithography was performed to define the patterns of the source and drain electrodes surrounding MoO_3/Gr. Subsequently, Cr/Pd/Au (2 nm/30 nm/40 nm) was deposited on MoO_3/Gr using an e-beam evaporator. The electrical measurements of the devices were performed using a parameter analyzer (Keithley 2400) under ambient conditions. The two-probe field-effect mobility (μ_{FE}) of MoO_3/Gr was calculated using the following equation

$$\mu_{FE} = g_m \frac{L}{WV_{DS}C} \quad (2)$$

where c is the unit back-gate capacitance of 285-nm SiO_2, $g_m = dI_{DS}/dV_G$ is the transconductance, V_{DS} is the drain voltage, and L and W are the channel length and width, respectively. The channel width is defined as the width of the metal electrodes. The transconductance was obtained by linearly fitting the transfer curve.

DFT calculations

To investigate the electronic and transport properties of the MoO_3/graphene heterostructure, we performed first-principles calculations based on DFT (*58*, *59*) using the VASP code (*60*, *61*). Projector-augmented wave potentials (*62*, *63*) were used to describe the valence electrons. The cutoff energy for the plane wave basis was set to 450 eV, and atomic relaxation was performed until the Hellmann-Feynman force acting on every atom decreased below 0.01 eV $Å^{-1}$. Dipole correction was included for a more precise calculation. For the exchange-correlation function, the rev-vdW-DF2 method (*64*) was adopted to consider vdW interactions. The BZ was sampled using a 2 × 8 × 1 k-grid for the rectangular supercell of MoO_3/graphene. To avoid spurious interlayer interaction along the out-of-plane direction, a vacuum region of 15 Å was introduced.

Supplementary Materials

This PDF file includes:

Supplementary Text
Figs. S1 to S7
References

REFERENCES AND NOTES

1. L. A. Walsh, C. L. Hinkle, Van der Waals epitaxy: 2D materials and topological insulators. *Appl. Mater. Today* **9**, 504–515 (2017).
2. H. Kum, D. Lee, W. Kong, H. Kim, Y. Park, Y. Kim, Y. Baek, S.-H. Bae, K. Lee, J. Kim, Epitaxial growth and layer-transfer techniques for heterogeneous integration of materials for electronic and photonic devices. *Nat. Electron.* **2**, 439–450 (2019).
3. A. K. Geim, I. V. Grigorieva, Van der Waals heterostructures. *Nature* **499**, 419–425 (2013).
4. A. Koma, Van der Waals epitaxy—A new epitaxial growth method for a highly lattice-mismatched system. *Thin Solid Films* **216**, 72–76 (1992).
5. K. Ueno, K. Saiki, T. Shimada, A. Koma, Epitaxial growth of transition metal dichalcogenides on cleaved faces of mica. *J. Vac. Sci. Technol. A* **8**, 68–72 (1990).
6. Z. Lin, A. Yin, J. Mao, Y. Xia, N. Kempf, Q. He, Y. Wang, C.-Y. Chen, Y. Zhang, V. Ozolins, Scalable solution-phase epitaxial growth of symmetry-mismatched heterostructures on two-dimensional crystal soft template. *Sci. Adv.* **2**, e1600993 (2016).
7. G. Tang, P. You, Q. Tai, A. Yang, J. Cao, F. Zheng, Z. Zhou, J. Zhao, P. K. L. Chan, F. Yan, Solution-phase epitaxial growth of perovskite films on 2D material flakes for high-performance solar cells. *Adv. Mater.* **31**, e1807689 (2019).
8. Z. Wu, Y. Lyu, Y. Zhang, R. Ding, B. Zheng, Z. Yang, S. P. Lau, X. H. Chen, J. Hao, Large-scale growth of few-layer two-dimensional black phosphorus. *Nat. Mater.* **20**, 1203–1209 (2021).
9. K. Hermann, Periodic overlayers and moiré patterns: Theoretical studies of geometric properties. *J. Phys. Condens. Matter* **24**, 314210 (2012).

10. K. Tang, W. Qi, Moiré-pattern-tuned electronic structures of van der Waals heterostructures. *Adv. Funct. Mater.* **30**, 2002672 (2020).
11. Y. Liu, J. N. B. Rodrigues, Y. Z. Luo, L. Li, A. Carvalho, M. Yang, E. Laksono, J. Lu, Y. Bao, H. Xu, S. J. R. Tan, Z. Qiu, C. H. Sow, Y. P. Feng, A. H. C. Neto, S. Adam, J. Lu, K. P. Loh, Tailoring sample-wide pseudo-magnetic fields on a graphene–black phosphorus heterostructure. *Nat. Nanotechnol.* **13**, 828–834 (2018).
12. T. Akamatsu, T. Ideue, L. Zhou, Y. Dong, S. Kitamura, M. Yoshii, D. Yang, M. Onga, Y. Nakagawa, K. Watanabe, T. Taniguchi, J. Laurienzo, J. Huang, Z. Ye, T. Morimoto, H. Yuan, Y. Iwasa, A van der Waals interface that creates in-plane polarization and a spontaneous photovoltaic effect. *Science* **372**, 68–72 (2021).
13. G. H. Ahn, M. Amani, H. Rasool, D.-H. Lien, J. P. Mastandrea, J. W. Ager Iii, M. Dubey, D. C. Chrzan, A. M. Minor, A. Javey, Strain-engineered growth of two-dimensional materials. *Nat. Commun.* **8**, 608 (2017).
14. H. Negishi, S. Negishi, Y. Kuroiwa, N. Sato, S. Aoyagi, Anisotropic thermal expansion of layered MoO_3 crystals. *Phys. Rev. B* **69**, 064111 (2004).
15. S. Puebla, R. D'Agosta, G. Sanchez-Santolino, R. Frisenda, C. Munuera, A. Castellanos-Gomez, In-plane anisotropic optical and mechanical properties of two-dimensional MoO_3. *npj 2D Mater. Appl.* **5**, 37 (2021).
16. W.-B. Zhang, Q. Qu, K. Lai, High-mobility transport anisotropy in few-layer MoO_3 and its origin. *ACS Appl. Mater. Interfaces* **9**, 1702–1709 (2017).
17. B. Zheng, Z. Wang, Y. Chen, W. Zhang, X. Li, Centimeter-sized 2D α-MoO_3 single crystal: Growth, Raman anisotropy, and optoelectronic properties. *2D Mater.* **5**, 045011 (2018).
18. W. Ma, P. Alonso-González, S. Li, A. Y. Nikitin, J. Yuan, J. Martín-Sánchez, J. Taboada-Gutiérrez, I. Amenabar, P. Li, S. Vélez, In-plane anisotropic and ultra-low-loss polaritons in a natural van der Waals crystal. *Nature* **562**, 557–562 (2018).
19. L. Kihlborg, Least squares refinement of crystal structure of molybdenum trioxide. *Ark. Kemi* **21**, 357 (1963).
20. G. Andersson, A. Magneli, L. Sillén, M. Rottenberg, On the crystal structure of molybdenum trioxide. *Acta Chem. Scand.* **4**, 793–797 (1950).
21. A. J. Molina-Mendoza, J. L. Lado, J. O. Island, M. A. Niño, L. Aballe, M. Foerster, F. Y. Bruno, A. Lopez-Moreno, L. Vaquero-Garzon, H. S. Van Der Zant, Centimeter-scale synthesis of ultrathin layered MoO_3 by van der Waals epitaxy. *Chem. Mater.* **28**, 4042–4051 (2016).
22. H. Ding, K. G. Ray, V. Ozolins, M. Asta, Structural and vibrational properties of α-MoO_3 from van der Waals corrected density functional theory calculations. *Phys. Rev. B* **85**, 012104 (2012).
23. J. H. Kim, J. K. Dash, J. Kwon, C. Hyun, H. Kim, E. Ji, G.-H. Lee, Van der Waals epitaxial growth of single crystal α-MoO_3 layers on layered materials growth templates. *2D Mater.* **6**, 015016 (2018).
24. M. A. Py, P. E. Schmid, J. T. Vallin, Raman scattering and structural properties of MoO_3. *Il Nuovo Cimento B (1971-1996)* **38**, 271–279 (1977).
25. M. Dieterle, G. Weinberg, G. Mestl, Raman spectroscopy of molybdenum oxides. *Phys. Chem. Chem. Phys.* **4**, 812–821 (2002).
26. A. C. Ferrari, D. M. Basko, Raman spectroscopy as a versatile tool for studying the properties of graphene. *Nat. Nanotechnol.* **8**, 235–246 (2013).
27. L. M. Malard, M. A. Pimenta, G. Dresselhaus, M. S. Dresselhaus, Raman spectroscopy in graphene. *Phys. Rep.* **473**, 51–87 (2009).
28. J. H. Kim, C. Hyun, H. Kim, J. K. Dash, K. Ihm, G.-H. Lee, Thickness-insensitive properties of α-MoO_3 nanosheets by weak interlayer coupling. *Nano Lett.* **19**, 8868–8876 (2019).
29. J. C. Meyer, A. K. Geim, M. I. Katsnelson, K. S. Novoselov, T. J. Booth, S. Roth, The structure of suspended graphene sheets. *Nature* **446**, 60–63 (2007).
30. Q. Yu, L. A. Jauregui, W. Wu, R. Colby, J. Tian, Z. Su, H. Cao, Z. Liu, D. Pandey, D. Wei, T. F. Chung, P. Peng, N. P. Guisinger, E. A. Stach, J. Bao, S.-S. Pei, Y. P. Chen, Control and characterization of individual grains and grain boundaries in graphene grown by chemical vapour deposition. *Nat. Mater.* **10**, 443–449 (2011).
31. E. Ji, M. J. Kim, J.-Y. Lee, D. Sung, N. Kim, J.-W. Park, S. Hong, G.-H. Lee, Substrate effect on doping and degradation of graphene. *Carbon* **184**, 651–658 (2021).
32. J. E. Lee, G. Ahn, J. Shim, Y. S. Lee, S. Ryu, Optical separation of mechanical strain from charge doping in graphene. *Nat. Commun.* **3**, 1024 (2012).
33. S. Ryu, L. Liu, S. Berciaud, Y.-J. Yu, H. Liu, P. Kim, G. W. Flynn, L. E. Brus, Atmospheric oxygen binding and hole doping in deformed graphene on a SiO_2 substrate. *Nano Lett.* **10**, 4944–4951 (2010).
34. J. Son, M. Choi, J. Hong, I. S. Yang, Raman study on the effects of annealing atmosphere of patterned graphene. *J. Raman Spectrosc.* **49**, 183–188 (2018).
35. Y. Guo, J. Robertson, Origin of the high work function and high conductivity of MoO_3. *Appl. Phys. Lett.* **105**, 222110 (2014).
36. A. L. F. Cauduro, R. Dos Reis, G. Chen, A. K. Schmid, H.-G. Rubahn, M. Madsen, Work function mapping of MoO_x thin-films for application in electronic devices. *Ultramicroscopy* **183**, 99–103 (2017).
37. D. A. Kowalczyk, M. Rogala, K. Szalowski, W. Kozlowski, I. Lutsyk, M. Piskorski, P. Krukowski, P. Dabrowski, D. Belić, M. Cichomski, Z. Klusek, P. J. Kowalczyk, Local electronic structure of stable monolayers of α-MoO_{3-x} grown on graphite substrate. *2D Mater.* **8**, 025005 (2020).
38. Y. Hu, X. Liu, S. Xu, W. Wei, G. Zeng, H. Yuan, Q. Gao, J. Guo, M. Chao, E. Liang, Improving the thermal expansion and capacitance properties of MoO_3 by introducing oxygen vacancies. *J. Phys. Chem. C* **125**, 10817–10823 (2021).
39. D. Yoon, Y.-W. Son, H. Cheong, Negative thermal expansion coefficient of graphene measured by Raman spectroscopy. *Nano Lett.* **11**, 3227–3231 (2011).
40. T. Liang, W. G. Sawyer, S. S. Perry, S. B. Sinnott, S. R. Phillpot, First-principles determination of static potential energy surfaces for atomic friction in MoS2 and MoO3. *Phys. Rev. B* **77**, 104105 (2008).
41. T. Korhonen, P. Koskinen, Peeling of multilayer graphene creates complex interlayer sliding patterns. *Phys. Rev. B* **92**, 115427 (2015).
42. M. Huang, H. Yan, C. Chen, D. Song, T. F. Heinz, J. Hone, Phonon softening and crystallographic orientation of strained graphene studied by Raman spectroscopy. *Proc. Natl. Acad. Sci. U.S.A.* **106**, 7304–7308 (2009).
43. T. M. G. Mohiuddin, A. Lombardo, R. R. Nair, A. Bonetti, G. Savini, R. Jalil, N. Bonini, D. M. Basko, C. Galiotis, N. Marzari, K. S. Novoselov, A. K. Geim, A. C. Ferrari, Uniaxial strain in graphene by Raman spectroscopy: ***G*** peak splitting, Grüneisen parameters, and sample orientation. *Phys. Rev. B* **79**, 205433 (2009).
44. O. Frank, G. Tsoukleri, J. Parthenios, K. Papagelis, I. Riaz, R. Jalil, K. S. Novoselov, C. Galiotis, Compression behavior of single-layer graphenes. *ACS Nano* **4**, 3131–3138 (2010).
45. A. Castellanos-Gomez, Black phosphorus: Narrow gap, wide applications. *J. Phys. Chem. Lett.* **6**, 4280–4291 (2015).
46. H. Liu, A. T. Neal, Z. Zhu, Z. Luo, X. Xu, D. Tománek, P. D. Ye, Phosphorene: An unexplored 2D semiconductor with a high hole mobility. *ACS Nano* **8**, 4033–4041 (2014).
47. F. Xia, H. Wang, Y. Jia, Rediscovering black phosphorus as an anisotropic layered material for optoelectronics and electronics. *Nat. Commun.* **5**, 4458 (2014).
48. P. R. Wallace, The band theory of graphite. *Phys. Rev.* **71**, 622 (1947).
49. A. H. C. Neto, F. Guinea, N. M. R. Peres, K. S. Novoselov, A. K. Geim, The electronic properties of graphene. *Rev. Mod. Phys.* **81**, 109 (2009).
50. C.-H. Park, L. Yang, Y.-W. Son, M. L. Cohen, S. G. Louie, Anisotropic behaviours of massless Dirac fermions in graphene under periodic potentials. *Nat. Phys.* **4**, 213–217 (2008).
51. Y. Li, S. Dietrich, C. Forsythe, T. Taniguchi, K. Watanabe, P. Moon, C. R. Dean, Anisotropic band flattening in graphene with one-dimensional superlattices. *Nat. Nanotechnol.* **16**, 525–530 (2021).
52. P. V. C. Medeiros, S. Stafström, J. Björk, Effects of extrinsic and intrinsic perturbations on the electronic structure of graphene: Retaining an effective primitive cell band structure by band unfolding. *Phys. Rev. B* **89**, 041407 (2014).
53. P. V. C. Medeiros, S. S. Tsirkin, S. Stafström, J. Björk, Unfolding spinor wave functions and expectation values of general operators: Introducing the unfolding-density operator. *Phys. Rev. B* **91**, 041116 (2015).
54. S. Kim, J. Ihm, H. J. Choi, Y.-W. Son, Origin of anomalous electronic structures of epitaxial graphene on silicon carbide. *Phys. Rev. Lett.* **100**, 176802 (2008).
55. G. K. H. Madsen, J. Carrete, M. J. Verstraete, BoltzTraP2, a program for interpolating band structures and calculating semi-classical transport coefficients. *Comput. Phys. Commun.* **231**, 140–145 (2018).
56. M. S. Choi, A. Nipane, B. S. Y. Kim, M. E. Ziffer, I. Datta, A. Borah, Y. Jung, B. Kim, D. Rhodes, A. Jindal, Z. A. Lamport, M. Lee, A. Zangiabadi, M. N. Nair, T. Taniguchi, K. Watanabe, I. Kymissis, A. N. Pasupathy, M. Lipson, X. Zhu, W. J. Yoo, J. Hone, J. T. Teherani, High carrier mobility in graphene doped using a monolayer of tungsten oxyselenide. *Nat. Electron.* **4**, 731–739 (2021).
57. S.-J. Kwon, T.-H. Han, T. Y. Ko, N. Li, Y. Kim, D. J. Kim, S.-H. Bae, Y. Yang, B. H. Hong, K. S. Kim, S. Ryu, T.-W. Lee, Extremely stable graphene electrodes doped with macromolecular acid. *Nat. Commun.* **9**, 2037 (2018).
58. P. Hohenberg, W. Kohn, Inhomogeneous electron gas. *Phys. Rev.* **136**, B864 (1964).
59. W. Kohn, L. J. Sham, Self-consistent equations including exchange and correlation effects. *Phys. Rev.* **140**, A1133 (1965).
60. G. Kresse, J. Furthmüller, Efficient iterative schemes for ab initio total-energy calculations using a plane-wave basis set. *Phys. Rev. B* **54**, 11169 (1996).
61. G. Kresse, J. Hafner, Ab initio molecular dynamics for liquid metals. *Phys. Rev. B* **47**, 558 (1993).
62. P. E. Blöchl, Projector augmented-wave method. *Phys. Rev. B* **50**, 17953 (1994).
63. G. J. Kresse, D. Joubert, From ultrasoft pseudopotentials to the projector augmented-wave method. *Phys. Rev. B* **59**, 1758–1775 (1999).
64. I. Hamada, Van der Waals density functional made accurate. *Phys. Rev. B* **89**, 121103 (2014).

65. C.-F. Chen, C.-H. Park, B. W. Boudouris, J. Horng, B. Geng, C. Girit, A. Zettl, M. F. Crommie, R. A. Segalman, S. G. Louie, F. Wang, Controlling inelastic light scattering quantum pathways in graphene. *Nature* **471**, 617–620 (2011).
66. A. Das, B. Chakraborty, S. Piscanec, S. Pisana, A. K. Sood, A. C. Ferrari, Phonon renormalization in doped bilayer graphene. *Phys. Rev. B* **79**, 155417 (2009).
67. A. Das, S. Pisana, B. Chakraborty, S. Piscanec, S. K. Saha, U. V. Waghmare, K. S. Novoselov, H. R. Krishnamurthy, A. K. Geim, A. C. Ferrari, A. K. Sood, Monitoring dopants by Raman scattering in an electrochemically top-gated graphene transistor. *Nat. Nanotechnol.* **3**, 210–215 (2008).
68. M. Lazzeri, F. Mauri, Nonadiabatic Kohn anomaly in a doped graphene monolayer. *Phys. Rev. Lett.* **97**, 266407 (2006).
69. J. Son, J. Kwon, S. Kim, Y. Lv, J. Yu, J.-Y. Lee, H. Ryu, K. Watanabe, T. Taniguchi, R. Garrido-Menacho, N. Mason, E. Ertekin, P. Y. Huang, G.-H. Lee, A. M. van der Zande, Atomically precise graphene etch stops for three dimensional integrated systems from two dimensional material heterostructures. *Nat. Commun.* **9**, 3988 (2018).

Acknowledgments
Funding: This work was supported by Samsung Electronics Co. Ltd. IO201210-07987-01 (to H.K. and G.-H.L.), National Research Foundation of Korea grant 2021R1A2C3014316 (to H.K. and G.-H.L.), National Research Foundation of Korea grant 2021M3F3A2A01037858 (H.K. and G.-H.L.), National Research Foundation of Korea grant 2017R1A5A1014862 (SRC program: vdWMRC center) (to G.-H.L.), Research Institute of Advanced Materials (RIAM) at the Seoul National University (to G.-H.L.), Institute of Engineering Research (IER) at the Seoul National University (to G.-H.L.), Institute of Applied Physics (IAP) at the Seoul National University (to G.-H.L.), and Inter-University Semiconductor Research Center (ISRC) at the Seoul National University. **Author contributions:** Conceptualization: H.K. and G.-H.L. Methodology: H.K., J.H.K., J.K., J.P., K.P., J.-H.B., J.-C.S., J.S., S.R., Y.-W.S., H.C., and G.-H.L. Validation: H.K., J.S., S.R., Y.-W.S., H.C., and G.-H.L. Formal analysis: H.K., J.H.K., J.K., J.P., K.P., J.S., S.R., Y.-W.S., H.C., and G.-H.L. Investigation: H.K., J.K., J.P., K.P., J.-H.B., J.-C.S., and H.L. Resource: S.R., Y.-W.S., H.C., and G.-H.L. Data curation: H.K. and G.-H.L.. Writing—original draft: H.K., J.H.K., and G.-H.L. Writing—review and editing: H.K., J.H.K., J.K., J.P., K.P., J.-H.B., J.-C.S., H.L., J.S., S.R., Y.-W.S., H.C., and G.-H.L. Visualization: H.K., J.H.K., and G.-H.L. Supervision: G.-H.L. Project administration: G.-H.L. Funding acquisition: G.-H.L. **Competing interests:** The authors declare that they have no competing interests. **Data and materials availability:** All data needed to evaluate the conclusions in the paper are present in the paper and/or the Supplementary Materials.

Submitted 15 January 2023
Accepted 1 May 2023
Published 7 June 2023
10.1126/sciadv.adg6696

APPLIED SCIENCES AND ENGINEERING

The strength of surgical knots involves a critical interplay between friction and elastoplasticity

Paul Johanns[1], Changyeob Baek[2], Paul Grandgeorge[1,3], Samia Guerid[4], Shawn A. Chester[5], Pedro M. Reis[1]*

Knots are the weakest link in surgical sutures, serving as mechanical ligatures between filaments. Exceeding their safe operational limits can cause fatal complications. The empirical nature of present guidelines calls for a predictive understanding of the mechanisms underlying knot strength. We identify the primary ingredients dictating the mechanics of surgical sliding knots, highlighting the previously overlooked but critical effect of plasticity and its interplay with friction. The characterization of surgeon-tied knots reveals the relevant ranges of tightness and geometric features. Using model experiments coupled with finite element simulations, we uncover a robust master curve for the target knot strength versus the tying pre-tension, number of throws, and frictional properties. These findings could find applications in the training of surgeons and robotic-assisted surgical devices.

INTRODUCTION

Surgery is a delicate craft in which high-quality suturing requires precision manual skills (*1*, *2*). Knots are central to surgical procedures, where they are used as ligatures during suturing (*3*, *4*). Knots are the weakest link in a suture (*5*, *6*), with disastrous consequences when they fail if they fail (*7*, *8*). A typical complication in surgery is wound dehiscence, whereby a previously sutured incision reopens, thus preventing wound healing (*9*). The related incisional hernia can be as high as 20% within the first year following midline laparotomy (*10*). In many common surgical procedures, suturing using monofilaments (versus braided ones) is advantageous for lower infection risks, albeit more challenging to ensure mechanical safety (*11*).

Surgeons tie sliding knots daily, consciously, or unwittingly (*12*); all intended flat knots tied in monofilaments capsize into a sliding conformation (*13*). Typical sliding knots consist of a series of half-hitches around a nearly straight filament segment under tension. A notation has been developed (*5*, *12*, *14*, *15*) to describe these knot configurations: "S" denotes a sliding throw, and "||" or "×" indicates an identical or nonidentical subsequent throw, respectively. For example, S || S refers to the sliding granny knot with two identical throws, and S × S to the sliding square knot with two nonidentical throws. The more complex S || S × S configuration describes a sliding granny knot followed by a sliding square knot. This notation is used throughout.

Although a high variability of knot-tying techniques is found across surgeons (*1*), additional throws in a knot have been shown to consistently decreases spontaneous untying rates (*5*, *16*, *17*). Furthermore, the tying pre-tension applied by the surgeon to tighten each throw appears to depend more on individual perception than experience (*18*). Even if the importance of mechanical analysis of knots has long been recognized in the medical profession, existing guidelines for best practices are primarily empirical and historical, not relying on physics-based structural analyses (*5*). Despite their broad and practical relevance, the predictive understanding of the physical mechanisms underlying knots remains crude. Existing frameworks in the classic mathematical theory of knots or elastic rod theory (*19*) are limited to purely geometric abstractions (*20*–*22*) or loose physical knots (*23*, *24*) and, thus, cannot capture the mechanical behavior of tight physical knots with their three-dimensional (3D) deformations and frictional contact (*25*–*27*). In addition to the fundamental challenges related to topology, geometry, 3D elasticity, contact, and frictional interactions, knotted surgical monofilaments also undergo elastoplastic deformation (*28*, *29*). The consequences and potentials of plasticity in functional knots have, to the best of our knowledge, not been considered to date.

Here, we seek to establish physics-based operational and safety guidelines for the strength of surgical sliding knots, focusing on commercial polypropylene suturing monofilaments which are common in surgical practice. We develop a physical model system to study the resistance of the knot to slippage—the knot strength—by systematically varying the tying pre-tension, number of throws, and knot topology (|| versus × throws). Our data are consistent with a power law for the knot strength as a function of the applied pre-tension and a linear relation between the knot strength and the number of throws. In addition, we characterize knots tied by an experienced surgeon, finding that they intuitively leave a safety margin between the regimes where knots are too loose to be functional and the high-tension regime resulting in filament fracture. The influence of friction on knot safety is explored systematically, using finite element modeling(FEM) to simulate elastoplastic knots with varying frictional interactions. Last, we propose a normalization that collapses all the data onto a master curve, describing the knot strength of tight knots in all of the configurations we considered and a wide range of friction coefficients. Our analysis suggests a robust mechanism for the strength of these surgical knots.

[1]Flexible Structures Laboratory, Institute of Mechanical Engineering, École Polytechnique Fédérale de Lausanne (EPFL), Lausanne, Switzerland. [2]Department of Applied Mathematics, Harvard University, Cambridge, MA, USA. [3]Materials Science and Engineering Department, University of Washington, Seattle, WA, USA. [4]Independent Plastic Surgeon, Lausanne, Switzerland. [5]Department of Mechanical & Industrial Engineering, New Jersey Institute of Technology, Newark, NJ, USA.
*Corresponding author. Email: pedro.reis@epfl.ch

RESULTS

The photograph in Fig. 1A (and movie S1) shows a series of half-hitch throws tied by a surgeon in a polypropylene suturing filament (Prolene, Ethicon Inc., Johnson & Johnson). This monofilament of circular cross section and area, A, was used throughout the study in the diameters of 0.25 or 0.49 mm United States Pharmacopeia (USP) designation 3-0 and 1, respectively (*30*)]. The yield strength of as-received Prolene was determined from uniaxial stress-strain measurements to be σ_Y = 19.1 MPa [from the 0.1% offset yield point (*31*)]. Typically, multiple suturing knots allow binding tissue, sealing an accident tear or a surgical incision (*11*, *32*). In Fig. 1 (B1 to B3) (and movie S2), we illustrate the typical surgical failure mode of wound dehiscence using a suturing practice pad with three stitches (S || S × S each) of different tightness. The outer knots k_1 and k_3 are tighter than the middle knot k_2. The system was loaded by gradually increasing the far-field uniaxial stress field of magnitude σ_∞. At a sufficiently large stress level, the filament of the middle knot, k_2, starts sliding (Fig. 1B2) until it completely slips out and, from then on, no longer fulfills its binding function (Fig. 1B3).

In Fig. 1 (C and D), we present optical microscope images (top) of S || S and the S × S knots, tightened using a UTM (universal testing machine; Instron 5943), along with their topological diagram (bottom). The knots (surgeon- and machine-tied) were tied around rigid 3D-printed pins (stereolithography 3D printer: Form 2, Formlabs; Clear V4 resin), with a flat upper surface of width, $2L$ = 6 mm (Fig. 1E). This pin geometry was chosen on the basis of the common rule for skin closures (*33*), prescribing the distance between the needle's entry point and the wound's edge, L, to equal the thickness of the tissue, ranging from 1 to 4 mm in the human body. After the half-hitch (identical or nonidentical throw) was set manually in its loose configuration on the rigid pin, the two free extremities of the filament were clamped to the UTM. The protocol to tighten the knot to a set pre-tension, $\tilde{T}$, is described in Materials and Methods.

We characterized sliding knots by quantifying their slippage resistance as follows. The loop surrounding the pin was cut open (Fig. 1E), and the protruding sliding strand (extremity of the filament at the cut) was threaded through the hole of a rigid stopper plate, as schematized in Fig. 1F for the S || S knot. Then, the knotted configuration was pulled against this plate to measure the knot-slipping force, $\tilde{F}$. In this model system, the plate represents the bound tissue in the suturing system, where tractions may lead to wound dehiscence (Fig. 1B). Figure 2A1 presents the experimental setup, where the protruding (sliding) strand, previously part of the loop, was first slid through a clearance hole (0.30 − mm diameter for 3-0 USP filament) in a flat, rigid acrylic plate (4 − mm thickness). Using the UTM at the constant speed of 1 mm/s, the S || S knot is then pulled against the plate, blocking vertical translation, and eventually leading to the sliding mechanism (Fig. 2, A1 to A4). In Fig. 2B, we plot the resulting dimensionless slipping force $\tilde{F} = F/(\sigma_Y A)$ versus the normalized displacement $\tilde{\delta} = \delta/D$. Initially, $\tilde{F}$ increases as the

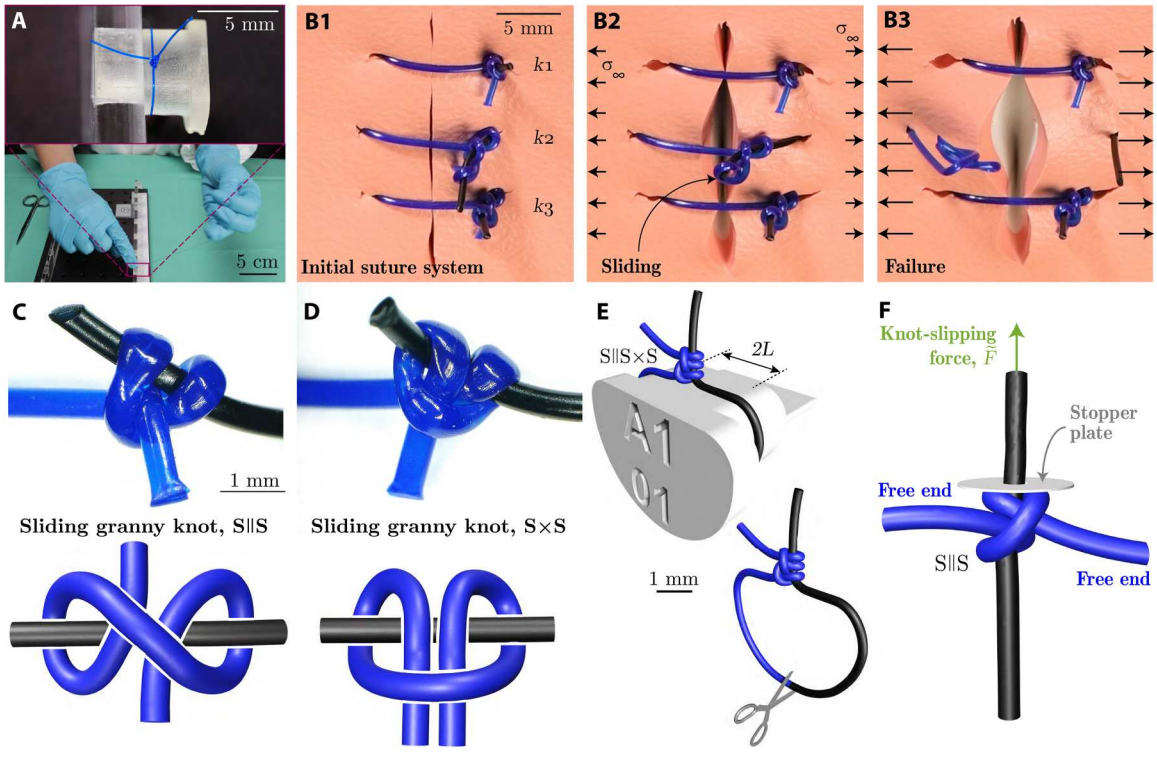

Fig. 1. Failure of surgical sliding knots. (**A**) Photograph of the tying of a common sliding knot by an experienced surgeon in a Prolene polypropylene filament on a rigid support. (**B1** to **B3**) Photographs illustrating knot safety and sliding for different levels of tightness of the S || S × S knot in a suture system on a practice pad, at increasing levels of the far-field stress, σ_∞. (**C** and **D**) Optical microscope image (top) and topological diagram (bottom) of the S || S (C), and S × S (D) sliding-knot topologies. (**E**) Schematic of the S || S × S knot tied around a 3D-printed pin and visualization of the cutting location in the suture loop. (**F**) FEM-computed configuration for a S || S knot tied with a pre-tension of $\tilde{T}$ = 10.9. The same configuration is implemented in the mechanical testing experiments to measure the slipping force, $\tilde{F}$, of the S || S knot (cf. Fig. 2).

vertical filament is pulled upward and the knotted filament is resisted by the stopper plate (Fig. 2A2). Past an initial transient, the force reaches a plateau, where the filament slides with a nearly constant slipping force (Fig. 2A3). This characteristic force, denoted nondimensionally as $\tilde{F}_0$, corresponds to the knot strength, ultimately, the cause of the knot's untying (Fig. 2A4). Note that forces are nondimensionalized in units of $\sigma_Y A$; applied dimensionless tensions greater than 1 involve plastic deformation of the straight filament strand.

Next, we use the mechanical testing described above to characterize the knot strength, $\tilde{F}_0$, while systematically varying the tying pre-tension, $\tilde{T}$, and the number of throws, n. First, we focus on the S || S × S topology (n = 3), with each throw pre-tensioned equally. Different levels of $\tilde{T}$ lead to the three distinct regimes showcased in Fig. 3A: (i) loose knots ($\tilde{T} < T_{\min}$), (ii) tight knots ($T_{\min} \leq \tilde{T} \leq T_{\max}$), and (iii) filament fracture ($\tilde{T} > T_{\max}$). Loose and tight knots were distinguished quantitatively using volume measurements on the sliding granny knot. In fig. S1, we report results on the knot's volume (measured from the convex hull of x-ray tomography data) as a function of $\tilde{T}$, demonstrating two distinct slopes. The transition between the two regimes is compatible with the convex hull computation applied on the ideal (purely geometric), tightest sliding granny knot, using the Ridgerunner algorithm (*34*). From this volumetric analysis, the minimum knot tying pre-tension is determined as $\tilde{T}_{\min} = T_{\min}/\sigma_Y A = 2.59 \pm 0.1$ 4 (leftmost vertical line in Fig. 3B), below which the knot is considered loose.

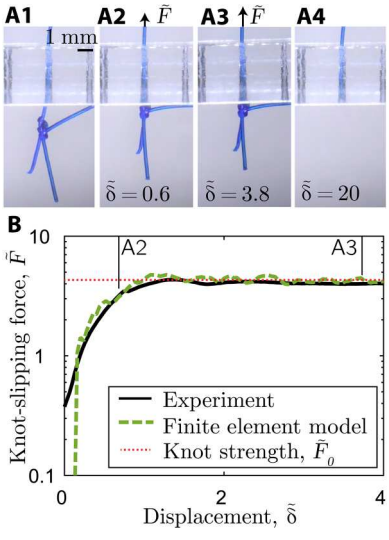

Fig. 2. Mechanical tests of the strength of a S||S knot. (**A1** to **A4**) Sequence of photographs during mechanical testing, visualizing the sliding process of a previously tied knot that is pulled against a stopper plate to measure the slipping force, $\tilde{F}$. The frames are shown at increasing values of dimensionless displacement, $\tilde{\delta} = \delta/D$, of the vertically pulled filament. (**B**) Representative curves (experiments and FEM) of $\tilde{F}$ versus displacement, $\tilde{\delta}$. The plateau of the curves defines the knot strength, $\tilde{F}_0$. The points A2 and A3 correspond to the photographs in (A2) to (A3). The S || S knot was tied to a pre-tension of $\tilde{T} = 10.9$.

Beyond the onset of tight knots, in the intermediate region (ii), the knot strength follows

$$\tilde{F}_0 = \tilde{K}\tilde{T}^{\alpha} \quad (1)$$

where the exponent α and the prefactor $\tilde{K}$ are two fitting parameters. Equation 1 provides an excellent fit to the data up to filament fracture. This upper limit is determined by rate- and temperature-dependent fracture tests on knotted Prolene filaments and represented by the rightmost vertical line at $\tilde{T}_{\max} = T_{\max}\sigma_Y A = 15.74 \pm 0.63$ (fig. S2).

We turn to surgeon-tied knots, mapping their strength to the model experiments described above. Using the same monofilaments, topology (S || S × S), and rigid supports as in the model experiments, an experienced surgeon was instructed to hand-tie 38 knots, tightened identically to their routine suturing procedure. The level of pre-tension of the manually tied knots was unknown (see the representative knot in Fig. 3C). Using our experimental setup, the surgeon-tied knots were then tested for their strength, $\tilde{F}_0$, which, as presented in Fig. 3D, exhibits a nearly uniform histogram in the range, $1.7 < \tilde{F}_0 < 7.7$. The probability distribution is summarized by the box plot with a median normalized strength of *3.2* and lower and upper quartiles at 2.7 and 5.2, respectively. Projecting the median knot strength and interquartile ranges (shaded region from Fig. 3D to Fig. 3B) onto the results from the model experiments on the S || S × S knot provides an estimate of the operating range of pre-tensions for surgeon-tied knots, $\tilde{T}_{\text{surgeon}} \in [6.6 - 10]$. We find that $\tilde{T}_{\text{surgeon}} \in [\tilde{T}_{\min}, \tilde{T}_{\max}]$; the surgeon targets the middle of the intermediate regime (ii) for tight knots identified by our model experiments while leaving safety margins between loose knot configurations, $\tilde{T}_{\min}$, and filament fracture, $\tilde{T}_{\max}$.

Thus far, we focused on the S || S × S knot, the simplest configuration comprising the two sliding topologies of interest: S || S and S × S. However, surgeons typically tie more than three half-hitches for increased knot safety. To explore the effect of the number of throws, n, on knot strength, we return to the model experiments and investigate configurations with an initial S || S knot followed by different numbers of non-identical (×) throws (Fig. 3E). In Fig. 3B, we plot $\tilde{F}_0$ versus the tying pre-tension, $\tilde{T}$. These more complex knots with additional throws exhibit the same functional dependence, Eq. 1, as the simpler S || S × S topology, with α = 1.59 ± 0.03. The consistency of α across the different tested topologies is notable, considering the underlying geometric complexity. These robust results call for a detailed theoretical analysis, which is beyond the scope of the present study. The knot strength increases with n with a prefactor $\tilde{K}$, which we denote as a multiplicative-strength factor. In Fig. 3F, we plot the fitted value of $\tilde{K}$ versus n, finding the linear relation $\tilde{K} = \beta_1 n$, with β_1 = 0.047 ± 0.003. All the fitted parameters are summarized in table S1.

In Fig. 3F, fig. S3, and table. S1, we show that the behavior according to Eq. 1 and the value of K are identical for the S || S × S and the S || S || S knots. In other words, these two topologies are equivalent regarding knot strength. Therefore, quantifying the mechanical performance of complex surgical knots with various topological combinations of multiple throws reduces to characterizing a single sliding knot (n = 2) with a single topology (e.g., S || S). Combining the above observations, we find that surgeon-tied sliding knots are in the tight regime, where the knot strength follows Eq.

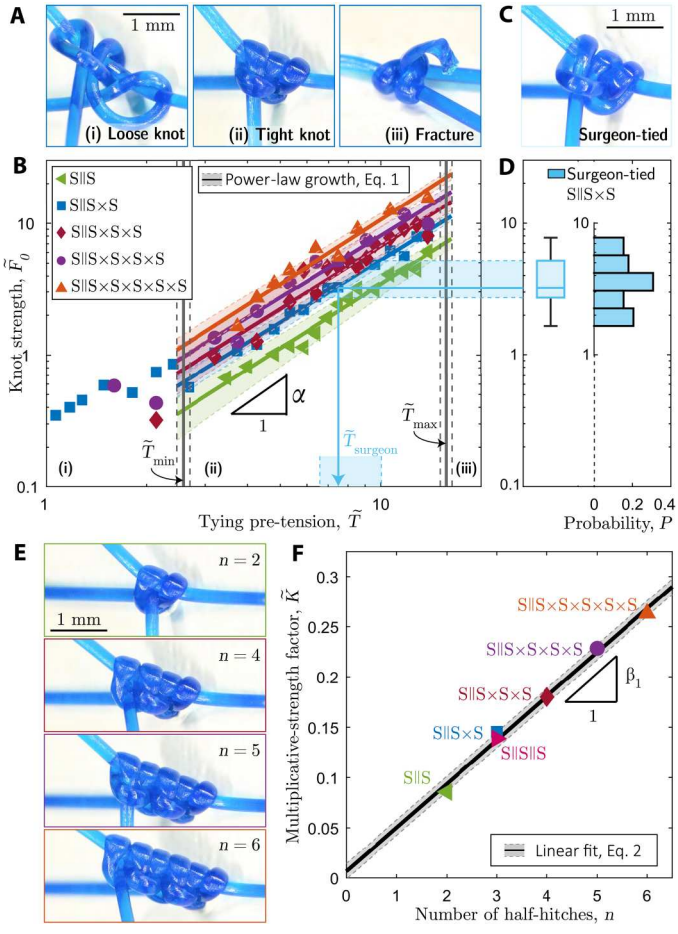

Fig. 3. Dependence of the knot strength on pre-tension and topology. (**A**) Photographs of representative S || S × S knots tied with different values of pre-tension: (i) loose knot ($\tilde{T} = 15$), (ii) tight knot ($\tilde{T} = 8.5$), and (iii) fracture of the last throw ($\tilde{T} = 20$). (**B**) Knot strength, $\tilde{F}_0$, versus tying pre-tension, $\tilde{T}$, for sliding knots with multiple throw. The solid lines represent the average power-law increase, and the corresponding shaded regions are the 65% confidence interval. The bounds of the intermediate region (ii), $\tilde{T}_{min}$ and $\tilde{T}_{max}$, are represented by vertical solid lines with their SD by the dashed lines. (**C**) Photograph of a surgeon-tied S || S × S knot. (**D**) Histogram and box plot of knot-strength measurements for surgeon-tied knots (S || S × S), with the mapping (shaded region) onto the experimental curve in (B). (**E**) Photographs of sliding knots with different numbers of throws, n = {2,4,5,6} ($\tilde{T} = 8.5$). (**F**) Multiplicative-strength factor, $\tilde{K}$, cf. Eq. 1, of the fitted curves in (B) as a function of the number of throws, n. The linear fit to Eq. 2 and the corresponding 65% confidence interval are represented by the solid line and shaded region, respectively.

1, with the same exponent, independently of the number of throws or the topological combination. The knot strength is described by a multiplicative-strength factor, $\tilde{K}$, which depends linearly on the number of throws, such that

$$\tilde{F}_0 = \beta_1 n \tilde{T}^{\alpha} \quad (2)$$

We proceed by complementing the experimental results with fully 3D finite element modeling (FEM) simulations to gain physical insight into the underlying mechanism leading to the knot strength in the tight regime. We used the commercial package ABAQUS/EXPLICIT (Simulia, Dassault Systèmes) to simulate knotted filaments, probing physical quantities not accessible in the experiments, especially the reactions on the surface of the filament. The self-contact of the monofilaments was modeled using Amontons-Coulomb friction enforced through normal penalty forces, combined with tangential frictional forces, with a prescribed dynamic friction coefficient, $\mu = 0.20 \pm 0.02$ (fig. S4). On the basis of (*35*, *36*), a 3D continuum-level constitutive model for elastic-viscoplastic mechanical behavior (specialized for uniaxial tension) was developed and implemented in the simulations (fig. S5 and table S2). The filaments used throughout this study undergo unknown deformation during manufacturing and packaging, leading to intrinsic curvature upon unpacking. To account for this (unknown) loading history in the simulations, we considered an effective residual bending stress, σ_R, applied on the initially straight model of the filament (fig. S6).

After calibrating the FEM simulations for uniaxial and bending deformations (Materials and Methods) of our filaments, we simulated S || S knots by applying a sequence of prescribed displacements and rotations to control the nodes located at each end and the central filament coordinate (see Materials and Methods and movie S5). For generality, the simulations were performed with a unit-diameter filament. The numerical configuration presented in Fig. 1F was tied with $\tilde{T} = 10.9$. The corresponding force-displacement curve is shown in Fig. 2B (dashed line). Note that, at this stage, the FEM has no adjustable parameters; all material parameters and mechanical properties were determined independently. As a final validation step of the numerics, we compared the computed knot strength against experiments over the full range of $\tilde{T}$ in the tight knots regime (ii). In Fig. 4A, we replot the experimental $\tilde{F}_0$ data for the S || S knot with the solid line representing the corresponding fit from Fig. 3B. In the same plot, we juxtapose the FEM data computed using the experimentally measured kinematic friction coefficient, $\mu = 0.2$ (* symbols). The agreement between experiments and FEM furthers the confidence in the numerical model and validates the choice for the nondimensionalization of the forces by $\sigma_Y A$, noting that all simulations were performed assuming unit diameter. Last, we leveraged the FEM to vary μ systematically; the data in Fig. 4A reveals that the knot strength increases with μ.

Zooming into the inner workings of the knot, we used the FEM to compute the normalized contact pressure, p/σ_Y, between the half-hitches and the quasi-straight sliding filament. For the representative case of an S || S knot ($n = 2$) with $\tilde{T} = 9.5$, Fig. 4B shows a 3D visualization of p/σ_Y and its projected 2D map, the latter focusing on the contacting regions. We distinguish two main contact domains related to the two half-hitches, with four distinct pressure hot spots. Integrating the local normal tractions over the entire surface of the knotted rod yields the integrated normal contact force, $\tilde{F}_n = F_n/\sigma_Y A$. It is useful to define the prereleased configuration as the state when the pre-tension is still applied before freeing the ends and the released configuration when the ends have been freed for testing. Their respective renderings are shown in Fig. 4C (left and right, respectively). The inset in Fig. 4C plots the integrated normal contact force in the released versus that in the prereleased configurations, i.e., $\tilde{F}_n^r$ versus $\tilde{F}_n^{pr}$. For $\mu \geq 0.15$, we find $\tilde{F}_n^r \approx \tilde{F}_n^{pr}$ (dashed line), meaning that the released configuration maintains the normal contact force onto the sliding filament due to the plastic deformation accumulated during the pre-tensioning step. For $\mu < 0.15$, $\tilde{F}_n^r < \tilde{F}_n^{pr}$ as the knot dilates (elastic springback)

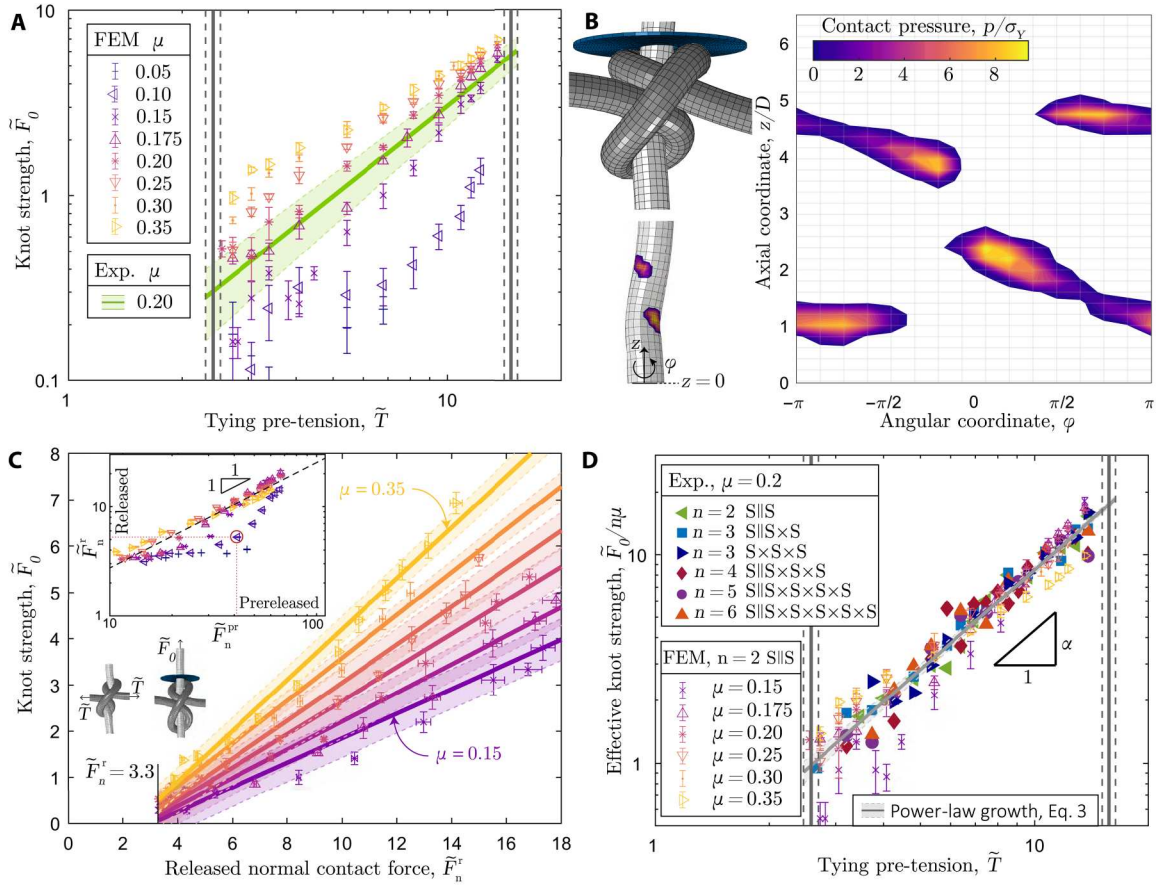

Fig. 4. Analysis of surface tractions and master curve for knot strength. (**A**) FEM-computed knot strength, $\tilde{F}_0$, versus tying pre-tension, $\tilde{T}$, for the S || S ($n = 2$) configuration, over a range of friction coefficients, $\mu \in [0.05 - 0.35]$. The green line corresponds to the experimental fit of the data in Fig. 3B to Eq. 1; the shaded region represents the 65% confidence interval of the fit. The experimental value of the friction coefficient is $\mu = 0.2$ (fig. S4). (**B**) Three-dimensional visualization of the S || S knot system ($\tilde{T} = 95$) simulated using FEM (top). Contact pressure, p/σ_Y, visualized on the pulled 3D rod (bottom) and mapped in 2D along the axial coordinate, z/D, and the angular coordinate, ϕ(right). (**C**) Knot strength, $\tilde{F}_0$, versus released integrated normal contact force, $\tilde{F}_n^r$, for friction coefficients in the range, $\mu \in [0.15 - 0.35]$; see legend in (A). Linear fit of the data (lines) and 65% confidence interval (shaded regions). Inset: Released normal contact force, $\tilde{F}_n^r$ versus the prereleased normal contact force, $\tilde{F}_n^{pr}$, for all the simulated values of μ; see legend in (A). Spring back (dilation) of the knots is observed for the datasets with $\mu = 0.05, 0.10$, an example of which is shown in the adjacent FEM configuration corresponding to the red-circled data point ($\mu = 0.10$, $\tilde{T} = 6.8$). (**D**) Effective knot strength, $\tilde{F}_0/n\mu$, versus $\tilde{T}$, combining all the experimental and numerical results obtained in this study.

after the pre-tension is released with an insufficient level of plastic deformation. In these low-friction cases, the desired constricting geometry around the sliding filament is insufficient; consequently, the normal tractions in the released configuration are low. Thus, plasticity turns out to be crucial to prevent the complete unraveling of the knot, even for vanishing friction coefficients ($\mu = 0.05$). The plastically bent filament guarantees the knot topology, while the same knots on a purely elastic rod would unravel (movie S3).

Focusing on the tight, nondilated configurations ($\mu \geq 0.15$), the data in Fig. 4C evidence that the global knot strength depends linearly on the integrated local normal force; $\tilde{F}_0 \propto \tilde{F}_n^r$. Therefore, despite the strong underlying geometric nonlinearities, the Amontons-Coulomb friction law is at the source of this proportionality (as implemented in the FEM model), relating the total integrating tangential force, $\tilde{F}_t$, and hence the knot strength, to $\tilde{F}_n^r$. Combining the friction-related dependence with Eq. 2, the knot strength is expected to behave as

$$\tilde{F}_0 = \beta_2 n \mu \tilde{T}^{\alpha} \quad (3)$$

with the prefactor $\beta_2 = \tilde{K}/(n\mu) = 0.21 \pm 0.07$ measured by fitting. In Fig. 4D, we plot $\tilde{F}_0/(n\mu)$ versus $\tilde{T}$ for the experimental data ($n \in [2,6]$, from Fig. 2) together with the FEM data ($n = 2$ and $\mu \in [0.15,0.35]$). Consistently with Eq. 3, the data collapse onto a master curve with $\alpha = 1.56 \pm 0.23$. These results confirm that the frictional interactions dictate the knot strength with the required normal contact forces ensured by the plastic deformation accumulated during pre-tensioning. As evidenced in Fig. 4C, note that the description of Eq. 3 is valid only for tight knots (above T_{min}). These findings call for future theoretical efforts to rationalize the measured values of α and β_2, which are independent of the filament diameter, the number of throws, and the friction coefficient (for $\mu \geq 0.15$), in the tension range of the tight-knots regime.

DISCUSSION

Our results on both surgeon-tied knots and model experiments, combined with FEM, enabled us to identify the ingredients dictating the strength of surgical sliding knots. In addition to topology, geometry, and elasticity, the interplay between plastic deformation and frictional interactions is crucial in a knotted monofilament. Our findings could be translated into practical guidelines on how to tie a safe surgical knot in a given suturing monofilament with friction coefficient, $\mu \geq 015$, and yield strength, σ_Y. The surgeon can adapt the filament caliber and the number of throws, or control the tying pre-tension to induce an appropriate level of plastic deformation and hence normal-contact pressures, which, through friction, establish a desired knot strength. Since we only considered dry conditions, the master curve of the effective knot strength is applicable to dry suturing environments. In the presence of fluids during surgical procedures, lower knot strengths are to be expected, which can be compensated by $\tilde{T}$ and n.

We hope that our investigation will raise awareness of the physical ingredients in surgical knots among experienced surgeons and will be valuable in the training of entry-level surgeons. Furthermore, our quantitative description of the mechanism underlying sliding knots could be implemented into emerging robotic-assisted surgical devices containing haptic feedback to target effective knot-tying at a level akin to an experienced surgeon (*37*).

MATERIALS AND METHODS

Experimental procedure for knot-tying in our physical model system

To reproducibly tie knots of well-defined pre-tension, we used the following protocol. Rigid 3D-printed pins were used as support for manually tying an initial half-hitch in its loose configuration. One end of the filament was kept straight by applying a slight tension (far below the yield strength), while the other end was wound around the straight filament segment. The manually applied tension should be just enough to keep the half-hitch in place before the two free filament extremities were clamped on the UTM. Then, the knots were tightened under displacement-controlled conditions, followed by a load-controlled holding step to account for any viscous material effects. The pulling speed was 1 mm/s (i.e., engineering strain rate $\dot{\varepsilon} = 0.01/\mathrm{s}$) up to the set value of the tying pre-tension, $\tilde{T}$, and held constant for 100 s to account for any potential viscoelastic effects. Subsequently, the sample was unmounted from the UTM, and anotherhalf-hitch (identical or nonidentical throw) was added manually in its loose configuration, and then tightened with the UTM. This protocol was repeated for every additional throw (increasing n).

Threshold to define tight knots

As demonstrated in the main text, tight knots, compared to loose knots, exhibit higher knot strength due to the increased self-contact pressure between different segments of the filament. In general, the transition from loose to tight physical knots is a continuous process without an abrupt change in geometry or mechanical behavior (see fig. S1A). Still, we developed a method to define an approximate threshold separating the two regimes, combining a volumetric analysis based on x-ray micro–computed tomography (μCT) and a purely geometric rod model. We focus on the elementary, sliding granny knot, S || S, since knots with higher throw numbers are not necessary for the procedure described.

The notion of "tightest knot" is well-defined in the mathematical framework of ideal (geometric) knot theory: A prescribed diameter and arc length of an ideal filament enable the computation of the tightest knot shape for the maximal end-to-end shortening (*21*, *26*). An ideal filament is characterized by an undeformable circular cross section, inextensible centerline, and vanishing bending stiffness (*22*). On the basis of this geometric theory of knots, we computed the shape of the tightest S || S knot using the software Ridgerunner, developed by Ashton *et al.* (*34*). This software iteratively increases the tightness of an initial (ansatz) knot geometry. The tightening algorithm is based on a C-language code for tightening ideal knots (*38*), combining a polygonal thickness version (*39*–*41*) with a constrained gradient descent. In our case, this ansatz was provided by the centerline coordinates of an FEM simulation of a loose knot. In fig. S1B, we present the tightest S || S knot configuration. The compactness of the resulting knot was characterized as the volume of the 3D convex hull [convhulln function in Matlab 2019, based on Qhull (*42*)], around the bulk knot, excluding the protruding filaments. The computed convex hull on the tightest sliding granny knot is represented as a semi-transparent envelope in fig. S1B and was measured to have a dimensionless volume of $4V_{\mathrm{ideal}}/\pi D^3 \approx 32.3$. A cylinder of diameter and height D (normalized volume, $\pi D^3/4$) is used as the reference volume.

Next, we make use of 3D μCT images of physical knots to quantify their compactness as a function of the pre-tension applied to both throws. First, the S || S knots were machine-tied on monofilaments (Prolene 1 USP 0.49 mm in diameter) within the range of tying pre-tensions, $1.5 \leq \tilde{T} \leq 6.8$. Second, as shown in the photograph in fig. S1A, the knots were mounted in an array of increasing pre-tensions, $\tilde{T}$, labeled (1) to (7). Then, the samples were slid along a narrow cylindrical sample holder (diameter, 14 mm) and scanned with the maximum spatial resolution of 4.9 μm (voxel size) using μCT imaging (μCT100, Scanco Medical).

In fig. S1C, we show the 3D reconstruction of the μCT-scanned tightest knot (7) with four protruding strands. To quantify only the volume of the knot, we excluded the four protruding strands by implementing the following cropping steps using MATLAB (Matlab 2019b, MathWorks). The 3D image consisted of grayscale values, representing the local material density of the voxels, ranging from 0 (nonoccupied voxels outside filament) to 1 (occupied voxels inside filament). The dataset was binarized using the voxel value 0.5 as the threshold. The gradient profile (gradient function in MATLAB), representing the change in the number of occupied voxels, was computed in each of the three spatial directions, {x, y, and z}. The gradient profile (along each spatial direction) exhibits peaks (gradient values larger than 25) at the transition between the bulk knot and either surrounding air or a single protruding strand. Beyond each peak location, the voxel values were set to 0 (nonoccupied voxels), such that the long protruding strands were cut off from the bulk knot, leaving a confined knot region. This technique was repeated by rotating the knot in each of the three spatial directions (incremental rotation angle: $\pi/4$ rad) and smoothly removing all protruding strands. Similar to the compactness measurement of the tightest ideal knot, we constructed the 3D convex hull on the bulk physical knot, as shown by the semi-transparent cover in fig. S1D.

In fig. S1E, we plot the volume measurements of the convex hull obtained from the μCT, $4V/\pi D^3$, as a function of the tying pre-tension, $\tilde{T}$. Each experimental data point is based on three scanned knot samples. We observe two regimes with different slopes, whose transition was determined by performing a linear fit to each of the two regions and determining the intersect, fitting seven consecutive data points in each regime. The uncertainty of each best fit is at the basis of the error analysis on the intersection point. The resulting onset of tight knots is given by the tying pre-tension, $\tilde{T}_{\min} = T_{\min}/\sigma_Y A = 2.59 \pm 0.14$ (vertical line). At this tightness level, the experimental knot volume is $4V_0/\pi D^3 \approx 28.1$ and corresponds to knot (7) in fig. S1A. The transition between the two regimes is compatible with the result of the tightest knot volume from the purely geometric model, $4V_{\text{ideal}}/\pi D^3 \approx 32.3$, reported above and represented by the dotted horizontal line in fig. S1E. We conclude that the transition between the distinct behavior in volume reduction is an appropriate definition for the onset of tight knots. Note that the smaller convex hull volume of experimental knots at the transition compared to the purely geometric case is presumably due to cross-sectional elastoplastic deformations, which induce a decrease in volume for the same amount of confined arc length.

Note that since the knot tightness is dictated by the volume of each individual throw, the tight-knot onset depends only on the applied tying pre-tension. In the main text, we report a change in the knot strength behavior between lower and higher tying pre-tensions, i.e., between loose and tight knots. The transition between the two regimes corresponds to the transition tension determined using the critical knot volume described above, $\tilde{T}_{\min}$, further asserting the validity of the knot volume method to describe the onset of tight knots.

Material testing and fracture

All the experiments presented in the main text were performed at room temperature (21°C) and with constant engineering strain rate $\dot{\varepsilon} = 0.01/\text{s}$ for the knot tying and strength testing. Here, we describe the mechanical tests performed to quantify the material response, including fracture, aiming to evaluate the range of applicability of our results for different tying rates and operating room temperatures.

We tested the tensile properties of single-filament specimens following the ISO 11566 (*43*) standard, which is designed to avoid filament fracture at the clamps. In fig. S2 (A and B), we present schematic illustrations of the sample preparation procedure with either straight, unknotted (A), or knotted (B) monofilaments. Since the knotted case is used for fracture tests, an S || S knot was tied manually on the rigid pin (described in the main text). For both cases (A) and (B), the Prolene 3-0 USP filament was glued with epoxy on a rectangular polyvinyl chloride shim stock frame (thickness: 0.1 mm, outer dimensions of the frame: 70×20 mm^2) with a gauge length of $L = 50$ mm. Besides setting reference length precisely, this technique also reinforces the filament at the ends by the epoxy layer, preventing fracture at the clamping due to stress concentration. Once the sample is clamped in a UTM (Instron 5943), the frame is cut along the y direction (orthogonal to the filament). Then, the mechanical response is measured by pulling along the axial direction of the filament (x direction in fig. S2, A and B) and recording the traction force throughout the imposed displacement.

In fig. S2C, we present the cyclic engineering stress-strain behavior (maximum strain, $\varepsilon = 0.5$) of the straight Prolene 3-0 USP filament at room temperature (21°C) as a function of the applied strain rate, ranging from $\dot{\varepsilon} = 0.0025/\text{s}$ to $\dot{\varepsilon} = 0.16/\text{s}$. Each curve shows the mean (solid line) and SD (shaded region) of three tests on five different Prolene 3-0 USP samples. We notice a slight increase in the stress quantities for higher strain rates. Still, despite the vast range of explored strain rates (variation of 6300%), the relative change in measured engineering stress at $\varepsilon_{\text{eng}} = 0.5$ is only 6.7%. The nominal fracture strength is determined by the maximum recorded engineering tensile force on straight filaments and represented by the blue box plots in fig. S2D. Similarly to the stress at $\varepsilon_{\text{eng}} = 0.5$, the fracture strength does not change considerably for different strain rates. Adding an S || S knot to the filament reduces the macroscopic fracture strength by 40 to 50% (see gray box plots), which is in agreement with the experimental observations reported in (*6*, *26*, *28*, *44*), although the underlying mechanism remains poorly understood.

In fig. S2E, we present results for the engineering stress-strain response of filaments under cyclic loading (constant strain rate, $\dot{\varepsilon} = 0.01/\text{s}$) while controlling temperature. The tests were conducted at 21°, 37°, and 45°C, within clinically relevant temperature ranges. In the operating room, the temperature is crucial to avoid intraoperative hypothermia (core temperature < 35°C) (*45*, *46*): in orthopedics, the room temperature is regulated to 16°C to reduce the infection risk (*47*); in obstetrics, the well-being of the newborn requires a temperature of 20° to 21°C (*48*); and in burn surgery, the operating room is heated to 30° − 40°C (*49*). Three tests on three different Prolene 3-0 USP samples were performed for each curve in fig. S2E. High reproducibility was achieved, as suggested by the small uncertainty regions (shaded region) around the average curve (solid curve). The Prolene filaments are somewhat temperature-dependent, exhibiting softening in their mechanical response to higher temperatures. Temperature dependence is less prominent in the nominal fracture strength of S || S-knotted filaments, plotted in fig. S2F as a function of the three temperature-regulated environments. The relative difference between the median values of the fracture strength at 21°C versus 45°C is only 3.6%.

As expected, the mechanical response of straight Prolene monofilaments exhibits some rate and temperature dependence. In the current case study, however, we are mostly concerned with the uncertainty of the macroscopic fracture strength in knotted samples since this fracture strength defines the upper boundary of applicable pre-tension during knot tightening. Relative changes of 12.3 and 6.1% are to be expected for the ranges of explored strain rates ($\dot{\varepsilon} = [0.0025 - 0.16]\text{s}^{-1}$) and temperature (21° − 45°C), respectively. Therefore, given the vast ranges of parameters, the rate and temperature effects are relatively small. Consequently, for the study described in the main text, we consider the mean fracture strength with its SD, $\sigma_c = 300.6$ MPa ± 12.1 MPa, for the case of a strain rate, $\dot{\varepsilon} = 0.01/\text{s}$, and at room temperature (21°C). Last, the normalized maximal tying tension, $\tilde{T}_{\max} = \sigma_c/\sigma_Y = 15.74 \pm 0.63$, is considered as the upper force limit, corresponding to the vertical lines in Fig. 3B of the main text.

Topological effect on knot strength

In Fig. 1C of the main text, we visualized the two possible sliding knot topologies, S || S and S × S, comprising two consecutive half-hitches. Although the topologies differ, we are interested in the resulting knot performance for a given tying pre-tension. In fig. S3, we compare the knot strength, $\tilde{F}_0$, as a function of the tying pre-tension, $\tilde{T}$, between the S || S × S and the S || S || S knot. Note that the first two throws share the same topology for both cases to avoid contact effects from the underlying pin during tying. Unlike the log-log plots on knot strength in the main text, here, we use linear axes to better contrast the difference in the response of the two knots, especially for higher tying pre-tensions. Again, the knot-strength data are consistent with the functional increase described by Eq. 1 of the main text. We find that the knot strength is equivalent for the two-knot topologies throughout the whole range of tight knots. We conclude that the resistance to sliding of surgical sliding knots does not depend on the throw direction (identical versus nonidentical throws). Within this study, this observation enables us to reduce the complexity from various topological combinations to a single topology, e.g., S || S.

Frictional contact interaction

Inspired by the apparatus reported in (*50*), we have designed an experimental setup to measure the frictional properties of two filaments in sliding contact using an orthogonal-crossing configuration in dry conditions. The upper end of the first filament (Prolene 1 USP) was attached to a 50-N load cell of the UTM (Instron 5943), and a dead load of 100 g was attached at the other end of the filament. A second filament (Prolene 1 USP) was tightly coiled (10 turns) around a rigid acrylic post (square cross section of 20×20 mm^2 with rounded corners), as shown in the photograph of fig. S4A. The straight vertical filament was pressed by an annular ball bearing (external diameter: 30 mm) against the coiled filament with a normal load, F_n, using a mass-pulley system (not shown in the photograph). Next, the vertical filament was displaced upward at a speed of 1 mm/s, which is the same displacement velocity imposed in the knot untying experiments reported in the main text. In fig. S4B, we plot the measured tangential contact force, F_t, as a function of the applied normal force, F_n. We find a linear relationship between the two, as expected for Amontons-Coulomb friction behavior. The linear fit, $F_t = \mu_d F_n$ (solid line in fig. S4B), of the experimental data yields a dynamic friction coefficient, $\mu_d = 0.20 \pm 0.02$, in agreement with values reported in the literature for Prolene monofilaments (*29*).

Elastoplastic constitutive material model

During the tying and testing of surgical knots, the Prolene filament can undergo considerable plastic deformation. Quantitatively reproducing this mechanical behavior in the FEM simulations requires an appropriate constitutive material model for the elastoplastic behavior of the polymer filament. Before describing the plasticity model, we implemented in FEM, we must first characterize the constitutive response of the Prolene filaments experimentally.

In fig. S5A, we present results for the cyclic stress-strain behavior of a straight (unknotted) Prolene monofilament (1 USP, gauge length, L = 50 mm), plotting the axial true stress, α, versus true strain, ε. The tests were performed at the constant engineering strain rate of $\dot{\varepsilon}_{eng} = 0.01/\text{s}$. For these characterization tests, we used the ISO11566 protocol for large-strain measurements. In the lower inset of fig. S5A, we show a schematic of the tested specimens prepared identically to those described in the "Material testing and fracture" section above. The plot in the upper inset of fig. S5A quantifies the dissipated energy density per cycle, W, measured from the area enclosed by each loading-unloading σ(ε) curve, for a particular cycle. We find that W decreases by ≈500% between the first and the second cycles before converging into a steady cycle. This seemingly large dissipated energy observed in the first cycle may be attributed to the unknown state of the material due to prior deformation history. We interpret the straightening of the intrinsically curved filament from the packaging and the preparation of the specimen for testing as the first loading cycle. To account for this first loading cycle, we will calibrate the constitutive model from the uniaxial tensile tests of a filament that has been preconditioned by prestretching it first to ε = 0.215 (i.e., after it has undergone the first cycle), and then unloaded for subsequent testing. In fig. S5B, we plot the σ(ε) experimental curves (solid lines) for the three subsequent loading-unloading cycles (2, 3, and 4); these data will be used to calibrate the elastoplastic constitutive model described next.

The 3D continuum-level constitutive model for elastic-viscoplastic mechanical behavior that we developed and implemented for the FEM simulations is based on (*35*, *36*). Hence, only a summary of the relevant content underlying the model is provided here. Overall, the model includes isotropic hardening since the filaments only undergo one single loading cycle during the knot-tying and tightening process. Furthermore, the model is rate-dependent, a choice that is supported by the data presented in fig. S2. The total deformation gradient is decomposed into elastic and plastic parts

$$\mathbf{F} = \mathbf{F}^e\mathbf{F}^p \tag{4}$$

We assume that plastic flow is incompressible, meaning that $\det \mathbf{F}^p = J^p = 1$, where $J = \det = \mathbf{F}$. The evolution equation for $\mathbf{F}^p$ is

$$\frac{\mathrm{d}\mathbf{F}^p}{\mathrm{d}t} = \mathbf{D}^p\mathbf{F}^p \tag{5}$$

The flow rule may be written in the form

$$\mathbf{D}^p = \sqrt{\frac{1}{2}}\nu^p\mathbf{N}^p \tag{6}$$

where the equivalent plastic shear strain rate is

$$\nu^p = \nu_0\left(\frac{\bar{\tau}}{S}\right)^{1/m} \tag{7}$$

the equivalent shear stress is

$$\bar{\tau} = \sqrt{\frac{1}{2}(\mathbf{M}_0^e : \mathbf{M}_0^e)} \tag{8}$$

and the direction of plastic flow is given by

$$\mathbf{N}^p = \frac{\mathbf{M}_0^e}{\sqrt{2}\bar{\tau}} \tag{9}$$

In the expressions above, the notation $(\bullet)_0$ denotes the deviator of $(\bullet)$. The Mandel stress in Eq. 6 is given by the constitutive relation

$$\mathbf{M}^e = 2G\mathbf{E}^e + \lambda(\mathrm{Tr}\mathbf{E}^e)\mathbf{1} = 2G\mathbf{E}_0^e + K(\mathrm{Tr}\mathbf{E}^e)\mathbf{1} \tag{10}$$

where G, K, and $\lambda = K - (2/3)G$ are the shear modulus, bulk modulus, and Lamé parameter, respectively. Note that the strain measure used is $\mathbf{E}^e = \ln \mathbf{U}^e$, where $\mathbf{U}^e$ is the elastic stretch, $\mathbf{F}^e = \mathbf{R}^e\mathbf{U}^e$, and accounts for large deformations. The Cauchy stress is related to the Mandel stress by

$$\mathbf{T} = J^{-1}\mathbf{R}^e\mathbf{M}^e\mathbf{R}^{eT} \tag{11}$$

The strength model is given by an evolution equation for the deformation resistance S, which enters Eq. 4, taking the form

$$\dot{S} = h(S_{sat} - S)\nu^p, S(t=0) = S_0 \tag{12}$$

where S_{sat} is a saturation level for the deformation resistance, and h controls how quickly S approaches S_{sat}.

In summary, the elasto-viscoplastic model with isotropic hardening presented above involves the following material parameters, E, S_0, S_{sat}, h. Moreover, we define initial yield strength σ_0 as the initial condition for S. These parameters must be determined by fitting to the experimental data presented in fig. S5B, for the three consecutive loading and unloading cycles of a straight, unknotted, and prestretched Prolene monofilament.

The 3D constitutive model has been specialized for uniaxial tension, and the reduced model is implemented into MATLAB for the purpose of calibrating the parameters E, σ_0, S_{sat}, h. On the basis of the experimental data presented in fig. S5B, the built-in MATLAB function lsqnonlin was used to perform a nonlinear least-square optimization of the four parameters with a prescribed initial guess and lower and upper bounds, as summarized in table S2. The rate-sensitivity parameter was assumed as $m = 0.08$ to improve the numerical convergence of the optimization process. The shear strain rate was set to $\nu_0 0001$. Furthermore, we constrained the values of E using the initial slope of the test curves in the unloading region, which was measured to be ≈7000 MPa. Assuming material incompressibility, the shear modulus is related to the Young's modulus by $G = E/3$. The optimization process yields the calibrated quantities presented in table S2, with the model fitted (dashed lines) to the experimental cyclic stress-strain curves (solid lines), as shown in fig. S5B.

Residual stress

The Prolene filament used throughout the experiments came originally packaged in a stadium-shaped spool (with straight sides of length 55 mm and semi-circular caps of radius 10 mm) and exhibits natural curvature upon unpacking. As is common in plasticity problems, this prior loading history affects any subsequent material response. To account for this (unknown) deformation history in the FEM simulations, we consider the effective residual bending stress, σ_R, as a predefined stress field on the initially straight reference configuration of the filament and treat it as an additional fitting parameter. We specify σ_R by assuming elastic-perfectly plastic (small) deformation of a beam with a circular cross section of diameter, D, with curvature $\kappa(x)$ along the axial direction, x, of the beam, the axial strain in the bending direction, y, can be expressed as $\varepsilon_{xx}xy$.

For a fully plastic beam with yield strength, σ_Y, the cross section consists of two regions: the lower half, $-D/2 \le y \le 0$, with $\sigma_{xx} = \sigma_Y$ and area, A_1; and the upper half, $0 \le y \le D/2$, with $\sigma_{xx} = -\sigma_Y$ and area, A_2. Thus, two regions of integration (A_1 and A_2) are considered to compute the bending moment:

$$M_p = -\int_{A_1} y\sigma_Y dA_1 - \int_{A_2} y(-\sigma_Y)dA_2 = \frac{D^3\sigma_Y}{6} \tag{13}$$

The residual stress is then expressed as the difference between the fully loaded and the elastically unloaded case,

$$\sigma_{xx}(\text{unloaded}) = \sigma_{xx}(\text{loaded}) - \Delta\sigma_{xx} \tag{14}$$

with the stress difference due to elastic spring-back,

$$\Delta\sigma_{xx} = E\Delta\varepsilon_{xx} = E(\kappa_{\text{loaded}} - \kappa_{\text{unloaded}})y \tag{15}$$

Furthermore, from the moment-curvature relation, $M_{\text{loaded}} = EI(\kappa_{\text{loaded}} - \kappa_{\text{unloaded}})$, we get

$$\kappa_{\text{loaded}} - \kappa_{\text{unloaded}} = \frac{M_{\text{loaded}}}{EI} \tag{16}$$

Plugging Eq. 13 into Eq. 12 yields the axial stress difference

$$\Delta\sigma_{xx} = -\frac{M_p y}{I} \tag{17}$$

where we considered loading to the fully plastic state ($M_{\text{loaded}} \equiv M_p$). Thus, Eq. 11 is written in the form

$$\sigma_{xx}(\text{unloaded}) = \sigma_{xx}(\text{loaded}) + \frac{M_p y}{I} \tag{18}$$

Considering a fully plastic deformation [$\sigma_{xx}(\text{loaded}) = \pm\sigma_Y$], and plugging Eq. 10 into Eq. 15 gives the residual stress field as a function of the yield strength

$$\sigma_R y \begin{cases} \left(1 + \frac{32y}{3\pi D}\right)\sigma_Y \text{ for } y < 0 \\ \left(-1 + \frac{32y}{3\pi D}\right)\sigma_Y \text{ for } y < 0 \end{cases} \tag{19}$$

In ABAQUS/EXPLICIT, the predefined stress field—Eq. 16—was applied on the initially straight reference configuration, $\sigma_R(\sigma_Y = 0$ MPa), of the filament of diameter, $D_{\text{Fil}} = 0.49$ mm (1 USP), and axial length,300 mm. Note that, whereas the calibration tests described next used this physical value of D_{Fil}, subsequent simulations (including all of those reported in the main text) were done with unit-diameter filaments for generality. The rod was meshed with reduced hybrid 3D solid elements (C3D8I) such that the number of elements along the axial direction was 200, with 26 elements per cross section. In fig. S6A, we show typical initial configurations of the filament for the different values $\sigma_Y = \{10,20,30\}$ MPa; different values of σ_R relate to different natural curvatures of the filament.

Figure S6B presents a photograph of the apparatus developed to calibrate the parameters of our plasticity model. In this configuration, which we refer to as plastic capstan, we quantify the tension drop, ΔT, between the free end and the pulled end (displacement-controlled with 1 mm/s) of a Prolene monofilament (1 USP) passing through a grooved pin with the diameter in the range $0.5 \text{ mm} \le D_{\text{Pin}} \le 9$ mm. Given that the pin is mounted on an air-bearing, and the two constraining ball bearings minimize friction, the ensemble rotates as a frictionless gear when pulling the filament (movie S4). Hence, there is minimal sliding frictional dissipation; the dissipation is only due to plastic bending deformation of the filament around the pin, which causes the tension to drop between the two extremities. By contrast, in the classic capstan problem (*50*, *51*), the tension drop is due to the friction interaction alone.

Using FEM, we simulate this same plastic capstan configuration for filaments subjected to residual bending stresses. The pin of diameter, D_{Pin}, and the gap walls were simulated as rigid bodies according to the fabrication tolerances of the pins, leaving a groove of depth D_{Fil} + 0.01 mm and width D_{Fil} + 0.11 mm. In fig. S6C, we present an FEM-computed configuration of the plastic capstan (D_{Pin} = 0.5 mm), color-coded by the equivalent plastic shear strain, γ^p, which increases along the filament from the free end (right) to the pulled end (left) as a result of the accumulated plastic deformation. A horizontal cut (purple dashed line) at the height of the pin exposes the in-plane profile of γ^p. In fig. S6D, we plot experimental and FEM data for the normalized tension difference, $\Delta T/(\sigma_Y A)$, as a function of normalized curvature imposed by the pin of diameter D_{Pin} on the filament of diameter D_{Fil}: $2D_{Fil}/(D_{Pin} + D_{Fil})$. Tuning the residual stresses allows for the calibration of the numerical model by matching its results to the experimental data to determine the fitting parameter. With the fitted value of $\sigma_R(\sigma_Y = 30 \pm 2\text{MPa})$, we find that the FEM simulations accurately represent the experimental data across the full range. Note that the fitted yield strength is of the same order of magnitude as the experimentally determined 0.1% offset yield strength, σ_Y = 19.1 MPa (*31*).

Finite element modeling—Knot tying, tightening, and testing procedure

In the commercial package ABAQUS/EXPLICIT (Simulia, Dassault Systèmes), two initially straight filaments were implemented, each with unit diameter, $D_{Fil} = 1$. The filament (1) forming the two half-hitches was modeled with axial length, $L_1 = 35D_{Fil}$. The sliding filament (2) was chosen to be half as long. The two filaments were oriented such that their centerlines cross with a relative angle of 10°. Both filaments were meshed with 3D solid elements, enhanced with incompatible modes for bending (C3D8I). The number of elements along the axial direction was 230 for filament (1) and 115 for filament (2), with 40 elements per cross section in both cases. Two circular plates ($5D_{Fil}$ in diameter, $0.1D_{Fil}$ in thickness) with a central clearance hole of diameter, $1.10D_{Fil}$, were modeled as rigid bodies and aligned with the centerline axis of filament (2), leaving a relative distance $7D_{Fil}$ between the two plates.

The tying, tightening, and testing procedure described next is visualized in movie S5. In an initial step, the central region of filament (1), $0.25L_1 < L_{center} < 0.75L_1$, was subject to the residual stress field $\sigma_R(\sigma_Y = 30 \pm 2\text{MPa})$ since the filament extremities are not part of the knot. Mimicking the tying procedure of the surgeon, a dead load (Mg = 50 N) was applied to one of the extremities of filament (2), keeping the other end clamped. Next, by applying a sequence of prescribed displacements and rotations to control the nodes located at each end and the central coordinate of filament (1), two half-hitches were formed around filament (2), corresponding to the sliding granny knot. A similar tying protocol was introduced in (*52*), in the context of the clove hitch knot. Both knots share the same topology but differentiate by their application: A clove hitch knot attaches a rod to a rigid cylinder (typically larger than the rod diameter), whereas the sliding granny knot is a binding knot, connecting two rods (of equal diameters). We made use of the tying algorithm used in (*52*), with minor adaptations to tie the S || S knots.

After the S || S topology was set, both rigid plates were displaced, leaving a relative distance of $6D_{Fil}$, to help keep filament (2) in place (in addition to the applied dead load) during the subsequent tightening step. Then, the two extremities of filament (1) were gradually loaded by the tying pre-tension of the same magnitude, $\tilde{T}$, but in opposite directions to yield a symmetric knot. Next, the pre-tensions were released symmetrically to free the ends of filament (1), while one of the two plates was displaced along the centerline axis of filament (2), away from the actual system since, subsequently, it is no longer needed. At this stage, the clamped boundary condition at the extremity of filament (2) was also released, such that the filament could be displaced with the constant unit speed 1 s^{-1}. Last, the S || S knot was pulled against the rigid stopper plate, and the slipping force, $\tilde{F}$, was measured.

Supplementary Materials

This PDF file includes:

Figs. S1 to S6
Tables S1 and S2
Legends for movies S1 to S5
Legend for data S1

Other Supplementary Material for this manuscript includes the following:

Movies S1 to S5
Data S1

REFERENCES AND NOTES

1. L. Fischer, T. Bruckner, B. P. Müller-Stich, J. Höer, H.-P. Knaebel, M. W. Büchler, C. M. Seiler, Variability of surgical knot tying techniques: Do we need to standardize? *Langenbecks Arch. Surg.* **395**, 445–450 (2010).
2. S. S. Ching, C. W. Mok, Y. X. Koh, S.-M. Tan, Y. K. Tan, Assessment of surgical trainees' quality of knot-tying. *J. Surg. Educ.* **70**, 48–54 (2013).
3. F. Dubrana, P. Pasquier, *Ligatures et Sutures Chirurgicales* (Springer-Verlag, 2011).
4. P. Calhoun, *Advanced Surgical Knot Tying* (Independently Published, ed. 2, 2016).
5. J. B. Trimbos, E. J. C. Van Rijssel, P. J. Klopper, Performance of sliding knots in monofilament and multifilament suture material. *Obstet. Gynecol.* **68**, 425–430 (1986).
6. J. A. von Fraunhofer, R. J. Storey, B. J. Masterson, Tensile properties of suture materials. *Biomaterials* **9**, 324–327 (1988).
7. M. B. Myers, G. Cherry, Functional and angiographic vasculature in healing wounds. *Am. Surg.* **36**, 750–756 (1970).
8. L. C. Bartlett, Pressure necrosis is the primary cause of wound dehiscence. *Can. J. Surg.* **28**, 27–30 (1985).
9. N. J. Slater, R. P. Bleichrodt, H. van Goor, Wound dehiscence and incisional hernia. *Surgery* **30**, 282–289 (2012).
10. H. J. Sugerman, J. M. Kellum, H. D. Reines, E. J. DeMaria, H. H. Newsome, J. W. Lowry, Greater risk of incisional hernia with morbidly obese than steroid-dependent patients and low recurrence with prefascial polypropylene mesh. *Am. J. Surg.* **171**, 80–84 (1996).
11. R. Singh, W. Hawkins, Sutures, ligatures and knots. *Surgery* **38**, 123–127 (2020).
12. H. Tera, C. Aberg, Tensile strengths of twelve types of knot employed in surgery, using different suture materials. *Acta Chir. Scand.* **142**, 1–7 (1976).
13. D. A. Davis, D. M. Pellowski, E. J. Rawdon, All monofilament knots assume sliding conformation in vivo. *Dermatol. Surg.* **39**, 729–733 (2013).
14. C. A. Zimmer, J. G. Thacker, D. M. Powell, K. T. Bellian, D. G. Becker, G. T. Rodeheaver, R. F. Edlich, Influence of knot configuration and tying technique on the mechanical performance of sutures. *J. Emerg. Med.* **9**, 107–113 (1991).
15. D. C. Schubert, J. B. Unger, D. Mukherjee, J. F. Perrone, Mechanical performance of knots using braided and monofilament absorbable sutures. *Am. J. Obstet. Gynecol.* **187**, 1438–1442 (2002).
16. J. J. Ivy, J. B. Unger, J. Hurt, D. Mukherjee, The effect of number of throws on knot security with nonidentical sliding knots. *Am. J. Obstet. Gynecol.* **191**, 1618–1620 (2004).
17. E. Silver, R. Wu, J. Grady, L. Song, Knot security- how is it affected by suture technique, material, size, and number of throws? *J. Oral Maxillofac. Surg.* **74**, 1304–1312 (2016).
18. K.-T. von Trotha, J. Grommes, N. Butz, A. Lambertz, C. D. Klink, U. P. Neumann, M. Jacobs, M. Binnebösel, Surgical sutures: Coincidence or experience? *Hernia* **21**, 505–508 (2017).
19. B. Audoly, Y. Pomeau, *Elasticity and Geometry* (Oxford Univ. Press, 2010).
20. J. A. Calvo. *Physical and Numerical Models in Knot Theory: Including Applications to the Life Sciences* (World Scientific, 2005).

21. P. Pierański, S. Przybył, A. Stasiak, Tight open knots. *Eur. Phys. J. E* **6**, 123–128 (2001).
22. M. Carlen, B. Laurie, J. H. Maddocks, J. Smutny. Biarcs, global radius of curvature, and the computation of ideal knot shapes, in *Physical and Numerical Models in Knot Theory* (World Scientific, 2005), pp. 75–108.
23. B. Audoly, N. Clauvelin, S. Neukirch, Elastic knots. *Phys. Rev. Lett.* **99**, 164301 (2007).
24. M. K. Jawed, P. Dieleman, B. Audoly, P. M. Reis, Untangling the mechanics and topology in the frictional response of long overhand elastic knots. *Phys. Rev. Lett.* **115**, 118302 (2015).
25. P. Grandgeorge, C. Baek, H. Singh, P. Johanns, T. G. Sano, A. Flynn, J. H. Maddocks, P. M. Reis, Mechanics of two filaments in tight orthogonal contact. *Proc. Natl. Acad. Sci. U.S.A.* **118**, e2021684118 (2021).
26. P. Johanns, P. Grandgeorge, C. Baek, T. G. Sano, J. H. Maddocks, P. M. Reis, The shapes of physical trefoil knots. *Extreme Mech. Lett* **43**, 101172 (2021).
27. C. Baek, P. Johanns, T. G. Sano, P. Grandgeorge, P. M. Reis, Finite element modeling of tight elastic knots. *J. Appl. Mech.* **88**, 024501 (2021).
28. H. Uehara, H. Kimura, A. Aoyama, T. Yamanobe, T. Komoto, Effects of knot characteristics on tensile breaking of a polymeric monofilament. *New J. Phys.* **9**, 65–65 (2007).
29. B. S. Gupta. Surgical Knot Performance in Sutures, in *Biotextiles as Medical Implants* (Elsevier, 2013), pp. 335–365.
30. The United States Pharmacopeia. *The National Formulary* (The United States Pharmacopeia, 1979).
31. ASTM Standard D0638-14, Test Method for Tensile Properties of Plastics, ASTM International, West Conshohocken, PA (2014). DOI: 10.1520/d0638-14, www.astm.org
32. P. B. Price, Stress, strain and sutures. *Ann. Surg.* **128**, 408–421 (1948).
33. J. Armitage, S. Lockwood, Skin incisions and wound closure. *Surgery* **29**, 496–501 (2011).
34. T. Ashton, J. Cantarella, M. Piatek, E. J. Rawdon, Knot tightening by constrained gradient descent. *Exp. Math.* **20**, 57–90 (2011).
35. L. Anand, N. M. Ames, V. Srivastava, S. A. Chester, A thermo-mechanically coupled theory for large deformations of amorphous polymers. part I: Formulation. *Int. J. Plast.* **25**, 1474–1494 (2009).
36. N. M. Ames, V. Srivastava, S. A. Chester, L. Anand, A thermo-mechanically coupled theory for large deformations of amorphous polymers. part II: Applications. *Int. J. Plast.* **25**, 1495–1539 (2009).
37. F. Tendick, M. Downes, T. Goktekin, M. Cenk Cavusoglu, D. Feygin, X. Wu, R. Eyal, M. Hegarty, L. W. Way, A virtual environment testbed for training laparoscopic surgical skills. *Presence Teleop. Virt.* **9**, 236–255 (2000).
38. J. Cantarella, M. Piatek, E. Rawdon. Visualizing the tightening of knots, in *VIS 05. IEEE Visualization* (IEEE, 2005).
39. A. Stasiak, V. Katritch, L. H. Kauffman, *Ideal Knots* (World Scientific, 1998).
40. R. J. Rawdon, Approximating smooth thickness. *J. Knot Theory Ramif.* **9**, 113–145 (2000).
41. E. J. Rawdon, Can computers discover ideal knots? *Exp. Math.* **12**, 287–302 (2003).
42. C. B. Barber, D. P. Dobkin, H. Huhdanpaa, The quickhull algorithm for convex hulls. *ACM Trans. Math. Soft.* **22**, 469–483 (1996).
43. International Organization for Standardization, ISO 11566:1996 Carbon fibre — Determination of the tensile properties of single-filament specimens (1996). Retrieved from https://www.iso.org/standard/19518.html.
44. P. Pierański, S. Kasas, G. Dietler, J. Dubochet, A. Stasiak, Localization of breakage points in knotted strings. *New J. Phys.* **3**, 10 (2001).
45. M. John, D. Crook, K. Dasari, F. Eljelani, A. El-Haboby, C. M. Harper, Comparison of resistive heating and forced-air warming to prevent inadvertent perioperative hypothermia. *Br. J. Anaesth.* **116**, 249–254 (2016).
46. J. Yi, Y. Lei, S. Xu, Y. Si, S. Li, Z. Xia, Y. Shi, X. Gu, J. Yu, G. Xu, E. Gu, Y. Yu, Y. Chen, H. Jia, Y. Wang, X. Wang, X. Chai, X. Jin, J. Chen, M. Xu, J. Xiong, H. Wang, K. Lu, W. Yu, W. Lei, Z. Qin, J. Xiang, L. Li, Z. Xiang, S. Pan, L. Zhan, K. Qiu, M. Yao, Y. Huang, Intraoperative hypothermia and its clinical outcomes in patients undergoing general anesthesia: National study in china. *PLOS ONE* **12**, e0177221 (2017).
47. M. A. Ritter, E. M. Olberding, R. A. Malinzak, Ultraviolet lighting during orthopaedic surgery and the rate of infection. *J. Bone Joint Surg.* **89**, 1935–1940 (2007).
48. S. Aluri, I. J. Wrench, Enhanced recovery from obstetric surgery: A UK survey of practice. *Int. J. Obstet. Anesth.* **23**, 157–160 (2014).
49. J. A. Rizzo, M. P. Rowan, I. R. Driscoll, R. K. Chan, K. K. Chung, Perioperative temperature management during burn care. *J. Burn Care Res.* **38**, e277–e283 (2017).
50. J. A. Eytelwein, *Handbuch der Mechanik fester Körper und der Hydraulik: mit vorzüglicher Rücksicht auf ihre Anwendung in der Architektur aufgesetzt* (Fleischer, 1842).
51. L. Euler. Remarques sur l'effet du frottement dans l'equilibre. *Memoires de l'academie des sciences de Berlin* (1769); http://eulerarchive.maa.org/, https://scholarlycommons.pacific.edu/euler-works/382/.
52. T. G. Sano, P. Johanns, P. Grandgeorge, C. Baek, P. M. Reis, Exploring the inner workings of the clove hitch knot. *Ext. Mech. Lett.* **55**, 101788 (2022).

Acknowledgments: We are grateful to E. Rawdon for computing the tightest, ideal S || S knot. We also thank A. Herzog for assistance with the photographs in Fig. 1A and movie S1. **Funding:** This work was partially supported by the Fonds National de la Recherche, Luxembourg (12439430). **Author contributions:** Conceptualization: P.J., P.G., and P.M.R. Formal analysis, investigation, experiments, validation: P.J. Methodology, writing—review and editing: P.J., C.B., P.G., S.A.C., and P.M.R. Resources: S.G. Software: P.J., C.B., S.A.C. Supervision: P.M.R. Visualization: P.J. and P.G. Writing—original draft: P.J., S.A.C., and P.M.R. **Competing interests:** The authors declare that they have no competing interests. **Data and materials availability:** All data needed to evaluate the conclusions in the paper are present in the paper and/or the Supplementary Materials.

Submitted 27 January 2023
Accepted 2 May 2023
Published 7 June 2023
10.1126/sciadv.adg8861

MATERIALS SCIENCE

Enhanced sub-1 eV detection in organic photodetectors through tuning polymer energetics and microstructure

Polina Jacoutot[1], Alberto D. Scaccabarozzi[2], Davide Nodari[1], Julianna Panidi[1], Zhuoran Qiao[1], Andriana Schiza[3], Alkmini D. Nega[4], Antonia Dimitrakopoulou-Strauss[4], Vasilis G. Gregoriou[3,5], Martin Heeney[1,6], Christos L. Chochos[3,5], Artem A. Bakulin[1], Nicola Gasparini[1]*

One of the key challenges facing organic photodiodes (OPDs) is increasing the detection into the infrared region. Organic semiconductor polymers provide a platform for tuning the bandgap and optoelectronic response to go beyond the traditional 1000-nanometer benchmark. In this work, we present a near-infrared (NIR) polymer with absorption up to 1500 nanometers. The polymer-based OPD delivers a high specific detectivity D^* of 1.03×10^{10} Jones (−2 volts) at 1200 nanometers and a dark current J_d of just 2.3×10^{-6} ampere per square centimeter at −2 volts. We demonstrate a strong improvement of all OPD metrics in the NIR region compared to previously reported NIR OPD due to the enhanced crystallinity and optimized energy alignment, which leads to reduced charge recombination. The high D^* value in the 1100-to-1300-nanometer region is particularly promising for biosensing applications. We demonstrate the OPD as a pulse oximeter under NIR illumination, delivering heart rate and blood oxygen saturation readings in real time without signal amplification.

INTRODUCTION

Light detection is at the core of modern technology. With the growing variety of electronic devices to support the Internet of Things services, the research community needs to address the rising demand. By 2030, more than 25 billion devices are forecasted to be connected, and about 15% of the global value is allocated to the health sector (*1*, *2*). Visible and infrared (IR) photodetectors based on silicon and indium gallium arsenide (InGaAs) dominate the current market thanks to their outstanding optoelectronic properties, with specific detectivity exceeding 10^{12} Jones. Notwithstanding, their lack of flexibility and costly manufacturing processes have left room for other emerging technologies such as organic photodetectors (OPDs) (*3*, *4*). Organic optoelectronics can address the fast-growing demand for portable, lightweight, cost-effective sensors that are flexible and easy to integrate and scale (*5*–*8*). Among notable benefits of organic semiconductors are broad and tunable absorption, solution processing, and a choice of deposition techniques onto soft, curved, or large surface areas. Moreover, these advantages over the established photodetector technology make OPD technology a desirable choice for large-area flexible imagers (*9*, *10*), on-the-go monitoring (*11*), and skin-grafted sensors and bioelectronics (*12*).

To overcome the exciton binding energy in organic semiconductors, a bulk heterojunction device architecture is realized by blending electron-donating (D) and electron-accepting (A) organic molecules in the photoactive layer (*13*, *14*). Now, the widely accepted benchmarks for IR OPDs consist of conjugated donor polymers and small-molecule non-fullerene acceptors (*15*, *16*). In the visible region, the photoactive layer materials arise from broad and intense research on organic photovoltaic technology, which helps visible OPDs to achieve metrics comparable with benchmark inorganic photodetectors (*9*, *17*, *18*). However, we rarely see IR materials with absorption onset above 1000 nm, as the solar spectrum irradiance drops off strongly in the IR. The additional difficulty in going further into the IR region arises from synthetic challenges in developing solution-processable, scalable IR–absorbing organic materials (*19*–*21*).

D-A polymers with absorption extending into the IR carry a vast potential for the OPD community (*22*–*24*). These near-infrared (NIR) polymers provide a wide scope for synthetic chemists to fine-tune the energetic levels, microstructure, solubility, and other properties (*23*, *25*). The electron-deficient A moiety largely determines the lowest unoccupied molecular orbital (LUMO) of the polymer, while the electron-rich D unit strongly influences the highest occupied molecular orbital (HOMO) energy. The former, for instance, can be used to lower the LUMO through the stabilization of the quinoid form of the acceptor unit (*23*, *26*). In our previous work, we demonstrated an NIR OPD based on thiadiazoloquinoxaline-thiophene (TQ-T) polymer and IEICO-4F with photocurrent response up to 1800 nm (*27*). However, those photodetectors suffered from high J_d under reverse bias. Given the ultranarrow optical bandgap of TQ-T polymer, it is expected that nonradiative recombination strongly limits the specific detectivity (D^*) of the device, while the energetic alignment with the charge blocking layers results in high injection current at the electrodes at reverse bias (*28*, *29*). The resulting D^* is far below the established background-limited IR photodetection detectivity limits for OPDs (*30*).

For biosensing and imaging applications, it is advantageous to focus on improving D^* in the second NIR detection window (1100 to 1300 nm), where tissue penetration is greater than with visible light, and light attenuation is minimized (*31*–*33*). To suppress the carrier injection from the electrodes at reverse bias, a

[1]Department of Chemistry and Centre for Processable Electronics, Imperial College London, London W12 0BZ, UK. [2]Center for Nano Science and Technology@PoliMi, Istituto Italiano di Tecnologia, via Raffaele Rubattino 81, Milano 20134, Italy. [3]Institute of Chemical Biology, National Hellenic Research Foundation, 48 Vassileos Constantinou Avenue, Athens 11635, Greece. [4]Clinical Cooperation Unit Nuclear Medicine, German Cancer Research Center, 69120 Heidelberg, Germany. [5]Advent Technologies SA, Stadiou Street, Platani, Rio, Patras 26504, Greece. [6]King Abdullah University of Science and Technology (KAUST), KAUST Solar Center (KSC), Thuwal 23955, Saudi Arabia.
*Corresponding author. Email: n.gasparini@imperial.ac.uk

deeper HOMO level of D is beneficial for increasing the injection barrier and forming a better ohmic contact with hole-transporting layers (HTLs), i.e., poly(3,4-ethylenedioxythiophene) polystyrene sulfonate (PEDOT:PSS) or molybdenum oxide (MoO_x) (*34*, *35*). Therefore, a strategy for OPD optimization should include fine-tuning of D molecular orbital energy levels and improving carrier mobility through control of the microstructure and optimized blend morphology (*36*–*38*).

In this work, we report a newly synthesized IR polymer that, in combination with IEICO-4F, realized an OPD with high D^* of 10^{10} Jones at 1200 nm. We compare the OPD and material parameters with those previously reported for the TQ-T:IEICO-4F system and demonstrate a strong performance improvement. We assign this improvement to higher crystallinity of the newly synthesized polymer, which affords improved molecular packing and carrier mobility both in the pristine material and in the blend, while its deeper HOMO minimizes the effect of dark charge injection at reverse bias. Through a careful analysis of the charge generation dynamics in the blend and of the OPD response kinetics, we observe efficient charge generation under NIR illumination within <2 ps, accompanied by rapid 2- to 5-μs rise and fall times of the photoresponse owing to the higher carrier mobility and suppressed recombination in the blend. The resulting specific detectivity is among the highest reported values for solution processable OPDs in the second NIR detection window (*17*, *22*, *24*, *39*). This allows us to demonstrate an application of the sensor as a pulse oximeter, which successfully and accurately measures heart rate and blood oxygen saturation under NIR illumination.

RESULTS

Materials characterizations

Figure 1A depicts the chemical structures of two solution-processable conjugated polymers based on the TQ building block. We previously demonstrated an OPD based on TQ-T push-pull polymer blended with IEICO-4F to achieve spectral responsivity up to 1800 nm (*27*). We showed that the effect of blend morphology played a key role in achieving higher D^* in the short-wave IR region beyond 1000 nm. However, those OPDs suffered from relatively high dark currents J_d due to the energetic alignment and the amorphous nature of the ultralow bandgap polymer. Here, we report a newly synthesized solution-processable IR polymer TQ-3T with three electron-rich thiophene units extending along the backbone. The new polymer was synthesized by Stille cross-coupling polymerization reaction (outlined in figs. S1 to S6).

Normalized absorption spectra of TQ-3T, TQ-T, and IEICO-4F are displayed in Fig. 1B. Peak absorption for TQ-3T is observed at 1150 nm, and the absorption onset occurs at 1470 nm, corresponding to an optical bandgap of 0.84 eV. The formation of multiple absorption peaks in TQ-3T suggests a higher degree of crystallinity, which will be discussed later in the morphology section. Relative to TQ-T, in the new polymer, we observe a deepening of the HOMO energy level from −4.6 to −4.7 eV, according to photoelectron spectroscopy measurements in air (fig. S7). At a first glance, it is expected that the introduction of an additional (electron-rich) T comonomers leads to a slight deepening of the HOMO. However, we speculate that this is due to the unusual properties of the TQ monomer. TQ is known to promote quinoidal character along the backbone, assisted by the formal aromatization of the pyrazine ring, leading in some cases to an open-shell ground state character and very low bandgaps (*40*, *41*). By extending the number of aromatic comonomers from one (T) to three (3T), we believe that the degree of quinoidal character of the polymer is reduced, leading to the measured changes in energy levels. This is beneficial in reducing the leakage current from carrier injection at reverse bias (*9*, *42*). By having better energy alignment with the MoO_x HTL, a better Ohmic contact is formed in the inverted OPD devices than previously with TQ-T polymer. While the introduction of the two more electron-rich T donor units deepened the HOMO energy in TQ-3T, the LUMO energy calculated as HOMO + E_g remains similar in the two polymers with an identical TQ acceptor unit.

Another effect of the backbone modification is the improved crystal order of the TQ-3T thin films, which was observed with grazing-incidence wide-angle x-ray scattering (GIWAXS) measurements. Figure 1 (D to F) illustrates the two-dimensional (2D) GIWAXS patterns for the D:A blend and the pristine materials. We have previously shown that TQ-T has a semicrystalline structure with a low degree of order, which also disrupts the high packing order of IEICO-4F in the D:A blend (*27*). Although a peak at 3.1 nm^{-1} associated with IEICO-4F was also observed in the TQ-T:IEICO-4F blend, this blend remains largely amorphous. Compared to its predecessor, TQ-3T displays an increased order and anisotropy, with a preferential face-on orientation in a thin film. The high crystal order of IEICO-4F and TQ-3T is also maintained in the blend. Sharp in-plane diffraction peaks at 2 and 3 nm^{-1} are ascribed to TQ-3T and IEICO-4F, respectively. The out-of-plane peak for IEICO-4F at 5 nm^{-1} is preserved in the blend, along with other diffractions from the polymer at lower angles. Therefore, TQ-3T:IEICO-4F blend shows the same crystal quality and orientation of its neat components.

To get an insight into the materials′ charge transport properties, organic thin-film transistors (OTFTs) were fabricated in bottom-contact, top-gate architecture. Both TQ-T and TQ-3T films showed high ambipolarity (fig. S8), with the former exhibiting mainly n-type and the latter p-type character. TQ-3T achieved a substantially higher hole mobility of 7×10^{-2} cm^2 V^{-1} s^{-1} in the saturation regime when compared with TQ-T, which reached 3.5×10^{-3} cm^2 V^{-1} s^{-1}. Regarding their n-type operation, TQ-T showed highest electron charge transport in the order of 3×10^{-2} cm^2 V^{-1} s^{-1}, whereas TQ-3T reached a mobility of 3×10^{-3} cm^2 V^{-1} s^{-1}. The mostly p-type operation of TQ-3T devices can be assigned to the deeper HOMO and workfunction value (see Fig. 1C), which reduces the energetic barrier with the source/drain electrodes. Moreover, the relatively high hole mobility of TQ-3T can also be assigned to the improved microstructure, as observed from the GIWAXS measurements (*43*, *44*).

Near-infrared OPDs

To evaluate the ability of TQ-3T to convert NIR light into current, we fabricated OPDs with an inverted device architecture by blending the IR polymer with IEICO-4F in a 1:1 optimized ratio (Fig. 2A). Photodetectors require efficient light-to-current conversion and low J_d for good light detection. One of the key methodologies for improving the photodetector′s sensitivity to light, i.e., increasing signal-to-noise ratio, linear dynamic range (LDR), and specific detectivity, is the minimization of the leakage current generated at reverse bias. A well-established practice is to use HTL and electron-transporting layer to suppress parasitic currents across the

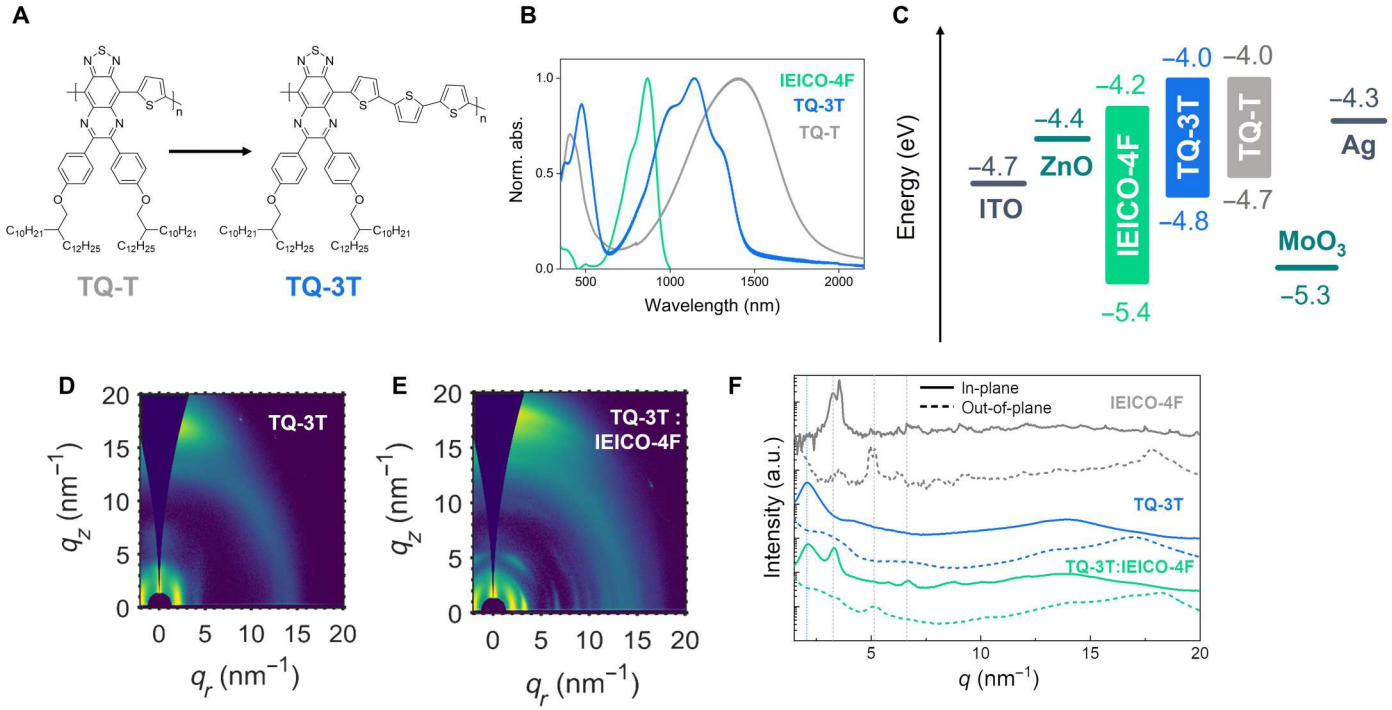

Fig. 1. TQ-3T polymer structure and OPD materials characterization. (**A**) Chemical structure of low bandgap conjugated polymers TQ-T and TQ-3T. (**B**) Normalized visible-IR absorption spectra of conjugated donor polymers and non-fullerene acceptor IEICO-4F. (**C**) Energy diagram of the materials used in OPD measured by air photoelectron spectroscopy (APS), with workfunction values of 4.7 and 4.6 eV for TQ-3T and TQ-T, respectively, obtained by Kelvin probe measurements. 2D GIWAXS maps of (**D**) TQ-3T and (**E**) TQ-3T:IEICO-4F; (**F**) in-plane and out-of-plane profiles of pristine films and the D:A blend. a.u., arbitrary units.

device under reverse bias, which we also adopted in this work. Effective suppression of J_d can also be achieved by deepening the HOMO of D or shallowing of A LUMO levels, which, unfortunately, presents a trade-off for ultralow bandgap materials (*42*, *45*–*47*).

Previously studied system TQ-T:IEICO-4F suffered from the relatively high dark currents of 8.4×10^{-5} A cm^{-2} (fig. S9), which were improved in this work by suppressing dark current injection from the HTL. As a result, in Fig. 2B, we observe dark current of 2.3×10^{-6} A cm^{-2} at −2 V with TQ-3T:IEICO-4F OPD. Under the illumination conditions, we observe higher photocurrent (J_L) values of 6.3×10^{-2} A cm^{-2} at −2 V, and an open circuit voltage of 0.32 V under one sun equivalent illumination. The improved OPD sensitivity in TQ-3T–based devices compared to TQ-T is demonstrated by the spectral responsivity (R) in Fig. 2C.

The OPD's photocurrent response to incident photons of varying energy is known as responsivity R. We calculated R from the following equation

$$R = \frac{J_{ph}}{P_{in}} = \eta \frac{\lambda q}{hc} \quad (1)$$

where P_{in} is the power, λ is the wavelength of incident light, η is the external quantum efficiency, q is the elementary charge, h is the Planck's constant, and c is the speed of light.

The spectral responsivity covers the NIR region up to 1500 nm, with R of 0.05 A W^{-1} measured at 1200 nm. This is significantly higher across the whole NIR spectral range than previously observed with TQ-T:IEICO-4F.

A key parameter for light-sensing applications is the specific detectivity, D^*, calculated according to the equation below

$$D^* = \frac{R\sqrt{A\Delta f}}{i_{noise}} \quad (2)$$

where A is the photoactive area of the device, Δf is the detection bandwidth, and i_{noise} is the noise current. To avoid an overestimation of D^*, the total experimental noise currents should be considered in the calculation (figs. S10 and S11). Because other sources of white noise, such as flicker and thermal noise, provide a significant contribution to the overall noise of the device, J_d cannot be considered as its main contributor (*48*). We calculated D^* to be 1.03×10^{10} Jones at 1200 nm under −2-V applied bias.

So far, we have presented steady-state characteristics of the OPD. However, to compete with existing benchmarks for imaging, video, or communication applications, we need to meet the minimum detection speed requirements of 10 kHz (*49*). Therefore, we examine dynamic characteristics by measuring the electrical bandwidth and rise t_r and fall t_f times of the OPD with IR light illumination. The bandwidth of a photodetector is known as a frequency of an incident modulated light at which the photocurrent response of the device has diminished by 3 dB from its low-frequency value. It is limited by the transit time of carriers to the electrodes and parasitic capacitance in the photoactive layer.

$$\text{Damping (dB)} = 20\log\frac{i(f_{3dB})}{i_{max}} \quad (3)$$

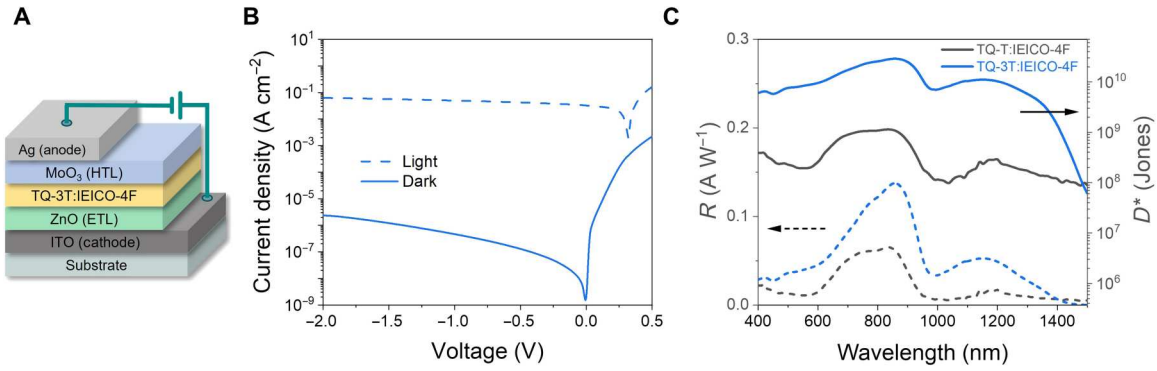

Fig. 2. OPD architecture and performance. (**A**) Inverted OPD device structure of the TQ-3T–based device. (**B**) Current-voltage characteristics of TQ-3T:IEICO-4F OPDs under light and dark conditions. (**C**) Responsivity and specific detectivity at −2 V applied bias.

Dynamic measurements were performed to evaluate the speed of the OPD. Figure 3A illustrates the electrical bandwidth of 470 kHz under 940-nm light at −2 V. Similar values were obtained under 1100- and 1300-nm illumination (fig. S12), confirming the high response speed of these NIR devices. The OPD demonstrates 2 μs t_r and t_f under 940-nm illumination and 3 and 5 μs t_r and t_f, respectively, under 1100-nm light (fig. S13). At applied reverse bias, an OPD is operated in the linear light intensity regime, known as LDR. LDR has been calculated to be 84 dB at 940 nm, which, again, is an improvement over the TQ-T–based system (Table 1). Last, the extrapolation of the LDR into the noise floor allowed the calculation of the noise equivalent power (NEP). We obtained a NEP value of 0.3 nW/$\sqrt{}$Hz, which results in D^* values of 7×10^9 Jones at 940 nm. This value is in line with the D^* calculated in Fig. 2C.

From Table 1, we can clearly see an improvement across most OPD parameters, with the only exception of responsivity extending further in the IR window in the TQ-T–based system. We attribute the improved OPD performance of the TQ-3T blend to an enhanced crystalline order and better energy alignment in the device to lower the dark current contributions, resulting in higher detectivity across the entire spectral window.

Ultrafast spectroscopy analysis

The photocurrent generation efficiency in the TQ-3T:IEICO-4F can be expected given the low offset of LUMO levels. To elucidate the underlying carrier dynamics in the D:A blend on the ultrafast time scale and kinetic limitations of device performance, we studied the blend and pristine films using pump-probe spectroscopy. Global analysis (GA) was applied to the transient absorption data of the blends to deconvolute varying spectral components.

Figure 4A presents a broad (visible-NIR) spectrum of the D:A blend under low-intensity excitation with 1300-nm pump illumination. The IR part of the spectrum is dominated by the ground state bleaching (GSB), representing the ground state absorption of the donor. The ground state absorption of the acceptor is expected in the 700-to-900-nm region. This GSB feature of the A is not observed at early times, as the polymer is selectively excited, but appears at later times when electron is transferred to the A. In addition, the dominant GSB feature from the polymer may be masking the photoinduced absorption from IEICO-4F, which peaks at 1160 nm (fig. S15). The visible part of the probe spectrum presents convoluted spectra from both D and A components as we see a spectral shape distortion and peak shifting beyond ~5 ps. This visible region was closely examined, and a GA was performed using the reference spectra of the pristine materials in figs. S14 and S15. The resulting deconvoluted spectra of the two components are shown in Fig. 4B with their associated kinetics in Fig. 4C. GA is

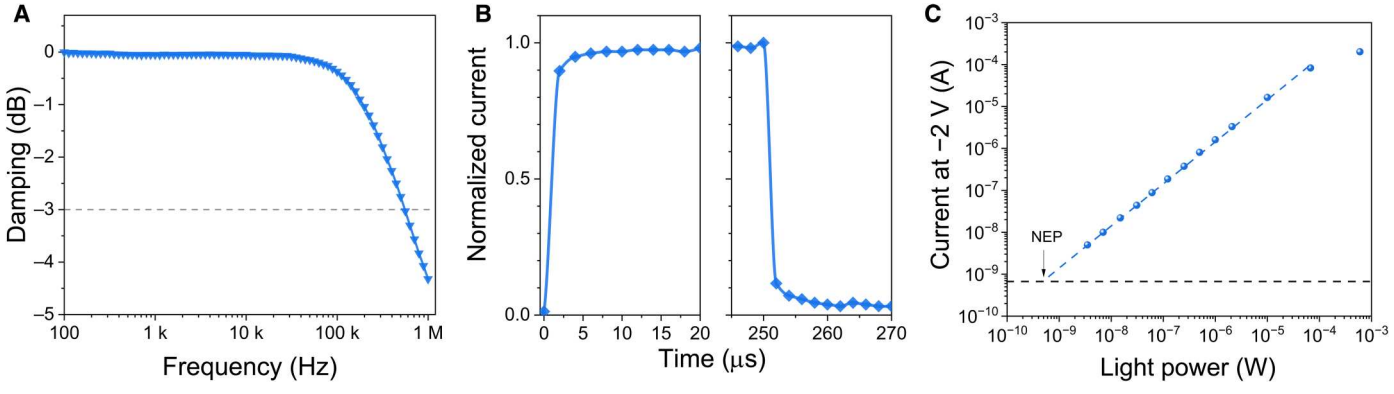

Fig. 3. OPD response speed and dynamic range. Dynamic measurements with TQ-3T:IEICO-4F all performed at 940-nm illumination and −2 V applied bias. (**A**) Cut-off frequency at −3 dB. (**B**) Transient photocurrent measurements with rise and fall times. (**C**) LDR measurements and extrapolation of the LDR into the noise floor, with calculation of the NEP.

Table 1. Comparison of the OPD figures of merit for TQ-3T– and TQ-T–based devices.

Active layer	E_g (eV)	λ_{onset} (nm)	J_d (A cm^{-2})	D^* (Jones)	R (A W^{-1})	Cut-off frequency (kHz)	LDR (dB)
TQ-3T:IEICO-4F	0.84	1470	2.3×10^{-6}	1.03×10^{10} at 1200 nm	0.05 at 1200 nm	470 kHz	84 at 940 nm
TQ-T:IEICO-4F	0.67	1800	8.4×10^{-5}	3.04×10^{8} at 1200 nm	0.02 at 1200 nm	100 kHz	46 at 940 nm

based on a genetic algorithm, which identifies spectral footprints of multiple components within the system, provided that they have different dynamics (*50*). Hence, we were able to identify spectral components associated with the TQ-3T exciton and charges (electrons). A rapid TQ-3T exciton decay within 2 ps is observed from fitting a single exponent. This correlates well with the exponential rise in the second component, which we ascribe to fast charge formation. Through TAS data analysis, we demonstrate that this D:A blend shows rapid exciton separation and charge generation within 2 ps or less. To improve the light-to-current conversion in the NIR region even further, future work will be focusing on the selection of HTLs with a better ohmic contact with the HOMO of the ultralow E_g polymers.

Real-time heartbeat monitoring and SpO_2 measurements

Last, we demonstrate a practical application of the new OPD as an NIR pulse oximeter with high-accuracy heart rate monitoring and SpO_2 saturation. A photoplethysmogram (PPG) was obtained from a healthy young volunteer in a resting state at three different wavelengths: 880, 940, and 1100 nm. PPGs were collected in transmission mode, whereby the fingertip was placed between the light-emitting diode (LED) and the OPD according to the setup described previously (fig. S16). Transmission mode pulse oximetry is useful at locations such as fingers, ears, and toes. For larger body parts, reflectance mode oximeters are a more suitable choice (*51*, *52*).

The LED light was attenuated by pulsating blood in the microvascular network and the surrounding tissue. The transmitted light was directly read out as OPD photocurrent. The resulting waveforms under three different illumination wavelengths are presented in Fig. 5A. Examining the amplitude of the signal and the overall current, the best signal-to-noise ratio was observed under 940-nm light. This is in line with high responsivity at this wavelength.

Despite lower current amplitude at 1100 nm, sharp and well-resolved peaks are still observed, which is valuable in combination with the enhanced tissue penetration and reduced attenuation at this wavelength (*32*, *53*, *54*). From all three waveforms, we calculated average resting heart rates of 58, 56, and 54 bpm, which are in good agreement and were not collected simultaneously. Furthermore, we obtained second derivative waveforms (Fig. 5B), known as the acceleration plethysmogram (APG), which are useful for examining the heart rate variability bypassing contour analysis errors in raw PPG signals (*55*, *56*). APG is also used to extract valuable physiological information about arterial health. The APG waveform has four systolic waves [*a* to *d* in Fig. 5B] and one diastolic wave (*e*). The points indicated in Fig. 5B on the APG wave are known as early systolic positive wave (*a*), early systolic negative wave (*b*), late systolic reincresing wave (*c*), late systolic redecreasing wave (*d*), and early diastolic positive wave (*e*) (*56*, *57*). Peak detection from *a* to *a* can be used to accurately calculate the heart rate, while *b*/*a* ratio is an indicator of arterial stiffness, which increases with age (*58*, *59*). We calculated the average *b*/*a* index for our volunteer to be 0.81, which is in perfect agreement with the *b*/*a* index for the fourth-decade age group in healthy males (*58*, *60*).

PPG is also used in pulse oximetry to extract arterial oxygen saturation (SpO_2). The pulsatile component AC is superimposed onto the lower-frequency DC component, which are analyzed to obtain the AC/DC ratio at different wavelengths (*61*). The SpO_2 of 98% was calculated from PPG waveform. The calculations were carried out according to the equation below (*62*)

$$SpO_2 = \frac{\varepsilon_{\lambda_1,Hb} - \varepsilon_{\lambda_2,Hb} R}{(\varepsilon_{\lambda_1,Hb} - \varepsilon_{\lambda_1,HbO_2}) + (\varepsilon_{\lambda_2,HbO_2} - \varepsilon_{\lambda_2,Hb}) R} \quad (4)$$

where εHbO_2 and εHb are absorption coefficients for oxyhemoglobin and deoxyhemoglobin, taken from (*52*) and R is the ratio of ac to dc at two different wavelengths. This SpO_2 value is within range for a healthy young volunteer and demonstrates the new OPD system as an effective pulse oximeter under NIR illumination.

DISCUSSION

We have synthesized a new IR push-pull polymer based on the TQ-3T backbone with absorption onset at 1470 nm. Using this polymer as a donor material in the bulk heterojunction (BHJ) blend with IEICO-4F, we have realized an NIR OPD with high specific detectivity of 10^{10} Jones at 1200 nm, exceeding previously reported OPD with TQ-T donor polymer by two orders of magnitude. GIWAXS measurements related this improvement to the superior crystalline order of TQ-3T compared to TQ-T polymer. The order was also preserved in the D:A blend where TQ-3T was shown to not disrupt the ordering of IEICO-4F significantly. The improved microstructure in TQ-3T contributed to a reduced charge recombination leading to a faster charge extraction. In addition, efficient photon to charge conversion and fast response speed were observed at different NIR wavelengths, which we attribute to the fast charge generation and extraction in this blend. The novel OPD system demonstrated a reduction in J_d at reverse bias by an order or magnitude, which we accredited to a better ohmic contact with the HTL through deepening of HOMO (D). Besides an improvement across all the device metrics, we also demonstrated an application as a pulse oximeter, performing heart rate variability and SpO_2 analysis.

MATERIALS AND METHODS

Materials

TQ-3T polymer was synthesized according to the details outlined in the Supplementary Materials. The NFA IEICO-4F was purchased from 1-Material.

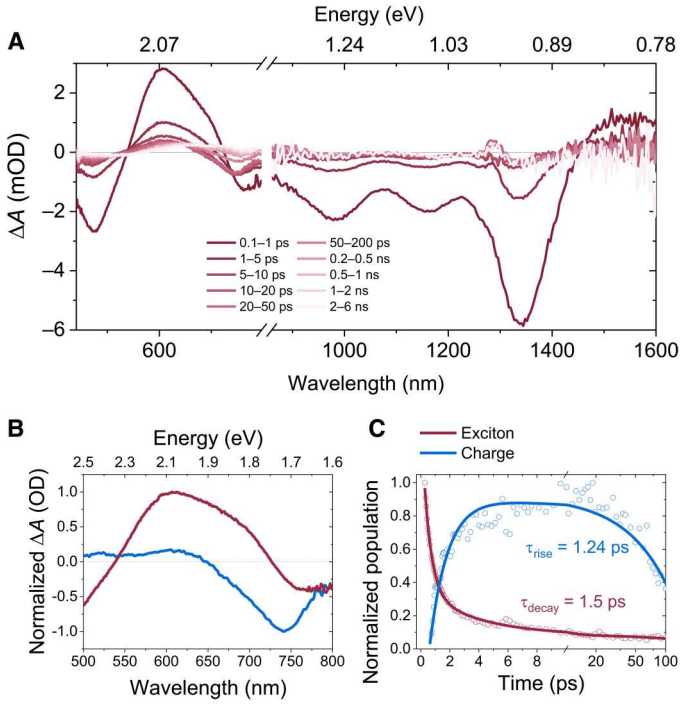

Fig. 4. TAS analysis of the OPD blend. (**A**) Broadband visible-IR transient absorption spectra of TQ-3T:IEICO-4F blend upon 1300-nm pump excitation. Decomposed spectra (**B**) and kinetics (**C**) of the two-component GA depicting decaying excitonic and growing charge dynamic. mOD, mean optical density; OD, optical density.

Device fabrication

OPDs were fabricated in an inverted architecture of indium tin oxide (ITO)/ZnO (30 nm)/active layer (120 nm)/MoO_x (10 nm)/Ag (100 nm). Glass substrates prepatterned with ITO were cleaned by sequential sonication in acetone, deionized water, Decon 90 detergent, and propan-2-ol each for 10 min. Following this, an 8-min oxygen plasma treatment was performed. Zinc oxide (ZnO) precursor solution was prepared from zinc acetate dihydrate (219.5 mg), ethanolamine (60 μl), and 2-methoxyethanol (2 ml). This ZnO precursor solution was filtered through a 0.45-μm Acrodisc filter, spin-coated onto the plasma-treated substrates at 4000 rpm/40 s, and annealed at 150°C/20 min. The TQ-3T:IEICO-4F (1:1) and TQ-T:IEICO-4F (1:1) were dissolved in chlorobenzene solutions with total concentrations of 15 and 20 mg/ml, respectively, and stirred overnight at 60°C in a glove box. The active layers were deposited by spin coating at 2000 rpm/40 s in inert conditions and then annealed at 100°C/10 min in the glove box. MoO_x (10 nm) and silver (Ag) (100 nm) were then deposited by evaporation through a shadow mask giving photodiodes with pixel areas of 0.045 cm^2.

OTFTs fabrication

Bottom-contact, top-gate OTFTs were fabricated on glass substrates. Substrates were sonicated in Decon 90/deionized water solution for 5 min, followed by sequential sonication in acetone and isopropanol. Gold (40 nm) was deposited via thermal evaporation in high vacuum (10^{-6} mbar) to form the source/drain electrodes, resulting in transistor devices with channel length in the range of 30 to 100 μm and width of 1 mm. For the hole-only TFTs, a self-assembled monolayer, pentafluorothiophenol (PFBT) was used to treat the workfunction. Substrates with source/drain contacts were immersed in 7 mmol of PFBT solution in isopropanol. No further treatment was conducted for the electron-only TFTs. Organic semiconductors were spin-coated from a solution (5 mg/ml) in anhydrous chlorobenzene at 2000 rpm for 30 s, followed by thermal annealing at 100°C for 10 min. CYTOP (90 nm) was used as dielectric layer, followed by 50-nm thermal evaporated aluminum, which formed the gate electrode. Device fabrication and electrical measurements were performed in a nitrogen glovebox. Transistor characterization was carried out using a Keithley 4200 semiconductor parameter analyzer.

J-V measurements

Current density-voltage (*J-V*) characteristics were measured using a Keithley 4200 Source-Measure unit (scan rate of 25 mV s^{-1}). An Oriel Instruments Solar Simulator with a Xenon lamp and calibrated to a silicon reference cell was used to provide AM1.5G irradiance. For determination of the LDR, a neutral white light LED driven by a function generator (Thorlabs, DC2200) was used. The LED light was attenuated using a selection of neutral density filters placed between the lamp and OPD. The photocurrent (J_{ph}) was calculated as the difference in response between the illuminated current density (J_L) and dark current density (J_d) at each light intensity. All the devices were tested in nitrogen atmosphere.

NEP measurements

To calculate the NEP, OPD devices were connected to a lock-in amplifier (MFLI, Zurich Instruments AG) and illuminated with a 940-nm IR light. A frequency of 77 Hz was used and controlled with an optical chopper.

Responsivity

Responsivity was measured using an integrated system from Quantum Design PV300. All the devices were tested in ambient air.

Dynamic measurements

Dynamic measurements were performed using a digital oscilloscope (Tektronix, TDS3032B). The PPDs were illuminated with a neutral white light LED driven by a function generator (Thorlabs, DC2200). For determination of the rise and fall time, a 1-kHz square wave pulse was applied to the LED using the function generator. For determination of the cut-off frequency, sinusoidal functions with varying frequencies between 100 Hz and 1 MHz were used to drive the LED. All the devices were tested in nitrogen atmosphere.

GIWAXS measurements

GIWAXS measurements were performed at the noncrystalline diffraction beamline (BL11-NCD-Sweet) at ALBA Synchrotron Radiation Facility in Barcelona (Spain). A detector (Rayonix, WAXS LX255-HS) with a resolution of 1920 × 5760 pixels was used to collect the scattering signals. Sample holder position was calibrated with chromium oxide (Cr_2O_3) standard. The incident energy was 12.4 eV, and the sample-to-detector distance was set at 200.93 mm. The angle of incidence αi was set between 0.1 and 0.15, and the exposure time was 5 s. 2D GIWAXS patterns were corrected as a function of the components of the scattering vector with a

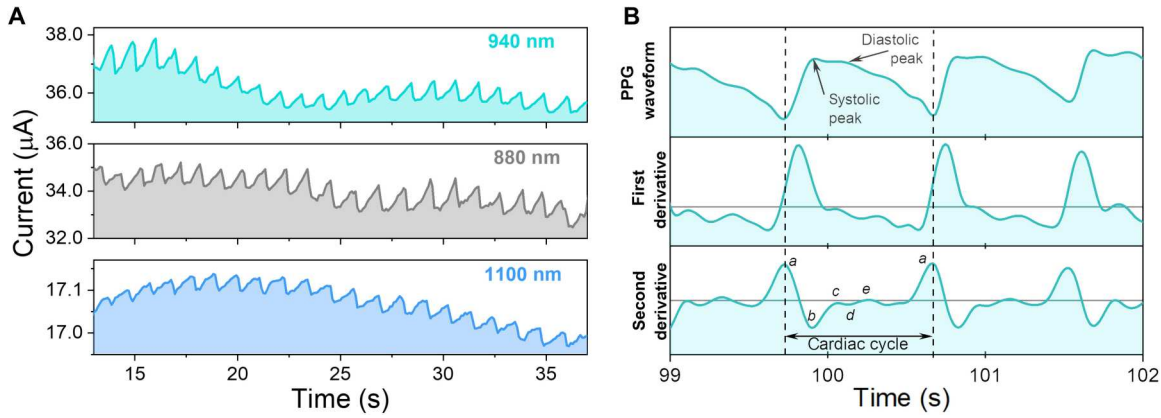

Fig. 5. Finger PPG testing under NIR illumination. (**A**) Transmittance PPG collected from a volunteer's finger under different NIR illumination wavelengths. (**B**) Comparison of PPG waveform and its derivatives, including the second derivative APG, highlighting the key areas of interest in a cardiac cycle.

MATLAB script developed by A. Nogales and E. Gutiérrez. Thin films were cast onto highly doped silicon substrates following same processing route used for the device fabrication.

Transient absorption spectroscopy

A broadband femtosecond transient absorption spectrometer Helios (Spectra Physics, Newport Corp.) was used for pump-probe measurements on the neat polymer and acceptor films and their blends. A 1-kHz Ti:Sapphire regenerative amplifier (Solstice, Spectra Physics, Newport Corp.) delivered ultrafast laser pulses (800 nm, <100 fs full width at half maximum) to an optical parametric amplifier (TOPAS Prime, Spectra Physics) and a frequency mixer (Niruvis, Light Conversion) to generate pump pulses at 850 and 1500 nm, which were modulated at 500 Hz by an optical chopper system (Thorlabs). Seed pulses (800 nm) were also delayed on the 6-ns mechanical delay stage and passed through a sapphire crystal to produce a white light probe (400 to 900 nm). Spatial and temporal overlap of the pump and the focused probe beams was achieved on the thin-film samples, contained in a quartz cuvette under a constant flow of nitrogen. The fluences were calculated on the basis of the probe beam size of 0.5 mm^2 at the sample. Background and chirp corrections were applied to the spectra after measurement using the Surface Xplorer software.

Photoplethysmography

Photoplethysmography measurements (fig. S16) were performed by directly connecting the OPD devices to a Keithley 4200 Source-Measure unit and recording the current as a function of time upon illumination with different LEDs driven by a function generator (Thorlabs, DC2200).

Supplementary Materials

This PDF file includes:

Supplementary Text
Figs. S1 to S16
Table S1

REFERENCES AND NOTES

1. Statista dossier on the internet of things (IoT), 2022, pp. 1–34, www.statista.com/study/27915/internet-of-things-iot-statista-dossier/.
2. V. Jahmunah, V. K. Sudarshan, S. L. Oh, R. Gururajan, R. Gururajan, X. Zhou, X. Tao, O. Faust, E. J. Ciaccio, K. H. Ng, U. R. Acharya, Future IoT tools for COVID-19 contact tracing and prediction: A review of the state-of-the-science. *Int. J. Imaging Syst. Technol.* **31**, 455–471 (2021).
3. R. Ollearo, X. Ma, H. B. Akkerman, M. Fattori, M. J. Dyson, A. J. J. M. Van Breemen, S. C. J. Meskers, W. Dijkstra, R. A. J. Janssen, G. H. Gelinck, Vitality surveillance at distance using thin-film tandem- like narrowband near-infrared photodiodes with light-enhanced responsivity. *Sci. Adv.* **9**, eadf9861 (2023).
4. N. Li, N. Eedugurala, J. D. Azoulay, T. N. Ng, A filterless organic photodetector electrically switchable between visible and infrared detection. *Cell Rep. Phys. Sci.* **3**, 100711 (2022).
5. S. Park, K. Fukuda, M. Wang, C. Lee, T. Yokota, H. Jin, H. Jinno, H. Kimura, P. Zalar, N. Matsuhisa, S. Umezu, G. C. Bazan, T. Someya, Ultraflexible near-infrared organic photodetectors for conformal photoplethysmogram sensors. *Adv. Mater.* **30**, 1802359 (2018).
6. S. Wang, J. Y. Oh, J. Xu, H. Tran, Z. Bao, Skin-inspired electronics: An emerging paradigm. *Acc. Chem. Res.* **51**, 1033–1045 (2018).
7. H. Bristow, P. Jacoutot, A. D. Scaccabarozzi, M. Babics, M. Moser, A. Wadsworth, T. D. Anthopoulos, A. Bakulin, I. McCulloch, N. Gasparini, Nonfullerene-based organic photodetectors for ultrahigh sensitivity visible light detection. *ACS Appl. Mater. Interfaces* **12**, 48836–48844 (2020).
8. Y. Zhong, A. Koklu, D. R. Villalva, Y. Zhang, L. H. Hernandez, M. Moser, R. K. Hallani, I. McCulloch, D. Baran, S. Inal, An organic electrochemical transistor integrated photodetector for high quality photoplethysmogram signal acquisition. *Adv. Funct. Mater.* **33**, 2211479 (2022).
9. G. Simone, M. J. Dyson, S. C. J. Meskers, R. A. J. Janssen, G. H. Gelinck, Organic photodetectors and their application in large area and flexible image sensors: The role of dark current. *Adv. Funct. Mater.* **30**, 1904205 (2020).
10. N. Gasparini, A. Gregori, M. Salvador, M. Biele, A. Wadsworth, S. Tedde, D. Baran, I. McCulloch, C. J. Brabec, Visible and near-infrared imaging with nonfullerene-based photodetectors. *Adv. Mater. Technol.* **3**, 1800104 (2018).
11. J. H. Kim, C. Marcus, R. Ono, D. Sadat, A. Mirzazadeh, M. Jens, S. Fernandez, S. Zheng, T. Durak, C. Dagdeviren, A conformable sensory face mask for decoding biological and environmental signals. *Nat. Electron.* **5**, 794–807 (2022).
12. T. Yokota, T. Nakamura, H. Kato, M. Mochizuki, M. Tada, M. Uchida, S. Lee, M. Koizumi, W. Yukita, A. Takimoto, T. Someya, A conformable imager for biometric authentication and vital sign measurement. *Nat. Electron.* **3**, 113–121 (2020).
13. G. Yu, J. Gao, J. C. Hummelen, F. Wudl, A. J. Heeger, Polymer photovoltaic cells: Enhanced efficiencies via a network of internal donor-acceptor heterojunctions. *Science* **270**, 1789–1791 (1995).
14. N. Gasparini, F. V. A. Camargo, S. Frühwald, T. Nagahara, A. Classen, S. Roland, A. Wadsworth, V. G. Gregoriou, C. L. Chochos, D. Neher, M. Salvador, D. Baran, I. McCulloch, A. Görling, L. Lüer, G. Cerullo, C. J. Brabec, Adjusting the energy of interfacial states in organic photovoltaics for maximum efficiency. *Nat. Commun.* **12**, 1772 (2021).
15. N. Li, P. Mahalingavelar, J. H. Vella, D. S. Leem, J. D. Azoulay, T. N. Ng, Solution-processable infrared photodetectors: Materials, device physics, and applications. *Mater. Sci. Eng. R Rep.* **146**, 100643 (2021).
16. S. Holliday, R. S. Ashraf, A. Wadsworth, D. Baran, S. A. Yousaf, C. B. Nielsen, C. H. Tan, S. D. Dimitrov, Z. Shang, N. Gasparini, M. Alamoudi, F. Laquai, C. J. Brabec, A. Salleo,

J. R. Durrant, I. McCulloch, High-efficiency and air-stable P3HT-based polymer solar cells with a new non-fullerene acceptor. *Nat. Commun.* **7**, 11585 (2016).
17. Y. Wang, J. Kublitski, S. Xing, F. Dollinger, D. Spoltore, J. Benduhn, K. Leo, Narrowband organic photodetectors-towards miniaturized, spectroscopic sensing. *Mater. Horiz.* **9**, 220–251 (2022).
18. A. Wadsworth, Z. Hamid, J. Kosco, N. Gasparini, I. McCulloch, The bulk heterojunction in organic photovoltaic, photodetector, and photocatalytic applications. *Adv. Mater.* **32**, 2001763 (2020).
19. D. Meng, R. Zheng, Y. Zhao, E. Zhang, L. Dou, Y. Yang, Near-infrared materials: The turning point of organic photovoltaics. *Adv. Mater.* **34**, 2107330 (2022).
20. A. E. London, H. Chen, M. A. Sabuj, J. Tropp, M. Saghayezhian, N. Eedugurala, B. A. Zhang, Y. Liu, X. Gu, B. M. Wong, N. Rai, M. K. Bowman, J. D. Azoulay, A high-spin ground-state donor-acceptor conjugated polymer. *Sci. Adv.* **5**, eaav2336 (2019).
21. J. H. Vella, L. Huang, N. Eedugurala, K. S. Mayer, T. Nga Ng, J. D. Azoulay, Broadband infrared photodetection using a narrow bandgap conjugated polymer. *Sci. Adv.* **7**, eabg2418 (2021).
22. Q. Li, Y. Guo, Y. Liu, Exploration of near-infrared organic photodetectors. *Chem. Mater.* **31**, 6359–6379 (2019).
23. J. Qi, W. Qiao, Z. Y. Wang, Advances in organic near-infrared materials and emerging applications. *Chem. Rec.* **16**, 1531–1548 (2016).
24. J. Huang, J. Lee, J. Vollbrecht, V. V. Brus, A. L. Dixon, D. Xi Cao, Z. Zhu, Z. Du, H. Wang, K. Cho, G. C. Bazan, T.-Q. Nguyen, A high-performance solution-processed organic photodetector for near-infrared sensing. *Adv. Mater.* **32**, e1906027 (2020).
25. A. A. Mohapatra, Y. Dong, P. Boregowda, A. Mohanty, A. Sadhanala, X. Jiao, A. Narayan, C. R. Mcneill, J. R. Durrant, S. Patil, Rational design of donor–acceptor based semiconducting copolymers with high dielectric constants. *J. Phys. Chem. C* **125**, 6886–6896 (2021).
26. T. Hasegawa, M. Ashizawa, J. Hiyoshi, S. Kawauchi, J. Mei, Z. Bao, H. Matsumoto, An ultranarrow bandgap derived from thienoisoindigo polymers: Structural influence on reducing the bandgap and self-organization. *Polym. Chem.* **7**, 1181–1190 (2016).
27. P. Jacoutot, A. D. Scaccabarozzi, T. Zhang, Z. Qiao, F. Aniés, M. Neophytou, H. Bristow, R. Kumar, M. Moser, A. D. Nega, A. Schiza, A. Dimitrakopoulou-Strauss, V. G. Gregoriou, T. D. Anthopoulos, M. Heeney, I. McCulloch, A. A. Bakulin, C. L. Chochos, N. Gasparini, Infrared organic photodetectors employing ultralow bandgap polymer and non-fullerene acceptors for biometric monitoring. *Small* **18**, e2200580 (2022).
28. S. Karuthedath, J. Gorenflot, Y. Firdaus, N. Chaturvedi, C. S. P. De Castro, G. T. Harrison, J. I. Khan, A. Markina, A. H. Balawi, T. A. Dela Peña, W. Liu, R. Z. Liang, A. Sharma, S. H. K. Paleti, W. Zhang, Y. Lin, E. Alarousu, S. Lopatin, D. H. Anjum, P. M. Beaujuge, S. De Wolf, I. McCulloch, T. D. Anthopoulos, D. Baran, D. Andrienko, F. Laquai, Intrinsic efficiency limits in low-bandgap non-fullerene acceptor organic solar cells. *Nat. Mater.* **20**, 378–384 (2021).
29. E. Collado-Fregoso, S. N. Pugliese, M. Wojcik, J. Benduhn, E. Bar-Or, L. Perdigón Toro, U. Hörmann, D. Spoltore, K. Vandewal, J. M. Hodgkiss, D. Neher, Energy-gap law for photocurrent generation in fullerene-based organic solar cells: The case of low-donor-content blends. *J. Am. Chem. Soc.* **141**, 2329–2341 (2019).
30. S. Gielen, C. Kaiser, F. Verstraeten, J. Kublitski, J. Benduhn, D. Spoltore, P. Verstappen, W. Maes, P. Meredith, A. Armin, K. Vandewal, Intrinsic detectivity limits of organic near-infrared photodetectors. *Adv. Mater.* **32**, 2003818 (2020).
31. J. Spigulis, L. Gailite, A. Lihachev, R. Erts, Simultaneous recording of skin blood pulsations at different vascular depths by multiwavelength photoplethysmography. *Appl. Opt.* **46**, 1754–1759 (2007).
32. P. D. Mannheimer, J. R. Casciani, M. E. Fein, S. L. Nierlich, Wavelength selection for low-saturation pulse oximetry. *IEEE Trans. Biomed. Eng.* **44**, 148–158 (1997).
33. F. F. Jobsis, Noninvasive, infrared monitoring of cerebral and myocardial oxygen sufficiency and circulatory parameters. *Science* **198**, 1264–1267 (1977).
34. J. Zhang, W. Liu, M. Zhang, Y. Liu, G. Zhou, S. Xu, F. Zhang, H. Zhu, F. Liu, X. Zhu, Revealing the critical role of the HOMO alignment on maximizing current extraction and suppressing energy loss in organic solar cells. *iScience* **19**, 883–893 (2019).
35. J. Huang, J. Lee, H. Nakayama, M. Schrock, D. X. Cao, K. Cho, G. C. Bazan, T. Q. Nguyen, Understanding and countering illumination-sensitive dark current: Toward organic photodetectors with reliable high detectivity. *ACS Nano* **15**, 1753–1763 (2021).
36. J. Liu, Y. Wang, H. Wen, Q. Bao, L. Shen, L. Ding, Organic photodetectors: Materials, structures, and challenges. *Sol. RRL* **4**, 2000139 (2020).
37. T. Zhang, M. Moser, A. D. Scaccabarozzi, H. Bristow, P. Jacoutot, A. Wadsworth, T. D. Anthopoulos, I. McCulloch, N. Gasparini, Ternary organic photodetectors based on pseudo-binaries nonfullerene-based acceptors. *J. Phys. Mater.* **4**, 045001 (2021).
38. S. M. Menke, A. Cheminal, P. Conaghan, N. A. Ran, N. C. Greehnam, G. C. Bazan, T.-Q. Nguyen, A. Rao, R. H. Friend, Order enables efficient electron-hole separation at an organic heterojunction with a small energy loss. *Nat. Commun.* **9**, 277 (2018).
39. F. Verstraeten, S. Gielen, P. Verstappen, J. Raymakers, H. Penxten, L. Lutsen, K. Vandewal, W. Maes, Efficient and readily tuneable near-infrared photodetection up to 1500 nm enabled by thiadiazoloquinoxaline-based push-pull type conjugated polymers. *J. Mater. Chem. C.* **8**, 10098–10103 (2020).
40. Y. Joo, L. Huang, N. Eedugurala, A. E. London, A. Kumar, B. M. Wong, B. W. Boudouris, J. D. Azoulay, Thermoelectric performance of an open-shell donor–acceptor conjugated polymer doped with a radical-containing small molecule. *Macromolecules* **51**, 3886–3894 (2018).
41. L. Huang, N. Eedugurala, A. Benasco, S. Zhang, K. S. Mayer, D. J. Adams, B. Fowler, M. M. Lockart, M. Saghayezhian, H. Tahir, E. R. King, S. Morgan, M. K. Bowman, X. Gu, J. D. Azoulay, Open-shell donor–acceptor conjugated polymers with high electrical conductivity. *Adv. Funct. Mater.* **30**, 1909805 (2020).
42. G. Simone, M. J. Dyson, C. H. L. Weijtens, S. C. J. Meskers, R. Coehoorn, R. A. J. Janssen, G. H. Gelinck, On the origin of dark current in organic photodiodes. *Adv. Opt. Mater.* **8**, 1901568 (2020).
43. G. Schweicher, Y. Olivier, V. Lemaur, Y. H. Geerts, What currently limits charge carrier mobility in crystals of molecular semiconductors? *Isr. J. Chem.* **54**, 595–620 (2014).
44. S. Chen, Z. Li, Y. Qiao, Y. Song, Solution-processed organic semiconductor crystals for field-effect transistors: From crystallization mechanism towards morphology control. *J. Mater. Chem. C.* **9**, 1126–1149 (2021).
45. F. Furlan, D. Nodari, E. Palladino, E. Angela, L. Mohan, J. Briscoe, M. J. Fuchter, T. J. Macdonald, G. Grancini, M. A. McLachlan, N. Gasparini, Tuning halide composition allows low dark current perovskite photodetectors with high specific detectivity. *Adv. Opt. Mater.* **10**, 2201816 (2022).
46. W. Jang, T. Q. Nguyen, D. H. Wang, Theoretical and experimental investigation of barrier-energy-dependent charge injection mechanisms in organic photodetectors. *Adv. Funct. Mater.* **33**, 2209615 (2023).
47. O. J. Sandberg, C. Kaiser, S. Zeiske, N. Zarrabi, S. Gielen, W. Maes, K. Vandewal, P. Meredith, A. Armin, Mid-gap trap state-mediated dark current in organic photodiodes. *Nat. Photonics* **17**, 368–374 (2023).
48. Y. Fang, A. Armin, P. Meredith, J. Huang, Accurate characterization of next-generation thin-film photodetectors. *Nat. Photonics* **13**, 1–4 (2019).
49. R. D. Jansen-van Vuuren, A. Armin, A. K. Pandey, P. L. Burn, P. Meredith, Organic photodiodes: The future of full color detection and image sensing. *Adv. Mater.* **28**, 4766–4802 (2016).
50. S. Gélinas, A. Rao, A. Kumar, S. L. Smith, A. W. Chin, J. Clark, T. S. Van Der Poll, G. C. Bazan, R. H. Friend, Ultrafast long-range charge separation in organic semiconductor photovoltaic diodes. *Science* **343**, 512–516 (2014).
51. G. Simone, D. Tordera, E. Delvitto, B. Peeters, A. J. J. M. Van Breemen, S. C. J. Meskers, R. A. J. Janssen, G. H. Gelinck, High-accuracy photoplethysmography array using near-infrared organic photodiodes with ultralow dark current. *Adv. Opt. Mater.* **8**, 1901989 (2020).
52. Y. Khan, D. Han, A. Pierre, J. Ting, X. Wang, C. M. Lochner, G. Bovo, N. Yaacobi-Gross, C. Newsome, R. Wilson, A. C. Arias, A flexible organic reflectance oximeter array. *Proc. Natl. Acad. Sci. U.S.A.* **115**, E11015–E11024 (2018).
53. F. Scholkmann, M. Wolf, General equation for the differential pathlength factor of the frontal human head depending on wavelength and age. *J. Biomed. Opt.* **18(10)**, 105004 (2013).
54. L. A. Sordillo, Y. Pu, S. Pratavieira, Y. Budansky, R. R. Alfano, Deep optical imaging of tissue using the second and third near-infrared spectral windows. *J. Biomed. Opt.* **19**, 056004 (2014).
55. J. M. Ahn, Wave detection in acceleration plethysmogram. *Healthc. Inform. Res.* **21**, 111–117 (2015).
56. M. Elgendi, On the analysis of fingertip photoplethysmogram signals. *Curr. Cardiol. Rev.* **8**, 14–25 (2012).
57. M. Elgendi, I. Norton, M. Brearley, D. Abbott, D. Schuumans, Detection of *a* and *b* waves in the acceleration photoplethysmogram. *Biomed. Eng. Online* **13**, 139 (2014).
58. K. Takazawa, N. Tanaka, M. Fujita, O. Matsuoka, T. Saiki, M. Aikawa, S. Tamura, C. Ibukiyama, Assessment of vasoactive agents and vascular aging by the second derivative of photoplethysmogram waveform. *Hypertension* **32**, 365–370 (1998).
59. I. Imanaga, H. Hara, S. Koyanagi, K. Tanaka, Correlation between wave components of the second derivative of plethysmogram and arterial distensibility. *Jpn. Heart J.* **39**, 775–784 (1998).
60. K. Pilt, K. Meigas, R. Ferenets, K. Temitski, M. Viigimaa, Photoplethysmographic signal waveform index for detection of increased arterial stiffness. *Physiol. Meas.* **35**, 2027–2036 (2014).
61. P. D. Mannheimer, The light-tissue interaction of pulse oximetry. *Anesth. Analg.* **105**, S10–S17 (2007).
62. J. G. Webster, *Design of Pulse Oximeters* (IOP Publishing Ltd, 1997).

Acknowledgments: P.J. thanks Optoelectronics group (University of Cambridge) for providing access to the GA script in MATLAB. **Funding:** C.L.C., V.G.G., A.D.-S., A.N., and A.D.S. would like to thank the Helmholtz European partnering program for the cooperation between German Cancer Research Center (DKFZ) and National Hellenic Research Foundation (NHRF) to build the Athens Comprehensive Cancer Center (ACCC) for the financial support. A.A.B. and P.J. thank Royal Society for support via URF grant. **Author contributions:** P.J. and N.G. conceived and developed the ideas. P.J. designed the experiments and performed ultrafast measurements and data analysis under the supervision of A.A.B. D.N. and Z.Q. fabricated the OPD devices and performed the electrical characterizations. J.P. fabricated the OTFT devices and analyzed the data. A.D.S. performed GIWAXS measurements and analyses. A.S., A.D.N., and A.D-S. synthetized TQ-3T polymer under the supervision of V.G.G and C.L.C. M.H. interpreted the data. P.J. and N.G. wrote the manuscript. All authors commented on the manuscript. **Competing interests:** The other authors declare that they have no competing interests. **Data and materials availability:** All data needed to evaluate the conclusions in the paper are present in the paper and/or the Supplementary Materials.

Submitted 23 February 2023
Accepted 4 May 2023
Published 7 June 2023
10.1126/sciadv.adh2694

CANCER

Quantitative intravital imaging for real-time monitoring of pancreatic tumor cell hypoxia and stroma in an orthotopic mouse model

Timothy Samuel[1,2], Sara Rapic[1], Cristiana O'Brien[1,2], Michael Edson[1], Yuan Zhong[1], Ralph S. DaCosta[1,2]*

Pancreatic cancer is a lethal disease with few successful treatment options. Recent evidence demonstrates that tumor hypoxia promotes pancreatic tumor invasion, metastasis, and therapy resistance. However, little is known about the complex relationship between hypoxia and the pancreatic tumor microenvironment (TME). In this study, we developed a novel intravital fluorescence microscopy platform with an orthotopic mouse model of pancreatic cancer to study tumor cell hypoxia within the TME in vivo, at cellular resolution, over time. Using a fluorescent BxPC3-DsRed tumor cell line with a hypoxia-response element (HRE)/green fluorescent protein (GFP) reporter, we showed that HRE/GFP is a reliable biomarker of pancreatic tumor hypoxia, responding dynamically and reversibly to changing oxygen concentrations within the TME. We also characterized the spatial relationships between tumor hypoxia, microvasculature, and tumor-associated collagen structures using in vivo second harmonic generation microscopy. This quantitative multimodal imaging platform enables the unprecedented study of hypoxia within the pancreatic TME in vivo.

INTRODUCTION

Despite decades of research, the current standard of care for pancreatic cancer, on average, provides only a few months of survival benefit (*1*, *2*). The poor outcomes associated with this disease are due in combination to its late diagnosis (*3*) as well as both inherent and acquired treatment resistance (*4*). Pancreatic tumors tend to be resistant to both chemo- and radiotherapy (*5*–*7*), as well as more contemporary immunotherapies (*8*).

The complex pancreatic tumor microenvironment (TME), characterized by hypoxia and desmoplasia, plays a crucial role in treatment response (*9*–*13*). As cancer cells proliferate and invade the surrounding tissues, they develop a pronounced stromal compartment, made up of dense fibrotic tissue (*14*). Proliferating fibroblasts secrete extracellular matrix (ECM) proteins [primarily type I collagen; (*15*)], which can act as a physical barrier to treatments (*16*) and cause disruption of vascular networks, leading to impaired blood perfusion and the development and exacerbation of tumor hypoxia (*16*–*20*). Hypoxia up-regulates hypoxia-inducible factors (HIFs) in tumor cells that, besides promoting cancer progression, invasion, and metastasis (*21*), can further stimulate collagen deposition (*22*, *23*), creating a positive feedback loop and the emergence of a more invasive phenotype (*24*).

These characteristics not only make pancreatic cancer difficult to treat but also pose several challenges in studying the development, progression, and treatment of pancreatic tumors in vivo (*25*–*27*). While major advancements in genetically engineered mouse models (GEMMs) (*28*, *29*) and genomics (*30*) have been used to improve our knowledge of pancreatic tumor biology, current preclinical research methodologies are still limited in their ability to study the dynamic changes of the pancreatic TME in the in vivo, orthotopic setting. Conventional murine–based studies of pancreatic cancer largely rely on resected tumor tissue specimens collected at fixed time points from euthanized mice. While such an approach enables detailed examination of histological and immunohistological tumor features and their spatial variation under various experimental conditions, it lacks temporal information within the same mouse. This experimental limitation inhibits our understanding of the biological and treatment-induced spatiotemporal changes affecting pancreatic tumors, as well as their supporting vasculature and TME. Previously, some approaches have used ultrasound and magnetic resonance imaging to study changes in bulk properties, e.g., tumor volume and perfusion, of pancreatic tumors in the same animal serially over time (*31*). However, these methods lack the spatial resolution required to visualize the distinct heterogeneity of tumor cells, stroma, microvasculature, and hypoxia in pancreatic tumors at a cellular level in vivo.

To overcome these challenges, we designed and surgically implanted a pancreatic imaging window (PIW) to perform intravital fluorescence microscopy (IVFM) in an orthotopic mouse model of pancreatic cancer. Using this technique, we were able to directly image pancreatic cancer cells and their TME at cellular resolution, within the same animal, for up to 4 weeks. Using a dually fluorescent human pancreatic cancer cell line, we demonstrate that it is possible to visualize DsRed fluorescent pancreatic tumor cells together with a HIF-driven green fluorescent protein (GFP) reporter in vivo and quantitatively validate this GFP fluorescence as an in vivo biomarker of pancreatic tumor cell hypoxia. We also use allophycocyanin (APC)–conjugated anti-CD31 fluorescent dye and second harmonic generation (SHG) microscopy to simultaneously image tumor microvasculature and collagen structures in the stromal compartment and quantitatively characterize their spatial relationship with tumor cell HIF activity in vivo. Overall, our findings elucidate an intricate relationship between tumor hypoxia, microvasculature, and collagen structures within the pancreatic TME. Future studies with our in vivo IVFM model can be designed to

[1]Princess Margaret Cancer Centre, University Health Network, Toronto, Canada. [2]Department of Medical Biophysics, University of Toronto, Toronto, Canada.
*Corresponding author. Email: ralph.dacosta@uhnresearch.ca

further explore these complex relationships sustaining pancreatic tumor development and explore mechanisms of treatment resistance to help develop more effective treatment strategies and improve outcomes of pancreatic cancer.

RESULTS

BxPC3 5xHRE/GFP expression is driven by hypoxia in vitro

In vitro live-cell fluorescence microscopy was performed daily (for up to 4 days) to investigate the time course of BxPC3 tumor cell 5xHRE (5x hypoxia-response element)/GFP expression under 0.2, 1, and 21% O_2. We found that, for both 0.2 and 1% O_2, tumor cell GFP expression rose gradually over the course of 4 days, with the fastest rise occurring under 0.2% O_2 (Fig. 1C). Cells that were returned to normoxia (21% O_2) after 3 days in 0.2% O_2 returned to baseline GFP fluorescence within 1 day. By performing hourly time-lapse imaging on cells that were kept under 0.2% O_2 for 3 days and subsequently returned to 21% O_2, we found that tumor cell GFP fluorescence intensity had a half-life of approximately ~2 hours, returning to baseline values within 8 to 12 hours (Fig. 1D). Because cellular GFP synthesis is known to be oxygen dependent (*32*), Western blots were also performed to confirm GFP expression (Fig. 1E). Quantitative densitometric analysis of BxPC3-DsRed-5xHRE/GFP cell lysates demonstrated a similar trend, with GFP expression rising gradually over the course of 4 days under 0.2% O_2 (Fig. 1F). However, for cells that were kept under 0.2% O_2 for 3 days and subsequently returned to 21% O_2 for 1 day ("3 + 1R"), GFP was still detected (although not statistically significant, $P = 0.84$). Only after exposing cells to 2 days under 0.2% O_2 followed by 2 days under 21% O_2 ("2 + 2R") did GFP expression return to baseline levels ($P > 0.99$).

In vivo BxPC3 5xHRE/GFP fluorescence increases with distance from tumor blood vessels

To investigate BxPC3 5xHRE/GFP fluorescence, in vivo IVFM was performed by combining an orthotopic mouse model of pancreatic cancer with a custom-designed PIW (Fig. 2). Using this animal model, we were able to serially and simultaneously visualize BxPC3 cells (DsRed), BxPC3 HIF activity (5xHRE/GFP), blood vessels (APC-CD31), and fibrillar collagen (SHG) in real time, at cellular resolution (Figs. 3 and 4). To understand how blood vessel density affected 5xHRE/GFP expression in our tumor model, we decided to investigate this relationship across all images that were taken ($n = 861$). From these data, we found a negative correlation between tumor vascular density and GFP-positive fraction of tumor regions of interest (ROIs) [correlation coefficient (r) = −0.39, $P < 0.0001$; Fig. 5B]. By analyzing the distance of each tumor cell to the nearest blood vessel and aggregating these values across all tumor ROIs (n = 1,783,797 cells), we found a positive relationship between each tumor cell's GFP fluorescence intensity and its distance to the nearest blood vessel ($r = 0.48$, $P < 0.0001$). This was visualized using a bivariate histogram (Fig. 5C) with the probability of each tumor cell's GFP fluorescence intensity increasing with its distance to the nearest blood vessel. "Low" GFP fluorescence intensity (empirically determined to be below background fluorescence) was largely localized to distances less than 100 μm, while "high" GFP fluorescence intensity was localized to distances greater than 100 μm (Fig. 5D).

BxPC3 5xHRE/GFP expression colocalizes with histological markers of tumor hypoxia

The correlation between BxPC3 cell 5xHRE/GFP expression and other known biomarkers of tumor hypoxia [pimonidazole and carbonic anhydrase IX (PIMO and CA9, respectively)] was assessed using 10 different ex vivo tumor samples, each serially sectioned (5 μm thick) and immunofluorescence-stained against GFP, PIMO, and CA9 (Fig. 6A). Pixel intensity–based colocalization analysis (*33*, *34*) across each of these tumor sections found that anti-GFP stain fluorescence intensity had the strongest correlation with anti-CA9 stain fluorescence intensity, with a mean Pearson $\overline{r}$ of 0.84 (SD = 0.09). Anti-PIMO and anti-GFP stains had an $\overline{r}$ of 0.74 (SD = 0.09), while anti-PIMO and anti-CA9 stains had an $\overline{r}$ of 0.66 (SD = 0.13) (Fig. 6B).

Intravital 5xHRE/GFP fluorescence is representative of tumor hypoxic fraction

To assess whether BxPC3 5xHRE/GFP fluorescence intensity measured using IVFM is representative of hypoxia throughout the tumor, we compared the mean tumor cell GFP fluorescence intensity in vivo (using IVFM) to the tumor hypoxic fraction from 11 different tumors, immunofluorescence-stained for both PIMO and CA9 (Fig. 6C). The mean in vivo GFP fluorescence intensity from IVFM was found to strongly correlate with the positive ex vivo stain fraction of PIMO ($r = 0.89$, $P = 0.0003$) and CA9 ($r = 0.88$, $P = 0.0003$). These relationships indicate that the mean BxPC3 5xHRE/GFP fluorescence intensity is representative of hypoxia throughout the tumor.

Relationship between BxPC3 5xHRE/GFP fluorescence and tumor-associated fibrillar collagen

To investigate the relationship between 5xHRE/GFP fluorescence and tumor-associated collagen in our BxPC3 tumor model, fibrillar collagen structures were visualized using in vivo SHG microscopy and analyzed along the tumor-collagen interface. A circular, moving "peritumoral ROI" with a diameter of 100 μm was used to compare local GFP fluorescence intensity with three different collagen features: mean SHG intensity, collagen fiber alignment, and collagen orientation (relative to the tumor edge) (Fig. 7A). By aggregating these measurements for all peritumoral ROIs across all images ($n = 6846$), we found a weak positive correlation between the mean GFP fluorescence intensity and mean SHG intensity ($r = 0.21$, $P < 0.0001$; Fig. 7B). Peritumoral ROIs with a high mean SHG intensity were found to have significantly higher mean GFP fluorescence intensity than peritumoral ROIs with a low mean SHG intensity (12.50 versus 7.50, $P < 0.0001$; Fig. 7C). GFP fluorescence intensity was also found to have a weak positive Pearson r with alignment score of collagen fibers ($r = 0.09$, $P < 0.0001$; Fig. 7D). Peritumoral ROIs with a high alignment score were found to have a higher mean GFP fluorescence intensity than peritumoral ROIs with a low alignment score (10.57 versus 8.63, $P < 0.0001$; Fig. 7E). Last, GFP fluorescence intensity was found to have a weak negative correlation with the orientation of collagen fibers relative to the tumor edge ($r = -0.05$, $P < 0.05$; Fig. 7F). Peritumoral ROIs where collagen fibers were perpendicular to the tumor edge were found to have a lower mean GFP intensity than peritumoral ROIs with collagen fibers running parallel to the tumor edge (10.96 versus 9.82, $P < 0.0001$; Fig. 7G).

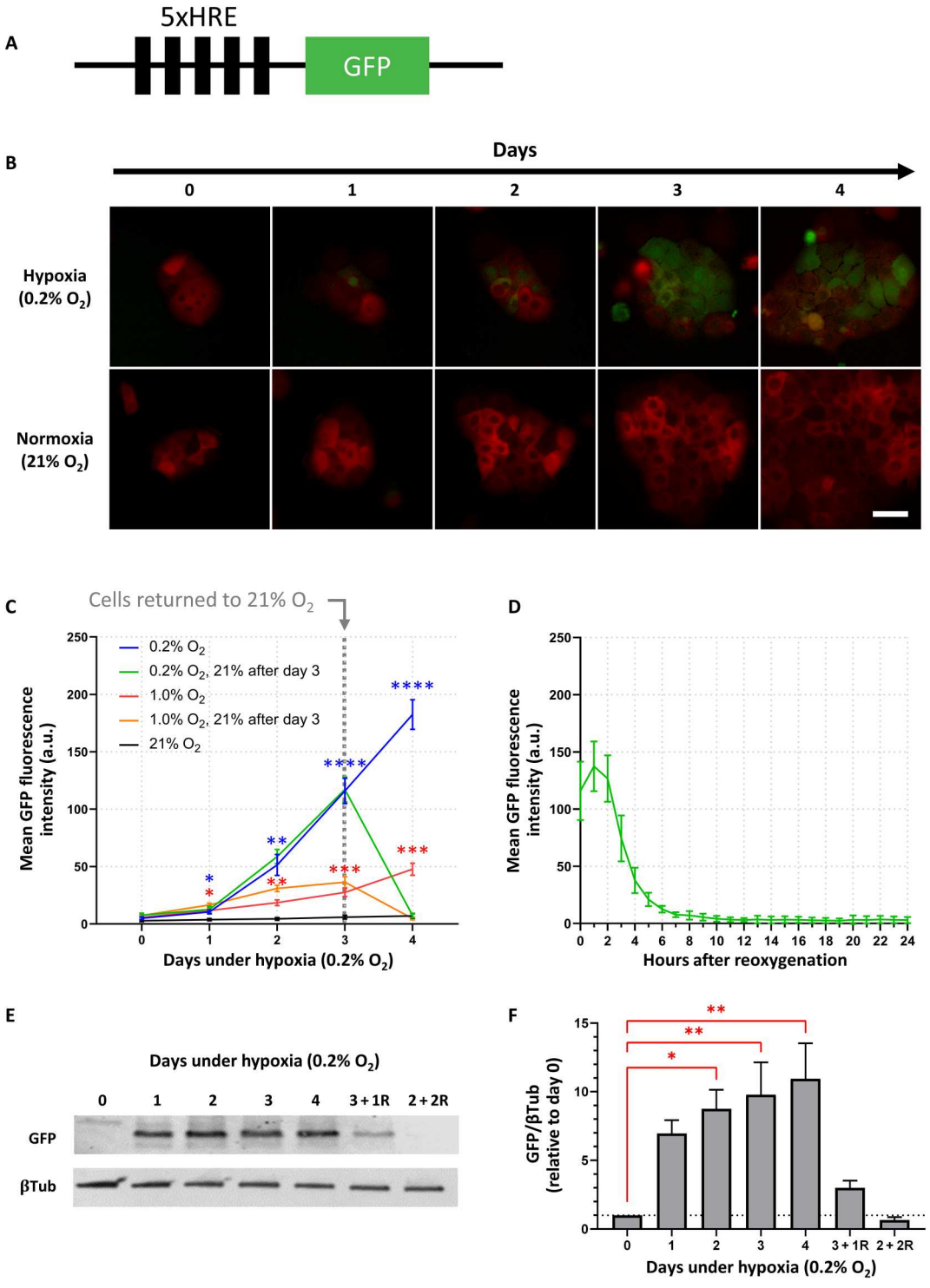

Fig. 1. Hypoxia drives 5xHRE-induced GFP expression in BxPC3-DsRed-5xHRE/GFP cells. (**A**) Schematic of 5xHRE/GFP construct. (**B**) Representative images of BxPC3-DsRed-5xHRE/GFP cells growing under hypoxia (0.2% O_2) and normoxia (21% O_2) using in vitro live-cell fluorescence microscopy. Scale bar, 50 μm. (**C**) Quantification of GFP fluorescence intensity at 0.2, 1, and 21% O_2. The green and orange lines indicate cells returned to 21% O_2 between days 3 and 4. $n = 9$ replicates per group. (**D**) Hourly time lapse of the mean GFP fluorescence intensity after BxPC3-DsRed-5xHRE/GFP cells (previously incubated under 0.2% O_2 for 3 days) were transferred to 21% O_2 confirms the oxygen dependence of 5xHRE/GFP construct. $n = 9$ replicates per group. a.u., arbitrary units. (**E**) Western blot and (**F**) densitometric analysis of GFP expression [relative to β-tubulin (βTub)] after various time durations under 0.2% O_2. Columns labeled with letter "R" indicate the number of days cells were reoxygenated at 21% O_2 before protein collection. Data were obtained from three independent experiments. *$P < 0.05$, **$P < 0.01$, ***$P < 0.001$, and ****$P < 0.0001$.

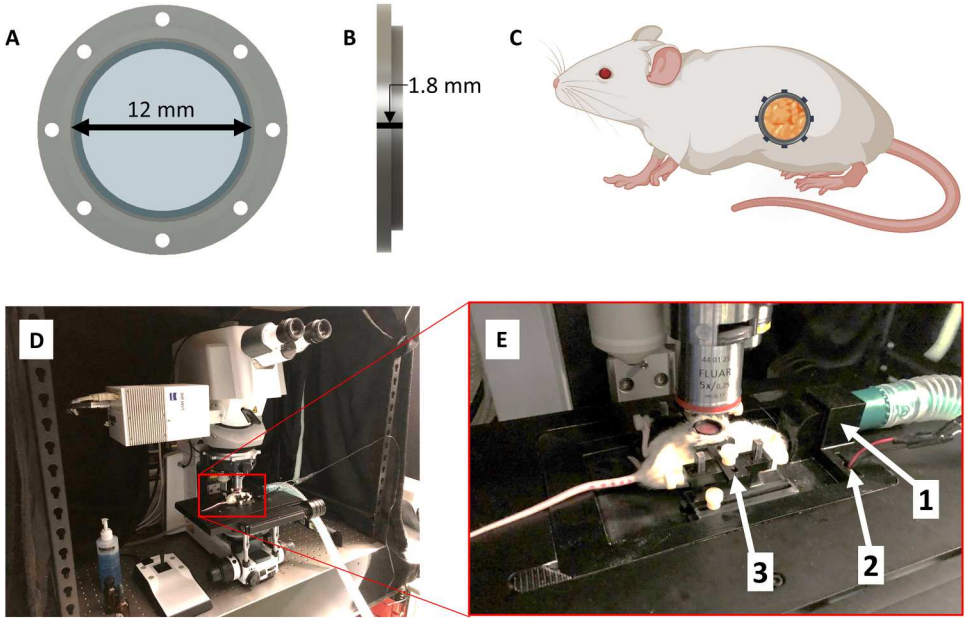

Fig. 2. Surgically implanted abdominal imaging window allows longitudinal intravital imaging of pancreatic tumors in vivo. (**A** and **B**) Computer-aided design of an abdominal PIW frame holding a circular glass coverslip (12 mm diameter). (**C**) Diagram of a mouse (using BioRender.com) indicating the anatomical location of the surgically implanted PIW, providing longitudinal imaging access to the pancreas in vivo. (**D**) Photo of the laser scanning confocal microscope with (**E**) a custom-designed, three-dimensionally (3D) printed stage insert to stabilize the animal for anesthesia and imaging. The stage is equipped with (1) a gas anesthesia port, (2) an electrical heating element, and (3) a holder to minimize motion artifacts during imaging and produce consistent images.

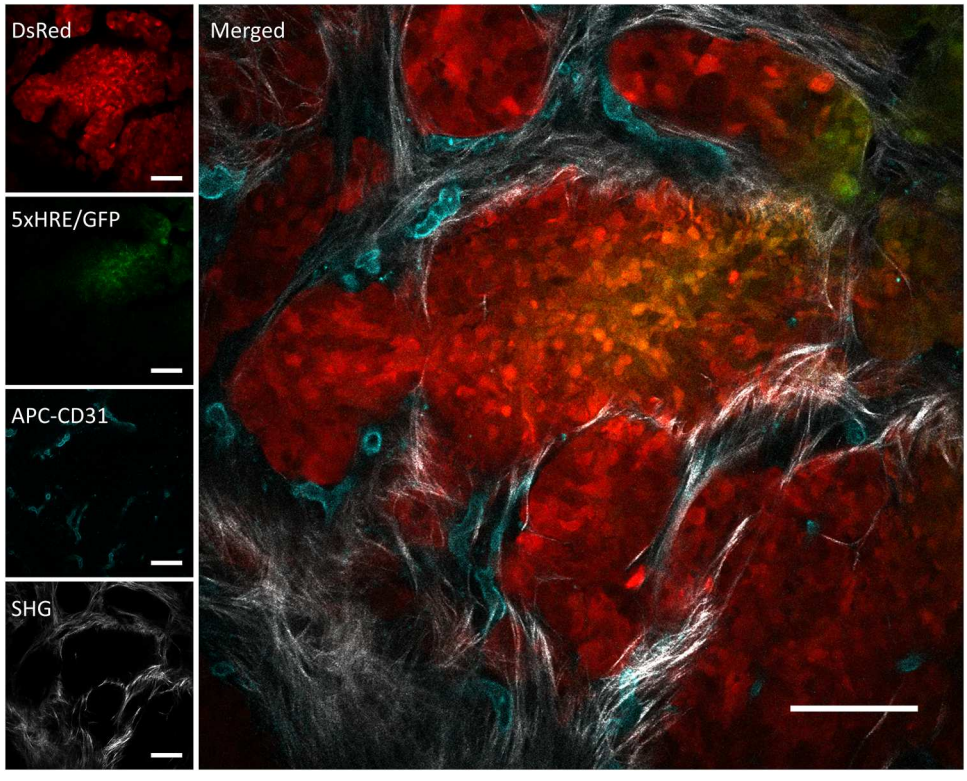

Fig. 3. A representative image of an in vivo orthotopic BxPC3-DsRed-5xHRE/GFP tumor foci, taken using intravital fluorescence and SHG microscopy. BxPC3 cells (DsRed) are shown in red, HIF activity (5xHRE/GFP) in green, blood vessels (APC-CD31) in cyan, and fibrillar collagen (SHG) in white. Scale bars, 100 μm.

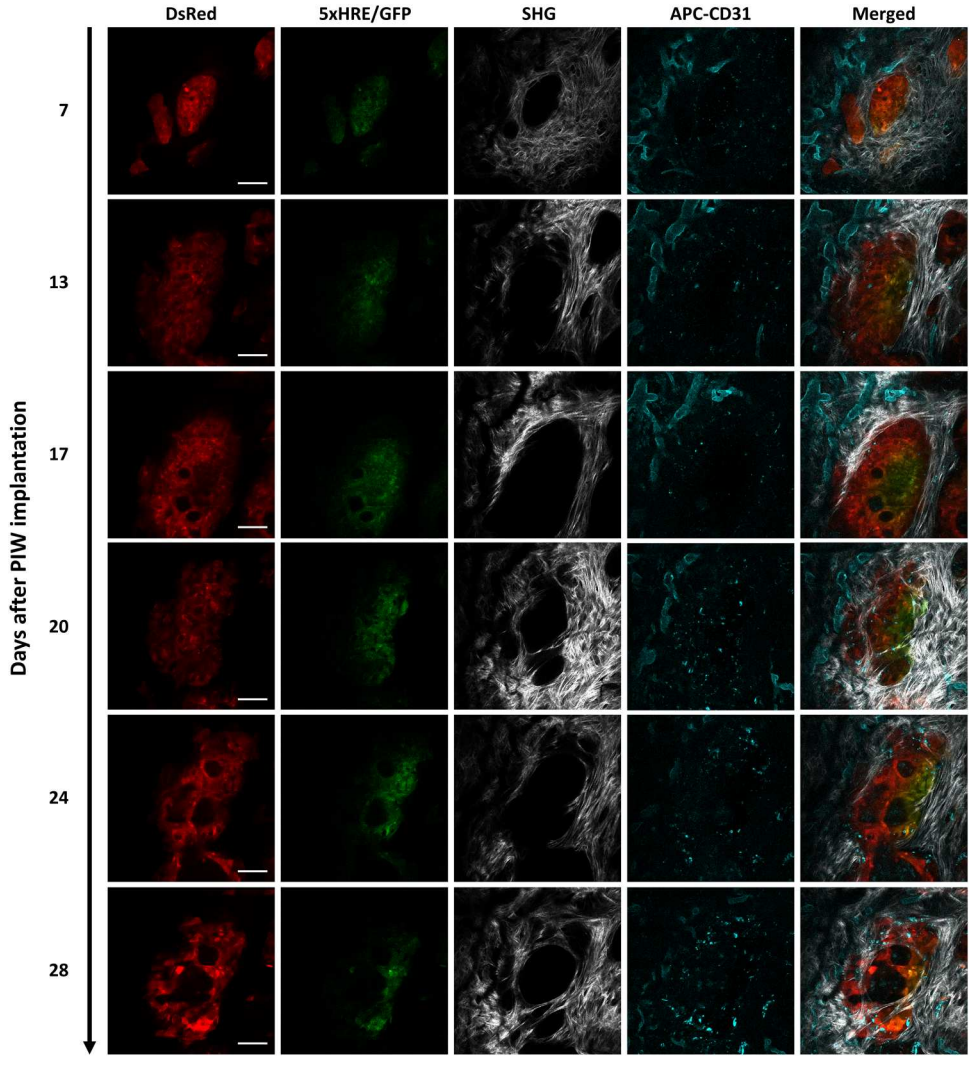

Fig. 4. Longitudinal intravital images of an orthotopic BxPC3-DsRed-5xHRE/GFP tumor region of interest (ROI), up to 28 days after PIW implantation. BxPC3 cells (DsRed) are shown in red, HIF activity (5xHRE/GFP) in green, blood vessels (APC-CD31) in cyan, and fibrillar collagen (SHG) in white. Scale bars, 100 μm.

DISCUSSION

The pancreatic TME is characterized by hypoxia and desmoplasia, both of which play a major role in affecting treatment response (*9*–*13*). Accumulating evidence suggests that understanding the complex interactions between components of the pancreatic TME is necessary to identify new therapeutic targets and improve treatment strategies (*35*). However, there are several challenges in studying these interactions in vivo due to substantial heterogeneity, both within the TME and between different tumor samples (*25*–*27*). In addition, the pancreatic TME is constantly changing in composition and structure as cancer cells proliferate and invade the surrounding tissues (*25*) and in response to therapeutic interventions (e.g., chemo- and radiotherapy) (*36*). While preclinical studies are invaluable in studying how the pancreatic tumors respond to therapy, existing in vivo animal models of pancreatic tumors are limited. In this study, we undertook the development and validation of a novel intravital imaging model to study pancreatic tumors in vivo and quantitatively image tumor cells, stroma, microvasculature, and hypoxia simultaneously and in real time within the pancreatic TME.

To reliably monitor tumor cell hypoxia in vivo, we developed a dually fluorescent BxPC3-DsRed-5xHRE/GFP cell line. This human pancreatic cancer cell line constitutively expresses red fluorescent protein (DsRed) and GFP, the latter being driven by the 5xHRE/GFP reporter under hypoxia. It should be noted, however, that this model does not directly measure partial pressure of oxygen (or pO_2) but rather the tumor cell transcriptional response to hypoxia in the microenvironment, characterized by increased tumor cell HIF activity. While it is well established in the literature that HIFs drive cellular protein expression under hypoxic conditions by binding to the HRE promoter (*37*), the time scale of different HIF transcription complexes (e.g., HIF-1 and HIF-2) in regulating cellular hypoxic response is an active area of investigation (*38*). Nevertheless, using in vitro live-cell fluorescence microscopy (Fig. 1B), we confirmed that 5xHRE/GFP is a sensitive and reliable fluorescent marker of BxPC3 cell hypoxia and was tested in cell culture for up to 4 days under 0.2, 1, and 21% O_2. Our data show

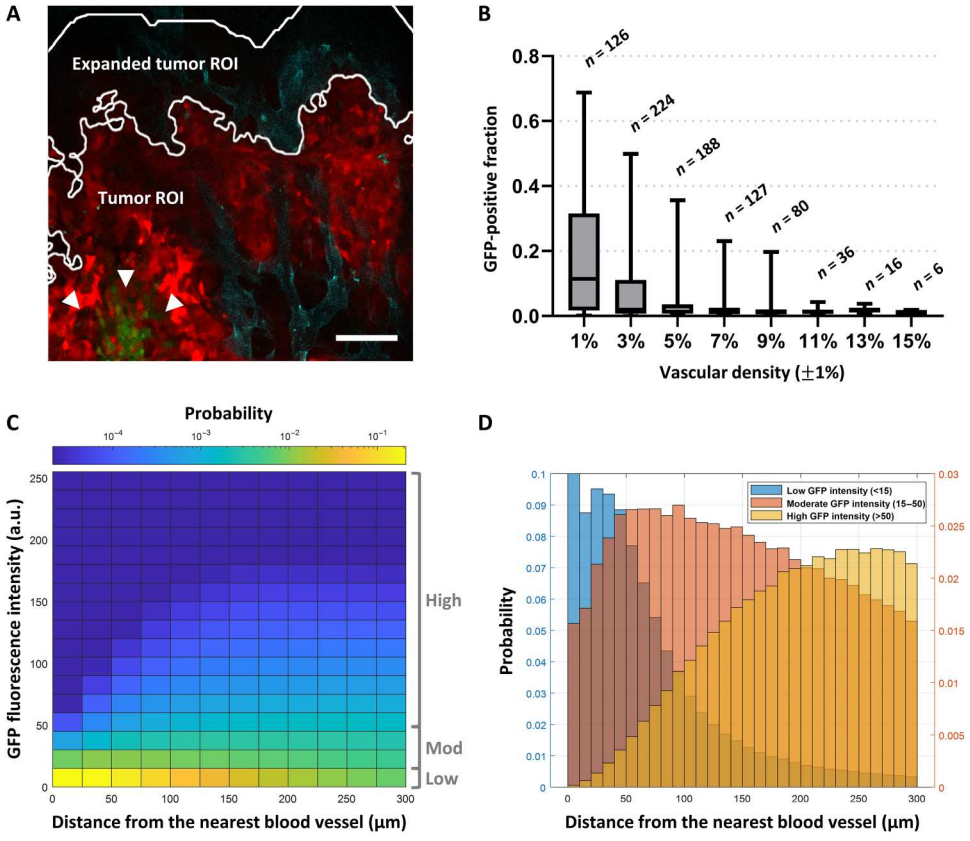

Fig. 5. Quantitative intravital fluorescence imaging reveals an inverse relationship between tumor cell 5xHRE/GFP expression and vascular density. (**A**) An example intravital fluorescence image shows BxPC3-DsRed cells in red, GFP fluorescence (HIF activity) in green (arrowheads), and APC-CD31 (blood vessels) in cyan. The tumor ROI outlines the analysis region for BxPC3-DsRed–positive tumor pixels. The expanded tumor ROI outlines a concentric analysis region, expanded radially by 100 μm, to include blood vessels along the tumor periphery. Scale bar, 100 μm. (**B**) Aggregate data from 861 intravital fluorescence images (2429 μm by 2429 μm) of BxPC3 tumors in vivo show an inverse relationship between tumor vascular density (%) and GFP-positive fraction of tumor ROIs. $r = -0.39$, $P < 0.0001$. (**C**) A bivariate probability histogram from aggregate tumor cell fluorescence data reveals a positive relationship between BxPC3 GFP fluorescence intensity and distance to the nearest blood vessel ($r = 0.48$, $P < 0.0001$). Bins are colored from blue to yellow, indicating low to high probability within the dataset, respectively. (**D**) Grouping BxPC3 GFP fluorescence intensity ("low," "moderate," and "high") demonstrates its relationship with the distance of the BxPC3 tumor cells to the nearest blood vessel. Probabilities for low GFP intensity are plotted on the left *y* axis, and probabilities for moderate/high GFP intensity are plotted on the right *y* axis.

that HRE-driven GFP fluorescence intensity increases with both the duration and severity of low oxygen conditions, although this reporter may not be able to distinguish between severe, acute hypoxia and moderate, chronic hypoxia. We also show that this fluorescent reporter is reversible, with GFP fluorescence intensity returning to baseline levels within 8 to 12 hours of reoxygenation (half-life of ~2 hours; Fig. 1D). GFP was still detected using Western blot for up to 2 days after reoxygenation (Fig. 1, E and F), which is consistent with the previously reported degradation half-life of GFP (approximately 26 hours) (*39*). The difference between these two measurements is likely due to the fact that fluorescence imaging can only detect mature GFP, while Western blot assay can detect both premature and mature GFP (*40*). It is also possible that the GFP fluorescence intensity in tumor cells decreased at a faster rate than the previously reported degradation half-life of GFP due to proteins being diluted through cell division (*41*). Nevertheless, the temporal behavior of BxPC3 cell 5xHRE/GFP fluorescence suggests that fluorescence microscopy is a suitable technique for detecting cells undergoing chronic hypoxia (on the order of hours to days).

To validate the expression of 5xHRE/GFP as a marker of BxPC3 tumor cell hypoxia in vivo, we performed immunofluorescence staining on 10 individual BxPC3 tumor samples to correlate GFP expression with conventional markers of tumor hypoxia (i.e., PIMO and CA9). It is well established that hypoxic conditions in tumor cells induce CA9 expression through the HIF transcription factor, which binds to the HRE site in the CA9 promoter (*42*, *43*). Because 5xHRE/GFP and CA9 are driven by the same promoter, it is not unexpected that their cellular expression is strongly correlated with one another, with a mean Pearson $\bar{r}$ of 0.84 (SD = 0.09) across 10 tumor samples. The weaker correlations measured between 5xHRE/GFP and PIMO ($\bar{r} = 0.74$, SD = 0.11) and CA9 and PIMO ($\bar{r} = 0.67$, SD = 0.13) are likely due to the differences in each marker's sensitivity to low oxygen conditions. PIMO is typically reduced at oxygen tensions less than 10 mmHg (~1% O_2) (*44*), while CA9 is generally expressed at oxygen tensions less than 20 mmHg (~3% O_2) (*45*). Because CA9 has a higher oxygen threshold than PIMO, it is not unexpected that we observed CA9 staining closer to tumor blood vessels (Fig. 6A). The differences in oxygen sensitivity between these markers, although subtle, can be used to

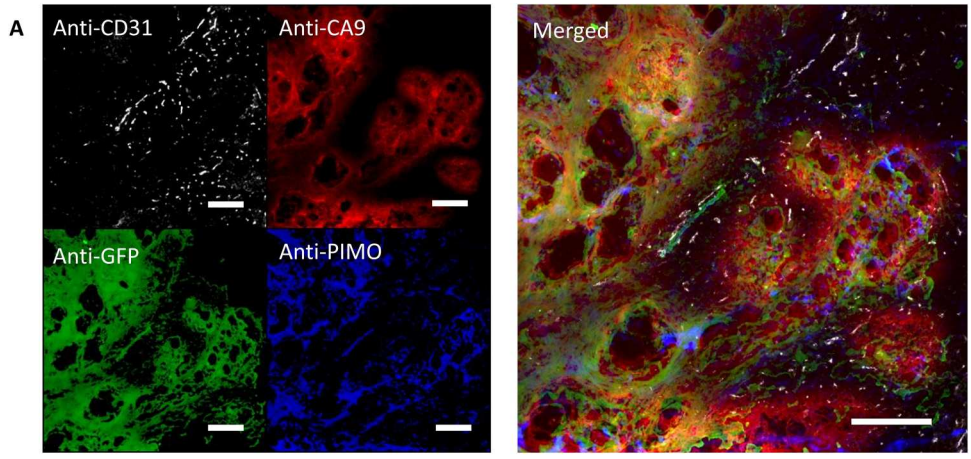

B

Pearson correlation matrix

	Anti-GFP	Anti-CA9
Anti-PIMO	0.74 ± 0.11	0.67 ± 0.13
Anti-CA9	0.84 ± 0.09	

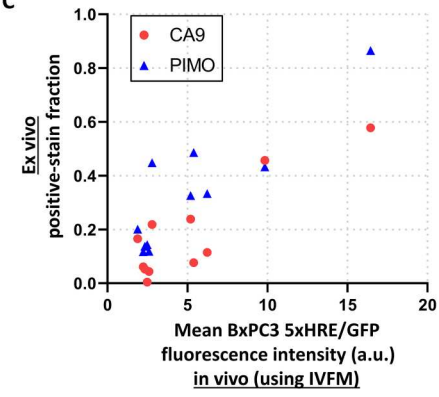

Fig. 6. In vivo expression of 5xHRE/GFP in BxPC3 tumor cells correlates with conventional biomarkers of tumor hypoxia. (**A**) Representative immunofluorescence (IF) images from serial BxPC3 pancreatic tumor tissue sections (5 μm thick). Tumors were excised immediately after the final in vivo imaging time point. Sections were stained with anti-CD31, anti-CA9, anti-GFP, and anti-PIMO. Scale bars, 200 μm. (**B**) A correlation matrix shows the mean Pearson correlation coefficients between each IF stain, across 10 tumor samples (± SD). (**C**) A scatter plot shows the relationship between the hypoxic biomarker (CA9 and PIMO) IF positive-stain fraction in ex vivo tumor tissue sections versus the mean GFP fluorescence intensity of the same tumors in vivo, using IVFM. $r = 0.88$ ($P = 0.0003$) and 0.89 ($P = 0.0003$), respectively. $n = 11$ tumors.

measure the relative severity of tumor hypoxia. Healthy tissue oxygen levels range between 3 and 7% O_2 (*46*). Once oxygen falls below this range [termed "physiological hypoxia"; (*47*)], several physiological processes begin to respond to maintain oxygen homeostasis, e.g., vasodilation, increasing blood flow, and up-regulation of hypoxia response genes (primarily driven by HIF) (*48*). "Pathological hypoxia," defined as oxygen levels below 8 mmHg (1% O_2) (*47*), suggests a disruption to normal oxygen homeostasis resulting in the persistence of poor oxygenation. While PIMO is a more suitable marker for pathological hypoxia in tissues and, as an exogenous molecule, provides more dynamic measurements of pO_2 (*49*), it does not provide any information regarding each tumor cell's biological response to hypoxia. In contrast, endogenous biomarkers CA9 and 5xHRE/GFP provide direct measurements of the cellular transcriptional response to hypoxia, and we have shown in vitro that tumor cell GFP expression responds dynamically to changing oxygen conditions (Fig. 1C). Future studies should explore the dynamics of tumor cell 5xHRE/GFP expression in experimental orthotopic tumors using compounds such as carbogen and hydralazine to modulate tumor hypoxia in vivo in mice (*49*). Nevertheless, the data presented here demonstrate that 5xHRE/GFP expression can measure the relative magnitude of hypoxic stress experienced by BxPC3 tumor cells in vivo.

Within the pancreatic TME, the lack of functional vasculature plays an important role in the establishment and sustained presence of tumor hypoxia (*50*). Using IVFM, we observed an inverse relationship between the vascular density and the hypoxic (GFP-positive) fraction of BxPC3 cells ($r = -0.39$, $P < 0.0001$; Fig. 5B). This is not unexpected because hypovascular tumor regions typically have less access to oxygen, making cells more susceptible to hypoxic stress (*50*, *51*). Furthermore, we demonstrate the spatial relationship between blood vessels and BxPC3 HIF activity by analyzing the distance transform of tumor blood vessels to tumor cells (Fig. 5, C and D). We consistently observed a spatial gradient of BxPC3 5xHRE/GFP fluorescence intensity that increases with the distance of the BxPC3 cells from blood vessels ($r = 0.48$, $P < 0.0001$). This is consistent with previously observed "hypoxia gradients" in tumor tissues (*52*, *53*). However, given that our study analyzed intravital images from specific ROIs, we may have excluded blood vessels outside the field of view and optical depth of field. Thus, it is possible that our BxPC3 cell distance–to–nearest blood vessel measurements overestimated the actual Euclidean distance between pancreatic tumor cells and their nearest blood vessel. In addition,

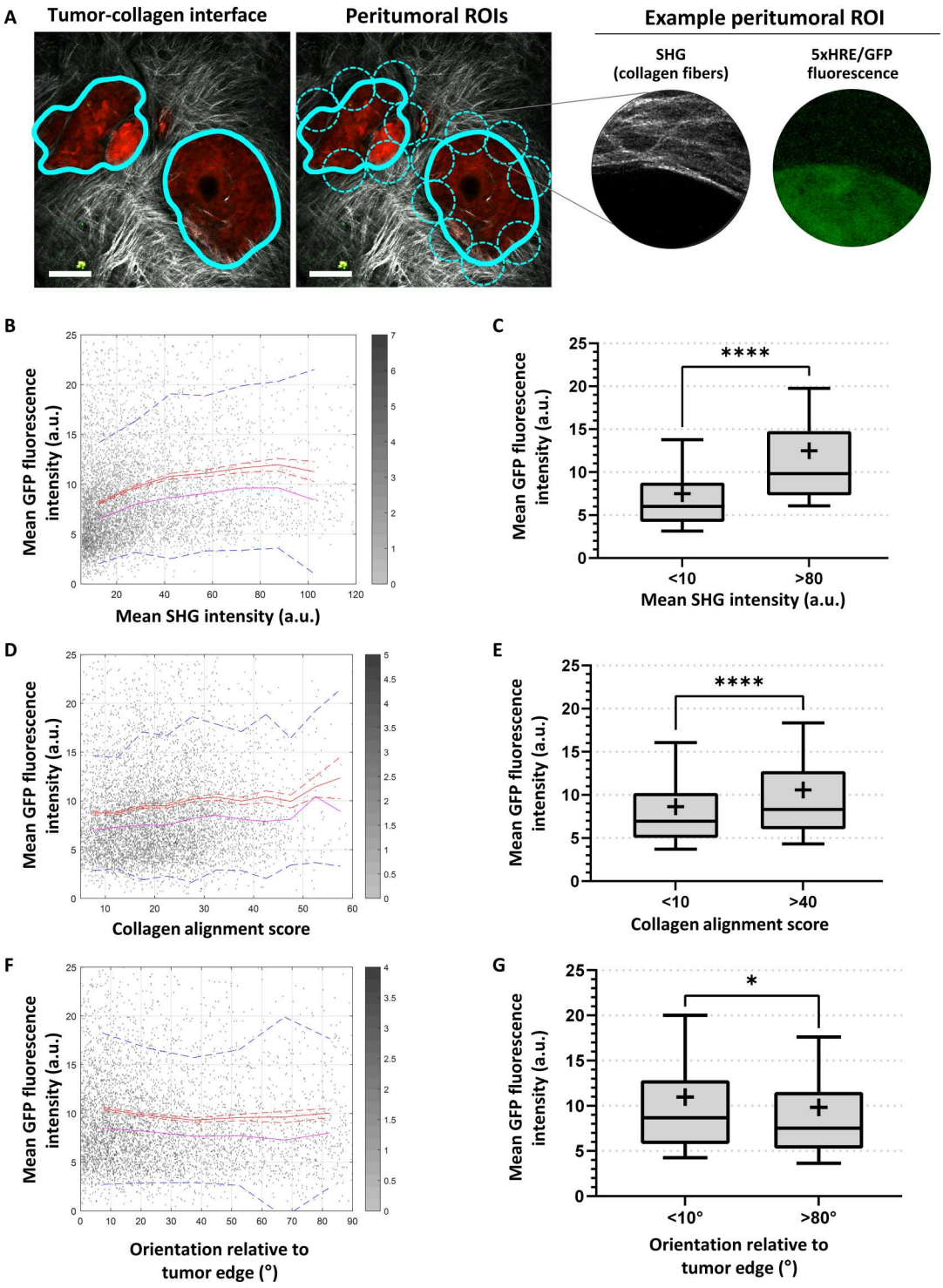

Fig. 7. Peritumoral collagen production is associated with BxPC3 5xHRE/GFP expression. (**A**) Image analysis framework used to analyze collagen and BxPC3 5xHRE/GFP expression along the tumor-collagen interface (thick cyan line). Dashed cyan circles indicate each peritumoral ROI, with a diameter of 100 μm, spaced 100 μm apart. Scale bars, 100 μm. (**B**, **D**, and **F**) Scatter plots show the mean GFP fluorescence intensity versus mean SHG intensity ($r = 0.21$, $P < 0.0001$), alignment score ($r = 0.09$, $P < 0.0001$), and orientation relative to tumor edge ($r = -0.05$, $P < 0.0001$), respectively. $n = 6846$. The red lines indicate mean values, red dashed lines are SEM, pink lines are median values, and blue dotted lines show SD. (**C**, **E**, and **G**) Box plots show the mean GFP fluorescence intensity of BxPC3 cells for different ranges of SHG intensity, alignment score, and collagen orientation relative to tumor edge, respectively. Mean values are indicated by the "+" symbol on each boxplot. Whiskers show 10th to 90th percentile of mean GFP fluorescence intensity in peritumoral ROIs. *$P < 0.05$ and ****$P < 0.0001$.

because the microvasculature of tumors is known to be irregular and dysfunctional (*54*, *55*), the presence of blood vessels in the fluorescence images may not necessarily mean that sufficient levels of oxygen are being delivered to those tissues. Nevertheless, this intravital imaging model can be used to measure oxygen diffusion gradients in pancreatic tumors in vivo and potentially study its effects on tumor progression. Oxygen gradients have been shown to influence macrophage recruitment, which plays a critical role in cancer progression (*56*). In addition, the slope of the spatial oxygen diffusion gradient (as a function of distance from blood vessels; Fig. 5, C and D) may be used to study changes in metabolic oxygen consumption rates (*53*) of cancer cells over time or in response to treatment (such as radiotherapy). For example, shorter oxygen gradients from blood vessels could indicate that tumor cells may have higher oxygen consumption (*57*) and are actively proliferating. Longer oxygen gradients may indicate that the cancer cells have lower oxygen consumption rates, becoming tolerant to hypoxia in the TME, affecting overall malignancy and treatment efficacy (*58*, *59*). Thus, our quantitative intravital imaging model may serve as a platform for future investigation of tissue oxygen gradients within the pancreatic TME and their spatiotemporal relationship to tumor blood vessels, immune cells (e.g., macrophages), and cellular oxygen consumption rates in vivo.

Clinical findings indicate that one of the most prominent features of pancreatic tumors is their highly desmoplastic TME (*25*, *35*, *60*, *61*). This desmoplasia creates a physical barrier around the tumor (*35*), which can alter blood flow resulting in hypoxia (*62*), decreased drug delivery (*16*), and immune infiltration (*63*), ultimately increasing resistance to chemotherapy (*16*), radiotherapy (*64*, *65*), anti-angiogenic therapy (*66*), and immunotherapy (*63*). Previous studies have shown that pancreatic tumor–associated collagen can induce tumor hypoxia and vice versa (*21*). Using our model, we can image tumor-associated collagen in vivo using intravital SHG microscopy. By analyzing fibrillar collagen surrounding the tumor from SHG images, we found a weak positive relationship between the mean 5xHRE/GFP fluorescence intensity of tumor cells and mean SHG intensity ($r = 0.21$, $P < 0.0001$; Fig. 7). These findings are consistent with previous studies showing that tumor-associated collagen coincides with hypoxic regions within tumors (*50*, *67*–*69*). Several studies have demonstrated that hypoxia modifies tumor ECM components, increasing collagen deposition in the TME as well as ECM density and stiffness (*70*–*72*). Both cancer cells and cancer-associated fibroblasts are known to contribute to ECM remodeling in response to hypoxia (*72*, *73*). Conversely, a desmoplastic stroma contributes to tumor hypoxia by displacing capillaries with high amounts of ECM, further reducing the supply of oxygen and perpetuating a cycle leading to even more hypoxia and metabolic stress (*20*, *74*–*78*). Nevertheless, there is still controversy in the literature about whether the fibrotic reaction in the pancreatic TME ultimately promotes or inhibits disease progression (*24*, *79*). Our model may facilitate the study of the dynamic interactions between tumor hypoxia and desmoplasia and how this relationship affects tumor growth, metastasis, or treatment response.

In addition to an increase in collagen production in the TME, the spatial alignment of collagen fibers around the tumor was also found to be related to BxPC3 5xHRE/GFP fluorescence intensity ($r = 0.09$, $P < 0.0001$; Fig. 7, D and E). This relationship is consistent with previous studies showing that, through multiple mechanisms, hypoxic fibroblasts generate and organize highly aligned ECM (*80*–*82*). However, given that the relationship between hypoxia and collagen alignment was relatively weak in our dataset, it is still unclear what other factors contribute to collagen alignment in the pancreatic TME and how this ultimately affects disease progression. Drifka *et al.* (*83*) have shown that spatially aligned stromal collagen is a negative prognostic factor in pancreatic cancer, associated with poor survival. In contrast, Bolm *et al.* (*84*) have shown that pancreatic tumors with randomly oriented stromal fibers were associated with larger tumor size, nodal-positive disease, margin-positive resection rates, and poorer overall survival. This inconsistency in the literature suggests that a more detailed, mechanistic understanding is needed to uncover how the spatial alignment of collagen fibers in the pancreatic TME affects tumor progression. Using our intravital model of pancreatic cancer, we can continue to explore what factors contribute to collagen fiber alignment and how this may have downstream effects on pancreatic tumor growth, remodeling of the TME, and metastasis.

We also found that collagen fibers oriented parallel (<10°) to the tumor boundary were weakly associated with increased local BxPC3 5xHRE/GFP fluorescence intensity, especially when compared to tumor regions with collagen fibers oriented perpendicular (>80°) to the tumor boundary (Fig. 7G). Collagen fiber orientation has been previously shown to steer both angiogenesis and endothelial cell migration (*85*, *86*). Thus, it is possible that radially oriented collagen fibers (perpendicular to the tumor boundary) may allow blood vessels to more easily migrate into the tumor and increase tumor oxygenation. Emerging evidence suggests that radially oriented collagen fibers can also provide avenues for tumor cells to invade the surrounding tissues to escape their hostile microenvironment (*87*). Conversely, tangentially oriented collagen fibers (parallel to the tumor boundary) may be confining tumor cells as they continue to proliferate, causing an increase in solid stress and interstitial fluid pressure (*88*, *89*). As desmoplasia progresses in pancreatic tumors, an increase in solid stress can contribute to reduced vascular patency along the tumor boundary, leading to increased tumor hypoxia (*77*, *90*). This leads to a vicious cycle—whereby tumor growth leads to solid stress, solid stress leads to hypoxia, hypoxia leads to collagen remodeling (*91*), and collagen remodeling influences angiogenesis and tumor cell invasion—further driving tumor growth and disease progression. Remodeling of the tumor ECM along the tumor boundary is an ongoing and dynamic process (*92*). Future studies can potentially benefit from using our pancreatic intravital imaging model to study the relationship between tumor hypoxia and ECM remodeling, which collectively influence tumor cell invasion and metastasis (*80*). The successful development of novel treatments targeting the TME stromal compartment depends on a more complete understanding of these tumor-stromal interactions.

Together, this study presents a key advancement over conventional methodologies of studying the pancreatic TME and previously adopted methods of intravital imaging in pancreatic tumor models. By combining multispectral IVFM and SHG microscopy with a custom-desigend, surgically implanted imaging window, we were able to consistently and simultaneously image pancreatic cancer cells, tumor microvasculature, and fibrillar collagen at cellular resolution in vivo, for up to 4 weeks. We also developed and validated a novel, dually fluorescent pancreatic DsRed-5xHRE/GFP reporter cell line for real-time monitoring of tumor hypoxia in the orthotopic setting. In this study, we used the 5xHRE/GFP

reporter to quantify tumor cell hypoxia and hypoxic gradients in the orthotopic in vivo tumor setting and postulated a potential means of measuring oxygen consumption rates of tumor cells relative to tumor microvasculature. Last, we used this model to quantify the spatial relationship between tumor cell hypoxia and tumor-associated collagen structures and hypothesized potential mechanisms by which collagen fiber density, alignment, and orientation could affect tumor hypoxia, growth, invasion, metastasis, and treatment response.

While cell line–derived tumor models, such as the one used in this study, are ideal for intravital imaging experiments due to their consistent and predictable tumor growth kinetics, they are limited in their ability to study the TME due to their severely immunodeficient host system. Thus, future work should continue to build on this fluorescent reporter model, adapting it to new cell lines to show broad utility of this reporter system, as well as immunocompetent GEMMs that can better recapitulate the pancreatic TME in human disease. This could substantially enhance the clinical translational aspect of such research. By combining these emerging technologies with the intravital imaging platform described in this work, we can improve our understanding of the biological processes that promote pancreatic cancer progression and help us identify mechanisms of treatment resistance within the pancreatic TME.

METHODS

Cell line and live-cell fluorescence microscopy

Fluorescently labeled BxPC3-DsRed human pancreatic adenocarcinoma cells (AntiCancer, San Diego, CA, USA) (*93*) were grown in RPMI 1640 medium supplemented with 2 mM L-glutamine, 10% fetal bovine serum, and 1% penicillin-streptomycin at 37.0°C and 5% CO_2. To report on tumor cellular HIF activity, BxPC3 cells were stably transfected with a 5xHRE-GFP construct ["5xHRE/GFP" (Fig. 1A), a gift from M. Brown and T. Foster; Addgene, plasmid no. 46926], as previously described (*94*). The GFP expression of this modified cell line, hereinafter referred to as BxPC3-DsRed-5xHRE/GFP, was characterized in vitro at various oxygen concentrations (0.2, 1.0, and 21% O_2) using an H45 HEPA HypOxystation (HypOxygen Inc., Frederick, MD, USA). Cells were seeded in 12-well plates at 15% cell confluence and placed in a normoxic (21% O_2) incubator for 24 hours. Cell plates were then transferred to incubators at each respective oxygen concentration, for up to 4 days (reaching approximately 80% cell confluence). Live-cell fluorescence imaging was performed at intermittent (daily/hourly) time points using a Zeiss AxioObserver Z.1 inverted microscope (Carl Zeiss Ltd., Toronto, Canada) with a large chamber microscope incubator (Pecon GmbH, Erbach, Germany).

Western blot

To confirm and quantify the relative expression of GFP, BxPC3-DsRed-5xHRE/GFP cell lysates were collected at several time points under either hypoxia (0.2% O_2) or normoxia (21% O_2). Cells were washed with ice-cold phosphate-buffered saline and harvested in radioimmunoprecipitation assay (RIPA) buffer and protease inhibitor cocktail (BioShop, diluted 1:100 in RIPA buffer). Cell lysates were incubated for 1 hour on ice (vortexed every 30 min). The soluble fractions of cell lysates were isolated by centrifugation at 11,000*g* for 20 min (4°C), and a bicinchoninic assay (Pierce BCA Protein Assay Kit, Thermo Fisher Scientific) was used to normalize protein concentrations. Cell lysates were diluted 1:1 in 2x Laemmli buffer, and gel electrophoresis and membrane blotting were performed using equipment purchased from Bio-Rad Laboratories (CA, USA). Polyvinylidene fluoride membranes were incubated for 24 hours at 4°C in an antibody solution (see Table 1 for antibody and dilutions used). All membranes were scanned using the LI-COR Odyssey Imaging System and analyzed in Empiria Studio software (LI-COR Biosciences Inc.). Band intensity was quantified using Fiji ImageJ software (*95*).

Mouse model and PIW surgery

All animal experiments were conducted in accordance with regulatory standards approved by the University Health Network Animal Care Committee (Animal Use Protocol no. 2613). Orthotopic BxPC3-DsRed-5xHRE/GFP pancreatic tumors were established in 8- to 10-week-old female NOD-Rag1^{null} IL2rg^{null} (NRG) mice (Jackson Laboratory, no. 007799) as previously described (*96*).

Table 1. Antibodies and dilutions used in the study. N/A, not applicable.

	Primary antibody	Company, catalog no.	Dilution	Secondary antibody/reagent	Company, catalog no.	Dilution
Western blot	Anti-GFP	Novus Biologicals, NB600-308	1:2000	IRDye 680RD Detection Reagent	LI-COR Biosciences, 926-69100	1 μl/ml
	Anti–β-tubulin	MilliporeSigma, 05-661	1:10,000			
IVFM	APC-conjugated anti-CD31	BD Biosciences, 551262	0.03 mg/ml		N/A	
Tissue immunofluorescence	Anti-CD31	BD Biosciences, 550274	1:100	Anti-rat Alexa Fluor 488	Thermo Fisher Scientific, A-11066	1:200
	Anti-PIMO	Hypoxyprobe, Pab2627	1:100	Anti-rabbit Alexa Fluor 555	Thermo Fisher Scientific, A-21428	1:200
	Anti-CA9	Novus Biologicals, NB100-479SS	1:50	Anti-rabbit Alexa Fluor 555	Thermo Fisher Scientific, A-21428	1:200
	Anti-GFP	Novus Biologicals, NB600-308SS	1:500	Anti-rabbit Alexa Fluor 555	Thermo Fisher Scientific, A-21428	1:200

Once tumors reached ~5 mm in diameter (5 weeks after inoculation), a custom-designed PIW, with an inner diameter of 12 mm, a thickness of 1.8 mm, and eight equally spaced 1-mm holes (Fig. 2, A and B), was three-dimensionally (3D) printed with acrylonitrile butadiene styrene plastic and surgically implanted over the tumor site (Fig. 2C). The surgical procedure for PIW implantation was performed as previously described (*97*), with modifications. Briefly, anesthetized animals received buprenorphine (0.1 mg/kg) and were maintained with 2% isoflurane in oxygen in right-lateral position on a heated pad. Fur was removed on the left lateral side, and the surgical site was prepared with iso-betadine and ethanol solutions. A 15-mm paramedian incision was made in the left flank of the mouse, above the pancreas. The PIW was positioned under the skin and interrupted, and 4-0 nonabsorbable sutures (Prolene, Ethicon) were placed in each hole around the PIW, securing it to the skin. A lobe of the pancreas (containing the pancreatic tumor) was extracorporated through the center of the PIW using sterile cotton swabs. One to two interrupted, 4-0 absorbable sutures (Polysorb, Covidien) were placed in the abdominal muscle to prevent the tumor from retracting back into the abdominal cavity. A #2 glass microscopic coverslip (Electron Microscopy Sciences, no. 72226) was inserted in the PIW and kept in place with a plastic snap ring. Mice were given 7 days to recover before imaging. In total, 33 animals were used in this study.

Intravital fluorescence and SHG microscopy

After 1 week of recovery from PIW implantation, serial intravital fluorescence and SHG imaging of pancreatic tumors was performed using a LSM710 laser scanning confocal microscope (Carl Zeiss Canada Ltd.; Fig. 2D). To facilitate live-animal imaging on the microscope and obtain consistent images, a custom-designed, 3D printed microscope stage insert was used with a built-in isoflurane port to maintain anesthesia, an electrical heating pad to maintain physiological body temperature, and a PIW holder to reduce motion artifacts while imaging (Fig. 2E). All animals were anesthetized using isoflurane in oxygen (5% induction and 2% maintenance) and kept at 37°C throughout each imaging session. Tumor blood vessels were fluorescently labeled via intravenous injection of 6 μg of APC-conjugated rat anti-mouse CD31 antibody (see Table 1). Lasers at 488 and 633 nm were used to excite GFP/DsRed and APC, respectively. An 840-nm laser was also used to create an SHG signal for visualization of fibrillar collagen within the pancreatic tumors in vivo.

In total, 33 mice were subject to intravital imaging. Mice were imaged every 3 to 5 days for up to 28 days after PIW implantation. This was previously determined to be a reliable period for imaging before the PIW was dislodged from the abdominal wall or skin (*98*). For each mouse-imaging session, four unique fields of view (FOVs) within the imaging window were taken using a 5×/0.25 numerical aperture (NA) lens (FOV = 2429 μm by 2429 μm), and 10 unique FOVs were taken with a W Plan-Apochromat 20×/1.0 NA water immersion lens (FOV = 607 μm by 607 μm). All analyses involving tumor vasculature and collagen structures were performed using images collected under 5× and 20× FOVs, respectively.

Intravital image analysis

All intravital images were analyzed using a custom MATLAB script (vR2021A, The MathWorks Inc.). Before quantification, linear unmixing of all spectral image data was performed using an algorithm previously described by Zimmerman (*99*). Briefly, a coefficient matrix (R) was first created using control samples of each fluorophore to measure their relative contribution to each channel. Then, the measured signal intensity in each channel (S) was used to determine the amount of each fluorophore (A) by solving matrix Eq. 1

$$S = A \times R \tag{1}$$

To quantify 5xHRE/GFP fluorescence intensity in BxPC3 cells, a binary image was first created using DsRed fluorescence intensity to identify the tumor cell ROI ("tumor ROI," Fig. 5A). Thresholds for both DsRed and GFP fluorescence intensities were empirically determined to be above background fluorescence. The GFP-positive fraction was calculated by taking the number of GFP-positive pixels within the tumor ROI divided by the total number of pixels in the tumor ROI. Mean tumor cell GFP fluorescence intensity was calculated as the sum of each pixel's GFP fluorescence intensity within the tumor ROI divided by the number of pixels in the tumor ROI.

To quantify tumor vasculature, the tumor ROI binary image was morphologically dilated by 100 μm beyond the tumor boundary (creating an "expanded tumor ROI," Fig. 5A) to account for blood vessels along the tumor periphery [and within the nominal diffusion limit of O_2 in tissues; (*100*)]. Blood vessels were segmented from APC-CD31 fluorescence intensity by performing simple linear iterative clustering (*101*) followed by adaptive thresholding (*102*). Tumor vascular density was calculated as the number of APC-positive pixels within the expanded tumor ROI divided by the total number of pixels in the expanded tumor ROI.

To analyze BxPC3 cell 5xHRE/GFP fluorescence intensity in the images, equally spaced pixels within the tumor ROI (spaced 20 μm apart, the average diameter of BxPC3 cells) were sampled to approximate individual tumor cell GFP fluorescence intensity. The distance of each tumor cell to the nearest blood vessel was determined using a distance transform (*103*) of all APC-CD31 fluorescence-positive pixels, where each cell in the tumor ROI is assigned a distance value to the nearest blood vessel wall.

To investigate the correlation between tumor-associated collagen fibers and BxPC3 5xHRE/GFP fluorescence (using the in vivo SHG and fluorescence images, respectively), a 100-μm-diameter circular, moving peritumoral ROI was analyzed every 100 μm center to center along the peritumoral border of the tumor-collagen interface (Fig. 7A). We chose 100 μm as the diameter for each peritumoral ROI as this spans the approximate limit of O_2 diffusion in tissues (*100*). Within each peritumoral ROI, mean GFP fluorescence intensity was calculated in all pixels that overlapped with the tumor ROI (see above). Mean SHG intensity was calculated as the sum of each pixel's SHG intensity divided by the total number of pixels. To determine the spatial alignment and orientation of collagen fibers within each peritumoral ROI, a 2D fast Fourier transform was used to generate a power spectrum, as previously described (*104*–*106*). A circular selection in the center of the power spectrum was summed radially, and the resultant data were projected onto a polar plot and fit with an ellipse. The tilt angle of the ellipse indicated the dominant "orientation" of collagen fibers within each peritumoral ROI. An identical procedure was performed on the tumor-collagen interface line to determine the orientation of the tumor edge. The difference in orientation of collagen fibers and the tumor edge was used

to calculate the orientation of collagen fibers relative to the tumor edge. The ratio of minor (b) and major (a) axes of the ellipse was used to calculate the "alignment score" using Eq. 2. An alignment score of 0 indicates collagen fibers that are completely unaligned with one another, whereas a score of 100 indicates that collagen fibers are perfectly aligned

$$\text{Alignment score} = \left(1 - \frac{b}{a}\right) \times 100 \quad (2)$$

Immunofluorescence staining and analysis of excised tumors

Twenty-eight days after PIW implantation, mice were euthanized, and whole tumors were excised from the pancreas. Tumor tissue was embedded in optimal cutting temperature compound (Tissue-Tek) and flash-frozen in liquid nitrogen. Eleven tumors were then randomly selected for immunofluorescence staining. From the center of each tumor, four serial 5-μm-thick sections were cut using a cryostat. Tissue sections were stained with antibodies for DsRed (BxPC3 tumor cells), GFP (driven by HIF activity), CD31 (endothelial cells), and hypoxia markers: PIMO and CA9. Each section was subsequently stained with a secondary antibody (see Table 1 for antibodies and dilutions used). Slides were scanned at ×20 magnification, digitalized using a whole-slide scanner (Zeiss AzioScan.Z1), and uploaded into the HALO Image Analysis software (v3.3.2541.301, Indica Labs). Consecutive images from serially sectioned tumors were registered using HALO's Serial Stain Registration module and exported as .tiff files. All subsequent analysis was performed in MATLAB (vR2021a, The MathWorks Inc.).

To investigate the relationship between BxPC3 5xHRE/GFP expression and established biomarkers of hypoxia (PIMO and CA9), pixel intensity–based colocalization analysis (*33*, *34*) was performed on images from immunofluorescence-stained tumor tissue sections. One tissue sample was excluded from this analysis as there was no tumor hypoxia and, thus, no positive staining. Before colocalization analysis, the resolution of each image was reduced by a factor of 100 to account for errors in spatial image registration between serial sections (using MATLAB's "resize" function with bicubic interpolation). With each resized pixel representing an area of 32.5 μm by 32.5 μm, a Pearson r was calculated to determine the relationship between GFP, PIMO, and CA9 staining intensities. To determine the positive stain fraction of PIMO and CA9 for each tumor, the top 10th percentile of fluorescence intensity across all stained tissues was thresholded in MATLAB to create a binary image of positively stained tissue. The total area of CA9- and PIMO-positive tissue within the area of viable tumor tissue (DsRed fluorescence positive) was divided by the total area of viable tumor tissue.

Statistical analysis

All statistical analyses were performed using GraphPad Prism v9.3.1. For in vitro live-cell fluorescence data, a repeated-measures analysis of variance (ANOVA) followed by Dunnett's multiple comparisons test was performed to compare multiple oxygen conditions to normoxia (21% O_2) at each time point. For densitometric analysis of Western blot data, a one-way ANOVA followed by Dunnett's multiple comparisons test was used to compare each condition to "0 days" under hypoxia. All correlations were determined using the Pearson r. Comparisons between two groups were performed using an unpaired t test with Welch's correction. All data are represented as means ± SEM unless otherwise specified, with significance determined at $P < 0.05$.

View/request a protocol for this paper from *Bio-protocol*.

REFERENCES AND NOTES

1. A. McGuigan, P. Kelly, R. C. Turkington, C. Jones, H. G. Coleman, R. S. McCain, Pancreatic cancer: A review of clinical diagnosis, epidemiology, treatment and outcomes. *World J. Gastroenterol.* **24**, 4846–4861 (2018).
2. C. S. Yabar, J. M. Winter, Pancreatic cancer: A review, in *Gastrointestinal Neoplasia, An Issue of Gastroenterology Clinics of North America*, vol. 45, P. J. Limburg, D. A. Dixon, D. A., eds. (Elsevier Health Sciences, 2016).
3. A. Vincent, J. Herman, R. Schulick, R. H. Hruban, M. Goggins, Pancreatic cancer. *Lancet* **378**, 607–620 (2011).
4. G. L. Beatty, G. Werba, C. A. Lyssiotis, D. M. Simeone, The biological underpinnings of therapeutic resistance in pancreatic cancer. *Genes Dev.* **35**, 940–962 (2021).
5. S. P. Pereira, L. Oldfield, A. Ney, P. A. Hart, M. G. Keane, S. J. Pandol, D. Li, W. Greenhalf, C. Y. Jeon, E. J. Koay, C. V. Almario, C. Halloran, A. M. Lennon, E. Costello, Early detection of pancreatic cancer. *Lancet Gastroenterol. Hepatol.* **5**, 698–710 (2020).
6. P. Weibel, M. Pavic, N. Lombriser, S. Gutknecht, M. Weber, Chemoradiotherapy after curative surgery for locally advanced pancreatic cancer: A 20-year single center experience. *Surg. Oncol.* **36**, 36–41 (2021).
7. Q. Liu, Q. Liao, Y. Zhao, Chemotherapy and tumor microenvironment of pancreatic cancer. *Cancer Cell Int.* **17**, 68 (2017).
8. R. Jahanban-Esfahlan, M. de la Guardia, D. Ahmadi, B. Yousefi, Modulating tumor hypoxia by nanomedicine for effective cancer therapy. *J. Cell. Physiol.* **233**, 2019–2031 (2018).
9. T. M. A. Carvalho, D. di Molfetta, M. R. Greco, T. Koltai, K. O. Alfarouk, S. J. Reshkin, R. A. Cardone, Tumor microenvironment features and chemoresistance in pancreatic ductal adenocarcinoma: Insights into targeting physicochemical barriers and metabolism as therapeutic approaches. *Cancers (Basel)* **13**, 6135 (2021).
10. S. Wang, Y. Li, C. Xing, C. Ding, H. Zhang, L. Chen, L. You, M. Dai, Y. Zhao, Tumor microenvironment in chemoresistance, metastasis and immunotherapy of pancreatic cancer. *Am. J. Cancer Res.* **10**, 1937–1953 (2020).
11. J. Tao, G. Yang, W. Zhou, J. Qiu, G. Chen, W. Luo, F. Zhao, L. You, L. Zheng, T. Zhang, Y. Zhao, Targeting hypoxic tumor microenvironment in pancreatic cancer. *J Hematol. Oncol.* **14**, 14 (2021).
12. M. Erkan, S. Hausmann, C. W. Michalski, A. A. Fingerle, M. Dobritz, J. Kleeff, H. Friess, The role of stroma in pancreatic cancer: Diagnostic and therapeutic implications. *Nat. Rev. Gastroenterol. Hepatol.* **9**, 454–467 (2012).
13. M. Erkan, C. Reiser-Erkan, C. W. Michalski, J. Kleeff, Tumor microenvironment and progression of pancreatic cancer. *Exp. Oncol.* **32**, 128–131 (2010).
14. A. Cannon, C. Thompson, B. R. Hall, M. Jain, S. Kumar, S. K. Batra, Desmoplasia in pancreatic ductal adenocarcinoma: Insight into pathological function and therapeutic potential. *Genes Cancer* **9**, 78–86 (2018).
15. M. G. Bachem, M. Schünemann, M. Ramadani, M. Siech, H. Beger, A. Buck, S. Zhou, A. Schmid-Kotsas, G. Adler, Pancreatic carcinoma cells induce fibrosis by stimulating proliferation and matrix synthesis of stellate cells. *Gastroenterology* **128**, 907–921 (2005).
16. P. P. Provenzano, C. Cuevas, A. E. Chang, V. K. Goel, D. D. von Hoff, S. R. Hingorani, Enzymatic targeting of the stroma ablates physical barriers to treatment of pancreatic ductal adenocarcinoma. *Cancer Cell* **21**, 418–429 (2012).
17. R. K. Jain, Antiangiogenesis strategies revisited: From starving tumors to alleviating hypoxia. *Cancer Cell* **26**, 605–622 (2014).
18. V. P. Chauhan, Y. Boucher, C. R. Ferrone, S. Roberge, J. D. Martin, T. Stylianopoulos, N. Bardeesy, R. A. DePinho, T. P. Padera, L. L. Munn, R. K. Jain, Compression of pancreatic tumor blood vessels by hyaluronan is caused by solid stress and not interstitial fluid pressure. *Cancer Cell* **26**, 14–15 (2014).
19. P. P. Provenzano, S. R. Hingorani, Hyaluronan, fluid pressure, and stromal resistance in pancreas cancer. *Br. J. Cancer* **108**, 1–8 (2013).
20. M. Erkan, M. Kurtoglu, J. Kleeff, The role of hypoxia in pancreatic cancer: A potential therapeutic target? *Expert Rev. Gastroenterol. Hepatol.* **10**, 301–316 (2016).
21. A. Yuen, B. Díaz, The impact of hypoxia in pancreatic cancer invasion and metastasis. *Hypoxia* **2**, 91–106 (2014).
22. A. Masamune, K. Kikuta, T. Watanabe, K. Satoh, M. Hirota, T. Shimosegawa, Hypoxia stimulates pancreatic stellate cells to induce fibrosis and angiogenesis in pancreatic cancer. *Am. J. Physiol. Gastrointest. Liver Physiol.* **295**, G709–G717 (2008).

23. K. T. Ostapoff, N. Awasthi, B. Kutluk Cenik, S. Hinz, K. Dredge, R. E. Schwarz, R. A. Brekken, PG545, an angiogenesis and heparanase inhibitor, reduces primary tumor growth and metastasis in experimental pancreatic cancer. *Mol. Cancer Ther.* **12**, 1190–1201 (2013).
24. C. Chandler, T. Liu, R. Buckanovich, L. G. Coffman, The double edge sword of fibrosis in cancer. *Transl. Res.* **209**, 55–67 (2019).
25. C. Feig, A. Gopinathan, A. Neesse, D. S. Chan, N. Cook, D. A. Tuveson, The pancreas cancer microenvironment. *Clin. Cancer Res.* **18**, 4266–4276 (2012).
26. Group Young Researchers in Inflammatory Carcinogenesis, A. M. Wandmacher, A.-S. Mehdorn, S. Sebens, The heterogeneity of the tumor microenvironment as essential determinant of development, progression and therapy response of pancreatic cancer. *Cancer* **13**, 4932 (2021).
27. N. C. Dhani, S. Serra, M. Pintilie, J. Schwock, J. Xu, S. Gallinger, R. P. Hill, D. W. Hedley, Analysis of the intra- and intertumoral heterogeneity of hypoxia in pancreatic cancer patients receiving the nitroimidazole tracer pimonidazole. *Br. J. Cancer* **113**, 864–871 (2015).
28. A. Gopinathan, J. P. Morton, D. I. Jodrell, O. J. Sansom, GEMMs as preclinical models for testing pancreatic cancer therapies. *Dis. Model. Mech.* **8**, 1185–1200 (2015).
29. Y. Ding, J. D. Cravero, K. Adrian, P. Grippo, Modeling pancreatic cancer in vivo: From xenograft and carcinogen-induced systems to genetically engineered mice. *Pancreas* **39**, 283–292 (2010).
30. A. Hayashi, J. Hong, C. A. Iacobuzio-Donahue, The pancreatic cancer genome revisited. *Nat. Rev. Gastroenterol. Hepatol.* **18**, 469–481 (2021).
31. T. Yin, Y. Liu, R. Peeters, Y. Feng, Y. Ni, Pancreatic imaging: Current status of clinical practices and small animal studies. *World J Methodol.* **7**, 101–107 (2017).
32. R. Y. Tsien, The green fluorescent protein. *Annu. Rev. Biochem.* **67**, 509–544 (1998).
33. K. W. Dunn, M. M. Kamocka, J. H. McDonald, A practical guide to evaluating colocalization in biological microscopy. *Am. J. Physiol. Cell Physiol.* **300**, C723–C742 (2011).
34. V. Zinchuk, O. Zinchuk, T. Okada, Quantitative colocalization analysis of multicolor confocal immunofluorescence microscopy images: Pushing pixels to explore biological phenomena. *Acta Histochem. Cytochem.* **40**, 101–111 (2007).
35. W. J. Ho, E. M. Jaffee, L. Zheng, The tumour microenvironment in pancreatic cancer — Clinical challenges and opportunities. *Nat. Rev. Clin. Oncol.* **17**, 527–540 (2020).
36. E. Hirata, E. Sahai, Tumor microenvironment and differential responses to therapy. *Cold Spring Harb. Perspect. Med.* **7**, a026781 (2017).
37. G. N. Masoud, W. Li, HIF-1α pathway: Role, regulation and intervention for cancer therapy. *Acta Pharm. Sin. B* **5**, 378–389 (2015).
38. M. Y. Koh, G. Powis, Passing the baton: The HIF switch. *Trends Biochem. Sci.* **37**, 364–372 (2012).
39. P. Corish, C. Tyler-Smith, Attenuation of green fluorescent protein half-life in mammalian cells. *Protein Eng.* **12**, 1035–1040 (1999).
40. X. Li, X. Zhao, Y. Fang, X. Jiang, T. Duong, C. Fan, C. C. Huang, S. R. Kain, Generation of destabilized green fluorescent protein as a transcription reporter. *J. Biol. Chem.* **273**, 34970–34975 (1998).
41. E. Eden, N. Geva-Zatorsky, I. Issaeva, A. Cohen, E. Dekel, T. Danon, L. Cohen, A. Mayo, U. Alon, Proteome half-life dynamics in living human cells. *Science* **331**, 764–768 (2011).
42. E. Švastová, A. Hulíková, M. Rafajová, M. Zat'ovič̌ová, A. Gibadulinová, A. Casini, A. Cecchi, A. Scozzafava, C. T. Supuran, J. Pastorek, S. Pastoreková, Hypoxia activates the capacity of tumor-associated carbonic anhydrase IX to acidify extracellular pH. *FEBS Lett.* **577**, 439–445 (2004).
43. T. van den Beucken, M. Koritzinsky, H. Niessen, L. Dubois, K. Savelkouls, H. Mujcic, B. Jutten, J. Kopacek, S. Pastorekova, A. J. van der Kogel, P. Lambin, W. Voncken, K. M. A. Rouschop, B. G. Wouters, Hypoxia-induced expression of carbonic anhydrase 9 is dependent on the unfolded protein response. *J. Biol. Chem.* **284**, 24204–24212 (2009).
44. J. C. Walsh, A. Lebedev, E. Aten, K. Madsen, L. Marciano, H. C. Kolb, The clinical importance of assessing tumor hypoxia: Relationship of tumor hypoxia to prognosis and therapeutic opportunities. *Antioxid. Redox Signal.* **21**, 1516–1554 (2014).
45. M. A. Proescholdt, C. Mayer, M. Kubitza, T. Schubert, S.-Y. Liao, E. J. Stanbridge, S. Ivanov, E. H. Oldfield, A. Brawanski, M. J. Merrill, Expression of hypoxia-inducible carbonic anhydrases in brain tumors. *Neuro Oncol.* **7**, 465–475 (2005).
46. A. Carreau, B. E. Hafny-Rahbi, A. Matejuk, C. Grillon, C. Kieda, Why is the partial oxygen pressure of human tissues a crucial parameter? Small molecules and hypoxia. *J. Cell. Mol. Med.* **15**, 1239–1253 (2011).
47. S. R. McKeown, Defining normoxia, physoxia and hypoxia in tumours-implications for treatment response. *Br. J. Radiol.* **87**, 20130676 (2014).
48. M. Höckel, P. Vaupel, Tumor hypoxia: Definitions and current clinical, biologic, and molecular aspects. *J. Natl. Cancer Inst.* **93**, 266–276 (2001).
49. H. S. Kyung, J. A. Diaz-Gonzalez, J. Russell, Q. Chen, P. Burgman, X.-F. Li, C. C. Ling, Detecting changes in tumor hypoxia with carbonic anhydrase IX and pimonidazole. *Cancer Biol. Ther.* **6**, 70–75 (2007).
50. V. Petrova, M. Annicchiarico-Petruzzelli, G. Melino, I. Amelio, The hypoxic tumour microenvironment. Oncogenesis 7, 10 (2018).
51. J. Pouysségur, F. Dayan, N. M. Mazure, Hypoxia signalling in cancer and approaches to enforce tumour regression. *Nature* **441**, 437–443 (2006).
52. H. K. Haugland, V. Vukovic, M. Pintilie, A. W. Fyles, M. Milosevic, R. P. Hill, D. W. Hedley, Expression of hypoxia-inducible factor-1alpha in cervical carcinomas: Correlation with tumor oxygenation. *Int. J. Radiat. Oncol. Biol. Phys.* **53**, 854–861 (2002).
53. M. Zaidi, F. Fu, D. Cojocari, T. D. M. Kee, B. G. Wouters, Quantitative visualization of hypoxia and proliferation gradients within histological tissue sections. *Front. Bioeng. Biotechnol.* **7**, 397 (2019).
54. J. C. Forster, W. M. Harriss-Phillips, M. J. Douglass, E. Bezak, A review of the development of tumor vasculature and its effects on the tumor microenvironment. *Hypoxia* **5**, 21–32 (2017).
55. D. W. Siemann, The unique characteristics of tumor vasculature and preclinical evidence for its selective disruption by tumor-vascular disrupting agents. *Cancer Treat. Rev.* **37**, 63–74 (2011).
56. N. Campillo, B. Falcones, J. Otero, R. Colina, D. Gozal, D. Navajas, R. Farré, I. Almendros, Differential oxygenation in tumor microenvironment modulates macrophage and cancer cell crosstalk: Novel experimental Setting and proof of concept. *Front. Oncol.* **9**, 43 (2019).
57. V. E. Zannella, A. Dal Pra, H. Muaddi, T. D. McKee, S. Stapleton, J. Sykes, R. Glicksman, S. Chaib, P. Zamiara, M. Milosevic, B. G. Wouters, R. G. Bristow, M. Koritzinsky, Reprogramming metabolism with metformin improves tumor oxygenation and radiotherapy response. *Clin. Cancer Res.* **19**, 6741–6750 (2013).
58. B. G. Wouters, T. van den Beucken, M. G. Magagnin, P. Lambin, C. Koumenis, Targeting hypoxia tolerance in cancer. *Drug Resist. Updat.* **7**, 25–40 (2004).
59. E. Butturini, A. Carcereri de Prati, D. Boriero, S. Mariotto, Tumor dormancy and interplay with hypoxic tumor microenvironment. *Int. J. Mol. Sci.* **20**, 4305 (2019).
60. M. Orth, P. Metzger, S. Gerum, J. Mayerle, G. Schneider, C. Belka, M. Schnurr, K. Lauber, Pancreatic ductal adenocarcinoma: Biological hallmarks, current status, and future perspectives of combined modality treatment approaches. *Radiat. Oncol.* **14**, 141 (2019).
61. C. J. Whatcott, C. H. Diep, P. Jiang, A. Watanabe, J. L. Bello, C. Sima, G. Hostetter, H. M. Shepard, D. D. Von Hoff, H. Han, Desmoplasia in primary tumors and metastatic lesions of pancreatic cancer. *Clin. Cancer Res.* **21**, 3561–3568 (2015).
62. M. A. Jacobetz, D. S. Chan, A. Neesse, T. E. Bapiro, N. Cook, K. K. Frese, C. Feig, T. Nakagawa, M. E. Caldwell, H. I. Zecchini, M. P. Lolkema, P. Jiang, A. Kultti, C. B. Thompson, D. C. Maneval, D. I. Jodrell, G. I. Frost, H. M. Shepard, J. N. Skepper, D. A. Tuveson, Hyaluronan impairs vascular function and drug delivery in a mouse model of pancreatic cancer. *Gut* **62**, 112–120 (2013).
63. H. Salmon, K. Franciszkiewicz, D. Damotte, M. C. Dieu-Nosjean, P. Validire, A. Trautmann, F. Mami-Chouaib, E. Donnadieu, Matrix architecture defines the preferential localization and migration of T cells into the stroma of human lung tumors. *J. Clin. Invest.* **122**, 899–910 (2012).
64. T. S. Mantoni, S. Lunardi, O. al-Assar, A. Masamune, T. B. Brunner, Pancreatic stellate cells radioprotect pancreatic cancer cells through β1-integrin signaling. *Cancer Res.* **71**, 3453–3458 (2011).
65. T. Suwa, M. Kobayashi, J. M. Nam, H. Harada, Tumor microenvironment and radioresistance. *Exp. Mol. Med.* **53**, 1029–1035 (2021).
66. N. R. Smith, D. Baker, M. Farren, A. Pommier, R. Swann, X. Wang, S. Mistry, K. McDaid, J. Kendrew, C. Womack, S. R. Wedge, S. T. Barry, Tumor stromal architecture can define the intrinsic tumor response to VEGF-targeted therapy. *Clin. Cancer Res.* **19**, 6943–6956 (2013).
67. Y. Kang, M. R. Roh, S. Rajadurai, A. Rajadurai, R. Kumar, C.-N. Njauw, Z. Zheng, H. Tsao, Hypoxia and HIF-1α regulate collagen production in keloids. *J. Invest. Dermatol.* **140**, 2157–2165 (2020).
68. S. Xu, H. Xu, W. Wang, S. Li, H. Li, T. Li, W. Zhang, X. Yu, L. Liu, The role of collagen in cancer: From bench to bedside. *J. Transl. Med.* **17**, 309 (2019).
69. L. Bentovim, R. Amarilio, E. Zelzer, HIF1α is a central regulator of collagen hydroxylation and secretion under hypoxia during bone development. *Development* **139**, 4473–4483 (2012).
70. L. Hui, Y. Chen, Tumor microenvironment: Sanctuary of the devil. *Cancer Lett.* **368**, 7–13 (2015).
71. N. Willumsen, L. B. Thomsen, C. L. Bager, C. Jensen, M. A. Karsdal, Quantification of altered tissue turnover in a liquid biopsy: A proposed precision medicine tool to assess chronic inflammation and desmoplasia associated with a pro-cancerous niche and response to immuno-therapeutic anti-tumor modalities. *Cancer Immunol. Immunother.* **67**, 1–12 (2018).
72. M. Erkan, C. Reiser-Erkan, C. W. Michalski, S. Deucker, D. Sauliunaite, S. Streit, I. Esposito, H. Friess, J. Kleeff, Cancer-stellate cell interactions perpetuate the hypoxia-fibrosis cycle in pancreatic ductal adenocarcinoma. *Neoplasia* **11**, 497–508 (2009).

73. D. M. Gilkes, S. Bajpai, C. C. Wong, P. Chaturvedi, M. E. Hubbi, D. Wirtz, G. L. Semenza, Procollagen lysyl hydroxylase 2 is essential for hypoxia-induced breast cancer metastasis. *Mol. Cancer Res.* **11**, 456–466 (2013).
74. E. Henke, R. Nandigama, S. Ergün, Extracellular matrix in the tumor microenvironment and its impact on cancer therapy. *Front. Mol. Biosci.* **6**, 160 (2019).
75. P. Baril, R. Gangeswaran, P. C. Mahon, K. Caulee, H. M. Kocher, T. Harada, M. Zhu, H. Kalthoff, T. Crnogorac-Jurcevic, N. R. Lemoine, Periostin promotes invasiveness and resistance of pancreatic cancer cells to hypoxia-induced cell death: Role of the beta4 integrin and the PI3k pathway. *Oncogene* **26**, 2082–2094 (2007).
76. A. D. Rhim, P. E. Oberstein, D. H. Thomas, E. T. Mirek, C. F. Palermo, S. A. Sastra, E. N. Dekleva, T. Saunders, C. P. Becerra, I. W. Tattersall, C. B. Westphalen, J. Kitajewski, M. G. Fernandez-Barrena, M. E. Fernandez-Zapico, C. Iacobuzio-Donahue, K. P. Olive, B. Z. Stanger, Stromal elements act to restrain, rather than support, pancreatic ductal adenocarcinoma. *Cancer Cell* **25**, 735–747 (2014).
77. H. T. Nia, L. L. Munn, R. K. Jain, Physical traits of cancer. *Science* **370**, eaaz0868 (2020).
78. R. K. Jain, J. D. Martin, T. Stylianopoulos, The role of mechanical forces in tumor growth and therapy. *Annu. Rev. Biomed. Eng.* **16**, 321–346 (2014).
79. Y. Chen, J. Kim, S. Yang, H. Wang, C.-J. Wu, H. Sugimoto, V. S. LeBleu, R. Kalluri, Type I collagen deletion in αSMA^+ myofibroblasts augments immune suppression and accelerates progression of pancreatic cancer. *Cancer Cell* **39**, 548–565.e6 (2021).
80. D. M. Gilkes, S. Bajpai, P. Chaturvedi, D. Wirtz, G. L. Semenza, Hypoxia-inducible Factor 1 (HIF-1) promotes extracellular matrix remodeling under hypoxic conditions by inducing *P4HA1*, *P4HA2*, and *PLOD2* expression in fibroblasts. *J. Biol. Chem.* **288**, 10819–10829 (2013).
81. D. M. Gilkes, L. Xiang, S. J. Lee, P. Chaturvedi, M. E. Hubbi, D. Wirtz, G. L. Semenza, Hypoxia-inducible factors mediate coordinated RhoA-ROCK1 expression and signaling in breast cancer cells. *Proc. Natl. Acad. Sci. U.S.A.* **111**, E384–E393 (2014).
82. K. R. Levental, H. Yu, L. Kass, J. N. Lakins, M. Egeblad, J. T. Erler, S. F. T. Fong, K. Csiszar, A. Giaccia, W. Weninger, M. Yamauchi, D. L. Gasser, V. M. Weaver, Matrix crosslinking forces tumor progression by enhancing integrin signaling. *Cell* **139**, 891–906 (2009).
83. C. R. Drifka, A. G. Loeffler, K. Mathewson, A. Keikhosravi, J. C. Eickhoff, Y. Liu, S. M. Weber, W. J. Kao, K. W. Eliceiri, Highly aligned stromal collagen is a negative prognostic factor following pancreatic ductal adenocarcinoma resection. *Oncotarget* **7**, 76197–76213 (2016).
84. L. Bolm, P. Zghurskyi, H. Lapshyn, E. Petrova, S. Zemskov, Y. K. Vashist, S. Deichmann, K. C. Honselmann, P. Bronsert, T. Keck, U. F. Wellner, Alignment of stroma fibers, microvessel density and immune cell populations determine overall survival in pancreatic cancer—An analysis of stromal morphology. *PLOS ONE* **15**, e0234568 (2020).
85. H. E. Balcioglu, B. van de Water, E. H. J. Danen, Tumor-induced remote ECM network orientation steers angiogenesis. *Sci. Rep.* **6**, 22580 (2016).
86. M. G. McCoy, J. M. Wei, S. Choi, J. P. Goerger, W. Zipfel, C. Fischbach, Collagen fiber orientation regulates 3D vascular network formation and alignment. *ACS Biomater Sci. Eng.* **4**, 2967–2976 (2018).
87. S. M. Kakkad, M. F. Penet, A. Akhbardeh, A. P. Pathak, M. Solaiyappan, V. Raman, D. Leibfritz, K. Glunde, Z. M. Bhujwalla, Hypoxic tumor environments exhibit disrupted collagen I fibers and low macromolecular transport. *PLOS ONE* **8**, e81869 (2013).
88. M. D. Nieskoski, K. Marra, J. R. Gunn, S. C. Kanick, M. M. Doyley, T. Hasan, S. P. Pereira, B. Stuart Trembly, B. W. Pogue, Separation of solid stress from interstitial fluid pressure in pancreas cancer correlates with collagen area fraction. *J. Biomech. Eng.* **139**, 0610021–0610028 (2017).
89. T. Stylianopoulos, J. D. Martin, V. P. Chauhan, S. R. Jain, B. Diop-Frimpong, N. Bardeesy, B. L. Smith, C. R. Ferrone, F. J. Hornicek, Y. Boucher, L. L. Munn, R. K. Jain, Causes, consequences, and remedies for growth-induced solid stress in murine and human tumors. *Proc. Natl. Acad. Sci. U.S.A* **109**, 15101–15108 (2012).
90. V. P. Chauhan, J. D. Martin, H. Liu, D. A. Lacorre, S. R. Jain, S. V. Kozin, T. Stylianopoulos, A. S. Mousa, X. Han, P. Adstamongkonkul, Z. Popović, P. Huang, M. G. Bawendi, Y. Boucher, R. K. Jain, Angiotensin inhibition enhances drug delivery and potentiates chemotherapy by decompressing tumour blood vessels. *Nat. Commun.* **4**, 2516 (2013).
91. Y. Dekker, S. E. le Dévédec, E. H. J. Danen, Q. Liu, Crosstalk between hypoxia and extracellular matrix in the tumor microenvironment in breast cancer. *Genes* **13**, 1585 (2022).
92. P. Lu, V. M. Weaver, Z. Werb, The extracellular matrix: A dynamic niche in cancer progression. *J. Cell Biol.* **196**, 395–406 (2012).
93. M. H. Tan, N. J. Nowak, R. Loor, H. Ochi, A. A. Sandberg, C. Lopez, J. W. Pickren, R. Berjian, H. O. Douglass, T. M. Chu, Characterization of a new primary human pancreatic tumor line. *Cancer Invest.* **4**, 15–23 (1986).
94. D. Vordermark, T. Shibata, J. M. Brown, Green fluorescent protein is a suitable reporter of tumor hypoxia despite an oxygen requirement for chromophore formation. *Neoplasia* **3**, 527–534 (2001).
95. J. Schindelin, I. Arganda-Carreras, E. Frise, V. Kaynig, M. Longair, T. Pietzsch, S. Preibisch, C. Rueden, S. Saalfeld, B. Schmid, J.-Y. Tinevez, D. J. White, V. Hartenstein, K. Eliceiri, P. Tomancak, A. Cardona, Fiji: An open-source platform for biological-image analysis. *Nat. Methods* **9**, 676–682 (2012).
96. S. Rapic, T. Samuel, P. E. Lindsay, S. Ansell, R. A. Weersink, R. S. Da Costa, Assessing the accuracy of bioluminescence image-guided stereotactic body radiation therapy of orthotopic pancreatic tumors using a small animal irradiator. *Radiat. Res.* **197**, 626–637 (2022).
97. L. Ritsma, E. J. A. Steller, S. I. J. Ellenbroek, O. Kranenburg, I. H. M. Borel Rinkes, J. van Rheenen, Surgical implantation of an abdominal imaging window for intravital microscopy. *Nat. Protoc.* **8**, 583–594 (2013).
98. L. Ritsma, E. J. A. Steller, E. Beerling, C. J. M. Loomans, A. Zomer, C. Gerlach, N. Vrisekoop, D. Seinstra, L. van Gurp, R. Schäfer, D. A. Raats, A. de Graaff, T. N. Schumacher, E. J. P. de Koning, I. H. B. Rinkes, O. Kranenburg, J. Rheenen, Intravital microscopy through an abdominal imaging window reveals a pre-micrometastasis stage during liver metastasis. *Sci. Transl. Med.* **4**, 158ra145 (2012).
99. T. Zimmermann, Spectral imaging and linear unmixing in light microscopy. *Adv. Biochem. Eng. Biotechnol.* **95**, 245–265 (2005).
100. A. B. Baker, A. D. Farmery, Inert gas transport in blood and tissues. *Compr. Physiol.* **1**, 569–592 (2011).
101. R. Achanta, A. Shaji, K. Smith, A. Lucchi, P. Fua, S. Süsstrunk, SLIC superpixels compared to state-of-the-art superpixel methods. *IEEE Trans. Pattern Anal. Mach. Intell.* **34**, 2274–2282 (2012).
102. D. Bradley, G. Roth, Adaptive thresholding using the integral image. *J. Graph. Tools* **12**, 13–21 (2011).
103. C. R. Maurer, R. Qi, V. Raghavan, A linear time algorithm for computing exact Euclidean distance transforms of binary images in arbitrary dimensions. *IEEE Trans. Pattern Anal. Mach. Intell.* **25**, 265–270 (2003).
104. E. C. Rentchler, K. L. Gant, R. Drapkin, M. Patankar, P. J. Campagnola, Imaging collagen alterations in STICs and high grade ovarian cancers in the fallopian tubes by second harmonic generation microscopy. *Cancers (Basel)* **11**, 1805 (2019).
105. B. K. Robinson, E. Cortes, A. J. Rice, M. Sarper, A. Del Río Hernández, Quantitative analysis of 3D extracellular matrix remodelling by pancreatic stellate cells. *Biol. Open* **5**, 875–882 (2016).
106. E. Cortes, D. Lachowski, B. Robinson, M. Sarper, J. S. Teppo, S. D. Thorpe, T. J. Lieberthal, K. Iwamoto, D. A. Lee, M. Okada-Hatakeyama, M. T. Varjosalo, A. E. Del Río Hernández, Tamoxifen mechanically reprograms the tumor microenvironment via HIF-1A and reduces cancer cell survival. *EMBO Rep.* **20**, e46557 (2019).

Acknowledgments: We thank M. Minden and R. He (Princess Margaret Cancer Center, University Health Network, Toronto, Canada) for help in transfecting the BxPC3-DsRed cell line with the 5xHRE/GFP reporter. R. Vallanki (Princess Margaret Cancer Center, University Health Network, Toronto, Canada) provided valuable training and guidance using the H45 HEPA HypOxystation. Napoleon Law and Feryal Sarraf (STTARR Pathology, University Health Network, Toronto, Canada) processed and stained all ex vivo tumor tissue sections. J. Jonkman (Advanced Optical Microscopy Facility, University Health Network, Toronto, Canada) provided valuable guidance and discussion for all microscopy experiments. **Funding:** Funding for this study was provided by a peer-reviewed research grant to R.S.D. from the Terry Fox Research Institute (TFRI; grant no. 1056). **Author contributions:** T.S., S.R., and R.S.D. developed the concept for this study. T.S. performed all in vitro experiments, animal surgeries, image processing, and data analysis. T.S. and S.R. developed the orthotopic PIW, fluorescence, and SHG intravital microscopy imaging platform and collected intravital images and ex vivo tissues for immunostaining. T.S., C.O., and M.E. performed Western blot experiments. T.S. and Y.Z. performed statistical analyses. T.S. wrote the manuscript. All authors reviewed and edited the manuscript as well as approved the final version. **Competing interests:** The authors declare that they have no competing interests. **Data and materials availability:** All data needed to evaluate the conclusions in the paper are present in the paper.

Submitted 14 September 2022
Accepted 5 May 2023
Published 7 June 2023
10.1126/sciadv.ade8672

IMMUNOLOGY

3D deconvolution of human skin immune architecture with Multiplex Annotated Tissue Imaging System

Manon Scholaert[1,2]†, Raissa Houmadi[1]†, Jeremy Martin[1]†, Nadine Serhan[1]†, Marie Tauber[1,3,4,5], Emilie Braun[2], Lilian Basso[1], Eric Merle[6], Pascal Descargues[6], Manuelle Viguier[7], Cécile Lesort[4,8], Benoît Chaput[9], Jean Kanitakis[4,8], Denis Jullien[4,8], Cristina Bulai Livideanu[1,10], Laurence Lamant[11], Emeline Pagès[2], Nicolas Gaudenzio[1,2]*

Routine clinical assays, such as conventional immunohistochemistry, often fail to resolve the regional heterogeneity of complex inflammatory skin conditions. We introduce MANTIS (Multiplex Annotated Tissue Imaging System), a flexible analytic pipeline compatible with routine practice, specifically designed for spatially resolved immune phenotyping of the skin in experimental or clinical samples. On the basis of phenotype attribution matrices coupled to α-shape algorithms, MANTIS projects a representative digital immune landscape while enabling automated detection of major inflammatory clusters and concomitant single-cell data quantification of biomarkers. We observed that severe pathological lesions from systemic lupus erythematosus, Kawasaki syndrome, or COVID-19–associated skin manifestations share common quantitative immune features while displaying a nonrandom distribution of cells with the formation of disease-specific dermal immune structures. Given its accuracy and flexibility, MANTIS is designed to solve the spatial organization of complex immune environments to better apprehend the pathophysiology of skin manifestations.

INTRODUCTION

The skin acts as a barrier organ that separates the body from the external environment. Upon inflammation, blood-circulating immune cells are recruited to help orchestrate the cutaneous immunity and are often nested nearby key structural elements (e.g., postcapillary venules, hair follicles, dermal-epidermal junction, etc.) (*1*, *2*). In pathological settings, the nature and activation status of the skin immune landscape often represent precious biological information that can help establish an accurate diagnosis, apprehend interpatient heterogeneity, and select the most appropriate treatment. The use of imaging-based approaches to identify cutaneous immune cells is still challenging because of the high level of autofluorescence arising from the tissue itself, the potential spectral spillover when more than four fluorochromes are used simultaneously, and the entanglement of all cells within thick and polarized structural appendages.

The vast majority of microscopic diagnoses of inflammatory skin conditions relies on repeated immunohistochemistry analysis of one or two proteins and/or hematoxylin and eosin (H&E) staining in thin (2 to 5 μm) formalin-fixed, paraffin-embedded (FFPE) specimens (*3*, *4*). While such two-dimensional (2D) approaches are reproducible and suitable for routine practice, they do not permit to apprehend the complex topology and heterogeneity of immune cells (*5*), particularly those nested in-between epidermal appendices. The development of image-based histo-cytometry, which consists of analyzing segmented multicolor images with classical flow cytometry gating strategies, has paved the way toward the development of sophisticated image generation systems coupled to computational imaging (*6*). Recently, highly multiplexed imaging systems have substantially advanced our understanding of tissue-resident immune subsets and of their spatial distribution with regard to tissue structures, with a strong focus on cancer samples and tumor heterogeneity, such as CODEX (Co-detection by indexing) (*7*, *8*), MIBI-TOF (Multiplex Ion Beam Imaging by Time Of Flight) (*9*), IMC (Imaging Mass Cytometry) (*10*), MuSIC (Multiplexing using Spectral Imaging and Combinatorics) (*11*), CyCIF (tissue-based cyclic immunofluorescence) (*12*), Cell Dive (*13*), and others (*14*). While multiplexed imaging has an immense potential, there is a strong need to democratize these methods with the use of inexpensive instrumentation compatible with standard tissue processing and coupled to an analysis interface that is user-friendly enough to be used in routine practice.

Here, we present an integrated framework primarily designed for spatially resolved immune cells phenotyping in FFPE human skin biopsies. We first set up a simple and inexpensive method to acquire 10 fluorescent signals simultaneously and in 3D using a classical confocal microscope. We next designed MANTIS (Multiplex Annotated Tissue Imaging System), an adaptable and interactive analytical system that automatically generates a digitalized version of the skin immune landscape and enables single-cell quantitative data visualization. On the basis of these settings, MANTIS could be implemented in most laboratories coupled to existing confocal equipment to bridge the gap between sophisticated research tools

[1]Toulouse Institute for Infectious and Inflammatory Diseases (Infinity), INSERM UMR1291, CNRS UMR5051, and University Toulouse III, Toulouse, France. [2]Genoskin SAS, Toulouse, France. [3]Department of Allergology and Clinical Immunology, Hospices Civils de Lyon, Centre Hospitalier Lyon Sud, Pierre-Bénite, France. [4]Centre International de Recherche en Infectiologie (CIRI; Team Immunology of Skin Allergy and Vaccination), Inserm U1111, Université Claude Bernard Lyon 1, and CNRS, UMR5308, Lyon, France. [5]ENS de Lyon, F-69007 Lyon, France. [6]Genoskin Inc, Salem, MA, USA. [7]Dermatology Department, Hôpital Robert Debré, EA7509 IRMAIC, Université Reims Champagne Ardenne, Reims, France. [8]Department of Dermatology Edouard Herriot Hospital, Hospices Civils de Lyon, Lyon, France. [9]Department of Plastic, Reconstructive and Aesthetic Surgery, Rangueil Hospital, CHU Toulouse, Toulouse, France. [10]Department of Dermatology, Paul Sabatier University, Toulouse University Hospital, Toulouse, France. [11]Department of Pathology, Institut Universitaire du Cancer Toulouse Oncopole, avenue Joliot-Curie, 31049 Toulouse, France.
*Corresponding author. Email: nicolas.gaudenzio@inserm.fr
†These authors contributed equally to this work.

and standard-of-care diagnostic procedures with minimal human intervention.

RESULTS

Extraction of single-cell statistics from skin sections by combining conventional confocal laser scanning microscopy and computational imaging

We developed a simple method to generate 3D multiplexed fluorescent images from FFPE (10-μm-thick) or fresh frozen (50-μm-thick) skin biopsies that could be implemented in most research or clinical laboratories on existing equipment. Skin sections were first stained with different panels of commercially available fluorochrome-coupled antibodies added simultaneously and then quenched to avoid excessive natural autofluorescence of skin structural elements (Fig. 1A). We acquired 3D fluorescent multiplexed images with a conventional inverted confocal laser scanning microscope equipped with five laser lines, five detectors, and a 40× oil immersion objective, using a strategy of sequential acquisition composed of fast consecutive steps (Fig. 1B; the detailed description of optical paths and lasers of our 8-year-old Leica SP8 system is provided in Materials and Methods). This setting enabled the acquisition of 8 to 10 fluorescent channels, on a system primarily designed for four colors, over a skin section of the following three dimensions, 0.6 mm (x) by 0.4 mm (y) by 20 μm (z), within 25 min. The obtained 3D images were then deconvoluted and compensated to correct 3D fluorescent spectral spillovers (Fig. 1, C and D) using the Huygens software (Scientific Volume Imaging), a strategy routinely applied in flow cytometry to combine multiple fluorochromes simultaneously (*6*, *15*). Compared to classical segmentation strategies based on nucleus expansion (*16*), which often lead to under- or overestimation of cellular cluster composition, we used the general immune biomarker CD45 as a robust immune staining visualized in most skin-resident immune cells to constitute the core of our cell segmentation strategy for future single immune cell statistics extraction (Fig. 1, E and F). Using the isosurface algorithm of the Imaris software (Bitplane), we next modeled the 3D fluorescence signal of CD45 for individual immune cells and exported a corresponding single-cell database composed of the mean fluorescence intensity (MFI) of all individual biomarkers and precise x, y, and z tissue coordinates obtained with a resolution of 299 nm by 299 nm by 999 nm per voxel (Fig. 1F). We found that CD45-based segmentation enabled an efficient isolation of single immune cell characteristics, even when those were found aggregated around dermal structural elements. Overall, we demonstrate that it is possible to extract a 10-parameter single-cell database using regular confocal equipment coupled to basic computational imaging steps.

Analysis of the skin immune landscape using MANTIS phenotype attribution matrices

On the basis of the literature, we designed two panels composed of antibodies directed against immune biomarkers suitable to generate a non-exhaustive overview of lymphoid cell (LC) and myeloid cell landscape of the skin, with an average cost of approximately $65 per sample. The combination of CD45, CD3e, CD4, CD8, γδ T cell receptor (TCRγδ), CD20, and CD57 [a terminally sulfated glycan carbohydrate epitope shared by natural killer (NK) and T cells with high cytotoxic potential (*17*, *18*)] allows us to identify the following LCs: conventional CD4 and CD8 T cells (being $CD57^{low}$ or $CD57^{high}$), $CD4^+$ $CD8^+$ double-positive (dp) T cells (*19*), $CD4^-$ $CD8^-$ double-negative (dn) T cells (*20*), γδ T cells, B cells, and NK cells (table S1). The combination of CD45, CD207, CD1c, human leukocyte antigen DR [HLA-DR (Human Leukocyte Antigen - DR isotype)], CD123, Siglec8, myeloperoxidase (MPO), and tryptase allows us to identify the following myeloid cells: Langerhans cells, $Langerin^+$ ($CD207^+$) dermal dendritic cells (dDCs) and $Langerin^-$ dDCs, eosinophils, basophils, neutrophils, and mast cells (table S1). The activation status of DC, $Langerin^+$ DC, and LC was investigated using levels of HLA-DR expression. A detailed list of excitation/emission/detection strategies is provided in table S2.

We next aimed to develop an adaptable analytical system that could integrate and batch-process extracted single-cell databases and enable an unsupervised phenotyping of immune subsets. To address this latter challenge, we developed MANTIS, an interactive digital tool based on phenotype attribution matrices inspired by the analytical logic of single-cell RNA sequencing that identifies correlations between the single-cell database and the expression profiles of different cell types (Fig. 2A and fig. S1A). Such an analysis is possible by computing Spearman′s ρ correlation, which accommodates nonlinear relationships in the expression values (i.e., in our case, the collected MFI of each biomarker). In practice, MANTIS runs instantaneously a pairwise Spearman′s correlation analysis, for each detected single-cell, against selected combinations of biomarkers to identify the immune subsets annotated in the phenotype attribution matrices. The output information is the attribution of specific ρ values per single cell, which then automatically finds the best match of cellular identity and generates associated quantitative statistics (Fig. 2, A to C, and fig. S1, B and C). When analyzed side by side with conventional flow cytometry, we found that the same populations were detected; however, MANTIS enabled the identification of more LCs and CD4 T cells (and less dn T cells), while flow cytometry enabled the identification of more $HLA\text{-}DR^{high}$ dDCs and eosinophils (fig. S2). As a proof of concept, we generated data from two serial sections of an acral lesion from a patient with systemic lupus erythematosus (SLE; i.e., lupus chilblains) stained with a lymphoid and a myeloid panel. The fast 3D acquisition of one region of interest (ROI) composed of six fields of view [i.e., 0.6 mm (x) by 0.4 mm (y) by 20 μm (z)] enabled the annotation of 519 myeloid cells and 708 LCs for a total of 19 different immune subsets identified (Fig. 2D and fig. S1D). One can then decide to visualize annotated immune populations using either a heatmap, in which the MFI of individual biomarkers is displayed per single cell (fig. S1E), or a graph-based dimensionality reduction, i.e., t-distributed stochastic neighbor embedding (t-SNE), specifically designed for visualizing clusters of populations and corresponding expression of biomarkers per cluster (Fig. 2E).

A particularly challenging aspect of multiplexed imaging technologies is to circumvent the spatial distribution of immune cells with respect to longitudinal and polarized structural elements (e.g., epidermal appendages of the skin) in thick tissue sections. We developed an interactive software interface that contextualizes the immune topology of the skin by replacing all annotated single immune cells within their 3D spatial context and leverages the natural autofluorescence of keratinocytes to model the epidermal layer to facilitate biopsy orientation (Fig. 2F and fig. S1, F and G). The algorithm allows us to use two complementary analytical approaches and to switch from one to the other with a simple drawing tool (movie S1). The analysis can start from the

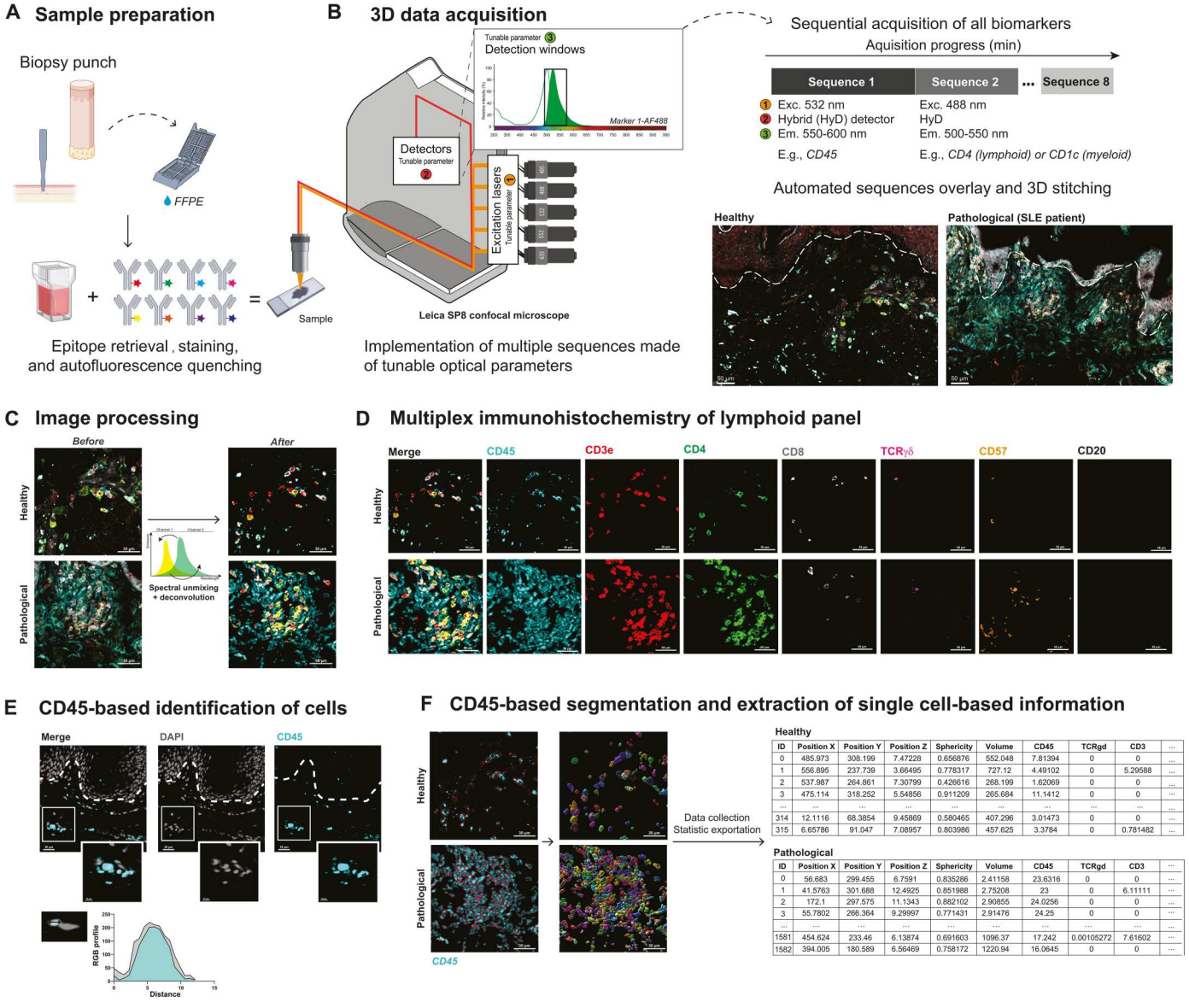

Fig. 1. Between-stack microscope configuration allows sequential acquisition of 7+ channels with classical image processing. (**A**) Sample preparation. FFPE-skin sections were cut and stained for myeloid and lymphoid panels after appropriate epitope retrieval and autofluorescence quenching. Sample images were then acquired using an SP8 confocal microscope from Leica Microsystems as described in (B). (**B**) Microscope configuration and acquisition settings. Mosaic sequential images were acquired using the between-stack configuration with tunable detection windows. Sequences were overlaid and 3D-stitched. An example of data acquisition is given for healthy (left) and pathological [systemic lupus erythematosus (SLE)] (right) skin. (**C**) Deconvolution of regions of interest and spectral unmixing. Acquired 3D images were deconvoluted and compensated to correct optical aberrations and 3D fluorescent spectral spillovers. (**D**) Representative 3D multiplex image of healthy (top) and pathological SLE (bottom) skin sample for lymphoid panel, staining CD45, CD3, CD4, CD8, TCRγδ, CD57, and CD20. (**E**) Colocalization of DAPI (4′,6-diamidino-2-phenylindole) and CD45 staining and respective RGB profiles. (**F**) Segmentation and single-cell database creation. Cell segmentation using the CD45 fluorescence channel allowed efficient isolation of individual objects, i.e., immune cells. Individual object statistics (*xyz* coordinates, sphericity, volume, and MFI) were extracted for each sample. Scale bars, 30 μm.

visualization of the skin digital immune landscape and then be pursued with the investigation of the immune composition of defined microregions via instantaneous recomputation of drawn ROI. Conversely, it is also possible to start from all annotated immune cells on a t-SNE graph, draw around subsets of interest, and immediately visualize their anatomical distribution in the skin digital immune landscape (Fig. 2G and movie S1). Together, these data suggest that the MANTIS interactive analytical system can be used to compute the 3D spatial organization of immune and structural elements of inflammatory skin samples from patients.

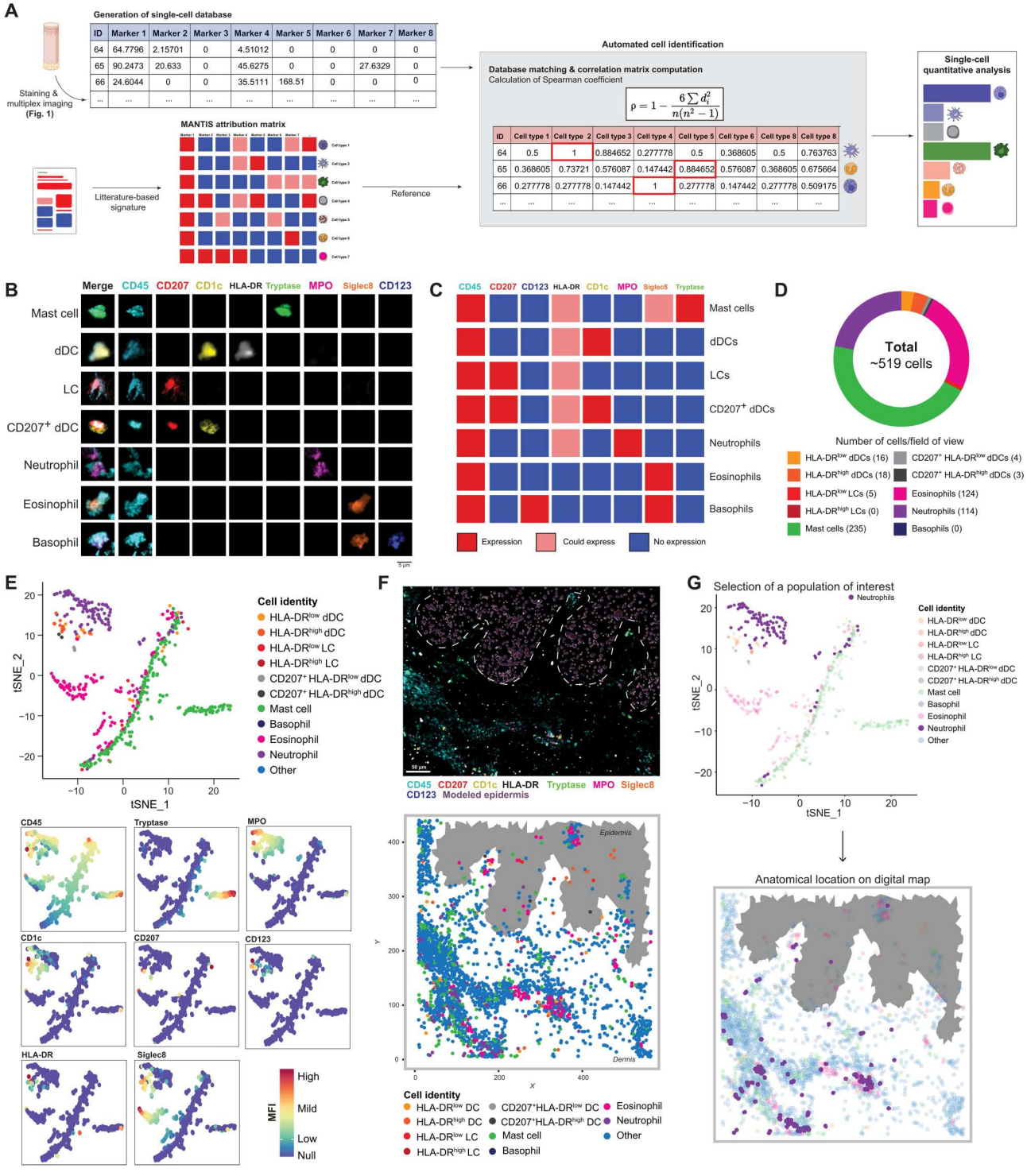

Fig. 2. MANTIS algorithm allows automated cell type attribution and interactive exploration of skin myeloid immune topology. (**A**) Automated tissue annotation. A reference attribution matrix defining the literature-based theoretical signature of a particular cell type was constructed and designated as MANTIS attribution matrix. A correlation matrix calculating Spearman coefficient between the single-cell database and MANTIS attribution matrix was computed. Each segmented cell was annotated to the cell type having the highest correlation coefficient, and cell type proportions were extracted. (**B**) Single-cell staining of all used biomarkers in identified myeloid cells. Scale bar, 5 μm. (**C**) MANTIS-simplified attribution matrix for myeloid panel. (**D**) Tissue annotation and cell proportion of pathological (SLE) skin. (**E**) Representative t-SNE plot of myeloid cell populations (top) and MFI levels of used markers (colored intensity scale) (bottom). (**F**) Representative 3D confocal multiplex image (top) and associated digital map (bottom) of predesigned MANTIS myeloid panel of pathological (SLE) skin. Scale bar, 50 μm. (**G**) Interactive reverse-gating. A population of interest (neutrophils) was selected on the t-SNE plot. Recomputation of the corresponding digital map enabled the visualization of the anatomical distribution of this particular population in the skin biopsy.

Quantitative validation of MANTIS annotation system using healthy-looking skin and inflammatory pathological lesions

With the constant increase in the number of cases, a large panel of putative skin manifestations of coronavirus disease 2019 (COVID-19) have been observed worldwide (*21*, *22*), including an unprecedented high rate of acral lesions, which represent ~75% of all cases and commonly named "COVID-toes" (*23*–*26*). Such manifestations (fig. S3A), compared to non-inflamed healthy-looking skin (fig. S3B), are associated with an important immune cell infiltration (fig. S3C) and tend to develop in young patients with no or very mild respiratory symptoms (*26*, *27*). While some pathological features of those lesions have been described (*3*, *28*, *29*), a precise analysis of their spatial immune profile is currently missing, which impairs the development of a clear readout to better diagnose and treat these rare cutaneous lesions. A possible explanation could be a collateral clinical manifestation of an efficient antiviral type 1 interferon response because acral lesions are also commonly observed in patients with interferonopathies, such as the Aicardi-Goutières syndrome (*30*) and SLE (*31*). With this in mind, we decided to benchmark the effective performance of MANTIS to resolve the immune topology of skin lesions of similar clinical severity from five patients with COVID-toes, two patients with the multisystem inflammatory syndrome, which is clinically similar to Kawasaki syndrome (i.e., a rare severe systemic inflammatory condition triggered by severe acute respiratory syndrome 2 infection, named hereafter "Kawasaki syndrome"), and three patients with SLE chilblains. Abdominal skin biopsies from five healthy-looking controls were used to set the baseline of a natural steady-state immune environment, albeit from a distant anatomical region.

We validated the quantitative performance of MANTIS to annotate immune cells by calculations of statistical correlations with a supervised approach of histo-cytometry (*6*, *15*) applied on the same datasets for each antibody panel in all skin samples. This last method consists of a manual gating of immune subsets on the same principle used in traditional flow cytometry. A total of 20,464 single CD45$^+$ immune cells were identified with the following distribution per condition: 1670 immune cells in five healthy-looking

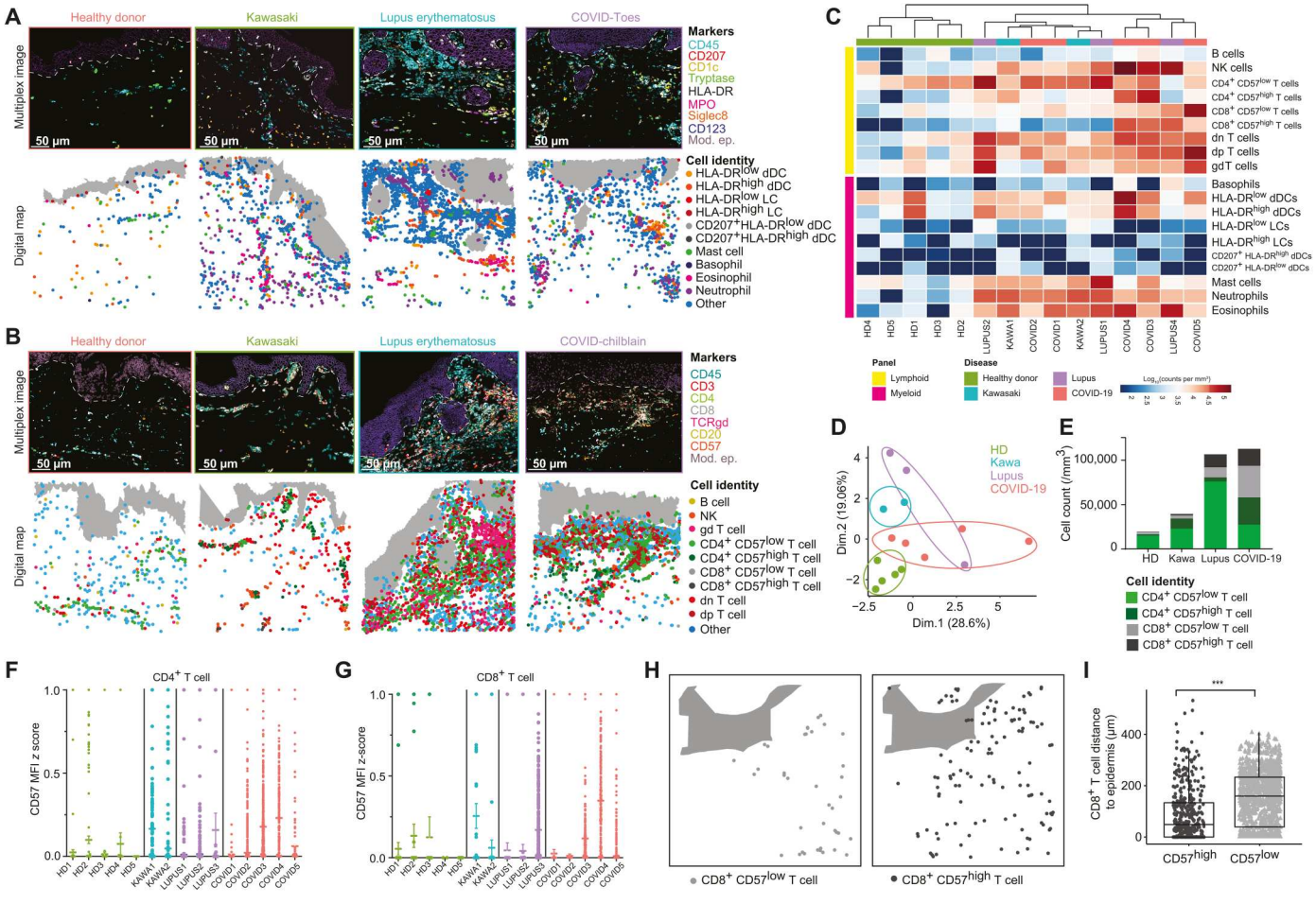

Fig. 3. 3D quantitative and spatial analysis of skin immune cells at the cellular level provide insight into disease signatures. (**A** and **B**) Representative 3D confocal multiplex images (top) and associated digital maps (bottom) of predesigned MANTIS myeloid (A) and lymphoid (B) panels of healthy and pathological skin. Scale bar, 50 µm. (**C**) Representative heatmap of LC and myeloid cell densities in logarithmic scale with hierarchical clustering. (**D**) Principal components analysis (PCA) of immune signatures of healthy and diseased skin. (**E**) Cell count per cubic millimeter of CD57^{low} and CD57^{high} T cells. (**F** and **G**) Dot plot of CD57 MFI *z* score in CD4$^+$ (F) and CD8$^+$ (G) T cells in healthy and diseased skin. (**H** and **I**) Representative digital map (H) and mean distance to epidermis (in µm) (I) of CD8$^+$ CD57^{low} (left) and CD57^{high} (right) T cells in COVID-19 skin lesions. Means + SEM; ***P < 0.001, Mann-Whitney test.

skin samples (i.e., with 895 myeloid cells and 775 LCs), 1703 in two patients with Kawasaki syndrome (i.e., with 932 myeloid cells and 775 LCs), 5076 in three patients with SLE chilblain (i.e., with 1560 myeloid cells and 3516 LCs), and 12,015 in five patients with COVID-toes (i.e., with 2838 myeloid cells and 9177 LCs). A classical gating strategy based on mutually exclusive biomarkers was used to assess the presence of myeloid cell (fig. S4A) and LC (fig. S5A) subsets by histo-cytometry. We identified a total of 19 different immune subsets and found very similar distributions of cell counts by either supervised histo-cytometry or unsupervised MANTIS algorithm (figs. S4, B to E, and S5, B to E). The calculated *R* coefficients were between 0.75 and 1, regardless of the antibody panel, the patients analyzed, or the disease (figs. S4F and 5F). We observed that all healthy-looking skin samples exhibited a proportion of immune cells aligned with previously described skin-resident immune populations at steady state in human (*1*, *32*). However, we noted a slightly higher tendency to detect rare populations of blood-circulating $CD45^+CD3^-CD20^+$ B cells or $CD45^+HLA\text{-}DR^-CD123^+Siglec8^+$ basophils, only when 3D images were computationally analyzed with MANTIS (figs. S4B and 5B). This is consistent with the fact that the skin is a highly vascularized tissue and that recent studies identified rare B cells in healthy skin (*33*).

Having validated the quantitative and qualitative performance of MANTIS-based annotation, we next defined a high-level view of the complex immune environment of pathological lesions from all 10 patients. Compared to healthy-looking samples, pathological lesions contained large immune infiltrates, confirming their inflammatory status (Fig. 3, A and B). All three conditions were associated with an infiltration of myeloid cells composed of a large number of neutrophils, eosinophils, mast cells, and conventional $CD45^{+-}CD1c^+CD207^-HLA\text{-}DR^+$ dDCs (Fig. 3, A and C). While detected in relatively low numbers in all analyzed skin samples, no difference was observed between healthy-looking and pathological samples for $CD45^+CD1c^-CD207^+HLA\text{-}DR^+$ LC or $CD45^+CD1c^+CD207^+HLA\text{-}DR^+$ dDC populations.

Compared to patients with Kawasaki syndrome, patients with SLE and COVID-19 tended to have an increased proportion of LCs (Fig. 3, B and C), with an enrichment in conventional $CD4^+$ or $CD8^+$ T cells and NK cells and, to a lesser extent, in γδ T cells. We also observed dp $CD45^+CD4^+CD8^+CD3^+TCR\gamma\delta^-$ and dn $CD45^+CD4^-CD8^-CD3^+TCR\gamma\delta^-$ T cells in all inflamed and some healthy-looking samples, albeit in smaller numbers (Fig. 3, B and C, and fig. S4). Such populations of T cells were often understudied, as CD4 and CD8 biomarkers are thought to be mutually exclusive; however, they have been often reported in autoimmune and chronic inflammatory disorders (*19*, *34*), including SLE (*35*, *36*).

We next performed an unsupervised clustering of all patients and healthy-looking controls based on the quantitative analysis of their immune signature using both a detailed heatmap based on immune profiles (Fig. 3C) and a principal components analysis (PCA) per patient (Fig. 3D). Healthy-looking skin samples clustered together, with no apparent relationship with the pathological samples (Fig. 3, C and D). Patients with Kawasaki syndrome and COVID-toes had a tendency to form disease-specific clusters, while patients with SLE were distributed between both conditions (Fig. 3, C and D). Although these data were obtained on a restricted number of patients, they suggest that all analyzed pathological lesions displayed common quantitative immune features (Fig. 3C), with nevertheless potential disease-intrinsic characteristics suggested upon analysis with a dimensional reduction PCA (Fig. 3D). To explore this hypothesis further, we refined our analysis by investigating the activation status of conventional $CD4^+$ and $CD8^+$ T cells based on their expression level of CD57, a biomarker classically associated with a high cytotoxic potential (i.e., pro-tissue damage) during viral infections and autoimmune disorders, including COVID-19 (*37*). We found that, compared to other pathological conditions, three COVID-toes cases were particularly enriched in $CD4^+$ and $CD8^+$ T cells, exhibiting high levels of CD57 (i.e., $CD57^{high}$; calculated as CD57 MFI *z* score; Fig. 3, E to G).

During inflammatory skin conditions, cytotoxic immune cells can relocate nearby to/in contact with keratinocytes and contribute to severe epidermal damage (*38*, *39*). To calculate the anatomical location of all immune cells with respect to the epidermal layers, we acquired the spatial coordinates of the modeled epidermis. We next incorporated into MANTIS a *k*-dimensional tree algorithm (*40*, *41*), which automatically decomposes the structural element coordinates (i.e., as exemplified here with the epidermis) into virtual subspaces and enables us to calculate the nearest neighbor to each immune cell (fig. S6A). A batch calculation of the distance of each individual cell can then be visualized under the format of a heatmap, providing a quick overview of the dataset (fig. S6B). We found that HLA^{high} dDCs (fig. S6C), NK cells (fig. S6D), and $CD8^+$ $CD57^{high}$ T cells (fig. S6E) were all significantly enriched near the epidermal layer in cases of COVID-toes. $CD8^+$ $CD57^{low}$ T cells were not found enriched in the epidermis (Fig. 3, H to K), suggesting a biological link between the expression levels of CD57 and epidermal migration in CD8 T cells. Although the number of patients studied is limited, these findings strongly suggest the potential formation of tissue-damaging subepidermal inflammatory clusters composed of cytotoxic T cells and NK cells in COVID-toes.

MANTIS enables topographic exploration of skin lesions by solving the α-shape of in situ immune substructures

Inflammatory dermatoses are characterized by the presence of large inflammatory infiltrates composed of specific immune cells and thought to be critical for the development of the pathology (e.g., type 2 immune cells and eosinophils in atopic dermatitis). To better understand the regional heterogeneity of pathological lesions from SLE, Kawasaki syndrome, and COVID-toes, we took advantage of α-shape algorithms that enable us, by tuning the α parameter, to define a precise shape of sets of points by drawing bounding polygons based on the principle of Delaunay triangulation (*42*). When combined with the digital immune landscapes generated with MANTIS, α-shape algorithms automatically generate polymorphic α-shapes around n-clusters composed of a minimum of 15 cells (i.e., 15 being the minimum number of cells often found in clusters of inflammatory but not in healthy-looking samples; Fig. 4A). This method enables us to automatically detect and quantify the major inflammatory clusters (i.e., named hereafter "αROIs") to provide a high-level view of the in situ immune architecture of the skin lesion for each patient and disease. We generated lymphoid (Fig. 4, B and C) and myeloid (Fig. 4, D and E) αROIs for all the samples. Healthy-looking controls displayed a few lymphoid αROIs, and four of five controls did not show myeloid αROIs. These data indicate that, in human skin at the steady state, LCs have a tendency to form aggregates [i.e., composed of perivascular T lymphocytes (*1*)], while myeloid cells are more likely to be randomly

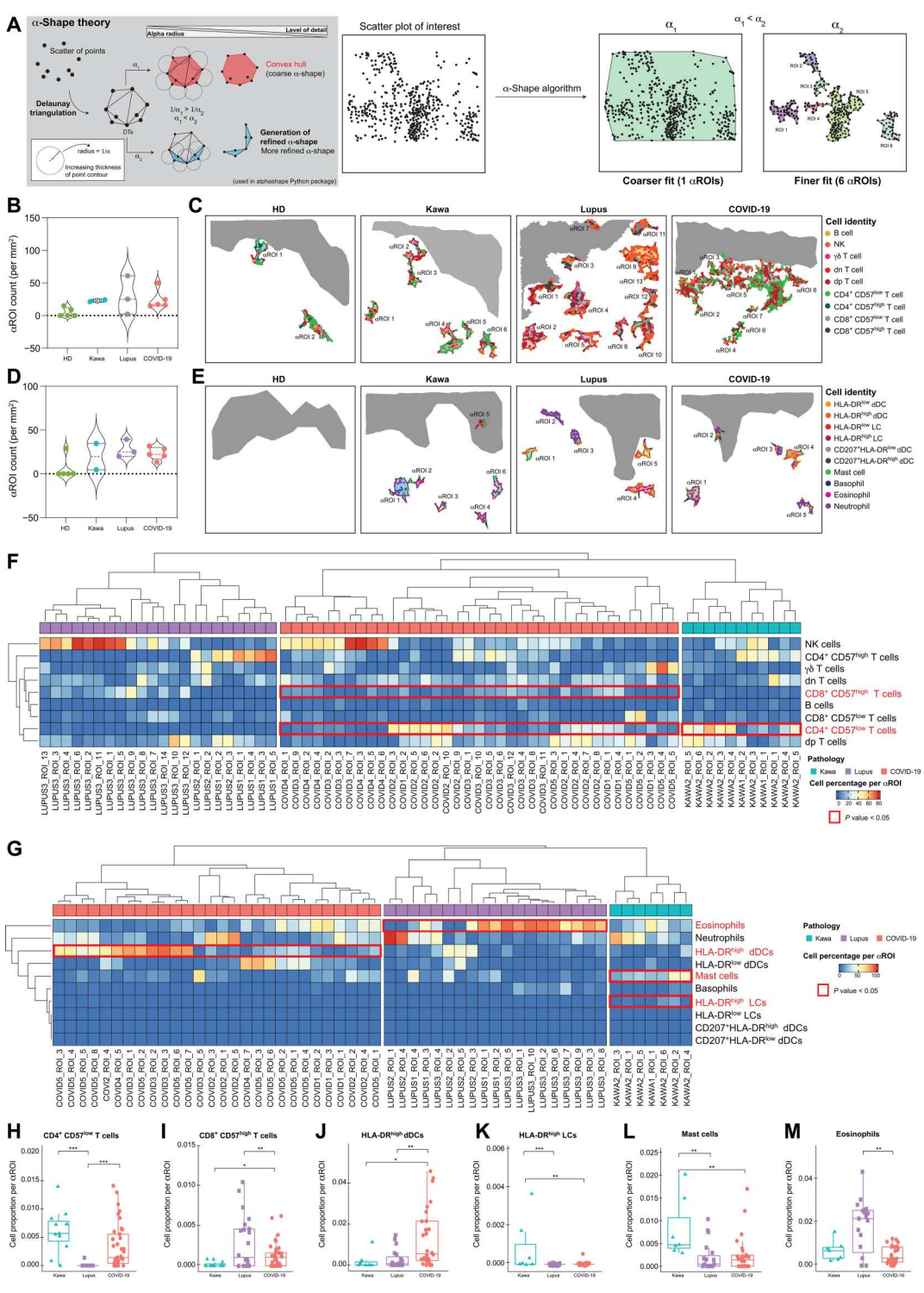

Fig. 4. Automatic detection of αROI enables exploration of inflammatory cluster topography in healthy and diseased skin. (**A**) α-Shape algorithm. Delaunay triangulation of a given set of points formed a bounding polygon that contains all the points of the set. The α parameter was defined by the value α, and a circle with 1/α radius was drawn around each point of the dataset. The line between two circles' meeting points formed a side of the bounding polygon, i.e., the α-shape. α value defines the detail level of the α-shape and allows modeling of voluminous structures ($1/\alpha_1$) or smaller structures ($1/\alpha_2$) having $1/\alpha_1 > 1/\alpha_2$. (**B** and **C**) Violin plot (B) and representative digital maps (C) of lymphoid αROI density in healthy and pathological skin. (**D** and **E**) Violin plot (D) and representative digital maps (E) of myeloid αROI density in healthy and diseased skin. (**F** and **G**) Representative heatmaps of cell proportions in lymphoid (F) and myeloid (G) αROIs in pathological skin. A hierarchical clustering was applied on rows and on each pathology's column. (**H** to **M**) Mean proportion of $CD4^+$ $CD57^{low}$ T cells (H), $CD8^+$ $CD57^{high}$ T cells (I), HLA-DR^{high} dDCs (J), HLA-DR^{high} LCs (K), mast cells (L), and eosinophils (M) per αROI in diseased skin. Means ± SEM; $*P < 0.05$, $**P < 0.01$, and $***P < 0.001$, one-way analysis of variance (ANOVA) (H to M).

distributed. In line with the data presented in Fig. 3, we found a higher proportion of both lymphoid and myeloid αROIs in pathological samples as compared to healthy-looking controls (Fig. 4, B to E). Using global unsupervised hierarchical clustering of αROIs per disease, we can generate a high-level view of inflammatory cluster composition and observe trends in disease-specific immune responses (Fig. 4, F and G). Notably, lymphoid αROIs of both Kawasaki syndrome and COVID-toes exhibited a significantly higher proportion of $CD4^+CD57^{low}$ T cells than that of patients with SLE (Fig. 4, F and H). Both COVID-toes and SLE lesions displayed significant clusters of $CD8^+CD57^{high}$ cytotoxic T cells, highlighting the cytolytic aspect of pathological lesion microenvironment in these conditions (Fig. 4, F and I). We next analyzed myeloid αROIs for all cases. We found that, COVID-toes had

a particularly high density of clusters enriched in activated HLA-DR^{high} dDCs (Fig. 4, G and J). Conversely, Kawasaki syndrome lesions showed an enrichment in both HLA-DR^{high} LCs (Fig. 4, G and K) and mast cells (Fig. 4, G and L), while SLE lesions displayed large aggregates of eosinophils (Fig. 4, G and M). This finding is consistent with previous reports of strong eosinophilia in SLE (*43*–*45*). No significant differences were observed regarding other immune cell subsets in αROIs. While the precise role played by specific inflammatory clusters of immune cells in each disease remains elusive, these data strongly suggest that combining MANTIS digital maps with α-shape–based algorithms can reveal a significant nonrandom distribution of skin immune cells in skin lesions, with the presence of disease-specific immune structures. MANTIS analytic pipeline can thus enable us to quickly solve the spatial organization of complex immune environments and open interesting perspectives for future investigations in the field of dermatopathology.

DISCUSSION

Here, we propose a general framework for 3D quantitative and spatial analysis of skin immune cells at the cellular level. We first describe a simple method to perform a fast 3D acquisition of up to 10 biomarkers simultaneously and extract a single-cell database containing the biological identity (including spatial coordinates) of skin lymphoid and myeloid cells. We then analyze the extracted databases using an automated and interactive analytic pipeline composed of phenotype attribution matrices coupled with cell-to-structure distance calculations and α-shape algorithm–based detection of major inflammatory clusters. Our analysis was focused on FFPE samples, as it is still the most easily available source of pathological tissues and can enable analysis of patients′ skin-sampled in routine clinical practice. However, the use of cryopreserved samples is compatible with the approach that we describe here and enables the analysis of thicker tissue sections (fig. S2).

We identified that the first step of the process, which consists of the generation of good-quality 3D multiplexed images with a great ratio signal over noise, is critical for the rest of the study. This is why we emphasized the capability of a conventional 8-year-old (non–custom-built) confocal laser scanning system to acquire 10 different fluorochromes simultaneously. This method of acquisition can be democratized to most academic/clinical facilities because it involves a conventional equipment coupled to basic spectral spillover compensation and single-cell data extraction strategies, via the use of commercially available software (Huygens and Imaris; described in detail in Materials and Methods).

Single-cell segmentation is also very critical, as it will constitute the very core of the future analysis of immune subpopulations and expression of biomarkers. Possible mistakes made at this step, e.g. the inability to separate immune cells in large infiltrates, would then result in misinterpretation of MANTIS-generated results. We tested different approaches to automatically segment healthy-looking and inflammatory skin samples, including random forest-based classifiers (e.g., ilastik machine learning). While such a method was suitable to segment healthy-looking images with a low concentration of immune cells, it failed to segment complex inflammatory lesions, where large and packed immune clusters were present. We thus opted for a semisupervised segmentation of single immune cells using the software Imaris, in which the segmentation of each inflammatory cluster was quality-controlled manually and was in 3D (Fig. 1F). While this approach is probably more time-consuming, we could ensure a precise 3D segmentation and further extraction of an accurate single-cell database to be processed with MANTIS. A recent study has reported the use of an analysis pipeline, including a new segmentation strategy, adapted from the field of astronomy named "AstroPath" (*46*). Using this approach and only six biomarkers, they could identify important pathological features in biopsies from patients with melanoma. These results, in line with our findings, highlight the importance of carefully selecting a list of biomarkers to be studied and of having the right analytic pipeline to draw reliable insights.

Because immunologists are more commonly used to identifying immune cell populations with manual gating of populations based on flow cytometry, we validated the quantitative performance of MANTIS by analyzing the extracted single-cell databases for the 15 patients analyzed with the conventional flow cytometry software, FlowJo. We found that the MANTIS-based analysis on 3D images generated with two different panels and just a minimal number of 10 antibodies per panel were sufficient to distinguish 19 immune subsets and identify disease-specific trends in skin lesions.

Because MANTIS attribution matrices can be quickly adjusted to any set of markers, they could be compatible with single-cell databases generated using technology with high multiplexing capabilities such as CODEX (*7*, *8*), MIBI-TOF (*9*), IMC (*10*), MuSIC (*11*), CyCIF (*12*), Cell Dive (*13*), and others (*14*). We included in MANTIS the α-shape algorithm that enables us to define the precise shape of the inflammatory immune clusters based on the principle of Delaunay triangulation (*42*). When applied to digital immune landscapes, the α-shape algorithm automatically identifies and quantifies dermal and epidermal inflammatory clusters (i.e., αROIs) composed of a minimum of 15 immune cells (Fig. 4A). This method enables one to directly analyze the major αROIs to provide a fast high-level view of the skin immune architecture in a given lesion. Using this method, we could quickly identify that the immune subset (e.g., mast cells, HLA-DR^{high} dDCs, CD8^{+}CD57^{high} cytotoxic T cells, eosinophils, etc.) was specifically enriched in dermal areas only in some patient subgroups. These preliminary observations suggest that, depending on their etiology, pathological lesions could be due to distinct pathological mechanisms. This type of analysis opens interesting perspectives for the 3D cartography of complex inflammatory skin lesions and should be pursued by additional studies on a larger number of patients. While 2D immune landscapes are represented here to facilitate the visual assessment in the figures (3D graphs are hardly perceivable on static pictures), the single-cell segmentation and extraction of cellular spatial coordinates were all performed in 3D.

On the basis of CODEX high multiplexing capacity, previous studies (*8*, *47*) have shown that it is possible to generate a high-level view of the cell-to-cell interaction landscape based on the principle of the Delaunay neighborhood graph (*48*). The MANTIS α-shape algorithm is complementary, as it automatically identifies major immune structures while deciphering their cellular composition. Combining α-shape and neighborhood approaches could help quickly solve the biology of major inflammatory clusters in the skin, by drawing the ligand-receptor interactome of immune and structural cells within the identified cluster. Such a high-dimensional analysis of the skin immune architecture could provide a promising avenue for understanding the complexity of inflammatory skin

manifestations with potential benefits for patient stratification and/or diagnosis.

There is a strong need to design new tools to assist clinical decision-making and/or better apprehend the complexity of inflammatory dermatoses. While very promising processes have been made in the field of spatial biology (*49*–*51*), there is an unmet need for a non-expensive and standardized multiplexed imaging analytical framework capable of automatically resolving the immune architecture of an inflamed skin. Here, we show that the MANTIS analytical system is uniquely positioned to examine numerous questions in the fields of skin immunobiology and should lay the foundation for a fast and automated analysis pipeline of relevant in situ inflammatory environments in both research and clinical facilities.

MATERIALS AND METHODS

Human skin samples

The pathological biopsies were performed as part of routine care for diagnosis purposes in Lyon, Reims, and Toulouse university hospitals. All patients have given written informed consent to the publication of their case details. Skin biopsies from patients with lupus erythematosus were obtained from Toulouse University Hospital. Biopsies of COVID-toes were obtained from Toulouse, Reims, and Lyon university hospitals. Skin biopsies of multisystem inflammatory syndrome were obtained from Reims University Hospital. Anonymized healthy human skin samples were obtained from donors that underwent abdominoplasty procedures and had given their written informed consent. Donors did not have any record of allergies or dermatological disorders and did not use corticosteroids. Control healthy skin biopsies were age- and gender-matched with pathological samples and obtained from Genoskin SAS (www.genoskin.com/). Genoskin has obtained all legal authorizations necessary from the French Ministry of Higher Education, Research and Innovation (AC-2017-2897) and the Personal Protection Committee (2017-A01041-52). All studies were conducted according to Declaration of Helsinki protocols.

Skin section preparation, histology, and staining

Human skin samples were either frozen in optimal cutting temperature compounds (OCT, Tissue-Tek) or formalin-fixed and paraffin-embedded. FFPE-tissue sections (10 μm) were heated at 95°C for 20 min. Sections were subsequently immersed into xylene for 30 min, washed in a graded series of ethanol (100, 95, 70, 50, and 30% for 5 min each), and abundantly washed with distilled water. They were then treated using a heat-induced epitope retrieval method as previously described (*52*).

FFPE-tissue sections were blocked and permeabilized with phosphate-buffered saline (PBS), 0.5% (w/v)% bovine serum albumin (BSA; Sigma-Aldrich), and 0.3% Triton X-100 (Merck) for 30 to 60 min at room temperature and then incubated with fluorophore-coupled antibodies or unconjugated antibodies overnight at 4°C in the dark. The sections were then washed three times in PBS 0.5% (w/v)% BSA, 0.3% Triton X-100 and incubated, if needed, with secondary antibodies in PBS, 0.5% (w/v)% BSA, and 0.3% Triton X-100 for 2 hours at room temperature in the dark. Last, samples were treated with an autofluorescence quenching solution named TrueVIEW (Vector Laboratories) for 5 min. The slides were mounted in Mowiol medium (Sigma-Aldrich) and sealed with a coverslip. All conjugated and unconjugated antibodies used in this study were validated in single immunostainings of human skin and tonsils and are listed in table S1.

Acquisition

Z-stack images (512 × 512 pixel; 1 μm) were acquired using an 8-year-old confocal microscope SP8 (Leica Microsystems) equipped with an HC PL APO CS2 with 40× numerical aperture 1.3 oil objective, an ultraviolet diode (405 nm), and four lasers in visible range wavelengths (405, 488, 532, 552, and 635 nm). The setup was made up of five detectors [three hybrid detectors with high quantum yield compared to classical photomultiplier (PMT) detectors and two PMTs]. Mosaic sequential images were acquired using the between-stack configuration to simultaneously collect individual seven or eight channels and tiles before merging them to obtain one single image. Use of the between-stack configuration and the modulation of the detectors′ detection windows help reduce the leaking of fluorophores. Last, a digital zoom of 1.9 was applied during the acquisition and a mosaic multicolor image was obtained and exported into a .lif format. Detection windows and microscope configuration used in our study are listed in table S2.

Image deconvolution and correction of spectral spillover

3D mosaic images were then imported into Huygens SVI software to correct the signal by applying deconvolution and cross-talk correction. Two deconvolution methods were used: the express deconvolution (theoretical and fast) or the deconvolution wizard (possibility to use experimental or theoretical parameters and to adjust the background value). Automatic cross-talk correction estimation was obtained, and the coefficients were slightly adjusted manually, if needed, for optimal spillover correction.

Segmentation

3D mosaic images were imported into Imaris software to separate objects (cells) using a 3D surface segmentation. Before creating the surface objects in Imaris, classical image processing was required. For instance, defining a threshold, adding a median filter, and/or normalizing the layers were sometimes applied to clean the background. Images were either cleaned using the CD45 surface objects or other channels by applying appropriate masks for each channel. Then, segmentation was applied on the CD45 channel surface. Statistics were exported into .csv format.

Epidermis modeling

The epidermis was identified using the natural autofluorescence of the tissue. On the basis of the autofluorescence found in multiple appropriate channels, an epidermis surface was created using the Object Creation semi-automated tool of the Imaris software. The coordinates of the epidermis were then exported into .csv format. The modeling of the epidermis shape showed on the digital maps was obtained using the α-shape algorithm (described below).

Segmentation troubleshooting

In some cases, the surface creation parameters were not efficient in automatically obtaining good object creation, or the module was not sensitive enough to detect low-intensity objects. In this case, the creation of small objects was done manually, and the threshold selection was also reduced. If the detected object was below 1 μm, then a manual object unification with surrounding objects of the same intensity was performed.

Statistical data exportation

Statistical properties of each segmented object (cell) in the processed 3D Imaris Multiplex image were automatically calculated. Object volume, sphericity, area, *xyz* position, and MFI in all channels were exported as a .csv table.

Skin enzymatic digestion and gradient separation

Immune cells were isolated from fresh skin biopsies from Genoskin. Briefly, skin was harvested in predigestion medium, fragmented into pieces, and incubated at 37°C on a rotating plate to remove epithelial cells and other impurities. The supernatant was discarded, and the samples were digested for 45 min on a rotating plate with 1.25 mg of Liberase (Sigma Aldrich, #5401127001) and 2.5 mg of deoxyribonuclease I (Sigma Aldrich, #10104159001) to disaggregate the tissue. Samples were further dissociated with the Miltenyi gentleMACS Dissociator. Cells were then enriched with a Percoll gradient, washed, and used for staining with the same panels used for MANTIS. Data were acquired on a FACSymphony (BD) cytometer and were analyzed using FlowJo (Tree Star) software.

FlowJo analysis and gating strategies

Identification and density assessment of immune cell subsets were analyzed using classical histo-cytometry (*6*). Immune cell populations were gated in FlowJo software as follows: B cells, $CD45^+$ $CD20^+$; NK cells, $CD45^+$ $CD20^-$ $CD3^-$ $CD57^+$; $CD4^+$ T cells, $CD45^+$ $CD20^-$ $CD3^+$ $TCR\gamma\delta^-$ $CD4^+$ $CD8^-$ $CD57^{low\ or\ high}$; $CD8^+$ T cells, $CD45^+$ $CD20^-$ $CD3^+$ $TCR\gamma\delta^-$ $CD4^-$ $CD8^+$ $CD57^{low\ or\ high}$; γδ T cells, $CD45^+$ $CD20^-$ $CD3^+$ $TCR\gamma\delta^+$; dn T cells, $CD45^+$ $CD20^-$ $CD3^+$ $TCR\gamma\delta^-$ $CD4^-$ $CD8^-$; dp T cells, $CD45^+$ $CD20^-$ $CD3^+$ $TCR\gamma\delta^-$ $CD4^+$ $CD8^+$; mast cells, $CD45^+$ $Tryptase^+$; DC, $CD45^+$ $CD1c^+$ $CD207^-$ $HLA\text{-}DR^{low\ or\ high}$; LC, $CD45^+$ $CD1c^-$ $CD207^+$ $HLA\text{-}DR^{low\ or\ high}$; DC $CD207^+$, $CD45^+$ $CD1c^+$ $CD207^+$ $HLA\text{-}DR^{low\ or\ high}$; neutrophils, $CD45^+$ $CD1c^-$ $CD207^-$ $Tryptase^-$ $Siglec8^-$ MPO^+; eosinophils, $CD45^+$ $CD1c^-$ $CD207^-$ MPO^- $Tryptase^-$ $Siglec8^+$ $CD123^-$; and basophils, $CD45^+$ $CD1c^-$ $CD207^-$ MPO^- $Siglec8^+$ $CD123^+$.

Tissue annotation using MANTIS

Implementation of MANTIS reference panels

To enable cell identification, we built a binary table containing a literature-based theoretical signature of biomarkers expressed in each cell population identified by the used panel (naturally depending on the used set of antibodies), known as the reference attribution panel. If a cell population is positive for a marker, then the value is set to 1; otherwise, it is set to 0. If a cell population can be positive for a marker, then there are two columns, one with the value set to 1 and the other with the value set to 0 (i.e., γδ T cells can express CD4 or not). Two reference tables were implemented and designated by lymphoid and myeloid reference attribution matrices.

Dynamic adaptation of reference matrices

Sample heterogeneity led to different acquisition parameters (laser power, gain, etc.). To standardize data processing, we scaled the reference tables and dynamically adapted, for each sample, the table values according to the MFI values. In practice, the value "1" in the binary table was replaced by the maximum MFI value acquired in the corresponding channel from the tested sample.

Automatic cell type identification

To annotate the segmented objects, a correlation matrix between the MFI table and the adapted reference panel was generated by performing a pairwise Spearman's rank correlation using the R software (2021). Each object was then phenotypically assigned to the cell type having the highest correlation coefficient. Objects with multiple highest correlation coefficients were assigned as "Other" cell types.

Accuracy validation

The accuracy of MANTIS automatic cell identification was verified by comparing quantification results to classical histo-cytometry (*6*). Briefly, linear regression of cell type density was computed between both attribution methods, and regression coefficients were calculated. Regression coefficients ranging between 0.75 and 1 reflect MANTIS technique robustness.

Activation status detection

MANTIS panels were designed to include not only discriminant markers for cell attribution but also nondiscriminant and informative markers, for instance, activation markers. The cell populations of interest ($CD4^+$ and $CD8^+$ T cells in the lymphoid panel and DCs, LCs, and $CD207^+$ DCs in the myeloid panel) and the activation markers that reflect the activation status of these populations (CD57 in the lymphoid panel and HLA-DR in the myeloid panel) were defined in the MANTIS algorithm. The latter automatically computes the MFI density curve associated with the activation markers within the selected populations. Subsequently, the MFI corresponding to the first peak of the density curve is defined as the MFI value above which the cell is considered positive for the activation marker.

α-Shape calculation

α-Shape was calculated using the alphashape Python package. Briefly, Delaunay triangulation of a given set of points formed a bounding polygon that contains all the points of the set. The α parameter was defined by the value α, and a circle with 1/α radius was drawn in such a way that two points of the dataset are located on the boundaries of the circle and the circle is empty. For each empty circle found, the line between the two points formed a side of the bounding polygon, i.e., the α-shape. As α decreased, the α-shape changed from a convex hull (e.g., epidermis α-shape, α = 0.4) to a more tightly fitting bounding box, resulting in more refined α-shapes [e.g., ROI α-shape (αROI), α = 0.1].

Cell-to-structure distance calculation and nearest-neighbor search

x-y coordinates of epidermis α-shape contours were stored using the *k*-dimensional tree method, which allows data ranking and structuration. Briefly, data points were classified on the basis of nodes and branches space-partitioning, allowing a fast nearest-neighbor calculation. For a given point (cell) of the dataset, the nearest neighbor in the epidermis α-shape was found, and the distance defined by *r* was calculated using the scipy.spatial Python package (*40*). The distance of cells contained in the epidermis α-shape was set to 0.

Data clustering and αROI analysis

ROIs (αROI, i.e., inflammatory cell clusters) were identified using the α-shape algorithm with a tuned α parameter (α = 0.1), allowing correct detection of high–cell density areas. αROI with less than 15 cells were removed from the analysis. For each selected αROI, specific characteristics were calculated and extracted, such as area, total number of cells, cell number, proportion by cell type, and αROI center coordinates.

Data visualization

Visualization charts were obtained using the ggplot2, Pigengene, and ComplexHeatmap R packages and matplotlib and seaborn Python packages. t-SNE was computed with Rtsne.

Statistics

Statistical tests were performed using Prism 8 (GraphPad Software) and the Rstats and rstatix R packages. One-way analysis of variance (ANOVA) with Tukey's test for multiple comparisons or Mann-Whitney test was performed on samples as noted in the respective figure legends. A *P* value of less than 0.05 was considered statistically significant.

Supplementary Materials

This PDF file includes:
Figs. S1 to S6
Tables S1 to S4
Legend for movie S1

Other Supplementary Material for this manuscript includes the following:
Movie S1

View/request a protocol for this paper from *Bio-protocol*.

REFERENCES AND NOTES

1. W. R. Heath, F. R. Carbone, The skin-resident and migratory immune system in steady state and memory: Innate lymphocytes, dendritic cells and T cells. *Nat. Immunol.* **14**, 978–985 (2013).
2. F. O. Nestle, P. Di Meglio, J. Z. Qin, B. J. Nickoloff, Skin immune sentinels in health and disease. *Nat. Rev. Immunol.* **9**, 679–691 (2009).
3. J. Kanitakis, C. Lesort, M. Danset, D. Jullien, Chilblain-like acral lesions during the COVID-19 pandemic ("COVID toes"): Histologic, immunofluorescence, and immunohistochemical study of 17 cases. *J. Am. Acad. Dermatol.* **83**, 870–875 (2020).
4. I.-I. Morar, F.-A. Tabăran, T. Mocan, E.-M. Jianu, M.-S. Orăsan, A.-D. Pop, R.-I. Orăsan, Immunohistochemical study of psoriatic plaques and perilesional skin in psoriasis vulgaris patients: A pilot study. *Exp. Ther. Med.* **18**, 888–894 (2019).
5. K. Heinzmann, L. M. Carter, J. S. Lewis, E. O. Aboagye, Multiplexed imaging for diagnosis and therapy. *Nat. Biomed. Eng.* **1**, 697–713 (2017).
6. M. Y. Gerner, W. Kastenmuller, I. Ifrim, J. Kabat, R. N. Germain, Histo-cytometry: A method for highly multiplex quantitative tissue imaging analysis applied to dendritic cell subset microanatomy in lymph nodes. *Immunity* **37**, 364–376 (2012).
7. S. Black, D. Phillips, J. W. Hickey, J. Kennedy-Darling, V. G. Venkataraaman, N. Samusik, Y. Goltsev, C. M. Schürch, G. P. Nolan, CODEX multiplexed tissue imaging with DNA-conjugated antibodies. *Nat. Protoc.* **16**, 3802–3835 (2021).
8. Y. Goltsev, N. Samusik, J. Kennedy-Darling, S. Bhate, M. Hale, G. Vazquez, S. Black, G. P. Nolan, Deep profiling of mouse splenic architecture with CODEX multiplexed imaging. *Cell* **174**, 968–981.e15 (2018).
9. L. Keren, M. Bosse, S. Thompson, T. Risom, K. Vijayaragavan, E. McCaffrey, D. Marquez, R. Angoshtari, N. F. Greenwald, H. Fienberg, J. Wang, N. Kambham, D. Kirkwood, G. Nolan, T. J. Montine, S. J. Galli, R. West, S. C. Bendall, M. Angelo, MIBI-TOF: A multiplexed imaging platform relates cellular phenotypes and tissue structure. *Sci. Adv.* **5**, eaax5851 (2019).
10. C. Giesen, H. A. O. Wang, D. Schapiro, N. Zivanovic, A. Jacobs, B. Hattendorf, P. J. Schüffler, D. Grolimund, J. M. Buhmann, S. Brandt, Z. Varga, P. J. Wild, D. Günther, B. Bodenmiller, Highly multiplexed imaging of tumor tissues with subcellular resolution by mass cytometry. *Nat. Methods* **11**, 417–422 (2014).
11. H. Y. Holzapfel, A. D. Stern, M. Bouhaddou, C. M. Anglin, D. Putur, S. Comer, M. R. Birtwistle, Fluorescence multiplexing with spectral imaging and combinatorics. *ACS Comb. Sci.* **20**, 653–659 (2018).
12. J.-R. Lin, B. Izar, S. Wang, C. Yapp, S. Mei, P. M. Shah, S. Santagata, P. K. Sorger, Highly multiplexed immunofluorescence imaging of human tissues and tumors using t-CyCIF and conventional optical microscopes. *eLife* **7**, e31657 (2018).
13. A. Corwin, E. McDonough, C. Surrette, P. Dumpuri, A. Sood, F. M. Ginty, Abstract 1448: Cell DIVE: A robust and standardized platform for multiplexed whole slide imaging and single cell analysis. *Cancer Res.* **80**, 1448 (2020).
14. S. K. Saka, Y. Wang, J. Y. Kishi, A. Zhu, Y. Zeng, W. Xie, K. Kirli, C. Yapp, M. Cicconet, B. J. Beliveau, S. W. Lapan, S. Yin, M. Lin, E. S. Boyden, P. S. Kaeser, G. Pihan, G. M. Church, P. Yin, Immuno-SABER enables highly multiplexed and amplified protein imaging in tissues. *Nat. Biotechnol.* **37**, 1080–1090 (2019).
15. W. Li, R. N. Germain, M. Y. Gerner, High-dimensional cell-level analysis of tissues with Ce3D multiplex volume imaging. *Nat. Protoc.* **14**, 1708–1733 (2019).
16. M. Y. Lee, J. S. Bedia, S. S. Bhate, G. L. Barlow, D. Phillips, W. J. Fantl, G. P. Nolan, C. M. Schürch, CellSeg: A robust, pre-trained nucleus segmentation and pixel quantification software for highly multiplexed fluorescence images. *BMC Bioinformatics* **23**, 46 (2022).
17. R. Ahmed, K. L. Miners, J. Lahoz-Beneytez, R. E. Jones, L. Roger, C. Baboonian, Y. Zhang, E. C. Y. Wang, M. K. Hellerstein, J. M. McCune, D. M. Baird, D. A. Price, D. C. Macallan, B. Asquith, K. Ladell, CD57^{+} memory T cells proliferate in vivo. *Cell Rep.* **33**, 108501 (2020).
18. H. Kared, S. Martelli, T. P. Ng, S. L. Pender, A. Larbi, CD57 in human natural killer cells and T-lymphocytes. *Cancer Immunol. Immunother.* **65**, 441–452 (2016).
19. Y. Parel, C. Chizzolini, CD4^{+} CD8^{+} double positive (DP) T cells in health and disease. *Autoimmun. Rev.* **3**, 215–220 (2004).
20. Z. Wu, Y. Zheng, J. Sheng, Y. Han, Y. Yang, H. Pan, J. Yao, CD3^{+}CD4^{-}CD8^{-} (double-negative) T cells in inflammation, immune disorders and cancer. *Front. Immunol.* **13**, 816005 (2022).
21. D. Fernandez-Nieto, D. Ortega-Quijano, G. Segurado-Miravalles, C. Pindado-Ortega, M. Prieto-Barrios, J. Jimenez-Cauhe, Comment on: Cutaneous manifestations in COVID-19: A first perspective. Safety concerns of clinical images and skin biopsies. *J. Eur. Acad. Dermatol. Venereol.* **34**, e252–e254 (2020).
22. B. Joob, V. Wiwanitkit, COVID-19 can present with a rash and be mistaken for dengue. *J. Am. Acad. Dermatol.* **82**, e177 (2020).
23. V. Piccolo, I. Neri, C. Filippeschi, T. Oranges, G. Argenziano, V. C. Battarra, S. Berti, F. Manunza, A. B. Fortina, V. di Lernia, V. Boccaletti, G. de Bernardis, B. Brunetti, C. Mazzatenta, A. Bassi, Chilblain-like lesions during COVID-19 epidemic: A preliminary study on 63 patients. *J. Eur. Acad. Dermatol. Venereol.* **34**, e291–e293 (2020).
24. N. Landa, M. Mendieta-Eckert, P. Fonda-Pascual, T. Aguirre, Chilblain-like lesions on feet and hands during the COVID-19 pandemic. *Int. J. Dermatol.* **59**, 739–743 (2020).
25. C. G. Casas, A. Català, G. C. Hernández, P. Rodríguez-Jiménez, D. Fernández-Nieto, A. R.-V. Lario, I. N. Fernández, R. Ruiz-Villaverde, D. Falkenhain-López, M. L. Velasco, J. García-Gavín, O. Baniandrés, C. González-Cruz, V. Morillas-Lahuerta, X. Cubiró, I. F. Nart, G. Selda-Enriquez, J. Romaní, X. Fustà-Novell, A. Melian-Olivera, M. R. Riesco, P. Burgos-Blasco, J. S. Ortigosa, M. F. Rodriguez, I. García-Doval, Classification of the cutaneous manifestations of COVID-19: A rapid prospective nationwide consensus study in Spain with 375 cases. *Br. J. Dermatol.* **183**, 71–77 (2020).
26. D. E. McMahon, A. E. Gallman, G. J. Hruza, M. Rosenbach, J. B. Lipoff, S. R. Desai, L. E. French, H. Lim, J. G. Cyster, L. P. Fox, M. S. Fassett, E. E. Freeman, Long COVID in the skin: A registry analysis of COVID-19 dermatological duration. *Lancet Infect. Dis.* **21**, 313–314 (2021).
27. A. M. Jimenez-Cebrian, A. Castro-Mendez, B. García-Podadera, R. Romero-Galisteo, M. Medina-Alcántara, I. Garcia-Paya, J. Páez-Moguer, A. Córdoba-Fernández, Clinical manifestations of COVID-19 in the feet: A review of reviews. *J. Clin. Med.* **10**, 2201 (2021).
28. T. G. Olsen, M. A. Shrit, T. A. Feeser, J. J. Wargo, COVID purpura (Toes) case series: A chilblains-like vasculopathy. *Am. J. Dermatopathol.* **43**, e47–e50 (2021).
29. I. Colmenero, C. Santonja, M. Alonso-Riaño, L. Noguera-Morel, A. Hernández-Martín, D. Andina, T. Wiesner, J. L. Rodríguez-Peralto, L. Requena, A. Torrelo, SARS-CoV-2 endothelial infection causes COVID-19 chilblains: Histopathological, immunohistochemical and ultrastructural study of seven paediatric cases. *Br. J. Dermatol.* **183**, 729–737 (2020).
30. C. Piccoli, N. Bronner, F. Gavazzi, H. Dubbs, M. de Simone, V. de Giorgis, S. Orcesi, E. Fazzi, J. Galli, S. Masnada, D. Tonduti, C. Varesio, A. Vanderver, A. Vossough, L. Adang, Late-onset Aicardi-Goutières syndrome: A characterization of presenting clinical features. *Pediatr. Neurol.* **115**, 1–6 (2021).
31. A. Ramondetta, M. Panzone, P. Dapavo, M. Ortoncelli, M. T. Giura, M. Licciardello, G. Rozzo, N. Siliquini, M. T. Fierro, S. Ribero, Chilblain acral lesions in the COVID -19 era. Are they

marker of infection in asymptomatic patients? *J. Eur. Acad. Dermatol. Venereol.* **34**, e440–e441 (2020).
32. K. Kabashima, T. Honda, F. Ginhoux, G. Egawa, The immunological anatomy of the skin. *Nat. Rev. Immunol.* **19**, 19–30 (2019).
33. G. F. Debes, S. E. McGettigan, Skin-associated B cells in health and inflammation. *J. Immunol.* **202**, 1659–1666 (2019).
34. H. Li, G. C. Tsokos, Double-negative T cells in autoimmune diseases. *Curr. Opin. Rheumatol.* **33**, 163–172 (2021).
35. P. A. Sieling, S. A. Porcelli, B. T. Duong, F. Spada, B. R. Bloom, B. Diamond, B. H. Hahn, Human double-negative T cells in systemic lupus erythematosus provide help for IgG and are restricted by CD1c. *J. Immunol.* **165**, 5338–5344 (2000).
36. J. C. Crispín, M. Oukka, G. Bayliss, R. A. Cohen, C. A. Van Beek, I. E. Stillman, V. C. Kyttaris, Y.-T. Juang, G. C. Tsokos, Expanded double negative T cells in patients with systemic lupus erythematosus produce IL-17 and infiltrate the kidneys. *J. Immunol.* **181**, 8761–8766 (2008).
37. R. Srivastava, N. Dhanushkodi, S. Prakash, P. G. Coulon, H. Vahed, L. Zayou, A. Quadiri, L. B. Mohamed, High frequencies of phenotypically and functionally senescent and exhausted $CD56^+$ $CD57^+$ $PD\text{-}1^+$ natural killer cells, SARS-CoV-2-specific memory $CD4^+$ and $CD8^+$ T cells associated with severe disease in unvaccinated COVID-19 patients. bioRxiv 2022.07.26.501655 [Preprint] (2022). 10.1101/2022.07.26.501655
38. A. W. Ho, T. S. Kupper, T cells and the skin: From protective immunity to inflammatory skin disorders. *Nat. Rev. Immunol.* **19**, 490–502 (2019).
39. D. Hijnen, E. F. Knol, Y. Y. Gent, B. Giovannone, S. J. P. Beijn, T. S. Kupper, C. A. F. M. Bruijnzeel-Koomen, R. A. Clark, $CD8^+$ T cells in the lesional skin of atopic dermatitis and psoriasis patients are an important source of IFN-γ, IL-13, IL-17, and IL-22. *J. Invest. Dermatol.* **133**, 973–979 (2013).
40. P. Virtanen, R. Gommers, T. E. Oliphant, M. Haberland, T. Reddy, D. Cournapeau, E. Burovski, P. Peterson, W. Weckesser, J. Bright, S. J. van der Walt, M. Brett, J. Wilson, K. J. Millman, N. Mayorov, A. R. J. Nelson, E. Jones, R. Kern, E. Larson, C. J. Carey, İ. Polat, Y. Feng, E. W. Moore, J. V. Plas, D. Laxalde, J. Perktold, R. Cimrman, I. Henriksen, E. A. Quintero, C. R. Harris, A. M. Archibald, A. H. Ribeiro, F. Pedregosa, P. van Mulbregt; SciPy 1.0 Contributors, SciPy 1.0: Fundamental algorithms for scientific computing in Python. *Nat. Methods* **17**, 261–272 (2020).
41. S. Maneewongvatana, D. M. Mount. (arXiv, 1999).
42. J. D. Gardiner, J. Behnsen, C. A. Brassey, Alpha shapes: Determining 3D shape complexity across morphologically diverse structures. *BMC Evol. Biol.* **18**, 184 (2018).
43. M. Thomeer, P. Moerman, R. Westhovens, A. van den Eeckhout, J. Dequeker, M. Demedts, Systemic lupus erythematosus, eosinophilia and Löffler's endocarditis. An unusual association. *Eur. Respir. J.* **13**, 930–933 (1999).
44. S. Aydoğdu, O. Uçar, M. Cetin, A case of systemic lupus erythematosus presenting with hypereosinophilia and Loeffler endocarditis. *Acta Cardiol.* **65**, 571–573 (2010).
45. H. M. Markusse, R. Schravenhoff, H. Beerman, Hypereosinophilic syndrome presenting with diarrhoea and anaemia in a patient with systemic lupus erythematosus. *Neth. J. Med.* **52**, 79–81 (1998).
46. S. Berry, N. A. Giraldo, B. F. Green, T. R. Cottrell, J. E. Stein, E. L. Engle, H. Xu, A. Ogurtsova, C. Roberts, D. Wang, P. Nguyen, Q. Zhu, S. Soto-Diaz, J. Loyola, I. B. Sander, P. F. Wong, S. Jessel, J. Doyle, D. Signer, R. Wilton, J. S. Roskes, M. Eminizer, S. Park, J. C. Sunshine, E. M. Jaffee, A. Baras, A. M. de Marzo, S. L. Topalian, H. Kluger, L. Cope, E. J. Lipson, L. Danilova, R. A. Anders, D. L. Rimm, D. M. Pardoll, A. S. Szalay, J. M. Taube, Analysis of multispectral imaging with the AstroPath platform informs efficacy of PD-1 blockade. *Science* **372**, eaba2609 (2021).
47. D. Phillips, M. Matusiak, B. R. Gutierrez, S. S. Bhate, G. L. Barlow, S. Jiang, J. Demeter, K. S. Smythe, R. H. Pierce, S. P. Fling, N. Ramchurren, M. A. Cheever, Y. Goltsev, R. B. West, M. S. Khodadoust, Y. H. Kim, C. M. Schürch, G. P. Nolan, Immune cell topography predicts response to PD-1 blockade in cutaneous T cell lymphoma. *Nat. Commun.* **12**, 6726 (2021).
48. K. R. Gabriel, R. R. Sokal, A new statistical approach to geographic variation analysis. *Syst. Biol.* **18**, 259–278 (1969).
49. S. M. Lewis, M. L. Asselin-Labat, Q. Nguyen, J. Berthelet, X. Tan, V. C. Wimmer, D. Merino, K. L. Rogers, S. H. Naik, Spatial omics and multiplexed imaging to explore cancer biology. *Nat. Methods* **18**, 997–1012 (2021).
50. E. Lundberg, G. H. H. Borner, Spatial proteomics: A powerful discovery tool for cell biology. *Nat. Rev. Mol. Cell Biol.* **20**, 285–302 (2019).
51. C. G. Williams, H. J. Lee, T. Asatsuma, R. Vento-Tormo, A. Haque, An introduction to spatial transcriptomics for biomedical research. *Genome Med.* **14**, 1–18 (2022).
52. N. Serhan, L. Basso, R. Sibilano, C. Petitfils, J. Meixiong, C. Bonnart, L. L. Reber, T. Marichal, P. Starkl, N. Cenac, X. Dong, M. Tsai, S. J. Galli, N. Gaudenzio, House dust mites activate nociceptor-mast cell clusters to drive type 2 skin inflammation. *Nat. Immunol.* **20**, 1435–1443 (2019).

Acknowledgments: We thank all members of the Gaudenzio laboratory at Infinity and of Genoskin for discussions and technical assistance. We thank S. Allart and S. Lachambre for technical assistance at the cellular imaging facility of Inserm UMR 1291, Toulouse. We thank S. Milia and T. Durand-Plavis for technical assistance at the experimental histopathology platform US06/CREFRE. **Funding:** This work was supported by the Agence Nationale pour la Recherche (ANR), the European Research Council (ERC-2018-STG #802041), and Genoskin (to N.G.). **Author contributions:** N.G. conceived the project. M.S., R.H., J.M., N.S., M.T., and N.G. were involved in experimental design. M.S., R.H., J.M., N.S., and N.G. performed most experiments and compiled the data. M.T., E.P., and E.B. provided important help with experiments. M.T., L.L., D.J., B.C., C.L., C.B.L., and J.K. provided clinical samples and expertise. All authors participated in analyzing the data and writing or editing the paper. **Competing interests:** Co-patent applications between Inserm and Genoskin have been filed related to the subject matter of this publication. N.G. acts as chief scientific officer, P.D. is the founder and chief executive officer, and E.M. is the chief business innovation officer at Genoskin, and N.G., E.M., P.D. are shareholders at Genoskin. The authors declare no other competing interests. **Data and materials availability:** Single-cell databases (.csv file) of all healthy and pathological samples and patients used to generate the presented data are available in the nonprofit repository Dryad (doi:10.5061/dryad.rxwdbrvdm). All data needed to evaluate the conclusions in the paper are present in the paper and/or the Supplementary Materials.

Submitted 25 November 2022
Accepted 2 May 2023
Published 7 June 2023
10.1126/sciadv.adf9491

CORONAVIRUS

Structural and computational design of a SARS-CoV-2 spike antigen with improved expression and immunogenicity

James A. Williams, Marco Biancucci, Laura Lessen, Sai Tian, Ankita Balsaraf†, Lynn Chen†, Chelsy Chesterman, Giulietta Maruggi, Sarah Vandepaer, Ying Huang‡, Corey P. Mallett, Ann-Muriel Steff§, Matthew James Bottomley||, Enrico Malito¶, Newton Wahome*#, Wayne D. Harshbarger*

Severe acute respiratory syndrome coronavirus 2 (SARS-CoV-2) variants of concern challenge the efficacy of approved vaccines, emphasizing the need for updated spike antigens. Here, we use an evolutionary-based design aimed at boosting protein expression levels of S-2P and improving immunogenic outcomes in mice. Thirty-six prototype antigens were generated in silico and 15 were produced for biochemical analysis. S2D14, which contains 20 computationally designed mutations within the S2 domain and a rationally engineered D614G mutation in the SD2 domain, has an ~11-fold increase in protein yield and retains RBD antigenicity. Cryo–electron microscopy structures reveal a mixture of populations in various RBD conformational states. Vaccination of mice with adjuvanted S2D14 elicited higher cross-neutralizing antibody titers than adjuvanted S-2P against the SARS-CoV-2 Wuhan strain and four variants of concern. S2D14 may be a useful scaffold or tool for the design of future coronavirus vaccines, and the approaches used for the design of S2D14 may be broadly applicable to streamline vaccine discovery.

INTRODUCTION

Severe acute respiratory syndrome coronavirus 2 (SARS-CoV-2), the causative agent for coronavirus disease 2019 (COVID-19), was first identified in Wuhan, China before spreading globally and being declared a pandemic in March 2020. With more than 613 million confirmed cases globally, resulting in more than 6.5 million deaths, COVID-19 remains a notable global health burden. Vaccines, such as mRNA-1273 (Moderna), BNT162b2 (Pfizer/BioNTech), and Ad.26.COV2.S (Janssen), are all based on the sequence of the original Wuhan-Hu-1 strain of the spike fusion glycoprotein (S), engineered to remain in the prefusion state, which is the primary target of neutralizing antibodies (nAbs). However, the efficacies of these first-generation vaccines are diminished against newly circulating variants of concern (VoCs) such as Alpha (B.1.1.7), Beta (B.1.351), Delta (B.1.617.2), and Omicron (BA.1, BA.2, BA.4/5, XBB, and BQ.1.1), which evade nAbs due to mutations in the S protein (*1*–*8*). Although booster vaccines have been developed to match S protein sequences of circulating variants (*9*–*12*), there is no guarantee that these updated vaccines will protect against future strains of the virus (*7*, *8*, *13*–*15*). Therefore, there is a need for the development of vaccine antigens that can elicit Abs that are more efficient in neutralizing future variants, thus providing broader and/or longer-lasting protection.

The S glycoprotein is composed of S1 and S2 subunits that mediate host-cell attachment to initiate virus-cell fusion (*16*, *17*). The S1 subunit comprises the N-terminal domain (NTD) and the receptor binding domain (RBD) with subdomains SD1 and SD2 undergoing hinge-like motions that promote RBD movement between closed and opened conformations (*18*, *19*). Engagement of the RBD open conformation with human angiotensin-converting enzyme 2 receptor (hACE2) triggers a large-scale conformational rearrangement in the S2 domain, which contains the fusion machinery necessary to mediate viral fusion and infectivity (*17*, *20*). A large portion of the nAb response elicited during natural infection or vaccination is directed toward epitopes spanning the RBD (*21*–*24*). Epitopes in less accessible regions of the RBD are more conserved among circulating coronaviruses, consistent with Abs targeting these regions being able to cross-neutralize other coronaviruses (*21*, *25*, *26*). Several groups have developed adjuvanted RBD-only vaccines based on the monomeric or multivalent display of the RBD, with several human phase 1/2 and phase 3 trials showing a safe and immunogenic response, thus making the RBD, or S in the RBD open state, an attractive vaccine antigen (*27*–*36*).

Engineering of the S protein to remain in the prefusion state was accomplished through the rational, structure-guided insertion of two proline residues, K986P and V987P (named S-2P), which are located between the heptad repeat region 1 (HR1) and the central helix (CH) domain (*20*). S-2P was later modified to have higher thermostability and greater protein expression through the incorporation of additional prolines (F817P, A892P, A899P, and A942P) (referred to as S-6P or HexaPro), which are located between the fusion peptide proximal region, HR1, and the CH domain (*37*). Similar structure-based approaches have also been instrumental in

GSK, Rockville, MD, USA.
*Corresponding author. Email: newton@wahome.org (N.W); wayne.d.harshbarger@gsk.com (W.D.H)
†Present address: AstraZeneca, Gaithersburg, MD, USA.
‡Present address: Merck Research Laboratories, Merck & Co. Inc., Kenilworth, NJ, USA.
§Present address: Coalition for Epidemic Preparedness Innovations (CEPI), Oslo, Norway.
||Present address: Dynavax Technologies Corporation, Emeryville, CA 94608, USA.
¶Present address: Schrödinger, Inc., New York City, New York 10036, USA.
#Present address: Exscientia, Miami, FL, USA.

the design of vaccine antigens for other pathogens such as the respiratory syncytial virus fusion protein F, metapneumovirus fusion protein F, influenza hemagglutinin (HA), and HIV-1 envelope (*38*–*43*). However, the identification of an antigen with the preferred qualities (i.e., conformation, stability, and expression) often requires testing hundreds of single-point mutations followed by rounds of combinatorial design which can lead to many failures.

Data-driven computational approaches have the potential to reveal mutable space within a protein's structure that may not be obvious in a rational-based setting and assist antigen design by identifying sequences that yield desired protein characteristics (*44*–*48*). One such computational method is PROSS (Protein Repair One-Stop Shop), which is a design algorithm using evolutionary information in multisequence alignments to focus the protein design search on residues that are functional in nature (*44*). Combined with the Rosetta design suite and energy scoring function (*49*, *50*), false positive predictions can be minimized and the number of variants that must be experimentally tested is reduced (*44*, *51*, *52*). Success has been shown for multiple enzymes and the HIV gp140 glycoprotein, where using PROSS led to enhanced protein stability and greater expression of functional protein compared to wild type (*44*, *52*, *53*).

Here, we adapted the PROSS workflow to perform antigen design based on a multisequence alignment of related coronavirus glycoproteins and incorporated symmetry protocols to uniformly mutate the S protein's trimeric structure. The evolutionary consensus design strategy resulted in a novel prefusion S antigen that had biochemical and biophysical characteristics comparable to S-2P, but with greater expression and capable of eliciting higher levels of nAb titers against Wuhan and VoCs in mice. High-resolution cryo–electron microscopy (cryo-EM) structures of our top design, S2D14, confirm the structural integrity of the spike protein and the dynamic nature of the RBDs, thus allowing exposure of potently neutralizing epitopes. This work provides a computational and experimental workflow for improving antigen characteristics, such as expression and immunogenicity, and may be valuable for informing the design of future spike-based vaccines that can elicit broad protection against emerging and future strains of the virus.

RESULTS

Computational design of SARS-CoV-2 spike antigens

The evolutionary consensus design workflow combines three distinct steps, as previously described (*44*). First, we generated a multisequence alignment of 500 nonredundant spike protein sequences from various betacoronavirus lineages (lineages *A* to *D*), which we obtained from the BLAST database (data S1) (*54*), allowing for the identification of residues with natural variation. Next, Rosetta atomistic design simulations (*50*) were used to curate which set(s) of single-point mutations could be applied to the above-identified residues to obtain unique spike designs with predicted lower free energy (i.e., improved stability) compared to the sequence of the target S antigen model (*20*). To generate an initial S protein model, we chose to incorporate a symmetry-based protocol (*55*) with a molecular structure that has all three RBDs in the open conformation which places the RBDs away from the neighboring S protomers (Fig. 1) (see Materials and Methods). We believed that this would prevent the possibility of designs being stabilized in the three-RBD closed conformation, therefore ensuring that important neutralizing epitopes remained accessible. Specifically, our starting model contained three mutations: (i and ii) the S-2P di-proline mutations (K986P, V987P) which were used to ensure that the prefusion conformation of the spike was maintained (*20*) and (iii) a D614G mutation, located within the SD2 domain, which was included because it was an overrepresented mutation in the above sequence alignments from circulating strains at the time of this study (*56*, *57*). Modification of these mutations was prohibited during design simulations and is therefore conserved across all designed sequences (data S2). In the final design step, Rosetta combinatorial sequence optimization was used to generate constructs with energy profiles more favorable (lower energy) than the initial S antigen model (fig. S1).

Because of the difficulty of modeling large and dynamic proteins such as S, and facing the substantial sequence diversity in coronavirus families, three independent strategies were used for this final design step to increase the probability of identifying sequences that yield desirable protein characteristics. The first strategy incorporated mutations across the full S ectodomain, the second strategy limited the design space to the NTD + S2 domain, and the third strategy further restricted the mutations to the S2 domain (Fig. 1A). A total of 36 designs (12 constructs per strategy) were created, where each design contained a total of 28 to 141 mutations (full S ectodomain), 17 to 103 mutations (NTD + S2), or 12 to 25 mutations (S2 domain). To narrow the candidate pool for in vitro analysis, the 12 designs per strategy were placed into five groups based on phylogenetic analysis, and one representative S antigen from each of these groups was selected for production and purification, followed by biochemical and biophysical characterization (fig. S1, A to C).

Expression, antigenicity, and stability of spike designs

Genes containing sequences for each of the 15 selected constructs were cloned into a mammalian expression vector and tested for expression in human embryonic kidney (HEK) 293 cells. Among the 15 designs selected, 7 (three for the NTD + S2 and four for the S2 domain only) displayed expression levels in cell culture supernatants that exceeded S-2P, with five of those designs (numbers 8, 9, 12, 13, and 14) also having expression levels in supernatant higher than S-6P (Fig. 1B). Specifically, design 8 (NTD + S2 domain) and designs 12, 13, and 14 (S2 domain only) displayed the largest increase in nonpurified protein expression relative to S-2P (>6-fold) or S-6P (>3-fold) and exceeded the upper limit of quantification of the assay, while design 9 (NTD + S2 domain) had an ~4-fold and ~1.5-fold increase compared to S-2P and S-6P, respectively. The expression levels of designs targeting the full S ectodomain were considerably lower than those detected for S-2P (~1.5-fold) or S-6P (~4-fold). This is consistent with observations that, despite the high tolerance for variability within the RBD, many mutations can result in deleterious effects on protein expression (*58*). Designs 6 and 7 (NTD + S2 domain) and design 11 (S2 domain) also had expression levels lower than S-2P. On the basis of these results, full S ectodomain designs, as well as designs 6, 7, and 11, were not considered for further biochemical or biophysical characterization, leaving seven designs for further analysis.

Considering that the majority of the most potent SARS-CoV-2 nAbs isolated to date target epitopes spanning the surface of the RBD, surface plasmon resonance (SPR) was used to determine whether incorporated mutations within the NTD or S2 domain

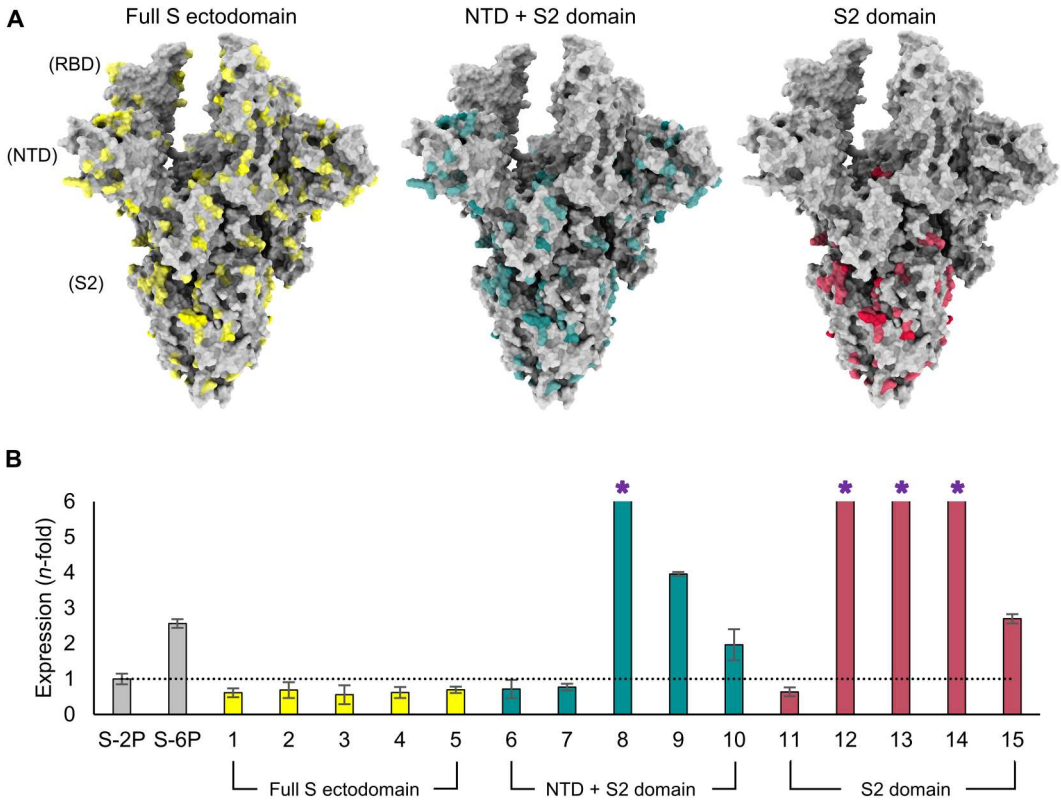

Fig. 1. Evolutionary-based design strategy and expression levels of spike mutants. (**A**) Model of the SARS-CoV-2 spike (S) protein structure with all three RBDs in the open conformation. The first design strategy (left) allowed for mutations (yellow) across the full S ectodomain. The second design strategy (center) limited the design landscape to the NTD + S2 domain (mutations in teal). The third design strategy (right) only modified the S2 domain and mutations are colored red. (**B**) Protein expression level (determined by biolayer interferometry using anti-HIS biosensors) of spike mutants normalized to S-2P (shown by dotted line) and grouped according to domain-specific design strategies in (A). S-6P (HexaPro) was used as an additional comparator. Error bars were determined from duplicate measurements, and asterisks indicate designs where expression exceeded the assay's limit of quantitation.

inadvertently altered the presentation or accessibility of key RBD epitopes. CR3022, which requires at least two RBDs in the open state, S309, which recognizes open or closed RBDs, and the hACE2 receptor, which binds a single RBD in the open conformation, were all found to bind designs 8, 9, and 10 (NTD + S2 domain) as well as designs 12, 13, and 14 (S2 domain) with equilibrium dissociation binding constants (K_d values) in the picomolar range (Table 1, fig. S2, and table S1). These values were comparable to those found for binding to S-2P, thus indicating no structural disruptions to these RBD epitopes.

Next, the binding of monoclonal antibodies (mAbs) VRC-118 and VRC-112, which target the NTD and S2 domains, respectively, was tested as these domains have also been shown to contribute to neutralization breadth and potency (*21*, *22*, *59*–*61*). All the designs tested were found to bind VRC-118 with picomolar affinity and with a similar K_d as S-2P. However, binding to VRC-112 was abolished for all designs, revealing that the S2 domain mutations do disrupt at least this S2 domain epitope (Table 1, figs. S2 and S3, and table S1). Despite this result, we reasoned that further characterization was warranted on the basis of the high levels of protein expression and the confirmation of intact RBD and NTD epitopes.

To assess the impact of thermal stress, purified proteins were subjected to a differential scanning fluorimetry (DSF) assay. S-2P has previously been shown to have two distinct melting transitions (T_m1 and T_m2) with an increase in T_m1 being indicative of improved stability (*37*). All three NTD + S2 designs (8, 9, and 10) had T_m1 values greater than S-2P (T_m1 = 44°C), with design 9 having the largest, yet modest, increase of 4.2°C (T_m1 = 48°C) (Table 1). T_m1 values for all four S2 domain designs (12, 13, 14, and 15) were comparable to S-2P. The T_m2 values for most designs were also comparable to S-2P, with only designs 12 and 15 showing an ~10°C increase in melting temperature, though the impact of this improvement is not clear.

Design 14 forms stable prefusion trimers

Considering the loss of binding to VRC-112 for each of the designs, we next sought to determine whether modifications had inadvertently altered the S2 domain architecture or overall protein morphology. To accomplish this task, a Glacios 200-kV electron microscope was used to quickly assess one construct from the NTD + S2 designs and one construct from the S2 domain designs. Design 9 was chosen from the NTD + S2 designs based on the high expression and thermostability; however, particles resembling the prefusion S trimer were infrequently observed on the cryo-EM micrographs (fig. S4A). This may be due to dissociation into monomers or other misfolded states during storage or vitrification, consistent with known issues of cold handling with spike proteins (*62*). From the S2 domain designs, design 14 was selected

Table 1. Thermal stability and binding affinity measurements for spike protein designs. The T_m values are the average of triplicate measurements with the exception of design 10, which was limited by protein quantity. For binding affinity values, the average and SD of triplicate measurements are shown with the exception of design 15, which was not measured because of limited protein quantity. The binding of design 10 to VRC-118 was limited to a single measurement because of limited protein quantity. NM, not measured; NB, no binding.

Designed mutant	Design strategy	T_m1 (°C)	T_m2 (°C)	Binding affinity, K_d (pM)				
				ACE2	CR3022	S309	VRC-118	VRC-112
8	NTD + S2	46.38	76.34	160 ± 14	27 ± 4	19 ± 16	9.7 ± 0.4	NB
9	NTD + S2	48.35	79.65	150 ± 5	370 ± 240	44 ± 6	2.9 ± 0.5	NB
10	NTD + S2	46.99	77.44	44 ± 4	2.4 ± 3.3	0.16 ± 0.07	1.9	NB
12	S2 domain	43.72	86.86	100 ± 2	9.0 ± 0.9	11 ± 2	14 ± 8	NB
13	S2 domain	43.75	77.96	65 ± 1	2.2 ± 1.1	20 ± 3	11 ± 1	NB
14	S2 domain	44.18	78.65	190 ± 5	110 ± 51	70 ± 14	25 ± 1	NB
15	S2 domain	44.00	86.54	NM	NM	NM	NM	NM
S-2P		44.13	77.58	200 ± 18	58 ± 26	70 ± 0	42 ± 5	53 ± 4

on the basis of the high level of protein expression and similar thermostability and antigenicity as S-2P. Cryo-EM micrographs of design 14 revealed the expected S protein trimers with the anticipated particle size and secondary structural features (Fig. 2A and fig. S4B).

Two distinct conformational states for design 14 were identified during three-dimensional (3D) classification: one conformation with all three RBDs in the closed state and the second conformation with a single RBD domain in the open state (Fig. 2, B and C, and fig. S5A). The refinement of each population resulted in 7.1-Å resolution (three RBDs closed) and 8.5-Å resolution (one RBD open) maps, respectively (Fig. 2, B and C, Table 2, and fig. S5B). The sampling of RBD open states is consistent with the recognition of the hACE2 receptor and mAb CR3022. Docking of previously published structures for either the closed spike trimer [Protein Data Bank (PDB) accession number: 6VXX] or a single RBD open trimer (PDB accession number: 6VSB) into the corresponding electron density maps revealed a high degree of similarity across the S2 domains for either model, indicating that engineered S2 mutations were well tolerated and did not alter the S protein morphology. At this stage, design 14 was considered our top candidate for further evaluation and renamed S2D14 for simplicity.

Next, we wanted to evaluate whether the high expression of S2D14 in HEK293 cell culture supernatants translated into higher

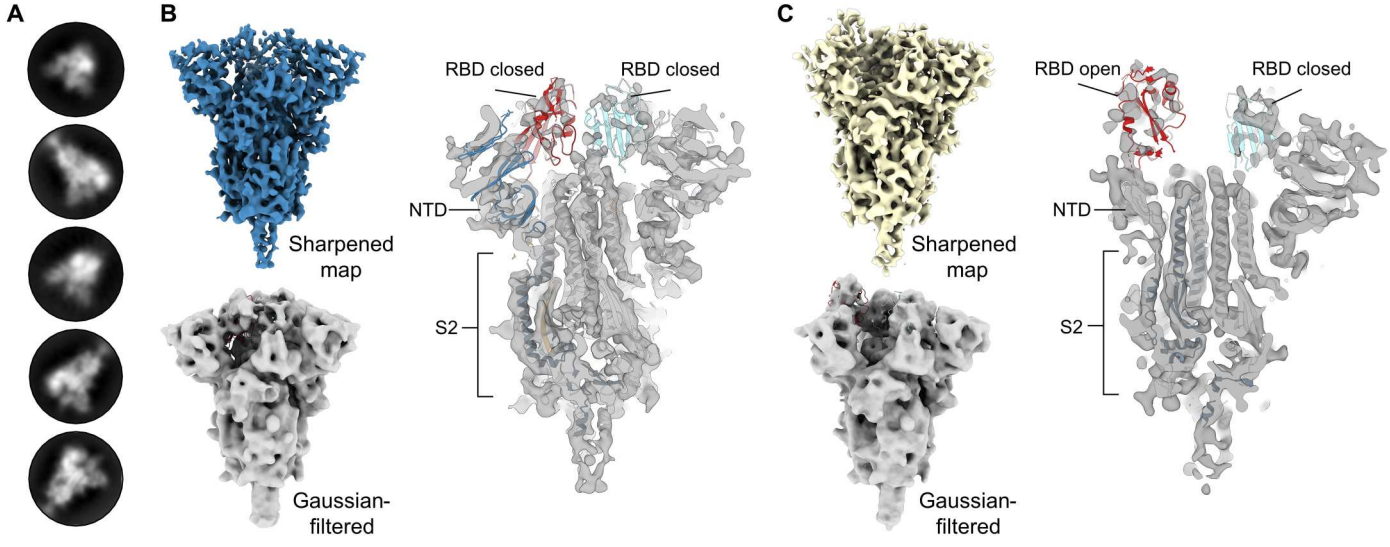

Fig. 2. S2D14 (design 14) adopts the trimeric prefusion S conformation and exhibits RBD conformational heterogeneity. (**A**) Representative two-dimensional classes of S2 domain design S2D14 from cryo-EM micrographs, confirming the expected S protein trimers. (**B**) The cryo-EM map of S2D14 in a three-RBD closed state at 7.1-Å resolution is shown above and colored blue. A Gaussian-filtered volume with a rigid body fit of the S protein in the closed conformation [Protein Data Bank (PDB) accession number: 6VXX] is shown below the cryo-EM map and more clearly displays the three-RBD closed state. Shown on the right is a cross section of the sharpened map with a rigid body fit of the S protein in the closed conformation (PDB accession number: 6VXX). (**C**) The cryo-EM map of S2D14 with one RBD in the open conformation at 8.5-Å resolution and obtained from the same dataset as (B) is shown above and colored yellow. A Gaussian-filtered volume with a rigid body fit of the S protein in the one-RBD open state is shown below the cryo-EM map and, more clearly, displays the one-RBD open state. Shown on the right is a cross section of the EM map with a rigid body fit of the spike protein in the one-RBD open state (PDB accession number: 6VSB).

Table 2. Cryo-EM data collection and image processing statistics for S2D14. EMDB, Electron Microscopy Data Bank; PDB, Protein Data Bank; RMSD, root mean square deviation.

Data collection					
Microscope	**Glacios**		**TitanKrios**		
Voltage (kV)	200		300		
Detector	Falcon 3		Falcon 4		
Magnification	120,000		120,000		
Pixel size (Å/pixel)	0.91		0.67		
Exposure (e/Å^2)	48		43		
No. of frames	50		42		
Defocus range (μm)	0.75–2.5		0.8–2.2		
Software	EPU		EPU		
Total micrographs	1425		6169		
Data processing					
Particles extracted	92,933		724,002		
After 2D classification	44,459		566,825		
	3-RBD down	1-RBD open	3-RDB down	2-RBD exposed	2-RBD open
Particles in refinement	7759	9154	33,173	47,773	87,614
Symmetry	C3	C1	C3	C1	C1
Map sharpening B-factor	−389.99	−592.139	−17.18	−5.35	−7.2
Unmasked resolution at 0.5/0.143 FSC (Å)	10/7.5	13/9.1	4.2/3.5	7.9/4.1	7.3/3.9
Masked resolution at 0.5/0.143 FSC (Å)	8.1/7.1	9.0/8.5	3.3/2.8	3.9/3.3	3.7/3.1
PDB ID			8EPN	8EPQ	8EPP
EMDB ID			28531	28533	28532
Model statistics					
MolProbity score			1.50	1.60	1.67
Clash score			6.70	7.20	7.58
Composition					
Amino acids			2991	2984	2939
Glycans			126	66	66
RMSD bonds (Å)			0.003	0.003	0.002
RMSD angles (°)			0.579	0.609	0.491
C-beta outliers (%)			0.00	0.00	0.00
CC (mask)			0.87	0.81	0.84
Rotamer outliers (%)			0.84	0.12	0.35
Ramachandran plot					
Favored (%)			97.34	96.75	96.21
Allowed (%)			2.66	3.21	3.65
Disallowed (%)			0.00	0.03	0.14

levels of purified, functional protein compared to S-2P and S-6P. In addition, to compare the possible contribution of the D614G mutation for enhancing the expression of S-2P, an S-2P variant that contains the D614G mutation, named S-2P–D614G, was created and tested as well. Purified S2D14 protein yielded an ~11-fold increase relative to S-2P and an ~5.4-fold increase relative to S-6P (Fig. 3, A to C). The purified yield of S-2P–D614G was nearly identical to S-2P, confirming that the increased expression obtained for S2D14 is attributed to the mutations incorporated through computational design.

Immunization with S2D14 elicits high neutralizing antibody titers

To assess the immunogenicity of S2D14 in comparison to S-2P, we immunized BALB/c mice with AS03 (oil-in-water emulsion) adjuvanted proteins at either 0.3- or 3.0-μg doses. Intramuscular

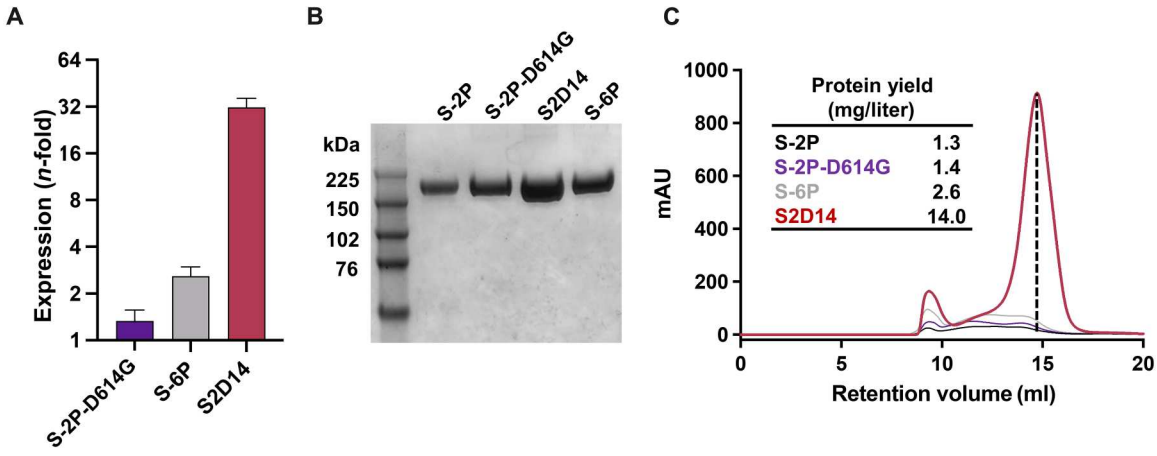

Fig. 3. S2 domain mutations in S2D14 enhance expression of functional prefusion trimer. (**A**) Total protein expression in cell culture supernatant for S proteins showing an *n*-fold increase relative to S-2P. A total of six replicate measurements were taken, and error bars represent SD from the means. (**B**) SDS–polyacrylamide gel electrophoresis analysis of size exclusion chromatography (SEC)–purified S proteins. Relevant bands for the molecular weight ladder (lane 1) are labeled in kilodaltons. (**C**) Overlay of the SEC chromatograms for S protein antigens. The dashed vertical line indicates the peak retention volume for the S2D14 trimer. The final yield of purified S protein trimers is shown in the inset.

injections were given on days 0 and 21, with serum collected 3 weeks post-I (first immunization) injection and two weeks post-II (second immunization) injection (Fig. 4A). Total anti-spike immunoglobulin G (IgG) titers [assessed by anti-spike enzyme-linked immunosorbent assay (ELISA)] indicated that S2D14 was immunogenic at both the 0.3- and 3.0-μg doses and that titers were boosted after the second dose (Fig. 4, B and C). Anti-spike IgG titers were comparable between S-2P and S2D14 at both post-I and post-II time points at the 0.3-μg dose and for the 3.0-μg dose (Fig. 4, B and C).

S2D14 elicited a robust neutralizing antibody response to the Wuhan strain at post-II for each vaccine dose (Fig. 4, D and E). At post-II for the 0.3-μg dose, S2D14 induced statistically significant higher neutralizing antibody titers compared to S-2P (9.1-fold increase). In addition, both S-2P and S2D14 had low neutralizing titers post-I at either dose (fig. S6), but noticeably higher neutralizing titers at either dose at post-II than for human convalescent serum (HCS) (Fig. 4, D and E) (*63*). The post-II neutralizing titers were highly similar between 0.3- and 3.0-μg doses. While it is possible that nAb titers reached saturation, the saturating dose in each assay is not known.

Next, we determined neutralizing antibody titers against VoCs that were available at the time of this study: Alpha (B1.1.7), Beta (B.1.351), Delta (B.1.617.2), and Omicron (BA.1) strains (Fig. 5, A and B). S2D14 elicited a neutralizing antibody response to all the variant strains when immunized at both the 0.3- and 3.0-μg doses but with an overall decrease in neutralizing antibody titers compared to the Wuhan strain for the Beta (~10-fold), Delta (~5-fold), and Omicron (~100-fold) variants. Compared to S-2P at post-II for the 0.3-μg dose, S2D14 induced statistically significant higher neutralizing antibody responses against the Alpha (10.8-fold increase), Beta (8.2-fold increase) and Delta (23.4-fold increase) variants (Fig. 5A). Regarding the Omicron strain, although many mice did not show measurable titers (4 out of 10 in the S2D14 group and 7 out of 10 in the S-2P group), and the difference was not statistically significant, at 0.3-μg dose, S2D14 did elicit an ~10-fold higher neutralizing antibody response than S-2P. At post-II for the 3.0-μg dose, S2D14 elicited statistically significant higher neutralizing antibody responses against the Alpha and Beta variants but were comparable to S-2P for the Delta and Omicron variants (Fig. 5B). Together, these data show that S2D14 is immunogenic and capable of eliciting high levels of IgG binding antibodies (Wuhan) and nAbs (Wuhan and VoC strains). In addition, although the total IgG titers are similar between S2D14 and S-2P after vaccination, the antibody response elicited by S2D14 at the 0.3-μg dose is superior in neutralization potency and breadth.

Cryo-EM structures of S2D14 reveal a range of RBD conformational states

To better understand the molecular basis for the improved breadth and immunogenicity of S2D14, a more extensive cryo-EM dataset was collected for high-resolution structural analysis using a Titan Krios 300-kV electron microscope. From a single dataset, we were able to determine the structure of S2D14 in three distinct conformations: two RBDs open (43% of particles, 3.1-Å resolution), three RBDs closed (16% of total particles, 2.8-Å resolution), and two RBDs exposed with one RBD down (23% of total particles, 3.3-Å resolution) (Fig. 6, A to D, Table 2, and fig. S7, A and B). Although this final class most closely aligned to the one-RBD open mask used during focused classification, two of the RBDs lacked clear density suggesting a state with two dynamic RBDs, each sampling an RBD open state, yet distinguishable from the two-RBD open structure (Fig. 6, B to D). Together, these conformations reveal that ~66% of particles contain at least two RBDs in the open or exposed states and are consistent with binding to hACE2 and CR3022. Docking of Fabs S309 (*64*), S2X259, or S2K146 (*25*, *26*) onto S2D14 confirms that neutralization-sensitive RBD epitopes, in particular those exposed only in an RBD open state (recognized by S2X259 and S2K146), are accessible with no apparent clashes (Fig. 6E).

To better assess the relative proportion of RBDs in the open conformation, we performed BLI experiments measuring the peak binding levels for hACE2 and CR3022 to S-2P, S-6P, S2D14, and the S-2P–D614G variant. In this assay, an increase in peak binding signal indicates greater accessibility of the RBDs (i.e.,

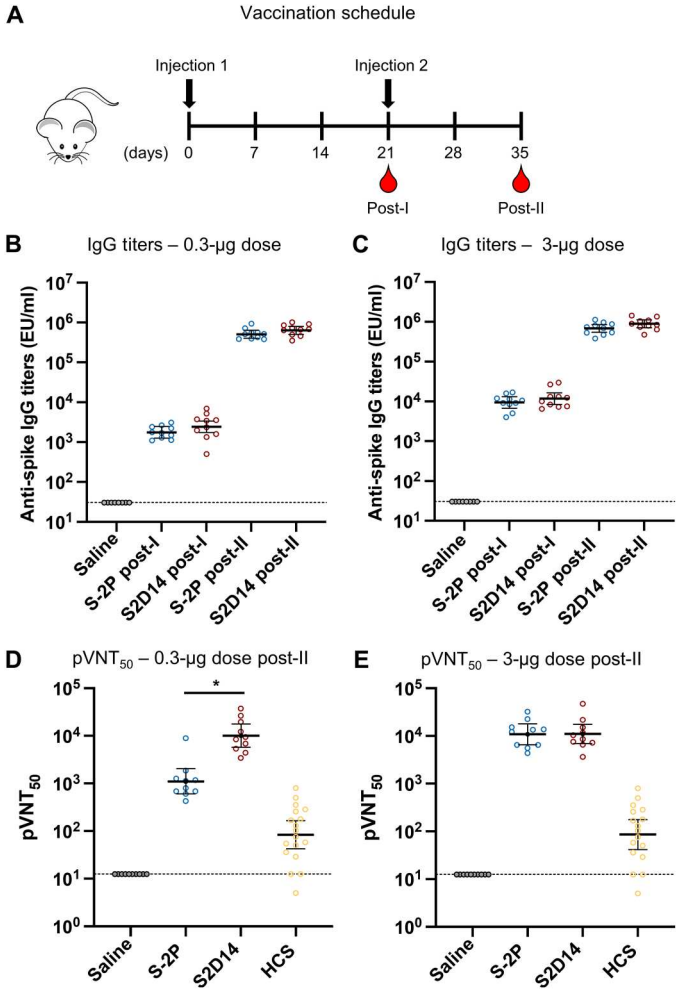

Fig. 4. IgG and neutralizing antibody titers from mice immunized with adjuvanted S2D14 or S-2P. (**A**) Mouse immunization schedule. Mice were immunized with either a 0.3- or 3.0-μg doses containing AS03 adjuvanted S2D14 or S-2P. Serum was collected 3 weeks after the first immunization (post-I) and 2 weeks after the second immunization (post-II). (**B** and **C**) Enzyme-linked immunosorbent assay immunoglobulin G (IgG) titers of S2D14 compared to S-2P at both 0.3-μg (B) and 3.0-μg (C) doses for both post-I and post-II serum collections. Individual data with geometric mean titers (GMT) and 95% confidence intervals (CIs) are presented. (**D** and **E**) 50% pseudovirus neutralization titers ($pVNT_{50}$) against the Wuhan strain were analyzed 2 weeks post-II at two antigen dosages, 0.3 (D) and 3.0 μg (E). Neutralizing antibody titers at either dose post-II were noticeably greater than for human convalescent sera (HCS). Individual data with GMT and 95% CIs are presented. For HCS samples, GMT and 95% CIs were calculated separately from vaccination groups in GraphPad Prism. Asterisks, *, indicate a statistically significant increase in neutralization response based on geometric mean ratio (GMR) comparisons with a two-sided 90% CI. Ratios for which the CI does not include 1 are considered statistically significant. See Materials and Methods for a description of the sera panel.

more open states) (*65*). Although the peak binding signal for S2D14 to hACE2 was greater than both S-2P–D614G and S-6P by ~2.2-fold and ~1.6-fold, respectively, S2D14 only reached 80% of the peak binding signal for S-2P (fig. S8A). The S-2P–D614G mutant showed the lowest peak binding levels, which was unexpected given previous data showing that the D614G mutation can enhance RBD exposure (*66*). A similar trend was also observed for binding to CR3022 (fig. S8B). Nonetheless, the PROSS mutations within S2D14 do appear to recover most of the loss in peak binding levels that may have occurred by the inclusion of the D614G mutation, which is consistent with the cryo-EM analysis showing a mix of open and closed RBD states.

The 23 total mutations (20 PROSS designed mutations, D614G, K986P, and V987P) present in S2D14 are all well resolved with clear side chain densities (Fig. 7, A to C). Analysis of the structures provides molecular details for the three main types of mutations incorporated by the evolutionary consensus design: (i) improvement of complementary electrostatic potential between interprotomer contact regions (Fig. 7A), (ii) optimization of hydrophobicity and van der Waals (VDW) contacts (Fig. 7B), and/or (iii) introduction of hydrogen bond interactions (Fig. 7C). Although the minimal number of mutations that are necessary to have the same properties as S2D14 was not explored, the analysis of the structure does allow for speculation of how these mutations may influence local interactions and trimer stability. For example, the mutation T998N introduces a hydrogen bond between the asparagine oxygen with the side chain of Y756, located on the same protomer, while the mutation T1027E within the CH forms a hydrogen bonding network between the E1027 side chain and R1039 of an adjacent S protomer (Fig. 8, A to C). Notably, several hydrogen bonds are also lost because of mutations such as T734V, S1003A, and Q1005N (fig. S9, A and B). However, as shown by DSF, the overall thermostability of S2D14 is the same as S-2P, suggesting that this loss of energy is well compensated not only by the formation of additional hydrogen bonds but also by the VDWs and electrostatic mutations that are introduced. One example of the addition of an electrostatic interaction is the A701E mutation, which positions the E701 side chain within ~5 Å of the K786 side chain of an adjacent S protomer and creates a complementary charged surface (Fig. 8D and fig. S9, C to E).

Superposition of the S2 domain (residues 821 to 1147) of S2D14 in the two-RBD open conformation with S-2P reveals a root mean square deviation of 1.6 Å over all C_α atoms (fig. S10). Despite this high structural similarity, there is a marked difference in the positioning of the loop connecting the α10 and α11 helices (residues G885 to Q895) near mutations A1070T and E1072Y located on the adjacent S protomer. These mutations reduce the overall charge of the interface between these two S protomers, creating a more hydrophobic patch that displaces the loop connecting α10 and α11 by 7.2 Å (measured from the C_α atom of residue A890) (Fig. 8E and fig. S11, A to E). Of note, the modification of this loop with an A892P mutation has been shown to provide an increase in protein expression and to stabilize the trimeric S protein (*37*, *67*). Although other S2 domain mutations, such as those that are surface-exposed, may also influence trimer expression and/or solubility, they are not easily rationalized by the structure and further experiments performing single-point mutations or reversions would be necessary to fully understand individual contributions.

DISCUSSION

The emergence of SARS-CoV-2 variants has heightened concerns about the efficacy of currently approved vaccines, which are based on the prefusion stabilized S protein antigen, S-2P (*1*–*4*, *68*). Taking a computational approach starting with S-2P plus the inclusion of a

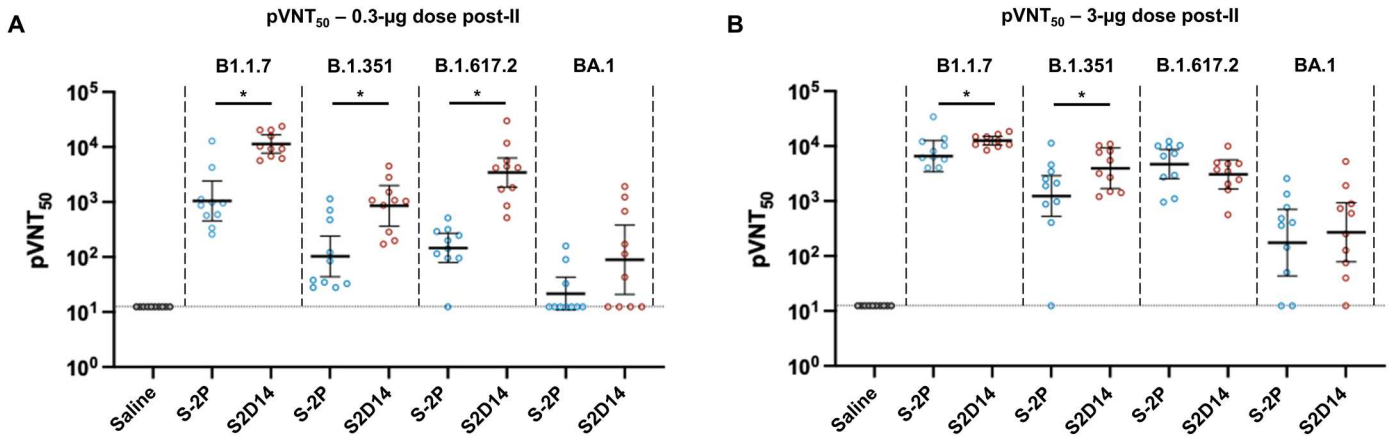

Fig. 5. S2D14 elicits neutralizing antibody titers in mice capable of neutralizing variants of concern. (**A**) Neutralization of VoCs compared between S2D14 and S-2P at low doses for post-II serum collection. S2D14 induced statistically significant higher neutralization responses against the Alpha (B1.1.7), Beta (B.1.351), and Delta (B.1.617.2) variants compared to S-2P. (**B**) Neutralization of VoCs compared between S2D14 and S-2P at high doses for post-II serum collection. S2D14 induced statistically significant higher neutralization responses against the Alpha (B1.1.7) and Beta (B.1.351) variants compared to S-2P. Individual data with GMT and 95% CIs are presented. Asterisks, *, indicate a statistically significant increase in neutralization response based on GMR comparisons with a two-sided 90% CIs. Ratios for which the CI does not include 1 are considered statistically significant.

predominant D614G mutation and modeled to have three RBDs in the open conformation, we used evolutionary consensus design for the in silico optimization of trimeric S antigens. These antigens were then biochemically, biophysically, structurally, and immunogenically characterized leading to the selection of design 14, named S2D14, which yielded an ~11-fold improvement in purified protein expression from HEK293 cells compared to S-2P. Immunization of mice with S2D14 resulted in higher levels of neutralizing antibody titers against Wuhan and VoC strains. Although we could not assess this experimentally, the increased expression yield suggests a greater stability of the protein in solution and offers a potential mechanism for the improved quality of the antibody response through better preservation of properly folded protein in mice after injection. Future studies should aim to experimentally compare the long-term stability between S2D14 and S-2P.

Cryo-EM structures revealed that roughly two-thirds of the S2D14 particles have either one or more RBDs in an open or exposed state, and an assessment of binding to hACE2 and CR3022 confirmed that the dynamic RBDs are not hindered by the incorporated mutations. The mutations found in S2D14 reflect strategies that would typically be used in rational-based approaches, such as improving VDW contacts, adding hydrogen bond interactions, and the insertion of complementary electrostatics (*69*). Although many modifications to the S protein have been reported in the literature to improve expression and thermostability (*70*), none of the mutations incorporated in S2D14 have been reported, providing previously unrecognized chemical space, and improving our understanding of how spike may be modified. Therefore, the advantages of the evolutionary-based strategy used here are that mutable space can be explored, which may not be obvious from a rational approach, and unique combinations of mutations that may improve protein folding and expression can be rapidly determined. In addition, since computational energetics guide the assessment, a more restricted set of constructs will likely be generated for testing in vitro, as opposed to often much larger numbers of designs if a rational approach was taken. One drawback, however, is that the computationally determined sequences contain a large number of mutations per design (20 for S2D14 not including D614G, K986P, and V987P) and the individual contribution for each mutation is not clear. Some mutations may be providing the opposite effect than what is desired. Another consideration is that other widely adopted strategies used to arrest the prefusion conformation of glycoproteins, such as incorporating non-natural disulfide bonds and helix-capping prolines, are unlikely to be inserted by an evolutionary-based approach since the design landscape is influenced by sequences circulating in nature which must contain fusion-competent S glycoproteins. Therefore, the engineering of an antigen with the desired characteristics (i.e., expression, stability, and immunogenicity) may benefit from the incorporation of both evolutionary consensus design and rational-based strategies.

Despite the development of bivalent vaccines, variants continue to emerge that challenge vaccine efficacy and durability (*71*, *72*), highlighting an urgent need for improved vaccines capable of broad protection again VoCs. Some strategies taken to improve protective efficacy have included focusing the immune response toward the RBD through multivalent display of the RBD on nanoparticles, or through the modification of the RBD sequence (*27*, *28*). In the case of nanoparticles, mosaic display of RBDs from diverse sarbecoviruses was capable of neutralizing SARS-CoV-2 variants, including Omicron, and was protective against challenges with SARS-2 Delta variant and SARS-1 in non-human primates (*27*). Alternatively, modification of the RBD sequence was shown to focus the immune response to potently neutralizing epitopes and to elicit neutralizing titers greater than the unmodified RBD in mice (*28*).

Aside from the RBD, vulnerable epitopes have also been described for the NTD, SD1, and S2 domains (*21*, *22*, *59*, *60*, *73*–*79*). The S2 domain, in particular, is highly conserved among coronaviruses, and it was found that non–SARS-CoV-2–exposed individuals had IgG that bound the CoV-2 S2 domain but not S1, perhaps by previous infection with a related human coronavirus (*61*). Recently, stabilization of the MERS-CoV S2 domain was shown to elicit cross-reactive betacoronavirus antibodies in mice

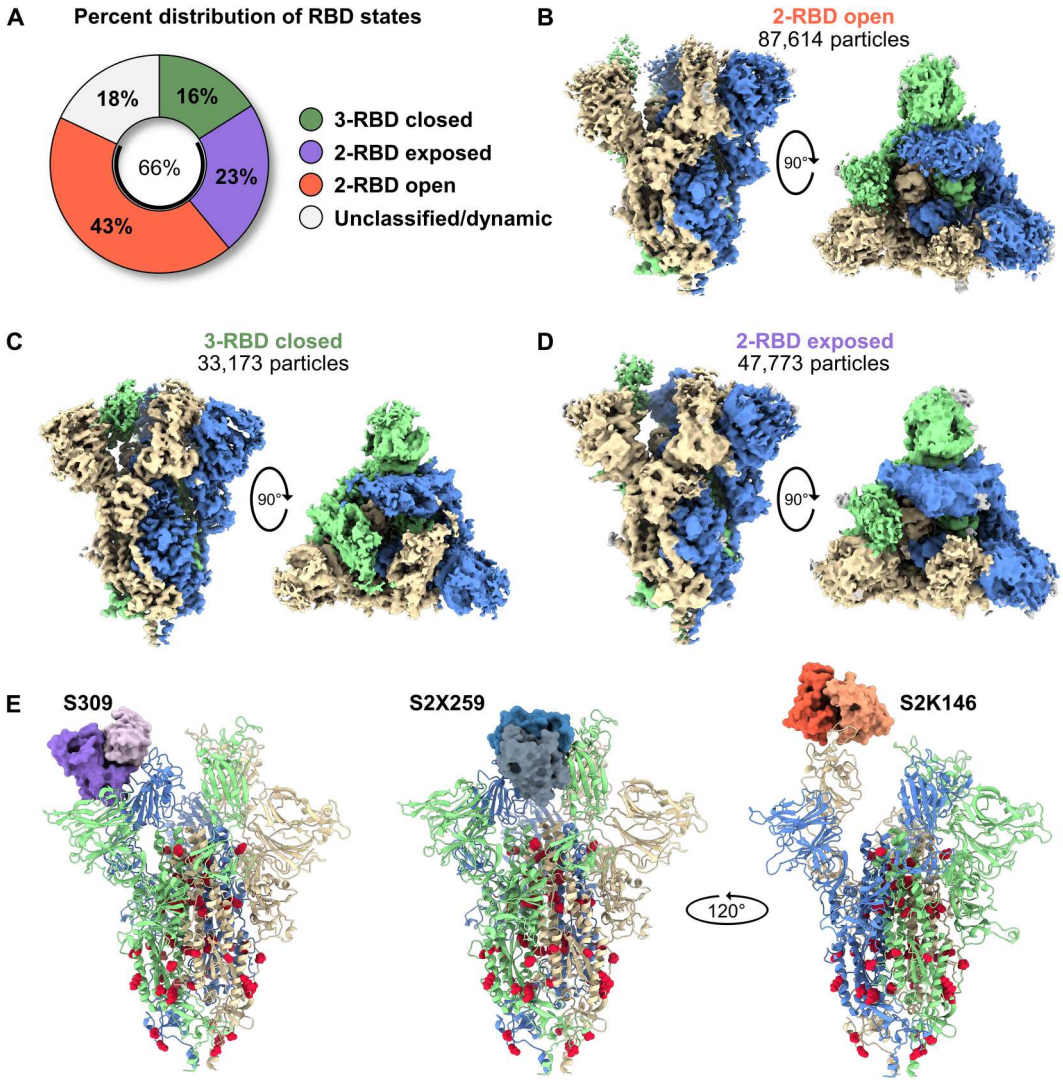

Fig. 6. S2D14 displays RBD open conformational states and is accessible for binding RBD nAbs. (**A**) Pie chart illustrating the percent distribution of RBD conformational states. (**B**) The cryo-EM structure of S2D14 in the two-RBD open conformations (3.1-Å resolution) was the dominant population and represents 43% of total particles. (**C**) The cryo-EM structure of S2D14 in the three-RBD closed conformation (2.8-Å resolution) was the minority population with 16% of total particles. (**D**) The cryo-EM structure (3.3-Å resolution) of S2D14 in the two-RBD exposed state was representative of 23% of the total population. Eighteen percent of the particles could not be classified into a distinct conformation. Side and top views are shown for each structure, and monomers are individually colored for clarity. (**E**) Docking of Fabs of S309 (left), S2X259 (center), and S2K146 (right) onto S2D14 in the two-RBD open conformation confirms the accessibility of these broadly neutralizing RBD epitopes. S2D14 protomers are colored blue, green, or tan, and mutations are shown as red spheres.

suggesting that the S2 domain has the potential to elicit broad coronavirus protection (*51*). For S2D14, a subset of the 20 S2 domain mutations computationally found to be stabilizing is surface-exposed, and four of those mutations (Q872A, S929K, S937G, and A1070T) are shared between all seven designs that were tested for antigenicity and may play a role in the loss of binding to VRC-112. The extent of the effect on other S2 domain epitopes and whether they can be recovered without compromising protein expression and stability is unknown and should be investigated in future studies. Despite the loss of this epitope, immunization with S2D14 resulted in high levels of neutralizing antibody titers. One possible explanation for this could be that, by inadvertently knocking out this epitope, the immune response is more focused toward the highly neutralizing epitopes on the RBDs. EM-based polyclonal epitope mapping, which has described the antibody landscape for other vaccine targets such as HIV-1 envelope (*80*–*82*) and influenza HA (*83*), has recently been applied to characterize antibody specificities against the spike protein in SARS-CoV-2 convalescent sera (*84*) and could be used to provide a detailed molecular map of the immune response elicited by S2D14. The role of T cell immunity is another important consideration for optimized S antigens which is suggested to play a role in limiting severe-to-critical COVID-19 (*85*). S-6P was shown to induce higher frequencies of antigen-specific $CD8^+$ T cells producing T helper 1 cytokines than S-2P, while trimeric RBD linked to the HR1 and HR2 domain of S2 induced RBD-specific interleukin-4 and interferon-γ–producing memory

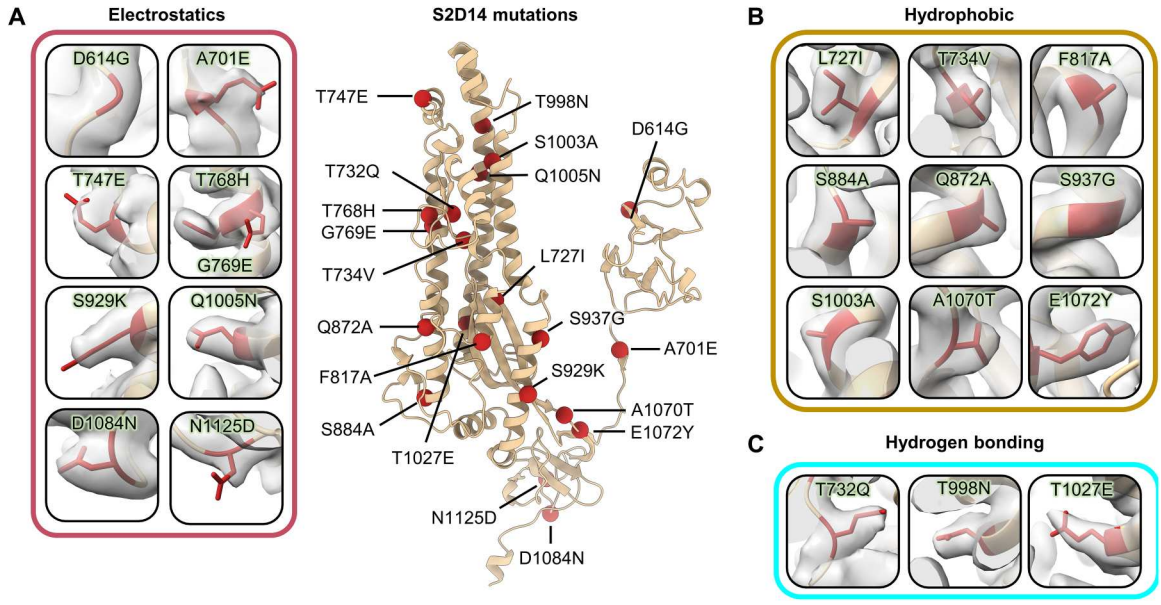

Fig. 7. PROSS mutations incorporated in S2D14 are well resolved by cryo-EM. A single protomer of S2D14 residues 600 to 1147 is shown in the center in ribbon representation with mutations indicated as red spheres. Mutations are grouped on the basis of changes in either (**A**) electrostatic complementarity, (**B**) alterations in hydrophobicity, or (**C**) the introduction of hydrogen bonds. Residue side chains are depicted as sticks and cryo-EM density is shown as a transparent surface.

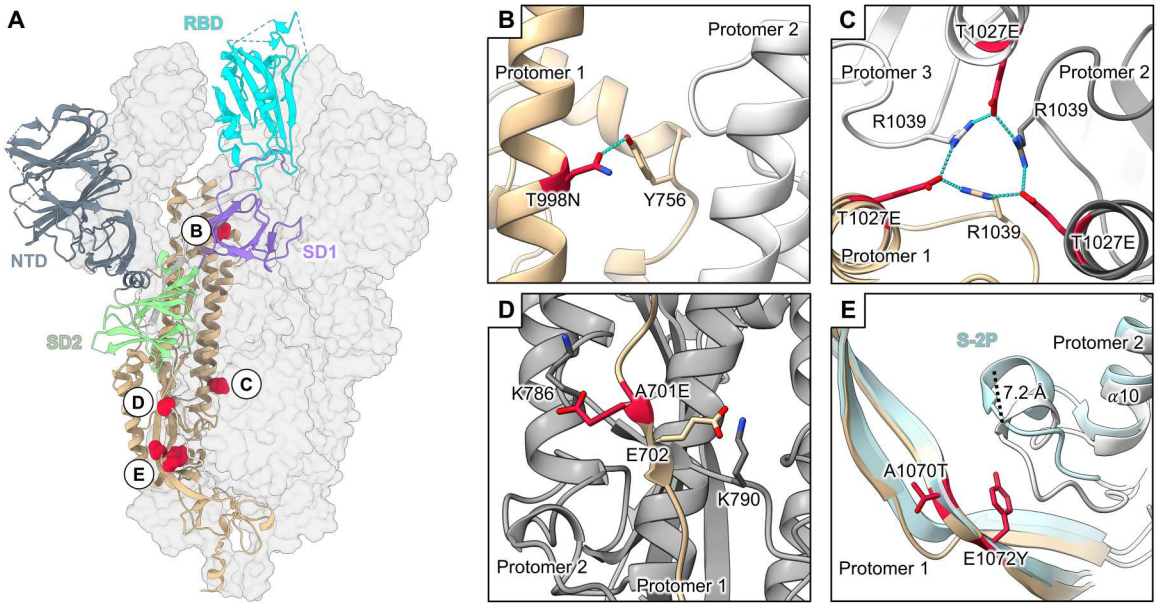

Fig. 8. Mutations within S2D14 that may influence S2 domain stability. (**A**) S2D14 is shown with two protomers as transparent surfaces, and a single protomer is depicted as a cartoon with domains colored as labeled in the figure. Mutations that may stabilize the S2 domain are colored red and shown as spheres. (**B**) A T998N mutation in the CH domain introduces a hydrogen bond with Y756 within the same protomer. (**C**) A T1027E mutation in the S2 core forms an interprotomer hydrogen bond network between R1039 residues. (**D**) An A701E mutation creates a negative patch at the S1/S2 linker region in proximity to a positively charged lysine residue K786 on an adjacent protomer. (**E**) The E1072Y mutation creates a hydrophobic surface that displaces an adjacent loop away from the trimer interior by ~7.2 Å. The positioning of this loop for S-2P is shown for comparison (light blue).

T cells (*86*, *87*). Although, for this work, we only measured the humoral response as the primary way to evaluate the immunogenicity of S2D14, future studies should aim to examine the impact of mutations in S2D14 on the overall T cell response.

A major finding of this work is that although vaccination of mice with either S2D14 or S-2P results in the elicitation of similar IgG titers, S2D14 elicits a higher functional response that was more effective than S-2P in neutralizing the ancestral Wuhan strain and VoCs (Alpha, Beta, and Delta). A recent report of the

immunogenicity of recombinant VSV vectored S-6P found that the enhanced stability and expression of S-6P led to the elicitation of a more effective nAb response at lower doses than S-2P against the Wuhan strain and VoC including Alpha (B.1.1.7), Gamma (P.1), Beta (B.1.351), Epsilon (B.1.427), and Delta (B.1.617.2) strains (*86*). Combined with enhanced expression, vaccination with S2D14 not only could translate well into dose-sparing effects when delivered in a recombinant setting but also may translate to a lower dose when delivered by alternative platforms such as mRNA or replication-competent viral vectors. For adjuvanted protein-based vaccines, the ability to increase expression yields of recombinant antigens would also be advantageous by providing a more cost-effective manufacturing process. Regarding the neutralization of the Omicron strain, immunization of mice with the 0.3-μg dose of S2D14 resulted in reduced nAbs when compared to titers observed against the Wuhan strain but was ~10-fold greater than titers elicited by S-2P. Therefore, S2D14 could serve as a scaffold for additional modifications which further improve nAb responses against Omicron or future variants. Overall, this work highlights the benefits of using an evolutionary consensus approach for antigen design and supports additional investigation into S2D14 as a potential tool for translational research and as a scaffold for further design and use as an immunogen for combating future coronaviruses.

MATERIALS AND METHODS

Computational design

Rosetta comparative modeling (RosettaCM) (*88*) was used to build a model, with cyclic symmetry constraints (*55*), of the SARS-CoV-2 S antigen with the RBD in the open conformation (PDB accession numbers: 6VSB and 6VYB). The model reconstruction strategy used a combination of x-ray and cryo-EM structures [PDB accession numbers: 6VYB, 6VW1, and 6NB7 (SARS-CoV-1)]. The symmetric interface design was performed on the lowest energy RosettaCM trimer, focusing on a monomeric chain with two virtual and identical partners, adapting protocols from the PROSS, with the updated beta energy scoring function (*49*, *50*).

To design mutations of the spike protein from SARS-CoV-2 using evolutionary constraints for the introduction of stabilizing residues, homologous sequences were obtained from the nonredundant BLAST database (*54*) and narrowed to 500 glycoprotein sequences from various coronavirus lineages (data S1). These aligned sequences were calculated into a position-specific scoring matrix (PSSM) with the PSI-BLAST algorithm (*54*). The matrix represents the likelihood for each of the 20 amino acids being present at each residue position, within the aligned sequences.

The Rosetta FilterScan mover (*89*) was used to perform single-point mutagenesis of all the residues to the preferred PSSM mutations, targeting the full spike (S) ectodomain, NTD plus S2 domain (NTD + S2), or the S2 domain only. The mutation scan was binned within 12 different energy thresholds (−0.5, −1, −1.5, −2, −2.5, −3, −3.5, −4, −4.5, −5, −5.5, and −6 kcal/mol) to increase mutation sequence diversity. A RosettaScripts (*90*) algorithm that energetically combined the proposed single mutations was used to reduce the search space onto a single monomer which was replicated across the identical protomers, yielding 12 total stabilizing designs for each round of mutations and representing each energy threshold.

S-2P and spike mutant expression and quantification

The gene encoding the sequence of designed S mutants was synthesized and cloned into an in-house mammalian expression vector pBW, with a hexahistidine sequence added to the C terminus. For the design of the S-2P–D614G variant, cloning was performed according to the protocol in the Agilent Quickchange II Kit using the S-2P backbone as a template. The spike designs were expressed in HEK293 cells using 3.0 ml of Expi293 expression in each well of a 24-deep-well high-throughput expression system. Each design was tested in duplicate wells. Cell culture supernatants were harvested on days 5 to 6 when viability was approximately 50%.

The Octet quantification assay for protein expression level was performed on an Octet 96 Red system (Sartorius). Harvested cell media were centrifuged and cell supernatants were prepared in a 96-well plate with S-2P or S-6P standards diluted in media from 20 to 0.3125 μg/ml. The standard and mutant binding curves were measured using anti-polyhistidine biosensors (anti-HIS), where the concentration of each mutant in media was calculated by fitting the measured initial binding rate to the calibration curve. The expression levels were measured in duplicate wells of each mutant's media and the average readout was reported.

Purification of mutants

The culture supernatant of selected SARS-CoV-2 S mutants produced in a 1-liter scale was directly loaded through 5 ml of nickel–nitrilotriacetic acid Excel column (Cytiva Life Sciences). The column was washed with 300 mM sodium chloride and 50 mM imidazole in 20 mM Hepes buffer (pH 7.5) and captured S mutants were eluted with 300 mM sodium chloride and 250 mM imidazole in 20 mM Hepes buffer (pH 7.5). The collected samples from appropriate elution fractions were pooled and concentrated before further purification of the S trimer by gel filtration using a Superose 6 increase 10/300 GL column (Cytiva Life Sciences) with 1× phosphate-buffered saline (PBS), pH 7.4, as a running buffer. The fractions corresponding to the targeted S mutants based on SDS–polyacrylamide gel electrophoresis analysis were pooled together and quantitated using the absorbance at 280 nm.

Surface plasmon resonance

SPR experiments were performed in a running buffer composed of 0.01 M Hepes (pH 7.4), 0.15 M NaCl, 3 mM EDTA, and 0.005% v/v surfactant P20 at 25°C using the Biacore 8K (GE Healthcare), with a series S protein A sensor chip (GE Healthcare). The ACE2 receptor or SARS-CoV-2 spike-specific antibodies (CR3022 or S309) were immobilized on the protein A sensor chip (GE Healthcare) at a ligand capture level of ~100 RU. Serial dilutions of purified spike designs were injected, at concentrations ranging from 10 to 1.25 nM. The resulting data were fit to a 1:1 binding model using the Biacore Evaluation Software (GE Healthcare).

Differential scanning fluorimetry

Nano-DSF was used to assess the thermal stability of purified spike designs on a Prometheus NT.48 instrument (NanoTemper Technologies). Samples were diluted to 0.2 mg/ml with PBS and 20 μl of each sample was loaded into capillary tubes. A temperature ramp was set to 1°C/minute, ranging from 20° to 95°C. The reported values are the mean of the first derivative of the ratio of intrinsic tryptophan fluorescence emission wavelengths for protein unfolding/folding (350 nm/330 nm), measured in triplicate.

Biolayer interferometry binding assays

Octet binding assays were performed using the Octet RH96 system (Sartorius). Freshly purified S-2P, S-2P–D614G, S2D14, and S-6P at 10 μg/ml were loaded onto 16 HIS1K biosensors before being dipped into 200 nM CR3022 mAb or hACE2 (Sino Biological). Immobilized antigen was allowed to associate with hACE2 or CR3022 for 10 min to achieve a signal plateau before a 10-min dissociation phase. The maximum binding signal of CR3022 and hACE2 was measured in triplicate.

Mouse immunization studies

An in vivo study was performed to assess the immunogenicity of S2D14 compared to S-2P in a mouse model. Female BALB/c mice, 7 to 8 weeks of age at the start of the study, were immunized (N = 10 mice per group) with AS03-adjuvanted (an oil-in-water emulsion adjuvant system containing 1.186 mg of alpha-tocopherol per dose) spike proteins at two dosage levels of 3.0 or 0.3 μg (*91*). A saline placebo control group was also included in the study (N = 4) but was not considered for statistical analysis. Spike proteins and AS03 were admixed shortly before injection. Mice were injected intramuscularly twice 3 weeks apart and bled 3 weeks after the initial immunization (post-I) and 2 weeks after the second immunization (post-II).

The in vivo study was conducted in accordance with the GSK Policy on the Care, Welfare and Treatment of Laboratory Animals and was reviewed by the Institutional Animal Care and Use Committee by the ethical review process at the institution where the work was performed. All studies followed ARRIVE (Animal Research: Reporting of In Vivo Experiments) Guidelines as applicable and were conducted in compliance with provisions of the United States Department of Agriculture Animal Welfare Act, the Public Health Service Policy on Humane Care and Use of Laboratory Animals and the U.S. Interagency Research Animal Committee Principles for the Utilization and Care of Research Animals.

Neutralization assays and ELISA

The serum CoV2-specific antibody responses were assessed using a Wuhan strain pseudo-virus neutralization assay to measure functional antibodies as described previously (*63*) and an ELISA (prefusion S-2P antigen absorbed to the solid phase) to measure IgG binding antibodies for all mice (Nexelis, Laval, Quebec). Human SARS-CoV-2 infection/COVID-19 convalescent sera (n = 22) were obtained at CHU Tivoli, Belgium, from donors 23 to 61 years of age, mostly from females, after polymerase chain reaction–confirmed diagnosis and at least 28 days after the participants were asymptomatic. Human samples were obtained with informed consent. All recruitment, sample collection, and experimental procedures using human samples have been approved by relevant institutional review boards and by GSK human sample management board. nAbs in post-II serum samples from mice immunized with S-2P, and S2D14 or placebo were additionally measured using a pseudo-virus neutralization assay with the Alpha, Beta, Delta, and Omicron variant strains (Nexelis, Laval, Quebec).

Statistical analysis of IgG binding and neutralization data

To assess differences between S-2P and S2D14 vaccines, for IgG binding titers, an analysis of variance (ANOVA) model for repeated measures was fitted on $\log_{10}$-transformed data including vaccine, dose, time, and their interaction as fixed factors and considering homogeneity of variances between groups. For post-II neutralization data, except with the Omicron strain, an ANOVA model was fitting on $\log_{10}$-transformed data with vaccine and dose as fixed factors. For the Omicron assay, a model accounting for left censored data was fitted on $\log_{10}$-transformed data. Homogeneity of variances between study groups was considered for all except Alpha and Omicron assays.

Geometric mean titers (GMTs) with corresponding 95% confidence intervals and geometric mean ratios (GMRs) with 90% confidence intervals (two-sided test with alpha = 0.05) were computed from these models to compare responses to S-2P and S2D14 vaccines by dose. GMRs for which the confidence interval does not include 1 are considered statistically significant. The analyses included more vaccination groups than reported (14 for IgG data and 6 for neutralization data) as the in vivo study initially consisted of additional vaccinated groups irrelevant to this study, but a multiplicity of comparisons was not considered. GMTs with corresponding 95% confidence intervals for HCS samples were computed separately from vaccination groups using Prism (GraphPad Software, San Diego, California USA).

Cryo-EM sample preparation

SARS-CoV-2 S designs 9 and S2D14, previously isolated by nickel-affinity chromatography, were further purified by size exclusion chromatography using a Superose 6 10/300 GL column (Cytiva Life Sciences) with tris-buffered saline buffer composed of 10 mM tris (pH 7.5) and 150 mM NaCl. Fractions containing purified spike protein were diluted to a final concentration of 0.4 mg/ml before specimen preparation on EM grids. Prepared samples (3.0 μl) were then applied to glow-discharged Quantifoil 1.2/1.3-400 mesh copper grids, blotted, and plunged into liquid ethane using an FEI Vitrobot Mark IV vitrification apparatus set at 100% relative humidity and 4°C (Thermo Fisher Scientific).

Cryo-EM image processing and modeling

Glacios TEM

A total of 1425 movies were collected using an FEI Glacios TEM at 200 kV equipped with a Falcon 3 direct electron detector at a magnification of ×120,000 corresponding to a pixel size of 0.91 Å/pixel. A more detailed description of imaging parameters used during data collection can be found in Table 2.

Cryo-EM single-particle analysis was carried out using the RELION 3.1 image processing suite (*92*). Briefly, frame alignment was performed using RELION′s implementation of MotionCor2 followed by contrast transfer function (CTF) estimation using CTFFIND4.1 (*93*, *94*). A subset of images was used to manually select particles to build a set of 2D templates for automated particle picking across the entire dataset. Using the 2D templates for autopicking, a total of 92,933 particles were selected from the full set of images. Particles were next subjected to 2D classification, which resulted in the selection of 44,459 particles. Next, 3D classification was performed against a reference structure built using RELION′s de novo 3D model generation and applying C3 symmetry. Three classes retained the trimeric morphology, and the fourth class was discarded because of poor structure quality. The three classes consisting of 39,718 particles were subjected to an additional round of 3D classification using C1 symmetry, which resulted in one class of particles with three RBDs in a closed state (7759 particles) and a second class with one RBD in the open state (9154 particles).

For particles in the closed conformation, 3D refinement was performed using C3 symmetry, while C1 symmetry was used for 3D refinement for the one-RBD open conformation. After initial 3D refinement, both datasets were followed by CTF refinement to correct for beam aberrations and determine per-particle defocus values. Bayesian polishing of the CTF-refined particles was then performed to correct for per-particle motion. A final 3D refinement of both structures converged to 7.1 Å for the RBD closed conformation and 8.5 Å for the single RBD open conformation according to the gold-standard 0.143 Fourier shell correlation (FSC) criteria.

Titan Krios

A total of 6169 movies were collected using an FEI Titan Krios operating at 300 kV and equipped with a Falcon 4 direct electron detector (Nanosciences Center, Cambridge University, UK) at a magnification of ×120,000 corresponding to a pixel size of 0.67 Å/pixel. A more detailed description of settings used for imaging during data collection can be found in Table 2.

Cryo-EM single-particle analysis was carried out using the RELION 3.1 image processing suite (*92*). For a visual depiction of the single-particle workflow, refer to fig. S7. Briefly, alignment of the raw movie frames was performed using RELION′s implementation of MotionCor2 followed by CTF estimation using CTFFIND4.1 (*93*, *94*). Next, a subset of particles was manually selected and used to generate 2D classes that were then used as templates for particle-picking across the entire set of 6169 micrographs, which resulted in the selection of 724,002 particles. Particles were initially extracted at 4× binning with a pixel size of 2.68 Å/pixel. The binned particle stack was subjected to a single round of 2D classification and classes showing that features consistent with the S trimer were selected for further processing. The 566,825 particles selected from 2D classification were subjected to one round of 3D classification against a reference model that was generated using RELION′s de novo 3D model generation. Among the generated classes was a single population resembling the known trimeric S morphology. This stack of 205,674 particles was then re-extracted as the unbinned particle set. A consensus C1 refinement was performed to estimate correct particle poses resulting in a 3.8-Å resolution cryo-EM map. The focused 3D classification was then performed using individual masks encompassing the NTD and RBD for RBDs in the closed state, one-RBD open, and two-RBD open conformations, which resulted in the separation of the particles into three distinct classes: a three-RBD closed class (33,173 particles), a two-RBD exposed class (47,773 particles), and a two-RBD open class (87,614 particles). Initial 3D auto-refinement for the three-RBD closed, two-RBD exposed, and two-RBD open conformations resulted in 3.9-, 3.5-, and 3.5-Å resolution cryo-EM maps, respectively. Three-dimensional refined particles for each set were further subjected to CTF refinement and Bayesian polishing to estimate per-particle defocus values and correct for individual particle motions. A final 3D refinement resulted in an improved resolution for each map according to the gold-standard 0.143 FSC criteria. Final resolutions for the three-RBD closed, two-RBD exposed, and two-RBD open conformations were 2.8, 3.3, and 3.1 Å, respectively.

Modeling of each cryo-EM structure was performed using Phenix and COOT (*95*, *96*). For the three-RBD closed conformation, PDB 6VXX was used as a starting structure where mutations for S2D14 were inserted using ChimeraX (*17*, *97*). For the RBD exposed and RBD open structures, a model for the two-RBD open conformation was built from PDB 6VSB, and mutations for S2D14 were inserted using ChimeraX (*20*). For each model and corresponding map, real-space refinement was performed in Phenix, initially by applying morphing, simulated annealing, and applying secondary structure restraints. To rebuild loops missing in the original PDB files and fit into the corresponding cryo-EM density, RosettaCM was performed using the initial Phenix models and structural templates for known NTD and RBD structures (PDB accession numbers: 7LY3 and 7DEU). Once the full homology model was built, Rosetta Cartesian refinement was performed (*98*), followed by torsional refinement to build glycan structures (*99*, *100*). A final real-space refinement applying minimization, atomic displacement parameter refinement, and occupancy optimization was performed using Phenix. For the RBD exposed and RBD open structures, 0.14 and 0.03% of their residues were classified in the disallowed regions of Ramachandran space, but models were not further adjusted because of poor map quality in these regions. Loops, disordered regions, and glycans lacking structural information in the cryo-EM density were removed in the resulting Rosetta models.

Supplementary Materials

This PDF file includes:

Figs. S1 to S11
Table S1
Legends for data S1 and S2

Other Supplementary Material for this manuscript includes the following:

Data S1 and S2

View/request a protocol for this paper from *Bio-protocol*.

REFERENCES AND NOTES

1. E. Volz, S. Mishra, M. Chand, J. C. Barrett, R. Johnson, L. Geidelberg, W. R. Hinsley, D. J. Laydon, G. Dabrera, Á. O'Toole, R. Amato, M. Ragonnet-Cronin, I. Harrison, B. Jackson, C. V. Ariani, O. Boyd, N. J. Loman, J. T. McCrone, S. Gonçalves, D. Jorgensen, R. Myers, V. Hill, D. K. Jackson, K. Gaythorpe, N. Groves, J. Sillitoe, D. P. Kwiatkowski; COVID-19 Genomics UK (COG-UK) consortium, S. Flaxman, O. Ratmann, S. Bhatt, S. Hopkins, A. Gandy, A. Rambaut, N. M. Ferguson, Assessing transmissibility of SARS-CoV-2 lineage B.1.1.7 in England. *Nature* **593**, 266–269 (2021).
2. H. Tegally, E. Wilkinson, M. Giovanetti, A. Iranzadeh, V. Fonseca, J. Giandhari, D. Doolabh, S. Pillay, E. J. San, N. Msomi, K. Mlisana, A. von Gottberg, S. Walaza, M. Allam, A. Ismail, T. Mohale, A. J. Glass, S. Engelbrecht, G. van Zyl, W. Preiser, F. Petruccione, A. Sigal, D. Hardie, G. Marais, N. Y. Hsiao, S. Korsman, M. A. Davies, L. Tyers, I. Mudau, D. York, C. Maslo, D. Goedhals, S. Abrahams, O. Laguda-Akingba, A. Alisoltani-Dehkordi, A. Godzik, C. K. Wibmer, B. T. Sewell, J. Lourenço, L. C. J. Alcantara, S. L. Kosakovsky Pond, S. Weaver, D. Martin, R. J. Lessells, J. N. Bhiman, C. Williamson, T. de Oliveira, Detection of a SARS-CoV-2 variant of concern in South Africa. *Nature* **592**, 438–443 (2021).
3. H. Jhun, H. Y. Park, Y. Hisham, C. S. Song, S. Kim, SARS-CoV-2 Delta (B.1.617.2) variant: A unique T478K mutation in receptor binding motif (RBM) of spike gene. *Immune Netw.* **21**, e32 (2021).
4. H. Zhou, B. M. Dcosta, N. R. Landau, T. Tada, Resistance of SARS-CoV-2 omicron BA.1 and BA.2 variants to vaccine-elicited sera and therapeutic monoclonal antibodies. *Viruses* **14**, 1334 (2022).
5. S. Jangra, C. Ye, R. Rathnasinghe, D. Stadlbauer, F. Krammer, V. Simon, L. Martinez-Sobrido, A. García-Sastre, M. Schotsaert, H. Alshammary, A. A. Amoako, M. H. Awawda, K. F. Beach, M. C. Bermúdez-González, R. L. Chernet, L. Q. Eaker, E. D. Ferreri, D. L. Floda, C. R. Gleason, G. Kleiner, D. Jurczyszak, J. C. Matthews, W. A. Mendez, L. C. F. Mulder, K. T. Russo, A. B. T. Salimbangon, M. Saksena, A. S. Shin, L. A. Sominsky, K. Srivastava, SARS-CoV-2 spike E484K mutation reduces antibody neutralisation. *Lancet Microbe* **2**, e283–e284 (2021).
6. K. B. Pouwels, E. Pritchard, P. C. Matthews, N. Stoesser, D. W. Eyre, K. D. Vihta, T. House, J. Hay, J. I. Bell, J. N. Newton, J. Farrar, D. Crook, D. Cook, E. Rourke, R. Studley, T. E. A. Peto,

I. Diamond, A. S. Walker, Effect of Delta variant on viral burden and vaccine effectiveness against new SARS-CoV-2 infections in the UK. *Nat. Med.* **27**, 2127–2135 (2021).

7. Y. Cao, A. Yisimayi, F. Jian, W. Song, T. Xiao, L. Wang, S. du, J. Wang, Q. Li, X. Chen, Y. Yu, P. Wang, Z. Zhang, P. Liu, R. An, X. Hao, Y. Wang, J. Wang, R. Feng, H. Sun, L. Zhao, W. Zhang, D. Zhao, J. Zheng, L. Yu, C. Li, N. Zhang, R. Wang, X. Niu, S. Yang, X. Song, Y. Chai, Y. Hu, Y. Shi, L. Zheng, Z. Li, Q. Gu, F. Shao, W. Huang, R. Jin, Z. Shen, Y. Wang, X. Wang, J. Xiao, X. S. Xie, BA.2.12.1, BA.4 and BA.5 escape antibodies elicited by Omicron infection. *Nature* **608**, 593–602 (2022).
8. Y. Cao, F. Jian, J. Wang, Y. Yu, W. Song, A. Yisimayi, J. Wang, R. An, N. Zhang, Y. Wang, P. Wang, L. Zhao, H. Sun, L. Yu, S. Yang, X. Niu, T. Xiao, Q. Gu, F. Shao, X. Hao, Y. Xu, R. Jin, Y. Wang, X. S. Xie, Imprinted SARS-CoV-2 humoral immunity induces convergent Omicron RBD evolution. *bioRxiv* 2022.09.15.507787 (2022). https://doi.org/10.1101/2022.09.15.507787
9. X. Wang, X. Zhao, J. Song, J. Wu, Y. Zhu, M. Li, Y. Cui, Y. Chen, L. Yang, J. Liu, H. Zhu, S. Jiang, P. Wang, Homologous or heterologous booster of inactivated vaccine reduces SARS-CoV-2 Omicron variant escape from neutralizing antibodies. *Emerg. Microbes Infect.* **11**, 477–481 (2022).
10. Z. Zhang, Q. He, W. Zhao, Y. Li, J. Yang, Z. Hu, X. Chen, H. Peng, Y. X. Fu, L. Chen, L. Lu, A heterologous V-01 or variant-matched bivalent V-01D-351 booster following primary series of inactivated vaccine enhances the neutralizing capacity against SARS-CoV-2 delta and Omicron strains. *J. Clin. Med.* **11**, 4164 (2022).
11. S. M. Scheaffer, D. Lee, B. Whitener, B. Ying, K. Wu, H. Jani, P. Martin, N. J. Amato, L. E. Avena, D. M. Berrueta, S. D. Schmidt, S. O'Dell, A. Nasir, G.-Y. Chuang, G. Stewart-Jones, R. A. Koup, N. A. Doria-Rose, A. Carfi, S. M. Elbashir, L. B. Thackray, D. K. Edwards, M. S. Diamond, Bivalent SARS-CoV-2 mRNA vaccines increase breadth of neutralization and protect against the BA.5 Omicron variant. *bioRxiv* 2022.09.12.507614 (2022). https://doi.org/10.1101/2022.09.12.507614
12. A. Muik, B. G. Lui, M. Bacher, A.-K. Wallisch, A. Toker, Carla Iris Cadima Couto, A. Güler, V. Mampilli, G. J. Schmitt, J. Mottl, T. Ziegenhals, S. Fesser, J. Reinholz, F. Wernig, K.-G. Schraut, H. Hefesha, H. Cai, Q. Yang, K. C. Walzer, J. Grosser, S. Strauss, A. Finlayson, K. Krüger, O. Ozhelvaci, K. Grikscheit, N. Kohmer, S. Ciesek, K. A. Swanson, A. B. Vogel, Ö. Türeci, U. Sahin, Exposure to BA.4/BA.5 Spike glycoprotein drives pan-Omicron neutralization in vaccine-experienced humans and mice. *bioRxiv* 2022.09.21.508818 (2022). https://doi.org/10.1101/2022.09.21.508818
13. J. Tubiana, Y. Xiang, L. Fan, H. J. Wolfson, K. Chen, D. Schneidman-Duhovny, Y. Shi, Reduced antigenicity of Omicron lowers host serologic response. *bioRxiv* 2022.02.15.480546 (2022). https://doi.org/10.1101/2022.02.15.480546
14. E. Andreano, R. Rappuoli, SARS-CoV-2 escaped natural immunity, raising questions about vaccines and therapies. *Nat. Med.* **27**, 759–761 (2021).
15. Y. Cao, J. Wang, F. Jian, T. Xiao, W. Song, A. Yisimayi, W. Huang, Q. Li, P. Wang, R. An, J. Wang, Y. Wang, X. Niu, S. Yang, H. Liang, H. Sun, T. Li, Y. Yu, Q. Cui, S. Liu, X. Yang, S. du, Z. Zhang, X. Hao, F. Shao, R. Jin, X. Wang, J. Xiao, Y. Wang, X. S. Xie, Omicron escapes the majority of existing SARS-CoV-2 neutralizing antibodies. *Nature* **602**, 657–663 (2022).
16. B. J. Bosch, R. van der Zee, C. A. de Haan, P. J. Rottier, The coronavirus spike protein is a class I virus fusion protein: Structural and functional characterization of the fusion core complex. *J. Virol.* **77**, 8801–8811 (2003).
17. A. C. Walls, Y. J. Park, M. A. Tortorici, A. Wall, A. T. McGuire, D. Veesler, Structure, function, and antigenicity of the SARS-CoV-2 spike glycoprotein. *Cell* **183**, 1735 (2020).
18. D. J. Benton, A. G. Wrobel, P. Xu, C. Roustan, S. R. Martin, P. B. Rosenthal, J. J. Skehel, S. J. Gamblin, Receptor binding and priming of the spike protein of SARS-CoV-2 for membrane fusion. *Nature* **588**, 327–330 (2020).
19. R. Henderson, R. J. Edwards, K. Mansouri, K. Janowska, V. Stalls, S. M. C. Gobeil, M. Kopp, D. Li, R. Parks, A. L. Hsu, M. J. Borgnia, B. F. Haynes, P. Acharya, Controlling the SARS-CoV-2 spike glycoprotein conformation. *Nat. Struct. Mol. Biol.* **27**, 925–933 (2020).
20. D. Wrapp, N. Wang, K. S. Corbett, J. A. Goldsmith, C. L. Hsieh, O. Abiona, B. S. Graham, J. S. McLellan, Cryo-EM structure of the 2019-nCoV spike in the prefusion conformation. *Science* **367**, 1260–1263 (2020).
21. T. N. Starr, N. Czudnochowski, Z. Liu, F. Zatta, Y. J. Park, A. Addetia, D. Pinto, M. Beltramello, P. Hernandez, A. J. Greaney, R. Marzi, W. G. Glass, I. Zhang, A. S. Dingens, J. E. Bowen, M. A. Tortorici, A. C. Walls, J. A. Wojcechowskyj, A. de Marco, L. E. Rosen, J. Zhou, M. Montiel-Ruiz, H. Kaiser, J. R. Dillen, H. Tucker, J. Bassi, C. Silacci-Fregni, M. P. Housley, J. di Iulio, G. Lombardo, M. Agostini, N. Sprugasci, K. Culap, S. Jaconi, M. Meury, E. Dellota Jr., R. Abdelnabi, S. Y. C. Foo, E. Cameroni, S. Stumpf, T. I. Croll, J. C. Nix, C. Havenar-Daughton, L. Piccoli, F. Benigni, J. Neyts, A. Telenti, F. A. Lempp, M. S. Pizzuto, J. D. Chodera, C. M. Hebner, H. W. Virgin, S. P. J. Whelan, D. Veesler, D. Corti, J. D. Bloom, G. Snell, SARS-CoV-2 RBD antibodies that maximize breadth and resistance to escape. *Nature* **597**, 97–102 (2021).
22. L. Premkumar, B. Segovia-Chumbez, R. Jadi, D. R. Martinez, R. Raut, A. J. Markmann, C. Cornaby, L. Bartelt, S. Weiss, Y. Park, C. E. Edwards, E. Weimer, E. M. Scherer, N. Rouphael, S. Edupuganti, D. Weiskopf, L. V. Tse, Y. J. Hou, D. Margolis, A. Sette, M. H. Collins, J. Schmitz, R. S. Baric, A. M. de Silva, The receptor binding domain of the viral spike protein is an immunodominant and highly specific target of antibodies in SARS-CoV-2 patients. *Sci. Immunol.* **5**, eabc8413 (2020).
23. E. Andreano, I. Paciello, G. Piccini, N. Manganaro, P. Pileri, I. Hyseni, M. Leonardi, E. Pantano, V. Abbiento, L. Benincasa, G. Giglioli, C. de Santi, M. Fabbiani, I. Rancan, M. Tumbarello, F. Montagnani, C. Sala, E. Montomoli, R. Rappuoli, Hybrid immunity improves B cells and antibodies against SARS-CoV-2 variants. *Nature* **600**, 530–535 (2021).
24. E. Andreano, E. Nicastri, I. Paciello, P. Pileri, N. Manganaro, G. Piccini, A. Manenti, E. Pantano, A. Kabanova, M. Troisi, F. Vacca, D. Cardamone, C. de Santi, J. L. Torres, G. Ozorowski, L. Benincasa, H. Jang, C. di Genova, L. Depau, J. Brunetti, C. Agrati, M. R. Capobianchi, C. Castilletti, A. Emiliozzi, M. Fabbiani, F. Montagnani, L. Bracci, G. Sautto, T. M. Ross, E. Montomoli, N. Temperton, A. B. Ward, C. Sala, G. Ippolito, R. Rappuoli, Extremely potent human monoclonal antibodies from COVID-19 convalescent patients. *Cell* **184**, 1821–1835.e16 (2021).
25. M. A. Tortorici, N. Czudnochowski, T. N. Starr, R. Marzi, A. C. Walls, F. Zatta, J. E. Bowen, S. Jaconi, J. di Iulio, Z. Wang, A. de Marco, S. K. Zepeda, D. Pinto, Z. Liu, M. Beltramello, I. Bartha, M. P. Housley, F. A. Lempp, L. E. Rosen, E. Dellota Jr., H. Kaiser, M. Montiel-Ruiz, J. Zhou, A. Addetia, B. Guarino, K. Culap, N. Sprugasci, C. Saliba, E. Vetti, I. Giacchetto-Sasselli, C. S. Fregni, R. Abdelnabi, S. Y. C. Foo, C. Havenar-Daughton, M. A. Schmid, F. Benigni, E. Cameroni, J. Neyts, A. Telenti, H. W. Virgin, S. P. J. Whelan, G. Snell, J. D. Bloom, D. Corti, D. Veesler, M. S. Pizzuto, Broad sarbecovirus neutralization by a human monoclonal antibody. *Nature* **597**, 103–108 (2021).
26. Y. J. Park, A. de Marco, T. N. Starr, Z. Liu, D. Pinto, A. C. Walls, F. Zatta, S. K. Zepeda, J. E. Bowen, K. R. Sprouse, A. Joshi, M. Giurdanella, B. Guarino, J. Noack, R. Abdelnabi, S. Y. C. Foo, L. E. Rosen, F. A. Lempp, F. Benigni, G. Snell, J. Neyts, S. P. J. Whelan, H. W. Virgin, J. D. Bloom, D. Corti, M. S. Pizzuto, D. Veesler, Antibody-mediated broad sarbecovirus neutralization through ACE2 molecular mimicry. *Science* **375**, 449–454 (2022).
27. A. A. Cohen, N. van Doremalen, A. J. Greaney, H. Andersen, A. Sharma, T. N. Starr, J. R. Keeffe, C. Fan, J. E. Schulz, P. N. P. Gnanapragasam, L. M. Kakutani, A. P. West Jr., G. Saturday, Y. E. Lee, H. Gao, C. A. Jette, M. G. Lewis, T. K. Tan, A. R. Townsend, J. D. Bloom, V. J. Munster, P. J. Bjorkman, Mosaic RBD nanoparticles protect against challenge by diverse sarbecoviruses in animal models. *Science* **377**, eabq0839 (2022).
28. T. H. Dickey, W. K. Tang, B. Butler, T. Ouahes, S. Orr-Gonzalez, N. D. Salinas, L. E. Lambert, N. H. Tolia, Design of the SARS-CoV-2 RBD vaccine antigen improves neutralizing antibody response. *Sci. Adv.* **8**, eabq8276 (2022).
29. W. Sun, L. He, H. Zhang, X. Tian, Z. Bai, L. Sun, L. Yang, X. Jia, Y. Bi, T. Luo, G. Cheng, W. Fan, W. Liu, J. Li, The self-assembled nanoparticle-based trimeric RBD mRNA vaccine elicits robust and durable protective immunity against SARS-CoV-2 in mice. *Signal Transduct. Target. Ther.* **6**, 340 (2021).
30. A. C. Walls, B. Fiala, A. Schäfer, S. Wrenn, M. N. Pham, M. Murphy, L. V. Tse, L. Shehata, M. A. O'Connor, C. Chen, M. J. Navarro, M. C. Miranda, D. Pettie, R. Ravichandran, J. C. Kraft, C. Ogohara, A. Palser, S. Chalk, E. C. Lee, K. Guerriero, E. Kepl, C. M. Chow, C. Sydeman, E. A. Hodge, B. Brown, J. T. Fuller, K. H. Dinnon III, L. E. Gralinski, S. R. Leist, K. L. Gully, T. B. Lewis, M. Guttman, H. Y. Chu, K. K. Lee, D. H. Fuller, R. S. Baric, P. Kellam, L. Carter, M. Pepper, T. P. Sheahan, D. Veesler, N. P. King, Elicitation of potent neutralizing antibody responses by designed protein nanoparticle vaccines for SARS-CoV-2. *Cell* **183**, 1367–1382.e17 (2020).
31. L. Dai, L. Gao, L. Tao, S. R. Hadinegoro, M. Erkin, Z. Ying, P. He, R. T. Girsang, H. Vergara, J. Akram, H. I. Satari, T. Khaliq, U. Sughra, A. P. Celi, F. Li, Y. Li, Z. Jiang, D. Dalimova, J. Tuychiev, S. Turdikulova, A. Ikram, N. Flores Lastra, F. Ding, M. Suhardono, E. Fadlyana, J. Yan, Z. Hu, C. Li, I. Y. Abdurakhmonov, G. F. Gao; ZF2001 Global Trial Group, Efficacy and safety of the RBD-dimer-based COVID-19 vaccine ZF2001 in adults. *N. Engl. J. Med.* **386**, 2097–2111 (2022).
32. N. A. Kaabi, Y. K. Yang, L. F. du, K. Xu, S. Shao, Y. Liang, Y. Kang, J. G. Su, J. Zhang, T. Yang, S. Hussein, M. S. ElDein, S. S. Yang, W. Lei, X. J. Gao, Z. Jiang, X. Cong, Y. Tan, H. Wang, M. Li, H. M. Mekki, W. Zaher, S. Mahmoud, X. Zhang, C. Qu, D. Y. Liu, J. Zhang, M. Yang, I. Eltantawy, J. W. Hou, Z. H. Lei, P. Xiao, Z. N. Wang, J. L. Yin, X. Y. Mao, J. Zhang, L. Qu, Y. T. Zhang, X. M. Yang, G. Wu, Q. M. Li, Safety and immunogenicity of a hybrid-type vaccine booster in BBIBP-CorV recipients in a randomized phase 2 trial. *Nat. Commun.* **13**, 3654 (2022).
33. N. A. Kaabi, Y. K. Yang, J. Zhang, K. Xu, Y. Liang, Y. Kang, J. G. Su, T. Yang, S. Hussein, M. S. ElDein, S. Shao, S. S. Yang, W. Lei, X. J. Gao, Z. Jiang, H. Wang, M. Li, H. M. Mekki, W. Zaher, S. Mahmoud, X. Zhang, C. Qu, D. Y. Liu, J. Zhang, M. Yang, I. Eltantawy, P. Xiao, Z. N. Wang, J. L. Yin, X. Y. Mao, J. Zhang, N. Liu, F. J. Shen, L. Qu, Y. T. Zhang, X. M. Yang, G. Wu, Q. M. Li, Immunogenicity and safety of NVSI-06-07 as a heterologous booster after priming with BBIBP-CorV: A phase 2 trial. *Signal Transduct. Target. Ther.* **7**, 172 (2022).
34. J. Zhang, Z. B. Han, Y. Liang, X. F. Zhang, Y. Q. Jin, L. F. du, S. Shao, H. Wang, J. W. Hou, K. Xu, W. Lei, Z. H. Lei, Z. M. Liu, J. Zhang, Y. N. Hou, N. Liu, F. J. Shen, J. J. Wu, X. Zheng, X. Y. Li, X. Li, W. J. Huang, G. Z. Wu, J. G. Su, Q. M. Li, A mosaic-type trimeric RBD-based COVID-19

vaccine candidate induces potent neutralization against Omicron and other SARS-CoV-2 variants. *eLife* **11**, e78633 (2022).

35. F. Hernández-Bernal, M. C. Ricardo-Cobas, Y. Martín-Bauta, Z. Navarro-Rodríguez, M. Piñera-Martínez, J. Quintana-Guerra, K. Urrutia-Pérez, K. Urrutia-Pérez, C. O. Chávez-Chong, J. L. Azor-Hernández, J. L. Rodríguez-Reinoso, L. Lobaina-Lambert, E. Colina-Ávila, J. Bizet-Almeida, J. Rodríguez-Nuviola, S. Del Valle-Piñera, M. Ramírez-Domínguez, E. Tablada-Ferreiro, M. Alonso-Valdés, G. Lemos-Pérez, G. E. Guillén-Nieto, A. Palenzuela-Díaz, E. Noa-Romero, M. Limonta-Fernández, J. M. Fernández-Ávila, N. A. Ali-Mros, L. Del Toro-Lahera, R. Remedios-Reyes, M. Ayala-Ávila, V. L. Muzio-González, Safety, tolerability, and immunogenicity of a SARS-CoV-2 recombinant spike RBD protein vaccine: A randomised, double-blind, placebo-controlled, phase 1-2 clinical trial (ABDALA Study). *EClinicalMedicine* **46**, 101383 (2022).
36. M. Eugenia-Toledo-Romaní, L. Verdecia-Sánchez, M. Rodríguez-González, L. Rodríguez-Noda, C. Valenzuela-Silva, B. Paredes-Moreno, B. Sánchez-Ramírez, R. Pérez-Nicado, R. González-Mugica, T. Hernández-García, G. Bergado-Baez, F. Pi-Estopiñán, O. Cruz-Sui, A. Fraga-Quintero, M. García-Montero, A. Palenzuela-Díaz, G. Baró-Román, I. Mendoza-Hernández, S. Fernandez-Castillo, Y. Climent-Ruiz, D. Santana-Mederos, U. R. Gonzalez, Y. García-Vega, B. Pérez-Massón, Guang-Wu-Chen, T. Boggiano-Ayo, E. Ojito-Magaz, D. G. Rivera, Y. Valdés-Balbín, D. García-Rivera, V. Vérez-Bencomo; SOBERANA Research Group, Y. Gómez-Maceo, R. Reyes-Matienzo, J. M. Coviella-Artime, I. Morffi-Cinta, M. Martínez-Pérez, I. Castillo-Quintana, A. Garcés-Hechavarría, R. Valera-Fernández, D. Martínez-Bedoya, R. Garrido-Arteaga, F. C.-S. Jorge, L. Q. Moreno, I. Ontivero-Pino, M. T. Pérez-Guevara, M. Morales-García, E. Noa-Romero, I. Orosa-Vázquez, M. Díaz-Hernández, G. Rojas, Y. Tundidor, E. García-López, Y. Muñoz-Morejon, E. Galano-Frutos, J. Rodríguez-Alvarez, A. Arteaga, M. M. Nápoles, J. E. Ávila, M. F. Fernández, Safety and immunogenicity of anti-SARS CoV-2 vaccine SOBERANA 02 in homologous or heterologous scheme: Open label phase I and phase IIa clinical trials. *Vaccine* **40**, 4220–4230 (2022).
37. C. L. Hsieh, J. A. Goldsmith, J. M. Schaub, A. M. DiVenere, H. C. Kuo, K. Javanmardi, K. C. le, D. Wrapp, A. G. Lee, Y. Liu, C. W. Chou, P. O. Byrne, C. K. Hjorth, N. V. Johnson, J. Ludes-Meyers, A. W. Nguyen, J. Park, N. Wang, D. Amengor, J. J. Lavinder, G. C. Ippolito, J. A. Maynard, I. J. Finkelstein, J. S. McLellan, Structure-based design of prefusion-stabilized SARS-CoV-2 spikes. *Science* **369**, 1501–1505 (2020).
38. J. S. McLellan, M. Chen, M. G. Joyce, M. Sastry, G. B. E. Stewart-Jones, Y. Yang, B. Zhang, L. Chen, S. Srivatsan, A. Zheng, T. Zhou, K. W. Graepel, A. Kumar, S. Moin, J. C. Boyington, G. Y. Chuang, C. Soto, U. Baxa, A. Q. Bakker, H. Spits, T. Beaumont, Z. Zheng, N. Xia, S. Y. Ko, J. P. Todd, S. Rao, B. S. Graham, P. D. Kwong, Structure-based design of a fusion glycoprotein vaccine for respiratory syncytial virus. *Science* **342**, 592–598 (2013).
39. M. B. Battles, V. Más, E. Olmedillas, O. Cano, M. Vázquez, L. Rodríguez, J. A. Melero, J. S. McLellan, Structure and immunogenicity of pre-fusion-stabilized human metapneumovirus F glycoprotein. *Nat. Commun.* **8**, 1528 (2017).
40. C. L. Hsieh, S. A. Rush, C. Palomo, C. W. Chou, W. Pickens, V. Más, J. S. McLellan, Structure-based design of prefusion-stabilized human metapneumovirus fusion proteins. *Nat. Commun.* **13**, 1299 (2022).
41. G. B. E. Stewart-Jones, J. Gorman, L. Ou, B. Zhang, M. G. Joyce, L. Yang, C. Cheng, G. Y. Chuang, K. E. Foulds, W. P. Kong, A. S. Olia, M. Sastry, C. H. Shen, J. P. Todd, Y. Tsybovsky, R. Verardi, Y. Yang, P. L. Collins, D. Corti, A. Lanzavecchia, D. G. Scorpio, J. R. Mascola, U. J. Buchholz, P. D. Kwong, Interprotomer disulfide-stabilized variants of the human metapneumovirus fusion glycoprotein induce high titer-neutralizing responses. *Proc. Natl. Acad. Sci. U.S.A.* **118**, e2106196118 (2021).
42. L. Godley, J. Pfeifer, D. Steinhauer, B. Ely, G. Shaw, R. Kaufmann, E. Suchanek, C. Pabo, J. J. Skehel, D. C. Wiley, S. Wharton, Introduction of intersubunit disulfide bonds in the membrane-distal region of the influenza hemagglutinin abolishes membrane fusion activity. *Cell* **68**, 635–645 (1992).
43. R. W. Sanders, M. Vesanen, N. Schuelke, A. Master, L. Schiffner, R. Kalyanaraman, M. Paluch, B. Berkhout, P. J. Maddon, W. C. Olson, M. Lu, J. P. Moore, Stabilization of the soluble, cleaved, trimeric form of the envelope glycoprotein complex of human immunodeficiency virus type 1. *J. Virol.* **76**, 8875–8889 (2002).
44. A. Goldenzweig, M. Goldsmith, S. E. Hill, O. Gertman, P. Laurino, Y. Ashani, O. Dym, T. Unger, S. Albeck, J. Prilusky, R. L. Lieberman, A. Aharoni, I. Silman, J. L. Sussman, D. S. Tawfik, S. J. Fleishman, Automated structure- and sequence-based design of proteins for high bacterial expression and stability. *Mol. Cell* **63**, 337–346 (2016).
45. V. Frappier, A. E. Keating, Data-driven computational protein design. *Curr. Opin. Struct. Biol.* **69**, 63–69 (2021).
46. D. S. Marks, L. J. Colwell, R. Sheridan, T. A. Hopf, A. Pagnani, R. Zecchina, C. Sander, Protein 3D structure computed from evolutionary sequence variation. *PLOS ONE* **6**, e28766 (2011).
47. T. A. Hopf, J. B. Ingraham, F. J. Poelwijk, C. P. I. Schärfe, M. Springer, C. Sander, D. S. Marks, Mutation effects predicted from sequence co-variation. *Nat. Biotechnol.* **35**, 128–135 (2017).
48. A. J. Riesselman, J. B. Ingraham, D. S. Marks, Deep generative models of genetic variation capture the effects of mutations. *Nat. Methods* **15**, 816–822 (2018).
49. H. Park, P. Bradley, P. Greisen Jr., Y. Liu, V. K. Mulligan, D. E. Kim, D. Baker, F. DiMaio, Simultaneous optimization of biomolecular energy functions on features from small molecules and macromolecules. *J. Chem. Theory Comput.* **12**, 6201–6212 (2016).
50. R. F. Alford, A. Leaver-Fay, J. R. Jeliazkov, M. J. O'Meara, F. P. DiMaio, H. Park, M. V. Shapovalov, P. D. Renfrew, V. K. Mulligan, K. Kappel, J. W. Labonte, M. S. Pacella, R. Bonneau, P. Bradley, R. L. Dunbrack Jr., R. das, D. Baker, B. Kuhlman, T. Kortemme, J. J. Gray, The rosetta all-atom energy function for macromolecular modeling and design. *J. Chem. Theory Comput.* **13**, 3031–3048 (2017).
51. C. L. Hsieh, A. P. Werner, S. R. Leist, L. J. Stevens, E. Falconer, J. A. Goldsmith, C. W. Chou, O. M. Abiona, A. West, K. Westendorf, K. Muthuraman, E. J. Fritch, K. H. Dinnon III, A. Schäfer, M. R. Denison, J. D. Chappell, R. S. Baric, B. S. Graham, K. S. Corbett, J. S. McLellan, Stabilized coronavirus spike stem elicits a broadly protective antibody. *Cell Rep.* **37**, 109929 (2021).
52. G. Lapidoth, O. Khersonsky, R. Lipsh, O. Dym, S. Albeck, S. Rogotner, S. J. Fleishman, Highly active enzymes by automated combinatorial backbone assembly and sequence design. *Nat. Commun.* **9**, 2780 (2018).
53. S. K. Malladi, D. Schreiber, I. Pramanick, M. A. Sridevi, A. Goldenzweig, S. Dutta, S. J. Fleishman, R. Varadarajan, One-step sequence and structure-guided optimization of HIV-1 envelope gp140. *Curr. Res. Struct. Biol.* **2**, 45–55 (2020).
54. S. F. Altschul, T. L. Madden, A. A. Schäffer, J. Zhang, Z. Zhang, W. Miller, D. J. Lipman, Gapped BLAST and PSI-BLAST: A new generation of protein database search programs. *Nucleic Acids Res.* **25**, 3389–3402 (1997).
55. F. DiMaio, A. Leaver-Fay, P. Bradley, D. Baker, I. Andre, Modeling symmetric macromolecular structures in Rosetta3. *PLOS ONE* **6**, e20450 (2011).
56. B. Korber, W. M. Fischer, S. Gnanakaran, H. Yoon, J. Theiler, W. Abfalterer, B. Foley, E. E. Giorgi, T. Bhattacharya, M. D. Parker, D. G. Partridge, C. M. Evans, TI de Silva, on behalf of the Sheffield COVID-19 Genomics Group, CC La Branche, D. C. Montefiori, Spike mutation pipeline reveals the emergence of a more transmissible form of SARS-CoV-2. *bioRxiv* 2020.04.29.069054 (2020). https://doi.org/10.1101/2020.04.29.069054
57. A. Brufsky, Distinct viral clades of SARS-CoV-2: Implications for modeling of viral spread. *J. Med. Virol.* **92**, 1386–1390 (2020).
58. T. N. Starr, A. J. Greaney, S. K. Hilton, D. Ellis, K. H. D. Crawford, A. S. Dingens, M. J. Navarro, J. E. Bowen, M. A. Tortorici, A. C. Walls, N. P. King, D. Veesler, J. D. Bloom, Deep mutational scanning of SARS-CoV-2 receptor binding domain reveals constraints on folding and ACE2 binding. *Cell* **182**, 1295–1310.e20 (2020).
59. G. Cerutti, Y. Guo, P. Wang, M. S. Nair, M. Wang, Y. Huang, J. Yu, L. Liu, P. S. Katsamba, F. Bahna, E. R. Reddem, P. D. Kwong, D. D. Ho, Z. Sheng, L. Shapiro, Neutralizing antibody 5-7 defines a distinct site of vulnerability in SARS-CoV-2 spike N-terminal domain. *Cell Rep.* **37**, 109928 (2021).
60. G. Cerutti, Y. Guo, T. Zhou, J. Gorman, M. Lee, M. Rapp, E. R. Reddem, J. Yu, F. Bahna, J. Bimela, Y. Huang, P. S. Katsamba, L. Liu, M. S. Nair, R. Rawi, A. S. Olia, P. Wang, B. Zhang, G. Y. Chuang, D. D. Ho, Z. Sheng, P. D. Kwong, L. Shapiro, Potent SARS-CoV-2 neutralizing antibodies directed against spike N-terminal domain target a single supersite. *Cell Host Microbe* **29**, 819–833.e7 (2021).
61. P. Nguyen-Contant, A. K. Embong, P. Kanagaiah, F. A. Chaves, H. Yang, A. R. Branche, D. J. Topham, M. Y. Sangster, S protein-reactive IgG and memory B cell production after human SARS-CoV-2 infection includes broad reactivity to the S2 subunit. *MBio* **11**, e01991-20 (2020).
62. R. J. Edwards, K. Mansouri, V. Stalls, K. Manne, B. Watts, R. Parks, K. Janowska, S. M. C. Gobeil, M. Kopp, D. Li, X. Lu, Z. Mu, M. Deyton, T. H. Oguin III, J. Sprenz, W. Williams, K. O. Saunders, D. Montefiori, G. D. Sempowski, R. Henderson, S. Munir Alam, B. F. Haynes, P. Acharya, Cold sensitivity of the SARS-CoV-2 spike ectodomain. *Nat. Struct. Mol. Biol.* **28**, 128–131 (2021).
63. G. Maruggi, C. P. Mallett, J. W. Westerbeck, T. Chen, G. Lofano, K. Friedrich, L. Qu, J. T. Sun, J. McAuliffe, A. Kanitkar, K. T. Arrildt, K. F. Wang, I. McBee, D. McCoy, R. Terry, A. Rowles, M. A. Abrahim, M. A. Ringenberg, M. J. Gains, C. Spickler, X. Xie, J. Zou, P. Y. Shi, T. Dutt, M. Henao-Tamayo, I. Ragan, R. A. Bowen, R. Johnson, S. Nuti, K. Luisi, J. B. Ulmer, A. M. Steff, R. Jalah, S. Bertholet, A. H. Stokes, D. Yu, A self-amplifying mRNA SARS-CoV-2 vaccine candidate induces safe and robust protective immunity in preclinical models. *Mol. Ther.* **30**, 1897–1912 (2022).
64. D. Pinto, Y. J. Park, M. Beltramello, A. C. Walls, M. A. Tortorici, S. Bianchi, S. Jaconi, K. Culap, F. Zatta, A. de Marco, A. Peter, B. Guarino, R. Spreafico, E. Cameroni, J. B. Case, R. E. Chen, C. Havenar-Daughton, G. Snell, A. Telenti, H. W. Virgin, A. Lanzavecchia, M. S. Diamond, K. Fink, D. Veesler, D. Corti, Cross-neutralization of SARS-CoV-2 by a human monoclonal SARS-CoV antibody. *Nature* **583**, 290–295 (2020).
65. T. Sztain, S. H. Ahn, A. T. Bogetti, L. Casalino, J. A. Goldsmith, E. Seitz, R. S. McCool, F. L. Kearns, F. Acosta-Reyes, S. Maji, G. Mashayekhi, J. A. McCammon, A. Ourmazd, J. Frank,

J. S. McLellan, L. T. Chong, R. E. Amaro, A glycan gate controls opening of the SARS-CoV-2 spike protein. *Nat. Chem.* **13**, 963–968 (2021).
66. L. Yurkovetskiy, X. Wang, K. E. Pascal, C. Tomkins-Tinch, T. P. Nyalile, Y. Wang, A. Baum, W. E. Diehl, A. Dauphin, C. Carbone, K. Veinotte, S. B. Egri, S. F. Schaffner, J. E. Lemieux, J. B. Munro, A. Rafique, A. Barve, P. C. Sabeti, C. A. Kyratsous, N. V. Dudkina, K. Shen, J. Luban, Structural and functional analysis of the D614G SARS-CoV-2 spike protein variant. *Cell* **183**, 739–751.e738, 751.e8 (2020).
67. J. Juraszek, L. Rutten, S. Blokland, P. Bouchier, R. Voorzaat, T. Ritschel, M. J. G. Bakkers, L. L. R. Renault, J. P. M. Langedijk, Stabilizing the closed SARS-CoV-2 spike trimer. *Nat. Commun.* **12**, 244 (2021).
68. C. Huang, Y. Wang, X. Li, L. Ren, J. Zhao, Y. Hu, L. Zhang, G. Fan, J. Xu, X. Gu, Z. Cheng, T. Yu, J. Xia, Y. Wei, W. Wu, X. Xie, W. Yin, H. Li, M. Liu, Y. Xiao, H. Gao, L. Guo, J. Xie, G. Wang, R. Jiang, Z. Gao, Q. Jin, J. Wang, B. Cao, Clinical features of patients infected with 2019 novel coronavirus in Wuhan, China. *Lancet* **395**, 497–506 (2020).
69. P. O. Byrne, J. S. McLellan, Principles and practical applications of structure-based vaccine design. *Curr. Opin. Immunol.* **77**, 102209 (2022).
70. J. M. Schaub, C. W. Chou, H. C. Kuo, K. Javanmardi, C. L. Hsieh, J. Goldsmith, A. M. DiVenere, K. C. le, D. Wrapp, P. O. Byrne, C. K. Hjorth, N. V. Johnson, J. Ludes-Meyers, A. W. Nguyen, N. Wang, J. J. Lavinder, G. C. Ippolito, J. A. Maynard, J. S. McLellan, I. J. Finkelstein, Expression and characterization of SARS-CoV-2 spike proteins. *Nat. Protoc.* **16**, 5339–5356 (2021).
71. S. Chalkias, C. Harper, K. Vrbicky, S. R. Walsh, B. Essink, A. Brosz, N. McGhee, J. E. Tomassini, X. Chen, Y. Chang, A. Sutherland, D. C. Montefiori, B. Girard, D. K. Edwards, J. Feng, H. Zhou, L. R. Baden, J. M. Miller, R. das, A bivalent omicron-containing booster vaccine against COVID-19. *N. Engl. J. Med.* **387**, 1279–1291 (2022).
72. C. Kurhade, J. Zou, H. Xia, M. Liu, H. C. Chang, P. Ren, X. Xie, P.-. Y. Shi, Low neutralization of SARS-CoV-2 Omicron BA.2.75.2, BQ.1.1 and XBB.1 by parental mRNA vaccine or a BA.5 bivalent booster. *Nat. Med.* **29**, 344–347 (2023).
73. B. Ju, Q. Zhang, J. Ge, R. Wang, J. Sun, X. Ge, J. Yu, S. Shan, B. Zhou, S. Song, X. Tang, J. Yu, J. Lan, J. Yuan, H. Wang, J. Zhao, S. Zhang, Y. Wang, X. Shi, L. Liu, J. Zhao, X. Wang, Z. Zhang, L. Zhang, Human neutralizing antibodies elicited by SARS-CoV-2 infection. *Nature* **584**, 115–119 (2020).
74. M. A. Tortorici, M. Beltramello, F. A. Lempp, D. Pinto, H. V. Dang, L. E. Rosen, M. McCallum, J. Bowen, A. Minola, S. Jaconi, F. Zatta, A. de Marco, B. Guarino, S. Bianchi, E. J. Lauron, H. Tucker, J. Zhou, A. Peter, C. Havenar-Daughton, J. A. Wojcechowskyj, J. B. Case, R. E. Chen, H. Kaiser, M. Montiel-Ruiz, M. Meury, N. Czudnochowski, R. Spreafico, J. Dillen, C. Ng, N. Sprugasci, K. Culap, F. Benigni, R. Abdelnabi, S. Y. C. Foo, M. A. Schmid, E. Cameroni, A. Riva, A. Gabrieli, M. Galli, M. S. Pizzuto, J. Neyts, M. S. Diamond, H. W. Virgin, G. Snell, D. Corti, K. Fink, D. Veesler, Ultrapotent human antibodies protect against SARS-CoV-2 challenge via multiple mechanisms. *Science* **370**, 950–957 (2020).
75. J. R. Byrnes, X. X. Zhou, I. Lui, S. K. Elledge, J. E. Glasgow, S. A. Lim, R. P. Loudermilk, C. Y. Chiu, T. T. Wang, M. R. Wilson, K. K. Leung, J. A. Wells, Competitive SARS-CoV-2 serology reveals most antibodies targeting the spike receptor-binding domain compete for ACE2 binding. *mSphere* **5**, e00802-20 (2020).
76. S. Tanaka, C. A. Olson, C. O. Barnes, W. Higashide, M. Gonzalez, J. Taft, A. Richardson, M. Martin-Fernandez, D. Bogunovic, P. N. P. Gnanapragasam, P. J. Bjorkman, P. Spilman, K. Niazi, S. Rabizadeh, P. Soon-Shiong, Rapid identification of neutralizing antibodies against SARS-CoV-2 variants by mRNA display. *Cell Rep.* **38**, 110348 (2022).
77. S. Xu, Y. Wang, Y. Wang, C. Zhang, Q. Hong, C. Gu, R. Xu, T. Wang, Y. Yang, J. Zang, Y. Zhou, Z. Li, Q. Liu, B. Zhou, L. Bai, Y. Zhu, Q. Deng, H. Wang, D. Lavillette, G. Wong, Y. Xie, Y. Cong, Z. Huang, Mapping cross-variant neutralizing sites on the SARS-CoV-2 spike protein. *Emerg. Microbes Infect.* **11**, 351–367 (2022).
78. Z. Wang, F. Muecksch, A. Cho, C. Gaebler, H.-H. Hoffmann, V. Ramos, S. Zong, M. Cipolla, B. Johnson, F. Schmidt, J. D. Silva, E. Bednarski, T. B. Tanfous, R. Raspe, K. Yao, Y. E. Lee, T. Chen, M. Turroja, K. G. Milard, J. Dizon, A. Kaczynska, A. Gazumyan, T. Y. Oliveira, C. M. Rice, M. Caskey, P. D. Bieniasz, T. Hatziioannou, C. O. Barnes, M. C. Nussenzweig, Conserved neutralizing epitopes on the N-terminal domain of variant SARS-CoV-2 spike proteins. *bioRxiv* 2022.02.01.478695 (2022). https://doi.org/10.1101/2022.02.01.478695
79. J. Seow, H. Khan, A. Rosa, V. Calvaresi, C. Graham, S. Pickering, V. E. Pye, N. B. Cronin, I. Huettner, M. H. Malim, A. Politis, P. Cherepanov, K. J. Doores, A neutralizing epitope on the SD1 domain of SARS-CoV-2 spike targeted following infection and vaccination. *Cell Rep.* **40**, 111276 (2022).
80. M. Bianchi, H. L. Turner, B. Nogal, C. A. Cottrell, D. Oyen, M. Pauthner, R. Bastidas, R. Nedellec, L. E. McCoy, I. A. Wilson, D. R. Burton, A. B. Ward, L. Hangartner, Electron-microscopy-based epitope mapping defines specificities of polyclonal antibodies elicited during HIV-1 BG505 envelope trimer immunization. *Immunity* **49**, 288–300.e8 (2018).
81. B. Nogal, M. Bianchi, C. A. Cottrell, R. N. Kirchdoerfer, L. M. Sewall, H. L. Turner, F. Zhao, D. Sok, D. R. Burton, L. Hangartner, A. B. Ward, Mapping polyclonal antibody responses in non-human primates vaccinated with HIV env trimer subunit vaccines. *Cell Rep.* **30**, 3755–3765.e7 (2020).
82. A. Antanasijevic, L. M. Sewall, C. A. Cottrell, D. G. Carnathan, L. E. Jimenez, J. T. Ngo, J. B. Silverman, B. Groschel, E. Georgeson, J. Bhiman, R. Bastidas, C. LaBranche, J. D. Allen, J. Copps, H. R. Perrett, K. Rantalainen, F. Cannac, Y. R. Yang, A. T. de la Peña, R. F. Rocha, Z. T. Berndsen, D. Baker, N. P. King, R. W. Sanders, J. P. Moore, S. Crotty, M. Crispin, D. C. Montefiori, D. R. Burton, W. R. Schief, G. Silvestri, A. B. Ward, Polyclonal antibody responses to HIV Env immunogens resolved using cryoEM. *Nat. Commun.* **12**, 4817 (2021).
83. J. Han, A. J. Schmitz, S. T. Richey, Y. N. Dai, H. L. Turner, B. M. Mohammed, D. H. Fremont, A. H. Ellebedy, A. B. Ward, Polyclonal epitope mapping reveals temporal dynamics and diversity of human antibody responses to H5N1 vaccination. *Cell Rep.* **34**, 108682 (2021).
84. S. Bangaru, A. Antanasijevic, N. Kose, L. M. Sewall, A. M. Jackson, N. Suryadevara, X. Zhan, J. L. Torres, J. Copps, A. T. de la Peña, J. E. Crowe Jr., A. B. Ward, Structural mapping of antibody landscapes to human betacoronavirus spike proteins. *Sci. Adv.* **8**, eabn2911 (2022).
85. P. Moss, The T cell immune response against SARS-CoV-2. *Nat. Immunol.* **23**, 186–193 (2022).
86. M. Lu, M. Chamblee, Y. Zhang, C. Ye, P. Dravid, J. G. Park, K. C. Mahesh, S. Trivedi, S. Murthy, H. Sharma, C. Cassady, S. Chaiwatpongsakorn, X. Liang, J. S. Yount, P. N. Boyaka, M. E. Peeples, L. Martinez-Sobrido, A. Kapoor, J. Li, SARS-CoV-2 prefusion spike protein stabilized by six rather than two prolines is more potent for inducing antibodies that neutralize viral variants of concern. *Proc. Natl. Acad. Sci. U.S.A.* **119**, e2110105119 (2022).
87. C. He, J. Yang, W. Hong, Z. Chen, D. Peng, H. Lei, A. Alu, X. He, Z. Bi, X. Jiang, G. Jia, Y. Yang, Y. Zhou, W. Yu, C. Tang, Q. Huang, M. Yang, B. Li, J. Li, J. Wang, H. Que, L. Chen, W. Ren, D. Wan, J. Li, W. Wang, G. Shen, Z. Zhao, L. Yang, J. Yang, Z. Wang, Z. Su, Y. Wei, X. Cen, Y. Tanaka, X. Song, S. Lu, X. Peng, G. Lu, X. Wei, A self-assembled trimeric protein vaccine induces protective immunity against Omicron variant. *Nat. Commun.* **13**, 5459 (2022).
88. Y. Song, F. DiMaio, R. Y. R. Wang, D. Kim, C. Miles, T. J. Brunette, J. Thompson, D. Baker, High-resolution comparative modeling with RosettaCM. *Structure* **21**, 1735–1742 (2013).
89. T. A. Whitehead, A. Chevalier, Y. Song, C. Dreyfus, S. J. Fleishman, C. de Mattos, C. A. Myers, H. Kamisetty, P. Blair, I. A. Wilson, D. Baker, Optimization of affinity, specificity and function of designed influenza inhibitors using deep sequencing. *Nat. Biotechnol.* **30**, 543–548 (2012).
90. S. J. Fleishman, A. Leaver-Fay, J. E. Corn, E. M. Strauch, S. D. Khare, N. Koga, J. Ashworth, P. Murphy, F. Richter, G. Lemmon, J. Meiler, D. Baker, RosettaScripts: A scripting language interface to the Rosetta macromolecular modeling suite. *PLOS ONE* **6**, e20161 (2011).
91. N. Garcon, D. W. Vaughn, A. M. Didierlaurent, Development and evaluation of AS03, an Adjuvant System containing α-tocopherol and squalene in an oil-in-water emulsion. *Expert Rev. Vaccines* **11**, 349–366 (2012).
92. S. H. Scheres, RELION: Implementation of a Bayesian approach to cryo-EM structure determination. *J. Struct. Biol.* **180**, 519–530 (2012).
93. S. Q. Zheng, E. Palovcak, J. P. Armache, K. A. Verba, Y. Cheng, D. A. Agard, MotionCor2: Anisotropic correction of beam-induced motion for improved cryo-electron microscopy. *Nat. Methods* **14**, 331–332 (2017).
94. A. Rohou, N. Grigorieff, CTFFIND4: Fast and accurate defocus estimation from electron micrographs. *J. Struct. Biol.* **192**, 216–221 (2015).
95. D. Liebschner, P. V. Afonine, M. L. Baker, G. Bunkóczi, V. B. Chen, T. I. Croll, B. Hintze, L. W. Hung, S. Jain, A. J. McCoy, N. W. Moriarty, R. D. Oeffner, B. K. Poon, M. G. Prisant, R. J. Read, J. S. Richardson, D. C. Richardson, M. D. Sammito, O. V. Sobolev, D. H. Stockwell, T. C. Terwilliger, A. G. Urzhumtsev, L. L. Videau, C. J. Williams, P. D. Adams, Macromolecular structure determination using X-rays, neutrons and electrons: Recent developments in Phenix. *Acta Crystallogr. D Struct. Biol.* **75**, 861–877 (2019).
96. P. Emsley, B. Lohkamp, W. G. Scott, K. Cowtan, Features and development of Coot. *Acta Crystallogr. D Biol. Crystallogr.* **66**, 486–501 (2010).
97. E. F. Pettersen, T. D. Goddard, C. C. Huang, E. C. Meng, G. S. Couch, T. I. Croll, J. H. Morris, T. E. Ferrin, UCSF ChimeraX: Structure visualization for researchers, educators, and developers. *Protein Sci.* **30**, 70–82 (2021).
98. P. Conway, M. D. Tyka, F. DiMaio, D. E. Konerding, D. Baker, Relaxation of backbone bond geometry improves protein energy landscape modeling. *Protein Sci.* **23**, 47–55 (2014).
99. B. Frenz, S. Rämisch, A. J. Borst, A. C. Walls, J. Adolf-Bryfogle, W. R. Schief, D. Veesler, F. DiMaio, Automatically fixing errors in glycoprotein structures with Rosetta. *Structure* **27**, 134–139.e3 (2019).
100. J. Adolf-Bryfogle *et al.*, Growing Glycans in Rosetta: Accurate de novo glycan modeling, density fitting, and rational sequon design. *bioRxiv* 2021.09.27.462000 (2021). https://doi.org/10.1101/2021.09.27.462000

Acknowledgments: We would like to thank K. Matsuoka and L. Feng for expression, harvesting, and buffer exchange of culture supernatants; N. Mehzabeen and C. Harelson for the purification of Spike antigens; K. Karl for cloning support; and L. Leloup for assistance with statistical analysis of the antibody data. VRC-118 and VRC-112 antibodies used in this study were provided by B. S. Graham, J. Mascola, L. Wang, W. Kong, O. Abiona, and K. Corbett (NIAID) (US patent

application no. 63/101,646). P. Cadot coordinated the manuscript development. **Funding:** This study was sponsored by GlaxoSmithKline Biologicals SA. The funder provided support in the form of salaries for all authors and provided support in the form of research material. GlaxoSmithKline Biologicals SA was involved in the study design, data collection, and analysis, decision to publish, and preparation of the manuscript. **Author contributions:** W.D.H., N.W., M.B., E.M., M.J.B., J.A.W., A.-M.S., C.P.M., G.M., Y.H., C.C., and L.L. were involved in the conception and design of the study and/or the development of the study protocol. J.A.W., S.T., L.L., A.B., L.C., and C.P.M. participated to the acquisition of data. W.D.H., N.W., M.B., J.A.W., S.T., L.L., C.C., C.P.M., G.M., and S.V. analyzed and interpreted the results. All authors were involved in drafting the manuscript or revising it critically for important intellectual content. All authors had full access to the data and approved the manuscript before it was submitted by the corresponding author. **Competing interests:** All authors are/were employees of the GSK group of companies at the time of the study and may own GSK shares and/or restricted GSK shares. M.B., E.M., and N.W. are inventors on international patent application no. PCT/IB2021/054903 ("Modified Betacoronavirus Spike Proteins") filed on 04 June 2021 by GlaxoSmithKline Biologicals SA. The other authors declare that they have no competing interests. **Data and materials availability:** All data needed to evaluate the conclusions in the paper are present in the paper and/or the Supplementary Materials. Cryo-EM maps of S2D14 in the two-RBD open, RBD exposed, and RBD closed conformations have been deposited in the Electron Microscopy Data Bank as EMD-28532, EMD-28533, and EMDB-28531, respectively. The atomic coordinates for the cryo-EM structures of S2D14 in the two-RBD open, two-RBD exposed, and RBD closed conformations have been deposited to the RCSB Protein Data Bank (PDB accession numbers: 8EPP, 8EPQ, and 8EPN, respectively).

Submitted 29 November 2022
Accepted 2 May 2023
Published 7 June 2023
10.1126/sciadv.adg0330

BIOCHEMISTRY

Discovering a uniform functional trade-off of the CBC-type 2,3-oxidosqualene cyclases and deciphering its chemical logic

Fan Zhang[1,2]†, Yunpeng Wang[2]†, Jingyang Yue[2], Rongrong Zhang[2], Yong-er Hu[2], Ruoshi Huang[2], Ai-jia Ji[2], B. Andes Hess Jr.[3], Zhongqiu Liu[2]*, Lixin Duan[2]*, Ruibo Wu[1]*

Many functionally promiscuous plant 2,3-oxidosqualene cyclases (OSCs) have been found, but complete functional reshaping is rarely reported. In this study, we have identified two new plant OSCs: a unique protostadienol synthase (*Ao*PDS) and a common cycloartenol synthase (*Ao*CAS) from *Alisma orientale* (Sam.) Juzep. Multiscale simulations and mutagenesis experiments revealed that threonine-727 is an essential residue responsible for protosta-13 (17),24-dienol biosynthesis in *Ao*PDS and that the F726T mutant completely reshapes the native function of *Ao*CAS into a PDS function to yield almost exclusively protosta-13 (17),24-dienol. Unexpectedly, various native functions were uniformly reshaped into a PDS function by introducing the phenylalanine → threonine substitution at this conserved position in other plant and non-plant chair-boat-chair–type OSCs. Further computational modeling elaborated the trade-off mechanisms of the phenylalanine → threonine substitution that leads to the PDS activity. This study demonstrates a general strategy for functional reshaping by using a plastic residue based on the decipherment of the catalytic mechanism.

INTRODUCTION

Triterpenoids are one of the largest groups of natural products with numerous pharmaceutical applications (*1*–*3*). 2,3-Oxidosqualene cyclases (OSCs; also known as triterpene synthases) are a unique enzyme family with more than 250 known isoforms that can catalyze the common, acyclic substrate to form multiple triterpenes products. They serve as key enzymes that are responsible for the cyclic skeleton diversity of triterpenoids. According to an earlier report, approximately 200 distinct carbon skeletons had been found (*4*), and to date, the number has increased to more than 300 in view of the most recent terpenoid database (*5*). Among them, several types of triterpenoids such as cycloartenol and lanosterol are produced along with a total of more than a thousand other structures (see Fig. 1). The protostadienol-type tetracyclic triterpenes are rarely found in nature and their distribution is primarily limited to the genus *Alisma* of the Alismataceae family (*6*), and the enzyme responsible for its biosynthesis has been rarely reported. The only previously reported enzyme is a promiscuous OSC from fungus *Aspergillus fumigatus* (*Af*PDS) that yields protosta-17 (20),24-dienol (*7*, *8*) as the major product, going through a chair-boat-chair (CBC) conformation of the first three fused rings of the tetracyclic protosteryl cation (Fig. 1) (*9*). It is well known that the CBC conformation triterpenes including cycloartenol, lanosterol, cucurbitadienol, parkeol, and others are mostly produced by undergoing a cascade of rearrangements from the protosteryl cation.

In this work, a unique plant source protostadienol-type tetracyclic triterpene cyclase (*Ao*PDS) with a common cycloartenol synthase (*Ao*CAS) was first characterized from *Alisma orientale* (Sam.) Juzep in a yeast heterologous expression system. Computational simulations of the enzymatic mechanism and experimental mutagenesis found a plastic substitution F726T of *Ao*CAS that could reshape its native function to yield the protostadienol product. Further experiments found that the uniform trade-off from native activity to protostadienol synthase (PDS) activity occurs widely in several other CBC-type OSCs (catalyzing the formation of CBC conformation products) by a single F → T substitution at the same position. Last, the mechanism insights of functional trade-off were revealed by combined quantum and molecular mechanics (QM/MM) calculation.

RESULTS AND DISCUSSION

Characterization of *Ao*CAS and *Ao*PDS from *A. orientale* (Sam.) Juzep

A. orientale (Alismataceae) is a traditional and widely used Chinese medicinal herb native to several Asian countries, including China, Korea, and Japan. Protostane tetracyclic triterpenoids are thought to be chemotaxonomic markers of the genus (*6*). Two candidate unigenes *Ao*OSC1 and *Ao*OSC2 were screened from the publicly available transcriptome sequence data of *A. orientale* (National Center for Biotechnology Information, accession no. PRJNA417185). These two unigenes were cloned into the express vector pESC-Ura and transformed into a high-yield squalene yeast engineering strain SE-MET (see full experimental procedures in the Supplementary Materials). *Ao*OSC2 (*Ao*CAS) exclusively produces cycloartenol, whereas *Ao*OSC1 (*Ao*PDS) only produces protosta-13 (17),24-dienol (Fig. 2 and figs. S1 to S3), the precursor of alisol compounds [such as alisol B 23-acetate (*10*, *11*) with hypolipidemic and

[1]School of Pharmaceutical Sciences, Guangdong Provincial Key Laboratory of New Drug Design and Evaluation, Sun Yat-sen University, Guangzhou 510006, P. R. China. [2]Guangdong Provincial Key Laboratory of Translational Cancer Research of Chinese Medicines, Joint International Research Laboratory of Translational Cancer Research of Chinese Medicines, International Institute for Translational Chinese Medicine, School of Pharmaceutical Sciences, Guangzhou University of Chinese Medicine, Guangzhou 510006, P. R. China. [3]Department of Chemistry, Vanderbilt University, Nashville, TN 37235, USA.
*Corresponding author. Email: liuzq@gzucm.edu.cn (Z.L.); nlizn@gzucm.edu.cn (L. D.); wurb3@mail.sysu.edu.cn (R.W.)
†These authors contributed equally to this work

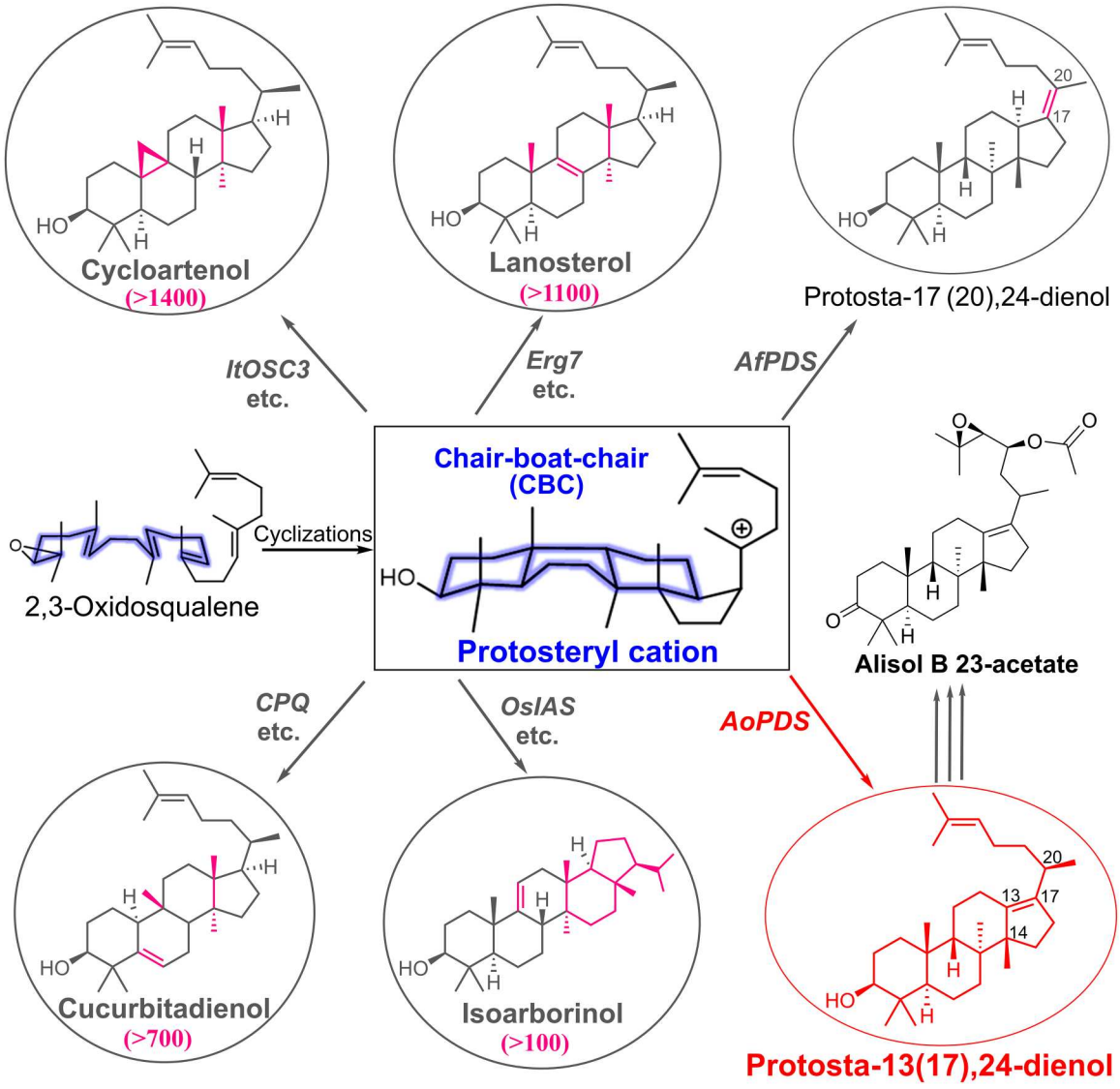

Fig. 1. The typical triterpenoids derived from CBC conformation protosteryl cation. The carbon-skeleton differences are highlighted by magenta, and the number of natural products with each carbon skeleton is given in parentheses. The only difference between the two rarely reported protostadienol compounds is the C=C double bond at C17.

anticancer activity]. *Ao*OSC1 was the first characterized plant source PDS with a typical double bond at 13 (17), while *Af*PDS from fungal protosta-17 (20),24-dienol was the only known PDS.

Identification of T727/F726 responsible for *Ao*PDS and *Ao*CAS product specificities

To decipher the different catalytic functions of *Ao*PDS and *Ao*CAS that share high sequence identity (>79%), we first performed QM/MM multiscale simulations to probe the catalytic mechanism from the common protosteryl cation. The plausible reaction pathways are proposed in Fig. 3A, starting from the protosteryl cation, followed by consecutive rearrangements including hydride shifts and methyl transfers, and finally deprotonation that leads to cycloartenol in *Ao*CAS, while early deprotonation from either A or B state produces protosta-13 (17),24-dienol in *Ao*PDS. The free energy profiles from protosteryl cation to the D state in *Ao*CAS and protosta-13 (17),24-dienol in *Ao*PDS were determined by QM/MM molecular dynamics (MD) simulations. The reaction energetic profiles are summarized in Fig. 3B, and corresponding structures for reaction intermediates are shown in Fig. 4.

For the catalytic reaction in *Ao*CAS, the 1,2-hydride shift in the protosteryl cation leads to the A state with a low barrier of 3.7 kcal/mol (Fig. 3B). The A state is unstable and is further converted to the B state through a different hydride shift with very low barrier (~1 kcal/mol). The next two steps involve 1,2-methyl transfers from the B state to D state (fig. S4) that also cross very low barriers (<3 kcal/mol). During the reactions, the aromatic side chain of F726 faces the D ring of the tetracyclic intermediate to stabilize the carbocation through cation-π interactions (Fig. 4). Accordingly, *Ao*CAS is a high-fidelity OSC responsible for the exclusive production of cycloartenol, as validated by our further experiments (see Fig. 2).

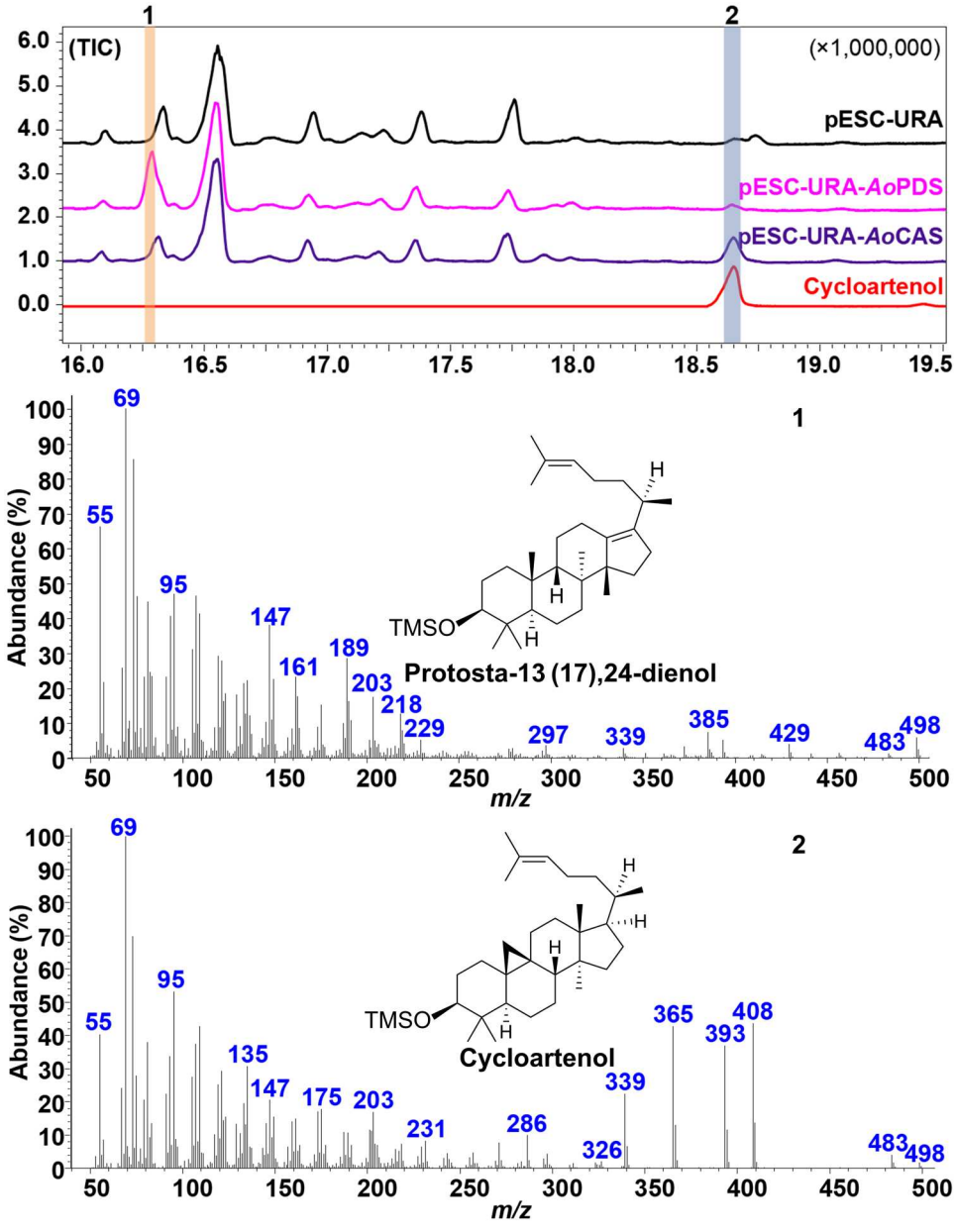

Fig. 2. Characterization of *Ao*CAS and *Ao*PDS. *Ao*CAS and *Ao*PDS were characterized as CAS and protosta-13 (17),24-dienol synthase, respectively. The mass spectra of the standard cycloartenol are shown in fig. S16. *m/z*, mass/charge ratio.

As for *Ao*PDS, the 1,2-hydride shift energy barriers (7.7 and 3.8 kcal/mol) are much higher than those in *Ao*CAS, and as a result, the premature deprotonation from A or B state occurs with T727 acting as a general base in *Ao*PDS, as shown in Fig. 4. The T727 in *Ao*PDS is located at the same position as the aromatic F726 in *Ao*CAS. We found a water hydrogen bond chain near the T727 and stably maintained during the MD simulations (Fig. 4). This may be due to the replacement of the hydrophobic residue F to the polar residue T. Although the hydroxyl group of T is not often regarded as a strong general base, the pK_a (where K_a is the acid dissociation constant) of a protonated alcohol is typically around −1 to −4 (*10*), and the formation of water chain will further increase the alkalinity of T727 and facilitate the proton transfer from intermediates (C13H of A state and C17H of B state; see Fig. 3A) to T727; thus, it is reasonable to regard T as the general base [T as a general base has also been discussed in previous studies (*11*, *12*)]. The deprotonation from C17H of B state with 6.1 kcal/mol barrier (Fig. 3B) is preferable to the C13H of A state because of its barrier (13.8 kcal/mol) (fig. S5). Therefore, the most plausible transformation from protosteryl cation to protosta-13 (17),24-dienol in *Ao*PDS is a premature deprotonation at intermediate B by T727. Accordingly, protosta-13 (17),24-dienol is the only product of *Ao*PDS detected in our experiments. Although several different amino acid residues do exist in the active pockets of these two enzymes, the above computational modeling verified that the F (or T) in the corresponding position

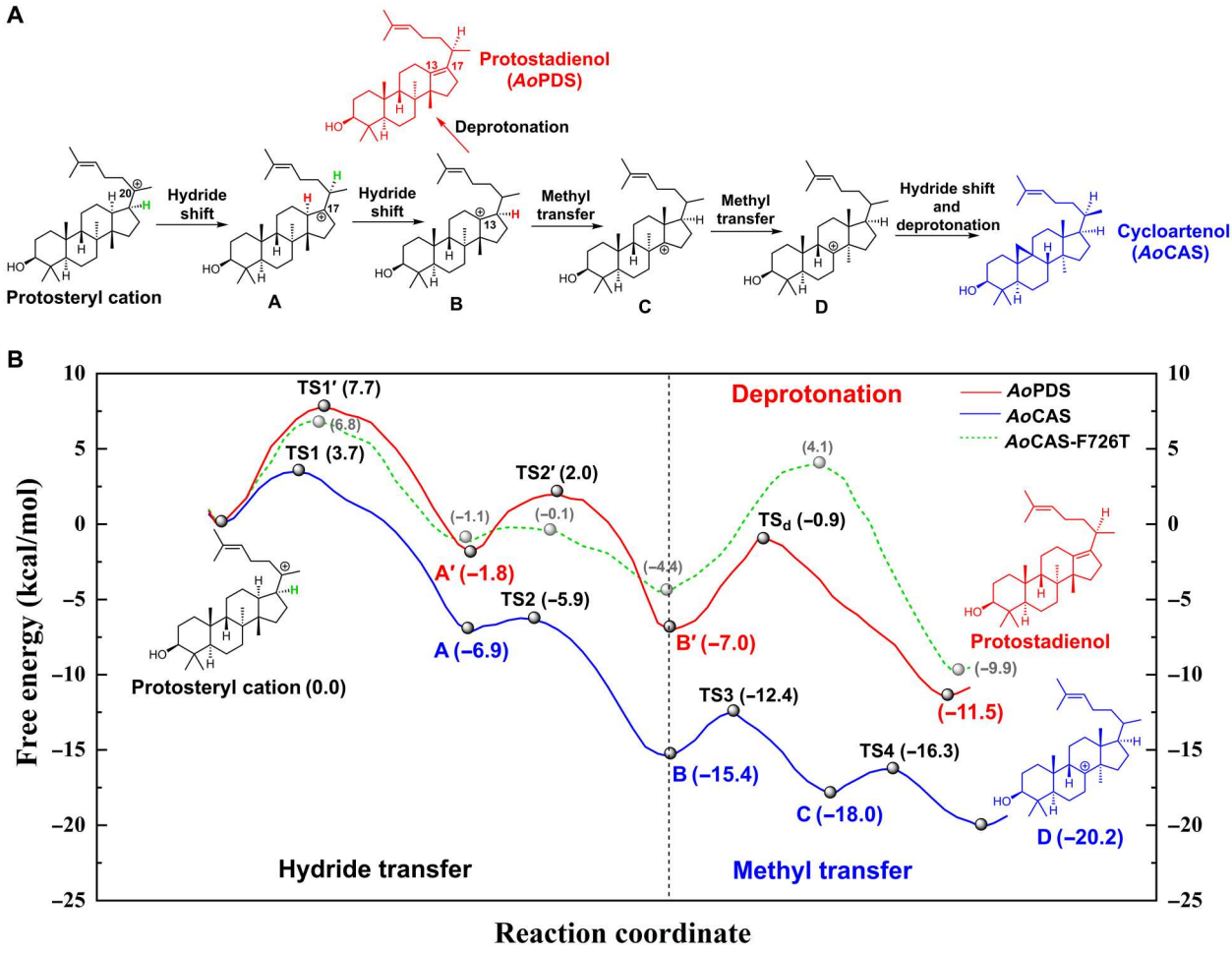

Fig. 3. QM/MM multiscale simulations of catalytic processes. (**A**) The plausible reaction pathways of *Ao*PDS and *Ao*CAS from the protosteryl cation. (**B**) Free energy profiles of *Ao*PDS (red), *Ao*CAS (blue), and *Ao*CAS-F726T (dashed green).

of 726 (or 727) is probably the main difference in the enzymatic reactions catalyzed by *Ao*CAS and *Ao*PDS.

The strong trade-off effect of *Ao*CAS-F726T from native activity to produce protosta-13 (17),24-dienol

To confirm the key catalytic roles of T727/F726 in *Ao*PDS/*Ao*CAS, site-directed mutagenesis experiments were carried out and the product profiles are summarized (Fig. 5 and figs. S6 and S7). Notably, F726T of *Ao*CAS reshapes its native function into the PDS function almost completely [99.7% protosta-13 (17),24-dienol]. Other F726 substitutions to residues with hydroxy group side chain such as T (including F726Y and F726S) will become inactive and not produce protosta-13 (17),24-dienol, while most of the *Ao*PDS mutants, especially substitutions of the T727 position, exhibited very low activity or even inactive, thus proving the essential deprotonation role of T727 in *Ao*PDS. The activity could be maintained to some extent in the *Ao*PDS-T727S mutant, which is likely because of S being somewhat similar to T with comparable side chain lengths and hydroxy groups, thus further confirming the aforementioned catalytic mechanism (Figs. 3 and 4) that T727 is the key residue for production of protosta-13 (17),24-dienol in *Ao*PDS. Regarding the other different residues in the *Ao*PDS/*Ao*CAS active site besides T727/F726, substitutions of V411/Y410 and V482/I481 show more or less activity loss (Fig. 5), indicating that these two positions were not related to the deprotonation and protosta-13 (17),24-dienol production. The product spectrum is sharply altered only by the F726T substitution in *Ao*CAS. Further QM/MM MD simulations on the *Ao*CAS-F726T mutant showed that the reaction energy profile is very similar to that of the wild-type *Ao*PDS (Fig. 3). Therefore, T727 is the key residue, as the general base for the premature deprotonation of the active carbocation, to yield protosta-13 (17),24-dienol exclusively in *Ao*PDS. Notably in *Ao*CAS, F726 is a plastic residue to harness the catalytic function of *Ao*CAS from the native product spectrum of cycloartenol to protosta-13 (17),24-dienol by a F726T single substitution. As far as we know, such a strong trade-off effect with high catalytic efficiency and specificity for a new function by a single-residue substitution has not been previously reported for the large OSCs enzyme family.

The uniform functional trade-off of the typical CBC-type OSCs

Inspired by the functional reshaping in *Ao*CAS-F726T and considering that F726 is highly conserved in most CBC-type OSCs (Fig. 6A

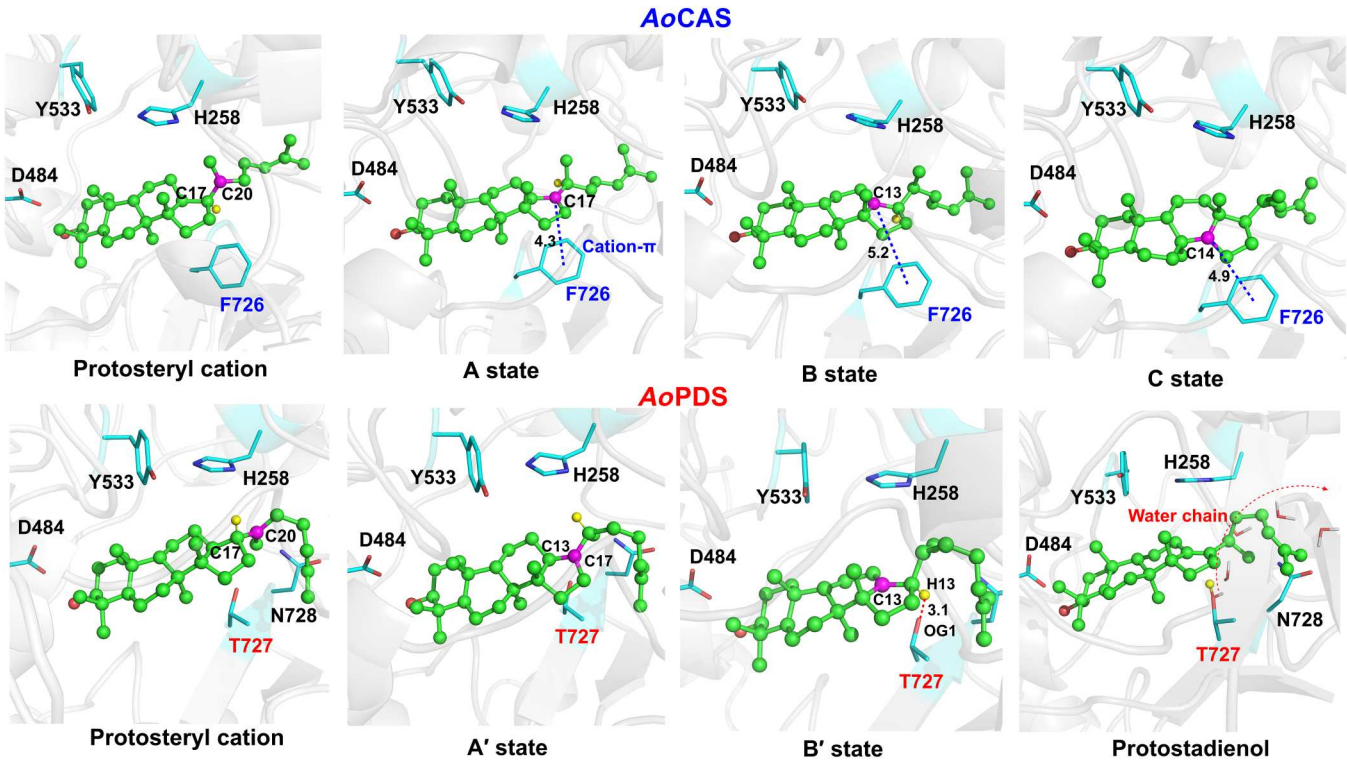

Fig. 4. Representative structures of reaction intermediates in *Ao*CAS/*Ao*PDS. The transition state structures are shown in figs. S8 and S9.

and figs. S10 and S11), the functional plasticity of the F in other OSCs was further investigated, including *It*OSC3 from *Iris tectorum Maxim* (*5*), *Sg*CBQ from *Siraitia grosvenorii* (*13*), *Aj*PS from *Apostichopus japonicus* (*14*, *15*), and ERG7 from *Saccharomyces cerevisiae* (*16*), as all these OSCs have F at the same site as F726 in *Ao*CAS.

For the strong trade-off effect of the F → T substitution, the native catalytic function of all the above four OSCs were consistently reshaped into PDS function to produce protostadienol. As summarized in Fig. 6B and fig. S12, the *It*OSC3, *Aj*PS, and ERG7 mutants were converted into PDS function almost completely (96.7, 90.7, and 99.8% protostadienol, respectively), and the *Sg*CBQ mutant shows a nearly half production proportion (49.5%). Sequence alignment of these selected CBC-type OSCs with *Ao*PDS/*Ao*CAS shows that the conversion to PDS function through the mutation is not limited by a certain level of sequence identity (fig. S17), because the *Aj*PS and ERG7 with relatively low sequence identity (~37 and 34%, respectively) and active site similarity (both with more than six residue differences) to *Ao*PDS still produce high percentage of protostadienol by the F → T substitutions. To decipher the intrinsic mechanism behind the high plasticity of the conserved F in these OSCs, QM/MM MD simulations were used to observe the dynamic interaction modes between F/T and the protosteryl cation (Fig. 6C). In wild-type enzymes, the protosteryl cation is stabilized by the aromatic F through cation-π interactions, which widely exists as a selectivity control factor in terpene synthases (*17*–*20*). As for the subsequent rearrangements from the protosteryl cation, CH-π interaction between C17 and F726 stabilizes the transition state to promote the 1,2-hydride transfer (C17 to C20); otherwise, it would take the route with the higher barrier as seen in *Ao*PDS and previously studied hLAS F696 mutants (*16*, *18*). While for the F → T mutants, the T supplements its hydroxy group to attract a proton from C17 or C13, causing the reactive carbocation to be quenched from A or B states. That is, the strong trade-off effect of F → T mutants is due to the supplemental deprotonation role of T, which replaces the original stabilizing contribution of F. Considering that the plasticity is commonly exhibited in the above four OSCs (all have the conserved F) and the high conservatism among CBC-type OSCs, we deduce that the specific F → T mutants are widely feasible (at least for those OSCs that yield tetracyclic products) for harnessing the new catalytic function to effectively biosynthesize the rare protostadienol.

The diverse trade-off effects of the same plastic position in chair-chair-chair–type OSC

Considering that the plastic F in CBC-type OSCs is also highly conserved in CCC-type (namely, chair-chair-chair conformation of the first three fused rings) OSCs, the potential plasticity of F in the CCC-type OSCs was also investigated. We found that the stabilization/quenching trade-off effect by F → T substitution is not well reproduced in CCC-type OSCs, which was proved by several typical OSCs with different products (figs. S13 to S15). Similar to *Gg*BAS (Fig. 7A), the activity was largely decreased and only trace amount of dammarenediol II was produced in the F728T mutant. Another reported substitution producing dammarenediol-II (oat β-amyrin synthase S728F) (*21*) was also tested, and the *Gg*BAS-N731F mutant did not obviously change the product spectrum. Instead, another notable trade-off between wild-type β-amyrin and abortive pentacyclic quenching activity was detected in the *Gg*BAS-F728S mutant (other hydroxy group side chain residues were further attempted by F728S and F728Y mutants) and produces germanicol

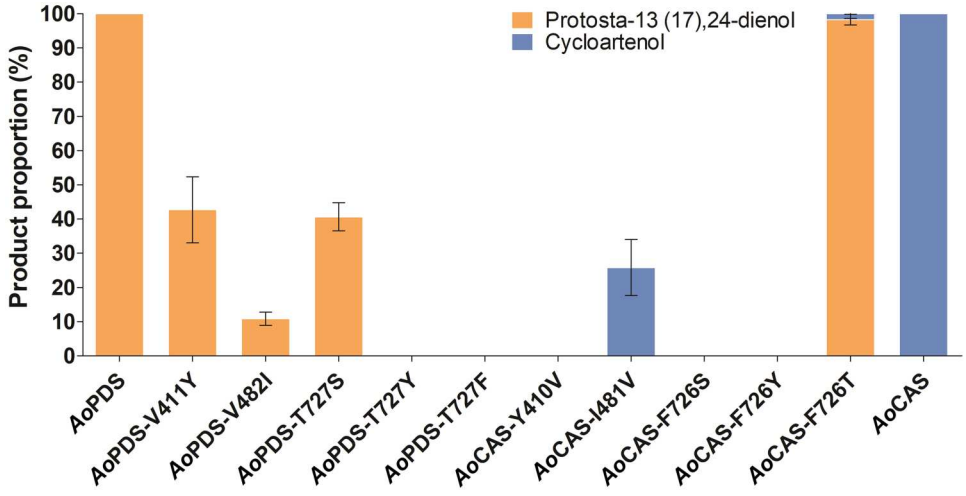

Fig. 5. The product variations of *Ao*PDS/*Ao*CAS mutations. The relative proportion of mutations was calculated by comparing with corresponding wide-type *Ao*PDS/*Ao*CAS that were set as 100%. The error bars were from three dependent mutation experiments.

as the major product. QM/MM MD simulation shows that the S728 closes to the E ring of the oleanane-type intermediate (especially C18 and C19) for deprotonation rather than the D ring (Fig. 7B). Because mutants of the same position bring nonuniform enzymatic activity in CCC-type OSCs and the functional trade-off is not as strong as observed in CBC-type OSCs, the diverse trade-off effects found in CCC-type OSC mutants might also be a good initial point for functional reshaping but requires further extensive studies. In addition, similar protostadienol products are yielded both in *Ao*PDS (this work) and in previously reported *Af*PDS; but as obviously shown in Fig. 7C, the *Ao*PDS has high similarity with plant CAS and is unique from the *Af*PDS, which is closer to fungal lanosterol synthase (LAS). This reminds us that the mutant of *Ao*CAS/*It*OSC3 and ERG7 (also belong to CAS or LAS family, respectively) shows much higher protostadienol product rate (>96%) than that in others (such as SgCBQ; <50%), as shown in Fig. 6B. Considering that F is highly conserved at the same position while the appearance of T is unique (only found in *Ao*PDS), the plastic F → T substitution likely causes a universal activity trade-off in many other CBC-type OSCs especially for CAS and LAS in plant.

In this work, inspired by deciphering the enzymatic catalytic mechanism for the unique *A. orientale* oxidosqualene cyclases (*Ao*PDS and *Ao*CAS), we found that the specific F → T substitution is a controllable factor to extensively produce protostadienol in CBC-type OSCs. It is remarkable that the uniform functional trade-off could be facilely realized by a single substitution, which will be instructive for other enzyme engineering, by combing multiscale simulations to reveal the plastic position with mutagenesis experiments to further validate its feasibility.

MATERIALS AND METHODS

Plant material and microbial strains

Ten- to 12-month-old *A. orientale* (Sam.) Juzep. (Alismataceae) plant was collected from JianOu, FuJian province, China. The plant was confirmed to be *A. orientale* belonging to the Alismataceae family by A. Ji (Guangzhou University of Chinese Medicine) and was maintained in the constant temperature incubator of Guangzhou University of Chinese Medicine. *Escherichia coli* DH5α was purchased from TransGen Biotech Co. Ltd. (Beijing, China). The *S. cerevisiae* strain SE-MET was constructed in our previous research.

Cloning of OSCs and construction of yeast expression plasmids

The full-length coding sequences were present for *Ao*OSC1 (*Ao*PDS) and *Ao*OSC2 (*Ao*CAS) in the transcriptome databases. These were directly amplified from the cDNA of *A. orientale* rhizomes using the Phanta Max Super-Fidelity DNA Polymerase (Vazyme Biotech Inc.) with gene-specific primers (table S4). Conditions for polymerase chain reaction amplification were as follows: 95°C for 3 min, (95°C for 15 s, 57°C for 15 s, 72°C for 2 min) × 32 cycles, and 72°C for 5 min. The resulting amplicons were constructed into the pESC-Ura vector (Agilent Technologies Inc.) between the Bam HI and Sma I restriction sites using the ClonExpressII One Step Cloning Kit (Vazyme Biotech, Nanjing, China) and validated by sequencing.

Phylogenetic and amino acid sequence analysis

The deduced amino acid sequences of *Ao*PDS, *Ao*CAS, and those of other OSCs (table S1) obtained from GenBank were subjected to phylogenetic analysis. All OSC proteins were aligned by ClustalW (*22*). The analysis was performed using the neighbor-joining method with MEGA 6.0 (*23*). Bootstrapping with 1000 replicates was used to estimate the strength of the nodes in the tree (*24*). Sequence similarities and secondary structure information of aligned sequences were rendered using ESPript 3.06 (*25*) based on the secondary structure of the human oxidosqualene cyclase (lanosterol cyclase) 1W6K, the only OSC for which experimentally determined structure information is available (*26*).

Metabolite extraction and gas chromatography–mass spectrometry analysis

Product analysis was collected by centrifugation of yeast cell biomass after fermentation. Transgenic yeast cells harboring the *AoPDS* and *AoCAS* genes were saponified in 2 ml of saponification reagent [20% (w/v) KOH in 50% (v/v) ethanol] at 100°C for 5 min and extracted three times with an equal volume of hexane,

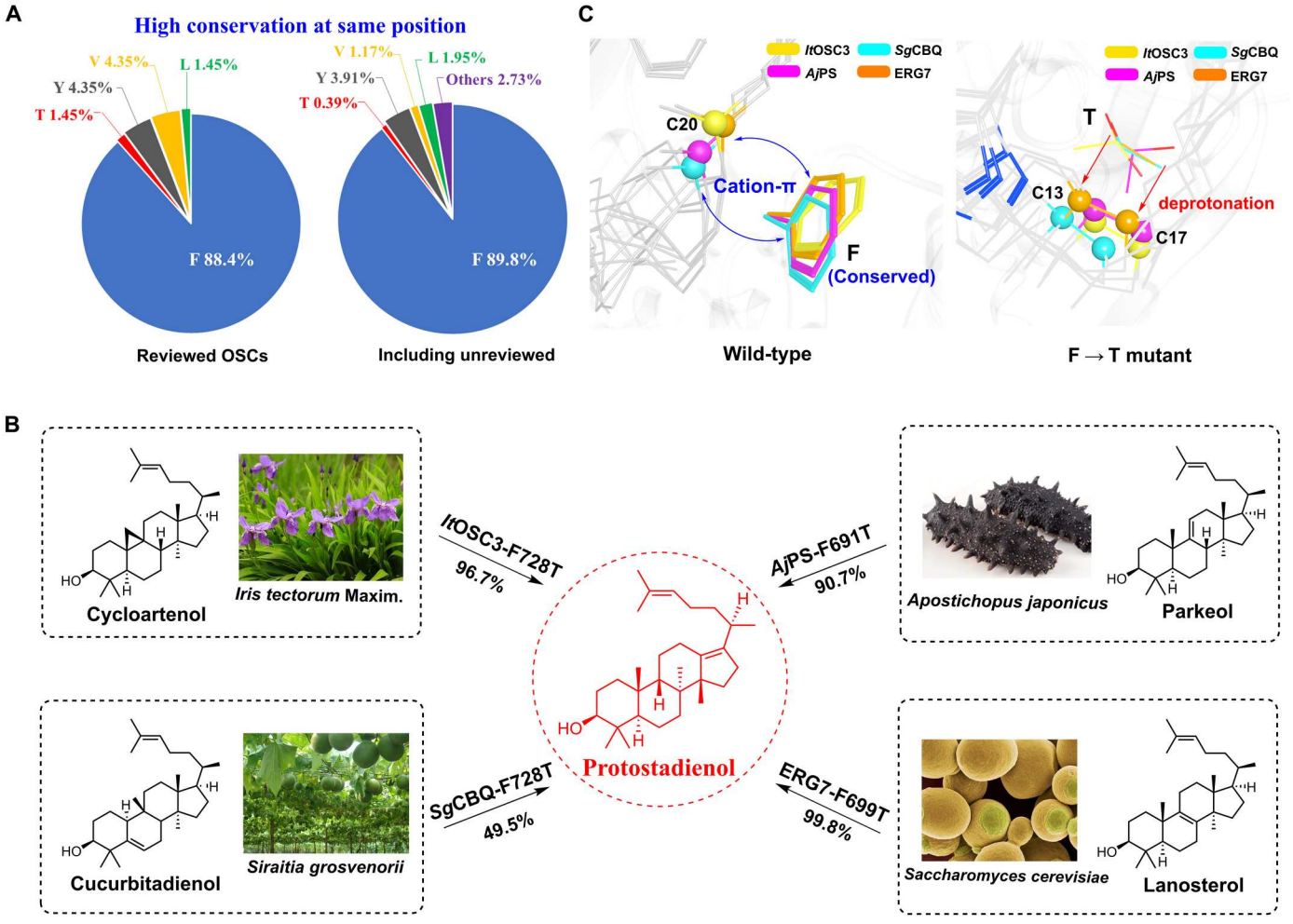

Fig. 6. The functional trade-off of typical CBC-type OSCs. (**A**) Sequence alignment analysis of reviewed OSCs (70 in total) and all available OSCs (256 in total including unreviewed sequences). (**B**) F → T substitution at same position as AoCAS in other CBC-type OSCs; the products of wild-type OSCs and their mutants are shown in dashed boxes and the circle, respectively [*It*OSC3, *Sg*CBQ, and *Aj*PS was done in this work and ERG7 was previously reported (*16*)]. (**C**) Comparisons of wild-type and F → T mutant models of OSCs.

combining organic phases and evaporating under reduced pressure to obtain the crude extract. Crude extracts were derivatized by treatment with 50 μl of *N*-methyl-*N*-trimethylsilyl-trifluoroacetamide at 90°C for 10 min and then analyzed using a gas chromatography–mass spectrometry (GC-MS) equipment. Three biological replicates were performed for each sample.

Purification of protosta-13 (17),20-dienol (the product of AoPDS)

Seven liters of *S. cerevisiae* SE-MET cells expressing *AoPDS* were cultured and collected by centrifuging the culture at 5000 rpm. Saponification was carried out in 1 liter of saponification reagent (3.57 M KOH with 10.87 M ethanol) and refluxed at 75°C for 3 hours. The products were extracted four times with an equal volume of hexane. The hexane extract was loaded onto a silica gel column (30 cm by 2.5 cm, 200- to 300-mesh particle size; Haiyang, Qingdao, China) and eluted with hexane:ethyl acetate = 15: 1 (v/v). Fifty-milliliter fractions were collected and analyzed by thin-layer chromatography and GC-MS. Full experimental details appear in the Supplementary Materials.

Computational modeling and QM/MM MD simulations

AlphaFold2 (*27*) was used for OSCs modeling, the protosteryl cation intermediate after cyclizations was used as the starting point for CBC OSCs system setup and subsequent computational studies, and the dammarenyl cation intermediate was used for CCC *Gg*BAS. The computational models were set up for further MD simulations to relax the structures of the proteins and the intermediates. Snapshots of each system from the stable trajectories were chosen to build the initial structures for the subsequent QM/MM simulations. The periodic boundary condition was also considered in the following QM/MM MD simulations. For *Ao*PDS/*Ao*CAS, the protosteryl cation and T727/F726 were included in the QM region, respectively (the charge of the QM region is 1). The same QM regions were used for *It*OSC3, *Sg*CBQ, *Aj*PS, and Erg7. For *Gg*BAS, the dammarenyl cation and F728 were included in the QM region. In all mutant models, the QM regions were kept the same as in the wild-type enzymes. All of these QM atoms were described with the M06-2X (*28*, *29*)/6-31G(d) basis set, which is widely used in studying cyclization reactions (*19*, *30*), and the

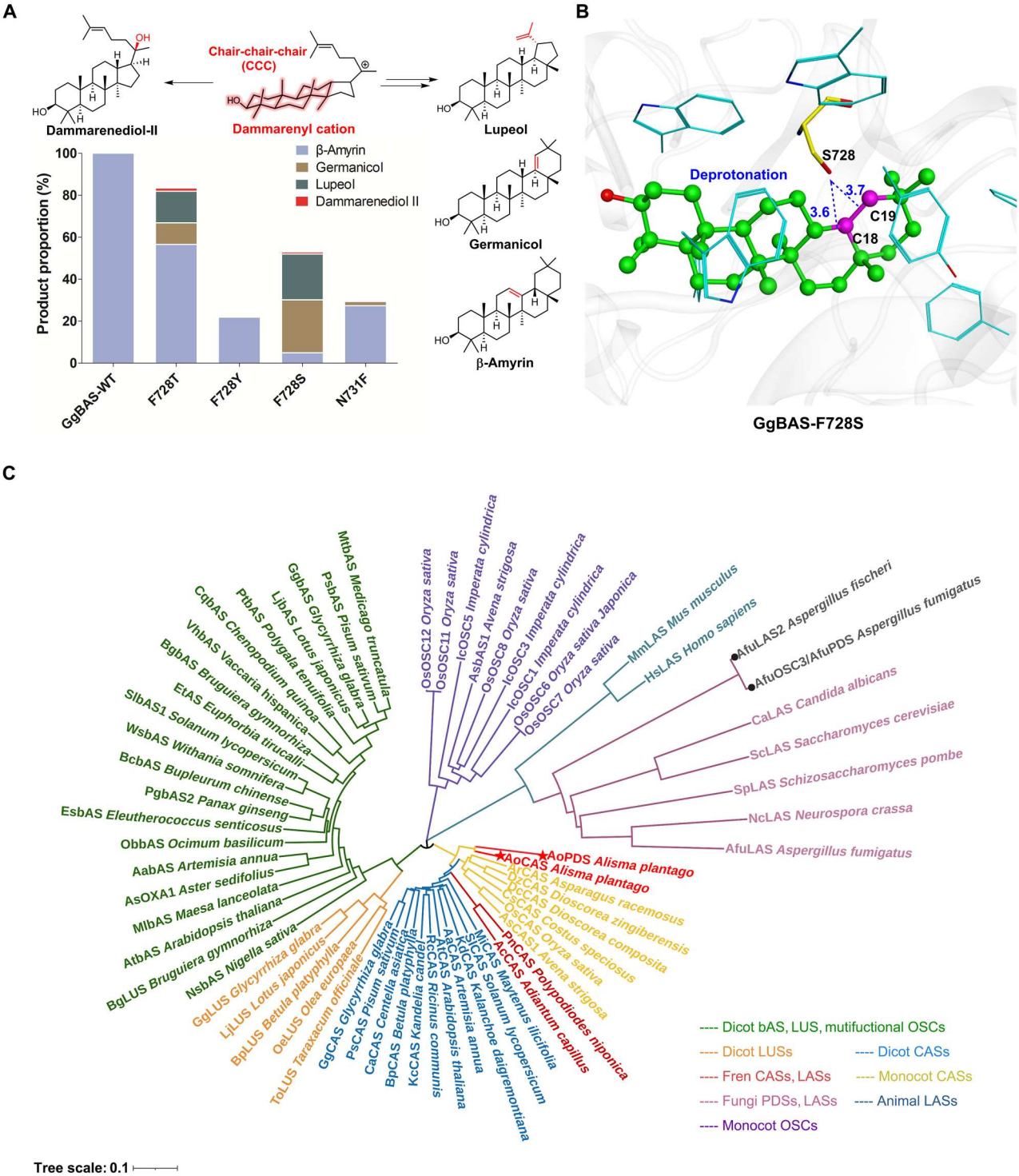

Fig. 7. The functional trade-off of typical CCC-type OSC *Gg*BAS. (**A**) Product profiles of wild-type *Gg*BAS and mutants. F728S mutant shows promiscous product spectrum with germanicol as the main product. (**B**) The model of *Gg*BAS F728S mutant with 6-6-6-6-6 oleanane-type intermediate. (**C**) Phylogenetic tree of characterized plant OSCs.

model contains more than 730 basis functions in total. All of these QM/MM calculations were performed with the interfaced QChem (*31*)–AMBER12 programs (*32*). Full computational details appear in the Supplementary Materials.

Supplementary Materials

This PDF file includes:
Supplementary Text
Figs. S1 to S18
Tables S1 to S5

View/request a protocol for this paper from *Bio-protocol*.

REFERENCES AND NOTES

1. R. Thimmappa, K. Geisler, T. Louveau, P. O'Maille, A. Osbourn, Triterpene biosynthesis in plants. *Annu. Rev. Plant Biol.* **65**, 225–257 (2014).
2. A. Osbourn, R. J. M. Goss, R. A. Field, The saponins – polar isoprenoids with important and diverse biological activities. *Nat. Prod. Rep.* **28**, 1261–1268 (2011).
3. J. M. Augustin, V. Kuzina, S. B. Andersen, S. Bak, Molecular activities, biosynthesis and evolution of triterpenoid saponins. *Phytochemistry* **72**, 435–457 (2011).
4. R. Xu, G. C. Fazio, S. P. T. Matsuda, On the origins of triterpenoid skeletal diversity. *Phytochemistry* **65**, 261–291 (2004).
5. T. Zeng, Z. Liu, J. Zhuang, Y. Jiang, W. He, H. Diao, N. Lv, Y. Jian, D. Liang, Y. Qiu, R. Zhang, F. Zhang, X. Tang, R. Wu, TeroKit: A database-driven web server for terpenome research. *J. Chem. Inf. Model.* **60**, 2082–2090 (2020).
6. M. Zhao, T. Gödecke, J. Gunn, J. A. Duan, C. T. Che, Protostane and fusidane triterpenes: A mini-review. *Molecules* **18**, 4054–4080 (2013).
7. H. Mitsuguchi, Y. Seshime, I. Fujii, M. Shibuya, Y. Ebizuka, T. Kushiro, Biosynthesis of steroidal antibiotic fusidanes: Functional analysis of oxidosqualene cyclase and subsequent tailoring enzymes from Aspergillus fumigatus. *J. Am. Chem. Soc.* **131**, 6402–6411 (2009).
8. S. Lodeiro, Q. Xiong, W. K. Wilson, Y. Ivanova, M. K. L. Smith, G. S. May, S. P. T. Matsuda, Protostadienol biosynthesis and metabolism in the pathogenic fungus aspergillus fumigatus. *Org. Lett.* **11**, 1241–1244 (2009).
9. M. J. Stephenson, R. A. Field, A. Osbourn, The protosteryl and dammarenyl cation dichotomy in polycyclic triterpene biosynthesis revisited: Has this 'rule' finally been broken? *Nat. Prod. Rep.* **36**, 1044–1052 (2019).
10. N. C. Deno, J. O. Turner, The basicity of alcohols and ethers. *J. Org. Chem.* **31**, 1969–1970 (1966).
11. K. Raz, S. Levi, P. K. Gupta, T. M. Dan, Enzymatic control of product distribution in terpene synthases: Insights from multiscale simulations. *Curr. Opin. Biotechnol.* **65**, 248–258 (2020).
12. M. Jia, Y. Zhang, J. B. Siegel, D. J. Tantillo, R. J. Peters, Switching on a nontraditional enzymatic base – deprotonation by serine in the ent-kaurene synthase from bradyrhizobium japonicum. *ACS Catal.* **9**, 8867–8871 (2019).
13. L. Dai, C. Liu, Y. Zhu, J. Zhang, Y. Men, Y. Zeng, Y. Sun, Functional characterization of cucurbitadienol synthase and triterpene glycosyltransferase involved in biosynthesis of mogrosides from siraitia grosvenorii. *Plant Cell Physiol.* **56**, 1172–1182 (2015).
14. R. Thimmappa, S. Wang, M. Zheng, R. C. Misra, A. C. Huang, G. Saalbach, Y. Chang, Z. Zhou, V. Hinman, Z. Bao, A. Osbourn, Biosynthesis of saponin defensive compounds in sea cucumbers. *Nat. Chem. Biol.* **18**, 774–781 (2022).
15. Y. Li, R. Wang, X. Xun, J. Wang, L. Bao, R. Thimmappa, J. Ding, J. Jiang, L. Zhang, T. Li, J. Lv, C. Mu, X. Hu, L. Zhang, J. Liu, Y. Li, L. Yao, W. Jiao, Y. Wang, S. Lian, Z. Zhao, Y. Zhan, X. Huang, H. Liao, J. Wang, H. Sun, X. Mi, Y. Xia, Q. Xing, W. Lu, A. Osbourn, Z. Zhou, Y. Chang, Z. Bao, S. Wang, Sea cucumber genome provides insights into saponin biosynthesis and aestivation regulation. *Cell Discov.* **4**, 29 (2018).
16. T.-K. Wu, C. H. Chang, H. Y. Wen, Y. T. Liu, W. H. Li, T. T. Wang, W. S. Shie, Alteration of the substrate's prefolded conformation and cyclization stereochemistry of oxidosqualene-lanosterol cyclase of saccharomyces cerevisiae by substitution at phenylalanine 699. *Org. Lett.* **12**, 500–503 (2010).
17. D. W. Christianson, Structural and chemical biology of terpenoid cyclases. *Chem. Rev.* **117**, 11570–11648 (2017).
18. H. Diao, N. Chen, K. Wang, F. Zhang, Y. H. Wang, R. Wu, Biosynthetic mechanism of lanosterol: A completed story. *ACS Catal.* **10**, 2157–2168 (2020).
19. N. Chen, S. Wang, L. Smentek, B. A. Hess Jr., R. Wu, Biosynthetic mechanism of lanosterol: Cyclization. *Angew. Chem. Int. Ed.* **54**, 8693–8696 (2015).
20. F. Zhang, T. An, X. Tang, J. Zi, H. B. Luo, R. Wu, Enzyme promiscuity versus fidelity in two sesquiterpene cyclases (TEAS versus ATAS). *ACS Catal.* **10**, 1470–1484 (2020).
21. M. Salmon, R. B. Thimmappa, R. E. Minto, R. E. Melton, R. K. Hughes, P. E. O'Maille, A. M. Hemmings, A. Osbourn, A conserved amino acid residue critical for product and substrate specificity in plant triterpene synthases. *Proc. Natl. Acad. Sci. U.S.A.* **113**, E4407–E4414 (2016).
22. J. D. Thompson, D. G. Higgins, T. J. Gibson, CLUSTAL W: Improving the sensitivity of progressive multiple sequence alignment through sequence weighting, position-specific gap penalties and weight matrix choice. *Nucleic Acids Res.* **22**, 1673–1680 (1994).
23. B. G. Hall, Building phylogenetic trees from molecular data with MEGA. *Mol. Biol. Evol.* **30**, 1229–1235 (2013).
24. B. Efron, E. Halloran, S. Holmes, Bootstrap confidence levels for phylogenetic trees. *Proc. Natl. Acad. Sci. U.S.A.* **93**, 13429–13434 (1996).
25. R. Xavier, G. Patrice, Deciphering key features in protein structures with the new ENDscript server. *Nucleic Acids Res.* **42**, W320–W324 (2014).
26. T. Ralf, R. Thoma, T. Schulz-Gasch, B. D'Arcy, J. Benz, J. Aebi, H. Dehmlow, M. Hennig, M. Stihle, A. Ruf, Insight into steroid scaffold formation from the structure of human oxidosqualene cyclase. *Nature* **432**, 118–122 (2004).
27. K. Tunyasuvunakool, J. Adler, Z. Wu, T. Green, M. Zielinski, A. Žídek, A. Bridgland, A. Cowie, C. Meyer, A. Laydon, S. Velankar, G. J. Kleywegt, A. Bateman, R. Evans, A. Pritzel, M. Figurnov, O. Ronneberger, R. Bates, S. A. A. Kohl, A. Potapenko, A. J. Ballard, B. Romera-Paredes, S. Nikolov, R. Jain, E. Clancy, D. Reiman, S. Petersen, A. W. Senior, K. Kavukcuoglu, E. Birney, P. Kohli, J. Jumper, D. Hassabis, Highly accurate protein structure prediction for the human proteome. *Nature* **596**, 590–596 (2021).
28. Y. Zhao, D. G. Truhlar, The M06 suite of density functionals for main group thermochemistry, thermochemical kinetics, noncovalent interactions, excited states, and transition elements: Two new functionals and systematic testing of four M06-class functionals and 12 other functionals. *Theor. Chem. Acc.* **120**, 215–241 (2008).
29. Y. Zhao, D. G. Truhlar, Exploring the limit of accuracy of the global hybrid meta density functional for main-group thermochemistry, kinetics, and noncovalent interactions. *J. Chem. Theory Comput.* **4**, 1849–1868 (2008).
30. N. Chen, J. Zhou, J. Li, J. Xu, R. Wu, Concerted cyclization of lanosterol C-ring and D-ring under human oxidosqualene cyclase catalysis: An ab initio QM/MM MD study. *J. Chem. Theory Comput.* **10**, 1109–1120 (2014).
31. Y. Shao, L. F. Molnar, Y. Jung, J. Kussmann, C. Ochsenfeld, S. T. Brown, A. T. B. Gilbert, L. V. Slipchenko, S. V. Levchenko, D. P. O'Neill, R. A. Di Stasio Jr., R. C. Lochan, T. Wang, G. J. O. Beran, N. A. Besley, J. M. Herbert, C. Y. Lin, T. Van Voorhis, S. H. Chien, A. Sodt, R. P. Steele, V. A. Rassolov, P. E. Maslen, P. P. Korambath, R. D. Adamson, B. Austin, J. Baker, E. F. C. Byrd, H. Dachsel, R. J. Doerksen, A. Dreuw, B. D. Dunietz, A. D. Dutoi, T. R. Furlani, S. R. Gwaltney, A. Heyden, S. Hirata, C.-P. Hsu, G. Kedziora, R. Z. Khalliulin, P. Klunzinger, A. M. Lee, M. S. Lee, W. Z. Liang, I. Lotan, N. Nair, B. Peters, E. I. Proynov, P. A. Pieniazek, Y. M. Rhee, J. Ritchie, E. Rosta, C. D. Sherrill, A. C. Simmonett, J. E. Subotnik, H. Lee Woodcock III, W. Zhang, A. T. Bell, A. K. Chakraborty, D. M. Chipman, F. J. Keil, A. Warshel, W. J. Hehre, H. F. Schaefer III, J. Kong, A. I. Krylov, P. M. W. Gilla, M. Head-Gordon, Advances in methods and algorithms in a modern quantum chemistry program package. *Phys. Chem. Chem. Phys.* **8**, 3172–3191 (2006).
32. Y. Zhou, S. Wang, Y. Li, Y. Zhang, Born-oppenheimer ab initio QM/MM molecular dynamics simulations of enzyme reactions. *Methods Enzymol.* **577**, 105–118 (2016).

Acknowledgments: We thank the Guangzhou and Shenzhen Supercomputer Center for providing computational source. We also thank Y. Zhang and S. g. Wang at NYU, as well as Y. Zhou at NJU, for help using the QChem-AMBER program. **Funding:** This research was supported by the Key-Area Research and Development Program of Guangdong Province (2022B1111080005 to R.W.), the National Natural Science Foundation of China (22103098 to F.Z., 81874333 to L.D., 81930114 to Z.L., and 21773313 to R.W.), and the Postdoctoral Research Foundation of China (2020TQ0390 and 2020M683144 to F.Z.). **Author contributions:** R.W. and L.D. supervised the whole research. R.W. designed the computational subproject. L.D. and Z.L. designed the experimental subprojects. R.Z. and Y.-e.H. isolated and identified the products. J.Y. and R.H. analyzed the sequences and data. A.-j.J. identified the plants and did the bioinformatic analysis. F.Z., R.W., and L.D. wrote the manuscript. B.A.H. and Z.L. made important contributions on revising the manuscript. F.Z. contributed many concepts and most computational simulations. Y.W. performed the experiments and data analysis. All authors contributed to the interpretation of the results. All authors reviewed and approved the final manuscript. **Competing interests:** The authors declare that they have no competing interests. **Data and materials availability:** All data needed to evaluate the conclusions in the paper are present in the paper and/or the Supplementary Materials.

Submitted 14 February 2023
Accepted 1 May 2023
Published 7 June 2023
10.1126/sciadv.adh1418

PLANT SCIENCES

Bilirubin is produced nonenzymatically in plants to maintain chloroplast redox status

Kazuya Ishikawa[1,2], Xiaonan Xie[1], Yasuhide Osaki[1], Atsushi Miyawaki[3,4], Keiji Numata[5,6], Yutaka Kodama[1,6]*

Bilirubin, a potent antioxidant, is a product of heme catabolism in heterotrophs. Heterotrophs mitigate oxidative stress resulting from free heme by catabolism into bilirubin via biliverdin. Although plants also convert heme to biliverdin, they are generally thought to be incapable of producing bilirubin because they lack biliverdin reductase, the enzyme responsible for bilirubin biosynthesis in heterotrophs. Here, we demonstrate that bilirubin is produced in plant chloroplasts. Live-cell imaging using the bilirubin-dependent fluorescent protein UnaG revealed that bilirubin accumulated in chloroplasts. In vitro, bilirubin was produced nonenzymatically through a reaction between biliverdin and reduced form of nicotinamide adenine dinucleotide phosphate at concentrations comparable to those in chloroplasts. In addition, increased bilirubin production led to lower reactive oxygen species levels in chloroplasts. Our data refute the generally accepted pathway of heme degradation in plants and suggest that bilirubin contributes to the maintenance of redox status in chloroplasts.

INTRODUCTION

Bilirubin is a yellow pigment that is a product of heme catabolism in heterotrophs such as mammals. Heme is an essential biological molecule consisting of a tetrapyrrole ring and an iron cation. After being synthesized in mitochondria, heme is distributed throughout the cell and binds to various proteins as a cofactor, playing essential roles in cellular functions such as oxygen transport and electron transfer. However, free heme released from the breakdown of heme-containing proteins (hemoproteins) is a strong prooxidant that promotes cellular oxidative stress, and its levels are therefore tightly controlled via catabolism (*1*–*3*). Heme oxygenases open and oxidize the heme ring into the linear tetrapyrrole biliverdin, which is subsequently reduced to bilirubin by biliverdin reductase. Biliverdin reductase uses reduced form of nicotinamide adenine dinucleotide phosphate ($NADP^+$) (NADPH) as an electron donor to reduce biliverdin (*4*), making the activity of biliverdin reductase NADPH dependent. Although bilirubin is toxic and causes kernicterus at high concentrations, it is also a potent antioxidant. Mildly elevated bilirubin levels in the body lower the risk of diseases such as arterial hypertension and diabetes mellitus by preventing cellular oxidative damage (*5*–*7*).

In plants, heme is biosynthesized and degraded in chloroplasts, unlike the typical mitochondrial biosynthetic pathway of heterotrophs. Aside from their different subcellular localizations, heme biosynthesis and degradation pathways are identical in plants and heterotrophs until the point of biliverdin biosynthesis via heme oxygenase. In plants, biliverdin is reduced to phytochromobilin by the plant-specific enzyme phytochromobilin synthase (*8*). Phytochromobilin is the chromophore of phytochromes, the red/far-red photoreceptors that promote photomorphogenesis and light-mediated development in plants. Phytochromobilin is believed to be the end product of heme degradation, since biliverdin reductase activity has not been detected in plant extracts (*9*, *10*). However, the sum of free and bound heme pools is estimated to far exceed the abundance of phytochromobilin in plants (*11*–*13*), suggesting the existence of other end products in the plant heme degradation pathway. Consistent with this idea, a few studies have reported the presence of bilirubin in the flowers and fruits of specific plant species, such as bird of paradise (*Strelitzia* spp.) (*14*, *15*).

Enzymes improve reaction rates and reaction specificities by catalyzing chemical reactions to control cellular functions. On the other hand, chemical reactions sometimes proceed in the absence of enzymes, with examples of nonenzymatic reactions playing important roles in cell metabolism (*16*, *17*). Several cases have been reported in which a reduced cofactor reacts nonenzymatically as an electron donor in vitro (*18*, *19*). However, the contribution of nonenzymatic reactions to cellular functions in vivo is largely unknown because genetic approaches are limited in their ability to investigate nonenzymatic reactions.

In this study, we used UnaG, a bilirubin-dependent fluorescent protein isolated from the muscle tissue of Japanese eel (*Anguilla japonica*), to demonstrate that bilirubin biosynthesis takes place in plants universally. UnaG has a specific and ultrahigh affinity for bilirubin (bilirubin IXα) and does not bind to biliverdin or any bilirubin analogs such as ditauro-bilirubin (*20*). Furthermore, we revealed that NADPH and biliverdin react nonenzymatically to produce bilirubin in chloroplasts, which have a considerably higher NADPH concentration than animal cells (*21*–*23*). Because increased bilirubin production diminished oxidative stress, we propose that nonenzymatically produced bilirubin contributes to the maintenance of redox status in chloroplasts.

[1]Center for Bioscience Research and Education, Utsunomiya University, Tochigi 321-8505, Japan. [2]Graduate School of Medicine, Dentistry, and Pharmaceutical Sciences, Okayama University, Okayama 700-8530, Japan. [3]Laboratory for Cell Function Dynamics, RIKEN Center for Brain Science, Saitama 351-0198, Japan. [4]Biotechnological Optics Research Team, RIKEN Center for Advanced Photonics; Saitama, 351-0198, Japan. [5]Department of Material Chemistry, Graduate School of Engineering, Kyoto University; Kyoto, 615-8246, Japan. [6]Biomacromolecules Research Team, RIKEN Center for Sustainable Resource Science, Saitama 351-0198, Japan.
*Corresponding author. Email: kodama@cc.utsunomiya-u.ac.jp

RESULTS

Bilirubin production in plants

We tested whether bilirubin accumulates in plants using the bilirubin biosensor UnaG. Since plant heme is biosynthesized and catabolized in chloroplasts, we transiently expressed a construct encoding a plastid (chloroplast)–targeted version of UnaG, with an N-terminal plastid transit peptide from Arabidopsis (*Arabidopsis thaliana*) Rubisco small subunit 1A (Rbcs1A) [transit peptide–fused UnaG (TP-UnaG)], in the leaves of *Nicotiana benthamiana*, Arabidopsis, and liverwort (*Marchantia polymorpha*). UnaG exhibited bright green fluorescence in the chloroplasts of all tested plants (Fig. 1A).

To ascertain whether UnaG is associated with endogenous bilirubin inside plant cells, we transiently expressed a construct encoding FLAG-tagged TP-UnaG (TP-UnaG-FLAG) in *N. benthamiana* leaves and immunopurified UnaG-FLAG using an anti-FLAG antibody. Immunoblot analysis demonstrated the efficiency of UnaG-FLAG immunoprecipitation (Fig. 1B). Immunopurified UnaG-FLAG (ipUnaG) emitted green fluorescence when excited with blue light (Fig. 1C). The excitation and emission spectra for ipUnaG and the control, holorcUnaG (recombinant UnaG complexed with commercial standard bilirubin), were identical (Fig. 1D). The perfect overlap in fluorescence spectra between ipUnaG and holorcUnaG suggests that UnaG-FLAG bound exclusively to bilirubin in plant cells.

To identify bilirubin bound to ipUnaG, we performed high-performance liquid chromatography (HPLC)–electrospray ionization mass spectrometry. A total ion chromatogram (TIC) of ipUnaG showed a major peak (Fig. 1E) with a tandem mass spectrum that was identical to that of standard bilirubin (fig. S1). Other peaks in Fig. 1E likely represent molecules derived from bilirubin isomers

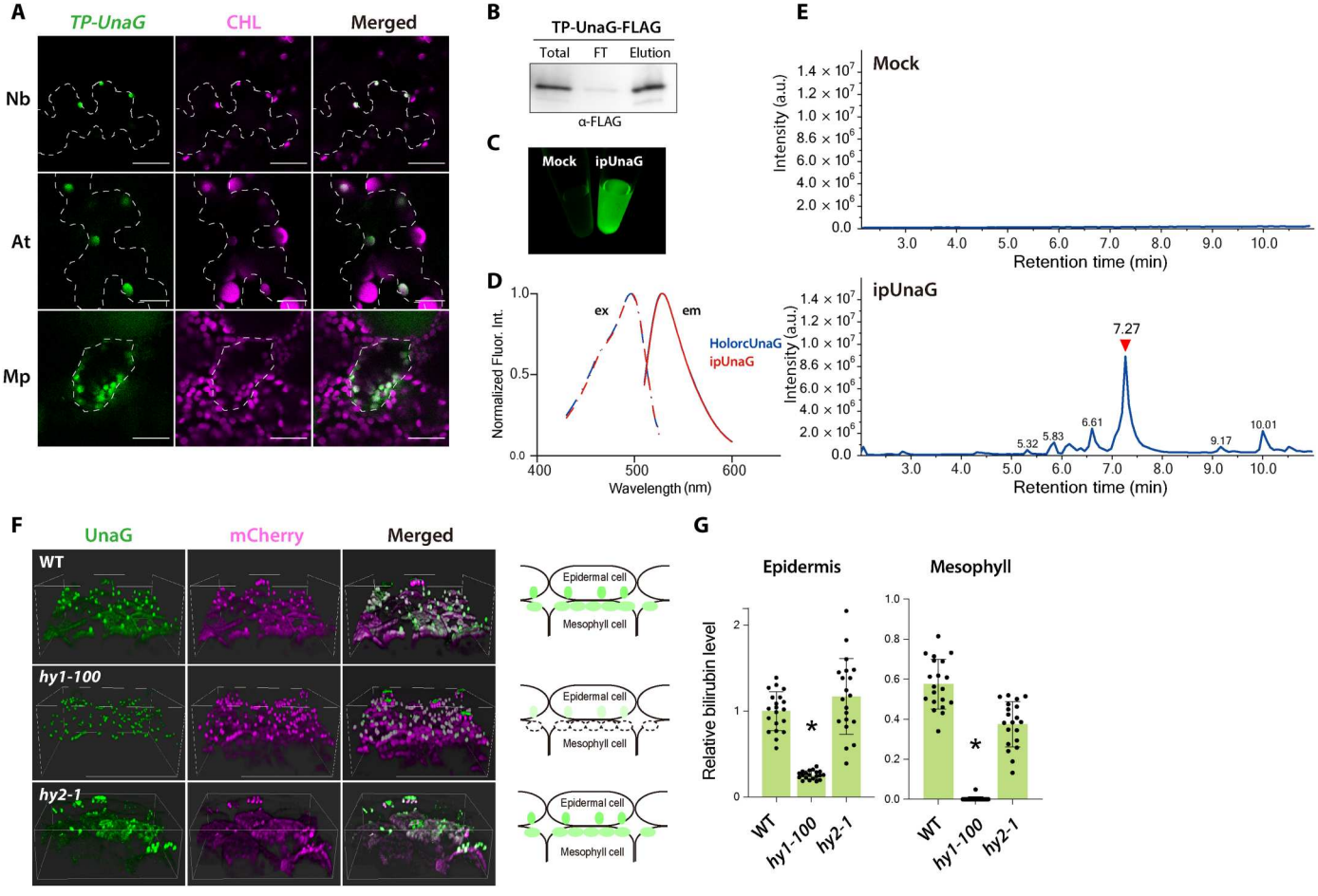

Fig. 1. Bilirubin is synthesized in planta. (**A**) Transient expression of constructs encoding TP-UnaG after particle bombardment of *N. benthamiana* (Nb) and Arabidopsis (At) leaves and *M. polymorpha* (Mp) thalli. CHL, chlorophyll autofluorescence. Successfully transfected cells are outlined by dashed lines. Scale bars, 25 μm. (**B** to **E**) Immunopurification of holoUnaG from *N. benthamiana* leaves transiently expressing *TP-UnaG-FLAG*. (B) Immunoblot of immunopurified UnaG-FLAG (ipUnaG) using an anti-FLAG antibody. FT, flow-through fraction. (C) ipUnaG fluorescence under blue light excitation. A mock immunoprecipitated sample from nontransgenic leaves was processed in parallel. (D) Excitation (ex; dashed lines) and emission (em; solid lines) spectra of ipUnaG (red) and recombinant holoUnaG (holorcUnaG; blue). (E) Total ion chromatograms (TICs) of ipUnaG. The mock control is a sample immunoprecipitated from nontransgenic leaves. The red arrowhead indicates a peak with a product ion spectrum corresponding to bilirubin standards (fig. S1A). a.u., arbitrary unit. (**F** and **G**) *TP-mCherry-UnaG* expression in a mutant lacking either heme oxygenase 1 (*hy1-100*) or phytochromobilin synthase (*hy2-1*). (F) Three-dimensional (3D) visualization of UnaG and mCherry fluorescence in epidermal cells and mesophyll cells of 7-day-old seedlings from the wild-type (WT) and *hy1-100* and *hy2-1* mutants. The diagrams to the right illustrate side views of the 3D fluorescence images. Green, UnaG fluorescence. (G) Quantification of plastid UnaG fluorescence intensity in the WT and mutants. Intensity in the leaf epidermis of the WT was set to 1. Data are means ± SD (n = 20); asterisks indicate significant differences from the WT and *hy2-1*, $P < 0.01$, using Tukey's multiple comparisons test.

and fragmented ipUnaG. These results provide strong evidence that exogenously expressed UnaG specifically bound to bilirubin present in plant cells. Collectively, these data suggest that bilirubin is produced in a wide range of plant species and accumulates in chloroplasts.

Next, we expressed a construct encoding chloroplast-targeted mCherry-UnaG (TP-mCherry-UnaG) in Arabidopsis mutants lacking enzymes involved in heme degradation: heme oxygenase 1 (AtHO1) and phytochromobilin synthase (Fig. 1F). mCherry provided visual confirmation of UnaG expression in chloroplasts. In a mutant lacking AtHO1 (*hy1-100*, for *long hypocotyl 1*), which converts heme to biliverdin in wild-type (WT) plants (*24*), UnaG fluorescence was four times lower than in WT cotyledon epidermal cells (Fig. 1, F and G). In mesophyll cells, the fluorescence was almost undetectable in *hy1-100* (Fig. 1, F and G). In a mutant lacking phytochromobilin synthase (*hy2-1*), the enzyme that catalyzes the formation of phytochromobilin from biliverdin (*8*), UnaG fluorescence in both cotyledon epidermal cells and mesophyll cells was comparable to that in the WT (Fig. 1, F and G). These results suggest that the bilirubin production takes place after biliverdin but not after phytochromobilin biosynthesis.

Biliverdin is nonenzymatically converted to bilirubin in the presence of higher concentrations of NADPH in vitro

The heme oxygenase reaction in plants requires coordination between ferredoxin and other electron donors with heme oxygenase (*25*). Considering that homologs of biliverdin reductase genes have not been identified in plant genomes, we hypothesized that both biliverdin and bilirubin are produced by the action of ferredoxin and/or other electron donors during the heme degradation reaction. We thus performed an in vitro heme oxygenase assay that reconstitutes the natural internal environment of chloroplasts (*25*, *26*). This assay contains recombinant AtHO1, hemin (ferric heme), a ferredoxin-$NADP^+$ oxidoreductase/ferredoxin electron transfer system, and an NADPH-regeneration system based on glucose-6 phosphate dehydrogenase (G6PD). After incubation at 25°C for 8 hours, the reaction solution with AtHO1 had a yellow-green color, whereas the buffer control remained the red color of heme (Fig. 2A). After stopping the reaction and removing the enzymes with organic solvents, we concentrated the reaction products and dissolved them in dimethyl sulfoxide (DMSO). Using liquid chromatography–mass spectrometry analysis, we determined whether bilirubin and biliverdin were synthesized. The TICs exhibited peaks with product ion mass spectra corresponding to bilirubin and biliverdin standards (Fig. 2, C and D), indicating the synthesis of bilirubin and biliverdin. These results suggest that bilirubin is produced during heme degradation despite the lack of biliverdin reductase.

We performed the following experiments to elucidate how bilirubin is produced in the in vitro heme oxygenase assay. Biliverdin was converted into bilirubin even in the absence of hemin and AtHO1 (Fig. 2E, lane: all-in). This observation indicated that enzymes and cofactors other than AtHO1 convert biliverdin to bilirubin. Therefore, we omitted additional enzymes and cofactors one by one to delineate the factors required for the conversion of biliverdin to bilirubin. We detected no bilirubin only when G6PD was omitted (Fig. 2E). G6PD is an enzyme that converts $NADP^+$ to NADPH, and biliverdin is reduced to bilirubin using NADPH as an electron donor in heterotrophs. This led us to hypothesize that NADPH reduces biliverdin nonenzymatically to produce bilirubin. When mixing biliverdin and NADPH, we observed bilirubin production in an NADPH concentration–dependent manner (Fig. 2F). We thus reacted different concentrations of NADPH with biliverdin and monitored the decrease in biliverdin over time. Biliverdin was converted to bilirubin in NADPH and biliverdin concentration–dependent manners (Fig. 2G). The degradation rate of biliverdin appeared to be proportional to the two-thirds power of the concentrations of NADPH and biliverdin. When the reaction products of biliverdin and NADPH were separated by thin-layer chromatography, we detected two bilirubin-like yellow spots at high and low R_f values at the NADPH concentrations of 0.1 mM or higher (Fig. 2H, top). Spots with high R_f values were bilirubin, as they were consistent with the bilirubin standard. Yellow spots with low R_f values were predominantly produced at low NADPH concentrations and are thus presumed to be semireduced intermediates in which one hydrogen ion was introduced into the biliverdin molecule. Subsequently, another hydrogen ion would be introduced from NADPH to produce bilirubin. These results indicate that NADPH and biliverdin react nonenzymatically to produce bilirubin.

Increased NADPH levels promote bilirubin production in planta

High light exposure excites photosystem I and increases NADPH concentration in chloroplasts (*27*). If bilirubin is synthesized directly by reacting with NADPH, then bilirubin production would be expected to increase transiently during irradiation with high-intensity light. Therefore, we intermittently irradiated Arabidopsis leaves expressing *TP-mCherry-UnaG* with 470-, 530-, 590-, or 650-nm lasers for 2 hours by confocal laser scanning microscopy. Irradiation with 590- or 650-nm lasers significantly increased UnaG fluorescence and the UnaG/mCherry ratio (Fig. 3, A and B). The fluorescence intensity of mCherry was not attenuated, confirming that bleaching of the fluorescent protein did not occur. Wavelengths of 590 and 650 nm have higher relative quantum efficiencies for photosynthesis than 470 or 530 nm (*28*), suggesting that the photosystems were activated more strongly by these wavelengths and produced larger amounts of NADPH.

To further test for the nonenzymatic production of bilirubin in chloroplasts, we assessed TP-UnaG fluorescence in *N. benthamiana* cells overexpressing Arabidopsis *NAD KINASE 2* (*NADK2*). NADK2 phosphorylates NAD and increases the amount of NADP(H) in chloroplasts (*29*). We observed stronger UnaG fluorescence in the chloroplasts of cells expressing *NADK2-tagRFP* compared to those expressing *TP-tagRFP* [encoding red fluorescent protein (RFP) with a plastid transit peptide] (Fig. 3C). Quantification of UnaG fluorescence in chloroplasts revealed that *NADK2-tagRFP* overexpression significantly increases fluorescence intensity to twice that of the control (Fig. 3D), suggesting that increased NADPH levels promote bilirubin production in chloroplasts.

These results indicate that increasing NADPH concentration in chloroplasts promotes bilirubin production, supporting the idea that bilirubin production occurs in planta through the nonenzymatic reaction between biliverdin and NADPH.

Bilirubin production lowers reactive oxygen species levels in chloroplasts

We next explored the physiological functions of bilirubin in plants. High light irradiation stimulates bilirubin production (Fig. 3, C and

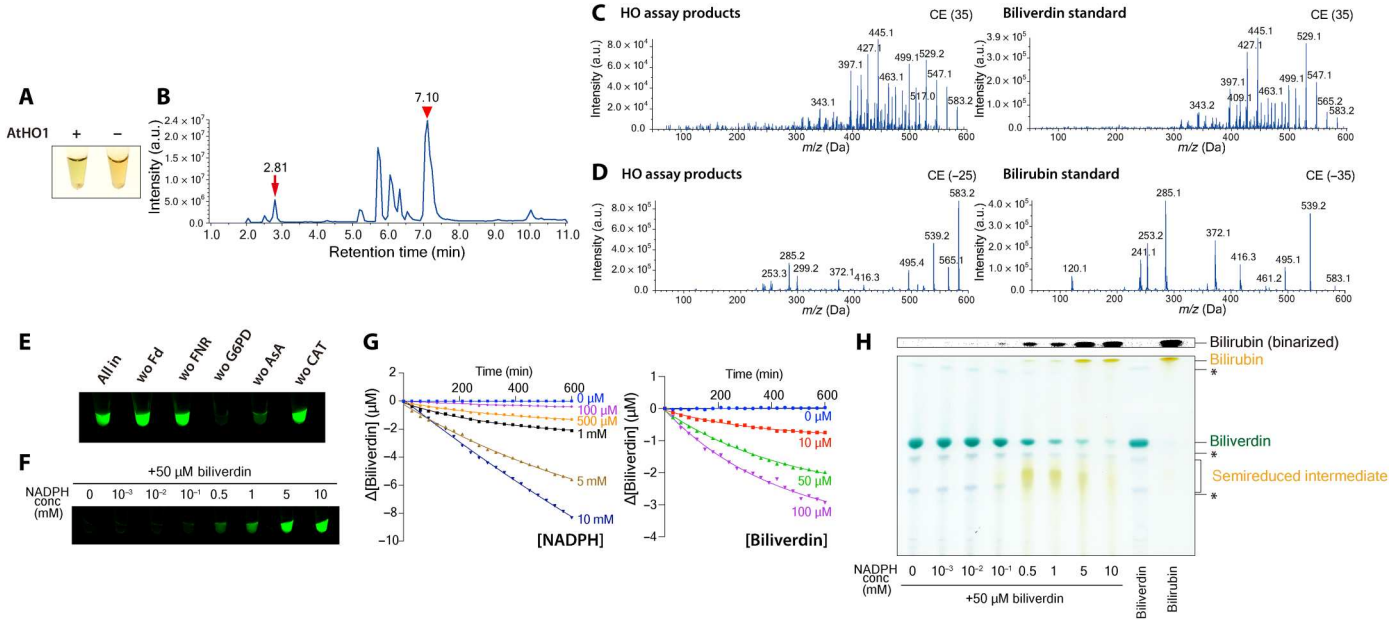

Fig. 2. Bilirubin is converted from biliverdin nonenzymatically in the presence of high concentrations of NADPH. (**A** to **D**) In vitro heme oxygenase assay using recombinant AtHO1. (A) Reaction mixtures with recombinant AtHO1 (+AtHO1) or buffer (−AtHO1). (B) to (D) Mass spectrometry detection of biliverdin and bilirubin from the reaction products of the heme oxygenase assay. (B) TIC of the reaction products. The arrow at 2.81 min and the arrowhead at 7.10 min indicate peaks with a product ion mass spectrum matching that of the biliverdin standard (C) and bilirubin standard (D), respectively. (C) and (D) Product ion mass spectra derived from the precursor ion [M-H] + [mass/charge ratio (*m/z*) 583.1] (C) and [M-H] − (*m/z* 583.1) (D) were detected in positive or negative ion mode with the indicated collision energies (CEs) (left, reaction products; right, biliverdin and bilirubin standards). (**E** to **H**) Nonenzymatic production of bilirubin from biliverdin and NADPH. (E) Biliverdin was mixed with the materials required for heme oxygenase assay other than hemin and AtHO1 (all-in) or without the indicated materials [ferredoxin (Fd), ferredoxin-NADP$^+$ reductase (FNR), G6PD, sodium ascorbate (AsA), and catalase (CAT)]. Bilirubin production was detected by the addition of recombinant apoUnaG. (F) Biliverdin (50 μM) was incubated with a series of concentrations of NADPH, and bilirubin production was detected by the addition of recombinant apoUnaG. (G) Time course of bilirubin production, measured at various concentrations of NADPH (with 50 μM biliverdin) or biliverdin (with 1 mM NADPH). (H) Thin-layer chromatography analysis of reaction products that were incubated with biliverdin and various concentrations of NADPH. Asterisks indicate biliverdin isomers. Top: A binarized image obtained by extracting yellow colors at the spot position of bilirubin IXα using Fiji software.

D), but Arabidopsis seedlings grown in the dark for 24 hours showed increased bilirubin concentrations in leaves compared to light-grown seedlings (Fig. 4A). In mesophyll cells, chloroplast bilirubin levels were 9.1 times higher after 24 hours in the dark compared to those of light-grown seedlings (Fig. 4B). However, plastid bilirubin levels did not significantly change in root epidermal cells of dark-treated seedlings after 24 hours. As bilirubin has antioxidant properties in mammals (*5*–*7*), we hypothesized that, under moderate light conditions, bilirubin is degraded by reactive oxygen species (ROS) generated by photosynthesis faster than it is produced. To investigate the ROS scavenging activity of bilirubin, we examined ROS accumulation in *N. benthamiana* leaves in which chloroplast bilirubin accumulation was elevated by the heterologous expression of a plastid-targeted version of rat (*Rattus rattus*) biliverdin reductase A (*TP-BVRA*; fig. S2), an enzyme that catalyzes the reduction of biliverdin to bilirubin (*9*). *TP-BVRA* expression increased the chloroplast bilirubin pool relative to that seen in plants expressing *TP-tagRFP* (Fig. 4, C and D). Previous studies have shown that stable expression of *BVRA* affects photosynthesis (*9*, *10*), but this transient *BVRA* expression did not affect photosynthetic efficiency (fig. S3). To analyze ROS levels, we used the ROS indicator 2′,7′-dichlorodihydrofluorescein diacetate (H_2DCFDA), which becomes fluorescent when it is oxidized in the presence of cellular ROS after the acetate groups are removed by intracellular esterases. Confocal microscopy revealed that TP-BVRA accumulation decreases H_2DCFDA fluorescence in chloroplasts compared to control leaves expressing *TP-tagRFP* (Fig. 4E). Quantification of H_2DCFDA fluorescence intensity in chloroplasts showed that the accumulation of TP-BVRA significantly lowers ROS levels (Fig. 4F), suggesting that the production of bilirubin diminishes chloroplast ROS levels. Therefore, we propose that bilirubin is constantly degraded in chloroplasts under light conditions by reacting with ROS generated by photosynthesis.

DISCUSSION

This study provides evidence that bilirubin, believed to be an animal pigment, is produced from biliverdin in plants nonenzymatically. Since we detected bilirubin in the early-diverging land plant *M. polymorpha* as well as the angiosperms *N. benthamiana* and Arabidopsis (Fig. 1A), we propose that almost all land plants, including crops, probably produce bilirubin. Our findings also revise the generally accepted pathway for heme degradation of plants (Fig. 5).

The NADPH-mediated nonenzymatic conversion of biliverdin described here appears to be kinetically slower than the biliverdin reductase–mediated reaction in mammals. Considering the physiological differences between animals and plants, we posit two potential reasons for the nonenzymatic bilirubin production in plants.

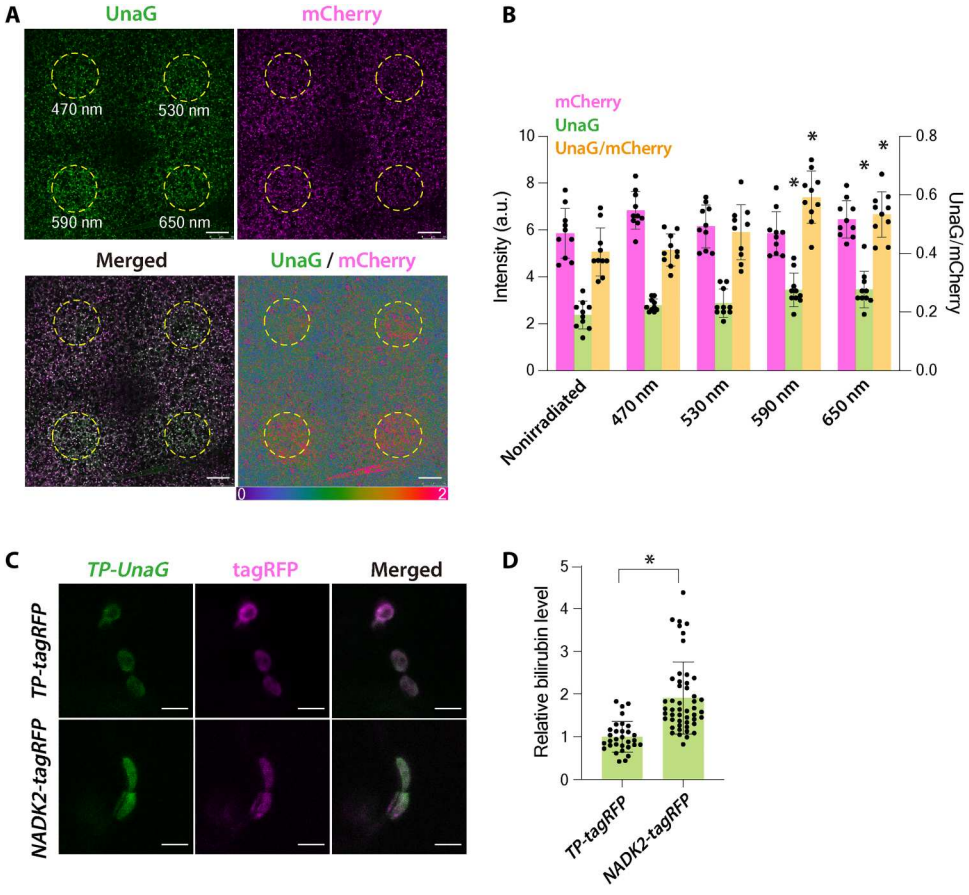

Fig. 3. Increase in NADPH levels by *NADK2* overexpression or red light irradiation promotes bilirubin production. (**A** and **B**) High light irradiation increases bilirubin accumulation. (A) Eleven-day-old *TP-mCherry-UnaG*–expressing Arabidopsis true leaves were irradiated with a 470-, 530-, 590-, or 650-nm laser. The areas surrounded by the yellow dashed lines were irradiated intermittently for 2 hours. Scale bars, 50 μm. (B) Quantification of UnaG and mCherry fluorescence intensities and the UnaG/mCherry ratio in (A). Data are means ± SD ($n = 10$); *$P < 0.01$, using Dunnett's multiple comparisons test. (**C** and **D**) Enhanced bilirubin accumulation upon the expression of Arabidopsis *NADK2* cloned in-frame with *tagRFP* (*NADK2-tagRFP*). (C) Confocal microscopy images of *N. benthamiana* cells transiently expressing *TP-UnaG* and *TP-tagRFP* or *NADK2-tagRFP*. Epidermal cells were observed 3 days after Agrobacterium-mediated infiltration. Scale bars, 5 μm. (D) Quantification of plastid bilirubin levels in *N. benthamiana* cells shown in (C). Plastid bilirubin levels in the cells coexpressing *TP-UnaG* and *TP-tagRFP* were set to 1. Data are means ± SD ($n = 31$ for *TP-mCherry-UnaG* and $n = 49$ for *TP-tagRFP*); *$P < 0.01$, using two-tailed Student's *t* test.

First, plants catabolize much less heme than animals. In adult humans, 375 mg of heme, which corresponds to approximately 10 nmol/g, is degraded each day (*16*), mainly due to hemoglobin turnover associated with oxygen transport in the blood. By contrast, the unbound heme content in aerial tissues of 3-week-old Arabidopsis plants was estimated to be 0.75 nmol/g of fresh weight (*11*). Even if all heme were degraded in 1 day, the amount of degraded heme by body mass in plants would be approximately $^1/_{10}$ that of humans. Therefore, plants may simply not need a high-speed heme degradation system comparable to that of animals. Second, NADPH concentrations in plant cells are higher than in animal cells. The NADPH concentration in animal cells is estimated to be 3 μM in the cytoplasm and 37 μM in mitochondria (*21*). By contrast, NADPH concentrations in the chloroplast stroma are estimated to be 0.29 to 0.5 mM (*22*, *23*). This high NADPH concentration probably enables nonenzymatic production of bilirubin with a relatively high reaction rate. On the basis of our results, we estimate that biliverdin is degraded at approximately 0.27 μM/hour when 50 μM biliverdin is incubated with 0.5 mM NADPH (Fig. 2G). In human cell cultures, the rate of bilirubin production, which is primarily mediated by BVRA, is estimated to be a few micromolars per hour (*30*), indicating that the estimated bilirubin production rate in plant cells is not much slower than that in mammal cells. This reaction rate would be further increased if NADPH and biliverdin were concentrated in subdomains within the chloroplast. Ferredoxin transfers electrons generated by photosystem I to $NADP^+$, resulting in NADPH production, but ferredoxin is also required as an electron donor for heme oxygenase activity (*25*). The production of biliverdin and NADPH therefore increases simultaneously when photosystem I is activated. On the thylakoid membrane, where photosystem I is located, higher concentrations of biliverdin and NADPH than those mentioned above may occur locally, resulting in higher bilirubin production rates than our estimation.

We propose that nonenzymatic bilirubin production in plants temporarily stores and mitigates excess reducing power (Fig. 5). Plants contain photosystem I, a system that produces NADPH using absorbed light energy, since they consume a large amount of NADPH for CO_2 assimilation and photorespiration under light

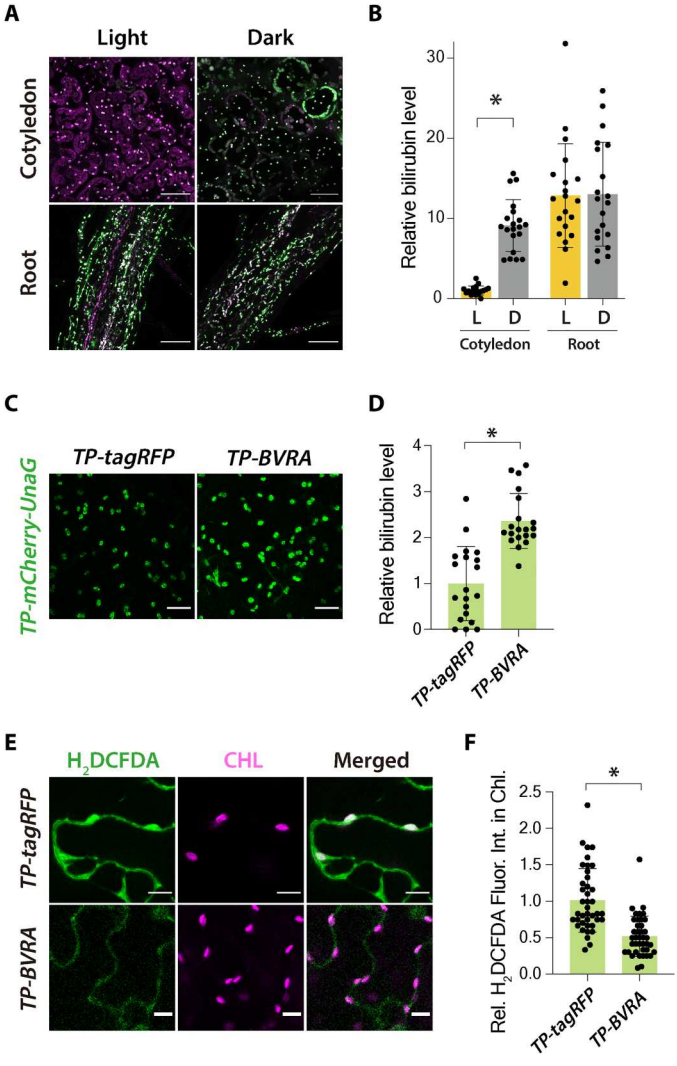

Fig. 4. Bilirubin production decreases ROS accumulation in chloroplasts. (**A**) UnaG and mCherry fluorescence in cotyledons and the root elongation zone from 7-day-old Arabidopsis seedlings expressing *TP-mCherry-UnaG* exposed to light or darkness for 24 hours. Scale bars, 50 μm. (**B**) Quantification of plastid bilirubin levels in cotyledon mesophyll cells and root epidermal cells in (A). Plastid bilirubin levels in the cotyledons of light-grown seedlings were set to 1. L, light. D, dark. Data are means ± SD (n = 20); *P < 0.01, using two-tailed Student's t test. (**C** to **F**) ROS accumulation in *N. benthamiana* leaves transiently expressing *TP-tagRFP* or *TP-BVRA*. (C) *TP-mCherry-UnaG* and *TP-tagRFP* or *TP-BVRA* were coexpressed in *N. benthamiana* leaves. Scale bars, 25 μm. (D) Quantification of chloroplast bilirubin levels. Data are means ± SD (n = 20). An asterisk indicates significant difference from the TP-tagRFP, *P < 0.01, two-tailed Student's t test. (E) Epidermal cells stained with 50 μM of the ROS indicator H_2DCFDA. Scale bars, 10 μm. (F) Quantification of H_2DCFDA fluorescence intensity in chloroplasts. The mean value of *TP-tagRFP*–expressing leaves was set to 1. Data are means ± SD (n = 30); the asterisk indicates significant difference from *TP-tagRFP*, *P < 0.01, two-tailed Student's t test.

conditions. However, when exposed to high-intensity light, an excess of NADPH is produced and the electrons that can no longer be received by $NADP^+$ are transferred to oxygen instead, causing the generation of ROS. Biliverdin may act as a reservoir of excess reducing power, attenuating photosystem I–mediated increases in NADPH levels while producing bilirubin as a potent antioxidant. This idea is consistent with the transient increase in bilirubin accumulation seen upon exposure to high-intensity light (Fig. 3, A and B). Bilirubin accumulated even in the dark, when photosynthesis is stopped and chloroplast NADPH consumption is low (Fig. 4, A and B). This bilirubin is likely derived from NADPH synthesized from the pentose phosphorylation pathway and may serve as a reservoir of reducing power for the regulation of ROS levels during photosynthesis. The ROS scavenging function of bilirubin in plant cells was suggested by the lower chloroplast ROS levels observed when bilirubin production was promoted by ectopic *BVRA* expression (Fig. 4, C to F). The bilirubin level calculated based on UnaG fluorescence intensity approximately doubled upon *BVRA* expression, while the ROS level was approximately halved, suggesting that bilirubin is a potent antioxidant. This notion is compatible with the removal of a 10,000-fold molar excess of H_2O_2 by bilirubin in human cells (*31*, *32*). However, we cannot conclude that the decrease in ROS levels is solely due to the effect of bilirubin because the animal enzyme BVRA was ectopically expressed in chloroplasts. One concern is that BVRA functions as a transcription factor in addition to bilirubin production, as reported previously for animal cells (*33*). Although BVRA is unlikely to function as a transcription factor in the present study because BVRA was targeted to the chloroplasts, the possibility of exhibiting side effects, such as binding to the chloroplast genome, cannot be denied. Furthermore, our results seem to be inconsistent with several papers suggesting that biliverdin, which is produced as a result of increased heme oxygenase expression, plays a protective role against oxidative stress in plants (*34*–*37*). The nonenzymatic production of bilirubin revealed in the present study points out that the antioxidative activity seen in the previous studies may include the effect of bilirubin. On the other hand, biliverdin also exhibits antioxidant activity in animal cells, although at a lower level than that of bilirubin (*38*). Increased heme oxygenase expression may provide resistance to oxidative stress through the combined antioxidant effects of biliverdin and bilirubin.

Recent studies revealed that bilirubin functions in signal transduction and regulation of metabolism as a hormone-like substance in animals (*39*, *40*). Similarly, in plants, the heme degradation pathway involves retrograde signaling from the chloroplast to the nucleus (*41*). Heme and bilin pigments produced by the heme degradation are generally thought to regulate photosynthetic gene expression as signaling molecules (*42*, *43*). Furthermore, ROS produced in photosynthesis also function as retrograde signaling molecules (*44*–*46*). Bilirubin and/or bilirubin-regulated ROS may function as retrograde signaling molecules or have hormone-like effects in plant cells similar to those seen in animals.

Cells contain a mixture of chemical substances, including unstable molecules, and nonenzymatic reactions are thought to occur everywhere. Furthermore, plants grow in an environment exposed to fluctuating light, whose energy frequently induces nonenzymatic reactions. Gene expression changes, which take tens of minutes to several hours, are not sufficient to respond to the constantly changing light environment. Plants may use a variety of nonenzymatic

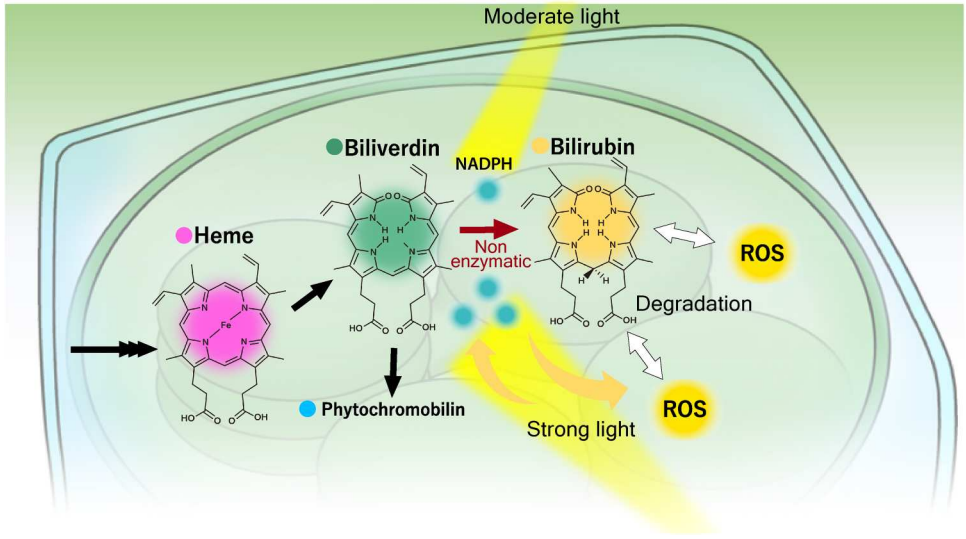

Fig. 5. The bilirubin production pathway and its physiological functions. The conversion of heme to biliverdin is catalyzed by heme oxygenases, while the conversion of biliverdin to phytochromobilin is catalyzed by phytochromobilin synthase (black arrows). Biliverdin reacts nonenzymatically with NADPH and is converted to bilirubin (brown arrows). An excess of NADPH is produced upon the exposure to high-intensity light, and ROS and biliverdin production are accelerated (yellow arrows). Bilirubin may contribute to the maintenance of the redox status in chloroplasts by reacting with excessive NADPH generated under high light and by reacting with ROS generated by photosynthesis (white arrows).

reactions to buffer the effect of fluctuating environments. However, there are few cases in which the physiological roles of these nonenzymatic reactions have been elucidated due to the difficulty of genetic analysis and in vivo experiments. Using a bilirubin biosensor called UnaG, we found that bilirubin is produced nonenzymatically in plants and maintains the redox status of chloroplasts. Further research with new perspectives and approaches is needed to elucidate additional physiologically important nonenzymatic reactions that have yet to be found in plants.

MATERIALS AND METHODS

Plant materials and growth conditions

We used Arabidopsis (*A. thaliana*) accession Columbia-0 (Col-0; CS60000) as the WT. Mutant lines were obtained from the Arabidopsis Biological Resource Center (*hy1-100*, CS236; *hy2-1*, CS2068). Arabidopsis seeds were surface sterilized and sown on Murashige and Skoog (MS) medium with 0.5% (w/v) gellan gum and 1% (w/v) sucrose. Arabidopsis seedlings were grown under continuous light (fluorescent tubes, 25 μmol m^{-2} s^{-1}) at 22°C and were transferred to vermiculite 11 days after sowing to set seeds. *N. benthamiana* plants were grown under a 16-hour light/8-hour dark photoperiod at 25°C. *M. polymorpha* plants (Takaragaike-1) were grown as previously reported (*47*).

Plasmid construction and transformation

All primers used for plasmid construction are listed in table S1. Unless otherwise noted, polymerase chain reaction (PCR)–amplified DNA fragments and a synthetic DNA fragment were cloned into the pENTR1a vector (Invitrogen) at the Sal I and Eco RV sites using the In-Fusion HD Cloning Kit (Clontech) according to the manufacturer's instructions. For the cloning of *TP-mCherry-UnaG*, DNA fragments that encode the N-terminal transit peptide (79 amino acids) from Rbcs1A (*48*) were amplified by PCR using Col-0 genomic DNA as a template. Genomic DNA was extracted from Col-0 with the DNeasy Plant Mini Kit (QIAGEN) according to the manufacturer's instructions. The PCR products were joined with the fragments encoding mCherry-UnaG, which was amplified from pcDNA3-mCherry-UnaG, by recombinant PCR. For the cloning of *TP-UnaG*, a linear pENTR1A-TP-UnaG fragment was amplified by inverse PCR using pENTR1A-TP-mCherry-UnaG as a template and circularized using the In-Fusion HD Cloning Kit. The *TP-UnaG-FLAG* fragment was amplified from pENTR1A-TP-UnaG. The synthetic DNA fragment encoding TP-BVRA was designed according to a previous study (*49*) and prepared as a synthetic double-stranded DNA (Integrated DNA Technologies; fig. S3). For the cloning of *NADK2*, the full-length coding sequence of *NADK2* (*29*) was amplified by PCR using Col-0 cDNA as a template. For the cloning of *TP-tagRFP*, the fragment encoding the N-terminal transit peptide of Rbcs1A and the *tagRFP* fragment amplified from the pGWB459 vector (*50*) were joined by recombinant PCR. The *TP-mCherry-UnaG* fragments cloned in pENTR1A were recombined into the pGWB602 binary vector, which was designed to express the cloned genes under the control of the cauliflower mosaic virus 35*S* promoter (*50*), using the Gateway LR reaction (Invitrogen). Transgenic Arabidopsis plants were generated using the floral dip method (*51*). The *TP-UnaG-FLAG*, *TP-BVRA*, and *TP-tagRFP* fragments were transferred to the pGWB511 binary vector (*50*), which expresses the cloned genes as a C-terminal FLAG-tagged fusion protein driven by the 35*S* promoter. The *NADK2* fragment was transferred to the pGWB560 binary vector (*50*), which expresses the cloned genes as a C-terminal tagRFP-tagged fusion protein driven by the 35*S* promoter. For particle bombardment, the *TP-UnaG* fragment was transferred to the pGWT35S vector, which places the cloned gene under the control of the 35*S* promoter (*52*), using the Gateway LR reaction. For the preparation of recombinant protein, *UnaG* fragments were amplified from pcDNA3-mCherry-UnaG and cloned into pDONR207

using the Gateway BP reaction (Invitrogen). A DNA fragment encoding amino acids 51 to 231 of AtHO1 was amplified from Arabidopsis cDNA (*26*) and cloned into the pENTR1a vector. Total RNA extraction and reverse transcription were performed according to a previous study (*53*). The *UnaG* and *AtHO1* fragments were transferred to the pDEST17 vector (Invitrogen), which is designed to express the cloned genes as a 6×His-tag fusion protein in *Escherichia coli*, using the LR reaction.

Transient expression by particle bombardment and agroinfiltration

pGWT35S-TP-UnaG was delivered into *N. benthamiana*, Arabidopsis, and *M. polymorpha* by particle bombardment according to previously published protocols with minor modifications (*54*). True leaves of 4-week-old *N. benthamiana* plants or 11-day-old Arabidopsis seedlings were placed on top of plates containing 0.4% (w/v) agarose and bombarded using 650 and 900 psi of rupture discs, respectively. One-day-old gemmalings of *M. polymorpha* growing on the medium were bombarded using 900 psi of rupture discs (*55*). All samples were visualized by confocal microscopy 24 hours after bombardment. For agroinfiltration, Agrobacterium (*Rhizobium radiobacter*) strain GV2260 harboring pGWB602-TP-UnaG, pGWB602-TP-mCherry-UnaG, pGWB560-NADK2, pGWB511-TP-UnaG-FLAG, pGWB511-TP-BVRA, or pGWB511-TP-tagRFP was cultured, and the cells were collected by centrifugation and resuspended in pure water to a final optical density of 1.0 at 600 nm. Single or mixed Agrobacterium cultures were infiltrated into true leaves of 4-week-old *N. benthamiana*. The leaves were used for experiments 2 or 3 days after infiltration.

Immunopurification of holoUnaG from plant cells

About 1 g of *N. benthamiana* leaves infiltrated with pure water or Agrobacterium cells harboring pGWB511-TP-UnaG-FLAG was collected. All subsequent procedures were performed at 4°C. The leaves were ground in a mortar and pestle with 5 ml of 1× phosphate-buffered saline (PBS; pH 7.4). The homogenate was filtered through two layers of Miracloth (Merck) and centrifuged at 3000*g* for 10 min. The supernatant was mixed with 100 μl of anti-DYKDDDDK (FLAG) tag antibody beads (Wako) and rotated for 5 hours. The mixture was transferred to a Poly-Prep Chromatography Column (Bio-Rad) to trap the affinity beads, which were subsequently washed twice with 5 ml of 1× PBS. The affinity beads were resuspended in 150 μl of 1× PBS, and UnaG florescence was observed under blue light. Further analysis was performed with UnaG bound to the affinity beads. Immunoblot analysis was carried out as described previously using an anti-DYKDDDDK (FLAG) antibody (Wako) and an anti-mouse antibody (Thermo Fisher Scientific) (*56*). Fluorescence excitation and emission spectra of ipUnaG were acquired using an F-2700 fluorescence spectrophotometer (Hitachi).

Recombinant protein preparation

The recombinant proteins 6×His-tagged UnaG and AtHO1 were purified using the QIAexpress Ni-NTA Protein Purification System (QIAGEN). The pDEST17-UnaG and pDEST17-AtHO1 plasmids were transformed into *E. coli* BL21-AI (Invitrogen). The *E. coli* cells harboring each plasmid were cultured in LB medium at 37°C to an optical density at 600 nm of 0.4, and the production of UnaG was induced by the addition of 20% (w/v) D-(−)-arabinose (final concentration of 0.1%, w/v). After cultivation at 16°C for 24 hours, the cells were pelleted and resuspended in 1× tris-buffered saline (TBS) [20 mM tris-HCl (pH 7.9) and 500 mM NaCl]. The resuspended cells were sonicated on ice (SONIFIER 250, Branson) and centrifuged at 12,000*g* at 4°C for 15 min. Only when purifying recombinant holoUnaG (holorcUnaG) was a solution of bilirubin (Wako) added to the supernatant to a final concentration of 100 μM for holoUnaG formation. The supernatant was mixed with Ni-NTA Agarose (QIAGEN) and rotated at 4°C for 30 min. The mixture was transferred to a Poly-Prep Chromatography Column to trap the agarose resin and subsequently washed twice with five bed volumes of 1× TBS. The recombinant proteins were eluted from the resin by adding elution buffer [20 mM tris-HCl (pH 7.9), 500 mM NaCl, and 1 M imidazole] and buffer exchanged by PD-10 gel filtration column (Cytiva) for further experiments [1× PBS for apoUnaG and holorcUnaG or 100 mM potassium phosphate buffer (pH 7.2) for AtHO1]. Fluorescence excitation and emission spectra of holorcUnaG were acquired using an F-2700 fluorescence spectrophotometer (Hitachi).

In vitro heme oxygenase assay

An in vitro heme oxygenase assay was performed according to a previous study (*25*, *26*). The following reagents were mixed and incubated at 25°C for 8 hours in a final volume of 100 μl: 5 μM recombinant AtHO1, 40 μM hemin (Tokyo Chemical Industry, catalog no. H0008), bovine serum albumin (60 μg/ml; Merck, catalog no. A9647), 4.6 μM ferredoxin (Merck, catalog no. F5875), ferredoxin-$NADP^+$ reductase (0.025 U/ml; Merck, catalog no. F0628), 10 μM catalase (Merck, catalog no. 219261), 6.5 mM glucose-6-phosphate (Merck, catalog no. 10127647001), G6PD (Merck, catalog no. G7877), 0.82 mM $NADP^+$ (Wako, catalog no. 308-50463), and 5 mM sodium ascorbate (Tokyo Chemical Industry, catalog no. A0539). These reagents were dissolved in 100 mM potassium phosphate buffer (pH 7.2) or DMSO according to the previous study (*26*). The reactions were stopped and their proteins removed by mixing water (reaction solution), methanol, and chloroform to a 0.9:1:1 ratio. Following centrifugation at 13,000*g* for 5 min, the upper layer was collected, dried, and then dissolved in 10 μl of DMSO. In Fig. 2E, biliverdin was added in place of AtHO1, hemin, and the indicated enzymes or coenzyme. The reaction products were mixed with an equal volume of 10 μM apoUnaG, and UnaG florescence was observed under blue light.

Nonenzymatic reaction of biliverdin and NADPH in vitro

Biliverdin (Toronto Research Chemicals, catalog no. B386400) and NADPH (Wako Chemicals, catalog no. 44332000) were dissolved in DMSO and 100 mM potassium phosphate buffer (pH 7.2) and then mixed in 100 mM potassium phosphate buffer (pH 7.2) at 25°C. After 8 hour incubation, the reaction products were mixed with an equal volume of 10 μM apoUnaG, and UnaG florescence was observed under blue light. Biliverdin degradation was monitored by absorbance at 620 nm with a Multiskan FC Microplate Reader (Thermo Fisher Scientific) at 25°C. The reaction product (250 μl) after 24-hour incubation was lyophilized and dissolved in 15 μl of chloroform:methanol (1:1). The bilirubin and biliverdin standards were diluted in chloroform:methanol (1:1). The samples and 10 nmol of commercial biliverdin and bilirubin were loaded onto Merck 60 F254-coated silica gel plates (0.25 mm in thickness) and separated in chloroform:methanol:water (65:25:3).

Confocal microscopy

Live-cell fluorescence imaging was performed with an SP8X confocal microscope system (Leica Microsystems) equipped with Fluotar VISIR 25× and HC PL APO CS 63× water-immersion lenses. Plant samples were mounted onto glass slides in pure water and topped with a coverslip. All images were taken in photon counting mode with the time-gating method (*57*). UnaG, mCherry, and H_2DCFDA were excited with 498-, 554-, and 484-nm lasers from the white light laser source and detected at 510 to 545, 565 to 636, and 494 to 545 nm by hybrid detectors, respectively. Chlorophyll autofluorescence was detected at 655 to 743 nm by a photomultiplier tube detector. Images were taken at 100 Hz/1024 × 1024 pixels in sequential scan mode. The *z*-projection images of Figs. 3A and 4A were reconstructed from *z*-stack images captured in 3.5-μm intervals. Three-dimensional (3D) images of Fig. 1F were reconstructed from *z*-stack images taken at 100 Hz/256 × 256 pixels in 0.35-μm intervals using 3D viewer in Leica Application Suite X software. Lasers were irradiated using a sequential scan between frames. In each frame, lasers of 470, 530, 590, or 650 nm with 15% intensity from the 70% power white light laser source were irradiated to the regions of interest. The lasers of four different wavelengths were irradiated at 400 Hz/512 × 512 pixels (1.295 s per frame) in turn for 2 hours.

Measurement of bilirubin levels

For the quantification of bilirubin levels or UnaG and mCherry fluorescence intensities, confocal images of UnaG and mCherry were taken at 100 Hz/1024 × 1024 pixels with the Fluotar VISIR 25× water-immersion lens. Each circular region of interest with 5 × 5 pixels was randomly set on the target plastids in different cells, and fluorescence intensities of UnaG and mCherry were measured with Fiji software (*58*). Bilirubin levels in *N. benthamiana* leaf epidermal cells were calculated as the mean value of UnaG fluorescence intensity. Bilirubin levels in epidermal cells of Arabidopsis were calculated with the following formula

$$\text{bilirubin level} = \frac{1}{n}\sum_{i=1}^{n}\left(x_i\frac{\overline{y}}{y_i}\right)$$

where x is UnaG fluorescence intensity, y is mCherry fluorescence intensity, and $\overline{y}$ is average mCherry fluorescence intensity.

For mesophyll cells, the following formula was used to normalize the fluorescence attenuation due to sample thickness

$$\text{bilirubin levels} = \frac{\overline{y}_{\text{epi}}}{\overline{y}}\left[\frac{1}{n}\sum_{i=1}^{n}\left(x_i\frac{\overline{y}}{y_i}\right)\right] = \frac{1}{n}\sum_{i=1}^{n}\left(x_i\frac{\overline{y}_{\text{epi}}}{y_i}\right)$$

where $\overline{y}_{\text{epi}}$ is average mCherry fluorescence intensity in the epidermis of cotyledons.

Investigation of the antioxidant function of bilirubin in planta

N. benthamiana leaves from the same position along the main stem were infiltrated with Agrobacterium cells harboring pGWB511-TP-BVRA or pGWB511-TP-tagRFP and analyzed 2 days after infiltration. The quantum yield photochemistry of photosystem II (F_v/F_m) was measured with a JUNIOR-PAM chlorophyll fluorometer (Walz). Measurements were made on the Agrobacterium-infiltrated leaves of three individual plants. The F_v/F_m values were measured at three points on a leaf, and the average value was used as single-sample data. Three leaf discs (5 mm in diameter) that were taken from the Agrobacterium-infiltrated leaves in three plants were immersed in 50 μM H_2DCFDA (Invitrogen) for 30 min by pressure infiltration with a syringe and subsequently washed with pure water. Fluorescence images were taken with a Leica SP8X as described above. H_2DCFDA fluorescence intensities in chloroplasts were measured with Fiji software.

Mass spectrometry analysis

Mass spectrometry analysis of proton adduct ions was performed with a triple quadrupole/linear ion trap instrument (LIT) (QTRAP5500, AB Sciex) with an electrospray source. MS and MS2 spectra were recorded in product ion scan mode using LIT. Ion source was maintained at 450°C with curtain gas at 30 psi, collisionally activated dissociation gas at 9 psi (12 psi for LIT), ion source gas at 80 psi, and ion source gas 2 at 70 psi. Ion spray voltage was set to 5000 V in positive ion mode and − 3500 V in negative ion mode. Declustering, entrance, and collision cell exit potentials were maintained at 60, 15, and 9 V, respectively. HPLC separation was performed on an ultrahigh-performance liquid chromatograph (Nexera X2, Shimadzu) equipped with a C8 column (YMC-Triart C8, ϕ 2.1 × 150 mm, 1.9 μm; YMC). The column oven temperature was maintained at 40°C. The mobile phase consisted of acetonitrile (solvent A) and water (solvent B), both of which contained 0.1% (v/v) acetic acid. HPLC separation was conducted with a linear gradient of 10% A (0 min) to 45% A (15 min) at a flow rate of 0.2 ml/min.

Supplementary Materials

This PDF file includes:

Figs. S1 to S3
Table S1

REFERENCES AND NOTES

1. D. Chiabrando, F. Vinchi, V. Fiorito, S. Mercurio, E. Tolosano, Heme in pathophysiology: A matter of scavenging, metabolism and trafficking across cell membranes. *Front. Pharmacol.* **5**, 61 (2014).
2. S. Kumar, U. Bandyopadhyay, Free heme toxicity and its detoxification systems in human. *Toxicol. Lett.* **157**, 175–188 (2005).
3. M. Shepherd, A. E. Medlock, H. A. Dailey, Porphyrin metabolism, in *Encyclopedia of Biological Chemistry: Second Edition* (Elsevier, 2013), vol. 60, pp. 544–549.
4. R. K. Kutty, M. D. Maines, Purification and characterization of biliverdin reductase from rat liver. *J. Biol. Chem.* **256**, 3956–3962 (1981).
5. S. Jangi, L. Otterbein, S. Robson, The molecular basis for the immunomodulatory activities of unconjugated bilirubin. *Int. J. Biochem. Cell Biol.* **45**, 2843–2851 (2013).
6. C. Mancuso, Bilirubin and brain: A pharmacological approach. *Neuropharmacology* **118**, 113–123 (2017).
7. Q. Yao, X. Jiang, L. Kou, A. T. Samuriwo, H.-L. Xu, Y.-Z. Zhao, Pharmacological actions and therapeutic potentials of bilirubin in islet transplantation for the treatment of diabetes. *Pharmacol. Res.* **145**, 104256 (2019).
8. T. Kohchi, K. Mukougawa, N. Frankenberg, M. Masuda, A. Yokota, J. C. Lagarias, The Arabidopsis *HY2* gene encodes phytochromobilin synthase, a ferredoxin-dependent biliverdin reductase. *Plant Cell* **13**, 425–436 (2001).
9. D. M. Lagarias, M. W. Crepeau, M. D. Maines, J. C. Lagarias, Regulation of photomorphogenesis by expression of mammalian biliverdin reductase in transgenic Arabidopsis plants. *Plant Cell* **9**, 675–688 (1997).
10. B. L. Montgomery, K. A. Franklin, M. J. Terry, B. Thomas, S. D. Jackson, M. W. Crepeau, J. C. Lagarias, Biliverdin reductase-induced phytochrome chromophore deficiency in transgenic tobacco. *Plant Physiol.* **125**, 266–277 (2001).

11. N. A. Espinas, K. Kobayashi, S. Takahashi, N. Mochizuki, T. Masuda, Evaluation of unbound free heme in plant cells by differential acetone extraction. *Plant Cell Physiol.* **53**, 1344–1354 (2012).
12. J. C. Lagarias, H. Rapoport, Chromopeptides from phytochrome. The structure and linkage of the PR form of the phytochrome chromophore. *J. Am. Chem. Soc.* **102**, 4821–4828 (1980).
13. R. A. Sharrock, T. Clack, Patterns of expression and normalized levels of the five Arabidopsis phytochromes. *Plant Physiol.* **130**, 442–456 (2002).
14. C. Pirone, J. V. Johnson, J. M. E. Quirke, H. A. Priestap, D. Lee, Bilirubin present in diverse angiosperms. *AoB Plants* **2010**, 785–788 (2010).
15. C. Pirone, J. V. Johnson, J. M. E. Quirke, H. A. Priestap, D. Lee, The animal pigment bilirubin identified in *Strelitzia reginae*, the bird of paradise flower. *HortScience* **45**, 1411–1415 (2010).
16. E. Nagababu, J. M. Rifkind, Heme degradation by reactive oxygen species. *Antioxid. Redox Signal.* **6**, 967–978 (2004).
17. M. A. Keller, G. Piedrafita, M. Ralser, The widespread role of non-enzymatic reactions in cellular metabolism. *Curr. Opin. Biotechnol.* **34**, 153–161 (2015).
18. S. Nam, V. Renganathan, Non-enzymatic reduction of azo dyes by NADH. *Chemosphere* **40**, 351–357 (2000).
19. C. Dupuy, J. Kaniewski, R. Ohayon, D. Dème, A. Virion, J. Pommier, Nonenzymatic NADPH-dependent reduction of 2,6-dichlorophenol-indophenol. *Anal. Biochem.* **191**, 16–20 (1990).
20. A. Kumagai, R. Ando, H. Miyatake, P. Greimel, T. Kobayashi, Y. Hirabayashi, T. Shimogori, A. Miyawaki, A bilirubin-inducible fluorescent protein from eel muscle. *Cell* **153**, 1602–1611 (2013).
21. R. Tao, Y. Zhao, H. Chu, A. Wang, J. Zhu, X. Chen, Y. Zou, M. Shi, R. Liu, N. Su, J. Du, H.-M. Zhou, L. Zhu, X. Qian, H. Liu, J. Loscalzo, Y. Yang, Genetically encoded fluorescent sensors reveal dynamic regulation of NADPH metabolism. *Nat. Methods* **14**, 720–728 (2017).
22. U. Takahama, M. Shimizu-Takahama, U. Heber, The redox state of the NADP system in illuminated chloroplasts. *Biochim. Biophys. Acta Bioenerg.* **637**, 530–539 (1981).
23. D. Heineke, B. Riens, H. Grosse, P. Hoferichter, U. Peter, U. I. Flügge, H. W. Heldt, Redox transfer across the inner chloroplast envelope membrane. *Plant Physiol.* **95**, 1131–1137 (1991).
24. M. J. Terry, Phytochrome chromophore-deficient mutants. *Plant Cell Environ.* **20**, 740–745 (1997).
25. T. Muramoto, N. Tsurui, M. J. Terry, A. Yokota, T. Kohchi, Expression and biochemical properties of a ferredoxin-dependent heme oxygenase required for phytochrome chromophore synthesis. *Plant Physiol.* **130**, 1958–1966 (2002).
26. B. Gisk, Y. Yasui, T. Kohchi, N. Frankenberg-Dinkel, Characterization of the haem oxygenase protein family in *Arabidopsis thaliana* reveals a diversity of functions. *Biochem. J.* **425**, 425–434 (2010).
27. S.-L. Lim, C. P. Voon, X. Guan, Y. Yang, P. Gardeström, B. L. Lim, *In planta* study of photosynthesis and photorespiration using NADPH and NADH/NAD^+ fluorescent protein sensors. *Nat. Commun.* **11**, 3238 (2020).
28. K. J. McCree, The action spectrum, absorptance and quantum yield of photosynthesis in crop plants. *Agric. Meteorol.* **9**, 191–216 (1971).
29. H. Takahashi, K. Takahara, S. N. Hashida, T. Hirabayashi, T. Fujimori, M. Kawai-Yamada, T. Yamaya, S. Yanagisawa, H. Uchimiya, Pleiotropic modulation of carbon and nitrogen metabolism in Arabidopsis plants overexpressing the NAD kinase2 gene. *Plant Physiol.* **151**, 100–113 (2009).
30. T. Takeda, A. Mu, T. T. Tai, S. Kitajima, S. Taketani, Continuous *de novo* biosynthesis of haem and its rapid turnover to bilirubin are necessary for cytoprotection against cell damage. *Sci. Rep.* **5**, 10488 (2015).
31. D. E. Baranano, M. Rao, C. D. Ferris, S. H. Snyder, Biliverdin reductase: A major physiologic cytoprotectant. *Proc. Natl. Acad. Sci. U.S.A.* **99**, 16093–16098 (2002).
32. A. F. McDonagh, The biliverdin-bilirubin antioxidant cycle of cellular protection: Missing a wheel? *Free Radic. Biol. Med.* **49**, 814–820 (2010).
33. L. O'Brien, P. A. Hosick, K. John, D. E. Stec, T. D. Hinds, Biliverdin reductase isozymes in metabolism. *Trends Endocrinol. Metab.* **26**, 212–220 (2015).
34. Y.-H. Chen, Y.-Y. Chao, Y. Y. Hsu, C.-Y. Hong, C. H. Kao, Heme oxygenase is involved in nitric oxide- and auxin-induced lateral root formation in rice. *Plant Cell Rep.* **31**, 1085–1091 (2012).
35. G. O. Noriega, K. B. Balestrasse, A. Batlle, M. L. Tomaro, Heme oxygenase exerts a protective role against oxidative stress in soybean leaves. *Biochem. Biophys. Res. Commun.* **323**, 1003–1008 (2004).
36. Y. Y. Hsu, Y. Y. Chao, C. H. Kao, Biliverdin-promoted lateral root formation is mediated through heme oxygenase in rice. *Plant Signal. Behav.* **7**, 885–887 (2012).
37. K. B. Balestrasse, G. G. Yannarelli, G. O. Noriega, A. Batlle, M. L. Tomaro, Heme oxygenase and catalase gene expression in nodules and roots of soybean plants subjected to cadmium stress. *Biometals* **21**, 433–441 (2008).
38. T. Jansen, M. Hortmann, M. Oelze, B. Opitz, S. Steven, R. Schell, M. Knorr, S. Karbach, S. Schuhmacher, P. Wenzel, T. Münzel, A. Daiber, Conversion of biliverdin to bilirubin by biliverdin reductase contributes to endothelial cell protection by heme oxygenase-1-evidence for direct and indirect antioxidant actions of bilirubin. *J. Mol. Cell. Cardiol.* **49**, 186–195 (2010).
39. L. Vítek, C. Tiribelli, Bilirubin: The yellow hormone? *J. Hepatol.* **75**, 1485–1490 (2021).
40. J. F. Creeden, D. M. Gordon, D. E. Stec, T. D. Hinds Jr., Bilirubin as a metabolic hormone: The physiological relevance of low levels. *Am. J. Physiol. Endocrinol. Metab.* **320**, E191–E207 (2021).
41. R. H. Calderon, Å. Strand, How retrograde signaling is intertwined with the evolution of photosynthetic eukaryotes. *Curr. Opin. Plant Biol.* **63**, 102093 (2021).
42. D. Duanmu, D. Casero, R. M. Dent, S. Gallaher, W. Yang, N. C. Rockwell, S. S. Martin, M. Pellegrini, K. K. Niyogi, S. S. Merchant, A. R. Grossman, J. C. Lagarias, Retrograde bilin signaling enables *Chlamydomonas* greening and phototrophic survival. *Proc. Natl. Acad. Sci. U.S.A.* **110**, 3621–3626 (2013).
43. T. M. Wittkopp, S. Schmollinger, S. Saroussi, W. Hu, W. Zhang, Q. Fan, S. D. Gallaher, M. T. Leonard, E. Soubeyrand, G. J. Basset, S. S. Merchant, A. R. Grossman, D. Duanmu, J. C. Lagarias, Bilin-dependent photoacclimation in *Chlamydomonas reinhardtii*. *Plant Cell* **29**, 2711–2726 (2017).
44. S. Zhang, K. Apel, C. Kim, Singlet oxygen-mediated and EXECUTER-dependent signalling and acclimation of *Arabidopsis thaliana* exposed to light stress. *Philos. Trans. R. Soc. Lond. B Biol. Sci.* **369**, 20130227 (2014).
45. S. Munné-Bosch, Vitamin E function in stress sensing and signaling in plants. *Dev. Cell* **48**, 290–292 (2019).
46. F. Ramel, S. Birtic, C. Ginies, L. Soubigou-Taconnat, C. Triantaphylidès, M. Havaux, Carotenoid oxidation products are stress signals that mediate gene responses to singlet oxygen in plants. *Proc. Natl. Acad. Sci. U.S.A.* **109**, 5535–5540 (2012).
47. Y. Fujii, H. Tanaka, N. Konno, Y. Ogasawara, N. Hamashima, S. Tamura, S. Hasegawa, Y. Hayasaki, K. Okajima, Y. Kodama, Phototropin perceives temperature based on the lifetime of its photoactivated state. *Proc. Natl. Acad. Sci. U.S.A.* **114**, 9206–9211 (2017).
48. Y. Osaki, Y. Kodama, Particle bombardment and subcellular protein localization analysis in the aquatic plant *Egeria densa*. *PeerJ* **5**, e3779 (2017).
49. B. L. Montgomery, K. C. Yeh, M. W. Crepeau, J. C. Lagarias, Modification of distinct aspects of photomorphogenesis via targeted expression of mammalian biliverdin reductase in transgenic Arabidopsis plants. *Plant Physiol.* **121**, 629–640 (1999).
50. T. Nakagawa, T. Suzuki, S. Murata, S. Nakamura, T. Hino, K. Maeo, R. Tabata, T. Kawai, K. Tanaka, Y. Niwa, Y. Watanabe, K. Nakamura, T. Kimura, S. Ishiguro, Improved gateway binary vectors: High-performance vectors for creation of fusion constructs in transgenic analysis of plants. *Biosci. Biotechnol. Biochem.* **71**, 2095–2100 (2007).
51. S. J. Clough, A. F. Bent, Floral dip: A simplified method for *Agrobacterium*-mediated transformation of *Arabidopsis thaliana*. *Plant J.* **16**, 735–743 (1998).
52. Y. Fujii, A. Yoshimura, Y. Kodama, A novel orange-colored bimolecular fluorescence complementation (BiFC) assay using monomeric Kusabira-Orange protein. *Biotechniques* **64**, 153–161 (2018).
53. K. Ishikawa, K. Tamura, Y. Fukao, T. Shimada, Structural and functional relationships between plasmodesmata and plant endoplasmic reticulum-plasma membrane contact sites consisting of three synaptotagmins. *New Phytol.* **226**, 798–808 (2020).
54. T. Muranaka, M. Okada, J. Yomo, S. Kubota, T. Oyama, Characterisation of circadian rhythms of various duckweeds. *Plant Biol.* **17**, 66–74 (2014).
55. R. Konno, H. Tanaka, Y. Kodama, SKLPT imaging: Efficient in vivo pre-evaluation of genome-editing modules using fluorescent protein with peroxisome targeting signal. *Biochem. Biophys. Res. Commun.* **503**, 235–241 (2018).
56. K. Ishikawa, C. Miura, K. Maejima, K. Komatsu, M. Hashimoto, T. Tomomitsu, M. Fukuoka, A. Yusa, Y. Yamaji, S. Namba, Nucleocapsid protein from fig mosaic virus forms cytoplasmic agglomerates that are hauled by endoplasmic reticulum streaming. *J. Virol.* **89**, 480–491 (2015).
57. Y. Kodama, Time gating of chloroplast autofluorescence allows clearer fluorescence imaging *in planta*. *PLOS ONE* **11**, e0152484 (2016).
58. J. Schindelin, I. Arganda-Carreras, E. Frise, V. Kaynig, M. Longair, T. Pietzsch, S. Preibisch, C. Rueden, S. Saalfeld, B. Schmid, J.-Y. Tinevez, D. J. White, V. Hartenstein, K. Eliceiri, P. Tomancak, A. Cardona, Fiji: An open-source platform for biological-image analysis. *Nat. Methods* **9**, 676–682 (2012).

Acknowledgments: We thank D. Inomata (Suana Science) for the illustrations; T. Kohchi (Kyoto University) for the kind gift of *M. polymorpha* plants (Takaragaike-1); T. Nakagawa (Shimane University) for the kind gift of pGWB vectors; T. Shinomura (Teikyo University), K. Toyooka

(Riken), T. Morohoshi (Utsunomiya University), and T. Suzuki (Utsunomiya University) for valuable discussions; and members of Y.K.'s laboratory for support. **Funding:** This work was supported by Japan Science and Technology Agency Exploratory Research for Advanced Technology program JPMJER1602 (to K.N. and Y.K.) and MEXT KAKENHI 20H05905 (to Y.K.).
Author contributions: Conceptualization: K.I., A.M., K.N., and Y.K. Methodology: K.I. and X.X. Investigation: K.I., X.X., Y.O., and Y.K. Visualization: K.I. Funding acquisition: K.N. and Y.K. Project administration: K.N. and Y.K. Supervision: A.M., K.N., and Y.K. Writing: K.I. and Y.K.. **Competing interests:** A.M. is an inventor of patents JP 6674687, US 9957308, and EP 2963115 granted by RIKEN that cover the creation and use of UnaG. The other authors declare that they have no competing interests. **Data and materials availability:** All data needed to evaluate the conclusions in the paper are present in the paper and/or the Supplementary Materials. The plasmid DNA containing UnaG (UnaG/pcDNA3-FLAG) is available from the RIKEN Bio-Resource Center under a material transfer agreement with RIKEN (https://dnaconda.riken.jp/search/RDB_clone/RDB15/RDB15703.html). The plasmids used in this study can be provided by Addgene pending scientific review and a completed material transfer agreement. Requests for the plasmids should be submitted to Addgene or to the corresponding author (Y.K.).

Submitted 6 March 2023
Accepted 1 May 2023
Published 7 June 2023
10.1126/sciadv.adh4787

VIROLOGY

Human SAMD9 is a poxvirus-activatable anticodon nuclease inhibiting codon-specific protein synthesis

Fushun Zhang[1], Quanquan Ji[2], Juhi Chaturvedi[3], Marisol Morales[1], Yuanhui Mao[2], Xiangzhi Meng[1], Leiming Dong[2], Junpeng Deng[3], Shu-Bing Qian[2]*, Yan Xiang[1]*

As a defense strategy against viruses or competitors, some microbes use anticodon nucleases (ACNases) to deplete essential tRNAs, effectively halting global protein synthesis. However, this mechanism has not been observed in multicellular eukaryotes. Here, we report that human SAMD9 is an ACNase that specifically cleaves phenylalanine tRNA ($tRNA^{Phe}$), resulting in codon-specific ribosomal pausing and stress signaling. While SAMD9 ACNase activity is normally latent in cells, it can be activated by poxvirus infection or rendered constitutively active by SAMD9 mutations associated with various human disorders, revealing $tRNA^{Phe}$ depletion as an antiviral mechanism and a pathogenic condition in SAMD9 disorders. We identified the N-terminal effector domain of SAMD9 as the ACNase, with substrate specificity primarily determined by a eukaryotic $tRNA^{Phe}$–specific 2′-*O*-methylation at the wobble position, making virtually all eukaryotic $tRNA^{Phe}$ susceptible to SAMD9 cleavage. Notably, the structure and substrate specificity of SAMD9 ACNase differ from known microbial ACNases, suggesting convergent evolution of a common immune defense strategy targeting tRNAs.

INTRODUCTION

Transfer RNAs (tRNAs) are one of the most conserved components of protein synthesis machinery. They are also a major target for protein toxins used by microbes to impede virus infection, mitigate cellular stress, or eliminate competing organisms (*1*). Many tRNA-targeting protein toxins are anticodon nucleases (ACNases) that cleave at the anticodon stem loops (ASLs), leading to depletion of specific tRNAs from cellular pools and a block in protein synthesis. Notable examples of ACNases include *Escherichia coli* PrrC, which is activated upon T4 phage infection and serves as an innate defense against phages (*2*), and *E. coli* Colicin E5 (*1*) and *Kluyveromyces lactis* γ-toxin (*3*), which are secreted from producing cells to arrest growth of competing bacterial or yeast cells. tRNA cleavage is also associated with some stress responses in eukaryotic cells (*4*), but the cleavage does not substantially reduce cellular tRNA pools, and no tRNA-depleting ACNases have been reported for multicellular eukaryotes.

In vertebrate animals, interferon-regulated innate immune system serves as the first line of defense against viruses, and innate antiviral factors can pose as host restriction factors that block the replication of certain groups of viruses. A paralogous pair of mammalian interferon-stimulated gene products, sterile alpha motif domain–containing 9 (SAMD9) and SAMD9-like (SAMD9L) (SAMD9/9L), are potent restriction factors for poxviruses (*5*–*7*), a family of DNA viruses that include monkeypox virus and vaccinia virus (VACV). Conversely, mammalian poxviruses have evolved multiple inhibitors of SAMD9/9L (*5*, *6*, *8*, *9*), without which they would fail to replicate in mammalian cells due to a block in protein synthesis (*10*–*12*). In addition to their antiviral activities, SAMD9/9L also have antiproliferative activities. Germline mutations in SAMD9/9L cause a range of human diseases, including around 10% of the inherited bone marrow failure syndromes (*13*, *14*) and several rare multisystem disorders (*15*–*17*). The mutations are mostly missense mutations that result in a gain of function (GoF) in inhibition of cell proliferation (*14*, *15*) and protein synthesis (*18*–*20*).

SAMD9/9L are ubiquitously expressed cytosolic proteins with a predicted domain architecture (*21*) resembling that of the STAND (signal transduction adenosine triphosphatases with numerous associated domains) (*22*) superfamily of immune sensors, which includes the nucleotide-binding oligomerization domain (NOD)–like receptors (*23*). STAND proteins share a conserved tripartite domain architecture, consisting of a C-terminal sensor that recognizes danger- or pathogen-associated molecular patterns (PAMPs), a central NOD that mediates the formation of a supramolecular complex, and an N-terminal effector that is allosterically activated to exert the downstream effect. Consistently, an N-terminal effector domain was recently identified in SAMD9/9L, and its functions were found to be closely linked to its ability to bind double-stranded nucleic acid (dsNA) in vitro (*18*). In this study, we found how SAMD9/9L inhibit viral replication and protein synthesis with the effector domain, which unexpectedly shares a functional connection with microbial ACNases.

RESULTS

FTSJ1-mediated 2′-*O*-methylation of tRNA wobble position is critical for host restriction of VACV

SAMD9, WD repeat domain 6 (WDR6), and FtsJ RNA 2′-*O*-methyltransferase 1 (FTSJ1) were previously identified by a human genome-wide RNA interference screen (*6*) and subsequently confirmed with individual gene knockout in HeLa cells (*11*), as host restriction factors for a VACV mutant that lacks two viral SAMD9/9L inhibitors (*7*) (referred to as $vK1^{-}C7^{-}$). However, how they are connected in restricting VACV was unknown. FTSJ1 is an RNA

[1]Department of Microbiology, Immunology and Molecular Genetics, University of Texas Health Science Center at San Antonio, 7703 Floyd Curl Drive, San Antonio, TX 78229, USA. [2]Division of Nutritional Sciences, Cornell University, Ithaca, NY 14853, USA. [3]Department of Biochemistry and Molecular Biology, Oklahoma State University, 246 Noble Research Center, Stillwater, OK 74078, USA.
*Corresponding author. Email: xiangy@uthscsa.edu (Y.X.); sq38@cornell.edu (S.-B. Q.)

methyltransferase that interacts separately with thyroid adenoma-associated protein (THADA) and WDR6 to install 2′-*O*-ribose methylation at positions 32 and 34 of certain tRNA species (*24*), respectively. The coidentification of WDR6 but not THADA from the same genome-wide screen suggests that tRNA methylation at position 34 is important for the host restriction. To test this idea, we knocked out *FTSJ1* from HeLa cells and reconstituted the *FTSJ1* KO cells (ΔFTSJ1) with a Dox-inducible *FTSJ1* allele. As expected, FTSJ1-deficient cells failed to restrict vK1^{-}C7^{-}. Induction of *FTSJ1*–wild type (WT) expression to different levels restored the restriction in a dose-dependent manner (Fig. 1A). By contrast, *FTSJ1* with K28A or A26P mutation failed to restore the restriction (Fig. 1B). The K28A mutation of the catalytic site completely inactivates the methyltransferase activity, while the A26P mutation specifically disrupts methylation at position 34 but leaves methylation at position 32 intact (*25*). These results indicate that 2′-*O*-methylation at position 34—the wobble position of the anticodon—is critical for host restriction of vK1^{-}C7^{-}.

SAMD9 is a VACV-activatable endoribonuclease with an exquisite specificity for 2′-*O*-methylated tRNA^{Phe}

In human cells, tRNA^{Phe}, tryptophan tRNA (tRNA^{Trp}), and leucine tRNA with CAA anticodon (tRNA$^{Leu(CAA)}$) are known to be methylated at position 34 by FTSJ1 (*26*, *27*). Among them, tRNA^{Phe} has been identified as the most biologically important substrate for FTSJ1 across eukaryotes (*26*, *28*). We thus focused on tRNA^{Phe} to decipher the functional connection between SAMD9 and FTSJ1/WDR6 in host restriction of vK1^{-}C7^{-}. We infected WT and ΔFTSJ1 HeLa cells with vK1^{-}C7^{-} and analyzed tRNA^{Phe} by Northern blot (Fig. 1C). In WT HeLa cells, tRNA^{Phe} level decreased continuously during the first few hours of infection, reaching a steady state of ~40 to 50% of the original level by 4 to 6 hours postinfection (hpi). Two tRNA^{Phe} fragments appeared at 2 hpi when full-length (FL) tRNA^{Phe} level was still relatively high, suggesting that tRNA^{Phe} was cleaved into two fragments before being completely degraded. The degradation only requires the early phase of viral replication, as it was not affected when replication was blocked at genome replication by cytosine arabinoside (AraC). In ΔFTSJ1 cells, tRNA^{Phe} level was also reduced after vK1^{-}C7^{-} infection, but the degree of reduction was relatively small. tRNA^{Phe} was not degraded in HeLa cells after WT VACV infection or in SAMD9 and SAMD9L KO (ΔSAMD9&L) cells after vK1^{-}C7^{-} infection (shown later), indicating that SAMD9 or SAMD9L is required for the degradation.

We recently identified an effector domain in SAMD9/9L that binds to dsNAs (*18*). Given that tRNA is highly structured and contains many ds regions, we reasoned that this effector domain was responsible for degrading tRNA^{Phe}. The incubation of recombinant SAMD9$^{134–385}$ protein with total RNA from HeLa cells produced two distinct RNA fragments, which were abundant enough to be visualized with only nucleic acid staining (Fig. 1C). Northern blot identified the large [~50 nucleotides (nt)] and the small (~30 nt) fragments to be 3′ and 5′ end of tRNA^{Phe}, respectively. They were identical in size to the two tRNA^{Phe} fragments transiently present in infected cells. With increasing incubation time, an increasing amount of tRNA^{Phe} was cleaved by SAMD9$^{134–385}$, but the cleavage products were not degraded (Fig. 1D), suggesting that further degradation of tRNA fragments in infected cells is likely mediated by a separate exonuclease. Notably, tRNA$^{Leu(CAA)}$ as well as six other tRNAs that we specifically tested for were not cleaved by SAMD9$^{134–385}$ or degraded in cells infected with vK1^{-}C7^{-} (Fig. 1C and fig. S1). SAMD9$^{134–385}$ did not cleave tRNA^{Phe} from ΔFTSJ1 cells under our in vitro assay condition (Fig. 1E), indicating that tRNA 2′-*O*-methylation is critical for substrate specificity. Because of its unique specificity for 2′-*O*-methylated tRNA^{Phe}, we named the SAMD9 effector domain (SAMD9$^{134–385}$) tRNA ribonuclease (tRNase) SA (for SAMD9/9L).

tRNA binding and active site of tRNase SA

We previously solved the crystal structure of SAMD9$^{156–385}$ in complex with DNA and identified a dsNA binding site that is essential for antiviral and antiproliferative activities of SAMD9 (Fig. 2A) (*18*). With a gel mobility shift assay, we found that tRNase SA formed a stable complex with purified yeast tRNA^{Phe}, and the binding is mediated by the previously identified dsNA binding residues, including K198, K214, and R221. Specifically, K198E, K214E, and R221E mutations abolished, while K350E and K242E mutations reduced the binding (Fig. 2B). Consistently, these mutations affected the cleavage of human tRNA^{Phe} by tRNase SA to different degrees (Fig. 2C).

We found that a divalent cation is required for tRNase SA cleavage of tRNA^{Phe}. While Mn^{2+} is preferred over Mg^{2+}, Ca^{2+} and Zn^{2+} do not support the cleavage of tRNA^{Phe} (Fig. 2D). This rather stringent selection of divalent cation is a characteristic of nucleases that use two metal ions, coordinated by acidic residues, for catalysis (*29*). Upon close examination of the structure of SAMD9$^{156–385}$/dsDNA complex, we identified a cluster of conserved acidic residues on the protein's surface near the dsNA binding site (Fig. 2A and fig. S2A). To investigate whether this cluster could represent the active site, we performed mutagenesis studies on these residues. In SAMD9, D345A substitution had no significant effect on its antiviral activity against VACV, while D192A partially reduced the antiviral activity (Fig. 2E). Furthermore, E184A, E196A, E218A, and D241A substitutions resulted in complete loss of the antiviral activity (Fig. 2E), indicating that these four acidic residues are essential for SAMD9 function. Recombinant SAMD9$^{156–385}$ proteins with E184A, E196A, E218A, or D241A substitutions could be purified similarly to the WT version and exhibited comparable binding to yeast tRNA^{Phe} (Fig. 2B), suggesting that the mutations do not affect protein folding. However, the mutations abolished the cleavage of human tRNA^{Phe} (Fig. 2C). These data collectively support the idea that E184, E196, E218, and D241 serve as the active site residues for tRNase SA in SAMD9.

tRNase SA targets the ASL with a 2′-*O*-methylguanosine

While tRNase SA forms a stable complex with yeast tRNA^{Phe} at 4°C with no sign of cleavage (Fig. 2B), we found that it cleaves yeast tRNA^{Phe} at 37°C (fig. S3A). To identify the cleavage site, we isolated the cleavage products and determined their molecular weights (MWs) by mass spectrometry (fig. S3A). This analysis revealed that SAMD9$^{134–385}$ cleaves between nucleotides 31 and 32, producing termini with 5′-phosphate and 3′-OH. We next examined the cleavage products using total RNAs from HeLa cells. Only the small cleavage product was purified with sufficient quantity for MW determination, and it belongs to the first 31 nucleotides of human tRNA^{Phe} with a 3′-OH (fig. S3A). Therefore, tRNase SA specifically cleaves tRNA^{Phe} among the numerous RNA species in human cells by targeting the same cleavage site as that of yeast

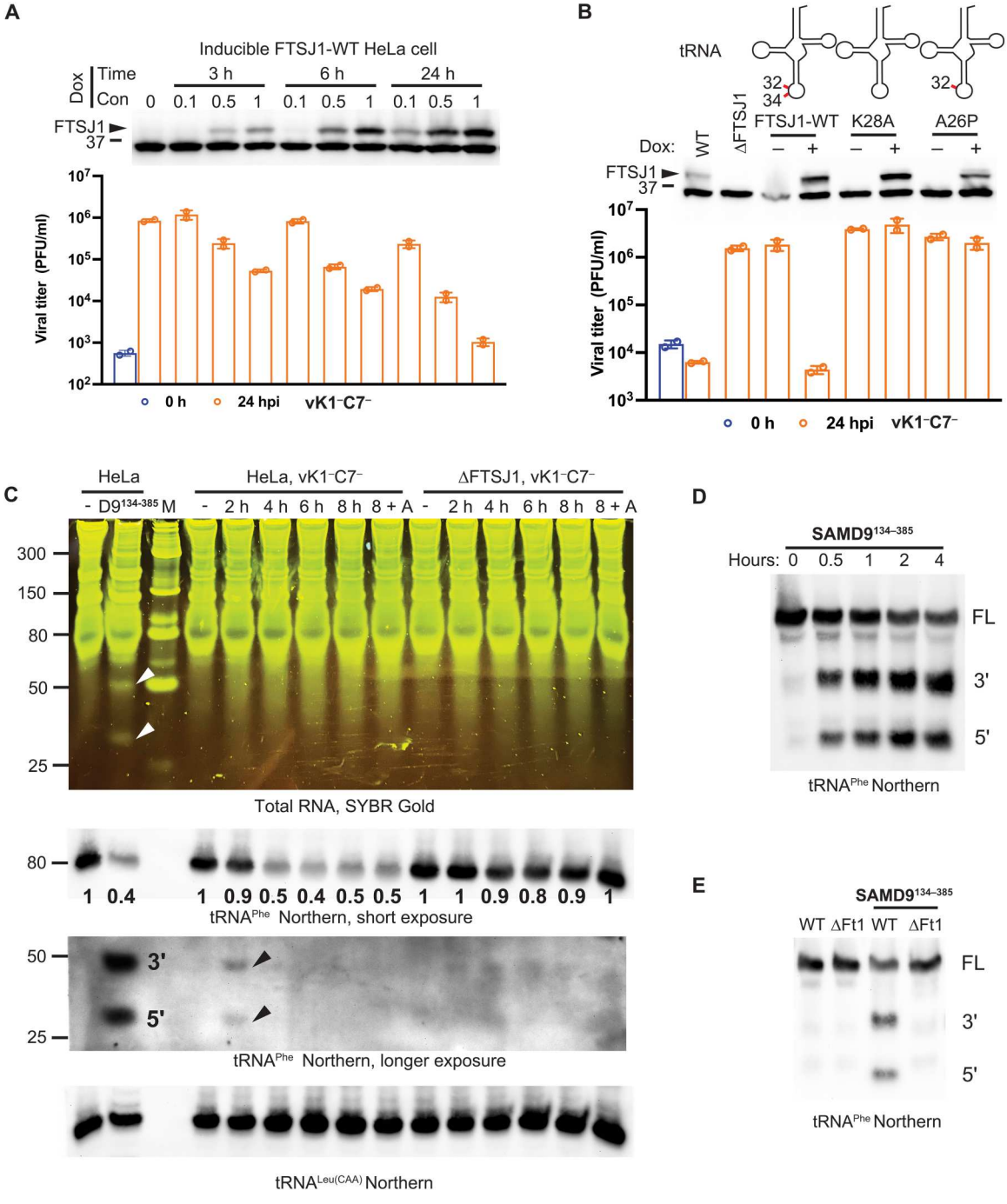

Fig. 1. SAMD9 is a VACV-activatable endoribonuclease specifically targeting tRNA^{Phe}. (**A**) HeLa cells with a Dox-inducible *FTSJ1*–wild type (WT) allele were induced to express different amount of FTSJ1 with varied Dox concentrations (0.1 to 1 μg/ml) for various time (3 to 24 hours). The FTSJ1 protein (arrowhead) and a nonspecific protein were detected by the anti-FTSJ1 antibody. The position of the 37-kDa molecular weight (MW) marker is shown. The abilities of the cells to restrict a SAMD9-sensitive mutant VACV (vK1^{-}C7^{-}) were determined by measuring the viral titers [plaque-forming units (PFU) per milliliter] at 0 and 24 hours postinfection (hpi) with plaque assays on Vero cells. (**B**) HeLa cells were engineered to express no FSTJ1 (ΔFTSJ1) or different FTSJ1 mutants under a Dox-inducible promoter. FTSJ1-K28A mutant is catalytically inactive, while FTSJ1-A26P mutant is defective of methylating at position 34 of certain tRNAs. 2′-*O*-methylations are indicated by the red lines in the tRNA schematics. (**C**) WT and ΔFTSJ1 HeLa cells were infected with vK1^{-}C7^{-} for the indicated time (2 to 8 hours). 8 + A, infection for 8 hours in the presence of cytosine arabinoside (AraC). Separately, total RNAs from uninfected HeLa cells were incubated with recombinant SAMD9$^{134–385}$ protein. RNAs resolved on a denaturing gel were stained with SYBR Gold. Lane M contains an RNA ladder, the sizes of which (in bases) are indicated on the left. Northern blots were performed with two probes complementary to 5′ or 3′ end of tRNA^{Phe} or one probe complementary to 3′ end of tRNA$^{Leu(CAA)}$. Numbers below the gel are relative band intensities with respect to that in uninfected cells. Black or white arrowheads point to the tRNA^{Phe} cleavage products. (**D**) Total RNAs from HeLa cells were incubated with SAMD9$^{134–385}$ protein for the indicated time (0.5 to 4 hours). FL, full-length tRNA. (**E**) Total RNAs from HeLa (WT) or ΔFTSJ1 (ΔFt1) cells were incubated with SAMD9$^{134–385}$ protein for 1 hour.

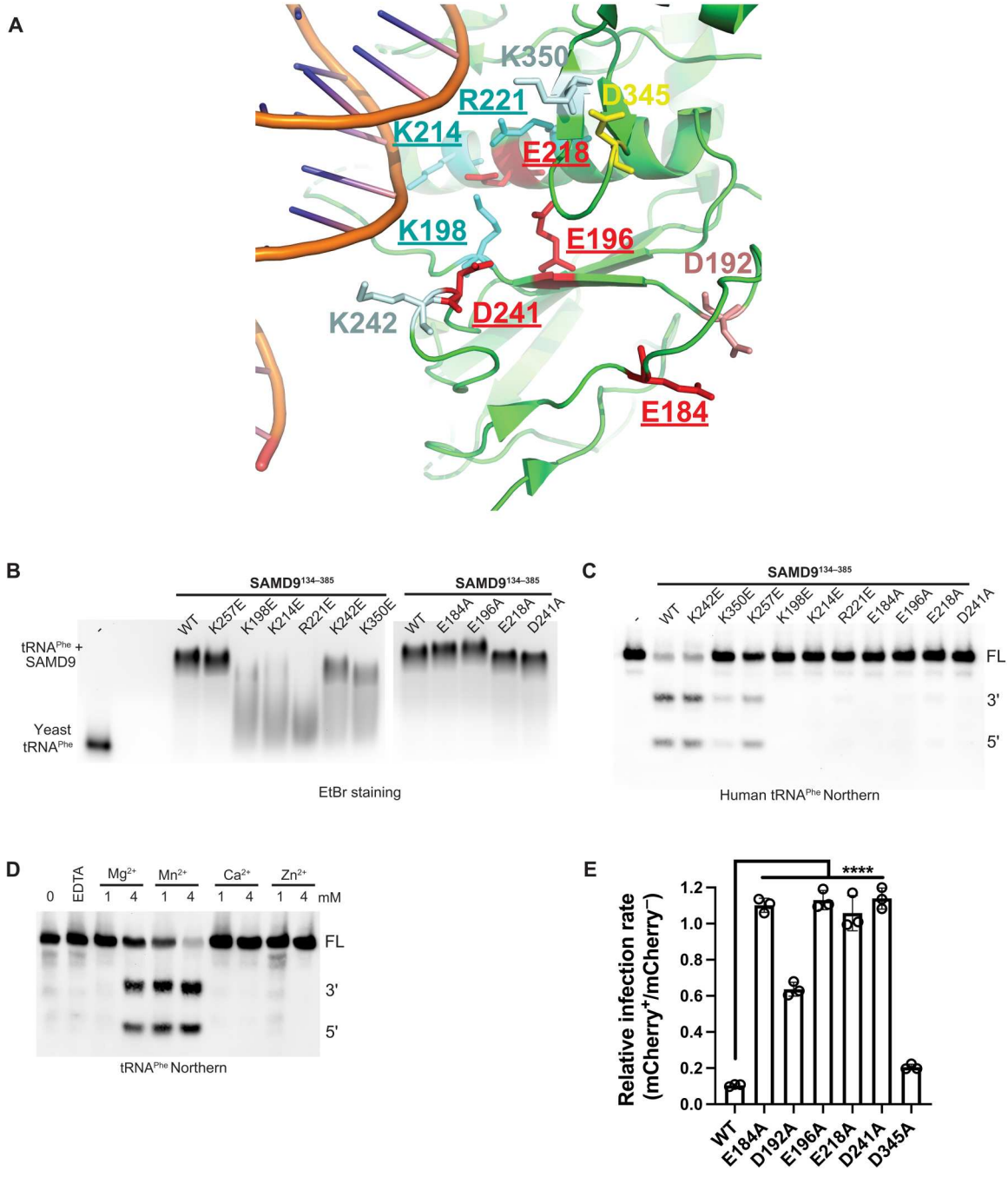

Fig. 2. tRNA binding and active site of SAMD9$^{134–385}$. (**A**) Part of the crystal structure of SAMD9$^{156–385}$/DNA complex (Protein Data Bank, 7ksp) is shown with residues that have been targeted for mutagenesis depicted. Residues that are essential for SAMD9$^{134–385}$ cleavage of tRNA^{Phe} are underlined with putative binding and active site residues colored in cyan and red, respectively. (**B**) Effects of the mutations on SAMD9$^{134–385}$ binding of yeast tRNA^{Phe} in a gel mobility shift assay. Purified SAMD9$^{134–385}$ proteins were incubated with yeast tRNA^{Phe} at 2:1 molar ratio and ran on an agarose gel. Ethidium bromide (EtBr)–stained gel is shown. (**C**) Effects of the mutations on SAMD9$^{134–385}$ cleavage of human tRNA^{Phe}. Total RNAs from HeLa cells were incubated with SAMD9$^{134–385}$ protein for 1 hour. tRNA^{Phe} fragments were detected by Northern blot. (**D**) Divalent cation requirements for SAMD9$^{134–385}$ activities. Total RNAs from HeLa cells were incubated with SAMD9$^{134–385}$ in the presence of the indicated concentrations (1 or 4 mM) of cations for 1 hour. tRNA^{Phe} fragments were detected by Northern blot. FL, full-length tRNA. (**E**) The effect of the mutations on SAMD9 antiviral activities. Human embryonic kidney (HEK) 293T cells were transfected with mCherry-SAMD9 fusions for 36 hours and infected with vK1^{-}C7^{-}/GFP^{+} for 15 hours. Infection rates (GFP^{+}%) among SAMD9-expressing and nontransfected control cells from the same culture well were simultaneously determined with flow cytometry. Relative infection rates between SAMD9-expressing and nontransfected cells are derived from the flow cytometry data shown in fig. S2B. Statistics: one-way ANOVA compared to the WT (****$P <$ 0.0001).

tRNA^{Phe}, which is the phosphodiester 5′ to the first nucleotides of the anticodon loop.

To determine the tRNase SA substrate specificity, we focused initially on regions conserved between human and yeast tRNA^{Phe}, which include the D arm and most of the anticodon arm (fig. S3A). tRNase SA efficiently cleaved a 38-nt synthetic RNA, containing only the D arm, the anticodon arm, and the variable loop, at the phosphodiester 5′ to the anticodon loop (Fig. 3A). The 3′ cleavage product was readily degraded by yeast exonuclease Xrn-1 (Fig. 3B), confirming that it has the 5′ monophosphate, which is required for Xrn-1 degradation. Deletion of the variable loop or base substitutions of the anticodon stem or the last two positions of the anticodon did not affect the cleavage efficiency or the cleavage site (fig. S3B). Last, a 17-nt synthetic RNA containing only the anticodon arm was found to be efficiently cleaved at 5′ to the anticodon loop (fig. S3C). Notably, these RNAs were all synthesized with 2′-*O*-methylation at the wobble position but lack all other modifications in human tRNA^{Phe} (fig. S3A).

We further assessed the substrate specificity of tRNase SA using additional synthetic variants of the 17-nt RNA. The absence of 2′-*O*-methylation at the wobble position greatly reduced cleavage, even if the position corresponding to tRNA^{Phe} C32 was 2′-*O*-methylated (Fig. 3C). A 17-nt linear RNA incapable of forming a stem was not cleaved, while a 13-nt RNA forming just a stem of 3 base pairs (bp) was cleaved (Fig. 3D). Substituting the wobble base with pyrimidines greatly reduced cleavage, while substituting its adjacent position with any bases had no negative impact (Fig. 3E). Unlike metal-independent RNases (*29*), 2′-OH immediate 5′ to the scissile phosphodiester was not required for the cleavage, but substituting ribose with deoxyribose in the stem or the loop abolished the cleavage (fig. S3F). These and additional results in fig. S3 (E and F) collectively showed that tRNase SA cleaves an RNA stem loop with the feature shown in Fig. 3F: (i) a loop of 7 or 8 nt and a stem of at least 3 bp, (ii) a pyrimidine base at the first position of the loop, and (iii) a 2′-*O*-methylated purine base at the third position of the loop (corresponding to wobble position). The substrate specificity of tRNase SA therefore fully explains the exquisite specificity of SAMD9 on tRNA^{Phe} and the requirement of FTSJ1 for SAMD9 activity, as tRNA^{Phe} is the only tRNA that is known to have the 2′-*O*-methylated purine at position 34. Other eukaryotic tRNAs known or suspected to be methylated by FTSJ1 at position 34, including tRNA$^{Trp(CCA)}$ and tRNA$^{Leu(CAA)}$, have a pyrimidine base at the wobble position.

To further delineate the boundary of the tRNase SA domain, we tested a more compact domain of SAMD9, SAMD9$^{156–385}$, which removes 22 amino acids from the N terminus of SAMD9$^{134–385}$. In addition, to expand our study to SAMD9L, we expressed and purified the corresponding fragment of SAMD9L, SAMD9L$^{158–388}$. Both SAMD9$^{156–385}$ and SAMD9L$^{158–388}$ cleaved the natural tRNA^{Phe} and the 38-nt synthetic substrate (fig. S3, G to I).

SAMD9 depletes cellular tRNA^{Phe} and causes codon-specific ribosomal pausing

To comprehensively evaluate the effect of SAMD9 on intracellular tRNAs, we used a modified tRNA sequencing approach to quantify tRNA levels in cells infected with VACV. Relative to cells infected with WT VACV, vK1$^-$C7$^-$ infection markedly reduced the level of tRNA^{Phe} by nearly 10-fold, but not other tRNAs (Fig. 4A and fig. S4A). We next conducted ribosome profiling [ribosome sequencing (Ribo-seq)] to determine the impact of tRNA^{Phe} depletion on global protein synthesis. With superior 3-nt periodicity of ribosome footprints, ribosome positions can be determined with high precision as evidenced by prominent peaks at start and stop codons (fig. S4B). We calculated the A-site ribosome occupancy at individual codons by averaging the read density from the entire transcriptome. This analysis revealed a marked increase in the read density at two Phe codons UUU (~3.6-fold) and UUC (~2.6-fold) that are decoded by the single tRNA^{Phe}, in cells infected with vK1$^-$C7$^-$, relative to that in cells infected with WT VACV or uninfected cells (fig. S4D). To avoid the cascading effect of viral replication on cell physiology and to synchronize WT and vK1$^-$C7$^-$ VACV replication at the early stage (fig. S5B), we repeated the experiments by conducting virus infection in the presence of AraC to block viral DNA replication. Under this condition, the elevated read density at both Phe codons became more prominent in cells infected with vK1$^-$C7$^-$ (~5.8-fold for UUU and ~3.6-fold for UUC) (Fig. 4B).

To substantiate this finding further, we performed additional studies on BT20 cells with Dox-inducible expression of WT SAMD9 or a GoF mutant SAMD9^{R1293W} that we characterized recently (*18*). Without virus infection, the expression of SAMD9^{R1293W}, but not WT SAMD9, decreased cellular tRNA^{Phe} level by ~50% with Northern blot analysis (Fig. 4C). The level of tRNA$^{Leu(CAA)}$ remained comparable, supporting the specificity of tRNA targeting by SAMD9. Furthermore, we tested additional GoF SAMD9/9L variants in 293T cells, including R982C and E1136Q of SAMD9, as well as W1180R and F886Lfs*11 of SAMD9L, by transient transfection in 293T cells. All the GoF variants that we tested depleted tRNA^{Phe} but had little effect on tRNA$^{Leu(CAA)}$ (fig. S4, E to H). A single substitution in the effector domain (R221E or R223E) that disrupted tRNA^{Phe} binding in vitro also prevented the GoF variants from depleting tRNA^{Phe}. Mutations of other tRNA binding residues and the putative catalytic site also prevented SAMD9^{R982C} from depleting tRNA^{Phe} (fig. S4E).

We performed Ribo-seq analysis on BT20 cells with Dox-inducible expression of SAMD9^{R1293W}. The two Phe codons UUU and UUC showed a marked increase of read density at the A-site (~8.6- and 5.3-fold, respectively) upon Dox treatment (Fig. 4D). Similar to vK1$^-$C7$^-$ infection, the pausing at the UUU codon was greater than at the UUC codon, presumably because the relatively weaker binding affinity of the UUU codon with tRNA^{Phe}, due to the non–Watson-Crick U:G base pairing at the wobble position, makes it more vulnerable to tRNA^{Phe} depletion.

Activated SAMD9 triggers ribotoxic stress

To find out the common signaling cascade downstream of SAMD9 activation, we performed transcriptome analysis on the infected HeLa cells and compared it to previous results from a GoF SAMD9 variant (Fig. 5A and fig. S5A). SAMD9^{R1293W} was previously shown to significantly induce 41 genes that are mostly associated with proteotoxic stress response (*18*). Nine of the 41 genes were also induced by more than fourfold in response to infection by vK1$^-$C7$^-$ but not by WT VACV (Fig. 5A). Among the nine genes, activating transcription factor 3 (ATF3) was induced the most with an increase of >60-fold. This was validated by reverse transcription quantitative polymerase chain reaction (RT-qPCR) analysis, which additionally showed that the ATF3 induction in infected cells requires SAMD9 and partially requires FTSJ1 (Fig. 5B).

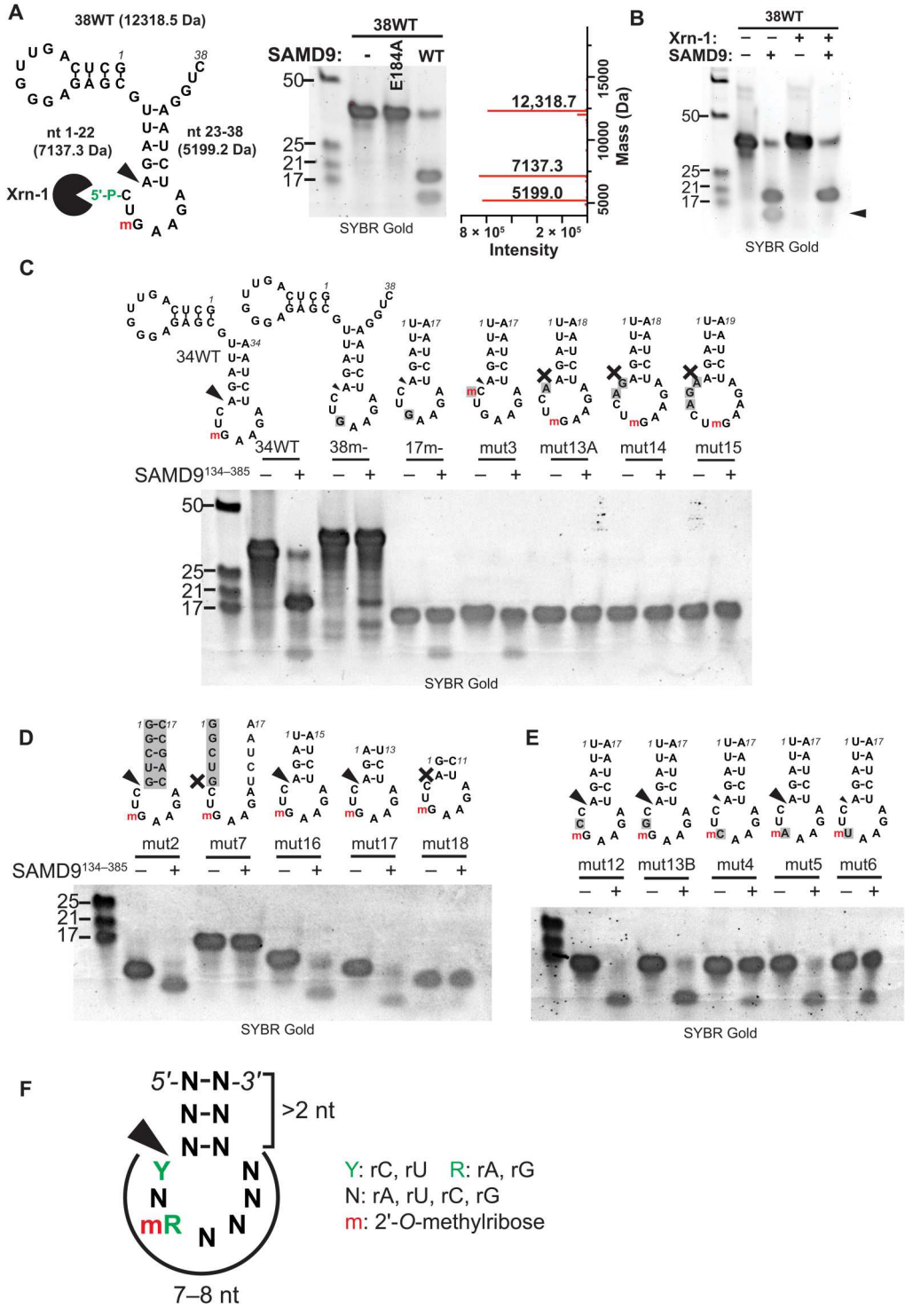

Fig. 3. SAMD9$^{134–385}$ is an ACNase with a specificity for the eukaryotic tRNA^{Phe}. (**A**) A 38-nt synthetic RNA with the depicted secondary structure was incubated with SAMD9$^{134–385}$ (WT or E184A) for 1 hour. The black arrowhead points to the cleavage site. MWs of different fragments are listed. The Xrn-1 symbol indicates that the 3′ fragment can be degraded by Xrn-1. m, 2′-*O*-methylation. The cleavage products were resolved on a denaturing gel and visualized after SYBR Gold staining. The sizes of the RNA ladder (in bases) are shown on the left of the gel. The cleavage products were analyzed with electrospray ionization liquid chromatography mass spectroscopy. The relative intensity and the MWs of the RNA species are shown. (**B**) The cleavage reaction was performed in the absence or presence of Xrn-1. The black arrowhead points to the 3′ product that disappeared in the presence of Xrn-1. Note that the RNA was synthesized with a 5′-OH group. (**C** to **E**) Synthetic RNAs with the depicted sequences were incubated with SAMD9$^{134–385}$ for 1 hour. Sequences that differ from that of tRNA^{Phe} were shown in gray background. The size of the arrows reflects the relative cleavage efficiency. "X" indicates no cleavage. (**F**) The consensus RNA structure cleaved by SAMD9$^{134–385}$.

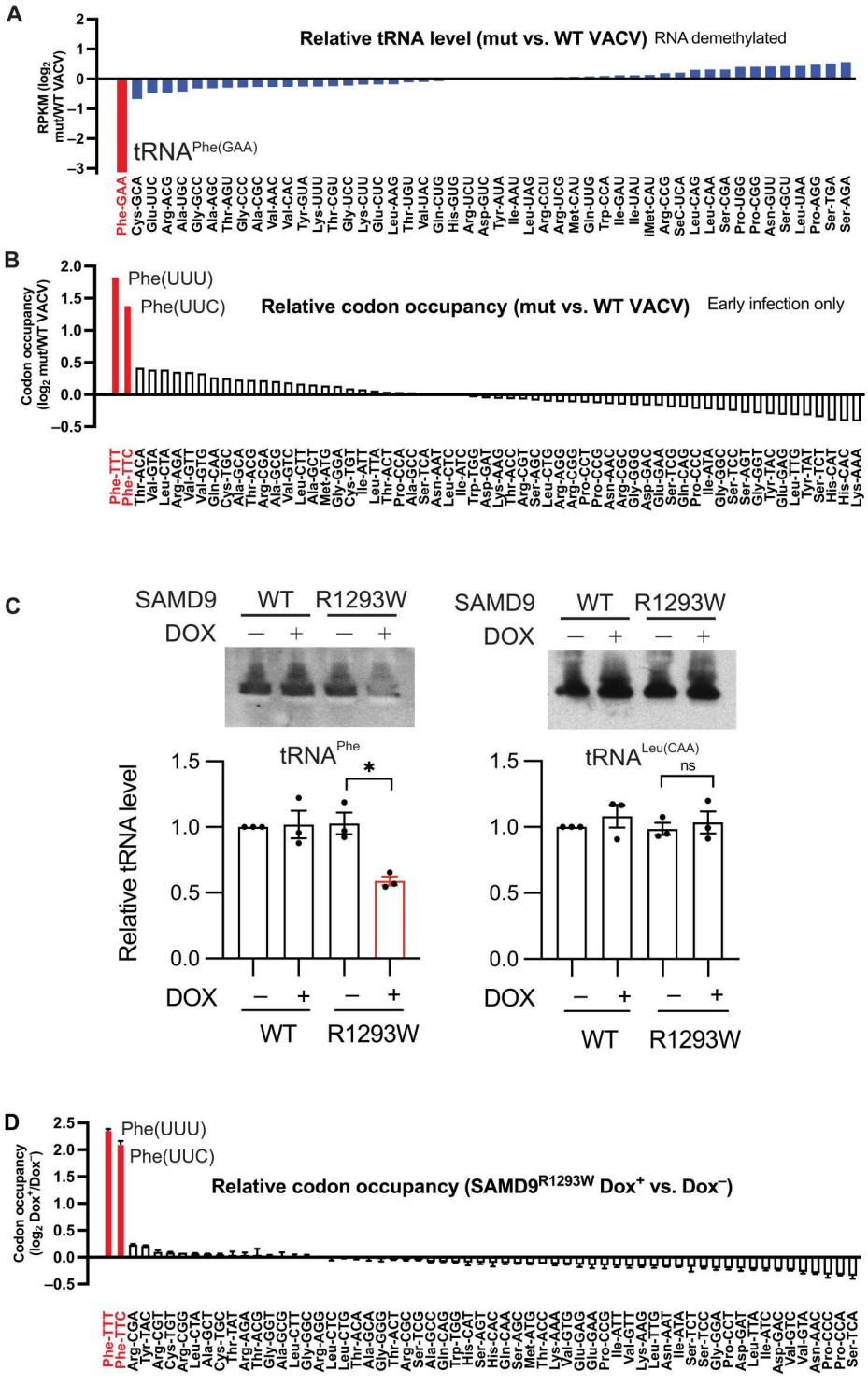

Fig. 4. SAMD9 activated by VACV or through a GoF mutation specifically depletes cellular tRNA^{Phe} and causes ribosomal pausing at Phe codons. (**A**) HeLa cells were uninfected or infected with either WT or vK1^{-}C7^{-} VACV for 8 hours. tRNAs were isolated from total RNAs resolved on a denaturing gel, treated with a tRNA demethylase and subjected to tRNA-seq. Levels of different tRNA species in vK1^{-}C7^{-}-infected cells with respect to that in WT VACV–infected cells are ranked from the lowest to the highest. tRNA^{Phe} is highlighted in red. (**B**) HeLa cells were infected as in (A) but in the presence of AraC to limit the infection to the early phase. Ribosome sequencing (Ribo-seq) was conducted, and global codon occupancy of all cellular transcripts was analyzed. Codon occupancies in vK1^{-}C7^{-}-infected cells with respect to that in WT VACV–infected cells are ranked from the highest to the lowest. Phe codons are shown in red. (**C**) BT20 cell lines with a Dox-inducible SAMD9 allele (WT or SAMD9^{R1293W}) were either uninduced or induced with Dox for 24 hours. tRNA^{Phe} and tRNA$^{Leu(CAA)}$ levels in the cells were determined by Northern blot. The graph summarizes the results from three biological replicates. ns, not significant. (**D**) BT20 cells with a Dox-inducible SAMD9^{R1293W} allele were either uninduced or induced with Dox for 24 hours. Ribo-seq was conducted, and global codon occupancy of all cellular transcripts was analyzed. Codon occupancies in Dox-induced cells with respect to that in uninduced cells are ranked from the highest to the lowest. Phe codons are shown in red.

Persistent ribosome pausing is expected to cause ribosome collision and subsequent ribotoxic stress, which is characterized by increased eukaryotic translation initiation factor 2 subunit alpha (eIF2α) phosphorylation and ATF3 induction (*30*). BT20 cells with the expression of SAMD9^{R1293W} induced ATF3 expression at mRNA and protein levels (Fig. 5C and fig. S5C). Intriguingly, knocking down tRNA^{Phe} was sufficient to induce ribotoxic stress as evidenced by eIF2α phosphorylation and the up-regulated ATF3 expression (Fig. 5D). Notably, silencing tRNA^{Leu} showed minimal effects on ATF3 induction (fig. S5D), presumably due to its relative abundance.

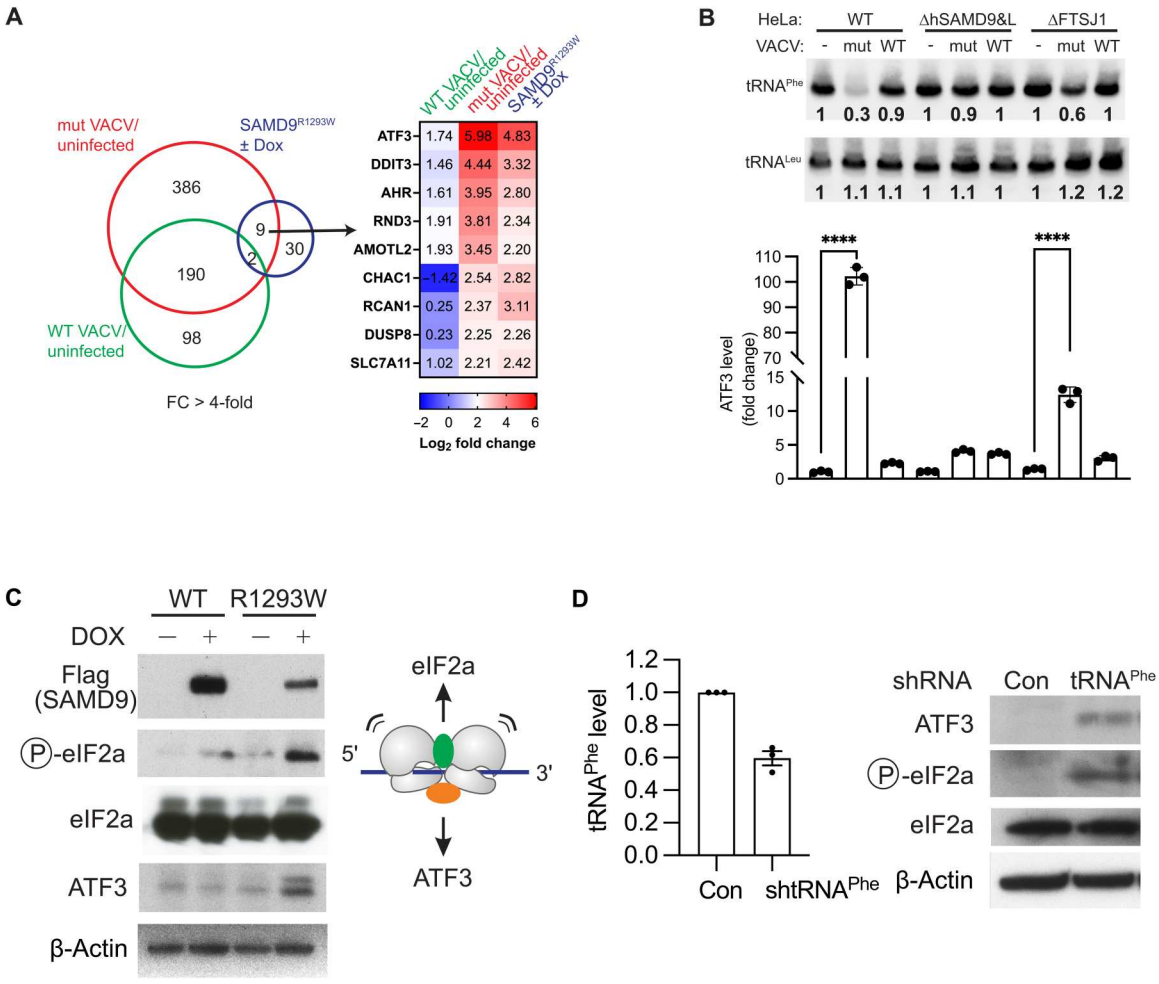

Fig. 5. Activated SAMD9 causes stress response associated with ATF3 induction. (**A**) RNA-seq was performed on HeLa cells that were uninfected or infected with either WT or vK1^{-}C7^{-} (mut) VACV for 8 hours. Numbers of genes in mut VACV and WT VACV–infected cells that showed RPKM (reads per kilobase of transcript, per million mapped reads) fold change (FC) greater than 4 with respect to uninfected cells are shown. A common set of nine genes were induced by SAMD9^{R1293W} in BT20 cells and by infection with the mut VACV (but not the WT VACV) in HeLa cells. The fold changes are shown in the heatmap. (**B**) Depletion of cellular tRNA^{Phe} and induction of ATF3 in VACV-infected cells in a SAMD9- and FTSJ1-dependent manner. HeLa cells with SAMD9 and SAMD9L KO (ΔhSAMD9&L) or FTSJ1 KO (ΔFTSJ1) were infected with vK1^{-}C7^{-} or WT VACV for 8 hours. tRNA^{Phe} and ATF3 levels in the cells were determined by Northern blot and reverse transcription quantitative polymerase chain reaction (RT-qPCR), respectively. ATF3 level is normalized with a mitochondrial mRNA level in the cells. (**C**) SAMD9^{R1293W} induces ATF3 expression and eIF2a phosphorylation. BT20 cell lines with a Dox-inducible SAMD9 allele (WT or SAMD9^{R1293W}) were either uninduced or induced with Dox for 24 hours. Proteins were detected with the indicated antibodies in immunoblots. (**D**) Knockdown of cellular tRNA^{Phe} induces ATF3 expression. Short hairpin RNA (shRNA) against tRNA^{Phe} was transduced into BT20 cells. tRNA^{Phe} level was determined by RT-qPCR, and ATF3 and phosphorylated eIF2a levels were determined by immunoblots.

Overexpression of tRNA^{Phe} restores protein synthesis and viral replication

We next tested whether SAMD9/9L–mediated inhibition of protein synthesis and VACV replication can be alleviated by overexpression of tRNA^{Phe}. To assess protein synthesis at single-cell level, we fluorescently labeled nascent cellular proteins with a puromycin analog and performed flow cytometry analysis. As we showed previously (*18*), transfection of mCherry-SAMD9^{R982C} fusion into 293T cells resulted in a strong inhibition of cellular protein synthesis in transfected (mCherry^{+}) cells, relative to nontransfected cells (mCherry^{-}) from the same culture well (Fig. 6A). Cotransfection of a plasmid overexpressing tRNA^{Phe} significantly increased cellular protein synthesis, including the synthesis of mCherry-SAMD9^{R982C} itself, in transfected cells (Fig. 6C). In comparison, cotransfection of a plasmid overexpressing tRNA^{Leu} had a minor effect (Fig. 6B). The effect of tRNA^{Phe} on cellular protein synthesis could also be detected from the total cell population by Western blot of puromycin-labeled proteins (fig. S6C).

To quantify the antiviral activity, 293T cells transfected with mCherry-SAMD9^{R982C} were infected with vK1^{-}C7^{-} and analyzed by flow cytometry. The antiviral activity of SAMD9^{R982C} was reflected by ~10-fold reduction in infection rate in mCherry-SAMD9^{R982C}–expressing cells relative to that in nontransfected cells from the same culture well (Fig. 6, E and N). Cotransfection of the tRNA^{Phe} plasmid increased the relative infection rate in transfected cells by ~60% (Fig. 6, G and N), although the cellular level of mCherry-SAMD9^{R982C} was more than doubled by tRNA^{Phe} overexpression (Fig. 6, G and M), indicating that the antiviral activity of

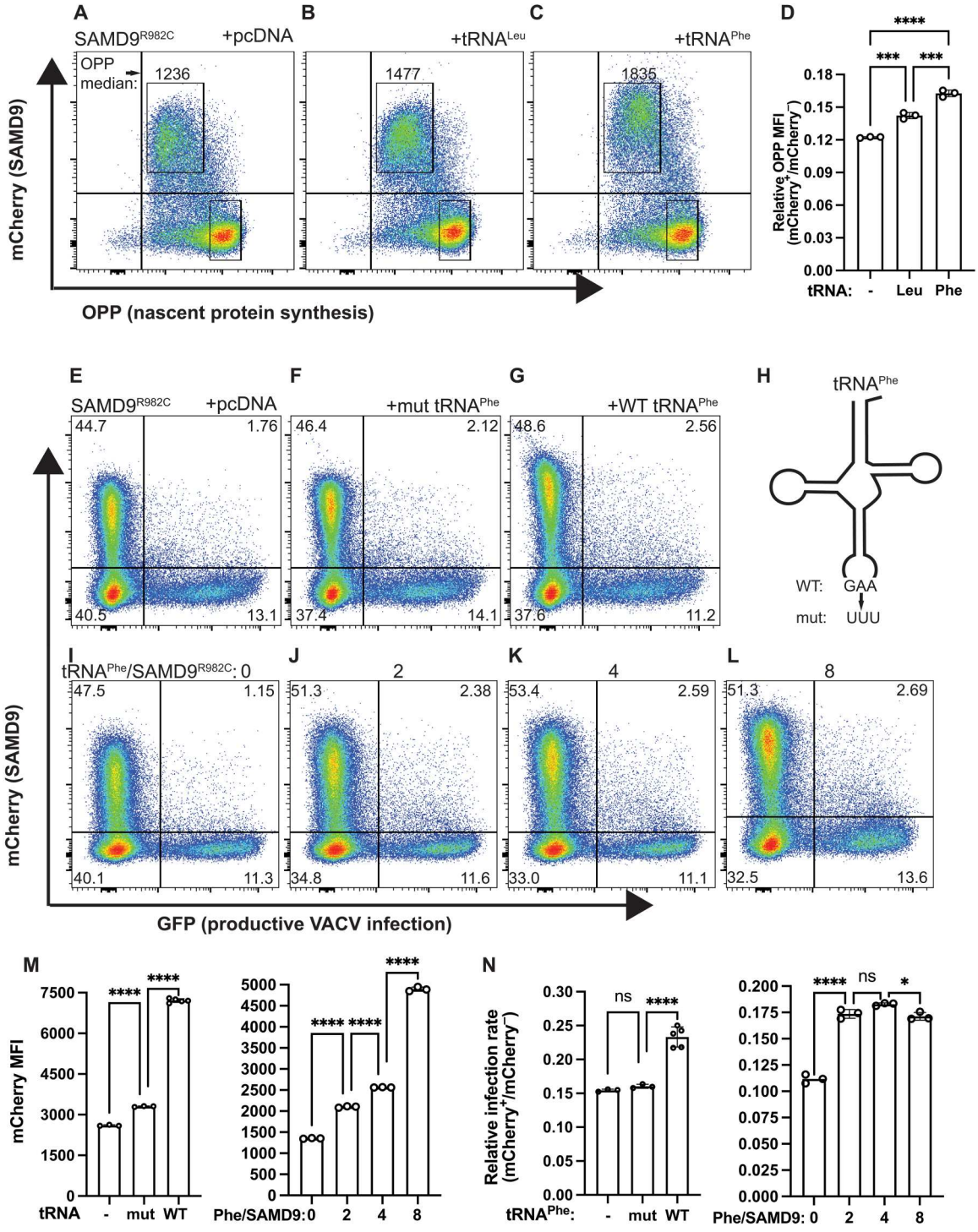

Fig. 6. Overexpression of tRNA^{Phe} reduces SAMD9 activities. (**A** to **C**) SAMD9 inhibition of global protein synthesis was reduced by tRNA^{Phe} overexpression. HEK 293T cells were transfected with mCherry-SAMD9^{R982C} and a plasmid expressing tRNA^{Phe} or tRNA^{Leu} and labeled with *O*-propargyl-puromycin (OPP) for 30 min. Representative flow cytometry plots of OPP level relative to cellular mCherry level are shown. The OPP median fluorescence intensities in SAMD9-expressing cells are listed. (**D**) Nascent protein synthesis levels in SAMD9^{R982C}-expressing cells relative to nontransfected cells from the same culture wells are derived from the flow cytometry. (**E** to **L**) SAMD9 inhibitions of protein synthesis and viral replication were reduced by tRNA^{Phe} in a dose-dependent manner. HEK 293T cells were cotransfected with a plasmid expressing mCherry-SAMD9^{R982C} and a plasmid expressing tRNA^{Phe} or a mutant tRNA^{Phe} and infected with vK1^{-}C7^{-}/GFP^{+}. Infections among SAMD9-expressing and nontransfected control cells from the same culture well were simultaneously determined with flow cytometry. Representative flow cytometry plots are shown. (**M**) The mean fluorescence intensity (MFI) of mCherry-SAMD9 in transfected cells and (**N**) the relative infection rates between SAMD9-expressing and nontransfected cells are derived from the flow cytometry data. Statistics: one-way ANOVA (ns, not significant; *$P < 0.1$; ***$P < 0.001$; ****$P < 0.0001$).

SAMD9^{R982C} was attenuated. A mutant tRNA^{Phe} with a 3-nt anticodon substitution had no effect on viral replication (Fig. 6, F and N). tRNA^{Phe} overexpression increased the cellular synthesis of SAMD9^{R982C} proteins in a dose-dependent manner (Fig. 6, I to M), but the increase in the relative infection rate was nearly constant (Fig. 6, I to L and N), probably because further reduction in SAMD9 antiviral activity was counterbalanced by the increased SAMD9 protein level in the same cells. Last, we obtained similar results using WT and additional GoF mutants of SAMD9/9L by showing that overexpression of tRNA^{Phe} restored protein synthesis and viral replication (fig. S6, A to C).

DISCUSSION

SAMD9/9L have recently emerged as critical antiviral factors and myeloid tumor suppressors, with studies revealing their role as host restriction factors for poxviruses (*5*–*7*) and GoF mutations in SAMD9/9L as the underlying cause for a spectrum of human diseases with myeloid involvement (*14*, *15*, *31*). SAMD9/9L are predicted to function similarly to the STAND superfamily of signaling molecules, which share a conserved tripartite domain architecture with an N-terminal effector, a central NOD, and a C-terminal sensor. Recently, we identified an N-terminal dsNA binding domain of SAMD9/9L as the effector responsible for their antiviral and antiproliferative activities (*18*). However, the precise function of this effector has remained elusive until our current study, where we found that the effector acts as an ACNase, functioning as a specific tRNA restriction enzyme that inhibits cellular protein synthesis and restricts viral replication. This discovery of an intrinsic effector function in eukaryotic STAND-like proteins is unexpected, as previously characterized eukaryotic STAND proteins all rely on adaptors to recruit additional cellular proteins to exert their effect (*23*). For instance, the prototypical STAND protein, apoptotic peptidase activating factor 1 (APAF1), a component of the apoptosome, uses a caspase activation and recruitment domain (CARD) as its effector to recruit and activate caspase 9, thereby initiating apoptosis (*32*). The reliance on an intrinsic effector may enable SAMD9/9L to mount a more rapid response to viral infections without the need for an additional signaling step. Intriguingly, recent findings have also revealed the presence of STAND proteins with intrinsic effector functions in prokaryotes (*33*). A family of bacterial STAND proteins that sense tailed phages was found to exert their antiviral functions with diverse N-terminal nucleases (*33*), making SAMD9/9L mechanistically more similar to these prokaryotic antiviral STAND proteins.

SAMD9/9L are ubiquitously expressed in various tissues (*34*), but, under normal physiological conditions in HeLa cells and presumably other cells, they do not inhibit cellular protein synthesis or degrade tRNA. Previous studies by us and others have demonstrated that frameshift mutations truncating nearly the C-terminal half of SAMD9L lead to a GoF phenotype, rendering SAMD9L constitutively active in suppressing protein synthesis (*18*–*20*). This suggests that SAMD9/9L are typically maintained in an inactive state through autoinhibition by the C-terminal half, similar to other STAND proteins involved in innate immunity. These STAND proteins are allosterically activated once their C-terminal sensors bind to specific PAMPs. Supporting this activation model, we found that SAMD9 ACNase activity is activated upon VACV infection in HeLa cells, resulting in cleavage of tRNA^{Phe} and ribosomal pausing (Figs. 1C and 4B). Although the molecular patterns that activate SAMD9 have not yet been uncovered, it is evident that they are already present during the early stage of VACV infection, even when viral genome replication is blocked, as shown by the tRNA^{Phe} degradation and ribosomal pausing under this condition (Figs. 1C and 4B). Furthermore, the aforementioned SAMD9/9L activation model is supported by the phenotypes of various GoF mutations. The mechanisms by which GoF mutations render SAMD9/9L constitutively active in inhibiting cell proliferation are not fully understood, but it is believed that these mutations eliminate self-inhibition mediated by the C-terminal half, where nearly all GoF mutations occur. All the GoF SAMD9/9L mutations that we analyzed, including frameshift and missense mutations, result in constitutive ACNase activity (fig. S4, E to H).

The utilization of ACNases to deplete essential tRNAs and thereby halt global protein synthesis represents a previously unknown antiviral and antiproliferative mechanism in multicellular eukaryotes. Recent studies have identified members of the mammalian Schlafen protein family, which include several viral restriction factors, as having an endoribonuclease domain that targets ribosomal RNA (rRNA) and/or tRNAs (*35*, *36*). Among these, human schlafen11 solely targets tRNAs, and it cleaves type II tRNAs (tRNA^{Ser} and tRNA^{Leu}) at the acceptor stem (*37*), inhibiting the synthesis of a subset of proteins with atypical codon usage, including HIV-1 proteins (*38*). In contrast, SAMD9 cleaves the essential tRNA^{Phe} at the anticodon loop, leading to the depletion of tRNA^{Phe} and inhibition of global protein synthesis. Similar mechanisms involving ACNase depletion of essential tRNAs are found in the microbial world, although the microbial ACNases differ from tRNase SA in terms of structure and substrate specificity. For example, *E. coli* PrrC contains a higher eukaryotes and prokaryotes nucleotide-binding (HEPN) domain (*39*) and cleaves tRNA$^{lys(UUU)}$ 5′ to the wobble position (*2*), *E. coli* Colicin E5 contains a barnase, EndoU, colicinD, RelE (BECR) domain and cleaves four different tRNA species 3′ to the wobble position (*40*), and enteric bacterial toxin VapC contains a PilT N-terminus (PIN) domain and cleaves tRNA^{fMET} at 3′ end of the anticodon loop (*41*). Most of these microbial ACNases produce termini with a 2′-3′-cyclic phosphate and a 5′-OH group. In contrast, tRNase SA adopts a fold that has no close match to others in the Protein Data Bank (*18*) and cleaves tRNA^{Phe} at the 5′ end of the anticodon loop, yielding termini with a 3′-OH and 5′-phosphate group. Despite these differences, SAMD9 and the microbial ACNases have the similar effects of depleting essential tRNAs and inhibiting global protein synthesis, highlighting the importance of tRNAs as regulators of protein synthesis and innate immunity in all domains of life.

Mature tRNAs are the most extensively modified RNA species in cells (*42*), although the physiological roles of the modifications are often not fully understood. The activities of SAMD9 and some microbial ACNases are influenced by different tRNA modifications at the ASLs. For instance, PrrC activity is enhanced by the presence of the 6-threonylcarbamoyl adenosine modification at position 37 (*43*), while γ-toxin activity requires the 5-methoxycarbonylmethyl-2-thiouridine modification at the wobble position (*3*). tRNase SA specificity is primarily determined by the presence of a 2′-*O*-methylated purine base at the wobble position, which is unique to eukaryotic tRNA^{Phe} and not present in other tRNAs or most of the prokaryotic tRNA^{Phe} (fig. S7). Notably, the 2′-*O*-methylation in tRNA^{Phe} is important for organismal health, as its absence leads

to slow growth in diverse yeast species (*28*) and intellectual disability in humans (*25*, *26*). Hypomodification of $tRNA^{Phe}$ in FTSJ1 KO mice selectively reduced the steady-state level of $tRNA^{Phe}$ in the brain, resulting in decreased translation of genes that are important for brain functions (*26*). Intriguingly, GoF SAMD9L mutations are associated with ataxia-pancytopenia syndrome characterized by cerebellar ataxia, raising the possibility that $tRNA^{Phe}$ deficiency could underlie the neurological manifestation of the disease. We showed that overexpression of $tRNA^{Phe}$ could restore protein synthesis and virus replication caused by GoF SAMD9/9L (Fig. 6), suggesting that restoring $tRNA^{Phe}$ levels by overexpressing $tRNA^{Phe}$ or inhibiting SAMD9/9L ACNase activity could be a potential therapeutic strategy for diseases associated with GoF SAMD9/9L mutations.

MATERIALS AND METHODS

Reagents

The following antibodies were used in the immunoblotting: anti-FTSJ1 (Santa Cruz Biotechnology, SC-390355), anti-Flag (Sigma-Aldrich, F1804), anti-ATF3 (Cell Signaling Technology, 18665S), anti–β-actin (Sigma-Aldrich, A5441), anti-phosphorylated eIF2α (Cell Signaling Technology, 3398P), anti-eIF2α (Cell Signaling Technology, 5324), and anti-puromycin antibody (Developmental Studies Hybridoma Bank, PMY-2A4). Yeast Xrn-1 [New England Biolabs (NEB), M0338], yeast tRNA (Sigma-Aldrich, R4018), the microRNA marker (NEB, N2102S), and the Low Range ssRNA Ladder (NEB, N0364S) were acquired commercially.

Viruses

WT VACV Western Reserve (WR) strain and the K1L and C7L deletion mutant ($vK1^{-}C7^{-}$) were previously described (*10*, *44*, *45*). They were propagated and titrated on Vero cells.

Cells

Vero (ATCC CCL-81) and HeLa 229 (ATCC CCL-2.1) cells were from American Type Culture Collection (ATCC). Human embryonic kidney (HEK) 293FT cells were from Thermo Fisher Scientific (catalog no. R70007). HeLa cells with SAMD9 and SAMD9L KO (ΔSAMD9&L) (*7*) and BT cells (*18*) with Dox-inducible expression of SAMD9-WT or $SAMD9^{R1293W}$ were described before.

Plasmids construction

To overexpress $tRNA^{Leu}$(CAA) in vivo, the sequence including promoter region, tRNA sequence and terminator region was amplified by PCR using genomic DNA extracted from BT20 cells as the template and cloned into EcoR I and Pst I sites of pcDNA3.1. To overexpress $tRNA^{Phe}$ in vivo, the Q5 Site-Directed Mutagenesis Kit (NEB) was used to replace the $tRNA^{Leu}$ sequence with $tRNA^{Phe}$.

To knock out FTSJ1 gene, a pair of complementary oligonucleotides (table S1) that contain the guide sequence for FTJS1 (5′-ATCTGTACCACACCTGGTAG-3′) was cloned into lenti-CRISPRv2 (Addgene, plasmid no. 52961) that had been digested with Esp3 I, essentially as described (*46*).

Lentiviral plasmids for expressing FTSJ1 were constructed by PCR amplification of a FTSJ1 complementary DNA (cDNA) clone (Transomic Technologies) and subcloning the PCR fragment into Nhe I and BamH I sites of pCW57.1 (Addgene, no. 41393), a doxycycline-inducible lentiviral vector with rtTA-VP16-2A-puro. To decrease FTSJ1 basal expression level, the minimal CMV promoter upstream of the FTSJ1 gene was modified to match that in pTRE3G-IRES vector (Takara Bio) by using a synthetic DNA fragment (Eurofins). FTSJ1 K28A and A26P mutations were introduced into the plasmid through PCR with primers containing the desired mutations (table S1) and subcloning the PCR fragments between Nhe I and EcoR I sites of the vector.

Plasmids for expressing mCherry-SAMD9/9L fusion (pcDNA6.2/mCherry-SAMD9/9L) were described previously (*18*). Specific mutations of SAMD9/9L were introduced into the plasmids through recombinant PCR-based site-directed mutagenesis as described previously (*44*).

Generation of HeLa cell lines that express FTSJ1 allele under the Dox-inducible promoter

A FTSJ1 KO HeLa cell line was first generated by transient transfection of the plasmid containing the guide sequence for FTSJ1 to HeLa cells, followed by selection with puromycin (3 μg/ml) for 2 days. Cells that survived the selection were cultured in the absence of puromycin, and multiple cell clones were isolated and tested for FTSJ1 expression by Western blotting. Cell clones that showed no FTSJ1 expression by Western blot were also tested for the FTSJ1 genotype by Sanger sequencing as described previously (*7*). The FTSJ1 KO cells were transduced with lentivirus encoding FTSJ1 WT or mutant alleles, similar as described previously (*9*). Transduced cells were selected with puromycin at 3 μg/ml.

Viral growth analysis

Cells in 12-well plates were incubated with 1 plaque-forming unit per cell of the VACV for 2 hours at room temperature. Following adsorption, the cells were washed twice with phosphate-buffered saline. One set of the cells was harvested immediately as the 0 hpi sample, while the other set was moved to 37°C incubator to initiate viral entry and harvested at 24 hpi. The viral titers in the cell lysates were determined by plaque assays on Vero cells.

Protein purification

Recombinant $SAMD9^{134–385}$, $SAMD9^{156–385}$, and $SAMD9L^{158–388}$ proteins were expressed in *E. coli* as a small ubiquitin-like modifier (SUMO) fusion with a 6xHis-tag and purified as previously described (*18*).

Assay of SAMD9/9L activities in HEK 293T cells

HEK 293T cells in 24-well plates were transfected with pcDNA6.2/mCherry-SAMD9/9L plasmids before they were subjected to the following assays. For assessing antiviral activities, cells that had been transfected for 36 hours were infected with $vK1^{-}C7^{-}/GFP^{+}$ at a multiplicity of infection of 1 for 15 hours. For assessing protein synthesis level, cells that had been transfected for 24 hours were treated with 10 μM of *O*-propargyl-puromycin (OPP) for 30 min before they were processed with the Click-iT Plus OPP Alexa Fluor 488 Protein Synthesis Assay Kit according to the manufacturer's instruction (Thermo Fisher Scientific). The cells were harvested using trypsin-EDTA solution, fixed with 4% paraformaldehyde for 20 min, washed twice with Hanks' balanced salt solution (HBSS) (Sigma Life Science) supplemented with 1% bovine serum albumin, resuspended in 400 μl of HBSS, filtered with 40-μm mesh, and analyzed with an LSR II cell analyzer (BD Biosciences). Flow data were analyzed using FlowJo software (TreeStar). Protein

synthesis rates in total transfected cells were also assessed by labeling the cells with puromycin (10 μg/ml; InvivoGen) for 10 min followed by Western blot with an anti-puromycin antibody (PMY-2A4, Developmental Studies Hybridoma Bank).

Electrophoretic mobility shift assay

The binding of the purified SAMD9 proteins with yeast tRNA was studied by electrophoretic mobility shift assay on a 0.8% native agarose gel as previously described (*18*).

In vitro cleavage assay

Total RNA (10 μg) extracted from HeLa cells or 20 pmol of synthetic RNAs (table S1) was incubated with 0.8 to 14 μg of recombinant SAMD9$^{134–385}$ protein in the cleavage buffer at 37°C for 60 min. The cleavage buffer was made of 40 mM tris-HCl (pH 8.0), 20 mM KCl, 4 mM $MgCl_2$ (or $MnCl_2$), and 2 mM dithiothreitol (DTT). The cleavage products were mixed with gel loading dye (Invitrogen, 8546G) and resolved on 8% or 15% denaturing polyacrylamide gel containing 8 M urea. The gels were stained with SYBR Gold (Invitrogen, S11494) or subjected to Northern blot analysis.

Northern blot analysis

Northern blots were performed as described (*47*). Briefly, RNAs resolved on denaturing urea-polyacrylamide gel were transferred onto a positive charged nylon membrane. RNAs on the membrane were visualized and photographed after ethidium bromide staining. The staining was washed away, and the RNAs on the membrane were cross-linked with short-wave ultraviolet light. The membrane was probed with digoxigenin (DIG)–labeled DNA oligonucleotides against specific tRNAs. The labeling of oligonucleotides was performed with a DIG oligonucleotide 3′-End labeling kit (Roche). The signal is detected with chemiluminescence with CDP-Star as the substrate (Roche).

Mass spectroscopy

Oligonucleotide mass was determined with electrospray ionization liquid chromatography mass spectroscopy by Novatia, LLC (Newtown, PA).

Immunoblotting

SDS–polyacrylamide gel electrophoresis gel (12%) was used to separate proteins with different mass, and proteins were transferred to polyvinylidene difluoride or nitrocellulose membranes (Thermo Fisher Scientific). Membranes were blocked in blocking buffer containing tris-buffered saline (TBS), 5% nonfat milk, and 0.1% Tween 20 for 1 hour at room temperature with shaking. Primary antibodies were diluted in blocking buffer (1:1000) and added to membrane overnight at 4°C. After incubation with horseradish peroxidase–coupled secondary antibodies for 1 hour at room temperature, the membrane was washed three times with Tris-buffered saline with 0.1% Tween 20 detergent (TBST), and immunoblots were visualized using enhanced chemiluminescence (ECL-Plus, GE Healthcare).

Lentiviral shRNAs

Short hairpin RNA (shRNA) sequence targeting tRNA^{Phe} (GAA) is 5′-TCAGTTGGGAGAGCGTTAGAC-3′. shRNA sequence targeting tRNA^{Leu} (CAA) is 5′-TCTAAGGCGCCAGACTCAAGT-3′. All the shRNA targeting sequences were cloned into DECIPHER pRSI9-U6-(sh)-UbiC-TagRFP-2A-Puro (Cellecta). Lenti-X 293T cells (Clontech) were used to package lentiviral particles. The supernatants containing virus were collected and filtered at 48 hours after transfection. Then, the lentivirus was added to cells for 24 hours. After selection by puromycin (2 μg/μl), tRNA knockdown cells were collected and characterized.

Reverse transcription quantitative polymerase chain reaction

For detecting mRNA levels, the cDNA was obtained by reverse transcription using the High-Capacity cDNA Reverse Transcription Kit (Invitrogen) or the iScript Select cDNA Synthesis Kit (Bio-Rad). For detecting tRNA levels, the cDNA was obtained by the rtStar tRNA-optimized First-Strand cDNA Synthesis Kit (ArrayStar). Real-time PCR was performed using the Power SYBR Green PCR Master Mix (Applied Biosystems) and run on the LightCycler 480 Real-Time PCR System (Roche Applied Science) or a CFX96 Real-Time system (Bio-Rad). Relative expression was calculated using the $2^{-\Delta\Delta Ct}$ method.

tRNA sequencing

Total RNA was deacylated in 50 mM tris-HCl (pH 9.0) at 37°C for 45 min and then resolved by 10% polyacrylamide tris-borate EDTA (TBE)–urea gel (Invitrogen). tRNA (60 to 100 nt) were collected by gel excision and resolved in RNA elution buffer [300 mM NaOAc (pH 5.2), 1 mM EDTA, SUPERase In (0.1 U/μl)] overnight. After ethanol precipitation, tRNA was treated with demethylase (rtStar tRNA-optimized First-Strand cDNA Synthesis Kit, ArrayStar) and cleaned up. tRNA (1 μg) was used for library construction. Briefly, tRNA was dephosphorylation in the 15-μl mixture containing 1 × T4 polynucleotide kinase buffer, SUPERase In (1 U/μl), and T4 polynucleotide kinase (1 U/μl) at 37°C for 30 min and followed by 65°C for 20 min. After ethanol precipitation, RNA was pelleted by centrifugation for 15 min at 20,000*g* at 4°C and dissolved in nuclease-free H_2O. Poly(A) tailing and 5′ adenylation reaction was carried in the mixture containing 1× poly(A) tailing reaction buffer, 1 mM adenosine 5′-triphosphate, SUPERase In (1 U/μl), poly(A) polymerase (1 U/μl), and Ezra (1 U/μl) (*48*) at 37°C for 30 min and followed by 65°C for 20 min. RNA sample was then mixed with 1 μl of 1 μM ligation adaptor (5′-AATGATACGGCGACCACCGAGATCTACACTCTTTCCCTACACGACGCTCTTCCGATCT rGrGrG-3′) and heated at 65°C for 2 min and then immediately put on ice for 1 min. Ligation was performed in a 5-μl mixture containing 1× T4 RNL2 reaction buffer, SUPERase In (1 U/μl), 15% PEG8000, and T4 RNA ligase 2 (20 U/μl) truncated at 22°C for 1.5 hours. For reverse transcription reaction, 1 μl of 1 μM RT primer (5′-GCATCTCGGTGGTCCAATCTGAACTCCAGTCGTGTGACTGGAGTTCAGACGTGTGCTCTTCCGATCTTTTTTTTTTTTTVN-3′) was added to the ligation products and denatured at 65°C for 2 min and cooled down on ice for 1 min. The linker-ligated RNA was then mixed with 1× first strand buffer, 0.5 mM deoxynucleotide triphosphate (dNTP), 5 mM DTT, RNaseOUT (2 U/μl), and SuperScript IV (200 U/μl) at 50°C for 1 hour, followed by 80°C for 10 min. PCR was performed in a 20-μl mixture containing 1× Phusion HF buffer (NEB), 0.2 mM dNTP, 0.5 μM forward PCR primer (5′-AATGATACGGCGACCACCGAGATCTACACTCTTTCCCTACACGACGCTCT-3′), 0.5 μM reverse PCR primer with barcode (see below), and 0.5 U of Phusion polymerase. The PCR was initiated at 98°C for 30 s, then 98°C for 5 s, 68°C for 20 s, and 72°C for 15 s for 12 cycles. PCR

products were separated on a nondenaturing 8% polyacrylamide TBE gel. Expected DNA at 200 to 240 bp was excised and soaked by 400 μl of DNA elution buffer (300 mM NaCl and 1 mM EDTA) overnight. After removal of gel debris using Spin-X column, samples were ethanol precipitated and dissolved in 15 μl of nuclease-free H_2O. Last, samples were sequenced (Illumina HiSeq) by using sequencing primers: library-PCR-R-13: 5′-CAAGCAGAAGACGGCATACGAGATTGTTGACTGTGACTGGAGTTCAGACGTGTGCTCT-3′; library-PCR-R-14: 5′-CAAGCAGAAGACGGCATACGAGATACGGAACTGTGACTGGAGTTCAGACGTGTGCTCT-3′; library-PCR-R-15: 5′-CAAGCAGAAGACGGCATACGAGATTCTGACATGTGACTGGAGTTCAGACGTGTGCTCT-3′; library-PCR-R-16: 5′-CAAGCAGAAGACGGCATACGAGATCGGGACGGGTGACTGGAGTTCAGACGTGTGCTCT-3′; library-PCR-R-18: 5′-CAAGCAGAAGACGGCATACGAGATGTGCGGACGTGACTGGAGTTCAGACGTGTGCTCT-3′; library-PCR-R-19: 5′-CAAGCAGAAGACGGCATACGAGATCGTTTCACGTGACTGGAGTTCAGACGTGTGCTCT-3′; library-PCR-R-20: 5′-CAAGCAGAAGACGGCATACGAGATAAGGCCACGTGACTGGAGTTCAGACGTGTGCTCT-3′; library-PCR-R-21: 5′-CAAGCAGAAGACGGCATACGAGATTCCGAAACGTGACTGGAGTTCAGACGTGTGCTCT-3′.

Ribosome sequencing

Ribo-seq in BT20 cells was performed as follows. Ribosome fractions separated by sucrose gradient sedimentation were pooled and digested with *E. coli* RNase I (Ambion, 750 U per 100 A260 units) by incubation at 4°C for 1 hour. SUPERase inhibitor (50 U per 100 U of RNase I) was then added into the reaction mixture to stop the digestion. Total RNA was extracted using TRIzol reagent. RNA was separated on a 15% polyacrylamide TBE-urea gel (Invitrogen), and the ribosome-protected fractions were excised (25 to 35 nt). After gel soaking and RNA precipitation, RNA was collected for library construction as described above. Last, expected DNA at 160 to 180 bp was excised and collected for sequencing.

Ribo-seq in VACV-infected cells was performed essentially as described (*49*). The steps include RNase I treatment, ribosome recovery, footprint fragment purification, 3′ adaptor ligation, rRNA depletion, reverse transcription, circularization, and PCR amplification (*49*).

Alignment of sequencing reads

The 3′ adapter was trimmed by Cutadapt (*50*). Trimmed reads with length < 15 nt were excluded. For Ribo-seq and RNA sequencing (RNA-seq), the remaining reads were mapped to a household database including all putative human rRNAs by using Bowtie (*51*). Mismatch is not permitted. The reads that cannot be aligned to rRNAs were aligned to human transcriptome using STAR (*52*). To construct the transcriptome, the annotation file from the Ensembl database (GRCh38) was used. For each gene, the mRNA with the longest coding sequence (CDS) was selected. In the case of equal CDS length, the longest transcript was used. For read alignment, a maximum of two mismatches were permitted. To avoid ambiguity, reads that were mapped to multiple positions were excluded. For tRNA-seq, the adaptor-trimmed reads were aligned to human genome (GRCh38) using HISAT2 (*53*), and the reads that were aligned to the human tRNAs were extracted and then were aligned to a household tRNA database that contains a unique tRNA sequence for each type of tRNAs. Mismatch is not permitted. For the reads that can be aligned to multiple tRNAs, the read is counted as $1/n$ for each tRNA (n is the total number of tRNAs that can be aligned).

Aggregation plot of footprint reads near the start and stop codons

The ribosome P-site was defined as positions +12, +13, and + 14 from the 5′ end of the reads (the first position of the reads is recorded as 0). For each mRNA, the mRNA with total reads in the CDS < 32 was excluded from analysis. Ribosome densities at individual mRNA sites were counted and then normalized by the average ribosome density of the CDS. Ribosome densities with the same distance from the start or stop codon were averaged over the whole transcriptome.

Estimation of ribosome density on mRNAs and mRNA levels

For each mRNA, an RPKM (reads per kilobase of transcript, per million mapped reads) value was calculated and used to measure the relative ribosome density on individual mRNAs. For Ribo-seq, only the reads aligned to the CDS were used. For RNA-seq, the reads aligned to mRNAs were used. mRNAs with RPKM values < 1 were excluded.

Calculation of ribosome occupancy

For each mRNA, ribosome densities at individual codons of the CDS were normalized to the average density of the CDS. Then, ribosome occupancies at the same codons were averaged over the whole transcriptome.

Figure preparation

SAMD9/9L amino acid sequence alignment was performed with secondary-structure matching (SSM) server (*54*), and the alignment figure was created with ESPript (*55*). $tRNA^{Phe}$ modification status in different species was obtained from the RNA modification database (*56*).

Statistical analysis

Data were analyzed using GraphPad Prism 9 software. We obtained the P value of the difference between different groups by performing Student's t test and one-way analysis of variance (ANOVA). When $P < 0.05$, differences were considered statistically significant.

Supplementary Materials

This PDF file includes:

Figs. S1 to S7
Table S1

REFERENCES AND NOTES

1. H. Masaki, T. Ogawa, The modes of action of colicins E5 and D, and related cytotoxic tRNases. *Biochimie* **84**, 433–438 (2002).
2. G. Kaufmann, Anticodon nucleases. *Trends Biochem. Sci.* **25**, 70–74 (2000).
3. J. Lu, B. Huang, A. Esberg, M. J. O. Johansson, A. S. Bystrom, The *Kluyveromyces lactis* γ-toxin targets tRNA anticodons. *RNA* **11**, 1648–1654 (2005).
4. D. M. Thompson, R. Parker, Stressing out over tRNA cleavage. *Cell* **138**, 215–219 (2009).
5. J. Liu, S. Wennier, L. Zhang, G. McFadden, M062 is a host range factor essential for myxoma virus pathogenesis and functions as an antagonist of host SAMD9 in human cells. *J. Virol.* **85**, 3270–3282 (2011).
6. G. Sivan, P. Ormanoglu, E. C. Buehler, S. E. Martin, B. Moss, Identification of restriction factors by human genome-wide RNA interference screening of viral host range mutants

exemplified by discovery of SAMD9 and WDR6 as inhibitors of the vaccinia virus K1L-C7L-mutant. *MBio* **6**, e01122 (2015).
7. X. Meng, F. Zhang, B. Yan, C. Si, H. Honda, A. Nagamachi, L. Z. Sun, Y. Xiang, A paralogous pair of mammalian host restriction factors form a critical host barrier against poxvirus infection. *PLOS Pathog.* **14**, e1006884 (2018).
8. X. Meng, B. Krumm, Y. Li, J. Deng, Y. Xiang, Structural basis for antagonizing a host restriction factor by C7 family of poxvirus host-range proteins. *Proc. Natl. Acad. Sci. U.S.A.* **112**, 14858–14863 (2015).
9. F. Zhang, X. Meng, M. B. Townsend, P. S. Satheshkumar, Y. Xiang, Identification of CP77 as the third orthopoxvirus SAMD9 and SAMD9L inhibitor with unique specificity for a rodent SAMD9L. *J. Virol.* **93**, e00225-19 (2019).
10. X. Meng, J. Chao, Y. Xiang, Identification from diverse mammalian poxviruses of host-range regulatory genes functioning equivalently to vaccinia virus C7L. *Virology* **372**, 372–383 (2008).
11. G. Sivan, S. G. Glushakow-Smith, G. C. Katsafanas, J. L. Americo, B. Moss, Human host range restriction of the vaccinia virus C7/K1 double deletion mutant is mediated by an atypical mode of translation inhibition. *J. Virol.* **92**, e01329-18 (2018).
12. R. Drillien, D. Spehner, A. Kirn, Host range restriction of vaccinia virus in Chinese hamster ovary cells: Relationship to shutoff of protein synthesis. *J. Virol.* **28**, 843–850 (1978).
13. S. S. Sahoo, V. B. Pastor, C. Goodings, R. K. Voss, E. J. Kozyra, A. Szvetnik, P. Noellke, M. Dworzak, J. Stary, F. Locatelli, R. Masetti, M. Schmugge, B. De Moerloose, A. Catala, K. Kallay, D. Turkiewicz, H. Hasle, J. Buechner, K. Jahnukainen, M. Ussowicz, S. Polychronopoulou, O. P. Smith, O. Fabri, S. Barzilai, V. de Haas, I. Baumann, S. Schwarz-Furlan; European Working Group of MDS in Children (EWOG-MDS), M. R. Niewisch, M. G. Sauer, B. Burkhardt, P. Lang, P. Bader, R. Beier, I. Muller, M. H. Albert, R. Meisel, A. Schulz, G. Cario, P. K. Panda, J. Wehrle, S. Hirabayashi, M. Derecka, R. Durruthy-Durruthy, G. Gohring, A. Yoshimi-Noellke, M. Ku, D. Lebrecht, M. Erlacher, C. Flotho, B. Strahm, C. M. Niemeyer, M. W. Wlodarski, Clinical evolution, genetic landscape and trajectories of clonal hematopoiesis in SAMD9/SAMD9L syndromes. *Nat. Med.* **27**, 1806–1817 (2021).
14. J. R. Schwartz, J. Ma, T. Lamprecht, M. Walsh, S. Wang, V. Bryant, G. Song, G. Wu, J. Easton, C. Kesserwan, K. E. Nichols, C. G. Mullighan, R. C. Ribeiro, J. M. Klco, The genomic landscape of pediatric myelodysplastic syndromes. *Nat. Commun.* **8**, 1557 (2017).
15. S. Narumi, N. Amano, T. Ishii, N. Katsumata, K. Muroya, M. Adachi, K. Toyoshima, Y. Tanaka, R. Fukuzawa, K. Miyako, S. Kinjo, S. Ohga, K. Ihara, H. Inoue, T. Kinjo, T. Hara, M. Kohno, S. Yamada, H. Urano, Y. Kitagawa, K. Tsugawa, A. Higa, M. Miyawaki, T. Okutani, Z. Kizaki, H. Hamada, M. Kihara, K. Shiga, T. Yamaguchi, M. Kenmochi, H. Kitajima, M. Fukami, A. Shimizu, J. Kudoh, S. Shibata, H. Okano, N. Miyake, N. Matsumoto, T. Hasegawa, SAMD9 mutations cause a novel multisystem disorder, MIRAGE syndrome, and are associated with loss of chromosome 7. *Nat. Genet.* **48**, 792–797 (2016).
16. B. Tesi, J. Davidsson, M. Voss, E. Rahikkala, T. D. Holmes, S. C. C. Chiang, J. Komulainen-Ebrahim, S. Gorcenco, A. Rundberg Nilsson, T. Ripperger, H. Kokkonen, D. Bryder, T. Fioretos, J. I. Henter, M. Mottonen, R. Niinimaki, L. Nilsson, C. J. Pronk, A. Puschmann, H. Qian, J. Uusimaa, J. Moilanen, U. Tedgard, J. Cammenga, Y. T. Bryceson, Gain-of-function SAMD9L mutations cause a syndrome of cytopenia, immunodeficiency, MDS, and neurological symptoms. *Blood* **129**, 2266–2279 (2017).
17. D. H. Chen, J. E. Below, A. Shimamura, S. B. Keel, M. Matsushita, J. Wolff, Y. Sul, E. Bonkowski, M. Castella, T. Taniguchi, D. Nickerson, T. Papayannopoulou, T. D. Bird, W. H. Raskind, Ataxia-pancytopenia syndrome is caused by missense mutations in SAMD9L. *Am. J. Hum. Genet.* **98**, 1146–1158 (2016).
18. S. Peng, X. Meng, F. Zhang, P. K. Pathak, J. Chaturvedi, J. Coronado, M. Morales, Y. Mao, S. B. Qian, J. Deng, Y. Xiang, Structure and function of an effector domain in antiviral factors and tumor suppressors SAMD9 and SAMD9L. *Proc. Natl. Acad. Sci. U.S.A.* **119**, e2116550119 (2022).
19. E. J. Allenspach, F. Soveg, L. S. Finn, L. So, J. A. Gorman, A. B. I. Rosen, S. Skoda-Smith, M. M. Wheeler, K. A. Barrow, L. M. Rich, J. S. Debley, M. J. Bamshad, D. A. Nickerson, R. Savan, T. R. Torgerson, D. J. Rawlings, Germline SAMD9L truncation variants trigger global translational repression. *J. Exp. Med.* **218**, e20201195 (2021).
20. A. J. Russell, P. E. Gray, J. B. Ziegler, Y. J. Kim, S. Smith, W. A. Sewell, C. C. Goodnow, SAMD9L autoinflammatory or ataxia pancytopenia disease mutations activate cell-autonomous translational repression. *Proc. Natl. Acad. Sci. U.S.A.* **118**, e2110190118 (2021).
21. S. L. Mekhedov, K. S. Makarova, E. V. Koonin, The complex domain architecture of SAMD9 family proteins, predicted STAND-like NTPases, suggests new links to inflammation and apoptosis. *Biol. Direct* **12**, 13 (2017).
22. D. D. Leipe, E. V. Koonin, L. Aravind, STAND, a class of P-loop NTPases including animal and plant regulators of programmed cell death: Multiple, complex domain architectures, unusual phyletic patterns, and evolution by horizontal gene transfer. *J. Mol. Biol.* **343**, 1–28 (2004).
23. J. D. G. Jones, R. E. Vance, J. L. Dangl, Intracellular innate immune surveillance devices in plants and animals. *Science* **354**, aaf6395 (2016).
24. J. Li, Y.-N. Wang, B.-S. Xu, Y.-P. Liu, M. Zhou, T. Long, H. Li, H. Dong, Y. Nie, P. R. Chen, E.-D. Wang, R.-J. Liu, Intellectual disability-associated gene *ftsj1* is responsible for 2′-O-methylation of specific tRNAs. *EMBO Rep.* **21**, e50095 (2020).
25. M. P. Guy, M. Shaw, C. L. Weiner, L. Hobson, Z. Stark, K. Rose, V. M. Kalscheuer, J. Gecz, E. M. Phizicky, Defects in tRNA anticodon loop 2′-*O*-methylation are implicated in non-syndromic X-linked intellectual disability due to mutations in *FTSJ1*. *Hum. Mutat.* **36**, 1176–1187 (2015).
26. Y. Nagayoshi, T. Chujo, S. Hirata, H. Nakatsuka, C. W. Chen, M. Takakura, K. Miyauchi, Y. Ikeuchi, B. C. Carlyle, R. R. Kitchen, T. Suzuki, F. Katsuoka, M. Yamamoto, Y. Goto, M. Tanaka, K. Natsume, A. C. Nairn, T. Suzuki, K. Tomizawa, F. Y. Wei, Loss of Ftsj1 perturbs codon-specific translation efficiency in the brain and is associated with X-linked intellectual disability. *Sci. Adv.* **7**, eabf3072 (2021).
27. L. Kawarada, T. Suzuki, T. Ohira, S. Hirata, K. Miyauchi, T. Suzuki, ALKBH1 is an RNA dioxygenase responsible for cytoplasmic and mitochondrial tRNA modifications. *Nucleic Acids Res.* **45**, 7401–7415 (2017).
28. M. P. Guy, E. M. Phizicky, Conservation of an intricate circuit for crucial modifications of the tRNAPhe anticodon loop in eukaryotes. *RNA* **21**, 61–74 (2015).
29. W. Yang, Nucleases: Diversity of structure, function and mechanism. *Q. Rev. Biophys.* **44**, 1–93 (2011).
30. C. C. Wu, A. Peterson, B. Zinshteyn, S. Regot, R. Green, Ribosome collisions trigger general stress responses to regulate cell fate. *Cell* **182**, 404–416.e14 (2020).
31. O. Bluteau, M. Sebert, T. Leblanc, R. Peffault de Latour, S. Quentin, E. Lainey, L. Hernandez, J. H. Dalle, F. Sicre de Fontbrune, E. Lengline, R. Itzykson, E. Clappier, N. Boissel, N. Vasquez, M. Da Costa, J. Masliah-Planchon, W. Cuccuini, A. Raimbault, L. De Jaegere, L. Ades, P. Fenaux, S. Maury, C. Schmitt, M. Muller, C. Domenech, N. Blin, B. Bruno, I. Pellier, M. Hunault, S. Blanche, A. Petit, G. Leverger, G. Michel, Y. Bertrand, A. Baruchel, G. Socie, J. Soulier, A landscape of germ line mutations in a cohort of inherited bone marrow failure patients. *Blood* **131**, 717–732 (2018).
32. O. Danot, E. Marquenet, D. Vidal-Ingigliardi, E. Richet, Wheel of Life, wheel of death: A mechanistic insight into signaling by STAND proteins. *Structure* **17**, 172–182 (2009).
33. L. A. Gao, M. E. Wilkinson, J. Strecker, K. S. Makarova, R. K. Macrae, E. V. Koonin, F. Zhang, Prokaryotic innate immunity through pattern recognition of conserved viral proteins. *Science* **377**, eabm4096 (2022).
34. C. F. Li, J. R. MacDonald, R. Y. Wei, J. Ray, K. Lau, C. Kandel, R. Koffman, S. Bell, S. W. Scherer, B. A. Alman, Human sterile alpha motif domain 9, a novel gene identified as down-regulated in aggressive fibromatosis, is absent in the mouse. *BMC Genomics* **8**, 92 (2007).
35. J. Y. Yang, X. Y. Deng, Y. S. Li, X. C. Ma, J. X. Feng, B. Yu, Y. Chen, Y. L. Luo, X. Wang, M. L. Chen, Z. X. Fang, F. X. Zheng, Y. P. Li, Q. Zhong, T. B. Kang, L. B. Song, R. H. Xu, M. S. Zeng, W. Chen, H. Zhang, W. Xie, S. Gao, Structure of Schlafen13 reveals a new class of tRNA/rRNA- targeting RNase engaged in translational control. *Nat. Commun.* **9**, 1165 (2018).
36. M. Li, E. Kao, D. Malone, X. Gao, J. Y. J. Wang, M. David, DNA damage-induced cell death relies on SLFN11-dependent cleavage of distinct type II tRNAs. *Nat. Struct. Mol. Biol.* **25**, 1047–1058 (2018).
37. F. J. Metzner, S. J. Wenzl, M. Kugler, S. Krebs, K. P. Hopfner, K. Lammens, Mechanistic understanding of human SLFN11. *Nat. Commun.* **13**, 5464 (2022).
38. M. Li, E. Kao, X. Gao, H. Sandig, K. Limmer, M. Pavon-Eternod, T. E. Jones, S. Landry, T. Pan, M. D. Weitzman, M. David, Codon-usage-based inhibition of HIV protein synthesis by human schlafen 11. *Nature* **491**, 125–128 (2012).
39. V. Anantharaman, K. S. Makarova, A. M. Burroughs, E. V. Koonin, L. Aravind, Comprehensive analysis of the HEPN superfamily: Identification of novel roles in intra-genomic conflicts, defense, pathogenesis and RNA processing. *Biol. Direct* **8**, 15 (2013).
40. Y.-L. Lin, Y. Elias, R. H. Huang, Structural and mutational studies of the catalytic domain of colicin E5: A tRNA-specific ribonuclease. *Biochemistry* **44**, 10494–10500 (2005).
41. K. S. Winther, K. Gerdes, Enteric virulence associated protein VapC inhibits translation by cleavage of initiator tRNA. *Proc. Natl. Acad. Sci. U.S.A.* **108**, 7403–7407 (2011).
42. B. El Yacoubi, M. Bailly, V. de Crécy-Lagard, Biosynthesis and function of posttranscriptional modifications of transfer RNAs. *Annu. Rev. Genet.* **46**, 69–95 (2012).
43. Y. Jiang, S. Blanga, M. Amitsur, R. Meidler, E. Krivosheyev, M. Sundaram, A. C. Bajji, D. R. Davis, G. Kaufmann, Structural features of tRNALys favored by anticodon nuclease as inferred from reactivities of anticodon stem and loop substrate analogs. *J. Biol. Chem.* **277**, 3836–3841 (2002).
44. X. Meng, Y. Xiang, Vaccinia virus K1L protein supports viral replication in human and rabbit cells through a cell-type-specific set of its ankyrin repeat residues that are distinct from its binding site for ACAP2. *Virology* **353**, 220–233 (2006).
45. X. Meng, C. Jiang, J. Arsenio, K. Dick, J. Cao, Y. Xiang, Vaccinia virus K1L and C7L inhibit antiviral activities induced by type I interferons. *J. Virol.* **83**, 10627–10636 (2009).
46. N. E. Sanjana, O. Shalem, F. Zhang, Improved vectors and genome-wide libraries for CRISPR screening. *Nat. Methods* **11**, 783–784 (2014).

47. D. C. Rio, Northern blots for small RNAs and microRNAs. *Cold Spring Harb. Protoc.* **2014**, 793–797 (2014).
48. Y. Mao, L. Jia, L. Dong, X. E. Shu, S.-B. Qian, Start codon-associated ribosomal frameshifting mediates nutrient stress adaptation. *bioRxiv*, 2023.02.15.528768 (2023).
49. N. T. Ingolia, G. A. Brar, S. Rouskin, A. M. McGeachy, J. S. Weissman, The ribosome profiling strategy for monitoring translation in vivo by deep sequencing of ribosome-protected mRNA fragments. *Nat. Protoc.* **7**, 1534–1550 (2012).
50. M. Martin, Cutadapt removes adapter sequences from high-throughput sequencing reads. *EMBnet J* **17**, 10 (2011).
51. B. Langmead, C. Trapnell, M. Pop, S. L. Salzberg, Ultrafast and memory-efficient alignment of short DNA sequences to the human genome. *Genome Biol.* **10**, R25 (2009).
52. A. Dobin, C. A. Davis, F. Schlesinger, J. Drenkow, C. Zaleski, S. Jha, P. Batut, M. Chaisson, T. R. Gingeras, STAR: Ultrafast universal RNA-seq aligner. *Bioinformatics* **29**, 15–21 (2013).
53. D. Kim, B. Langmead, S. L. Salzberg, HISAT: A fast spliced aligner with low memory requirements. *Nat. Methods* **12**, 357–360 (2015).
54. E. Krissinel, K. Henrick, Secondary-structure matching (SSM), a new tool for fast protein structure alignment in three dimensions. *Acta Crystallogr. D Biol. Crystallogr.* **60**, 2256–2268 (2004).
55. P. Gouet, X. Rober, E. Courcelle, E. Courcelle, ESPript/ENDscript: Extracting and rendering sequence and 3D information from atomic structures of proteins. *Nucleic Acids Res.* **31**, 3320–3323 (2003).
56. P. Boccaletto, F. Stefaniak, A. Ray, A. Cappannini, S. Mukherjee, E. Purta, M. Kurkowska, N. Shirvanizadeh, E. Destefanis, P. Groza, G. Avşar, A. Romitelli, P. Pir, E. Dassi, S. G. Conticello, F. Aguilo, J. M. Bujnicki, MODOMICS: A database of RNA modification pathways. 2021 update. *Nucleic Acids Res.* **50**, D231–D235 (2022).

Acknowledgments: Flow cytometry data were generated in the UT Health San Antonio Flow Cytometry Shared Resource Facility (supported by NIH-NCI P30 CA054174 and UL1 TR002645). Sequencing data were generated in the UT Health San Antonio Genome Sequencing Facility (supported by NIH-NCI P30 CA054174 and 1S10OD021805-01). **Funding:** This work was supported by National Institutes of Health grant AI151638 (Y.X.). **Author contributions:** Conceptualization: Y.X. and S.-B.Q. Methodology: F.Z., Q.J., J.C., M.M., Y.M., X.M., and L.D. Investigation: F.Z., Q.J., J.C., M.M., Y.M., Z.M., and L.D. Visualization: F.Z., Q.J., J.C., M.M., Y.M., J.D., S.-B.Q., and Y.X. Funding acquisition: Y.X. Project administration: Y.X., S.-B.Q., and J.D. Supervision: Y.X., S.-B.Q., and J.D. Writing—original draft: Y.X. Writing—review and editing: F.Z., Q.J., Y.M., J.D., S.-B.Q., and Y.X. **Competing interests:** Y.X., S.-B.Q., J.D., and Z.F. are inventors on a patent application related to this work filed by the University of Texas Health Science Center. The other authors declare that they have no competing interests. **Data and materials availability:** All data needed to evaluate the conclusions in the paper are present in the paper and/or the Supplementary Materials. The Ribo-seq and RNA-seq data have been deposited to Gene Expression Omnibus with accession numbers GSE229979 and GSE230043. The materials used in the paper can be obtained from the corresponding authors pending scientific review and a completed material transfer agreement.

Submitted 17 March 2023
Accepted 2 May 2023
Published 7 June 2023
10.1126/sciadv.adh8502